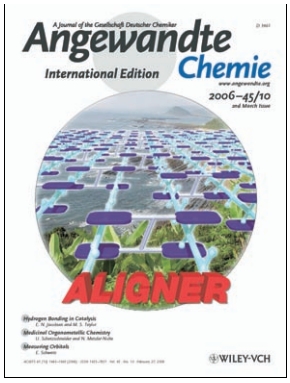
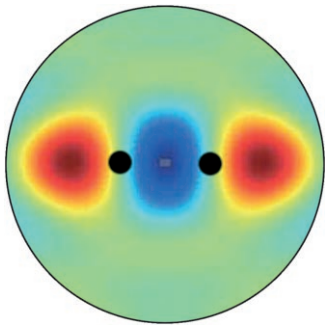
# Cover Picture

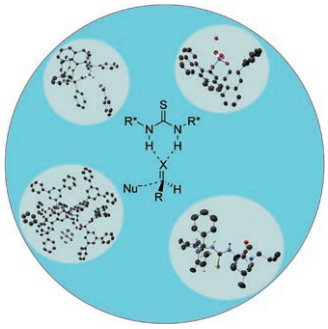



**Yohei Kubo, Yumiko Kitada, Rie Wakabayashi, Takanori Kishida, Masatsugu Ayabe, Kenji Kaneko, Masayuki Takeuchi,* and Seiji Shinkai***

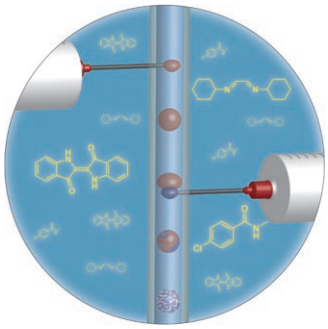
**Synthetic bundling molecules** organize conjugated polymers into aligned supramolecular assemblies in an approach inspired by actin-filament bundling proteins. In their Communication on page 1548 ff., M. Takeuchi, S. Shinkai, and co-workers describe how the use of these "aligner molecules" complements existing techniques in supramolecular assembly and provides a new means of generating complex and programmed assemblies of conjugated polymers with defined arrangements, as shown in the cover picture.



***Orbital measurements***
For a long time, it has been possible to reconstruct orbital functions from measured data and now even a femtosecond timescale can be used. In the Review on page 1508 ff., E. Schwarz asks whether complex orbitals can really be measured.




***Hydrogen Bonding in Catalysis***
Can the use of hydrogen-bond donors be transferred to synthetic systems for general acid catalysis? E. N. Jacobsen and M. S. Taylor search for analogies to an important enzyme mechanism in the Review on page 1520 ff.



***Microreactors***
D. T. McQuade et al. describe in their Communication on page 1544 ff. how a monodisperse flow in a microreactor provides an efficient method for keeping solid products away from the channel walls, thereby enabling solids to be synthesized without clogging of the reactor channels.

# Contents

**VIP** *The following Communications have been judged by at least two referees to be "very important papers" and will be published online at www.angewandte.org soon:*


*D. P. Curran,* G. Moura-Letts, M. Pohlman*
**Solution-Phase Mixture Synthesis with Fluorous Tagging En Route: Total Synthesis of an Eight-Member Stereoisomer Library of Passifloricins**

*H. Zhang, H. Xia,* G. He, T. B. Wen, L. Gong, G. Jia**
**Synthesis and Characterization of Stable Ruthenabenzenes**

*X. Mo, Y. An, C.-S. Yun, S. M. Yu**
**Nanoparticle-Assisted Visualization of Binding Interactions between Collagen Mimetic Peptide and Collagen Fibers**

*M. B. Harney, Y. Zhang, L. R. Sita**
**Discrete, Multiblock Isotactic–Atactic Stereoblock Polypropene Microstructures of Differing Block Architectures by Programmable Stereomodulated Living Ziegler–Natta Polymerization**

*Y. Weizmann, Z. Cheglakov, V. Pavlov, I. Willner**
**Autonomous Fueled Mechanical Replication of Nucleic Acid Templates for the Amplified Optical Detection of DNA**

*B. Botta, F. Caporuscio, D. Subissati, A. Tafi,* M. Botta, A. Filippi, M. Speranza**
**Flattened-Cone 2,8,14,20-Tetrakis(L-valinamido)[4]resorcinarene: Enantioselective Allosteric Receptors in the Gas Phase**


## Obituary


Arthur Schweiger (1946–2006) — *G. Jeschke, S. Stoll* — ***1500***


## Books


Soft Materials — John R. Dutcher, Alejandro G. Marangoni — *reviewed by P. Baglioni* — **1501**

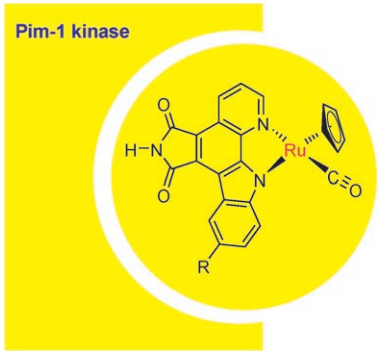
Inorganic and Organometallic Polymers — Vadapalli Chandrasekhar — *reviewed by I. Manners* — **1501**


## Highlights

***Bioorganometallic Chemistry***


U. Schatzschneider,*
N. Metzler-Nolte* — **1504 – 1507**

New Principles in Medicinal Organometallic Chemistry


**Hard-core drugs**: Recent structural and spectroscopic studies demonstrate the versatility of organometallic drug candidates, for example, as novel protein kinase inhibitors and hormone-independent breast cancer prodrugs. The presence of a transition-metal center in such systems allows both the organization of ligands in 3D space (see picture) and the control of redox-activation processes in biological systems.

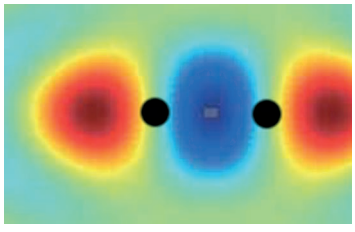
## Essays

***Chemical Concepts***


W. H. E. Schwarz* — **1508 – 1517**

Measuring Orbitals: Provocation or Reality?


**Can complex orbitals really be measured?** Orbital functions can indeed be reconstructed from measured data by various approaches. Now even femtosecond measurements can be used, though the results are still less accurate than those achieved with purely theoretical methods. The HOMO of the $N_2$ molecule (see picture) has been reconstructed directly from experimental laser-spectroscopic



interference intensity measurements by means of computer algorithms.

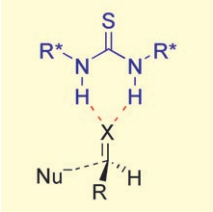


InterScience


© 2006 Wiley-VCH Verlag GmbH & Co. KGaA, Weinheim

# Reviews

**Copied from Nature**: A dominant mechanism used by enzymes, substrate activation by general acid catalysis, is emerging as a powerful and versatile strategy for enantioselective synthesis with small-molecule catalysts (see scheme). The mechanistic links between natural and synthetic hydrogen-bond-donor catalysts are explored, and the remarkable recent progress in asymmetric catalysis is reviewed.





**Reaction Mechanisms**

M. S. Taylor,
E. N. Jacobsen* ——— **1520 – 1543**

Asymmetric Catalysis by Chiral Hydrogen-Bond Donors


# Communications

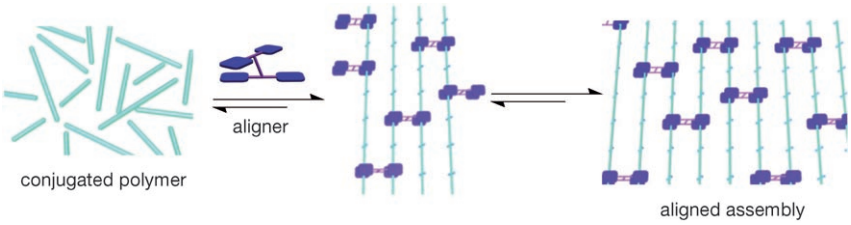
**Solids go with the flow**: A monodisperse flow in a microreactor provides an efficient method for keeping solid products away from channel walls. The use of a carrier phase, such as mineral oil, hexane, or toluene, enables solids to be synthesized without clogging of the reactor channels. Further injection points can be added to the microreactor to perform multistep syntheses (see picture).




**Microreactors**

S. L. Poe, M. A. Cummings, M. P. Haaf,
D. T. McQuade* ——— **1544 – 1548**

Solving the Clogging Problem: Precipitate-Forming Reactions in Flow


**All line up together**! A new concept for the alignment and assembly of conjugated polymers through the action of supramolecular bundling ("aligner") molecules is inspired by actin-filament bundling proteins. The approach provides a general means of preparing complex, ordered assemblies of conjugated polymers.


**Supramolecular Chemistry**

Y. Kubo, Y. Kitada, R. Wakabayashi,
T. Kishida, M. Ayabe, K. Kaneko,
M. Takeuchi,* S. Shinkai* — **1548 – 1553**

A Supramolecular Bundling Approach toward the Alignment of Conjugated Polymers



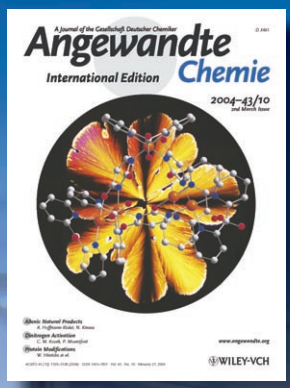
**For the USA and Canada:**
ANGEWANDTE CHEMIE International Edition (ISSN 1433-7851) is published weekly by Wiley-VCH PO Box 191161, D 69451 Weinheim, Germany. Air freight and mailing in the USA by Publications Expediting Inc. 200 Meacham Ave., Elmont, NY 11003. Periodicals postage paid at Jamaica NY 11431. US POSTMASTER: send address changes to *Angewandte Chemie*, Wiley-VCH, 111 River Street, Hoboken, NJ 07030. Annual subscription price for institutions: US$ 5685/5168 (valid for print and electronic / print or electronic delivery); for individuals who are personal members of a national chemical society prices are available on request. Postage and handling charges included. All prices are subject to local VAT/sales tax.



© 2006 Wiley-VCH Verlag GmbH & Co. KGaA, Weinheim

# The best in chemistry –

## for more than a hundred years




A Journal of the Gesellschaft Deutscher Chemiker

**Angewandte**
**International Edition** **Chemie**

**www.angewandte.org**

***1888:*** ***The beginning of a success story***

### Constant Innovations

***1962:*** *First issue of the International Edition*
***1976:*** *Graphical abstracts*
***1979:*** *Cover pictures*
***1988:*** *Centenary of Angewandte*
***1989:*** *Routine use of color*
***1991:*** *New section: Highlights*
***1992:*** *Computerized editorial tracking system*
***1995:*** *Internet service for readers*
***1998:*** *Regular press service; full-text online*
***2000:*** *New section: Essays; EarlyView: Communications available online ahead of the printed version*
***2001:*** *New section: Minireviews*
***2002:*** *Online submission of manuscripts*
***2003:*** *Weekly publication; new section: News; new layout*
***2004:*** *Backfiles (1962-1997); ManuscriptXpress: Online system for authors and referees*



### Angewandte's advisors...

***Hartmut Wiezer***
*Clariant International AG, Sulzbach am Taunus*

*»**Angewandte Chemie** is a highly acknowledged international chemical journal. Its attraction is based on excellence in content and presentation. It is a pleasure to commit myself to further the quality and success of **Angewandte Chemie**.«*

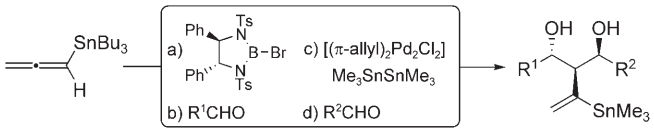
***Angewandte Chemie International Edition*** *is a journal of the German Chemical Society (GDCh)*

GDCh

WILEY InterScience® DISCOVER SOMETHING GREAT

WILEY-VCH

1191404_gu

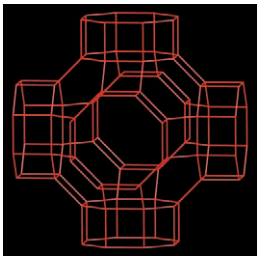



**More adventures of tin–tin**: The stereospecific synthesis of 2-stannylvinyl-1,3-diols was achieved through a one-pot allylic transfer/distannation/allylic transfer reaction sequence (see scheme). The method was applied to the concise asymmetric syntheses of (−)-avenaciolide and (−)-isoavenaciolide.

## Synthetic Methods

C.-M. Yu,* J. Youn, J. Jung — **1553 – 1556**

Asymmetric Sequential Allylic Transfer Reaction for the Synthesis of 2-(1-Stannylvinyl)-1,3-diols: Concise Synthesis of (−)-Avenaciolide and (−)-Isoavenaciolide

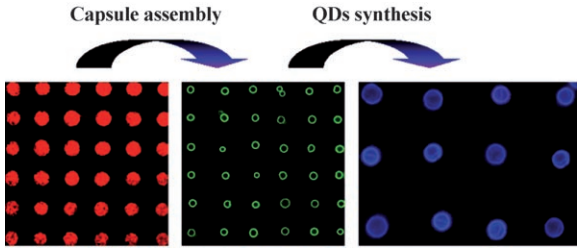


**Thermally robust** porous metal–organic frameworks (MOFs) with zeolitic topologies were constructed by means of a ligand-directed strategy involving molecular tailoring of simple bridging imidazolates with coordinatively unimportant substituents. This led to the isolation of three new MOFs having unusually high symmetries, intriguing topologies such as the supercage shown in the picture, and high thermal stability.

## Metal–Organic Frameworks

X.-C. Huang, Y.-Y. Lin, J.-P. Zhang, X.-M. Chen* — **1557 – 1559**

Ligand-Directed Strategy for Zeolite-Type Metal–Organic Frameworks: Zinc(II) Imidazolates with Unusual Zeolitic Topologies



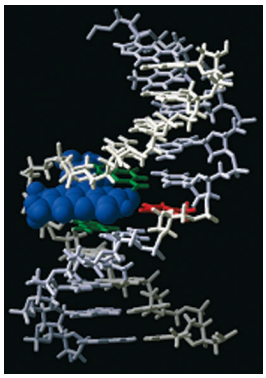

**Spaced capsules**: Polyelectrolyte hollow microcapsules are individually and covalently patterned on a flexible polymer film through specific biotin–avidin recognition. ZnS quantum dots (QDs) and other nanoparticles can be spatially synthesized in situ by using the aligned capsules as microreactors (see picture). Release of the QDs can be tuned by additional layers on the capsule walls.

## Microreactors

B. Wang, Q. Zhao, F. Wang, C. Gao* — **1560 – 1563**

Biologically Driven Assembly of Polyelectrolyte Microcapsule Patterns To Fabricate Microreactor Arrays

**Finding flavins:** A new class of DNA-duplex aptamers that bind to riboflavin by utilizing an abasic (AP) site has been developed (see model). An optimized duplex shows high selectivity for riboflavin over flavin mononucleotide and flavin adenine dinucleotide. Such riboflavin–duplex interactions are discussed as a basis for the further development of AP-site-based DNA aptamers.



## DNA-Aptamers

N. B. Sankaran, S. Nishizawa, T. Seino, K. Yoshimoto, N. Teramae* — **1563 – 1568**

Abasic-Site-Containing Oligodeoxynucleotides as Aptamers for Riboflavin


© 2006 Wiley-VCH Verlag GmbH & Co. KGaA, Weinheim

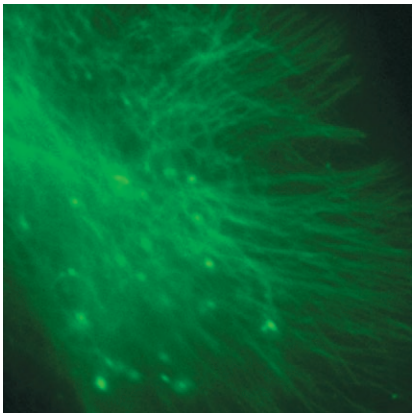
# Contents


## Transport of Nonviral Vectors

R. Bausinger, K. von Gersdorff, K. Braeckmans, M. Ogris, E. Wagner, C. Bräuchle,* A. Zumbusch* ——— **1568 – 1572**

The Transport of Nanosized Gene Carriers Unraveled by Live-Cell Imaging

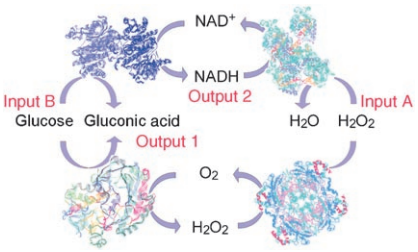
**Tracking transport**: Cationic polyethylenimine nanoparticles serve as nonviral vectors and deliver DNA to the nucleus of cells. Fluorescence live-cell imaging highlights the interactions between these polyplexes and the cytoskeleton during the subsequent stages of transfection (see picture). The analysis of the underlying transport processes gives new impulse to further chemical-synthesis approaches.



## Enzyme Systems

R. Baron, O. Lioubashevski, E. Katz, T. Niazov, I. Willner* ——— **1572 – 1576**

Elementary Arithmetic Operations by Enzymes: A Model for Metabolic Pathway Based Computing

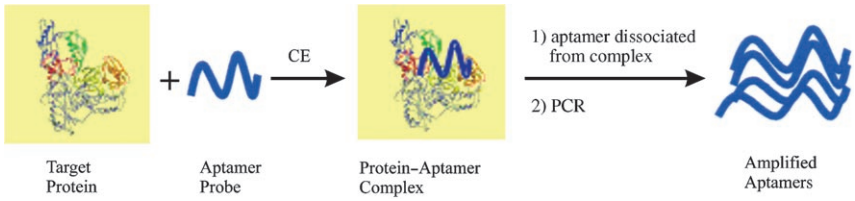



**Physio-logical**: A system of four enzymes, horseradish peroxidase, glucose dehydrogenase, glucose oxidase, and catalase, operate in parallel in the presence of NADH and $NAD^+$ to yield AND and XOR gates (see picture). Glucose and $H_2O_2$ act as the inputs, and the absorbance that follows the production of gluconic acid or NADH provide the outputs of the AND and XOR gates, respectively.

## Protein Detection

H. Zhang, Z. Wang, X.-F. Li, X. C. Le* ——— **1576 – 1580**

Ultrasensitive Detection of Proteins by Amplification of Affinity Aptamers

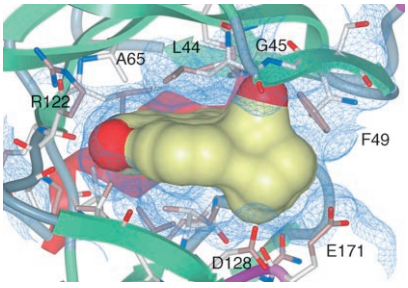



**Superdetective**: The detection of 180 molecules of a protein was achieved by amplification of DNA aptamers that bind to the target protein. The protein–aptamer complex is separated from the unbound aptamer by capillary electrophoresis (CE). The complex fraction is collected and the aptamer amplified by the polymerase chain reaction (PCR). Such amplification dramatically improves the sensitivity of the detection of proteins.

## Bioinorganic Chemistry

J. É. Debreczeni, A. N. Bullock, G. E. Atilla, D. S. Williams, H. Bregman, S. Knapp,* E. Meggers* ——— **1580 – 1585**

Ruthenium Half-Sandwich Complexes Bound to Protein Kinase Pim-1

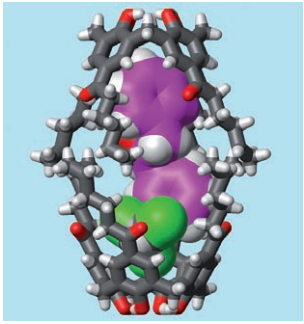



**Keeping in shape with half a sandwich**: The structure of a picomolar organoruthenium inhibitor bound to the ATP-binding site of the protein kinase Pim-1 (see picture) demonstrates that the ruthenium center has solely a structural role in organizing the organic ligands in the three-dimensional receptor space, thus yielding a structure that is complementary in shape and functional group presentation to the active site of Pim-1.



© 2006 Wiley-VCH Verlag GmbH & Co. KGaA, Weinheim

**Currency exchange**! Amphiphilic *para*-hexanoylcalix[4]arenes can form hydrophobic van der Waals nanocapsules (see picture) which are flexible enough to allow efficient guest exchange without destroying the crystal lattice. Purple: C (dibenzylketone), green: Cl($CHCl_3$), red: O, white: H.



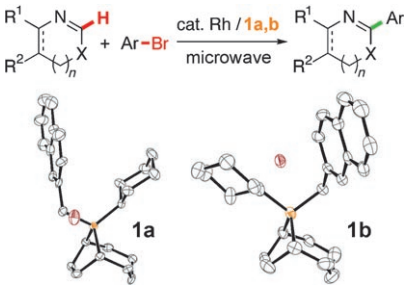
## Calixarenes

G. S. Ananchenko,* K. A. Udachin, A. Dubes, J. A. Ripmeester, T. Perrier, A. W. Coleman ——— **1585 – 1588**

Guest Exchange in Single Crystals of van der Waals Nanocapsules

---

**Performance-enhancing ligands**: Two new bridged bicyclic phosphines **1a,b** based on the "phoban" skeleton (see structures of their naphth-2-ylmethyl bromide salts; P yellow, Br brown, C white) are central to a practical catalytic method for the direct arylation of a variety of nitrogen heterocycles using aryl bromides. Broad functional-group tolerance was observed, and the use of microwave radiation allowed for short reaction times.

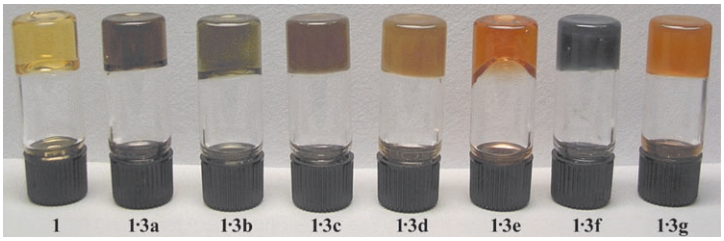



## C–H Activation

J. C. Lewis, J. Y. Wu, R. G. Bergman,* J. A. Ellman* ——— **1589 – 1591**

Microwave-Promoted Rhodium-Catalyzed Arylation of Heterocycles through C–H Bond Activation

---




**Like a color palette**: A naphthalenediimide-based organogel colorimetric sensor allows recognition of the positional isomers of dihydroxynaphthalene in the gel phase with the naked eye. Intercalation of the dihydroxynaphthalene into the gel matrix produces a donor–acceptor interaction, which gives the gel a distinct color that depends on the strength of noncovalent (H-bonding, π-stacking, van der Waals) interactions.

## Organogels

P. Mukhopadhyay, Y. Iwashita, M. Shirakawa, S.-i. Kawano, N. Fujita, S. Shinkai* ——— **1592 – 1595**

Spontaneous Colorimetric Sensing of the Positional Isomers of Dihydroxynaphthalene in a 1D Organogel Matrix

---




**Selective digestion**: α-Chymotrypsin was used to synthesize a cyclodextrin azo dye rotaxane and to digest it back to its components. *E*→*Z* photoisomerization of the rotaxane completely changes its affinity for the enzyme. The presence of the cyclodextrin accelerates digestion of the *E* isomer and prevents that of the *Z* isomer.

## Rotaxanes

A. G. Cheetham, M. G. Hutchings, T. D. W. Claridge, H. L. Anderson* ——— **1596 – 1599**

Enzymatic Synthesis and Photoswitchable Enzymatic Cleavage of a Peptide-Linked Rotaxane

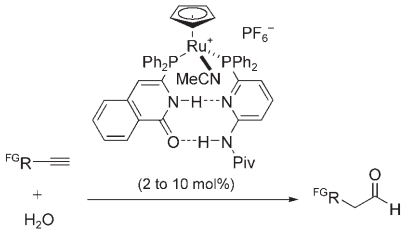

© 2006 Wiley-VCH Verlag GmbH & Co. KGaA, Weinheim

# Contents


## Homogeneous Catalysis

F. Chevallier, B. Breit* ——— **1599 – 1602**

Self-Assembled Bidentate Ligands for Ru-Catalyzed *anti*-Markovnikov Hydration of Terminal Alkynes

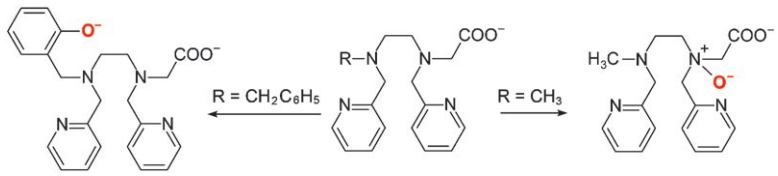



**In pairs**: Bidentate ligands are generated by the self-assembly of monodentate ligands through complementary hydrogen bonding. A ruthenium complex bearing such self-assembled heterodimeric ligands is used as the catalyst in the regioselective hydration of terminal alkynes. FG = functional group, Piv = pivaloyl.

## Non-heme Iron Complex

A. Nielsen, F. B. Larsen, A. D. Bond, C. J. McKenzie* ——— **1602 – 1606**

Regiospecific Ligand Oxygenation in Iron Complexes of a Carboxylate-Containing Ligand Mediated by a Proposed $Fe^{V}$–Oxo Species

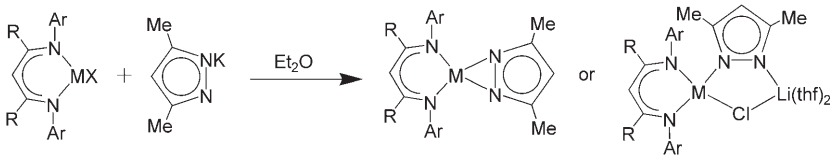



**Mimicked**: Through biomimetic iron activation of peroxides ($H_2O_2$ or *t*BuOOH), the shown $N_4O$ ligands in their iron(III) complexes can be oxygenated selectively at either an aromatic carbon atom or an aliphatic nitrogen atom.

## Coordination Modes

J. Vela, S. Vaddadi, S. Kingsley, C. J. Flaschenriem, R. J. Lachicotte, T. R. Cundari,* P. L. Holland* ——— **1607 – 1611**

Bidentate Coordination of Pyrazolate in Low-Coordinate Iron(II) and Nickel(II) Complexes

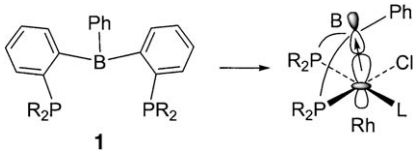



**The first $Fe^{II}$ and $Ni^{II}$ complexes** with bidentate pyrazolate ligands have been prepared (see scheme; M = $Fe^{II}$, $Ni^{II}$; R = *t*Bu, Me; Ar = 2,6-*i*$Pr_2C_6H_3$; X = Cl, $(\mu\text{-Cl})_2\text{Li(thf)}_2$). The coordination mode of the pyrazolate ligand $\eta^2$ or $\mu\text{-}(\eta^1{:}\eta^1)$ and the geometry of the resulting complex depends on the steric bulk of the diketiminate ligand, the d-electron configuration of the metal center, the solvent, and the relative stabilities of the σ- and π-type frontier orbitals.

## Ambiphilic Ligands

S. Bontemps, H. Gornitzka, G. Bouhadir, K. Miqueu, D. Bourissou* ——— **1611 – 1614**

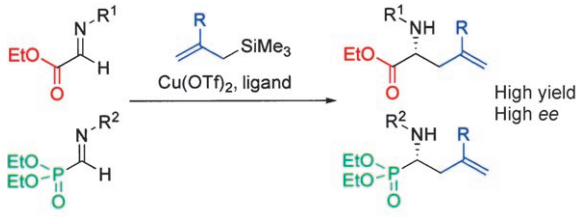
Rhodium(I) Complexes of a PBP Ambiphilic Ligand: Evidence for a Metal→Borane Interaction




**To and fro**: Diphosphanylborane derivative **1** behaves as a tridentate, ambiphilic ligand towards rhodium(I) fragments (see picture). The presence of metal→borane interactions in the resulting square-pyramidal complexes is highlighted by structural analyses and DFT calculations.



© 2006 Wiley-VCH Verlag GmbH & Co. KGaA, Weinheim

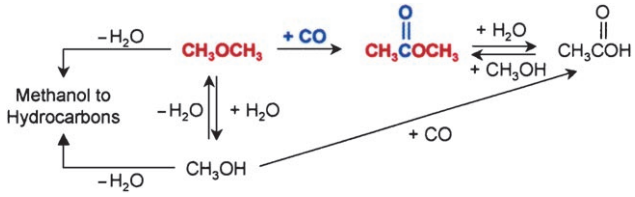



**α-Amino acid derivatives** are obtained in high yields through the catalytic enantioselective allylation of iminoesters using environmentally benign allylsilanes as nucleophiles in the presence of a copper complex prepared from $Cu(OTf)_2$ and a chiral diamine (see scheme; Tf = trifluoromethanesulfonyl, Nap = naphthyl). The reaction is also extended to iminophosphonates.

## Amino Acid Synthesis

H. Kiyohara, Y. Nakamura, R. Matsubara, S. Kobayashi* ——— **1615 – 1617**

Enantiomerically Enriched Allylglycine Derivatives through the Catalytic Asymmetric Allylation of Iminoesters and Iminophosphonates with Allylsilanes



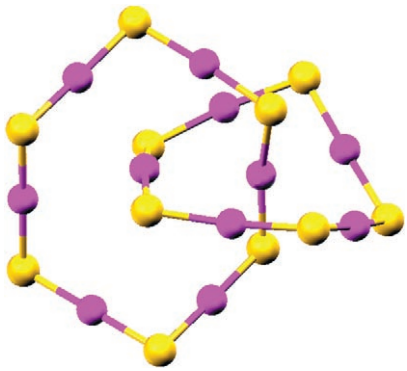

**A simpler way**: Acidic zeolites catalyze dimethyl ether carbonylation to methyl acetate at low temperatures with high selectivity and catalyst stability. This approach provides a halide-free heterogeneous catalytic route to acetic acid and methyl acetate.

## Heterogeneous Catalysis

P. Cheung, A. Bhan, G. J. Sunley, E. Iglesia* ——— **1617 – 1620**

Selective Carbonylation of Dimethyl Ether to Methyl Acetate Catalyzed by Acidic Zeolites

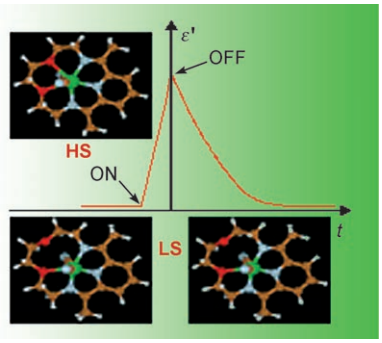
**Worth its weight in gold**: A homoleptic gold(I) glycosylated thiolate precursor for the antiarthritic drug auranofin has been structurally characterized. The undecagold(I) cluster forms an unusual chiral [2]catenane (see picture; Au violet, S yellow) and displays interesting photophysical behavior in the solid state and in solution.



## Cluster Compounds

S. S.-Y. Chui, R. Chen, C.-M. Che* ——— **1621 – 1624**

A Chiral [2]Catenane Precursor of the Antiarthritic Gold(I) Drug Auranofin




**Photoswitching of the dielectric constant** has been observed for the first time in the spin-crossover complex $[Fe(L)(CN)_2]\cdot H_2O$ (L = 2,13-dimethyl-6,9-dioxa-3,12,18-triazabicyclo[12.3.1]octadeca-1(18),2,12,14,16-pentaene, see picture). The electrical detection of a photoinduced change in spin state could allow the use of such complexes in optical information-storage devices.

## Spin-Crossover Complexes

S. Bonhommeau, T. Guillon, L. M. Lawson Daku, P. Demont, J. Sanchez Costa, J.-F. Létard, G. Molnár, A. Bousseksou* ——— **1625 – 1629**

Photoswitching of the Dielectric Constant of the Spin-Crossover Complex $[Fe(L)(CN)_2]\cdot H_2O$

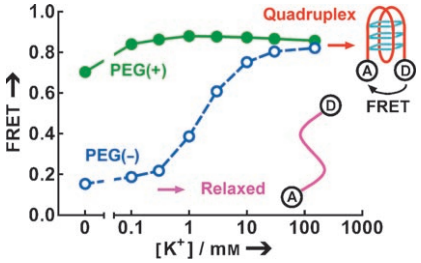

© 2006 Wiley-VCH Verlag GmbH & Co. KGaA, Weinheim

# Contents


## DNA Structures

Z.-y. Kan, Y. Yao, P. Wang, X.-h. Li, Y.-h. Hao, Z. Tan* ——— **1629 – 1632**

Molecular Crowding Induces Telomere G-Quadruplex Formation under Salt-Deficient Conditions and Enhances its Competition with Duplex Formation

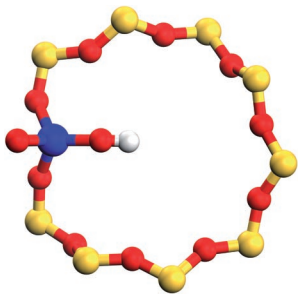



**Impact of crowding**: Molecular crowding with poly(ethylene glycol) (PEG) induces the formation of a G-quadruplex structure in the guanine-rich strand of telomeric DNA at a $K^+$-ion concentration that is unable to induce G-quadruplex formation alone. The picture shows the folding and unfolding of the telomeric DNA, revealed by fluorescence resonance energy transfer (FRET), the efficiency of which is inversely dependent on the distance between the donor (D) and acceptor (A).

## Zeolites

J. To,* A. A. Sokol, S. A. French, C. R. A. Catlow, P. Sherwood, H. J. J. van Dam ——— **1633 – 1638**

Formation of Heteroatom Active Sites in Zeolites by Hydrolysis and Inversion

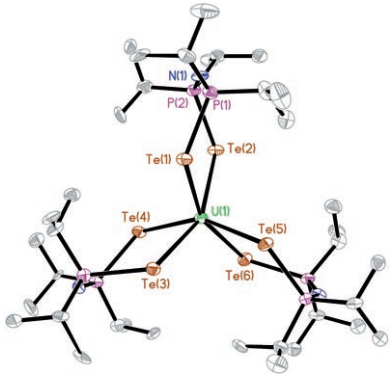


**A break and a flip**: Quantum mechanical/molecular mechanical calculations are used to investigate the structures of the active sites in silicalite doped with heteroatoms from Groups 4 and 14. These calculations reveal that tripodal (see picture; Si yellow, O red, H white, heteroatom blue) or bipodal sites, formed through hydrolysis and inversion, are preferred.

## Tellurium Ligands

A. J. Gaunt, B. L. Scott, M. P. Neu* ——— **1638 – 1641**

A Molecular Actinide–Tellurium Bond and Comparison of Bonding in $[M^{III}\{N(TeP\mathit{i}Pr_2)_2\}_3]$ (M = U, La)



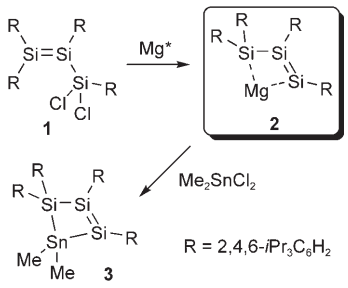

**Are the actinides going soft?** The first molecular complexes containing an actinide–tellurium bond, $[U\{N(TeP\mathit{i}Pr_2)_2\}_3]$ (see picture) and the isostructural complex $[La\{N(TeP\mathit{i}Pr_2)_2\}_3]$ have been crystallographically characterized. The $U^{III}$–Te bond is shorter than the $La^{III}$–Te bond by 0.06 Å, which suggests a greater degree of covalency in the bonding of actinides with soft donors.

## Low-Valent Silicon Compounds

K. Abersfelder, D. Güclü, D. Scheschkewitz* ——— **1643 – 1645**

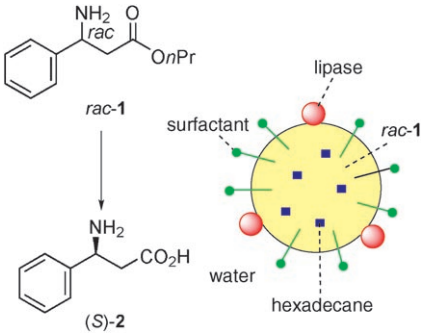
An Unsaturated α,ω-Dianionic Oligosilane

**A trisilenediide**: The reduction of dichlorotrisilene **1** with active magnesium leads to α,ω-dianionic trisilene **2**, which is characterized by NMR spectroscopy and X-ray diffraction. The potential of **2** as a precursor in the synthesis of heterocycles incorporating a Si=Si double bond is demonstrated by the formation of stannatrisilacyclobutene **3**.






© 2006 Wiley-VCH Verlag GmbH & Co. KGaA, Weinheim

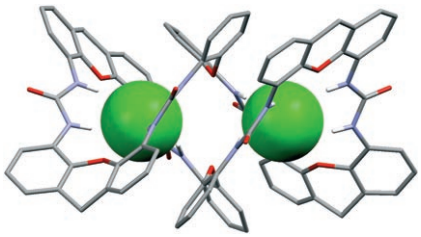



**Phasing in**: Miniemulsions are homogenous mixtures in which the organic phase is dispersed in the form of nanometer-scale droplets, which can act as efficient "nanoreactors" for enantioselective enzymatic transformations. Very high substrate concentrations are possible, and both α- and β-amino acids were prepared with high conversions and up to >99% *ee*.

## Miniemulsions

H. Gröger,* O. May, H. Hüsken, S. Georgeon, K. Drauz, K. Landfester* ——— **1645 – 1648**

Enantioselective Enzymatic Reactions in Miniemulsions as Efficient "Nanoreactors"



**It takes two to template:** A cyclic hexaurea with four xanthene and two diphenyl ether units is predominantly formed by reaction of two diisocyanate molecules with two diamine molecules in the presence of chloride (see picture; green Cl, blue N, red O). The formation of a 1:2 complex with chloride was confirmed by X-ray analysis, solution NMR spectroscopy, and ESI-MS. The complexation constants were determined by microcalorimetry and UV spectrometry.

## Host–Guest Systems

D. Meshcheryakov, V. Böhmer,* M. Bolte, V. Hubscher-Bruder, F. Arnaud-Neu, H. Herschbach, A. Van Dorsselaer, I. Thondorf, W. Mögelin ——— **1648 – 1652**

Two Chloride Ions as a Template in the Formation of a Cyclic Hexaurea

**Sources**

***Product and Company Directory***

You can start the entry for your company in "Sources" in any issue of *Angewandte Chemie*.

If you would like more information, please do not hesitate to contact us.

**Wiley-VCH Verlag – Advertising Department**
Tel.: 0 62 01 - 60 65 65
Fax: 0 62 01 - 60 65 50
E-Mail: MSchulz@wiley-vch.de

## Service

*Keywords* ——— *1654*

*Authors* ——— *1655*

*Angewandte's Sister Journals* ——— *1656 – 1657*

*Preview* ——— *1659*




***For more information on ChemMedChem see www.chemmedchem.org***


© 2006 Wiley-VCH Verlag GmbH & Co. KGaA, Weinheim

# Corrigendum

Construction of Quaternary Stereocenters by Efficient and Practical Conjugate Additions to α,β-Unsaturated Ketones with a Chiral Organic Catalyst

F. Wu, H. Li, R. Hong, L. Deng* **947–950**

*Angew. Chem. Int. Ed.* **2006**, *45*

DOI 10.1002/anie.200502658

Footnotes [e] and [g] for Table 3 should read as follows:
[e] The reaction was performed by treatment of **2B** (0.3 mmol) with **5a** (0.75 mmol, 2.5 equiv) and QD-**1b** in $CH_2Cl_2$ (0.6 mL).
[g] The reaction was performed by treatment of **2B** (0.3 mmol) with **5b** (0.75 mmol, 2.5 equiv) and QD-**1b** in $CH_2Cl_2$ (0.6 mL).


## Vacancies

HUMBOLDT-UNIVERSITÄT ZU BERLIN

**The Faculty of Mathematics and Natural Sciences I, Institute of Chemistry at Humboldt-Universität zu Berlin announces the position of a**

**Full Professor (W2) "Inorganic Chemistry"**

Applicants should have an outstanding record of achievement in important areas of synthetic inorganic molecular chemistry which complement the existing research activities of the institute for chemistry. The ideal candidate is able to participate in the research foci of the institute and has a record of close collaborations. Scientific exchange with research institutes within and outside Humboldt-Universität and with high tech companies at the science park Berlin-Adlershof and in the Berlin area will be appreciated. The candidate will be involved in the teaching of students covering the entire field of inorganic chemistry.
Applicants must meet the legal requirements for an university professor as stipulated in § 100 BerlHG. Humboldt-Universität zu Berlin is an equal opportunity employer, committed to the advancement of individuals without regard to ethnicity, religion, sex, age, disability or any other protected status.

Applications with necessary documents should be sent to Dekan der Mathematisch-Naturwissenschaftlichen Fakultät I, Prof. Buckhout, PhD, Humboldt-Universität zu Berlin, code number **PR/004/06**, 10099 Berlin, Unter den Linden 6, within four weeks after publication of this offer.

## Deadline for recruitment adverts

| | | | |
|---|---|---|---|
| 14/06 | March 9 | Publication date: | March 27 |
| 15/06 | March 16 | Publication date: | April 3 |

*Angewandte Chemie International Edition*
Advertising Sales Department:
Marion Schulz
Phone: 0 62 01 – 60 65 65
Fax: 0 62 01 – 60 65 50
E-Mail: MSchulz@wiley-vch.de

Place an advert in the printed version and have it made available online for 1 month, free of charge!

## Sources

*Product and Company Directory*

You can start the entry for your company in "Sources" in any issue of ***Angewandte Chemie***.

If you would like more information, please do not hesitate to contact us.

**Wiley-VCH Verlag – Advertising Department**
Tel.: 0 62 01 - 60 65 65
Fax: 0 62 01 - 60 65 50
E-Mail: MSchulz@wiley-vch.de


 © 2006 Wiley-VCH Verlag GmbH & Co. KGaA, Weinheim 

## Arthur Schweiger (1946–2006)

Arthur Schweiger, Professor of Physical Chemistry at ETH Zürich, passed away unexpectedly on January 4, 2006, at the age of only 59.



Having grown up in Zürich, he studied physics at the ETH and graduated with a diploma in 1970 and then joined H. H. Günthard at the Physical Chemistry Laboratory there for his dissertation. Günthard's group of young researchers was pursuing almost all aspects of molecular spectroscopy that were conceivable and exciting at that time. Schweiger's companions, A. Bauder, U. P. Wild, and the already independent R. R. Ernst, all became leading scientists in their respective fields. Schweiger worked on electron paramagnetic resonance (EPR) spectroscopy and, likewise, became one of its undisputed leaders. The hallmark of his research, an intimate mixture of the development of cutting-edge spectrometers, ingenious spin physics, and application to intricate transition-metal complexes, was established already in his dissertation with work on a computer-controlled electron nuclear double resonance (ENDOR) spectrometer, generalized spin operator transforms, and the structure of vitamin $B_{12}$. For this dissertation, which was completed in 1976, Schweiger was awarded the medal of the ETH.

In the following years, Schweiger applied his deep intuitive understanding of spin physics to the development of new EPR methods. A series of new continuous-wave ENDOR techniques[1] established his reputation as a "spin magician". From then on, he would continuously design new experiments that were highly aesthetic and opened up surprising new perspectives. Both these attributes certainly applied to his first rendezvous with pulse EPR spectroscopy.[2] An experimental signal trace from that work found its way both into the emblem of the International EPR/ESR Society and onto the title page of the issue of *Angewandte Chemie* in which his first review on pulse EPR spectroscopy appeared (Figure 1).[3] For years to come, this review, and another on pulse ENDOR spectroscopy,[4] remained the only introductions into pulse EPR techniques that could be understood by those who were not yet masters of the mysteries of spin dynamics themselves. Arguably, these two reviews transformed pulse EPR from a research field for a select few to an analytical technique accessible to chemists and biologists. It would take ten years before they were surpassed—by a monograph of his own.[5]

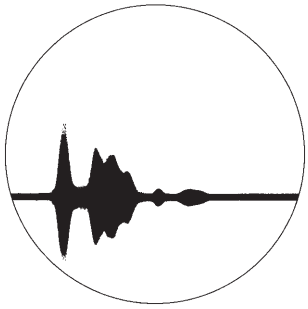


***Figure 1.***

That it took an entire decade was due to one of Schweiger's main character traits: a great reluctance to sacrifice quality for speed. He knew quite well that human works can never be perfect but wanted to get as close to perfection as possible. Before a manuscript from his group would be allowed to be submitted to a journal, he ensured that everything from the quality of experimental data down to minute typographic details met his elevated standards. His conference talks had the air of an artistic performance, thanks to an abundance of creative ideas matched with careful and often time-consuming preparation. Away from the conference podium Schweiger was a man of extraordinary modesty, bordering on shyness. However, that did not prevent him from successfully managing a sizeable research group. He led by example rather than by command and considered himself not the leader but the humble chauffeur of his group. Now and then he brought one of his ideas to the group seminar or the coffee break, where you could pursue it or ignore it. He never insisted. However, if you worked on it you would usually end up with a paper full of insight.

This quiet man gathered prizes—and friends—throughout his career. Besides the prestigious Werner price of the Swiss Chemical Society, he collected many honors in the field of EPR spectroscopy: the Zavoisky Prize in 1993, the Bruker Lecture of the Royal Society of Chemistry in 1994, and the Gold Medal of the International EPR/ESR Society in 1998. He served the community as an editor of the *Journal of Magnetic Resonance* and in several functions in the International EPR/ESR society. His lectures at the European Summer Schools on EPR were lucid and inspiring.

The aesthetic quality of Schweiger's research and publications was a consequence of his broad interests beyond science. He enjoyed classical music, good meals, and artistic photography, and he was unerring in his judgement about the quality of opera performances, restaurants, and art exhibitions. However, he was not one of those who criticize fine works out of their own artistic inability. With his own photographs, he built a reputation that, judged by rave reviews on the internet, came close to matching his reputation as a scientist.[6]

Arthur Schweiger has gone, but he has left us with impetus and inspiration to continue his work.

*Gunnar Jeschke*
Max Planck Institute for Polymer Research
*Stefan Stoll*
ETH Zürich

[1] A. Schweiger, *Struct. Bonding* **1982**, 51, R1-119.
[2] A. Schweiger, L. Braunschweiler, J. M. Fauth, R. R. Ernst, *Phys. Rev. Lett.* **1985**, 54, 1241 – 1246.
[3] A. Schweiger, *Angew. Chem.* **1991**, 103, 223 – 250; *Angew. Chem. Int. Ed.* **1991**, 30, 265 – 292.
[4] C. Gemperle, A. Schweiger, *Chem. Rev.* **1991**, 91, 1481 – 1505.
[5] A. Schweiger, G. Jeschke, *Principles of Pulse Electron Paramagnetic Resonance*, Oxford University Press, Oxford, **2001**.
[6] http://www.fotocommunity.de/pc/pc/mypics/592001.

DOI: 10.1002/anie.200600428


WILEY InterScience DISCOVER SOMETHING GREAT
© 2006 Wiley-VCH Verlag GmbH & Co. KGaA, Weinheim

Bioorganometallic Chemistry

DOI: 10.1002/anie.200504604

# New Principles in Medicinal Organometallic Chemistry

*Ulrich Schatzschneider* and Nils Metzler-Nolte**

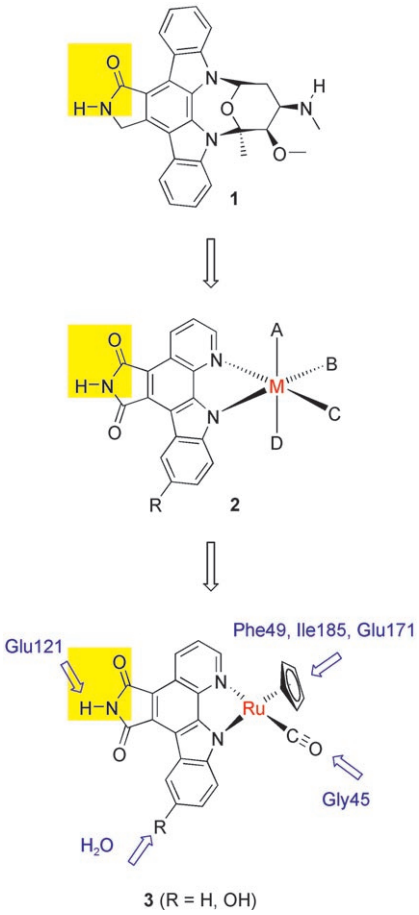
**Keywords:**
antitumor agents · bioorganometallic chemistry · inhibitors · medicinal chemistry · ruthenium

Transition-metal-based drugs are of steadily increasing importance in the therapy of cancer and other diseases.[1,2] Probably the most prominent example is cisplatin, *cis*-$[(NH_3)_2PtCl_2]$, which is in clinical use against testicular and other forms of cancer. Although DNA is now well-established as its primary cellular target, the recognition of DNA–cisplatin adducts by proteins and following events that eventually lead to cell death are, however, still not understood in detail.[3,4] The same is even more true concerning other recently described cytotoxic organometallic compounds such as the arene ruthenium half-sandwich complexes investigated by Sadler and Melchart.[5] It is of interest that most of these groups of metal-based drugs so far were discovered by serendipity or random screening. Herein, we highlight two new organometallic drug candidates that were carefully designed to interact with their molecular target and which take advantage of the very specific properties inherent to the transition-metal center.

[*] Dr. U. Schatzschneider,
Prof. Dr. N. Metzler-Nolte
Institut für Pharmazie
und Molekulare Biotechnologie
Ruprecht-Karls-Universität Heidelberg
Im Neuenheimer Feld 364
69120 Heidelberg (Germany)
and
Ruhr-Universität Bochum
Universitätsstraße 150
44801 Bochum (Germany)
E-mail: Ulrich.Schatzschneider@ruhr-uni-bochum.de
Nils.Metzler-Nolte@ruhr-uni-bochum.de

## Organometallic Mimics of Enzyme Inhibitors

It was only very recently that the first organometallic compound designed to specifically bind to a well-defined target site in a biomolecule was described (Scheme 1). Meggers and coworkers reported on a ruthenium cyclopentadienylcarbonyl {Ru(Cp)CO} complex **3**, which acts as an extremly potent inhibitor of certain protein kinases (PKs) at low nanomolar concentrations, with an affinity that is two orders of magnitude higher for certain PKs than established purely organic inhibitors.[6,7] Protein kinases are key players in the modulation of enzyme activity by transfer of the γ-phosphate group of the ATP (adenosine triphosphate) co-substrate to hydroxy groups of either serine, threonine, or tyrosine in the target protein. This phosphorylation is especially important in the control of cellular signal transduction pathways, and deregulated kinase activity is a frequent cause of diseases.




***Scheme 1.*** Retrosynthetic design of organometallic protein kinase inhibitor **3** from organic compound staurosporine (**1**). The interactions of **3** with the binding sites of Pim-1 are indicated by the blue arrows.

Organometallic compound **3** was modeled after the organic PK inhibitor (+)-staurosporine (**1**). The essential features of its planar indolo[2,3-*a*]carbazole aglycon, which mimics the hydrogen-bonding pattern of adenine in the original ATP substrate, were retained in a novel pyridocarbazole ligand. However, the globular carbohydrate moiety, which forms hydrophobic contacts and hydrogen bonds with the ribose-binding site, was replaced by the {Ru(Cp)CO} scaffold. Compound **3** is stable in vitro and was utilized as a tool to switch on signal transduction pathways in *Xenopus* frog embryos, which could be visualized by changes in the phenotype.[7] This results from the ATP-binding site being blocked by the organoruthenium compound. A cocrystal structure of enantiomerically pure (*S*)-**3**-OH bound to full-length human serine/threonine protein kinase Pim-1 was solved to a resolution of 1.9 Å (see Reference [8]). It is only the third crystal structure of an artificial organometallic compound bound to a protein.[8–10] Moreover, it is the first system that was specifically designed as a mimic of an enzyme inhibitor.


InterScience
© 2006 Wiley-VCH Verlag GmbH & Co. KGaA, Weinheim

Three hydrogen bonds and a number of van der Waals contacts fix (*S*)-**3**-OH in the ATP-binding site of Pim-1 (see Scheme 1). The imide NH group of the pyridocarbazole ligand binds to the backbone carbonyl oxygen atom of Glu121 in the hinge region, while the hydroxy group forms two hydrogen bonds to ordered water molecules. The structure thus resembles the binding pattern of ATP. Interestingly, the two typical organometallic ligands bound to ruthenium are also involved in close contacts with the active site of the enzyme. The cyclopentadienyl ring forms van der Waals contacts with Phe49, Ile185, and the methylene group of Glu171. There is also evidence for dipolar interactions between the CO ligand and the methylene and carbonyl groups of Gly45, which seem to be required for high potency. This point is further illustrated in Figure 1, with a comparison of the electrostatic potentials of **1** and **3**. The overall shape and potential of the organometallic inhibitor (in particular the {Ru(Cp)CO} moiety) resembles staurosporin quite well. In addition, it is conceivable that the stronger electronegative potential of the metal carbonyl group (pointing upwards in Figure 1) enhances the dipolar interaction with Gly45.

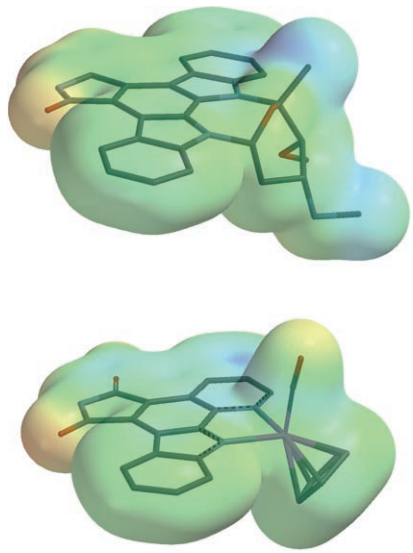


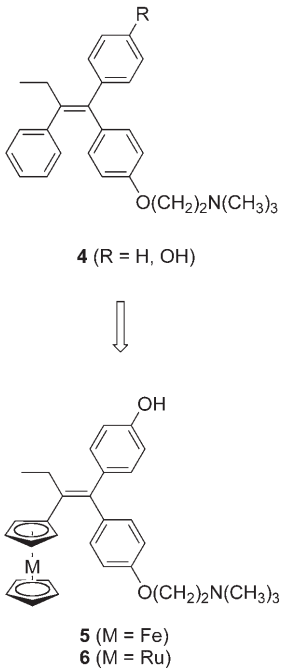
***Figure 1.*** Electrostatic potentials plotted on the surface of staurosporin (**1**; top) and its organometallic analogue **3** (bottom). (SPARTAN04 for Macintosh, v 1.0.3).

Pim-1 is especially interesting since it is distinct from all other PKs by a unique proline insertion in the hinge region that connects the two main domains. This precludes the formation of a hydrogen bond between N1 of the adenine substrate and the amide backbone which is conserved in all other enzymes of this type.[11,12] Interestingly, Pim-1 is overexpressed in human prostate cancer cells. Compound (*S*)-**3**-OH or its derivatives might therefore find application as novel chemotherapeutic agents by blocking its hormone-independent activation of the androgen receptor, which is typical for advanced prostate cancer with poor prognosis.

## *Redox Activation of Organometallic Prodrugs*

The principle of using an organometallic moiety as a globular shape mimic of an organic group was also exploited in the metal-containing derivatives **5** and **6** of the estrogen receptor (ER) modulator, tamoxifen (**4**; Scheme 2).[13–15]

Tamoxifen is the front-line chemotherapeutic agent for patients with hormone-dependent breast cancer. In general, breast tumors can be divided into two groups that are distinguished by the presence (ER(+)) or absence (ER(−)) of the estrogen receptor. About two-thirds of all cases belong to the ER(+) type, which is susceptible to hormone therapy by selective estrogen receptor modulators (SERMs) such as **4**. In the ER(+) cell lines, there exist two receptor subtypes ERα and ERβ. The antiproliferative action of tamoxifen (**4**) arises from the competitive binding to ERα, thus repressing estradiol-mediated DNA transcription in the tumor tissue.[16] The activity of ferrocifen (**5**) against ER(+) cancer cell lines is thought to follow the same principle. Recently, however, **5** was shown to also act against ER(−) tumor cells, which lack the molecular target of **4** and **5**, thus indicating a yet unknown mode of action. Interestingly, the ruthenocene derivative **6** also acts as an antiestrogen in ER(+) breast cancer cells but lacks the antiproliferative effect of **5** against ER(−) cell lines.[17] As the structural differences between ferrocene and ruthenocene derivatives are small (M–$Cp_{centroid}$: 2.03 Å in $[Cp_2Fe]$ versus 2.21 Å in $[Cp_2Ru]$), it is likely that the different redox properties for the two metallocenes are responsible for this distinct difference in activity.




***Scheme 2.*** Organometallic estrogen receptor modulators ferrocifen (**5**) and ruthenocifen (**6**) derived from the purely organic breast cancer drug tamoxifen (**4**).

The influence of the $Fe^{II/III}$ redox potential and the pH of the solution on the cytotoxic properties of **5** and several isomers that differ in the position and number of hydroxy groups was explored in a series of electrochemical experiments by Jaouen, Amatore, and coworkers.[18] This allowed the identification of important structure–activity relationships (SARs) that are required for cytotoxicity against ER(−) cell lines. The presence of a ferrocene moiety attached to a 1,1-diarylethene unit with a *para*-hydroxy substituent on the phenyl ring that lies *trans* to $[Cp_2Fe]$ seems to be a minimum structural requirement, as only these compounds showed a substantial cytotoxic effect.

The redox activation process shown in Scheme 3 can then be envisioned. Upon oxidation of the ferrocene group, the positive charge is partially imparted to the *para*-hydroxy group through the conjugated π system, thus rendering the proton acidic for abstraction by a base. The resulting open-shell species can be


© 2006 Wiley-VCH Verlag GmbH & Co. KGaA, Weinheim

described by various resonance structures, including $Fe^{III}$–phenol and $Fe^{II}$–phenoxyl valence tautomers $\mathbf{5a}^+$ and $\mathbf{5b}^+$, respectively, and is prone to deprotonation by base. A DFT calculation of the spin density distribution in deprotonated **7** (Figure 2) shows the typical

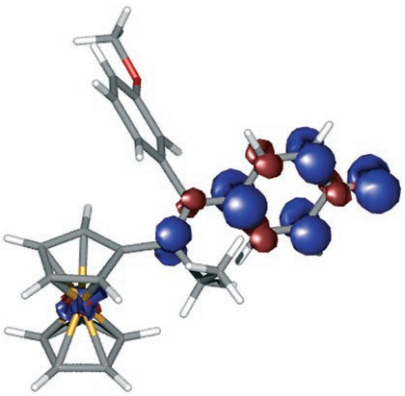


***Figure 2.*** Spin density distribution in **7** at 0.003 $e a_0^{-3}$ (Gaussian03, UB3LYP, 6-31G).

pattern of a phenoxyl radical with additional contributions from both the ethylene linker and the ferrocene metal d orbitals.[19]

In a subsequent second oxidative step, which is accompanied by another proton abstraction from the ethyl group, quinone methide **8** is formed. Quinone methides of 4-hydroxytamoxifen (**4**-OH) are known to be exceptionally stable with a half-life of about 3 h under physiological conditions. Follow-up reactions mostly involve 1,6- and 1,8-Michael additions by thiol nucleophiles, while the 5-position is more reactive towards amino nucleophiles.[20] Adducts of such tamoxifen metabolites with gluthatione and nucleobases are thought to be responsible for its general toxicity and mutagenic potential,[20–22] and similar modes of action might be involved in the organometallic derivatives described here. A redox-activation process was also discussed by Biot for the ferrocene-based antimalarial agents ferroquine, although the mechanism of action and molecular target is still not known in detail.[23] A ruthenium analogue (ruthenoquine) exhibits similar activity.

## Conclusion

These recent reports show that, by careful ligand design, organometallic compounds can be developed into highly active and specific drugs—a realm generally thought to be reserved for organic compounds. They specifically bind to well-defined biological target structures by making use of the extended opportunities of the metal center to organize organic ligands in three-dimensional space. The role of the metal in bioactive organometallic compounds is however not restricted to a purely structural one. The tunable redox properties inherent to transition-metal centers can also be exploited to control their action in biological systems, given that the cellular redox state is carefully balanced and deviations are associated with diseases. More exciting developments that make use of these new design principles in medicinal organometallic chemistry can be expected.

Published online: February 2, 2006


[1] Z. Guo, P. J. Sadler, *Angew. Chem.* **1999**, *111*, 1610–1630; *Angew. Chem. Int. Ed.* **1999**, *38*, 1512–1531.

[2] Special issue on *Medicinal Inorganic Chemistry* (Eds.: C. Orvig, M. J. Abrams): *Chem. Rev.* **1999**, *99*.

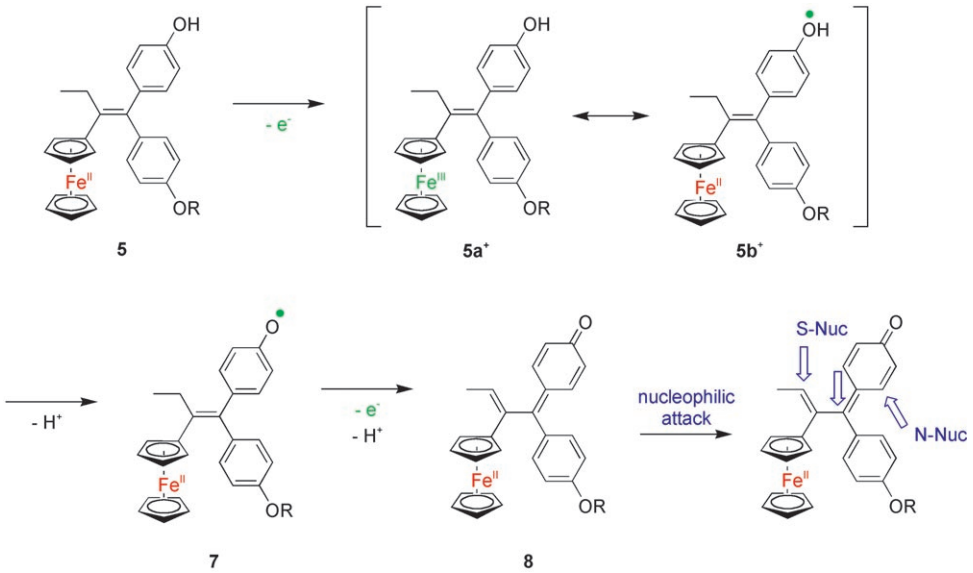
[3] B. Lippert, *Cisplatin—Chemistry and Biochemistry of a Leading Anticancer Drug*, Wiley-VCH, Weinheim, **1999**.

[4] D. Wang, S. J. Lippard, *Nat. Rev. Drug Discovery* **2005**, *4*, 307–320.

[5] M. Melchart, P. J. Sadler in *Bioorganometallics* (Ed.: G. Jaouen), Wiley-VCH, Weinheim, **2006**, pp. 39–64.

[6] H. Bregman, D. S. Williams, G. K. Atilla, P. J. Carroll, E. Meggers, *J. Am. Chem. Soc.* **2004**, *126*, 13594–13595.

[7] D. S. Williams, G. E. Atilla, H. Bregman, A. Arzoumanian, P. S. Klein, E. Meggers, *Angew. Chem.* **2005**, *117*, 2020–2023; *Angew. Chem. Int. Ed.* **2005**, *44*, 1984–1987.


***Scheme 3.*** Redox activation of ferrocifen (**5**) leads to quinone methide **8**, which is activated for nucleophilic attack by sulfur- and nitrogen-donor groups from biomolecules.

 © 2006 Wiley-VCH Verlag GmbH & Co. KGaA, Weinheim 

[8] J. E. Debreczeni, A. N. Bullock, G. E. Atilla, D. S. Williams, H. Bregman, S. Knapp, E. Meggers, *Angew. Chem.* **2006**, *118*; *Angew. Chem. Int. Ed.* **2006**, *45*, in press.
[9] K. Di Gleria, D. P. Nickerson, H. A. O. Hill, L.-L. Wong, V. Fülöp, *J. Am. Chem. Soc.* **1998**, *120*, 46–52.
[10] I. W. McNae, K. Fishburne, A. Habtemariam, T. M. Hunter, M. Melchart, F. Wang, M. D. Walkinshaw, P. J. Sadler, *Chem. Commun.* **2004**, 1786–1787.
[11] M. D. Jacobs, J. Black, O. Futer, L. Swenson, B. Hare, M. Fleming, K. Saxena, *J. Biol. Chem.* **2005**, *280*, 13728–13734.
[12] A. Kumar, V. Mandiyan, Y. Suzuki, C. Zhang, J. Rice, J. Tsai, D. R. Artis, P. Ibrahim, R. Bremer, *J. Mol. Biol.* **2005**, *348*, 183–193.
[13] V. C. Jordan, *J. Med. Chem.* **2003**, *46*, 883–908.
[14] V. C. Jordan, *J. Med. Chem.* **2003**, *46*, 1081–1111.
[15] G. Jaouen, S. Top, A. Vessieres, G. Leclercq, M. J. McGlinchey, *Curr. Med. Chem.* **2004**, *11*, 2505–2517.
[16] A. K. Shiau, D. Barstad, P. M. Lorisa, L. Cheng, P. J. Kushner, D. A. Agard, G. L. Greene, *Cell* **1998**, *95*, 927–937.
[17] P. Pigeon, S. Top, A. Vessieres, M. Huché, E. Hillard, E. Salomon, G. Jaouen, *J. Med. Chem.* **2005**, *48*, 2814–2821.
[18] E. Hillard, A. Vessiéres, L. Thouin, G. Jaouen, C. Amatore, *Angew. Chem.* **2006**, *118*, 291–296; *Angew. Chem. Int. Ed.* **2006**, *45*, 285–290.
[19] R. Schnepf, A. Sokolowski, J. Müller, V. Bachler, K. Wieghardt, P. Hildebrandt, *J. Am. Chem. Soc.* **1998**, *120*, 2352–2364.
[20] P. W. Fan, F. Zhang, J. L. Bolton, *Chem. Res. Toxicol.* **2000**, *13*, 45–52.
[21] F. Zhang, P. W. Fan, X. Liu, L. Shen, R. B. van Breemen, J. L. Bolton, *Chem. Res. Toxicol.* **2000**, *13*, 53–62.
[22] I. Terashima, N. Suzuki, S. Shibutani, *Cancer Res.* **1999**, *59*, 2091–2095.
[23] C. Biot, *Curr. Med. Chem. Anti-Infect. Agents* **2004**, *3*, 135–147.




 © 2006 Wiley-VCH Verlag GmbH & Co. KGaA, Weinheim 

Chemical Concepts

DOI: 10.1002/anie.200501333

# Measuring Orbitals: Provocation or Reality?**

*W. H. Eugen Schwarz**

**Keywords:**
femtochemistry · orbitals · quantum chemistry · single-molecule studies · wave functions

## 1. Introduction

The question in the title of this article has two aspects: How can one obtain the quantum mechanical description of matter through wave functions by reconstruction from experimental data? And can one represent chemical phenomena within a well-defined orbital approximation?

Wave functions, density matrices, orbital functions, Wigner functions etc. of electrons and atoms (i.e. nuclei) approximately reconstructed from experimental data have been published in scientific journals for decades. In the meantime reconstructions have been achieved even on the femtosecond timescale, which is of particular relevance for chemical reactions. An important step in this direction has recently been highlighted in a more general journal. The paper has provoked heated discussions in the scientific community focusing on secondary aspects. In the spirit of the "Einstein Year" 2005,[1] it seems timely to analyze scientific concepts and their experimental realization also in the present context.

Quantum reaction control and quantum stereochemistry control, quantum computers and quantum cryptography form a new and innovative field of research.[2] This area contributes both to basic quantum theoretical understanding and to new promising techniques of applied physicochemical quantum engineering. Essential in this research are ultrafast manipulation methods: "femto techniques".[3] The timescale for movements of valence electrons is $10^{-17}$ s (10 as), and for molecular rearrangements by movements of nuclei, $10^{-13}$ s (100 fs). After more than a dozen years of continuous achievements, the field was acknowledged with the Nobel Prize in 1999 for molecular femtosecond investigations (Zewail).[3b]

Quantum theory is a formal concept in effect "always and everywhere". The philosophical interpretation, however, still creates problems. Basic quantum mechanical experiments are of help both for a deeper understanding of nature and for the further development of experimental techniques. And it is very satisfactory for a scientist to confirm experimentally the still-striking predictions of quantum theory. However, each time a paper with the provocative title "Orbital Measured" appears in a journal addressed to a more general readership, heated discussions are initiated in the pubs and on the Internet on whether the fundamental statements make any sense or the experiments have any meaning. This is remarkable, since orbitals reconstructed from experimental data have been described in the literature for decades (Section 4). Some epistemological annotations therefore seem appropriate (Section 3).

Towards the end of 2004 a paper was published in *Nature* entitled "Tomographic imaging of molecular orbitals".[4a] The first response was: Again some orbital-like picture in *Nature*, or this time an orbital in real nature? Eloquent colleagues asked: "Imaging or Imagination?" Some background information: The paper was about an orbital corresponding to a specific electronic excitation, that is, an orbital well-defined by a photophysical process.[5] Not a whole set of molecular orbitals (MOs) but only a single MO. Specifically, a nonbonding one of rather simple structure and high symmetry,[6] which simplifies the experimental problems significantly. The amplitudes and phases of such an orbital function in three-dimensional space were reconstructed from measured data of higher harmonics generation (HHG) of laser pulses with the help of theoretical modeling. The most important aspect of this work was, however, the impressively short femtosecond timescale. Accordingly, an accompanying article in the same issue of *Nature* was entitled "Electrons frozen in motion".[4b]

For more than thirty years specific orbitals have been generated from experimental data of electron or X-ray scattering with the help of approximate theoretical assumptions. About twenty years ago sophisticated spectroscopic femtosecond techniques and the corresponding modern algorithms for processing the data were developed in order to reconstruct wave functions as empirically as possible.[7] Attosecond experiments are already being designed.[3,4,8] At present it is in general only possible to determine the wave function of a single particle or quasiparticle (phonon)

[*] Prof. emer. Dr. W. H. E. Schwarz
Theoretische Chemie
Universität Siegen
57068 Siegen (Germany)
and
School of Chemistry
Jiao Tong University
200240 Shanghai (China)
Fax: (+49) 271-740-4338
E-mail: schwarz@chemie.uni-siegen.de

[**] W.H.E.S. thanks three anonymous referees and also the colleagues Bucksbaum (Ann Arbor), Frenking (Marburg), Köppel (Heidelberg), Lorke (Duisburg), Manz (Berlin), Maercker (Siegen), Sillescu (Mainz), Schirmer (Heidelberg), Stapelfeld (Århus), Villeneuve (Ottawa), Weyrich (Constance), and Zeidler (Ottawa) for many useful ideas, enlightening discussions, and for some figures. He is grateful for financial support from the Fonds der Chemischen Industrie.


InterScience
© 2006 Wiley-VCH Verlag GmbH & Co. KGaA, Weinheim

in one to three dimensions of space. In a few cases the quantum description of two-particle correlations could be reconstructed. All this refers to free atoms in a trap, to bound atoms in small molecules (rotation, vibration, dissociation), to electrons in free or bound atoms (e.g. d AOs in transition-metal complexes), to electrons in molecules or nanostructures (quantum dots).

On the other hand, it must be noted that the phrase "orbital measurement" is often used only as a catchword. Genuine "orbital measurements" have little in common with the determination of total electron density plots in position or momentum spaces, and certainly nothing to do with the somewhat arbitrary creation of difference densities between a "measured" density of unknown accuracy and a reference density of "clever" choice.[9] It is also misleading to label photoelectron spectroscopy as "measuring orbitals on the energy scale", or symmetry assignments of spectra as "measuring orbitals on the quantum number scale". However, we may consider the experimental determination of some one-electron orbital densities as an acceptable limiting case of orbital measurement.

The recent reports in general scientific journals and in magazines of the scientific societies pose an interesting case for the sociology of science. Questions concerning the sources of experimental error or the serious approximations in the data analysis could have been commented on by experts. Mechanistic chemists could have commented on the potentialities of the femtosecond timescale. However, the discussion focused on only some secondary aspects, which were either positively exaggerated or incorrectly represented and then criticized on the basis of philosophical principles instead of scientific facts. Some comments were prefaced by the remark that familiarity with the new techniques, with modern quantum theory, or with the details of the respective publications is not required. However, the experiment[4] will be reviewed and commented on in some detail in Section 2.

## 2. The Experiment

### 2.1. The Three Steps of the Experimental Procedure

*Step 1:* First the molecules of an $N_2$ molecular beam are aligned by the electric field of a linearly polarized red intense laser pulse of 60 fs ($h\nu = 1.5$–$1.6$ eV).[10] Because of the different quantized rotational frequencies of the $N_2$ molecule, the molecular axis becomes smeared over all directions (Heisenberg uncertainty), but roughly every 4100 fs it becomes oriented (Figure 1, left).

*Step 2:* At this moment, a second significantly more intense laser pulse of only 30 fs is shot onto the oriented $N_2$, which becomes electronically excited in the keV range through multiphoton absorption of $mh\nu$ (Figure 1, middle). The partly ionized nonstationary state is many eV broad and emits higher harmonics $mh\nu$ of the original laser pulse.[11] In the case at hand, these processes can be reasonably described within the orbital approximation: Large amplitude "vibrations" of a single electron from the least strongly binding $\sigma_g$ orbital of the $N_2$ molecule (the lone-pair HOMO) in the direction of the polarization of the laser pulse are induced. Nineteen different angles 0°, 5°, 10°, … 90° (±1–2°) between molecular axis and polarization were applied.

The laser field changes direction every 1.3 fs. In the quasiclassical description, the electrons (with mass $M_e$) move in this timespan up to a few 10 Å forth and back, as a wave packet of about 10-Å width. This wave packet $\varphi$ can be approximated as a superposition of plane waves $e^{ikr}$ of different speeds with electronic wave vectors $k$ [Eq. (1)];[12] $a(k)$ is the complex "form factor" of the wave packet $\varphi$. $\varphi$ coherently interferes with the partly ionized $\sigma_g$ "home orbital" of the excited electron and will "scan" it: the photon emission by the time-dependent excited one-electron function $\sigma_g + \varphi$ carries the information about its amplitudes and phases (Figure 1, right). The interferences of $\varphi$ with the other $N_2$ orbitals are incoherent and do not contribute to the photon emission. The important aspects of coherence and the common, though incorrect, arguments against short-time "chemistry at the uncertainty limit" have been discussed by Zewail.[3c]

$$\varphi = \sum\nolimits_m a(k_m)\, e^{i k_m r}\, e^{i\pi 2m\nu t} \qquad k_m = \sqrt{2\, m\nu\, M_e/h} \tag{1}$$

The maxima of the emission spectra at multiples $mh\nu$ of the irradiated photon energies $h\nu$ decay roughly exponentially. In the first Born and in dipole length approximations the intensities $I(m\nu)$ of the emitted photons of frequencies $m\nu$ are proportional to the square of the value of the optical transition dipole moment $\langle r \rangle$ and to the square of the number $n$ of the simultaneously formed ions $N_2^+$ [Eq. (2)].

$$I(m\nu) \approx n^2\, (m\nu)^4 |\langle \sigma_g(r)|e\, r|\exp(i\, k_m\, r)\rangle|^2\, |a(k_m)|^2 \tag{2}$$

This comparatively simple expression results due to the inversion symmetry of the $\sigma_g$ MO and from the simplifying assumption that in the moment of emission the $N_2$ wave function is deformed neither by the intense laser field nor by the field of the excited electron. Namely, in this moment the

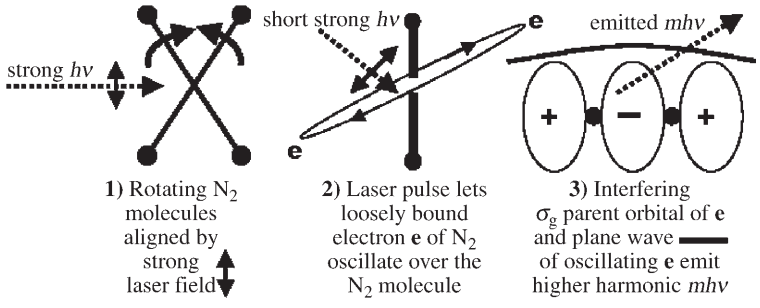



***Figure 1.*** Sketch of the three experimental steps to reconstruct the highest occupied orbital of $N_2$ molecules.


© 2006 Wiley-VCH Verlag GmbH & Co. KGaA, Weinheim

laser field changes direction, and the electron is near the center of the molecule. Experiments have corroborated the theoretical prediction that a quadratic relation exists between the higher harmonics generation (HHG) intensity $I$ and the ionization probability $n$.[11] A quadratic relation between optical intensity and particle number is well known, for instance, for coherent X-ray diffraction by defect-free crystal domains.[13] Another fortuitous circumstance is that electronic excitation of the nonbonding $\sigma_g$ HOMO hardly excites nuclear vibrations of $N_2$.[6]

*Step 3:* The optical emission intensities $I(mv)$ and polarizations were measured as functions of the energies $mhv$ in the X-ray range $\lambda = 15$–$50$ nm (photon energies 25–70 eV) for 27 higher harmonics of the initial laser frequency $v$ at the above-mentioned 19 angles. The relative phases of $a(k)$ were hypothetically determined by similar experiments with Ar and $N_2$/Ar mixtures, and were in agreement with theoretical predictions.[14]

### 2.2. Data Processing

From the experimentally determined form factors $a$, ion numbers $n$, HHG intensities $I$, and HHG frequencies $mv$ of sufficiently many energies, directions, and polarizations, the $\sigma_g$ orbital function in 3D space can be reconstructed by a double Fourier and Radon transformation of $|\langle\sigma_g|\,e\,r|\,e^{ik_{mr}}\rangle|$ in Equation (2). Several points facilitate the procedure.

Because of the high symmetry of the $\sigma_g$ HOMO, the phase of the optical transition moment $\langle\sigma_g|\,e\,r|\,i\,e^{ikr}\rangle = \langle\sigma_g|\,r\,|\sin(kr)\rangle = \mu(k)$ is purely real $\pm 1$. From the theoretical analysis for an MO of 2p-$\sigma_g$ topology with a length of a few Å, it follows that $\mu(k)$ for emission in the direction of the molecular axis should change sign at medium photon energies ($\lambda \approx 30$ nm), while $\mu(k)$ for emission orthogonal to the molecular axis should exhibit constant sign.[15] The expected sign changes of $\mu$ show up as minima in the measured intensity "curves". The most important term is the form factor $a(k)$.

Argon atoms and $N_2$ molecules have similar ionization potentials and polarizabilities, and similar excitation and ionization characteristics. The complex form factor $a(k)$ has been determined from the measurements of Ar atoms, $N_2$ molecules, and Ar/$N_2$ mixtures under the constraint that the data for Ar yield the theoretically calculated canonical Hartree–Fock 3p atomic orbital. Accordingly, errors in the diverse parameters of the instruments, detector, sensitivities etc. should basically cancel out in the reconstructed MO of $N_2$.

The $\sigma_g$ orbital function of $N_2$ was then reconstructed on a three-dimensional grid from the $27 \times 19$ basically empirical values of amplitude, phase, and polarization of the transition dipole moment vectors $\mu(k)$. This was achieved by Fourier unfolding of $\langle r\sigma_g|\sin(kr)\rangle$, and, for the transition matrix and the orbital function in different directions, by an algorithm similar to the Radon transformation used in medical tomography.[16] The one-electron orbital obtained reproduces the measured excitation and emission processes within the independent-particle approximation.

Since the most weakly bound canonical Hartree–Fock orbital of Ar was used for calibration, the function generated from $N_2$ laser-pulse spectra shown in Figure 2 may be assumed to be a canonical Hartree–Fock HOMO or some similar type of orbital such as a Dyson orbital (see Section 3.9).[17] Careful theoretical analyses of the experimental data production and of the data transformations are needed to distinguish between these cases in the future. However, the accuracy of the fs-spectroscopic data achievable at present and the approximations introduced in the data processing so far do not permit the detection of differences between these different orbital types. In any case, the experimentally reconstructed function of Figure 2 qualitatively reproduces the typical topology of an N2sp-N2sp-$\sigma_g$ lone-pair MO with a negative lobe between the N nuclei and strong positive lobes on the left and right sides.

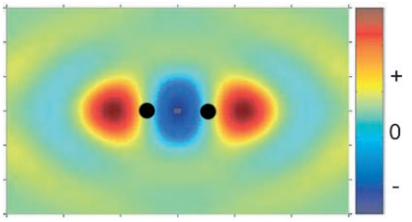



***Figure 2.*** Orbital of the most weakly bound electrons of $N_2$ molecules, which reproduces (within the orbital approximation) the higher harmonics generation of a laser pulse interacting with $N_2$ (tomographically reconstructed from experimentally determined transition dipole moments of the short-wave XUV emission and complex form factors). The plot is in a plane passing through the $N_2$ molecular axis. The two dots indicate the positions of the N nuclei. The color scale on the right codes the positive and negative values of the orbital function.[4a]

### 2.3. Evaluation

What has been measured on a femtosecond timescale are the optical intensities and polarizations of the higher harmonics generated by laser pulses interacting with $N_2$ molecules, with Ar atoms, and with $N_2$/Ar mixtures to determine the relative interference phases (selected curves through the $mv$ intensity values are shown in Figure 3 of reference [4a]).

Most remarkable is the timescale. Within 1 fs a quasiclassical electron would revolve several times on Bohr's hydrogen orbit. Concerning nuclear motions in chemistry, 1 fs covers only a small fraction of a rotation, a vibration or a direct bond-rearrangement. Femtosecond measurements can analyze the electronic rearrangements during the comparatively slow nuclear motions in some detail. The "electron shifts" in reaction mechanisms can become more than just chemistry on paper, namely "well-defined quantum chemistry", its experimental proof being within sight. The paper in *Nature*[4] is indeed another step on this difficult path. The details described above indicate the large number of simplifications thrown in and the large number of problems still to be solved. Some of them have already been mentioned explicitly in the cited paper.[4] In any case, at present the quantum chemical calculation of orbitals is the simpler and more reliable procedure.

An important aspect of experimental determination of orbitals is the well-defined orientation of the molecules. In the case of the gaseous phases, as in molecular beams, the molecular rotational states must be coherently super-

 © 2006 Wiley-VCH Verlag GmbH & Co. KGaA, Weinheim 

posed in an appropriate fashion. This was done here by a polarized laser pulse. Strongly polar molecules can be aligned with microwaves in multipole fields. Since the orientation of free molecules oscillates quantum mechanically, the "orbital measurement" must occur quickly. In the case of solids, the building blocks are in general stationary. Simpler, tried-and-true techniques can be applied easily (see Section 4.2).

Another point is the approximation of a complex many-electron phenomenon within the framework of the one-electron orbital model and the experimental reconstruction of the respective orbitals. Some theoretician's wisdom on orbitals will be communicated below, which should be considered in future "philosophical" discussions among experimental and computational chemists and in the community of philosophers of material sciences.

Some experimental scientists argue that one should perform measurements in a well-defined manner and present only slightly processed raw data. They argue that representations of model concepts based on extensive theoretical analysis, or even the philosophical or linguistic analysis of those concepts, are irrelevant in experimental science. Quantum chemists argue correctly that theoretically and computationally experienced theoreticians can generate wave functions and orbitals quite reliably. But some argue furthermore that any efforts to develop experimental alternatives are pointless, since at present even small molecules require terribly complicated procedures. Both groups of readers should proceed to Section 4.

## 3. "Philosophy" of Orbitals and of Their Reconstructions

### 3.1. Objects

In the (natural) sciences only sections of the world are investigated. Considering an isolated object means that its interactions with the environment are neglected. Measurements of data of an object are always performed within the framework of some approximate theory of the isolated object. If these data can or could help answer a given question satisfactorily, then the relations of the theoretical model represent some objective structure of reality. Whether an object may be said to exist objectively in this sense therefore depends on the internal physics of the system, its state, its environment,[18] the type of question, and the timescale. For instance, the concept of an $H_2O$ molecule makes sense in steam, but not in concentrated sulfuric acid, in particular not on an extended timescale.

### 3.2. Fields and Sets of Functions

Physical objects such as sections of electromagnetic or matter fields are represented by functions for fields and potentials.[36] Fields on microscopic scales are at best determined from interference patterns with a carefully prepared reference wave. However, it is much easier to measure only the amplitudes or values of multicomponent field functions, for example, the light intensity or the electron density.

An electromagnetic field is represented by a "gauge-invariant set" of four-component potential functions $\{A(X,t)+\bigtriangledown f_j(X,t)\}$ at space-position $X$ and time $t$. Here $f_j$ is an arbitrary function, and $\bigtriangledown$ the four-dimensional $(X,t)$ derivative. All individual potential functions $A+\bigtriangledown f_j$ from the set $\{A+\bigtriangledown f_j\}$ are equivalent and yield the same, experimentally verifiable results. Similarly, a matter field is represented by a "gauge-invariant set" of complex wave functions $\{\Psi(X,t)\,e^{if_j(X,t)}\}$. All individual wave functions $\Psi e^{if_j}$ are equivalent. It depends on the personal preference whether $\{A+\bigtriangledown f\}$ and $\{\Psi e^{if}\}$ are interpreted as "elements of a deduced reality" or only as "mathematical constructs" that reproduce the reality as exactly as detectable by measurements.

### 3.3. Measured Intervals, Numbers, and Complex Components

Any elementary measurement yields numbers with a few decimal places; that is, there are no real numbers with an infinite number of digits in experimental science. All measured values come from a "small" set of discrete numbers. Multiply reproduced data, not just individual measured values, form the basis of science. Because of the uncertainty of any experimental value, one can apply a mathematical simplification: calculations are performed with the help of continuous real values instead of the reliability intervals (of, say, $\pm 2\sigma$) obtained from repeated measurements. The basic equations of theoretical physics and chemistry hold in general for continuous differentiable functions.

Most physical quantities have several components. A vector field has three components; the so-called complex refraction index has two components for refraction and absorption; the nonrelativistically approximated wave function also has two complex components, in simple cases. Complex differentiable functions are mathematically distinguished and can represent the interrelationships of nature particularly clearly.

### 3.4. Wave Functions and Their Equivalents

All chemically interesting phenomena are many-particle phenomena that can often be described at the microscopic level with the help of many-particle wave functions $\Psi(X_1,\ldots,X_N)$. Here, $X_i$ may, for instance, indicate the position and spin direction of electron $i$ in 3D space. Other variables can also be used as alternatives to the position representation. In the momentum representation, $\Theta(P)$ (an equivalent to $\Psi(X)$) is obtained by a Fourier transformation, $\Theta(P)=\int dX\, e^{iPX}\Psi(X)$.

If quantum electrodynamical and environmental effects can be neglected, an isolated molecular system can be approximately represented by a wave function, but only in the case where all observable parameters are well specified ("pure state"). If one has some ensemble (e.g. a thermodynamic one), several wave functions are needed to construct the "density operator kernel" $D(X_i,X_j')$. In the simplest case of a pure state, $D(X_i,X_j')=\Psi(X_i)\Psi(X_j')^*$. In general, $D(X_i,X_j')$ is complex. Equivalent descriptions of reality can be obtained by variable transformations, yielding the real Wigner function $W(X_i,P_j)$ or the positive Husimi function $H(X_i,P_j)$ as a quantum mechanical generalization of the classical $X_i$–$P_j$ phase space density.[19]

 © 2006 Wiley-VCH Verlag GmbH & Co. KGaA, Weinheim 

### 3.5. Orbitals

All experimental concepts are based on some idealized approximations. Correspondingly, any comparably accurate theoretical description also comprises approximations. It is important to introduce further approximations to obtain simple and intuitively clear theoretical explanations. The wave functions $\Psi$ of many, though definitely not of all, states of an $N$-electron molecule can be approximated for many purposes by a "symmetry-adapted" product $\Phi$ of one-electron orbital functions $\varphi_j(X_i)$ ($j = \mathrm{a}$ to $n$) for electrons $i = 1$ to $N$ [Eq. (3)].

$$\Psi(X_1,\ldots,X_N) \approx \Phi(X_1,\ldots,X_N) = \mathrm{A}\{\varphi_\mathrm{a}(\mathrm{X}_1)\,\varphi_\mathrm{b}(X_2)\ \ldots\ \varphi_n(X_N)\} \quad (3)$$

Whether $\Phi$ is a satisfactory orbital approximation to $\Psi$ depends on the type of the molecule, on its state, and also on the type of the question. The statement "this object or structure exists" has the meaning that there is some objective structure in the real world that is satisfactorily described by the applied approximate concepts (theory) for the chosen section of reality (the object). In this sense, also orbitals can "exist" depending on the circumstances, just as NaCl molecules can exist in the gaseous phase though in general not in condensed phases. If a molecule exists, then orbitals often exist in the above-mentioned sense in the molecular ground state. Concerning excited states, however, the orbital approximation often fails. For instance, the orbital approximation of Equation (3) does in general not work for states with an electron excited from a lower subshell, such as 3 s of transition metal atoms, or the lowest valence MO of a molecule. These are cases of "breakdown of the orbital approximation".[20] In such physical situations "there are no" orbitals.

### 3.6. Measurement of Model Parameters

There is a whole continuum of different cases of measurements with more or less theory-laden data conversion—from the simple direct "measurement" of a single number (e.g. the comparison of the "length of a desk" with a meter stick) to the sophisticated semiempirical analysis of a large data set (e.g. the fitting of the parameters of a "static electron density model of a crystal" to the X-ray diffraction intensities). Concerning the extraction of physically relevant model parameters from the measured raw data, the last example is particularly strongly "theory- and model-laden". Parameters such as "dynamically averaged chemical shifts" from NMR measurements, or "vibrationally averaged internuclear distances" from microwave measurements are comparatively closer to the measurements. The reconstruction of orbital functions from HHG intensity measurements lies somewhere in between. Any reconstruction of a continuous function from the limited number of measured data bears some model load, such as the concentration distribution in a reactor, or the Born–Oppenheimer energy surface of a molecule.

Another aspect is the amount of chemically useful information connected with experimentally determined parameters. It is quite considerable for internuclear distance distributions from X-ray diffraction intensities, which characterize the structure and flexibility of a molecule. At present the amount of chemically useful information is still low for experimentally based orbital pictures.

Some repeated experiments are performed with the same object. In other cases, different identically prepared objects have to be used, not only in the quantum regime. For example, for the determination of a single classical activation energy, several similar reaction mixtures at different temperatures are needed. For the determination of the HOMO of $N_2$ many differently aligned $N_2$ molecules are required.

### 3.7. Reconstruction from Insufficient Data

In the reconstruction of physical functions from experimental data sets on the basis of a theoretical model, two problems must be overcome: 1) Since the measured data carry errors, more data than absolutely necessary must be determined, for error reduction and reproducibility. 2) In many cases one always has an insufficient amount of data. A typical example is the so-called "X-ray measurement of the electron density" of a crystal.[13] For finite wavelength $\lambda$ there is only a limited number of $\sin\theta/\lambda$ data. Their Fourier transform yields the Patterson density correlation function, and that only at an entirely insufficient quality. Therefore the broad qualitative and quantitative theoretical knowledge of chemistry is introduced. The approximate electron density distribution is constructed by fitting a superposition of vibrating "frozen" and "reasonably deformed" quantum-theoretical atomic densities, under the constraints of the already known chemical composition and under the restraints of "chemically reasonable" bonding and nonbonding interatomic distances. This approach now works routinely quite well after the introduction of a large number of tricks and educated guesses into the data-processing procedures, based on decades of experimental and computational experience.[13] However, it still can happen that significantly different "measured electron densities" fit the same experimental data set.[21]

### 3.8. Data Transformations

Fourier transformations of IR, NMR, and X-ray data are nowadays common between the time and energy domains, or between momentum transfers and position distances. In the cases of medical tomography and of atomic, electronic, or photonic scattering, projections upon different directions are measured. The data must be "inverted" to reconstruct the three-dimensional profile that causes the measured data. The previously mentioned Radon transformation developed for medical tomography and material investigations is also applied for "measuring orbitals".[16] It is not at all unique that engineering methods are also applied in quantum chemistry. The "Finite Elements" procedure, for instance, is used to predict tsunamis as well as the performance of new airplanes or cars, of large buildings and bridges, and of nanotubes, molecular orbitals, and nuclear dynamics in elementary chemical reaction steps.

 © 2006 Wiley-VCH Verlag GmbH & Co. KGaA, Weinheim 

### 3.9. Operational Definitions of Orbitals

"Orbitals" are concepts that are useful to approximately describe and efficiently manipulate structures, properties, and processes of real molecules, crystals, etc.[5] Accordingly, orbitals are essentially determined by the nature of the molecules, as well as by the aspects to be highlighted by the experimental investigation and the theoretical analysis. The relation between wave function $\Psi$ and corresponding orbital set $\{\varphi_j\}$ is made unique through the definition of the mathematical meaning of the "$\approx$" in Equation (3).

There are not "the orbitals" in molecules, just as there are not "the charges" on atoms in molecules. There are many kinds of atomic charges such as the Bader, Ahlrichs, Mulliken, IR, and dipole charges.[22] Similarly, rigorous quantum theory offers a wealth of different, well-defined types of orbitals, appropriate for different physical phenomena, to be described in different frameworks.[6,17] First, the *exact* wave function $\Psi$ and the *exact* energy $E$ can be generated from a simple orbital product function $\Phi$ by several theoretically well-defined techniques, for example, with the help of the Möller operator $\Omega$ or the coupled-cluster (CC) operator $\Xi$ according to $\Psi = \Omega\,\Phi$ or $\Psi = e^{\Xi}\Phi$. Second, the popular density functional (DF) approaches of Kohn and Sham (KS) all aim at the calculation of highly *reliable* molecular energies with the help of a product wave function of "KS orbitals" of different kinds.[23] Third, the most famous orbital approach for *approximate* energies is the first-principles (or ab initio) model of the self consistent field of Hartree and Fock (HF). There are also many semiempirical variants such as iterative extended Hückel (IEHT), CNDO, AM1, etc. For any of these approaches, there is a whole "continuum" of various equivalent sets of orbitals, such as the "canonically chosen" or the "localized-chosen" sets.

The description of arenes and pericyclic reactions, of periodic chains and crystals, of photo- and electrochemical excitations, and of charge-transfer processes by canonical orbitals delocalized over the molecule is particularly simple and concise. On the other hand, the discussion of $\sigma$ systems, ordinary conjugated $\pi$ systems and their substitution reactions, of valence-bond approaches, and of Lewis and VEPR models is most simple and straightforward, if orbitals are used that are localized according to Boys, von Niessen, Mezey etc. (the particular choice usually making no big difference).[24]

Diagonalization of an (experimentally reconstructed) one-electron density kernel $D$ yields the so-called ("experimental") "natural orbitals".[17] The analysis of experimental data of simple one-electron ionization processes $M \rightarrow M^+ + e$ within the orbital approach according to the approximation in Equation (4) yields the "Dyson orbitals".[5,17] The analysis of experimental HHG [Eq. (5)] in the framework of the Hartree–Fock model should yield "experimental" "Hartree–Fock orbitals".

$$\Psi(M) \approx A\{\Psi(M^+)\,\varphi(e)\} \qquad (4)$$

$$N_2 + mh\nu \rightarrow \{N_2^+ + e + n'h\nu\} \rightarrow N_2 + h\nu \qquad (5)$$

### 3.10. The HOMOs of $N_2$

In the framework of the Hartree–Fock approximation of closed-shell systems, the energies of orbitals (chosen canonically delocalized) approximate simple direct one-electron ionization energies (theorem of Koopmans). Two assumptions are implicit: The orbitals of $M^+$ are taken over from M as unmodified (ionization reorganization error). And no change upon ionization of the total correlation effect between any two electrons due to their Coulomb repulsion is postulated (ionization correlation error).

Figure 3 shows the one-electron orbital ionization energies of N and $N_2$ (from reliable many-particle calculations and from reliable experiments) in the form of an MO scheme. The 2s AOs of the two N atoms give rise to the lowest bonding $\sigma_g$(b) MO, which is particularly stable as a result of sp hybridization; the 2p$\pi$ AOs give rise to the lower pair of binding $\pi_u$(b) MOs. Also because of hybridization, the "antibonding" complement of $\sigma_g$(b) becomes a nonbonding $\sigma_u$(n) MO, and the "bonding" linear combination of the 2p$\sigma$ AOs becomes a nonbonding $\sigma_g$(n) MO. The two canonical MOs $\sigma_u$(n) and $\sigma_g$(n) correspond to the two localized $N_2$ lone pairs.

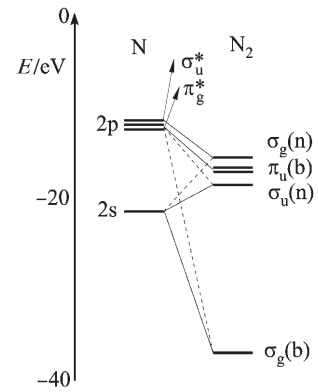



*Figure 3.* Negative one-electron orbital ionization energies $E$ (in eV) of the N atom (2s and 2p, configuration average values) and the $N_2$ molecule ($2s\sigma_g$(b), $2s\sigma_u$(n), $2p\pi_u$(b), $2p\sigma_g$(n)), with AO–MO correlations. (Note the deviation from the order of Hartree–Fock model orbital energies with $\pi_u$ above $\sigma_g$.)

It has been known for decades that the $\pi^4$ correlation energy (e.g. of $N_2$) is particularly large. Reorganization and correlation errors nearly cancel each other in the case of the $N_2(\pi_u)$ ionization. The 2p-2p-$\pi_u$(b) orbitals give rise to a vertical ionization potential (IP) at 17 eV; the corresponding orbital energy of the Hartree–Fock model is $\varepsilon_{HF}(\pi_u) = -17.0$ eV. The smallest ionization energy of 15.6 eV is sufficient to eliminate an electron from the nonbonding 2p-2p-$\sigma_g$ lone pair MO.[6] Here the "Koopmans error" is as large as 1.8 eV ($\varepsilon_{HF}(\sigma_g) = -17.4$ eV). While $IP(\sigma_g) < IP(\pi_u)$ holds for the ionization energies (according to experiment and theory), the Hartree–Fock approximation yields $|\varepsilon_{HF}(\sigma_g)| > |\varepsilon_{HF}(\pi_u)|$ for the orbital energies.[25]

According to a theorem of Janak for the KS-DF approach, the energies of the delocal KS orbitals (approximately accounting for electron correlation) describe the occupation tendencies of the orbitals in the electronic ground state.[23] Often the order of the approximate KS orbital energies corresponds to the order of the IPs. Indeed, we find $|\varepsilon_{KS}(\sigma_g)| < |\varepsilon_{KS}(\pi_u)|$. However, the values of the $\varepsilon_{KS}$ are smaller than those of the IPs, as usual, by up to a few eV.

 © 2006 Wiley-VCH Verlag GmbH & Co. KGaA, Weinheim 

### 4. Different Experimental Reconstructions of Wave Functions

The reconstructions of total electron densities and orbital densities, of many-electron wave functions, and of one-electron orbitals each have their own problems related to the applied experimental procedures. Kapale noted that "*quantum state measurement is an immensely complicated endeavor*".[26a] A wealth of approaches for experimental data collection and for computational data processing have been suggested or realized. Neglecting transition cases, the "experimental" reconstructions of electronic quantum states can be classified as four or five types. The broad field of photonic and of nuclear wave functions (molecular translations, rotations, vibrations, dissociations) shall not be considered here.

#### 4.1. Orbitals Reconstructed from Sufficient Experimental Data

Data sets sufficiently comprehensive for the direct reconstruction of amplitudes and phases of orbitals can be obtained from a whole series of different quite sophisticated experimental approaches. There are the spectroscopic homodyne and heterodyne techniques, the absorption, emission, fluorescence, and interference techniques of nonlinear and short pulse optics, which exploit the interaction of molecules with photons or electrons.[26] The most recent example is reviewed in Section 2. If the state under investigation is nonstationary, changing on the fs or ns timescales, the orbital wave function is complex at each instance of time. Such an orbital, though a simple one of an alkali-metal atom, had been "measured" by Weihnacht et al. already in 1998 (Figure 4).[27]

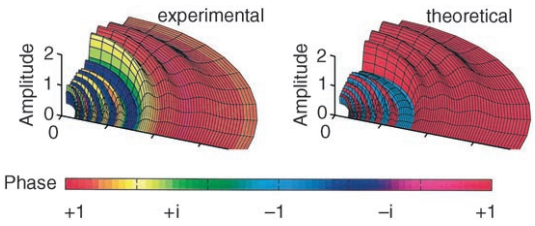



***Figure 4.*** Nonstationary complex $p_z$ orbital of a Cs atom (superposition of eight p states 25 p to 32 p obtained in a two-step excition from 6 s by an appropriately shaped short laser pulse). Right: Theoretically expected orbital. Left: Reconstructed from experimental data. Plots are shown in a quadrant of the *x*–*z* plane. The complex values (phases) of the AO function from $+1$ to $+i$ to $-1$ to $-i$ to $+1$ are color coded.[27]

#### 4.2. Model Orbitals from Complementary Experimental Data Sets

An experimentally simpler approach towards orbitals, wave functions, density kernels, etc. is based on fitting a not-too-flexible orbital model ansatz to a data set that is still insufficient for direct reconstruction. The resulting orbitals depend both on the experimental data and on the model assumptions. The most elaborate of such procedures is the joint use of complementary electron densities in position and momentum spaces for the generation of a "one-electron density matrix ".[28] The one-electron position density expresses the multicenter character of the molecule, the momentum density succinctly describes the quantum chemical character of the covalent bonds. The eigenvectors of the density matrix are the "natural orbitals" projected onto the model basis. These "semiexperimental" orbitals also account for electron correlation effects, in contrast to those of the Hartree–Fock approximation. For instance, assuming $1s^2\ 2s^{2-\delta}\ 2p^{\delta}$ for beryllium with weakly occupied p shell, one obtains the shapes of 1s, 2s, and 2p, and the orbital occupations with $\delta \approx 0.15$. Most investigators do not plot orbital figures explicitly but construct the orbitals only implicitly on the computer and use them to calculate molecular properties from the reconstructed orbital wave function: measured data→[semiempirical orbitals]→property values.

#### 4.3. Construction of Orbital Densities

Densities of individual Dyson orbitals can be reconstructed, first in momentum space, from inelastic energy-resolved triply differential electron-scattering data (e–2e spectra of electron momenta spectroscopy, EMS).[29] Similar results can be obtained from inelastic scattering data of high-energy photons (Compton spectroscopy) instead of high-energy electrons.[28b,c,30] Unfortunately the highly resolved gas-phase spectra yield only spherical averages of the orbital densities. We note a similarity between the EMS and HHG methods: The orbitals are scanned in momentum space by electronic plane waves, in the case of EMS by an "external" electron beam, in the case of HHG by a strongly oscillating electron from the excited molecule itself. Dyson orbital densities can also be generated from atomic scanning tunneling microscopic (ASTM) data, in position space (Figure 5[31]) or in momentum space (Figure 6[29g]).

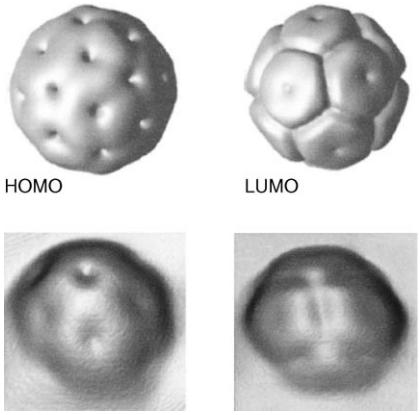



***Figure 5.*** HOMO and LUMO densities of fullerene $C_{60}$. Top: from DFT calculations. Bottom: from scanning tunnel microscopy at $+2$ V (left) and $-2$ V bias (right).[31a]

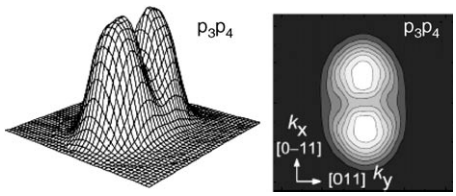



***Figure 6.*** Momentum density of a localized p-like electronic state in an (InAs) quantum dot in gallium arsenide, in the [001] plane, from scanning tunnelling data in a sweeping magnetic field.[29g]

#### 4.4. Combined Theoretical–Experimental Determination of Wave Functions

Various authors have suggested solving the comparably simple theoretically

 © 2006 Wiley-VCH Verlag GmbH & Co. KGaA, Weinheim 

approximate Hartree–Fock orbital equations so that simultaneously reasonable agreement with some experimental data sets is achieved, for instance X-ray crystallographic data sets ("quantum crystallography").[32] In this way, not only electron correlation effects can be introduced semiempirically into molecular Hartree–Fock calculations but also environmental influences of the solid surrounding the molecule in the crystal. In principle, these are theoretical orbitals, obeying experimentally determined conditions.

In a highly simplified version one chooses a rather small atomic orbital basis set that is known to yield still reasonable results in approximate molecular quantum calculations. Introducing some further restrictions (e.g. the single-determinant approximation, leading to the idempotency condition of the one-electron density matrix), the MO coefficients can then be fitted to some experimental data sets.[13a,33] For different opinions and critical comments on such semi-empirical and model-dependent MOs see footnote 1 in reference [28e].

### 4.5. Model Orbitals

It is common in crystallographic electron density studies to simulate the experimentally fitted total density distribution by a superposition of theoretical, empirically slightly deformed atomic orbital densities.[34] In this approach, however, the quantum mechanical interference effects between bonded atoms (the physical origin of the covalences) are not explicitly accounted for in the density reconstruction. Thereby one can get only roughly approximated AO occupation numbers of the d shells of transition metal ions in complexes, or of p shells of bonded main-group elements.

## 5. Summary

### 5.1. So-Called Measurements

Every experimental result is obtained in the framework of some approximate model concepts and has only some mediocre numerical accuracy. Every theoretical result is also based on some approximate assumptions and possesses only some numerical accuracy. This holds, for instance, even for the so-called exact hydrogen one-electron orbitals, which do not at all exactly reproduce reality.[35]

The various experimental or theoretical approaches do not differ in principle, but in the extent and amount of approximations and accuracies. A "rather directly measured" quantity and one reconstructed in a complicated manner from sophisticated measurements do not differ in principle but in the amount of intervening concepts and theories. Formerly one could apply simple measurement procedures that were analyzed with simple theories (e.g. Euclidean geometry as an approximate theory of physical space). Nowadays highly developed equipments must be combined with elaborate theories. Present measurement devices often directly display results theoretically reconstructed with the help of integrated computational hard- and software. The statement that some quantity has been "measured" just means that it has been reconstructed from some measurements that were performed and analyzed on the background of conceptual and numerical approximations, assumed to be appropriately valid and reliable in the given case.

Electromagnetic and matter fields of molecules are idealized objects excised from their environment. Such objects can be described mathematically, in many cases by a "gauge-invariant set" of real or complex or vectorial numbers or functions. In order to perform a concrete computation, a single representative from that set must be selected, for example, an electromagnetic potential in "Coulomb gauge", or a nonrelativistic wave function with $\alpha$ and $\beta$ spin factors and a position space function with real phase. What is the most appropriate choice among more or less equivalent concepts depends on the case and on the purpose.

An $N$-electron wave function describing an approximately isolated molecule in an approximate manner can be represented, depending on the theoretical approach, more or less accurately with the help of $N$ or more one-electron spin-orbitals. Whether canonical or localized orbitals, Hartree–Fock, density functional, or natural orbitals, or Dyson, Brückner, or Möller orbitals are most appropriate in a real problem also depends on the case and the accuracy desired. Anyhow, if one talks about orbitals one must always specify what kind is actually meant. This holds for calculated as well as for experimentally reconstructed orbitals.

### 5.2. Reconstruction of Orbitals and Orbital Densities from Experiments

Several experimental–theoretical hybrid approaches are on the market (Sections 2 and 4). The most developed one is based on a three-step femtosecond process consisting of: 1) tunnel ionization of an aligned molecule; 2) laser-driven motion of an electron in the continuum; 3) short-wave photoemission upon recombination. Whether and where the "experimental" constructions of total or orbital densities or wave functions are or may become superior to the purely theoretical ones depends on the molecular size and the thermodynamic conditions. When referring to empirically based electron deformation density maps or Laplacian density maps with all their incorporated assumptions as "measured ones", then it is even more justifiable to call orbital maps directly reconstructed from experimental data also "measured ones". However, the transformation of experimental data into orbitals has often not been analyzed sufficiently to specify the type of the reconstructed orbital. Today's sophisticated experimental and theoretical techniques call for more cooperation between theory and experiment in physics and in particular in chemistry. The chemistry curricula must take this into account. The pertinent problems of orbital reconstruction lie in the technical details which should be discussed in an interdisciplinary fashion by the specialists. In Section 3 we have tried to clarify the more "trivial" principles.

[1] "Albert Einstein and the Miraculous Year", *Phys. J.* **2005**, *4(3)*, 28–29, 35–38, 69–75; A. Einstein, *Ann. Phys. Chem. IV* **1905**, *17*, 891.

 © 2006 Wiley-VCH Verlag GmbH & Co. KGaA, Weinheim 

[2] a) S. A. Rice, M. Zhao, *Optical Control of Molecular Dynamics*, Wiley, New York, **2000**; b) H. Rabitz, R. de Vivie-Riedle, M. Motzkus, K. Kompa, *Science* **2000**, *288*, 824; c) T. Brixner, N. H. Damrauer, G. Gerber, *Adv. At. Mol. Opt. Phys.* **2001**, *46*, 1; d) T. Brixner, G. Gerber, *ChemPhysChem* **2003**, *4*, 418; e) M. Shapiro, P. Brumer, *Principles of Quantum Control of Molecular Processes*, Wiley-VCH, New York, **2003**; f) G. Leuchs, T. Beth, *Quantum Information Processing*, Wiley-VCH, New York, **2003**; g) N. Gisin, G. Ribordy, W. Tittel, H. Zbinden, *Rev. Mod. Phys.* **2002**, *74*, 145; J. Audretsch, *Verschränkte Systeme*, Wiley-VCH, Berlin, **2005**.

[3] a) J. Manz, A. W. Castleman, *J. Phys. Chem.* **1993**, *97*(48), 12423 – 12649; A. W. Castleman, V. Sundström, *J. Phys. Chem. A* **1998**, *102(23)*, 4021 – 4404; b) A. H. Zewail, *Angew. Chem.* **2000**, *112*, 2688; *Angew. Chem. Int. Ed.* **2000**, *39*, 2586; c) A. H. Zewail, *Angew. Chem.* **2001**, *113*, 4501; *Angew. Chem. Int. Ed.* **2001**, *40*, 4371; A. H. Zewail, *Nature* **2001**, *412*, 279.

[4] a) J. Itatani, J. Levesque, D. Zeitler, H. Niikura, H. Pépin, J. C. Kieffer, P. B. Corkum, D. M. Villeneuve, *Nature* **2004**, *432*, 867; J. Itatani, J. Levesque, D. Zeitler, H. Niikura, H. Pépin, J. C. Kieffer, P. B. Corkum, D. M. Villeneuve, *Phys. Rev. Lett.* **2005**, *94*, 123902; b) H. Stapelfeldt, *Nature* **2004**, *432*, 809; c) J. Itatani, J. Levesque, D. Zeitler, H. Niikura, P. B. Corkum, D. M. Villeneuve, *Laser Phys.* **2005**, *15*, 525.

[5] Orbitals of a given stationary molecular state are not uniquely defined by nature. Orbitals can be specified by more or less arbitrary or appropriate theoretical settings, or by a comparison of two different states, for example, ground state $N_2$ and ionized $N_2^+$ or excited $N_2^*$, that is, by a physical process! Chemistry is the "art of changing"; molecules and orbitals are typical concepts appropriate to chemistry. Different types of orbitals can be defined by different theoretical considerations.

[6] Constructive bonding AO interference in the overlap region is typical for two-center $\sigma_g$ MOs. However, density accumulation of the second $\sigma_g$ in the "lone-pair regions behind the nuclei" due to sp hybridization (see Figure 1) causes a nonbonding character: Vibrations are hardly excited, bond strength and length are hardly changed upon ionization of $^1\Sigma_g$ $N_2$ to $^2\Sigma_g$ $N_2^+$. In contrast, ionization from the bonding $\pi_u$ MO leading to $^2\prod_u$ $N_2^+$ extends the bond length by 8 pm and reduces the force constant by one-third, see K. P. Huber, G. Herzberg, *Molecular Spectra and Molecular Structure IV*, Van Nostrand Reinhold, New York, **1979**.

[7] a) Special issue (Eds.: W. P. Schleich, M. G. Raymer), *J. Mod. Opt.* **1997**, *44*-(11/12); b) M. Freyberger, P. Bardroff, C. Leichtle, G. Schrade, W. Schleich, *Phys. World* **1997**, *10*(11), 41.

[8] H. Niikura, D. M. Villeneuve, P. B. Corkum, *Phys. Rev. Lett.* **2005**, *94*, 083003, and references therein.

[9] a) C. J. Humphreys, *Nature* **1999**, *401*, 21; b) J. M. Zuo, M. Kim, M. O'Keeffe, J. C. H. Spence, *Nature* **1999**, *401*, 49; c) compare the critical evaluation of both by S. G. Wang, W. H. E. Schwarz, *Angew. Chem.* **2000**, *112*, 1827; *Angew. Chem. Int. Ed.* **2000**, *39*, 1757; S. G. Wang, W. H. E. Schwarz, *Angew. Chem.* **2000**, *112*, 3950; *Angew. Chem. Int. Ed.* **2000**, *39*, 3794.

[10] H. Stapelfeld, T. Seidemann, *Rev. Mod. Phys.* **2003**, *75*, 543.

[11] a) N. B. Delone, V. P. Krainov, *Multiphoton Processes in Atoms*, Springer, Heidelberg, **2000**; b) P. B. Corkum, *Phys. Rev. Lett.* **1993**, *71*, 1994; J. Itatani, D. Zeitler, J. Levesque, M. Spanner, D. M. Villeneuve, P. B. Corkum, *Phys. Rev. Lett.* **2005**, *94*, 123902; c) M. Lewenstein, P. Balcou, M. Y. Ivanov, A. L'Huillier, P. B. Corkum, *Phys. Rev. A* **1994**, *49*, 2117; d) R. Velotta, N. Hay, M. B. Mason, M. Castillejo, J. P. Marangos, *Phys. Rev. Lett.* **2001**, *87*, 183901; N. Hay, R. Velotta, M. Lein, R. de Nalda, E. Heesel, M. Castillejo, J. P. Marangos, *Phys. Rev. A* **2002**, *87*, 053805; e) T. Kanai, S. Minemoto, H. Sakai, *Nature* **2005**, *435*, 470.

[12] We use "atomic units": Plancks reduced constant $\hbar = h/2\pi = 1$, electronic mass $M_e = 1$, electronic charge $e = -1$. The electronic wave vector $k$ then has the same value as the momentum or the velocity.

[13] a) P. Coppens, *X-Ray Charge Densities and Chemical Bonding*, Oxford University Press, **1997**; b) V. G. Tsirelson, R. P. Ozerov, *Electron Density and Bonding in Crystals*, Institute of Physics Publishing, Bristol, **1996**.

[14] J. Levesque, D. Zeidler, P. B. Corkum, D. M. Villeneuve, personal communication.

[15] N. Hay, *J. Mod. Opt.* **2003**, *50*, 561.

[16] A. C. Kak, M. Slaney, *Principles of Computerized Tomographic Imaging*, Soc. Indust. Appl. Math., New York, NY, **2001**.

[17] A Dyson orbital is the best approximation in the sense of Equation (4) for the difference of the quantum mechanical states of a molecule and its cation, which is obtained by a "simple direct one-electron ionization process". Brückner orbitals yield the highest overlap of the accurate wave function with its orbital approximation. Strongly and weakly occupied natural orbitals are the eigenfunctions of an accurate "reduced one-electron density operator". See, e.g., J. V. Ortiz, *Int. J. Quantum Chem.* **2004**, *100*, 1131.

[18] D. Giulini, E. Joos, C. Kiefer, J. Kupsch, I. O. Stamatescu, H. D. Zeh, *Decoherence and the Appearance of a Classical World in Quantum Theory*, Springer, Heidelberg, **2002**.

[19] W. H. E. Schwarz, *Bunsen-Mag.* **2001**, *3*, 59; http://www.tc.chemie.uni-siegen.de/mess_wellenfkt.pdf.

[20] a) L. S. Cederbaum, J. Schirmer, W. Domcke, W. von Niessen, *J. Phys. B* **1977**, *10*, L549; b) L. S. Cederbaum, W. Domcke, J. Schirmer, W. von Niessen, *Adv. Chem. Phys.* **1986**, *65*, 115.

[21] P. G. Jones, *Chem. Soc. Rev.* **1984**, *13*, 157; R. E. Marsh, *Acta Crystallogr. Sect. B* **1997**, *53*, 317.

[22] J. Meister, W. H. E. Schwarz, *J. Phys. Chem.* **1994**, *98*, 8245.

[23] The KS density functional approach is an orbital-based approach. Theory and computational and experimental data demonstrate the physical significance of KS-DF orbitals. The exact KS-DF orbital energies are closely related to the one-elecron ionization potentials, while common approximate ones may deviate significantly. See, for example, a) P. Chong, O. V. Gritsenko, E. J. Baerends, *J. Chem. Phys.* **2002**, *116*, 1760; O. V. Gritsenko, E. J. Baerends, *J. Chem. Phys.* **2004**, *120*, 1937; O. V. Gritsenko, B. Braida, E. J. Baerends, *J. Chem. Phys.* **2003**, *119*, 1937; b) R. Stowasser, R. Hofmann, *J. Am. Chem. Soc.* **1999**, *121*, 3414; c) M. J. Hussey, A. J. Marray, *J. Phys. B* **2002**, *35*, 3399; C. E. Brion, G. Cooper, Y. Zheng, I. V. Litvinyuk, I. E. McCarthy, *Chem. Phys.* **2001**, *270*, 13.

[24] K. Ruedenberg in *Modern Quantum Chemistry I* (Ed: O. Sinanoğlu), Academic Press, New York **1965**, p. 85; W. Von Niessen, *J. Chem. Phys.* **1972**, *56*, 4290; C. Edmiston in *Theoretical Models of Chemical Bonding 2* (Ed.: Z. B. Maksić), Springer, Berlin, **1990**, p. 257, and references therein.

[25] a) L. S. Cederbaum, G. Hohlneicher, W. von Niessen, *Chem. Phys. Lett.* **1973**, *18*, 503; b) L. S. Cederbaum, *Chem. Phys. Lett.* **1974**, *25*, 562.

[26] a) K. T. Kapale, S. Qamar, M. S. Zubairy, *Phys. Rev. A* **2003**, *67*, 023805; b) G. M. D'Ariano, M. G. A. Paris, M. F. Sacchi, *Adv. Imaging Electron Phys.* **2003**, *128*, 205; c) Q. Thommen, V. Zehnle, J. G. Garreau, *Phys. Rev. A* **2003**, *67*, 013418.

[27] T. C. Weihnacht, J. Ahn, P. H. Bucksbaum, *Phys. Rev. Lett.* **1998**, *80*, 5508; T. C. Weihnacht, J. Ahn, P. H. Bucksbaum, **1998**, *81*, 3050; T. C. Weih-


 © 2006 Wiley-VCH Verlag GmbH & Co. KGaA, Weinheim 

nacht, J. Ahn, P. H. Bucksbaum, *Phys. Rev. Focus* **1998**, *1*, 21; T. C. Weihnacht, J. Ahn, P. H. Bucksbaum, *Nature* **1999**, *397*, 233.

[28] a) J. M. Gillet, P. J. Becker, *J. Phys. Chem. Solids* **2004**, *65*, 2017; J. M. Gillet, P. J. Becker, *Phys. Rev.* **2001**, *63*, 235115; b) G. T. Smith, H. L. Schmider, V. H. Smith, *Phys. Rev. A* **2002**, *65*, 032508; H. Schmider, V. H. Smith, W. Weyrich, *J. Chem. Phys.* **1992**, *96*, 8411; H. Schmider, V. H. Smith, W. Weyrich, *Z. Naturforsch. A* **1993**, *48*, 211; c) R. J. F. Nicholson, I. E. McCarthy, W. Weyrich, *J. Phys. B* **1999**, *32*, 3873; R. J. F. Nicholson, I. E. McCarthy, M. J. Brunger, *Aust. J. Phys.* **1998**, *51*, 691; d) J. E. Harriman, *Z. Naturforsch. A* **1993**, *48*, 203; e) W. H. E. Schwarz, A. Langenbach, L. Birlenbach, *Theor. Chim. Acta* **1994**, *88*, 437; f) W. H. E. Schwarz, B. Müller, *Chem. Phys. Lett.* **1990**, *166*, 621; g) J. M. Herbert, J. E. Harriman, *Int. J. Quantum Chem.* **2002**, *90*, 355.

[29] a) C. E. Brion, G. Cooper, Y. Zheng, I. V. Litvinyuk, I. E. McCarthy, *Chem. Phys.* **2001**, *270*, 13; S. Tixier, W. A. Shapley, Y. Zheng, D. P. Chong, C. E. Brion, Z. Shi, S. Wolfe, *Chem. Phys.* **2001**, *270*, 263, and references therein, in particular A. O. Bawagan, L. Y. Lee, K. T. Leung, C. E. Brion, *Chem. Phys.* **1985**, *99*, 367; A. O. Bawagan, C. E. Brion, E. R. Davidson, D. Feller, *Chem. Phys.* **1987**, *113*, 19; b) M. J. Hussey, A. J. Marray, *J. Phys. B* **2002**, *35*, 3399; c) X. G. Ren, G. L. Su, S. F. Zhang, C. G. Ning, H. Zhou, B. Li, E. Huang, G. Q. Li, J. K. Deng, *Phys. Lett. A* **2004**, *331*, 64; X. G. Ren, C. G. Ning, J. K. Deng, S. F. Zhang, G. L. Su, F. Huang, G. Q. Li, *Chem. Phys. Lett.* **2005**, *404*, 279; S. F. Zhang, G. L. Su, X. G. Ren, C. G. Ning, H. Zhou, B. Li, G. Q. Li, J. K. Deng, *Acta Phys. Sin.* **2005**, *54*, 1552; d) M. S. Deleuze, W. N. Pang, A. Salam, R. C. Shang, *J. Am. Chem. Soc.* **2001**, *123*, 4049; e) R. J. F. Nicholson, I. E. McCarthy, W. Weyrich, *J. Phys. B* **1999**, *32*, 3873; R. J. F. Nicholson, I. E. McCarthy, M. J. Brunger, *Aust. J. Phys.* **1998**, *51*, 691; f) M. Takahashi, Y. Idagawa, *J. Phys. Chem. Solids* **2004**, *65*, 2055; g) I. E. McCarthney, E. Weigold, *Rep. Prog. Phys.* **1991**, *54*, 789; h) O. S. Wibbelhoff, A. Lorke, D. Reuter, A. D. Wieck, *Appl. Phys. Lett.* **2005**, *86*, 092104.

[30] H. Schmider, V. H. Smith, W. Weyrich, *Trans. Am. Crystallogr. Assoc.* **1990**, *26*, 125; H. Schmider, V. H. Smith, W. Weyrich, *J. Chem. Phys.* **1992**, *96*, 8986; H. Schmider, V. H. Smith, W. Weyrich, *Z. Naturforsch. A* **1993**, *48*, 221; B. Barbiellini, A. Bansil, *J. Phys. Chem. Solids* **2004**, *65*, 2031.

[31] a) M. Grobis, X. H. Lu, K. H. Khoo, S. G. Louie, M. F. Crommie, *AIP Conf. Proc.* **2003**, *696*, 20; X. H. Lu, M. Grobis, K. H. Khoo, S. G. Louie, M. F. Crommie, *Phys. Rev. Lett.* **2003**, *90*, 096802; b) A. Biedermann, O. Genser, W. Hebenstreit, M. Schmid, J. Redinger, R. Podloucky, P. Varga, *Phys. Rev. Lett.* **1996**, *76*, 4179; c) X. Lu, K. W. Hipps, *J. Phys. Chem. B* **1997**, *101*, 5391; U. Mazur, K. W. Hipps, *J. Phys. Chem. B* **1999**, *103*, 9721; L. Scudiero, D. E. Barlow, K. W. Hipps, *J. Am. Chem. Soc.* **2001**, *123*, 4073; d) E. E. Vdovin, A. Levin, A. Patane, L. Eaves, P. C. Main, Y. N. Khanin, Y. V. Dubrovskii, M. Heinini, G. Hill, *Science* **2000**, *290*, 368075; A. Patane, R. J. A. Hill, L. Eaves, P. C. Main, M. Heinini, M. L. Zambrano, A. Levin, N. Mori, C. Hamaguchi, Y. V. Dubrovskii, E. E. Vdovin, D. G. Austing, S. Tarucha, G. Hill, *Phys. Rev. B* **2002**, *65*, 165308; e) T. K. Johal, R. Rinaldi, A. Passaseo, R. Cingolani, A. Vasanelli, R. Ferriera, G. Bastard, *Phys. Rev. B* **2002**, *66*, 075336.

[32] D. Jayatilaka, D. J. Grimwood, *Acta Crystallogr. Sect. A* **2001**, *57*, 76, 87; D. J. Grimwood, I. Bytheway, D. Jayatilaka, *Acta Crystallogr. Sect. A* **2002**, *58*, 232, 244; I. Bytheway, D. J. Grimwood, D. Jayatilaka, *J. Comput. Chem.* **2003**, *24*, 470.

[33] a) W. L. Clinton, L. J. Massa, *Phys. Rev. Lett.* **1972**, *29*, 1363; L. Massa, M. Goldberg, C. Frishberg, R. F. Boehme, S. J. LaPlaca, *Phys. Rev. Lett.* **1985**, *55*, 622; L. Huang, L. Massa, J. Karle, *Int. J. Quantum Chem.* **1999**, *73*, 439–450; b) S. T. Howard, J. P. Huke, P. R. Mallinson, C. S. Frampton, *Phys. Rev. B* **1994**, *49*, 7124.

[34] a) A. Holladay, P. C. Leung, P. Copperns, *Acta Crystallogr. Sect. A* **1983**, *39*, 377; b) K. Tanaka, M. Konishi, F. Maramo, *Acta Crystallogr. Sect. B* **1983**, *39*, 561, 557; c) L. L. Miller, R. A. Jacobson, K. Tuedenberg, J. Niu, W. H. E. Schwarz, *Helv. Chim. Acta* **2001**, *84*, 1907, and references therein; W. H. E. Schwarz, K. Ruedenberg, L. Mensching, *J. Am. Chem. Soc.* **1989**, *111*, 6926.

[35] Differences are due to the spatial extension and quantum smearing of the proton, its electric charge and magnetic dipole distribution, the "weak interaction" and the gravitational interaction between proton and electron, quantum electrodynamic effects (Lamb shift due to electromagnetic vacuum fluctuation and virtual electron-positron pair creation in the vicinity of the nucleus), the suppression of the exponentially decaying tail of the electronic orbital at large distances due to environmental perturbations by radiation fields and particle fluxes, etc.

[36] T. Y. Cao, *Synthese* **2003**, *136*(3), 25.

 © 2006 Wiley-VCH Verlag GmbH & Co. KGaA, Weinheim 

E. N. Jacobsen and M. S. Taylor

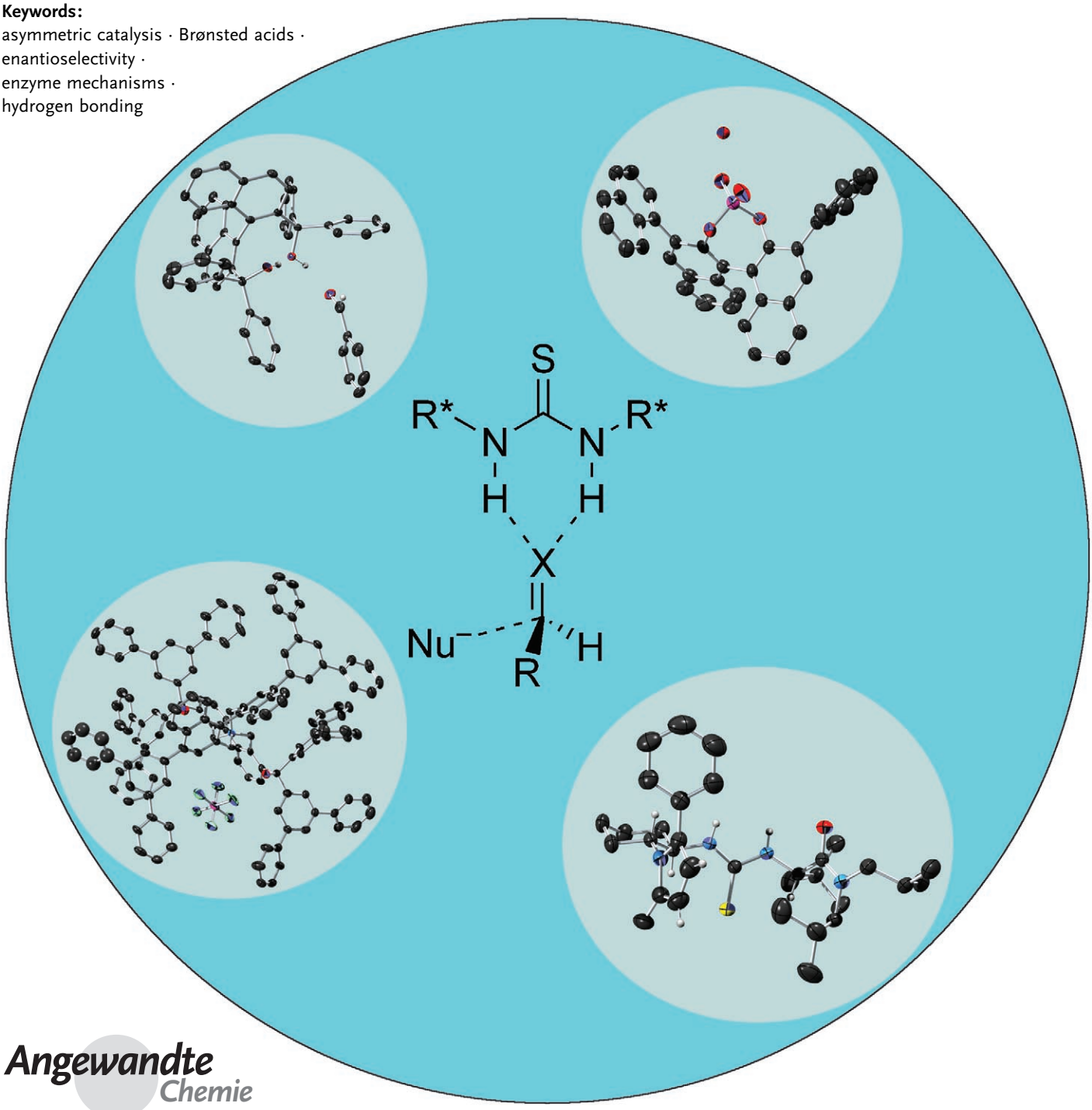
DOI: 10.1002/anie.200503132

Reaction Mechanisms

# Asymmetric Catalysis by Chiral Hydrogen-Bond Donors

*Mark S. Taylor and Eric N. Jacobsen**

**Keywords:**
asymmetric catalysis · Brønsted acids · enantioselectivity · enzyme mechanisms · hydrogen bonding






© 2006 Wiley-VCH Verlag GmbH & Co. KGaA, Weinheim

*Hydrogen bonding is responsible for the structure of much of the world around us. The unusual and complex properties of bulk water, the ability of proteins to fold into stable three-dimensional structures, the fidelity of DNA base pairing, and the binding of ligands to receptors are among the manifestations of this ubiquitous noncovalent interaction. In addition to its primacy as a structural determinant, hydrogen bonding plays a crucial functional role in catalysis. Hydrogen bonding to an electrophile serves to decrease the electron density of this species, activating it toward nucleophilic attack. This principle is employed frequently by Nature's catalysts, enzymes, for the acceleration of a wide range of chemical processes. Recently, organic chemists have begun to appreciate the tremendous potential offered by hydrogen bonding as a mechanism for electrophile activation in small-molecule, synthetic catalyst systems. In particular, chiral hydrogen-bond donors have emerged as a broadly applicable class of catalysts for enantioselective synthesis. This review documents these advances, emphasizing the structural and mechanistic features that contribute to high enantioselectivity in hydrogen-bond-mediated catalytic processes.*

**From the Contents**


| | |
|---|---|
| 1. Introduction | 1521 |
| 2. Hydrogen Bonding in Biological Catalysis | 1523 |
| 3. Hydrogen Bonding in Small-Molecule Synthetic Catalysis | 1525 |
| 4. Summary and Outlook | 1539 |


## 1. Introduction

Over the past four decades, the dominant strategy for enantioselective catalysis of nucleophile–electrophile reactions has involved electrophile activation by metal-centered chiral Lewis acids.[1] Rate acceleration results from the decrease in energy of the electrophile's lowest unoccupied molecular orbital (LUMO) accompanying the formation of a dative bond. The application of Lewis acids in organic chemistry has as its foundations the work of Friedel and Crafts, who discovered that electrophilic aromatic substitutions are accelerated by aluminum chloride.[2] The 1960 report by Yates and Eaton of aluminum chloride catalyzed Diels–Alder cycloadditions[3] signaled the onset of a period of intensive research activity on metal-centered Lewis acid catalysis that continues today.[4] The landmark discovery of Yates and Eaton was *not*, however, the first demonstration of catalysis of the Diels–Alder reaction: eighteen years earlier, Wassermann had reported that protic additives such as carboxylic acids and phenols accelerate the cycloaddition of cyclopentadiene with benzoquinone.[5] Why did the report of Yates and Eaton, and not that of Wassermann, capture the imagination of the vast majority of early practitioners of asymmetric catalysis, leading to the current situation where chiral Lewis acid catalysis, rather than chiral Brønsted acid catalysis, is the dominant strategy for promotion of enantioselective additions to electrophiles? The answer is clearly not that Brønsted acids are ineffective as catalysts: hydrogen bonding features prominently in biocatalysis, playing a central role in the acceleration of a diverse array of reactions, including acyl and phosphoryl transfer, carbonyl addition, and pericyclic processes.[6]

On the surface, metal-centered Lewis acids might appear to have several key advantages over hydrogen bond (abbreviated as H-bond) donors as small-molecule asymmetric catalysts (Figure 1). Lewis acids are highly tunable, a critical aspect of catalyst design. Variation of the identity of the Lewis acidic element, the counterion, and the chiral ligand framework provide the ability to fine-tune the steric and electronic environment of the catalyst. Methods to tune R*B–H bonds while retaining hydrogen bond donating ability seem limited in comparison. Moreover, many Lewis acid/base interactions are considerably stronger and more directional than H-bonds, features that should permit both enhanced LUMO-lowering ability and more effective communication of stereochemical information to the transition state.

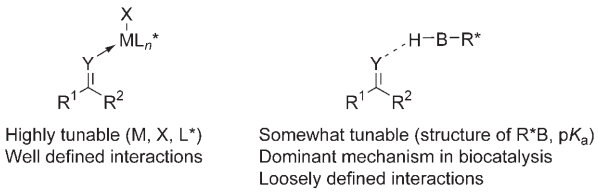



***Figure 1.*** Considerations in Lewis acid versus Brønsted acid activation of a generic electrophile (usually, Y = O, NR$^3$). L$_n$ = chiral ligand, X = counterion, R*BH = chiral Brønsted acid.

Nevertheless, electrophile activation by small-molecule chiral H-bond donors has emerged as an important paradigm for enantioselective catalysis, with new applications and developments appearing at a rapidly increasing pace.[7] To gain a thorough understanding of the principles and features underlying these catalysts, a definition and brief discussion of H-bonding is provided. More detailed discussions are the

[*] M. S. Taylor, Prof. E. N. Jacobsen
Department of Chemistry and Chemical Biology
Harvard University
12 Oxford St, Cambridge MA 02138 (USA)
Fax: (+1) 617-496-1836
E-mail: jacobsen@chemistry.harvard.edu

 © 2006 Wiley-VCH Verlag GmbH & Co. KGaA, Weinheim 

subject of a number of authoritative reviews and monographs.[8]

The relatively strong intramolecular interactions of molecules bearing X–H bonds, with proton acceptors A, were observed as early as the 19th century. Faraday's 1823 discovery of chlorine hydrate and Nernst's investigations of the properties of molecules containing hydroxy groups are notable examples. Huggins, Pauling, Bernal, Latimer, and Rodebush were among the first to recognize the generality of this phenomenon, and laid the foundations for the modern concept of H-bonding. A suitably inclusive definition of the H-bond was provided in a recent review by Steiner:

"*An X–H···A interaction is called a 'hydrogen bond', if 1. it constitutes a local bond, and 2. X–H acts as a proton donor to A.*"[9]

This concept applies to a wide diversity of intramolecular interactions, varying in strength from 0.4 to 40 kcal mol$^{-1}$. The range of observed hydrogen bond strengths reflects the variety of proton donors and acceptors capable of participating in this interaction: the subdivision of H-bonds into weak, moderate, and strong categories is often useful (Table 1).[8f] Bond directionality, as well as stability, differs among these categories. While the maximum H-bond strength is achieved when the X–H···A angle is 180°, this preference is most pronounced for strong hydrogen bonds, and is relaxed considerably in the case of moderate and weak bonds. The physical basis for hydrogen bonding also appears to differ between strong, moderate, and weak categories. The most successful approaches to deriving theoretical models have divided the interaction into components, such as electrostatic, polarization, exchange repulsion, charge-transfer, and coupling terms, with the relative contributions of these terms depending upon the bond strength. The majority of the H-bonding interactions discussed herein are of moderate strength, with classical electrostatic effects likely playing a dominant role.

Years of study have provided chemists with a relatively detailed understanding of catalysis by proton donors.[10] Brønsted acids can accelerate organic reactions by either of two fundamental mechanisms: reversible protonation of the electrophile in a pre-equilibrium step prior to nucleophilic attack (*specific* acid catalysis); or proton transfer to the transition state in the rate-determining step (*general* acid catalysis).

An increased appreciation of the scope of enzyme-catalyzed processes involving general acid catalysis likely contributed to the research efforts into synthetic H-bonding catalysts that began in the late 1990s. Organic chemists at this time also benefited from a relatively sophisticated understanding of the opportunities offered by H-bonding as a structural and functional element, due to research in several subdisciplines. Advances in supramolecular chemistry demonstrated that multiple, appropriately oriented H-bonds are sufficiently strong and directional to program the assembly of complex noncovalent structures, both in the solid state[11] and in solution.[12] The ability of well-defined achiral hydrogen bond donors to catalyze useful organic transformations was discovered in pioneering studies beginning in the mid 1980s (see Sections 3.1.1 and 3.2.1). Rapid progress in other areas of organocatalysis, which occurred contemporaneously with

***Table 1:*** Properties of hydrogen bonds.[8f]

| | Strong | Moderate | Weak |
|---|---|---|---|
| type of bonding | mostly covalent | mostly electrostatic | electrostatic |
| length of H-bond [Å] | 1.2–1.5 | 1.5–2.2 | 2.2–3.2 |
| bond angles [°] | 175–180 | 130–180 | 90–150 |
| bond energy [kcal mol$^{-1}$] | 14–40 | 4–15 | $<4$ |
| typical example | intramolecular NH···N bond in conjugate acid of proton sponge | NH···O=C bonds in peptide helices and sheets | bonds involving CH donors to N or O acceptors |



*Mark S. Taylor was born in Oxford (England) in 1977. After attending Saint Michael's Choir School (Toronto, Canada), he obtained his B.Sc. in chemistry (2000) at the University of Toronto, where he pursued undergraduate research in the laboratory of Prof. Mark Lautens. He recently completed Ph.D. studies at Harvard University (Cambridge, USA), under the supervision of Prof. E. N. Jacobsen. His research involved the discovery of enantioselective, catalytic carbon–carbon bond-forming reactions, including asymmetric Michael reactions and chiral thiourea-catalyzed transformations of N-acyliminium ions. He began postdoctoral studies in the laboratories of Prof. T. M. Swager at MIT (Cambridge, USA) in September 2005.*



*Eric N. Jacobsen was born in 1960 in New York. He obtained his primary and secondary school education at the Lycée Français de New York, then earned his BS degree from New York University (1982) and his PhD from UC Berkeley (1986, with Robert Bergman). After a postdoctoral fellowship at MIT with Barry Sharpless, he began his independent career at the University of Illinois in 1988. He moved to Harvard University in 1993, and he was named the Sheldon Emory Professor of Organic Chemistry in 2001. His research interests lie in the discovery, mechanistic elucidation, and application of new synthetic methods, with special emphasis on asymmetric catalytic processes.*

 © 2006 Wiley-VCH Verlag GmbH & Co. KGaA, Weinheim 

early developments in chiral hydrogen-bond-donor catalysis, rendered chemists keenly aware of the potential of simple organic molecules in asymmetric catalysis.[13]

A number of general design features may be identified that characterize the most generally applicable classes of small-molecule chiral hydrogen-bond donors. Species capable of simultaneously donating two hydrogen bonds, such as ureas, thioureas, as well as guanidinium and amidinium ions, are emerging as a class of privileged[14] catalyst structures, finding application in such mechanistically diverse transformations as 1,2-addition, acyl transfer, 1,4-addition, and cycloaddition reactions (Section 3.1). Efficient strategies for obtaining high enantiomeric excess using only a single hydrogen bond are beginning to emerge, with additional noncovalent interactions engaged to direct the assembly of a well-defined catalyst–substrate complex (Section 3.2). Bifunctional species incorporating H-bond donors in addition to other Brønsted basic, nucleophilic, or acidic functional groups constitute a highly successful catalyst class (Section 3.3). In addition to activating electrophiles through hydrogen bonding, chiral general acids also mediate enantioselective protonation reactions of prochiral substrates. In particular, highly enantioselective proton transfer to enolates and enolate equivalents has been achieved by employing a variety of structurally diverse catalysts. This important, but mechanistically distinct application of chiral Brønsted acids has been the subject of recent reviews[15] and will not be discussed here.

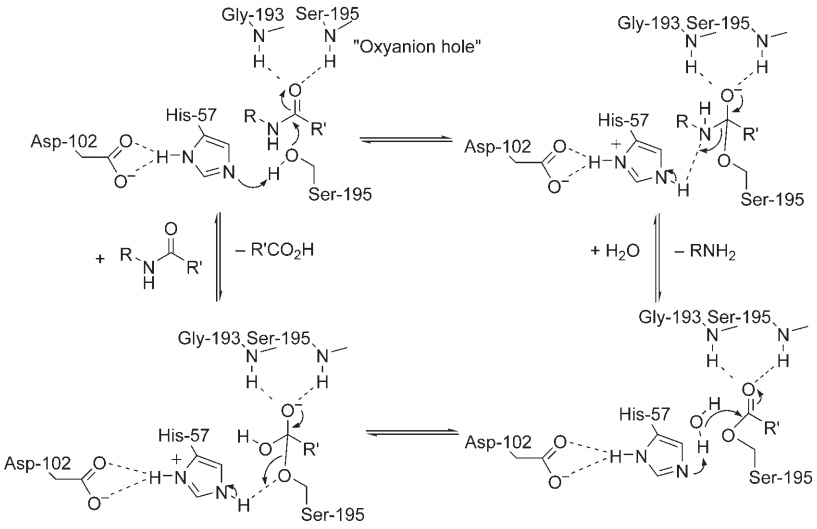
Parallels may be drawn between the design concepts mentioned above and the characteristics of biomolecules that activate electrophiles by hydrogen bonding. We therefore begin this review with a discussion of H-bonding in biocatalysis (Section 2), drawing attention to the mechanistic features shared with synthetic catalyst systems.

## 2. Hydrogen Bonding in Biological Catalysis

The serine proteases, enzymes that catalyze the hydrolysis of amide bonds, provide a useful starting point for discussion of electrophile activation by H-bonding in biocatalysis. The mechanism of amide hydrolysis catalyzed by serine protease, in which double hydrogen bonding, multiple noncovalent catalyst–substrate contacts, and bifunctional catalysis play key roles, is described in Section 2.1. These features of serine protease catalysis are common to many of the biological catalyst systems that employ H-bonding. A few illustrative examples, spanning a range of reaction mechanisms, are discussed in Sections 2.2–2.4.

### 2.1. Serine Proteases

Serine proteases have been studied in depth using a wide range of spectroscopic and kinetic techniques, and as a result, a detailed description of the mechanism of operation of this class of enzymes is possible.[16] The key feature of the catalytic machinery is a highly conserved active-site nucleophilic serine residue that effects alcoholysis of the amide substrate (through the presumed intermediacy of a tetrahedral adduct) to generate an acylated enzyme. The amide carbonyl group is activated by the "oxyanion hole" composed of two H-bond donors, while activation of the serine hydroxy group is accomplished by general base catalysis using a histidine/aspartate proton shuttle system. Hydrolysis of the acylenzyme regenerates the active site serine moiety and releases the product (Scheme 1). The fact that H-bonding alone serves to activate the amide electrophile is striking, given the poor




***Scheme 1.*** Serine protease: Acceleration of amide hydrolysis by double H-bonding, multiple noncovalent catalyst–substrate interactions and bifunctional catalysis. (From reference [16]).

electrophilicity of the amide functional group. Indeed, the serine proteases serve to illustrate several of the general principles by which the relatively weak H-bonding interaction is used by enzymes for electrophile activation.

1) *Double hydrogen bonding*: The simultaneous donation of two H-bonds, exemplified by the serine protease oxyanion hole, appears to be a particularly effective method for electrophile activation, both in enzymes and in synthetic catalysts. The interaction of carbonyl groups and tetrahedral intermediate mimics with the oxyanion hole is among the most well-studied hydrogen-bonding systems in catalysis. Computational and model studies suggest that the chymotrypsin acylenzyme is stabilized by 4–7.5 kcal mol$^{-1}$ (depending upon the structure of the acyl group) by binding of the ester carbonyl group in the oxyanion hole.[17] The importance of the double H-bonding interaction in the oxyanion hole is highlighted by the result of a study in which one of the H-bond donors was removed: site-directed mutagenesis of asparagine 155, which makes up half of the oxyanion hole in subtilisin, results in a 300-fold drop in the $k_{cat}$ value, and the loss of the low-frequency carbonyl IR shift diagnostic of a H-bonded acylenzyme.[18]

 © 2006 Wiley-VCH Verlag GmbH & Co. KGaA, Weinheim 

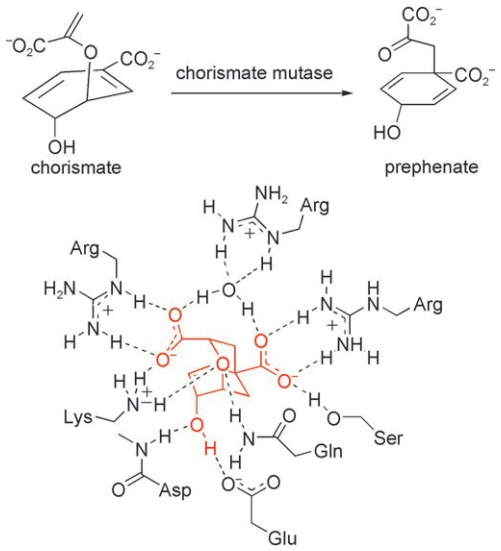
Current theories of enzyme catalysis hold that biomolecules have evolved to bind and stabilize transition states and reactive intermediates in preference to either starting materials or products.[19] The oxyanion hole provides an illustration of this concept: its name refers to its postulated role in the stabilization of the high-energy tetrahedral intermediates along the amide hydrolysis reaction coordinate. Organic molecules mimicking the structure and charge distribution of the tetrahedral intermediate function as serine protease inhibitors, demonstrating the ability of the oxyanion hole to tightly bind such species. In contrast, rate acceleration by metal-based Lewis acid and Brønsted acid synthetic catalysts is generally rationalized by a LUMO-lowering effect, and it is less well established whether the selective transition state binding principles that apply to enzymatic catalysis are also relevant in small-molecule systems.

2) *Multiple noncovalent interactions* with substrate: Serine proteases have evolved to recognize and selectively cleave certain amino acid sequences. This substrate specificity is achieved by formation of an antiparallel β sheet between the amino acids flanking the site of protein hydrolysis and enzyme residues that make up a cleft in the protease surface containing the active site. These additional H-bonding and van der Waals interactions not only confer substrate specificity, but also enhance catalytic activity. The value of $k_{cat}$ (a measure of the rate of alcoholysis of the bound substrate by enzyme) and not $K_M$ (a measure of enzyme–substrate binding affinity) changes when unnatural, rather than natural, serine protease substrates are processed.[20] The mechanism by which these secondary interactions are relayed to greater catalytic rates is not well understood: possible explanations include the distortion of the amide bond from planarity upon substrate binding, or changes in enzyme conformation that bring about a more favorable orientation of catalytic residues.

3) *Bifunctional catalysis*: The serine/histidine/aspartate triad is conserved in all members of the serine protease family. The presence of the catalytic triad in both bacterial and mammalian serine proteases, which bear essentially no other structural or sequence homology, appears to be an example of convergent evolution, or the development of a common phenotype from two independent evolutionary pathways.[16] Site-directed mutagenesis studies further highlight the crucial importance of the histidine and aspartate moieties in activating the serine hydroxy group for nucleophilic attack.[21] The prevalence of multifunctional catalysis in enzyme catalysis has served as the inspiration for many synthetic catalyst systems that rely upon simultaneous activation of nucleophile and electrophile (see Section 3.3).

### 2.2. Chorismate Mutase

Chorismate mutase, which catalyzes the conversion of chorismate to prephenate through a [3,3]-sigmatropic rearrangement, has been the subject of intensive mechanistic study.[22] Interest in chorismate mutase stems not only from the importance of the chorismate–prephenate transformation in the biosynthesis of the aromatic amino acids, but also from the ability of this enzyme to accelerate a pericyclic reaction using Brønsted acid/base catalysis alone: no metals are incorporated into the active site. Crystal structures of a bound inhibitor, along with site-directed mutagenesis studies, suggest that double H-bond donation to the vinyl ether oxygen atom serves to activate the substrate (Scheme 2).[23]



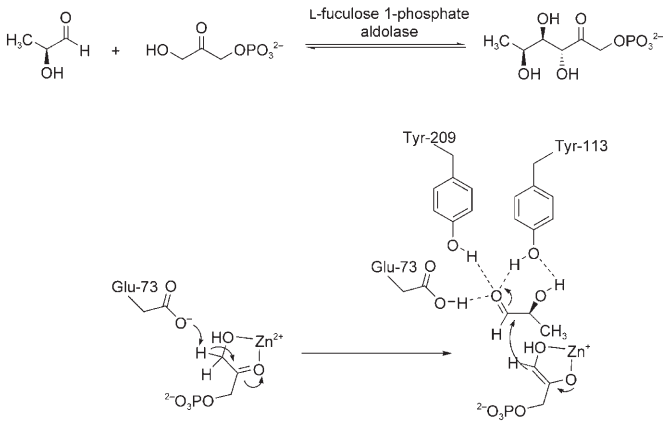

***Scheme 2.*** Chorismate mutase: Acceleration of a [3,3]-sigmatropic rearrangement by double hydrogen bonding and multiple noncovalent catalyst–substrate interactions. (From reference [22b]).

An analogous double H-bond interaction between water and a vinyl ether has been deduced from computational simulations of the Claisen rearrangement in aqueous solution.[24] Additional H-bonding and electrostatic interactions between substrate and chorismate mutase are of crucial importance, serving to hold the substrate in a reactive conformation. These interactions pay the entropic cost of the rearrangement reaction: whereas the entropy of activation ($\Delta S^{\neq}$) for uncatalyzed Claisen rearrangements is large and negative,[25] the enzyme-catalyzed reaction is characterized by a $\Delta S^{\neq}$ value close to zero.[26]

### 2.3. Type II Aldolases

Although H-bonding is frequently employed by biomolecules for electrophile activation, Nature rarely appears to use it for the purpose of enantioselective catalysis. Among the few enzymes that catalyze highly enantioselective reactions by means of H-bonding are type II aldolases such as L-fuculose 1-phosphate aldolase, which catalyzes the stereoselective aldol reaction of dihydroxyacetone phosphate (DHAP) with L-lactaldehyde (Scheme 3).[27] This enzyme and related DHAP-dependent aldolases exhibit substantial tolerance for unnatural aldehyde substrates, permitting enantioselective reactions of prochiral acceptors and kinetic resolutions of chiral α-substituted aldehydes. L-Fuculose 1-phosphate aldolase generates a nucleophilic enolate species under mild conditions using a zinc cofactor, which coordinates to dihydroxyacetone phosphate (DHAP), acidifying it to such

 © 2006 Wiley-VCH Verlag GmbH & Co. KGaA, Weinheim 

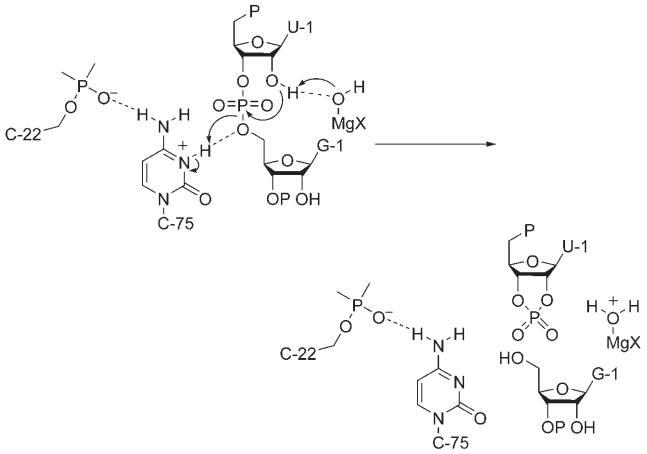



***Scheme 3.*** Type II aldolase: Promotion of a stereoselective aldol reaction by bifunctional catalysis.

an extent that it is deprotonated by Glu-73, a weak base. Three acidic residues play roles in orienting and activating the L-lactaldehyde electrophile: the phenolic hydroxy groups of Tyr-113 and Tyr-209, and the carboxylic acid group resulting from the action of Glu-73 in the enolization step.[28] The importance of these residues for catalysis has been demonstrated by site-directed mutagenesis experiments, in which significant decreases in reaction rate and enantioselectivity were observed.

### 2.4. Hepatitis Delta Virus Ribozyme

The discovery that RNA oligomers are capable of catalysis has generated tremendous interest among scientists studying the origins of life on earth, since RNA catalysis provides a plausible mechanism for the evolution of modern organisms, based on DNA, RNA, and proteins, from a prebiotic "RNA world". Since the initial identification of the *Tetrahymena thermophila* self-cleaving ribozyme, seven classes of catalytic RNA have been found in nature, all of which mediate cleavage or ligation reactions of the phosphodiester backbone.[29] In addition to their possible implications for origin-of-life theories, ribozymes are of fundamental mechanistic interest to organic chemists, who seek to elucidate how the limited range of functional groups present in the oligoribonucleotide structure are employed in catalysis. In particular, the naturally occurring ribonucleotide bases contain no functional groups with p$K_a$ values lower than 4.6 or higher than 9.4, typically the critical range for performing catalysis in an aqueous environment at or near neutral pH.[30] Many catalytic RNAs rely upon the presence of metal cofactors, not only to stabilize their folded structure, but also to play functional roles. The hepatitis delta virus (HDV) ribozyme, an RNA oligomer that undergoes self-cleavage as a crucial part of the hepatitis virus life cycle, is unique among naturally occurring ribozymes in that it does not require a specific metal cofactor for activity. Analysis of the X-ray crystal structure,[31] along with detailed kinetic studies,[32] suggest a general acid/base catalysis mechanism for this catalytic RNA. The mechanistic proposal involves activation of the phosphate electrophile by H-bonding from the N-H group of the protonated form of cytosine 75 (Scheme 4). The ability of cytosine 75 to act as an H-bond donor hinges on a perturbation of the acidity of this residue by H-bonding of its




***Scheme 4.*** The hepatitis delta virus ribozyme: Acceleration of a phosphoryl transfer reaction by bifunctional catalysis and modulation of p$K_a$.

exocyclic amino group with an anionic phosphate, an interaction that causes a substantial increase in p$K_a$, from 4.2 in the free nucleoside to approximately 7. The HDV ribozyme is a bifunctional catalyst: general base catalysis by a metal-bound hydroxide moiety serves to activate the 2′-hydroxy group as a nucleophile.

## 3. Hydrogen Bonding in Small-Molecule Synthetic Catalysis

The vast majority of small-molecule general acid enantioselective catalysts has been discovered only within the last few years. As a result, for the most part they have not yet been subjected to the same level of mechanistic scrutiny as have biological catalysts, and less is known with precision about the different modes by which they effect rate acceleration by H-bond donation. Still, it is possible at this early stage in the field to classify synthetic general acid catalysts into fundamentally different mechanistic classes, and this review of the field is organized accordingly.

### 3.1. Double Hydrogen-Bond-Donor Catalysts

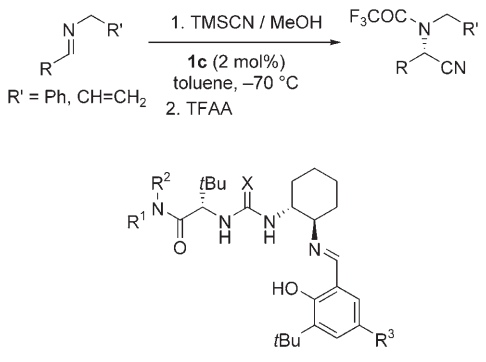
The simultaneous donation of two hydrogen bonds has proven to be a highly successful strategy for electrophile activation, both in enzymes (see Section 2) and in synthetic catalyst systems. Several properties of the bifurcated hydrogen bond may contribute to its utility in catalysis. Such interactions benefit from increased strength and directionality relative to a single hydrogen bond: in an analogous manner, two-point binding is an extremely powerful strategy for asymmetric catalysis with metal-centered Lewis acids.[33]

 © 2006 Wiley-VCH Verlag GmbH & Co. KGaA, Weinheim 

However, while the requirement for multidentate coordination to a chiral Lewis acid often imposes limitations upon substrate structure, in principle any Lewis base is capable of engaging in bifurcated hydrogen bonds. Electrophiles shown thus far to be activated by double hydrogen-bond donors include aldehydes, ketones, esters, a variety of imine derivatives, *N*-acyliminium ions, and nitro compounds.

#### 3.1.1. Ureas and Thioureas

The discovery that Schiff bases **1a–c** catalyze asymmetric hydrocyanation reactions of a wide variety of imine substrates revealed for the first time that chiral urea and thiourea derivatives are capable of mediating highly enantioselective transformations (Scheme 5).[34] These compounds had been



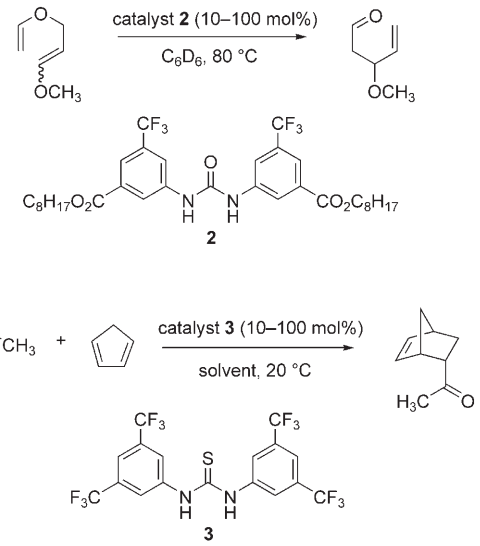

**1a**: $R^1$ = Bn, $R^2$ = H, $R^3$ = $OCH_3$, X = S
**1b**: $R^1$ = Bn, $R^2$ = H, $R^3$ = OCO*t*Bu, X = O
**1c**: $R^1$ = $R^2$ = $CH_3$, $R^3$ = OCO*t*Bu, X = S
**1d**: $R^1$ = Bn, $R^2$ = $CH_3$, $R^3$ = *t*Bu, X = S

***Scheme 5.*** Enantioselective Strecker reactions catalyzed by urea and thiourea Schiff bases. TFAA = trifluoroacetic acid anhydride, TMS = trimethylsilyl.

designed originally as potential ligands for Lewis acidic metals, and the observation that highest enantioselectivity was observed in the absence of metal additives was unanticipated. The mechanism by which these catalysts activate imines was subsequently investigated by using a number of approaches, such as structural modification, NMR, kinetic, and computational studies.[35] The data thus obtained were all consistent with a double H-bond between the acidic NH protons and the imine lone pair serving to activate the electrophile towards attack by cyanide.

The notion that ureas and thioureas could act as chiral catalysts by activating electrophiles through a double H-bonding mechanism finds solid precedent in the work of a number of research groups. The relatively strong and directional H-bonds donated by ureas in noncovalent assemblies represent an important facet of supramolecular chemistry.[11,12] Etter and co-workers demonstrated that electron-poor diaryl ureas can be cocrystallized with a wide variety of Lewis bases by formation of double H-bonds.[36] The interaction of ureas with anions and neutral molecules, such as phosphates, sulfates, benzoates, esters, and nitroarenes was investigated in the solution phase.[37]

Catalysis of several synthetically important organic transformations by achiral ureas and thioureas constitutes the most direct precedent for the results described above (Scheme 6). Curran and co-workers studied radical allylations of sulf-



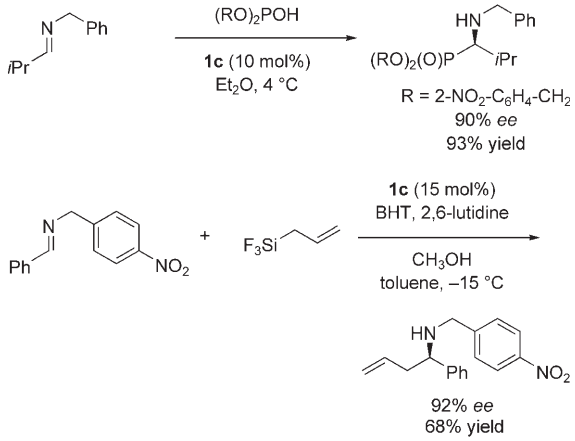

***Scheme 6.*** Achiral urea and thiourea catalysts.

oxides and Claisen rearrangements of allyl vinyl ethers catalyzed by electron-poor diaryl urea **2**.[38] The related diaryl thiourea **3** was found to catalyze Diels–Alder and dipolar cycloaddition reactions of α,β-unsaturated carbonyl compounds, even with water as the reaction solvent.[39]

In each of these examples of catalysis with achiral diaryl ureas or diaryl thioureas, maximum rate acceleration was observed with derivatives bearing strongly electron-withdrawing groups in the 3- and 5-positions. Diaryl ureas of this type were also identified by Etter and co-workers as being unique in their ability to cocrystallize with a wide range of acceptors. Several factors may contribute to the special behavior of these species. The presence of electron-withdrawing groups serves to decrease the p$K_a$ of the N–H bonds, increasing their H-bond donating ability. It has been further suggested that an intramolecular H-bond between the relatively acidic *ortho* C–H bonds of the aromatic system and the urea carbonyl group may play a role in catalyst activation.[36] Such an interaction would decrease the basicity of the carbonyl group, favoring cocrystallization over catalyst dimerization in the solid state; furthermore, it would serve to enhance H-bonding ability by acidifying the N–H bonds. In comparison, it is clear that the relatively electron-rich chiral thiourea and urea catalysts **1** used in the asymmetric Strecker reaction are substantially weaker H-bond donors. It therefore might have been anticipated that the scope of this type of enantioselective catalyst system might be restricted to a relatively small set of reactions. The converse has proven to be true: chiral ureas and thioureas related to **1** catalyze a remarkable variety of enantioselective transformations, and currently constitute the most generally applicable class of chiral H-bond donors.

 © 2006 Wiley-VCH Verlag GmbH & Co. KGaA, Weinheim 

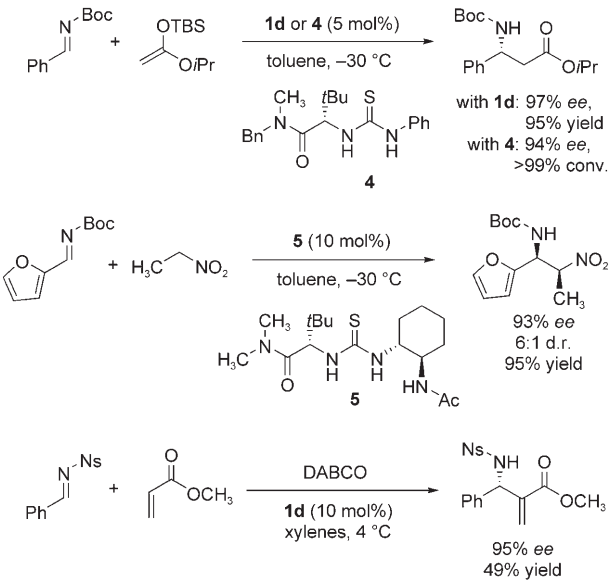
In addition to hydrogen cyanide, a number of nucleophiles undergo enantioselective addition to *N*-benzyl imines in the presence of thiourea catalysts **1**. Addition of di-(2-nitrobenzyl) phosphite to imines derived from aliphatic and aromatic aldehydes, followed by hydrogenolysis of the *N*- and *O*-benzyl groups, constitutes an efficient asymmetric synthesis of aminophosphonic acids.[40] Thiourea **1c** also mediates allylations of *N*-(4-nitrobenzyl) imines with allyltrifluorosilane, although this reaction exhibits limited substrate scope (Scheme 7).[41]




***Scheme 7.*** Nucleophilic additions to *N*-benzyl imines catalyzed by thiourea **1c**. BHT = 2,6-di-*tert*-butyl-4-methylphenol.

The observation that **1c** catalyzes enantioselective additions of a number of nucleophiles to *N*-benzyl imines is consistent with the mechanistic hypothesis that the thiourea serves to activate the electrophile alone by H-bonding. It is remarkable, however, that highly enantioselective additions to a range of functionally diverse electrophiles are promoted by thiourea catalysts. The first indications of this generality arose from studies of Mannich reactions of *N*-*tert*-butoxycarbonyl (Boc) imines, a reaction of interest for the preparation of enantioenriched β-amino acid derivatives. Thiourea **1d** catalyzes this reaction with high enantiomeric excess, despite the significant steric and electronic differences between *N*-Boc imines and the *N*-benzyl and *N*-allyl imines employed in the Strecker reaction (Scheme 8).[42] Vinylogous Mannich reactions are also catalyzed by **1d**, providing access to δ-aminocarbonyl compounds, useful intermediates for the preparation of nitrogen heterocycles.[43] Systematic variation of catalyst structure demonstrated that the mechanisms of asymmetric induction at work in the Strecker and Mannich reactions differ substantially: in particular, the diaminocyclohexane-derived Schiff base portion of the catalyst was not necessary for high enantioselectivity in Mannich reactions. This moiety could be replaced with a simple phenyl group as in **4**, resulting in an easily prepared catalyst that exhibited improved activity.[44]

The ability of thioureas to activate imines bearing a wide variety of protecting groups forms the basis of several enantioselective carbon-carbon bond-forming methodologies (Scheme 8). *N*-Boc imines participate in nitro-Mannich

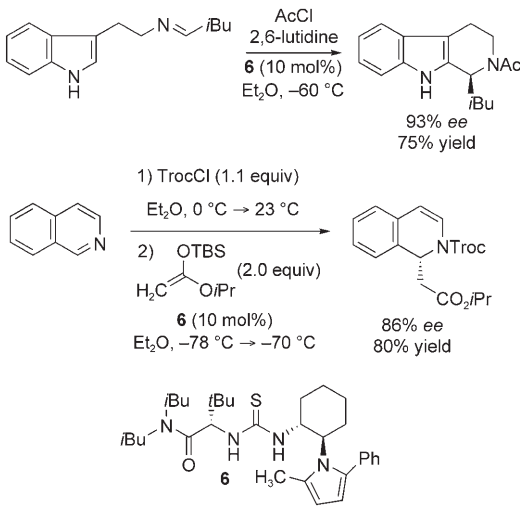



***Scheme 8.*** Carbon–carbon bond-forming reactions of *N*-Boc and *N*-Nosyl imines catalyzed by thioureas. Bn = benzyl, TBS = *tert*-butyldimethylsilyl.

reactions in the presence of thiourea **5**, which bears an acetamidocyclohexane substituent.[45] The function of this group is not well understood: the possibility that this catalyst operates by a cooperative bifunctional mechanism, activating both imine and nitroalkane nucleophile, was suggested. Recently, the scope of thiourea catalysis was extended to include *N*-(2-nitrobenzene)sulfonyl (nosyl, Ns) imines, useful substrates by virtue of their high electrophilicity and the ease of removal of the nosyl group.[46] In the presence of **1d** and stoichiometric quantities of diazabicyclo[2.2.2]octane (DABCO) as nucleophilic activator, *N*-nosyl imines undergo enantioselective aza-Baylis–Hillman reactions with methyl acrylate.

*N*-Acyliminium ions are among the most reactive imine derivatives, and methodology based upon these intermediates has been applied extensively to the synthesis of nitrogen-containing compounds.[47] Developing chiral catalysts capable of activating such species towards enantioselective addition reaction constitutes a significant challenge: in particular, their cationic nature should lead to diminished Lewis basicity relative to the neutral amide products of nucleophile addition. The highly enantioselective acyl-Pictet–Spengler reaction catalyzed by thiourea **6** not only represents the first example of asymmetric catalysis of this useful heterocycle-forming reaction, but also demonstrates for the first time that *N*-acyliminium ions can be activated by chiral H-bond donors (Scheme 9).[48] Although the mechanism by which these electron-poor intermediates are activated by the thiourea is unclear, early indications suggest that this catalysis concept may prove to be general. Catalyst **6** is also effective for Mannich-type reactions of acylisoquinolinium ions, providing access to enantioenriched dihydroisoquinoline products.[49] The use of the unsymmetrically substituted 2-methyl-5-phenylpyrrole group was crucial for obtaining high enantioselectivity in both the acyl-Pictet–Spengler and acyl-Mannich

 © 2006 Wiley-VCH Verlag GmbH & Co. KGaA, Weinheim 




***Scheme 9.*** Enantioselective, catalytic acyl-Pictet–Spengler and acyl-Mannich reactions. Troc = 2,2,2-trichloroethoxycarbonyl.

reactions. In the solid-state structure of this catalyst, the phenyl substituent is positioned to interact closely with substrate as it undergoes H-bonding to the acidic thiourea protons (Figure 2).

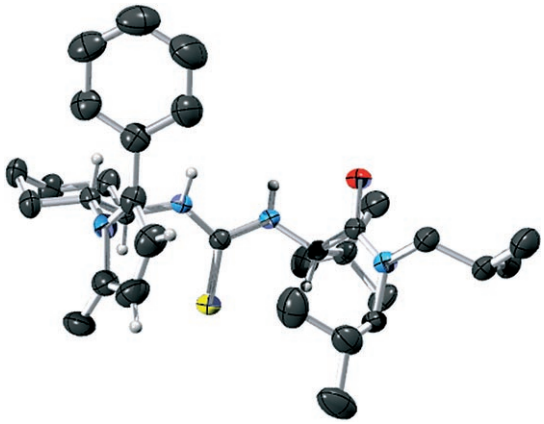


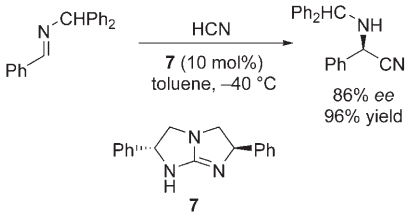
***Figure 2.*** X-ray crystal structure of thiourea catalyst **6**. C black, H white, N blue, O red, S yellow.

A number of features of the urea structure likely contribute to the ability of this catalyst class to effect enantioselective reactions of a range of nucleophilic and electrophilic partners. As was observed in solid-phase and solution-phase studies, the double H-bonding interaction enables ureas to interact with structurally diverse acceptors. Furthermore, ureas are both easily prepared and highly tunable. The choice of urea or thiourea provides a method for altering H-bond-donating ability, while variation of the nitrogen substituents permits a high degree of fine-tuning of catalyst steric and electronic properties. The urea structure also lends itself readily to the preparation of bifunctional catalysts, using amine coupling partners incorporating additional acidic or basic groups. This approach has resulted in further expansion of the scope of this catalyst class to include reactions of nitroalkenes, aldehydes, ketones, and carboxylic acid derivatives (see Section 3.3.4).

### *3.1.2. Chiral Guanidinium and Amidinium Ions*

Guanidinium and amidinium ions, structural relatives of ureas and thioureas, are also capable of participating in double H-bonding interactions. Indeed, the amino acid arginine, possessing a guanidinium functional group, frequently plays the role of double H-bond donor in biological systems. The positively charged nature of these species results in an increased hydrogen-bond donor ability relative to neutral ureas and thioureas, raising the possibility that guanidinium or amidinium catalysis might be more reactive general acid catalysts. Their positive charge also introduces potential problems for asymmetric catalysis, however, including the potential for nonproductive binding with the counteranion, and the possibility of specific, rather than general acid catalysis. That these problems are surmountable is evident from several recent examples of highly enantioselective carbon–carbon bond-forming reactions catalyzed by guanidinium and amidinium ions.

Pioneering work in this area was carried out by Corey and Grogan, who discovered that chiral bicyclic guanidine **7** mediates asymmetric Strecker reactions of *N*-diphenylmethyl imines (Scheme 10).[50] High yield and enantioselectivity were



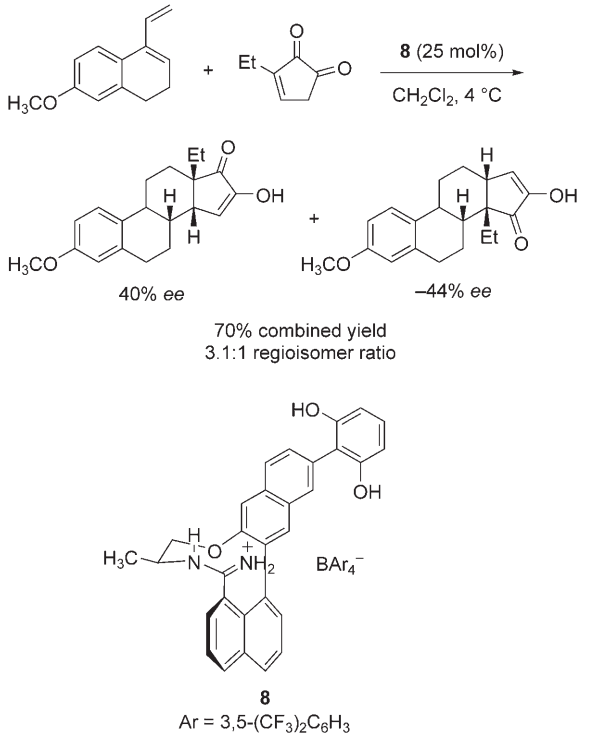

***Scheme 10.*** Bicyclic guanidine catalyst for asymmetric Strecker reactions.

obtained by using imines derived from a variety of aromatic and aliphatic aldehydes, with a strict requirement for the presence of the *N*-diphenylmethyl protecting group. Their mechanistic proposal involves the generation of a guanidinium cyanide species from **7** and hydrogen cyanide, followed by H-bond-accelerated attack of the cyanide ion on the imine electrophile, with π-stacking interactions between substrate and catalyst playing a key role. Although a single H-bond to the imine substrate was proposed, a double H-bond interaction is also possible. Support for the latter possibility is provided by the crystal structure of the benzoic acid complex of **7**, which reveals such an interaction.

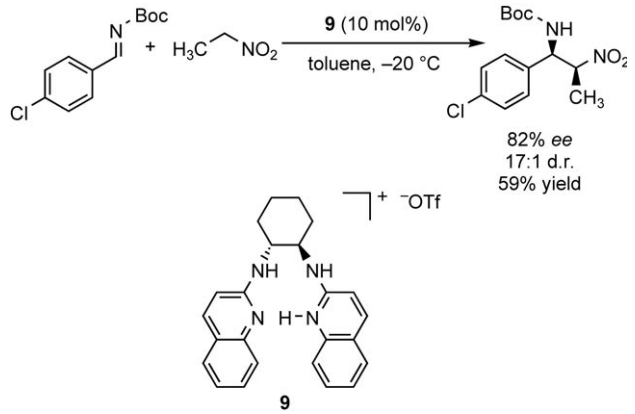
Göbel and co-workers have studied the acceleration of Diels–Alder cycloadditions by amidinium ions. Their initial studies, employing achiral amidinium ions derived from palmitic acid, highlighted the importance of non-coordinating counterions, such as the tetrakis(3,5-bis(trifluoromethyl)phenyl)borate ($BAr^{F}_{4}{}^{-}$) anion, for high catalyst activity.[51]


© 2006 Wiley-VCH Verlag GmbH & Co. KGaA, Weinheim

Modest enantioselectivity in the Diels–Alder reaction was achieved by using catalyst **8** (Scheme 11).[52] The possibility that the phenol groups of **8** participate in additional H-bonding contacts with the diketone electrophile was suggested. High enantioselectivity in an amidinium-catalyzed reaction was reported more recently by Johnston and co-workers.[53] Treatment of a diaminocyclohexane-derived bisamidine with trifluoromethanesulfonic acid (TfOH) gave rise to catalyst **9**, which is capable of effecting enantioselective nitro-Mannich reactions of *N*-Boc imines (Scheme 12).



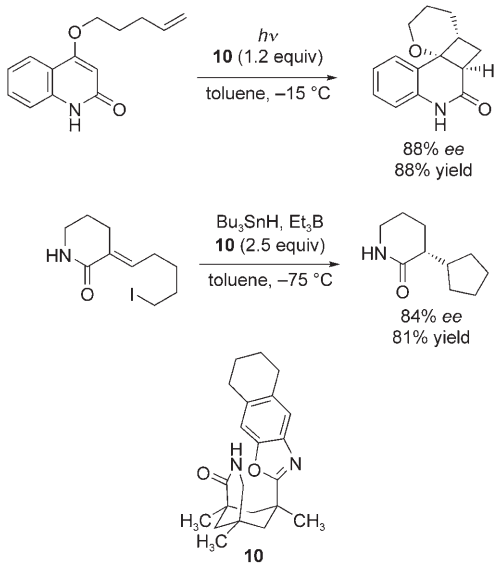

***Scheme 11.*** Diels–Alder reaction catalyzed by a chiral amidinium cation.




***Scheme 12.*** Amidinium-catalyzed asymmetric nitro-Mannich reaction.

### *3.1.3. Chiral Lactams*

Bach and co-workers have developed chiral lactam **10**, derived from Kemp's triacid, for several enantioselective transformations of prochiral secondary lactams. A strong double hydrogen bonding interaction between the two lactam moieties, in which each functions simultaneously as a donor and acceptor, facilitates the tight association of the auxiliary and substrate. Alternating donor–acceptor relationships of this type are reminiscent of those in nucleotide base pairs and are a common property of the strong hydrogen bonding motifs that serve as the basis of complex supramolecular structures.[12] Among the enantioselective reactions mediated by **10** are asymmetric photochemical [2+2][54] and [4+2][55] reactions, Norrish–Yang photocyclizations,[56] 6π photocyclizations,[57] and asymmetric radical cyclizations (Scheme 13).[58] Although the systems described above require the use of stoichiometric quantities of the chiral promoter, they currently represent state-of-the-art methods for effecting transformations of this type, and may point the way towards the development of enantioselective and catalytic variants.[59]




***Scheme 13.*** Enantioselective transformations mediated by chiral lactam **10**.

### *3.2. Catalysis by Single Hydrogen-Bond Donation*

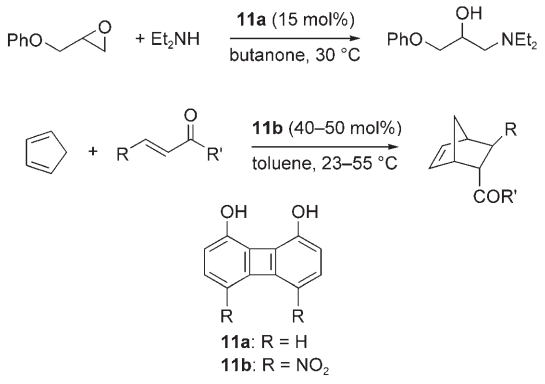
Highly enantioselective transformations involving the donation of a single H-bond as the sole mechanism of activation are considerably less common than those employing either double H-bonding interactions or bifunctional catalysis. The challenge associated with the development of chiral single H-bond donors likely stems from the moderate strength and directionality of most isolated H-bonds, which present difficulties for achieving a suitably rigid catalyst–substrate complex. As discussed in the following section,

 © 2006 Wiley-VCH Verlag GmbH & Co. KGaA, Weinheim 

compelling structural evidence exists for a single H-bonding mechanism in catalysis by TADDOL derivatives, despite the fact that these are in fact chiral diols. The mechanism of general acid catalysis by chiral biphenols is less certain at this stage, but that chemistry is included in this section because of the likely relationship to diol catalysts. For both TADDOL and BINOL derivatives, transition structure organization is probably achieved by means of an intramolecular H-bonding interaction, which defines the orientation and increases the acidity of the O–H bond, and by the encompassing of this hydroxy group by aromatic moieties, which likely further define the position of bound substrate through combinations of steric and electronic interactions. These features may be useful design elements for the development of new catalysts: indeed, structural similarities exist between TADDOL derivatives and chiral phosphoric acids, the other existing class of single H-bond donors capable of highly enantioselective catalysis.

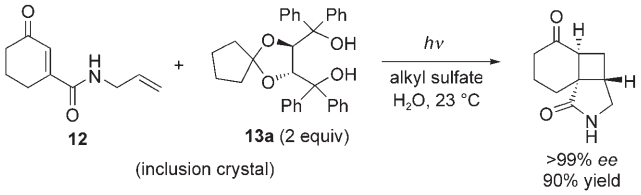
### 3.2.1. Diols, Biphenols, and Hydroxy Acids

Chiral diols and biphenols have long occupied a position of importance in the field of asymmetric catalysis: 1,1′-bi-2-naphthol (BINOL) and α,α,α′,α′-tetraaryl-1,3-dioxolane-4,5-dimethanol (TADDOL) derivatives are extraordinarily useful ligands for enantioselective Lewis acid mediated processes.[60] In comparison to the well-studied application of chiral diols as ligands, their emergence as effective general acid asymmetric catalysts is very recent. Suggestions that catalysis of this type was possible appeared in the literature as early as 1985: the biphenylenediol-accelerated epoxide aminolysis and Diels–Alder reactions were among the first examples of catalysis by well-defined hydrogen-bond donors (Scheme 14).[61] These findings, in turn, found their basis in studies by Hine and co-workers, who observed that biphenylenediols form doubly H-bonded structures with carbonyl compounds in the solid state and in solution.[62] Although these foundational studies suggest that chiral diols and biphenols may act as double H-bond donors, recent investigations of enantioselective variants suggest that, at least in certain cases, mechanisms involving single H-bond activation may be operative.



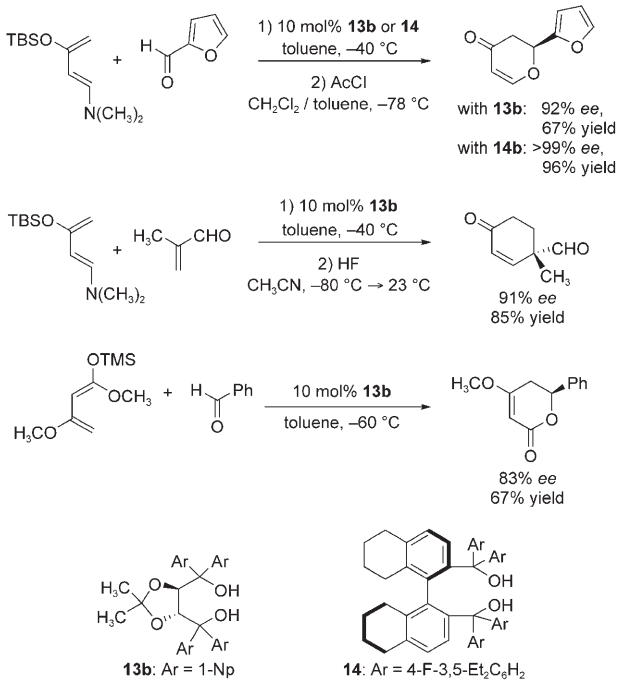

*Scheme 14.* Biphenylenediol-accelerated epoxide opening and cycloaddition reactions.

Pioneering research in the area of chiral recognition by TADDOL derivatives was carried out by Toda and co-workers. They discovered that these compounds are efficient resolving agents for a variety of basic species, such as amines, alcohols, carbonyl compounds, and sulfoxides, through the formation of H-bonded inclusion compounds.[60,63] These observations provided the impetus for the subsequent development of enantioselective photochemical reactions employing inclusion complexes of prochiral guest molecules with TADDOL hosts.[64] For example, irradiation of the cocrystal of diene **12** and TADDOL **13a** results in highly enantioselective [2+2] cycloaddition (Scheme 15).[65] Other solid-state enantioselective photochemical reactions mediated by chiral TADDOL derivatives include intermolecular [2+2] cycloadditions, Norrish type II reactions, and Ninomiya-type electrocyclizations.




*Scheme 15.* Enantioselective solid-state photochemical [2+2] cycloaddition.

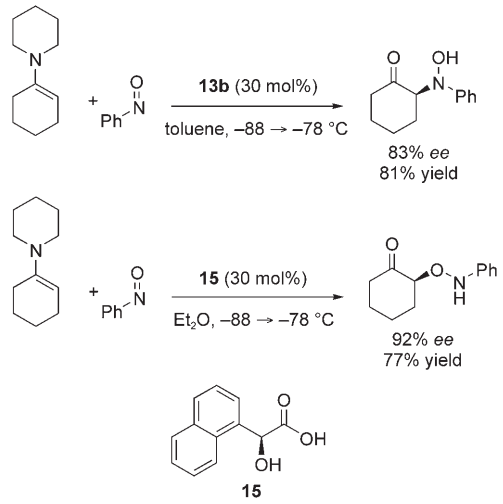
The report by Rawal and co-workers that TADDOL derivative **13b** catalyzes asymmetric hetero-Diels–Alder reactions of aminodienes with aromatic and aliphatic aldehydes marks the first successful application of chiral diols as enantioselective H-bonding catalysts (Scheme 16).[66] These




*Scheme 16.* Enantioselective cycloadditions mediated by TADDOL derivatives. Np = naphthyl.

 © 2006 Wiley-VCH Verlag GmbH & Co. KGaA, Weinheim 

investigations arose from observations that hetero-Diels–Alder reactions are accelerated in H-bond-donating solvents such as 2-butanol and chloroform.[67] Subsequent research has extended this mode of catalysis to carbon Diels–Alder reactions of aminodienes[68] and hetero-Diels–Alder reactions of Brassard's diene with aldehydes.[69] Modifications to the chiral diol backbone structure have been investigated by Yamamoto, Rawal, and co-workers. Axially chiral diol **14** provides high yields and selectivites for hetero-Diels–Alder reactions of a wide range of aldehyde substrates.[70] Momiyama and Yamamoto recently demonstrated that electrophiles other than aldehydes may be activated towards enantioselective transformations by **13b**: the asymmetric *N*-nitroso aldol reaction of enamines presumably involves H-bond activation of nitrosobenzene (Scheme 17).[71]




***Scheme 17.*** *N*- and *O*-nitrosoaldol reactions of enamines.

Crystallographic studies have been useful in elucidating the structural features of TADDOL that enable it to function effectively as a chiral catalyst. Structures of a large number of TADDOL derivatives have been solved: with very few exceptions, these structures feature an intramolecular H-bond between the two hydroxy groups. As a result of this interaction, the proton not engaged in H-bonding is both acidified and orientationally defined. Crystal structures of inclusion complexes of chiral carbonyl and imino acceptors are instructive: in each case, the "free" TADDOL hydroxy proton engages in a single H-bond with the acceptor.[62] By analogy, reactions involving this catalyst class also likely involve activation by means of a single H-bonding interaction. The cocrystal structure of an axially chiral diol with benzaldehyde is consistent with this hypothesis (Figure 3).[70]

The axial chirality characteristic of BINOL finds frequent application in the design of asymmetric catalysts. The ability of this species to function as a chiral H-bond donor was discovered by McDougal and Schaus in the context of enantioselective Morita–Baylis–Hillman reactions (Scheme 18).[72] The observation that acidic additives such as phenols accelerate Morita–Baylis–Hillman reactions constitutes important precedent for this work.[73] Optimization of

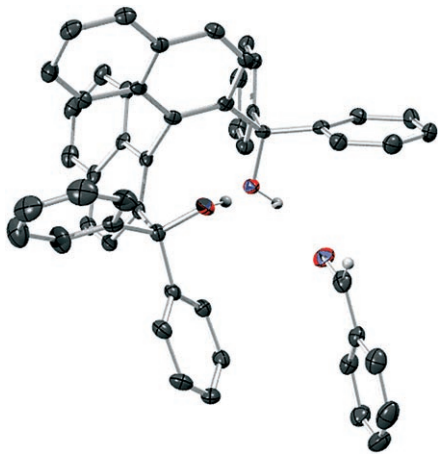
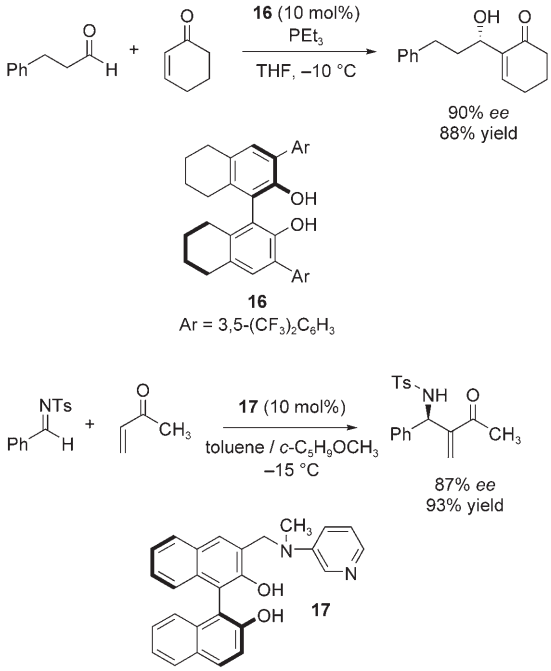


***Figure 3.*** Cocrystal structure of an axially chiral diol catalyst with benzaldehyde. C black, H gray, O red.



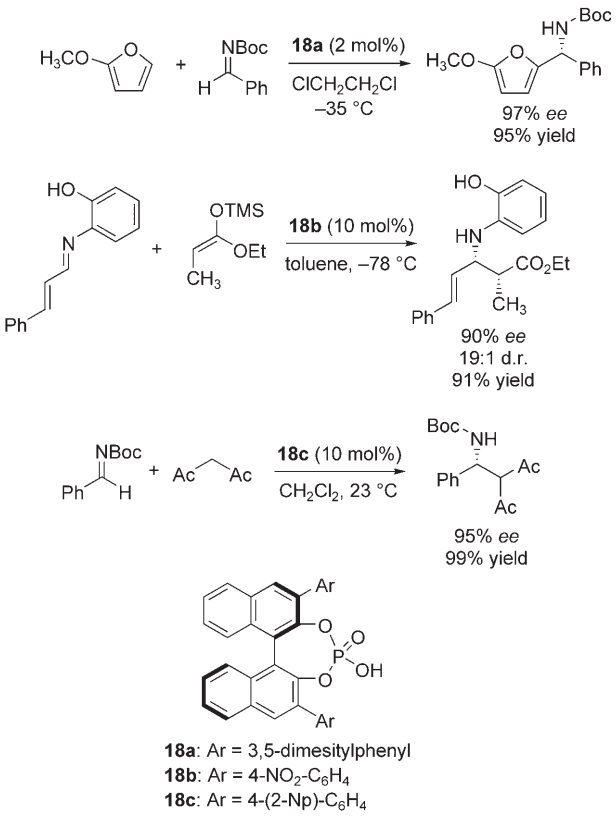

***Scheme 18.*** Morita–Baylis–Hillman and aza-Baylis–Hillman reactions catalyzed by BINOL derivatives. Ts = *para*-toluenesulfonyl.

the binaphthol structure revealed that arene-substituted octahydro(BINOL) derivatives such as **16** afforded high enantioselectivity for reactions of a range of aldehyde partners with 2-cyclohexenone in the presence of triethylphosphine. Whether the catalyst serves as a single or double H-bond donor in these reactions is not clear: methylation of one phenol hydroxy group resulted in low activity and complete loss of enantioselectivity, but this observation could be consistent with either a double H-bonding mechanism or a mechanism similar to TADDOL catalysis involving an intramolecular H-bond.[7b,e] The identity of the acceptor is also uncertain. Activation of the enone to nucleophilic attack by phosphine, generating a catalyst-bound enolate, H-bond-

 © 2006 Wiley-VCH Verlag GmbH & Co. KGaA, Weinheim 

ing to the aldehyde to accelerate enolate attack, or rate-limiting elimination of phosphonium from a H-bonded zwitterionic intermediate may be invoked. Enantioselective aza-Baylis–Hillman reactions catalyzed by BINOL derivative **17** have also been reported.[74] This catalyst appears to play a bifunctional role, with the phenol hydroxy protons activating the electrophile and the pyridyl group functioning as a nucleophile to generate the required enolate. That the poorly nucleophilic 3-aminopyridine is effective in this context is somewhat surprising, but catalyst modification studies support the bifunctional mechanism hypothesis. Further catalyst variations also suggest that a single H-bond is donated by the 2′-hydroxy group.

In their investigations of nitrosoaldol reactions of enamines, Momiyama and Yamamoto identified a new class of alcohol-based H-bonding catalysts.[71] While TADDOL derivatives were suitable for *N*-nitroso aldol reactions, *O*-nitroso aldol reactions could be achieved by using 1-naphthyl glycolic acid **15** as the catalyst (Scheme 17). Questions remain regarding the mechanism of this reaction, but the possibility that an intramolecular H-bond plays a role in the structure and function of the chiral hydroxy acid catalyst was advanced. This result suggests that the placement of an acidic group in proximity to an alcohol may be a general chiral catalyst design, in which p$K_a$ as well as steric properties may be varied systematically.




***Scheme 19.*** BINOL-based chiral phosphoric acids.

### *3.2.2. Chiral Phosphoric Acid Derivatives*

Axially chiral phosphoric acids derived from binaphthols have well-established utility in molecular recognition applications: their diastereoselective cocrystallization with Cinchona alkaloids served for several years as the primary method for the preparation of enantioenriched BINOLs.[75] Enantioselective Mannich reactions of imines catalyzed by these species were reported independently by two research groups in 2004 (Scheme 19).[76] Activation of imines by phosphoric acids also forms the basis for aza-Friedel–Crafts reactions of furans, amidoalkylations of α-diazocarbonyl compounds, asymmetric hydrophosphonylations of aldimines, and transfer hydrogenations of ketoimines.[77] In each of these reactions, the presence of aryl substituents at the 3- and 3′-positions of the catalyst framework was crucial for high enantioselectivity, and subtle variations of the electronic and steric properties of these aryl groups had pronounced effects. These observations, as well as the apparent limitation of this chemistry to substrates derived from aromatic or α,β-unsaturated aldehydes, suggest that these aryl groups play an important role in orienting the bound substrate through π–π interactions.

## *3.3. Bifunctional Hydrogen-Bond Donor Catalysts*

The development of chiral catalysts capable of simultaneous activation of nucleophile and electrophile is an active and fruitful area of investigation. Much of the pioneering research in this field has involved Lewis acids equipped with additional Brønsted or Lewis basic functionality;[78] the work of Shibasaki and co-workers demonstrates the impressive generality of this concept for catalyst design. Chiral bifunctional agents capable of H-bonding have been available to chemists for many years, and pioneering reports of proline- and Cinchona alkaloid catalyzed reactions (Sections 3.3.1 and 3.3.2) hinted at their potential utility in catalysis. Recent years have witnessed the maturation of dual activation strategies involving H-bonding for electrophile activation. Progress in this area has been accomplished through the discovery of new applications for existing, naturally occurring catalysts, as well as through the design and synthesis of novel bifunctional entities based on known hydrogen-bond-donor motifs.

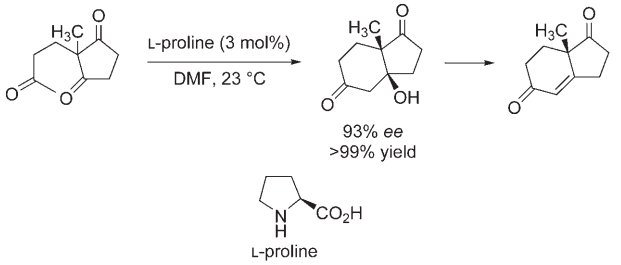
### *3.3.1. Proline and Proline Analogues*

α-Amino acids are among the simplest possible chiral bifunctional catalysts, bearing both an acidic carboxyl group and a basic amine moiety. No class of chiral catalysts rivals the amino acids in terms of accessibility: the 20 naturally occurring amino acids are commodity chemicals, and many unnatural analogues are commercially available in enantioenriched form. In retrospect, it is surprising that the opportunities for organocatalysis offered by the amino acids were, for the most part, ignored by organic chemists until recently.[79] Over the last five years, a multitude of useful enantioselective methodologies have been developed by using the cyclic amino acid proline as a catalyst. These studies highlight the diversity and scope of chemistry that is made possible by the well-

 © 2006 Wiley-VCH Verlag GmbH & Co. KGaA, Weinheim 

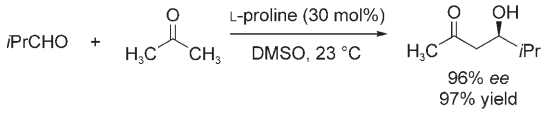
defined positioning of a H-bond donor and an amino group in a chiral framework.

The ability of proline to function as a chiral organocatalyst was discovered independently by Hajos and Parrish at Hoffman-La-Roche and Eder, Sauer, and Wiechert at Schering AG in the 1970s.[80] These groups demonstrated that triketones undergo highly enantioselective aldol cyclization in the presence of proline, giving rise to chiral bicyclic enones, useful starting materials for the synthesis of steroid structures (Scheme 20). Although this methodology was applied in a




***Scheme 20.*** Proline-catalyzed aldol cyclization.

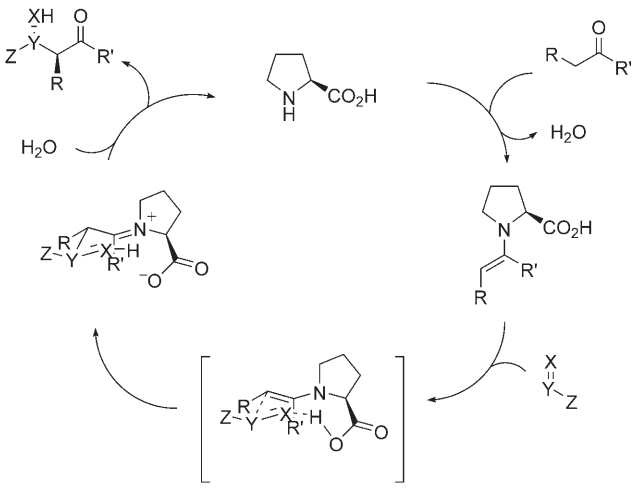
number of natural product total syntheses,[81] the potential generality of this catalyst system remained unappreciated until 2000, when List, Lerner, and Barbas reported the discovery of proline-catalyzed direct, asymmetric aldol reactions (Scheme 21).[82] Their report not only delineated a




***Scheme 21.*** Proline-catalyzed, intermolecular aldol addition.

remarkably simple solution to one of the most intensively studied problems in catalysis, but also marked a new beginning for the study of proline-catalyzed enantioselective reactions. Since 2000, research by a number of groups has demonstrated the tremendous generality of proline catalysis for the generation of carbon–carbon, carbon–nitrogen, carbon–oxygen, and carbon–halogen bonds α to ketone or aldehyde substrates. As a number of recent review articles summarize these advances,[83] the discussion herein will be confined to the mechanistic evidence for H-bonding in proline catalysis, and to recent novel proline derivatives designed to modulate the catalyst's H-bonding ability.

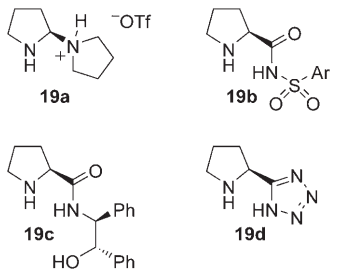
The now widely accepted mechanistic hypothesis for proline-catalyzed reactions is shown in Scheme 22. Here, the secondary amine group of the catalyst undergoes a condensation reaction with the ketone substrate, resulting in the formation of a nucleophilic enamine intermediate. H-bonding to the carboxylic acid group serves to activate the electrophile towards attack by the enamine. The high enantioselectivity observed for reactions of a wide range of electrophile and nucleophile partners may be attributed to the highly ordered nature of this transition state assembly. Although such a mechanistic scheme was proposed by Jung in 1976,[84]




***Scheme 22.*** Proposed mechanism for proline-catalyzed transformations.

experimental support for this proposal has emerged only recently. Proline-catalyzed asymmetric aldol reactions exhibit first-order kinetic dependence upon catalyst concentration, and a linear relationship between the enantiomeric excess of catalyst and that of product is observed, indicating that the transition state incorporates a single proline molecule.[85] Catalyst structure-variation studies demonstrate that both the secondary amine and the carboxylic acid functional groups are crucial for high yield and selectivity. The mechanism of proline-catalyzed reactions has also been investigated by using computational methods.[86] Houk and coworkers applied density functional theory methods (B3LYP/6-31G(d)) to lend support to the bifunctional catalysis mechanism, calculating that H-bonding activation of the aldehyde electrophile may lower the activation barrier for aldol addition by as much as 17 kcal mol$^{-1}$.

Building upon the practical advantages associated with the use of proline as a bifunctional catalyst, considerable effort has been dedicated to the development of unnatural analogues that might exhibit improved reactivity, selectivity, or scope. In this regard, tuning of the H-bond donating ability




of the catalyst by variation of the acidic moiety has proven particularly fruitful. Ammonium salts such as **19a**, prepared by treatment of a chiral diamine with an equimolar quantity of trifluoromethanesulfonic acid, mediate enantioselective aldol and Mannich reactions.[87] The positively charged ammonium group is proposed to play the role of H-bond

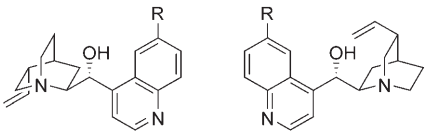
 © 2006 Wiley-VCH Verlag GmbH & Co. KGaA, Weinheim 

donor in these systems. Other functional groups bearing acidic N–H bonds, including secondary amides, sulfonamides, and acylsulfonamides, have been constructed from the proline framework.[88] In general, these modifications have provided only modest improvement upon the results obtained using proline itself. However, Wu and co-workers found that secondary amide **19c** derived from proline and a chiral amino alcohol provides systematically higher yields and selectivities than proline for direct aldol reactions of acetone with a variety of aromatic and aliphatic aldehydes.[89] Computational studies suggest that the aldehyde is activated by simultaneous H-bonding with the hydroxy and amido protons. This double H-bonding interaction, as well as the ability to vary the stereochemistry and steric properties of the H-bond donor, likely contribute to the effectiveness of this catalyst class. The replacement of proline's carboxylic acid group with tetrazole, a frequently employed carboxylic acid mimic in medicinal chemistry, has also afforded promising results.[90] The improved activity of catalyst **19d** in *O*-nitroso aldol reactions of ketones, Mannich reactions of imino esters, and aldol reactions of chloral may be ascribed to its altered $pK_a$ or increased solubility in comparison to proline.

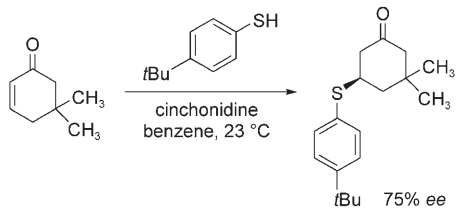
Detailed studies of proline-catalyzed oxygenation and amination reactions have led to the proposal that catalyst modification may be involved in the mechanism of these transformations.[91] The observation by Blackmond and co-workers of autoinductive rate behavior and amplification of enantiomeric excess over time provides compelling evidence that a more active catalyst is generated by the interaction of proline with the α-hydroxylamino or -hydrazinocarbonyl products.

### 3.3.2. Cinchona Alkaloids and Derivatives

Natural products isolated from the bark of evergreen trees belonging to the Cinchona and Remijia species have been applied extensively in asymmetric synthesis, as resolving agents, ligands in metal-mediated processes, and organocatalysts.[92] In addition to basic amine functionality, several of these alkaloids bear acidic hydroxy groups. The possibility




that these species could act as bifunctional catalysts was suggested by Wynberg and Hiemstra in 1981, in the context of enantioselective conjugate additions of aromatic thiols to cycloalkenones (Scheme 23).[93] They observed that alkaloids that possess a free hydroxy group, such as cinchonidine, cinchonine, quinine, and quinidine, promoted the conjugate addition with highest reaction rates and enantioselectivies. This led to the proposal that the catalyst serves to activate both the nucleophile, by general base catalysis, and the enone,

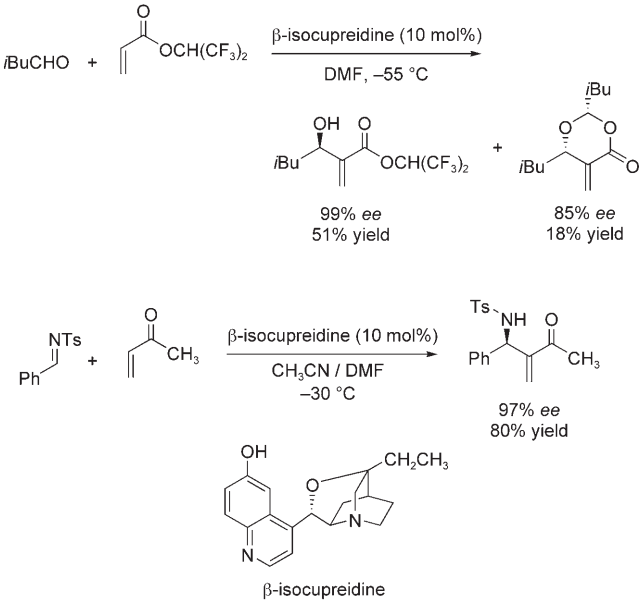



***Scheme 23.*** Cinchonidine-catalyzed thiol conjugate additions.

by H-bonding. Recently, Deng and co-workers reported a highly enantioselective variant of this transformation employing the dimeric ligands developed by Sharpless for asymmetric osmium-catalyzed dihydroxylation of alkenes.[94] The fact that high enantioselectity is achieved by using $(DHQD)_2PYR$, which lacks a free hydroxy group, suggests that this catalyst may operate by a different mechanism from that proposed by Wynberg.

The basic tertiary amine group present in the quinuclidine core of the Cinchona alkaloids has proven highly versatile in the context of asymmetric nucleophilic catalysts. Hatakeyama and co-workers discovered that β-isocupreidine, which bears an acidic phenolic hydroxy group, catalyzes enantioselective Baylis–Hillman reactions of hexafluoroisopropyl acrylate with aromatic and aliphatic aldehydes (Scheme 24).[95] Low enantioselectivity was obtained by using *O*-methyl β-isocupreidine as catalyst. The proposed mechanism involves a reversible aldol-type addition followed by enantioselectivity-determining elimination, in which a key H-bond between catalyst and intermediate is proposed. This system has been extended to aza-Baylis–Hillman reactions of *N*-sulfonyl and *N*-phosphinoyl imines.[96] As was observed with aldehyde electrophiles, the presence of the phenol group was crucial for effective catalysis.

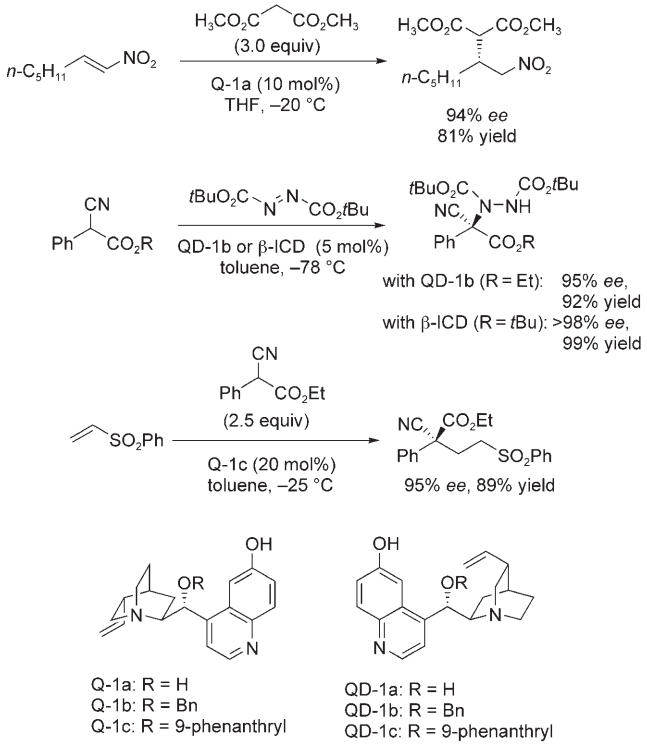
Semi-synthetic catalysts bearing the phenol and quinuclidine moeties characteristic of β-isocupreidine have been




***Scheme 24.*** Baylis–Hillman-type reactions catalyzed by β-isocupreidine.

 © 2006 Wiley-VCH Verlag GmbH & Co. KGaA, Weinheim 

developed by Deng and co-workers. These bifunctional species (QD-1a–c) and their pseudoenantiomers (Q-1a–c), which are available in one- or two-step procedures from quinidine and quinine, mediate a number of enantioselective nucleophile–electrophile reactions. Studies of the conjugate addition of β-dicarbonyl compounds to nitroalkenes catalyzed by QD-1a and Q-1a revealed that the phenolic groups were necessary for high yield and enantioselectivity, suggesting that H-bonding activation of the electrophile plays a key role (Scheme 25).[97] These results have been extended to

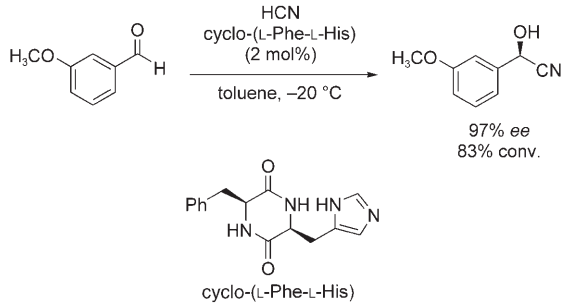



***Scheme 25.*** Cinchona alkaloid based bifunctional catalysts.

include conjugate additions of substituted β-dicarbonyl compounds, nitroesters, and cyanoesters to nitroalkenes, in which adjacent quaternary and tertiary stereocenters are generated simultaneously, as well as Michael additions to vinyl sulfones.[98] The enantioselective amination of α-cyanoacetates and β-dicarbonyl compounds with diazodicarboxylates is catalyzed by β-isocupreidine, QD-1b, Q-1b, cinchonine, and cinchonidine.[99] In these studies, results obtained with catalysts lacking Brønsted acid functionality were not described. The fact that the mechanistically related enantioselective Mannich reaction of α-cyanoacetates with imino esters is catalyzed by $(DHQD)_2PYR$, which lacks a free H-bond donor group, suggests that H-bond donation may be effected by the catalyst in its protonated form.[100]

### 3.3.3. *Oligopeptides, Catalytic Antibodies, and RNA*

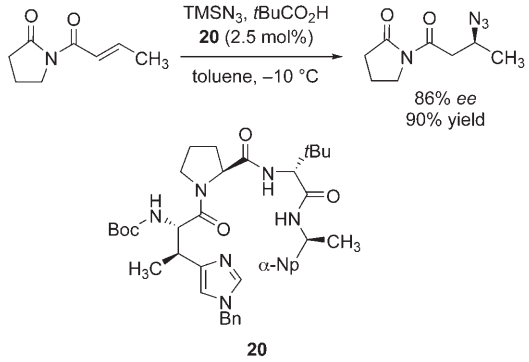
Oligopeptide structures are an attractive platform for catalyst development, particularly in light of the potential structural and functional diversity that may be accessed from commercially available bulding blocks using reliable amide coupling chemistry. The hydrocyanation of aldehydes developed by Inoue in 1981 was among the first-reported highly enantioselective oligopeptide-catalyzed reactions.[101] The diketopiperazine cyclo(L-phenylalanine-L-histidine) was found to mediate asymmetric hydrocyanation of a variety of aldehydes, with particularly high enantiomeric excess observed using electron-rich benzaldehyde substrates (Scheme 26). Despite the apparent simplicity of both the




***Scheme 26.*** Cyclo(L-phenylalanine-L-histidine)-catalyzed aldehyde hydrocyanation.

catalyst structure and the reaction taking place, many unanswered questions remain regarding the mechanism of this process. A second-order kinetic dependence upon catalyst concentration was observed, pointing to a dual activation mechanism involving two catalyst molecules in the rate-determing step.[102] Activation of the aldehyde electrophile by a H-bond, donated either from the secondary amide group or a protonated histidine moiety, has been proposed.[103]

Miller and co-workers have pursued a strategy for oligopeptide catalyst discovery based upon advances in the understanding of peptide structure and in high-throughput preparation and screening of catalyst candidates. A general design incorporating basic moieties into a β-turn structural motif has yielded catalysts for highly enantioselective acylation[104] and phosphorylation[105] of alcohols, as well as conjugate addition of hydrazoic acid to α,β-unsaturated imides (Scheme 27).[106] This latter transformation almost certainly involves activation of the nucleophile by general

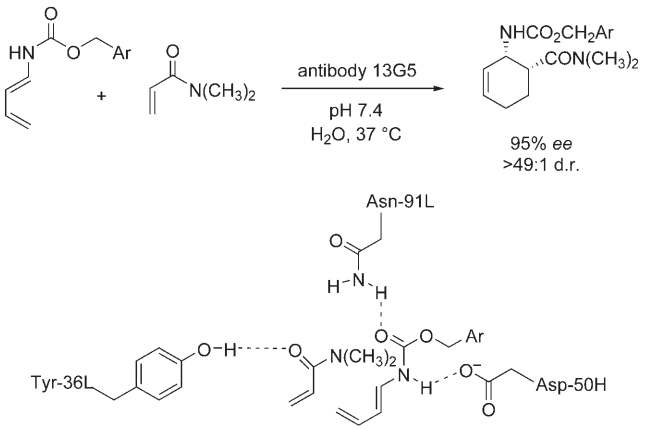



***Scheme 27.*** Peptide-catalyzed enantioselective conjugate addition of hydrazoic acid.

 © 2006 Wiley-VCH Verlag GmbH & Co. KGaA, Weinheim 

base catalysis, but the mechanism by which the electrophile is activated is less well understood. H-bonding to the imide carbonyl groups by one of the several acidic groups present in the catalyst is a possibility;[107] indeed, a thiourea-catalyzed Michael addition to *N*-acylpyrrolidinones has been reported,[108] and Diels–Alder reactions of similar α,β-unsaturated oxazolidinone imides are accelerated by achiral H-bond donors.[39]

The catalytic antibody approach to the development of complex polypeptide catalysts takes advantage of the mechanism of action of the immune system of living organisms, and the postulate that enzymes accelerate reactions by transition-state binding. A transition-state analogue, or hapten, for the reaction of interest, is designed, prepared, and used to elicit an immune response. The resulting antibodies are isolated and their ability to function as catalysts is tested. This approach has been used to generate antibodies capable of mediating a wide variety of transformations, including enantioselective processes.[109] Structural and mechanistic studies have provided insight into the basis for catalysis in a number of these systems: like enzymes, catalytic antibodies are multifunctional entities, and H-bonding often plays a key role in electrophile activation. The *exo*-Diels–Alderase antibody discovered by Janda and co-workers provides an illustrative example (Scheme 28).[110] While a number of

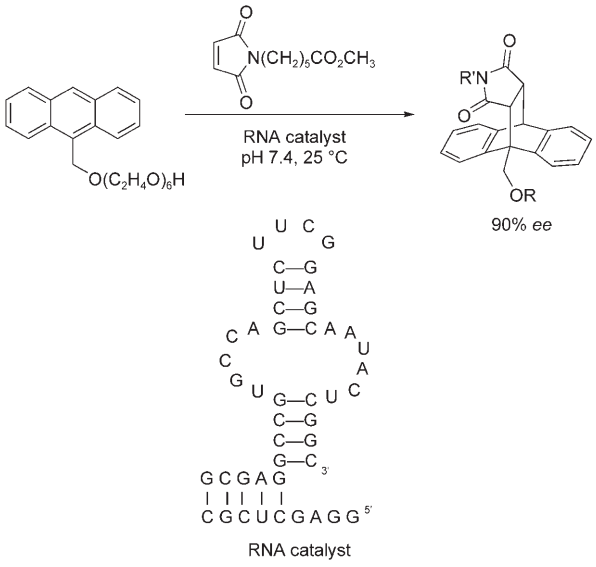



***Scheme 28.*** Antibody-catalyzed enantioselective, *exo*-selective Diels–Alder cycloaddition.

chiral Diels–Alder catalysts have been devised, these systems usually do not override the inherent substrate-controlled preference for formation of the *endo* diastereomer. In this respect, the ability of the catalytic antibody to selectively generate the *exo* diastereomer in high enantiomeric excess is noteworthy. Crystal structures of the antibody, both in the presence and the absence of inhibitor, provide compelling suggestions regarding the origins of catalytic activity and selectivity.[111] Analysis of these structures, complemented by computational studies, led to the proposal that the phenol group of a tyrosine residue serves to activate the *N*,*N*-dimethylacrylamide dienophile through H-bonding. The (acylamino)diene is activated by general base catalysis through an interaction between its acidic N–H bond and the carboxylate group of an aspartic acid moiety. Computational docking studies support the notion that these H-bonds, which are crucial for catalysis, cannot be formed upon binding of the putative transition states leading to the formation of *endo* products.

Oligonucleotide structures present interesting opportunities for catalyst discovery, due in particular to the possibility of evaluating large numbers of potential catalysts. The unique ability of DNA and RNA to function as templates for their own synthesis by polymerase enzymes renders them suitable for directed evolution approaches, which involve repeated cycles of selection for molecules possessing a property of interest, followed by amplification and diversification. However, as discussed in Section 2.4, the functional groups present in oligonucleotides are limited, in terms of both structure and $pK_a$, in comparison to oligopeptides. It might be anticipated that the scope of oligonucleotide-mediated chemistry would be correspondingly limited. In this regard, the report by Jäschke and co-workers of a synthetic RNA catalyst for the Diels–Alder reaction constitutes an important advance.[112] This catalyst was discovered using directed evolution, in which anthracene-linked random RNA sequences were selected, by streptavidin affinity chromatography, based upon their ability to undergo cycloaddition with a biotinylated maleimide. Ten rounds of selection yielded 35 diverse, catalytically active RNA sequences, the majority of which shared an 11-nucleotide consensus sequence. Synthesis of a minimal 49-mer incorporating this consensus sequence demonstrated that it is capable of acting as a multiple-turnover catalyst for the Diels–Alder reaction of hydroxymethylanthracenes with *N*-alkylmaleimides (Scheme 29). The cycloaddition product was obtained in 90% *ee*, a surprising result given that the selection strategy employed was based solely upon catalytic activity, not enantioselectivity.

Crystal structures of the Diels–Alder ribozyme, both alone and in complex with cycloaddition product, have recently been solved.[113] The oligonucleotide adopts a com-



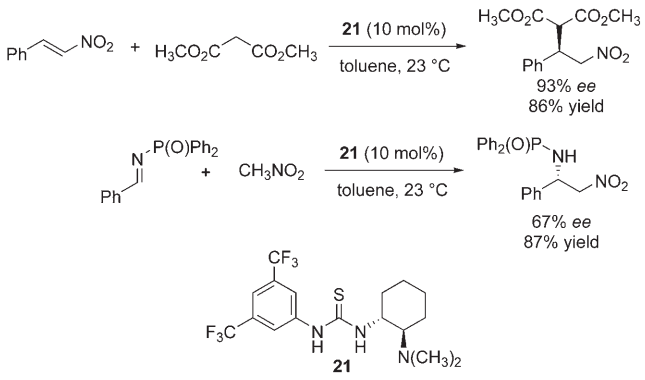

***Scheme 29.*** Enantioselective Diels–Alder reaction catalyzed by an evolved oligoribonucleotide.

 © 2006 Wiley-VCH Verlag GmbH & Co. KGaA, Weinheim 

plex and rigid three-dimensional architecture, including a well-defined binding pocket that accommodates the two substrate molecules in proximity through a number of hydrophobic and π-stacking contacts. Both the increase in effective molarity of the cycloaddition partners and the ability of the RNA active site to preferentially stabilize the transition structure play dominant roles in catalysis. Activation of the maleimide dienophile is accomplished by H-bond donation from the exocyclic amino group of guanine-24 and the 2′-hydroxy group of uracil-42, both elements of the consensus sequence required for activity.

### 3.3.4. *Bifunctional Thiourea Derivatives*

Thioureas bearing additional acidic or basic functional groups are readily accessed, due to the high functional group tolerance and reliability of the isothiocyanate coupling reaction used to prepare these species. The resulting bifunctional thioureas catalyze enantioselective reactions of a number of structurally diverse electrophiles, reflecting the generality of the double H-bond as a mode of activation. Takemoto and co-workers reported that thiourea **21**, which incorporates a basic dimethylamino group, catalyzes enantioselective Michael additions of malonates to nitroolefins (Scheme 30).[114] Reaction kinetic and catalyst modification

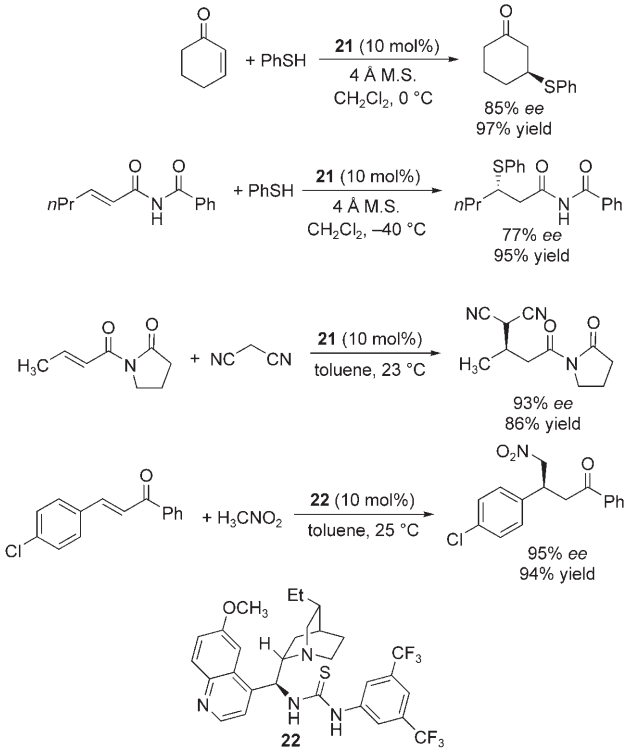



***Scheme 30.*** Michael and nitro-Mannich reactions mediated by bifunctional thiourea.

studies are consistent with the mechanistic proposal that the catalyst serves to activate both nucleophile, by general base catalysis, and electrophile, by H-bonding to the nitro group. This reactivity has been extended to include diastereo- and enantioselective additions of substituted ketoesters, and double Michael additions of γ,δ-unsaturated β-ketoesters.[115]

Recently, the scope of the Takemoto catalyst has been expanded to encompass reactions in which both the nucleophile and electrophile differ substantially from those for which it was initially developed. Reactions of *N*-phosphinoyl imines with nitroalkanes are catalyzed by **21**, affording the aza-Henry products with modest enantioselectivity.[116] That the nitroalkane plays the role of nucleophile, rather than electrophile, suggests that the mechanism of stereoinduction in this case may differ from that operating in the Michael addition chemistry.

Chen and co-workers reported that **21** catalyzes enantioselective conjugate additions of arenethiols to 2-cycloalkenones and α,β-unsaturated *N*-benzoyl imides, demonstrating that carbonyl groups at both the ketone and acid oxidation states are activated by this species.[117] Other recent results suggest that bifunctional thiourea catalysts may be of considerable utility for conjugate addition to carbonyl compounds (Scheme 31). Michael additions of malononitrile to α,β-

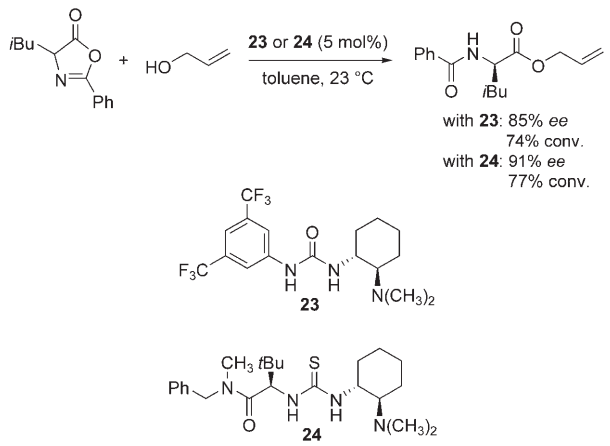



***Scheme 31.*** Enantioselective conjugate additions catalyzed by bifunctional thioureas.

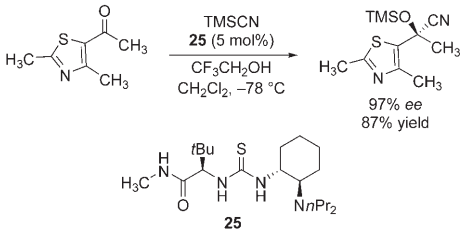
unsaturated imides catalyzed by **21** were reported by Takemoto and co-workers.[108] An interesting new epiquinine-derived thiourea **22** incorporating basic functionality mediates asymmetric conjugate additions of nitromethane to chalcones.[118] The analogous quinine-derived catalyst was inactive, highlighting the importance of correct relative orientation of acidic and basic functional groups.

Berkessel and co-workers have also employed bifunctional ureas for activation of carbonyl compounds, but in quite a different context: in the presence of urea **23** and allyl alcohol, chiral racemic azlactones undergo dynamic kinetic resolution, giving rise to protected, enantioenriched α-amino acid derivatives (Scheme 32).[119] In the proposed mechanism for this transformation, the catalyst performs the general functions of a serine protease: the carbonyl group is activated by a double H-bond, while allyl alcohol is activated by general base catalysis. An improvement in selectivity was achieved with thiourea **24**, incorporating the *tert*-leucine amide structural motif used frequently by our group. Indeed, a similar catalyst (**25**) was discovered independently by our group for the silylcyanation of ketones (Scheme 33).[120] Fine-tuning of

 © 2006 Wiley-VCH Verlag GmbH & Co. KGaA, Weinheim 



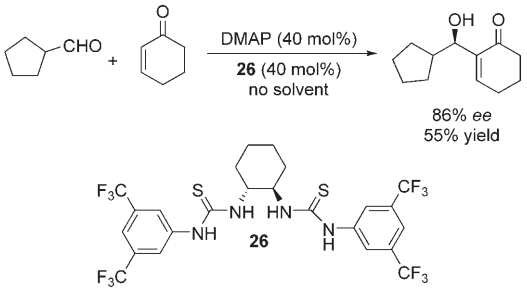

***Scheme 32.*** Dynamic kinetic resolution of azlactones.




***Scheme 33.*** Enantioselective, thiourea-catalyzed cyanosilylation of ketones.

both the amide substituent and the di-*n*-propylamino group was crucial for high enantioselectivity. Thus, within the past two years, bifunctional thioureas have been applied successfully as enantioselective catalysts for the three fundamental transformations of carbonyl compounds (1,2-addition, acyl transfer, and 1,4-addition). This provides a compelling indication of the generality of this catalyst class.

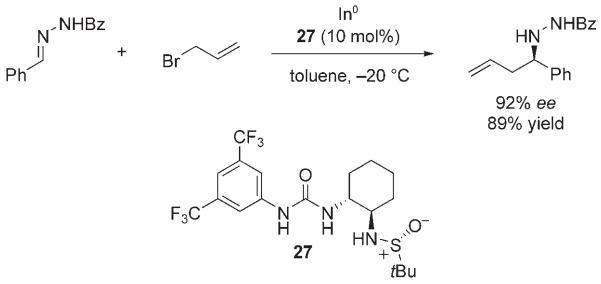
Thioureas incorporating additional acidic groups also show promise as bifunctional catalysts. Bis-thiourea **26** mediates enantioselective Baylis–Hillman reactions of cyclohexenone with aldehydes in the presence of *N*,*N*-(dimethylamino)pyridine or imidazole (Scheme 34).[121] Although detailed mechanistic studies were not reported, a proposal involving H-bonding to both the aldehyde electrophile and




***Scheme 34.*** Bis-thiourea-catalyzed Baylis–Hillman reaction. DMAP = 4-dimethylaminopyridine.

the enone (or enolate) was advanced. The thiourea developed by our group for nitro-Mannich reactions (Section 3.1) may also function as a bifunctional catalyst: although the role of the *N*-acetamido group has not been elucidated, its importance in catalyst performance was established unambiguously.[45]

Additions of organometallic nucleophiles constitute an important class of carbon–carbon bond-forming reactions, and substantial effort has been dedicated toward the discovery of enantioselective reactions of this type. The application of chiral H-bond donor catalysts to this problem is susceptible to several potential problems, including the possible incompatibility of organometallic agents with protic functional groups. Recent investigations of the addition of allylindium reagents to acylhydrazones demonstrate that despite these potential issues, bifunctional catalysis may be useful in this context (Scheme 35).[122] The optimal urea catalyst **27** bears a



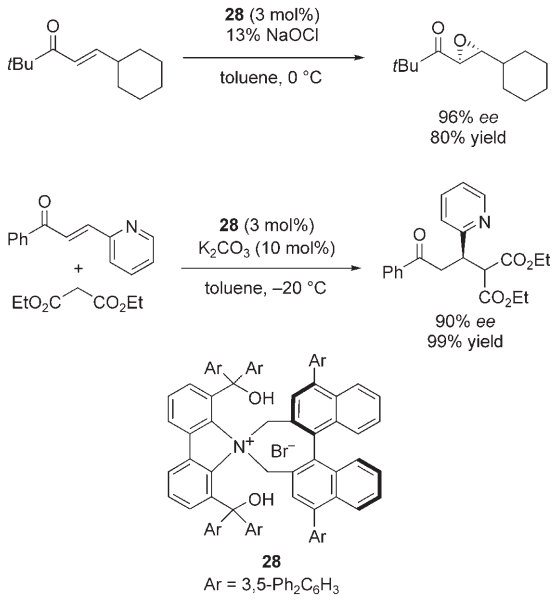

***Scheme 35.*** Enantioselective addition of allylindium to *N*-benzoylhydrazones. Bz = benzoyl.

configurationally defined, Lewis basic sulfinamide group, which is postulated to activate the incoming allylindium nucleophile towards attack. Given the well-studied ability of Lewis bases to activate organometallic and related reagents,[123] this general catalyst design may prove to have considerable utility for enantioselective methodology.

### *3.3.5. H-Bonding Phase-Transfer Catalysts*

In phase-transfer catalysis, stereochemical communication between a chiral cation and a substrate anion is achieved by an ion-pairing interaction. Pioneering studies by scientists at Merck demonstrated the utility of *N*-alkylated Cinchona alkaloids as phase-transfer catalysts for enolate alkylation and Michael addition reactions.[124] Subsequent studies have shown that this catalyst class is broadly applicable for reactions of a wide range of prochiral enolates.[125] Maruoka and co-workers have investigated the development of efficient phase-transfer catalyzed reactions of prochiral electrophiles by designing cationic catalysts capable of electrophile activation. Spiro-ammonium bromide **28** catalyzes highly enantioselective oxidations and Michael additions of α,β-unsaturated ketones (Scheme 36).[126] The diarylhydroxymethyl groups, which are crucial for high selectivity in these processes, are proposed to act as H-bond donors to the enone carbonyl group.

 © 2006 Wiley-VCH Verlag GmbH & Co. KGaA, Weinheim 




***Scheme 36.*** Asymmetric, hydrogen bond assisted phase-transfer catalysis.

## *4. Summary and Outlook*

Research in asymmetric H-bond donor catalysis is progressing at a rapid pace, and its scope will undoubtedly continue to expand through identification of new modes of reactivity and through the design of novel catalyst structures. As is true of any field that has reached a certain stage of maturity, new developments in this area will be held to increasingly high standards, in terms of innovation and practicality. Truly groundbreaking research will no longer simply demonstrate that H-bond donors are suitable alternative catalysts for reactions in which metal-centered chiral Lewis acids are of proven utility, but rather will highlight the unique features of this catalyst class. The ease of synthesis and modular nature of several of the catalyst structures described above are well-suited for combinatorial approaches to catalyst discovery. Such approaches were used successfully in the development of urea-catalyzed Strecker reactions, and it is to be anticipated that developing effective methodology to generate large numbers of structurally diverse catalyst candidates of high purity will be useful in the context of many other reaction types. It is clear that H-bonding activation will continue to play an important role in the development of bifunctional catalysts. The scope of the enantioselective chemistry mediated by a few simple acid/base molecules such as proline, cinchona alkaloid derivatives, and the diaminocyclohexane-derived thioureas suggests that research in this area has only begun to uncover what is possible with such simple bifunctional molecules.[127]

To realize the full potential of H-bond donor catalysis, a more detailed mechanistic understanding of this chemistry is certainly needed. At this stage, it cannot be disputed that enzymes are the best-understood catalyst systems involving H-bonding. As was noted in Section 2.1, many techniques, such as kinetics, computation, state-of-the art spectroscopic methods, and crystallography, have been brought to bear to elucidate the mechanism of action of the serine proteases. Several of these techniques are also appropriate for the study of synthetic catalyst systems: moreover, small-molecule catalysts are particularly well-suited for powerful physical-organic probes of mechanism such as substituent effect studies. Mechanistic studies will help to point the way to new catalysts and new transformations, and may also provide fundamental insight into the structure and function of hydrogen bonds.

Received: September 2, 2005


[1] a) *Lewis Acids in Organic Synthesis, Vols. 1 and 2* (Ed.: H. Yamamoto), Wiley, New York, **2000**; b) *Comprehensive Asymmetric Catalysis, Vols. 1–3* (Eds.: E. N. Jacobsen, A. Pfaltz, H. Yamamoto), Springer, Berlin, **1999**; c) M. Santelli, J.-M. Pons, *Lewis Acids and Selectivity in Organic Synthesis*, CRCs, Boca Raton, **1996**.

[2] C. Friedel, J.-M. Crafts, *C. R. Acad. Sci.* **1884**, 449–532.

[3] P. Yates, P. Eaton, *J. Am. Chem. Soc.* **1960**, *82*, 4436–4437.

[4] For a small sample of very recent, significant examples, see: a) D. A. Evans, J. Wu, *J. Am. Chem. Soc.* **2005**, *127*, 8006–8007; b) B. M. Trost, S. Shin, J. A. Sclafani, *J. Am. Chem. Soc.* **2005**, *127*, 8602–8603; c) E. R. Jarvo, B. M. Lawrence, E. N. Jacobsen, *Angew. Chem.* **2005**, *117*, 6197–6200; *Angew. Chem. Int. Ed.* **2005**, *44*, 6043–6046; d) S. Ishikawa, T. Hamada, K. Manabe, S. Kobayashi, *J. Am. Chem. Soc.* **2004**, *126*, 12236–12237; e) N. Momiyama, H. Yamamoto, *J. Am. Chem. Soc.* **2004**, *126*, 5360–5361; f) D. H. Ryu, G. Zhou, E. J. Corey, *J. Am. Chem. Soc.* **2004**, *126*, 4800–4802; g) M. P. Sibi, Z. Ma, C. P. Jasperse, *J. Am. Chem. Soc.* **2004**, *126*, 718–719; h) M. Braun, W. Kotter, *Angew. Chem.* **2004**, *116*, 520–523; *Angew. Chem. Int. Ed.* **2004**, *43*, 514–517.

[5] a) A. Wassermann, *J. Chem. Soc.* **1942**, 618–621; b) W. Rubin, H. Steiner, A. Wassermann, *J. Chem. Soc.* **1946**, 3046–3057.

[6] a) A. Fersht, *Structure and Mechanism in Protein Science*, Freeman, New York, NY, **1999**; b) R. B. Silverman, *The Organic Chemistry of Enzyme-Catalyzed Reactions*, Academic Press, San Diego, CA, **2000**; c) *Comprehensive Biological Catalysis, Vols. 1–3* (Ed.: M. Sinnott), Academic Press, London, **1998**; d) K. B. Schowen, H.-H. Limbach, G. S. Denisov, R. L. Schowen, *Biochim. Biophys. Acta* **2000**, *1458*, 43–62.

[7] For reviews: a) P. R. Schreiner, *Chem. Soc. Rev.* **2003**, *32*, 289–296; b) P. M. Pihko, *Angew. Chem.* **2004**, *116*, 2110–2113; *Angew. Chem. Int. Ed.* **2004**, *43*, 2062–2064; c) M. Oestreich, *Nachr. Chem.* **2004**, *52*, 35–38; d) C. Bolm, T. Rantanen, I. Schiffers, L. Zani, *Angew. Chem.* **2005**, *117*, 1788–1793; *Angew. Chem. Int. Ed.* **2005**, *44*, 1758–1763; e) H. Yamamoto, K. Futatsugi, *Angew. Chem.* **2005**, *117*, 1958–1977; *Angew. Chem. Int. Ed.* **2005**, *44*, 1924–1942.

[8] a) G. C. Pimentel, A. L. McClellan, *The Hydrogen Bond*, Freeman, San Francisco, **1960**; b) L. Pauling, *The Nature of the Chemical Bond, 3rd ed.*, Cornell University Press, Ithaca, **1968**; c) W. C. Hamilton, J. A. Ibers, *Hydrogen Bonding in Solids*, Benjamin, New York, **1968**; d) G. A. Jeffrey, W. Saenger, *Hydrogen Bonding in Biological Structures*, Springer, Berlin, **1991**; e) S. Scheiner, *Hydrogen Bonding. A Theoretical Perspective*, Oxford University Press, Oxford, **1997**; f) G. A. Jeffrey, *An Introduction to Hydrogen Bonding*, Oxford University Press, New York, **1997**; g) G. R. Desiraju, T. Steiner, *The Weak Hydrogen Bond in Structural Chemistry and Biology*, Oxford University Press, Oxford, **1999**; h) C. A. Hunter, *Angew. Chem.* **2004**, *116*, 5424–5439; *Angew. Chem. Int. Ed.* **2004**, *43*, 5310–5324.


 © 2006 Wiley-VCH Verlag GmbH & Co. KGaA, Weinheim 

[9] T. Steiner, *Angew. Chem.* **2002**, *114*, 50 – 80; *Angew. Chem. Int. Ed.* **2002**, *41*, 48 – 76.

[10] a) W. P. Jencks, *Acc. Chem. Res.* **1976**, *9*, 425 – 432; b) W. P. Jencks, *Acc. Chem. Res.* **1980**, *13*, 161 – 169; c) E. Ciuffarin, A. Loi, M. Isola, A. Lupetti, L. Sagramora, L. Senatore, *J. Org. Chem.* **1983**, *48*, 1047 – 1051; d) S. Scheiner, *Acc. Chem. Res.* **1994**, *27*, 402 – 408.

[11] a) G. R. Desiraju, *Crystal Engineering. The Design of Organic Solids*, Elsevier, Amsterdam, **1989**; b) G. R. Desiraju, *Angew. Chem.* **1995**, *107*, 2541 – 2558; *Angew. Chem. Int. Ed. Engl.Angew. Chem. Int. Ed.* **1995**, *34*, 2311 – 2327.

[12] L. J. Prins, D. N. Reinhoudt, P. Timmerman, *Angew. Chem.* **2001**, *113*, 2446 – 2492; *Angew. Chem. Int. Ed.* **2001**, *40*, 2382 – 2426.

[13] For reviews: a) P. I. Dalko, L. Moisan, *Angew. Chem.* **2001**, *113*, 3840 – 3864; *Angew. Chem. Int. Ed.* **2001**, *40*, 3726 – 3748; b) E. R. Jarvo, S. J. Miller, *Tetrahedron* **2002**, *58*, 2481 – 2495; c) M. Benaglia, A. Puglisi, F. Cozzi, *Chem. Rev.* **2003**, *103*, 3401 – 3430; d) A. Berkessel, H. Gröger, *Metal-Free Organic Catalysts in Asymmetric Synthesis*, Wiley-VCH, Weinheim, **2004**; e) "Special Issue: Asymmetric Organocatalysis", *Acc. Chem. Res.* **2004**, *37*, 487 – 631; f) P. I. Dalko, L. Moisan, *Angew. Chem.* **2004**, *116*, 5248 – 5286; *Angew. Chem. Int. Ed.* **2004**, *43*, 5138 – 5175; g) J. Seayad, B. List, *Org. Biomol. Chem.* **2005**, *3*, 719 – 724.

[14] T. P. Yoon, E. N. Jacobsen, *Science* **2003**, *299*, 1691 – 1693.

[15] a) A. Yanagisawa, H. Yamamoto in *Comprehensive Asymmetric Catalysis, Vol. III* (Eds.: E. N. Jacobsen, A. Pfaltz, H. Yamamoto), Springer, Berlin, **1999**; b) A. Yanagisawa in *Comprehensive Asymmetric Catalysis*, Supplement 2 (Eds.: E. N. Jacobsen, A. Pfaltz, H. Yamamoto), Springer, Berlin, **2004**; c) L. Duhamel, P. Duhamel, J.-C. Plaquevent, *Tetrahedron: Asymmetry* **2004**, *15*, 3653 – 3691.

[16] C. W. Wharton in *Comprehensive Biological Catalysis, Vol. 1* (Ed.: M. Sinnott), Academic Press, London, **1998**, pp. 345 – 379.

[17] A. J. White, C. W. Wharton, *Biochem. J.* **1990**, *270*, 627 – 637.

[18] P. Bryan, W. Pantoliano, S. G. Quill, H.-Y. Hsiao, T. Poulos, *Proc. Natl. Acad. Sci. USA* **1986**, *83*, 3743 – 3745.

[19] a) L. Pauling, *Chem. Eng. News* **1946**, *24*, 1375 – 1377. b) Recently, it has been suggested that the rate accelerations observed in enzyme-catalyzed reactions result from covalent, rather than noncovalent, interactions between the enzyme and transition state: X. Zhang, K. N. Houk, *Acc. Chem. Res.* **2005**, *38*, 379 – 385.

[20] a) R. C. Thompson, E. R. Blout, *Biochemistry* **1973**, *12*, 51 – 58; b) R. L. Stein, A. M. Strimpler, H. Hori, J. C. Powers, *Biochemistry* **1987**, *26*, 1301 – 1310; c) L. Hedstrom, L. Szilagi, W. J. Rutter, *Science* **1992**, *255*, 1249 – 1253.

[21] a) J. A. Wells, D. A. Estell, *Trends Biochem. Sci.* **1998**, *23*, 291 – 297; b) D. R. Corey, C. S. Craik, *J. Am. Chem. Soc.* **1992**, *114*, 1784 – 1790.

[22] For reviews: a) A. Y. Lee, J. D. Stewart , J. Clardy, B. Ganem, *Chem. Biol.* **1995**, *2*, 195 – 203; b) B. Ganem, *Angew. Chem.* **1996**, *108*, 1014 – 1023; *Angew. Chem. Int. Ed. Engl.* **1996**, *35*, 936 – 945.

[23] a) A. Y. Lee, P. A. Karplus, B. Ganem, J. Clardy, *J. Am. Chem. Soc.* **1995**, *117*, 3627 – 3628; b) Y.-M. Chook, J. V. Gray, H. Ke, W. N. Lipscomb, *J. Mol. Biol.* **1994**, *240*, 476 – 500.

[24] D. L. Severance, W. L. Jorgensen, *J. Am. Chem. Soc.* **1992**, *114*, 10966 – 10968.

[25] a) F. W. Schuler, G. W. Murphys, *J. Am. Chem. Soc.* **1950**, *72*, 3155 – 3159; b) H. J. Hansen, H. Schmid, *Tetrahedron* **1974**, *30*, 1959 – 1969.

[26] H. Gorisch, *Biochemistry* **1978**, *17*, 3700 – 3705.

[27] For reviews: a) C.-H. Wong, R. H. Halcomb, Y. Ichikawa, T. Kajimoto, *Angew. Chem.* **1995**, *107*, 453 – 472; *Angew. Chem. Int. Ed. Engl.* **1995**, *34*, 412 – 432; b) T. D. Machajewski, C.-H. Wong, *Angew. Chem.* **2000**, *112*, 1406 – 1430; *Angew. Chem. Int. Ed.* **2000**, *39*, 1352 – 1374.

[28] a) M. K. Dreyer, G. E. Schulz, *J. Mol. Biol.* **1996**, *259*, 458 – 466; b) A. C. Joerger, C. Gosse, W.-D. Fessner, G. E. Schulz, *Biochemistry* **2000**, *39*, 6033 – 6041.

[29] For reviews: a) T. R. Cech, D. Herschlag, J. A. Piccirill, A. M. Pyle, *J. Biol. Chem.* **1992**, *267*, 17479 – 17482; b) E. A. Doherty, J. A. Doudna, *Annu. Rev. Biochem.* **2000**, *69*, 597 – 615.

[30] G. M. Blackburn, M. J. Gait, *Nucleic Acids in Chemistry and Biology, 2nd ed.*,Oxford Press, Oxford, UK, **1996**.

[31] A. R. Ferré-D'Amaré, K. Zhou, J. A. Doudna, *Nature* **1998**, *395*, 567 – 574.

[32] a) A. T. Perrotta, I.-H. Shih, M. D. Been, *Science* **1999**, *286*, 123 – 216; b) S.-I. Nakano, D. M. Chadalavada, P. C. Bevilacqua, *Science* **2000**, *287*, 1493 – 1497.

[33] J. S. Johnson, D. A. Evans, *Acc. Chem. Res.* **2000**, *33*, 325 – 335.

[34] a) M. S. Sigman, E. N. Jacobsen, *J. Am. Chem. Soc.* **1998**, *120*, 4901 – 4902; b) P. Vachal, E. N. Jacobsen, *Org. Lett.* **2000**, *2*, 867 – 870; c) M. S. Sigman, P. Vachal, E. N. Jacobsen, *Angew. Chem.* **2000**, *112*, 1336 – 1338; *Angew. Chem. Int. Ed.* **2000**, *39*, 1279 – 1281.

[35] P. Vachal, E. N. Jacobsen, *J. Am. Chem. Soc.* **2002**, *124*, 10012 – 10014.

[36] a) M. C. Etter, T. W. Panunto, *J. Am. Chem. Soc.* **1988**, *110*, 5896 – 5897; b) M. C. Etter, Z. Urbañczyk-Lipkowska, M. Zia-Ebrahimi, T. W. Panunto, *J. Am. Chem. Soc.* **1990**, *112*, 8415 – 8426; c) M. C. Etter, *Acc. Chem. Res.* **1990**, *23*, 120 – 126.

[37] For early examples: a) E. Fan, S. A. Van Arman, S. Kincaid, A. D. Hamilton, *J. Am. Chem. Soc.* **1993**, *115*, 369 – 370; b) B. C. Hamann, N. R. Branda, J. Rebek, Jr., *Tetrahedron Lett.* **1993**, *34*, 6837 – 6840; c) T. R. Kelly, M. H. Kim, *J. Am. Chem. Soc.* **1994**, *116*, 7072 – 7080; d) S. Nishizawa, P. Bühlmann, M. Iwao, Y. Umezawa, *Tetrahedron Lett.* **1995**, *36*, 6483 – 6486.

[38] a) D. P. Curran, L. H. Kuo, *J. Org. Chem.* **1994**, *59*, 3259 – 3261; b) D. P. Curran, L. H. Kuo, *Tetrahedron Lett.* **1995**, *36*, 6647 – 6650.

[39] a) P. R. Schreiner, A. Wittkopp, *Org. Lett.* **2002**, *4*, 217 – 220; b) A. Wittkopp, P. R. Schreiner, *Chem. Eur. J.* **2003**, *9*, 407 – 414.

[40] G. D. Joly, E. N. Jacobsen, *J. Am. Chem. Soc.* **2004**, *126*, 4102 – 4103.

[41] T. Kuribayashi, A. M. Lerchner, E. N. Jacobsen, unpublished results.

[42] A. G. Wenzel, E. N. Jacobsen, *J. Am. Chem. Soc.* **2002**, *124*, 12964 – 12965.

[43] Y. Chen, E. N. Jacobsen, unpublished results.

[44] A. G. Wenzel, M. P. Lalonde, E. N. Jacobsen, *Synlett* **2003**, *12*, 1919 – 1922.

[45] T. P. Yoon, E. N. Jacobsen, *Angew. Chem.* **2005**, *117*, 470 – 472; *Angew. Chem. Int. Ed.* **2005**, *44*, 466 – 468.

[46] I. T. Raheem, E. N. Jacobsen, *Adv. Synth. Catal.* **2005**, *347*, 1701 – 1708.

[47] B. E. Maryanoff, H.-C. Zhang, J. H. Cohen, I. J. Turchi, C. A. Maryanoff, *Chem. Rev.* **2004**, *104*, 1431 – 1628.

[48] M. S. Taylor, E. N. Jacobsen, *J. Am. Chem. Soc.* **2004**, *126*, 10558 – 10559.

[49] M. S. Taylor, N. Tokunaga, E. N. Jacobsen, *Angew. Chem.* **2005**, *117*, 6858 – 6862; *Angew. Chem. Int. Ed.* **2005**, *44*, 6700 – 6704.

[50] E. J. Corey, M. J. Grogan, *Org. Lett.* **1999**, *1*, 157 – 160.

[51] T. Schuster, M. Kurz, M. W. Göbel, *J. Org. Chem.* **2000**, *65*, 1697 – 1701.

[52] T. Schuster, M. Bauch, G. Dürner, M. W. Göbel, *Org. Lett.* **2000**, *2*, 179 – 181.

[53] B. M. Nugent, R. A. Yoder, J. N. Johnston, *J. Am. Chem. Soc.* **2004**, *126*, 3418 – 3419.

[54] a) T. Bach, H. Bergmann, K. Harms, *Angew. Chem.* **2000**, *112*, 2391 – 2393; *Angew. Chem. Int. Ed.* **2000**, *39*, 2302 – 2304; b) T.


 © 2006 Wiley-VCH Verlag GmbH & Co. KGaA, Weinheim 

Bach, H. Bergmann, B. Grosch, K. Harms, *J. Am. Chem. Soc.* **2002**, *124*, 7982 – 7990.
[55] B. Grosch, C. N. Orlebar, E. Herdweck, M. Kaneda, T. Wada, Y. Inoue, T. Bach, *Chem. Eur. J.* **2004**, *10*, 2179 – 2189.
[56] T. Bach, T. Aechtner, B. Neumüller, *Chem. Eur. J.* **2002**, *8*, 2464 – 2475.
[57] T. Bach, B. Grosch, T. Strassner, E. Herdtweck, *J. Org. Chem.* **2003**, *68*, 1107 – 1116.
[58] T. Aechtner, M. Dressel, T. Bach, *Angew. Chem.* **2004**, *116*, 5974 – 5976; *Angew. Chem. Int. Ed.* **2004**, *43*, 5849 – 5851.
[59] Enantioselective photocyclization using catalytic quantities of a chiral secondary lactam was reported during the final stages of preparation of this manuscript: A. Bauer, F. Westkämper, S. Grimme, T. Bach, *Nature* **2005**, *436*, 1139 – 1140.
[60] For reviews: a) D. Seebach, A. K. Beck, A. Heckel, *Angew. Chem.* **2001**, *113*, 1, 96 – 142; *Angew. Chem. Int. Ed.* **2001**, *40*, 92 – 138; b) J. M. Brunel, *Chem. Rev.* **2005**, *105*, 857 – 897.
[61] a) J. Hine, S.-M. Linden, V. M. Kanagasabapathy, *J. Am. Chem. Soc.* **1985**, *107*, 1082 – 1083; b) J. Hine, S.-M. Linden, V. M. Kanagasabapathy, *J. Org. Chem.* **1985**, *50*, 5096 – 5099; c) T. R. Kelly, P. Meghani, V. S. Ekkundi, *Tetrahedron Lett.* **1990**, *31*, 3381 – 3384.
[62] a) J. Hine, K. Ahn, J. C. Gallucci, S.-M. Linden, *J. Am. Chem. Soc.* **1984**, *106*, 7980 – 7981; b) J. Hine, K. Ahn, *J. Org. Chem.* **1987**, *52*, 2083 – 2086; c) J. Hine, K. Ahn, *J. Org. Chem.* **1987**, *52*, 2089 – 2091.
[63] a) F. Toda, K. Tanaka, L. Infantes, C. Foces-Foces, R. M. Claramunt, J. Elguero, *J. Chem. Soc. Chem. Commun.* **1995**, 1453 – 1454; b) Y. Takemoto, S. Kuraoka, N. Hamaue, K. Aoe, H. Hiramatsu, C. Iwata, *Tetrahedron* **1996**, *52*, 14177 – 14188.
[64] For a review: F. Toda, *Acc. Chem. Res.* **1995**, *28*, 480 – 486.
[65] K. Tanaka, F. Toda, *J. Chem. Soc. Chem. Commun.* **1983**, 593 – 594.
[66] Y. Huang, A. K. Unni, A. N. Thadani, V. H. Rawal, *Nature* **2003**, *424*, 146.
[67] Y. Huang, V. H. Rawal, *J. Am. Chem. Soc.* **2002**, *124*, 9662 – 9663.
[68] A. N. Thadani, A. R. Stankovic, V. H. Rawal, *Proc. Natl. Acad. Sci. USA* **2004**, *101*, 5846 – 5850.
[69] H. Du, D. Zhao, K. Ding, *Chem. Eur. J.* **2004**, *10*, 5964 – 5970.
[70] A. K. Unni, N. Takenaka, H. Yamamoto, V. H. Rawal, *J. Am. Chem. Soc.* **2005**, *127*, 1336 – 1337.
[71] N. Momiyama, H. Yamamoto, *J. Am. Chem. Soc.* **2005**, *127*, 1080 – 1081.
[72] a) N. T. McDougal, S. E. Schaus, *J. Am. Chem. Soc.* **2003**, *125*, 12094 – 12095; b) N. T. McDougal, W. L. Trevellini, S. A. Rodgen, L. T. Kliman, S. E. Schaus, *Adv. Synth. Catal.* **2004**, *346*, 1231 – 1240.
[73] T. M. A. Yamada, S. Ikegami, *Tetrahedron Lett.* **2000**, *41*, 2165 – 2169.
[74] K. Matsui, S. Takizawa, H. Sasai, *J. Am. Chem. Soc.* **2005**, *127*, 3680 – 3681.
[75] For lead references: a) J. Brussee, A. C. A. Jansen, *Tetrahedron Lett.* **1983**, *24*, 3261 – 3262; b) S. Miyano, K. Kawahara, Y. Inoue, H. Hashimoto, *Chem. Lett.* **1987**, 355 – 356; c) G. Bringmann, W. Rainer, R. Weirich, *Angew. Chem.* **1990**, *102*, 1006 – 1019; *Angew. Chem. Int. Ed. Engl.* **1990**, *29*, 977 – 991; .
[76] a) T. Akiyama, J. Itoh, K. Yokota, K. Fuchibe, *Angew. Chem.* **2004**, *116*, 1592 – 1594; *Angew. Chem. Int. Ed.* **2004**, *43*, 1566 – 1568; b) D. Uraguchi, M. Terada, *J. Am. Chem. Soc.* **2004**, *126*, 5356 – 5357.
[77] a) D. Uraguchi, K. Sorimachi, M. Terada, *J. Am. Chem. Soc.* **2004**, *126*, 11804 – 11805; b) D. Uraguchi, K. Sorimachi, M. Terada, *J. Am. Chem. Soc.* **2005**, *127*, 9360 – 9361; c) T. Akiyama, H. Morita, J. Itoh, K. Fuchibe, *Org. Lett.* **2005**, *7*, 2583 – 2585; d) M. Rueping, E. Sugiono, C. Azap, T. Theissmann, M. Bolte, *Org. Lett.* **2005**, *7*, 3781 – 3783.
[78] For reviews: a) M. Shibasaki, H. Sasai, T. Arai, *Angew. Chem.* **1997**, *109*, 1290 – 1311; *Angew. Chem. Int. Ed. Engl.* **1997**, *36*, 1236 – 1256; b) H. Gröger, *Chem. Eur. J.* **2001**, *7*, 5246 – 5251; c) G. J. Rawlands, *Tetrahedron* **2001**, *57*, 1865 – 1882; d) M. Shibasaki, N. Yoshikawa, *Chem. Rev.* **2002**, *102*, 2187 – 2209; e) J.-A. Ma, D. Cahard, *Angew. Chem.* **2004**, *116*, 4666 – 4683; *Angew. Chem. Int. Ed.* **2004**, *43*, 4566 – 4583; M. Kanai, N. Kato, E. Ichikawa, M. Shibasaki, *Synlett* **2005**, *10*, 1491 – 1508.
[79] M. Movassaghi, E. N. Jacobsen, *Science* **2002**, *298*, 1904 – 1905.
[80] a) Z. G. Hajos, D. R. Parrish, (Hoffman-La-Roche), German Patent DE 2102623, **1971** [*Chem. Abstr.* **1972**, *76*, 59072]; b) U. Eder, G. Sauer, R. Wiechert, (Schering AG), German Patent DE 2014757, **1971** [*Chem. Abstr.* **1972**, *76*, 59072]; c) U. Eder, G. Sauer, R. Wiechert, *Angew. Chem.* **1971**, *83*, 472 – 473; *Angew. Chem. Int. Ed. Engl.* **1971**, *10*, 496 – 497; d) Z. G. Hajos, D. R. Parrish, *J. Org. Chem.* **1974**, *39*, 1615 – 1621.
[81] a) S. Danishefsky, P. Cain, *J. Am. Chem. Soc.* **1976**, *98*, 3975 – 4983; b) N. Cohen, *Acc. Chem. Res.* **1976**, *9*, 412 – 417; c) R. B. Woodward, E. Logusch, K. P. Nambiar, K. Sakan, D. E. Ward, B. W. Au-Yeung, P. Balaram, L. J. Browne, P. J. Card, C. H. Chen, *J. Am. Chem. Soc.* **1981**, *103*, 3210 – 3213; d) A. B. Smith III, J. Kingery-Wood, T. L. Leenay, E. G. Nolen, T. Sunazuka, *J. Am. Chem. Soc.* **1992**, *114*, 1438 – 1449.
[82] B. List, R. A. Lerner, C. F. Barbas III, *J. Am. Chem. Soc.* **2000**, *122*, 2395 – 2396.
[83] a) H. Gröger, J. Wilken, *Angew. Chem.* **2001**, *113*, 545 – 548; *Angew. Chem. Int. Ed.* **2001**, *40*, 529 – 532; b) B. List, *Synlett* **2001**, *11*, 1675 – 1686; c) B. List, *Tetrahedron* **2002**, *58*, 5573 – 5590; d) B. List, *Acc. Chem. Res.* **2004**, *37*, 548 – 557; e) W. Notz, F. Tanaka, C. F. Barbas III, *Acc. Chem. Res.* **2004**, *37*, 580 – 591; f) P. Merino, T. Tejero, *Angew. Chem.* **2004**, *116*, 3055 – 3058; *Angew. Chem. Int. Ed.* **2004**, *43*, 3995 – 3997.
[84] M. E. Jung, *Tetrahedron* **1976**, *32*, 3 – 31.
[85] L. Hoang, S. Bahmanyar, K. N. Houk, B. List, *J. Am. Chem. Soc.* **2003**, *125*, 16 – 17.
[86] See referemce [85], and: a) S. Bahmanyar, K. N. Houk, *J. Am. Chem. Soc.* **2001**, *123*, 11273 – 11283; b) S. Bahmanyar, K. N. Houk, *J. Am. Chem. Soc.* **2001**, *123*, 12911 – 12912; c) S. Bahmanyar, K. N. Houk, H. J. Martin, B. List, *J. Am. Chem. Soc.* **2003**, *125*, 2475 – 2479; d) K. N. Rankin, J. W. Gauld, R. J. Boyd, *J. Phys. Chem. A* **2002**, *106*, 5155 – 5159; e) M. Arno, L. R. Domingo, *Theor. Chem. Acc.* **2002**, *108*, 232 – 239; f) C. Allemann, R. Gordillo, F. R. Clemente, P. H.-Y. Cheong, K. N. Houk, *Acc. Chem. Res.* **2004**, *37*, 558 – 569; g) F. R. Clemente, K. N. Houk, *Angew. Chem.* **2004**, *116*, 5890 – 5892; *Angew. Chem. Int. Ed.* **2004**, *43*, 5766 – 5768.
[87] a) S. Saito, M. Nakadai, H. Yamamoto, *Synlett* **2001**, *8*, 1245 – 1248; b) K. Sakthivel, W. Notz, T. Bui, C. F. Barbas III, *J. Am. Chem. Soc.* **2001**, *123*, 5260 – 5267; c) W. Notz, K. Sakthivel, T. Bui, G. Zhong, C. F. Barbas III, *Tetrahedron Lett.* **2001**, *42*, 199 – 201; d) M. Nakadai, S. Saito, H. Yamamoto, *Tetrahedron* **2002**, *58*, 8167 – 8177; e) S. Saito, H. Yamamoto, *Acc. Chem. Res.* **2004**, *37*, 570 – 579.
[88] a) H. J. Martin, B. List, *Synlett* **2003**, *12*, 1901 – 1902; b) J. Kofoed, J. Nielsen, J.-L. Reymond, *Bioorg. Med. Chem. Lett.* **2003**, *13*, 2445 – 2447; c) N. Dahlin, A. Bøgevig, H. Adolfsson, *Adv. Synth. Catal.* **2004**, *346*, 1101 – 1105; d) A. Berkessel, B. Koch, J. Lex, *Adv. Synth. Catal.* **2004**, *346*, 1141 – 1146.
[89] Z. Tang, F. Jiang, L.-T. Yu, X. Cui, L.-Z. Gong, A.-Z. Mi, Y.-Z. Jiang, Y.-D. Wu, *J. Am. Chem. Soc.* **2003**, *125*, 5262 – 5263.
[90] a) H. Torii, M. Nakadai, K. Ishihara, S. Saito, H. Yamamoto, *Angew. Chem.* **2004**, *116*, 2017 – 2020; *Angew. Chem. Int. Ed.* **2004**, *43*, 1983 – 1986; b) N. Momiyama, H. Torii, S. Saito, H. Yamamoto, *Proc. Natl. Acad. Sci. USA* **2004**, *101*, 5374 – 5378; c) A. J. A. Cobb, D. M. Shaw, S. V. Ley, *Synlett* **2004**, *3*, 558 – 560; d) A. Hartikka, P. I. Arvidsson, *Tetrahedron: Asymmetry* **2004**, *15*, 1831 – 1834.


© 2006 Wiley-VCH Verlag GmbH & Co. KGaA, Weinheim

[91] a) S. P. Mathew, H. Iwamura, D. G. Blackmond, *Angew. Chem.* **2004**, *116*, 3379 – 3383; *Angew. Chem. Int. Ed.* **2004**, *43*, 3317 – 3321; b) H. Iwamura, S. P. Mathew, D. G. Blackmond, *J. Am. Chem. Soc.* **2004**, *126*, 11770 – 11771; c) H. Iwamura, D. H. Wells, Jr., S. P. Mathew, M. Klussmann, A. Armstrong, D. G. Blackmond, *J. Am. Chem. Soc.* **2004**, *126*, 16312 – 16313.

[92] a) K. Kacprzak, J. Gawronski, *Synthesis* **2001**, 961 – 998; b) S.-K. Tian, Y. Chen, J. Hang, L, Tang, P. McDaid, L. Deng, *Acc. Chem. Res.* **2004**, *37*, 621 – 631.

[93] H. Hiemstra, H. Wynberg, *J. Am. Chem. Soc.* **1981**, *103*, 417 – 430.

[94] P. McDaid, Y. Chen, L. Deng, *Angew. Chem.* **2002**, *114*, 348 – 350; *Angew. Chem. Int. Ed.* **2002**, *41*, 338 – 340.

[95] Y. Iwabuchi, M. Nakatani, N. Yokoyama, S. Hatakeyama, *J. Am. Chem. Soc.* **1999**, *121*, 10219 – 10220.

[96] a) M. Shi, Y.-M. Xu, *Angew. Chem.* **2002**, *114*, 4689 – 4692; *Angew. Chem. Int. Ed.* **2002**, *41*, 4507 – 4510; b) S. Kawahara, A. Nakano, T. Esumi, Y. Iwabuchi, S. Hatakeyama, *Org. Lett.* **2003**, *5*, 3103 – 3105; c) D. Balan, H. Adolfsson, *Tetrahedron Lett.* **2003**, *44*, 2521.

[97] H. Li, Y. Wang, L. Tang, L. Deng, *J. Am. Chem. Soc.* **2004**, *126*, 9906 – 9907.

[98] a) H. Li, Y. Wang, L. Tang, F. Wu, X. Liu, C. Guo, B. M. Foxman, L. Deng, *Angew. Chem.* **2004**, *116*, 107 – 110; *Angew. Chem. Int. Ed.* **2005**, *44*, 105 – 108; b) H. Li, J. Song, X. Liu, L. Deng, *J. Am. Chem. Soc.* **2005**, *127*, 8948 – 8949.

[99] a) S. Saaby, M. Bella, K. A. Jørgensen, *J. Am. Chem. Soc.* **2004**, *126*, 8120 – 8121; b) X. Liu, H. Li, L. Deng, *Org. Lett.* **2005**, *7*, 167 – 169; c) P. M. Pihko, A. Pohjakallio, *Synlett* **2004**, 2115 – 2118.

[100] T. B. Poulsen, C. Alemparte, S. Saaby, M. Bella, K. A. Jørgenson, *Angew. Chem.* **2005**, *117*, 2956 – 2959; *Angew. Chem. Int. Ed.* **2005**, *44*, 2896 – 2899.

[101] a) S. Inoue, J.-I. Oku, *J. Chem. Soc. Chem. Commun.* **1981**, 229 – 230; b) K. Tanaka, A. Mori, S. Inoue, *J. Org. Chem.* **1990**, *55*, 181 – 185; Lipton and co-workers reported application of a similar catalyst system to the enantioselective hydrocyanation of imines: c) M. S. Ivery, K. M. Gigstad, N. D. Namedev, M. Lipton, *J. Am. Chem. Soc.* **1996**, *118*, 4910 – 4911; however, subsequent studies reveal that the reported catalyst system does not in fact induce enantioselective catalysis of Strecker reactions: d) C. Becker, C. Hoben, D. Schollmeyer, G. Scherr, H. Kunz, *Eur. J. Org. Chem.* **2005**, 1497 – 1499.

[102] Y. Shvo, M. Gal, Y. Becker, A. Elgavi, *Tetrahedron: Asymmetry* **1996**, *7*, 911 – 924.

[103] See reference [101b], and: W. R. Jackson, G. S. Jayatilak, B. R. Matthews, C. Wilshire, *Aust. J. Chem.* **1988**, *41*, 203 – 213.

[104] a) B. R. Sculimbrene, S. J. Miller, *J. Am. Chem. Soc.* **2001**, *123*, 10125 – 10126; b) M. M. Vasbinder, E. R. Jarvo, S. J. Miller, *Angew. Chem.* **2001**, *113*, 2824 – 2827; *Angew. Chem. Int. Ed.* **2001**, *40*, 2824 – 2827; c) N. Papaioannou, C. A. Evans, J. T. Blank, S. J. Miller, *Org. Lett.* **2001**, *3*, 2879 – 2882; d) E. R. Jarvo, C. A. Evans, G. T. Copeland, S. J. Miller, *J. Org. Chem.* **2001**, *66*, 5522 – 5527; e) G. T. Copeland, S. J. Miller, *J. Am. Chem. Soc.* **2001**, *123*, 6496 – 6502; f) B. R. Sculimbrene, A. J. Morgan, S. J. Miller, *J. Am. Chem. Soc.* **2002**, *124*, 11653 – 11656; g) N. Papaioanno, J. T. Blank, S. J. Miller, *J. Org. Chem.* **2003**, *68*, 2728 – 2734; h) M. B. Fierman, D. J. O'Leary, W. E. Steinmetz, S. J. Miller, *J. Am. Chem. Soc.* **2004**, *126*, 6967 – 6971.

[105] a) B. R. Sculimbrene, S. J. Miller, *J. Am. Chem. Soc.* **2001**, *123*, 10125 – 10126; b) B. R. Sculimbrene, A. J. Morgan, S. J. Miller, *J. Am. Chem. Soc.* **2002**, *124*, 11653 – 11656.

[106] D. J. Guerin, S. J. Miller, *J. Am. Chem. Soc.* **2002**, *124*, 2134 – 2136.

[107] Computational studies suggest that the protonated imidazole moiety may function as the hydrogen-bond donor: D. J. Harriman, G. Deslongchamps, *J. Comput.-Aided Mol. Des.* **2004**, *18*, 303 – 308.

[108] Y. Hoashi, T. Okino, Y. Takemoto, *Angew. Chem.* **2005**, *117*, 4100 – 4103; *Angew. Chem. Int. Ed.* **2005**, *44*, 4032 – 4035.

[109] For a review: P. Wentworth, Jr., K. D. Janda in *Comprehensive Asymmetric Catalysis, Vol. 3*. (Eds: E. N. Jacobsen, A. Pfaltz, H. Yamamoto), Springer, **1999**, Berlin, pp. 1403 – 1426.

[110] a) J. T. Yli-Kauhaluoma, J. A. Ashley, C.-H. Lo, L. Tucker, M. M. Wolfe, K. D. Janda, *J. Am. Chem. Soc.* **1995**, *117*, 7041 – 7047; b) for an earlier report of an *exo*-Diels–Alder antibody catalyst: V. E. Gouverneur, B. de Pascual-Teresa, B. Beno, K. D. Janda, R. A. Lerner, *Science* **1993**, *262*, 204 – 208.

[111] A. Heine, E. A. Stura, J. T. Yli-Kauhaluoma, C. Gao, Q. Deng, B. R. Beno, K. N. Houk, K. D. Janda, I. A. Wilson, *Science* **1998**, *279*, 1934 – 1940.

[112] a) B. Seelig, A. Jäschke, *Chem. Biol.* **1999**, *6*, 167 – 176; b) B. Seelig, S. Keiper, F. Stuhlmann, A. Jäschke, *Angew. Chem.* **2000**, *112*, 4764 – 4768; *Angew. Chem. Int. Ed.* **2000**, *39*, 4576 – 4579.

[113] A. Serganov, S. Keiper, L. Malinina, V. Tereshko, E. Skripkin, C. Höbartner, A. Polonskaia, A. T. Phan, R. Wombacher, R. Micura, Z. Dauter, A. Jäschke, D. J. Patel, *Nat. Struct. Mol. Biol.* **2005**, *12*, 218 – 224.

[114] T. Okino, Y. Hoashi, Y. Takemoto, *J. Am. Chem. Soc.* **2003**, *125*, 12672 – 12673.

[115] a) Y. Hoashi, T. Yabuta, Y. Takemoto, *Tetrahedron Lett.* **2004**, *45*, 9185 – 9188; b) T. Okino, Y. Hoashi, T. Furukawa, X. Xu, Y. Takemoto, *J. Am. Chem. Soc.* **2005**, *127*, 119 – 125.

[116] T. Okino, S. Nakamura, T. Furukawa, Y. Takemoto, *Org. Lett.* **2004**, *6*, 625 – 627.

[117] a) B.-J. Li, L. Jiang, M. Liu, Y.-C. Chen, L.-S. Ding, Y. Wu, *Synlett* **2005**, *4*, 603 – 606. Subsequent to completion of this review, other interesting reports appeared describing asymmetric conjugate additions catalyzed by epiquinine- and epicinchonine thiourea derivatives: b) S. H. McCooey, S. J. Connon, *Angew. Chem.* **2005**, *117*, 6525 – 6528; *Angew. Chem. Int. Ed.* **2005**, *44*, 6367 – 6370; c) J. Ye, D. J. Dixon, P. S. Hynes, *Chem. Commun.* **2005**, 4481 – 4483.

[118] B. Vakulya, S. Varga, A. Czámpai, T. Sóos, *Org. Lett.* **2005**, *7*, 1967 – 1969.

[119] a) A. Berkessel, F. Cleemann, S. Mukherjee, T. N. Müller, J. Lex, *Angew. Chem.* **2005**, *117*, 817 – 821; *Angew. Chem. Int. Ed.* **2005**, *44*, 807 – 811; b) A. Berkessel, S. Mukherjee, F. Cleemann, T. N. Müller, J. Lex, *Chem. Commun.* **2005**, 1898 – 1900.

[120] D. E. Fuerst, E. N. Jacobsen, *J. Am. Chem. Soc.* **2005**, *127*, 8964 – 8965.

[121] Y. Sohtome, A. Tanatani, Y. Hashimoto, K. Nagasawa, *Tetrahedron Lett.* **2004**, *45*, 5589 – 5592.

[122] K. L. Tian, E. N. Jacobsen, unpublished results.

[123] S. E. Denmark, R. A. Stavenger, *Acc. Chem. Res.* **2000**, *33*, 432 – 440.

[124] a) U.-H. Dolling, P. Davis, E. J. J. Grabowski, *J. Am. Chem. Soc.* **1984**, *106*, 446 – 447; b) R. S. E. Conn, A. V. Lovell, S. Karady, L. M. Weinstock, *J. Org. Chem.* **1986**, *51*, 4710 – 4711.

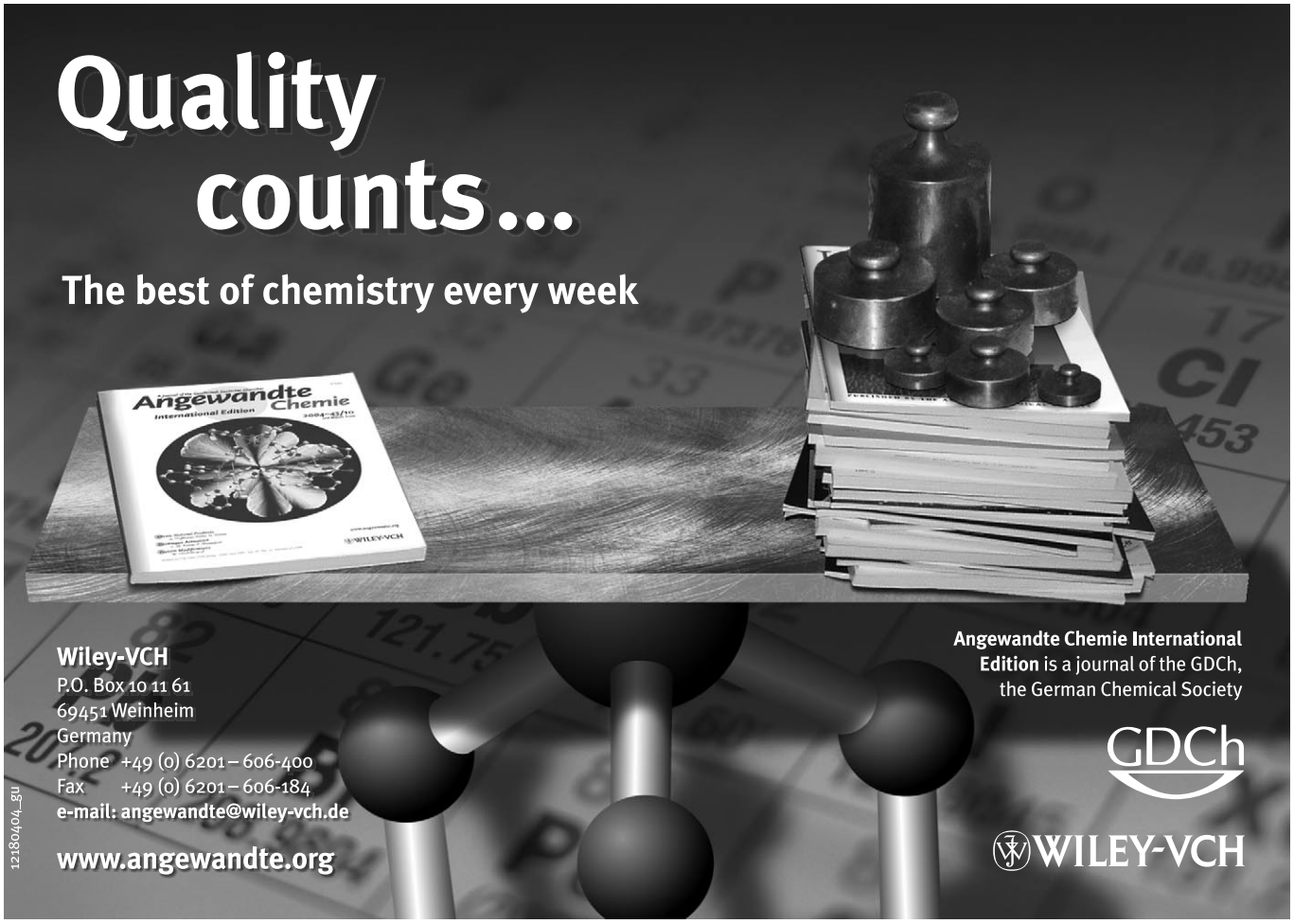
[125] T. Shiori in *Handbook of Phase-Transfer Catalysis* (Eds.: Y. Sasson, R. Neumann), Blackie Academic & Professional, London, **1997**, chap. 14.

[126] a) T. Ooi, D. Ohara, M. Tamura, K. Maruoka, *J. Am. Chem. Soc.* **2004**, *126*, 6844 – 6845; b) T. Ooi, D. Ohara, K. Fukumoto, K. Maruoka, *Org. Lett.* **2005**, *7*, 3195 – 3197.

[127] An indication of the accelerating pace of progress in this area is provided by the number of papers on bifunctional general acid catalysts that have appeared since completion of this review: proline and other amino acid derivatives: a) A. Córdova, W. Zou, I. Ibrahem, E. Reyes, M. Engqvist, W.-W. Liao, *Chem. Commun.* **2005**, 3586 – 3588; b) P. Krattiger, R. Kovasy, J. D. Revell, S. Ivan, H. Wennemers, *Org. Lett.* **2005**, *7*, 1101 – 1103;

 © 2006 Wiley-VCH Verlag GmbH & Co. KGaA, Weinheim 

Cinchona alkaloid derivatives: references [117b], [117c]; c) S. Lou, B. M. Taoka, A. Ting, S. E. Schaus, *J. Am. Chem. Soc.* **2005**, *127*, 11256 – 11257; thiourea derivatives: d) J. Wang, H. Li, X. Yu, L. Zu, W. Wang, *Org. Lett.* **2005**, *7*, 4293 – 4296; e) R. P. Herrera, V. Sgarzani, L. Bernardi, A. Ricci, *Angew. Chem.* **2005**, *117*, 6734 – 6737; *Angew. Chem. Int. Ed.* **2005**, *44*, 6576 – 6579; f) S. B. Tsogoeva, M. J. Hateley, D. A. Yalalov, K. Meindl, C. Weckbecker, K. Huthmacher, *Bioorg. Med. Chem.* **2005**, *13*, 5680 – 5685.

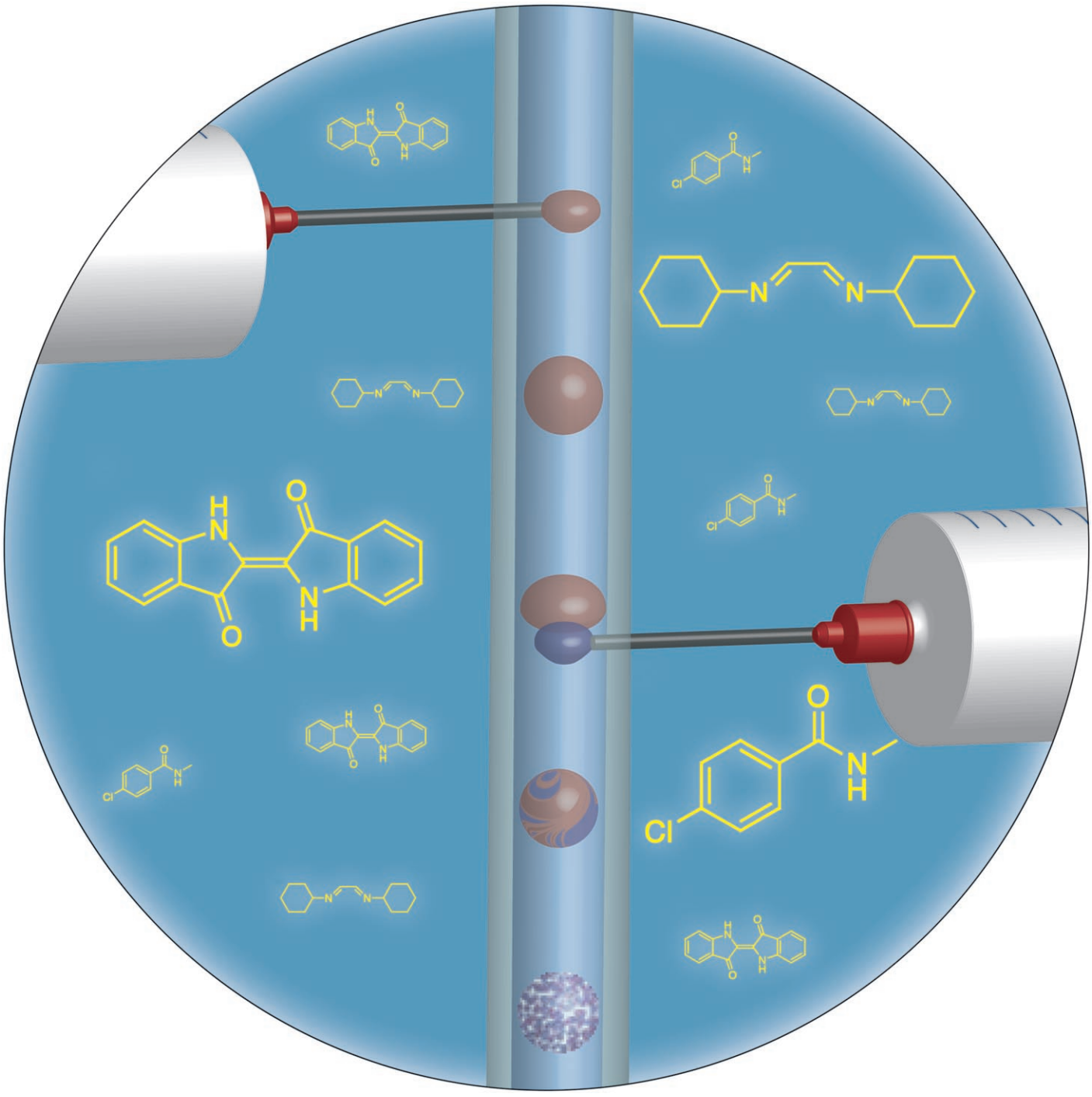




© 2006 Wiley-VCH Verlag GmbH & Co. KGaA, Weinheim

# Communications

DOI: 10.1002/anie.200503925



A major drawback to the synthesis of solid products within microreactors is the clogging of the reactor channels. In their communication on the following pages, D.T. McQuade and co-workers report a solution to this problem by using a monodisperse droplet flow to isolate the solid particles from the walls of the reactor tubing.


WILEY InterScience DISCOVER SOMETHING GREAT
© 2006 Wiley-VCH Verlag GmbH & Co. KGaA, Weinheim

Microreactors

DOI: 10.1002/anie.200503925

# Solving the Clogging Problem: Precipitate-Forming Reactions in Flow**

*Sarah L. Poe, Meredith A. Cummings, Michael P. Haaf, and D. Tyler McQuade**

Techniques developed in recent decades have done little to change the fundamental processes of chemistry. Reaction vessels of a century ago continue to be the standard reactors of today. Recently, however, increasing attention has been paid to chemical reactions performed in microreactors.[1] Reactions are performed in these microfluidic devices by flowing reactants through channels that generally range in size from 10 to 500 μm. On account of its small proportions, a flat microchannel with a width of 100 μm has a specific surface-area-to-volume ratio that is 200 times larger than that of a 100-mL flask and over 3000 times larger than a tank that occupies a cubic meter.[2] This increased surface-area-to-volume ratio allows for better molecular-diffusion and heat-transfer properties, which allow faster and more-selective chemical reactions.[3]

From an industrial standpoint, microreactors are advantageous because they eliminate the need to scale up a reaction. Whereas in traditional process chemistry bench-top syntheses must be redesigned for industrial compatibility, a method known as numbering-up involves the addition of microreactors to achieve the desired throughput.[4] As every reactor is identical to the pilot reactor, there is no need to change dimensions or conditions. Other advantages include increased safety,[5] lower costs, and more environmentally friendly chemistry owing to efficient reactions that require less solvent.

Despite the numerous advantages of microreactors, they are not without their drawbacks.[6] Researchers in an academic setting have been slow to embrace these systems because of their cost and inflexibility.[7] The manufacture of a single microreactor can be a very time- and cost-intensive process, and once a microreactor has been developed, there is rarely any opportunity to make variations to the device.[8] Another commonly cited concern is the clogging of the channels that occurs upon precipitate formation.[9] The handling and processing of solids make up a significant proportion of laboratory and industrial processes, and current microreactor technology is not yet ready to handle these syntheses efficiently.[10] There has recently been an increased effort to deal with this problem, although many industrial solutions come at a large expense. A less expensive approach incorporates a periodic purging step to flush out solids that have formed on the channel walls.[11] However, this method is not effective if significant solid buildup occurs before purging. A more attractive alternative involves performing reactions in droplets that travel through the microreactor channels inside a carrier phase.[12]

Fluid fields generated in microfluidic devices can control reagent mixing[13] and allow the formation of an emulsion upon the collision of two immiscible liquids. We have recently reported a simple microfluidic device that can replicate these flow phenomena.[14] Our device is composed of syringe pumps, syringes, needles, and ordinary laboratory tubing—all of which are relatively inexpensive and commercially available (Figure 1). Development of our microreactor to facilitate chemical syntheses would potentially ameliorate some of the problems still plaguing microreactors, namely their cost and channel clogging. By utilizing disperse-phase droplets as individual reactors, we can confine the solid products to these droplets, thus keeping them away from the tubing walls and avoiding clogged channels. Herein, we present the results of the first chemical syntheses performed in our microreactor and show that our device is practical and efficient for the production of solids in a microfluidic device.[15]

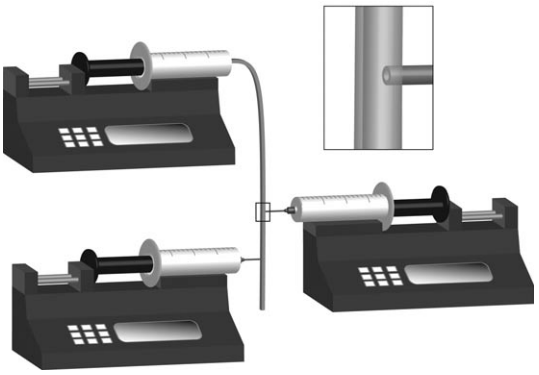


***Figure 1.*** Basic design of our microfluidic reactor. The top-left syringe pump contains the carrier phase, the right pump contains the first disperse phase, and the bottom-left pump contains the second disperse phase. Reagents are injected through a 30-gauge blunt-edge needle (see inset).

By nature of its design, our microfluidic device is versatile, bearing the essential features of the reactor illustrated in Figure 1. Additional fluid junctions may be added as needed simply by inserting a needle anywhere along the tubing.

To demonstrate the suitability of our device for the synthesis of solid particles, we chose a simple system in which aqueous reagents combine to form a solid precipitate. Having successfully demonstrated the ability to synthesize solids by

[*] S. L. Poe, Prof. D. T. McQuade
Department of Chemistry and Chemical Biology
Cornell University
Ithaca, NY 14853 (USA)
Fax: (+1) 607-255-4137
E-mail: dtm25@cornell.edu
M. A. Cummings, Prof. M. P. Haaf
Chemistry Department
Center for Natural Sciences
Ithaca College
Ithaca, NY 14850 (USA)

[**] This work was supported by NSF Sensors (CTS-0329899), ARO MAP-MURI, Cornell Center for Materials Science, and the Beckman Foundation.

 © 2006 Wiley-VCH Verlag GmbH & Co. KGaA, Weinheim 

interfacial polymerization in a two-flow system,[14] we took advantage of the versatility of our device and added a third fluid flow. In each case, an inert carrier fluid was employed as the continuous phase, and disperse-phase reagents were injected into the tubing through separate syringe pumps located downstream from the carrier-phase source. Reagent mixing occurred in one of two ways. If both disperse phases are immiscible with the carrier phase, the mixing of the reagents is initiated by the collision of two different reagent-phase droplets (Figure 2a). This type of mixing was observed when mineral oil was used as the carrier phase. On the other hand, reagents that are miscible with the carrier phase are injected coaxially as the final reagent. In this case, the mixing is caused both by infusion of the second reagent into the first and by diffusion from the carrier phase into the disperse phase (Figure 2b). In both of these cases, chaotic advection could be induced by passing the fluid stream through winding tubing (Figure 2c).[16] We used 30-gauge (0.15 mm i.d.) blunt-edge needles for reagent introduction to obtain spherical droplets (Figure 1, inset); beveled needles do not result in clean snap-off of the droplets.

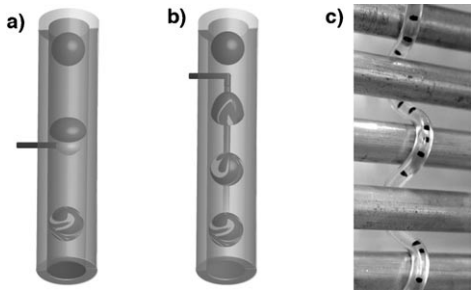



***Figure 2.*** Reagents are mixed inside the tubing by droplet–droplet collision (a) or infusion followed by diffusion (b). Mixing can be enhanced by chaotic advection induced by passing the reaction stream through winding tubing (c).

A number of research groups have employed fluorinated solvents as carrier phases for microfluidic processes to minimize the possibility of side reactions.[17] These solvents, however, can be expensive and are rarely used as common laboratory reagents. Instead, we chose mineral oil, hexane (mixture of isomers), and toluene as relatively inert and readily available carrier phases.

The first reaction we performed was the synthesis of indigo (**1**), which involves a base-catalyzed aldol condensation between acetone and 2-nitrobenzaldehyde (**2**; Scheme 1). The synthesis of this dye was appealing not only because it results in the precipitation of a solid, but also because the product stains the poly(vinyl chloride) (PVC) tubing upon contact, which provides an easy means of determining the effectiveness of our method for isolating the solid from the channel walls. We found that a mineral oil flow rate of 3 mL min$^{-1}$ produces sufficiently small droplets that are confined to the center of the tubing. Figure 3 illustrates the differences observed when indigo is synthesized in the presence and absence of a carrier phase.

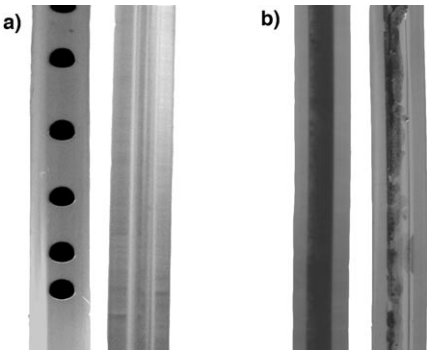
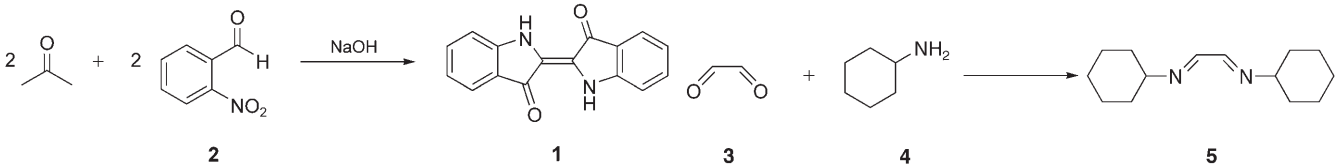



***Figure 3.*** Demonstration of the effectiveness of the carrier phase in the formation of solids. Comparison of the tubing during (left tube) and after (right tube) the synthesis of indigo in the presence (a) and absence (b) of a mineral oil carrier phase.

The reagent collision shown in Figure 2a and b induces some mixing of the reagents. It has been shown that a further enhancement is observed when the droplets are flowed through a winding channel, which causes mixing by chaotic advection.[16] We observed a qualitatively similar phenomenon when we wound our tubing through a series of parallel horizontal bars. When the indigo synthesis was performed inside this tubing, the indigo formation (observed by a color change) occurred more rapidly than it did in straight tubing. Characterization was not performed for this reaction due to well-established purification issues.[18]

This method of producing solids in microreactors by using a monodisperse droplet flow can be extended to carrier phases other than mineral oil. The reaction of glyoxal (**3**) with cyclohexylamine (**4**) results in the precipitation of *N*,*N*′-dicyclohexylethylenediimine (**5**; Scheme 2). When mineral oil is used as the carrier phase, the droplet–droplet phenomenon shown in Figure 2a is observed. However, as **5** is soluble in mineral oil, product recovery is difficult. In contrast, the use of hexane (mixture of isomers) as the carrier phase allows both the formation of solid in the monodisperse flow as well as easier extraction of the solid. Owing to the decreased viscosity and density of the hexane carrier phase relative to mineral oil, higher flow rates are required to achieve the




**2** **1** **3** **4** **5**

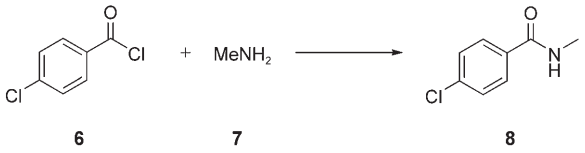
***Scheme 1.*** Synthesis of indigo (**1**).

***Scheme 2.*** Synthesis of *N*,*N*′-dicyclohexylethylenediimine (**5**).

 © 2006 Wiley-VCH Verlag GmbH & Co. KGaA, Weinheim 

desired flow type. We found that a flow rate of at least 12 mL min$^{-1}$ for the hexane phase yields desirable conditions for the formation of solid without channel blockage, although a rate as low as 5 mL min$^{-1}$ acts as an efficient purging system by keeping the channel walls free of solids.

The final microfluidic reaction we studied was the conversion of 4-chlorobenzoyl chloride (**6**) and methylamine (**7**) into 4-chloro-*N*-methylbenzamide (**8**; Scheme 3). This




**6** **7** **8**

***Scheme 3.*** Synthesis of 4-chloro-*N*-methylbenzamide (**8**).

highly exothermic reaction was performed in our microreactor with no safety concerns. The small dimensions of the device not only mitigated the violence with which the reaction took place, but they have also increased the yield of **8** (Table 1). The use of toluene as the carrier phase for this reaction further demonstrates the versatility of our system.

***Table 1:*** Synthesis of solids in our microfluidic device.

| Product | System | Yield [%][a] | Purity [%][b] | STY[c] | Rel. STY |
|---|---|---|---|---|---|
| **5** | flow | 97.0 | 94.5 | 11.44 | 25.55 |
| **5** | batch | 99.4 | 96.6 | 0.4478 | 1.00 |
| **8** | flow | 87.6 | >99 | 9.150 | 20.43 |
| **8** | batch | 76.9 | >99 | 0.7140 | 1.59 |

[a] Crude yields are reported for **5**; purified yields are reported for **8**. [b] The purities were determined from $^{13}$C satellites in the $^{1}$H NMR spectra. The purities of the crude product are reported for **5**; the purities of the purified product are reported for **8**. [c] Space–time yields are reported in mol m$^{-3}$ min$^{-1}$.

Batch syntheses were carried out as a control by stirring the reagents for the same amount of time as the microreactor experiments were allowed to run. As indicated in Table 1, the yields for the microreactor products are comparable to—if not greater than—those for the batch reactions. Also, space–time yields (STY) for the solids formed by microscale flow were much higher than those for solids formed in the macroscale batch reactions. High yields were obtained in the microfluidic system even when one reagent was miscible with the carrier phase. Although we expected lower yields as a result of the miscible reactant flowing into both the carrier and reactant phases, this was not observed, which suggests that diffusion is fast enough in our system to ensure reagent mixing.

In summary, we have reported a practical method for producing solids in microreactors. As demonstrated by the indigo synthesis, by performing these reactions in a monodisperse droplet flow, the solid particles are effectively isolated from the walls of the tubing. Our device not only allows the practical synthesis of solids in microfluidic devices, it also retains the advantages of traditional microreactors. Its ease of use, the widespread availability of many of its components, and its versatility provide further benefits. Future work with our microfluidic device includes temperature-controlled experiments as well as multistep syntheses in a single device.

## Experimental Section

**1**: Mineral oil (15 mL, 3 mL min$^{-1}$) was used as the carrier phase in 0.0625 inch (1.59 mm) internal diameter (i.d.) PVC tubing. NaOH (1 M in water, 3 mL, 0.6 mL min$^{-1}$) was injected into the center of the carrier phase. **2** (0.66 M in acetone, 3 mL, 0.6 mL min$^{-1}$) was introduced into the tubing further downstream. The pumps were allowed to run for 5 minutes while the product was collected over an ice–water bath.

**5**: Hexane (mixture of isomers, 60 mL, 6 mL min$^{-1}$) was used as the carrier phase in 0.066 inch (1.68 mm) i.d. polyethylene (PE) tubing. **3** (0.40 M in water, 12 mL, 1.2 mL min$^{-1}$) was injected into the center of the carrier phase. **4** (4.368 M in water, 2.4 mL, 0.24 mL min$^{-1}$) was introduced into the tubing further downstream. The pumps were allowed to run for 10 minutes while the product was collected at room temperature. Evaporation of the solvent yielded a white solid.

**8**: Toluene (70 mL, 7 mL min$^{-1}$) was used as the carrier phase in 0.066 inch (1.68 mm) i.d. PE tubing. **7** (1.44 M in water, 3 mL, 0.3 mL min$^{-1}$) was injected into the center of the carrier phase. **6** (1.0 mL, 0.1 mL min$^{-1}$) was introduced into the tubing further downstream. The pumps were allowed to run for 10 minutes while the product was collected at room temperature. Evaporation of the solvent and recrystallization from MeOH/$H_2O$ afforded needles of white solid.

Received: November 5, 2005
Published online: January 13, 2006

**Keywords:** aldol reaction · flow reactions · microreactors · synthesis design

[1] a) T. Schwalbe, A. Kursawe, J. Sommer, *Chem. Eng. Technol.* **2005**, *28*, 408; b) T. Wu, Y. Mei, J. T. Cabral, C. Xu, K. L. Beers, *J. Am. Chem. Soc.* **2004**, *126*, 9880; P. Watts, S. J. Haswell, *Chem. Eng. Technol.* **2005**, *28*, 290; c) E. Comer, M. G. Organ, *J. Am. Chem. Soc.* **2005**, *127*, 8160; d) X. Zhang, S. Stefanick, F. J. Villani, *Org. Process Res. Dev.* **2004**, *8*, 455; e) J. Yoshida, *Chem. Commun.* **2005**, 4509.
[2] S. Taghavi-Moghadam, A. Kleemann, K. G. Golbig, K, *Org. Process Res. Dev.* **2001**, *5*, 652.
[3] a) T. Bayer, K. Himmler, *Chem. Eng. Technol.* **2005**, *28*, 285; b) J. Yoshida, A. Nagaki, T. Iwasaki, S. Suga, *Chem. Eng. Technol.* **2005**, *28*, 259.
[4] W. Ehrfeld, V. Hessel, H. Lowe, *Microreactors: New Technology for Modern Chemistry*, Wiley-VCH, Weinheim, **2000**, p. 9.
[5] R. D. Chambers, M. A. Fox, D. Holling, T. Nakano, T. Okazoe, G. Sanford, *Chem. Eng. Technol.* **2005**, *28*, 344.
[6] a) E. R. Delsman, M. H. J. M. de Croon, G. D. Elzinga, P. D. Cobden, G. J. Kramer, J. C. Schouten, *Chem. Eng. Technol.* **2005**, *28*, 367; b) Y. Kikutani, T. Kitamori, *Macromol. Rapid Commun.* **2004**, *25*, 158.
[7] K. Shah, W. C. Shin, R. S. Besser, *Sens. Actuators B* **2004**, 157.
[8] R. D. Chambers, M. A. Fox, D. Holling, T. Nakano, T. Okazoe, G. Sanford, *Lab Chip* **2005**, *5*, 191.
[9] C. Boswell, *Chem. Mark. Rep.* **2004**, *266*(11), 8.
[10] D. M. Roberge, L. Ducry, N. Bieler, P. Cretton, B. Zimmerman, *Chem. Eng. Technol.* **2005**, *28*, 318.
[11] A. M. Thayer, *Chem. Eng. News* **2005**, *83*(22), 43.

 © 2006 Wiley-VCH Verlag GmbH & Co. KGaA, Weinheim 

[12] I. Shestopalov, J. D. Tice, R. F. Ismagilov, *Lab Chip* **2004**, *4*, 316.
[13] B. Zheng, J. D. Tice, R. F. Ismagilov, *Anal. Chem.* **2004**, *76*, 4977.
[14] E. Quevedo, J. Steinbacher, D. T. McQuade, *J. Am. Chem. Soc.* **2005**, *127*, 10498.
[15] Z. Chang, G. Liu, Y. Tian, Z. Zhang, *Mater. Lett.* **2004** *58*, 522.
[16] D. L. Chen, C. J. Gerdts, R. F. Ismagilov, *J. Am. Chem. Soc.* **2005**, *127*, 9672.
[17] H. Song, J. D. Tice, R. F. Ismagilov, *Angew. Chem.* **2003**, *115*, 792; *Angew. Chem. Int. Ed.* **2003**, *42*, 768.
[18] R. Kohlhaupt, U. Bergmann, U.S. Patent No. 5,424,453, **1995**.

 © 2006 Wiley-VCH Verlag GmbH & Co. KGaA, Weinheim 

Supramolecular Chemistry

DOI: 10.1002/anie.200503128

# A Supramolecular Bundling Approach toward the Alignment of Conjugated Polymers**

*Yohei Kubo, Yumiko Kitada, Rie Wakabayashi, Takanori Kishida, Masatsugu Ayabe, Kenji Kaneko, Masayuki Takeuchi,* and Seiji Shinkai**

Exploring new methods for controlling the orientation and electronic state of π-conjugated oligomers and polymers is of importance for the production of materials with optimized properties and for their ultimate assembly into molecular circuitry. In addition to supramolecular assembly schemes,[1–4] methods for aligning conjugated polymers, which lead to many new photophysical functions, include the use of metastable states enforced by liquid-crystalline phases,[5–7] Langmuir monolayers at the air–water interface,[8] incorporation into prealigned host matrixes,[9,10] and rubbing.[11,12] Unlike synthetic macromolecular systems, the bundling proteins found in animal cells bind one-dimensional (1D) actin filaments in high affinity to elicit the formation of actin bundles.[13] The bundling proteins possess two interactive modules for cross-linking actin filaments; their distinct properties determine the type of assembly. If one can reconstruct such modules interacting with 1D materials in a supramolecular manner, not only would these systems provide a new means of aligning the materials but also would create complex mesoscopic structures and networks akin to those found in nature. Herein, we report a new concept for aligning and assembling conjugated polymers through the action of supramolecular bundling ("aligner") molecules. We demonstrate this concept by utilizing the dative bonds formed between porphyrinatozinc and amine derivatives because of the high affinity and distinct bonding geometry of these species.[14] We designed the aligner molecules **1** and **2**, which are porphyrinatozinc oligomers,[14,15] to elicit positive homotropic allosterism[16–18] during their binding of the amino-functionalized conjugated polymers CP and CCP in an effort to organize the polymers into aligned, rather than random, assemblies (Figure 1). Although the distances between pairs of porphyrinatozinc units in **1** and **2** aligned in parallel can vary through conformational rearrangements about their rotational axes (the butadiyne unit for **1** and the ethylene bridges for **2**), the distances between the binding subunits when in a cofacial orientation are 2.5 and 2.0 nm, respectively. Each pair of cofacially aligned porphyrinatozinc tweezers in **1** and **2** binds to a diamine moiety of the polymer in an allosteric manner to form polymer bundles (Figure 1 B); in this process, the binding of the first polymer to an aligner molecule facilitates the second binding, which results in the ready formation of aligned assemblies (Figure 1 C).

To confirm the cooperativity of the binding of CP and CCP by **1** and **2**, we used MCP as a guest molecule for **1** and **2**. We noted the formation of the [**1**·MCP] or [**2**·MCP] complexes in $CHCl_3$ from changes in the UV/Vis absorption spectra that occurred upon the successive addition of MCP (see the Supporting Information). The values of $\lambda_{max}$ of the Soret and Q bands shifted to longer wavelengths with tight isosbestic points; these changes are consistent with those observed from studies of other porphyrinatozinc–amine coordination systems.[14] We estimated the stoichiometries of the complexes formed between MCP and both **1** or **2** from molar ratio plots, which clearly indicated the formation of 1:2 [**1**·$(MCP)_2$] and 1:3 [**2**·$(MCP)_3$] complexes. Importantly, plots of absorbance at the Q band (607 nm) versus [MCP] possessed sigmoidal curvature. From analyses of these binding isotherm using nonlinear-curve-fitting and Hill-plot[19] methods, we calculated the association constants ($K_n$/MCP) and Hill coefficients ($n_H$) to be $K_1 = 1.6 \times 10^5$, $K_2 = 3.0 \times 10^5$, and $n_H = 1.9$ for [**1**·$(MCP)_2$] and $K_1 = 8.8 \times 10^5$, $K_2 = 9.2 \times 10^5$, $K_3 = 4.8 \times 10^6$, and $n_H = 2.8$ for [**2**·$(MCP)_3$]. These results clearly indicate that highly cooperative binding occurs between MCP and both **1** and **2**. Extrapolating from the cooperativity and high association constants in the binding of MCP with **1** and **2**, we expected that the diamine moieties in CP and CCP would become juxtaposed and aligned by the clefts in the porphyrinatozinc units in **1** and **2** in a positive homotropic allosteric

[*] Y. Kubo, Y. Kitada, R. Wakabayashi, T. Kishida, Dr. M. Ayabe, Dr. M. Takeuchi, Prof. S. Shinkai
Department of Chemistry and Biochemistry
Graduate School of Engineering
Kyushu University, Fukuoka 819-0395 (Japan)
Fax: (+81) 92-802-2820
E-mail: taketcm@mbox.nc.kyushu-u.ac.jp
seijitcm@mbox.nc.kyushu-u.ac.jp
Prof. K. Kaneko
HVEM Laboratory
Kyushu University
Fukuoka 812-8581 (Japan)

[**] We thank Dr. N. Fujita and Dr. M. Ikeda for fruitful discussions. M.T. and Y.K. thank Prof. A. Ikeda for kindly supplying compound **2**. Y.K. thanks the JSPS Research Fellowship for Young Scientists for financial support. This study was supported partially by a Sumitomo Chemical Award in Synthetic Organic Chemistry Japan, a Grant-in-Aid for Scientific Research B (17350071), and the 21st Century COE Program, "Functional Innovation of Molecular Informatics," of the Ministry of Education, Culture, Science, Sports, and Technology (Japan).

Supporting information for this article is available on the WWW under http://www.angewandte.org or from the author.


InterScience DISCOVER SOMETHING GREAT
© 2006 Wiley-VCH Verlag GmbH & Co. KGaA, Weinheim

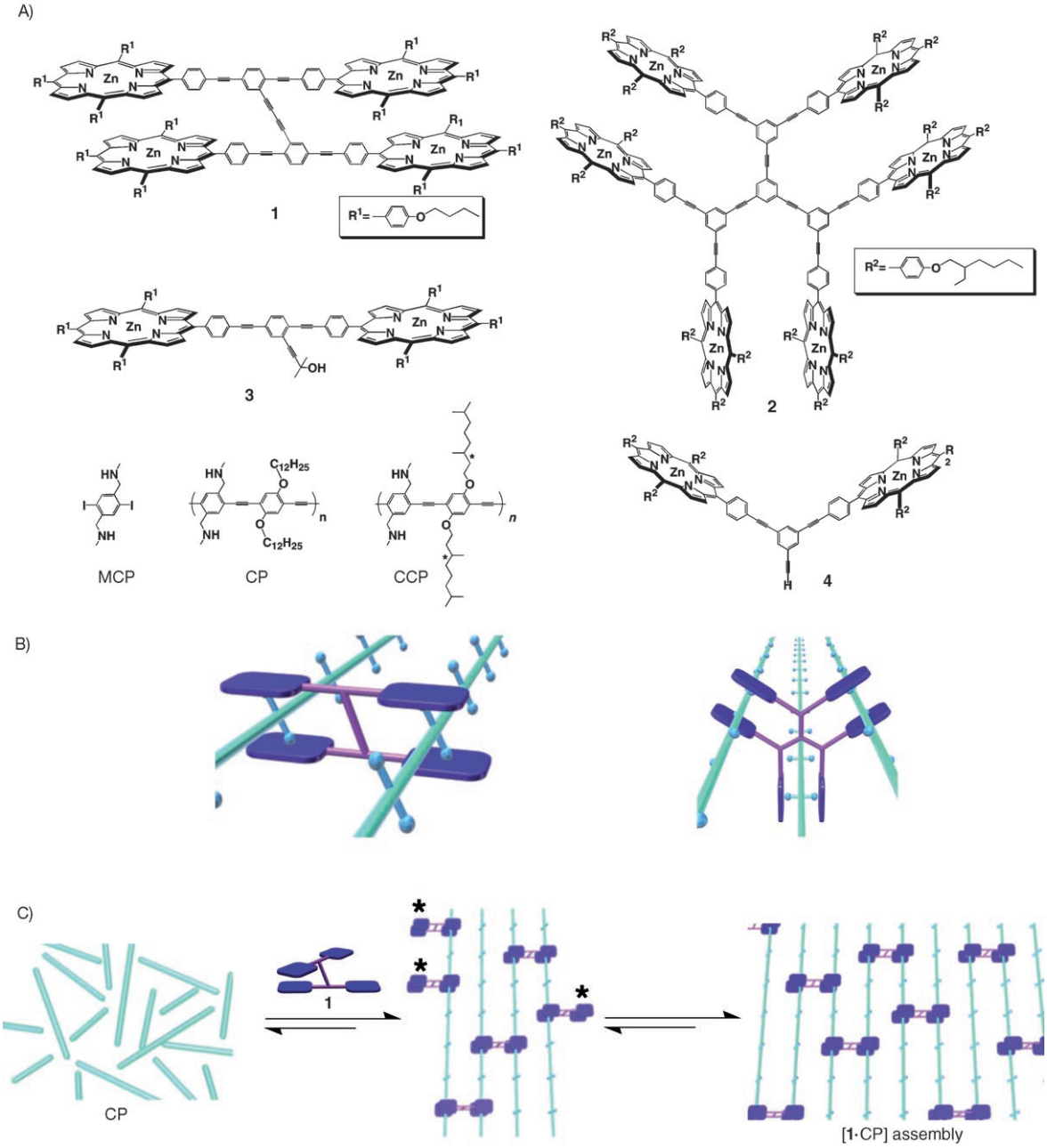



***Figure 1.*** A) Chemical structures of the aligner molecules and conjugated polymers studied herein. CP: number-average molecular mass ($M_n$) = 48 000; CPP: $M_n$ = 18 000. B) Schematic representation of the modes of bundling of the conjugated polymers with **1** (left) and **2** (right). Blue plates denote the porphyrinatozinc complexes in **1** and **2**; sky-blue fibers and spheres denote the polymer backbones and methylaminomethyl moieties, respectively, in the conjugated polymers. C) Schematic illustration of the alignment of the conjugated polymer CP mediated by **1**. The first polymer binding event to the porphyrinatozinc cleft preorganizes the second cleft (denoted by the asterisk) such that it has an even higher affinity toward the second polymer. The conjugated polymers are expected to be juxtaposed to each other to form aligned assemblies.

manner. That is to say that we expected the first polymer binding event to enhance the affinity of the second (and, for **2**, the third) polymer binding event to form aligned supramolecular assemblies; such a process is necessary if we are to avoid the formation of random assemblies. In fact, the addition of CP to a solution of **1** (3.5 μM) or **2** (0.43 μM) in $CHCl_3$ at 25 °C resulted in similar bathochromic shifts in the Soret and Q bands as those observed for **1** or **2** upon the addition of MCP (see Figure 2 and the Supporting Information). The emission intensity of CP ($[CP_{unit}] = 24$ μM; $\lambda_{ex} = 400$ nm) in $CHCl_3$ decreased, without a change in its shape when it was mixed with **1** (see the Supporting Information). This phenomenon is due to efficient energy transfer from CP to **1** within the complex because the emission wavelength of CP overlaps considerably with the absorption of **1**. Deposition of a homogeneous solution of CP ($[CP_{unit}] = 240$ μM) in $CHCl_3$ containing 5.0 wt% polystyrene ($M_w = 200\,000$) on a quartz plate provided us with a solution-cast film. The emission

 © 2006 Wiley-VCH Verlag GmbH & Co. KGaA, Weinheim 

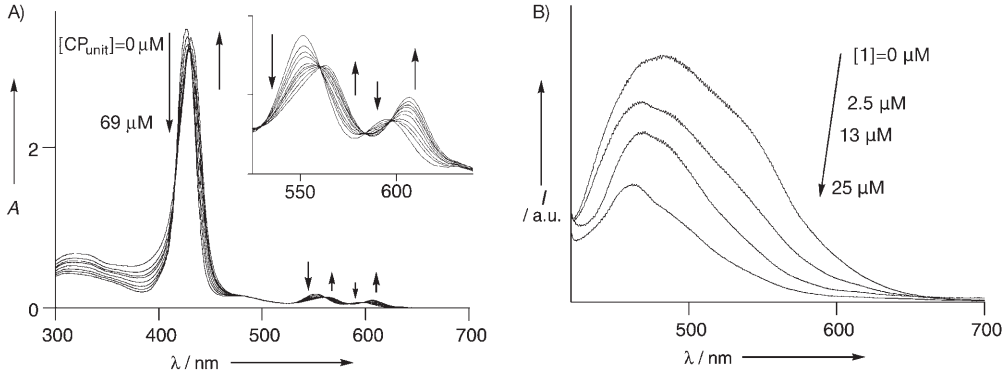



***Figure 2.*** A) UV/Vis spectra of **1** (3.7 μM) upon addition of CP in $CHCl_3$ at 25 °C. Inset: magnified spectra about the Q bands. B) Fluorescence spectral change of CP ($[CP_{unit}] = 240$ μM) in the presence and absence of **1** in the film cast from a solution of $CHCl_3$ containing polystyrene (5 wt%). The fluorescence intensity was normalized with respect to the absorption at 400 nm ($\lambda_{ex}$).

spectrum of this CP film is broadened relative to that recorded in dilute solution ($[CP_{unit}] = 24$ μM); this effect is probably due to random aggregation of the polymer main chains in the film. Interestingly, the addition of **1** turned the broad emission—even that obtained in the solid state—into the sharp one observed for a dilute solution of the [**1**·CP] complex (Figure 2B). Because the distance between the two distinct binding sites in **1** is 2.5 nm, the bundled assemblies of CP no longer emit the broad emission because of their random aggregation. Polarized optical microscopy images of [**1**·CP], as well as UV/Vis and fluorescence spectroscopic studies, also support the formation of ordered assemblies in the solid state (see the Supporting Information). These findings suggest that the structures of the supramolecular polymer bundles are maintained in the solid state; we further confirmed this situation by using atomic force microscopy (AFM) and transmission electron microscopy (TEM).

Figure 3A displays an AFM image of CP (deposited from a 1.3 μM solution in $CHCl_3$), in which the CP assembly is well dispersed in a rectangular shape on highly oriented pyrolytic graphite (HOPG). We calculated the average height to be 0.3 nm from the height profile. Polymer CP probably lies on HOPG in a monolayer with a face-on orientation (Figure 3A). From the height profile of the deposition samples of **1** and **2**, their thickness was shown to be 0.6 nm, thus indicating that porphyrins in **1** and **2** lie on the HOPG in a face-on orientation as much as possible. By mixing CP ($[CP_{unit}] = 1.2$ μM) with **1** (0.08 μM), the assemblies assigned to CP or **1** itself disappeared, and we observed a 20–25-fold larger (in area ratio) homothetic shape for the CP assemblies

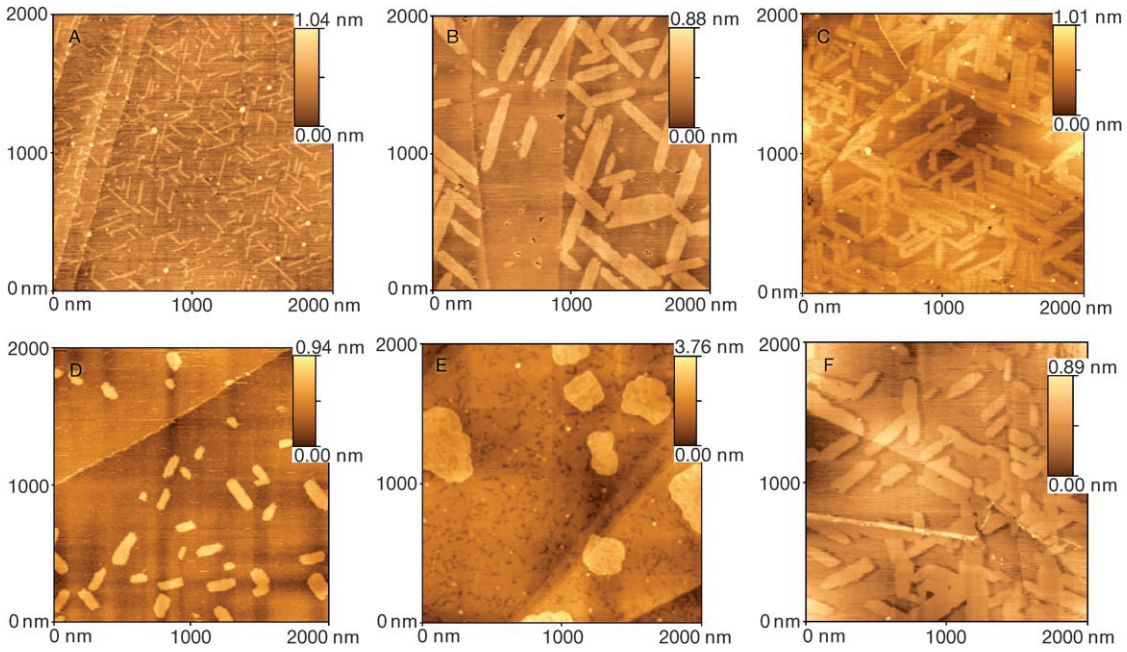



***Figure 3.*** Representative AFM images of CP and [**1**·CP] assemblies deposited from solution of $CHCl_3$ onto HOPG. Compounds **1** and **2** formed amorphous assemblies on HOPG. The mixing ratio ($\alpha$) is defined as $\alpha = [CP]/[\mathbf{1}$ or $\mathbf{2}]$ (mol/mol). A) CP ($[CP_{unit}] = 1.3$ μM); B) [**1**·CP] assemblies ($\alpha = 15$); C) [**1**·CP] assemblies ($\alpha = 9.1$); D) [**1**·CP] assemblies ($\alpha = 3.1$); E) [**1**·CP] assemblies aged for 24 h under the same conditions as those in (B); F) [**2**·CP] assemblies prepared under the conditions in which $[CP_{unit}] = 1.3$ μM and $[\mathbf{2}] = 0.17$ μM ($\alpha = 5.9$).

 © 2006 Wiley-VCH Verlag GmbH & Co. KGaA, Weinheim 

that had a height of 0.35 nm (see Figure 3B and the Supporting Information). Under the conditions in Figure 3B, every seventh repeating unit of CP on average was complexed with one porphyrin cleft of **1**, thus showing that **1** was not so densely packed in [**1**·CP] assemblies. The fact that the overall assembly height is larger than observed for CP itself shows that CP remain aligned in a porous-like solid-state morphology rather than collapsing on the surface. Given the degree of polymerization of CP, **1** must bundle with, and noncovalently splice, CP to form such aligned supramolecular assemblies. The polymer bundling and splicing caused by **1** is highly dependent upon the mixing ratio between CP and **1** and the aging period in solution. A higher molar ratio of **1** decreased the size of the assemblies (see Figure 3C and D); that is, the dimensions of the superstructure are readily controllable by changing the mixing ratio of CP and **1**. Aging the [**1**·CP] complex for 24 h in $CHCl_3$ at 25 °C resulted in further growth of three-dimensional (3D) assemblies to a height of 1.5 nm (Figure 3E). From these results, we infer that the bundling and splicing processes caused by **1** in solution take place thermodynamically to form initially two-dimensional and then 3D aligned structures. Compound **2** also aligned CP into sheetlike assemblies that had an average height of 0.3 nm and 9–16-fold larger areas than that of CP itself (Figure 3F). The clefts of the porphyrinatozinc units in **1** and **2** are essential for the bundling and noncovalent splicing of the polymers, as evidenced by the fact that neither **3** nor **4** was capable of producing similar assemblies.

The electron micrograph images of the complexes provide information regarding how **1** and **2** align the polymer. We observed highly ordered structures in the TEM and high-resolution TEM (HRTEM) images (see Figure 4 and the Supporting Information). We prepared solution-cast films of the polymer—in the presence and absence of **1** or **2**—on a TEM grid without staining. An HRTEM image of the CP assemblies was observed (see the Supporting Information) in which the periodicity of the dark layers was 0.4 nm, as determined from the Fourier-filtered image. We suggest that the dark sections in the electron micrographs to be regions that contain the ordered π-stacked layers. This hypothesis is supported by the fact that the periodic distance of 0.4 nm is comparable with the distance between π-conjugated molecules that are associated through π–π stacking interactions.[20] In the low-magnification micrograph, crystalline sheets (see the Supporting Information) and a multilamellar morphology (Figure 4A) with a periodicity of 2.0 nm over a 200-nm-wide distance was observed for the mixture of CP and **1**; this superstructure is totally different from that formed from CP itself. We believe that the dark regions observed in the TEM images of the assembly of CP and **1** to be domains that contained ordered π-stacked layers and/or the heaviest atom (Zn) in **1**; the results of energy dispersive X-ray spectroscopy (EDX) support this hypothesis (see the Supporting Information). The period of 2.0 nm corresponds to the distance between CP units when they are bundled in a parallel manner (Figure 5A). We recorded an HRTEM image of one of the sections of the assemblies constructed from CP and **1** to obtain additional evidence for the highly aligned nature of the polymer units. The micrograph in Figure 4B demonstrates

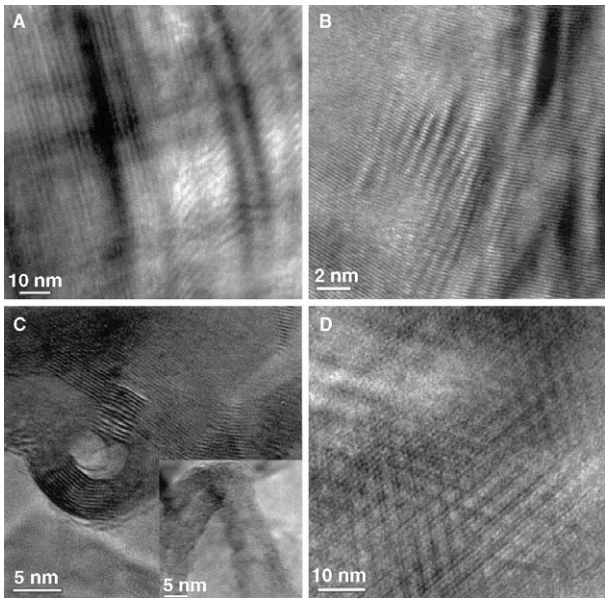



***Figure 4.*** Electron micrographs (no staining) of conjugated polymers aligned by **1** or **2**. A) A TEM image of aligned [**1**·CP] assemblies consisting of dark and light bands. The periodicity between the dark bands is 2.0 nm. B) An HRTEM image of [**1**·CP] assemblies with 0.2 nm periodicity, as revealed from the Fourier-filtered image. C) An HRTEM image of [**2**·CP] assemblies displaying multiwalled tubular and lamellar contrasts. The image in the inset displays a multiwalled tube that has bent from the back to the front. D) An HRTEM image of the [**1**·CCP] assemblies displaying a kagomé lattice contrast. The periodicity of the kagomé lattice is 0.8 nm.

that the film comprised many dark/light layers and that the periodicity of the dark contrast was 0.2 nm, which is much shorter than the π–π-stacking distances of common organic molecules. We infer that the dark/light contrast arises from the phase contrast provided by the zinc atoms in **1** aligned in [**1**·CP] assemblies when we observe the image in Figure 4A at an oblique angle. Figure 4C displays the supramolecular assemblies formed from CP and **2**, which we expected to bundle three CP strands to form 3D superstructures. We observe in this image unique supramolecular assemblies that possess both lamellar and multiwalled tubular contrast; the inside diameters of the tubes varied between 2 and 5 nm. The dark periodicities of the lamellar and multiwalled tubular assemblies were both 0.35 nm; this observation indicates that these assemblies were both constructed from the same structural unit (Figure 5B). Polymer CCP is also bound to **1** in $CHCl_3$ in a manner similar to that of CP and **1**. In addition to changes in the UV/Vis and fluorescence spectra, our circular dichroism (CD) spectroscopic measurements also support the formation of a complex between CCP and **1** (see the Supporting Information). The split-type CD signal that we observed in the Soret-band region indicates that the chiral side chains in CCP influence the orientation of the porphyrin plane in **1** to produce an induced-CD (ICD) signal, which should reflect the contrast pattern of the [**1**·CCP] assemblies. In fact, Figure 4D represents the HRTEM micrograph of the aligned assemblies constructed from CCP and **1**; the kagomé lattice and triangular grid patterns[21,22] with a 0.8-nm-

 © 2006 Wiley-VCH Verlag GmbH & Co. KGaA, Weinheim 

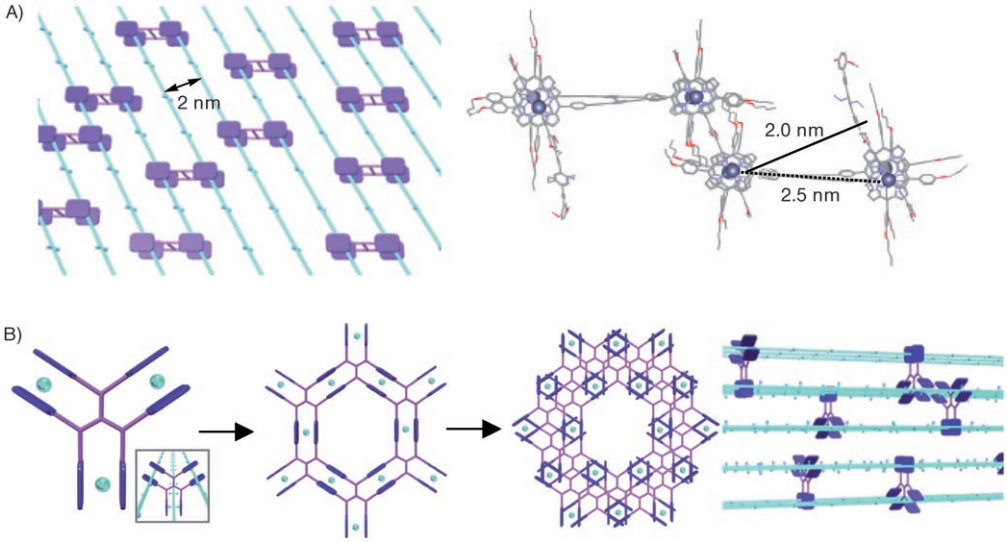



***Figure 5.*** Schematic representations of how A) **1** might align CP to form aligned assemblies and how B) [**2**·CP] assemblies might form multiwalled tubular structures.

periodicity dark contrast regions are clearly apparent. The differences between the contrast patterns of CP (lamellar) and CCP (kagomé lattice) might arise from the orientation of **1** in the assemblies being affected differently by the alkyl chains of CP and CCP.[23] These micrographs demonstrate that the conjugated polymers were aligned by both **1** and **2** to form highly ordered supramolecular assemblies and that the spacings and arrangements of the polymer binding sites in the aligner molecules—and the nature of the peripheral alkyl chains of CP and CCP—should determine the mode of polymer assembly.

The exploitation of the supramolecular bundling that we have described herein was inspired by the mode of action of actin-filament bundling proteins. Our approach provides a new, general means of preparing complex, ordered assemblies of conjugated polymers. Introducing interactive sites for the aligner molecules at special positions along the conjugated polymers allows control over the dimensions, morphologies, and interpolymer spacings. The concepts that we have introduced complement the existing techniques for supramolecular and macromolecular assembly; in addition, they allow the interpolymer spacing and orientation to be controlled so that they can influence the photophysical properties of the conjugated polymer. Moreover, this approach permits the construction of alternating arrays of different conjugated polymers. We believe that such a system could be realized by utilizing an aligner molecule that displays positive heterotropic allosterism toward such polymers.

## *Experimental Section*

All starting materials and solvents were purchased from Tokyo Kasei Chemicals or Wako Chemicals and used as received. The $^1$H NMR spectra were recorded on a Brucker DRX 600 (600 MHz) spectrometer. Chemical shifts are reported in ppm downfield from tetramethylsilane as the internal standard. Mass-spectral data were obtained using a Perseptive Voyager RP MALDI-TOF mass spectrometer and/or a JEOL JMS HX110A high-resolution magnetic sector FAB mass spectrometer. UV/Vis and fluorescence spectra were recorded using Shimadzu UV-2500 PC and Perkin-Elmer LS55 spectrophotometers.

Binding isotherm analysis: The cooperative guest-binding process was analyzed according to the Hill equation: $\log[y/(1-y)] = n\log[\text{guest}] + \log K$, where $K$, $y$, and $n_H$ are the association constant, the extent of complexation, and the Hill coefficient, respectively. The slope and the intercept of the linear (Hill) plots allow $K$ and $n_H$ to be estimated; these values are useful measures of cooperativity. A higher value of $n_H$ is related to a higher degree of cooperativity; the maximum value is equal to the number of binding sites. In the analysis of the binding isotherm from the Hill plot, we evaluated the concentration of the unbound guest ([guest]) by assuming that the 1:2 complex of **1** is formed quantitatively when the absorption change is saturated.

Sample preparation for AFM and TEM measurements: The following provides a typical example of the approach. A solution of CP in $CHCl_3$ ($[CP_{unit}] = 290\ \mu M$) and **1** (20.0 μM) was prepared; UV/Vis spectroscopy confirmed that the [**1**·CP] complex had formed quantitatively. This solution was then diluted because the higher-concentration [**1**·CP] assemblies covered the whole area of the HOPG or TEM grid. The resultant dilute solution of [**1**·CP] assemblies in $CHCl_3$ was cast on HOPG or a copper TEM grid upon a holey carbon-support film.

TEM and HRTEM images were acquired using a JEOL TEM-2010 (accelerating voltage: 120 kV) and a TECNAI-20 FEI (accelerating voltage: 200 kV), respectively. A sample solution was placed on a copper TEM grid upon a holey carbon-support film. The TEM grid was dried under reduced pressure for 6 h prior to TEM observation.

AFM images were acquired in air using a Topo METRIX SPM 2100 (noncontact mode). The sample was cast on HOPG and dried for 1 h under reduced pressure prior to AFM observation.

Received: September 2, 2005

**Keywords:** alignment · allosterism · conjugated polymers · porphyrinoids · supramolecular chemistry

 © 2006 Wiley-VCH Verlag GmbH & Co. KGaA, Weinheim 

[1] J.-M. Lehn, *Supramoleculer Chemistry*, VCH, New York, **1995**.
[2] S. I. Stupp, V. LeBonheur, K. Walker, L. S. Li, K. E. Huggins, M. Keser, A. Amstutz, *Science* **1997**, *276*, 384 – 389.
[3] S. Park, J.-H. Lim, S.-W. Chung, C. A. Mirkin, *Science* **2004**, *303*, 348 – 351.
[4] H. Sirringhaus, P. J. Brown, R. H. Friend, M. M. Nielsen, K. Bechgaard, B. M. W. Langeveld-Voss, A. J. H. Spiering, R. A. J. Janssen, E. W. Meijer, P. Herwig, D. M. de Leeuw, *Nature* **1999**, *401*, 685 – 688.
[5] H. Goto, K. Akagi, H. Shirakawa, *Synth. Met.* **1997**, *84*, 373 – 374.
[6] T. M. Long, T. M. Swager, *J. Am. Chem. Soc.* **2002**, *124*, 3826 – 3827.
[7] K. P. Fritz, G. D. Scholes, *J. Phys. Chem. B* **2004**, *108*, 10141 – 10147.
[8] J. Kim, T. M. Swager, *Nature* **2001**, *411*, 1030 – 1034.
[9] A. Montali, C. Bastiaansen, P. Smith, C. Weder, *Nature* **1998**, *392*, 261 – 264.
[10] W. C. Molenkamp, M. Watanabe, H. Miyata, S. H. Tolbert, *J. Am. Chem. Soc.* **2004**, *126*, 4476 – 4477.
[11] M. Hamaguchi, K. Yoshino, *Appl. Phys. Lett.* **1995**, *67*, 3381 – 3383.
[12] P. Dyreklev, M. Berggren, O. Inganas, M. R. Anderson, O. Wennestrom, T. Hjertberg, *Adv. Mater.* **1995**, *7*, 43 – 45.
[13] B. Alberts, A. Johnson, J. Lewis, M. Raff, K. Roberts, P. Walter, *Molecular Biology of the Cell*, Garland Science, New York, **2002**.
[14] Y. Kubo, M. Ikeda, A. Sugasaki, M. Takeuchi, S. Shinkai, *Tetrahedron Lett.* **2001**, *42*, 7435 – 7438.
[15] M. Ayabe, A. Ikeda, Y. Kubo, M. Takeuchi, S. Shinkai, *Angew. Chem.* **2002**, *114*, 2914 – 2916; *Angew. Chem. Int. Ed.* **2002**, *41*, 2790 – 2792.
[16] M. Takeuchi, M. Ikeda, A. Sugasaki, S. Shinkai, *Acc. Chem. Res.* **2001**, *34*, 865 – 873.
[17] S. Shinkai, M. Ikeda, A. Sugasaki, M. Takeuchi, *Acc. Chem. Res.* **2001**, *34*, 494 – 503.
[18] L. Kovbasyuk, R. Kramer, *Chem. Rev.* **2004**, *104*, 3161 – 3188.
[19] K. A. Connors, *Binding Constants*, Wiley, New York, **1987**.
[20] S. Tanaka, M. Shirakawa, K. Kaneko, M. Takeuchi, S Shinkai, *Langmuir* **2005**, *21*, 2163 – 2172.
[21] J. L. Atwood, *Nat. Mater.* **2002**, *1*, 91 – 92.
[22] D. G. Nocera, B. M. Bartlett, D. Grohol, D. Papoisakis, M. P. Shores, *Chem. Eur. J.* **2004**, *10*, 3850 – 3859.
[23] At the present stage, we cannot rule out the possibility that the difference in the molecular weights of CP and CCP influenced the morphological difference of the supramolecular assemblies.

 © 2006 Wiley-VCH Verlag GmbH & Co. KGaA, Weinheim 

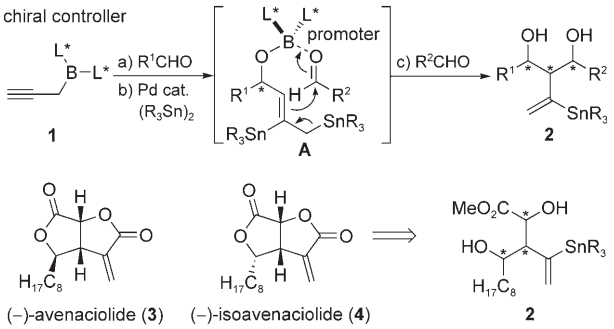
Synthetic Methods

DOI: 10.1002/anie.200503863

# Asymmetric Sequential Allylic Transfer Reaction for the Synthesis of 2-(1-Stannylvinyl)-1,3-diols: Concise Synthesis of (−)-Avenaciolide and (−)-Isoavenaciolide**

*Chan-Mo Yu,* Jinsuop Youn, and Juyoung Jung*

Stereocontrolled consecutive processes can offer advantages over stepwise transformations by increasing chemical efficacy and saving efforts as a result of a simple operation.[1] During the course of our research program aimed at developing new synthetic methods for the stereoselective construction of pyran rings through stepwise allylic transfer reactions,[2] we disclosed our investigations on transition-metal-catalyzed intramolecular allylations mainly between allene and carbonyl functionalities to afford cyclic compounds with high levels of stereoselectivity.[3] With these observations in hand, we became interested in designing a sequential allylic transfer reaction from **1** with two aldehydes to form acyclic 2-(1-stannylvinyl)-1,3-diols **2**, which contain versatile functional groups (Scheme 1).




***Scheme 1.*** General strategy for the synthesis of **2**, and thus natural products **3** and **4**, by a sequential approach. L* = chiral ligand.

It was envisaged that the sequential allylic transfer reaction starting from **1** could be realized by a three-step sequence as shown in Scheme 1. To provide direct access to **2**, we considered the bis(stannyl) compound **A** as a crucial intermediate. The transformation involves propargylboration

[*] Prof. Dr. C.-M. Yu, J. Youn, J. Jung
Department of Chemistry and Institute of Basic Sciences
Sungkyunkwan University
Suwon 440-746 (Korea)
Fax: (+82) 31-290-7075
E-mail: cmyu@chem.skku.ac.kr

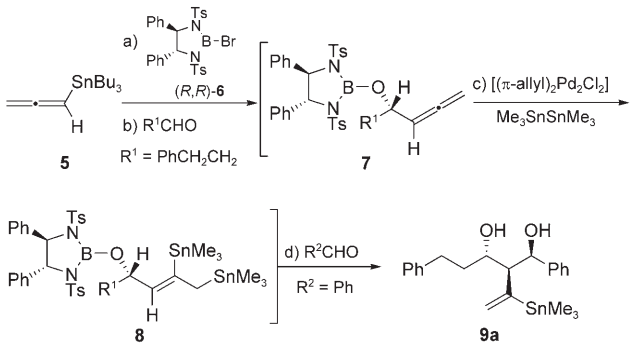
[**] Generous financial support from the Korea Science & Engineering Foundation (R01-2005-000-10381-0) and the Center for Molecular Design and Synthesis (CMDS, KOSEF-SRC) at KAIST is gratefully acknowledged.

Supporting information for this article is available on the WWW under http://www.angewandte.org or from the author.


© 2006 Wiley-VCH Verlag GmbH & Co. KGaA, Weinheim

with an aldehyde to yield an allenic species, distannation of the allene moiety using a palladium catalyst to form the allylic tin reagent **A**, and a second allylic transfer reaction with another aldehyde by activation of the existing boronyl group. Thus, the boronyl moiety would play two important roles—as a chiral controller and a Lewis acid promoter—to regulate reactivity and stereoselectivity during the reaction sequence. Herein, we report a one-pot sequential transformation for the stereoselective synthesis of 2-(1-stannylvinyl)-1,3-diols with the generation of three contiguous stereogenic centers, and application of this method to the synthesis of (−)-avenaciolide and (−)-isoavenaciolide in three steps.

We began with **5** and **6** for the first allylic transfer, as developed by Corey et al.,[4] to give easy access to **7** with excellent enantioselectivity (Scheme 2). Initial attempts of a



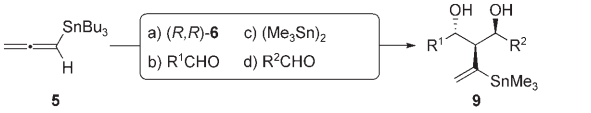

***Scheme 2.*** Preliminary investigations of the asymmetric sequential allylic transfer reaction. Ts = *p*-toluenesulfonyl.

distannation reaction of **7** ($R^1 = PhCH_2CH_2$) with $Bu_3SnSnBu_3$ in the presence of a palladium complex followed by addition to benzaldehyde to give **9a** were unsuccessful under various reaction conditions, presumably owing to a lack of reactivity caused by the steric bulkiness of the tributylstannyl group.[5] We subsequently observed that the use of $Me_3SnSnMe_3$ in the presence of $[(\pi\text{-allyl})_2Pd_2Cl_2]$, which was previously utilized for the cyclization of allene-aldehydes,[3a] could also be employed for this purpose. Upon surveying numerous conditions, the following observations emerged: 1) for the first allylic transfer, the use of 1.3 equivalents of **5** and **6** was optimum to prevent subsequent addition of the same aldehyde; 2) for the distannation reaction, the use of 3 mol% of $[(\pi\text{-allyl})_2Pd_2Cl_2]$ in $CH_2Cl_2$ at −40 °C for 4 h was most efficient in terms of reaction yields; 3) the formation of **8** was confirmed by NMR spectroscopy after quenching with pH 7 buffer solution; 4) only $Me_3SnSnMe_3$ proved to be effective for the transformation; and 5) the use of $CH_2Cl_2$ resulted in optimum chemical yields in comparison to other solvents.

Under optimal conditions, the reaction was conducted by dropwise addition of **5** (1.3 equiv) to (*R*,*R*)-**6** (1.3 equiv) at −10 °C in $CH_2Cl_2$. After 11 h at −10 °C the reaction mixture was cooled to −78 °C, and $PhCH_2CH_2CHO$ (1 equiv) was added during 2 h. To the resulting mixture was then added $Me_3SnSnMe_3$ (1.3 equiv) followed by $[(\pi\text{-allyl})_2Pd_2Cl_2]$ (3 mol%), and the reaction mixture was maintained for 4 h at −40 °C. After cooling to −78 °C, benzaldehyde (1 equiv) was added. Aqueous workup and silica gel chromatography afforded **9a** as a single stereoisomer in 77% isolated yield. Note that although an excess of propargylborane **6** (1.3 equiv) was used, the formation of allenyl carbinol resulting from its reaction with benzaldehyde was not observed. A control experiment clearly revealed that the propargylborane **6** was poisoned during the distannation process presumably by the formation of 2,3-distannylallylborane, which does not react with benzaldehyde at −78 °C.

With the notion that this approach might lead to a general and efficient method, we set out to determine the scope of the reaction (Table 1). Indeed, the method is successful with a

***Table 1:*** Scope of the sequential allylic transfer reaction of **5** and (*R*,*R*)-**6**.[a]



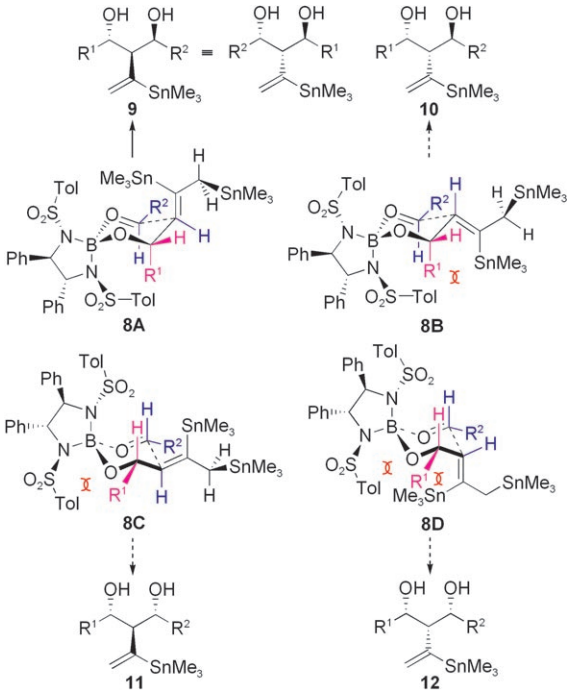

| Entry | $R^1$ | $R^2$ | **9** | Yield [%][b] |
|---|---|---|---|---|
| 1 | $PhCH_2CH_2$ | Ph | **a** | 77 |
| 2 | Ph | $PhCH_2CH_2$ | **b** | 68 |
| 3 | $PhCH_2CH_2$ | $PhCH_2CH_2$ | **c** | 78 |
| 4 | $PhCH_2CH_2$ | $C_5H_{11}$ | **d** | 81 |
| 5 | $C_5H_{11}$ | Ph | **e** | 73 |
| 6 | $Me_2CHCH_2$ | $C_5H_{11}$ | **f** | 68 |
| 7 | $PhCH_2CH_2$ | $Me_2CHCH_2$ | **g** | 71 |
| 8 | $PhCH_2CH_2$ | 4-BrPh | **h** | 72 |
| 9 | $PhCH_2CH_2$ | $C_3H_7CH{=}CH$ | **i** | 63 |
| 10 | $Me_2CH$ | $C_5H_{11}$ | **j** | 66 |
| 11 | $PhCH_2CH_2$ | $Me_2CH$ | **k** | 74 |

[a] Reactions were run in $CH_2Cl_2$. Reagents and conditions: a) −10 °C, 11 h; b) −78 °C, 2 h; c) $Me_3SnSnMe_3$ (1.3 equiv), $[(\pi\text{-allyl})_2Pd_2Cl_2]$ (3 mol%), −40 °C, 4 h; d) −78 °C, 4 h. [b] Refers to yield after purification.

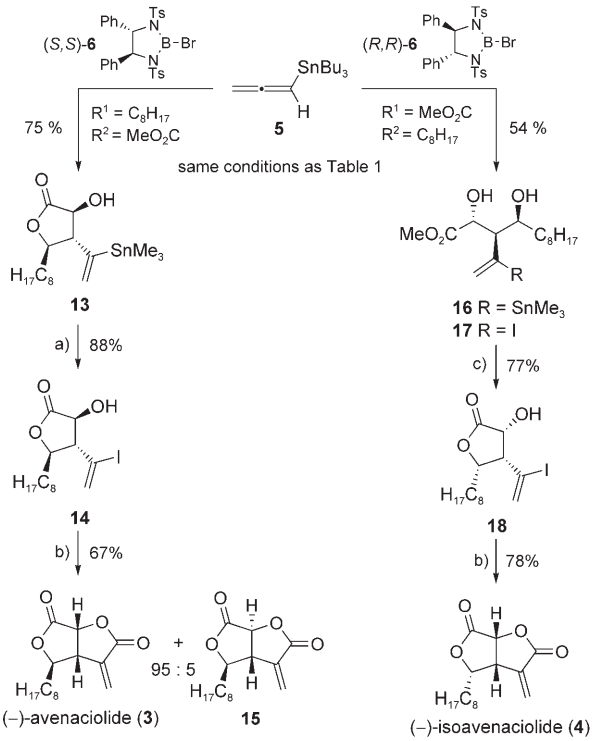
variety of aldehydes to yield the 2-(1-stannylvinyl)-1,3-diols **9** in good yields. It is important to note that the reaction produced no, or only detectable amounts (less than 1%), of minor stereoisomers according to analysis by $^1H$ NMR spectroscopy and HPLC with chiral column (Chiralcel OD-H or OD-RH) in comparison with authentic samples prepared from (*S*,*S*)-**6**.

The stereochemical outcome for the transformations can be explained by the analysis of stereochemical models as depicted in Scheme 3.[6] There are two possibilities governing the stereocontrol of the second allylic transfer reaction. First, the remote stereogenic center attached to $R^1$ was envisioned to impact stereoselectivity during the allylic transfer through the favored model **8C** for **11**. However, the results obtained (Table 1, entries 1–3) did not support this claim: the stereochemical relationship between **9a** and **9b** turned out to be diastereomeric rather than enantiomeric, and **9c** is an optically active species. Therefore, the preference for the absolute and relative configurations for adducts from (*R*,*R*)-**8** with aldehydes could be explained on the basis of the geometrical preference of the chairlike stereochemical model **8A** (Scheme 3). The stereoselectivity for both the

 © 2006 Wiley-VCH Verlag GmbH & Co. KGaA, Weinheim 



***Scheme 3.*** Stereochemical routes.



***Scheme 4.*** Synthesis of (−)-avenaciolide (**3**) and (−)-isoavenaciolide (**4**): a) NIS, −78 °C, 2 h, $CH_2Cl_2$; b) $[Pd(PPh_3)_4]$ (2 mol %), CO (100 atm), $K_2CO_3$, $CH_3CN$, 70 °C, 1 h; c) NIS, −78 °C, 1 h, $CH_2Cl_2$, then $CF_3CO_2H$ (10 mol %), 2 h. NIS = *N*-iodosuccinimide.

first and second allylic transfer reactions must be controlled by the chiral ligand. The exceptional stereoselectivity can also be explained by assuming that a tight coordination of the aldehyde to the boronyl moiety must be required for the formation of the new C–C bond, such that the overlap between the carbonyl group and the double bond leads to optimum stereoelectronic effects and minimum steric repulsions.

In light of the above results for the stereospecific sequential allylic transfer reaction, we next turned our attention to the application of this approach to the synthesis of the natural products (−)-avenaciolide (**3**) and (−)-isoavenaciolide (**4**; Scheme 1), which exhibit antifungal activities.[7] Interestingly, the diastereomer **10** can be obtained simply by changing the addition sequence of the aldehydes as illustrated in Scheme 3. Thus, we envisaged that the enantioselective synthesis of **3** and **4** could be realized by the sequential addition of aldehydes and appropriate selection of the chiral bromoborane **6** to obtain the correct absolute configurations. Even though the C–OH stereogenic center in **13** is not matched with that in **3**, we predicted that it could be epimerized to the desired product owing to the greater thermodynamic stability of a *cis*-fused bicyclic ring relative to the *trans* isomer.

We undertook the synthesis of **3** from the allenylstannane **5** and (*S*,*S*)-**6** as shown in Scheme 4. Lactone **13** was cleanly obtained under standard conditions in 75 % yield through the sequential allylic transfer reaction. Conversion of **13** into **14** was achieved in 88 % yield by using NIS.[8] Surprisingly, our attempts to convert **14** into **3** under a CO atmosphere using palladium catalysis according to standard procedures[9] were not efficient in terms of the desired epimerization from **15** to **3**. For example, treatment of **14** with CO (10 atm) in the presence of $[Pd(PPh_3)_4]$ (2 mol %) and $Et_3N$ in $CH_3CN$ at 50 °C for 5 h afforded **3** and **15** in a ratio of 2:1 (71 %). Longer reaction times resulted in decomposition of the products. Fortunately, we found that modified Stille conditions were effective for our purpose.[10] Thus, treatment of **14** under an atmosphere of CO (100 atm) in the presence of $[Pd(PPh_3)_4]$ (2 mol %) and $K_2CO_3$ in $CH_3CN$ at 70 °C for 1 h afforded (−)-avenaciolide (**3**, 67 %) along with **15** in a ratio of 95:5 as judged by $^1H$ NMR spectra of the crude mixture.

We then turned our attention to the synthesis of (−)-isoavenaciolide (**4**). Compound **16** was obtained in moderate (54 %) yield, probably because intramolecular chelation of the boronyl group with the ester in **8** resulted in diminished reactivity with nonanal (12 h at −78 °C; Scheme 4). Treatment of **16** with NIS to obtain the corresponding vinyl iodide **17** afforded a 1:1 mixture of **17** and the lactone **18**. However, after complete consumption of **16** in its reaction with NIS at −78 °C for 1 h, addition of $CF_3CO_2H$ (10 mol %) at −78 °C resulted in the formation of **18** in 77 % yield. A modified Stille reaction of **18** completed the synthesis of **4**.

In summary, we have described a sequential allylic transfer reaction for the synthesis of enantiomerically enriched 2-(1-stannylvinyl)-1,3-diols which provides three contiguous stereogenic centers through a four-component assembly. The approach is efficient and promises to be synthetically useful, as demonstrated here with the concise syntheses of (−)-avenaciolide and (−)-isoavenaciolide.

 © 2006 Wiley-VCH Verlag GmbH & Co. KGaA, Weinheim 

## Experimental Section

General procedure—preparation of **9a** from (*R*,*R*)-**6**: A flame-dried 20-mL Schlenk flask containing (+)-(1*R*,2*R*)-1,2-diphenyl-1,2-bis-*p*-toluenesulfonylamide (0.50 g, 0.96 mmol) was charged with dry $CH_2Cl_2$ (7 mL), and the resulting mixture was cooled to 0 °C and treated with $BBr_3$ (1.1 mL of a freshly prepared 1 M solution in $CH_2Cl_2$, 1.1 mmol). The solution was stirred at 0 °C for 1 h, warmed to 20 °C and maintained at this temperature for 5 h, and then concentrated under vacuum (1 mm Hg). Dryness of the vacuum line was maintained with a drying tube containing anhydrous $CaSO_4$ and two traps (one containing NaOH pellets, and the other a cold trap at −78 °C). Freshly distilled $CH_2Cl_2$ (5 mL) was added and evaporated under vacuum as above.

Freshly distilled $CH_2Cl_2$ (4 mL) was again added to the residue, and the homogeneous solution of (*R*,*R*)-**6** was cooled to −10 °C and treated dropwise with 1,2-propadienyl-tributylstannane (**5**, 0.33 g, 1.00 mmol) in $CH_2Cl_2$ (1 mL). The reaction mixture was maintained at −10 °C overnight (ca. 11 h) and then cooled to −78 °C. A solution of hydrocinnamaldehyde (purified and distilled, 100 mg, 0.74 mmol) in $CH_2Cl_2$ (1 mL) was added over 10 min to the cooled reaction mixture along the wall of the flask while keeping the temperature below −78 °C. The mixture was then stirred for 2 h, then hexamethyldistannane (0.21 mL, 0.33 g, 1.01 mmol) in $CH_2Cl_2$ (0.5 mL) was added followed by $[(\pi\text{-allyl})_2Pd_2Cl_2]$ (8.3 mg, 0.022 mmol) in $CH_2Cl_2$ (0.5 mL). The mixture was then allowed to warm to −40 °C and was stirred for 4 h.

The resulting solution of **8** was cooled to −78 °C, and a solution of benzaldehyde (0.08 mL, 83.6 mg, 0.78 mmol) in $CH_2Cl_2$ (1 mL) was added dropwise to the flask. The reaction was allowed to proceed for 4 h at −78 °C and then quenched by addition of aqueous buffer solution (pH 7, 10 mL) followed by $CH_2Cl_2$ (ca. 10 mL) to dissolve the white bis(sulfonamide) precipitate. The aqueous layer was extracted with $CH_2Cl_2$ (ca. 10 mL × 2), and the combined organic extracts were washed with saturated solutions of $NaHCO_3$ (1 ×) and NaCl (1 ×), dried over anhydrous $Na_2SO_4$, and filtered. The solvents were evaporated, and the residue was taken up in diethyl ether (ca. 30 mL). The solution was cooled to 0 °C for 20 min to complete the precipitation of (+)-(1*R*,2*R*)-1,2-diphenyl-1,2-bis-*p*-toluenesulfonylamide, which was then removed by filtration through a sintered glass funnel. The filtrate was washed with cold 20% KF solution (1 ×) and saturated aqueous $NaHCO_3$ solution (1 ×). The organic layer was separated, dried over anhydrous $Na_2SO_4$, filtered, and concentrated under reduced pressure to give the crude product. Final purification was effected by $SiO_2$ chromatography (4:1 hexanes/EtOAc) to afford pure **9a** as a colorless oil (0.255 g, 0.57 mmol, 77%).

Received: November 1, 2005
Revised: November 29, 2005

**Keywords:** asymmetric synthesis · boranes · natural products · synthetic methods · tin

[1] For recent examples, see: a) E. Flamme, W. R. Roush, *J. Am. Chem. Soc.* **2002**, *124*, 13644–13645; b) X. Wang, Q. Meng, A. J. Nation, J. L. Leighton, *J. Am. Chem. Soc.* **2002**, *124*, 10672–10673; c) M. Nakamura, T. Hatekeyama, K. Hara, H. Hukudome, E. Nakamura, *J. Am. Chem. Soc.* **2004**, *126*, 14344–14345; d) N. H. Halland, P. S. Aburel, K. A. Jorgensen, *Angew. Chem.* **2004**, *116*, 1292–1297; *Angew. Chem. Int. Ed.* **2004**, *43*, 1272–1277, and references therein.

[2] a) C.-M. Yu, J.-Y. Lee, B. So, J. Hong, *Angew. Chem.* **2002**, *114*, 169–171; *Angew. Chem. Int. Ed.* **2002**, *41*, 161–163; b) C.-M. Yu, J.-M. Kim, M.-S. Shin, M.-O. Yoon, *Chem. Commun.* **2003**, 1744–1745.

[3] a) C.-M. Yu, J. Youn, M.-K. Lee, *Org. Lett.* **2005**, *7*, 3733–3736; b) C.-M. Yu, J. Youn, S.-K. Yoon, Y.-T. Hong, *Org. Lett.* **2005**, *7*, 4507–4510; c) C.-M. Yu, Y.-T. Hong, J. Lee, *J. Org. Chem.* **2004**, *69*, 8506–8509; d) S. Kang, Y.-T. Hong, J.-H. Lee, W.-Y. Kim, I. Lee, C.-M. Yu, *Org. Lett.* **2003**, *5*, 2813–2816.

[4] a) E. J. Corey, C.-M. Yu, D.-H. Lee, *J. Am. Chem. Soc.* **1990**, *112*, 878–879; b) E. J. Corey, C.-M. Yu, S. S. Kim, *J. Am. Chem. Soc.* **1989**, *111*, 5495–5496.

[5] For reviews, see: a) T. N. Mitchell, *Synthesis* **1992**, 803–815; b) R. Zimmer, C. U. Dinesh, E. Nandann, F. A. Khan, *Chem. Rev.* **2000**, *100*, 3067–3125; c) T. Mandai, in *Modern Allene Chemistry, Vol. 2* (Eds.: N. Krause, A. S. K. Hashmi), Wiley-VCH, Weinheim, **2004**, pp. 925–972.

[6] For discussions on the mechanism of allylations, see: a) M. Santelli, J.-M. Pons, *Lewis Acids and Selectivity in Organic Synthesis*, CRC Press, Boca Raton, **1996**, pp. 91–184; b) S. E. Denmark, N. G. Almstead in *Modern Carbonyl Chemistry* (Ed.: J. Otera), Wiley-VCH, Weinheim, **2000**, pp. 299–401; c) S. R. Chemler, W. R. Roush in *Modern Carbonyl Chemistry* (Ed.: J. Otera), Wiley-VCH, Weinheim, **2000**, pp. 403–490; d) J. A. Marshall, *Chem. Rev.* **2000**, *100*, 3163–3185.

[7] a) V. K. Aggarwal, P. W. Davies, A. T. Schmidt, *Chem. Commun.* **2004**, 1232–1233; b) E. Alcazar, M. Kassou, I. Metheu, S. Castillon, *Eur. J. Org. Chem.* **2000**, 2285–2289; c) M.-J. Chen, K. Narkuran, R.-S. Liu, *J. Org. Chem.* **1999**, *64*, 8311–8318; d) V. S. Martin, C. M. Rodriguez, T. Martin, *Org. Prep. Proced. Int.* **1998**, *30*, 291–323, and references therein.

[8] a) R. A. Britton, E. Piers, B. O. Patrick, *J. Org. Chem.* **2004**, *69*, 3068–3075; b) R. S. Paley, A. De Dios, L. A. Estroff, J. A. Lafontaine, C. Montero, D. J. McCulley, M. B. Rubio, M. P. Ventura, H. L. Weers, R. F. de la Pradilla, S. Castro, R. Dorado, M. Morente, *J. Org. Chem.* **1997**, *62*, 6326–6343.

[9] V. Farina, M. Eriksson in *Handbook of Organopalladium Chemistry for Organic Synthesis, Vol. II* (Eds.: E. Negishi, A. de Meijere), Wiley-Interscience, New York, **2002**, pp. 2351–2355.

[10] L. D. Martin, J. K. Stille, *J. Org. Chem.* **1982**, *47*, 3630–3633.

 © 2006 Wiley-VCH Verlag GmbH & Co. KGaA, Weinheim 

*Metal–Organic Frameworks*

DOI: 10.1002/anie.200503778

# Ligand-Directed Strategy for Zeolite-Type Metal–Organic Frameworks: Zinc(II) Imidazolates with Unusual Zeolitic Topologies**

*Xiao-Chun Huang, Yan-Yong Lin, Jie-Peng Zhang, and Xiao-Ming Chen**

Because of their high stability and structural diversity, inorganic zeolites have been extensively studied as microporous materials for applications in separation, storage, and heterogeneous catalysis.[1] More recently, porous metal–organic frameworks (MOFs) have been explored as a new kind of zeolite-analogous materials that are expected to be more designable in pore sizes and shape, as well as exhibiting wide structural diversity.[2–4] However, crystal engineering of MOFs is still facing great challenges in control of network topology and stability. In particular, zeolite networks, as the most significant topologies for porous materials, are extremely scarce for porous MOFs.[5–7] On the other hand, it can be envisaged that: 1) strong metal–ligand bonding and the enhanced rigidity of bridging ligands may result in more robust and stable porous MOFs; 2) curved bidentate ligands may yield complicated and interesting polymeric structures when bridging metal ions;[8] and 3) MOFs with zeolitic topologies of large cages and small apertures may be expected to have advantages for molecular exchange and storage compared to porous MOFs with straight tubular channels.

As very simple, angular, monovalent anions, imidazolates can form neutral binary MOFs having three-dimensional (3D) frameworks with divalent and tetrahedral metal ions. However, only a few zeolite-like microporous cobalt(II) imidazolates have been synthesized by template-directed methods,[7] and most divalent metal imidazolates (im), such as $[\{M(im)_2\}_\infty]$ (M = Zn, Co, Cu),[9] are densely packed. We demonstrated recently that simple modification of the imidazolate ligand with a methyl or ethyl substituent at the 2-position produced polygonal or helical structures,[10] while the unsubstituted imidazolate led to simple zigzag chainlike structures in copper(I) imidazolates,[11] and triazolate ligands with different substituents could furnish different 3D MOFs of copper(I) triazolates.[12] Moreover, we have synthesized a porous zinc(II) benzimidazolate which has a distorted zeolitic sodalite topology with fairly small pores (ca. $6.3 \times 4.1$ Å).[13] These observations inspired us to establish a new strategy for the generation of zeolite-type MOFs with larger pores by using simple imidazolate ligands with a smaller substituent such as a methyl or ethyl group at the 2-position. This led to the isolation of three new zeolite-type MOFs, namely, $[\{Zn(mim)_2 \cdot 2H_2O\}_\infty]$ (**1**), $[\{Zn(eim)_2 \cdot H_2O\}_\infty]$ (**2**), and $[\{Zn(eim/mim)_2 \cdot 1.25H_2O\}_\infty]$ (**3**) (Hmim = 2-methylimidazole, Heim = 2-ethylimidazole) by the liquid-phase diffusion method.

X-ray crystallographic analysis revealed that **1** crystallizes in the cubic space group $I\bar{4}3m$, and each $Zn^{II}$ ion is tetrahedrally coordinated by four nitrogen atoms from bridging imidazolates (Zn–N 1.984(3) Å, N-Zn-N 109.5(1) and 109.4(2)°) to furnish an infinite 3D framework. The secondary building units (SBUs) of **1** are $Zn_6(mim)_6$ and $Zn_4(mim)_4$ rings, from which the subunits of truncated octahedra are constructed when the mim ligands are regarded as spacers between the metal centers (Figure 1a). The effective diameter of these cages is about 12.5 Å, while the effective hexagonal window size is about 3.3 Å (Figure 1b).[14] Each truncated octahedral cage has six square faces and eight hexagonal faces, which are all shared with neighboring cages. Sharing of the hexagonal faces with neighboring cages leads to 1D channels in the four body-diagonal directions of its cubic lattice (see Supporting Information). The overall network of **1** resembles a regular zeolitic sodalite (SOD) topology ($4^26^4$) with a solvent-accessible volume of 47.0% of the crystal volume. This value is comparable to the void fractions of 0.47–0.50 of the most open zeolites, such as the faujasite, paulingite, and zeolite A families.[1b]

Compound **2** crystallizes in the cubic space group $Ia\bar{3}d$, which has the highest crystallographic symmetry. The local coordination geometry of $Zn^{II}$ ions (Zn–N 2.001(2) and 2.017(2) Å, N-Zn-N 104.4(1)–112.6(1)°) in **2** is similar to that in **1**. However, the MOF of **2** contains highly distorted $Zn_4(eim)_4$, $Zn_6(eim)_6$, and $Zn_8(eim)_8$ rings (Figure 1c). A view along the [111] direction of the cubic cell reveals 1D channels with distorted hexagonal apertures, which intersect with other irregular channels to provide a 3D microporous network (see Supporting Information). The effective hexagonal pore diameter is only 2.2 Å (Figure 1d), and the whole net has a zeolitic analcime (ANA) topology ($4^26^28^2$), which is unprecedented in MOFs. The solvent-accessible volume of **2** is about 38.6%.

One might expect that the pore sizes of **1** and **2** could be enlarged by reducing the size of the substituents. However, when simple imidazole (Him) was used as starting material, we usually obtained the dense banalsite $Zn(im)_2$ structure that was documented in the literature.[9a] These phenomena indicate that the substituents in the 2-position of imidazole play an essential role in the generation of the SOD and ANA network structures of **1** and **2**. Similar to the formation of different 3D MOFs of copper(I) triazolates owing to the effect of different substituents on the triazolate ligands,[12] the 2-methyl and 2-ethyl groups may have slightly but significantly

[*] Dr. X.-C. Huang, Y.-Y. Lin, Dr. J.-P. Zhang, Prof. Dr. X.-M. Chen
State Key Laboratory of Optoelectronic Materials and Technologies
School of Chemistry and Chemical Engineering
Sun Yat-Sen University
Guangzhou 510275 (China)
Fax: (+86) 20-8411-2245
E-mail: cxm@mail.sysu.edu.cn
Dr. X.-C. Huang
Department of Chemistry
Shantou University
Shantou, Guangdong 515063 (China)

[**] This work was supported by the National Natural Science Foundation of China (No. 20531070) and the Guangdong Provincial Science and Technology Bureau (No. 04205405).

Supporting information for this article is available on the WWW under http://www.angewandte.org or from the author.

 © 2006 Wiley-VCH Verlag GmbH & Co. KGaA, Weinheim 

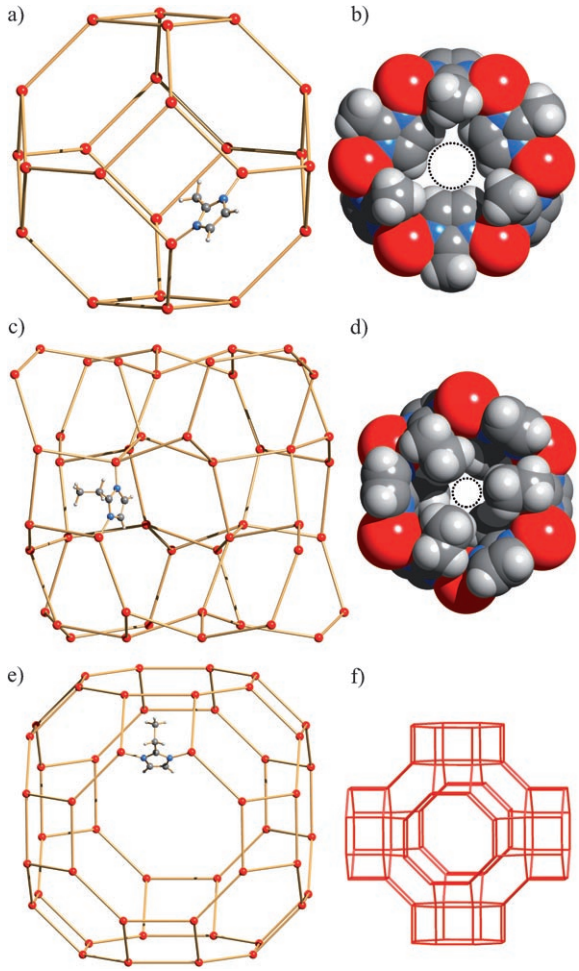



***Figure 1.*** Structures of **1**–**3**. Topological sodalite (SOD) net (a) and space-filling diagram of a hexagonal aperture with a diameter of 3.3 Å (b) in **1**; topological analcime (ANA) net (c) and space-filling diagram of a hexagonal aperture with a diameter of 2.2 Å (d) in **2**; a truncated cuboctahedron (e) and the topological $4^3 6$ supercage (f) constructed from six eight-membered rings, eight six-membered rings, and twelve four-membered rings, and surrounded by six topological $4^2 8^2$ cages, each constructed from two eight-membered rings and eight four-membered rings in **3**. Color code: Zn red, N blue, C gray, H white.

different effects on the orientations of adjacent metal coordination polyhedra, which lead to different configurations in the interconnection of these metal ions and thus result in formation of different 3D MOFs.

Thermogravimetric (TG) analysis of **1** showed release of the included water molecules below 100 °C (ca. 14 wt %, corresponding to the structural analysis), no further weight loss below 400 °C, and framework decomposition in the temperature range of 400–550 °C; the final product was ZnO (ca. 31 wt %). The TG curve of **2** indicated no weight loss below 400 °C, and the framework collapsed in the temperature range of 400–500 °C before formation of the final product (ZnO, ca. 30 wt %), which implied that the guest water molecules could not be released before the framework collapsed. Thermal stability of **1** and **2** was also investigated by X-ray thermodiffraction analysis, which showed that they are stable up to temperatures of 420 and 400 °C, respectively (see Supporting Information). Their stability is thus comparable to that of the most thermostable porous MOFs.[15] The $N_2$ sorption properties of **1** and **2** were also investigated. Compound **1** exhibited a typical type I isotherm with a Langmuir surface area of 1400 $m^2 g^{-1}$ (BET surface area 1030 $m^2 g^{-1}$). Furthermore, the adsorption isotherm of methanol vapor for **1** showed an adsorbed amount of 2.7 methanol molecules per metal atom, which also confirmed the nanoporosity of **1** (Figure 2). However, **2** only exhibited surface

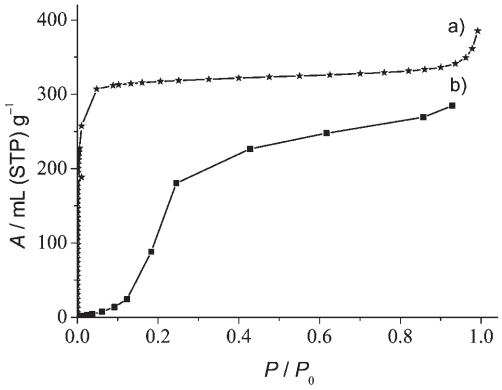



***Figure 2.*** Isotherm for $N_2$ adsorption at 77 K (a) and MeOH vapor adsorption at 298 K (b) for **1**. $P_0$ = saturated vapor pressure.

adsorption with a Langmuir surface area of 40.8 $m^2 g^{-1}$ (BET surface area 28.7 $m^2 g^{-1}$). These observations are consistent with the different aperture sizes of **1** and **2** (ca. 3.3 and 2.2 Å, respectively), which may account for the difference in gas-sorption properties.[16] The structural features and TG analysis of **2** imply that it cannot serve as a potential gas-sorption material.

By considering the very similar coordination abilities of mim and eim, we assumed that eim in **2** may be partially replaced by mim to enlarge the resultant windows of the MOF of **2**. However, isolation of the mixed-ligand complexes failed. In several trials with mixed mim/eim ligands, **1** was obtained as the major product, while only a few single crystals isolated from one trial were identified as a new MOF **3**. Although we were unable to further measure any properties and the mim/eim ratio of **3**, X-ray crystallography revealed that it crystallizes in the cubic space group $Im\bar{3}m$. The MOF of **3** consists of truncated cuboctahedral supercages and octagonal prisms. The supercage is constructed from $Zn_4(eim)_4$, $Zn_6(eim)_6$, and $Zn_8(eim)_8$ SBUs (Figure 1 e), each supercage contacts with six octagonal prisms through the octagonal faces (Figure 1 f), and each octagonal prism links two supercages through its opposite octagonal faces. In other words, each supercage is surrounded by six supercages through six octagonal-prism linkers in three axial directions of the lattice. The resulting microporous 1D channels have octagonal apertures with a pore diameter of 7.4 Å (see Supporting Information). The diameter of the supercage is 18.1 Å, and the void volume is 14352 $Å^3$ (55.4 % of the cell volume). It is noteworthy that the MOF of **3** has a regular zeolitic rho (RHO) topology ($4^3 6^3$), which has not been observed in MOFs. Although **3** was a byproduct, its formation implies that

 © 2006 Wiley-VCH Verlag GmbH & Co. KGaA, Weinheim 

the mixture of ligands could possibly be one of the factors controlling the formation of this MOF.

In conclusion, by taking advantage of simple modifications of imidazolates at the coordinatively unimportant 2-position, we could tune the orientation of adjacent metal coordination polyhedra and thus successfully synthesize three new MOFs with unusually high symmetries, 3D zeolitic topologies, and very high thermal stabilities, whereby **2** and **3** are the first examples of expanded ANA and RHO topologies in MOFs. In contrast to the traditional template method, we employed a ligand-directed strategy for constructing porous MOFs with zeolitic topologies by molecular tailoring of simple organic spacers with apparently unimportant groups. Our method may lead to zeolitic MOFs for applications in guest sorption, exchange, storage, and catalysis. Further exploration of the generation of zeolite-like MOFs and their gas-sorption properties are in progress.

## Experimental Section

**1**: A solution of Hmim (0.2 mmol, 0.016 g) in MeOH (5.0 mL) was slowly and carefully layered onto a solution of $Zn(OH)_2$ (0.1 mmol, 0.010 g) in aqueous ammonia (25%, 2.0 mL). Colorless polyhedral crystals began to appear after several days. After one month, they were collected, washed (methanol/water 1:1), and dried in air (yield 70%). **2**: The procedure was similar to that of **1**, except that Heim (0.2 mmol, 0.019 g) was used instead of Hmim (yield 60%). **3**: The procedure was similar to that of **1**, except that a mixture of Hmim (0.1 mmol, 0.008 g) and Heim (0.1 mmol, 0.010 g) was used instead of Hmim. In one of the trials, **1** was obtained as major product together with a couple of tiny prismatic crystals of **3**, which were different in shape and were manually isolated for X-ray diffraction studies.

Crystal data of **1**: cubic, $I\bar{4}3\,m$ (no. 217); $a = 17.012(1)$ Å, $V = 4923.1(3)$ Å$^3$, $Z = 12$, $\rho = 1.067\ g\,cm^{-3}$, $\mu = 1.488\ mm^{-1}$, final $R_1 = 0.0515$, $wR_2 = 0.1287$ for $I > 2\sigma(I)$; **2**: cubic, $Ia\bar{3}d$ (no. 230); $a = 26.5309(12)$ Å, $V = 18674.8(8)$ Å$^3$, $Z = 48$, $\rho_{calcd} = 1.168\ g\,cm^{-3}$, $\mu = 1.567\ mm^{-1}$, $R_1 = 0.0365$, $wR_2 = 0.1106$ for $I > 2\sigma(I)$; **3**: cubic, $Im\bar{3}m$ (no. 229); $a = 29.2582(5)$ Å, $V = 25046.3(7)$ Å$^3$, $Z = 48$, $\rho = 0.885\ g\,cm^{-3}$, $\mu = 1.170\ mm^{-1}$, $R_1 = 0.0442$, $wR_2 = 0.1327$ for $I \geq 2\sigma(I)$. X-ray diffraction data were recorded on a Bruker SMART Apex CCD system with graphite-monochromated $Mo_{K\alpha}$ radiation ($\lambda = 0.71073$ Å) at 123 K. The structures were solved by direct methods and refined by full-matrix least-squares techniques on $F^2$.[17] Non-hydrogen atoms of the host frameworks were refined anisotropically and organic hydrogen atoms were generated geometrically and refined isotropically. All guest atoms were refined isotropically. Solvent-accessible volumes were calculated by Platon2003.[18] CCDC-287180 (**1**), 287181 (**2**), and 287182 (**3**) contain the supplementary crystallographic data for this paper. These data can be obtained free of charge from The Cambridge Crystallographic Data Centre via www.ccdc.cam.ac.uk/data_request/cif.

Thermogravimetric analysis (TGA) was performed under a static air atmosphere on a Perkin-Elmer 7 thermogravimetric analyzer with a heating rate of $10\,°C\,min^{-1}$. The sorption isotherms for $N_2$ gas and MeOH were measured with an automatic volumetric adsorption apparatus (Micromertics ASAP 2010) and an automatic gravimetric adsorption apparatus (IGA-003 series, Hiden Isochema Ltd) at 77 and 298 K, respectively. The as-synthesized samples (weight 50–100 mg) were placed in the quartz tube and dried under high vacuum at 373 K for 10 h to remove water of hydration prior to measurements.

Received: October 25, 2005
Published online: January 27, 2006

**Keywords:** bridging ligands · crystal engineering · N ligands · zeolite analogues · zinc

[1] a) C. Baerlocher, W. M. Meier, D. H. Olson, *Atlas of Zeolite Framework Types*, 5th ed., Elsevier, Amsterdam, **2001**; b) D. W. Breck, *Zeolite Molecular Sieves*, Wiley, New York, **1974**; c) X. Bu, P. Feng, G. D. Stucky, *Science* **1997**, *278*, 2080.

[2] S. Kitagawa, R. Kitaura, S. Noro, *Angew. Chem.* **2004**, *116*, 2388; *Angew. Chem. Int. Ed.* **2004**, *43*, 2334.

[3] a) O. M. Yaghi, M. O'Keeffe, N. W. Ockwig, H. K. Chae, M. Eddaoudi, J. Kim, *Nature* **2003**, *423*, 705; b) S. S.-Y. Chui, S. M.-F. Lo, J. P. H. Charmant, A. G. Orpen, I. D. Williams, *Science* **1999**, *283*, 1148.

[4] a) G. Férey, C. Serre, C. Mellot-Draznieks, F. Millange, S. Surblé, J. Dutour, I. Margiolaki, *Angew. Chem.* **2004**, *116*, 6456; *Angew. Chem. Int. Ed.* **2004**, *43*, 6296; b) G. Férey, C. Mellot-Draznieks, C. Serre, F. Millange, *Acc. Chem. Res.* **2005**, *38*, 217; c) G. Férey, C. Mellot-Draznieks, C. Serre, F. Millange, J. Dutour, S. Surblé, I. Margiolaki, *Science* **2005**, *309*, 2040.

[5] Q. Fang, G. Zhu, M. Xue, J. Sun, Y. Wei, S. Qiu, R. Xu, *Angew. Chem.* **2005**, *117*, 3913; *Angew. Chem. Int. Ed.* **2005**, *44*, 3845.

[6] E. B. Rusanov, V. V. Ponomarova, V. V. Komarchuk, H. Stoeckli-Evans, E. Fernandez-Ibañez, F. Stoeckli, J. Sieler, K. V. Domasevitch, *Angew. Chem.* **2003**, *115*, 2603; *Angew. Chem. Int. Ed.* **2003**, *42*, 2499.

[7] a) Y.-Q. Tian, C.-X. Cai, J. Ji, X.-Z. You, S.-M. Peng, G.-H. Lee, *Angew. Chem.* **2002**, *114*, 1442; *Angew. Chem. Int. Ed.* **2002**, *41*, 1384; b) Y.-Q. Tian, C.-X. Cai, X.-M. Ren, C.-Y. Duan, Y. Xu, S. Gao, X.-Z. You, *Chem. Eur. J.* **2003**, *9*, 5673; c) Y.-Q. Tian, Z.-X. Chen, L.-H. Weng, H.-B. Guo, S. Gao, D.-Y. Zhao, *Inorg. Chem.* **2004**, *43*, 4631.

[8] For recent examples, see a) X.-M. Chen, G.-F. Liu, *Chem. Eur. J.* **2002**, *8*, 4811; b) Y.-T. Wang, M.-L. Tong, H.-H. Fan, H.-Z. Wang, X.-M. Chen, *Dalton Trans.* **2005**, 424; c) X.-L. Wang, C. Qin, E.-B. Wang, Y.-G. Li, Z.-M. Su, L. Xu, L. Carlucci, *Angew. Chem.* **2005**, *117*, 5974; *Angew. Chem. Int. Ed.* **2005**, *44*, 5824.

[9] a) R. Lehnert, F. Z. Seel, *Z. Anorg. Allg. Chem.* **1980**, *464*, 187; b) M. Sturm, F. Bromdl, D. Engel, W. Hoppe, *Acta Crystallogr. Sect. B* **1975**, *31*, 2369; c) N. Masciocchi, S. Bruni, E. Cariati, F. Cariati, S. Galli, A. Sironi, *Inorg. Chem.* **2001**, *40*, 5897.

[10] a) X.-C. Huang, J.-P. Zhang, X.-M. Chen, *J. Am. Chem. Soc.* **2004**, *126*, 13218; b) X.-C. Huang, J.-P. Zhang, Y.-Y. Lin, X.-M. Chen, *Chem. Commun.* **2005**, 2232.

[11] Y.-Q. Tian, H.-J. Xu, L.-H. Weng, Z.-X. Chen, D.-Y. Zhao, X.-Z. You, *Eur. J. Inorg. Chem.* **2004**, 1813.

[12] J.-P. Zhang, Y.-Y. Lin, X.-C. Huang, X.-M. Chen, *J. Am. Chem. Soc.* **2005**, *127*, 5495.

[13] X.-C. Huang, J.-P. Zhang, X.-M. Chen, *Chin. Sci. Bull.* **2003**, *48*, 1531.

[14] The size was determined by considering van der Waals radii for constituent atoms (C 1.7, H 1.2, N 1.55, Zn 2.25 Å). Hereafter, all pore sizes reported in this paper are defined in this way. A. Bondi, *J. Phys. Chem.* **1964**, *68*, 441.

[15] a) T. Devic, C. Serre, N. Audebrand, J. Marrot, G. Férey, *J. Am. Chem. Soc.* **2005**, *127*, 12788; b) T. K. Maji, K. Uemura, H.-C. Chang, R. Matsuda, S. Kitagawa, *Angew. Chem.* **2004**, *116*, 3331; *Angew. Chem. Int. Ed.* **2004**, *43*, 3269.

[16] For **1**, the effective window size of 3.3 Å is slightly larger than the van der Waals diameter of a nitrogen atom (3.1 Å), whereas for **2** the effective windows size is 2.2 Å.

[17] Shelxtl 6.10, Bruker Analytical Instrumentation, Madison, Wisconsin, USA, **2000**.

[18] A. L. Spek, *Acta Crystallogr. Sect. A* **1990**, *46*, C34.

 © 2006 Wiley-VCH Verlag GmbH & Co. KGaA, Weinheim 

Microreactors

DOI: 10.1002/anie.200502822

# Biologically Driven Assembly of Polyelectrolyte Microcapsule Patterns To Fabricate Microreactor Arrays**

*Bo Wang, Qinghe Zhao, Feng Wang, and Changyou Gao**

Microcapsules with polyelectrolyte multilayer walls assembled using the layer-by-layer process have attracted great attention because of their potential applications in medicine, drug delivery, artificial cells (viruses), and catalysis.[1] The most notable feature of such hollow microcapsules is the switchable permeability of the walls in response to environmental stimuli such as pH, salt, and temperature.[2] Therefore, it is possible to conveniently manipulate the interior content of the capsules by various approaches[3] with respect to specific application requirements. Meanwhile, many applications require confinement of the capsules with fine spatial selectivity. For example, space-confined materials are a prerequisite for high-throughput multipurpose sensors.[4] Stimulus-responsive microcapsules have potential for targeting drug carriers, as the intracellular pH value and ionic strength of tumor tissues differ from those of normal tissues.[5] Therefore, the targeting and selective immobilization of the microcapsules is of both scientific and technological interest and a key issue in this context.

Actually, patterning of the capsules has been fulfilled with both passive[6] (electron-beam lithography) and active[7] (electrostatic coupling) approaches. The active approaches are more promising for biological systems, but the stable immobilization of the capsules to maintain the as-prepared patterns is still an unsolved problem.[7b] Herein, a method that allows isolation of the individual capsules and patterned assembly with satisfactory spatial selectivity is developed on the basis of the biological affinity of avidin and biotin[8] (Figure 1). The selective immobilization of capsules is performed on receptor patterns fabricated by microcontact printing,[9] with a flexible, biocompatible polymer film as substrate. The stable microcapsule arrays are further used as microreactors to synthesize quantum dots (QDs) and other nanoparticles. In addition, the release of the spatially

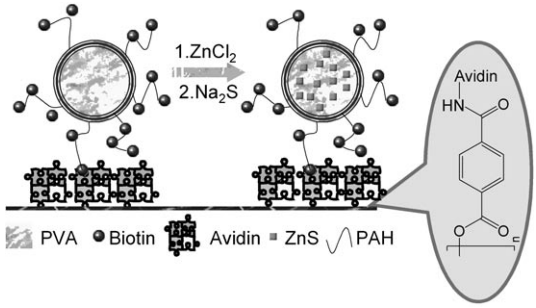



***Figure 1.*** Schematic illustration showing the strategy and bioaffinity force for capsule patterning. Avidin molecules are covalently patterned on a PET film containing pentafluorophenyl ester groups by microcontact printing, and are used to guide the spatial location of biotinylated capsules. Polymers with chelating groups (exemplified here by PVA) are loaded in the capsules to facilitate precipitation or reduction reactions to synthesize QDs, nanocrystals, and nanoparticles (illustrated by the production of ZnS QDs). PET = poly(ethylene terephthalate), PVA = poly(vinyl alcohol).

synthesized products can be readily tuned. Herein, a flexible polymer was chosen as the substrate as it may be further manipulated into various shapes, such as tubes. Moreover, the polymer is more like tissue than the commonly used silicon and glass substrates.

Biotin was covalently immobilized on the capsule walls by the reaction of biotinamidohexanoic acid 3-sulfo-*N*-hydroxysuccinimide (biotin-NHS) and the primary amine groups of poly(allylamine hydrochloride) (PAH; the outermost layer of the capsules) at pH 7–9. Infrared spectroscopy (Figure 2a) recorded the characteristic absorbance bands of biotin at 1710 and 1480 $cm^{-1}$, thus confirming the existence of the biotin molecules on the capsule walls. This is further evidenced by

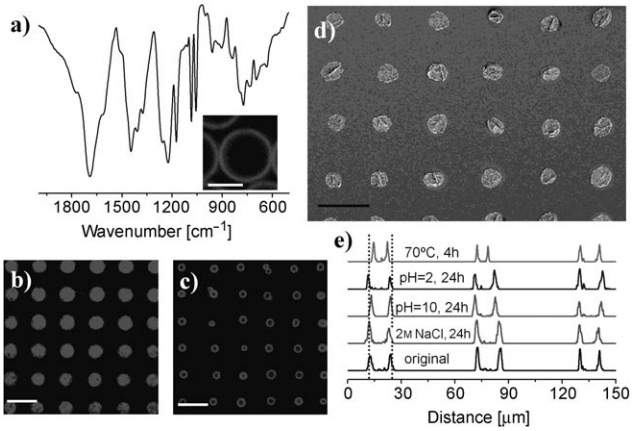



***Figure 2.*** a) FTIR spectrum of the biotinylated microcapsules after subtraction of the spectrum of the unmodified capsules. Inset: CLSM image of biotinylated microcapsules bound with Rd-avidin. The scale bar is 10 μm. b) CLSM image of the Rd-avidin covalent patterns on the PET film. c) CLSM image of the microcapsule arrays immobilized on the avidin patterns recorded at the same place as (b). A drop of fluorescein solution (0.05 mg $mL^{-1}$) was applied for visualization. d) SEM image of the microcapsule arrays immobilized on the avidin patterns. e) Line profiles of the fluorescence intensity depict the capsule wall positions after treatment under various conditions. The scale bars in b)–d) are 60 μm. CLSM = confocal laser scanning microscopy; Rd-avidin = rhodamine B isothiocyanate-labeled avidin.

[*] B. Wang, Q. Zhao, F. Wang, Prof. Dr. C. Gao
Department of Polymer Science and Engineering
Zhejiang University
Hangzhou 310027 (China)
Fax: (+86) 571-8795-1948
E-mail: cygao@mail.hz.zj.cn

[**] We thank Prof. Y. Y. Chen and Prof. J. C. Shen for their stimulating discussions and continuous support. Prof. H. Möhwald is greatly acknowledged for his critical reading and corrections of the manuscript. This study was financially supported by the Natural Science Foundation of China (Nos. 20434030 and 90206006) and the National Science Fund for Distinguished Young Scholars of China (No. 50425311).


InterScience
© 2006 Wiley-VCH Verlag GmbH & Co. KGaA, Weinheim

the fact that the biotinylated capsules adsorbed ten times more avidin (driven by the bioconjugation force; Figure 2a, inset) than the unmodified capsules (driven by electrostatic forces). A water-soluble biotinylation reagent with a negatively charged headgroup ($SO_3^{2-}$) was selected to improve the biotinylation activity. The spacer segment $-(CH_2)_6-$ can provide freedom for the ligand[10] to recognize its receptor in an optimal manner.

Avidin patterns on a poly(ethylene terephthalate) (PET) film were fabricated by microstamping onto an activated polymer surface (MAPS), which was initially developed by Chilkoti and co-workers.[11] The COOH groups that were introduced onto the PET film by hydrolysis[12] were converted into active pentafluorophenyl esters in a solution of pentafluorophenol (PFP) and 1-ethyl-3-(dimethylamino)propylcarbodiimide (EDAC).[13] The hydrolysis time, which was tracked by scanning force microscopy (SFM) and contact angle measurement, was set at 3 hours to give a homogeneous, flat surface with sufficient COOH groups, which is very important for the selectivity of the capsule assembly.[7b] The activated surface was then brought into conformal contact with a plasma-pretreated poly(dimethylsiloxane) (PDMS) stamp having periodic pillars inked with avidin solution. The avidin was stably patterned through formation of amide linkages with the PET film,[14] as shown by confocal laser scanning microscopy (CLSM; Figure 2b). Post-rinsing with buffer was performed, and the unreacted pentafluorophenyl esters were deactivated with lysine.

Then the patterned polymer film was placed in a suspension of biotinylated capsules (diameter $\approx 15$ μm). Capsule arrays were formed within 30 minutes, as observed by CLSM (Figure 2c, wet state) and scanning electron microscopy (SEM; Figure 2d, dry state). The location of each capsule corresponded exactly to the site of the avidin receptor (see Figure 2b and c). Control experiments showed that no capsule patterns could be formed by incubating the same patterned film in unmodified capsule or avidin-saturated biotinylated capsule suspensions, which demonstrates that the capsule patterns shown in Figure 2c were mediated by ligand–receptor recognition. Although the process has to be fine-tuned, satisfactory capsule arrays with a dimension of several millimeters can be obtained. Actually, reducing the nonspecific adsorption of the capsules is a key issue. The introduction of poly(ethylene glycol) (PEG) onto capsules[15] or vesicles[16] has been demonstrated as an effective method. Tween 20 detergent was added to our capsule suspension to avoid any potential influence on the capsule permeability by the grafted PEG nonfouling chains.[15] This detergent covered the capsule surfaces and showed a very effective blocking ability.[17]

To ensure that only one capsule is placed on a single pattern, the sizes of the patterns and the capsules should be matched. We used patterns with diameters of 4, 20, and 40 μm and a spacing of 6, 40, and 60 μm, respectively, and capsules with diameters of 4, 5, and 15 μm. Isolated individual capsule arrays were obtained only in cases where the ratio between the capsule diameters and the pattern sizes was approximately 1:2 to 3:4. When the capsule diameter was too large, the capsules bridged the spaces between patterns, whereas several capsules located on a single pattern if the capsule diameter was relatively small. However, no precise control over the number of capsules deposited was achieved by varying the dimensions, which can probably be attributed to the softness of the capsule wall.

Notably, biotin and avidin have to be covalently coupled to the capsule or substrate. If the avidin (positively charged at neutral pH)[18] was attached to the substrate through electrostatic interaction, the very strong affinity (binding constant of biotin and avidin ca. $10^{15}\,M^{-1}$)[19] would detach the avidin molecules.

The strong binding and the stability of the avidin molecules[20] endow the capsule patterns with enough stability to withstand relatively harsh conditions. In fact, the as-prepared capsule arrays could survive treatments by ultrasonication, concentrated salt, acid, and base, as well as elevated temperature (Figure 2e). The representative fluorescence intensity line profiles obtained by CLSM confirm that the intact periodicity of the capsule patterns was preserved, except that the annealed capsules shrank to some extent as a result of the rearrangement of polyelectrolytes within the multilayers.[21]

In a subsequent step, the interiors of such aligned microcontainers were manipulated by the incorporation of metal ions and subsequent chemical reactions to synthesize QDs. Polymers with chelating groups, for example poly(vinyl alcohol) (PVA), were incorporated into a $CaCO_3$ template as a crystallization manipulator.[22] After layer-by-layer assembly and dissolution of the cores with ethylenediaminetetraacetic acid disodium salt (EDTA-Na), PVA was simultaneously incorporated into the capsules during their formation, which was confirmed by the absorbance at 1085 $cm^{-1}$ in the infrared spectrum. After incubation of the capsule arrays in $ZnCl_2$ solution for 2 h, $Zn^{2+}$ ions were adsorbed onto the PVA matrix in the capsules by complexation with the hydroxy groups.[23] Successively immersing the capsule arrays into $Na_2S$ solution yielded ZnS QDs[24] exclusively within the capsules, with no detected fluorescence in solution. Raman spectroscopy also confirmed the formation of ZnS nanoparticles.[25] Under UV radiation, blue capsule arrays were observed by fluorescence microscopy (Figure 3a). The size of the ZnS QDs was estimated as ca. 1 nm according to the fluorescence spectrum (Figure 3b). Neither the excitation nor the emission maxima were changed after complete desiccation of the capsules (Figure 3b), which indicates that no agglomeration of the QDs occurred because of stabilization by the PVA matrix.

When capsule arrays loaded with ZnS QDs were incubated in buffer, the QDs were steadily released into the solution (Figure 3c, solid line). This effect lasted up to 40 days (Figure 3c, left inset image). We regard this as a refreshing process, which can be followed by a new reaction cycle. Actually, three cycles were carried out, and no change in properties of the produced ZnS was found during these cycles. On the other hand, the leaching of the QDs could be blocked to create stable QD-loaded capsule arrays of long durability. For instance, by assembling six additional polyelectrolyte layers on the capsules to reseal the pores,[26] less than 5% of the QDs escaped from the capsules within 40 days (Figure 3c, dashed line and right inset image).

 © 2006 Wiley-VCH Verlag GmbH & Co. KGaA, Weinheim 

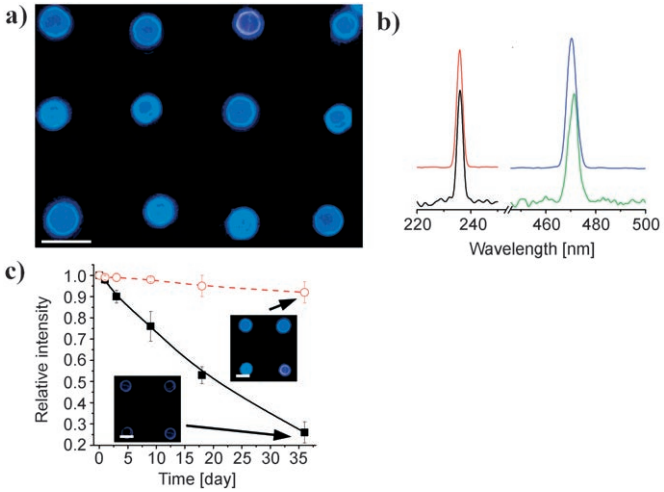



***Figure 3.*** a) Fluorescence image showing the existence of ZnS QDs formed exclusively within the patterned microcapsules. b) Excitation and emission spectra of aligned microcapsules containing ZnS QDs. Black: excitation at dry state, red: excitation in suspensions, green: emission at dry state, blue: emission in suspensions. c) Evolution of the fluorescence emission at 470 nm as a function of time. The solid and dashed lines represent the fluorescence intensity from the as-prepared QDs containing capsule arrays without and with additional $(PSS/PAH)_3$ layers, respectively. The insets show the fluorescence images of capsule patterns after incubation in buffer for 36 days. The scale bars in (a) and (c) are 30 and 20 μm, respectively. PSS = poly(styrene sulfonate) sodium salt; PAH = poly(allylamine hydrochloride).

To illustrate the versatility of this approach, carboxymethyl cellulose, poly(acrylic acid) (PAA), poly(vinyl pyrrolidone) (PVP), and chitosan were incorporated into the capsules as well. Cadmium(II), copper(II), silver(I), and gold(III) ions were similarly coordinated within the capsules through the ligand groups of these polymers, respectively. Nanocrystals or nanoparticles of cadmium sulfide (CdS), copper sulfide (CuS), silver, and gold were successfully synthesized by precipitation or reduction reactions. Immobilization of the capsules on the surface facilitated the fabrication and refreshing processes, as separation of the capsules and excess reagents could be accomplished by simply washing instead of centrifugation, filtration, and/or dialysis.

In conclusion, micropatterning of polyelectrolyte microcapsules has been realized on a polymer film with high spatial selectivity driven by specific biotin–avidin recognition. For this to occur, biotin is covalently immobilized on microcapsules with PAH as the outermost layer, while avidin is covalently patterned onto the PET film with pentafluorophenol groups on its surface by microcontact printing. The created microcapsule arrays are very stable against harsh treatments, such as ultrasonication, acid, base, and elevated temperature. Several kinds of polymers with chelating groups (with PVA as a representative example) are loaded into the capsules to site-specifically synthesize ZnS QDs, nanocrystals, and nanoparticles through precipitation and reduction reactions. The QDs can be released from the aligned capsules for up to 40 days. The synthesis can be performed again and such a cycle has been repeated several times. The leaching of the QDs can also be blocked to create stable QD-loaded capsule arrays with long durability by simply coating additional layers onto the capsules. A flexible polymer is chosen as the substrate, which facilitates the further shaping of devices. This study also provides a model for active drug targeting.

## *Experimental Section*

Capsule fabrication: $Ca(NO_3)_2$ solution (0.025 M, 100 mL) was mixed with 5% PVA solution ($M_w = 85$–$124$ kDa, 4 mL), and $Na_2CO_3$ solution (0.025 M, 100 mL) was added rapidly under strong agitation. $CaCO_3$ particles with an average diameter of 15 μm were formed immediately and collected by filtration. The suspension of $CaCO_3$ particles (concentration ca. 5 wt%) was alternately incubated for 10 min in solutions of poly(styrene sulfonate) sodium salt (PSS, Aldrich, $M_w = 70$ kDa, 1 mg mL$^{-1}$) and PAH (Aldrich, $M_w = 70$ kDa), both containing NaCl (0.5 M). A centrifugation/washing protocol was applied to remove excess polyelectrolytes. After $(PSS/PAH)_5$ was deposited, the $CaCO_3$ cores were dissolved by incubation in EDTA-Na solution (0.2 M) three times, each for 30 min. Capsules with diameters of 4 or 5 μm were similarly obtained by using commercial silicon dioxide colloids as templates.

Biotinylation of the capsules: Biotin-NHS (1.0 mg) was added to the capsule suspension ($\approx 10^5$ capsules mL$^{-1}$, 2 mL) in phosphate-buffered saline (pH 8.0). After incubation for 1 h at room temperature, centrifugation and washing were performed to purify the resulting capsules.

Activation of the PET film: A PET film (Melinex, DuPont) was cleaned by sequentially rinsing in distilled water, methanol, and refluxing hexane, each for 2 h. The cleaned film was incubated in NaOH solution (1 M) for 3 h. After hydrolysis, the film was sequentially rinsed with HCl (0.1 M) and distilled water, then dried under reduced pressure at 50 °C for 24 h. The COOH groups on the film were activated by immersion in EDAC (0.1 M, Sigma) and PFP (0.2 M, Aldrich) ethanolic solution for 15 min. The film was rinsed with anhydrous ethanol, dried by a nitrogen flow, and used immediately.

Fabrication of the avidin patterns: A PDMS (Dow Corning) stamp with periodic pillars[9] was inked with rhodamine B isothiocyanate-labeled avidin (Rd-avidin, Sigma) solution (0.1 mg mL$^{-1}$) for 30 min, rinsed with water, and dried with a gentle nitrogen stream. The stamp was immediately pressed onto the PET substrate with a normalized force of 2 N cm$^{-2}$ for 30 min. The patterned substrate was then removed from the stamp, washed with ethanol, cleaned by ultrasonication for 2 min, and finally dried by a nitrogen flow. The unreacted pentafluorophenyl esters in both the avidin patterns and the continuous regions were decomposed by reaction with lysine (0.1 M) for 20 min.

Capsule assembly: Capsules were assembled by incubating an avidin-patterned film in biotinylated capsule suspensions ($\approx 10^5$ capsules mL$^{-1}$) for 30 min, followed by rinsing with water. Tween 20 (0.02% v/v) was supplemented in the capsule suspension before assembly. After mixing for 20 min, the excess Tween 20 was removed by centrifugation. Tween 20 was also occasionally used during the rinsing step.

In situ synthesis of ZnS QDs within the microcapsules: The PET film with capsule arrays was incubated in $ZnCl_2$ aqueous solution (0.01 M) for 2 h, followed by ultrasonication and extensive washing. Then it was immersed in $Na_2S$ solution (0.05 M) for 30 min. Finally, the film was washed with distilled water to remove the excess $Na_2S$.

Characterization: The CLSM and SEM images were obtained with a Bio-Rad Radiance 2100 confocal laser scanning microscope and a Stereoscan 260 Cambridge electron microscope, respectively. Fluorescence spectra were recorded on a fluorescence spectrophotometer (Hitachi F-4500). The infrared spectra were obtained with a Bruker Vector 22 spectrometer on dry capsules.

Received: August 9, 2005
Published online: January 27, 2006

 © 2006 Wiley-VCH Verlag GmbH & Co. KGaA, Weinheim 

**Keywords:** microreactors · nanostructures · polyelectrolytes · polymers · quantum dots


[1] a) E. Donath, G. B. Sukhorukov, F. Caruso, S. Davis, H. Möhwald, *Angew. Chem.* **1998**, *110*, 2324; *Angew. Chem. Int. Ed.* **1998**, *37*, 2202; b) F. Caruso, R. A. Caruso, H. Möhwald, *Science* **1998**, *282*, 1111.

[2] G. B. Sukhorukov, M. Brumen, E. Donath, H. Möhwald, *J. Phys. Chem. B* **1999**, *103*, 6434.

[3] a) D. G. Shchukin, A. A. Patel, G. B. Sukhorukov, Y. M. Lvov, *J. Am. Chem. Soc.* **2004**, *126*, 3374; b) D. G. Shchukin, G. B. Sukhorukov, *Adv. Mater.* **2004**, *16*, 671; c) N. Gaponik, I. L. Radtchenko, G. B. Sukhorukov, H. Weller, A. L. Rogach, *Adv. Mater.* **2002**, *14*, 879; d) C. Y. Gao, E. Donath, H. Möhwald, J. C. Shen, *Angew. Chem.* **2002**, *114*, 3943; *Angew. Chem. Int. Ed.* **2002**, *41*, 3789.

[4] a) D. Trau, W. Yang, M. Seydack, F. Caruso, N.-T. Yu, R. Renneberg, *Anal. Chem.* **2002**, *74*, 5480; b) C. P. Chan, M. Haeussler, B. Z. Tang, Y. Dong, K. Sin, W. Mak, D. Traud, M. Seydack, R. Renneberg, *J. Immunol. Methods* **2004**, *295*, 111.

[5] a) B. Fischer, B. Müller, K.-G. Fischer, N. Baur, W. Kreutz, *Clin. Immunol.* **2000**, *96*, 252; b) M. Stubbs, R. L. Veechi, J. R. Griffiths, *Adv. Enzyme Regul.* **1995**, *35*, 101.

[6] T. Berzina, S. Erokhina, D. Shchukin, G. Sukhorukov, V. Erokhin, *Macromolecules* **2003**, *36*, 6493.

[7] a) M. Nolte, A. Fery, *Langmuir* **2004**, *20*, 2995; b) J. Feng, B. Wang, C. Y. Gao, J. C. Shen, *Adv. Mater.* **2004**, *16*, 1940.

[8] S. A. Walker, M. T. Kennedy, J. A. Zasadzinski, *Nature* **1997**, *387*, 61.

[9] a) Y. Xia, G. M. Whitesides, *Angew. Chem.* **1998**, *110*, 568; *Angew. Chem. Int. Ed.* **1998**, *37*, 550; b) A. Bernard, E. Delamarche, H. Schmid, B. Michel, H. R. Bosshard, H. Biebuyck, *Langmuir* **1998**, *14*, 2225; c) C. D. James, R. C. Davis, L. Kam, H. G. Craighead, M. Isaacson, J. N. Turner, W. Shain, *Langmuir* **1998**, *14*, 741; d) J. Feng, C. Y. Gao, B. Wang, J. C. Shen, *Colloids Surf. B* **2004**, *36*, 177.

[10] M. K. Ali, C. Bergson, *J. Biol. Chem.* **2003**, *278*, 51654.

[11] Z. Yang, A. Chilkoti, *Adv. Mater.* **2000**, *12*, 413.

[12] W. Chen, T. J. McCathy, *Macromolecules* **1998**, *31*, 3648.

[13] M. Adamczyk, J. R. Fishpaugh, P. G. Mattingly, *Tetrahedron Lett.* **1995**, *36*, 8345.

[14] J. Hyun, Y. Zhu, A. Liebmann-Vinson, T. P. Beebe, Jr., A. Chilkoti, *Langmuir* **2001**, *17*, 6358.

[15] R. Heuberger, G. Sukhorukov, J. Vörös, M. Textor, H. Möhwald, *Adv. Funct. Mater.* **2005**, *15*, 357.

[16] D. Stamou, C. Duschl, E. Delamarche, H. Vogel, *Angew. Chem.* **2003**, *115*, 5738; *Angew. Chem. Int. Ed.* **2003**, *42*, 5580.

[17] a) F. H. Pruslin, S. E. To, R. Winston, T. C. Rodman, *J. Immunol. Methods* **1991**, *137*, 27; b) H. Andersson, C. Jönsson, C. Moberg, G. Stemme, *Talanta* **2002**, *56*, 301.

[18] J. Anzai, T. Hoshi, N. Nakamura, *Langmuir* **2000**, *16*, 6306.

[19] Y.-S. Lo, J. Simons, T. P. Beebe, Jr., *J. Phys. Chem. B* **2002**, *106*, 9847.

[20] M. González, C. E. Argaraña, G. D. Fidelio, *Biomol. Eng.* **1999**, *16*, 67.

[21] S. Leporatti, C. Y. Gao, A. Voigt, E. Donath, H. Möhwald, *Eur. Phys. J. E* **2001**, *5*, 13.

[22] T. Kato, A. Sugawara, N. Hosoda, *Adv. Mater.* **2002**, *14*, 869.

[23] H. Yokoi, S. Kawata, M. Iwaizumi, *J. Am. Chem. Soc.* **1986**, *108*, 3358.

[24] P. Calandra, A. Longo, V. T. Liveri, *J. Phys. Chem. B* **2003**, *107*, 25.

[25] M. Abdulkhadar, B. Thomas, *Nanostruct. Mater.* **1995**, *5*, 289.

[26] G. Ibarz, L. Dähne, E. Donath, H. Möhwald, *Macromol. Rapid Commun.* **2002**, *23*, 474.


 © 2006 Wiley-VCH Verlag GmbH & Co. KGaA, Weinheim 

DNA-Aptamers

DOI: 10.1002/anie.200502979

# Abasic-Site-Containing Oligodeoxynucleotides as Aptamers for Riboflavin**

*N. B. Sankaran, Seiichi Nishizawa, Takehiro Seino, Keitaro Yoshimoto, and Norio Teramae**

Aptamers, short nucleic acid binding species, have emerged as promising candidates for molecular-recognition events on account of their significant ability to bind large numbers of ligands,[1–10] including amino acids such as arginine[3] and citrulline;[4] ribose-containing cofactors, such as adenosine triphosphate[5] and flavins;[6–8] and drugs, such as theophylline[9] and cocaine.[10] The high affinity and specificity of these aptamers toward target ligands are generally achieved by a combination of complementary molecular shapes, hydrogen-bonding, and stacking interactions.[1] Such binding events typically involve ligand-induced structural changes in the aptamers, which result in the formation of unique secondary structures that are responsible for ligand binding; the internal- or stem-loop structures are representative of the active sites for binding events. However, in the further design of both RNA and DNA aptamers for small ligands, little attention has been paid to other types of non-base-pairing moieties, despite their potential as binding pockets.

Herein, we report a new class of DNA-duplex aptamers for selective and strong binding to a biologically important ligand, where an abasic (AP) site[11–15] in the duplex is utilized as an active cavity for binding events. While it is well known that AP sites are formed by spontaneous hydrolysis of an N-

[*] Dr. N. B. Sankaran, Dr. S. Nishizawa, T. Seino, Prof. Dr. N. Teramae
Department of Chemistry
Graduate School of Science
Tohoku University
and
CREST, Japan Science and Technology Agency (JST)
Aoba-ku, Sendai 980-8578 (Japan)
Fax: (+81) 22-795-6552
E-mail: tera@anal.chem.tohoku.ac.jp

Dr. K. Yoshimoto
Bioengineering Laboratory
Discovery Research Institute
The Institute of Physical and Chemical Research
Wako, Saitama 351-0198 (Japan)

[**] This work was partially supported by Grants-in-Aid for Scientific Research (A) (no. 17205009), for Encouragement of Young Scientist (B) (no. 16750058), and for the COE Project "Giant Molecules and Complex Systems" from the Ministry of Education, Culture, Sports, Science and Technology, Japan. Partial support by RFTF from the Japan Society for the Promotion of Science (JSPS) is also acknowledged. N.B.S. would like to thank the JSPS for a fellowship. We thank Dr. Takeyoshi Kondo (Instrumental Analysis Center for Chemistry, Graduate School of Science, Tohoku University) for performing the $^1$H NMR spectroscopic measurements.

Supporting information for this article is available on the WWW under http://www.angewandte.org or from the author.

 © 2006 Wiley-VCH Verlag GmbH & Co. KGaA, Weinheim 

glycosidic bond[11] or by the removal of damaged or inappropriate bases by N-glycosylases,[12] we intentionally incorporate such lesion sites into the duplex, for which a normal DNA is complementarily hybridized with an AP-site-containing DNA. For our DNA aptamers, we strongly expect that, by stacking with two nucleotides flanking the AP site, a target ligand will be intercalated into the AP site and this will be accompanied by the formation of hydrogen bonds with a receptor nucleotide opposite the AP site (Figure 1). In

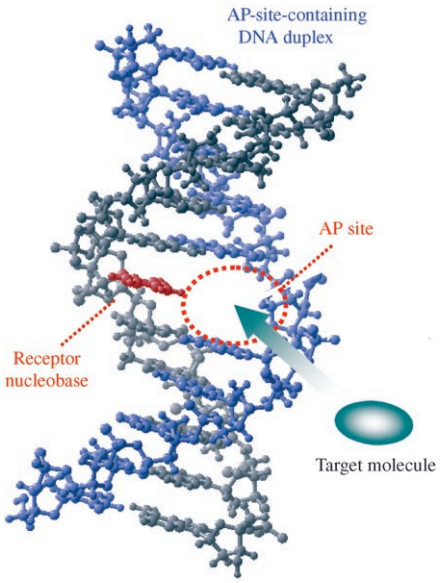
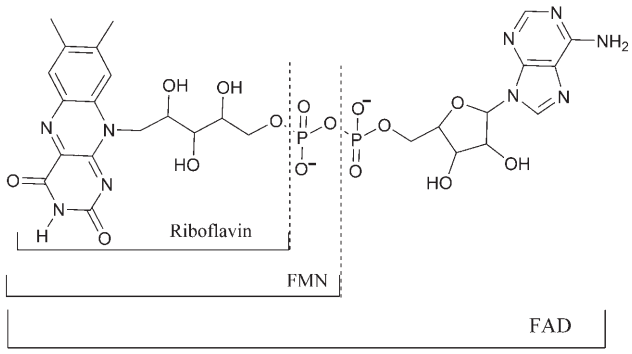



***Figure 1.*** Illustration of the binding motif of an AP-site-containing DNA duplex as an aptamer for small ligands. The pale-blue strand represents the AP-site-containing strand and the gray strand represents the complementary strand with the receptor nucleobase (red).

contrast to the relatively unspecific intercalation of aromatic ligands into double-stranded nucleic acids, this kind of binding motif would allow strong and selective binding to target ligands. Indeed, we have recently demonstrated that small aromatic ligands, such as naphthyridines, are able to bind with high affinity and selectivity to nucleotides opposite the AP site, and we have proposed a ligand-based fluorescence assay for single-nucleotide-polymorphism (SNP) typing.[16–18] Herein, we focus on the development of AP-site-containing DNA aptamers for riboflavin (vitamin $B_2$; Scheme 1), which is a biological redox cofactor that is essential for human and animal health because of its crucial role in metabolism.[19] A 23-mer duplex containing thymidine as a receptor nucleotide (**23T**) is found to strongly recognize riboflavin with a 1:1 binding stoichiometry based on examinations of the receptor nucleotides, the length of the duplexes, and the nucleotides flanking the AP site. Despite the simplicity of the binding motif, the 1:1 binding affinity of **23T** for riboflavin reaches $5.3 \times 10^5\,\text{M}^{-1}$ (at 20 °C, pH 7.0, $I = 0.11$ M), which is comparable to the binding affinities of RNA aptamers developed previously for flavin derivatives, in which the formation of the loop structures[6,8] or intramolecular G quartets[7] was responsible for the flavin binding. Moreover, the aptamer **23T** is found to show selectivity for riboflavin




***Scheme 1.*** Chemical structures of riboflavin, flavin mononucleotide (FMN), and flavin adenine dinucleotide (FAD).

over flavin mononucleotide (FMN) and flavin adenine dinucleotide (FAD). These features of the riboflavin–duplex interactions are discussed as a potential basis for the further development of AP-site-containing DNA aptamers.

Firstly, the effect of nucleobases opposite the AP site on the riboflavin–duplex interactions was examined by means of melting temperature ($T_m$) measurements. For this, we prepared four kinds of 11-mer oligodeoxynucleotide (ODN) duplexes that contain guanine (**11G**), adenine (**11A**), cytosine (**11C**), or thymine (**11T**) as the respective receptor nucleobase for binding with riboflavin. The sequences of these duplexes are given in Figure 2, together with those of other duplexes (**23C**, **23T**, **23BT**, **41T**, and **51T**) that are discussed later.

**11G** 5′-TCC AG**X** GCA AC-3′ / 3′-AGG TCG CGT TG-5′

**11A** 5′-TCC AG**X** GCA AC-3′ / 3′-AGG TCA CGT TG-5′

**11C** 5′-TCC AG**X** GCA AC-3′ / 3′-AGG TCC CGT TG-5′

**11T** 5′-TCC AG**X** GCA AC-3′ / 3′-AGG TCT CGT TG-5′

**23C** 5′-TCT GCG TCC AG**X** GCA ACG CAC AC-3′ /3 ′-AGA CGC AGG TCC CGT TGC GTG TG-5′

**23T** 5′-TCT GCG TCC AG**X** GCA ACG CAC AC-3′ / 3′-AGA CGC AGG TCT CGT TGC GTG TG-5′

**23BT** 5′-TCT GCG TCC AGG CAA CGC ACA C-3′ / 3′-AGA CGC AGG TCT CGT TGC GTG TG-5′

**41T** 5′-CAG CCG ATA ACG AAG TCC AG**X** GCA ACG ACA CGC ATA TGT GC-3′ / 3′-GTC GGC TAT TGC TTC AGG TCT CGT TGC TGT GCG TAT ACA CG-5′

**51T** 5′-GTG ACA CGC GAT TAA GAC AGT CCA G**X**G CAA CGC ACA CCA ATG CAA GGT CCA-3′ / 3′-CAC TGT GCG CTA ATT CTG TCA GGT CTC GTT GCG TGT GGT TAC GTT CCA GGT-5′

***Figure 2.*** The names and sequences of the ODN duplex aptamers. **X** = the AP site (spacer $C_3$, a propylene residue).

As shown in Table 1, the changes in $T_m$ value strongly depend on the nucleobase opposite the AP site. In solutions buffered to pH 7.0 ($I = 0.11$ M), the largest change in $T_m$ value is observed for the 11-mer duplex containing the thymine base as the receptor (**11T**), for which the $T_m$ value of the duplex (30 μM) increases by 4.0 °C in the presence of riboflavin (46 μM). An increase in $T_m$ value is also observed for the

 © 2006 Wiley-VCH Verlag GmbH & Co. KGaA, Weinheim 

***Table 1:*** Melting temperatures $T_m$ [°C] for the aptamers in the absence and presence of riboflavin.[a]

| Aptamer | $T_{m(-)}$ | $T_{m(+)}$ | $\Delta T_m$ |
|---|---|---|---|
| **11G** | 34.6 | 33.9(±0.1) | −0.7 |
| **11A** | 33.9 | 33.4(±0.1) | −0.5 |
| **11C** | 30.9 | 32.9(±1.0) | +2.0 |
| **11T** | 29.1 | 33.1(±0.8) | +4.0 |
| **23C** | 68.3 | 68.7(±0.8) | +0.4 |
| **23T** | 66.5 | 67.3(±1.0) | +0.8 |

[a] The DNA samples were annealed before the $T_m$ measurements. $T_m$ measurements were done on a Shimadzu UV-2450 UV/Vis spectrophotometer equipped with a thermoelectrically temperature-controlled micromulticell holder (8 cells; optical pathlength = 1 mm). [DNA] = 30 μM, [riboflavin] = 46 μM, [NaCl] = 100 mM, [sodium cacodylate buffer] = 10 mM, [ethylenediamine tetraacetate] = 1 mM; pH 7.0; heating rate = 1.5 °C min$^{-1}$. $T_{m(-)}$ = Melting temperature of the riboflavin-free DNA, $T_{m(+)}$ = melting temperature of the DNA with riboflavin added, $\Delta T_m = T_{m(+)} - T_{m(-)}$.

***Table 2:*** Binding constants $K_{1:1}$ [M$^{-1}$][a] at 20 °C for the binding of riboflavin with various aptamers and the corresponding thermodynamic parameters calculated by using a van't Hoff plot.[b]

| Aptamer | $K_{1:1}$ | $-\Delta H$ [kcal mol$^{-1}$] | $-\Delta S$ [e.u.][c] | $-\Delta G_{25\,°C}$ [kcal mol$^{-1}$] |
|---|---|---|---|---|
| **11G** | $3.3\times10^3$ | 18.1 | 45.3 | 4.6 |
| **11A** | $1.3\times10^4$ | 10.0 | 15.3 | 5.5 |
| **11C** | $8.1\times10^4$ | 17.6 | 37.6 | 6.4 |
| **11T** | $2.0\times10^5$ | 23.6 | 56.2 | 6.9 |
| **23C** | $2.0\times10^5$ | 12.4 | 18.1 | 7.0 |
| **23T** | $5.3\times10^5$ | 16.2 | 29.0 | 7.5 |
| **23BT** | $1.3\times10^4$ | 5.1 | −1.6 | 5.5 |
| **41T** | $6.7\times10^5$ | 13.2 | 18.5 | 7.7 |
| **51T** | $5.3\times10^5$ | 12 | 14.8 | 7.6 |

[a] Value ±10%. [b] The DNA samples were annealed before the fluorescence experiments. Fluorescence spectra were measured with a Jasco FP-6500 spectrofluorophotometer. [riboflavin] = 23 μM, [sodium cacodylate buffer] = 10 mM, [NaCl] = 100 mM, [ethylenediamine tetraacetate] = 1 mM; pH 7.0. The concentration of ODN duplex was varied from 5–80 μM. The measurement temperatures were 293, 288, 283, and 278 K. [c] e.u. = entropy unit = 4.184 J K$^{-1}$ mol$^{-1}$.

cytosine-containing duplex **11C** (+2.0 °C), but it is not as significant as that for **11T**. By contrast, the $\Delta T_m$ values are almost negligible when the receptor nucleobases are adenine (**11A**: −0.5 °C) or guanine (**11G**: −0.7 °C). Apparently, among these four kinds of 11-mer duplex, the thermal stability of **11T** is effectively increased in the presence of riboflavin, a result that indicates the incorporation of riboflavin into the AP site. The strongest binding with riboflavin is therefore expected when the receptor nucleobase opposite the AP site is thymine.

The binding affinity of the 11-mer duplexes with riboflavin was further examined quantitatively by fluorescence titration experiments, for which complexation-induced changes in the fluorescence of riboflavin were utilized (see the Supporting Information). While riboflavin (1.0 μM) shows no obvious changes for the normal 11-mer duplexes containing no AP sites (2.0 μM), its fluorescence is significantly quenched in the presence of AP-site-containing duplexes (2.0 μM). In accordance with the $T_m$ measurements, the largest quenching is observed when the receptor nucleobase at the AP site is thymine (**11T**), followed by cytosine (**11C**), adenine (**11A**), and guanine (**11G**). For all cases, the resulting changes in the fluorescence spectra can be explained by the formation of a 1:1 complex, a result that gives a 1:1 binding constant ($K_{1:1}$; at 20 °C, pH 7.0, $I = 0.11$ M) of $2.0\times10^5$ for **11T**, $0.81\times10^5$ for **11C**, $0.13\times10^5$ for **11A**, and $0.033\times10^5$ M$^{-1}$ for **11G** (Table 2). For effective binding with riboflavin, thymine is therefore the most suitable nucleobase as the receptor in the AP-site-containing duplex.

Interestingly, the binding affinity for riboflavin is further strengthened by the use of longer duplexes. As given in Table 2, the 1:1 binding constant with the 23-mer duplex containing thymine opposite the AP site, **23T** (see Figure 2), reaches $5.3\times10^5$ M$^{-1}$, which is at least two times larger than that with the corresponding 11-mer duplex, **11T** ($2.0\times10^5$ M$^{-1}$). Similarly, the 1:1 binding affinity with the 23-mer duplex **23C** ($2.0\times10^5$ M$^{-1}$) is stronger than its shorter counterpart, **11C** ($0.81\times10^5$ M$^{-1}$). On a further increase in the duplex length, from 23- to 51-mer, however, the increasing trend in $K_{1:1}$ values is rather insignificant (see Table 2), so the use of longer duplexes is not necessary. We therefore conclude that the 23-mer ODN duplex **23T** qualifies as an ideal aptamer in our investigations.

To understand such an effect of the ODN length on the riboflavin–duplex interactions, the nature of the thermodynamic profile was examined by construction of a van't Hoff plot from temperature-dependant fluorescence titration experiments (see Table 2 and the Supporting Information). As can be seen in Table 2, the riboflavin–duplex interaction is enthalpy driven for all the duplexes containing AP sites. However, the enthalpy term becomes destabilizing as the duplex length is increased from an 11-mer to a 23-mer. This is highly compensated for by less negative values of entropy that result in a more favorable free energy change ($\Delta G_{25\,°C}$). In the case of ODN duplexes containing thymine as the receptor base (**11T** and **23T**), the loss of enthalpy from the 11-mer to the 23-mer is approximately 7 kcal mol$^{-1}$, whereas the gain in entropy is approximately 27 e.u. Similarly, the increase in the binding affinity from **11C** to **23C** is due to the favorable gain in entropy ($\Delta\Delta H = 5.2$ kcal mol$^{-1}$; $\Delta\Delta S = -19.5$ e.u.). For the higher homologues, such as **41T** and **51T**, the overall loss of entropy reaches the minimum values among those of the series of thymine-containing duplexes (**11T**–**51T**); the reduced gain in enthalpy is compensated for by this. These favorable gains in entropy between complexes of different length may be a result of minimal conformational changes associated with the ODN duplexes on binding with riboflavin. Indeed, as revealed by melting temperature measurements (Table 1), the complexation-induced change in the $T_m$ value is almost negligible for 23-mer ODN duplexes ($\Delta T_m$: **23C**: +0.4 °C; **23T**: +0.8 °C), a fact that indicates that the thermal stabilities of these longer duplexes hardly change upon binding with riboflavin. It is therefore likely that, as compared to the binding affinities of 11-mer duplexes, the enhanced binding ability of the longer duplexes towards riboflavin is accompanied by rather less conformational change of the aptamers. This kind of binding event contrasts with those of typical RNA/DNA aptamers containing 30–40 nucleotides,

 © 2006 Wiley-VCH Verlag GmbH & Co. KGaA, Weinheim 

wherein effective binding is generally achieved by folding and conformational reorientation of the aptamers.[20]

Another interesting feature of the binding events compared to those with the previous flavin-binding aptamers[6,20] is the difference in the receptor nucleotides responsible for effective binding with riboflavin. In the RNA aptamers developed for flavins earlier,[6,20] an adenine that is coplanar with the flavin recognizes the polar groups along the edge of the isoalloxazine ring through hydrogen bonding. The uracil-like edge of isoalloxazine hydrogen bonds to the Hoogsteen edge of an adenine residue in such aptamers. However, in the present case, as is evident from the melting temperature and fluorescence studies, the binding of riboflavin with **11T**, in which a thymidine moiety locates opposite the AP site, is stronger than with **11A**, where the receptor nucleobase is adenine. The formation of hydrogen bonding between the receptor thymine base and riboflavin is confirmed by $^1$H NMR spectroscopic measurements by using the Watergate technique.[21,22] As shown in Figure 3, the signals for the imino

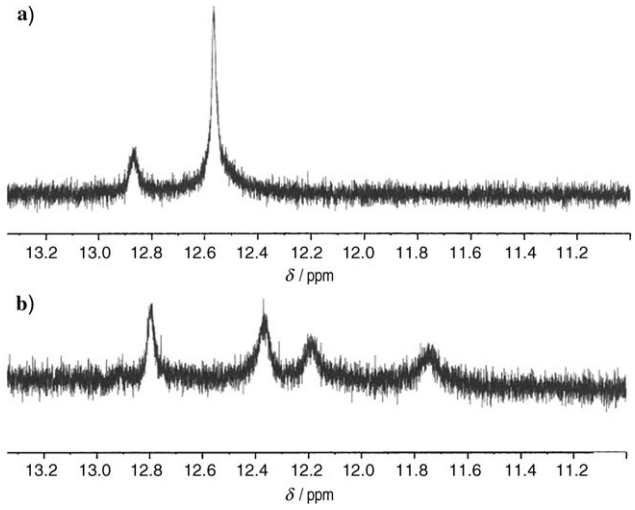



***Figure 3.*** $^1$H NMR spectra showing the imino proton region of the spectrum for the AP-site-containing DNA duplex **11T** in the absence (a) and in the presence (b) of riboflavin. The results support the formation of hydrogen bonds between the thymine receptor nucleobase and riboflavin. NMR spectra were measured with an Avance 600 spectrometer (600 MHz, Bruker) by employing the Watergate method. [DNA duplex] = 0.80 mM, [riboflavin] = 0.82 mM, [tris(hydroxymethyl)aminomethane buffer] = 10 mM, [NaCl] = 100 mM, [ethylenediamine tetraacetate] = 1 mM; pH 8.3, $T$ = 288 K. 5% $D_2O$ was added to lock the signals.

protons due to G–C base pairing are observed at $\delta = 12.86$ and 12.57 ppm for the 11-mer ODN duplex (spectrum a), whereas riboflavin alone does not generate any signals (spectrum not shown). Upon complexation, new signals appear at $\delta = 12.18$ and 11.75 ppm accompanied by upfield shifts of the signals for the imino protons due to G–C base pairing (spectrum b). The new signals can be assigned to imino protons due to binding of a thymine base with riboflavin, as has been observed for mismatched base pairings, such as T–T, that give signals in a more upfield region than those from fully matched base pairs.[22] It is therefore likely that at the AP site a pseudo base pair is formed with a thymine base along the uracil-like edge of the isoalloxazine ring of riboflavin, as shown in the energy-minimized structure of the complex obtained by molecular-modeling studies (see the Supporting Information). From the calculated structure (see the Supporting Information), we also see that the isoalloxazine ring is located at the AP site, in which the ring moiety is stacked with two guanines flanking the AP site. This indicates that, as has previously been revealed for the binding events of some RNA aptamers,[1] the high stability of the AP-site-based aptamer is achieved by a cooperative binding event, that is, not only by hydrogen bonding with target molecules but also by stacking with nucleobases flanking the AP site. Indeed, examination of the influence of the nucleobases flanking the AP site on fluorescence quenching of riboflavin with **23T** reveals that the fluorescence of riboflavin is quenched strongly when the nucleobases flanking the AP site were guanines, whereas other nucleobases flanking the AP site have considerably less influence on the fluorescence of riboflavin (see the Supporting Information). Apparently, the binding events at the AP site depend on the flanking nucleobases and an appropriate environment can be provided for riboflavin to effectively bind with the receptor thymine base when the flanking nucleobases are both guanines (G**X**G, **X** = AP site).

In connection with these effects of flanking nucleobases on the binding events, it is also of interest to note that the binding ability of the thymine base toward riboflavin depends on the size of the binding pockets in ODN duplexes. The 1:1 binding constant of riboflavin with **23BT**, a 23-mer ODN duplex where a single bulge structure is produced with thymine as the receptor nucleobase but with no AP sites (see Figure 2), is only $0.13 \times 10^5\,\text{M}^{-1}$, which is considerably less than that of the corresponding AP-site-containing duplex **23T** ($5.3 \times 10^5\,\text{M}^{-1}$). The examination of the thermodynamic profile of **23BT** shows that the interaction of the bulged thymine with riboflavin is both enthalpy and entropy driven, with a $\Delta G$ value of $-5.5$ kcal mol$^{-1}$, a $\Delta H$ value of $-5.1$ kcal mol$^{-1}$, and a $T\Delta S$ value of 0.4 kcal mol$^{-1}$ at 25 °C (Table 2). The observed nature of the binding is clearly different from the enthalpy-driven binding at the AP site and is rather similar to that for outside-edge- and partial-insertion-binding drugs.[23] It is therefore likely, probably for steric reasons, that the isoalloxazine ring of riboflavin is not able to intercalate deeply between the nucleotides opposite the bulge structure and the effective formation of key molecular interactions, including stacking and hydrogen bonding, is not allowed with binding to the bulged thymine in **23BT**.

Finally, we examined the binding ability of **23T** with other flavin cofactors, such as FMN and FAD. As shown in Figure 4, the aptamer **23T** is found to quench fluorescence of these ligands, and the resulting changes in fluorescence can be analyzed based on the formation of a 1:1 complex. These results indicate that, similarly to the binding mode for riboflavin, **23T** also recognizes the isoalloxazine ring of FMN and FAD and the tricyclic ring intercalates into the AP site in the duplex. However, the binding affinity for FMN or FAD is significantly lower than the affinity for riboflavin. The 1:1 binding constants for FMN and FAD are $0.21 \times 10^5$

 © 2006 Wiley-VCH Verlag GmbH & Co. KGaA, Weinheim 

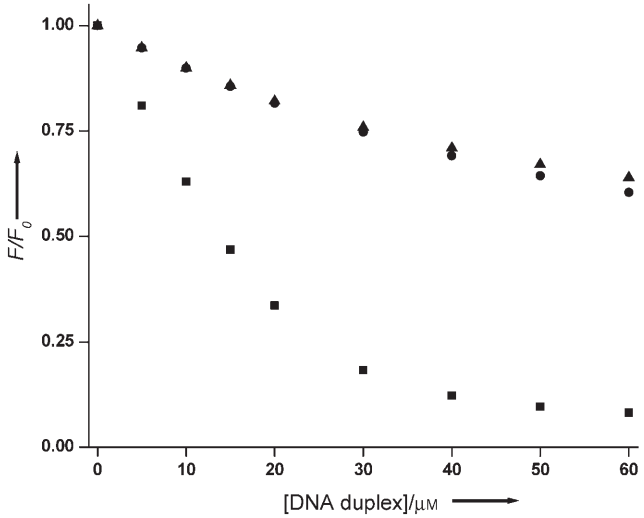



***Figure 4.*** Fluorescence titration curves of riboflavin (■), FMN (●), and FAD (▲) with **23T**. [flavins] = 23 μM, [**23T**] = 0, 5, 10, 15, 20, 30, 40, 50, or 60 μM, [sodium cacodylate buffer] = 10 mM, [NaCl] = 100 mM, [ethylenediamine tetraacetate] = 1 mM; pH 7.0. Fluorescence spectra were measured with a Jasco FP-6500 spectrofluorophotometer; $\lambda_{ex} = 448$ nm. $F_0$ is the fluorescence intensity (at 530 nm) of flavins before adding the ODN duplex and $F$ is the fluorescence intensity after addition of the ODN duplex.

and $0.25 \times 10^5\,\text{M}^{-1}$, respectively, under identical conditions to those in which riboflavin binding was examined. Such high selectivity for riboflavin over FMN and FAD was not obtained by the RNA aptamers developed previously, where the formation of intramolecular G quartets[7] or the internal-loop structure[8] was utilized as the binding motif for the flavin portion of these ligands.[24]

A simple explanation for the lower affinity of FMN and FAD is that of charge repulsion of the negatively charged phosphate groups of both ligands with the ODN phosphate backbone. In the case of riboflavin, this repulsive interaction is apparently absent and, even in the uncharged form, a favorable gain from the electrostatic free-energy contribution $\Delta G_{pe}$ can also be expected, as has been observed for the interaction of electrically neutral echinomycin with DNA duplexes.[25] This is generally attributed to lengthening and unwinding of the DNA, both of which increase the phosphate spacing along the helix axis. This results in a decrease in the charge density of the duplex, thereby releasing condensed counterions and providing an entropically favorable contribution to the binding free energy.[25] Indeed, in the present case, from the examination of the salt dependence of the binding constants, the effective number of charges on riboflavin is found to be +0.52 when binding to **11T**. At 110 mM $Na^+$ concentration (pH 7.0, at 5 °C), the polyelectrolyte contribution $\Delta G_{pe}$ is calculated to be $-0.56\,\text{kcal mol}^{-1}$, a result that reveals an effective contribution of $\Delta G_{pe}$ to the overall free energy of the riboflavin–ODN binding ($-7.97\,\text{kcal mol}^{-1}$). Under the same conditions, the apparent charge of riboflavin on binding with **23T** is +0.60 and $\Delta G_{pe}$ is $-0.65\,\text{kcal mol}^{-1}$ leads to a favorable entropy contribution to the overall binding free-energy ($-8.14\,\text{kcal mol}^{-1}$) of the longer duplex.

However, other possibilities should also be taken into account when it is considered that **23T** binds to FMN and FAD with equal affinity, despite the difference in the number of negative charges. In the case of FAD, for example, the difference in the hydrate shell from the other two ligands is evident since FAD is known to exist predominantly in a stacked conformation. The thermodynamic profile of the FAD–**23T** interaction shows that $\Delta G = -5.7\,\text{kcal mol}^{-1}$, $\Delta H = -16.0\,\text{kcal mol}^{-1}$, and $T\Delta S = -10.3\,\text{kcal mol}^{-1}$ at 25 °C, thereby indicating that the significant loss of binding entropy is responsible for the lower affinity as compared to the riboflavin–**23T** interaction. By contrast, loss of binding enthalpy is responsible for the lower affinity to FMN ($\Delta G = -5.7\,\text{kcal mol}^{-1}$, $\Delta H = -10.8\,\text{kcal mol}^{-1}$, and $T\Delta S = -5.1\,\text{kcal mol}^{-1}$ at 25 °C). We are currently investigating the flavin–ODN interactions in more detail to obtain a deeper insight into the origin of the binding affinity and selectivity.

In summary, we have demonstrated a new class of DNA aptamer in which AP sites in the duplex were utilized as the binding pockets for riboflavin recognition. By optimizing structural parameters, such as the receptor nucleotide, the length of the duplexes, and the flanking nucleotides to the AP site, the aptamer **23T** selectively bound to riboflavin over FMN and FAD, with a 1:1 binding constant of $5.3 \times 10^5\,\text{M}^{-1}$ (at 20 °C, pH 7.0, $I = 0.11$ M). The binding affinity of **23T** up to the micromolar range was indeed comparable with binding affinities of RNA aptamers developed earlier for flavin derivatives[6–8] and was significantly better than the millimolar affinity of polymer-bound zinc(II) azamacrocycles for riboflavin.[26] Although the fact that only four nucleobases are available for our design scheme may necessitate some synthetic modification of the nucleobases in order to make it suitable for binding with a large number of ligands, our DNA aptamer may have some advantages, such as its easy and low-cost synthesis and its higher chemical stability relative to typical RNA aptamers. These features of the AP-site-based DNA aptamer would allow various kinds of analytical applications, including the isolation of riboflavin from natural sources[26] and the determination of riboflavin in aqueous samples.[27–29] Moreover, our system can also be applied to the analysis of thymidine-related SNPs, for which riboflavin functions as a thymidine-selective fluorescence ligand and the complexation-induced quenching of its fluorescence is utilized to detect the single-base mutation (see the Supporting Information). We are now undertaking further studies in these directions.

Received: August 22, 2005
Revised: October 27, 2005
Published online: January 30, 2006

**Keywords:** abasic sites · aptamers · flavins · fluorescence probes · nucleic acids

[1] T. Hermann, D. J. Patel, *Science* **2000**, *287*, 820.
[2] A. D. Ellington, J. W. Szostak, *Nature* **1990**, *346*, 818.
[3] K. Harada, A. D. Frankel, *EMBO J.* **1995**, *14*, 5798.
[4] M. Famulok, *J. Am. Chem. Soc.* **1994**, *116*, 1698.

 © 2006 Wiley-VCH Verlag GmbH & Co. KGaA, Weinheim 

[5] a) S. D. Jhaveri, R. Kirby, R. Conrad, E. J. Maglott, M. Bowser, R. T. Kennedy, G. Glick, A. D. Ellington, *J. Am. Chem. Soc.* **2000**, *122*, 2469; b) S. Jhaveri, M. Rajendran, A. D. Ellington, *Nat. Biotechnol.* **2000**, *18*, 1293; c) E. J. Merino, K. M. Weeks, *J. Am. Chem. Soc.* **2003**, *125*, 12370.
[6] P. Burgstaller, M. Famulok, *Angew. Chem.* **1994**, *106*, 1163; *Angew. Chem. Int. Ed. Engl.* **1994**, *33*, 1084.
[7] C. T. Lauhon, J. W. Szostak, *J. Am. Chem. Soc.* **1995**, *117*, 1246.
[8] M. Roychowdhury-Saha, S. M. Lato, E. D. Shank, D. H. Burke, *Biochemistry* **2002**, *41*, 2492.
[9] R. D. Jenison, S. C. Gill, A. Pardi, B. Polisky, *Science* **1994**, *263*, 1425.
[10] M. N. Stojanovic, P. de Prada, D. W. Landry, *J. Am. Chem. Soc.* **2001**, *123*, 4928.
[11] T. Lindahl, B. Nyberg, *Biochemistry* **1972**, *11*, 3610.
[12] H. E. Krokan, R. Standal, G. Slupphaug, *Biochem. J.* **1997**, *325*, 1.
[13] T. Lindahl, *Nature* **1993**, *362*, 709.
[14] J. H. J. Hoeijmakers, *Nature* **2001**, *411*, 366.
[15] E. C. Friedberg, *Nature* **2003**, *421*, 436.
[16] K. Yoshimoto, S. Nishizawa, M. Minagawa, N. Teramae, *J. Am. Chem. Soc.* **2003**, *125*, 8982.
[17] K. Yoshimoto, C.-Y. Xu, S. Nishizawa, T. Haga, H. Satake, N. Teramae, *Chem. Commun.* **2003**, 2960.
[18] S. Nishizawa, K. Yoshimoto, T. Seino, C.-Y. Xu, M. Minagawa, H. Satake, A. Tong, N. Teramae, *Talanta* **2004**, *63*, 175.
[19] The importance of flavins in various biological processes has been highlighted; see, for example: a) *Flavins and Flavoproteins* (Eds.: S. K. Chapman, R. N. Perham, N. S. Scrutton), Rudolf Weber Agency for Scientific Publications, Berlin, **2002**; b) *Chemistry and Biochemistry of Flavoenzymes, Vol. 1* (Ed.: F. Müller), CRC, Boca Raton, **1991**.
[20] P. Fan, A. K. Suri, R. Fiala, D. Live, D. J. Patel, *J. Mol. Biol.* **1996**, *258*, 480.
[21] M. Piotto, V. Saudek, V. Sklenar, *J. Biomol. NMR* **1992**, *2*, 661.
[22] P. K. Bhattacharya, J. Cha, J. K. Barton, *Nucleic Acids Res.* **2002**, *30*, 4740.
[23] I. Haq, J. Ladbury, *J. Mol. Recognit.* **2000**, *13*, 188.
[24] The binding of RNA aptamers with 7,8-dimethylalloxazine, FMN, and FAD has been examined,[6] whereby aptamers for FMN or FAD were isolated by in vitro selection. While the RNA aptamers (FMN-2 and 35FMN-2) based on the internal-loop structure were not able to distinguish between these flavin derivatives, FAD-1 or 27FAD-1 containing the stem-loop structure as the binding motif showed moderate selectivity for 7,8-dimethylalloxazine over FMN and FAD: the dissociation constants of 27FAD-1 with 7,8-dimethylalloxazine, FMN, and FAD were reported to be 35, 280, and 273 μM, respectively.
[25] F. Leng, J. B. Chaires, M. J. Waring, *Nucleic Acids Res.* **2003**, *31*, 6191.
[26] B. König, H.-T. Gallmeier, R. Reichenbach-Klinke, *Chem. Commun.* **2001**, 2390.
[27] J. A. Tillotson, M. M. Bashor, *Anal. Biochem.* **1980**, *107*, 214.
[28] J. Becvar, G. Palmer, *J. Biol. Chem.* **1982**, *257*, 5607.
[29] I. Caelen, A. Kalman, L. Wahlström, *Anal. Chem.* **2004**, *76*, 137.

 © 2006 Wiley-VCH Verlag GmbH & Co. KGaA, Weinheim 

Transport of Nonviral Vectors

DOI: 10.1002/anie.200503021

# The Transport of Nanosized Gene Carriers Unraveled by Live-Cell Imaging**

*Ralf Bausinger, Katharina von Gersdorff, Kevin Braeckmans, Manfred Ogris, Ernst Wagner, Christoph Bräuchle,* and Andreas Zumbusch**

Nonviral vectors are increasingly attracting interest as tools for the transfer of genetic material into cells.[1] Compared to viral gene-transfer systems, they offer several advantages, especially flexibility regarding the size and type of nucleic acid to be transported, biosafety, and a chemically controllable structure. Based on different chemical building blocks, a broad variety of nonviral vectors have been designed. Polyethylenimines (PEIs) are especially attractive polymers for gene delivery because their high buffering capacity promotes endosomal release, thereby favoring high in vitro and in vivo transfection efficiencies of the PEI/DNA polyplexes.[2]

Current efforts in polyplex synthesis are aimed at further optimizing the transfection efficiencies. Insight into the behavior of polyplexes in live cells is a prerequisite for the development of new strategies and their validation. Fluorescence microscopy is an ideal tool for the elucidation of the respective mechanisms. Previous experiments gave the first insights into the interaction of polyplexes with negatively charged proteoglycans at the cell surface.[3,4] However, little is known about the transport processes that allow the polyplexes to overcome the barriers occurring between binding to the cell surface and the final transcription of the transgene. To unravel the dynamics of the processes involved, new single-particle tracking techniques are employed.[5–7] First results from such experiments indicate that, once inside the cell,

[*] R. Bausinger, Dr. K. Braeckmans,[+] Prof. Dr. C. Bräuchle, Priv.-Doz. Dr. A. Zumbusch
Department Chemie und Biochemie and Center for NanoScience (CeNS)
Ludwig-Maximilians-Universität München
Butenandtstrasse 11, 81377 München (Germany)
Fax: (+49) 89-2180-77548
E-mail: christoph.braeuchle@cup.uni-muenchen.de
zumbusch@fwf.ac.at

K. von Gersdorff, Dr. M. Ogris, Prof. Dr. E. Wagner
Department Pharmazie
Ludwig-Maximilians-Universität München

[+] Current address:
General Biochemistry & Physical Pharmacy
Gent University (Belgium)

[**] This work was supported by the Deutsche Forschungsgemeinschaft (Grant no. SFB 486). R.B. and K.v.G. contributed equally to this work. K.B. is a Postdoctoral Fellow of the Fund for Scientific Research—Flanders, Belgium.

Supporting information for this article is available on the WWW under http://www.angewandte.org or from the author.


WILEY InterScience DISCOVER SOMETHING GREAT
© 2006 Wiley-VCH Verlag GmbH & Co. KGaA, Weinheim

polyplexes are actively transported to the perinuclear region.[8] It was hypothesized that the cellular microtubule network plays a pivotal role in the transfection process. Herein we report how PEI/DNA polyplexes interact with different parts of the cytoskeleton. This is the first study to cover the complete cycle from binding at the cell surface to the behavior during cell division. We use a novel, simultaneous fluorescence-imaging scheme to follow the dynamic interaction of single PEI/DNA particles with the cytoskeleton. This proves the hitherto only indirectly inferred interactions of polyplexes with actin filaments and microtubules. Our investigations point at bottlenecks during the transfection and provide a basis for new synthetic strategies to optimize the transfection efficiencies of polyplexes.

A recently published model suggests that the actin cytoskeleton might be involved in the cellular uptake of PEI/DNA polyplexes after binding to the cell surface,[4] whereas microtubules are postulated to be involved in intracellular particle transport.[8] We therefore tracked single polyplexes and simultaneously imaged the respective parts of the cytoskeleton in live cells. From the data analysis (see the Experimental Section), we obtained the transport velocities $v$ and diffusion coefficients $D$ for the polyplexes. Three different types of motion emerge: polyplex diffusion with a broad range of diffusion coefficients, actin-associated transport with $v \approx 10^{-2}\ \mu m\,s^{-1}$, and active transport with $v \approx 0.2\ \mu m\,s^{-1}$ along microtubules (Figure 1). Simultaneous particle tracking and live-cell imaging allow us, for the first time, to show how the interaction of the polyplex with the cytoskeleton is correlated to the observed motion.

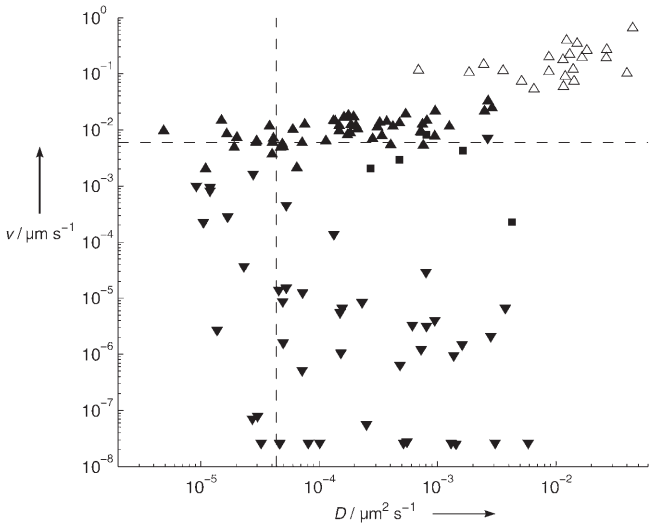



***Figure 1.*** Scatter plot of velocity $v$ versus diffusion coefficient $D$ for all analyzed trajectories of PEI/DNA polyplexes in HUH-7 cells. Three clusters are attributed to different motion behaviors of the polyplexes: fast, active transport along microtubules (△), slower, actin-associated active transport (▲), and quasifree (■) and anomalous (▼) diffusion with a broad range of diffusion coefficients. The exponent $\gamma$ (related to Equation (2); see the Experimental Section) shows values of $\gamma > 1.05$ (△, ▲), $0.95 < \gamma < 1.05$ (■), and $\gamma < 0.95$ (▼). The horizontal and vertical dashed lines mark the lowest detectable velocity ($v_{min} = 6 \times 10^{-3}\ \mu m\,s^{-1}$) and diffusion coefficient ($D_{min} = 4 \times 10^{-5}\ \mu m^2\,s^{-1}$), respectively, within the accuracy of our setup.

To unravel the role of actin filaments in the transfection process, we generated an HUH-7 cell line that stably expressed an actin–EGFP chimera (EGFP = enhanced green fluorescent protein). We observed the interaction of PEI/DNA-Cy3 polyplexes with these actin structures by imaging them both at the same time (Figure 2a; Cy3 = 5-*N*,*N*′-dialkyltetramethylindocarbocyanine derivative). Less than 10 min after incubation, polyplexes are found to be attached to the cell surface. Most of them are colocalized with actin filaments. In a few cases, we directly observed attachment of particles from the medium, as well as detachment from the cell surface (see movie 1 in the Supporting Information), which indicates that some particles are not yet internalized. Surface-bound polyplexes exhibit three different types of behavior: 2D free diffusion (Figure 2b,c), restricted diffusion up to the point of complete immobilization (Figure 2d,e), and active transport (Figure 2f,g).

Our experimental findings give a conclusive picture of the processes in the early stage of transfection with PEI/DNA polyplexes. Because of their positive surface charge, the polyplexes bind to syndecans, negatively charged heparan sulfate proteoglycans (HSPGs), in cell membranes.[3] It has been proposed that syndecan clustering around the particle triggers cytoplasmic binding of these transmembrane proteins to actin filaments through linker proteins and this process subsequently supports polyplex uptake through endocytotic vesicles.[4] Our data show that this association indeed occurs.

A fraction (5%) of the polyplexes diffuse freely (Figure 2b,c) and their mean-squared displacements $\langle r^2 \rangle(\Delta t)$ show a quasilinear dependence on $\Delta t$ with $0.95 < \gamma < 1.05$ according to Equation (2) (see the Experimental Section). Their diffusion coefficients $D$ range from $10^{-2}$ to $3 \times 10^{-4}\ \mu m^2\,s^{-1}$. We interpret this free diffusion as the first process after the attachment of a polyplex to the cell membrane through interaction with a negatively charged HSPG. The $D$ value then reflects the motion of the HSPG in the membrane. This interpretation is supported by similar diffusion coefficients found for particles attached to glycoproteins.[9]

In addition to free diffusion, we observe anomalous diffusion with $\gamma < 0.95$ and diffusion in a confined space separated by periods of free diffusion (Figure 2d,e). This means that the free volume accessible to the diffusing polyplexes is restricted. We interpret this as continuous binding and unbinding of polyplexes to and from actin filaments, mediated by linker proteins. This follows the putative triggering of a phosphorylation of the polyplex-bound syndecans and a subsequently increased ability of the polyplex–syndecan complex to bind to actin filaments. In this process, the particle will gradually be engulfed by the membrane, which corresponds to the observed diffusion in a confined space. Ultimately, the confinement immobilizes the polyplex. Indeed, we find that 90% of the observed polyplexes are colocalized with actin filaments and show strongly reduced diffusion coefficients of $D < 10^{-3}\ \mu m^2\,s^{-1}$ (Figure 1, Figure 2).

Engulfment has been demonstrated to be a prerequisite for active transport of polystyrene beads binding to actin. Active transport is then caused by cellular transport of the

 © 2006 Wiley-VCH Verlag GmbH & Co. KGaA, Weinheim 

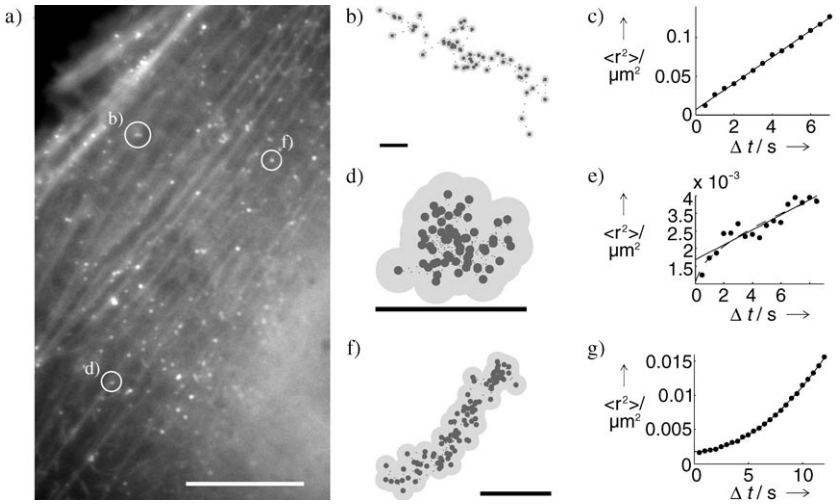



***Figure 2.*** PEI/DNA-polyplex interaction with actin structures in HUH-7 cells during the early stage of transfection. a) Fluorescence microscopy of EGFP–actin and Cy3-labeled polyplexes (scale bar: 10 µm). b)–g) Three different modes of motion can be distinguished; b), d), f) show the particles' trajectories (scale bars: 0.2 µm), c), e), g) the mean-squared displacements $\langle r^2 \rangle$ dependent on the time delay for a polyplex diffusing between actin fibers with $D = 4 \times 10^{-3}$ µm$^2$ s$^{-1}$ and $\gamma = 1.0$ ((b) and (c)), a nearly immobilized polyplex with $D = 5 \times 10^{-5}$ µm$^2$ s$^{-1}$ and $\gamma = 0.6$ ((d) and (e)), and a particle showing active transport parallel to actin fibers with $v = 10^{-2}$ µm s$^{-1}$ ((f) and (g)). The solid lines in (c), (e), and (g) are second-order polynomial fits to the data according to Equation (1) (see the Experimental Section), while the dashed lines represent a power-law fit corresponding to Equation (2) (see the Experimental Section). The gray areas denote the accuracy of the measured position with a radius of $3 \times 10^{-2}$ µm.

actin filaments to which the particles are bound.[10] We observe active transport with or along actin filaments in a number of cases (Figure 2 f, g). The data analysis yields average transport velocities of $v = 10^{-2}$ µm s$^{-1}$ and diffusion coefficients of $D = 2 \times 10^{-4}$ µm$^2$ s$^{-1}$. These values are the same as those reported for the transport of engulfed glycoprotein-binding beads on actin filaments.[9,10]

Polyplex observation more than 90 min after incubation reveals a distinctly different motion behavior. Its hallmarks are long-range directed motion with increased velocity and no correlation of this movement to actin filaments. We therefore performed experiments on HUH-7 cells expressing an EGFP–tubulin chimera, which allows the simultaneous monitoring of the microtubule network and polyplex motion. The results directly verify the proposition that active transport of polyplexes takes place along microtubules. This has previously been suggested, on the basis of the known effect of microtubule-disrupting drugs on the intracellular transport of polyplexes.[8]

We find that the polyplex movement occurs along tracks which are given by the microtubules (Figure 3 a, movie 2 in the Supporting Information). It is intriguing to consider the form in which the polyplexes are undergoing this fast transport. At the end of the polyplexes' interaction with the cellular actin network, they should be internalized by the formation of a vesicle around the polyplex. Fast transport would then be observed for particles that are inside vesicles. To test this hypothesis, we used a dextran–Alexa Fluor 647 conjugate as a fluid-phase marker and applied it together with Cy3-labeled polyplexes in investigations of unlabeled live cells. Colocalization experiments of polyplexes and the fluid-phase marker by using a confocal microscope reveal that, more than 180 min after incubation, 95 % of all polyplexes are inside vesicles.

Thus, polyplexes inside vesicles are moved along microtubules. Most probably, molecular motors such as kinesins or dyneins mediate this transport. We find average velocities of $v = 0.19$ µm s$^{-1}$, in agreement with reference [8], but these values are smaller than those reported for motor proteins by up to a factor of five. This discrepancy is explained by analyzing small parts of the trajectories separately (Figure 3 b, c). It is immediately revealed that fast transport only lasts for less than 3 s before the polyplexes stall or move in the opposite direction (Figure 3 d). This leads to the low mean velocities. The maximum values of $v_{max} = 0.65$ µm s$^{-1}$ from this analysis compare well with those reported for kinesin and dynein.[11]

During the rapid motion, particles are often seen to change direction (Figure 3 d). Competing processes with opposite directionality have been reported previously for the intracellular transport of influenza viruses and adenoviruses in live cells.[7,12] As in these cases, our observation is best explained by competition between plus and minus end-directed motors present on the vesicle.

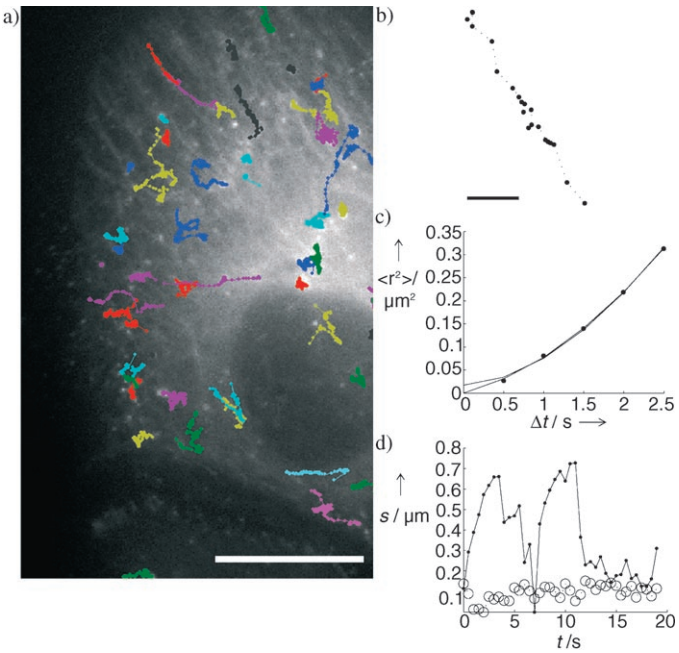



***Figure 3.*** Active transport of PEI/DNA polyplexes in HUH-7 cells along microtubules. a) Fluorescence image of EGFP-labeled microtubules with PEI/DNA-Cy3 complexes (scale bar: 10 µm). b) Trajectory (scale bar 1 µm) and c) mean-squared displacement plot for an actively transported particle along a microtubule with $v = 0.18$ µm s$^{-1}$. Positioning accuracies are given as gray areas. d) Bidirectional movement along a microtubule. Time dependence of the particle coordinates along (dots, solid line) and perpendicular to the filament (open circles, dashed line).

 © 2006 Wiley-VCH Verlag GmbH & Co. KGaA, Weinheim 

The observation of successful gene expression indicates that the transgene delivered by the polyplex becomes accessible to the transcriptional machinery. Direct entry of the polyplexes into the nucleus is inhibited by their size. Nevertheless, nuclear location of some PEI-polyplex formulations has been observed.[13] More recent work has shown that the transfection efficiency is cell-cycle dependent,[14] a fact that is ascribed to the breakdown of the nuclear membrane during cell division. To ascertain the fate of polyplexes during mitosis, we tracked single polyplexes in mitotic EGFP–tubulin-tagged cells. Polyplexes move along the microtubules of the spindle apparatus with velocities of up to 0.9 $\mu m\,s^{-1}$, a value that again corresponds to those known for motor proteins (Figure 4, movie 3 in the Supporting Information). Monitoring of the fate of the polyplexes over extended periods with simultaneous phase-contrast and fluorescence microscopy reveals their distribution at the poles of the spindle apparatus. It is remarkable that, at this stage, the majority of the polyplexes are associated with movement along the microtubules. This suggests that the concentration of polyplexes at the location of the emerging nuclei of the daughter cells strongly contributes to the transfection process.

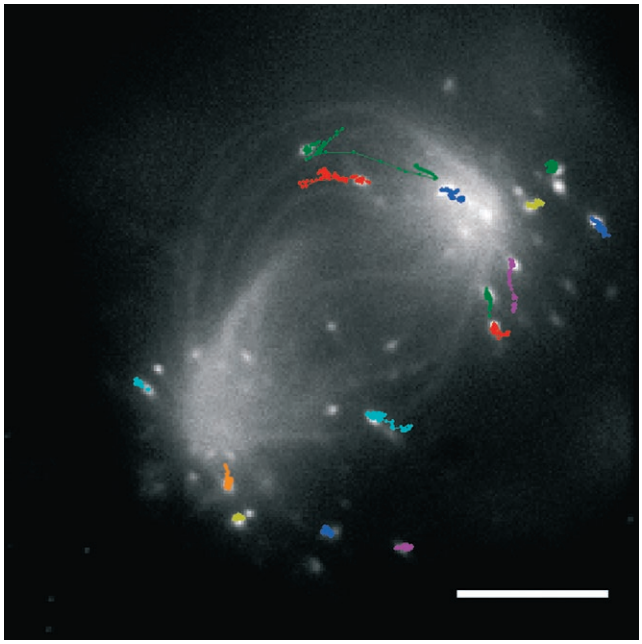


***Figure 4.*** Polyplex distribution during mitosis. PEI/DNA complexes are transported on astral microtubules towards the poles of the spindle apparatus with peak velocities of 0.9 $\mu m\,s^{-1}$ (scale bar: 5 μm).

In conclusion, simultaneous particle tracking and high-resolution live-cell imaging yields a conclusive image of the interaction between PEI/DNA nanoparticles and cellular components during transfection. In the early stage of transfection, PEI/DNA polyplexes bind to cell-membrane syndecans and diffuse freely on the cell surface. Progressive accumulation of syndecans around the polyplex induces its binding to actin filaments and engulfment by the plasma membrane. Subsequently, polyplexes inside vesicles are actively transported along microtubules by molecular motors. Finally, we have given evidence for the importance of mitosis in the transfection process. Knowledge of the binding, transport, and release mechanisms provides a basis for the improvement of transfection efficiencies with synthetic gene carriers. Current strategies based on these results include chemical surface modification with target-cell-specific ligands and the introduction of environment-sensitive groups that induce intracellular polyplex disassembly.[15,16]

## *Experimental Section*

Cell-culture reagents and Alexa Fluor 647 dextran (10 kDa) were purchased from Invitrogen (Karlsruhe, Germany). HUH-7 human hepatoma cells (JCRB 0403; Tokyo, Japan; cell diameters up to 70 μm) were cultured in Dulbecco's modified Eagle's medium:F12 (1:1) with Glutamax I medium containing 10% fetal calf serum. pEGFP–actin and pEGFP–tubulin vectors (encoding fusion proteins of EGFP and actin or tubulin, respectively, under the control of a CMV (CMV = cytomegalovirus) promoter) were purchased from Clontech (Palo Alto, CA). The plasmid pCMVLuc was covalently labeled with the fluorophore Cy3 as described earlier.[15] PEI/DNA polyplexes were generated with linear PEI (22 kDa) in 2-[4-(2-hydroxyethyl)-1-piperazinyl]ethanesulfonic acid (HEPES) buffered glucose (HBG, 5% glucose, 20 mM HEPES, pH 7.1) at a PEI/DNA ratio of 6:1. Light scattering (Zetasizer 3000HS; Malvern Instruments, Worcestershire, UK) revealed polyplex diameters of (85 ± 14) nm in HBG and (165 ± 18) nm in cell-culture medium.

For stably expressing EGFP–actin and EGFP–tubulin cells, vectors were linearized with the restriction enzymes ApaL I and MlU I, respectively. HUH-7 cells were transfected by using PEI22 polyplexes generated in HEPES-buffered saline (0.5× HBS, 75 mM NaCl, 2.5% glucose, 20 mM HEPES, pH 7.1) with a PEI/DNA ratio of 6:1. Cells were incubated in fresh medium for 48 h and then selected with G418 (200 $\mu g\,mL^{-1}$). After several days, surviving cells were seeded into six-well plates. Finally, single-cell clones were isolated and expanded.

A Nikon TE200 microscope with a Nikon PlanApo 100×/1.4 oil immersion objective was used. The samples were Köhler illuminated with 488 nm and 532 nm light. Fluorescence was collected in the epi direction, passed through a dichromatic mirror reflecting at 488, 532, and 633 nm (from AHF Analysentechnik, Tübingen, Germany), and was filtered from residual excitation light by a bandpass filter (HQ 575/70; AHF). Movies were captured with an electron multiplier (EM) CCD camera (Cascade 650; Roper Scientific, Tuscon, AZ, USA).

Particle positions were derived from the centroids of their diffraction-limited spots for each frame in a movie. The mode of motion was analyzed by calculating the mean-squared displacement $\langle r^2\rangle(\Delta t) = \langle\{x(t+\Delta t)-x(t)\}^2+\{y(t+\Delta t)-y(t)\}^2\rangle$ for a time interval of $\Delta t$ between pairs of frames. $\langle\ldots\rangle$ indicates the ensemble average over all such pairs in a movie. $\langle r^2\rangle(\Delta t)$ was fitted with a second-order polynomial [Eq. (1)], referring to diffusion with a diffusion coefficient $D$ overlaying transport with constant velocity $v$, and a power-law function [Eq. (2)], referring to free diffusion ($\gamma = 1$) and anomalous sub ($\gamma < 1$) and super($\gamma > 1$) diffusion.[17]

$$\langle r^2\rangle(\Delta t) = C + 4\,D\,\Delta t + v^2\,\Delta t^2 \quad (1)$$

$$\langle r^2\rangle(\Delta t) = C' + A\,\Delta t^{\gamma} \quad (2)$$

The constants $C$ and $C'$ consider the finite spatial and temporal resolution of our setup.[18] A particle-positioning accuracy of $\pm s =$ 30 nm was obtained from the variance of position measurements of an immobile particle. This results in a lowest detectable velocity of $v_{min} =$

 © 2006 Wiley-VCH Verlag GmbH & Co. KGaA, Weinheim 

$6 \times 10^{-3}$ μm s$^{-1}$ for pure transport and a lowest detectable diffusion coefficient of $D_{min} = 4 \times 10^{-5}$ μm$^2$ s$^{-1}$.

Received: August 24, 2005

**Keywords:** DNA · fluorescence microscopy · gene expression · intracellular transport · nanoparticles

[1] E. Wagner, *Pharm. Res.* **2004**, *21*, 8.
[2] O. Boussif, F. Lezoualc'h, M. A. Zanta, M. D. Mergny, D. Scherman, B. Demeneix, J.-P. Behr, *Proc. Natl. Acad. Sci. USA* **1995**, *92*, 7297.
[3] K. A. Mislick, J. D. Baldeschwieler, *Proc. Natl. Acad. Sci. USA* **1996**, *93*, 12349.
[4] I. Kopatz, J. S. Remy, J.-P. Behr, *J. Gene Med.* **2004**, *6*, 769.
[5] G. S. Harms, L. Cognet, P. H. M. Lommerse, G. A. Blab, H. Kahr, R. Gamsjäger, H. P. Spaink, N. M. Soldatov, C. Romanin, T. Schmidt, *Biophys. J.* **2001**, *81*, 2639.
[6] G. Seisenberger, M. U. Ried, T. Endreß, H. Büning, M. Hallek, C. Bräuchle, *Science* **2001**, *294*, 1929.
[7] M. Lakadamyali, M. J. Rust, H. P. Babcock, X. Zhuang, *Proc. Natl. Acad. Sci. USA* **2003**, *100*, 9280.
[8] J. Suh, D. Wirtz, J. Hanes, *Proc. Natl. Acad. Sci. USA* **2003**, *100*, 3878.
[9] M. P. Sheetz, S. Turney, H. Qian, E. L. Elson, *Nature* **1989**, *340*, 284.
[10] A. Caspi, O. Yeger, I. Grosheva, A. D. Bershadsky, M. A. Elbaum, *Biophys. J.* **2001**, *81*, 1990.
[11] S. J. King, T. A. Schroer, *Nat. Cell Biol.* **2000**, *2*, 20.
[12] M. Suomalainen, M. Y. Nakano, S. Keller, K. Boucke, R. P. Stidwill, U. F. Greber, *J. Cell Biol.* **1999**, *144*, 657.
[13] W. T. Godbey, K. K. Wu, A. G. Mikos, *Proc. Natl. Acad. Sci. USA* **1999**, *96*, 5177.
[14] S. Brunner, E. Fürtbauer, T. Sauer, M. Kursa, E. Wagner, *Mol. Ther.* **2002**, *5*, 80.
[15] K. von Gersdorff, M. Ogris, E. Wagner, *Eur. J. Pharm. Biopharm.* **2005**, *60*, 279.
[16] G. F. Walker, C. Fella, J. Pelisek, J. Fahrmeir, S. Boeckle, M. Ogris, E. Wagner, *Mol. Ther.* **2005**, *11*, 418.
[17] M. J. Saxton, K. Jacobson, *Annu. Rev. Biophys. Biomol. Struct.* **1997**, *26*, 373.
[18] H. Qian, M. P. Sheetz, E. L. Elson, *Biophys. J.* **1991**, *60*, 910.

 © 2006 Wiley-VCH Verlag GmbH & Co. KGaA, Weinheim 

Enzyme Systems

DOI: 10.1002/anie.200503314

# Elementary Arithmetic Operations by Enzymes: A Model for Metabolic Pathway Based Computing**

*Ronan Baron, Oleg Lioubashevski, Eugenii Katz, Tamara Niazov, and Itamar Willner**

The similarities in the processing of information by biological systems and human-designed devices are broadly recognized.[1–3] Computer technology relies on logic functions and arithmetic operations, whereby the insertion of signals into electronic circuits allows the differentiation and processing of the output signals. In chemical or biochemical computing systems, different stimuli trigger molecular architectures or biochemical ensembles, and the resulting chemical reactivity provides computing and processing functions. A variety of molecular and supramolecular[4–17] systems were reported to act as logic gates that perform molecular-scale arithmetic functions. The use of biomaterials as active computing elements attracts substantial research efforts. Biomolecules such as DNA or proteins were suggested as active components that function as logic gates. Gene-based artificial circuits acting as a bistable toggle switch[18] or as an oscillator[19] were developed. Enzymes and DNA were coupled to perform programmable biochemical transformations that mimic basic computing of finite automaton.[20] This led to the design of a biocomputer that logically analyses the content of messenger RNA and in response produces a molecule that controls the levels of gene expression.[21] The hemoprotein cytochrome c was employed as an active component for the development of AND, OR, and XOR logic operations by the application of different chemical inputs that induce changes in the protein. These structural changes altered the fluorescence of the protein, thus the emission was used as the output signal.[22]

The function of enzyme networks as mimics of Boolean logic gates was also discussed.[23] The use of enzymes as potential building blocks for designing high-density computing architectures, free from interconnection requirements, was also addressed theoretically.[1] Only a few studies, however, dealt with the practical realization of biocomputing devices using enzymes. The conformational dynamics of malate dehydrogenase in response to the concentrations of $Mg^{2+}$ and $Ca^{2+}$ ions was employed to construct an XOR

[*] Dr. R. Baron, O. Lioubashevski, Dr. E. Katz, T. Niazov, Prof. I. Willner
Institute of Chemistry
The Hebrew University of Jerusalem
Jerusalem 91904 (Israel)
Fax: (+972) 2-652-7715
E-mail: willnea@vms.huji.ac.il

[**] This research was supported by the MOLDYNLOGIC EC project.

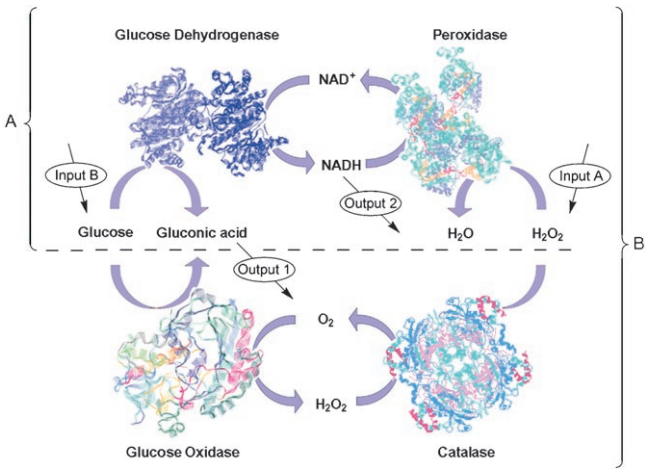
Supporting information for this article is available on the WWW under http://www.angewandte.org or from the author.


InterScience
© 2006 Wiley-VCH Verlag GmbH & Co. KGaA, Weinheim

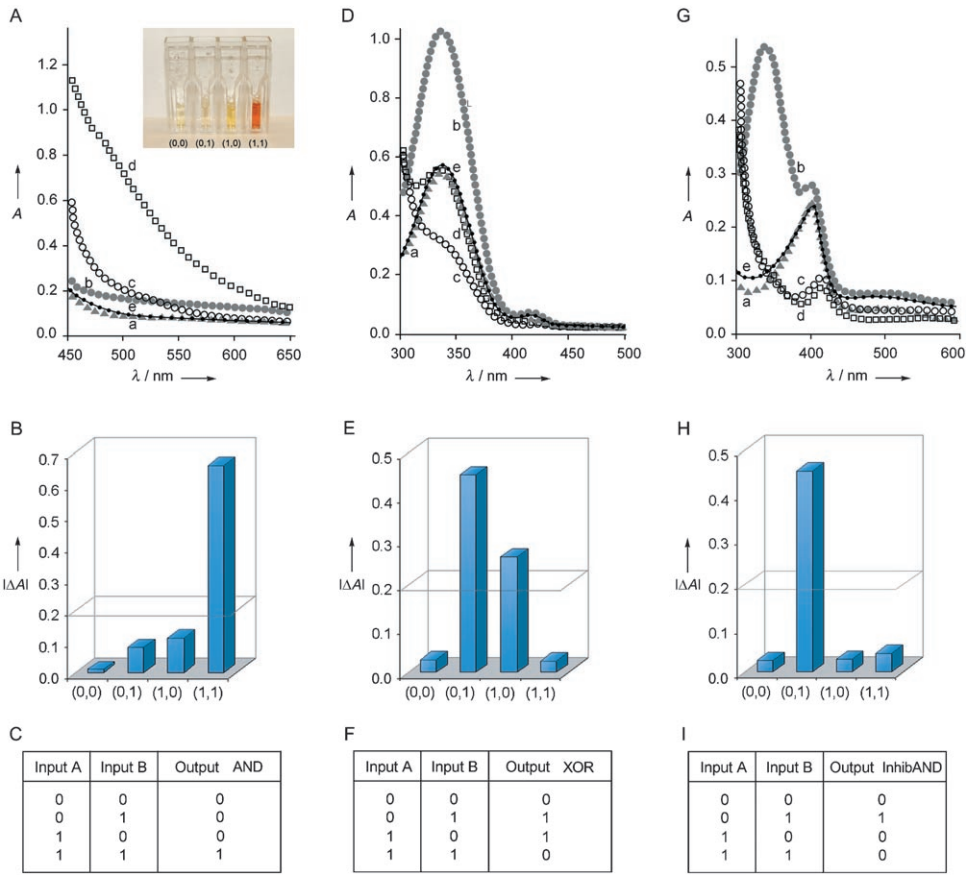
gate.[24] Recently, a modified enzyme and its inhibitor were used as two inputs for the operation of an AND logic gate.[25] Herein, we report the use of native enzyme systems as digital logic gates that perform arithmetic operations (half-adder or half-subtractor). In the future, such biochemical computers may follow in vivo metabolic pathways or regulate drug delivery. (Note that in the present discussion, "biochemical computers" are defined as biomolecule-based systems that mimic functions of logic gate circuits).

Modern computers rely on the parallel execution of particular logic gates that are based on Boolean operations activated by binary input signals "0" and "1" to produce a single binary output signal.[26] In the present study, we describe biocatalytic systems that comprise a combination of two enzymes—horseradish peroxidase (HRP) and glucose dehydrogenase (GDH)—in conjunction with two chemicals that act as activating signals, namely hydrogen peroxide (input A; $H_2O_2$) and glucose (input B). Scheme 1 A depicts the configuration of the two-enzyme system that performs AND, XOR, and InhibAND gate functions. The HRP/GDH enzyme system is coupled by the $NAD^+$/NADH cofactor system (NAD(H) = nicotinamide adenine dinucleotide, (reduced)). The biocatalyzed oxidation of glucose by $NAD^+$ yields NADH, while the peroxidase-mediated reduction of $H_2O_2$ by NADH completes the cycle. For all gates both inputs are present in equal amounts, and the output of the biocatalytic logic gates (the result of the enzymatic activity of the systems) is read out in terms of a change in absorbance at an appropriate wavelength. A measured threshold value, the modulus of the change in absorbance change ($|\Delta A|$), below 0.2 absorbance units (au) corresponds to the output 0, and a measured value above 0.2 au yields the output 1 (the absorbance values below or above the threshold value are analogous to the voltage regions of transistor logics that define "0" or "1" states). The parallel activation of different gates allows us to perform arithmetic operations consisting of half-adders and half-subtractors.

For the AND gate, in the presence of NADH the peroxidase-mediated transformation of input A yields $NAD^+$, which is consumed by GDH and used to catalyze the oxidation of input B, glucose, to gluconic acid. The gluconic acid product, output 1 (Scheme 1 A), is analyzed colorimetrically upon its reaction with hydroxylamine and subsequent production of the red compound generated by complexation of the hydroxamate with $Fe^{II}$.[27] From the spectra depicted in Figure 1 A it can be seen that the product is generated only if both inputs are present in the system (A = 1, B = 1), by observing the absorbance band at $\lambda = 500$ nm ($|\Delta A| > 0.2$, curve d). The changes in the absorbance presented




***Scheme 1.*** A) Logic gates based on two coupled enzymes. B) Half-adder based on four coupled biocatalysts.




| Input A | Input B | Output AND |
|---|---|---|
| 0 | 0 | 0 |
| 0 | 1 | 0 |
| 1 | 0 | 0 |
| 1 | 1 | 1 |

| Input A | Input B | Output XOR |
|---|---|---|
| 0 | 0 | 0 |
| 0 | 1 | 1 |
| 1 | 0 | 1 |
| 1 | 1 | 0 |

| Input A | Input B | Output InhibAND |
|---|---|---|
| 0 | 0 | 0 |
| 0 | 1 | 1 |
| 1 | 0 | 0 |
| 1 | 1 | 0 |

***Figure 1.*** A) Absorbance features of the AND gate. Inset: visual color output of the enzyme-based AND gate. B) Bar-chart presentation of the absorbance outputs of the AND gate. C) Truth table corresponding to the AND gate. D) Absorbance features of the XOR gate. E) Bar chart of the absorbance outputs of the XOR gate. F) Truth table corresponding to the XOR gate. G) Absorbance features of the InhibAND gate. H) Bar chart of the absorbance outputs of the InhibAND gate. I) Truth table corresponding to the InhibAND gate. Inputs correspond to a) (0,0) ▲; b) (0,1) ●; c) (1,0) ○; and d) (1,1) □; curve (e) –•–• shows the absorbance of the biocatalytic system prior to activation by the inputs. For the bar charts, the threshold absorbance value of 0.2 is marked.

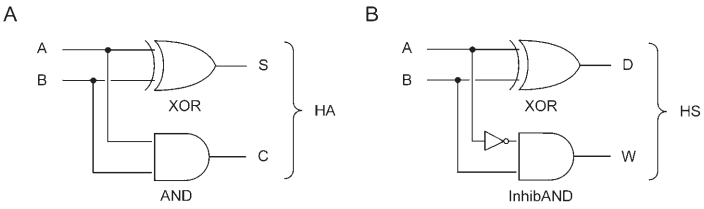
 © 2006 Wiley-VCH Verlag GmbH & Co. KGaA, Weinheim 

in Figure 1B demonstrate that an output of "1" exists only for a situation when the inputs are (1,1). This situation is also shown by the respective truth table (Figure 1C) and depicted in the inset to Figure 1A. Note that for all gates the changes in absorbance are analyzed after a fixed time interval of 20 minutes. This time interval was selected after studying the kinetic operation of the different enzyme-based logic gates which revealed a tendency of saturation of the absorbance values (see Supporting Information). Thus, although the operation of the gates is a result of kinetically controlled biotransformations, the steady-state features of the system allow us to read out the logic gate operation. (For the theoretical justification of the use of kinetically controlled systems for computations, see reference [28–29]).

An XOR (eXclusive OR) gate is created in a buffered solution that contains equal amounts of NADH and $NAD^+$. The output signal is the modulus, $|\Delta A|$, of the change in absorbance for NADH at $\lambda =$ 340 nm (Scheme 1A, output 2) measured after the biocatalytic reaction was allowed to proceed for 20 minutes. As depicted in Figure 1D, a TRUE output only exists if the configuration of inputs is (1,0) or (0,1). If only input A is added to the system, configuration (1,0), then the HRP-catalyzed oxidation of NADH to $NAD^+$ occurs, giving rise to a variation in the absorbance of NADH (Scheme 1A, curve b). In contrast, if only input B is added, configuration (0,1), then the GDH-biocatalyzed reduction of $NAD^+$ to NADH proceeds, resulting in a positive change in the absorbance of NADH (Scheme 1A, curve c). When both inputs are introduced into the system, (1,1), the glucose input generates NADH while the $H_2O_2$ input results in a depletion of NADH, leading to no net change in the absorbance of NADH (Scheme 1A, curve d), and the XOR gate gives a FALSE output. Figure 1E shows the schematic variations in absorbance of the XOR gate operation, while the respective truth table is shown in Figure 1F.

The third gate, InhibAND, has a TRUE output if one specific input is TRUE (input B), while the second TRUE input or a combination of two TRUE inputs yields a FALSE output (the InhibAND gate is equivalent to the output of a NOT gate acting as the input to an AND gate). This situation occurs when $NAD^+$ is added as a mediating cofactor that bridges the two enzymes. As with the XOR gate, the output is the formation of NADH (output 2; Scheme 1A) and is followed spectroscopically at $\lambda = 340$ nm. When no input is introduced into the system, configuration (0,0), there is no NADH in the system, as depicted by the spectral features shown in Figure 1G, curve a. Introduction of input A, configuration (1,0), also does not yield NADH (curve c). However, the introduction of input B, configuration (0,1), activates the reduction by GDH of $NAD^+$ to NADH and yields a TRUE output (curve b). When both inputs are introduced, configuration (1,1), GDH catalyzes the reduction of $NAD^+$ to NADH, but the HRP-mediated oxidation of NADH by $H_2O_2$ recycles $NAD^+$ and thus no change in absorbance is observed at $\lambda = 340$ nm. While only the configuration (0,1) results in a TRUE output (also depicted by the absorbance variations and the corresponding truth table shown in Figure 1H and I, respectively), for the configurations (0,0) and (0,1) an absorbance band is observed at $\lambda = 410$ nm, assigned to the reduced heme site of HRP. In configurations (1,0) and (1,1) there is a decrease in the absorbance of heme and the band is shifted to around 420 nm owing to the oxidized form of the heme center.

The combination of the AND and XOR gates, operating in parallel, yields a half-adder (Figure 2A); the half-adder is defined as a logic circuit that adds two one-bit binary numbers. The first input binary number is coded by the presence or absence of $H_2O_2$, whereas the second input binary number is coded by the presence or absence of glucose. The carry digit is given by the AND gate through the generation of the gluconic acid output, analyzed spectroscopically through the color of the $Fe^{III}$–hydroxamate complex at $\lambda =$ 500 nm. The output of the XOR gate represents the sum digit and is read out by the spectroscopic determination of NADH at $\lambda = 340$ nm. Figure 2C summarizes the truth table corresponding to the half-adder.




C

| First digit, input A | Second digit, input B | Carry digit, C | Sum digit, S |
|---|---|---|---|
| 0 | 0 | 0 | 0 |
| 0 | 1 | 0 | 1 |
| 1 | 0 | 0 | 1 |
| 1 | 1 | 1 | 0 |

D

| First digit, input A | Second digit, input B | Borrow digit, W | Difference digit, D |
|---|---|---|---|
| 0 | 0 | 0 | 0 |
| 0 | 1 | 1 | 1 |
| 1 | 0 | 0 | 1 |
| 1 | 1 | 0 | 0 |

***Figure 2.*** Circuitry for A) the half-adder (HA) and B) the half-subtractor (HS). C, D) Truth tables corresponding to the half-adder and the half-subtractor, respectively.

By analogy, the parallel activation of the InhibAND and XOR gates yields the half-subtractor (Figure 2B); the half-subtractor is defined as a logic circuit that subtracts two one-bit binary numbers. The outputs of the two gates correspond to the absorbance of NADH at $\lambda = 340$ nm. The borrow digit is the output of the InhibAND gate, while the difference digit is the output of the XOR gate. Figure 2D shows the truth table corresponding to the half-subtractor system.

The half-adder and half-subtractor enzyme-based systems suffer from the limitation that the gates operate in separate compartments and that the computation results from the outputs of the separate gates. However, one may design an integrated enzyme system of enhanced complexity that performs the half-adder computation in a single compart-

 © 2006 Wiley-VCH Verlag GmbH & Co. KGaA, Weinheim 

ment. This is exemplified in Scheme 1 B by the application of four enzymes—GDH, HRP, glucose oxidase (GOx), and catalase (Cat)—that operate in parallel, in the presence of NADH and $NAD^+$, to yield AND and XOR gates. Glucose and $H_2O_2$ act as the inputs, as described earlier, and the absorbance that follows the production of gluconate or NADH provide the outputs of the AND and XOR gates, respectively. For the AND gate, gluconate is generated by two complementary paths that include the GDH- and GOx-mediated formation of gluconate (Figure 3 A, B). For the XOR gate, the absorbance of NADH is the output and changes in the absorbance of NADH occur only in the presence of one input. The introduction of the two inputs results in the continuous transformation of $NAD^+$ to NADH and back, such that the steady-state $NAD^+$/NADH ratio remains constant (Figure 3 C and D).

In conclusion, the study has introduced a new paradigm for biomolecular computing that employs enzyme-based logic gates. The half-adder and half-subtractor systems described here were developed using identical inputs and coupled biocatalysts. Specifically, an integrated "single-compartment" half-adder was constructed. We believe that this model could be extended to other enzyme systems. For example, by using enzymes that participate in the metabolic regulatory cycle, biocomputing systems that follow physiological conditions may be envisaged. Furthermore, we employed redox enzymes and their substrates as input units, and the computational functions were read out by optical means. The "wiring" of the enzymes with electrodes[30] and the electrical readout of the biocatalytic computations could lead to enzyme-based electronic computers.

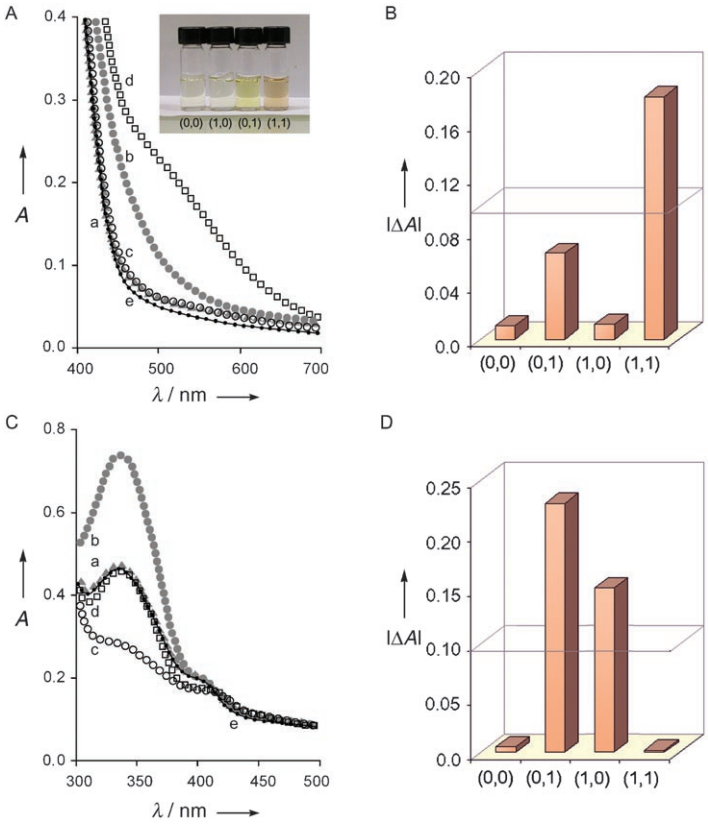



***Figure 3.*** A) Absorbance features of the AND gate corresponding to the four-enzyme system. Inset: visual color output of the enzyme-based AND gate. B) Bar-chart presentation of the absorbance outputs of the AND gate. C) Absorbance features of the XOR gate corresponding to the four-enzyme system. D) Bar-chart presentation of the absorbance outputs of the XOR gate. Inputs correspond to a) (0,0) ▲; b) (0,1) ▲; c) (1,0) ○; and d) (1,1) □; curve (e) –•–• shows the absorbance of the biocatalytic system prior to activation by the inputs. For the bar charts, the threshold absorbance value of 0.1 is marked.

## *Experimental Section*

Materials and methods: All chemicals and enzymes were purchased from Aldrich or Sigma. The enzymes used are glucose dehydrogenase from *Thermoplasma acidophilum* (E.C. 1.1.1.47), horseradish peroxidase (E.C. 1.11.1.7), glucose oxidase from *Aspergillus niger* (E.C. 1.1.3.4), and catalase from bovine liver (E.C. 1.11.1.6). For each gate, the amounts of enzymes and substrates were first roughly estimated and then optimized in order to keep the same inputs for all the gates as well as to get a significant difference of $|\Delta A|$ between the states "0" and "1". The absorbance measurements were performed using a Shimadzu UV-2401PC UV/Vis spectrophotometer. All measurements were performed at $25 \pm 2\,^{\circ}C$.

Composition of the gates for the two-enzyme systems (Scheme 1 A): The experiments were conducted in a 250-μl spectrophotometric quartz cell. For all gates, the modulus of the change in absorbance, $|\Delta A|$, was measured after a time interval of 20 min. The deviation of the $|\Delta A|$ values did not exceed $\pm 5\,\%$. The variations in absorbance correspond to the difference in absorbance before and after the enzymatic reaction. The inputs that were used for all the two-enzymes systems correspond to an addition of 0.30 M $H_2O_2$ (input A) and 1 M β-D(+)glucose (input B). For the AND gate, the system is composed of a solution (250 μl) of 4.5 U horseradish peroxidase, 12 U glucose dehydrogenase, and $1 \times 10^{-4}$ M NADH in 0.01 M phosphate buffer, pH 6.8. The enzymatic reaction takes place for 20 min. The gluconic acid product was measured according to a previously reported procedure.[27] Briefly, 250 μL of solution 1 ($5 \times 10^{-3}$ M EDTA and 0.15 M $Et_3N$ in water) and 25 μL of solution 2 (3 M $NH_2OH$ in water) were added to the system and the mixture was allowed to react for 15 min. Finally, 125 μL of solution 3 (1 M HCl, 0.1 M $FeCl_3$, and 0.25 M $CCl_3COOH$ in water) was added to the reaction medium, and the reaction was allowed to proceed for 5 min. The generated gluconic acid reacts with hydroxylamine, and after the addition $Fe^{3+}$ the red complex hydroxamate–$Fe^{3+}$ is formed. The TRUE output corresponds to the absolute value of the change in absorbance, $|\Delta A|$, at 500 nm that is above a predefined threshold value of 0.2 au. For the XOR gate, the system consists of a solution (250 μL) of 10 U horseradish peroxidase, 7.5 U glucose dehydrogenase, $1 \times 10^{-4}$ M $NAD^+$, and $1 \times 10^{-4}$ M NADH in 0.01 M phosphate buffer, pH 6.8 (the amounts of enzymes were balanced in such a way that the biocatalytic transformations proceeded at the same rate). The TRUE output corresponds to $|\Delta A| > 0.2$ au at 340 nm. For the InhibAND gate, the system is composed of a solution (250 μL) of 13.5 U horseradish peroxidase, 3 U glucose dehydrogenase, and $1 \times 10^{-4}$ M $NAD^+$ in 0.01 M phosphate buffer, pH 6.8. The TRUE output corresponds to $|\Delta A| > 0.2$ au at 340 nm.

Composition of the four-enzyme system (AND and XOR gates combined, Scheme 1 B): The system is composed of a solution (1.2 mL) of 13.5 U horseradish peroxidase, 10 U glucose dehydrogen-

 © 2006 Wiley-VCH Verlag GmbH & Co. KGaA, Weinheim 

ase, 40 U glucose oxidase, 400 U catalase, $1 \times 10^{-4}$ M $NAD^+$, and $1 \times 10^{-4}$ M NADH in 0.01M phosphate buffer, pH 6.8. The experiments were conducted in a 2-mL spectrophotometric glass cell connected by a long glass tube that can be hermetically closed. The reaction medium was degassed with argon that was purified from traces of oxygen by bubbling in an aqueous solution of sodium dithionate/methyl viologen. The variations in absorbance correspond to the difference in absorbance before and after the enzymatic reaction. The inputs correspond to an addition of 0.03 M $H_2O_2$ (input A) and 0.8 M β-D(+)glucose (input B). For the XOR gate, the modulus of absorbance change, $|\Delta A|$, was measured after a time interval of 10 min with the spectrophotometric cell hermetically closed, and a TRUE output corresponds to $|\Delta A| > 0.1$ au at 340 nm. For the AND gate, we then applied the procedure as described previously for the two-enzyme system AND gate, with the only modification being that the solutions were previously deoxygenated before being added to the spectrophotometric cell. The TRUE output corresponds to the absolute value of the change in absorbance, $|\Delta A|$, that is above a predefined threshold value of 0.1 au at 500 nm.

Received: September 18, 2005
Revised: November 30, 2005
Published online: January 27, 2006

**Keywords:** enzymes · logic gates · metabolism · redox chemistry

[1] M. Sugita, *J. Theor. Biol.* **1961**, *1*, 415 – 430.
[2] T. Pawson, *Nature* **1995**, *373*, 573 – 580.
[3] D. Bray, *Nature* **1995**, *376*, 307 – 312.
[4] A. Credi, V. Balzani, S. J. Langford, J. F. Stoddart, *J. Am. Chem. Soc.* **1997**, *119*, 2679 – 2681.
[5] C. P. Collier, E. W. Wong, M. Belohradský, F. M. Raymo, J. F. Stoddart, P. J. Kuekes, R. S. Williams, J. R. Heath, *Science* **1999**, *285*, 391 – 394.
[6] K. L. Kompa, R. D. Levine, *Proc. Natl. Acad. Sci. USA* **2001**, *98*, 410 – 414.
[7] A. P. de Silva, H. Q. N. Gunaratne, C. P. McCoy, *Nature* **1993**, *364*, 42 – 44.
[8] M. N. Stojanovic, T. E. Mitchell, D. Stefanovic, *J. Am. Chem. Soc.* **2002**, *124*, 3555 – 3561.
[9] A. Saghatelian, N. H. Völcker, K. M. Guckian, V. S.-Y. Lin, M. R. Ghadiri, *J. Am. Chem. Soc.* **2003**, *125*, 346 – 347.
[10] M. N. Stojanovic, D. Stefanovic, *J. Am. Chem. Soc.* **2003**, *125*, 6673 – 6676.
[11] S. J. Langford, T. Yann, *J. Am. Chem. Soc.* **2003**, *125*, 11198 – 11199.
[12] G. Ashkenasy, M. R. Ghadiri, *J. Am. Chem. Soc.* **2004**, *126*, 11140 – 11141.
[13] D. Margulies, G. Melman, C. E. Felder, R. Arad-Yellin, A. Shanzer, *J. Am. Chem. Soc.* **2004**, *126*, 15400 – 15401.
[14] J. Andreasson, G. Kodis, Y. Terazono, P. A. Lidell, S. Bandyopadhyay, R. H. Mitchell, T. A. Moore, A. L. Moore, D. Gust, *J. Am. Chem. Soc.* **2004**, *126*, 15926 – 15927.
[15] S. Uchiyama, G. D. McClean, K. Iwai, A. P. de Silva, *J. Am. Chem. Soc.* **2005**, *127*, 8920 – 8921.
[16] S. D. Straight, J. Andreasson, G. Kodis, S. Bandyopadhyay, R. H. Mitchell, T. A. Moore, A. L. Moore, D. Gust, *J. Am. Chem. Soc.* **2005**, *127*, 9403 – 9409.
[17] F. Remacle, J. R. Heath, R. D. Levine, *Proc. Natl. Acad. Sci. USA* **2005**, *102*, 5653 – 5658.
[18] T. S. Gardner, C. R. Cantor, J. J. Collins, *Nature* **2000**, *403*, 339 – 342.
[19] M. B. Elowitz, S. Leibler, *Nature* **2000**, *403*, 335 – 338.
[20] Y. Benenson, T. Paz-Elizur, R. Adar, E. Keinan, Z. Livneh, E. Shapiro, *Nature* **2001**, *414*, 430 – 434.
[21] Y. Benenson, B. Gil, U. Ben-Dor, R. Adar, E. Shapiro, *Nature* **2004**, *429*, 423 – 429.
[22] A. S. Deonarine, S. M. Clark, L. Konermann, *FGCS* **2003**, *19*, 87 – 97.
[23] A. Arkin, J. Ross, *Biophys. J.* **1994**, *67*, 560 – 578.
[24] K.-P. Zauner, M. Conrad, *Biotechnol. Prog.* **2001**, *17*, 553 – 559.
[25] S. Sivan, S. Tuchman, N. Lotan, *Biosystems* **2003**, *70*, 21 – 33.
[26] V. P. Heuring, H. F. Jordan, *Computer Systems: Design and Architecture*, Addison-Wesley, Menlo Park, CA, **1997**.
[27] E. T. Rakitzis, P. Papandreou, *Chem.-Biol. Interact.* **1998**, *113*, 205 – 216.
[28] M. O. Magnasco, *Phys. Rev. Lett.* **1997**, *78*, 1190 – 1193.
[29] A. Hjelmfelt, E. D. Weinberger, J. Ross, *Proc. Natl. Acad. Sci. USA* **1991**, *88*, 10983 – 10987.
[30] I. Willner, E. Katz, *Angew. Chem.* **2000**, *112*, 1180 – 1218; *Angew. Chem. Int. Ed.* **2000**, *39*, 1230 – 1269.

 © 2006 Wiley-VCH Verlag GmbH & Co. KGaA, Weinheim 

Protein Detection

DOI: 10.1002/anie.200503345

# Ultrasensitive Detection of Proteins by Amplification of Affinity Aptamers**

*Hongquan Zhang, Zhongwen Wang, Xing-Fang Li, and X. Chris Le**

Determination of low-abundance proteins is essential for characterizing proteomes and studying their biochemical functions. Although nucleic acids can be amplified by a polymerase chain reaction (PCR) to improve the sensitivity, there is no comparable technique to chemically amplify proteins. To improve the sensitivity and specificity of protein detection, the nanoparticle-based bio-barcode technique,[1] immuno-PCR,[2,3] and proximity-dependent DNA-ligation assays[4,5] have been developed, albeit each has its own advantages and drawbacks.

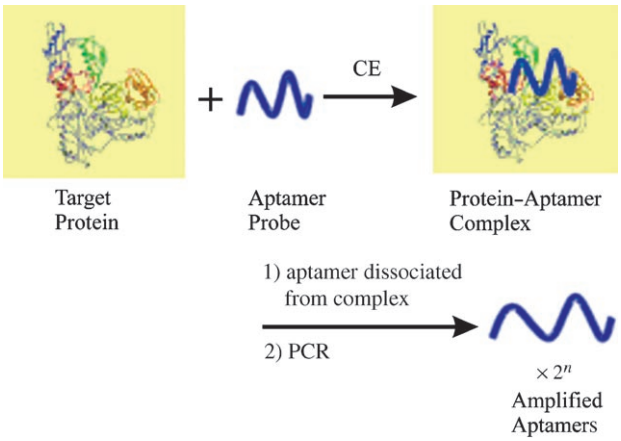
Herein we describe an ultrasensitive aptamer-based affinity-PCR technique for the determination of trace amounts of proteins (Scheme 1). First, we introduced an aptamer that bound with a target protein. The protein–aptamer complex was then separated from the unbound aptamer by using capillary electrophoresis (CE). We collected the protein–aptamer complex, dissociated the aptamer from the complex, and then amplified the aptamer by PCR. The amplification of the aptamer to which the protein binds

[*] H. Zhang, Dr. Z. Wang, Prof. Dr. X.-F. Li, Prof. Dr. X. C. Le
Department of Public Health Sciences, University of Alberta
Edmonton, Alberta, T6G 2G3 (Canada)
Fax: (+1) 780-492-7800
E-mail: xc.le@ualberta.ca

[**] We thank the Natural Sciences and Engineering Research Council of Canada and the Canada Research Chairs Program for financial support of this research.

Supporting information for this article is available on the WWW under http://www.angewandte.org or from the author.


WILEY InterScience DISCOVER SOMETHING GREAT
© 2006 Wiley-VCH Verlag GmbH & Co. KGaA, Weinheim




***Scheme 1.*** Concept and process of the affinity aptamer PCR technique.

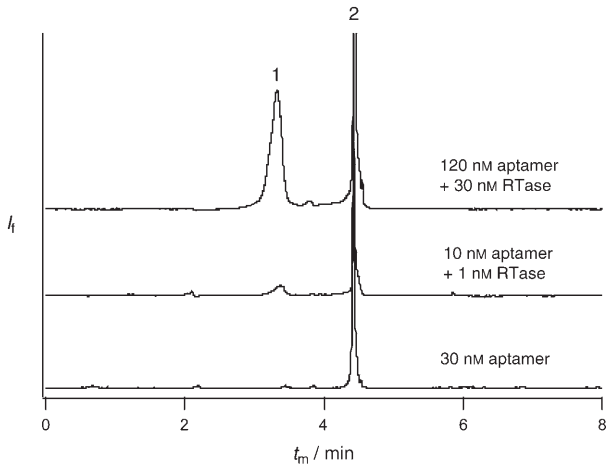



***Figure 1.*** CE analyses of mixtures that contain HIV-1 RTase (0–30 nM) and fluorescently labeled aptamer RT26 (10–120 nM) showed the presence of protein–aptamer complex (peak 1) and the unbound aptamer (peak 2). The aptamer was fluorescently labeled with carboxyfluorescein at the 5′ end. Separation was carried out on a 40 cm capillary, with Tris-glycine (pH 8.3) as the running buffer. The separation voltage was 15 kV. $t_m$ = migration time, $I_f$ = fluorescence intensity.

dramatically improves the sensitivity of the detection of proteins. We were able to detect as few as 180 protein molecules. This sensitivity represents an improvement of several orders of magnitude greater than that of other available methods of protein detection. The technique may be generalized and used for analysis of any other molecules that can bind to aptamers.

To demonstrate the proof of principle, we chose the reverse transcriptase of the human immunodeficiency virus type 1 (HIV-1 RTase) as the initial target protein because of the importance of this protein in the life cycle of the HIV virus. A high-affinity DNA aptamer (RT 26, $K_d = 1$ nM) for this protein had been previously selected by using the SELEX process.[6] To analyze for trace levels of HIV-1 RTase protein in a sample, the sample was incubated with aptamer RT-26 (0.1 nM), and an aliquot (10 nL) of the incubation solution was subjected to CE separation. In an open capillary and under free-zone electrophoresis conditions, the protein–aptamer complex migrated first (3–3.5 min) leaving the excess unbound aptamer behind. The fraction that contained the protein–aptamer complex was collected for subsequent amplification and detection. This fraction corresponded to the HIV-1 RTase protein present in the sample.

To determine the time intervals for fraction collection, we initially studied the separation of the protein–aptamer complex from the unbound aptamer by using a fluorescently labeled aptamer as a probe. We were able to detect the protein–aptamer complex (3–3.5 min) and the unbound aptamer (4–5 min) by laser-induced fluorescence (LIF). From the CE/LIF analysis of two incubation solutions, it was seen that one contained the aptamer (10 nM) and HIV-1 RTase (1 nM), and the other the aptamer (120 nM) and HIV-1 RTase (30 nM; Figure 1). To ensure that the protein-bound and the free aptamers are separately collected for subsequent analysis, we collected fractions at 0–2, 2–2.5, 2.5–3, 3–3.5, 3.5–4, and 4–5 min. Each fraction was subjected to PCR amplification and gel electrophoresis analysis.

Figure 2 shows the gel electrophoresis of the PCR products of the selected CE fractions from the analysis of HIV-1 RTase (Figure 2a) and control (Figure 2b). The fractions collected before 3 min do not contain any aptamer or protein–aptamer complex. In the fraction at $t = 3$–3.5 min, a strong band corresponding to the amplified aptamer (75 nucleotides) is present in the sample (Figure 2a) but not in the control (Figure 2b). This represents the protein–aptamer complex only. The fraction at $t = 3.5$–4 min contains a mixture of the protein–aptamer complex and the unbound aptamer. The fraction at $t = 4$–5 min contains the excess amount of the unbound aptamer (0.1 nM). As expected, the unbound aptamer is present in both the sample and the control. Both the negative (−ve) and positive (+ve) controls of the aptamer show the expected results. The band at 40 base pairs (bp; primer dimer) serves as a marker along with the DNA-ladder marker (the far left lane, 10 bp DNA ladder with 100 bp band ≈2–3 times darker than other bands). The CE migration behavior of the protein–aptamer complex and the unbound aptamer, as shown from the collected fractions, is consistent with that observed previously with CE separation and LIF detection of the fluorescently labeled aptamer and its complexes.[7]

To determine the specificity of the method, we have conducted parallel experiments with human IgG and RNase H reverse transcriptase in place of HIV-1 RTase. The results showed that these proteins did not bind to the specific aptamer for HIV-1 RTase or interfere with the detection of the target HIV-1 RTase.

To achieve reproducible detection of trace levels of proteins, we have optimized each component of the experiments, including the aptamer affinity complex formation (concentrations of aptamer and incubation conditions), CE separation and fraction collection, and PCR amplification. Varying concentrations of aptamer RT26 ($10^{-3}$, $10^{-2}$, 0.1, and 0.5 nM) were initially tested and the aptamer (0.1 nM) was chosen because it was sufficient enough to bind with low levels of protein and its unbound fraction was readily separated from its protein complex by CE. The aptamer

 © 2006 Wiley-VCH Verlag GmbH & Co. KGaA, Weinheim 

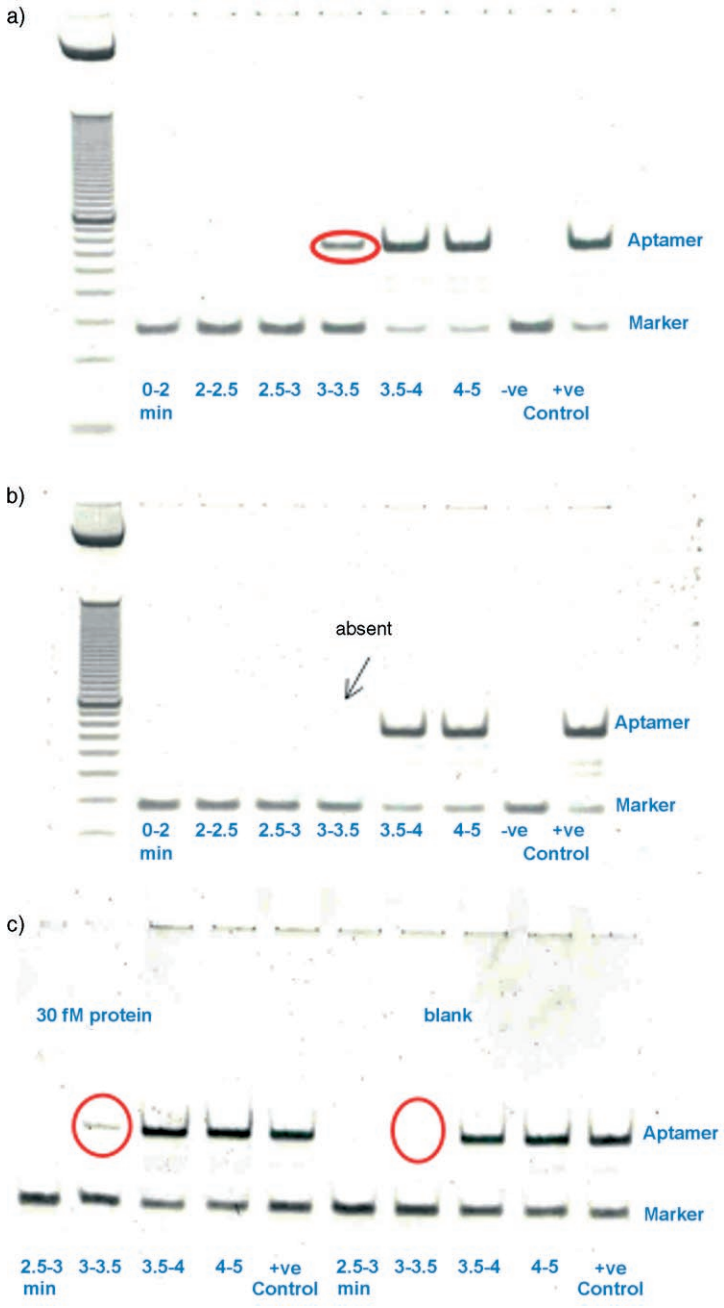



***Figure 2.*** PCR and gel electrophoresis of fractions collected from the CE analysis of approximately 10 nL mixture containing aptamer (0.1 nM) and either protein (150 fM) (a) or blank (b). c) PCR and gel electrophoresis of fractions collected from the CE analysis of approximately 10 nL mixture that contained aptamer (0.1 nM) and either protein (30 fM; $3\times10^{-14}$ M) or blank.

(0.1 nM) was incubated with the sample in Tris-borate–EDTA (60 μL; TBE) buffer solution on ice for 5 min. An aliquot of approximately 10 nL was injected into CE for analysis. Reproducibility was assessed through repeated anylysis of HIV-1 RTase (150 fM; $1.5\times10^{-13}$ M) in five consecutive experiments. Under the optimum conditions, consistent results were obtained from the five replicate analyses of HIV-1 RTase (150 fM).

We have obtained a calibration curve ($r^2 = 0.98$) with trace levels of HIV-1 RTase (0, $3\times10^{-14}$, $1.5\times10^{-13}$, $1.5\times10^{-12}$, and $1.5\times10^{-11}$ M) (see the Supporting Information). Figure 2c shows the representative PCR products from the CE analysis of an approximate 10 nL ($10^{-8}$ L) aliquot, which contained HIV-1 RTase ($3\times10^{-14}$ M) and aptamer RT26 ($10^{-10}$ M). A band from the aptamer bound to the HIV-1 RTase is also clearly visible here, but is absent in the control. The products resulted from approximately $3\times10^{-22}$ mole (or 180 molecules) of the HIV-1 RTase protein. The ability to detect as few as 180 protein molecules represents a major technological advance that will be particularly useful for proteomics research and medical diagnostics.

In the equilibrium-mixture solution that contained HIV-1 RTase ($3\times10^{-14}$ M) and aptamer RT26 ($10^{-10}$ M), the concentration of the aptamer complex of HIV-1 RTase is approximately $3\times10^{-15}$ M (based on a Kd value of 1 nM). With an injection volume of $10^{-8}$ L, approximately 18 molecules ($3\times10^{-23}$ mole) of the protein–aptamer complex were injected into the electrophoretic capillary. Taking into account the possible loss of the protein–aptamer complex owing to dissociation and adsorption, the number of the protein–aptamer complex molecules collected could be fewer than 18. To ensure that low number of aptamer molecules can be amplified by PCR and analyzed by gel electrophoresis, we carried out a series of PCR experiments by using serially diluted aptamer solutions that contained 6000, 600, 60, and 6 aptamer molecules (see the Supporting Information). Through PCR, we were able to amplify and detect six aptamer molecules, whereas in the duplicate blanks, no aptamer was detected.

To determine that the detected PCR product was the expected aptamer, we have sequenced the PCR product that was amplified from the collected protein–aptamer complex. Duplicate sequencing from both the forward and reverse primer directions confirmed that the sequence of the middle 35 nucleotides of the PCR product (excluding the two primer sequences) was identical to that of the aptamer.

To further demonstrate the specificity of the assay, we performed a control experiment by using a DNA molecule that was the same size as the aptamer. The DNA molecule had the same primer binding sites for PCR but with a scrambled sequence in the middle. This nonspecific oligonucleotide (0.1 nM) was incubated with HIV-1 RTase protein ($1.5\times10^{-12}$ M) and the mixture was subjected to CE separation. Analysis of the PCR products from the collected CE fractions showed the absence of a protein–DNA complex (Figure 3). This is compared with the strong signals observed when the specific aptamer was used under the same conditions (see Figure 2a and the Supporting Information). These results further support the validity of the affinity aptamer for the analysis of specific proteins.

The previously reported nanoparticle-based barcode technique[1] and the immuno-PCR assay[2,3] require the use of specific antibodies for the targeting of proteins and thus are limited by the availability and specificity of the antibodies. The proximity-dependent DNA-ligation assay[4,5] requires the ligation of two proximal probes that bind to a target protein in order to give rise to an amplifiable DNA sequence; thus it is useful mainly for the detection of targets that have two proximal binding probes. The aptamer-affinity technique

 © 2006 Wiley-VCH Verlag GmbH & Co. KGaA, Weinheim 

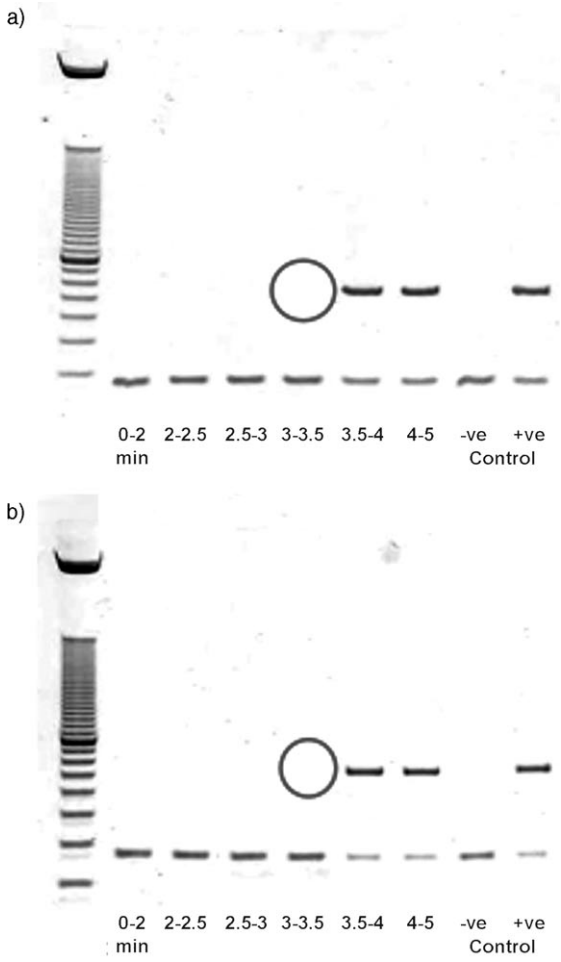



***Figure 3.*** Control experiments show the absence of protein–aptamer complex when a nonspecific DNA oligonucelotide was used as a substitution for the specific aptamer. a) PCR and gel electrophoresis analysis of fractions collected from the CE analysis of a mixture that contained nonspecific DNA oligonucelotides (0.1 nM) and HIV-1 RTase protein (1.5 pM), and b) parallel control that does not contain the HIV-1 RTase protein.

described herein requires only a single aptamer for each target molecule of interest, and the CE separation provides additional specificity. It is possible to scale this assay through the separation of multiple protein–aptamer complexes in a single capillary. The fractions that contain different protein–aptamer complexes can be PCR amplified by using unique primers for each aptamer sequence, thereby achieving the analysis of multiple proteins. The aptamer-affinity PCR assay can also be multiplexed by using CE systems with multiple capillaries, such as those used for genome sequencing,[9] to further improve the throughput of multiple-target analysis.

Potential applications of the aptamer-affinity PCR technique include detection of low-abundance proteins for proteomics research and medical diagnostics, studies of molecular interactions, and biosensing. Aptamers for a wide variety of molecular targets can be selected from a random nucleic acid library of $\approx 10^{13-15}$ different sequences.[8,10–13] Therefore, the principle of the aptamer-affinity PCR technique is not limited to the detection of proteins, it can be applied to the analysis of any other molecular targets that can bind to aptamers.

## Experimental Section

HIV-1 RTase was obtained from Worthington Biochemical (Lakewood, NJ). RT26 aptamer (5′-ATCCGCCTGATTAGCGATACTTACGTGAGCGTGCTGTCCCCTAAAGGTGATACGTCACTTGAGCAAAATCACCTGCAGGGG-3′), both the unlabeled and those labeled with 5′-FAM (carboxyfluorescein), were synthesized at the University Core DNA Services, University of Calgary (Canada). The underlined sequences (20 nucleotides) are the primer regions. Both the forward primer (5′-CCGCCTGATTAGCGATACTT-3′) and the reverse primer (5′-TGCAGGTGATTTTGCTCAAG-3′) were obtained from Integrated DNA Technologies (Coraville, IA). Platinum Pfx DNA polymerase and Platinum Taq DNA polymerase (both from Invitrogen, Burlington, Ontario) were initially tested, and Platinum Taq DNA polymerase was chosen for all the subsequent PCR experiments. Tris-borate–EDTA (TBE) buffer solution (89 mM Tris base, boric acid (89 mM), and EDTA (2 mM; pH 8.0) was prepared in autoclaved and deionized water by dissolving appropriate amounts of the reagent-grade materials. Tris-glycine (TG) buffer solution (Tris (25 mM) and glycine (192 mM); pH 8.3) was diluted with autoclaved, deionized water and 10 × TG buffer that was obtained from Bio-Rad Laboratories (Mississauga, ON, Canada).

As a negative control, a nonspecific DNA oligonucleotide with 5′-ATCCGCCTGATTAGCGATACTTGTAGACTGGAGACGAATGCGCATACGAGTCGAACGCTTGAGCAAAATCACCTGCAGGGG-3′ was obtained from Integrated DNA Technologies (Coraville, IA). It has the same size and primer regions (underlined) as those of the aptamer RT26, but the middle 35 nucleotide sequence is random and is different from that of the aptamer RT26.

Aptamers and proteins of desired concentrations were mixed in TBE buffer solution (60 μL) in 200 μL microcentrifuge vials. The vials were vortexed for 20 s and put on ice for 5 min prior to analysis by CE.

Uncoated fused-silica capillaries (50 μm inner diameter, 150 μm outer diameter, 40 cm in length, Polymicro Technologies, Phoenix, AZ) were used for CE separation. Electrophoresis was carried out at room temperature with a voltage of 15 kV (electric field 375 $V\,cm^{-1}$) with TG buffer solution as the running buffer. Samples were injected electrokinetically for 3 s at 15 kV. Following each CE run, the capillary was washed sequentially with TG buffer solution (10 min), water (5 min), and TG buffer solution (5 min).

Fractions from the outlet of the capillary were collected into separate 200 μL microcentrifuge vials, each containing TG buffer (15 μL). Fractions were collected for 30 s intervals of CE separation (initially 15 s collections were also used). Between fractions, the CE voltage was temporarily stopped to allow changes of new vials for collection of the subsequent fractions. From the initial CE/LIF analysis of an incubation solution that contained fluorescently labeled aptamer (10 nM) and HIV-1 RTase (1 nM), the protein–aptamer complex (3–3.5 min) and the unbound aptamer (4–5 min) were detected by LIF. However, further decreased concentrations of the aptamer and protein could not be detected even by the most sensitive LIF technique. Therefore, the fractions had to be collected without LIF monitoring. Fraction collection intervals of 15 s and 30 s were initially compared. Although 15 s fractions provided a better resolution of separation, the 30 s fractions provided a more reproducible collection of sufficient amounts for the subsequent PCR. Thus, fractions at 30 s intervals were collected and analyzed.

A fraction collected from CE was mixed with 10 × PCR buffer solution (5 μL; minus Mg), dNTP mixture (1 μL, 10 mM), $MgCl_2$ (1.5 μL, 50 mM), primer mix (1.5 μL, 10 μM), and 0.2 μL Platinum Taq DNA polymerase, in 50 μL autoclaved, distilled water. The mixture was initially heated to 94 °C for 3 min. The subsequent temperature cycling program included 94 °C for 30 s, 55 °C for 30 s,

 © 2006 Wiley-VCH Verlag GmbH & Co. KGaA, Weinheim 

and 72 °C for 30 s, and finally 10 min extension at 72 °C. PCR cycles of 25, 40, and 50 were compared, and the PCR with 50 cycles was chosen to maximize the products. At a lower number of cycles (25 cycles) no primer dimer was seen, at 50 cycles, however, the band was distinctly observed. A positive control (2 μL $10^{-13}$ M aptamer RT26) and a negative control (15 μL autoclaved, distilled water) were included with each set of PCR experiments.

The PCR products were separated by using gel electrophoresis on 8% polyacrylamide gels. The electric field was 8 $V\,cm^{-1}$ and the running buffer solution was TBE. The gel was stained by submerging it in ethidium bromide (0.5 $\mu g\,mL^{-1}$) for 5–10 min. The bands were visualized on a Syngene (Cambridge, UK) UV illuminator and the intensity was integrated by using Adobe Photoshop and Polaroid PhotoMaxPro. The DNA marker was a 10 bp DNA ladder consisting of 33 repeats of 10 bp plus a fragment at 1668 bp. The 100 bp band is approximately 2–3 times stronger than other ladder bands to provide internal orientation.

The PCR products were sequenced at the Molecular Biology Facility in the Department of Biological Sciences, University of Alberta. A solution containing aptamer RT26 (0.1 nM) and HIV-1 RTase protein (150 fM) was separated by CE and the fraction at $t = 3$–3.5 min, which contained the protein–aptamer complex, was collected and amplified by using PCR as described above. This PCR product was purified by Qiagen MinElute PCR Purification Kit (Mississauga, ON, Canada) and diluted to 200 μL with autoclaved deionized water, from which 5 μL was used for each of ten replicate PCR reactions. These ten PCR reactions were each carried out under the same conditions as described above, with the exception that 12 cycles were used. The PCR products were pooled, purified by a Qiagen MinElute PCR Purification Kit, and concentrated by ethanol precipitation. Sequencing from both the forward primer and the reverse primer directions was performed.

Received: September 20, 2005
Revised: November 22, 2005
Published online: January 27, 2006

**Keywords:** aptamers · DNA structures · polymerase chain reaction · protein detection · protein structures

[1] J.-M. Nam, C. S. Thaxton, C. A. Mirkin, *Science* **2003**, *301*, 1884–1886.
[2] T. Sano, C. L. Smith, C. R. Cantor, *Science* **1992**, *258*, 120–122.
[3] C. M. Niemeyer, M. Adler, R. Wacker, *Trends Biotechnol.* **2005**, *23*, 208–216.
[4] S. Fredriksson, M. Gullberg, J. Jarvius, C. Olsson, K. Pietras, S. M. Gustafsdottir, A. Ostman, U. Landegren, *Nat. Biotechnol.* **2002**, *20*, 473–477.
[5] M. Gullberg, S. Fredriksson, M. Taussig, J. Jarvius, S. Gustafsdottir, U. Landegren, *Curr. Opin. Biotechnol.* **2003**, *14*, 82–86.
[6] D. J. Schneider, J. Feigon, Z. Hostomsky, L. Gold, *Biochemistry* **1995**, *34*, 9599–9610.
[7] V. Pavski, X. C. Le, *Anal. Chem.* **2001**, *73*, 6070–6076.
[8] L. Gold, B. Polisky, O. Uhlenbeck, M. Yarus, *Annu. Rev. Biochem.* **1995**, *64*, 763–797.
[9] N. J. Dovichi, J. Z. Zhang, *Angew. Chem.* **2000**, *112*, 4635–4640; *Angew. Chem. Int. Ed.* **2000**, *39*, 4463–4468.
[10] S. E. Osborne, A. D. Ellington, *Chem. Rev.* **1997**, *97*, 349–370.
[11] M. Famulok, G. Mayer, M. Blind, *Acc. Chem. Res.* **2000**, *33*, 591–599.
[12] S. D. Mendonsa, M. T. Bowser, *J. Am. Chem. Soc.* **2004**, *126*, 20–21.
[13] M. Berezovski, A. Drabovich, S. M. Krylova, M. Musheev, V. Okhonin, A. Petrov, S. N. Krylov, *J. Am. Chem. Soc.* **2005**, *127*, 3165–3171.

 © 2006 Wiley-VCH Verlag GmbH & Co. KGaA, Weinheim 

Bioinorganic Chemistry

DOI: 10.1002/anie.200503468

# Ruthenium Half-Sandwich Complexes Bound to Protein Kinase Pim-1**

*Judit É. Debreczeni, Alex N. Bullock, G. Ekin Atilla, Douglas S. Williams, Howard Bregman, Stefan Knapp,* and Eric Meggers**

Structurally complicated natural products generally adopt very distinctive three-dimensional conformations, which, unquestionably, are important for their unique biological properties.[1] Consequently, an important challenge for the future design of synthetic compounds with superior biological activities is the development of methods for the economical synthesis of molecules with defined three-dimensional shapes.[2]

Some of us recently started a program that aims at exploring small-molecule chemical space with metal complexes.[3–9] In these molecules, the coordinative bonds are designed to be kinetically inert and thus stable in biological environments. Hence, such metal complexes should behave like purely organic compounds without displaying any metal-related cytotoxicities.[6] We believe that the addition of a metal to an otherwise organic scaffold opens new opportunities for the design of bioactive molecules by giving access to areas of the chemical space that may not be easily reachable with purely organic scaffolds. In this respect, we like to think of a chemically inert metal center as a "hypervalent carbon" with extended structural opportunities.

Herein, we demonstrate how a conceptually simple metal-complex scaffold can substitute for a structurally complicated natural product in its binding to a target protein. We prove that the metal center is not involved in any direct interactions but solely plays a structural role in organizing the organic ligands in the three-dimensional space. Specifically, we disclose cocrystal structures of a ruthenium half-sandwich

[*] Dr. J. É. Debreczeni, Dr. A. N. Bullock, Dr. S. Knapp
Oxford University
Centre for Structural Genomics
Botnar Research Centre
Oxford OX3 7LD (UK)
Fax: (+44) 1865-737-231
E-mail: stefan.knapp@sgc.ox.ac.uk

G. E. Atilla, D. S. Williams, H. Bregman, Prof. Dr. E. Meggers
Department of Chemistry
University of Pennsylvania
231 South 34th Street, Philadelphia, PA 19104 (USA)
Fax: (+1) 215-746-0348
E-mail: meggers@sas.upenn.edu

[**] We gratefully acknowledge support for this work from the US National Institutes of Health through grant 1 R01 GM071695-01A1 (E.M.). The Structural Genomics Consortium is a registered charity (no. 1097737) funded by the Wellcome Trust, GlaxoSmithKline, Genome Canada, the Canadian Institutes of Health Research, the Ontario Innovation Trust, the Ontario Research and Development Challenge Fund, and the Canadian Foundation for Innovation.


WILEY InterScience DISCOVER SOMETHING GREAT
© 2006 Wiley-VCH Verlag GmbH & Co. KGaA, Weinheim

scaffold with the human protein kinase Pim-1 and illustrate how closely the half-sandwich scaffold mimics the binding mode of staurosporine.[10]

The protein kinase inhibitor staurosporine (**1**) adopts a defined globular structure with the carbohydrate moiety oriented perpendicular to the plane of the indolocarbazole heterocycle (Figure 1). The indolo[2,3-*a*]carbazole moiety

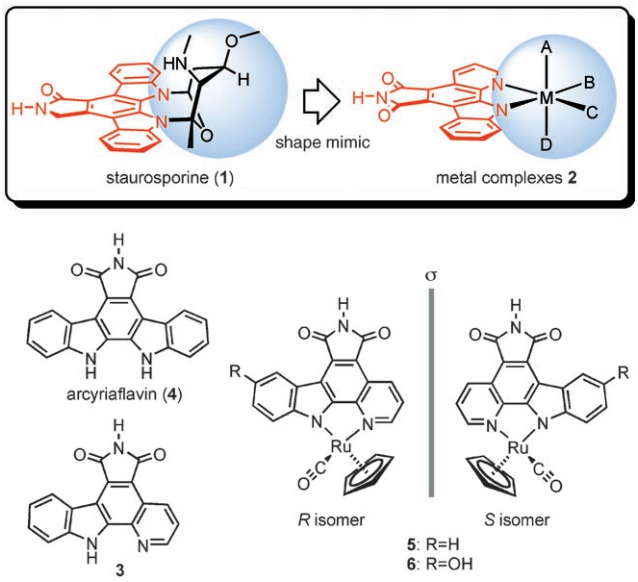



***Figure 1.*** Designing ruthenium complexes as protein kinase inhibitors by using the ATP-competitive natural product staurosporine as a lead structure. The half-sandwich compounds **5** and **6** are pseudotetrahedral and exist in two mirror-imaged configurations. The absolute configuration at the ruthenium center has been assigned according to the priority order of the ligands as $\eta^5$-$C_5H_5$ > pyridine [N(C,C,C)] > indole [N(C,C,lone pair)] > CO. However, the $\eta^5$-$C_5H_5$ ligand occupies three facial coordination sites of the ruthenium center (for example, B, C, and D in **2**), which means that the geometry of these compounds is also pseudooctahedral.

occupies the hydrophobic adenine-binding cleft with the lactam group mimicking the hydrogen-bonding pattern of the adenine base and the carbohydrate moiety forming hydrophobic contacts and hydrogen bonds within the globular ribose-binding site.[11] Thus, stauroporine closely matches the shape of the ATP-binding site which makes it a highly potent inhibitor for many protein kinases. This distinctive globular three-dimensional structure of staurosporine is in contrast to many synthetic protein kinase inhibitors which mainly fill the adenine-binding site with planar aromatic moieties and flexible side chains protruding into other areas of the active site, thus constituting promiscuous scaffolds with respect to their three-dimensional shapes.[12]

To match the overall shape of the ATP-binding site of protein kinases in a fashion similar to staurosporine, but with less synthetic effort and more extended structural options, we replaced the indolocarbazole alkaloid scaffold with simple metal complexes as in **2**, in which the main features of the indolocarbazole aglycon are retained in the metal-chelating pyridocarbazole ligand (highlighted red in **2**, Figure 1).[5,6] This places the metal center within the ribose-binding site and gives new opportunities to build defined globular shapes by assembling ligands around the metal center. Accordingly, we developed pyridocarbazole ligand **3**, derived from arcyriaflavin A (**4**) by substituting one indole moiety for a pyridine. We established that ligand **3** can serve as a bidentate ligand for metals and found that the half-sandwich ruthenium complexes **5** and **6** act as potent and ATP-competitive inhibitors for glycogen synthase kinase 3 (GSK-3).[5,6]

Profiling the racemic mixture of **5** against a panel of more than 50 protein kinases confirmed the high selectivity of this class of compounds for GSK-3 (data not shown). For example, the phylogenetically and structurally closely related cyclin-dependent kinases (CDK1/CyclinB, CDK2/CyclinE, CDK3/CyclinE, CDK5/p35, CDK6/CyclinD3, and CDK7/CyclinH) show activities between 74% and 97% at 100 nM of racemic **5**.[13] However, we found that the protein kinase Pim-1 is inhibited by racemic **5** with a potency that is similar to that with GSK-3.[14,15] The ruthenium scaffolds **5** and **6** display metal-centered chirality, and, interestingly, the *S* enantiomers, (*S*)-**5** and especially (*S*)-**6**, show a strong preference for Pim-1.[16–18] In fact, (*S*)-**6** has an $IC_{50}$ value for Pim-1 of 220 pM at 100 μM ATP compared to $IC_{50}$ values of 9 nM and 15 nM under the same conditions for GSK-3α and GSK-3β, respectively (see selectivity profile in Figure 2 and Experimental Section for details). Compared to staurosporine ($IC_{50}$ = 65 nM for Pim-1 at 100 μM ATP), (*S*)-**6** inhibits Pim-1 at concentrations that are more than two orders of magnitude lower (Figure 2). Thus, (*S*)-**6** is an extremely potent and potentially selective inhibitor for the protein kinase Pim-1.

To understand the binding mode of this class of organometallic scaffolds to protein kinases, we cocrystallized full-length human Pim-1 with the enantiomerically pure ruthenium compound (*S*)-**6** and solved the structure to a resolution of 1.9 Å (Table 1). The structure of (*S*)-**6** in Figure 3 shows the typical two-lobe protein kinase architecture, connected by a hinge region, with the catalytic domain positioned in a deep intervening cleft.[19] The N-terminal lobe is comprised primarily of antiparallel β-sheets and the C-terminal lobe is comprised mainly of α-helices. Figure 3 demonstrates that (*S*)-**6** occupies the ATP-binding site, in accordance with the initial design.

Superposition of the binding positions of cocrystallized (*S*)-**6** and staurosporine (PDB code 1YHS) with Pim-1 reveals how closely the half-sandwich complex (*S*)-**6** mimics the binding mode of staurosporine (Figure 4).[20] The pyridocarbazole moiety of (*S*)-**6** superimposes with the indolocarbazole moiety of staurosporine, and the rest of the metal complex fragment occupies the binding site of the carbohydrate moiety of staurosporine.

Organoruthenium compound (*S*)-**6** forms three hydrogen bonds within the ATP-binding site of Pim-1 (Figure 5a). The pyridocarbazole moiety mimics the hydrogen-bonding pattern of the adenine base of ATP and establishes one hydrogen bond between the imide NH group and the backbone carbonyl oxygen atom of Glu121 within the hinge region. Pim-1 is unique among protein kinases as a result of the presence of a proline residue at position 123 that precludes the formation of the canonical second hydrogen bond between the hinge backbone and the adenine moiety of

 © 2006 Wiley-VCH Verlag GmbH & Co. KGaA, Weinheim 

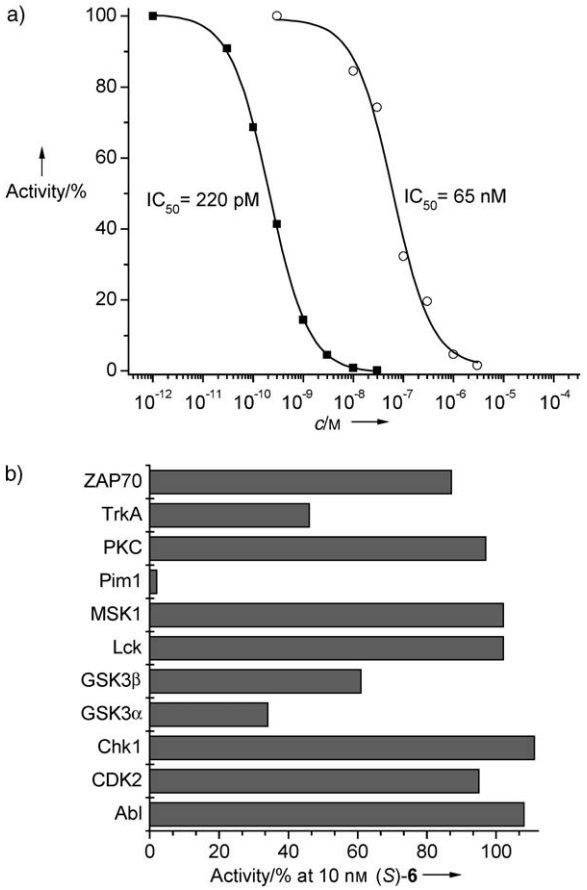



***Figure 2.*** a) Inhibition of Pim-1 with ruthenium compound (*S*)-**6** (■) and staurosporine (○). $IC_{50}$ curves and selectivity data (b) were obtained by phosphorylation of substrate peptides with [$\gamma$-$^{32}$P]ATP (ca. 0.2 $\mu$Ci $\mu$L$^{-1}$) and 100 $\mu$M ATP in the presence of (*S*)-**6** or staurosporine, followed by precipitation of the phosphorylated substrate on P81 phosphocellulose and measurement of the counts per minutes in a scintillation counter. See Experimental Section for more details.

***Table 1:*** Crystallographic data and refinement statistics.[a]

| Parameter | (*R*)-**5** | (*S*)-**6** |
|---|---|---|
| space group | $P6_5$ | $P6_5$ |
| cell dimensions [Å] | *a*,*b* = 97.53, *c* = 80.73 | *a*,*b* = 98.24, *c* = 80.89 |
| resolution [Å] | 1.9 | 1.9 |
| total observation (unique, redundancy) | 192106 (33487, 5.5) | 162104 (34114, 4.4) |
| completeness (outer shell) | 99 (97) | 97 (97) |
| $R_{merge}$ (outer shell) [%] | 5.9 (33.0) | 4.5 (21.8) |
| $I/\sigma$ (outer shell) | 14.4 (3.2) | 15.7 (3.5) |
| $R_{work}$ ($R_{free}$) [%] | 15.8 (18.9) | 21.5 (26.5) |
| hetero groups | (*R*)-**5** | (*S*)-**6** |
| rmsd bond length [Å] | 0.012 | 0.009 |
| rmsd bond angle [°] | 1.279 | 1.107 |
| Ramachandran [%] (allowed/generally allowed/disallowed) | 94.1/5.9/0 | 93.7/6.3/0 |

[a] rmsd = root-mean-square deviation.

ATP. Accordingly, (*S*)-**6** cannot form the second hydrogen bond. In addition, the hydroxy group of (*S*)-**6** forms two hydrogen bonds to ordered water molecules (Figure 5a).

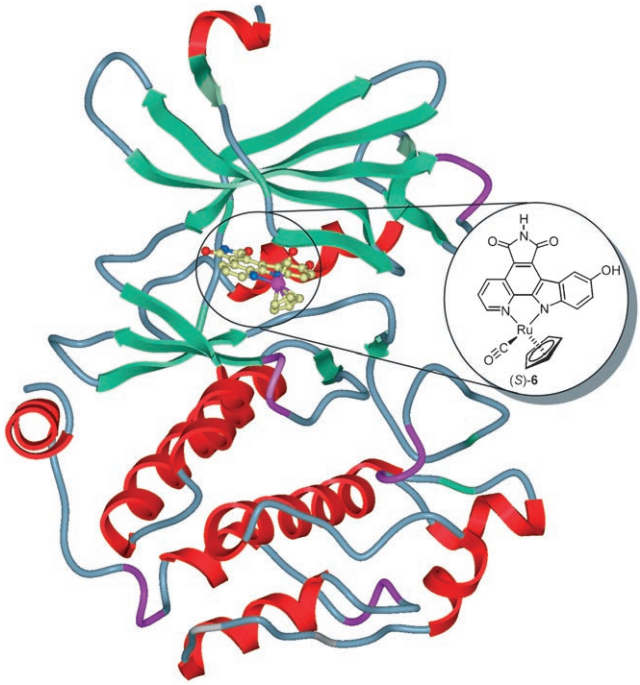



***Figure 3.*** Crystal structure of Pim-1 with the enantiomerically pure ruthenium complex (*S*)-**6** bound to the ATP-binding site.

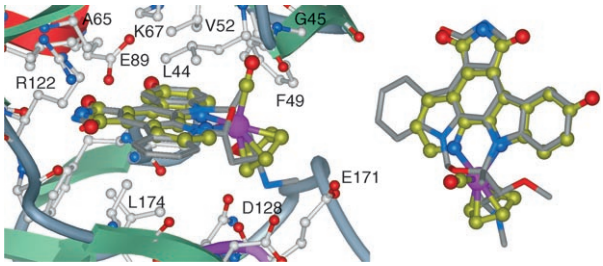



***Figure 4.*** Superimposed cocrystal structures of ruthenium compound (*S*)-**6** and staurosporine with Pim-1.

Furthermore, (*S*)-**6** is involved in extensive van der Waals contacts with Pim-1 (Figure 5b). Four amino acid side chains each of the N-terminal lobe (Leu44, Phe49, Val52, and Ala65) and the C-terminal lobe (Ile104, Val126, Leu174, and Ile185) form a hydrophobic pocket for the pyridocarbazole moiety. The cyclopentadienyl moiety packs against Phe49, Ile185, and the methylene group of Glu171.

Interestingly, the CO group does not form any hydrogen bonds. However, the distance between the carbonyl oxygen atom and Gly45 is surprisingly short. In particular, the methylene group of Gly45 lies at a distance of just 3.0 Å from the carbonyl oxygen atom of the CO ligand which is clearly below the typical van der Waals distance (Figure 5c). In addition, the distances to the amino group and amide carbon atom of Gly45 are 3.0 and 3.2 Å, respectively. These short distances are strong evidence for dipolar interactions of the CO ligand with the positively polarized methylene and carbonyl groups of Gly45.[21,22] In fact, we did not yet identify any ruthenium complex with similar potency for Pim-1 that

 © 2006 Wiley-VCH Verlag GmbH & Co. KGaA, Weinheim 

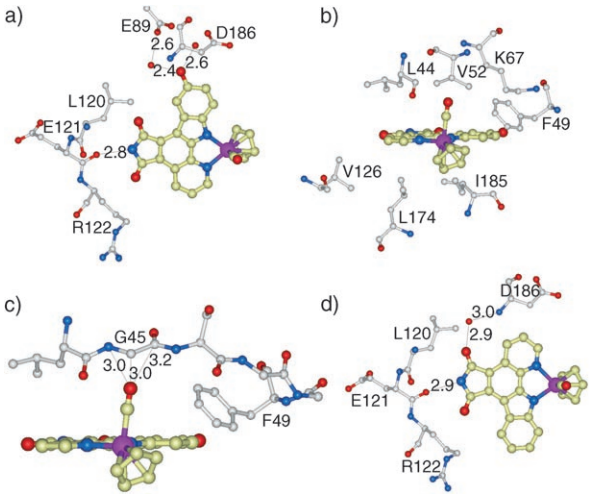



***Figure 5.*** Interactions of (*S*)-**6** (a–c) and (*R*)-**5** (d) within the active site of Pim-1 (distance indicated in Å). a) Hydrogen bond between the maleimide NH group of (*S*)-**6** and the backbone amide carbonyl group of Glu121, and water-mediated contacts of the hydroxy group. b) The most important hydrophobic interactions with (*S*)-**6**. c) Highlighting the close contact of the CO ligand of (*S*)-**6** with Gly45. d) Hydrogen bonding of (*R*)-**5** within the active site of Pim-1.

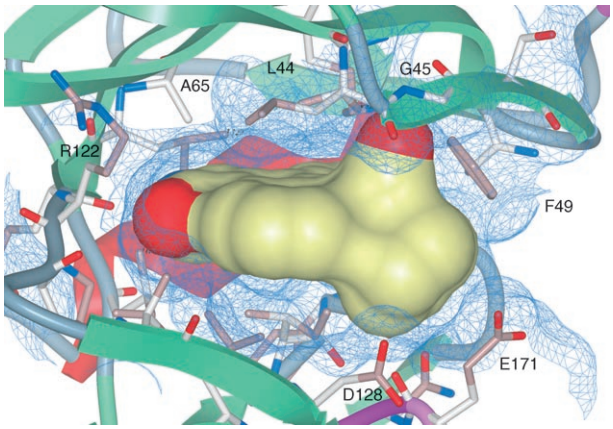



***Figure 6.*** Space-filling model of (*S*)-**6** in the binding pocket of Pim-1 which demonstrates the shape match.

does not contain a CO group perpendicular to the plane of the pyridocarbazole ligand (data not shown).

As both enantiomers of **5** and **6** bind to Pim-1, we were interested in comparing their binding modes and therefore also cocrystallized (*R*)-**5** with Pim-1 and solved the structure to a resolution of 1.9 Å. A comparison of cocrystallized (*R*)-**5** (Figure 5d) and (*S*)-**6** (Figure 5a) demonstrates indeed that in both enantiomers, the maleimide group, the cyclopentadienyl ring, and the CO group are in very similar positions. The differences are mainly limited to a pyridocarbazole moiety that has been flipped by 180°. The maleimide group of (*R*)-**5** forms an additional water-mediated hydrogen bond, which we cannot identify in (*S*)-**6** (Figure 5d). In addition, the hydroxy group at the indole moiety in (*S*)-**6** is involved in hydrogen bonds to two ordered water molecules, explaining at least in part the approximately 100-fold-lower $IC_{50}$ value of (*S*)-**6** compared to (*R*)-**5** ($IC_{50}$ of 25 nM at 100 μM ATP). Another factor appears to be the more extensive hydrophobic contacts between the indole moiety of (*S*)-**6** and Phe49, compared to the analogous but weaker hydrophobic interaction of the smaller and more electron-poor pyridine moiety of (*R*)-**5** with Phe49.

In conclusion, these cocrystal structures clearly demonstrate that the ruthenium complexes (*R*)-**5** and (*S*)-**6** bind to their target in a fashion typical for organic enzyme inhibitors. The metal center is not involved in any direct interactions with the active site of Pim-1. Instead, the metal controls the orientation of the organic ligands in the receptor space, thus yielding three-dimensional structures that are complementary in shape and functional group presentation to the active site of Pim-1. Indeed, the space-filling model of (*S*)-**6** in Figure 6 illustrates how closely the organometallic scaffold complements the shape of the Pim-1 active site. It is noteworthy that the organometallic complexes **5** and **6** are highly rigid and cannot change their three-dimensional shapes. Experiments to elucidate the importance of this rigidity for potency and kinase selectivity are underway.

## Experimental Section

Crystallization: Pim-1 was prepared as described previously.[23] Crystals of Pim-1 were grown at 4 °C in 1.8 μL sitting drops, by mixing Pim-1 (1.2 μL of a solution at 10 mg mL$^{-1}$ in 50 mM HEPES, pH 7.5, 250 mM NaCl, 5% glycerol, 10 mM DTT) with 0.6 μL precipitant stock. Crystals of the (*R*)-**5** complex were grown using nonphosphorylated Pim-1 protein and a precipitant stock containing 0.12 M potassium citrate, 60 mM BisTrisPropane (pH 6.5), 12% PEG3350, 6% ethylene glycol, and 0.3% DMSO. Crystals of the (*S*)-**6** complex were grown using singly phosphorylated Pim-1 protein (position Ser261) and a precipitant stock containing 0.12 M potassium thiocyanate, 60 mM BisTrisPropane (pH 7.5), 12% PEG3350, 6% ethylene glycol, and 0.3% DMSO. Ruthenium half-sandwich complexes were added to the protein from 10 mM stock solutions in DMSO to a final concentration of 1 mM.

Structure Determination: Diffraction data of the (*R*)-**5** complex of Pim-1 were collected on a cryofrozen crystal (100 K) on a Rigaku FRE X-ray generator equipped with multilayer mirrors and an R-AXIS HTC detector. Diffraction data of the (*S*)-**6** complex of Pim-1 were collected on a cryofrozen crystal (100 K) at the BESSY beamline BL2. Diffraction data were processed with HKL2000,[24] and the structures were solved using molecular replacement and the program Phaser using the structure of Pim-1 in complex with (2-[1-(3-dimethylaminopropyl)-1*H*-indol-3-yl]-3-(1*H*-indol-3-yl) maleimide (PDB code 1XWS) as a search model.[25] All structures were refined with REFMAC5 using iterative rounds of rigid-body refinement and restrained refinement with TLS, against maximum likelihood targets, interspersed with manual rebuilding of the model using Xfit/XtalView.[26,27] Coordinates for the two complexes have been deposited in the Protein Data Bank (PDB codes 2BZH and 2BZI for (*R*)-**5** and (*S*)-**6**, respectively).

Measurement of Protein Kinase Inhibition: Kinases (human) and substrates were purchased from Upstate Biotechnology USA, except for poly(Glu,Tyr) which was purchased from Sigma, and KKSPGEYVIEFG, which was purchased from Bachem. For determining the activities of Lck, Abl, ZAP70, CHK1, Pim1, GSK-3α, GSK3β, CDK2/CyclinA, and MSK1 in the presence of (*S*)-**6**, (*R*)-**5**, or staurosporine, the compounds were incubated at room temperature in 20 mM MOPS, 30 mM $MgCl_2$, 0.8 μg μL$^{-1}$ BSA, 5% DMSO (resulting from the stock solution of the inhibitor), pH 7.0, in the presence of substrate (Abltide for Abl: 25 μM; Src-peptide for Lck: 50 μM; poly(Glu,Tyr)

 © 2006 Wiley-VCH Verlag GmbH & Co. KGaA, Weinheim 

for ZAP70: 0.1 mg mL$^{-1}$; CHK1 substrate peptide for CHK1: 0.2 μg μL$^{-1}$; S6 kinase/Rsk2 substrate for Pim-1: 50 μM; phosphorglycogen synthase kinase-2 for GSK-3α and GSK-3β: 20 μM; histone H1 substrate for CDK2/CyclinA: 0.1 mg mL$^{-1}$; Crosstide for MSK1: 30 μM) and kinase (0.04 ng μL$^{-1}$ for Pim-1, MSK1, GSK3α, GSK3β, and CHK1; 0.4 ng μL$^{-1}$ for ZAP70; 0.08 ng μL$^{-1}$ for Lck and CDK2/CyclinA). In assays for measuring $IC_{50}$ values of (*S*)-**6** against GSK-3α, GSK-3β, and Pim-1, and staurosporine against Pim-1, the following concentrations of kinase were chosen: 730 pM GSK3α or GSK3β and 160 pM Pim-1. The measurement of the activity of PKCα at 10 nM (*S*)-**6** was performed in 10 mM HEPES, 0.025% Triton X-100, 10 mM $MgCl_2$, 0.3 mM $CaCl_2$, 0.1 mg mL$^{-1}$ phosphatidylserine, 0.01 mg mL$^{-1}$ diacylglycerol, 5 mM β-glycerophosphate, 0.2 mM sodium orthovanadate, 0.8 mg mL$^{-1}$ BSA, 5% DMSO (resulting from the stock solution of inhibitor), pH 7.5, in the presence of histone H1 (0.05 mg mL$^{-1}$) and PKCα (0.04 ng μL$^{-1}$). The measurement of the activity of TrkA at 10 nM (*S*)-**6** was performed in 8 mM MOPS/NaOH pH 7.2, 0.3 mM EDTA, 10 mM $Mg(OAc)_2$, 0.5% glycerol, 0.001% Brij-35, 0.01% β-mercaptoethanol, 0.1 mg mL$^{-1}$ BSA, in the presence of 250 μM substrate (KKSPGEYVIEFG), and 0.2 ng μL$^{-1}$ TrkA. After 15 minutes, the reaction was initiated by adding ATP to a final concentration of 100 μM including approximately 0.2 μCi μL$^{-1}$ [γ-$^{32}$P]ATP. Reactions were performed in a total volume of 25 μL. After 2 h, the reaction was terminated by spotting 17.5 μL on a circular P81 phosphocellulose paper (diameter 2.1 cm, Whatman) followed by washing five times (five minutes each wash) with 0.75% phosphoric acid and once with acetone. The dried P81 papers were transferred to a scintillation vial and 5 mL of scintillation cocktail were added. The counts per minute (CPM) were determined with a Beckmann 6000 scintillation counter. $IC_{50}$ values were defined to be the concentration of inhibitor at which the CPM was 50% of the control sample, corrected by the background.

Received: September 30, 2005
Published online: December 28, 2005

**Keywords:** bioinorganic chemistry · inhibitors · proteins · ruthenium

[1] a) D. J. Newman, G. M. Cragg, K. M. Snader, *Nat. Prod. Rep.* **2000**, *17*, 215 – 234; b) J. Clardy, C. Walsh, *Nature* **2004**, *432*, 829 – 837.
[2] a) S. L. Schreiber, *Science* **2000**, *287*, 1964 – 1969; b) M. D. Burke, S. L. Schreiber, *Angew. Chem.* **2004**, *116*, 48 – 60; *Angew. Chem. Int. Ed.* **2004**, *43*, 46 – 58.
[3] For chemical space, see: C. M. Dobson, *Nature* **2004**, *432*, 824 – 828.
[4] L. Zhang, P. J. Carroll, E. Meggers, *Org. Lett.* **2004**, *6*, 521 – 523.
[5] H. Bregman, D. S. Williams, G. E. Atilla, P. J. Carroll, E. Meggers, *J. Am. Chem. Soc.* **2004**, *126*, 13594 – 13595.
[6] D. S. Williams, G. E. Atilla, H. Bregman, A. Arzoumanian, P. S. Klein, E. Meggers, *Angew. Chem.* **2005**, *117*, 2020 – 2023; *Angew. Chem. Int. Ed.* **2005**, *44*, 1984 – 1987.
[7] Metal-based drugs: a) (Eds.: C. Orvig, M. J. Abrams), *Chem. Rev.* **1999**, *99*, 2201–2842; b) Z. Guo, P. J. Sadler, *Angew. Chem.* **1999**, *111*, 1610 – 1630; *Angew. Chem. Int. Ed.* **1999**, *38*, 1512 – 1531; c) (Ed.: N. Farrell), *Coord. Chem. Rev.* **2002**, *232*, 1–230.
[8] Metal complexes as enzyme inhibitors: A. Y. Louie, T. J. Meade, *Chem. Rev.* **1999**, *99*, 2711 – 2734.
[9] For bioorganometallic chemistry, see: a) K. Severin, R. Bergs, W. Beck, *Angew. Chem.* **1998**, *110*, 1722 – 1743; *Angew. Chem. Int. Ed.* **1998**, *37*, 1634 – 1654; b) D. B. Grotjahn, *Coord. Chem. Rev.* **1999**, *190*, 1125 – 1141; c) (Ed.: G. Jaouen), *J. Organomet. Chem.* **1999**, *589*, 1–126; d) N. Metzler-Nolte, *Angew. Chem.* **2001**, *113*, 1072 – 1076; *Angew. Chem. Int. Ed.* **2001**, *40*, 1040 – 1043; e) R. H. Fish, G. Jaouen, *Organometallics* **2003**, *22*, 2166 – 2177; f) R. Stodt, S. Gencaslan, I. M. Müller, W. S. Sheldrick, *Eur. J. Inorg. Chem.* **2003**, 1873 – 1882; g) D. Schlawe, A. Majdalani, J. Velcicky, E. Heßler, T. Wieder, A. Prokop, H.-G. Schmalz, *Angew. Chem.* **2004**, *116*, 1763 – 1766; *Angew. Chem. Int. Ed.* **2004**, *43*, 1731 – 1734; h) D. R. Van Staveren, N. Metzler-Nolte, *Chem. Rev.* **2004**, *104*, 5931 – 5985.
[10] For crystal structures of metal complexes bound to proteins, see: a) K. Di Gleria, D. P. Nickerson, H. A. O. Hill, L.-L. Wong, V. Fülöp, *J. Am. Chem. Soc.* **1998**, *120*, 46 – 52; b) W. Zhong, D. Alexeev, I. Harvey, M. Guo, D. J. B. Hunter, H. Zhu, D. J. Campopiano, P. J. Sadler, *Angew. Chem.* **2004**, *116*, 6040 – 6044; *Angew. Chem. Int. Ed.* **2004**, *43*, 5914 – 5918; c) I. W. McNae, K. Fishburne, A. Habtemariam, T. M. Hunter, M. Melchart, F. Wang, M. D. Walkinshaw, P. J. Sadler, *Chem. Commun.* **2004**, 1786 – 1787; d) M. V. Cherrier, L. Martin, C. Cavazza, L. Jacquamet, D. Lemaire, J. Gaillard, J. C. Fontecilla-Camps, *J. Am. Chem. Soc.* **2005**, *127*, 10075 – 10082; e) S. M. Contakes, G. A. Juda, D. B. Langley, N. W. Halpern-Manners, A. P. Duff, A. R. Dunn, H. B. Gray, D. M. Dooley, J. M. Guss, H. C. Freeman, *Proc. Natl. Acad. Sci. USA* **2005**, *102*, 13451 – 13456.
[11] For cocrystal structures of staurosporine with protein kinases, see, for example: a) L. M. Toledo, N. B. Lydon, *Structure* **1997**, *5*, 1551 – 1556; b) A. M. Lawrie, M. E. M. Noble, P. Tunnah, N. R. Brown, L. N. Johnson, J. A. Endicott, *Nat. Struct. Biol.* **1997**, *4*, 796 – 801; c) L. Prade, R. A. Engh, A. Girod, V. Kinzel, R. Huber, D. Bossemeyer, *Structure* **1997**, *5*, 1627 – 1637.
[12] For protein kinase inhibitor scaffolds, see: a) C. García-Echeverría, P. Traxler, D. B. Evans, *Med. Res. Rev.* **2000**, *20*, 28 – 57; b) A. J. Bridges, *Chem. Rev.* **2001**, *101*, 2541 – 2571.
[13] For CDKs, see: a) M. Knockaert, P. Greengard, L. Meijer, *Trends Pharmacol. Sci.* **2002**, *23*, 417 – 425; b) A. Huwe, R. Mazitschek, A. Giannis, *Angew. Chem.* **2003**, *115*, 2170 – 2187; *Angew. Chem. Int. Ed.* **2003**, *42*, 2122 – 2138.
[14] For Pim-1, see: M. Bachmann, T. Möröy, *Int. J. Biochem. Cell Biol.* **2005**, *37*, 726 – 730.
[15] For GSK-3, see: a) H. Eldar-Finkelman, *Trends Mol. Med.* **2002**, *8*, 126 – 132; b) B. W. Doble, J. R. Woodgett, *J. Cell Sci.* **2003**, *116*, 1175 – 1186; c) R. S. Jope, G. V. W. Johnson, *Trends Biochem. Sci.* **2004**, *29*, 95 – 102; d) P. Cohen, M. Goedert, *Nat. Rev. Drug Discovery* **2004**, *3*, 479 – 487.
[16] For optically active organometallic compounds, see: H. Brunner, *Angew. Chem.* **1999**, *111*, 1194 – 1208; *Angew. Chem. Int. Ed.* **1999**, *38*, 1248 – 1263.
[17] For the synthesis of **5** and **6**, see: H. Bregman, D. S. Williams, E. Meggers, *Synthesis* **2005**, 1521 – 1527.
[18] The racemic mixtures of **5** and **6** were separated into the pure enantiomers with a ChiralPak AD-H analytical HPLC column (Daicel/Chiral Technologies) using a gradient of hexanes and ethanol (7:3 to 1:4 in 20 minutes) with a flow rate of 0.95 mL min$^{-1}$. The enantiomers do not show any significant racemization in an acetonitrile solution over a time period of 12 h.
[19] S. S. Taylor, E. Radzio-Andzelm, *Structure* **1994**, *2*, 345 – 355.
[20] For the cocrystal structure of staurosporine with Pim-1, see: M. D. Jacobs, J. Black, O. Futer, L. Swenson, B. Hare, M. Fleming, K. Saxena, *J. Biol. Chem.* **2005**, *280*, 13728 – 13734.
[21] For attractive interactions between organic fluorine and carbonyl groups, see: a) F. Hof, D. M. Scofield, W. B. Schweizer, F. Diederich, *Angew. Chem.* **2004**, *116*, 5166 – 5169; *Angew. Chem. Int. Ed.* **2004**, *43*, 5056 – 5059; b) J. A. Olsen, D. W. Banner, P. Seiler, B. Wagner, T. Tschopp, U. Obst-Sander, M. Kansy, K. Müller, F. Diederich, *ChemBioChem* **2004**, *5*, 666 – 675.
[22] For orthogonal multipolar interactions in crystal structures, see: R. Paulini, K. Müller, F. Diederich, *Angew. Chem.* **2005**, *117*, 1820 – 1839; *Angew. Chem. Int. Ed.* **2005**, *44*, 1788 – 1805.
[23] A. N. Bullock, J. É. Debreczeni, O. Y. Fedorov, A. Nelson, B. D. Marsden, S. Knapp, *J. Med. Chem.* **2005**, *48*, 7604 – 7614.

 © 2006 Wiley-VCH Verlag GmbH & Co. KGaA, Weinheim 

[24] Z. Otwinowski, W. Minor, *Methods Enzymol.* **1997**, *276*, 307–326.
[25] L. C. Storoni, A. J. McCoy, R. J. Read, *Acta Crystallogr. Sect. D* **2004**, *60*, 432–438.
[26] G. N. Murshudov, A. A. Vagin, E. J. Dodson, *Acta. Crystallogr. Sect. D* **1997**, *53*, 240–255.
[27] D. E. McRee, *J. Struct. Biol.* **1999**, *125*, 156–165.

 © 2006 Wiley-VCH Verlag GmbH & Co. KGaA, Weinheim 

Calixarenes

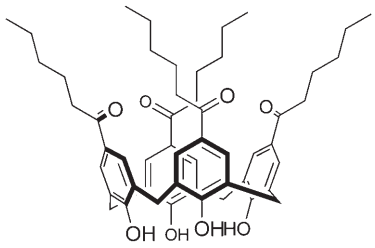
DOI: 10.1002/anie.200503553

# Guest Exchange in Single Crystals of van der Waals Nanocapsules**

*Gennady S. Ananchenko,* Konstantin A. Udachin, Alix Dubes, John A. Ripmeester, Thomas Perrier, and Anthony W. Coleman*

Container molecules and molecular capsules are likely to be of importance in the future both in biological and chemical applications,[1] for example, for drug transport and as nanoreactors. So far, most efforts have been directed at the formation of nanocontainers stabilized either by hydrogen bonding[2] or those constructed with metal–ligand or covalent bonds,[3] as they are able to capture and exchange guest molecules in solution. In contrast, nanocapsules formed from components that interact strictly by van der Waals forces (vdW) have received less attention.[4] It is clear that such nanocontainers are not sufficiently stable in solution as solvation forces may exceed the vdW interactions significantly. However, vdW interactions will be the only source of stabilization of the nanocapsules in the solid state, and the weak nature of these forces is likely to give the system the flexibility necessary to allow guest capture and release without disrupting the lattice. Guest exchange in such solid matrices would be very advantageous for applications in separations and clean organic syntheses. This has been illustrated, to some extent, for some simple calixarenes,[4a,c,5] in which the host molecule is not known to bind neutral guest molecules in solution, but single crystals can capture and release guest molecules under controlled conditions without disruption of the crystal lattice. However, the available void space in the aforementioned calixarenes is rather small, so herein we explore the possibility of producing larger vdW nanocapsules that still have the flexibility to support guest exchange.

The amphiphilic calixarenes, particularly *para*-acylcalix[4]arenes,[6] belong to one of the major groups of synthetic macrocyclic hosts in supramolecular chemistry. We have shown previously that interaction of these calixarenes with a guest in an appropriate solvent leads to inclusion complexes of different morphologies.[7] Now we present another type of inclusion complex of *para*-hexanoylcalix[4]arene in which encapsulation of a guest and guest exchange become possible at the solid–liquid interface without degrading the structure.




*para*-hexanoylcalix[4]arene

Crystals obtained at around −20 °C from a solution of *para*-hexanoylcalix[4]arene in $CHCl_3$ have the calixarene molecules arranged in tail-to-tail pairs to form a hydrophobic capsular complex (complex **1**) that is about 15 Å wide and 20 Å long and contains four molecules of $CHCl_3$ (Figure 1). Single-crystal X-ray diffraction (XRD) shows that the complex has tetragonal (*P*4/*nnc*) symmetry with unit-cell parameters $a, b = 15.57$ and $c = 22.68$ Å. Two $CHCl_3$ molecules are located at the poles of the nanocapsule with the chlorine atoms deep inside the cavity interacting weakly with the π systems of the benzene rings. The two remaining $CHCl_3$ molecules occupy equatorial positions.

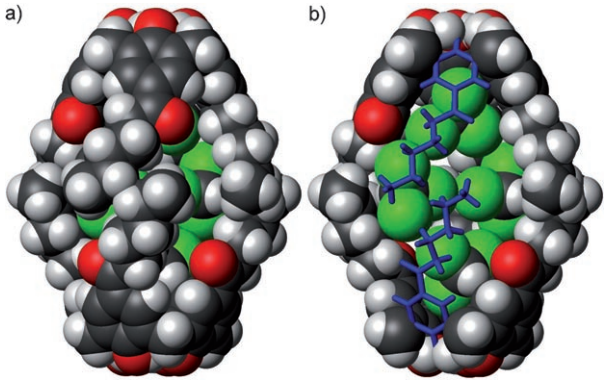



***Figure 1.*** The structure of the complex of *para*-hexanoylcalix[4]arene with $CHCl_3$ (complex **1**): a) the nanocapsule; b) a cutaway view.

[*] Dr. G. S. Ananchenko, Dr. K. A. Udachin, Dr. A. Dubes, Dr. J. A. Ripmeester
Steacie Institute for Molecular Sciences
National Research Council Canada
100 Sussex Drive, Ottawa, ON, K1A 0R6 (Canada)
Fax: (+1) 613-998-7833
E-mail: gennady.ananchenko@nrc-crnc.gc.ca
T. Perrier, Dr. A. W. Coleman
Institut de Chimie et Biologie des Proteins
7 Passage du Vercors, 69367 Lyon Cedex 07 (France)

[**] This work was supported in part by the CNRS–NRC collaborative program.

Supporting information for this article is available on the WWW under http://www.angewandte.org or from the author.


© 2006 Wiley-VCH Verlag GmbH & Co. KGaA, Weinheim

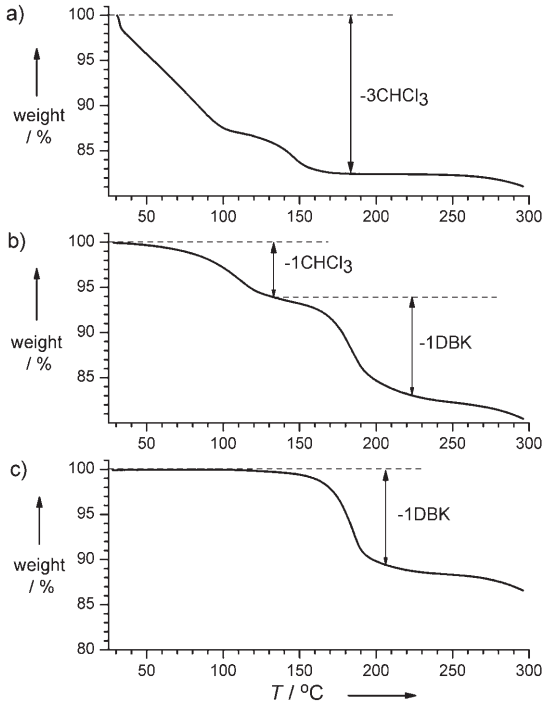



***Figure 2.*** TGA traces for the complexes: a) **1**; b) **2**; c) **3**.

The complex is not very stable thermally and instantly releases one $CHCl_3$ molecule, even below room temperature. Thermogravimetric analysis (TGA; Figure 2a) shows that the next two $CHCl_3$ molecules can be ejected easily from the cavity by heating to 80 °C; further heating removes the remaining guest.

As complex **1** is not very stable, we anticipated that the guest might be replaceable rather easily by another guest to form a more stable complex. We chose 1,3-diphenylpropan-2-one (dibenzylketone, DBK) as the new guest because its molecular size is suitable for the cavity and it remains liquid over a broad range of temperatures, thus allowing easy handling. Crystals of complex **1** were placed in a saturated solution of the calixarene in dibenzylketone at 70 °C for 3 days. The latter displaces some of the $CHCl_3$ in the capsule without destroying the crystals. The new crystals were also analyzed by single-crystal XRD, which showed that not all the molecules of $CHCl_3$ have been displaced by DBK (Figure 3), so that the capsule now contains two different guests (complex **2**).

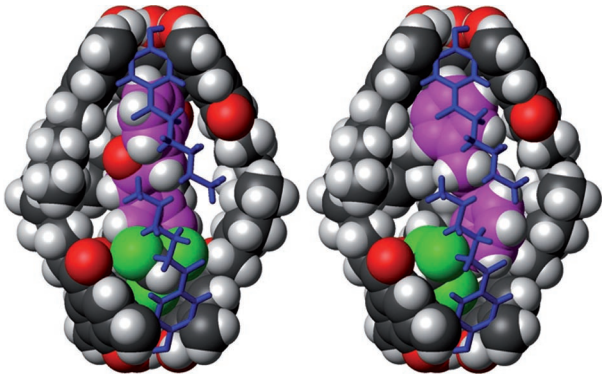


***Figure 3.*** The structure of complex **2** (two cutaway views).

Several methods were used to prepare crystals to confirm that **2** forms both by direct crystallization and by replacement of $CHCl_3$ by DBK. In one case, a single-crystal of complex **1** was treated with DBK after collecting a single crystal data set; the XRD study was repeated for the treated crystal. This proved that guest exchange is indeed a single-crystal-to-single-crystal transition. The $CHCl_3$ molecule in complex **2** is locked deep inside the cavity by the much larger DBK, with the shortest distance between the benzene rings of dibenzylketone and the Cl atoms of $CHCl_3$ being about 3.5 Å. According to the TGA trace (Figure 2b), this new complex is stable up to around 70 °C, at which temperature the residual $CHCl_3$ begins to leave; above about 140 °C the complex contains only DBK (complex **3**), which leaves the capsule slowly upon further heating. The release of $CHCl_3$ from complex **2** proceeds such that the single crystal remains intact and it may still be suitable for single-crystal XRD, although the quality of the crystal is not likely to be as good. This is completely different from the behavior of complex **1**, in which removal of only two molecules of $CHCl_3$ already destroys the crystal lattice.

CP-MAS $^{13}C$ NMR spectra of the complexes are shown in Figure 4. All signals in the spectrum of complex **1** are relatively broad, thus suggesting that exchange processes between the two $CHCl_3$ positions in the capsule are likely. The $CHCl_3$ signal ($\delta = 76.3$ ppm, marked with an asterisk) is shifted upfield by 1.3 ppm in comparison to that of the liquid phase measured by the same NMR probe. No other $CHCl_3$ signals were found in the spectra recorded at different spinning rates, in agreement with the presence of rapid exchange. The signals in complex **2** are sharper because the exchange process is likely slower due to steric restrictions within the capsule. It is worth noting that all of the lines in the spectrum have approximately the same width, which confirms that the complex is not a mixture of different types of nanocapsules (that is, capsules with only DBK and capsules with only $CHCl_3$). The signals of the carbon atoms of DBK in complexes **2** and **3** are shifted upfield in comparison with those of pure DBK (e.g., $\delta = 201.7$ vs. 204.9 ppm for C=O and $\delta = 132.6$ vs. 134.6 ppm for $C_{ipso}$), thus indicating the increased shielding of the DBK atoms in the capsule. After the $CHCl_3$ molecule has left the cavity, the lines become quite sharp (complex **3**) as there is no significant exchange between the different positions of DBK in the cavity.

The essential feature of the formation of complex **2** is the ability of DBK to displace $CHCl_3$ without a decomposition/reformation cycle, that is, both the nanocapsule and the entire crystal remain intact. To check the permeability of the capsule walls for small molecules we studied the complexes by hyperpolarized $^{129}Xe$ NMR (HP-Xe) spectroscopy, which lends itself well as an in situ probe of the temperature-dependent access to the guest sites in the complex.[4a,8]

Figure 5 shows a set of $^{129}Xe$ NMR spectra for complex **1** in contact with a flowing gas mixture (98 % He, 1 % $N_2$, 1 % Xe) containing HP-Xe as a function of temperature under static conditions. The room-temperature spectrum (Fig-

 © 2006 Wiley-VCH Verlag GmbH & Co. KGaA, Weinheim 

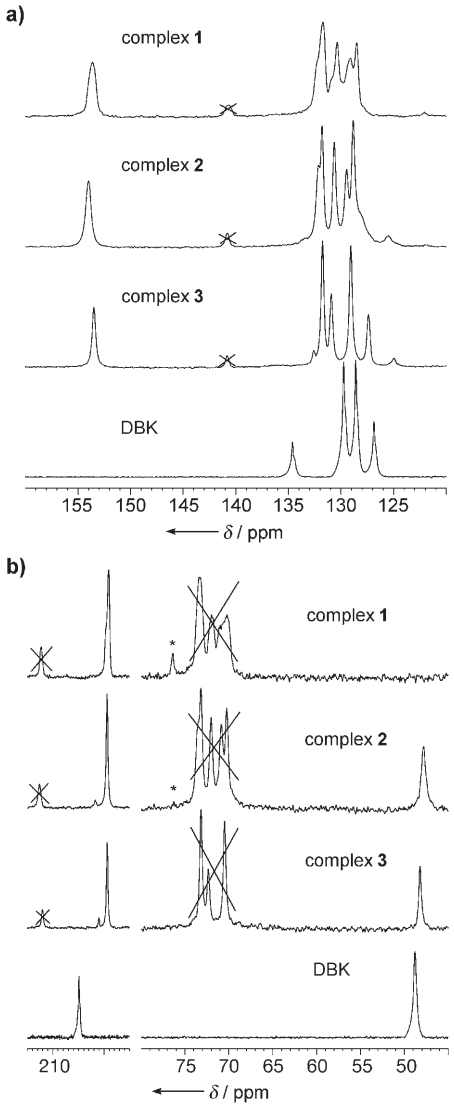



***Figure 4.*** CP-MAS $^{13}C$ NMR spectra of complexes **1**–**3**: a) aromatic region; b) carbonyl and part of the aliphatic regions. Spinning sidebands are crossed out. An asterisk denotes the signal of $CHCl_3$.

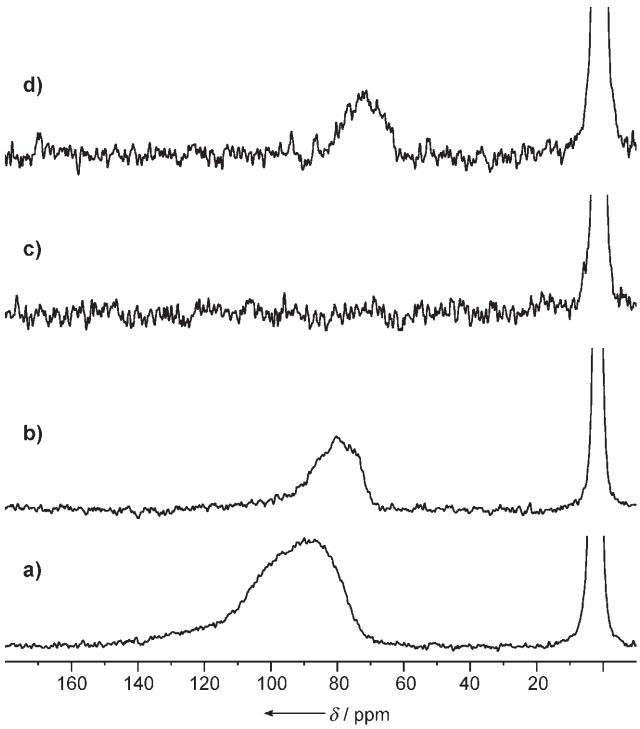



***Figure 5.*** In situ study of the transformation of complex **1** as monitored by continuous flow HP-$^{129}Xe$ NMR spectroscopy: a) room temperature; b) 60 °C; c) 120 °C; d) room temperature at the end of the reaction.

ure 5a) shows the resonance at $\delta = 0$ ppm of free xenon gas and a broad signal at around $\delta = 90$ ppm assigned to Xe occupying some available space within the capsule.[4a,9] Heating to 60 °C (Figure 5b) and further to 120 °C (Figure 5c) leads to a decrease in the signal-to-noise ratio and an upfield shift of this broad signal, followed by its complete disappearance. This correlates with the TGA data (Figure 2), in which most of the $CHCl_3$ is seen to leave the capsule in this temperature range. As soon as the capsule is empty it becomes unstable and immediately collapses. The absence of the signal of adsorbed xenon at this temperature clearly indicates that there is no void space available for gas adsorption, probably because of formation of a self-included complex. Upon cooling to room temperature some void space reappears in the material but it is very small, as can be concluded from the poor signal-to-noise ratio, and it is likely that Xe competes with included hydrocarbon chains for cavity space. Therefore, the capsule exists only because of the occupying guest, which provides additional vdW stabilization of the structure. This is in contrast to *p-tert*-butylcalix[4]arene and related nanocapsules,[4c,10] which can exist even without a guest, although the void spaces are small.

$^{129}Xe$ NMR spectra of the gas that interacts with complex **2** show a completely different behavior (Figure 6). At the start of the reaction, a small, broad signal appears at room temperature at around $\delta = 150$ ppm which corresponds to Xe interacting with the aliphatic chains of the capsule but without deep penetration into the latter.[9] An increase in temperature to 60 °C (Figure 6b) hardly affects the position, shape, or intensity of the line. The TGA trace (Figure 2b) shows that there is no major release of $CHCl_3$ from complex **2** at this temperature. Further heating to 120 °C (Figures 6c–e) leads to an upfield shift of the Xe signal. This correlates with the TGA results, which show the release of $CHCl_3$ at this temperature. The capsule can now provide more space for the adsorption of gas, although the chemical shift suggests that Xe is still in a state of rapid exchange. After cooling to room temperature the Xe signal moves upfield (Figure 6f) and its chemical shift of about $\delta = 85$ ppm corresponds approximately to that of Xe in complex **1** (Figure 5a) before thermal treatment, that is, Xe is localized in the capsule. Comparison of these two experiments allows us to conclude that complex **2** contains $CHCl_3$ and DBK in one capsule and the larger DBK molecule does not allow $CHCl_3$ to be released unless serious heating is applied. Furthermore, these experiments clearly illustrate the permeability of the crystal and the capsule walls.

 © 2006 Wiley-VCH Verlag GmbH & Co. KGaA, Weinheim 

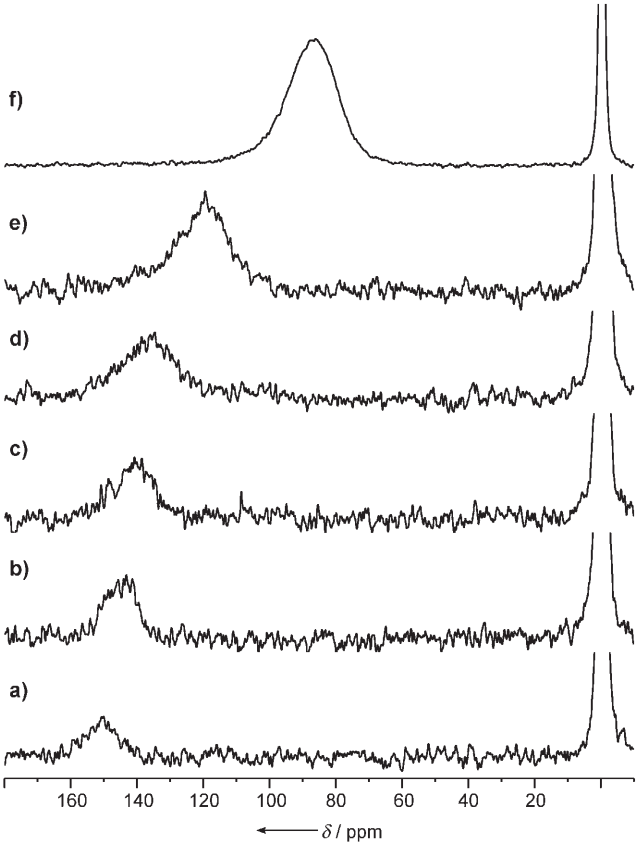



***Figure 6.*** In situ study of the transformation of complex **2** as monitored by continuous flow HP-$^{129}$Xe NMR spectroscopy: a) room temperature; b) 60 °C; c) 120 °C; d) 120 °C after 20 min; e) 120 °C after briefly heating to 140 °C; f) room temperature at end of reaction.

In summary, we have shown that *para*-hexanoylcalix[4]-arene can form hydrophobic tail-to-tail nanocapsules that can encapsulate various guests. The guests stabilize the nanocapsule through van der Waals interactions. The capsule is robust enough to trap larger guests at room temperature, but at the same time it is flexible enough to allow efficient guest exchange without destroying the crystal lattice. This suggests that thermal programming can be used to control the adsorption and release of guests of different volatility, and thus the nanocapsule can serve as a refillable nanocontainer. This nanocapsule may well play a role in the high loading previously observed for various solid lipid nanoparticles based on this host material.[9] It is clear that there are applications in separation science, in the preservation and the transport of active species, and as nanocontainers for chemical transformations.

Received: October 6, 2005
Published online: January 30, 2006

**Keywords:** calixarenes · crystal growth · host–guest systems · self-assembly · supramolecular chemistry

[1] a) C. D. Gutsche, *Calixarenes: Monographs in Supramolecular Chemistry*, The Royal Society of Chemistry, Cambridge, **1989**; b) J.-M. Lehn, *Supramolecular Chemistry: Concept and Perspectives*, VCH, Weinheim, **1995**; c) D. J. Cram, J. M. Cram, *Container Molecules and Their Guests*, The Royal Society of Chemistry, Cambridge, **1994**; d) L. R. MacGillivray, J. L. Atwood, *Angew. Chem.* **1999**, *111*, 1080 – 1096; *Angew. Chem. Int. Ed.* **1999**, *38*, 1018 – 1033; e) M. M. Conn, J. Rebek, Jr., *Chem. Rev.* **1997**, *97*, 1647 – 1668; f) A. Jasat, J. C. Sherman, *Chem. Rev.* **1999**, *99*, 931 – 967.

[2] a) R. Wyler, J. de Mendoza, J. Rebek, Jr., *Angew. Chem.* **1993**, *105*, 1820 – 1822; *Angew. Chem. Int. Ed. Engl.* **1993**, *32*, 1699 – 1701; b) J. Rebek, Jr., *Chem. Commun.* **2000**, 637 – 643; c) A. Shivanyuk, J. Rebek, Jr., *Chem. Commun.* **2001**, 2374 – 2375; d) L. R. MacGillivray, J. L. Atwood, *Nature* **1997**, *389*, 469 – 472.

[3] a) D. J. Cram, S. Karbach, Y. H. Kim, L. Baczynskyj, G. W. Kalleymeyn, *J. Am. Chem. Soc.* **1985**, *107*, 2575 – 2576; b) J. Gabard, A. Collet, *J. Chem. Soc. Chem. Commun.* **1981**, 1137 – 1138; c) R. G. Chapman, J. C. Sherman, *J. Am. Chem. Soc.* **1995**, *117*, 9081 – 9082; d) N. Chopra, J. C. Sherman, *Angew. Chem.* **1999**, *111*, 2109 – 2111; *Angew. Chem. Int. Ed.* **1999**, *38*, 1955 – 1957; e) M. Yoshizawa, T. Kusukawa, M. Fujita, K. Yamaguchi, *J. Am. Chem. Soc.* **2000**, *122*, 6311 – 6312.

[4] a) G. D. Enright, K. A. Udachin, I. L. Moudrakovski, J. A. Ripmeester, *J. Am. Chem. Soc.* **2003**, *125*, 9896 – 9897; b) C. L. D. Gibb, B. C. Gibb, *J. Am. Chem. Soc.* **2004**, *126*, 11 408 – 11 409; c) P. K. Thallapally, G. O. Lloyd, T. B. Wirsig, M. W. Bredenkamp, J. L. Atwood, L. J. Barbour, *Chem. Commun.* **2005**, 5272 – 5274.

[5] a) J. L. Atwood, L. J. Barbour, A. Jerga, B. L. Schottel, *Science* **2002**, *298*, 1000 – 1002; b) J. L. Atwood, L. J. Barbour, A. Jerga, *Science* **2002**, *296*, 2367 – 2369.

[6] a) P. Shahgaldian, A. W. Coleman, *Langmuir* **2001**, *17*, 6851 – 6854; b) P. Shahgaldian, A. W. Coleman, V. I. Kalchenko, *Tetrahedron Lett.* **2001**, *42*, 577 – 579; c) P. Shahgaldian, M. Cesario, P. Goreloff, A. W. Coleman, *Chem. Commun.* **2002**, 326 – 327.

[7] A. Dubes, K. A. Udachin, P. Shahgaldian, A. W. Coleman, J. A. Ripmeester, *New J. Chem.* **2005**, *29*, 1141 – 1146.

[8] a) I. L. Moudrakovski, A. Nossov, S. Lang, S. Breeze, C. I. Ratcliffe, B. Simard, G. Santyr, J. A. Ripmeester, *Chem. Mater.* **2000**, *12*, 1181 – 1183; b) A. V. Nossov, D. V. Soldatov, J. A. Ripmeester, *J. Am. Chem. Soc.* **2001**, *123*, 3563 – 3568.

[9] A. Dubes, I. L. Moudrakovski, P. Shahgaldian, A. W. Coleman, C. I. Ratcliffe, J. A. Ripmeester, *J. Am. Chem. Soc.* **2004**, *126*, 6236 – 6237.

[10] a) E. B. Brouwer, K. A. Udachin, G. D. Enright, J. A. Ripmeester, K. J. Ooms, *Chem. Commun.* **2001**, 565 – 566; b) E. B. Brouwer, G. D. Enright, K. A. Udachin, S. Lang, K. J. Ooms, P. A. Halchuk, J. A. Ripmeester, *Chem. Commun.* **2003**, 1416 – 1417.

 © 2006 Wiley-VCH Verlag GmbH & Co. KGaA, Weinheim 

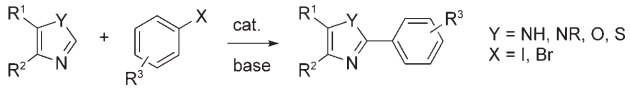
C–H Activation

DOI: 10.1002/anie.200504289

# Microwave-Promoted Rhodium-Catalyzed Arylation of Heterocycles through C–H Bond Activation**

*Jared C. Lewis, Jessica Y. Wu, Robert G. Bergman,* and Jonathan A. Ellman**

The advantages of directly forming carbon–carbon (C–C) bonds from carbon–hydrogen (C–H) bonds in organic synthesis[1] have driven the development and application of an expanding body of reactions proceeding through catalytic C–H activation.[2] One reaction that has recently received particular attention is the C2-arylation of azoles (Scheme 1), the products of which are commonly found in a wide array of pharmaceuticals and materials.[3]




***Scheme 1.*** General C2-arylation of azoles.

Despite the progress that has been made in direct azole–aryl iodide couplings,[4] only scattered examples of the use of aryl bromides have emerged.[5] In these cases, the scope with respect to either coupling partner is limited and the reactions typically require extended reaction times at high temperatures in sealed reaction vessels. Our previously reported Rh-catalyzed arylation reactions in particular suffer from hydrodehalogenation of the starting aryl iodide and dehydrogenation of the tricyclohexylphosphine used as an added ligand.[6] Herein, we report the solution to several of these problems in the development of a new microwave-promoted[7] heterocycle–aryl bromide direct coupling reaction that employs rhodium catalysts in the presence of 9-cyclohexylbicyclo-[4.2.1]-9-phosphanonane ("cyclohexylphobane") ligands.

Our efforts to find phosphines that would maintain the unique steric and electronic qualities of $PCy_3$ while reducing the ability of the phosphine to undergo dehydrogenation led to the exploration of phobanes, such as **1** (Figure 1 a),[8] for the Rh-catalyzed C–H activation/olefin coupling of a dihydroquinazoline.[9] The efficacy of this phosphine for the alkylation reaction prompted further investigation into its use for arylation. While the use of **1** as a ligand in the coupling of benzimidazole and iodobenzene gave only a 27% yield after heating for 30 min at 250 °C in a microwave reactor, this yield represented an improvement over that obtained using $PCy_3$ (Table 1). The relative success of **1** also prompted our investigation of its isomer **2a**. However, while protocols exist for the synthesis of **1**/**2a** mixtures and pure **1**, neither **2a** nor **2b** have been prepared in isomerically pure form to our knowledge.[10] We were able to obtain a mixture of **2a**,**b** (ca. 2:1) from the alkylation of the corresponding secondary bicyclic phosphine in analogy to **1** (Figure 1 b).

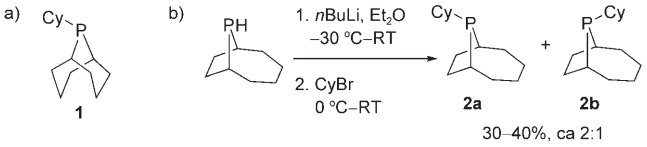
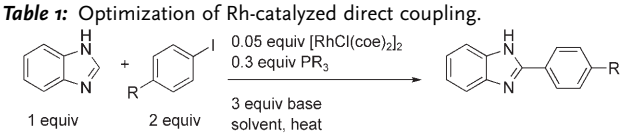



***Figure 1.*** a) Structure of **1**.[9] b) Synthesis of **2a**,**b**. Cy = cyclohexyl.

***Table 1:*** Optimization of Rh-catalyzed direct coupling.




| Entry | Base (equiv) | $PR_3$ | R | Product | Yield [%] |
|---|---|---|---|---|---|
| 1 | $Et_3N$ (4) | $PCy_3$ | H | **5** | 20[a] |
| 2 | $Et_3N$ (4) | **1** | H | **5** | 27[a] |
| 3 | $Et_3N$ (4) | **2a**,**b** | H | **5** | 40[a] |
| 4 | $iPr_2iBuN$ (4) | **2a**,**b** | H | **5** | 71[a] |
| 5 | $iPr_2iBuN$ (3) | **2a**,**b** | H | **5** | 91[b] (76)[c] |
| 6 | $iPr_2iBuN$ (3) | **2a**,**b** | $CF_3$ | **6** | 58[b] (68)[c] |
| 7 | $iPr_2iBuN$ (3) | **2a**,**b** | OMe | **7** | 10[a] (99)[c] |

[a] Yields were determined by GC analysis relative to hexamethylbenzene as internal standard; reactions were conducted in 1,2-dichlorobenzene (DCB) heated at 250 °C for 30 min in a microwave reactor. [b] Isolated yields of pure products; reactions were conducted in DCB heated at 250 °C for 40 min in a microwave reactor. [c] Isolated yields of pure products; reactions were conducted in THF heated at 150 °C for 24 h in a sealed tube. coe = cyclooctene.

The phosphine mixture was then used for the Rh-catalyzed arylation of benzimidazole with PhI (Table 1).

[*] Prof. R. G. Bergman
Department of Chemistry
University of California, Berkeley and
Division of Chemical Sciences
Lawrence Berkeley National Laboratory
Berkeley, CA 94720-1460 (USA)
Fax: (+1) 510-642-7714
E-mail: bergman@cchem.berkeley.edu
J. C. Lewis, J. Y. Wu, Prof. J. A. Ellman
Department of Chemistry
University of California, Berkeley
Berkeley, CA 94720-1460 (USA)
Fax: (+1) 510-642-8369
E-mail: jellman@cchem.berkeley.edu

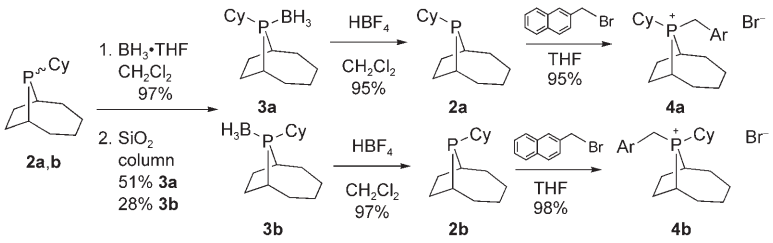
[**] This work was supported by the NIH (grant no. GM069559, to J.A.E.) and by the Director, Office of Energy Research, Office of Basic Energy Sciences, Chemical Sciences Division, US Department of Energy (contract no. DE-AC03-76SF00098, to R.G.B.). J.Y.W. is funded by the Jean Dreyfus Boissevain Award. We gratefully acknowledge Dr. Fredrick J. Hollander and Dr. Allen G. Oliver at the UCB X-ray diffraction facility (CHEXRAY) for solving the structures of **4a** and **4b**, and Jeffrey McMahon for many helpful discussions. Dr. Wolfgang Meyer of Sasol Corp. is acknowledged for helpful advice on phobane alkylation.

Supporting information for this article is available on the WWW under http://www.angewandte.org or from the author.

 © 2006 Wiley-VCH Verlag GmbH & Co. KGaA, Weinheim 

Gratifyingly, use of **2a**,**b** improved the yield of 2-phenylbenzimidazole to 40% and little to no hydrodehalogenation of PhI occurred over the course of a conventionally heated reaction, as monitored by in situ $^1$H NMR spectroscopy (Table 1, entry 3). The use of a more hindered amine base, diisopropylisobutylamine, in combination with **2a**,**b** provided the desired product in 71% yield (Table 1, entry 4). Further optimization of the reaction time and stoichiometry allowed isolation of 2-phenylbenzimidazole in 95% yield. Both electron-rich and electron-poor aryl iodides were observed to couple (Table 1, entries 6 and 7).[11] The desired products could also be obtained in good yields by conventionally heating the reaction mixtures in sealed tubes. Most importantly, bromobenzene was observed to couple in 80% isolated yield under the optimized reaction conditions.

To determine if there are any differences in reactivity between **2a** and **2b** and to confirm the previously unreported structure of **2b**, a protocol to isolate pure **2a** and pure **2b** was developed. Following protection of the mixture as the corresponding borane adducts **3a**,**b**, chromatography was successfully used to resolve the two isomers (Scheme 2). Acid




***Scheme 2.*** Separation and characterization of **2a** and **2b**.

deprotection provided the pure phosphines **2a** and **2b**,[12] which were alkylated with naphth-2-ylmethyl bromide to provide crystalline phosphonium salts **4a** and **4b**.

Single-crystal X-ray analysis revealed that **4a** and **4b** are indeed isomers differing in the orientation of the cyclohexyl substituent (**4a** *exo*, **4b** *endo*; Figure 2).[13] Starting from isolated **3a**,**b**, each step in sequence provided a single phosphorus-containing species as judged by $^{31}$P{$^1$H} NMR spectroscopy, suggesting that the configuration at phosphorus remained constant throughout. Heating a solution of **2a**,**b** to 150 °C for several hours led to no change of the mixture by in situ $^{31}$P{$^1$H} NMR spectroscopy. However, heating the mixture to 250 °C for 40 minutes in a microwave reactor led to complete conversion of the mixture into **2a** according to $^{31}$P{$^1$H} NMR spectroscopy. Possibly as a result of this isomerization, no significant differences in yield were observed when either isomerically pure **2a** or **2b** was used in the arylation of benzimidazole with iodobenzene. Therefore, the mixture **2a**,**b** was used exclusively in coupling experiments. The applicability of this mixture is of practical importance as it can be obtained by Kugelrohr distillation of the crude alkylation reaction mixture obtained in two steps from commercial materials, with no chromatography needed (Figure 1b).

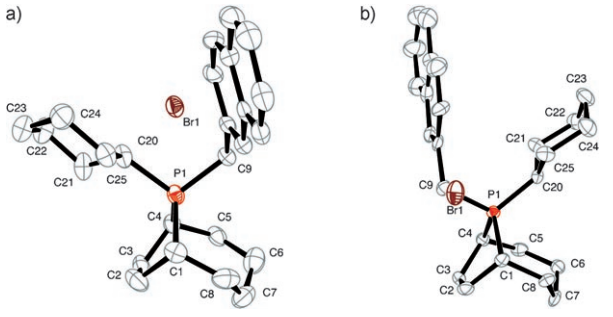
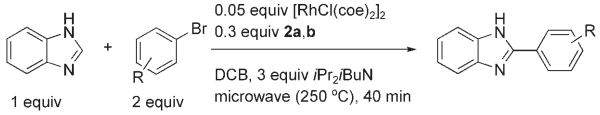



***Figure 2.*** ORTEP diagrams of a) **4a** and b) **4b**. Thermal ellipsoids are shown at the 50% probability level.

Compared to $[RhCl(coe)_2]_2/PCy_3$, **2a**,**b**-derived C–H arylation catalysts uniquely promote the direct coupling of benzimidazole to aryl bromides without significant interference from hydrodehalogenation. This reaction also exhibits considerable functional group tolerance. *para*-Substituted 2-arylbenzimidazoles incorporating a wide variety of functional groups, including nitrile, chloride, alkoxy, ketone, and amide substituents, were isolated in good to high yields under standard microwave reaction conditions (Table 2). While the reaction of aryl bromides that lack a sensitive functionality could be conducted at concentrations of 0.3 M, more-reactive functional groups required more-dilute conditions (0.05 or 0.1 M) to obtain high yields of the desired products. *meta*-Substitution had little effect on the outcome of the reaction, but *o*-$CH_3$ or *o*-$CF_3$ substitution completely suppressed the desired reaction, consistent with known difficulties for sterically hindered cross-coupling reactions.[14] Highly electron-rich aryl bromides led to decreased yields (Table 2, entries 9 and 12), but the use of aryl iodides circumvents this problem (Table 1, entry 7).

Besides tolerating various substituted aryl bromides, the optimized reaction conditions were compatible with a number of different heterocycles (Table 3). As previously observed for the conventionally heated coupling of aryl

***Table 2:*** Functional group tolerance under optimized arylation conditions.

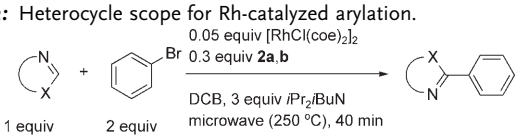


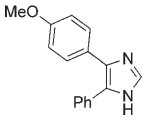
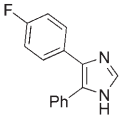
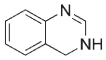

| Entry | R | Conc. [M][a] | Product | Yield [%][b] |
|---|---|---|---|---|
| 1 | *p*-$CF_3$ | 0.3 | **6** | 77 (60) |
| 2 | *p*-CN | 0.1 | **8** | 90 |
| 3 | *p*-Cl | 0.1 | **9** | 67 |
| 4 | *p*-COEt | 0.05 | **10** | 77 (59) |
| 5 | *p*-$CONH_2$ | 0.1 | **11** | 60 |
| 6 | *p*-Ph | 0.3 | **12** | 81 |
| 7 | *p*-H | 0.3 | **5** | 80 (28) |
| 8 | *p*-Me | 0.3 | **13** | 91 |
| 9 | *p*-OMe | 0.1 | **7** | 54 (24) |
| 10 | *m*-$CO_2Et$ | 0.05 | **14** | 70 |
| 11 | *m*-Me | 0.1 | **15** | 79 |
| 12 | *m*-OEt | 0.05 | **16** | 46 |

[a] Reaction concentration relative to azole starting material. [b] Isolated yields of pure products. Yields in parentheses were obtained from in situ NMR spectroscopic analysis of reactions that were conducted in [$D_8$]THF and conventionally heated at 150 °C for 24 h in a sealed tube.

 © 2006 Wiley-VCH Verlag GmbH & Co. KGaA, Weinheim 

***Table 3:*** Heterocycle scope for Rh-catalyzed arylation.




| Entry | Heterocycle | Conc. [M][a] | Product | Yield [%][b] |
|---|---|---|---|---|
| 1 |  | 0.1 | **17** | 55 |
| 2 |  | 0.1 | **18** | 63 |
| 3 |  | 0.05 | **19** | 45 |
| 4 |  | 0.05 | **20** | 75 |
| 5 |  | 0.1 | **21** | 86 |
| 6 |  | 0.1 | **22** | 50 |

[a] Reaction concentration relative to azole starting material. [b] Isolated yields of pure products.

iodides, both *N*-methylbenzimidazole and benzoxazole couple in moderate yields, but benzothiazole was incompatible with the reaction conditions. Dihydroquinazoline, which contains a non-aromatic heterocycle, provided 2-phenylquinazoline as observed previously.[6] Bis(aryl) imidazoles, a highly important class of bioactive compounds,[15] were also highly effective arylation substrates. The observed substrate scope is fully consistent with our mechanistic understanding based on N-heterocyclic carbene/rhodium complexes as intermediates in C–C bond formation.[16]

In conclusion, a highly general method for the direct coupling of azoles with aryl bromides has been developed and shown to provide rapid access to medicinally relevant compounds. The bulky trialkylphosphines **2a** and **2b** were synthesized and characterized and proved to be superior to $PCy_3$ under our arylation conditions, presumably because their rigid bicyclic structure prohibits dehydrogenation, a liability of $PCy_3$. The use of microwave radiation as a heat source for the arylation reactions allowed a convenient access to the temperatures needed to allow complete reaction in only 40 minutes and eliminated the safety concerns associated with sealed-tube conditions used for other arylation methods. Thus, information provided by mechanistic studies was used to guide relatively conservative modifications to our existing catalytic system and led to dramatic improvements in generality and practicality.

Received: December 2, 2005
Published online: January 30, 2006

**Keywords:** arylation · C–H activation · heterocycles · phosphane ligands · rhodium

[1] a) B. A. Arndsten, R. G. Bergman, T. A. Mobley, T. H. Peterson, *Acc. Chem. Res.* **1995**, *28*, 154–162; b) A. E. Shilov, G. B. Shul'pin, *Chem. Rev.* **1997**, *97*, 2879; c) R. H. Crabtree, *Dalton Trans.* **2001**, 2437–2450; d) J. E. Bercaw, J. A. Labinger, *Nature* **2002**, *417*, 507–514.

[2] a) G. Dyker, *Angew. Chem.* **1999**, *111*, 1808–1822; *Angew. Chem. Int. Ed.* **1999**, *38*, 1698–1712; b) M. Miura, M. Nomura, *Top. Curr. Chem.* **2002**, *219*, 212–237; c) F. Kakiuchi, S. Murai, *Acc. Chem. Res.* **2002**, *35*, 826–834; d) Y. Guari, S. Sabo-Etienne, B. Chaudret, *Eur. J. Inorg. Chem.* **1999**, 1047–1055; e) F. Kakiuchi, S. Murai, *Top. Curr. Chem.* **1999**, *3*, 47–77.

[3] D. J. Hlasta, C. A. Zificsak, *Tetrahedron* **2004**, *60*, 8991–9016.

[4] a) Nomura and co-workers found $Pd(OAc)_2/PPh_3$ to be a viable arylation catalyst in the presence of a carbonate base: S. Pivsa-Art, T. Satoh, Y. Kawamura, M. Miura, M. Nomura, *Bull. Chem. Soc. Jpn.* **1998**, *71*, 467–473; b) B. S. Lane, M. A. Brown, D. Sames, *J. Am. Chem. Soc.* **2005**, *127*, 8050–8057.

[5] a) A. Mori, A. Sekiguchi, K. Masui, T. Shimada, M. Horie, K. Osakada, M. Kawamoto, T. Ikeda, *J. Am. Chem. Soc.* **2003**, *125*, 1700–1701 (one example); b) Scattered examples of heterocycle–aryl bromide couplings are given in ref. [4a]; c) A. Yokooji, T. Okazawa, T. Satoh, M. Miura, M. Nomura, *Tetrahedron* **2003**, *59*, 5685–5689; d) Electron-rich aryl bromides were coupled with benzothiazole and benzoxazole in: D. Alagille, R. M. Baldwin, G. D. Tamagnan, *Tetrahedron Lett.* **2005**, *46*, 1349–1351.

[6] J. C. Lewis, S. H. Wiedemann, R. G. Bergman, J. A. Ellman, *Org. Lett.* **2004**, *6*, 35–38.

[7] a) M. Larhed, C. Moberg, A. Hallberg, *Acc. Chem. Res.* **2002**, *35*, 717–727; b) B. A. Roberts, C. R. Strauss, *Acc. Chem. Res.* **2005**, *38*, 653–661.

[8] "Phoban" is commerically available as a technical mixture of [3.3.1] and [4.2.1] isomers and has received limited but continual attention since its original patent in 1968: a) R. G. Mason, J. L. van Winkle (Shell Oil Co.), US Patent 3400163, **1968**; b) For separation of the isomers, see: J. H. Downing, V. Gee, P. G. Pringe, *Chem. Commun.* **1997**, 1527–1528; c) For its use as a ligand, see: H. C. L. Abbenhuis, U. Burckhardt, V. Gramlich, C. Köllner, P. S. Pregosin, R. Salzmann, A. Togni, *Organometallics* **1995**, *14*, 759–766; d) G. S. Forman, A. E. McConnell, M. J. Hanton, A. M. Z. Slawin, R. P. Tooze, W. J. van Rensburg, W. H. Meyer, C. Dwyer, M. M. Kirk, D. W. Serfontein, *Organometallics*, **2004**, *23*, 4824–4827.

[9] S. H. Wiedemann, R. G. Bergman, J. A. Ellman, *J. Org. Chem.*, in press.

[10] a) see ref. [8d]; b) C. L. Dwyer, M. M. Kirk, W. H. Meyer, W. J. van Rensburg, G. S. Forman, unpublished results.

[11] Significant amounts of demethylation were observed for the microwave-mediated arylation using iodoanisole, presumably due to nucleophilic displacement by iodide anion at high temperatures.

[12] Z. Chen, Q. Jiang, G. Zhu, D. Xiao, P. Cao, C. Guo, X. Zhang, *J. Org. Chem.* **1997**, *62*, 4521–4523.

[13] A number of reports have described the phenyl-substituted analogue of **2a**, but none have mentioned the *endo* isomer: a) S. T. Howard, J. P. Foreman, P. G. Edwards, *Inorg. Chem.* **1996**, *35*, 5805–5812; b) S. J. Coles, P. G. Edwards, M. B. Hursthouse, K. M. Abdul Malik, J. L. Thick, R. P. Tooze, *J. Chem. Soc. Dalton Trans.* **1997**, 1821–1830.

[14] G. Altenhoff, R. Goddard, C. W. Lehmann, F. Glorius, *J. Am. Chem. Soc.* **2004**, *126*, 15195–15201, and references therein.

[15] J. Sisko, A. J. Kassick, M. Mellinger, J. J. Filan, A. Allen, M. A. Olsen, *J. Org. Chem.* **2000**, *65*, 1516–1524, and references therein.

[16] a) K. L. Tan, R. G. Bergman, J. A. Ellman, *J. Am. Chem. Soc.* **2002**, *124*, 3202–3203; b) S. H. Wiedemann, J. C. Lewis, R. G. Bergman, J. A. Ellman, *J. Am. Chem. Soc.*, in press.

 © 2006 Wiley-VCH Verlag GmbH & Co. KGaA, Weinheim 

Organogels

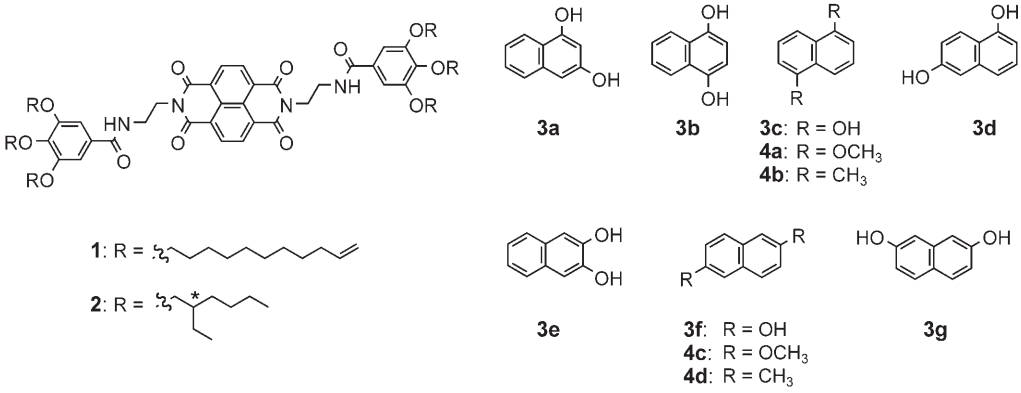
DOI: 10.1002/anie.200503158

# Spontaneous Colorimetric Sensing of the Positional Isomers of Dihydroxynaphthalene in a 1D Organogel Matrix**

*Pritam Mukhopadhyay, Yuya Iwashita, Michihiro Shirakawa, Shin-ichiro Kawano, Norifumi Fujita, and Seiji Shinkai**

The recent upsurge of interest in functional and stimuli-responsive organogels[1] has unraveled new and exciting properties of molecules hitherto unknown in solution and the solid state.[2] Hydrogen-bonding interactions between amide, urea, and sugar groups as well as the van der Waals interactions between cholesteryl groups have chiefly been utilized so far in the construction of one-dimensional (1D) architectures suitable for gelation. In contrast, examples of a relatively new design strategy that utilizes the π–π-stacking interaction to form 1D low-molecular-weight gels are rather limited.[3a–d] We employed this concept to produce 1D perylenediimide-based organogels with light-harvesting properties.[3e,f] Our interest in the development of a 1D naphthalenediimide-based organogel that exhibits recognition properties was driven by the following motives: Firstly, naphthalenediimide is a versatile molecule[4] with an extended π surface and has been applied in the design of conductive materials, artificial photosynthetic systems, as well as DNA intercalators. Secondly, the naphthalenediimide–alkoxynaphthalene system is an important supramolecular motif that has been applied in the design of a plethora of novel architectures:[5] for example, Sanders, Stoddart, and co-workers have reported [2]catenanes, [2]rotaxanes, and pseudo[2]rotaxanes, and Iverson and co-workers have designed folded aedamers—artificial duplexes based on this versatile donor–acceptor interaction. Surprisingly, however, this important motif has not been investigated in an organogel system to date.

Herein we present a highly efficient, versatile organogelator (**1**) that forms a robust 1D gel superstructure. We reasonably envisioned that the gel matrix of **1** would bind to 1,5-dialkoxynaphthalenes following the precedent of supramolecular architectures derived from the naphthalenediimide–alkoxynaphthalene motif.[5] However, to our astonishment, organogel **1** does not interact with this well-known complementary partner, whereas it shows selective recognition of the polar, hydrophilic dihydroxynaphthalenes. Thus, we have found serendipitously an alternative supramolecular binding motif that predominantly operates only in the gel state. We utilized this unusual recognition pattern and the remarkably amplified binding in the gel-phase environment to design a simple and straightforward colorimetric detection system. With this system, it is possible to distinguish clearly several positional isomers of dihydroxynaphthalenes with the naked eye; such a process is impossible to carry out in the conventional solution state. To our knowledge, this is the first example of an organogel matrix that has been employed in a colorimetric sensing system.




The gelator molecule **1** was designed to include a combination of π–π stacking, H-bonding, and van der Waals forces. We anticipated that the naphthalenediimide moiety would facilitate the formation of a 1D superstructure because of its propensity to form π-stacked structures. Interestingly, **1** was found to be a versatile gelator; it formed stable gels in 19 of the 26 common organic solvents evaluated.[6] This gel shows a reversible sol–gel transition, and the temperature-dependent spectral changes strongly indicate the existence of π–π-stacked naphthalenediimide units in the gel which unstack upon heating (see Supporting Information). The 1D morphology constructed from **1** was confirmed by TEM observations (see Supporting Information).

To investigate the recognition characteristics[7] in the gel matrix of **1**, we first chose 1,5-dimethoxynaphthalene (**4a**) as a substrate as it is known to form a strong donor–acceptor complex with naphthalenediimide that can be visualized by its plum/violet color.[8] Gelator **1** and compound **4a** were added

[*] Dr. P. Mukhopadhyay, Y. Iwashita, M. Shirakawa, S.-i. Kawano, Dr. N. Fujita, Prof. Dr. S. Shinkai
Department of Chemistry and Biochemistry
Graduate School of Engineering
Kyushu University
744 Moto-oka, Nishi-ku, Fukuoka 819-0395 (Japan)
Fax: (+81) 92-802-2820
E-mail: seijitcm@mbox.nc.kyushu-u.ac.jp

[**] Support was provided by a Grant-in-Aid for Young Scientists (B) (No. 16750122), the 21st Century COE Project "Functional Innovation of Molecular Informatics", and JSPS fellowships (for P.M., M.S., and S.-i.K.).

Supporting information for this article is available on the WWW under http://www.angewandte.org or from the author.


InterScience
© 2006 Wiley-VCH Verlag GmbH & Co. KGaA, Weinheim

in a 1:1 molar ratio to a screw-capped sample vial containing cyclohexane (1 mL),[9] and the mixture was heated gently until a clear solution was obtained. Gel formation occurred within a few minutes, but contrary to our expectation, no color change was observed even after keeping the gel for a few weeks at ambient temperature, which indicates that no donor–acceptor interaction is present in the gel matrix. Likewise, no color changes were observed for 2,6-dimethoxynaphthalene (**4c**) and other common donor analogues such as **4b**, **4d**, and pyrene (see Figure 1). This finding is very surprising because a large number of supramolecular architectures have been constructed in which dialkoxynaphthalene or pyrene[10] derivatives intercalate between naphthalenediimide moieties to form columnar π-stacked donor–acceptor superstructures.

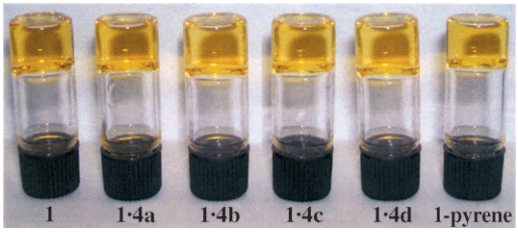



***Figure 1.*** The photograph shows there is no change in color upon addition of alkoxynaphthalenes (**4a** and **4c**), methylnaphthalenes (**4b** and **4d**), and pyrene to the gel matrix of **1** ([**1**] = 3.5 mM in cyclohexane, RT).

We then turned our attention to dihydroxynaphthalenes, which are also known to be environmental pollutants widely distributed in water and soil. Their recognition, sensing, and immobilization in a gel matrix would therefore be very important. However, carrying out recognition studies of dihydroxynaphthalenes in a nonpolar medium poses a serious challenge because of their hydrophilicity and poor solubility. Presumably, this is why dihydroxynaphthalenes have been studied mainly in aqueous media rather than in nonpolar solvents. Among the polar analogues of naphthalene, 2,6-dihydroxynaphthalene (**3f**) is known to form stable, violet-colored complexes with various acceptors in aqueous solution.[11] However, its complexation with naphthalenediimide in solution and the solid state has not been reported to date. Very surprisingly, although **3f** remains completely insoluble in solvents such as cyclohexane and decalin, it dissolves readily with gentle heating in the presence of **1**. A deep bluish-green color appears within a few minutes as the solution is cooled and transforms into a gel. The UV/Vis absorption spectrum exhibits a broad band in the visible region ($\lambda_{max} = 600$ nm), which is characteristic of a charge-transfer transition between the donor and acceptor molecules in the gel matrix (Figure 2). The charge-transfer band at 600 nm increases sharply with increasing amounts of **3f** in the gel matrix of **1**, while the intensity of the π–π* transition at 380 nm decreases. This observation indicates the facile transformation of a π-stacked naphthalenediimide structure to a naphthalenediimide–2,6-dihydroxynaphthalene complex in

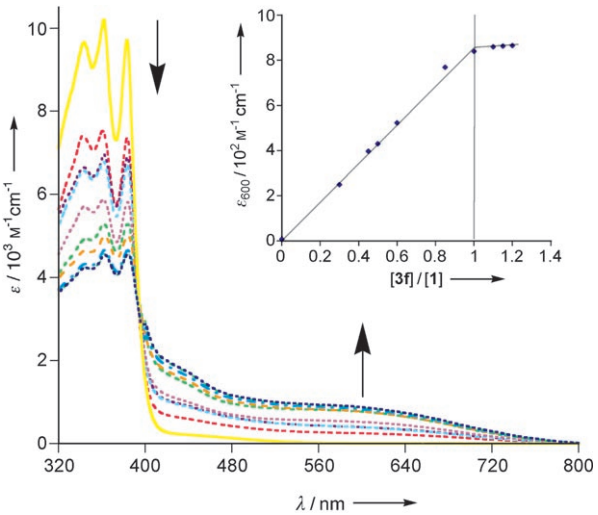



***Figure 2.*** UV/Vis spectra of gelator **1** (4.0 mM in cyclohexane) at various concentrations of **3f** (0.0–4.8 mM). The inset shows a plot of the molar absorption coefficient at 600 nm versus concentration of **3f** and confirms a 1:1 stoichiometry of the donor–acceptor complex ([**1**] = 4 mM).

the gel matrix. A 1:1 stoichiometry was confirmed by various spectroscopic methods[12] (e.g., see inset of Figure 2).

Encouraged by this observation, we then investigated the recognition of seven positional isomers of dihydroxynaphthalene (**3a–g**) in the gel matrix of **1**. Interestingly, all of the isomers spontaneously generate distinct colors visible to the naked eye (Figure 3a). To ascertain that the recognition

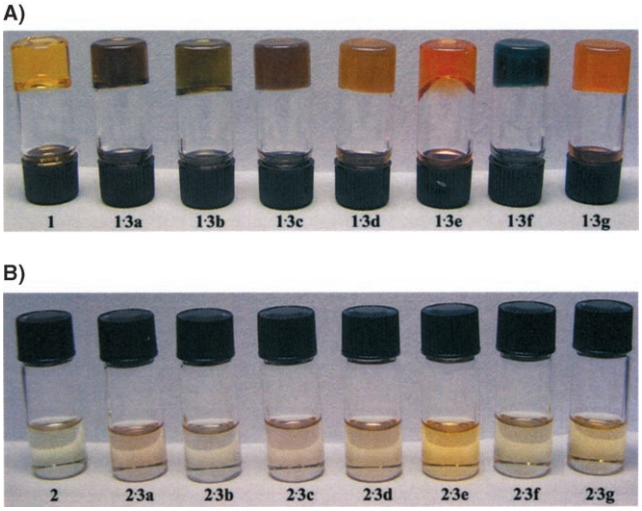



***Figure 3.*** A) The photograph depicts the spontaneous color changes of organogel **1** upon addition of positional isomers of dihydroxynaphthalene (**3a–3g**): **1** (yellow), **1·3a** (deep purple), **1·3b** (green), **1·3c** (purple), **1·3d** (light brown), **1·3e** (reddish-orange), **1·3f** (bluish-green) and **1·3g** (orange). B) The photograph shows the significantly reduced color changes in the solution state with nongelling compound **2** upon addition of dihydroxynaphthalenes **3a–3g**: **2** (colorless), **2·3a** (light violet), **2·3b** (colorless), **2·3c** (light purple), **2·3d** (light purple), **2·3e** (yellowish-orange), **2·3f** (yellowish-green), and **2·3g** (light yellow). Conditions: 1:1 complexes at 2.5 mM in **1·3a–3g** in cyclohexane gel, **2·3a**, **2·3d**, and **2·3f** in cyclohexane/$CHCl_3$ (1:1), and **2·3b**, **2·3c**, **2·3e**, and **2·3g** in cyclohexane.[9]


© 2006 Wiley-VCH Verlag GmbH & Co. KGaA, Weinheim

process operates only in the gel matrix, we synthesized the nongelling reference compound **2**, which has 2-ethylhexyl groups as solubilizing substituents. Figure 3b shows that the addition of the same isomers of **3** to the nongelling compound **2** in solution (in the same concentrations as before) generates drastically less-intense and less-distinct color changes. Hence, the determination of the positional isomers of dihydroxynaphthalenes with the naked eye is not possible in the solution state.

UV/Vis spectra of the various complexes (**1·3a–g**) in the gel state show clearly the significantly red-shifted and markedly more-intense charge-transfer bands relative to those in the solution state (**2·3a–g**; Figure 4). For example,

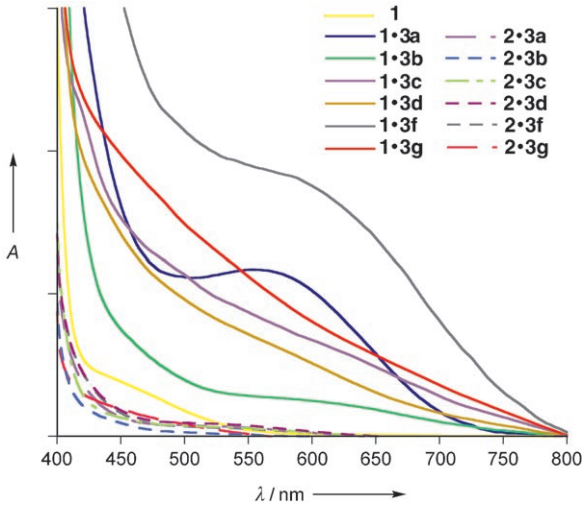



***Figure 4.*** UV/Vis spectra of **1** and the charge-transfer bands of the donor–acceptor complexes (4.0 mM) **1·3a–3g** in cyclohexane gel, **2·3a**, **2·3d**, and **2·3f** in cyclohexane/$CHCl_3$ (1:1), and **2·3b**, **2·3c**, **2·3e**, and **2·3g** in cyclohexane.[9]

the bluish-green gel of **1·3f** ($\varepsilon = 877\,M^{-1}\,cm^{-1}$) shows an impressive 70-fold enhancement in the molar absorption coefficient of the charge-transfer band relative to that of of **2·3f** in solution ($\varepsilon = 12.5\,M^{-1}\,cm^{-1}$) at $\lambda = 600$ nm. Moreover, all the color changes (from pale yellow to the respective colors) were found to be reversed by heating and could be repeated many times with the same sample (see Supporting Information). Furthermore, we found that the number of hydroxy groups is also important, since α- and β-naphthols, which are also insoluble in these solvents, do not show any binding in the gel matrix. These derivatives gradually precipitate from the gel matrix.

The **1·3f** complex exhibits the most-intense and red-shifted charge-transfer band of all of the complexes. We carried out molecular modeling studies of this complex to gain an insight into this unusually amplified recognition phenomenon. Close inspection of the energy-minimized structure of the **1·3f** complex suggested that **3f** can form the most complementary motif because the symmetrical disposition of its hydroxy groups and the carbonyl groups of the naphthalenediimide moiety result in cooperative interplay of weak H-bonding and π-stacking interactions between the electron-rich and electron-deficient rings along the 1D superstructure (see Supporting Information) of the gel matrix. Attenuated total reflectance infrared (ATR-IR) spectrometry of the xerogels (see Supporting Information) conclusively supports this view; the symmetrical and asymmetrical carbonyl group vibrations of the naphthalenediimide unit in **1** at 1706 and 1665 $cm^{-1}$ shift to 1700 and 1659 $cm^{-1}$, respectively, as a result of this weak H-bonding in the **1·3f** complex. This remarkably unusual binding property can now be rationalized as follows: a successful intercalation of the donor molecule in the gel matrix of **1** can take place only if it is energetically feasible to break the cooperatively associated π-stacked naphthalenediimides, amide H-bonds, and the closely packed alkyl chains. The dihydroxynaphthalenes, which show a cooperative H-bonding effect and π-stacked donor–acceptor interactions, can easily cross this uphill energy process, while alkoxynaphthalenes, which have a single donor–acceptor interaction, cannot compensate for the overall process.

It is notable that the solvophobic effect can facilitate the binding of the dihydroxynaphtahlenes in the organogel matrix. However, a solvophobic effect alone cannot explain this recognition process in the organogel matrix. The degree of color change with the various dihydroxynaphthalene isomers and the inability of the other hydrophilic and insoluble naphthalene derivatives (i.e. α- and β-naphthols) to bind show that a combination of various interactions such as H-bonding and donor–acceptor interactions have to be taken into account to explain this recognition process in the oragnogel matrix.[13]

The recognition of the dihydroxynaphthalene triggers a morphological modulation of the 1D fibers of organogel **1** as can be seen clearly from the SEM images (Figure 5). The long

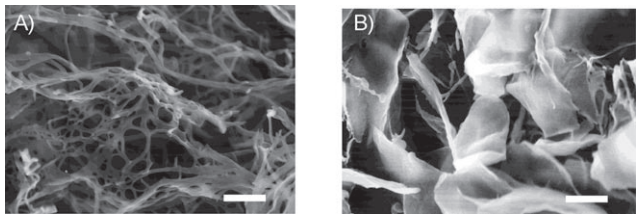



***Figure 5.*** SEM images of the xerogel of A) **1** and B) the **1·3f** complex prepared from the cyclohexane gel (4.0 mM); the scale bar denotes 1 μm.

1D fibrous network of **1** with fiber diameters of 100–200 nm, which is typical for organogels, has been transformed into a 2D sheetlike structure in the **1·3f** complex. This tranformation is not unsurprising when it is considered that the intercalation of the donor moiety creates a gap of around 7 Å between the gelator molecules (see Supporting Information); this intercalation triggers the 2D aggregation to maintain the close-packed nature of the alkyl chains.

Importantly, even minute quantities (0.2 equiv) of the dihydroxynaphthalenes (0.16 mg of **3f** in 5.0 mM of **1**) can be sensed by the naked eye with the gelator **1**. Furthermore, we found that the gel superstructure is extremely sensitive even to the upper limit of added donor molecules, since the

 © 2006 Wiley-VCH Verlag GmbH & Co. KGaA, Weinheim 

addition of more than 1.2 equivalents can readily transform the gel matrix into a sol phase (Figure 6). Therefore, this organogel-based approach becomes quite attractive, considering that conventional colorimetric sensors that operate in

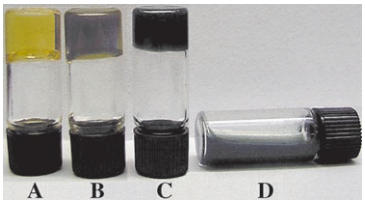



***Figure 6.*** Photograph of organogel **1** (5.0 mM in cyclohexane): A) without **3 f**; B) with 0.2 equivalents of **3 f**; C) with 1.0 equivalent of **3 f**, and D) with 1.2 equivalents of **3 f**.

solution require 10–100 equivalents of the analyte for sensing with the naked eye.[14] Although the present organogel matrix can detect analytes on the milligram scale, an improved design could lead to attractive systems that operate on the ppm scale. This development would make organogels attractive for future applications to determine environmental pollutants.

In summary, we have found a rare example of an organogel in which a multiple set of noncovalent interactions confers hostlike character to the gel matrix[15], and by virtue of this character, the organogel can perform several exciting functions. It can differentiate different classes of electron-rich naphthalene compounds such as dihydroxynaphthalenes from alkoxy- and hydroxynaphthalenes. Naked-eye differentiation of several positional isomers of dihydroxynaphthalene becomes possible as a result of an unprecedented coerced H-bonding-driven recognition that significantly amplifies the binding in the gel state.

## *Experimental Section*

Organogelator **1** and the nongelling reference compound **2** were synthesized from 1,4,5,8-naphthalenetetracarboxylic dianhydride. See the Supporting Information for experimental details on the synthesis, gelation tests, $^1$H NMR, ATR-FTIR, and UV/Vis spectrometry, MALDI TOF mass spectrometry, and SEM/TEM measurements.

Received: September 6, 2005

**Keywords:** donor–acceptor systems · host–guest systems · molecular recognition · sensors · supramolecular chemistry

[1] a) P. Terech, R. G. Weiss, *Chem. Rev.* **1997**, *97*, 3133–3159; b) J. H. van Esch, B. L. Feringa, *Angew. Chem.* **2000**, *112*, 2351–2354; *Angew. Chem. Int. Ed.* **2000**, *39*, 2263–2266; c) O. Gronwald, S. Shinkai, *Chem. Eur. J.* **2001**, *7*, 4328–4334, and references therein.

[2] a) S.-i. Kawano, N. Fujita, S. Shinkai, *J. Am. Chem. Soc.* **2004**, *126*, 8592–8593; b) S. Y. Ryu, S. Kim, J. Seo, Y.-W. Kim, O.-H. Kwon, D.-J. Jang, S. Y. Park, *Chem. Commun.* **2004**, 70–71; c) M. Ikeda, M. Takeuchi, S. Shinkai, *Chem. Commun.* **2003**, 1354–1355; d) Y. Iwashita, K. Sugiyasu, M. Ikeda, N. Fujita, S. Shinkai, *Chem. Lett.* **2004**, *33*, 1124–1125.

[3] a) K. Sugiyasu, N. Fujita, M. Takeuchi, S. Yamada, S. Shinkai, *Org. Biomol. Chem.* **2003**, *1*, 895–899; b) M. Shirakawa, S.-i. Kawano, N. Fujita, K. Sada, S. Shinkai, *J. Org. Chem.* **2003**, *68*, 5037–5044; c) M. Shirakawa, N. Fujita, S. Shinkai, *J. Am. Chem. Soc.* **2005**, *127*, 4164–4165; d) T. Kishida, N. Fujita, K. Sada, S. Shinkai, *J. Am. Chem. Soc.* **2005**, *127*, 7298–7299; e) A. Ajayaghosh, S. J. George, V. K. Praveen, *Angew. Chem.* **2003**, *115*, 346–349; *Angew. Chem. Int. Ed.* **2003**, *42*, 332–335; f) K. Sugiyasu, N. Fujita, S. Shinkai, *Angew. Chem.* **2004**, *116*, 1249–1253; *Angew. Chem. Int. Ed.* **2004**, *43*, 1229–1233.

[4] a) R. G. Duan, L. L. Miller, D. A. Tomalia, *J. Am. Chem. Soc.* **1995**, *117*, 10783–10784; b) L. Flamigni, M. R. Johnston, L. Giribabu, *Chem. Eur. J.* **2002**, *8*, 3938–3947; c) R. S. Lokey, Y. Kwok, V. Guelev, C. J. Pursell, L. H. Hurley, B. L. Iverson, *J. Am. Chem. Soc.* **1997**, *119*, 7202–7210.

[5] a) D. G. Hamilton, N. Feeder, L, Prodi, S. J. Teat, W. Clegg, J. K. M. Sanders, *J. Am. Chem. Soc.* **1998**, *120*, 1096–1097; b) D. G. Hamilton, J. E. Davies, L. Prodi, J. K. M. Sanders, *Chem. Eur. J.* **1998**, *4*, 608–620; c) S. A. Vignon, T. Jarrosson, T. Iijima, H.-R. Tseng, J. K. M. Sanders, J. F. Stoddart, *J. Am. Chem. Soc.* **2004**, *126*, 9884–9885; d) R. S. Lokey, B. L. Iverson, *Nature* **1995**, *375*, 303–305; e) J. Q. Nguyen, B. L. Iverson, *J. Am. Chem. Soc.* **1999**, *121*, 2639–2640; f) G. J. Gabriel, B. L. Iverson, *J. Am. Chem. Soc.* **2002**, *124*, 15174–15175.

[6] See the Supporting Information.

[7] Our work differs conceptually from the donor–acceptor-assisted gelation processes in that our work focuses on utilizing the 1D gel matrix to study the novel recognition processes. For donor–acceptor-induced gel formation, see: a) U. Maitra, P. V. Kumar, N. Chandra, L. J. D'Souza, M. D. Prasanna, A. R. Raju, *Chem. Commun.* **1999**, 595–596; b) A. Friggeri, O. Gronwald, K. J. C. van Bommel, S. Shinkai, D. N. Reinhoudt, *J. Am. Chem. Soc.* **2002**, *124*, 10754–10758; c) J. H. Jung, S. J. Lee, J. A, Rim, H. Lee, T.-S. Bae, S. S. Lee, S. Shinkai, *Chem. Mater.* **2005**, *17*, 459–462.

[8] A charge-transfer band due to this well-known donor–acceptor interaction has been observed by various groups: P. Talukdar, G. Bollot, J. Mareda, N. Sakai, S. Matile, *J. Am. Chem. Soc.* **2005**, *127*, 6528–6529.

[9] The recognition studies in the gel matrix of **1** were carried out in cyclohexane or decalin. Dichloromethane and chloroform, which are common solvents for studying donor–acceptor complexes, could not be used because of the inability of **1** to form a gel in these solvent. However, we had to use the mixed solvent cyclohexane/chloroform for **2**·**3 a**, **2**·**3 d**, and **2**·**3 f** to maintain the solubility of the complexes and overcome precipitation.

[10] Naphthalenediimide–pyrene complexes are well known both in solution and in the solid state. For a recent example that employs this motif, see: H. M. Colquhoun, Z. Zhu, D. J. Williams, *Org. Lett.* **2003**, *5*, 4353–4356.

[11] For donor–acceptor interactions of 2,6-dihydroxynaphthalenes in aqueous solution, see: a) H.-J. Kim, J. Heo, W. S. Jeon, E. Lee, J. Kim, S. Sakamoto, K. Yamaguchi, K. Kim, *Angew. Chem.* **2001**, *113*, 1574–1577; *Angew. Chem. Int. Ed.* **2001**, *40*, 1526–1529; b) J. W. Lee, K. Kim, S. W. Choi, Y. H. Ko, S. Sakamoto, K. Yamaguchi, K. Kim, *Chem. Commun.* **2002**, 2692–2693.

[12] ATR-IR observations show that the peaks due to C=O vibrations shifted gradually with the addition of small amounts of **3 f** from 1706 and 1665 cm$^{-1}$ to 1700 and 1659 cm$^{-1}$, respectively, until a 1:1 stoichiometry was achieved. No further changes in the C=O vibrations were observed with the addition of excess **3 f**.

[13] One of the referees has suggested that a solvophobic effect could be the major driving force for the observed interaction.

[14] R. M. Martinez, F. Sansenon *Chem. Rev.* **2003**, *103*, 4419, 4476.

[15] M. Shirakawa, N. Fujita, S. Shinkai, *J. Am. Chem. Soc.* **2003**, *125*, 9902–9903.

 © 2006 Wiley-VCH Verlag GmbH & Co. KGaA, Weinheim 

Rotaxanes

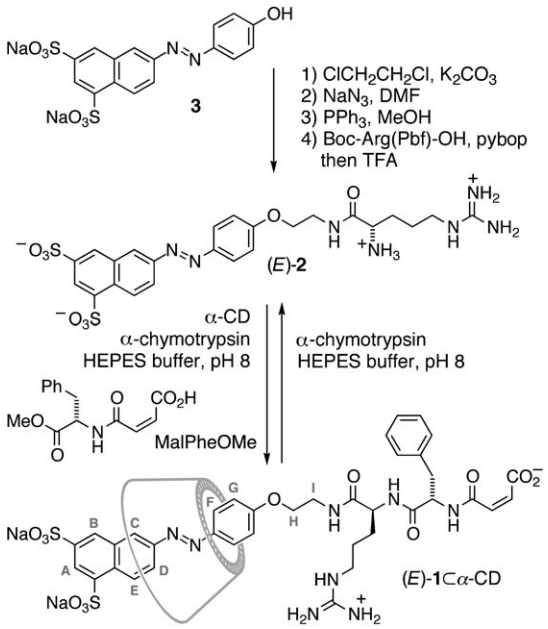
DOI: 10.1002/anie.200504064

# Enzymatic Synthesis and Photoswitchable Enzymatic Cleavage of a Peptide-Linked Rotaxane**

*Andrew G. Cheetham, Michael G. Hutchings, Tim D. W. Claridge, and Harry L. Anderson**

Cyclodextrin inclusion complexes often exhibit useful properties, such as enhanced chemical stability, fluorescence efficiency, and solubility.[1] An inclusion complex of this type can be converted into a kinetically robust rotaxane[2] by attaching bulky stoppers to both ends of the threaded guest, permanently locking it inside the cyclodextrin.[3] The hydrophobic effect is the main driving force for threading, so it is convenient to synthesize these rotaxanes in water, although this limits the range of chemistry available for covalent coupling. Enzymes are uniquely suited for catalyzing covalent-bond formation in water, so it seems surprising that they have not previously been used to catalyze rotaxane synthesis. Herein we report the chymotrypsin-catalyzed synthesis of a peptide-linked azo dye rotaxane, (*E*)-**1**⊂α-CD (CD = cyclodextrin). Rotaxanes of this type generally exhibit reversible photochemical *cis-trans* isomerization, with concomitant relocation of the cyclodextrin along the axle of the rotaxane.[4] Herein we show that photoisomerization of (*E*)-**1**⊂α-CD can be used to prevent its chymotrypsin-catalyzed hydrolysis. Although there are no previous examples of enzyme-catalyzed rotaxane synthesis, enzyme-catalyzed rotaxane cleavage has been studied in detail as an approach to drug delivery in which the enzymes naturally present are used to liberate the components of the rotaxane.[5] Photoswitchable rotaxane cleavage is relevant to this area, because it could enable a drug to be delivered selectively to cells that have a specific enzyme and that are being irradiated with light of the appropriate wavelength.

Protease-catalyzed synthesis of peptides has been investigated extensively because it offers distinct advantages over conventional chemical synthesis, such as high selectivity and lack of racemization.[6] The most common approach is amination of an amino acid ester under kinetic control. The ester acts as an acyl donor and gives an acyl enzyme intermediate, which then acylates the amine to form the peptide bond. A variety of serine and cysteine proteases can be used, and we chose the serine protease α-chymotrypsin because it is readily available and requires no preactivation. To effect efficient peptide coupling, the acyl donor (ester) and acyl acceptor (amine) must be tailored to suit the active site of the enzyme and to match the $S_1$ and $S_1'$ specificities ($S_1$ and $S_1'$ are the binding sites for amino acid residues on the donor and acceptor sides of the new amide bond, respectively).[7] For α-chymotrypsin, the $S_1$ site prefers large hydrophobic side chains, while the $S_1'$ site prefers cationic amino acid residues.[8] Accordingly, a phenylalanine-based donor, MalPheOMe, and an arginine-based acceptor, (*E*)-**2**, were chosen as the substrates for our enzyme-catalyzed rotaxane synthesis. The arginine-substituted azo dye, (*E*)-**2**, was synthesized in four steps from the phenol **3**, as shown in Scheme 1.




***Scheme 1.*** Enzymatic synthesis and hydrolysis of the rotaxane (*E*)-**1**⊂α-CD. Boc-Arg(Pbf)-OH = $N_\alpha$-*tert*-butoxycarbonyl-$N_\omega$-(2,2,4,6,7-pentamethyldihydrobenzofuran-5-sulfonyl)-L-arginine; DMF = *N*,*N*-dimethylformamide; HEPES = 4-(2-hydroxyethyl)piperazine-1-ethanesulfonic acid; Mal = maleyl; pybop = (benzotriazol-1-yloxy)tripyrrolidinophosphonium hexafluorophosphate; TFA = trifluoroacetic acid.

The α-chymotrypsin-catalyzed acylation of (*E*)-**2** was monitored by HPLC (Figure 1). Use of excess acyl donor (10 equiv) and excess α-cyclodextrin (15 equiv) gave 87% conversion into the rotaxane (*E*)-**1**⊂α-CD after 20 min. However, at longer reaction times the enzyme hydrolyzes the rotaxane back to (*E*)-**2** by selective cleavage of the PheArg link. Stopping the reaction after 20 min and purification by reversed-phase and anion-exchange chromatography enabled the rotaxane to be isolated in 37% yield. The same reaction in the absence of cyclodextrin gave the dumbbell peptide azo dye (*E*)-**1** in 48% yield. When a dumbbell with non-equivalent ends, such as (*E*)-**1**, is threaded through a cyclodextrin with non-equivalent rims, there is the

[*] A. G. Cheetham, Dr. T. D. W. Claridge, Prof. H. L. Anderson
Department of Chemistry, Chemistry Research Laboratory
University of Oxford
12 Mansfield Road, Oxford, OX1 3TA (UK)
Fax: (+44) 1865-28-5002
E-mail: harry.anderson@chem.ox.ac.uk
Dr. M. G. Hutchings
DyStar UK Ltd., School of Chemistry
University of Manchester
Oxford Road, Manchester, M13 9PL (UK)

[**] We thank the Engineering and Physical Sciences Council (EPSRC) and DyStar UK Ltd. for supporting this work.

Supporting information for this article is available on the WWW under http://www.angewandte.org or from the author.


InterScience
© 2006 Wiley-VCH Verlag GmbH & Co. KGaA, Weinheim

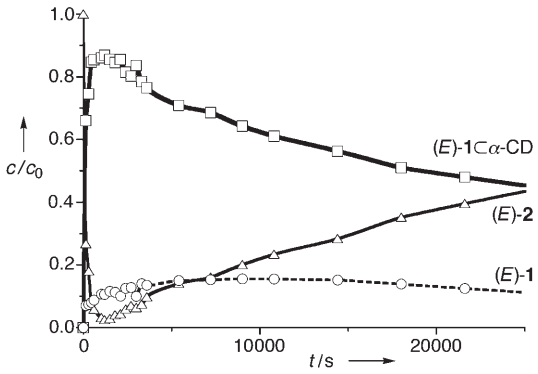



***Figure 1.*** HPLC data showing the formation of rotaxane (*E*)-**1**⊂α-CD over time, as in Scheme 1. All concentrations are normalized by dividing by the initial concentration of (*E*)-**2**. The conversion into (*E*)-**1**⊂α-CD peaks at 87% after 20 min, whereas the concentration of (*E*)-**1** peaks at 16% after 150 min, and the concentration of (*E*)-**2** reaches a minimum of 2.5% after 20 min. The concentration of MalPheOMe (not plotted here) becomes less than 1% of its initial value after 20 min. Initial concentrations: [(*E*)-**2**] = 1.57 mM, [MalPheOMe] = 15.7 mM, [α-CD] = 23.6 mM, [α-chymotrypsin] = 0.3 μM. Buffer: HEPES 0.1 M, NaCl 0.2 M, $CaCl_2$ 0.02 M, pH 8.

possibility of forming two stereoisomers. HPLC analysis indicates that rotaxane (*E*)-**1**⊂α-CD is formed as a single isomer, and this observation was supported by $^1$H and $^{13}$C NMR spectroscopic analysis. $^1$H NMR NOESY experiments showed that the wide 2,3-rim of the cyclodextrin is directed towards the sulfonate groups, while the narrower 6-rim is directed towards the peptide. For example, $H_C$ shows a strong NOE interaction with 3-H of the cyclodextrin (and a weak one with 5-H, but none with 6-H or 6′-H), whereas $H_F$ shows strong NOE interactions with 5-H, 6-H and 6′-H, but none with 3-H. Surprisingly, NOE investigations of the (*E*)-**2**⊂α-CD inclusion complex revealed that the dominant isomer of this complex has the opposite cyclodextrin orientation,[9] implying that the enzyme determines the stereochemistry of the rotaxane by kinetic selection of the less stable isomer of this inclusion complex.

The $E \rightarrow Z$ photoisomerization of (*E*)-**1**⊂α-CD and (*E*)-**1** in aqueous solution was monitored by HPLC and $^1$H NMR spectroscopy. Irradiation at 368 nm gave photostationary mixtures dominated by the *Z* isomers, whereas irradiation at 445 nm rapidly shifted the composition back towards the *E* isomers. This photochemistry is cleanly reversible and no by-products were detected by HPLC or NMR spectroscopy. The rate of dark thermal $Z \rightarrow E$ isomerization was measured for both the rotaxane (*Z*)-**1**⊂α-CD and the dumbbell (*Z*)-**1** in aqueous solution at 297 K and 277 K. In each case, the reaction is first order, and isomerization is faster in the rotaxane ($t_{1/2} = 5.4 \pm 0.3$ h at 297 K and $72 \pm 10$ h at 277 K) than in the dumbbell ($t_{1/2} = 34 \pm 3$ h at 297 K and $> 200$ h at 277 K). Thus the presence of the cyclodextrin destabilizes the *Z* isomer of the azo dye and decreases the activation energy for thermal isomerization (as noticed in similar rotaxanes by Nakashima and co-workers[4b]). NOE analysis of (*E*)-**1**⊂α-CD and (*Z*)-**1**⊂α-CD in $D_2O$ showed that $E \rightarrow Z$ photoisomerization of the rotaxane results in relocation of the α-cyclodextrin from the azo region to the phenoxyethyl moiety adjacent to the dipeptide stopper. For example, in (*Z*)-**1**⊂α-CD, $H_C$ shows no NOE interactions with cyclodextrin protons, whereas $H_F$ and $H_H$ show NOE interactions with 3-H and 5-H, respectively (Figure 2a).

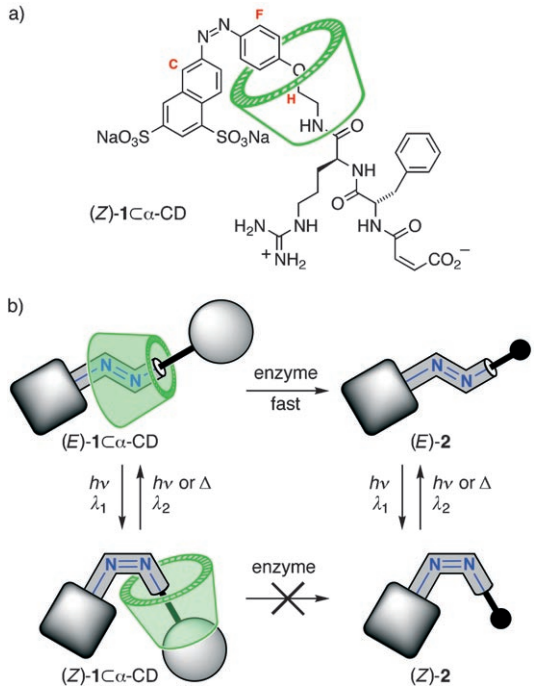



***Figure 2.*** a) Co-conformation of (*Z*)-**1**⊂α-CD deduced from NOE measurements. b) Schematic representation of photoisomerization and enzyme-catalyzed cleavage of the PheArg peptide bond, which decreases the bulk of the end group and results in unthreading of the cyclodextrin ($\lambda_1 = 368$ nm, $\lambda_2 = 445$ nm).

The relative rates of enzyme-catalyzed hydrolysis of (*E*)-**1**⊂α-CD, (*Z*)-**1**⊂α-CD, (*E*)-**1**, and (*Z*)-**1** were tested by monitoring the hydrolysis of a mixture of these four compounds simultaneously by HPLC, to test whether photoswitching can be used to control enzymatic hydrolysis (Figure 2b). The reaction was carried out at 277 K in the dark at high enzyme concentration to minimize thermal or photochemical $Z \rightarrow E$ isomerization. The data from this experiment were fitted to first order decay curves to give the pseudo-first-order rate constants indicated in Figure 3.[10] The *E* and *Z* isomers of the dumbbell **1** are hydrolyzed at the same rate, whereas (*E*)-**1**⊂α-CD is hydrolyzed more than 80 times faster than (*Z*)-**1**⊂α-CD. The slower hydrolysis of the *Z* rotaxane shows that when the cyclodextrin shifts towards the peptide link it hinders interaction with the enzyme; thus the reactivity of the peptide can be controlled by photoisomerization. (*Z*)-**1**⊂α-CD is hydrolyzed so slowly that, under the conditions of this experiment, thermal $Z \rightarrow E$ isomerization dominates, and we can only estimate an upper limit to its rate of hydrolysis.

It seems amazing that the bulky rotaxane (*E*)-**1**⊂α-CD is hydrolyzed 2.6 times faster than the corresponding dumbbell (*E*)-**1** (Figure 3). This implies that the cyclodextrin increases the affinity of the peptide for the active site of chymotryp-

 © 2006 Wiley-VCH Verlag GmbH & Co. KGaA, Weinheim 

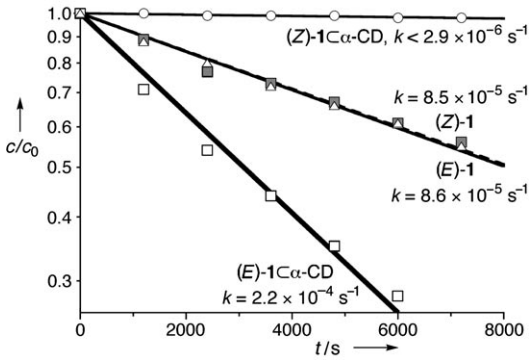



***Figure 3.*** Plot of normalized concentration ($c/c_0$) of (*E*)-**1**⊂α-CD (□), (*Z*)-**1**⊂α-CD (○), (*E*)-**1** (△), and (*Z*)-**1** (■) against time (*t*) during competitive α-chymotrypsin-catalyzed hydrolysis, showing values of pseudo-first-order rate constants. The reaction was monitored by HPLC at 277 K in the dark; initial concentrations: [**1**⊂α-CD] = 1.2 mM, [**1**] = 1.2 mM and [α-chymotrypsin] = 12 μM.[10] These rate constants have error margins of about 30%, but their relative values are accurate to ±5% owing to the nature of the competition experiment.

sin.[11] This conclusion is supported by the selective formation of this stereoisomer of the rotaxane (*E*)-**1**⊂α-CD, despite the fact that the other stereoisomer of the inclusion complex (*E*)-**2**⊂α-CD predominates in solution. We carried out molecular-mechanics calculations on the α-chymotrypsin/(*E*)-**1**⊂α-CD complex (with the PheArg peptide bound to the active site of the enzyme) to gain insight into the factors stabilizing this complex. The energy-minimized structure (Figure 4) shows that the cyclodextrin lies close to the surface of the enzyme and indicates a hydrogen-bonding interaction between the OH group of tyrosine 146 and O6 on the narrow rim of the cyclodextrin.[12] Interactions of this type may explain why the presence of the cyclodextrin increases the affinity of the peptide for the enzyme.

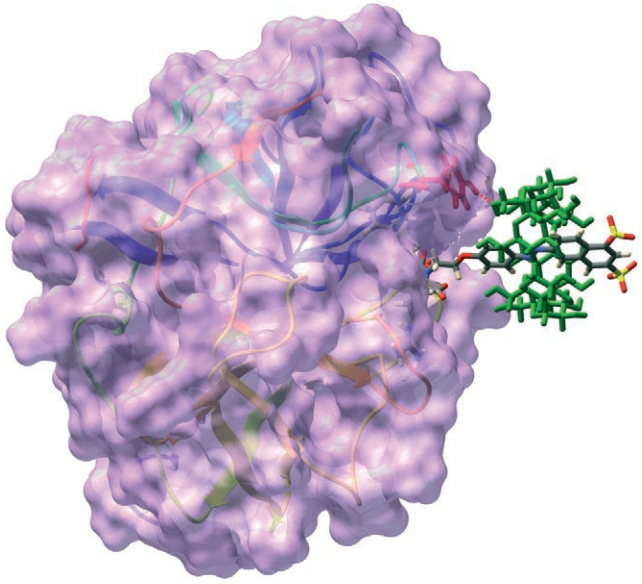


***Figure 4.*** Calculated structure of the α-chymotrypsin/(*E*)-**1**⊂α-CD complex, with PheArg bound in the active site of the enzyme. The tyrosine-146 residue (shown in red, top left of rotaxane) is hydrogen bonded to O6 of the cyclodextrin. (Other protein residues not displayed; enzyme surface: 1.4-Å probe radius; α-cyclodextrin green.)[12]

In conclusion, we have shown that enzymes can be used to synthesize cyclodextrin rotaxanes rapidly and selectively under mild conditions. This chemistry should be useful for the synthesis of encapsulated dyes[3] and insulated molecular wires.[13] The observation that photoisomerization of (*E*)-**1**⊂α-CD turns off its reactivity towards enzyme-catalyzed hydrolysis can also be regarded as a first step towards photoswitchable rotaxane-mediated drug delivery.

Received: November 15, 2005
Published online: February 3, 2006

**Keywords:** azo compounds · enzyme catalysis · peptides · photochemistry · rotaxanes

[1] *Comprehensive Supramolecular Chemistry, Vol. 3* (Eds: J. L. Atwood, J. E. D. Davies, D. D. MacNichol, F. Vögtle), Pergamon, Oxford, UK, **1996**.
[2] S. A. Nepogodiev, J. F. Stoddart, *Chem. Rev.* **1998**, *98*, 1959–1976; F. M. Raymo, J. F. Stoddart, *Chem. Rev.* **1999**, *99*, 1643–1663; A. Harada, *Acc. Chem. Res.* **2001**, *34*, 456–464.
[3] a) J. E. H. Buston, J. R. Young, H. L. Anderson, *Chem. Commun.* **2000**, 905–906; b) C. A. Stanier, M. J. O'Connell, W. Clegg, H. L. Anderson, *Chem. Commun.* **2001**, 493–494, 787; c) M. R. Craig, M. G. Hutchings, T. D. W. Claridge, H. L. Anderson, *Angew. Chem.* **2001**, *113*, 1105–1108; *Angew. Chem. Int. Ed.* **2001**, *40*, 1071–1074.
[4] a) H. Murakami, A. Kawabuchi, K. Kotoo, M. Kunitake, N. Nakashima, *J. Am. Chem. Soc.* **1997**, *119*, 7605–7606; b) H. Murakami, A. Kawabuchi, R. Matsumoto, T. Ido, N. Nakashima, *J. Am. Chem. Soc.* **2005**, *127*, 15891–15899; c) D.-H. Qu, Q.-C. Wang, J. Ren, H. Tian, *Org. Lett.* **2004**, *6*, 2085–2088.
[5] a) M. Eguchi, T. Ooya, N. Yui, *J. Controlled Release* **2004**, *96*, 301–307; b) T. Ooya, K. Arizono, N. Yui, *Polym. Adv. Technol.* **2000**, *11*, 642–651; c) T. Ooya, N. Yui, *J. Controlled Release* **1999**, *58*, 251–269.
[6] a) F. Bordusa, *Chem. Rev.* **2002**, *102*, 4817–4867; b) V. Schellenberger, H.-D. Jakubke, *Angew. Chem.* **1991**, *103*, 1440; *Angew. Chem. Int. Ed. Engl.* **1991**, *30*, 1437–1449.
[7] This nomenclature was introduced by I. Schechter, A. Berger, *Biochem. Biophys. Res. Commun.* **1969**, *37*, 157–162.
[8] V. Schellenberger, U. Schellenberger, Y. V. Mitin, H.-D. Jakubke, *Eur. J. Biochem.* **1990**, *187*, 163–167.
[9] UV/Vis titration of (*E*)-**2** and α-cyclodextrin, carried out under the same conditions as the enzymatic synthesis (HEPES buffer, pH 8, 22 °C), gave data which fit well to a 1:1 binding isotherm with a binding constant of $K = 2.5 \pm 0.2 \times 10^3\ \text{M}^{-1}$. $^1$H NMR titration showed the formation of two 1:1 complexes, in a ratio of 1:10. These complexes undergo slow exchange on the chemical shift timescale, with each other and with excess (*E*)-**2**, but exchange cross-peaks were observed during NOESY experiments, and the complexes appeared to form immediately on addition of the cyclodextrin; hence the exchange rate is probably in the 1-s$^{-1}$ regime. The dominant isomer of the (*E*)-**2**⊂α-CD inclusion complex gave NOE interactions of $H_C$ and $H_D$ with both 5-H and 6-H, $H_F$ with both 3-H and 5-H, and $H_G$ with 3-H, indicating that it has the opposite cyclodextrin orientation to the (*E*)-**1**⊂α-CD rotaxane. The $^1$H NMR spectrum of the minor isomer of the (*E*)-**2**⊂α-CD inclusion complex is very similar to that of the (*E*)-**1**⊂α-CD rotaxane, leading us to conclude that these two species have the same cyclodextrin

 © 2006 Wiley-VCH Verlag GmbH & Co. KGaA, Weinheim 

orientation, and this is supported by the observation of NOE interactions of $H_C$ with 3-H, and $H_G$ with 6-H, 6′-H, and 5-H.

[10] The pseudo-first-order rate constants marked in Figure 3 are simply the gradients of the straight-line fits. Under these conditions the rate constants for thermal $Z \rightarrow E$ isomerization of (*Z*)-**1** and (*E*)-**1**⊂α-CD are $< 1 \times 10^{-6}\ s^{-1}$ and $(2.7 \pm 0.4) \times 10^{-6}\ s^{-1}$, respectively; hence, thermal isomerization makes no significant contribution to the loss of (*Z*)-**1**, but it accounts for at least 90% of the loss of (*Z*)-**1**⊂α-CD.

[11] The presence of the cyclodextrin in (*E*)-**1**⊂α-CD may accelerate enzymatic hydrolysis by lowering the Michaelis constant $K_M$ or by increasing the turnover number $k_{cat}$. We plan to carry out Michaelis–Menten analysis to address this issue.

[12] The α-chymotrypsin/(*E*)-**1**⊂α-CD complex was modelled by using the Maestro software (from Schrödinger LLC) starting from the crystallographic coordinates of α-chymotrypsin (PDB ID: 6CHA; A. Tulinsky, R. A. Blevins, *J. Biol. Chem.* **1987**, *262*, 7737–7743) and of the methyl orange α-CD complex (K. Harata, *Bull. Chem. Soc. Jpn.* **1976**, *49*, 1493–1501). The structure was minimized by using MacroModel (Schrödinger LLC), with the MMFFs force field, with water as the solvent, and with the Polak–Ribier Convergence Gradient Method at a convergence threshold of 0.005. During this calculation the geometry of the azo group was constrained to be planar, and the carbonyl of the Phe residue of the rotaxane was constrained to be within hydrogen-bonding distance of Ser-195 and Gly-193. The calculated structure (Figure 4) features the following intercomponent hydrogen bonds: Gly193-NH to C=O of $Arg_{rotax}$ (2.2 Å); Arg-$NH_2(1)_{rotax}$ to C=O of Phe-41 (2.0 Å); Arg-NH-(Guan.)$_{rotax}$ to C=O of Phe-41 (1.8 Å); Arg-$NH_2(2)_{rotax}$ to C=O of Cys-58 (1.9 Å); Phe-$NH_{rotax}$ to N-imidazole of His-57 (2.8 Å); Phe-$NH_{rotax}$ to OH of Ser-195 (2.7 Å); Arg-$NH_{rotax}$ to OH of Ser-195 (1.7 Å); α-CD 2-OH to 3-$SO_3$ (1.8 Å); Tyr-146-OH to α-CD 6-OH (1.7 Å). Molecular-mechanics calculations were also performed on both isomers of the (*E*)-**2**⊂α-CD inclusion complex bound to the enzyme. Similar interactions were predicted for both isomers; however, the level of these calculations is not sufficient to probe the origins of the exclusive formation of one isomer of the rotaxane.

[13] F. Cacialli, J. S. Wilson, J. J. Michels, C. Daniel, C. Silva, R. H. Friend, N. Severin, P. Samori, J. P. Rabe, M. J. O'Connell, P. N. Taylor, H. L. Anderson, *Nat. Mater.* **2002**, *1*, 160–164.

 © 2006 Wiley-VCH Verlag GmbH & Co. KGaA, Weinheim 

Homogeneous Catalysis

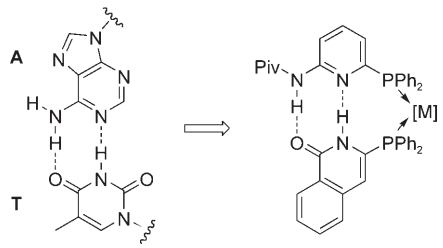
DOI: 10.1002/anie.200503826

# Self-Assembled Bidentate Ligands for Ru-Catalyzed *anti*-Markovnikov Hydration of Terminal Alkynes**

*Floris Chevallier and Bernhard Breit**

The regioselective functionalization of terminal alkynes is a fundamental process in organic synthesis since it allows the installation of a variety of important functional groups into an existing carbon skeleton.[1] Among these reactions, the addition of water across a triple bond generally follows the Markovnikov rule.[2] On the other hand, an *anti*-Markovnikov hydration of terminal alkynes could be a convenient way to the preparation of aldehydes, but so far only a few ruthenium complexes have been identified which allowed the catalysis of this unusual hydration mode.[3] The presence of bidentate phosphine ligands,[3b] the coordination of a water molecule stabilized by hydrogen bonding,[3e] and the use of phosphinopyridine ligands[3f] seem to be of major importance in these processes.

In the course of our investigation on the formation of bidentate ligands through hydrogen bonding,[4] we recently reported the construction of homodimeric[5] and heterodimeric[6] bidentate ligands by employing self-assembly.[7] In the latter case, an adenine/thymine base-pair analogous system was used: the aminopyridine/isoquinolone platform (Scheme 1).




***Scheme 1.*** Self-assembly through hydrogen bonding of the adenine/thymine and aminopyridine/isoquinolone systems.

The first bidentate-phosphine ligand library for homogeneous metal-complex catalysis based on self-assembly through hydrogen bonding was realized, and these ligands furnished an active rhodium catalyst for the regioselective

[*] Dr. F. Chevallier, Prof. Dr. B. Breit
Institut für Organische Chemie und Biochemie
Albert-Ludwigs-Universität Freiburg
Albertstrasse 21, 79104 Freiburg (Germany)
Fax: (+49) 761-203-8715
E-mail: bernhard.breit@orgmail.chemie.uni-freiburg.de

[**] The authors would like to thank the DFG (GRK 1038), the Fonds der Chemischen Industrie, the Alfried-Krupp Award for young university teachers (B.B.) for financial support, and Dr. M. Keller for solving the X-ray crystal structure analyses of **5**.

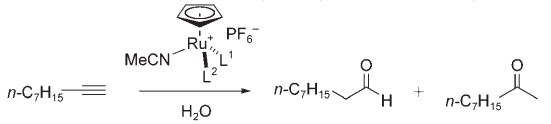

© 2006 Wiley-VCH Verlag GmbH & Co. KGaA, Weinheim

hydroformylation of terminal alkenes. Interestingly, these self-assembly systems incorporate a pyridinyl-functionalized phosphine ligand, emulate chelation, and contain a hydrogen-bonding network that may be suited to activating a molecule of water through further hydrogen bonding. Hence, the self-assembly ligand systems incorporate all the features that seem essential to allow a ruthenium-catalyzed *anti*-Markovnikov addition of water to a terminal alkyne.

In a first set of experiments, we studied the catalytic activity of a variety of half-sandwich ruthenium complexes bearing monodentate and bidentate phosphine ligands in the course of hydrating 1-nonyne as the test substrate. The ruthenium complexes used in this study were obtained in good yields (73–92%) by mixing one equivalent of each ligand in the presence of one equivalent of $[CpRu(CH_3CN)_3]PF_6$ (Cp = cyclopentadiene)[8] and subsequent precipitation with diethyl ether.

The results of the catalytic hydration are depicted in Table 1. Thus, triphenylphosphine, 2-diphenylphosphinopyridine and bis(diphenylphosphino)ethane (dppe) gave ruthenium complexes that performed with very low catalytic activity and selectivity. Using the 6-DPPon ligand, which should allow for self-dimerization based on hydrogen bonding between the pyridone form and its hydroxypyridine tautomer,[5] a similarly disappointing result was obtained. Conversely, on employing the self-assembled heterodimeric aminopyridine/isoquinolone bidentate ligands (entry 5; see also Scheme 1),[6] a catalyst was obtained that operated with outstanding activity and perfect regioselectivity. It is obvious from entries 6 and 7 that the self-assembled heterodimer is responsible for this interesting result. Thus, neither 6-DPPAP nor 3-DPICon ligands alone provided an active catalyst.

***Table 1:*** Ruthenium complex-catalyzed hydration of 1-nonyne.




| Entry | Cat. | L[1][a] | L[2][a] | *t* [h] | **a** [%][b] | **k** [%][b] |
|---|---|---|---|---|---|---|
| 1 | **1** | $PPh_3$ | $PPh_3$ | 140 | 1.2 | 18 |
| 2 | **2**[c] | dppy | dppy | 168 | 4.0 | 2.4 |
| 3 | **3** | dppe | – | 168 | 2.1 | 20 |
| 4 | **4**[c] | 6-DPPon | 6-DPPon | 168 | 2.1 | 25 |
| 5 | **5** | 6-DPPAP | 3-DPICon | 26 | 94 | 0 |
| 6 | **6**[c] | 6-DPPAP | 6-DPPAP | 72 | 39 | 3.8 |
| 7 | **7** | 3-DPICon | 3-DPICon | 48 | 1.9 | 0 |

[a] dppy: 2-diphenylphosphinopyridine, dppe: 1,2-bis(diphenylphosphino)ethane, 6-DPPon: 6-diphenylphosphino-2-pyridone, 6-DPPAP: 6-diphenylphosphino-*N*-pivaloyl-2-aminopyridine, 3-DPICon: 3-diphenylphosphinoisoquinolone. [b] Yield calculated from GC response factors relative to hexadecane internal standard. a = aldehyde, k = ketone. [c] $\eta^1$-P,$\eta^2$-P,N coordination of the phosphinopyridine with replacement of the acetonitrile ligand.

Moreover, modifications of the aminopyridine and isoquinolone ligands with electron-donating and electron-withdrawing substituents furnished a $3 \times 3$ library of self-assembling ligands (Table 2). As no superior catalyst could be identified, we decided to focus on **5**.

***Table 2:*** Ligand matrix ($3 \times 3$) of aminopyridine/isoquinolone-derived self-assembled bidentate ligands in the Ru-catalyzed hydration of 1-nonyne.

| | Aminopyridine[b] | | |
|---|---|---|---|
| Isoquinolone[b] | 6-DPPAP | 6-D(*p*-MeO)PPAP | 6-D(*p*-F)PPAP |
| 3-DPICon | 94:0[a] | 77:0 | 84:1.8 |
| 3-D(*p*-MeO)PICon | 60:0 | 60:1.2 | 66:1.8 |
| 3-D(*p*-F)PICon | 78:1.0 | 71:2.2 | 70:4.9 |

[a] Yield of aldehyde/ketone products (%) determined by GC after 26 h. [b] 6-D(*p*-MeO)PPAP: 6-bis-(4-methoxyphenyl)-phosphino-2-(pivaloylamino)-pyridine, 6-D(*p*-F)PPAP: 6-bis(4-fluorophenyl)phosphino-2-(pivaloylamino)-pyridine, 3-D(*p*-MeO)PICon: 3-bis(4-methoxyphenyl)phosphinoisoquinolone, 3-D(*p*-F)PICon: 3-bis(4-fluorophenyl)phosphinoisoquinolone.

To get more structural information on the optimal catalyst **5**, the heterodimer-ligand formation based on self-assembly through hydrogen bonding was studied in solution by $^{31}P$ NMR spectroscopic analysis. Thus, a clean AB system with a $^2J$(P-P) coupling constant of 35.9 Hz confirms the presence of two nonequivalent phosphine ligands coordinated at the same metal center (Figure 1).[9] Additionally, $^1H$ NMR experiments in $CDCl_3$ and [D$_6$]acetone show a substantial shift of the 6-DPPAP and 3-DPICon NH signals to low field after addition of $[CpRu(CH_3CN)_3]PF_6$, which is in agreement with hydrogen bonding. Furthermore NOE interactions observed in a solution of [D$_6$]acetone containing residual water confirm the existence of the hydrogen-bonding network under these conditions.

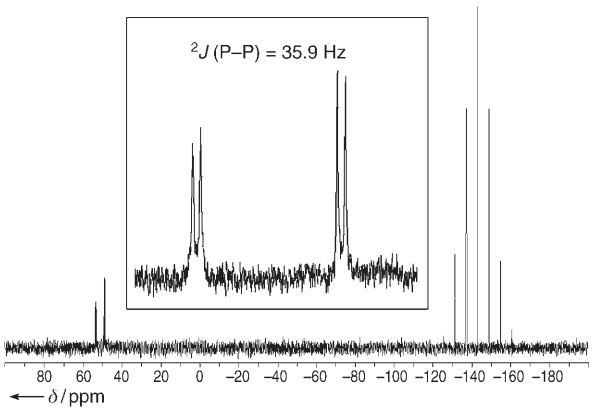



***Figure 1.*** $^{31}P$ NMR spectrum of $[CpRu(CH_3CN)(6\text{-DPPAP})(3\text{-DPICon})]PF_6$ (**5**) in solution with $CDCl_3$.

Single crystals suitable for X-ray diffraction were obtained from slow diffusion of cyclohexane into a concentrated solution of **5** in dichloromethane.[10,11] As proposed, the aminopyridine and isoquinolone ligands form the expected hydrogen-bonding network reminiscent of the Watson–Crick base pairing of A and T in DNA (Figure 2).[12]

 © 2006 Wiley-VCH Verlag GmbH & Co. KGaA, Weinheim 

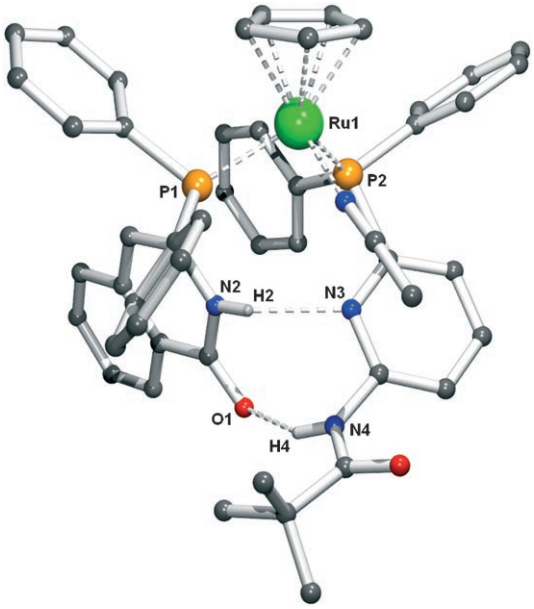
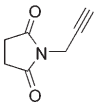
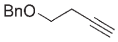
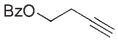
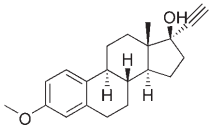



***Figure 2.*** PLATON plot of **5** (H atoms bound to the carbon atoms and the $PF_6^-$ counterion are omitted for clarity). Selected interatomic distances [Å] and angles [°]: Ru1-P1 2.3366(7), Ru1-P2 2.3193(8), H2···N3 2.811(3), O1···H4 2.846(3); P1-Ru1-P2 98.20(3), N2-H2···N3 135.35(3), O1···H4-N4 147.50(3).

The scope of the *anti*-Markovnikov hydration of various 1-alkynes was examined with **5** as the catalyst (Table 3). Reactions using 2–10 mol% of **5** gave the desired aldehydes in good yields. Linear terminal alkynes furnished the corresponding carbonyl products with complete regioselectivity, even if the catalyst seems to be partially inhibited by the presence of a nitrile group, which may act as a competing ligand for the ruthenium center (entries 1–3).[3b] 1,9-Decadiyne was converted into the corresponding dialdehyde in 78% yield, with only traces of the monoaldehyde (entry 4). The regioselectivity is excellent for a range of different functionalized substrates (entries 1–7, 9, and 10), with only one exception: a homopropargylic system bearing a benzoate function (entry 8). In this case, the regioselectivity is slightly diminished, which may be because of a chelation effect. Finally, a steroid ring system substituted by a propargylic alcohol reacted with water and gave the γ-hydroxy aldehyde selectively in 61% yield (entry 10). It should be noted that in this example the reaction was carried out at 70°C to avoid degradation of the product into an α,β-unsaturated aldehyde.[13]

In summary, the present study highlights the utility of bidentate ligands generated by the self-assembly of monodentate ligands through complementary hydrogen bonding for homogeneous catalysis. Thus, a new ruthenium catalyst was identified, which allows highly regioselective *anti*-Markovnikov hydration of terminal alkynes compatible with a wide range of functional groups. Although at this stage, the origin of the catalytic activity remains unknown, the hydrogen-bonding network may play an important role besides emulation of bidentate ligand binding.[14]

***Table 3:*** Regioselective hydration of functionalized terminal alkynes with **5** as the catalyst.

| Entry | Substrate | **5**[%] | *t* [h] | **a/k** [%][a] | Yield [%][b] |
|---|---|---|---|---|---|
| 1 | $n$-$C_7H_{15}$— | 2 | 26 | >99:1 | 89 |
| 2 | Ph— | 2 | 26 | >99:1 | 73 |
| 3 | N≡$(CH_2)_3$— | 10 | 96 | >99:1 | 78 |
| 4 | —$(CH_2)_6$— | 10 | 78 | 99:1[c] | 82 |
| 5 |  | 5 | 70 | >99:1 | 87 |
| 6 |  | 5 | 72 | 99:1 | 65 |
| 7 |  | 5 | 48 | 99:1 | 83 |
| 8 |  | 5 | 50 | 87:13 | 74 |
| 9 |  | 5 | 28 | 96:4 | 91 |
| 10[d] |  | 10 | 124 | >99:1 | 61 |

[a] Determined by GC analysis and $^1$H NMR spectroscopy. a = aldehyde, k = ketone. [b] Yield of isolated product. [c] Ratio of decane-1,10-dial/9-oxodecanal. [d] Reaction performed at 70°C.

## Experimental Section

Representative procedure: Freshly prepared **5** (21 mg, 2 mol%) was added to a solution of 1-nonyne (124 mg, 1.0 mmol) and water (90 mg, 5.0 mmol) in deoxygenated acetone (1.6 mL). The mixture was heated under Ar for 26 h at 120°C in a sealed tube and the reaction progress was monitored by GC. After cooling to room temperature, the solvent was removed in vacuo and the residue was extracted with diethyl ether. The solution was dried ($MgSO_4$), filtered through a plug of silica, and concentrated under reduced pressure to furnish nonanal (126 mg, 89%) as a colorless oil.

Received: October 28, 2005
Published online: January 31, 2006

**Keywords:** alkynes · homogeneous catalysis · hydrogen bonding · ruthenium · self-assembly

[1] M. Beller, J. Seayad, A. Tillack, H. Jiao, *Angew. Chem.* **2004**, *116*, 3448–3479; *Angew. Chem. Int. Ed.* **2004**, *43*, 3368–3398.

[2] a) Y. Fukuda, K. Utimoto, *J. Org. Chem.* **1991**, *56*, 3729–3731; b) J. Blum, H. Huminer, H. Alper, *J. Mol. Catal.* **1992**, *75*, 153–160; c) J. W. Hartman, W. C. Hiscox, P. W. Jennings, *J. Org. Chem.* **1993**, *58*, 7613–7614; d) W. Baidossi, M. Lahav, J. Blum, *J. Org. Chem.* **1997**, *62*, 669–672; e) T. Tsuchimoto, T. Joya, E. Shira-

 © 2006 Wiley-VCH Verlag GmbH & Co. KGaA, Weinheim 

kawa, Y. Kawakami, *Synlett* **2000**, 1777 – 1778; f) E. Mizushima, K. Sato, T. Hayashi, M. Tanaka, *Angew. Chem.* **2002**, *114*, 4745 – 4747; *Angew. Chem. Int. Ed.* **2002**, *41*, 4563 – 4565; g) R. Casado, M. Contel, M. Laguna, P. Romero, S. Sanz, *J. Am. Chem. Soc.* **2003**, *125*, 11925 – 11935; h) A. Vasudevan, M. K. Verzal, *Synlett* **2004**, 631 – 634.

[3] a) M. Tokunaga, Y. Wakatsuki, *Angew. Chem.* **1998**, *110*, 3024 – 3027; *Angew. Chem. Int. Ed.* **1998**, *37*, 2867 – 2869; b) T. Suzuki, M. Tokunaga, Y. Wakatsuki, *Org. Lett.* **2001**, *3*, 735 – 737; c) P. Alvarez, M. Bassetti, J. Gimeno, G. Mancini, *Tetrahedron Lett.* **2001**, *42*, 8467 – 8470; d) M. Tokunaga, T. Suzuki, N. Koga, T. Fukushima, A. Horiuchi, Y. Wakatsuki, *J. Am. Chem. Soc.* **2001**, *123*, 11917 – 11924; e) D. B. Grotjahn, C. D. Incarvito, A. L. Rheingold, *Angew. Chem.* **2001**, *113*, 4002 – 4005; *Angew. Chem. Int. Ed.* **2001**, *40*, 3884 – 3887; f) D. B. Grotjahn, D. A. Lev, *J. Am. Chem. Soc.* **2004**, *126*, 12232 – 12233.

[4] B. Breit, *Angew. Chem.* **2005**, *117*, 6976 – 6986; *Angew. Chem. Int. Ed.* **2005**, *44*, 6816 – 6825.

[5] B. Breit, W. Seiche, *J. Am. Chem. Soc.* **2003**, *125*, 6608 – 6609.

[6] B. Breit, W. Seiche, *Angew. Chem.* **2005**, *117*, 1666 – 1669; *Angew. Chem. Int. Ed.* **2005**, *44*, 1640 – 1643.

[7] For alternative approaches to bidentate ligands through self-assembly, see ref. [4] and: J. M. Takacs, D. S. Reddy, S. A. Moteki, D. Wu, H. Palencia, *J. Am. Chem. Soc.* **2004**, *126*, 4494 – 4495; M. J. Wilkinson, P. W. N. M. van Leeuwen, J. N. H. Reek, *Org. Biomol. Chem.* **2005**, *3*, 2371 – 2383; V. F. Slagt, M. Röder, P. C. J. Kamer, P. W. N. M. van Leeuwen, J. N. H. Reek, *J. Am. Chem. Soc.* **2004**, *126*, 4056 – 4057; V. F. Slagt, P. W. N. M. van Leeuwen, J. N. H. Reek, *Angew. Chem.* **2003**, *115*, 5777 – 5781; *Angew. Chem. Int. Ed.* **2003**, *42*, 5619 – 5623; V. F. Slagt, P. W. N. M. van Leeuwen, J. N. H. Reek, *Chem. Commun.* **2003**, 2474 – 2475.

[8] For reviews of the general use of cationic CpRu complexes, see: a) C. Slugovc, E. Ruba, R. Schmid, K. Kirchner, K. Mereiter, *Monatsh. Chem.* **2000**, *131*, 1241 – 1251; b) B. M. Trost, F. D. Toste, A. B. Pinkerton, *Chem. Rev.* **2001**, *101*, 2067 – 2096; an efficient synthesis of $[CpRu(CH_3CN)_3]PF_6$, see: B. M. Trost, C. M. Older, *Organometallics* **2002**, *21*, 2544 – 2546.

[9] $^{31}P$ NMR spectra of complex **5** was measured in $CDCl_3$ and [D$_6$]acetone; in both cases, the AB-spin system, depicted in Figure 1, was observed with identical chemical shifts and coupling constants (the septet at $\delta = -141.6$ ppm ($^1J$(P-F) = 707.7 Hz) belongs to the $PF_6$ counterion).

[10] CCDC 289523 (**5**) contains the supplementary crystallographic data for this paper. These data can be obtained free of charge from The Cambridge Crystallographic Data Centre via www.ccdc.cam.ac.uk/data_request/cif.

[11] Crystal data for **5**: $C_{50}H_{47}F_6N_4O_2P_3Ru$; $M_r = 1043.90$; $T = 100(2)$ K; $\lambda = 0.71073$ Å; triclinic; space group $P\bar{1}$, $a = 11.1195(4)$, $b = 13.0414(4)$, $c = 18.2113(8)$ Å, $\alpha = 92.169(2)$, $\beta = 106.9106(17)$, $\gamma = 97.314(2)°$; $V = 2498.32(16)$ Å$^3$; $Z = 2$; $D_c = 1.388$ Mg m$^{-3}$; $\mu = 0.474$ mm$^{-1}$; $F(000) = 1068$; crystal size = $0.08 \times 0.08 \times 0.06$ mm; $\theta$ range for data collection: 1.58–27.52°, limiting indices: $-14 \le h \le 14$, $-16 \le k \le 16$, $-23 \le l \le 23$; 30814 reflections collected; 11483 reflections unique ($R_{int} = 0.0509$); completeness to $\theta = 25.00°$: 100.0%; absorption correction: semiempirical from equivalents; max. and min. transmission: 0.975 and 0.937; refinement method: full-matrix least-squares on $F^2$; data/restraints/parameters: 11483/0/599; GOF on $F^2$: 0.987; final $R$ indices: ($I > 2\sigma(I)$): $R1 = 0.0438$, $wR2 = 0.0964$; $R$ indices (all data): $R1 = 0.0718$, $wR2 = 0.1047$; largest diff. peak and hole: 0.533 and $-0.585$ e Å$^{-3}$.

[12] a) J. D. Watson, F. H. C. Crick, *Nature* **1953**, *171*, 964 – 967; b) M. D. Topal, J. R. Fresco, *Nature* **1976**, *263*, 285 – 289.

[13] a) B. M. Trost, R. C. Livingston, *J. Am. Chem. Soc.* **1995**, *117*, 9586 – 9587; b) T. Suzuki, M. Tokunaga, Y. Wakatsuki, *Tetrahedron Lett.* **2002**, *43*, 7531 – 7533; c) N. d'Alessandro, M. Di Deo, M. Bonetti, L. Tonucci, A. Morvillo, M. Bressan, *Eur. J. Inorg. Chem.* **2004**, 810 – 817.

[14] A first confirmation for this assumption was obtained from the reaction of 6-DPPAP (1 equiv), 3-DPICon (1 equiv), and *cis*-[$PtCl_2$(cod)] (1 equiv; cod = cyclooctadiene) in toluene in the presence of water to give *cis*-[$PtCl_2$(6-DPPAP)(3-DPICon)-($H_2O$)] quantitatively.

 © 2006 Wiley-VCH Verlag GmbH & Co. KGaA, Weinheim 

Non-heme Iron Complex

DOI: 10.1002/anie.200502656

# Regiospecific Ligand Oxygenation in Iron Complexes of a Carboxylate-Containing Ligand Mediated by a Proposed $Fe^{V}$–Oxo Species**

*Anne Nielsen, Frank B. Larsen, Andrew D. Bond, and Christine J. McKenzie**

Metal-promoted oxidations of coordinated ligands in synthetic metal complexes mimic the reactions catalyzed by metalloenzymes involved in oxidation/oxygenation of substrates using $O_2$ or its activated derivatives as terminal oxidants. In the biomimetic non-heme genre, observed reactions include oxygen-atom insertion into aliphatic[1] and aromatic[2–4] C–H bonds, and oxidative N-dealkylation.[5]

Herein we communicate regiospecific oxygen-atom insertion into iron(III) complexes of carboxylate-containing pentadentate ligand systems based on *N*-carboxymethyl-*N*′-R-*N*,*N*′-bis(2-pyridylmethyl)-1,2-ethandiamine (R = methyl or benzyl;[6] Scheme 1a) and propose involvement of an $Fe^{V}$-based oxidant. A single oxygen atom can be inserted into these complexes in two ways, using $H_2O_2$ and *t*BuOOH as oxidants: a phenolato group is produced in the system containing the benzyl substituent (Scheme 1b), and an unprecedented iron(III) complex containing a coordinated *N*-oxide group is produced in the related methyl-substituted ligand (Scheme 1c).

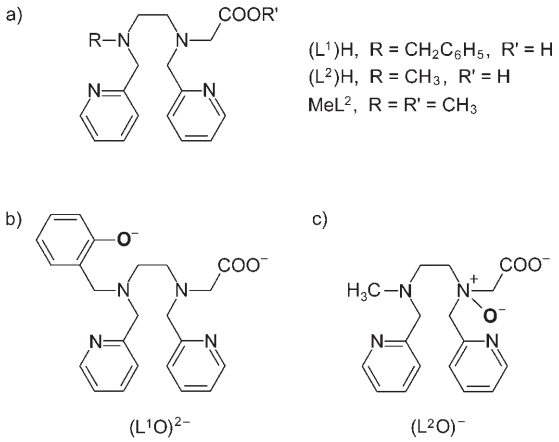
The monoanionic precursor ligands $(L^1)^-$ and $(L^2)^-$ contain one carboxylate donor, resembling in this respect

[*] A. Nielsen, F. B. Larsen, Dr. A. D. Bond, Prof. C. J. McKenzie
University of Southern Denmark
Department of Chemistry
Campusvej 55, 5230 Odense M (Denmark)
Fax: (+45) 6615-8780
E-mail: chk@chem.sdu.dk

[**] This work was supported by a grant (2058-03-0036) from the Danish Technical Research Council. We express our gratitude to the referees for helpful comments.

Supporting information for this article (syntheses and characterizations, full details of single-crystal X-ray analyses, list of structures considered for definition of average N–O bond distance in coordinated *N*-oxides, ESI MS of **5**-$FeCl_4 \cdot H_2O$ and the N-oxygenation reaction mixture in $H_2O$) is available on the WWW under http://www.angewandte.org or from the author.


WILEY InterScience DISCOVER SOMETHING GREAT
© 2006 Wiley-VCH Verlag GmbH & Co. KGaA, Weinheim




***Scheme 1.*** a) Protonated benzyl and methyl N-substituted pentadentate $N_4O$ ligands, $(L^1)^-$ and $(L^2)^-$, together with a methylated derivative, $MeL^2$. b) Hexadentate phenolate-containing ligand, $(L^1O)^{2-}$, prepared by the Fe-promoted oxygenation of $(L^1)^-$. c) *N*-oxide-containing pentadentate ligand $(L^2O)^-$, prepared by oxygenation of $(L^2)^-$.

many non-heme iron enzymes involved in $O_2$ metabolism. In these enzymes, the proteins furnish endogenous mononegative amino-acid donor sets containing one aspartate or glutamate group along with predominately histidine donors. A common motif is the 2-his-1-carboxylate triad which occurs in extradiol cleaving catechol dioxygenases, Rieske dioxygenases, α-ketoglutarate-dependent oxidases, pterin-dependent hydroxylases, and other non-heme iron oxidases.[7]

Reaction of $L^1H$ with iron(II) or iron(III) perchlorate in water, methanol, or acetonitrile gives the brown unsupported μ-oxo-bridged diiron(III) complex $[(L^1)FeOFe(L^1)](ClO_4)_2$ (**1**-$(ClO_4)_2$).[8] When water, acetonitrile, methanol, or $D_2O$ solutions of **1**-$(ClO_4)_2$ are treated with four equivalents of perchloric acid, evidence of hydrolysis and cleavage of the oxide bridge is furnished by the generation of mononuclear iron(III) cations $[(L^1)FeOH]^+$ (**2a**$^+$, *m*/*z* 462.3, in water or acetonitrile), $[(L^1)FeOCH_3]^+$ (**2b**$^+$, *m*/*z* 476.3, in methanol), and $[(L^1)FeOD]^+$ (**2c**$^+$, *m*/*z* 463.3, in $D_2O$). When 10–15 equivalents of $H_2O_2$ or *t*BuOOH per iron atom are subsequently added, a dark blue color evolves within minutes to hours, depending on concentration and the requirement that a final pH of 2 is reached. Above or below pH 2, bubbles are evolved, indicating catalase activity. The electrospray-ionization mass spectra (ESI MS) of all these blue solutions show that a new singly charged ion evolves at *m*/*z* 460.2, two mass units less than for **2a**$^+$. As the intense color of the solution ($\lambda = 588$ nm) is consistent with a phenolato–$Fe^{III}$ ligand-to-metal charge transfer (LMCT), the most reasonable assignment for this peak is the mononuclear iron(III) complex $[(L^1O)Fe]^+$ (**3**$^+$) of the previously unknown ligand $L^1O$ (Scheme 1).[9]

The best conditions found for the oxidation were those using $H_2O_2$ in methanol. Under these conditions **3**$^+$ as the perchlorate salt was isolated in good yield. At least 45% conversion is possible, as determined on the basis of UV/Vis spectroscopy ($\varepsilon$ 1900 $M^{-1}cm^{-1}$). The ESI MS of the mother liquors show that the cations **1**$^{2+}$ and **2a**$^+$ or **2b**$^+$ remain in solution, and further **3**$^+$ can be generated by addition of more oxidant. It is difficult to state precisely the number of equivalents of $H_2O_2$ required to optimize the reaction since the oxidant is also consumed by competing catalase activity. However, it is notable that the ESI MS does not identify ions that might arise from alternative oxidation reactions, in particular N-dealkylation.

X-ray analysis of **3**-$ClO_4$·0.5 MeOH·0.5 $H_2O$[10] (Figure 1) shows that the $Fe^{III}$ atom in the cation **3**$^+$ exhibits distorted

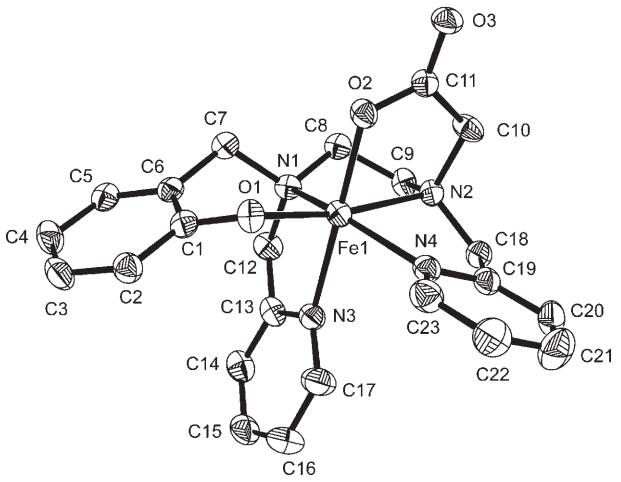


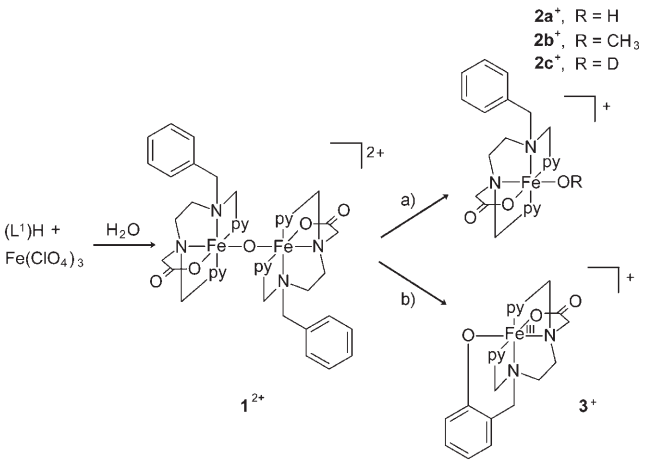

***Figure 1.*** $[(L^1O)Fe]^+$ ion in the crystal structure **3**-$ClO_4$·0.5 MeOH·0.5 $H_2O$, showing displacement ellipsoids at 50% probability. H atoms are omitted. Selected bond lengths [Å]: Fe1–O1 1.864(4), Fe1–O2 1.951(4), Fe1–N1 2.161(4), Fe1–N2 2.218(4), Fe1–N3 2.188(5), Fe1–N4 2.107(5), C1–O1 1.344(6).

octahedral coordination geometry, with the O atoms of the carboxylato and phenylato groups lying *cis* to each other. The $Fe–N_{arom.}$ and $Fe–N_{aliph.}$ bond lengths are consistent with those observed in comparable $Fe^{III}$ complexes and display the expected distortion on account of the *trans* influence of O.

Speculating that removal of the internal aromatic substrate may permit trapping of a reactive metal-based oxide or peroxide intermediate, we set out to examine the reactivity of iron complexes of the analogous methylated ligand $(L^2)^-$ (Scheme 1). Using this system we observed a second, unprecedented type of oxygen-atom insertion. Since an oxo-bridged analogue to **1**$^{2+}$ had not been adequately characterized for the methylated ligand $(L^2)^-$, we were not able to carry out the series of reactions exactly analogous to those depicted in Scheme 2. Instead, we examined the reactions of the iron(III) complex of the methyl ester derivative, $[FeCl_2(MeL^2)]ClO_4$ (**4**-$ClO_4$), which is prepared from reaction of equimolar amounts of $FeCl_3$ and $L^2H$ in methanol with approximately 10 equivalents of $HCl_{(aq)}$.[11] Treatment of a suspension of **4**-$ClO_4$ in dichloromethane with *t*BuOOH (in decane) gave a yellow solution, from which crystals of $[FeCl_2(HL^2O)][FeCl_4]·H_2O$, **5**-$FeCl_4·H_2O$ were isolated after a few days.

The single-crystal X-ray structure of **5**-$FeCl_4·H_2O$[12] (Figure 2) shows that the ligand in the cation has undergone two transformations: the methyl ester group of **4**$^+$ has been hydrolyzed, and, more significantly, one tertiary amine group

 © 2006 Wiley-VCH Verlag GmbH & Co. KGaA, Weinheim 




***Scheme 2.*** a) 4 equiv $HClO_4$ in $H_2O$ or $D_2O$ or MeOH; b) 4 equiv $HClO_4$, 20–30 equiv $H_2O_2$ or *t*BuOOH in $H_2O$ or MeOH or $CH_3CN$.

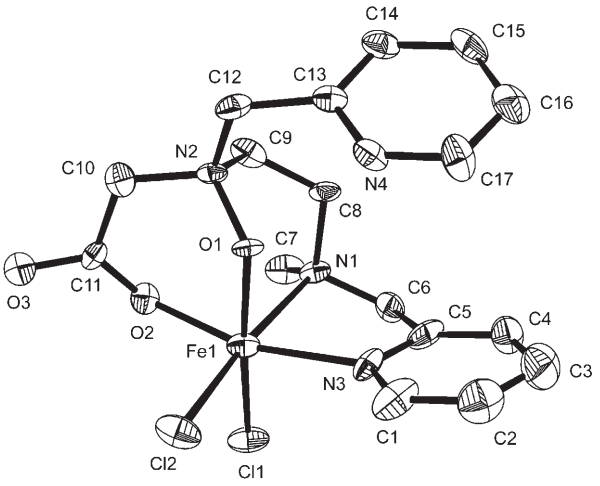
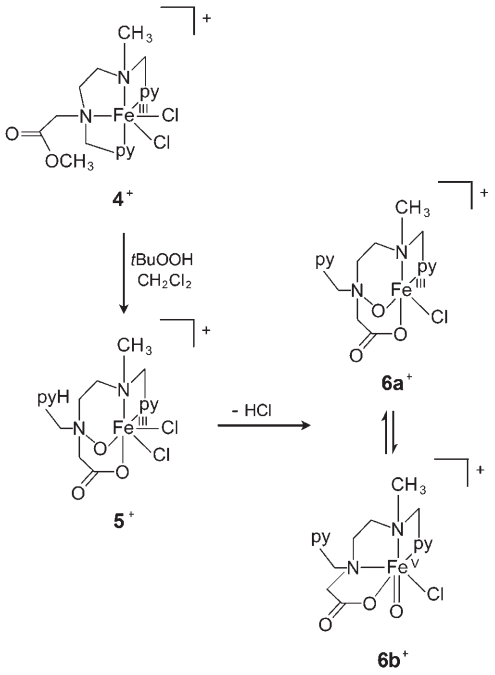



***Figure 2.*** $[FeCl_2(HL^2O)]^+$ ion in the crystal structure **5**-$FeCl_4{\cdot}H_2O$, showing displacement ellipsoids at 50% probability for non-H atoms. H atoms are omitted (atom N4 is protonated). Selected bond lengths [Å]: Fe1–O1 1.993(5), Fe1–O2 2.001(5), Fe1–N1 2.257(7), Fe1–N3 2.163(7), Fe1–Cl1 2.302(2), Fe1–Cl2 2.299(3), N2–O1 1.402(8).

has been oxygenated (Scheme 3). The methylpyridine arm attached to the resultant *N*-oxide nitrogen atom is decoordinated from the Fe atom and is protonated in the solid state (forming a strong hydrogen bond to the uncoordinated O atom of the carboxy group in an adjacent complex). The N–O bond length of 1.402(8) Å is that expected for a coordinated *N*-oxide, $R_3NO$ ($R \neq H$); the mean value from 29 such structures in the Cambridge Structural Database[13] is 1.404(19) Å.

The IR spectrum of **5**-$FeCl_4{\cdot}H_2O$ is consistent with the crystal structure: absorbances at 2962 and 2932 $cm^{-1}$ are assigned to the protonated pyridine group and the shift of $\nu$(C=O) from 1743 $cm^{-1}$ in **4**-$ClO_4$ to 1666 $cm^{-1}$ in **5**-$FeCl_4{\cdot}H_2O$ shows conversion of the ester to a monodentate carboxylate.[14] The ESI MS (THF or $CH_3CN$) also supports the crystallographic results: the cation assignable to $\mathbf{5}^+$ (*m*/*z* 456.2) is observed along with a much more intense ion at *m*/*z*




***Scheme 3.*** N-oxygenation reaction. Complexes $\mathbf{4}^+$ and $\mathbf{5}^+$ are isolated as their $ClO_4^-$ and $FeCl_4^-$ salts, respectively. Ions $\mathbf{6a}^+$ and $\mathbf{6b}^+$ are alternative assignments for the major ion in the ESI MS of **5**-$FeCl_4{\cdot}H_2O$.

420.3 ($\mathbf{6}^+$). This latter ion results from facile loss of the mass equivalent of HCl from $\mathbf{5}^+$. Two alternative structural assignments for *m*/*z* 420.3 are $[Fe^{III}(L^2O)Cl]^+$ ($\mathbf{6a}^+$) or $[Fe^{V}O(L^2)Cl]^+$ ($\mathbf{6b}^+$; Scheme 3).

The lack of color change as a visual aid in the N-oxygenation makes the reaction considerably more difficult to follow compared to the aromatic oxygenation. However, ESI MS suggests that the N-oxygenation also occurs in aqueous solution. In water, the ester group of **4**-$ClO_4$ is readily hydrolyzed and the oxo-bridged analogue of $\mathbf{1}^{2+}$, $[(L^2)Fe^{III}OFe^{III}(L^2)]^{2+}$ ($\mathbf{7}^{2+}$) at *m*/*z* 377.3, is the dominant species along with a peak for $[(L^2)Fe^{III}OH]^+$ ($\mathbf{8}^+$) at *m*/*z* 386.3.[15] Addition of 50 equivalents of *t*BuOOH causes no immediate significant change to the spectrum of the solution, but a new singly charged cation is observed at *m*/*z* 402.2 after standing for 24 h.[16] Possible structural assignments for this cation include the $Fe^{III}$–(*N*-oxide) species $[Fe^{III}(L^2O)OH]^+$ ($\mathbf{9a}^+$), the $Fe^{V}$–oxo species $[Fe^{V}O(L^2)OH]^+$ ($\mathbf{9b}^+$), and the $Fe^{III}$–hydroperoxo species $[Fe^{III}(L^2)OOH]^+$ ($\mathbf{9c}^+$), all expected at *m*/*z* 402.2. Cations $\mathbf{9a}^+$ and $\mathbf{9b}^+$ are isoelectronic with $\mathbf{6a}^+$ and $\mathbf{6b}^+$ (Scheme 3). An analogue of the cation $\mathbf{9c}^+$ has been identified previously as a transient species for the neutral $N_5$ Rtpen ligand system.[17] In the present case, however, cation $\mathbf{9c}^+$ seems an unlikely assignment since *t*BuOOH, and not $H_2O_2$, was used as the oxidant in this particular reaction, and since the species is unlikely to be stable in solution after standing under ambient conditions for a day. Furthermore the UV/Vis spectrum of the reaction mixture also lacks the characteristic CT band around 530 nm indicative of a $Fe^{III}$–OOH species. The emergence of a peak at *m*/*z* 385.3 on collision-induced dissociation of the *m*/*z* 402.2

 © 2006 Wiley-VCH Verlag GmbH & Co. KGaA, Weinheim 

species (an MS/MS experiment) shows that the mass equivalent of HO$^{\bullet}$ can be fragmented from the cation. This peak is assignable to either $[(L^2O)Fe^{II}]^+$ or $[(L^2)Fe^{IV}O]^+$ (both expected at $m/z$ 385.2), which would arise by HO$^{\bullet}$ loss from **9a**$^+$ and **9b**$^+$, respectively. On the basis of the structure of **5**$^+$, we favor the assignment of $m/z$ 402.2 to **9a**$^+$.

In general, complexes with aliphatic *N*-oxides are rare.[18] Examples are known for the early transition metals, but there are no previous examples for iron. Interestingly, both the aliphatic nitrogen atoms of ethylenediaminetetraacetate ($edta^{4-}$) (to which $(L^1)^-$ and $(L^2)^-$ are related by the common feature of a diaminoethane backbone) can be oxygenated in the presence of niobic acid[19] or tetraperoxotantalate[20] and excess $H_2O_2$ to give $[M(O_2)_2(edtaO_2)]^{3-}$ (M = Nb, Ta). In the context of these observations, it is clear that the $(L^2)^-$ system displays impressive selectivity: only one of the aliphatic nitrogen atoms is oxygenated, and neither of the aromatic nitrogen atoms is affected.

The mechanism of the oxygenation reactions conceivably involves O–O homolysis of a $[LFe^{III}OOR]^+$ species (R = H or *t*Bu) to give the oxygenating species $[LFe^{IV}O]^+$ and RO$^{\bullet}$, or O–O heterolysis to give $[LFe^{V}O]^{2+}$ and $RO^-$. That the oxygenation is not effected by HO$^{\bullet}$ or *t*BuO$^{\bullet}$ can be justified by 1) the regioselectivity, 2) the high yield, 3) the fact that *t*BuOOH can be used as terminal oxidant,[21] and 4) the fact that no other oxidation products are detected. Furthermore, Haber–Weiss chemistry would imply involvement of an $Fe^{II}$ species and our experience here with $(L^1)^-$ and $(L^2)^-$ indicates that $Fe^{II}$ complexes are not readily accessible for these ligands in condensed phases. This contrasts with the behavior of the neutral Rtpen ligands, for which mononuclear $Fe^{II}$ species are typically isolated in air.[17] If the proposed $Fe^{IV}$ species acts as the O-atom donor, Equations (1) and (2) apply. If the proposed $Fe^{V}$ species acts as the O-atom donor, Equations (3) and (4) apply. In each case, for simplicity, only the relevant parts of $(L^1)^-$ and $(L^2)^-$ are depicted as the substrate:

$$[Fe^{IV}{=}O]^+ + C_6H_5R \rightarrow [Fe^{III}{-}O{-}C_6H_4R]^+ + H^{\cdot} \quad (1)$$

$$[Fe^{IV}{=}O]^+ + NR_3 \rightarrow [Fe^{III}{-}O{-}NR_3]^{2+} + e^- \quad (2)$$

$$[Fe^{V}{=}O]^{2+} + C_6H_5R \rightarrow [Fe^{III}{-}O{-}C_6H_4R]^+ + H^+ \quad (3)$$

$$[Fe^{V}{=}O]^{2+} + NR_3 \rightarrow [Fe^{III}{-}O{-}NR_3]^{2+} \quad (4)$$

Of the two possibilities, Equations (3) and (4) are most consistent with our results. Proposal of an $Fe^{V}$–oxo species is supported by following observations: 1) An upward shift of one oxidation state is observed for mononuclear iron oxides of $(L^1)^-$ and $(L^2)^-$ relative to the related neutral aminopyridyl supported systems (such as Rtpen), for which the catalytically competent $[Fe^{IV}O]$ species have been proposed.[3] 2) The intramolecular two-electron, one-atom, oxygen transfer represented by Equation (4) resembles closely the mechanisms of the molybdenum oxotransferases and their models.[22] These systems have been shown to transfer an oxygen atom from $Mo^{VI}{=}O$ to an amine in two-electron reactions, giving a $Mo^{IV}$ species and an *N*-oxide, and vice versa. By analogy, it can be noted that minimal bond rearrangement is needed to interconvert the $Fe^{V}$–oxo species **6b**$^+$ and the *N*-oxide species **6a**$^+$. 3) Although we have so far avoided the use of buffers, we observe that it is essential to maintain a pH of 2 for both oxygenations in water. The acidic conditions would assist O–O heterolysis for $[LFe^{III}OOR]^+$ rather than homolysis, since water or *t*BuOH would be released as leaving groups. 4) N-oxygenation has been observed previously on reaction of $[Fe^{III}tmp(Cl)]$ (tmp = tetramesitylporphyrin) with *m*-chloroperoxybenzoic acid in toluene at 0 °C under dilute conditions ($< 10^{-4}$ M).[23] In that system, an intermediate $[Fe^{IV}(tmp^{\cdot+})]$ species was detected in $CH_2Cl_2$ solution, again indicating two-electron chemistry. 5) The results obtained using ligands $(L^1)^-$ and $(L^2)^-$ are in clear contrast to the neutral Rtpen systems, in which transient $Fe^{III}$ peroxides have been identified in the condensed phase,[17,24] but ligand oxygenation has not been observed.

The most interesting feature in our system is the biomimetic carboxylate donor and how this might tune the redox properties of iron complexes and their ability to form the iron centered oxidant/oxygen atom donor involved in these two regiospecific reactions. The pentadentate ligand system contains an inherent flexibility for alternative decoordination of either a pyridyl or carboxylate group during reactions, which might be useful for supporting various oxidation states and geometries.[25] We have not investigated whether solvent oxidation is occurring in parallel with ligand oxygenations. This, and the possibility that external substrates might be oxygenated, particularly in catalytic reactions, is clearly an area of interest for further work. As a final remark, we note that ESI MS is often a principal means of characterization for reactive biomimetic oxide and peroxide iron, manganese, and copper species. If our interpretation of the N-oxygenation reaction had been based solely on ESI MS, without knowledge from the X-ray structure analysis, the tempting but incorrect assignment of $[Fe^{V}O(L^2)Cl]^+$ (**6b**$^+$) might have been made for the ion **6**$^+$, without consideration of the unprecedented N-oxygenated $[Fe^{III}(L^2O)Cl]^+$ (**6a**$^+$). Likewise, an $Fe^{III}$–hydroperoxo species (**9c**$^+$) might have been assigned rather than **9a**$^+$ or **9b**$^+$.

Received: July 28, 2005
Revised: December 16, 2005

**Keywords:** hydroxylation · iron · N ligands · *N* oxides · peroxides

[1] V. Mahadevan, Z. Hou, A. P. Cole, D. E. Root, T. K. Lal, E. I. Solomon, T. D. P. Stack, *J. Am. Chem. Soc.* **1997**, *119*, 11996–11997; S. Hikichi, H. Komatsuzaki, N. Kitajima, M. Akita, M. Mukai, T. Kitagawa, Y. Moro-oka, *Inorg. Chem.* **1997**, *36*, 266–267; S. Hikichi, H. Komatsuzaki, M. Akita, Y. Moro-oka, *J. Am. Chem. Soc.* **1998**, *120*, 4699–4710.

[2] S. Ménage, J. B. Galey, G. Hussler, M. Seité, M. Fontecave, *Angew. Chem.* **1996**, *108*, 2535–2537; *Angew. Chem. Int. Ed. Engl.* **1996**, *35*, 2353–2355; S. Ménage, J. B. Galey, J. Dumats, G. Hussler, M. Seité, I. G. Luneau, G. Chottard, M. Fontecave, *J. Am. Chem. Soc.* **1998**, *120*, 13370–13382; F. Avenier, L. Dubois, J.-M. Latour, *New J. Chem.* **2004**, *28*, 782–784.

[3] M. P. Jensen, S. J. Lange, M. P. Mehn, E. L. Que, L. Que, Jr., *J. Am. Chem. Soc.* **2003**, *125*, 2113–2128; J.-U Rohde, S. Torelli, X.

 © 2006 Wiley-VCH Verlag GmbH & Co. KGaA, Weinheim 

Shan, M. H. Lim, E. J. Klinker, J. Kaizer, K. Chen, W. Nam, L. Que, Jr., *J. Am. Chem. Soc.* **2004**, *126*, 16750 – 16761.

[4] H. Furutachi, M. Murayama, A. Shiohara, S. Yamazaki, S. Fujinami, A. Uehara, M. Suzuki, S. Ogo, Y. Watanabe, Y. Maeda, *Chem. Commun.* **2003**, 1900 – 1901.

[5] S. Mahapatra. J. A. Halfen, E. C. Wilkinson, G. Pan, X. Wang, V. G. Young, Jr., C. J. Cramer, L. Que, Jr., W. B. Tolman, *J. Am. Chem. Soc.* **1996**, *118*, 11555 – 11574; S. Mahapatra, V. G. Young, Jr., S. Kaderli, A. D. Zuberbühler, W. B. Tolman, *Angew. Chem.* **1997**, *109*, 125 – 127; *Angew. Chem. Int. Ed. Engl.* **1997**, *36*, 130 – 133; Y. Mekmouche, S. Ménage, C. Toia-Duboc, M. Fontecave, J. B. Galey, C. Lebrun, J. Pécaut, *Angew. Chem.* **2001**, *113*, 975 – 978; *Angew. Chem. Int. Ed.* **2001**, *40*, 949 – 952.

[6] C. Baffert, M.-N. Collomb, A. Deronzier, S. Kjærgaard-Knudsen, J.-M. Latour, K. H. Lund, C. J. McKenzie, M. Mortensen, L. P. Nielsen, N. Thorup, *Dalton Trans.* **2003**, 1765 – 1772.

[7] L. Que, Jr., *Nat. Struct. Biol.* **2000**, *7*, 182 – 184; K. D. Koehntop, J. P. Emerson, L. Que, Jr., *J. Biol. Inorg. Chem.* **2005**, *10*, 87 – 93.

[8] **1**-$(ClO_4)_2$ has been characterized in the solid state as two different solvates, **1**-$(ClO_4)_2{\cdot}CH_3OH{\cdot}2H_2O$ and **1**-$(ClO_4)_2{\cdot}0.5H_2O$; see Supporting Information.

[9] Treatment of **1**-$(ClO_4)_2$ dissolved in methanol with 10 equivalents of ascorbic acid and exposure to dioxygen results in a less intense absorption at 585 nm suggesting that the combination of dioxygen and a reductant can also effect the oxygenation, albeit in a much lower yield.

[10] Crystal data for **3**-$(ClO_4){\cdot}0.5\,CH_3OH{\cdot}0.5\,H_2O$. $C_{23.5}H_{27}ClFeN_4O_8$, $M_r = 584.79$, monoclinic, $P2_1/m$, $Z = 4$, $a = 8.0335(2)$, $b = 36.5599(11)$, $c = 8.8232(2)$ Å, $\beta = 107.693(2)°$, $V = 2468.83(11)$ Å$^3$, $T = 180(2)$ K, $\rho_{calcd} = 1.573\ g\,cm^{-3}$, $\mu(Mo_{K\alpha}) = 0.777\ mm^{-1}$. Of 30287 data measured, 4750 were unique ($R_{int} = 0.079$). Final $R1 = 0.074$ (3300 data with $I > 2\sigma(I)$) and $wR2 = 0.185$ (all data).

[11] Crystal data for **4**-$(ClO_4){\cdot}0.25\,CH_3OH$. $C_{18.25}H_{25}Cl_3FeN_4O_{6.25}$, $M_r = 562.62$, triclinic, $P\bar{1}$, $Z = 4$, $a = 9.0165(8)$, $b = 14.8220(16)$, $c = 19.630(2)$ Å, $\alpha = 69.953(3)$, $\beta = 84.028(4)$, $\gamma = 80.974(4)°$, $V = 2430.3(4)$ Å$^3$, $T = 180(2)$ K, $\rho_{calcd} = 1.538\ g\,cm^{-3}$, $\mu(Mo_{K\alpha}) = 0.993\ mm^{-1}$. Of 39082 data measured, 8150 were unique ($R_{int} = 0.073$). Final $R1 = 0.064$ (4888 data with $I > 2\sigma(I)$) and $wR2 = 0.196$ (all data).

[12] Crystal data for **5**-$(FeCl_4){\cdot}H_2O$. $C_{17}H_{24}Cl_6Fe_2N_4O_4$, $M_r = 672.80$, monoclinic, $P2_1$, $Z = 2$, $a = 8.5123(11)$, $b = 9.9011(10)$, $c = 15.876(2)$ Å, $\beta = 102.141(5)°$, $V = 1308.2(3)$ Å$^3$, $T = 180(2)$ K, $\rho_{calcd} = 1.708\ g\,cm^{-3}$, $\mu(Mo_{K\alpha}) = 1.753\ mm^{-1}$. The crystal was twinned by two-fold rotation about $c^*$. Of 21521 data measured, 6516 were assigned exclusively to component 1, 6485 were assigned exclusively to component 2, and 8520 were overlapped. The structure was refined against both components (HKLF-5 in SHELXL). Final $R1 = 0.065$ (4760 data with $I > 2\sigma(I)$) and $wR2 = 0.157$ (all data). CCDC-276436 (**3**), -276438 (**4**), and -276439 (**5**) contain the supplementary crystallographic data for this paper. These data can be obtained free of charge from The Cambridge Crystallographic Data Centre via www.ccdc.cam.ac.uk/data_request/cif.

[13] F. H. Allen, *Acta Crystallogr. Sect. B* **2002**, *58*, 380 – 388. Cambridge Structural Database, November 2004 release plus 2 updates (347763 structures in total). Details of the structures used to define the average are included in the Supporting Information.

[14] There are no signals that can be assigned unambiguously to a coordinated tertiary amine *N*-oxide. These would be expected to be weak, appearing around 1270 and 860 $cm^{-1}$, in this case overlapping with ligand bands.

[15] Low intensity peaks are also present for the free ligands $[L^2H_2]^+$ ($m/z$ 314.9) and $[MeL^2H]^+$ ($m/z$ 329.0). This was not the case for the reactions starting with **1**-$(ClO_4)_2$. Ligand release is presumably promoted by the presence of chloride ions combined with the low pH. This is consistent with the formation of the $FeCl_4^-$ counteranion in **5**-$(FeCl_4){\cdot}H_2O$.

[16] Analysis of the analogous reaction with $H_2O_2$ in water is hampered by a competing catalase reaction. We have observed the $m/z$ 402.2 peak in the ESI MS of this solution, albeit as a weaker signal.

[17] Rtpen = *N*-R-*N*,*N*′,*N*′-tris(2-pyridylmethyl)ethane-1,2-diamine, R = $CH_3CH_2$, $CH_3CH_2CH_2$, $HOCH_2CH_2$, $(CH_3)_2CH$, $C_6H_5$, and $C_6H_5CH_2$. O. Horner, C. Jeandey, J.-L. Oddou, P. Bonville, C. J. McKenzie, J.-M. Latour, *Eur. J. Inorg. Chem.* **2002**, 3278 – 3283; A. Hazell, C. J. McKenzie, L. P. Nielsen, S. Schindler, M. Weitzer, *J. Chem. Soc. Dalton Trans* **2002**, 310 – 317; K. B. Jensen, C. J. McKenzie, L. P. Nielsen, J. Z. Pedersen, H. Molina Svendsen, *Chem. Commun.* **1999**, 1313 – 1314; I. Bernal, I.-M. Jensen, K. B. Jensen, C. J. McKenzie, H. Toftlund, J.-P. Tuchagues, *J. Chem. Soc. Dalton Trans.* **1995**, 3667 – 3675.

[18] W. R. Thiel, T. Priermeier, T. Bog, *J. Chem. Soc. Chem. Commun.* **1995**, 1871 – 1872; R. F. Bezerra, D. M. Araujo Melo, G. Vicentini, K. Zinner, K. L. B. Zinner, *J. Alloys Compd.* **2002**, *344*, 120 – 122; D. Bayot, B. Tinant, M. Devillers, *Inorg. Chem.* **2004**, *43*, 5999 – 6005; M. Capo, J. Gonzalez, H. Adams, *Eur. J. Inorg. Chem.* **2004**, *17*, 3405 – 3408; A. J. Bailey, M. G. Bhowon, W. P. Griffith, A. G. F. Shoair, A. J. P. White, D. J. Williams, *J. Chem. Soc. Dalton Trans.* **1997**, 3245 – 3250; R. B. Brown, M. M. Williamson, C. L. Hill, *Inorg. Chem.* **1987**, *26*, 1602 – 1608.

[19] D. Bayot, B. Tinant, B. Mathieu, J.-P. Declercq, M. Devillers, *Eur. J. Inorg. Chem.* **2003**, 737 – 743.

[20] D. Bayot, B. Tinant, M. Devillers, *Inorg. Chem.* **2004**, *43*, 5999 – 6005.

[21] Using the same argument as in Ref. [3]: aromatic hydrogen abstraction by *t*BuO$^{\bullet}$ is strongly disfavored on thermodynamic grounds.

[22] B. E. Schultz, S. F. Gheller, M. C. Muetterties, M. J. Scott, R. H. Holm, *J. Am. Chem. Soc.* **1993**, *115*, 2714 – 2722.

[23] J. T. Groves, Y. Watanabe, *J. Am. Chem. Soc.* **1988**, *110*, 8443 – 8452. Changed Soret bands were the only spectroscopic signature of the non-isolated oxidized complex. Subsequent demetalation and analysis of the isolated porphyrin by NMR spectroscopy showed that a pyrrole nitrogen atom was oxygenated in 25% yield.

[24] We have not yet detected $Fe^{III}$–peroxide species for L = $(L^1)^-$ and $(L^2)^-$ analogue to those obtained for Rtpen, despite attempts to generate them using similar reactions.[20] The failure to detect $[Fe^{III}(L)OOH]^+$ for $(L^1)^-$ and $(L^2)^-$ might imply that they are much more reactive than their Rtpen counterparts.

[25] A. K. Poulsen, A. Rompel, C. J. McKenzie, *Angew. Chem.* **2005**, *117*, 7076 – 7080; *Angew. Chem. Int. Ed.* **2005**, *44*, 6916 – 6920.

 © 2006 Wiley-VCH Verlag GmbH & Co. KGaA, Weinheim 

Coordination Modes

DOI: 10.1002/anie.200503535

# Bidentate Coordination of Pyrazolate in Low-Coordinate Iron(II) and Nickel(II) Complexes**

*Javier Vela, Sridhar Vaddadi, Savariraj Kingsley, Christine J. Flaschenriem, Rene J. Lachicotte, Thomas R. Cundari,* and Patrick L. Holland**

Pyrazolate ligands have rich coordination chemistry (Figure 1) that includes *exo*-bidentate bridging ($\mu$-$\eta^1$:$\eta^1$,

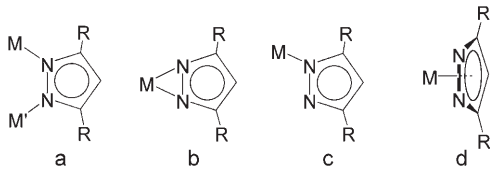



***Figure 1.*** Typical coordination modes of pyrazolate ligands (R = H, alkyl, or aryl) towards metal ions (M, M′). a) *exo*-bidentate; b) *endo*-bidentate; c) monodentate; d) pentadentate.

Figure 1a, most commonly observed),[1,2] *endo*-bidentate ($\eta^2$, Figure 1b), terminal monodentate ($\eta^1$, Figure 1c), and side-on, pentadentate ($\eta^5$, Figure 1d) coordination modes.[3,4] Because of this diversity in coordination modes, pyrazolates are potentially useful in devising synthetically useful processes in which the presence of a hemilabile ligand is required, as well as in the construction of metal architectures for catalysis,[5–8] luminescent materials,[9] and chemical vapor deposition.[10]

[*] S. Vaddadi, Prof. T. R. Cundari
Department of Chemistry
University of North Texas
Denton, TX 76203 (USA)
Fax: (+1) 940-565-4318
E-mail: tomc@unt.edu
Dr. J. Vela, Dr. S. Kingsley, C. J. Flaschenriem, Dr. R. J. Lachicotte, Prof. P. L. Holland
Department of Chemistry
University of Rochester
Rochester, NY 14627 (USA)
Fax: (+1) 585-276-0205
E-mail: holland@chem.rochester.edu

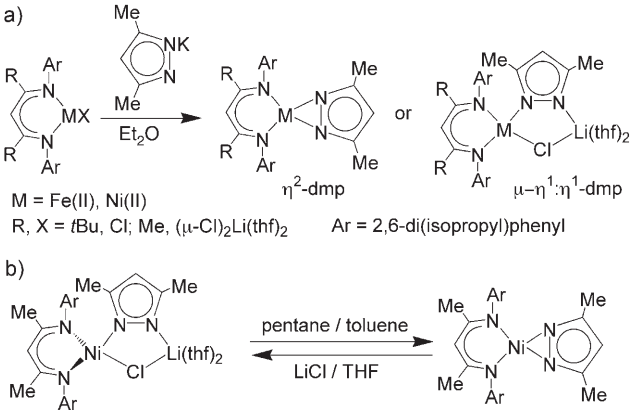
[**] The authors acknowledge funding from the Petroleum Research Fund (38275-G; P.L.H.), the A. P. Sloan Foundation (P.L.H.), the University of Rochester (Messersmith Fellowship; J.V.), and the US Departments of Education and Energy (DOE-FG02-97ER14811; T.R.C.). A portion of the calculations were performed on the UNT computational chemistry resource, for which S.V. and T.R.C. acknowledge the NSF for support through grant CHE-0342824. J.V. thanks Sandip Sur for help with DEPT and 2D NMR experiments and Dr. Azwana R. Sadique for advice on synthetic procedures.

Supporting information for this article is available on the WWW under http://www.angewandte.org or from the author.

The *endo*-bidentate ($\eta^2$-pyrazolate) coordination mode (Figure 1b) was long thought to be prevented by the opposing directionality of the two pyrazolate nitrogen lone pairs. More recently, $\eta^2$-pyrazolate coordination has been established for the lanthanides, actinides, alkali and alkaline earth metals, and early transition metals in high oxidation states.[11–13] $\eta^2$-Pyrazolate coordination to transition-metal ions with partially filled d shells is rare[11] and is limited to a few well-characterized examples with $Ti^{III}$ ($d^1$),[14] $V^{III}$($d^2$),[15] $Mo^{IV}$ ($d^2$),[8] $Cr^{III}$ ($d^3$),[16] $Mo^{II}$ ($d^4$),[17] and $Fe^{III}$ ($d^5$).[16]

Bulky β-diketiminate ancillary ligands have enabled the isolation and study of late, first-row transition-metal complexes with coordination numbers three and four.[18–20] Herein, it is shown that the steric protection of a β-diketiminate stabilizes the first $\eta^2$-pyrazolate complexes with $d^6$ and $d^8$ electron configurations, and these show different coordination geometries. Interestingly, a bridging pyrazolate binding mode is also accessible in the complexes, and the balance between the different pyrazolate coordination modes is explored through solution spectroscopic methods.

Treatment of [$L^{tBu}$MCl] ($L^{tBu}$ = 2,2,6,6-tetramethyl-3,5-bis(2,6-diisopropylphenylimino)hept-4-yl; M = Fe, Ni)[19] with a freshly prepared solution of potassium 3,5-dimethylpyrazolate (Kdmp) in tetrahydrofuran (THF) affords the complexes [$L^{tBu}$Fe($\eta^2$-dmp)] and [$L^{tBu}$Ni($\eta^2$-dmp)] in 89 and 72% yields, respectively (Scheme 1a).[21] The monomeric nature and *endo*-bidentate ligation of the dmp ligand in these complexes was confirmed by X-ray diffraction studies (Figure 2).




***Scheme 1.***

The coordination geometry around the iron center in the 14-electron complex [$L^{tBu}$Fe($\eta^2$-dmp)] is intermediate between tetrahedral and square planar; the twist angle between the pyrazolato and diketiminato ($C_3N_2Fe$) planes is 35.62(7)° (Figure 2a). The pyrazolate Fe–N bonds (2.031(1) and 2.048(1) Å) are longer than the diketiminate Fe–N bonds (1.988(1) and 2.001(1) Å). They are also longer than the Fe–N bonds reported for the homoleptic complex tris(3,5-di-*tert*-butylpyrazolato)iron(III) (2.009 Å).[16] The $^1$H NMR spectrum shows paramagnetically shifted resonances, which have been assigned on the basis of relative integrations (see the

 © 2006 Wiley-VCH Verlag GmbH & Co. KGaA, Weinheim 

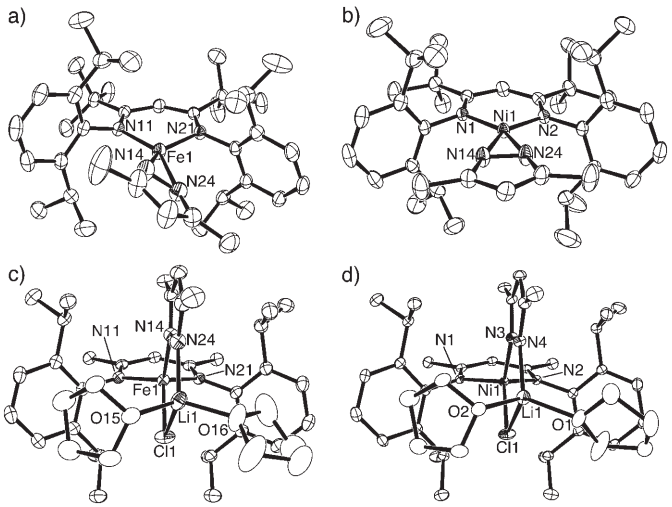



***Figure 2.*** Molecular structures of iron(II) (a, c) and nickel(II) (b, d) diketiminate complexes containing either *endo*-bidentate ($\eta^2$) (a, b) or *exo*-bidentate ($\mu$-($\eta^1$:$\eta^1$)) (c, d) 3,5-dimethylpyrazolato coordination. Thermal ellipsoids drawn at 50% probability; hydrogen atoms omitted for clarity.

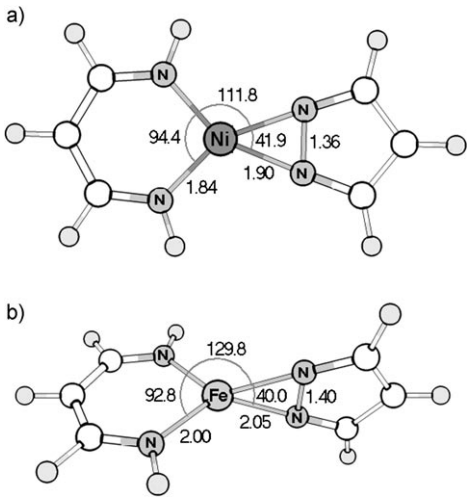



***Figure 3.*** B3LYP/SBKJC(d)-optimized geometries of singlet $C_{2v}$-symmetric [L′Ni($\eta^2$-pz)] (top) and quintet $C_2$-symmetric [L′Fe($\eta^2$-pz)] (bottom). All geometries correspond to energy minima. Bond lengths are in Å; bond angles are in degrees. The twist angle is 0° in the nickel compound and 90° in the iron compound.

Supporting Information). The solution magnetic moment is 5.1 $\mu_B$, which is consistent with a high-spin iron(II) center having four unpaired electrons and a spin state of $S=2$.

In the 16-electron complex [L$^{t\mathrm{Bu}}$Ni($\eta^2$-dmp)], the four nitrogen atoms and the nickel(II) center are roughly situated within a plane (Figure 2b). This is evidenced by a sum of angles around the metal center of 360.1(6)°, and there is only a small twist angle of 4.8(1)° between the pyrazolato and diketiminato ($C_3N_2Ni$) planes. The pyrazolate Ni–N bond lengths (1.901(1) and 1.906(1) Å) are again longer than the diketiminate Ni–N bond lengths (1.851(1) and 1.852(1) Å). The $^1$H NMR spectrum indicates a diamagnetic complex with well-defined proton resonances and coupling constants, and the complex has no measurable solution magnetic moment.

Thus, the $\eta^2$-pyrazolate iron(II) complex is nonplanar, and its nickel(II) analogue is planar. To understand whether this geometric difference arises from a steric or electronic effect, we performed density functional theory (DFT) calculations (B3LYP[22] in conjunction with both double- and triple-zeta-plus-polarization pseudopotential[23] and all-electron[24] basis sets) on $C_{2v}$-symmetric models [L′Fe($\eta^2$-pz)] and [L′Ni($\eta^2$-pz)] (L′ represents the truncated β-diketiminate $C_3N_2H_5^-$, and pz represents the parent pyrazolate $C_3N_2H_3^-$). The geometries (Figure 3) of the molecules were optimized in the quintet (Fe) and singlet (Ni) states. A parallel (i.e., square-planar) coordination geometry is greatly preferred for the nickel complex (32.2 kcal mol$^{-1}$ at the B3LYP/SBKJC(d) level), whereas the parallel and perpendicular conformers are closer in energy for the iron complex (3.8 kcal mol$^{-1}$ at the B3LYP/SBKJC(d) level), with the perpendicular conformer slightly preferred. The latter inference was confirmed by multiconfiguration self-consistent field (MCSCF)[25] geometry optimization on the [L′Fe(pz)] model complex, which showed the lowest-energy $^5A_1$ and $^5A_2$ states of the parallel and perpendicular conformations to be essentially at the same energy. As the truncated models used in the calculations do not suffer from steric obstructions, we infer that the planar geometry around the nickel center is determined electronically, whereas the geometry observed for the iron complex is probably dominated by steric factors.[26]

Treating [L$^{\mathrm{Me}}$M($\mu$-Cl)$_2$Li(thf)$_2$] (M = Fe, Ni)[18,19]—analogous complexes with the slightly smaller diketiminate ligand L$^{\mathrm{Me}}$ (2,4-bis(2,6-diisopropylphenylimino)pent-3-yl)—with Kdmp in THF gives the bridged complexes [L$^{\mathrm{Me}}$Fe{$\mu$-($\eta^1$:$\eta^1$)-dmp}($\mu$-Cl)Li(thf)$_2$] and [L$^{\mathrm{Me}}$Ni{$\mu$-($\eta^1$:$\eta^1$)-dmp}($\mu$-Cl)Li(thf)$_2$] in 85 and 76% yields, respectively (Scheme 1a). The bridging, *exo*-bidentate nature of the dmp ligand in these complexes was confirmed by X-ray diffraction studies (Figure 2).

Both the iron(II) and nickel(II) heterobridged complexes are tetrahedral (Figure 2). The pyrazolate Fe–N (2.033(1) Å) and Ni–N (1.959(1) Å) bond lengths are elongated with respect to those in the *endo*-bidentate complexes (see above). The $^1$H NMR spectrum of each complex shows broad and paramagnetically shifted resonances. The solution magnetic moment for the iron(II) complex is 5.2 $\mu_B$ and is consistent with a high-spin d$^6$ configuration with four unpaired electrons and a spin state of $S=2$. The nickel(II) complex has a magnetic moment of 3.1 $\mu_B$, which is consistent with a high-spin d$^8$ configuration ($S=1$).

The *tert*-butyl substituents in L$^{t\mathrm{Bu}}$ consistently push the aryl rings closer to the metal center than in the L$^{\mathrm{Me}}$ complex and increase the steric crowding around the metal center.[18,19] Thus, the different balance between bridging and $\eta^2$-pyrazolate ligation can be rationalized by the different steric requirements of the two diketiminate ligands used—the {Li(Cl)(dmp)} "ligand" is more sterically hindering than dmp itself, thus the bridging pyrazolate complex is forced to assume the more sterically accessible tetrahedral geometry.

Interestingly, the $\eta^2$ and bridging forms of the pyrazolate ligand interconvert in the nickel complexes of the smaller diketiminate ligand (Scheme 1b). Green solutions of [L$^{\mathrm{Me}}$Ni-

 © 2006 Wiley-VCH Verlag GmbH & Co. KGaA, Weinheim 

{μ-($\eta^1$:$\eta^1$)-dmp}(μ-Cl)Li(thf)$_2$] quickly become pink and form a white precipitate upon exposure to toluene. Filtration of this pink solution followed by evaporation of the solvent leads to a diamagnetic solid ([L$^{Me}$Ni($\eta^2$-dmp)]) whose $^1$H NMR and electronic spectra are reminiscent of those displayed by [L$'^{Bu}$Ni($\eta^2$-dmp)]. Each complex has a band between 522 and 547 nm ($\varepsilon = 440\,M^{-1}\,cm^{-1}$) that is typical of square-planar $d^8$ complexes,[27,28] along with a weaker band at 731–778 nm ($\varepsilon = 150\,M^{-1}\,cm^{-1}$; see Supporting Information). Treatment with a slight excess of LiCl in THF returned the compound to the green tetrahedral form. Therefore, we conclude that uptake and release of the alkali halide by the nickel(II) pyrazolate complexes are reversible, solvent-dependent processes. Toluene favors formation of the $\eta^2$-pyrazolate complex by decreasing the solubility of LiCl in the organic phase, thus promoting salt extrusion from the heterobridged species.

Considering that three-coordinate nickel and iron complexes of these bulky diketiminates have been synthesized,[18] it is surprising that $\eta^1$-pyrazolate ligands collapse so easily to the $\eta^2$ form in the absence of LiCl. DFT calculations of the nickel complexes were used to evaluate the cause of this phenomenon. Several different conformations of $\eta^1$-pyrazolate species of truncated [L′Ni(pz)] and full [L$'^{Bu}$Ni(dmp)] were constructed manually from the calculated or experimental $\eta^2$-pyrazolate structures. The truncated complex was studied with density functional (B3LYP/SBKJC(d)) methods and the full complex was studied with hybrid quantum mechanics/molecular mechanics (ONIOM(B3LYP/6-31G(d):UFF))[29] calculations. In all cases, $\eta^1$-pyrazolate complexes relaxed upon geometry optimization either back to the $\eta^2$ structures found previously or, in the case of the L′ models, to a higher-energy structure in which the noncoordinated pyrazolate nitrogen atom hydrogen bonds to one of the N–H bonds of L′. Hence, $\eta^1$-pyrazolate coordination in the nickel complex is disfavored with respect to $\eta^2$-pyrazolate coordination.

As the [L′Ni($\eta^1$-pz)] structure does not correspond to a stable stationary point, the geometry was constructed by constraining one Ni-N$_{pz}$-C$_{pz}$ angle and one N$_{pz}$-Ni-N$_{L'}$ angle while performing B3LYP/SBKJC(d) geometry optimization of all other degrees of freedom. Analysis of the frontier molecular orbitals (Figure 4) for the $\eta^2$-pz (left) and $\eta^1$-pz (right) geometry minima of [L′Ni(pz)] at the B3LYP/SBKJC(d) level reveals that the symmetric (in-phase) and antisymmetric (out-of-phase) combinations of the pyrazolate nitrogen lone pairs interact with the appropriate-symmetry Ni d orbitals. These "σ" frontier orbitals decrease in energy upon coordinating the second nitrogen atom, as described by Schlegel, Winter, and co-workers for early transition-metal pyrazolate complexes.[12b,15,16] Whereas the changes in frontier-orbital energies indicate a preference for $\eta^2$-pz bonding from the σ orbitals (top three orbitals in Figure 4), the frontier orbitals made up of Ni dπ orbitals and π electrons in the pyrazolate and L′ rings (bottom three orbitals in Figure 4) predominantly favor $\eta^1$-pz bonding. In the complexes described herein, the preference of the σ orbitals for $\eta^2$-pz bonding more than counterbalances the preference of the π orbitals for $\eta^1$-pz bonding, as can be inferred from the changes in the frontier-orbital energies. We speculate that the balance between $\eta^1$ and $\eta^2$ binding modes could be tuned through appropriate manipulation of these opposing electronic effects.

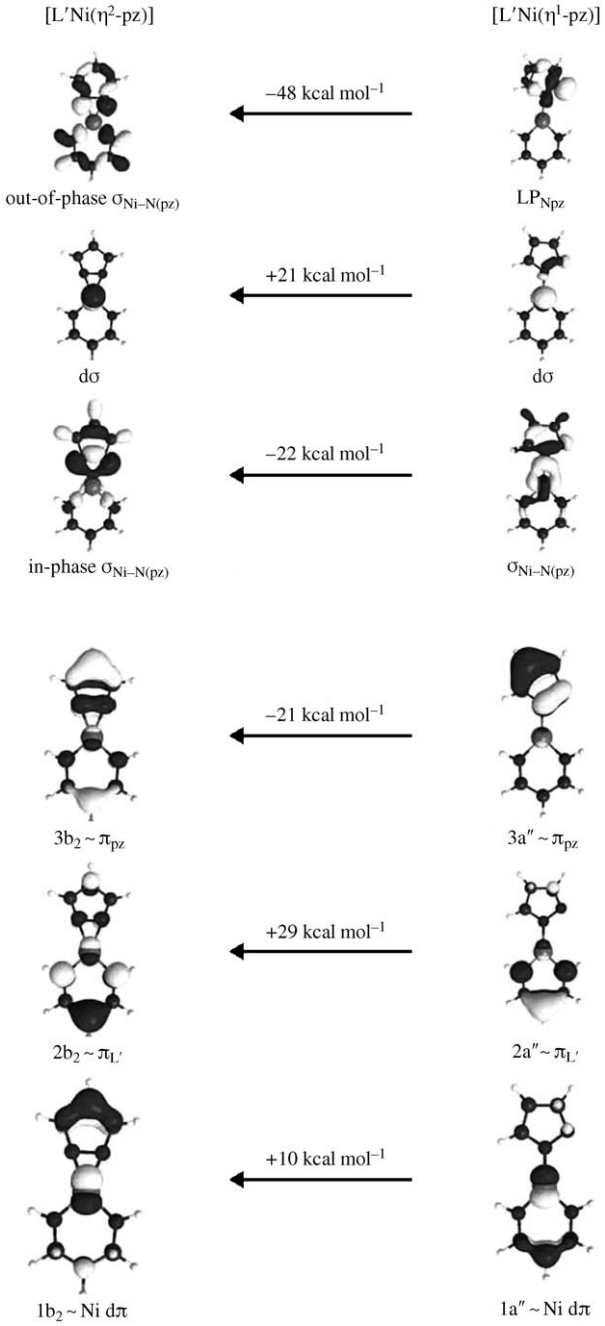



***Figure 4.*** Changes in σ and π frontier orbitals upon transforming [L′Ni($\eta^1$-pz)] (right) into [L′Ni($\eta^2$-pz)] (left).

In summary, we have shown the first examples of $\eta^2$-pyrazolate complexes of $d^6$ and $d^8$ metal ions. The high d-electron count of the late transition metals does not exclude this binding mode. Depending on the steric crowding imposed by the diketiminate ancillary ligand used, both $\eta^2$ and $\eta^1$ coordination to iron(II) and nickel(II) can be observed. The nickel(II) complexes show solvent-dependent behavior and

 © 2006 Wiley-VCH Verlag GmbH & Co. KGaA, Weinheim 

adopt either high-spin tetrahedral or diamagnetic square-planar configurations.

Received: October 5, 2005

**Keywords:** coordination modes · density functional calculations · iron · N ligands · nickel

[1] a) A. P. Sadimenko, *Adv. Heterocycl. Chem.* **2001**, *39*, 157 – 240; b) J. E. Cosgriff, G. B. Deacon, *Angew. Chem.* **1998**, *110*, 298 – 299; *Angew. Chem. Int. Ed.* **1998**, *37*, 286 – 287; c) G. La Monica, G. A. Ardizzoia, *Prog. Inorg. Chem.* **1997**, *46*, 151 – 238; d) A. P. Sadimenko, S. S. Basson, *Coord. Chem. Rev.* **1996**, *147*, 247 – 297; e) S. Trofimenko, *Prog. Inorg. Chem.* **1986**, *34*, 115 – 210.

[2] Bridging (*exo*-bidentate) pyrazolate ligation is formally present in bis and tris(pyrazolyl)borate complexes: a) S. Trofimenko, *Polyhedron* **2004**, *23*, 197 – 203; b) S. Trofimenko, *Chem. Rev.* **1993**, *93*, 943 – 980; c) S. Trofimenko, *Chem. Rev.* **1972**, *72*, 497 – 509.

[3] $\eta^5$-Pyrazolate coordination in ruthenium(II): J. R. Perera, M. J. Heeg, H. B. Schlegel, C. H. Winter, *J. Am. Chem. Soc.* **1999**, *121*, 4536 – 4537.

[4] Other pyrazolate coordination modes: G. B. Deacon, C. M. Forsyth, A. Gitlits, R. Harika, P. C. Junk, B. W. Skelton, A. H. White, *Angew. Chem.* **2002**, *114*, 3383 – 3385; *Angew. Chem. Int. Ed.* **2002**, *41*, 3249 – 3251.

[5] Initial studies suggest that the mechanism of oxo transfer in a Mo system involves switching from $\eta^2$- to $\eta^1$-pyrazolate ligation: K. Most, J. Hoßbach, D. Vidovic, J. Magull, N. C. Mösch-Zanetti, *Adv. Synth. Catal.* **2005**, *347*, 463 – 472.

[6] N. C. Mösch-Zanetti, A. Sachse, R. Pfoh, D. Vidovic, J. Magull, *Dalton Trans.* **2005**, 2124 – 2129.

[7] P. J. Baricelli, R. Santos, A. J. Pardey, *J. Mol. Catal. A* **2004**, *207*, 81 – 87.

[8] K. Most, N. C. Mösch-Zanetti, D. Vidovic, J. Magull, *Organometallics* **2003**, *22*, 5485 – 5490.

[9] a) H. V. Rasika Dias, H. V. K. Diyabalanage, M. G. Eldabaja, O. Elbjeirami, M. A. Rawashdeh-Omary, M. A. Omary, *J. Am. Chem. Soc.* **2005**, *127*, 7489 – 7501; b) T. R. Cundari, H. V. Rasika Dias, H. V. K. Diyabalanage, O. Elbjeirami, M. A. Gonzer, T. Grimes, M. A. Omary, M. Rawashdeh-Omary, *Inorg. Chem.* **2005**, *44*, 8200 – 8210.

[10] a) H. M. El-Kaderi, M. J. Heeg, C. H. Winter, *Eur. J. Inorg. Chem.* **2005**, 2081 – 2088; b) H. M. El-Kaderi, M. J. Heeg, C. H. Winter, *Polyhedron* **2005**, *24*, 645 – 653.

[11] a) C. W. Eigenbrot, Jr., K. N. Raymond, *Inorg. Chem.* **1981**, *20*, 1553 – 1556; b) C. W. Eigenbrot, Jr., K. N. Raymond, *Inorg. Chem.* **1982**, *21*, 2653 – 2660.

[12] Initial examples of $\eta^2$-pyrazolate coordination to transition metals, (e.g. $[ZrCp_2(\eta^2\text{-pz})(thf)][BPh_4]$; Cp = cyclopentadienyl) were explained in terms of their need to attain an 18-electron configuration: a) D. Röttger, G. Erker, M. Grehl, R. Fröhlich, *Organometallics* **1994**, *13*, 3897 – 3902; b) I. A. Guzei, A. G. Baboul, G. P. A. Yap, A. L. Rheingold, C. H. Schlegel, C. H. Winter, *J. Am. Chem. Soc.* **1997**, *119*, 3387 – 3388; c) I. A. Guzei, G. P. A. Yap, C. H. Winter, *Inorg. Chem.* **1997**, *36*, 1738 – 1739.

[13] A search of the CSD revealed 55 structures with $\eta^2$-pyrazolate coordination to f-block elements, 13 with alkali and alkaline-earth metals, 40 with $d^0$ early transition-metal ions, and only 8 with $\eta^2$-pyrazolate coordination to a metal ion with a partially filled d shell: Cambridge Structural Database, ConQuest version 1.7, November 2004 release, May 2005.

[14] N. C. Mösch-Zanetti, R. Krätzner, C. Lehmann, T. R. Schneider, I. Usón, *Eur. J. Inorg. Chem.* **2000**, 13 – 16.

[15] K. R. Gust, J. E. Knox, M. J. Heeg, H. B. Schlegel, C. H. Winter, *Eur. J. Inorg. Chem.* **2002**, 2327 – 2334.

[16] K. R. Gust, J. E. Knox, M. J. Heeg, H. B. Schlegel, C. H. Winter, *Angew. Chem.* **2002**, *114*, 1661 – 1664; *Angew. Chem. Int. Ed.* **2002**, *41*, 1591 – 1594.

[17] G. Zhu, J. M. Tanski, G. Parkin, *Polyhedron* **2003**, *22*, 199 – 203.

[18] Recent references: a) N. A. Eckert, E. M. Bones, R. J. Lachicotte, P. L. Holland, *Inorg. Chem.* **2003**, *42*, 1720 – 1725; b) N. A. Eckert, J. M. Smith, R. J. Lachicotte, P. L. Holland, *Inorg. Chem.* **2004**, *43*, 3306 – 3321; c) J. Vela, S. Vaddadi, T. R. Cundari, J. M. Smith, E. A. Gregory, R. J. Lachicotte, C. J. Flaschenriem, P. L. Holland, *Organometallics* **2004**, *23*, 5226 – 5239; d) J. Vela, J. M. Smith, Y. Yu, N. A. Ketterer, C. J. Flaschenriem, R. J. Lachicotte, P. L. Holland, *J. Am. Chem. Soc.* **2005**, *127*, 7857 – 7870.

[19] a) J. M. Smith, R. J. Lachicotte, P. L. Holland, *Chem. Commun.* **2001**, 1542 – 1543; b) P. L. Holland, T. R. Cundari, L. L. Perez, N. A. Eckert, R. J. Lachicotte, *J. Am. Chem. Soc.* **2002**, *124*, 14416 – 14424.

[20] Selected references: a) E. Kogut, A. Zeller, T. H. Warren, T. Strassner, *J. Am. Chem. Soc.* **2004**, *126*, 11984 – 11994; b) D. J. E. Spencer, A. M. Reynolds, P. L. Holland, B. A. Jazdzewski, C. Duboc-Toia, L. Le Pape, S. Yokota, Y. Tachi, S. Itoh, W. B. Tolman, *Inorg. Chem.* **2002**, *41*, 6307 – 6321; c) A. Panda, M. Stender, R. J. Wright, M. M. Olmstead, P. Klavins, P. P. Power, *Inorg. Chem.* **2002**, *41*, 3909 – 3916.

[21] Full synthetic, spectroscopic, and crystallographic details are given in the Supporting Information.

[22] a) A. D. Becke, *Phys. Rev. A* **1998**, *38*, 3098 – 3100; b) C. Lee, W. Yang, R. G. Parr, *Phys. Rev. B* **1998**, *37*, 785 – 789.

[23] The Stevens pseudopotentials and valence basis sets (W. J. Stevens, M. Krauss, H. Basch, P. G. Jasien, *Can. J. Chem.* **1992**, *70*, 612 – 630) were employed, augmented with d polarization functions for main-group elements within the GAMESS package (M. W. Schmidt, K. K. Baldridge, J. A. Boatz, S. T. Elbert, M. S. Gordon, J. J. Jensen, S. Koseki, N. Matsunaga, K. A. Nguyen, S. Su, T. L. Windus, M. Dupuis, J. A. Montgomery, *J. Comput. Chem.* **1993**, *14*, 1347 – 1363). This basis-set combination is referred to as SBKJC(d).

[24] All-electron calculations employed the 6-311G(d) basis set for all atoms within the Gaussian 03 suite of programs (Gaussian 03 (Revision B.03), M. J. Frisch, G. W. Trucks, H. B. Schlegel, G. E. Scuseria, M. A. Robb, J. R. Cheeseman, J. A. Montgomery, Jr., T. Vreven, K. N. Kudin, J. C. Burant, J. M. Millam, S. S. Iyengar, J. Tomasi, V. Barone, B. Mennucci, M. Cossi, G. Scalmani, N. Rega, G. A. Petersson, H. Nakatsuji, M. Hada, M. Ehara, K. Toyota, R. Fukuda, J. Hasegawa, M. Ishida, T. Nakajima, Y. Honda, O. Kitao, H. Nakai, M. Klene, X. Li, J. E. Knox, H. P. Hratchian, J. B. Cross, C. Adamo, J. Jaramillo, R. Gomperts, R. E. Stratmann, O. Yazyev, A. J. Austin, R. Cammi, C. Pomelli, J. W. Ochterski, P. Y. Ayala, K. Morokuma, G. A. Voth, P. Salvador, J. J. Dannenberg, V. G. Zakrzewski, S. Dapprich, A. D. Daniels, M. C. Strain, O. Farkas, D. K. Malick, A. D. Rabuck, K. Raghavachari, J. B. Foresman, J. V. Ortiz, Q. Cui, A. G. Baboul, S. Clifford, J. Cioslowski, B. B. Stefanov, G. Liu, A. Liashenko, P. Piskorz, I. Komaromi, R. L. Martin, D. J. Fox, T. Keith, M. A. Al-Laham, C. Y. Peng, A. Nanayakkara, M. Challacombe, P. M. W. Gill, B. Johnson, W. Chen, M. W. Wong, C. Gonzalez, J. A. Pople, Gaussian, Inc., Pittsburgh, PA, **2003**).

[25] For the MCSCF calculations, the five 3d orbitals of iron(II), subtending the irreducible representations $2a_1 + a_2 + b_1 + b_2$, and the six electrons contained within this orbital manifold comprised the active space. Geometry optimizations were carried out for the $^5A_1$, $^5A_2$, $^5B_1$, and $^5B_2$ states. The latter two states were found to be much higher in energy ($> 6$ kcal mol$^{-1}$) for both parallel and perpendicular conformations of [L′Fe(pz)]. MCSCF calculations employed the GAMESS package (see reference 23) and the SBKJC(d) basis set.

 © 2006 Wiley-VCH Verlag GmbH & Co. KGaA, Weinheim 

[26] Calculations on full models with the PM3(tm) Hamiltonian gave similar results, that is, a nearly planar geometry for [L$^{t\mathrm{Bu}}$Ni($\eta^2$-dmp)] and a nonplanar geometry for [L$^{t\mathrm{Bu}}$Fe($\eta^2$-dmp)].
[27] a) N. N. Greenwood, A. Earnshaw, *Chemistry of the Elements*, 2nd ed., Butterworth Heinemann, Oxford, **1997**, pp. 1091–1097, 1156–1166; b) R. L. Carter, *Molecular Symmetry and Group Theory*, Wiley, New York, **1998**, pp. 201–214.
[28] A. B. P. Lever, *Inorganic Electronic Spectroscopy*, 2$^{nd}$ ed., Elsevier, Amsterdam, **1984**, pp. 507–611.
[29] The ONIOM methodology is described in M. Svensson, S. Humbel, R. D. J. Froese, T. Matsubara, S. Sieber, K. Morokuma, *J. Phys. Chem.* **1996**, *100*, 19357–19363. The UFF force field is described in A. K. Rappé, C. J. Casewit, K. S. Colwell, W. A. Goddard III, W. M. Skiff, *J. Am. Chem. Soc.* **1992**, *114*, 10024–10035. In our calculations, the MM region included the aryl and *tert*-butyl substituents of L$^{t\mathrm{Bu}}$ and the methyl groups of dmp.

 © 2006 Wiley-VCH Verlag GmbH & Co. KGaA, Weinheim 

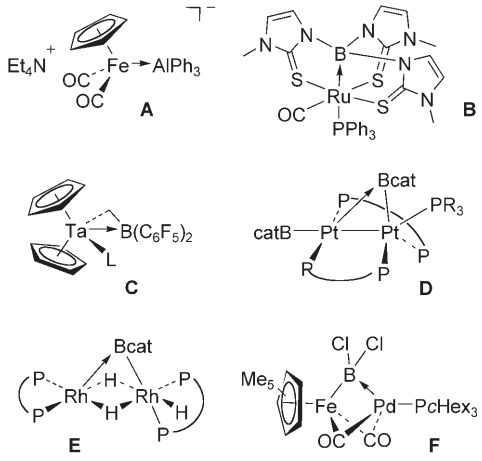
*Ambiphilic Ligands*

DOI: 10.1002/anie.200503649

# Rhodium(I) Complexes of a PBP Ambiphilic Ligand: Evidence for a Metal→Borane Interaction**

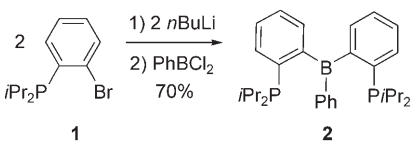
*Sébastien Bontemps, Heinz Gornitzka, Ghenwa Bouhadir, Karinne Miqueu, and Didier Bourissou**

Transition-metal complexes of Group 13 elements,[1] and especially of boron,[2] have attracted considerable interest over the last decade. A wide variety of coordination modes have been characterized structurally and investigated theoretically.[3] In particular, the possibility for Lewis acids $ER_3$ (E = B, Al…) to behave as σ-acceptor ligands has been demonstrated, although examples of such M→$ER_3$ interactions remain very rare. Indeed, despite the structural characterization of the transition metal→alane complex $Et_4N^+$-$[CpFe(CO)_2(AlPh_3)]^-$ (**A**) as early as 1979,[4] it was not until 1999 that Hill reported the first solid-state structure of a borane complex.[5a] The synthesis of the ruthenaboratrane **B** clearly represents a major breakthrough, the borane moiety being generated in the coordination sphere of the metal by B–H activation of a tris(azolyl)borate. Following the same strategy, a few related metallaboratranes (Os, Pt, Rh, Ir, Co) have recently been prepared.[5b–h] Notably, the contribution of M→B interactions[6] has also been pointed out in the bonding description of the tantalocene–borataalkene $\eta^2$-complexes **C**[7,8] and the boryl-bridged complexes **D**–**F** (cat = 1,2-$O_2C_6H_4$).[9]




Besides the fundamental aspects associated with the bonding description of such transition metal→borane interactions, new insights might also be expected for their use in organometallic catalysis. Indeed, ligands featuring pendant borane moieties can be reasonably assumed to interact with the coordination sphere of transition metals not only by activating an M–X bond[10,11] or anchoring a substrate,[12] but also by coordinating as σ-acceptor ligands. With this in mind, we have recently initiated a research program aimed at exploring the use of so-called ambiphilic ligands. Here we report the synthesis of a diphosphanylborane derivative and its tridentate coordination to $Rh^I$ fragments. The presence of a Rh→B interaction has been demonstrated by both structural analyses and DFT calculations.

To disfavor an intramolecular phosphane→borane interaction, a phenyl ring was chosen as a rigid two-carbon linker for the target PBP ambiphilic ligand.[13] Starting from readily available (*o*-bromophenyl)phosphane **1**,[14] the desired ligand **2** was obtained in 70% yield by bromine–lithium exchange followed by electrophilic trapping with dichlorophenylborane (Scheme 1). The monomeric structure of **2** was suggested by mass spectrometry and confirmed by multinuclear NMR




***Scheme 1.*** Synthesis of the diphosphanylborane **2**.

[*] S. Bontemps, Dr. H. Gornitzka, Dr. G. Bouhadir, Dr. D. Bourissou
Laboratoire Hétérochimie Fondamentale et Appliquée du CNRS (UMR 5069)
Université Paul Sabatier
118, route de Narbonne, 31062 Toulouse Cedex 09 (France)
Fax: (+33) 5-6155-8204
E-mail: dbouriss@chimie.ups-tlse.fr
Dr. K. Miqueu
Laboratoire de Chimie Théorique et Physico-Chimie Moléculaire (UMR 5624)
Avenue de l'Université, BP 1155, 64013 Pau Cedex (France)

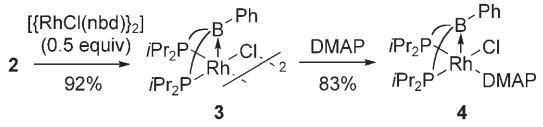
[**] We are grateful to the CNRS, UPS, and the French Ministry of Research and New Technologies (ACI JC4091) for financial support of this work. IDRIS (CNRS, Orsay, France) is acknowledged for calculation facilities.

Supporting information for this article is available on the WWW under http://www.angewandte.org or from the author.

 © 2006 Wiley-VCH Verlag GmbH & Co. KGaA, Weinheim 

spectroscopy. Indeed, the $^{31}P$ NMR chemical shift for **2** ($\delta =$ 11 ppm) is very similar to that of **1** ($\delta = 9$ ppm), and a broad signal is observed at $\delta = 43$ ppm in the $^{11}B$ NMR spectrum, as expected for a triaryl borane.

The presence of an occupied, nonbonding $d_{z^2}$ orbital makes square-planar $d^8$-$ML_4$ fragments ideal candidates for the study of metal→borane interactions.[15] The propensity of **2** for tridentate coordination through P→M and M→B interactions was thus investigated by treating it with half an equivalent of [{Rh(μ-Cl)(nbd)}$_2$] (nbd = 2,5-norbornadiene) in dichloromethane (Scheme 2). The yellow precipitate that




***Scheme 2.*** Synthesis of the rhodium(I) complexes **3** and **4**.

spontaneously formed at room temperature was collected by filtration and analyzed spectroscopically. The $^{31}P$ NMR spectrum at room temperature in solution is only poorly resolved, with several broad signals being observed, probably due to conformational restrictions. At −60 °C, however, one of the conformers becomes largely predominant. It exhibits two magnetically differentiated phosphorus atoms ($\delta = 74.7$ and 64.2 ppm ($J_{P,P} = 24.3$ Hz)) coupled to rhodium ($^1J_{P,Rh} = 151.9$ and 160.0 Hz, respectively), thereby unambiguously establishing the coordination of both phosphorus atoms to the rhodium center. Moreover, the mass spectrum is consistent with a dimeric structure of general formula [{RhCl(**2**)}$_2$]. All these features were confirmed by an X-ray diffraction study (Figure 1 a).[16] Complex **3** adopts a centrosymmetric and planar[17] chloro-bridged structure in the solid state. The rhodium center is surrounded by two phosphorus and two chlorine atoms organized in a perfectly planar arrangement ($\Sigma Rh_\alpha = 359.8°$). The bite angle of the diphosphane skeleton (P-Rh-P = 98.5°) is at the lower limit of those observed for related POP diphosphanes featuring donor diphenylether backbones (102–123°).[18] The two phenyl linkers adopt slightly different conformations (Rh-P-$C_{ipso}$-$C_{ortho}$ torsion angles of 17.8° and 24.1°), in agreement with the inequivalence of the two phosphorus atoms in the $^{31}P$ NMR spectrum in solution at −60 °C and in the solid state at room temperature ($\delta = 76.9$ ($^1J_{P,Rh} = 166.6$ Hz) and 66.5 ppm ($^1J_{P,Rh} =$ 162.8 Hz)). Interestingly, due to the folding of this rather rigid ligand, the boron atom comes close to the metal center, almost perpendicularly to the square coordination plane (P-Rh-B = 81.1° and 80.3°). The Rh–B distance (2.306 Å) is noticeably longer than the metal–boron distances observed in metallaboratranes (2.09–2.21 Å). Although these values cannot be rigorously compared to each other as the position *trans* to the borane is occupied by a donor ligand in metallaboratranes but not in complex **3**, the presence of a Rh→B interaction in **3** is further supported by the pyramidalization of the boron environment ($\Sigma B_\alpha = 338.8°$) and by the significant high-field shift of the $^{11}B$ NMR resonance signal ($\Delta\delta = -23$ ppm compared to that of the free ligand **2**).

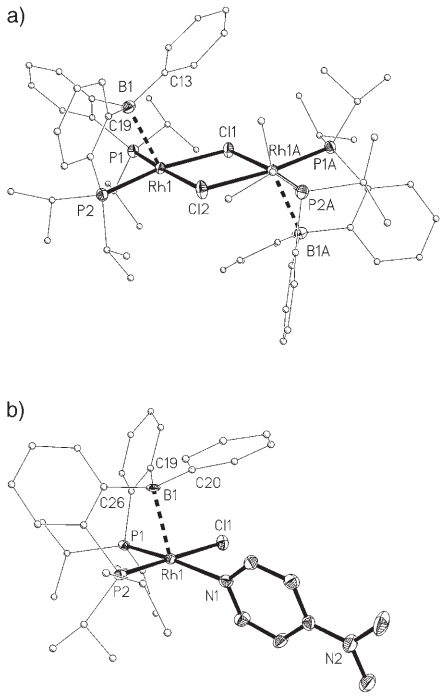



***Figure 1.*** Molecular views of **3** (a) and **4** (b) in the solid state. Hydrogen atoms have been omitted for clarity. The thermal ellipsoids are shown at 50% probability for (a) and 50% probability for (b). Selected bond lengths [Å] and angles [°]: **3**: Rh1–P1 2.2507(13), Rh1–P2 2.2710(13), Rh1–B1 2.306(3), Rh1–Cl2 2.4381(13), Rh1–Cl1 2.4492(13); P1-Rh1-P2 98.52(4), C13-B1-C19 116.3(3), C13-B1-C12 113.3(3), C19-B1-C12 109.2(3), P1-Rh1-B1 81.18(10), P2-Rh1-B1 80.41(10), B1-Rh1-Cl2 103.81(9), B1-Rh1-Cl1 106.09(10); **4**: Rh1–P2 2.2560(12), Rh1–P1 2.2856(12), Rh1–B1 2.295(5), Rh1–N1 2.153(4); P2-Rh1-P1 97.59(4), C20-B1-C19 117.6(4), C20-B1-C26 114.1(4), C19-B1-C26 108.5(4), N1-Rh1-B1 110.75(16), P2-Rh1-B1 83.55(13), P1-Rh1-B1 80.06(13), N1-Rh1-Cl1 83.63(10).

As a first evaluation of the strength of the Rh→B interaction, complex **3** was then treated with *N*,*N*-dimethylaminopyridine (DMAP) in dichloromethane (Scheme 2). Although the $^1H$ and $^{13}C$ NMR spectra revealed the presence of a coordinated DMAP in the ensuing complex **4**, no significant modification was observed by $^{11}B$ and $^{31}P$ NMR spectroscopy. An X-ray diffraction analysis (Figure 1 b)[16] revealed that cleavage of the chloro bridge had taken place due to the coordination of the Lewis basic pyridine to the metal center rather than to the boron atom. It is noteworthy that the Rh→B interaction is not significantly affected, as clearly indicated by the similarity in the geometric parameters of both complexes. Indeed, the rhodium center in the monomeric complex **4** also adopts an overall square-pyramidal geometry (P-Rh-P bite angle of 97.6°), the Rh–B distance (2.295 Å) is only marginally shorter than in **3**, and the boron environment is still significantly pyramidalized (340.3°).

To gain further insight into the nature of the Rh–B interaction, ab initio calculations[19] were performed for the mononuclear complex **4*** featuring model diphosphanylborane and DMAP ligands (methyl groups at phosphorus, hydrogen atoms at nitrogen). The key features of complex **4** (Rh–B and Rh–P bond lengths and boron pyramidalization) could be very well reproduced, especially at the BP86/[CEP-

 © 2006 Wiley-VCH Verlag GmbH & Co. KGaA, Weinheim 

31G(Rh),6-31G*(C,P,B,N,Cl,P,H)] level of theory (Table 1). Notably, the two-center, two-electron bonding interaction between the metal center and borane moiety is apparent from the frontier molecular orbitals of **4*** (major contribution from

***Table 1:*** Selected bond lengths [Å] and angles [°] for complexes **4** and **4***.

| | Rh–P | Rh–B | P-Rh-P | P-Rh-B | $\Sigma Rh_\alpha$ | $\Sigma B_\alpha$ |
|---|---|---|---|---|---|---|
| X-ray | 2.286(1) | 2.295(5) | 97.59(4) | 80.1(1) | 360.2 | 340.2 |
| | 2.256(1) | | | 83.6(1) | | |
| B3LYP/ | 2.296 | 2.458 | 97.52 | 78.13 | 359.3 | 344.6 |
| LanL2DZ(Rh)[a] | 2.265 | | | 81.38 | | |
| BP86/ | 2.282 | 2.392 | 97.39 | 78.61 | 359.2 | 342.8 |
| LanL2DZ(Rh)[a] | 2.249 | | | 82.04 | | |
| BP86/CEP- | 2.281 | 2.384 | 97.38 | 78.51 | 359.2 | 339.2 |
| 31G(Rh)[a] | 2.251 | | | 81.97 | | |
| BP86/SDD(Rh)[a] | 2.274 | 2.381 | 97.41 | 78.63 | 359.2 | 342.2 |
| | 2.241 | | | 82.10 | | |

[a] The 6-31G* basis set was used for C,P,B,Cl,N,P,H.

the $d_{z^2}$(Rh) orbital to the HOMO (Figure 2a) with little distortion due to its interaction with a vacant boron orbital, and antibonding combination of the $d_{z^2}$(Rh) and 2p(B) orbitals in the LUMO (Figure 2b)). This qualitative description was further confirmed by a natural bond orbital (NBO) analysis, second-order perturbation theory being particularly suitable for the description of donor–acceptor interactions. A natural localized molecular orbital (NLMO) was found to account for the Rh–B bonding interaction (Figure 2c) with about 79.3% contribution from the rhodium lone-pair ($d_{z^2}$) and major "delocalization tails" (17.1%) from a vacant boron orbital. In agreement with the pyramidalization of the boron environment, this transfer of electron density from the metal to the σ-acceptor ligand is accompanied by some hybridization of the formerly vacant 2p(B) orbital (the corresponding natural atomic orbital (NAO) decomposition of the NLMO features 12.7% of s character).[19] Although the precise value for this donor–acceptor interaction is meaningless (in the range 30–58 kcal mol$^{-1}$, depending on the level of calculations), its magnitude is remarkable and in good agreement with the observation of the cleavage of the chloro bridge and retention of the Rh→B interaction in the reaction of complex **3** with DMAP.

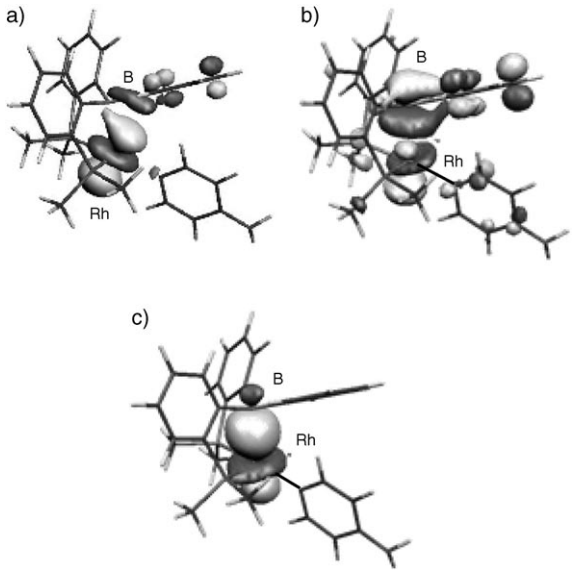



***Figure 2.*** Molekel plots (cutoff: 0.04) of the HOMO (a), LUMO (b), and NLMO (c) accounting for the Rh–B interaction in the model complex **4*** at the BP86/[CEP-31G(Rh),6-31G*(C,P,B,N,Cl,P,H)] level of theory.

In conclusion, evidence for Rh→B interactions has been provided by both structural analyses and DFT calculations for the 16-electron square-pyramidal $Rh^I$ complexes **3** and **4** derived from the ambiphilic PBP ligand **2**. This highlights that these very rare transition metal→borane interactions 1) are readily accessible by coordination of preformed borane-containing ligands, 2) exist even in complexes not featuring donor ligands in the position *trans* to the Lewis acid, and 3) are resistant to the action of a Lewis base such as DMAP. The influence of such M→B interactions on the reactivity of the resulting complexes is currently under investigation, as are variations of the metal fragment and of the stereoelectronic properties of the ambiphilic ligand.

## *Experimental Section*

All reactions and manipulations were carried out under an atmosphere of dry argon, using standard Schlenk techniques. Unless otherwise stated, the NMR spectra were recorded at 293 K.

***2***: *n*BuLi (2.5 M in hexane, 5.2 mL, 12.9 mmol) and dichlorophenylborane (0.84 mL, 6.5 mmol) were successively added at −40 °C and −78 °C, respectively, to a solution of **1** in toluene (20 mL). After warming to room temperature, the volatiles were removed under vacuum, the residue was dissolved in diethyl ether (20 mL), and the salts were removed by filtration. Diphosphanylborane **2** (2.04 g, 69%) was obtained as a white solid upon removal of the solvent. M.p. 95–97 °C; $^{11}$B NMR (128.4 MHz, $C_6D_6$): $\delta = 43.1$ ppm; $^{31}P\{^1H\}$ NMR (162.0 MHz, $C_6D_6$): $\delta = 11.0$ ppm; MS (EI, 70 eV): $m/z$: 474 $[M]^+$.

**3**: A solution of **2** (1.00 g, 2.1 mmol) in $CH_2Cl_2$ (6 mL) was added at −78 °C to a solution of $[\{Rh(\mu\text{-}Cl)(nbd)\}_2]$ (486 mg, 1.1 mmol) in $CH_2Cl_2$ (10 mL). After warming the mixture to room temperature and stirring for 1 h, complex **3** (921 mg, 72%) was collected by filtration. Crystals suitable for X-ray crystallography were obtained from a saturated toluene solution at −4 °C. M.p. 205 °C; $^{11}$B NMR (160.5 MHz, $CDCl_3$): $\delta = 20.0$ ppm; $^{31}P\{^1H\}$ NMR (161.8 MHz, solid state): $\delta = 76.9$ (d, $^1J_{P,Rh} = 166.6$ Hz), 66.5 ppm (d, $^1J_{P,Rh} = 162.8$ Hz); $^{103}$Rh NMR (15.8 MHz, $CDCl_3$, 213 K) $\delta = -7365$ ppm; MS (DCI/$NH_3$): $m/z$: 1242 $[M+NH_4]^+$; C,H analysis (%) calcd. for $C_{30}H_{41}BClP_2Rh$: C 58.80, H 6.74; found: C 58.99, H 7.11.

**4**: A solution of DMAP (40 mg, 0.33 mmol) in $CH_2Cl_2$ (2 mL) was added at −78 °C to a solution of **3** (200 mg, 0.16 mmol) in $CH_2Cl_2$ (10 mL). After warming to room temperature, complex **4** (203 mg, 83%) was collected by filtration. Crystals suitable for X-ray crystallography were obtained from a saturated THF/pentane solution at −20 °C. M.p. 137 °C; $^{11}$B NMR (160.5 MHz, $CDCl_3$): $\delta = 19.4$ ppm; $^{31}P\{^1H\}$ NMR (202.5 MHz, $CDCl_3$): $\delta = 66.8$ (dd, $^1J_{P,Rh} = 169.8$, $^2J_{P,P} = 31.0$ Hz), 65.3 ppm (dd, $^1J_{P,Rh} = 144.5$, $^2J_{P,P} = 31.0$ Hz); $^{103}$Rh NMR (15.8 MHz, $CDCl_3$): $\delta = -7552$ ppm.

Received: October 14, 2005

**Keywords:** σ-acceptor ligands · ab initio calculations · boranes · phosphanes · rhodium

 © 2006 Wiley-VCH Verlag GmbH & Co. KGaA, Weinheim 

[1] R. A. Fischer, J. Weiß, *Angew. Chem.* **1999**, *111*, 3002 – 3022; *Angew. Chem. Int. Ed.* **1999**, *38*, 2830 – 2850.

[2] a) H. Wadepohl, *Angew. Chem.* **1997**, *109*, 2547 – 2550; *Angew. Chem. Int. Ed. Engl.* **1997**, *36*, 2441 – 2444; b) H. Braunschweig, *Angew. Chem.* **1998**, *110*, 1882 – 1898; *Angew. Chem. Int. Ed.* **1998**, *37*, 1786 – 1801; c) G. J. Irvine, M. J. Lesley, T. B. Marder, N. C. Norman, C. R. Rice, E. G. Robins, W. R. Roper, G. R. Whittell, L. J. Wright, *Chem. Rev.* **1998**, *98*, 2685 – 2722; d) M. R. Smith III, *Prog. Inorg. Chem.* **1999**, *48*, 505 – 567; e) H. Braunschweig, M. Colling, *Coord. Chem. Rev.* **2001**, *223*, 1 – 51; f) N. N. Greenwood, *Coord. Chem. Rev.* **2002**, *226*, 61 – 69; g) H. Braunschweig, M. Colling, *Eur. J. Inorg. Chem.* **2003**, 393 – 403; h) S. Aldridge, D. L. Coombs, *Coord. Chem. Rev.* **2004**, *248*, 535 – 559.

[3] G. Frenking, N. Fröhlich, *Chem. Rev.* **2000**, *100*, 717 – 774.

[4] J. M. Burlitch, M. E. Leonowicz, R. B. Petersen, R. E. Hughes, *Inorg. Chem.* **1979**, *18*, 1097 – 1105.

[5] a) A. F. Hill, G. R. Owen, A. J. P. White, D. J. Williams, *Angew. Chem.* **1999**, *111*, 2920 – 2923; *Angew. Chem. Int. Ed.* **1999**, *38*, 2759 – 2761; b) M. R. St.-J. Foreman, A. F. Hill, G. R. Owen, A. J. P. White, D. J. Williams, *Organometallics* **2003**, *22*, 4446 – 4450; c) M. R. St.-J. Foreman, A. F. Hill, A. J. P. White, D. J. Williams, *Organometallics* **2004**, *23*, 913 – 916; d) I. R. Crossley, A. F. Hill, *Organometallics* **2004**, *23*, 5656 – 5658; e) D. J. Mihalcik, J. L. White, J. M. Tanski, L. N. Zakharov, G. P. A. Yap, C. D. Incarvito, A. L. Rheingold, D. Rabinovitch, *Dalton Trans.* **2004**, 1626 – 1634; f) I. R. Crossley, M. R. St.-J. Foreman, A. F. Hill, A. J. P. White, D. J. Williams, *Chem. Commun.* **2005**, 221 – 223; g) I. R. Crossley, A. F. Hill, A. C. Willis, *Organometallics* **2005**, *24*, 1062 – 1064; h) I. R. Crossley, A. F. Hill, E. R. Humphrey, A. C. Willis, *Organometallics* **2005**, *24*, 4083 – 4086.

[6] Metal→boron interactions have also been proposed to account for the bent structure of metallocenylboranes, and the delocalized through-space nature of such M→B interactions has been recently established theoretically for ferrocenylboranes: a) M. Scheibitz, M. Bolte, J. W. Bats, H.-W. Lerner, I. Nowik, R. H. Herber, A. Krapp, M. Lein, M. C. Holthausen, M. Wagner, *Chem. Eur. J.* **2005**, *11*, 584 – 603; b) K. Venkatasubbaiah, L. N. Zakharov, W. S. Kassel, A. L. Rheingold, F. Jäkle, *Angew. Chem.* **2005**, *117*, 5564 – 5569; *Angew. Chem. Int. Ed.* **2005**, *44*, 5428 – 5433, and references therein.

[7] a) K. S. Cook, W. E. Piers, R. McDonald, *Organometallics* **1999**, *18*, 1575 – 1577; b) K. S. Cook, W. E. Piers, R. McDonald, *Organometallics* **2001**, *20*, 3927 – 3937; c) K. S. Cook, W. E. Piers, R. McDonald, *J. Am. Chem. Soc.* **2002**, *124*, 5411 – 5418.

[8] Somewhat related zirconium and palladium complexes of boron-bridged diylides have recently been reported: F. Jiang, P. J. Shapiro, F. Fahs, B. Twamley, *Angew. Chem.* **2003**, *115*, 2755 – 2757; *Angew. Chem. Int. Ed.* **2003**, *42*, 2651 – 2653.

[9] a) D. Curtis, M. J. G. Lesley, N. C. Norman, A. G. Orpen, J. Starbuck, *J. Chem. Soc. Dalton Trans.* **1999**, 1687 – 1694; b) S. A. Westcott, T. B. Marder, R. T. Baker, R. L. Harlow, J. C. Calabrese, K. C. Lam, Z. Lin, *Polyhedron* **2004**, *23*, 2665 – 2677; c) H. Braunschweig, K. Radacki, D. Rais, G. R. Whittell, *Angew. Chem.* **2005**, *117*, 1217 – 1219; *Angew. Chem. Int. Ed.* **2005**, *44*, 1192 – 1193.

[10] For metallocene complexes featuring pendant boryl groups, see: a) W. E. Piers, *Chem. Eur. J.* **1998**, *4*, 13 – 18; b) M. Hill, G. Kehr, R. Fröhlich, G. Erker, *Eur. J. Inorg. Chem.* **2003**, 3583 – 3589; c) M. Hill, G. Erker, G. Kehr, R. Fröhlich, O. Kataeva, *J. Am. Chem. Soc.* **2004**, *126*, 11046 – 11057; d) S. J. Lancaster, S. Al-Benna, M. Thornton-Pett, M. Bochmann, *Organometallics* **2000**, *19*, 1599 – 1608.

[11] The activation of a nickel–methyl bond by a phosphanylalane has been reported in the context of silane polymerization: F.-G. Fontaine, D. Zargarian, *J. Am. Chem. Soc.* **2004**, *126*, 8786 – 8794.

[12] Boron analogs of 2,3-*O*-isopropylidene-2-3-dihydroxy-1,4-bis-(diphenylphosphanyl)butane (diop) have been simultaneously and independently investigated by the groups of Kagan and Jacobsen: a) A. Börner, J. Ward, K. Kortus, H. B. Kagan, *Tetrahedron: Asymmetry* **1993**, *4*, 2219 – 2228; b) L. B. Fields, E. N. Jacobsen, *Tetrahedron: Asymmetry* **1993**, *4*, 2229 – 2240.

[13] Transition metal complexes of bis(phosphanylmethyl)boranes have recently been reported, but here metal→boron interactions are geometrically prohibited by the short methylene linkers: a) L. Turculet, J. D. Feldman, T. D. Tilley, *Organometallics* **2004**, *23*, 2488 – 2502; b) J. C. Thomas, J. C. Peters, *Polyhedron* **2004**, *23*, 2901 – 2913.

[14] M. Tamm, B. Dreßel, K. Baum, T. Lügger, T. Pape, *J. Organomet. Chem.* **2003**, *677*, 1 – 9.

[15] G. Aullón, S. Alvarez, *Inorg. Chem.* **1996**, *35*, 3137 – 3144.

[16] Crystal data for **3**: $C_{35.25}H_{46.5}BClP_2Rh$, $M = 681.33$, tetragonal, space group $P4_22_12$, $a = b = 20.711(11)$, $c = 15.503(9)$ Å, $V = 6650(7)$ Å$^3$, $Z = 8$, $\mu(Mo_{K\alpha}) = 0.713$ mm$^{-1}$, crystal size $0.2 \times 0.3 \times 0.3$ mm$^3$, 39070 reflections collected (6801 independent, $R_{int} = 0.1009$), 453 parameters, $R1(I > 2\sigma(I)) = 0.0312$, $wR2$(all data) = 0.0711, largest diff. peak and hole: 0.750 and $-0.337$ e Å$^{-3}$. **4**: $C_{41}H_{59}BClN_2OP_2Rh$, $M = 807.01$, triclinic, space group $P\bar{1}$, $a = 10.0198(8)$, $b = 10.2336(8)$, $c = 21.9239(18)$ Å, $\alpha = 100.279(2)$, $\beta = 91.578(2)$, $\gamma = 115.263(1)°$, $V = 1986.8(3)$ Å$^3$, $Z = 2$, $\mu(Mo_{K\alpha}) = 0.612$ mm$^{-1}$, crystal size $0.1 \times 0.3 \times 0.4$ mm$^3$, 8716 reflections collected (5588 independent, $R_{int} = 0.0822$), 452 parameters, $R1(I > 2\sigma(I)) = 0.0434$, $wR2$(all data) = 0.0966, largest diff. peak and hole: 1.018 and $-0.578$ e Å$^{-3}$. Data for all structures were collected at 133(2) K for an oil-coated, shock-cooled crystal on a Bruker-AXS CCD 1000 diffractometer ($\lambda = 0.71073$ Å). The structures were solved by direct methods (SHELXS-97),[20] and refined using the least-squares method on $F^2$.[21] CCDC-286287 (**3**) and -286288 (**4**) contain the supplementary crystallographic data for this paper. These data can be obtained free of charge from The Cambridge Crystallographic Data Centre via www.ccdc.cam.ac.uk/data_request/cif.

[17] G. Aullón, G. Ujaque, A. Lledós, S. Alvarez, P. Alemany, *Inorg. Chem.* **1998**, *37*, 804 – 813.

[18] a) P. Dierkes, P. W. N. M. van Leeuwen, *J. Chem. Soc. Dalton Trans.* **1999**, 1519 – 1529; b) Z. Freixa, P. W. N. M. van Leeuwen, *Dalton Trans.* **2003**, 1890 – 1901.

[19] See Supporting Information for details.

[20] G. M. Sheldrick, *Acta Crystallogr. Sect. A* **1990**, *46*, 467 – 473.

[21] SHELXL-97, Program for Crystal Structure Refinement, G. M. Sheldrick, University of Göttingen, **1997**.


 © 2006 Wiley-VCH Verlag GmbH & Co. KGaA, Weinheim 

Amino Acid Synthesis

DOI: 10.1002/anie.200504196

# Enantiomerically Enriched Allylglycine Derivatives through the Catalytic Asymmetric Allylation of Iminoesters and Iminophosphonates with Allylsilanes**

*Hiroshi Kiyohara, Yoshitaka Nakamura, Ryosuke Matsubara, and Shū Kobayashi**

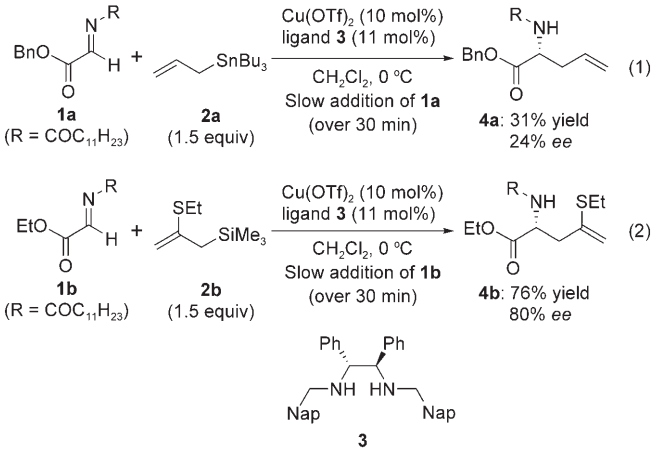
The synthesis of α-amino acids is one of the most important topics in modern medicinal chemistry.[1] Among the variety of synthetic methods so far reported, asymmetric carbon–carbon bond-forming reactions of iminoesters provide an efficient route to optically active α-amino acids. While catalytic asymmetric Mannich-type reactions of N-protected iminoesters have already been reported by several groups,[2] few examples of catalytic asymmetric allylations of iminoesters are known despite their utility in organic synthesis.[3] Lectka and co-workers reported that *N*,*O*-acetals react with β-phenylallyltrimethylsilane in the presence of a $Cu^{I}$/binap (binap = 2,2′-bis(diphenylphosphino)-1,1′-binaphthyl) complex,[3a] and they also disclosed reactions of *N*-tosyl iminoesters with β-arylallyltrimethylsilanes as well as nonsubstituted allyltrimethylsilane under similar conditions.[3d] However, only β-arylallylsilane gave the desired product with high enantiomeric purity while other allyltrialkylsilanes gave moderate selectivities (up to 72% *ee*). Jørgensen and co-workers reported highly enantioselective reactions of *N*-tosyl iminoesters with allyltributyltin.[3b,c] They showed that the use of allylsilanes resulted in low yields with low selectivity. Additionally, from a viewpoint of synthetic utility, a sulfonyl group at the nitrogen center is sometimes problematic for deprotection compared to amide or alkoxycarbonyl groups. Hence, the development of environmentally friendlier, efficient, and practical methods is strongly desired. Herein, we report a $Cu^{II}$-catalyzed, highly enantioselective allylation of *N*-acyl and *N*-alkoxycarbonyl iminoesters using environmentally benign allylsilanes as nucleophiles. The first example of catalytic enantioselective allylations of iminophosphonates for the synthesis of α-aminophosphonic acids and their phosphonate esters is also described.

[*] H. Kiyohara, Y. Nakamura, R. Matsubara, Prof. Dr. S. Kobayashi
Graduate School of Pharmaceutical Sciences
The University of Tokyo
The HFRE Division, ERATO
Japan Science Technology Agency (JST)
Hongo, Bunkyo-ku, Tokyo 113-0033 (Japan)
Fax: (+81) 3-5684-0634
E-mail: skobayas@mol.f.u-tokyo.ac.jp

[**] This work was partially supported by a Grant-in-Aid for Scientific Research from the Japan Society of the Promotion of Sciences (JSPS). H.K. and R.M. thank the JSPS for Fellowships for Japanese Junior Scientists.

Supporting information for this article is available on the WWW under http://www.angewandte.org or from the author.

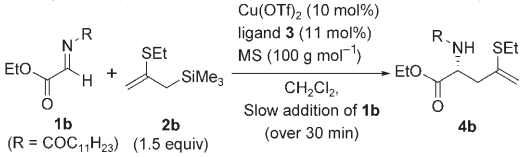
Allylation reactions of *N*-acyliminoester **1** with several allylating reagents were examined in the presence of a copper complex (10 mol%) prepared from $Cu(OTf)_2$ and diamine **3**, which was an efficient catalyst for Mannich-type reactions of iminoesters with silicon enolates.[2f,g] Relatively reactive allyltributylstannane (**2a**) was found to give the desired product, albeit in low yield with low selectivity (Scheme 1, Eq. (1)). On the other hand, when allylsilane **2b**, which bears a sulfur substituent at the β-position to the silicon atom, was employed[4] the allylated product was obtained in high yield with high selectivity [Scheme 1, Eq. (2)].




***Scheme 1.*** Allylation reactions of iminoester **1** with several allylating reagents **2** catalyzed by $Cu^{II}$/**3**. Bn = benzyl; Tf = trifluoromethanesulfonyl; Nap = α-naphthyl.

However, the result was not reproducible (66–76% yield, 68–80% *ee*) especially in terms of selectivity. To address this issue, we then examined the addition of dehydrating agents as well as several procedures to add the substrates (Table 1). The addition of 3-Å molecular sieves (3Å MS) and slow addition of the substrates were found to improve the yield, selectivity, and reproducibility (84% yield, 86% *ee*; entry 4, Table 1). The 3Å MS were essential for the removal of water, which

***Table 1:*** $Cu^{II}$/**3**-catalyzed reactions of iminoester **1b** with allylsilane **2b**.




| Entry | MS | *T* [°C] | Yield [%] | *ee* [%] |
|---|---|---|---|---|
| 1 | – | 0 | 66–76 | 68–80 |
| 2 | 3Å | 0 | 44 | 87 |
| 3 | 3Å | −20 | 56 | 80 |
| 4[a] | 3Å | 0 | 84 | 86 |
| 5[a] | 4Å | 0 | 77 | 80 |
| 6[a] | 5Å | 0 | 70 | 85 |
| 7[a,b] | 3Å | 0 | 76 | 93 |

[a] Allylsilane **2b** (1.36 equiv) was also slowly added (see Supporting Information). [b] Toluene was used as a cosolvent. MS = molecular sieves.

 © 2006 Wiley-VCH Verlag GmbH & Co. KGaA, Weinheim 

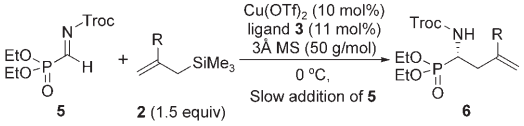
may induce partial hydrolysis of nucleophile **2b** to form a thiol (a potential copper poison). A lower temperature was not beneficial for this reaction (entry 3, Table 1). Slow addition of the substrates suppressed an uncatalyzed background reaction that otherwise furnished racemic product (entry 5, Table 1). Of the molecular sieves tested, 3Å MS were found to be superior to 4Å and 5Å MS. The best enantioselectivity (93% *ee*; entry 7, Table 1) was obtained when toluene was used as a co-solvent in the presence of 3Å MS and when both substrates were simultaneously added to the catalyst solution over 30 min.

Under these optimal conditions, various combinations of electrophiles and nucleophiles were then examined (Table 2). The use of allylsilane **2c** also led to a high yield with high selectivity (entry 2, Table 2). While *N*-acetyl iminoester **1c** gave high selecitivity (entry 3, Table 2), less reactive allylsilane **2d** afforded the desired product in good yield with high selectivity (entry 4, Table 2). Additionally, methallyltrimethylsilane (**2e**) gave a lower yield with high selectivity, and only a trace amount of the desired product was obtained when allyltrimethylsilane (**2f**) was treated with iminoester **1b** under the same conditions. These results, regarding yields, are consistent with a relative reactivity of allylsilane nucleophiles **2b–f** (entries 1–6, Table 2). Allylsilanes **2b** and **2c** also reacted with *N*-Boc iminoesters smoothly to afford the desired adducts in good yields with high selectivities (entries 10 and 11, Table 2).

We presumed the formation of a [4+2]-type self-condensation adduct of iminoester **1b** when less-nucleophilic allylsilanes were employed. We thought at this stage that if less-electrophilic iminoesters were used instead of **1b**, then the self-condensation may be suppressed and even less nucleophilic allylsilanes may react with iminoesters to afford the desired adducts. On the basis of this assumption, we conducted the reaction of *N*-Cbz iminoester **1d** with methallyltrimethylsilane (**2e**). To our delight, the reaction proceeded smoothly to afford the desired allylated adduct in excellent yield and with moderate selectivity. After optimization, the selectivity was improved to 88% *ee* (entry 8, Table 2). These optimal conditions were found to be applicable to the reaction with allyltrimethylsilane **2f** (entry 9, Table 2).[5]

Furthermore, we were pleased to find that this catalyst system could be successfully applied to allylations of iminophosphonate **5** (Table 3). As reported previously,[6] the catalyst turnover frequency was lower in reactions of iminophosphonates than in those of iminoesters. Therefore, slow addition of the electrophile was also essential in this allylation reaction. Note that even less reactive allylsilanes such as **2e** and **2f** afforded the desired products in good yields and with high enantioselectivities, and that highly enantioselective allylation of an iminophosphonate was attained for the first time.

***Table 3:*** $Cu^{II}$/**3a**-catalyzed reactions of iminophosphonate **5** with allylsilanes **2**.

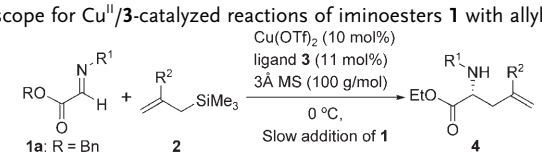



| Entry | 2 | Addition of 2 | Product | Yield [%] | *ee* [%] |
|---|---|---|---|---|---|
| 1[a,b] | **2b**: R = SEt | 0.14+1.36 | **6a** | 80 | 82 |
| 2[a,b] | **2c**: R = SPh | 0.14+1.36 | **6b** | 86 | 79 |
| 3[c] | **2d**: R = Ph | 1.5+0 | **6c** | 71 | 85 |
| 4[c] | **2e**: R = $CH_3$ | 1.5+0 | **6d** | 73 | 89 |
| 5[c] | **2f**: R = H | 1.5+0 | **6e** | 66 | 80 |

[a] $CH_2Cl_2$ as the solvent. [b] Simultaneous slow addition of **2**. [c] $CH_2Cl_2$/THF. Troc = trichloroethyloxycarbonyl.

In summary, highly enantioselective and efficient allylation reactions of iminoesters and an iminophosphonate using various allylsilanes, catalyzed by a copper complex prepared from $Cu(OTf)_2$ and chiral diamine **3**, have been developed. Whereas the study of catalytic asymmetric allylations with iminoesters was relatively neglected in relation to the corresponding Mannich-type reactions, this study provides a useful method for the preparation of a variety of amino acids as well as aminophosphonic acids based on the allylation protocol. Further investigations to improve the yields and enantioselectivity by optimization of the ligand are currently in progress.

***Table 2:*** Substrate scope for $Cu^{II}$/**3**-catalyzed reactions of iminoesters **1** with allylsilanes **2**.




| Entry | 1 | 2 | Addition of 2[a] | Product | Yield [%] | *ee* [%] |
|---|---|---|---|---|---|---|
| 1[b,c] | **1b**: $R^1$ = $C_{11}H_{23}CO$ | **2b**: $R^2$ = SEt | 0.14+1.36 | **4b** | 76 | 93 |
| 2[b,c] | **1b**: $R^1$ = $C_{11}H_{23}CO$ | **2c**: $R^2$ = SPh | 0.14+1.36 | **4c** | 84 | 92 |
| 3[c,d] | **1c**: $R^1$ = $CH_3CO$ | **2b**: $R^2$ = SEt | 0.14+1.36 | **4d** | 75 | 90 |
| 4[c,d] | **1b**: $R^1$ = $C_{11}H_{23}CO$ | **2d**: $R^2$ = Ph | 0.5+1.0 | **4e** | 68 | 91 |
| 5[d] | **1a**: $R^1$ = $C_{11}H_{23}CO$ | **2e**: $R^2$ = $CH_3$ | 3.0+0 | **4f** | 33 | 90 |
| 6[d] | **1a**: $R^1$ = $C_{11}H_{23}CO$ | **2f**: $R^2$ = H | 3.0+0 | **4g** | trace | – |
| 7[d] | **1d**: $R^1$ = Cbz | **2e**: $R^2$ = $CH_3$ | 3.0+0 | **4h** | 94 | 63 |
| 8[e] | **1d**: $R^1$ = Cbz | **2e**: $R^2$ = $CH_3$ | 3.0+0 | **4h** | 99 | 88 |
| 9[e] | **1d**: $R^1$ = Cbz | **2f**: $R^2$ = H | 3.0+0 | **4i** | 73 | 88 |
| 10[b,c] | **1e**: $R^1$ = Boc | **2b**: $R^2$ = SEt | 0.14+1.36 | **4j** | 84 | 86 |
| 11[b,c] | **1e**: $R^1$ = Boc | **2c**: $R^2$ = SPh | 0.14+1.36 | **4k** | 71 | 86 |

[a] For example, for entry 1, 0.14 equiv of **2b** was added initially, followed by the slow addition of a further 1.36 equiv of **2b** simultaneously with **1** (see Supporting Information for details). [b] $CH_2Cl_2$/toluene. [c] Simultaneous slow addition of **2**. [d] $CH_2Cl_2$ as the solvent. [e] $CH_2Cl_2$/THF. Cbz = benzyloxycarbonyl; Boc = *tert*-butoxycarbonyl.

Received: November 24, 2005
Published online: January 30, 2006

**Keywords:** allylation · amino acids · asymmetric catalysis · iminoesters · synthetic methods

 © 2006 Wiley-VCH Verlag GmbH & Co. KGaA, Weinheim 

[1] For reviews on enantioselective α-amino acid synthesis, see: a) H. Gröger, *Chem. Rev.* **2003**, *103*, 2795; b) M. J. Burk, *Acc. Chem. Res.* **2000**, *33*, 363.

[2] a) E. Hagiwara, A. Fujii, M. Sodeoka, *J. Am. Chem. Soc.* **1998**, *120*, 2474; b) D. Ferraris, B. Young, T. Dudding, T. Lectka, *J. Am. Chem. Soc.* **1998**, *120*, 4548; c) D. Ferraris, B. Young, C. Cox, W. J. Drury III, T. Dudding, T. Lectka, *J. Org. Chem.* **1998**, *63*, 6090; d) D. Ferraris, B. Young, C. Cox, T. Dudding, W. J. Drury III, L. Ryzhkov, A. E. Taggi, T. Lectka, *J. Am. Chem. Soc.* **2002**, *124*, 67, and references therein; e) N. Nishiwaki, K. R. Knudsen, K. V. Gothelf, K. A. Jørgensen, *Angew. Chem.* **2001**, *113*, 3080; *Angew. Chem. Int. Ed.* **2001**, *40*, 2992; f) K. Juhl, N. Gathergood, K. A. Jørgensen, *Angew. Chem.* **2001**, *113*, 3083; *Angew. Chem. Int. Ed.* **2001**, *40*, 2995; g) S. Kobayashi, R. Matsubara, H. Kitagawa, *Org. Lett.* **2002**, *4*, 143; h) S. Kobayashi, R. Matsubara, Y. Nakamura, H. Kitagawa, M. Sugiura, *J. Am. Chem. Soc.* **2003**, *125*, 2507; i) Y. Nakamura, R. Matsubara, H. Kiyohara, S. Kobayashi, *Org. Lett.* **2003**, *5*, 2481; j) R. Matsubara, Y. Nakamura, S. Kobayashi, *Angew. Chem.* **2004**, *116*, 1711; *Angew. Chem. Int. Ed.* **2004**, *43*, 1679.

[3] a) D. Ferraris, T. Dudding, B. Young, W. J. Drury III, T. Lectka, *J. Org. Chem.* **1999**, *64*, 2168; b) X. Fang, M. Johannsen, S. Yao, N. Gathergood, R. G. Hazell, K. A. Jørgensen, *J. Org. Chem.* **1999**, *64*, 4844; c) S. Sabby, M. Bayón, P. S. Aburel, K. A. Jørgensen, *J. Org. Chem.* **2002**, *67*, 4352; d) D. Ferraris, B. Young, C. Cox, T. Dudding, W. J. Drury III, T. Lectka, *J. Am. Chem. Soc.* **2002**, *124*, 67; For catalytic enantioselective allylation of imines and their equivalents, see: e) H. Nakamura, K. Nakamura, Y. Yamamoto, *J. Am. Chem. Soc.* **1998**, *120*, 4242; f) K. Nakamura, H. Nakamura, Y. Yamamoto, *J. Org. Chem.* **1999**, *64*, 2614; g) R. A. Fernandes, A. Stimac, Y. Yamamoto, *J. Am. Chem. Soc.* **2003**, *125*, 14133; h) T. Gastner, H. Ishitani, R. Akiyama, S. Kobayashi, *Angew. Chem.* **2001**, *113*, 1949; *Angew. Chem. Int. Ed.* **2001**, *40*, 1896; i) T. Hamada, K. Manabe, S. Kobayashi, *Angew. Chem.* **2003**, *115*, 4057; *Angew. Chem. Int. Ed.* **2003**, *42*, 3927; Erratum: T. Hamada, K. Manabe, S. Kobayashi, *Angew. Chem.* **2003**, *115*, 4714; *Angew. Chem. Int. Ed.* **2003**, *42*, 4565; For a review on enantioselective allylations, see: j) S. E. Denmark, J. Fu, *Chem. Rev.* **2003**, *103*, 2763; For a review on recent developments in allylsilane chemistry, see: k) L. Chabaud, P. James, Y. Landais, *Eur. J. Org. Chem.* **2004**, 3173.

[4] a) K. Narasaka, T. Shibata, Y. Hayashi, *Bull. Chem. Soc. Jpn.* **1992**, *65*, 8869; For the preparation of 2-alkylsulfanylallyl silanes, see: b) K. Narasaka, Y. Hayashi, H. Shimizu, S. Niihata, *J. Am. Chem. Soc.* **1992**, *114*, 8869.

[5] See the Supporting Information for deprotection steps and further transformations of the products.

[6] S. Kobayashi, H. Kiyohara, Y. Nakamura, R. Matsubara, *J. Am. Chem. Soc.* **2004**, *126*, 6558.

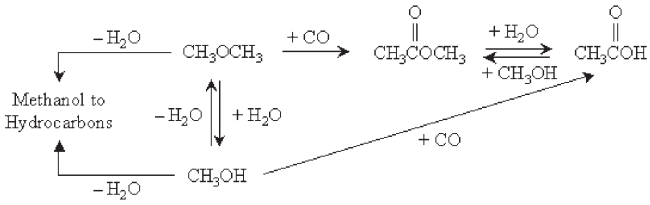
 © 2006 Wiley-VCH Verlag GmbH & Co. KGaA, Weinheim 

DOI: 10.1002/anie.200503898

# Selective Carbonylation of Dimethyl Ether to Methyl Acetate Catalyzed by Acidic Zeolites**

*Patricia Cheung, Aditya Bhan, Glenn J. Sunley, and Enrique Iglesia**

Methanol carbonylation is currently used to produce acetic acid with Rh and Ir organometallic complexes and iodide co-catalysts.[1–3] Zeolites[4–9] and Keggin polyoxometallate clusters[10–13] also catalyze the carbonylation of alcohols and ethers (Koch reaction) to form carboxylic acids and esters. Surface alkyl groups, formed by alcohol dissociation, alkene protonation, or alkane deprotonation at acidic sites react with CO to form acylium ions, which then form carboxylic acids and esters, as in the reactions of isobutane on sulfated zirconia[14] and *tert*-butyl alcohol[5,7,8] on acidic ZSM5, MOR, BEA, and Y-zeolites to form pivalic acid. Carbonylation of methanol and dimethyl ether (DME) on acidic zeolites and polyoxometallate clusters occurs concurrently with side reactions (Scheme 1) and significant catalyst deactivation.[4,6,9–13]




***Scheme 1.*** Network of carbonylation, hydration, dehydration, and methanol-to-hydrocarbon chemistries.

We report herein stable and highly selective (>99%) halide-free catalysts based on zeolites for DME carbonylation to methyl acetate at low temperatures (423–463 K). The reaction rates are much higher than for methanol carbonylation because water may adsorb competitively at CO binding sites and/or cause parallel methanol dehydration

[*] P. Cheung, A. Bhan, Professor E. Iglesia
Department of Chemical Engineering
University of California at Berkeley
Berkeley, CA 94720 (USA)
Fax: (+1) 510-642-4778
E-mail: iglesia@cchem.berkeley.edu
G. J. Sunley
BP Chemicals Limited
Hull Research and Technology Centre
Saltend, Hull HU128DS (UK)

[**] This work was supported by BP as part of the Methane Conversion Cooperative Research Program at the University of California at Berkeley. We acknowledge helpful technical discussions with Drs. Theo Fleisch, David Law, Sander Gaemers, and Ben Gracey of BP.

Supporting information for this article is available on the WWW under http://www.angewandte.org or from the author.

 © 2006 Wiley-VCH Verlag GmbH & Co. KGaA, Weinheim InterScience 

reactions. DME carbonylation involves the formation of methyl groups, which reform after reaction with CO to generate acetyl species and reactions of DME with acetyl species to give methyl acetate; these propagation steps avoid the formation of methyl groups by the initial direct reaction of DME with $H^+$, which causes an induction period during the early stages of reaction (see the Supporting Information).

DME carbonylation proceeds at approximately 423–463 K with 99% selectivity to methyl acetate; higher temperatures favor homologation and oligomerization reactions that form hydrocarbons. Figure 1 shows that the rate of methyl acetate synthesis (per total Al content) is highest on H-MOR (Si/Al = 10:1; lower on H-FER (Si/Al = 33.5), H-MOR (Si/Al = 45:1), and H-ZSM5 (Si/Al = 12.5:1); and undetectable on H-USY (Si/Al = 3:1), H-BEA (Si/Al = 12.5:1), and amorphous $SiO_2$–$Al_2O_3$ (Si/Al = 3:1) at 0.93 MPa CO, 20 kPa DME, and 420–513 K. The carbonylation rates did not show a clear correlation with the number of framework or extraframework Al atoms measured by $^{27}$Al MAS NMR spectroscopic analysis, thus suggesting that neither type of acidic site is sufficient by itself or uniform in reactivity for carbonylation turnover rates.

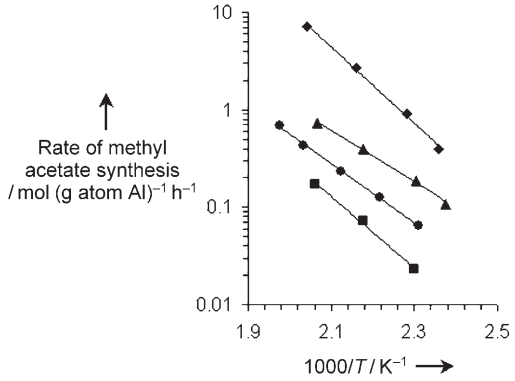



***Figure 1.*** The rate of methyl acetate formation (per total Al content) on H-MOR (Si/Al = 10:1; diamonds), H-FER (Si/Al = 33.5:1; triangles), H-MOR (Si/Al = 45:1; circles), and H-ZSM5 (Si/Al = 12.5:1; squares). Conditions: 0.93 MPa CO, 20 kPa DME, 50 kPa Ar.

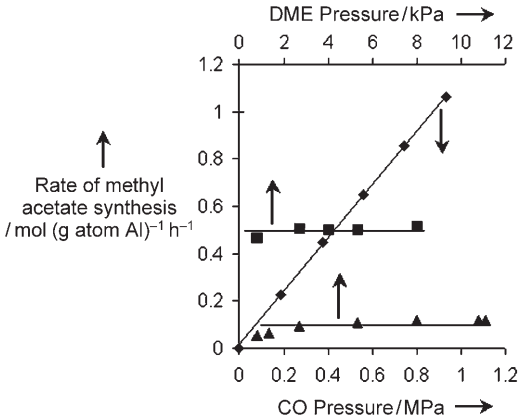



***Figure 2.*** Effects of DME (squares: 0.5 MPa CO, 438 K; triangles: 0.5 kPa $H_2O$, 0.5 MPa CO, 438 K) and CO (diamonds: 2–16 kPa DME, 438 K) concentration on the rate of methyl acetate formation on H-MOR (Si/Al = 10:1).

Kinetic and transient studies were conducted on H-MOR (Si/Al = 10:1) under conditions that led to > 99% selectivity for methyl acetate without detectable deactivation. Figure 2 shows that the rate of methyl acetate synthesis does not depend on DME pressure (0.8–8.0 kPa), which indicates that the active sites are saturated with DME-derived intermediates, and is proportional to CO pressure (0–0.93 MPa), thus showing that kinetically relevant steps involve reactions of gas-phase or adsorbed CO with DME-derived intermediates. The requirement for Brønsted acid sites is consistent with the stoichiometric effects of 2,6-dimethyl pyridine, a titrant selective to $H^+$ sites, on the rate of methyl acetate synthesis.

***Table 1:*** Steady-state carbonylation rates with methanol, DME, and DME–$H_2O$ reactants on H-MOR (Si/Al = 10:1).

| Reactants | $T$ [K] | $P_{MeOH}$ or $P_{DME}$ [kPa] | $P_{CO}$ [kPa] | $P_{H_2O}$ [kPa] | Rate of methyl acetate synthesis [mol (g atom Al)$^{-1}$ h$^{-1}$] |
|---|---|---|---|---|---|
| DME–CO | 423 | 26 | 120 | 0 | 0.034 |
| DME–CO–$H_2O$ | 423 | 26 | 120 | 1.1 | 0.0025 |
| DME–CO | 438 | 0.8–8 | 500 | 0 | 0.50 |
| DME–CO–$H_2O$ | 438 | 8–66.8 | 500 | 0.5 | 0.12 |
| $CH_3OH$–CO | 423 | 3.7 | 86 | 0 | not detected (< 0.001) |

The addition of water (0.5–1.1 kPa) to DME–CO reactants led to methanol formation and a lower rate of methyl acetate synthesis (Figure 2 and Table 1), without detectable formation of acetic acid. The rate of carbonylation gradually returned to initial values after the removal of water, which is consistent with reversible kinetic inhibition. During methanol carbonylation, parallel dehydration reactions form stoichiometric DME and $H_2O$, with the latter inhibiting the carbonylation steps. Inhibition by $H_2O$ does not reflect its competitive adsorption with DME on Brønsted acid sites or the displacement of DME-derived intermediates by $H_2O$ because the rates remain zero order with respect to DME pressure, even when $H_2O$ is present (Figure 2). $H_2O$ competes with CO for adsorption at the Lewis acid sites; this competition is possibly required to bind CO coreactants[15–18] or inhibit CO reactions with adsorbed methyl intermediates. IR spectra showed that $H_2O$ (pre-adsorbed at 298 K) prevents the binding of CO on Lewis acid sites on H-MOR at 123 K, but does not influence CO interactions with $H^+$.[19] The involvement of Lewis acid sites in DME carbonylation reactions remains equivocal at this time.

The potential role of surface methyl intermediates and the kinetic relevance of the CO addition steps were examined by DME pulsing studies (addition of DME/Al = 0.73:1–1.00:1) at 438 K on samples treated in flowing dry air at 773 K. Only DME and water were detected in the effluent during subsequent He treatment. DME adsorption ratios per Al

 © 2006 Wiley-VCH Verlag GmbH & Co. KGaA, Weinheim 

atom were approximately 0.5:1 (±0.05) on H-MOR (Si/Al = 6.5:1, 10:1) and H-ZSM5 (Si/Al = 12.5:1; Table 2), which is consistent with DME reactions with $H^+$ to form two methyl species [Eq. (1)]. The formation of the methyl species is

$$CH_3OCH_3 + 2\,[SiO(H)Al] \rightleftharpoons 2\,[SiO(CH_3)Al] + H_2O \quad (1)$$

consistent with IR and NMR spectral evidence of DME interactions with H-zeolites.[20–24]

***Table 2:*** Ratios of dosed and adsorbed DME per Al atom on zeolites at 438 K.

| Zeolite | Si/Al | $DME_{dosed}$/Al | $DME_{ads}$/Al |
|---|---|---|---|
| H-MOR | 10:1 | 1.00:1 | 0.45:1 |
| | 10:1 | 0.80:1 | 0.51:1 |
| | 10:1 | 0.73:1 | 0.45:1 |
| | 6.5:1 | 0.88:1 | 0.54:1 |
| H-ZSM5 | 12.5:1 | 0.83:1 | 0.51:1 |

Interactions of CO with these methyl groups were probed by replacing DME–CO reactants with pure CO for a specific time interval and then reintroducing DME–CO mixtures. CO reacts with methyl-saturated surfaces to form acetyl complexes that desorb only after DME is reintroduced, at which time the rate of methyl acetate formation increases sharply and then returns gradually to the steady-state values (Figure 3a). Exposing methyl-saturated samples to He led to an immediate return to steady-state rates after DME–CO mixtures were reintroduced. Precursors to methyl acetate form slowly during the contact of methyl groups with CO, but cannot desorb without methylation by DME to form methyl acetate and a new methyl intermediate.

The number of $CH_3$–CO complexes, measured from the excess methyl acetate formed as the DME–CO reactions approach steady-state, increased with CO exposure time (Figure 3b). The local slope in Figure 3b gives the rate of $CH_3$–CO formation; the dashed line shows predictions for rates proportional to the residual number of unreacted methyl species. The initial rate derived from Figure 3b is 0.42 methyl acetate (g atom Al)$^{-1}$ h$^{-1}$, which is approximately 50% of the steady-state rate (0.82 methyl acetate (g atom Al)$^{-1}$ h$^{-1}$). The reasonable agreement between the steady-state and transient rates indicates that the reaction of CO with the methyl-saturated sites is the sole kinetically relevant step in DME carbonylation reactions; the remaining differences may reflect a nonuniform reactivity of methyl groups or a different concentration of activated CO near such methyl groups, which would cause only some methyl species to form methyl acetate, while steady-state rates on the saturated surfaces reflect carbonylation rates of the most reactive methyl groups instead.

A plausible chain-transfer sequence involves initiation through reaction of DME with $H^+$ to form hydrogen-bonded DME [Eq. (2)] and methyl groups [Eqs. (3) and (4)] in steps

$$CH_3OCH_3 + [SiO(H)Al] \rightleftharpoons CH_3OCH_3 - [SiO(H)Al] \quad (2)$$

$$CH_3OCH_3 - [SiO(H)Al] \rightleftharpoons [SiO(CH_3)Al] + CH_3OH \quad (3)$$

$$CH_3OH + [SiO(H)Al] \rightleftharpoons [SiO(CH_3)Al] + H_2O \quad (4)$$

that lead to an induction period during DME–CO reactions (see the Supporting Information). CO and water adsorb competitively at sites responsible for CO binding [Eqs. (5) and (6)], and the propagation steps [Eqs. (6)–(8)] dominate in

$$H_2O + * \rightleftharpoons H_2O^* \quad (5)$$

$$CO + * \rightleftharpoons CO^* \quad (6)$$

the absence of water. The catalyst surface becomes saturated with stable methyl intermediates that react with CO in the kinetically relevant step to form adsorbed acetyl intermediates [Eq. (7)]. Methyl acetate and subsequent methyl species form by reactions of acetyl species with DME [Eq. (8)].

$$[SiO(CH_3)Al] + CO^* \rightarrow [SiO(COCH_3)Al] + * \quad (7)$$

$$[SiO(COCH_3)Al] + CH_3OCH_3 \rightarrow [SiO(CH_3)Al] + CH_3COOCH_3 \quad (8)$$

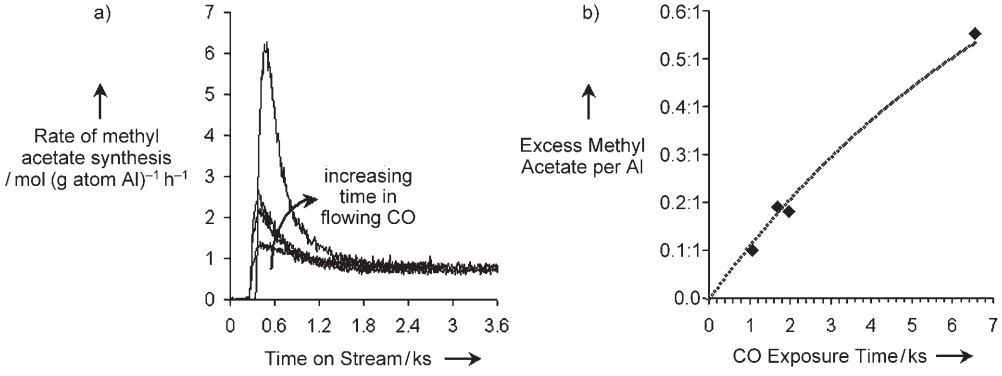



***Figure 3.*** a) The rate of methyl acetate synthesis upon reintroduction of DME–CO reactants on H-MOR (Si/Al = 10:1) after exposure to 0.95 MPa CO for varying intervals (0.93 MPa CO, 20 kPa DME, 50 kPa Ar, 438 K). b) Rate of excess methyl acetate formation (0.93 MPa CO, 20 kPa DME, 50 kPa Ar, 438 K) on H-MOR (Si/Al = 10:1) integrated over time per Al atom as a function of exposure time in 0.95 MPa CO.

In summary, acid zeolites catalyze DME carbonylation to methyl acetate at low temperatures (423–463 K) with high selectivity and catalyst stability. DME reacts with Brønsted protons to form methyl-saturated surfaces, which react with CO to form acetyl moieties. These species form methyl acetate by reaction with DME, which also restores the methyl groups initially formed by direct reaction of DME with $H^+$ during the induc-

 © 2006 Wiley-VCH Verlag GmbH & Co. KGaA, Weinheim 

tion period. DME carbonylation preserves anhydrous conditions, as conversion occurs and avoids inhibition of carbonylation pathways by $H_2O$, a process that leads to much lower carbonylation rates when methanol is used as the reactant. Kinetic and spectroscopic studies are on-going to address the nature of the CO binding sites responsible for these reactions and the apparent requirement for both Brønsted and CO binding centers in DME carbonylation catalysis. The current productivities are below the expected commercial targets but do increase linearly with CO pressure. Taken together with the remarkable selectivity for methyl acetate and the unprecedented low reaction temperatures, these initial reports show significant promise for the practical use of this catalytic chemistry as our knowledge of the nature of CO binding sites increases.

## Experimental Section

Amorphous silica alumina (Si/Al = 3:1) was obtained from Aldrich. $NH_4$-MOR (Si/Al = 10:1; Zeolyst), H-MOR (Si/Al = 45:1; Zeolyst), $NH_4$-FER (Si/Al = 33.5:1; Zeolyst), and $NH_4$-BEA (Si/Al = 12.5:1; Zeolyst), $NH_4$-ZSM5 (Si/Al = 12.5:1; AlSi-Penta Zeolithe), and $NH_4$-USY (Si/Al = 3:1; Engelhard) were treated in flowing dry air at 773 K for 3 h to form acid zeolites. Na-MOR (Si/Al = 6.5:1; Zeolyst) was converted into its $NH_4$ form by exchanging Na-MOR (10 g) with 1 M $NH_4NO_3$ (4 × 0.2 L) at 353 K for 12 h with washing and filtering in deionized water (0.2 L) after each exchange. After the last exchange, the samples were dried overnight in ambient air at 393 K before treatment in flowing dry air for 3 h at 773 K.

Carbonylation rates and selectivities were measured using a packed-bed stainless steel reactor (9.5 mm OD) equipped with a multipoint thermocouple held within a 1.6-mm outer thermowell aligned along the tube center. Catalysts (0.2–0.6 g, 125–250 μm) were treated in flowing dry air ($\approx 1.67\ cm^3 s^{-1} g^{-1}$) for 2 h at 773 K and cooled to reaction temperature (420–513 K) in flowing He (UHP, Praxair) before introducing 2% DME/93% CO/5% Ar (99.5% DME, UHP CO/Ar; Praxair), 16.7% DME/CO (99.5% DME, UHP CO; Praxair), and/or 95% CO/Ar (UHP, Praxair). Methanol was added through a saturator using He as the carrier gas, and water was added by a syringe pump (Cole-Parmer, Model 100 series) or by reaction of 1.25% $H_2$/Ar (UHP, Praxair) with CuO at 673 K. Heated lines (423–473 K) transferred the reactor effluent to a mass spectrometer (MKS Spectra Minilab) and a gas chromatograph (Agilent 6890) equipped with a methyl silicone column (HP-1, 50 m × 0.32 mm × 1.05 μm) connected to a flame-ionization detector and a Porapak Q column (80–100 mesh, 12 ft. × 1/8 in.) connected to a thermal conductivity detector.

Transient experiments were carried in the same equipment. He ($\approx 3.34\ cm^3 s^{-1} g^{-1}$, UHP; Praxair) was used to introduce DME (99.5%, Praxair) pulses (1.07 $cm^3$) at 120-s intervals. Samples were then flushed with He ($\approx 3.34\ cm^3 s^{-1} g^{-1}$) for 1.5–2 h to remove physisorbed DME and any water formed. CO, Ar, and He streams were purified of oil and water (Matheson, 451) and of metal carbonyls (Matheson, 454) prior to addition to mixtures containing DME. These streams were further dried using $CaH_2$ (Aldrich, 99%) held at ambient temperature.

Received: November 4, 2005
Published online: January 30, 2006

**Keywords:** carbonylation · carboxylic acids · ethers · heterogeneous catalysis · zeolites

[1] F. E. Paulik, J. F. Roth, *J. Chem. Soc. Chem. Commun.* **1968**, 1578.
[2] J. F. Roth, J. H. Craddock, A. Hershman, F. E. Paulik, *Chem. Technol.* **1971**, 600.
[3] G. J. Sunley, D. J. Watson, *Catal. Today* **2000**, *58*, 293.
[4] B. Ellis, M. J. Howard, R. W. Joyner, K. N. Reddy, M. B. Padley, W. J. Smith, *Stud. Surf. Sci. Catal.* **1996**, *101*, 771.
[5] T. Li, N. Tsumori, Y. Souma, Q. Xu, *Chem. Commun.* **2003**, 2070.
[6] W. J. Smith (BP Chemicals Limited), US 5420345, **1995**.
[7] A. G. Stepanov, M. V. Luzgin, V. N. Romannikov, V. N. Sidelnikov, K. I. Zamaraev, *J. Catal.* **1996**, *164*, 411.
[8] Q. Xu, S. Inoue, N. Tsumori, H. Mori, M. Kameda, M. Tanaka, M. Fujiwara, Y. Souma, *J. Mol. Catal. A* **2001**, *170*, 147.
[9] K. Fujimoto, T. Shikada, K. Omata, H. Tominaga, *Chem. Lett.* **1984**, 2047.
[10] A. Sardesai, S. Lee, T. Tartamella, *Energy Sources* **2002**, *24*, 301.
[11] G. G. Volkova, L. M. Plyasova, A. N. Salanov, G. N. Kustova, T. M. Yurieva, V. A. Likholobov, *Catal. Lett.* **2002**, *80*, 175.
[12] G. G. Volkova, L. M. Plyasova, L. N. Shkuratova, A. A. Budneva, E. A. Paukshtis, M. N. Timofeeva, V. A. Likholobov, *Stud. Surf. Sci. Catal.* **2004**, *147*, 403.
[13] R. W. Wegman, *J. Chem. Soc. Chem. Commun.* **1994**, 947.
[14] A. G. Stepanov, M. V. Luzgin, A. V. Krasnoslobodtsev, V. P. Shmachkova, N. S. Kotsarenko, *Angew. Chem.* **2000**, *112*, 3804; *Angew. Chem. Int. Ed.* **2000**, *39*, 3658.
[15] M. Maache, A. Janin, J. C. Lavalley, E. Benazzi, *Zeolites* **1995**, *15*, 507.
[16] L. Benco, T. Bucko, J. Hafner, H. Toulhoat, *J. Phys. Chem. B* **2004**, *108*, 13656.
[17] J. A. van Bokhoven, A. M. J. van der Eerden, D. C. Koningsberger, *J. Am. Chem. Soc.* **2003**, *125*, 7435.
[18] A. Zecchina, C. O. Arean, *Chem. Soc. Rev.* **1996**, *25*, 187.
[19] P. Cheung, A. Bhan, E. Iglesia, unpublished results.
[20] W. Wang, M. Seiler, M. Hunger, *J. Phys. Chem. B* **2001**, *105*, 12553.
[21] W. Wang, A. Buchholz, M. Seiler, M. Hunger, *J. Am. Chem. Soc.* **2003**, *125*, 15260.
[22] I. I. Ivanova, A. Corma, *J. Phys. Chem. B* **1997**, *101*, 547.
[23] S. M. Campbell, X. Z. Jiang, R. F. Howe, *Microporous Mesoporous Mater.* **1999**, *29*, 91.
[24] V. A. Veefkind, J. A. Lercher, *Appl. Catal. A* **1999**, *181*, 245.

 © 2006 Wiley-VCH Verlag GmbH & Co. KGaA, Weinheim 

Cluster Compounds

DOI: 10.1002/anie.200503431

# A Chiral [2]Catenane Precursor of the Antiarthritic Gold(I) Drug Auranofin**

*Stephen Sin-Yin Chui, Rong Chen, and Chi-Ming Che**

The self-assembled formation of molecular gold(I) [2]catenanes is known. For instance, gold(I) *tert*-butylacetylide,[1a] diacetylide,[1b–f] and thiolate complexes[2] without auxiliary ligands or with sterically unencumbered auxiliary ligands are reported to generate interlocking metallocycles that are stabilized by weak $Au^I\cdots Au^I$ interactions.[3] Among these complexes, homoleptic gold(I) thiolates have received our attention because of their photophysical[4] and antiarthritic properties.[5] However, most homoleptic gold(I) thiolates with aromatic or aliphatic substituents have a low solubility in common organic solvents. Also, they usually form cyclic or polymeric structures[6,7] or their solid-state structures are unknown.

The precursor of the orally administrated antiarthritic drug auranofin, namely, 2,3,4,6-tetra-*O*-acetyl-β-1-D-thioglucopyranosato-S gold(I), is a non-aromatic homoleptic gold(I) thiolate whose chiral glycosylated thiolate ligand may impart its medicinal properties. Although the structures for auranofin $[(PEt_3)Au(SR)]$[8a] and its oxidized product $[(PEt_3)_4Au_4(SR)_2](NO_3)_2$[8b] (RSH = 2,3,4,6-tetra-*O*-acetyl-β-1-D-thioglucose) have been determined, there has been no structural information on $[\{Au(SR)\}_n]$—a precursor material for the preparation of the clinically used auranofin. Herein, we describe the structure of an unprecedented glycosylated gold(I) thiolate, namely, undeca{2,3,4,6-tetra-*O*-acetyl-β-1-D-thioglucopyranosato-S gold(I)}, $[Au_{11}(SR)_{11}]$ (**1**). Besides its unique structural features, this undecagold(I) cluster displays interesting photoluminescent properties in the solid state and in solution.

[*] Dr. S. S.-Y. Chui, R. Chen, Prof. Dr. C.-M. Che
Department of Chemistry and
Open Laboratory of Chemical Biology
Institute of Molecular Technology for Drug Discovery and Synthesis
The University of Hong Kong
Pokfulam, Hong Kong (China)
Fax: (+852) 2857-1586
E-mail: cmche@hku.hk

[**] S.S.-Y.C. acknowledges the award of a postdoctoral fellowship from The University of Hong Kong (HKU). This work is supported by the Areas of Excellence Scheme (Project No. AoE/P10/01) administrated by The University Grants Council (HKSAR) and The University of Hong Kong (University Development Fund, HKU Nanotechnology Research Institute, 00600009). We are grateful to Prof. Ian D. Williams and Dr. Herman H. Y. Sung (HKUST) for performing low-temperature X-ray crystallography. Technical assistance from Dr. Laura Y. Cao (HKUST) for MALDI-MS, Dr. Annie F. M. Siu (HKU) for ESI-MS experiments, and Mr. Steven C. F. Kui (HKU) for emission studies is also acknowledged.

Supporting information for this article is available on the WWW under http://www.angewandte.org or from the author.

$[\{Au(SR)\}_n]$ was prepared according to a reported procedure and obtained as a white solid.[9] Recrystallization of the solid from common organic solvents usually gave a fine crystalline white powder that displayed a broad peak (*d* spacing values of ca. 15.80–16.38 Å) in the powder X-ray diffraction pattern. Slow diffusion of diethyl ether into a solution of $[\{Au(SR)\}_n]$ in benzene while adding a few drops of a mixture of fluorobenzene/nitrobenzene afforded **1** as colorless platelike crystals. Single-crystal X-ray diffraction data were collected in a sealed capillary tube at −100 °C and revealed an unprecedented molecular structure of undecagold [2]catenane,[10] which contains a pair of interlocking ten- and twelve-membered cyclic subunits, $[Au_5(SR)_5]$ and $[Au_6(SR)_6]$, and one molecule of solvent (benzene). Figure 1

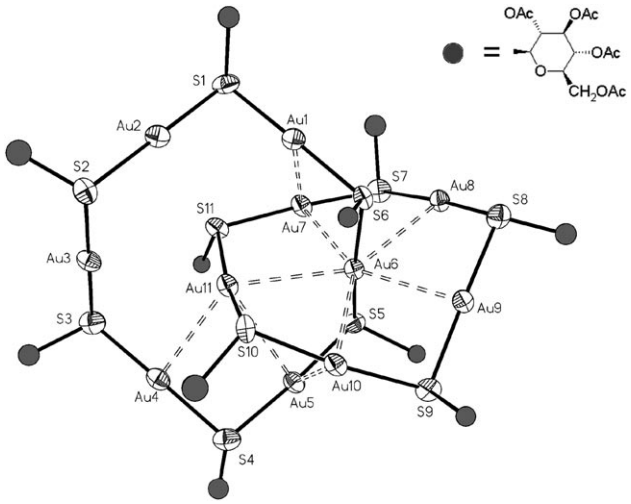



***Figure 1.*** ORTEP diagram of chiral [2]catenane **1** (ellipsoids are shown at the 40% probability level) showing interlocking cyclic $[Au_6(SR)_6]$ and $[Au_5(SR)_5]$ subunits (gray spheres represent R = 2,3,4,6-tetra-*O*-acetyl-glucopyranose rings) supported by Au···Au contacts (open dashed lines) [Å]: Au(6)–Au(7) 2.915(2), Au(6)–Au(8) 3.062(2), Au(6)–Au(9) 2.908(2), Au(6)–Au(10) 2.990(2), Au(6)–Au(11) 3.147(2), Au(11)–Au(4) 3.149(3), Au(11)–Au(5) 3.288(2), Au(1)–Au(7) 3.255(2), Au(5)–Au(10) 3.251(2).

shows the ORTEP drawing of **1** in which the two subunits are held together by weak $Au^I\cdots Au^I$ interactions (see Supporting Information for the Au–S distances and Au-S-Au/S-Au-S angles for each individual $[Au_6(SR)_6]$ and $[Au_5(SR)_5]$ subunit). Note that the undecagold [2]catenane contains $[Au_5S_5]$ and $[Au_6S_6]$ rings which interlock each other; this topology is unique, and only homoleptic gold(I) thiolate [2]catenanes that consist either of interlocking $[Au_5S_5]$ *or* $[Au_6S_6]$ rings have been reported previously.[2]

On the basis of the absolute structure parameter of 0.01(1), we determined that **1** crystallizes in a chiral space group $P2_1$ with homochiral molecular packing in the crystal structure. Interestingly, all the thioglucopyranose rings adopt the same β-anomeric configuration as that of the free ligand indicating that racemization or inversion of configuration of the coordinated ligands did not occur during the growth of the crystal. The chiral [2]catenane of **1** comprises 11 crystallographically inequivalent gold(I) cations and 11 glycosylated

 © 2006 Wiley-VCH Verlag GmbH & Co. KGaA, Weinheim 

thiolate monoanions. Each of the latter contains five stereogenic carbon atoms that preclude any inversion center and mirror symmetry within the molecule. A solution of crystalline **1** in $C_6D_6$ displays two positive (314 and 381 nm) and negative (280 and 348 nm) circular dichroism absorption bands, compatible with its chiral nature. This chiral structure is in contrast to that of myochrysin,[11] which contains racemic polymeric (*R*/*S*)-thiolmalate chains. Achiral or topologically chiral [2]catenanes containing $C_2$-symmetric ligands are assembled by template-directed synthesis, and the formation of [2]catenanes is directed by various noncovalent interactions such as hydrogen bonds, π–π stacking, hydrophobic packing, and metal–ligand coordination.[1,2,12–17] Several undecagold(I) phosphine clusters $[Au_{11}(PR_3)_7X_3]$ ($PR_3$ = phosphines, X = halides) with $C_{3v}$ and $D_{4d}$ molecular symmetry have been reported,[18] but these clusters form non-catenanes. In short, isolation of a non-topologically chiral undecagold(I) thiolate [2]catenane such as **1** that consists of enantiomerically pure ligands is unique with respect to the structural chemistry of gold(I) thiolates.

In contrast to auranofin,[8a] **1** exhibits several close $Au^I\cdots Au^I$ contacts (2.908–3.288(2) Å) between the cyclic $[Au_6(SR)_6]$ and $[Au_5(SR)_5]$ subunits, and these contacts are comparable to those found in $[(PEt_3)_4Au_4(SR)_2](NO_3)_2$ (3.106–3.171(1) Å).[8b] Longer $Au^I\cdots Au^I$ contacts (3.425–3.611(1) Å) are noted around the peripheral gold atoms of each subunit (Au2–Au3 3.521, Au3–Au4 3.571, Au6–Au1 3.593, Au7–Au8 3.611, Au10–Au11 3.570, Au11–Au7 3.597 Å). The Au–S bond lengths, which lie in the range 2.269–2.351(7) Å, are similar to those reported for auranofin (2.293 Å) and $[(PEt_3)_4Au_4(SR)_2](NO_3)_2$ (2.355 Å) and comparable to those found for homoleptic gold(I) thiolates (2.287–2.435(6) Å).[2,6] Each Au atom is two-coordinate (S-Au-S angles: 165.4–179.8°). The Au-S-Au angles (97.6–103.0° and 90.8–103.1° for the $[Au_5(SR)_5]$ and $[Au_6(SR)_6]$ subunits, respectively) deviate significantly from the idealized values for a regular pentagon (108°) and hexagon (120°). The dihedral angles Au-S-S-Au for the $[Au_5(SR)_5]$ and $[Au_6(SR)_6]$ subunits fall in the range $|24.6–61.5|°$ and $|72.6–89.2|°$, respectively. Alternatively, two different puckered gold–sulfur metallocycles for these subunits are formed in which the $[Au_5(SR)_5]$ subunit adopts a distorted pentameric ring whereas the $[Au_6(SR)_6]$ subunit forms a cyclohexane-like ring structure. Extensive weak intra- and intermolecular hydrogen bonds $CH_3C{=}O\cdots H{-}C$ are evident throughout the crystal lattice. These interactions stabilize intra-/intermolecular aggregations and minimize steric hindrance between $[Au_5(SR)_5]$ and $[Au_6(SR)_6]$ subunits (see Supporting Information).

The structure of **1** in solution was investigated by $^1$H NMR spectroscopy. Dissolution of crystals of **1** in $C_6D_6$ gave a pale yellow solution, which showed 36 resolved peaks with chemical shifts in the range $\delta = 1.670–2.781$ ppm. On the basis of integration ratios, these peaks were assigned to the 44 chemically non-equivalent methyl groups of the chiral undecagold(I) catenane. Less-resolved signals for protons of methyl groups were observed for solutions in $CCl_4$ ($\delta = 2.249–2.533$ ppm, 16 peaks), $CDCl_3$ ($\delta = 1.907–2.279$ ppm, 29 peaks), and $CD_3CN$ ($\delta = 1.902–2.288$ ppm, 14 peaks).

A single elution band with a polydispersity index of 1.12 was recorded in the gel permeation chromatograph for a solution of **1** in THF (see Supporting Information). The structure of **1** in $CH_3CN$ was studied by electrospray ionization mass spectrometry (ESI-MS); the spectrum features two prominent molecular cluster ion peaks centered at *m*/*z* 6163 and 3082, which match the simulated isotopic patterns based on $[M+H]^+$ and $[M+2H]^{2+}$ formulations, respectively (see Supporting Information). The intense $[M+H]^+$ and $[M+2H]^{2+}$ cluster ion peaks together with the $^1$H NMR spectral data reveal that the undecagold(I) structure of **1** remains intact in solution. In $C_6D_6$ solution, **1** gradually converts into a $[Au_4(SR)_4]$ complex over 24 h, and the latter was characterized by $^1$H NMR spectroscopy and MALDI-MS analyses.[19] Attempts to obtain crystals of $[Au_4(SR)_4]$ that are of suitable quality for diffraction studies were unsuccessful.

Both absorption and emission spectroscopic data suggest the presence of intramolecular $Au^I\cdots Au^I$ interactions within the undecagold(I) structure of **1** in solution. As depicted in Figure 2, the UV/Vis spectrum of **1** in $C_6H_6$ displays an intense

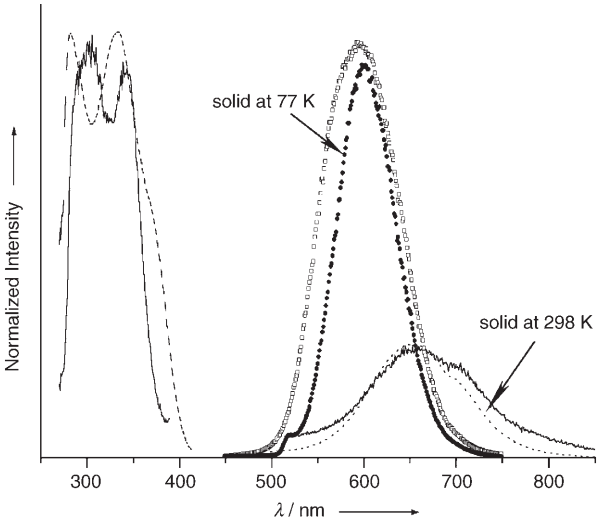



***Figure 2.*** Left: UV/Vis (-----) and excitation spectra (——; $\lambda_{em} = 650$ nm) of **1** in $C_6H_6$ solution. Right: Emission spectra of **1** at 77 K in the solid state (●) and as a glass in 2-methyltetrahydrofuran (□), and at 298 K in the solid state (-----; ×10) and in $C_6H_6$ solution (——; ×100).

absorption band at 330 nm ($\varepsilon = 13\,300\,M^{-1}cm^{-1}$) with a shoulder near 370 nm ($\varepsilon = 7800\,M^{-1}cm^{-1}$). There is little effect of the solvent on the $\lambda_{max}$ value of this band, as similar UV/Vis spectra were recorded for solutions of **1** in $CH_2Cl_2$ ($\lambda_{max}$ [nm] ($\varepsilon$ [$M^{-1}cm^{-1}$]) = 328 (12730) s; 368 (7280) sh) and $CH_3CN$ ($\lambda_{max}$ [nm] ($\varepsilon$ [$M^{-1}cm^{-1}$]) = 329 (11160) s; 363 (6690) sh). The UV/Vis spectrum of the tetrameric congener $[Au_4(SR)_4]$ ($\lambda_{max}$ [nm] ($\varepsilon$ [$M^{-1}cm^{-1}$]) = 332 (6320) in $CH_2Cl_2$; 323 (4960) in $CH_3CN$; and 339 (6170) in $C_6H_6$), obtained from heating a solution of **1** in benzene or acetonitrile at reflux for 24 h, is blue-shifted relative to that of **1**. The $\varepsilon$ values for **1** are significantly higher than those for $[Au_4(SR)_4]$ at $\lambda_{max} = 350$ nm (see Supporting Information). The absorption spectra of both **1** and $[Au_4(SR)_4]$ are significantly red-shifted with respect to that of auranofin ($\lambda_{max}$ [nm] ($\varepsilon$ [$M^{-1}cm^{-1}$]) = 242 (3950), 276 (460) in $CH_2Cl_2$; 242 (3920), 277 (350) in $CH_3CN$).

 © 2006 Wiley-VCH Verlag GmbH & Co. KGaA, Weinheim 

We also prepared $[Au_2(SR)_2(dcpm)]$ (dcpm = bis(dicyclohexylphosphanyl)methane), but its structure is unknown, making it difficult to compare its absorption spectrum ($\lambda_{max}$ [nm] ($\varepsilon$ [$M^{-1}cm^{-1}$] = 258 (25680), 292 (5360) in $CH_3CN$) with that of **1**. We ascribe the absorption bands of **1** at 330 and 370 nm in benzene to 5d(dσ*)→6p(pσ) transitions, modified by intramolecular $Au^I\cdots Au^I$ interactions present within the undecagold(I) structure. This transition lies at longer wavelengths compared to the analogous 5d(dσ*)→6p(pσ) transition of the salts $[Au_2(dppm)_2]^{2+}$ (dppm = bis(diphenylphosphanyl)methane) at $\lambda_{max} = 293$ nm ($\varepsilon \approx 21000\ M^{-1}cm^{-1}$)[20a,c] and $[Au_2(dcpm)_2]^{2+}$ at $\lambda_{max} = 277$ nm ($\varepsilon = 26000$–$29000\ M^{-1}cm^{-1}$)[20e,f] which also display $Au^I$–$Au^I$ distances of around 2.926–3.013 Å.[18b,d–f] The red shift in the 5d(dσ*)→6p(pσ) transition for **1** relative to those for the diphosphane salts could be ascribed to the anionic thiolate ligands, which destabilize the Au 5d orbitals through Au···S interactions.

Excitation of **1** at 325 nm in the solid state or in solution gives rise to a broad weak emission ($\Phi < 0.01$) with $\lambda_{em} \approx 650$ nm at 298 K. This orange emission band is significantly enhanced ($\approx$20-fold) and blue-shifted to $\lambda_{em} = 600$ nm upon cooling the solid to 77 K. A similar emission at $\lambda_{em} = 595$ nm was also observed for a frozen glassy solution of **1** in 2-methyltetrahydrofuran at 77 K. A freshly prepared solution of **1** in $CH_2Cl_2$ or $CH_3CN$ displayed multiple emission bands in the green ($\lambda_{em} = 521$–$528$ nm) and orange-red ($\lambda_{em} = 608$–614 nm with a shoulder near 650 nm) regions. The emission lifetimes ($\tau = 5.6$–$44.2$ μs) for these bands are suggestive of a triplet parentage. For $[Au_4(SR)_4]$, two weak emissions at 400 and 643 nm were observed in $CH_2Cl_2$ solution but only one emission band was observed in the solid state (see Supporting Information). As auranofin is non-emissive in both the solid and the solution states, the orange-red emission of **1** ($\lambda_{em} =$ 595–650 nm) is likely to be associated with its catenane structure. Note that polynuclear gold(I) thiolate complexes in the solid state at 298 K have been reported to emit in the visible region: mononuclear [(tpa)Au(SPhX)] (tpa = 1,3,5-triaza-7-phosphaadamantanetriylphosphine; X = H, *o*-OMe, *m*-OMe, *m*-Cl, *p*-Cl) with $\lambda_{em} = 589$–$702$ nm,[4a] dinuclear [Au(L)(pdt)Au] (pdt = 1,3-propanedithiol; L = 1,2-bis(diphenylphosphanyl)ethane, 1,3-bis(diphenylphosphanyl)propane, 1,4-bis(diphenylphosphanyl)butane, 1,5-bis(diphenylphosphanyl)pentane) with $\lambda_{em} = 500$–$515$ nm,[4b] and polymeric $[\{Au(SPh)\}_\infty]$ with $\lambda_{em} = 643$ nm.[4c] The large Stokes shift between the singlet [5d(dσ*)→6p(pσ)] absorption of **1** at 330 nm (in benzene solution) and its emission at 590–650 nm reveals that the latter could not directly originate from the metal–metal-bonded $^3$[5dσ*, 6pσ] excited state. With reference to recent work,[20e,21] the emission is assigned to originate from either exciplex formation of $Au^I$[20e,f] or a Jahn–Teller distortion of the excited state of $Au^I$,[21] both of which could involve $Au^I\cdots Au^I$ and/or Au···S excited-state bonding interactions. We note that both the absorption and emission spectra of **1** dissolved in a mixture of phosphate-buffered saline (PBS) and $CH_3CN$ (5% v/v) are similar to those recorded in benzene solution. The presence of an intense absorption band at 330 nm and the emission at 640 nm reveals that the intramolecular $Au^I\cdots Au^I$ interactions within the catenane structure of **1** are likely to be retained in PBS solution.

In summary, the self-assembled formation of the chiral [2]catenane **1** is facile. The structure-directing effect of glycosylated thiolate ligands on the formation of the chiral [2]catenane containing $[Au_5S_5]$ and $[Au_6S_6]$ rings interlocking with each other is unprecedented. As the emission of this undecagold(I) complex is related to intramolecular $Au^I\cdots Au^I$ interactions within the [2]catenane structure, it may be feasible to use emission spectroscopy to study the interaction of **1** with biomolecules.[23]

Received: September 28, 2005
Published online: January 30, 2006

**Keywords:** aurophilicity · catenanes · cluster compounds · gold · self-assembly

[1] a) D. M. P. Mingos, J. Yau, S. Menzer, D. J. Williams, *Angew. Chem.* **1995**, *107*, 2045–2047; *Angew. Chem. Int. Ed. Engl.* **1995**, *34*, 1894–1895; b) C. P. McArdle, M. J. Irwin, M. C. Jennings, R. J. Puddephatt, *Angew. Chem.* **1999**, *111*, 3571–3573; *Angew. Chem. Int. Ed.* **1999**, *38*, 3376–3378; c) R. J. Puddephatt, *Coord. Chem. Rev.* **2001**, *216*, 313–332; d) C. P. McArdle, M. J. Irwin, M. C. Jennings, J. J. Vittal, R. J. Puddaphatt, *Chem. Eur. J.* **2002**, *8*, 723–734; e) C. P. McArdle, S. Van, M. C. Jennings, R. J. Puddephatt, *J. Am. Chem. Soc.* **2002**, *124*, 3959–3965; f) F. Mohr, M. C. Jennings, R. J. Puddephatt, *Eur. J. Inorg. Chem.* **2003**, 217–223.

[2] M. R. Wiseman, P. A. Marsh, P. T. Bishop, B. J. Brisdon, M. F. Mahon, *J. Am. Chem. Soc.* **2000**, *122*, 12598–12599.

[3] a) P. Pyykkö, *Chem. Rev.* **1997**, *97*, 597–636; b) H. Schmidbaur, A. Grohmann, M. E. Olmos in *Gold: Progress in Chemistry, Biochemistry, and Technology* (Ed.: H. Schmidbaur), Wiley, Chichester, **1999**, chap. 18.

[4] a) J. M. Forward, D. Bohmann, J. P. Fackler, Jr., R. J. Staples, *Inorg. Chem.* **1995**, *34*, 6330–6336; b) W. B. Jones, J. Yuan, R. Narayanaswamy, M. A. Young, R. C. Elder, A. E. Bruce, M. R. M. Bruce, *Inorg. Chem.* **1995**, *34*, 1996–2001; c) R. E. Bachman, S. A. Bodolosky-Bettis, S. C. Glennon, S. A. Sirchio, *J. Am. Chem. Soc.* **2000**, *122*, 7146–7147.

[5] a) Z. Guo, P. J. Sadler, *Angew. Chem.* **1999**, *111*, 1610–1630; *Angew. Chem. Int. Ed.* **1999**, *38*, 1512–1531; b) C. F. Shaw III, *Chem. Rev.* **1999**, *99*, 2589–2600.

[6] a) I. Schroter, J. Strähle, *Chem. Ber.* **1991**, *124*, 2161–2164; b) P. J. Bonasia, D. E. Gindelberger, J. Arnold, *Inorg. Chem.* **1993**, *32*, 5126–5131; c) W. Wojnowski, B. Becker, J. Sassmannhausen, E. M. Peters, K. Peters, H. G. Von Schnering, *Z. Anorg. Allg. Chem.* **1994**, *620*, 1417–1421; d) D. J. LeBlanc, C. J. L. Lock, *Acta Crystallogr. Sect. C* **1997**, *53*, 1765–1768.

[7] P. J. Blower, J. R. Dilworth, *Coord. Chem. Rev.* **1987**, *76*, 121–185.

[8] a) D. T. Hill, B. M. Sutton, *Cryst. Struct. Commun.* **1980**, *9*, 679–686; b) A. A. Mohamed, J. Chen, A. E. Bruce, M. R. M. Bruce, *Inorg. Chem.* **2003**, *42*, 2203–2205.

[9] R. A. Bell, C. J. L. Lock, S. J. F. Valliant, *Inorg. Chim. Acta* **1998**, *274*, 137–142. A mixture of AuCl·DMS (0.295 g, 1 mmol; DMS = dimethyl sulfide, $(CH_3)_2S$) and 2,3,4,6-tetra-*O*-acetyl-β-D-1-thioglucose (0.400 g, 1.1 mmol) was stirred in dichloromethane (2 mL) for 10 min. The reaction mixture was evaporated to dryness, and diethyl ether (10 mL) was added to the residue. The white solid residue was filtered, washed with diethyl ether, and air-dried (0.280 g, 50%). Elemental analysis (%) calcd for $C_{154}H_{209}O_{99}S_{11}Au_{11}$: C 30.01, H 3.40; found: C 29.51, H

 © 2006 Wiley-VCH Verlag GmbH & Co. KGaA, Weinheim 

3.41. Specific rotation of **1**: $[\alpha] = -87.0°$ ($c = 0.01\ g\,mL^{-1}$ in benzene, $l = 10$ cm, $\lambda = 589$ nm, and $T = 20\,°C$; Perkin-Elmer Polarimeter Model 343). Circular dichroism spectra ($c = 400\ \mu M$; JASCO 720 spectropolarimeter): $\lambda\ nm^{-1}$ ($\Delta\varepsilon$ [mdeg]): 280 (−25.5), 314 (+26.1), 348 (−15.4), 381 (+4.3).

[10] Crystal data for **1**: $C_{160}H_{215}O_{101}S_{11}Au_{11}$, $M_r = 6273.61$, monoclinic, $P2_1$, $a = 19.547(4)$ Å, $b = 31.283(6)$ Å, $c = 21.821(4)$ Å, $\beta = 115.38(3)°$, $V = 12055(5)$ Å$^3$, $Z = 2$, $T = 173$ K, $\rho_{calcd} = 1.728\ g\,cm^{-3}$, $\mu(Mo_{K\alpha}) = 6.845\ mm^{-1}$, $F(000) = 6056$, absolute structure (Flack) parameter = −0.01(1),[22a] total number of observed [$F^2 > 2\sigma(I)$] and independent reflections 28163 ($R_{int} = 0.053$). Numbers of restraints/parameters = 3246/1230, $R1 = 0.079$ and $wR2 = 0.148$. CCDC-265292 contains the supplementary crystallographic data for this paper. These data can be obtained free of charge from The Cambridge Crystallographic Data Centre via www.ccdc.cam.ac.uk/data_request/cif. Intensity data were collected using a Bruker AXS diffractometer equipped with a Smart-Apex CCD detector at −100 °C with graphite-monochromatized $Mo_{K\alpha}$ X-ray radiation. The structure solution (SHELXS) and refinement (SHELXL) were performed using the SHELX-97 program.[22b] The structure was solved by direct methods, and the Au and S atoms were refined anisotropically, while the positions of C and O atoms of each glycosylated thiolate ligand were located subsequently and refined isotropically. All C–C and C–O distances of the glycosylated thiolate ligands were restrained to be equal to each other because they were chemically indistinguishable. One benzene solvate molecule was located and restrained as a perfect hexagon with C–C bond distances fixed at 1.390 Å. The positions of all H atoms were refined using a riding model with fixed isotropic thermal parameters (1.5-times that of attached atoms).

[11] R. Bau, *J. Am. Chem. Soc.* **1998**, *120*, 9380 – 9381.

[12] a) C. O. Dietrich-Buchecker, J. P. Sauvage, *Chem. Rev.* **1987**, *87*, 795 – 810; b) J. P. Sauvage, *Acc. Chem. Res.* **1990**, *23*, 319 – 327; c) J. F. Nierengarten, C. O. Dietrich-Buchecker, J. P. Sauvage, *J. Am. Chem. Soc.* **1994**, *116*, 375 – 376; d) D. B. Amabilino, C. O. Dietrich-Buchecker, A. Livoreil, L. Pérez-García, J. P. Sauvage, J. F. Stoddart, *J. Am. Chem. Soc.* **1996**, *118*, 3905 – 3913; e) J. P. Sauvage, C. Dietrich-Buchecker, *Molecular Catenanes, Rotaxanes, and Knots*, Wiley-VCH, Weinheim, **1999**; f) J. C. Chambron, J. P. Sauvage, K. Mislow, A. De Cian, J. Fischer, *Chem. Eur. J.* **2001**, *7*, 4085 – 4096; g) C. Dietrich-Buchecker, J. P. Sauvage, N. Geum, A. Hori, M. Fujita, S. Sakamoto, K. Yamaguchi, *Chem. Commun.* **2001**, 1182 – 1183; h) C. Dietrich-Buchecker, M. C. Jimenez-Molero, V. Sartor, J. P. Sauvage, *Pure Appl. Chem.* **2003**, *75*, 1383 – 1393.

[13] a) P. R. Ashton, T. T. Goodnow, A. E. Kaifer, M. V. Reddington, A. M. Z. Slawin, N. Spencer, J. F. Stoddart, C. Vicent, D. J. Williams, *Angew. Chem.* **1989**, *101*, 1404 – 1408; *Angew. Chem. Int. Ed. Engl.* **1989**, *28*, 1396 – 1399; b) M. Asakawa, P. R. Ashton, S. E. Boyd, C. L. Brown, S. Menzer, D. Pasini, J. F. Stoddart, M. S. Tolley, A. J. P. White, D. J. Williams, P. G. Wyatt, *Chem. Eur. J.* **1997**, *3*, 463 – 481; c) F. M. Raymo, J. F. Stoddart, *Chem. Rev.* **1999**, *99*, 1643 – 1663; d) J. F. Stoddart, *Acc. Chem. Res.* **2001**, *34*, 410 – 411.

[14] a) F. Vögtle, T. Dünnwald, T. Schmidt, *Acc. Chem. Res.* **1996**, *29*, 451 – 460; b) C. Yamamoto, Y. Okamoto, T. Schmidt, R. Jäger, F. Vögtle, *J. Am. Chem. Soc.* **1997**, *119*, 10547 – 10548; c) C. Reuter, A. Mohry, A. Sobanski, F. Vögtle, *Chem. Eur. J.* **2000**, *6*, 1674 – 1682.

[15] a) M. Fujita, *Acc. Chem. Res.* **1999**, *32*, 53 – 61; b) A. Hori, A. Akasaka, K. Biradha, S. Sakamoto, K. Yamaguchi, M. Fujita, *Angew. Chem.* **2002**, *114*, 3403 – 3406; *Angew. Chem. Int. Ed.* **2002**, *41*, 3269 – 3272; c) A. Hori, H. Kataoka, T. Okano, S. Sakamoto, K. Yamaguchi, M. Fujita, *Chem. Commun.* **2003**, 182 – 183; d) A. Hori, K. Yamashita, M. Fujita, *Angew. Chem.* **2004**, *116*, 5126 – 5129; *Angew. Chem. Int. Ed.* **2004**, *43*, 5016 – 5019.

[16] a) A. C. Try, M. M. Harding, D. G. Hamilton, J. K. M. Sanders, *Chem. Commun.* **1998**, 723 – 724; b) D. G. Hamilton, J. E. Davies, L. Prodi, J. K. M. Sanders, *Chem. Eur. J.* **1998**, *4*, 608 – 620; c) D. G. Hamilton, N. Feeder, S. J. Teat, W. Clegg, J. K. M. Sanders, *J. Am. Chem. Soc.* **1998**, *120*, 1096 – 1097.

[17] a) C. A. Hunter, *Chem. Soc. Rev.* **1994**, *23*, 101 – 109; b) H. Adams, F. J. Carver, C. A. Hunter, *J. Chem. Soc. Chem. Commun.* **1995**, 809 – 810; c) D. A. Leigh, K. Moody, J. P. Smart, K. J. Watson, A. M. Z. Slawin, *Angew. Chem.* **1996**, *108*, 326 – 331; *Angew. Chem. Int. Ed. Engl.* **1996**, *35*, 306 – 310; d) T. J. Kidd, D. A. Leigh, A. J. Wilson, *J. Am. Chem. Soc.* **1999**, *121*, 1599 – 1600; e) D. A. Leigh, P. J. Lusby, S. J. Teat, A. J. Wilson, J. K. Y. Wong, *Angew. Chem.* **2001**, *113*, 1586 – 1591; *Angew. Chem. Int. Ed.* **2001**, *40*, 1538 – 1543; f) B. Korybut-Daszkiewicz, A. Wieckowska, R. Bilewicz, S. Domagala, K. Wozniak, *J. Am. Chem. Soc.* **2001**, *123*, 9356 – 9366; g) Y. Nakamura, S. Minami, K. Iizuka, J. Nishimura, *Angew. Chem.* **2003**, *115*, 3266 – 3270; *Angew. Chem. Int. Ed.* **2003**, *42*, 3158 – 3162; h) M. R. Sambrook, P. D. Beer, J. A. Wisner, R. L. Paul, A. R. Cowley, *J. Am. Chem. Soc.* **2004**, *126*, 15364 – 15365; i) M. J. Gunter, S. M. Farquhar, K. M. Mullen, *New J. Chem.* **2004**, *28*, 1443 – 1449; j) G. D. Fallon, M. A. P. Lee, S. J. Langford, P. J. Nichols, *Org. Lett.* **2004**, *6*, 655 – 658; k) W. W. H. Wong, J. Cookson, E. A. L. Evans, E. J. L. McInnes, J. Wolowska, J. P. Maher, P. Bishop, P. D. Beer, *Chem. Commun.* **2005**, 2214 – 2216.

[18] a) F. Cariati, L. Naldini, *Inorg. Chim. Acta* **1971**, *5*, 172 – 174; b) P. Bellon, M. Manassero, M. Sansoni, *J. Chem. Soc. Dalton Trans.* **1972**, 1481 – 1487; c) F. A. Vollenbroek, D. C. P. Bouten, J. M. Trooster, J. P. van der Berg, J. J. Bour, *Inorg. Chem.* **1978**, *17*, 1345 – 1347; d) W. Bos, R. P. F. Kanters, C. J. Van Halen, W. P. Bosman, H. Behm, J. M. M. Smits, P. T. Beurskens, J. J. Bour, L. H. Pignolet, *J. Organomet. Chem.* **1986**, *307*, 385 – 398; e) R. C. B. Copley, D. M. P. Mingos, *J. Chem. Soc. Dalton Trans.* **1996**, 479 – 489.

[19] A solution of **1** in $C_6D_6$ displayed 12 additional peaks (see Supporting Informtaion) together with the 36 peaks for $[Au_{11}(SR)_{11}]$ after 24 h. These additional peaks were assigned to the 16 sets of chemically different methyl groups of the $[Au_4(SR)_4]$ cluster. Complete conversion of **1** into $[Au_4(SR)_4]$ was observed when solutions of **1** in acetonitrile or $CHCl_3$ were heated at reflux for 3 h. The solution of **1** in $C_6D_6$ and the solutions of "$[Au_4(SR)_4]$" in acetonitrile or $CHCl_3$ (after 3 h heating at reflux) also revealed two prominent peaks at *m*/*z* 2263.2 and 2279.0 in their MALDI-MS corresponding to $\{[Au_4(SR)_4] + Na\}^+$ and $\{[Au_4(SR)_4] + K\}^+$ formulations, respectively (see Supporting Information).

[20] a) C. King, J. C. Wang, M. N. I. Kahn, J. P. Fackler, Jr., *Inorg. Chem.* **1989**, *28*, 2145 – 2149; b) M. N. I. Kahn, C. King, D. D. Heinrich, J. P. Fackler, Jr., L. C. Porter, *Inorg. Chem.* **1989**, *28*, 2150 – 2154; c) C.-M. Che, H. L. Kwong, V. W. W. Yam, K. C. Cho, *J. Chem. Soc. Chem. Commun.* **1989**, 885 – 886; d) C.-M. Che, H. L. Kwong, C. K. Poon, *J. Chem. Soc. Dalton Trans.* **1990**, 3215 – 3219; e) W. F. Fu, K. C. Chan, V. M. Miskowski, C.-M. Che, *Angew. Chem.* **1999**, *111*, 2953 – 2955; *Angew. Chem. Int. Ed.* **1999**, *38*, 2783 – 2785; f) W. F. Fu, K. C. Chan, K. K. Cheung, C.-M. Che, *Chem. Eur. J.* **2001**, *7*, 4656 – 4664.

[21] K. A. Barakat, T. R. Cundari, M. A. Omary, *J. Am. Chem. Soc.* **2003**, *125*, 14228 – 14229.

[22] a) H. D. Flack, *Acta Crystallogr. Sect. A* **1983**, *39*, 876 – 881; b) G. M. Sheldrick, *SHELX-97* **1997**, University of Göttingen, Germany.

[23] a) P. A. Frey, T. G. Frey, *J. Struct. Biol.* **1999**, *127*, 94 – 100; b) D. Safer, *J. Struct. Biol.* **1999**, *127*, 101 – 105; c) W. Jahn, *J. Struct. Biol.* **1999**, *127*, 106 – 112.

 © 2006 Wiley-VCH Verlag GmbH & Co. KGaA, Weinheim 

*Spin-Crossover Complexes*

DOI: 10.1002/anie.200503252

# Photoswitching of the Dielectric Constant of the Spin-Crossover Complex $[Fe(L)(CN)_2]\cdot H_2O$**

*Sébastien Bonhommeau, Thomas Guillon, Latévi Max Lawson Daku, Philippe Demont, José Sanchez Costa, Jean-François Létard, Gábor Molnár, and Azzedine Bousseksou**

The interest in bistable molecular materials for information processing has been discussed by several authors.[1] Iron(II) spin-crossover (SCO) compounds[2] are particularly promising in this respect, because the conversion between the high-spin (HS) (S = 2) and low-spin (LS) (S = 0) states can be triggered not only by temperature, pressure,[3] and pulsed magnetic fields,[4] but also by irradiation with light.[5] This latter phenomenon—usually called light-induced excited-spin-state trapping (LIESST)—was discovered by Decurtins et al.,[6] who observed a light-induced LS→HS transition involving quantitative trapping of the molecules in the excited HS state at low temperatures (typically below 50 K). Our recent investigations demonstrated that it was feasible to trigger SCO by light even at room temperature by using a nanosecond laser pulse,[7] and potential applications of SCO compounds as active elements in optical devices were also discussed.[8]

Furthermore, we also observed hysteretic bistability in the dielectric properties of SCO materials.[9] The real part of the dielectric constant was found to be significantly different in the two spin states, which suggests that capacitance measurements can be used to "read" the information stored in the bistable system. Taking advantage of this property, we have constructed and patented a prototype of a thermal molecular memory device.[10] Within this context, the existence of a correlation between photomagnetic and dielectric properties would open interesting prospects because switchable dielectric properties and optical addressing are two physical principles widely used for information storage and processing. The possible advantages of using SCO materials for these aims include: a) the short addressing times (picosecond scale on the molecular level),[11] b) photostability over successive cycles, c) low addressing power (on the order of $mW\,cm^{-2}$), and d) high storage densities (because the LIESST effect is purely molecular).[8,12]

Herein, we report on the observation of the change in dielectric constant upon SCO induced by irradiation with light. A preliminary theoretical approach, based on density functional theory (DFT), to interpret the variation of the dielectric constant with the SCO is also presented. For this study, we selected the SCO complex $[Fe(L)(CN)_2]\cdot H_2O$[13,14] in which L is a Schiff base macrocyclic ligand derived from the condensation of 2,6-diacetylpyridine with 3,6-dioxaoctane-1,8-diamine (L = 2,13-dimethyl-6,9-dioxa-3,12,18-triazabicyclo[12.3.1]octadeca-1(18),2,12,14,16-pentaene). This molecule was chosen because its critical temperature ($T_{LIESST}$), defined as the temperature at which the light-induced HS information is erased,[8] is the highest (130 K) ever obtained for a SCO compound.[13] Dynamic dielectric spectroscopy was used to measure the light-induced and thermal variations of the complex dielectric permittivity ($\varepsilon^* = \varepsilon' - i\varepsilon''$) in the frequency range $10^2$–$10^6$ Hz. The imaginary part $\varepsilon''$ represents the dielectric losses and was found to be small and quasi-independent of temperature for each SCO complex investigated. The real part $\varepsilon'$ represents the displacement of the bounded charges under the effect of a time-dependent electric field. We will focus only on this latter physical quantity in the following discussion.

As reported previously,[13–15] the magnetic behavior of $[Fe(L)(CN)_2]\cdot H_2O$ is rather unusual: if the sample is quenched (at a rate of 20 $K\,min^{-1}$) from 300 to 77 K, the HS state may be "frozen in" and remains stable for several days. The sample transforms into a pure LS state when it is heated up to 150 K. Irradiation with light of the LS state at 10 K leads to an increase in the magnetic susceptibility (LIESST effect) as shown in Figure 1a. The magnetic behavior of the irradiated sample upon heating ($< 1\,K\,min^{-1}$) is quite complicated. First, a decrease in the $\chi_M T$ value occurs around

[*] S. Bonhommeau, T. Guillon, Dr. G. Molnár, Dr. A. Bousseksou
Laboratoire de Chimie de Coordination
CNRS UPR-8241
205, Route de Narbonne, 31077 Toulouse Cedex (France)
Fax: (+33) 5-6155-3003
E-mail: boussek@lcc-toulouse.fr
S. Bonhommeau
Laboratoire de Physique des Solides de Toulouse
CNRS UMR-5477
Université Toulouse III
118 Route de Narbonne, 31062 Toulouse Cedex (France)
Dr. L. M. Lawson Daku
Département de Chimie Physique
Université de Genève
30 quai Ernest-Ansermet, 1211 Genève 4 (Switzerland)
Prof. P. Demont
Laboratoire de Physique des Polymères-CIRIMAT
CNRS UMR-5085
Université Toulouse III
118 Route de Narbonne, 31062 Toulouse Cedex (France)
Dr. J. Sanchez Costa, Dr. J.-F. Létard
Institut de Chimie de la Matière Condensée de Bordeaux
CNRS UPR-9048
Université Bordeaux I
87 Avenue du Doc. A. Schweitzer, 33608 Pessac (France)

[**] L = 2,13-dimethyl-6,9-dioxa-3,12,18-triazabicyclo[12.3.1]octadeca-1(18),2,12,14,16-pentaene. Financial support from the Paul Sabatier University (BQR/2004) is acknowledged. DFT calculations have been performed thanks to the facilities provided by CALMIP (Calculs en Midi-Pyrénées, France), CINES (Centre Informatique National de l'Enseignement Supérieur, France), and IDRIS (Institut du Développement et des Ressources en Informatique Scientifique, France). L.M.L.D. thanks the Centro Svizzero di Calcolo Scientifico (CSCS) for the calculation resources allocated in the framework of the CSCS project entitled "Photophysics and Photochemistry of Transition Metal Compounds: Theoretical Approaches" and the Swiss National Science Foundation for financial support.

Supporting information for this article is available on the WWW under http://www.angewandte.org or from the author.

 © 2006 Wiley-VCH Verlag GmbH & Co. KGaA, Weinheim 

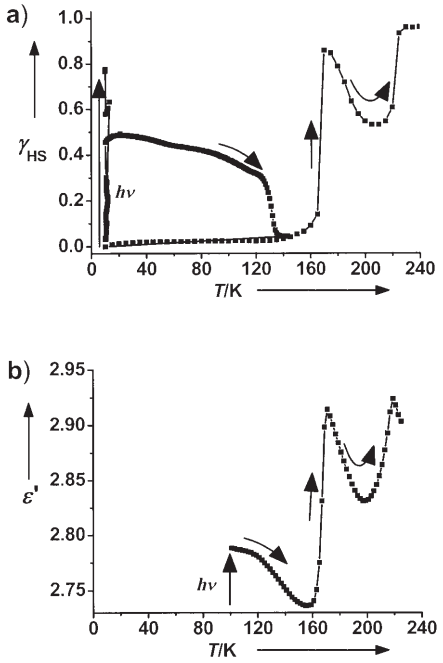



***Figure 1.*** a) Thermal variation of the fraction of high-spin molecules ($\gamma_{HS}$) in $[Fe(L)(CN)_2]\cdot H_2O$ obtained through magnetic-susceptibility measurements following irradiation with light at 10 K. b) Thermal variation of the dielectric constant in $[Fe(L)(CN)_2]\cdot H_2O$ following irradiation with light at 100 K.

130 K, which corresponds to the relaxation of the photo-induced HS species. Then, the thermally induced LS-to-HS transformation occurs at about 160 K, which is followed by a decrease in the $\chi_M T$ value around 170 K and a rise around 200 K. Finally, the pure HS state is reached at about 230 K. The change in magnetic properties around 170 K is thought to correspond to a phase transition leading to a 1:1 mixture of LS and HS species. Subsequent slow cooling of the sample ($< 1\,K\,min^{-1}$) also yields a population of this 1:1 mixture at around 170 K. Every subsequent (slow) sample heating cycle leads to a pure HS state and every cooling cycle leads to the above-mentioned mixture of spin states.

As it is impossible to observe the LIESST effect at 100 K with this mixture of states,[16] care must be taken to irradiate the sample in its pure LS state. Figure 1b shows the variation of $\varepsilon'$ (measured at 100 kHz) upon irradiation at 100 K and subsequent heating to 230 K. There is a clear similarity between the magnetic and dielectric behavior of the sample (Figure 1a and b), which proves that the dielectric polarization (dielectric constant) can be photoswitched and allows the light- and thermally induced spin-state changes to be followed as well. Figure 2 displays the temporal evolution of the dielectric constant upon irradiation at 100 K with light. A partial transition of the sample to the HS state occurs, and saturation is reached after approximately 2500 s of illumination. The relaxation from this light-induced metastable state after the laser is switched off is quite slow (Figure 2) and leads to the stable LS state after more than 12000 s at 115 K (inset Figure 2). Any quantitative interpretation of the relaxation rates would be rather doubtful, as the relation between the

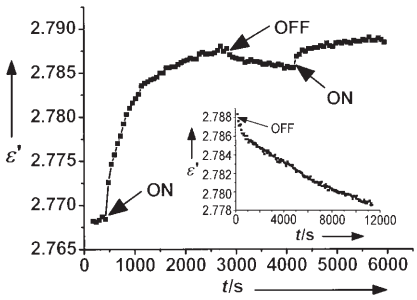



***Figure 2.*** Variation of the dielectric constant of the $[Fe(L)(CN)_2]\cdot H_2O$ complex (initially in a pure LS state) at 100 K upon irradiation with light. The labels "ON" and "OFF" indicate the points at which the light source was switched on and off, respectively. The inset shows the relaxation curve obtained at 115 K following the irradiation at 100 K.

HS fraction and the dielectric constant is not known, contrary to the case for magnetic susceptibility.

The change in dielectric constant of SCO materials results from structural modifications accompanying the spin-state change. The dielectric constant, and therefore the total polarizability, are always nearly independent of the frequency of the external applied electric field (quasi-static range) within the investigated frequency range (Figure 3). Also, no

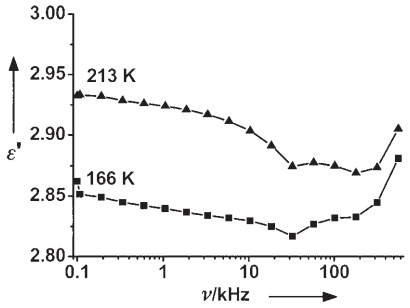



***Figure 3.*** Frequency dependence of the dielectric constant of $[Fe(L)(CN)_2]\cdot H_2O$ at 166 K (squares) and 213 K (triangles). Note that the data reported here and in Figure 1b were collected in the same experiment.

relaxation process, associated with an orientational polarization of permanent dipole moments, is observed in the $\varepsilon''$ versus frequency curve. Nevertheless, the dielectric constant sometimes increases slightly with temperature once the pure LS or HS state is reached;[9] this phenomenon is typically due to the presence of polar entities, such as water molecules, which are mobile or able to reorient themselves by rotation. These dipoles are able to align more readily with the applied electric field as the molecular mobility increases. In our consideration of the correlation between the macroscopically measurable relative permittivity and the microscopic polarizability, we rule out, in a first approximation, any effect of the dipolar polarization on the observed transition and thereby consider the polarizability to be composed mainly of electronic and ionic contributions. As the HS molecules are larger than the LS ones, their electronic polarizability and hence $\varepsilon_\infty$ value should decrease in going from the HS to the LS state. Furthermore, as the HS state has a more ionic nature, the

 © 2006 Wiley-VCH Verlag GmbH & Co. KGaA, Weinheim 

ionic polarizability must also decrease to some extent with the HS→LS spin-state change. Indeed, a decrease of the macroscopically measurable $\varepsilon'$ value was observed for most of the investigated SCO compounds during the HS-to-LS transition; the maximal switching magnitude of 0.3 was observed for the compound $[Fe(NH_2trz)_3](NO_3)_2$ (trz = triazole).[9] The title compound $[Fe(L)(CN)_2]\cdot H_2O$ (Figure 1b) exhibits an $\varepsilon'_{HS}$ value of approximately 2.92 and an $\varepsilon'_{LS}$ value of approximately 2.74; that is, a difference of 0.18 in the dielectric constants for the LS and HS states.

To gain a deeper insight into the origin of the variation of the dielectric constant upon SCO, a quantum chemical study of the $[Fe(L)(CN)_2]$ complex was performed by using DFT methods. The aim of this study was to determine the dependence on spin state of the microscopic electrical properties by evaluating the electronic polarizability of the molecule in the two spin states. Indeed, the large number of atoms in the SCO complexes prohibits the use of computationally demanding high-level ab initio (i.e. wavefunction-based) methods, whereas DFT methods can be applied efficiently to such large systems. DFT calculations have recently been carried out on several SCO compounds.[17] These studies were aimed at assessing the performance of available density functionals in describing the geometries of the complexes in both spin states, evaluating the HS–LS energy difference, and determining the vibrational spectra. Although the spin-state energetics were often calculated inaccurately, it was shown that DFT methods give structural parameters and vibrational frequencies in good agreement with the experimental data.

The optimized HS geometries were in good agreement with the X-ray structure of $[Fe(L)(CN)_2]\cdot H_2O$ in the HS state.[18] Table 1 gives the metal–ligand distances found for the experimental HS structure and the calculated HS and LS geometries (note that no experimental structural data are available for the LS species). The optimized metal–ligand bonds are approximately 0.2 to 0.3 Å longer in the HS state than in the LS state with the noticeable exception of the Fe–O2 bond, which is approximately 0.7 to 0.8 Å shorter in the HS state. Consequently, the spin-state change is related to a huge structural modification of the iron coordination sphere. The $Fe^{II}$ ion is seven-coordinate in the HS state and six-coordinate in the LS state (Figure 4). This original feature was first suggested by Nelson et al.[14] and corroborated recently by Guionneau et al.[18] through X-ray investigations. It is noteworthy that the same optimized six-coordinate LS geometry was successfully obtained with different basis sets by using the seven-coordinate HS structure as a starting geometry.

***Table 1:*** Experimental[16] and calculated Fe–ligand distances [Å] in $[Fe(L)(CN)_2]\cdot H_2O$.[a]

| HS state | X-ray[b] | B3LYP/6-31G* | B3LYP/6-311G** |
|---|---|---|---|
| Fe–N1 | 2.107(2) | 2.069 | 2.096 |
| Fe–N2 | 2.203(2) | 2.225 | 2.235 |
| Fe–N3 | 2.203(2) | 2.225 | 2.235 |
| Fe–C1 | 2.163(3) | 2.102 | 2.120 |
| Fe–C2 | 2.163(3) | 2.102 | 2.120 |
| Fe–O1 | 2.334(2) | 2.435 | 2.411 |
| Fe–O2 | 2.334(2) | 2.435 | 2.411 |
| LS state | | B3LYP/6-31G* | B3LYP/6-311G** |
| Fe–N1 | | 1.824 | 1.832 |
| Fe–N2 | | 1.929 | 1.937 |
| Fe–N3 | | 2.054 | 2.067 |
| Fe–C1 | | 1.944 | 1.958 |
| Fe–C2 | | 1.944 | 1.958 |
| Fe–O1 | | 2.415 | 2.409 |
| Fe–O2 | | 3.144 | 3.149 |

[a] Calculations were performed on $[Fe(L)(CN)_2]$. [b] X-ray crystal structure obtained at 293 K.

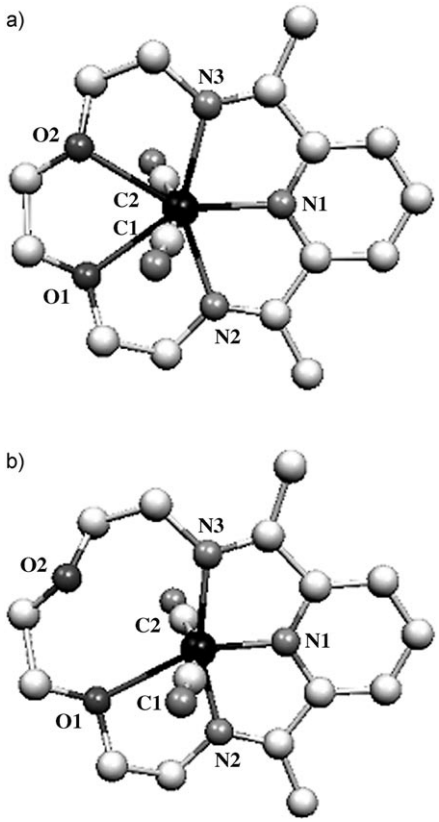



***Figure 4.*** Calculated (B3LYP/6-31G*) optimized structure of the $[Fe(L)(CN)_2]$ complex in the HS (a) and LS (b) states.

From the optimized structures, the mean (static) electronic polarizability of the complex $\alpha = \frac{1}{3}(\alpha_{xx}+\alpha_{yy}+\alpha_{zz})$ can be determined in both spin states as the analytic second derivative of the energy with respect to the electric field.[19] The calculated values of the LS ($\alpha_{LS}$) and HS ($\alpha_{HS}$) mean polarizabilities are given in Table 2. Notably, they increase with the quality of the basis sets and the HS value obtained

***Table 2:*** Calculated values of the HS and LS mean polarizabilities ($\Delta\alpha = \alpha_{HS}-\alpha_{LS}$) for $[Fe(L)(CN)_2]$ (in atomic units).

| | $\alpha_{LS}$ [a.u.] | $\alpha_{HS}$ [a.u.] | $\Delta\alpha$ [a.u.] |
|---|---|---|---|
| B3LYP/3-21G | 238.99 | 254.40 | 15.41 |
| B3LYP/6-31G* | 247.40 | 259.48 | 12.08 |
| B3LYP/6-311G** | 257.50 | 266.91 | 9.41 |
| PBE/TZVP | 287.52 | 302.80 | 15.28 |

 © 2006 Wiley-VCH Verlag GmbH & Co. KGaA, Weinheim 

with a given basis set is always higher than its LS counterpart ($\Delta\alpha_{HL} > 0$). This latter trend is also reproduced with the gradient-corrected PBE[20] functional and the TZVP basis set[21] (Table 2). Therefore, the change in the dielectric constant of the SCO compound appears to be correlated with the change in the mean polarizability of the complex. To confirm this result, similar calculations were performed at the B3LYP/6-31G* level for the $[Fe(phen)_2(NCS)_2]$ (phen = phenanthroline)[17c] and $[Fe\{5\text{-}NO_2\text{-}sal\text{-}N(1,4,7,10)\}]$ (5-$NO_2$-sal-N(1,4,7,10) = 1,10-bis(5-nitrosalicylaldehyde)-1,4,7,10-tetraazadecane-*O*,*O*′,*N*,*N*′,*N*″,*N*‴) SCO complexes. The LS and HS polarizabilities obtained for these two complexes are given in Table 3 together with those found for the title complex at the same theoretical level. The calculated electronic polarizabilities and the measured (quasi-static) dielectric constants in $[Fe(L)(CN)_2]\cdot H_2O$ and $[Fe(phen)_2(NCS)_2]$ both increase in going from the LS to the HS state. In contrast, the calculated decrease in the polarizability for $[Fe\{5\text{-}NO_2\text{-}sal\text{-}N(1,4,7,10)\}]$ corroborates the previously observed atypical decrease[9] in its dielectric constant upon spin-state change. The electronic polarizability and the dielectric constant of $[Fe\{5\text{-}NO_2\text{-}sal\text{-}N(1,4,7,10)\}]$ are indeed higher in the LS state than in the HS state. This counterintuitive behavior of the dielectric constant is therefore purely of structural origin.

***Table 3:*** Experimental change in the dielectric constant ($\Delta\varepsilon' = \varepsilon'_{HS} - \varepsilon'_{LS}$) and calculated (B3LYP/6-31G*) change in the mean electronic polarizability ($\Delta\alpha = \alpha_{HS} - \alpha_{LS}$) for selected SCO compounds.

| | $\Delta\varepsilon'$ | $\alpha_{LS}$ [a.u.] | $\alpha_{HS}$ [a.u.] | $\Delta\alpha$ [a.u.] |
|---|---|---|---|---|
| $[Fe(L)(CN)_2]\cdot H_2O$ | 0.18 | 247.40 | 259.48 | 12.08 |
| $[Fe(phen)_2(NCS)_2]$ | 0.015[9] | 414.33 | 469.78 | 55.45 |
| $[Fe\{5\text{-}NO_2\text{-}sal\text{-}N(1,4,7,10)\}]$ | −0.13[9] | 351.71 | 343.52 | −8.19 |

In summary, photoswitching of the dielectric constant has been demonstrated experimentally for the SCO compound $[Fe(L)(CN)_2]\cdot H_2O$ and correlated through DFT calculations with the change in electronic polarizability that accompanies the spin transition. The electrical detection of a photoinduced spin-state change promises new opportunities for the use of SCO compounds as switchable capacitors in electronic devices for information storage and processing. Further research is necessary to enhance the changes in the dielectric constant of SCO compounds upon irradiation with light. Such tailoring of the relative permittivity might be possible, for example, by the introduction of highly polarizable (i.e. voluminous) atoms into these materials. Moreover, the relationship between the permittivity change and the structural and electronic changes accompanying the SCO must also be investigated in detail.

## Experimental Section

Measurements of the dielectric constant were performed by using a Novocontrol BDS 4000 broad-band dielectric spectrometer for which the frequency of the external electric field applied to the sample was scanned between $10^2$ and $10^6$ Hz. Irradiation was carried out by applying an $Ar^+$ laser beam (457 –514 nm) on the polycrystalline sample located between a stainless steel electrode and an ITO (indium–tin oxide) electrode deposited on a glass plate, which allows uniform irradiation of the whole sample surface. The dielectric powder sample sandwiched between the two electrodes was ca. 100 μm thick with an effective diameter of 10 mm. The diameter of the laser beam was adjusted to slightly larger than that of the sample to ensure complete irradiation of the sample, and the power density at the sample was ca. 0.5 mW mm$^{-2}$.

DFT calculations were performed with the Gaussian 03 program package.[22] The Becke three-parameter hybrid functional B3LYP[23] was used with three different basis sets: 3-21G, 6-31G*, and 6-311G**. Calculations were also performed at the PBE/TZVP level.[20,21] The X-ray crystal structure was used as the starting point for the optimization of the HS geometry. As the low-temperature structure is not known because of the structural instability of the single crystals at low temperature, the optimized HS structure was used to initialize the optimization of the LS structure. The structures were optimized without constraints. The MOLDEN[24] and the MOLEKEL[25] software packages were used to visualize the calculated molecular structures. After completion of the optimization, the vibrational frequencies (within the harmonic approximation) and the static polarizability tensor were calculated. The optimized LS and HS geometries correspond to true minima since real frequencies were obtained in all cases.

Received: September 13, 2005
Revised: December 5, 2005

**Keywords:** density functional calculations · dielectric constant · magnetic properties · photophysics · spin crossover

[1] a) O. Kahn, C. J. Martinez, *Science* **1998**, *279*, 44; b) C. Joachim, J. K. Gimzewski, A. Aviram, *Nature* **2000**, *408*, 541; c) J. K. Gimzewski, C. Joachim, *Science* **1999**, *283*, 1683.
[2] a) P. Gütlich, A. Hauser, H. Spiering, *Angew. Chem.* **1994**, *106*, 2109; *Angew. Chem. Int. Ed. Engl.* **1994**, *33*, 2024; b) "Spin Crossover in Transition Metal Compounds I–III" (Ed.: P. Gütlich, H. A. Goodwin): *Top. Curr. Chem.* **2004**, 233 – 235.
[3] V. Ksenofontov, A. B. Gaspar, P. Gütlich, *Top. Curr. Chem.* **2004**, *235*, 23.
[4] A. Bousseksou, K. Boukheddaden, M. Goiran, J.-P. Tuchagues, F. Varret, *Top. Curr. Chem.* **2004**, *235*, 65.
[5] A. Hauser, *Top. Curr. Chem.* **2004**, *234*, 155.
[6] S. Decurtins, P. Gütlich, C. P. Köhler, H. Spiering, A. Hauser, *Chem. Phys. Lett.* **1984**, *105*, 1.
[7] S. Bonhommeau, G. Molnár, A. Galet, A. Zwick, J.-A. Real, J. J. McGarvey, A. Bousseksou, *Angew. Chem.* **2005**, *117*, 4137; *Angew. Chem. Int. Ed.* **2005**, *44*, 4069.
[8] J.-F. Létard, P. Guionneau, L. Goux-Capes, *Top. Curr. Chem.* **2004**, *235*, 221.
[9] A. Bousseksou, G. Molnár, P. Demont, J. Menegotto, *J. Mater. Chem.* **2003**, *13*, 2069.
[10] A. Bousseksou, C. Vieu, J.-F. Létard, P. Demont, J.-P. Tuchagues, L. Malaquin, J. Menegotto, L. Salmon, EP1430552, **2004**.
[11] C. Brady, J. J. McGarvey, J. K. McCusker, H. Toftlund, D. N. Hendrickson, *Top. Curr. Chem.* **2004**, *235*, 1.
[12] Besides the purely molecular LIESST effect, macroscopic domain switching by light pulses in solid spin-crossover materials has also been evidenced,[26] even at room temperature.[7] Freysz and co-workers reported that within the hysteresis loop, $[Fe(PM\text{-}BiA)_2(NCS)_2]$ (PM-BiA = *N*-(2-pyridylmethylene)-4-aminobiphenyl) was converted from the LS state into a pure HS state within the 8-ns light pulse and that the system relaxed to a mixture of HS/LS molecules in approximately 1 s.[26] However, more research is necessary to clarify the main characteristics

 © 2006 Wiley-VCH Verlag GmbH & Co. KGaA, Weinheim 

(domain size, switching times, and switching power) of this recently discovered phenomenon.

[13] a) S. Hayami, Z.-z. Gu, Y. Einaga, Y. Kobayasi, Y. Ishikawa, Y. Yamada, A. Fujishima, O. Sato, *Inorg. Chem.* **2001**, *40*, 3240; b) J. S. Costa, P. Guionneau, J.-F. Létard, *J. Phys. Conf. Ser.* **2005**, *21*, 67.

[14] S. M. Nelson, P. D. A. Mcllroy, C. S. Stevenson, E. König, G. Ritter, J. Waigel, *J. Chem. Soc. Dalton Trans.* **1986**, 991.

[15] E. König, G. Ritter, J. Dengler, S. M. Nelson, *Inorg. Chem.* **1987**, *26*, 3582.

[16] H. Liu, A. Fujishima, O. Sato, *Appl. Phys. Lett.* **2004**, *85*, 2295.

[17] a) G. Baranovic, *Chem. Phys. Lett.* **2003**, *369*, 668; b) G. Brehm, M. Reiher, S. Schneider, *J. Phys. Chem. A* **2002**, *106*, 12024; c) V. K. Pálfi, T. Guillon, H. Paulsen, G. Molnár, A. Bousseksou, *C. R. Chim.* **2005**, *8*, 1317; d) H. Paulsen, A. X. Trautwein, *Top. Curr. Chem.* **2004**, *235*, 197; e) H. Paulsen, A. X. Trautwein, *J. Phys. Chem. Solids* **2004**, *65*, 793; f) H. Paulsen, L. Duelund, H. Winkler, H. Toftlund, A. X. Trautwein, *Inorg. Chem.* **2001**, *40*, 2201; g) H. Paulsen, H. Winkler, A. X. Trautwein, H. Grunsteudel, V. Rusanov, H. Toftlund, *Phys. Rev. B* **1999**, *59*, 975; h) M. Reiher, *Inorg. Chem.* **2002**, *41*, 6928; i) A. Fouqueau, S. Mer, M. E. Casida, L. M. Lawson Daku, A. Hauser, T. Mineva, F. Neese, *J. Chem. Phys.* **2004**, *120*, 9473; j) A. Fouqueau, M. E. Casida, L. M. Lawson Daku, A. Hauser, F. Neese, *J. Chem. Phys.* **2005**, *122*, 044110; k) L. M. Lawson Daku, A. Vargas, A. Hauser, A. Fouqueau, M. E. Casida, *ChemPhysChem* **2005**, *6*, 1393.

[18] P. Guionneau, J. S. Costa, J.-F. Letard, *Acta Crystallogr. Sect. C* **2004**, *60*, m587.

[19] M. Frisch, M. Head-Gordon, J. Pople, *Chem. Phys.* **1990**, *141*, 189.

[20] a) J. P. Perdew, K. Burke, M. Ernzerhof, *Phys. Rev. Lett.* **1996**, *77*, 3865; b) J. P. Perdew, K. Burke, M. Ernzerhof, *Phys. Rev. Lett.* **1997**, *78*, 1396.

[21] A. Schäfer, C. Huber, R. Ahlrichs, *J. Chem. Phys.* **1994**, *100*, 5829.

[22] Gaussian 03 (Revision B.05): M. J. Frisch et al., see Supporting Information.

[23] a) A. D. Becke, *J. Chem. Phys.* **1993**, *98*, 5648; b) *Becke3LYP Method References and General Citation Guidelines*, *Gaussian News*, **1994**, *5*, 2.

[24] G. Schaftenaar, J. H. Noordik, *J. Comput.-Aided Mol. Des.* **2000**, *14*, 123.

[25] a) MOLEKEL 4.3: P. Flükiger, H. P. Lüthi, S. Portmann, J. Weber, Swiss Center for Scientific Computing, Manno, Switzerland, **2000–2002**; b) S. Portmann, H. P. Lüthi, *Chimia* **2000**, *54*, 766.

[26] a) E. Freysz, S. Montant, S. Létard, J.-F. Létard, *Chem. Phys. Lett.* **2004**, *394*, 318; b) J. Degert, N. Lascoux, S. Montant, S. Létard, E. Freysz, G. Chastanet, J.-F. Létard, *Chem. Phys. Lett.* **2005**, *415*, 206.

 © 2006 Wiley-VCH Verlag GmbH & Co. KGaA, Weinheim 

DNA Structures

DOI: 10.1002/anie.200502960

# Molecular Crowding Induces Telomere G-Quadruplex Formation under Salt-Deficient Conditions and Enhances its Competition with Duplex Formation**

*Zhong-yuan Kan, Yuan Yao, Ping Wang, Xiong-hui Li, Yu-hua Hao, and Zheng Tan**

Tandem-repetitive guanine-rich DNA can fold into a four-stranded structure termed a G-quadruplex through Hoogsteen hydrogen bonding.[1] Great interest in this structure arose because of its applications in supramolecular chemistry and nanotechnology,[2] and its involvement in many important biological processes. The G-quadruplex-forming sequences exist in many essential regions of chromosomes, for example telomeres,[3] promoters of oncogenes,[4,5] immunoglobulin switches,[6] and the insulin regulatory regions.[7] Evidence for the presence of the G-quadruplex in vivo is accumulating, and it is believed such a structure to be essential in certain biological processes, for instance, in the regulation of oncogene transcription.[4,8,9]

The aqueous environment in living cells is highly crowded with various biomolecules which can occupy as much as 30–40% of the internal cellular volume. The total concentration of proteins, nucleic acids, and polysaccharides can reach 300–400 $g\,L^{-1}$,[10,11] whereas in most in vitro biochemical studies it was less than 1 $g\,L^{-1}$.[12] In general, crowding may significantly alter the rates, equilibria, and mechanisms of biomolecular reactions.[12,13] Only a few studies of the effect of crowding on the G-quadruplex have been reported. It was observed that molecular crowding induced transition from the antiparallel to the parallel G-quadruplex,[14] dissociation of the duplex in *Oxytricha nova* $G_4T_4G_4$ telomeric DNA,[15] and transition from the intramolecular G-quadruplex to a long multi-stranded G-wire in *Tetrahymena* $(T_2G_4)_3T_2G_2$ but not in human $G_3(T_2AG_3)_3$ telomeric DNA.[16] The G-quadruplex

[*] Prof. Dr. Z. Tan
Laboratory of Biochemistry and Biophysics
College of Life Sciences, Wuhan University
Wuhan 430072 (P.R. China)
and
Institute of Zoology, Chinese Academy of Sciences
Beijing 100080 (P.R. China)
Fax: (+86) 27-6875-6661
E-mail: tanclswu@public.wh.hb.cn

Z.-y. Kan, Y. Yao, X.-h. Li, Y.-h. Hao
Laboratory of Biochemistry and Biophysics
College of Life Sciences, Wuhan University
Wuhan 430072 (P.R. China)

P. Wang
College of Chemical and Molecular Sciences
Wuhan University, Wuhan 430072 (P.R. China)

[**] This work was supported by grant nos. 30270314 and 20572082 from NSFC and G2000057001 from MSTC.


© 2006 Wiley-VCH Verlag GmbH & Co. KGaA, Weinheim

structure is stabilized by certain metal cations, most effectively by $K^+$ and $Na^+$.[17] While all the previous studies were conducted in cation-containing solutions, we report herein that molecular crowding can induce G-quadruplex formation under salt-deficient conditions. In addition, it greatly reduces the salt dependence of G-quadruplex formation, and alters the competition between G-quadruplex and duplex formation in the presence of complementary strands.

We used $G_3(T_2AG_3)_3$, the core sequence of the G-rich strand of human telomeric DNA, as a model molecule and poly(ethylene glycol) (PEG 200) as crowding agent. The structures of $G_3(T_2AG_3)_3$, $(T_2AG_3)_4$, $(T_2AG_3)_3$, and $(T_2AG_3)_2$, termed R3.5, R4, R3, and R2 respectively, were analyzed by gel electrophoresis. In the absence of added PEG and salt (Figure 1a), the oligonucleotides did not form a G-quadruplex[18,19] and displayed mobilities inversely proportional to their size. However, when the samples were prepared and subjected to electrophoresis in the presence of PEG without added salt, the mobility of R4 became comparable with that of R3, and R3.5 was faster than R3 (Figure 1b), while R2 and R3 retained their relative positions. The behavior of these oligonucleotides in the absence and presence of PEG is similar to that of the same sequences in the absence and presence of $Na^+$ ions.[18,19] The increased mobility of R3.5 and R4 suggests that they formed intramolecular G-quadruplexes in PEG, which are more compact and migrate faster than the relaxed equivalents. The concentrations of $K^+$, $Na^+$, and $Li^+$ ions in the buffer used in all the experiments, as determined by atomic absorption spectroscopy, were 0.03, 0.15, and 0.0006 mM, respectively, when no salt was added. At these levels the cations are known to be incapable of inducing G-quadruplex formation[20,21] (see also Figure 4b). Therefore, the G-quadruplex is formed under cation-deficient conditions.

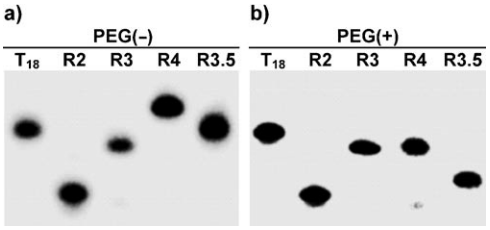



***Figure 1.*** Electrophoresis of $^{32}$P-labeled $T_{18}$, R2, R3, R4, and R3.5 in the absence (a) or presence (b) of PEG 200. No salt was added in either case.

The structure of R3.5 in PEG was verified by circular dichroism (CD) spectroscopy in comparison with the spectra obtained in $K^+$ and $Na^+$ solution (Figure 2). It is known that R3.5 forms an antiparallel G-quadruplex in $Na^+$ solution and a mixture of parallel and antiparallel G-quadruplexes in $K^+$ solution.[22] The spectra in the presence of $K^+$ or $Na^+$, or in the absence of these cations are the same as those previously reported,[22] whereas the spectrum in PEG was similar to that in $K^+$ solution, and features a negative peak near 240 nm and a positive peak near 290 nm, which are characteristic of parallel and antiparallel G-quadruplexes, respectively. This

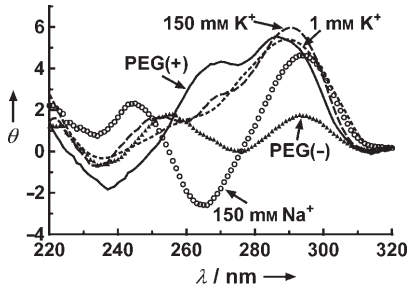



***Figure 2.*** CD spectra of R3.5 at 25 °C in the presence or absence of PEG 200 without addition of salt, and in 1 mM and 150 mM solutions of $K^+$ or a 150 mM solution of $Na^+$ without addition of PEG.

finding suggests that the oligonucleotide in PEG formed a mixture of both parallel and antiparallel G-quadruplexes.

The G-quadruplex formation induced by PEG was also verified by UV-melting analysis. Denaturation of the G-quadruplex is characterized by hypochromicity at 295 nm.[23] In a fluorescence quenching study (a technique similar to the fluorescence resonant energy transfer method used for Figure 4), it was shown that the G-quadruplexes formed by R3.5 in different concentrations of $K^+$ ions have a different stability, as reflected by their melting temperatures ($T_m$).[24] Figure 3 shows that R3.5 exhibited hypochromicity in PEG without addition of salt, whereas a random control sequence showed no transition under the same conditions. These results indicate that the oligonucleotide formed a G-quadruplex in PEG. Its $T_m$ value (36.6 °C) is close to that obtained in 1 mM $K^+$ solution but much lower than that in 150 mM $K^+$ solution in the absence of PEG, which suggests that the PEG mimicked the effect of 1 mM $K^+$ solution in terms of thermal stability.

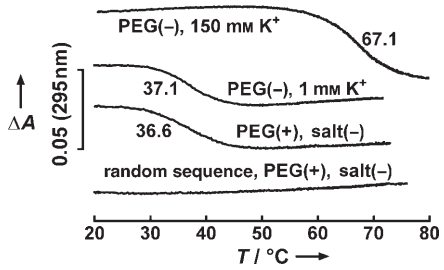



***Figure 3.*** UV-melting profiles of R3.5 and a random 21-mer TGCGTGAAACCTGAGAGGATG monitored at 295 nm in the presence of the indicated cosolutes. Curves are shifted up the vertical axis to avoid overlap. The numbers by the curves are the $T_m$ values in °C.

PEG-induced G-quadruplex formation was further evidenced by fluorescence resonant energy transfer (FRET).[20] We labeled the 5′ end of R3.5 with fluorescein (FAM) as donor and the 3′ end with tetramethylrhodamine (TMR) as acceptor. The efficiency of FRET is inversely dependent on the distance between the two fluorophores. The formation of the intramolecular G-quadruplex brings the two ends into close proximity. This allows FRET to occur between the two fluorophores, which results in a decrease in the emission intensity of the FAM and an increase in the emission intensity

 © 2006 Wiley-VCH Verlag GmbH & Co. KGaA, Weinheim 

of the TMR.[20,25,26] Figure 4a shows that fluorescent R3.5 displayed efficient FRET in PEG without added cation. A simultaneous increase in TMR fluorescence and decrease in FAM fluorescence was observed with time when the oligonucleotide was mixed with PEG (data not shown). Moreover, PEG greatly reduced but did not entirely remove the concentration dependence of G-quadruplex formation in $K^+$ solution (Figure 4b), because PEG mimics the effect of 1 mM $K^+$ solution (Figure 3). In the absence of PEG, a half-structural transition was observed at several millimoles per liter of $K^+$. When PEG was present, G-quadruplex formation reached a maximum at 0.1 mM of $K^+$.

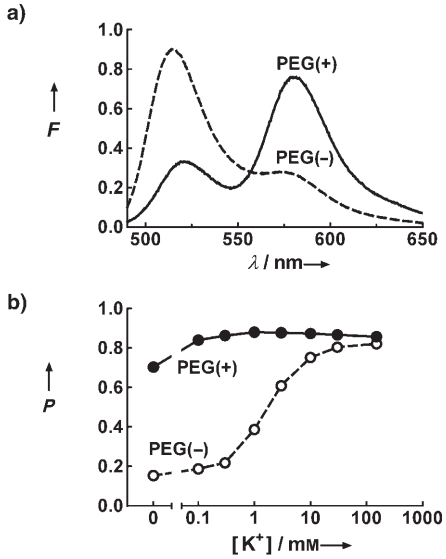



***Figure 4.*** a) Emission spectra of fluorescent R3.5 in the absence or presence of PEG 200 without addition of salt. b) Extent of FRET (in proximity ratio *P*) as a function of the $K^+$ concentration in the absence or presence of PEG 200. Measurements were carried out at 25 °C.

Except for the single-strand tail at the terminus of telomeres, all the G-rich sequences coexist with their complementary strands in chromosomes. Therefore, G-quadruplex formation in the double-stranded region, if any, must compete with the classical Watson–Crick duplex pairing.[27,28] To examine how molecular crowding might affect this process, the FRET of fluorescent R3.5 was studied in an equimolar mixture of G- and C-rich strands at different concentrations. The competitive formation of the duplex and G-quadruplex is dependent on the strand concentration, because of the intermolecular nature of the duplex formation. G-quadruplex formation was favored only at low strand concentration and PEG had a profound impact on the competition (Figure 5), elevating the half-transition concentration by roughly two orders of magnitude.

So far, several Group 1 and 2 metal cations and $NH_4^+$ ions have been identified as stabilizing the G-quadruplex,[17] among which $K^+$ and $Na^+$, which are the most abundant intracellular cations, have clear physiological relevance.[6,29] All previous studies on the effect of molecular crowding were conducted in the presence of cations at concentrations sufficient to induce G-quadruplex formation, but we observed

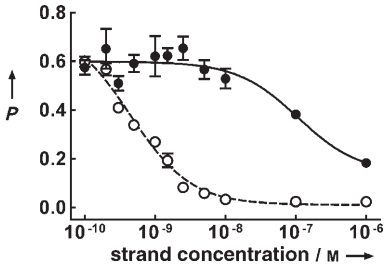



***Figure 5.*** Strand-concentration dependence of G-quadruplex formation in the presence of equimolar complementary C-rich strands. Measurements were carried out at 25 °C in 150 mM $K^+$ solution in the absence (-----) or presence (——) of PEG. The extent of FRET (in proximity ratio *P*) represents the average of three individual measurements with standard deviation.

that molecular crowding itself could induce G-quadruplex formation. Recently, Hurley and co-workers reported that the G-quadruplex-binding ligand telomestatin also has the ability to induce G-quadruplex formation without addition of salt.[30,31] A few other studies have shown that a G-quadruplex can form without or at very low concentration of cations under certain conditions, such as modification of nucleoside[32] or repeated freeze–thawing cycles.[33]

The promotion of G-quadruplex formation by molecular crowding under cation-deficient conditions provides an example of physiological relevance, which may have implications in cellular processes. It is believed that molecular crowding can function as a "metabolic buffer", which allows molecular interactions to occur under conditions that are inhibitory in noncrowded solutions, thus extending the range of intracellular conditions for such reactions.[34] By making the formation of G-quadruplexes insensitive to cation concentration (Figure 4b), we speculate that molecular crowding may work in a similar way to guarantee G-quadruplex formation against large fluctuations in cation concentration in living cells.[35] Moreover, the effect is not limited to cation-deficient conditions. The bulk concentration of intracellular $K^+$ ions is estimated to be 100–200 mM,[36] which is greater than that required for G-quadruplexes to reach maximal formation.[20,21] The fact that molecular crowding shifts G-quadruplex–duplex competition (Figure 5) in the presence of $K^+$ ions suggests it may participate in the regulation of G-quadruplex formation under both salt-abundant and -deficient conditions in vivo.

G-quadruplex formation under molecular crowding conditions also has implications in technical applications. Recently, unique potassium probes based on a fluorescently labeled G-quadruplex-forming sequence have been reported.[21,37] Such probes show great potential for the determination of $K^+$ concentration in living cells. Our data suggest that the effect of molecular crowding needs to be considered. Suitable calibration may be required for measurements in biological fluids, which may contain large numbers of macromolecules. Application in living cells might be difficult because, as is seen in Figure 4b, a probe may no longer be sensitive to $K^+$ concentration in the molecularly crowded intracellular environment. Thus, probes that are not sensitive to molecular crowding are desired. In

 © 2006 Wiley-VCH Verlag GmbH & Co. KGaA, Weinheim 

more general terms, molecular crowding should be given serious attention in the above and possibly other similar intracellular applications because of the effect it may impose.

## Experimental Section

Oligonucleotides were purchased from TaKaRa Biotech (Dalian, China) and AuGCT Biotech (Beijing, China). For fluorescence spectroscopy, the R3.5 was labeled with 5′-FAM and 3′-TMR and purified by HPLC. Oligonucleotide concentrations were determined from their absorbance at 260 nm, and the nearest-neighbor method was used to calculate the extinction coefficients.[38] For the fluorescent conjugates, $\varepsilon_{260} = 13000\ \text{M}^{-1}\text{cm}^{-1}$ for FAM and $\varepsilon_{260} = 34000\ \text{M}^{-1}\text{cm}^{-1}$ for TMR were added into the calculations.[39] In all experiments, the oligonucleotides were dissolved in Tris-HCl (10 mM) and EDTA (1 mM; pH 7.4) with the cosolute indicated. In all experiments with PEG added the concentration of PEG was 40% (w/v).

Electrophoresis was carried out on 12% polyacrylamide gel containing PEG 200 or no PEG. The oligonucleotides were 5′-end-labeled with [$\gamma$-$^{32}$P]ATP by using T4 polynucleotide kinase (Fermentas, Lithuania). After incubation for 3 h, the samples were loaded and run at 4 °C and 10 $\text{V cm}^{-1}$ in 1 × TBE buffer (Tris/borate/EDTA) without addition of cations, and autoradiographed on a Typhoon phosphor imager (Amersham Biosciences, Sweden).

Fluorescence measurements were carried out on a Spex Fluorolog-3 spectrofluorometer (HORIBA Jobin Yvon, France) at 25 °C. The excitation and emission slits were both 5 nm. Excitation was set at 480 nm, and emission was collected from 490 to 650 nm. Lamp fluctuations were corrected by using the reference channel. A buffer blank was subtracted for all spectra. The extent of FRET was expressed as proximity ratio $P$ using the definition[26] $P = I_A/(I_A+I_D)$, where $I_D$ and $I_A$ are the fluorescence intensities of the donor (FAM) and acceptor (TMR), respectively. The fluorescence intensities were calculated by integrating the emission spectra from 500 to 530 nm for the donor and from 565 to 595 nm for the acceptor. Cross talk from donor to acceptor emission areas, determined from the single-labeled-donor emission spectra, was 15%, and correction was made in the above calculation as described.[26] In the G-quadruplex–duplex competition experiments, fluorescent oligonucleotide was used at a fixed concentration of 1 nM and unlabeled oligonucleotide was added to adjust the final concentration. All samples were incubated at 25 °C for 3 days to allow them to reach equilibrium before measurement.

Thermal denaturation was carried out on a DU-640 UV/Vis spectrophotometer (Beckman, USA) equipped with a digital circulating water bath. The absorbance was monitored at 295 nm while the temperature was increased from 20 to 80 °C at about 1.0 $\text{K min}^{-1}$. A solution containing no oligonucleotide was used as reference. The temperature was simultaneously measured using a thermal probe immersed in the sample cell.

CD spectra were collected from 320 to 220 nm on a CD6 spectropolarimeter (HORIBA Jobin Yvon, France) with a 1-mm-pathlength cylindrical quartz cuvette at 25 °C. A buffer blank correction was made for all spectra.

Received: August 19, 2005
Revised: November 28, 2005

**Keywords:** DNA structures · FRET (fluorescence resonant energy transfer) · G-quadruplex · oligonucleotides · potassium

[1] J. R. Williamson, M. K. Raghuraman, T. R. Cech, *Cell* **1989**, *59*, 871 – 880.
[2] J. T. Davis, *Angew. Chem.* **2004**, *116*, 684 – 716; *Angew. Chem. Int. Ed.* **2004**, *43*, 668 – 698.
[3] E. H. Blackburn, *Nature* **1991**, *350*, 569 – 573.
[4] A. Siddiqui-Jain, C. L. Grand, D. J. Bearss, L. H. Hurley, *Proc. Natl. Acad. Sci. USA* **2002**, *99*, 11593 – 11598.
[5] T. Simonsson, P. Pecinka, M. Kubista, *Nucleic Acids Res.* **1998**, *26*, 1167 – 1172.
[6] D. Sen, W. Gilbert, *Nature* **1988**, *334*, 364 – 366.
[7] M. C. Hammond-Kosack, B. Dobrinski, R. Lurz, K. Docherty, M. W. Kilpatrick, *Nucleic Acids Res.* **1992**, *20*, 231 – 236.
[8] C. Schaffitzel, I. Berger, J. Postberg, J. Hanes, H. J. Lipps, A. Plückthun, *Proc. Natl. Acad. Sci. USA* **2001**, *98*, 8572 – 8577.
[9] C. C. Chang, I. C. Kuo, I. F. Ling, C. T. Chen, H. C. Chen, P. J. Lou, J. J. Lin, T. C. Chang, *Anal. Chem.* **2004**, *76*, 4490 – 4494.
[10] S. B. Zimmerman, S. O. Trach, *J. Mol. Biol.* **1991**, *222*, 599 – 620.
[11] B. Bohrmann, M. Haider, E. Kellenberger, *Ultramicroscopy* **1993**, *49*, 235 – 251.
[12] A. P. Minton, *J. Biol. Chem.* **2001**, *276*, 10577 – 10580.
[13] R. J. Ellis, *Trends Biochem. Sci.* **2001**, *26*, 597 – 604.
[14] D. Miyoshi, A. Nakao, N. Sugimoto, *Biochemistry* **2002**, *41*, 15017 – 15024.
[15] D. Miyoshi, S. Matsumura, S. Nakano, N. Sugimoto, *J. Am. Chem. Soc.* **2004**, *126*, 165 – 169.
[16] D. Miyoshi, H. Karimata, N. Sugimoto, *Angew. Chem.* **2005**, *117*, 3806 – 3810; *Angew. Chem. Int. Ed.* **2005**, *44*, 3740 – 3744.
[17] T. Simonsson, *Biol. Chem.* **2001**, *382*, 621 – 628.
[18] A. I. Murchie, D. M. Lilley, *EMBO J.* **1994**, *13*, 993 – 1001.
[19] T. M. Fletcher, D. Sun, M. Salazar, L. H. Hurley, *Biochemistry* **1998**, *37*, 5536 – 5541.
[20] T. Simonsson, R. Sjoback, *J. Biol. Chem.* **1999**, *274*, 17379 – 17383.
[21] H. Ueyama, M. Takagi, S. Takenaka, *J. Am. Chem. Soc.* **2002**, *124*, 14286 – 14287.
[22] W. Li, P. Wu, T. Ohmichi, N. Sugimoto, *FEBS Lett.* **2002**, *526*, 77 – 81.
[23] J. L. Mergny, A. T. Phan, L. Lacroix, *FEBS Lett.* **1998**, *435*, 74 – 78.
[24] A. Risitano, K. R. Fox, *Nucleic Acids Res.* **2004**, *32*, 2598 – 2606.
[25] J. L. Mergny, J. C. Maurizot, *ChemBioChem* **2001**, *2*, 124 – 132.
[26] J. J. Green, L. Ying, D. Klenerman, S. Balasubramanian, *J. Am. Chem. Soc.* **2003**, *125*, 3763 – 3767.
[27] A. T. Phan, J. L. Mergny, *Nucleic Acids Res.* **2002**, *30*, 4618 – 4625.
[28] W. Li, D. Miyoshi, S. Nakano, N. Sugimoto, *Biochemistry* **2003**, *42*, 11736 – 11744.
[29] D. Sen, W. Gilbert, *Nature* **1990**, *344*, 410 – 414.
[30] M. Y. Kim, M. Gleason-Guzman, E. Izbicka, D. Nishioka, L. H. Hurley, *Cancer Res.* **2003**, *63*, 3247 – 3256.
[31] E. M. Rezler, J. Seenisamy, S. Bashyam, M. Y. Kim, E. White, W. D. Wilson, L. H. Hurley, *J. Am. Chem. Soc.* **2005**, *127*, 9439 – 9447.
[32] J. L. Sessler, M. Sathiosatham, K. Doerr, V. Lynch, K. A. Abboud, *Angew. Chem.* **2000**, *112*, 1356 – 1359; *Angew. Chem. Int. Ed.* **2000**, *39*, 1300 – 1303.
[33] H. Penazova, M. Vorlickova, *Biophys. J.* **1997**, *73*, 2054 – 2063.
[34] R. Goobes, N. Kahana, O. Cohen, A. Minsky, *Biochemistry* **2003**, *42*, 2431 – 2440.
[35] M. T. Record, Jr., E. S. Courtenay, S. Cayley, H. J. Guttman, *Trends Biochem. Sci.* **1998**, *23*, 190 – 194.
[36] B. Alberts, A. Johnson, J. Lewis, M. Raff, K. Roberts, P. Walter, *Molecular Biology of the Cell*, 4th edition, Garland Publishing, New York, **2002**.
[37] S. Nagatoishi, T. Nojima, B. Juskowiak, S. Takenaka, *Angew. Chem.* **2005**, *117*, 5195 – 5198; *Angew. Chem. Int. Ed.* **2005**, *44*, 5067 – 5070.
[38] P. N. Borer in *Handbook of Biochemistry and Molecular Biology*: *Nucleic Acids, Vol. 1* (Ed.: G. D. Fasman), CRC, Cleveland, OH, **1975**, pp. 589 – 595.
[39] J. Wildeson, C. J. Murphy, *Anal. Biochem.* **2000**, *284*, 99 – 106.

 © 2006 Wiley-VCH Verlag GmbH & Co. KGaA, Weinheim 

Zeolites

DOI: 10.1002/anie.200503006

# Formation of Heteroatom Active Sites in Zeolites by Hydrolysis and Inversion**

*Judy To,* Alexey A. Sokol, Samuel A. French, C. Richard A. Catlow, Paul Sherwood, and Huub J. J. van Dam*

Following the discovery of the titanosilicalite zeolite TS-1 and its remarkable catalytic properties in selective oxidation reactions with aqueous $H_2O_2$,[1] there have been several reports on the possible use of other heteroatom-substituted zeolites. Of particular interest are tin and zirconium silicalites, which are efficient catalysts in the hydroxylation of phenol with aqueous $H_2O_2$.[2] Germanium-containing silicalites, as well as a number of Ti–Ge–Si zeolites, showing catalytic activity toward oxidation with $H_2O_2$, have also been successfully synthesized.[3] Other important examples are lead-containing zeolites with framework $Pb^{II}$ species; these compounds are promising photocatalysts in denitrification ($deNO_x$) reactions.[4,5] Despite the considerable effort that has been devoted to the synthesis and characterization of these interesting materials, there is still no well-defined model to explain the observed catalytic properties. As the heteroatoms are postulated to be the active sites for the oxidation reactions, accurate information on their coordination environment and electronic structure is of fundamental importance for understanding the catalytic behavior of the heteroatom-substituted zeolites and for designing new materials with predetermined properties.

Herein, we propose a new model for the formation of active sites in silicalite, which is based on the hydrolysis and inversion of tetrahedral sites in the zeolitic framework. We demonstrate that the inversion mechanism can help to stabilize the active sites, as well as increase their accessibility to guest molecules in the zeolite pores. This model is in agreement with early experimental studies on TS-1,[6] which suggested that hydrolysis of a Ti–O–Si bridge forces the titanium atom to move away from its tetrahedral configuration to a new more "external" relaxed position. In contrast, current models make a strong distinction between the modes of incorporation of titanium atoms: in zeolites they occupy tetrapodal sites within the framework, while in mesoporous materials they are grafted onto the silica surface and have a tripodal coordination environment.[7] Our calculations show that both configurations are realized within zeolites and that the hydrolysis-plus-inversion mechanism is the missing link between them.

The characteristic features of this model are closely related to a number of structures in silica. For example, it has been postulated that the hydrolysis step during silica synthesis occurs through an $S_N2$ mechanism with inversion of a silicon tetrahedron.[8] A similar mechanism was reported for the formation of positively charged oxygen-vacancy defects (E′ centers) in α-quartz and amorphous silica.[9] It was suggested that the E′ center undergoes a distortion to a stable puckered configuration, which is accompanied by a large relaxation of the silicon atoms adjacent to the oxygen vacancy. Recently, Sokol et al. advanced the hydrolysis-plus-inversion model for the stabilization of intrinsic defects, for example, vicinal disilanols and trigonal aluminum species, in hydrated siliceous and aluminosilicate zeolites.[10]

The early computational work on titanium sites was based on generic cluster models with no real distinction between micro- and mesoporous silicas. In particular, Sinclair et al. provided evidence of a tripodal configuration for titanium sites on a mesoporous support.[11] Although the hydrolysis of one or two of the Ti–O–Si bridges was calculated to be an endothermic process, it was argued that the formation of hydrogen bonds helps to stabilize the hydrolyzed sites further. Therefore, both tetra- and tripodal species should co-exist in the material. Ricchiardi et al. applied an embedded-cluster approach in a study of the hydrolysis of the titanium-containing zeolite chabazite and drew similar conclusions.[12] More recent computational studies followed the experimental lead and concentrated on tetrapodal models for the titanium sites in zeolites[13] and on tripodal models for the sites in mesoporous materials.[14] Herein, for the first time, we apply both types of model to zeolites and explore further related structures of the active sites.

During synthesis or post-synthetic treatments, the oxidation state of the heteroatoms can also change. Upon exposure of TS-1 to radiation, or $H_2$ or CO gas, the $Ti^{IV}$ centers can be reduced to $Ti^{III}$.[15,16] The chemistry of titanium, zirconium, and hafnium is dominated by the tetravalent oxidation state (although a few compounds containing the elements in the trivalent oxidation state are known).[17] Lower oxidation states of tin and lead are, of course, well characterized, with $Pb^{II}$ being the dominant valence state of this element.

We first explored the structure and stability of sites substituted by elements from Groups 4 and 14 in their main oxidation states. The structures we consider have four, three, or two T–O–Si bridges linking the metal T site with the framework; these configurations are referred to as tetrapodal, tripodal, and bipodal, respectively.

We employed the hybrid quantum mechanical/molecular mechanical (QM/MM) embedded-cluster approach, which was developed to treat localized states in extended systems. Herein, the zeolite system is represented by a QM/MM

[*] J. To, Dr. A. A. Sokol, Dr. S. A. French, Prof. C. R. A. Catlow
Davy Faraday Research Laboratory
The Royal Institution of Great Britain
21 Albemarle Street, London, W1S 4BS (UK)
Fax: (+44) 20-7670-2920
E-mail: judy@ri.ac.uk
P. Sherwood, H. J. J. van Dam
CCLRC Daresbury Laboratory
Warrington, WA4 4AD (UK)

[**] For the useful discussions, we thank Dr. J. M. Garcés, Dr. A. Kuperman, Dr. P. E. Sinclair, Dr. C. M. Barker, Prof. R. J. Davis, Dr. G. Berlier, Dr. A. M. Beale, Prof. G. Sankar, Dr. N. R. Shiju, and Prof. Sir J. M. Thomas. J.T. gratefully acknowledges EPSRC for the financial support and HPCx Materials Chemistry Consortium for the computational resources from grant GR/S13422.

 © 2006 Wiley-VCH Verlag GmbH & Co. KGaA, Weinheim 

cluster embedded in an array of point charges that models the electrostatic environment. The QM/MM model can be loosely partitioned into a QM and a MM region. The QM region, which contains the proposed active site, is treated with ab initio methods, whereas the MM region, which includes the rest of the system, is described using classical interatomic potentials. As part of the embedding procedure, the QM region is further terminated by hydrogen atoms to satisfy the valence of the Si–O bonds that are cut when defining the QM and MM regions. The methodology described is implemented in the computational-chemistry environment code ChemShell.[18]

Based on neutron diffraction and extended X-ray absorption fine structure (EXAFS) studies of TS-1,[19,20] the T(8) site of the structure was chosen for substitution and was placed at the centre of a QM/MM cluster of 18 Å radius. The atoms within three coordination spheres of the T(8) site (that is, shell-3 atoms), and those that are part of the connected five- and ten-membered rings (ring sizes are defined by the number of tetrahedral atoms) were all included in the QM region (Figure 1). Only the heteroatoms, shell-3 atoms, and atoms that are part of the five-membered ring were used for geometry optimization.

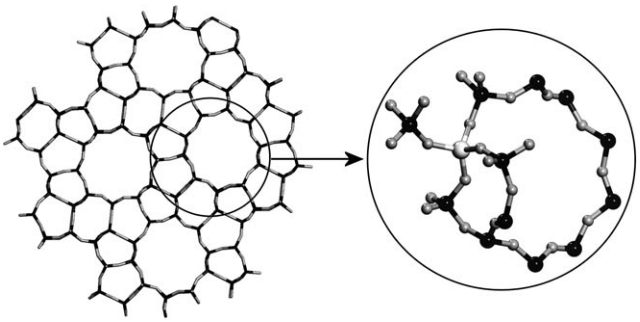


***Figure 1.*** A 2D view of the QM/MM cluster, highlighting the QM region. The hydrogen terminating atoms are omitted for clarity. Si black, O gray, heteroatom white.

For the QM treatment, we used the density functional theory (DFT) as implemented in the GAMESS-UK code.[21] We employed the BB1K exchange correlation functional,[22] which was shown in our cluster calculations to provide a very accurate description of the electronic structure of localized and paramagnetic defects in silica materials.[23] The heteroatoms and the other optimized atoms were described with TZVP and DZP basis sets, respectively, while the remaining QM atoms were treated with SV basis sets.[24] Interactions in the MM region were dealt with using the aluminosilicate interatomic potentials of Hill and Sauer[25] with modified charges,[18] using routines from DL_POLY[26] as incorporated in the ChemShell code. To include relativistic effects, small-core pseudopotentials were used for the heavier elements (tin, lead, zirconium, and hafnium).[27] Based on our calculations on selected cluster models of larger size and with more extensive basis sets, we estimate the error of our calculations to be within 10–20 kJ mol$^{-1}$, which is in line with state-of-the-art quantum-mechanical calculations in solid-state chemistry. This error arises from the embedding procedure, the limited size of the quantum mechanical and active regions, the accuracy of the BB1K density functional, and the basis set superposition error.

Let us first consider a tetravalent heteroatom occupying a tetrapodal framework site, which is expected to be its ground state under anhydrous conditions. Upon interaction with water, one of the T–O–Si bridges opens, and a stable two-membered ring is formed (Figure 2a, left). A reaction path to

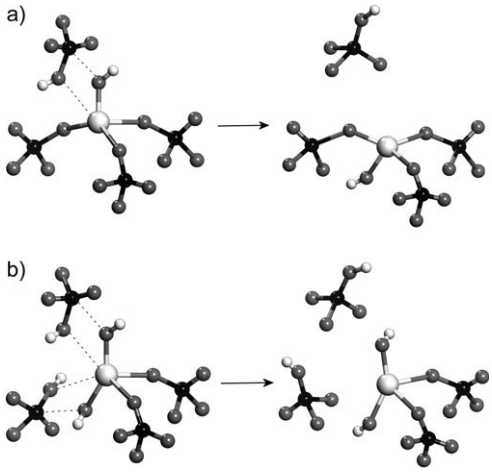



***Figure 2.*** a) The tripodal structure with (right) and without (left) inverted tetrahedral sites. b) The bipodal structure with (right) and without (left) inverted tetrahedral sites. Si black, O gray, H small white circles, heteroatom large white circles.

this structure can be achieved by transferring one proton from water to a bridging oxygen atom to yield a T–OH group, and then forming a Si–OH group with the remaining hydroxide ion. As the two hydroxy groups strongly repel each other in the confinement of the small space between the two framework T sites, this configuration is further transformed by inversion, resulting in two tripodal sites with terminal hydroxy groups [Figure 2a, right; Eq. (1)].[*]

$$(SiO)_4T^{IV} + H_2O\,(g) \rightarrow (SiO)_3T^{IV}_{tri}OH + Si_{tri}OH \qquad (1)$$

The mechanism of inversion should be fully analogous with that reported for vicinal disilanols.[10] A proton hopping to a neighboring bridging oxygen site leads to rotation of the oxygen tetrahedron surrounding the T atom. The T atom linked to the new hydroxy group moves from its central position into the channel of the zeolite. The deprotonated oxygen atom subsequently takes the place of the leaving bridging hydroxy group, thus restoring the T–O–Si bridge.

The mechanism of hydrolysis and inversion of the T–O–Si bridges is, of course, not exclusive to tetrapodal sites, but can also involve tripodal sites, leading to the bipodal configuration [Figure 2b; Eq. (2)]. Alternatively, the hydrolysis may

[*] For all reactions, active sites are represented by all atoms in the first two coordination shells of the T atoms. Subscripts tri and bi refer to tripodal and bipodal sites, respectively; T atoms without subscripts occupy tetrapodal sites.

 © 2006 Wiley-VCH Verlag GmbH & Co. KGaA, Weinheim 

proceed as a concerted process; combining Equations (1) and (2) gives Equation (3).

$$(SiO)_3T^{IV}_{tri}OH + H_2O\,(g) \rightarrow (SiO)_2T^{IV}_{bi}(OH)_2 + Si_{tri}OH \quad (2)$$

$$(SiO)_4T^{IV} + 2\,H_2O\,(g) \rightarrow (SiO)_2T^{IV}_{bi}(OH)_2 + 2\,Si_{tri}OH \quad (3)$$

Table 1 lists the energies of the reactions in Equations (1)–(3) and the ionic radii of the tetravalent heteroatoms.[28] The

***Table 1:*** Calculated energies [kJ mol$^{-1}$] for the hydrolysis reactions at $T^{IV}$ and $T^{IV}_{tri}$ sites given in Equations (1)–(3).

| T | Ionic radius [Å][a] | $T^{IV} \rightarrow T^{IV}_{tri}$ [Eq. (1)] | $T^{IV}_{tri} \rightarrow T^{IV}_{bi}$ [Eq. (2)] | $T^{IV} \rightarrow T^{IV}_{bi}$ [Eq. (3)] |
|---|---|---|---|---|
| Ti | 0.42 | −39 | 45 | 6 |
| Zr | 0.59 | −83 | 3 | −80 |
| Hf | 0.58 | −77 | 9 | −68 |
| C | 0.15 | −100 | −1 | −100 |
| Si | 0.26 | −36 | 74 | 39 |
| Ge | 0.39 | −43 | 59 | 16 |
| Sn | 0.55 | −69 | 11 | −58 |
| Pb | 0.65 | −97 | −4 | −101 |

[a] Data taken from Ref. [28].

opening of the T–O–Si bridges and the rearrangement of the local structure through inversion help to release the lattice strain associated with the heteroatoms and, hence, to stabilize the structure. The large negative energies of the reaction in Equation (1) reveal that the formation of all of the tripodal structures is energetically favorable. In contrast, the formation of all of the bipodal structures from their corresponding tripodal precursors is endothermic, except in the cases of carbon and lead sites. The stability of the bipodal structure is clearly dependent on the ionic size of the heteroatom. Being at the two size extremes of the series studied, the carbon and lead atoms are associated with the largest defect strain, which is released in the less-constrained bipodal configuration. As heteroatoms may be introduced into zeolites, not only in their synthesis, but also by impregnation, ion exchange, and/or grafting on pretreated silica matrices, we assessed the feasibility of these substitution methods. Figure 3 displays the substitution energies with respect to the pure-silica system for two ion-exchange routes [Eq. (4a) and (4b)].

$$(SiO)_4Si^{IV} + TCl_4\,(g) \rightarrow (SiO)_4T^{IV} + SiCl_4\,(g) \quad (4a)$$

$$(SiO)_4Si^{IV} + T(OH)_4\,(g) \rightarrow (SiO)_4T^{IV} + Si(OH)_4\,(g) \quad (4b)$$

In agreement with our previous observations for tetrapodal models,[29] the energies calculated for the reaction in Equation (4a) show that the larger the heteroatom, the greater the substitution energy for all of the configurations considered. For the larger atoms, the substitution energies are lower for the heteroatoms in the tri- and bipodal configurations; this effect can be attributed to the increased ability of the heteroatoms to enter a less-constrained framework. The large positive energies, which indicate highly endothermic processes, suggest that grafting may be preferred over ion

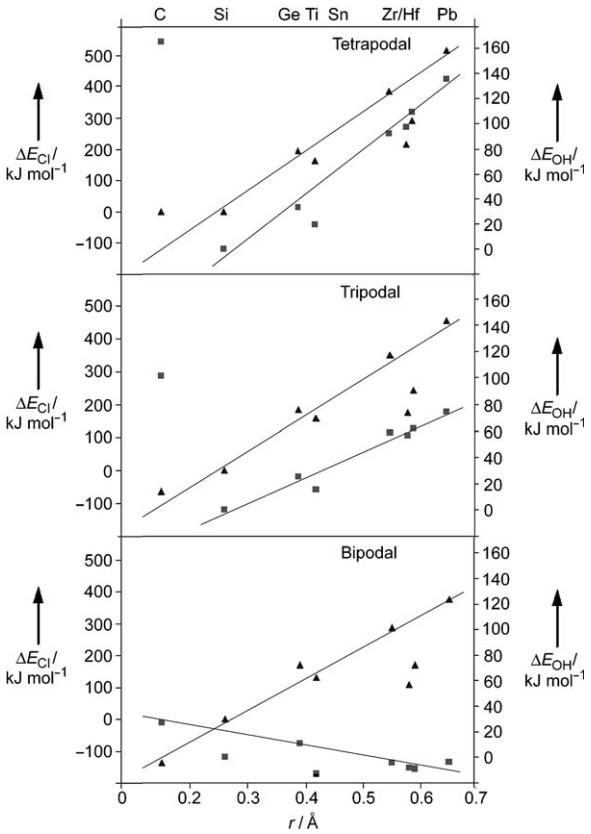



***Figure 3.*** Plot of the substitution energies for C, Si, Ge, Ti, Sn, Zr, Hf, and Pb atoms calculated from Equations (4a) ($\Delta E_{Cl}$ ▲) and (4b) ($\Delta E_{OH}$ ■) as a function of ionic radius ($r$) for tetrapodal (top), tripodal (middle), and bipodal (bottom) sites.

exchange as a preparation route. The substitution energies for the reaction in Equation (4b), apart from those of the carbon and silicon sites, are lower than the energies for the reaction in Equation (4a) for all configurations. Furthermore, the energies for the reaction in Equation (4b) are less dependent on the ionic radius of the heteroatom. They also span a much smaller range, which makes identification of the preferred degree of hydrolysis more difficult. In a recent review of TS-1,[7] it was suggested that tetra- and tripodal structures could be distinguished by their X-ray absorption, UV/Vis, Raman, and EPR spectroscopic signatures. Our initial calculations do not support the distinctive nature of the vibrational modes reported for these species. Similarly, Chaudhari et al. were unable to definitively assign the vibrational bands in the FT-IR spectra of mesoporous titano- and zirconosilicates.[30] However, in an attempt to determine the dominant titanium species in TS-1, an accurate refinement of EXAFS data based on our calculated structures is in progress.

We would expect that under aqueous conditions the heteroatom sites in silicalite would hydrolyze to a mixture of tri- and bipodal structures. Note that these heteroatom sites can undergo further hydrolysis, leading first to unipodal structures, and finally to the removal of the heteroatom from the framework and the formation of hydroxy-nest defects. The bipodal sites, which have fewer Ti–O–Si bridges, are more susceptible to such degradation. Therefore, the tripodal

 © 2006 Wiley-VCH Verlag GmbH & Co. KGaA, Weinheim 

structures are considered to be the dominant and more stable species under severe post-synthetic conditions.

Based on these results, the tripodal model was chosen as the starting structure for the reduction reactions of tetravalent heteroatoms. When substituted into a pure silica framework, heteroatoms with oxidation states less than IV will have negative effective charges, which must be compensated. Herein, the charge is neutralized either by adding protons or by removing hydroxy groups bonded to the heteroatom.

The results of our calculations on the structure and stability of $Ti^{III}$, $Zr^{III}$, and $Hf^{III}$ sites are summarized in Table 2, and the reaction scheme considered is outlined in Figure 4. The reduction step A in Figure 4 can be effected with either $H_2$ [Eq. (5a)] or CO [Eq. (5b)] as reducing agent.[31,32]

***Table 2:*** Calculated energies [kJ mol$^{-1}$] for the reduction of $T^{IV}_{tri}$ centers to $T^{III}_{tri}$, and the structural reorganization of the $T^{III}_{tri}$ sites, as depicted in Figure 4 and given in Equations (5)–(7).

| T | A = $T^{IV}_{tri} \rightarrow T^{III}_{tri}$ [a] [Eq. (5a)] | [Eq. (5b)] | B = $T^{III}_{tri} \rightarrow T^{III}_{bi}$ [a] [Eq. (6)] | C = $T^{III}_{tri} \rightarrow T^{III}$ [a] [Eq. (7)] |
|---|---|---|---|---|
| Ti | 175 | 120 | −70 | 290 |
| Zr | 287 | 232 | −118 | 292 |
| Hf | 391 | 336 | −114 | 247 |

[a] For steps A–C see Figure 4.

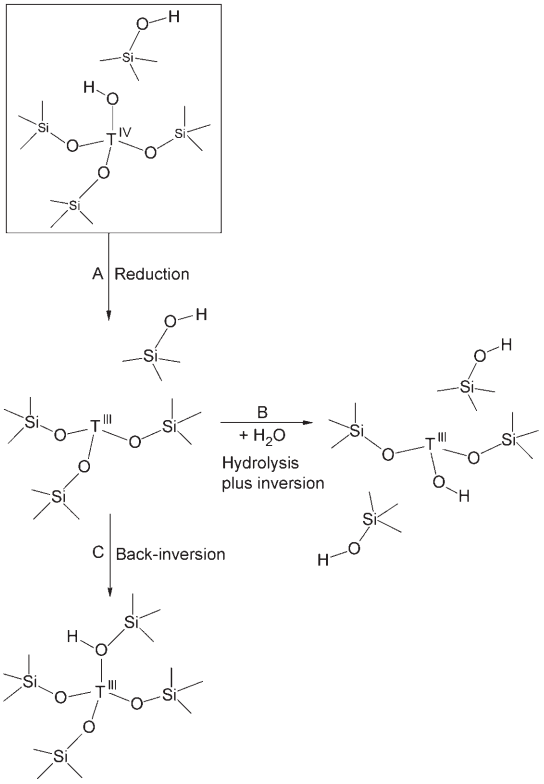



***Figure 4.*** Reduction of $T^{IV}_{tri}$ centers to $T^{III}_{tri}$, and structural reorganization of the $T^{III}_{tri}$ sites; T = Ti, Zr, Hf. See text for full details.

$$(SiO)_3T^{IV}_{tri}OH + Si_{tri}OH + 1/2\,H_2\,(g) \rightleftharpoons (SiO)_3T^{III}_{tri} + Si_{tri}OH + H_2O\,(g) \quad (5a)$$

$$(SiO)_3T^{IV}_{tri}OH + Si_{tri}OH + CO\,(g) \rightleftharpoons (SiO)_3T^{III}_{tri} + Si_{tri}OH + CO_2\,(g) + 1/2\,H_2\,(g) \quad (5b)$$

Treatment with $H_2$ or CO reduces the diamagnetic $T^{IV}$ ($nd^0$) transition-metal center to a paramagnetic, EPR-active $T^{III}_{tri}$ ($nd^1$) center. The formation of the trivalent-heteroatom site upon interaction with $H_2$ is calculated to be an endothermic process. Reduction with CO is also endothermic, although more energetically favorable (by approximately 55 kJ mol$^{-1}$). Characterization of titanium and zirconium species in micro- and mesoporous materials by EPR spectroscopy has confirmed the presence of trivalent metal centers in the framework structure after reduction.[31,32] In particular, Prakesh and Kevan investigated the formation of trivalent titanium centers in TS-1 upon treatment with $H_2$ or CO, and reported that both reduction processes occur above 673 K.[31] This observation indicates the presence of unidentified activation processes preceding reduction, which should shift the equilibrium to the right in Equations (5a) and (5b).

To probe the activation mechanisms of the trivalent-heteroatom sites, we further explored the structure and stability of the triply coordinated bipodal $T^{III}_{bi}$ site formed after hydrolysis step B in Figure 4 [Eq. (6)], and of the tetrapodal $T^{III}$ site formed after back-inversion step C [Eq. (7)].

$$(SiO)_3T^{III}_{tri} + Si_{tri}OH + H_2O\,(g) \rightarrow (SiO)_2T^{III}_{bi}OH + 2\,Si_{tri}OH \quad (6)$$

$$(SiO)_3T^{III}_{tri} + Si_{tri}OH \rightarrow (SiO)_4T^{III}OHSi \quad (7)$$

The calculated formation energies of the $Ti^{III}$, $Zr^{III}$, and $Hf^{III}$ centers in the different structural environments indicate the order of stability of these species as follows: bipodal > tripodal > tetrapodal. Interestingly, Bal et al.,[16] and Chaudhari et al.[30] gave EPR spectroscopic evidence for the presence of two different types of $Ti^{III}$ sites in both TS-1 and Ti-MCM-41, which were assigned as tetra- and tripodal structures by Ratnasamy et al.[7a] However, our results do not support the spectroscopic signatures, because we predict that $Ti^{III}$ centers are most stable in the less-constrained bipodal structure. The two different results can be attributed to the preparation procedures of the samples. Under dry conditions, we expect calcined anhydrous samples to contain a high proportion of tetrapodal $Ti^{IV}$ sites, which would first be reduced to the tetrapodal $Ti^{III}$ species, and then undergo inversion to the tripodal configuration, as observed in the published experiments. In the presence of water, however, we expect the sample to contain a large number of tripodal $Ti^{IV}$ sites, which would first be reduced to tripodal $Ti^{III}$ species, and then undergo hydrolysis and inversion to form the bipodal structure, as predicted by our calculations. Note that the overall formation processes of all bipodal $T^{III}_{bi}$ sites are endothermic, which explains the necessity of the high-temperature treatments mentioned above.

While the reduction of the Group 4 elements can be expected to proceed by the occupation of d shells, with trivalent species being of prime interest, lone pairs in s shells are known to define the chemistry of tin and lead; hence, we focus on oxidation state II for these elements. The results of

 © 2006 Wiley-VCH Verlag GmbH & Co. KGaA, Weinheim 

our calculations are summarized in Table 3, and the reaction scheme considered is outlined in Figure 5. As before, we consider two reactions for the reduction step D in Figure 5 [Eqs. (8a) and (8b)].

$$(SiO)_3T^{IV}_{tri}OH + Si_{tri}OH + H_2\,(g) \rightarrow (SiO)_2T^{II}_{tri}OHSi + Si_{tri}OH + H_2O\,(g) \quad (8a)$$

$$(SiO)_3T^{IV}_{tri}OH + Si_{tri}OH + CO\,(g) \rightarrow (SiO)_2T^{II}_{tri}OHSi + Si_{tri}OH + CO_2\,(g) \quad (8b)$$

***Table 3:*** Calculated energies [kJ mol$^{-1}$] for the reduction of $T^{IV}_{tri}$ centers to $T^{II}_{tri}$, and the structural reorganization of the $T^{II}_{tri}$ sites, as depicted in Figure 5 and given in Equations (8)–(10).

| T | $D = T^{IV}_{tri} \rightarrow T^{II}_{tri}$ [a] | | $E = T^{II}_{tri} \rightarrow T^{II}_{bi}$ [a] | $F = T^{II}_{tri} \rightarrow T^{II}$ [a] |
|---|---|---|---|---|
| | [Eq. (8a)] | [Eq. (8b)] | [Eq. (9)] | [Eq. (10)] |
| Sn | −133 | −188 | 44 | 302 |
| Pb | −384 | −439 | 30 | −23[b] |

[a] For steps D–F see Figure 5. [b] $T^{II}_{tri}$ (noninverted).

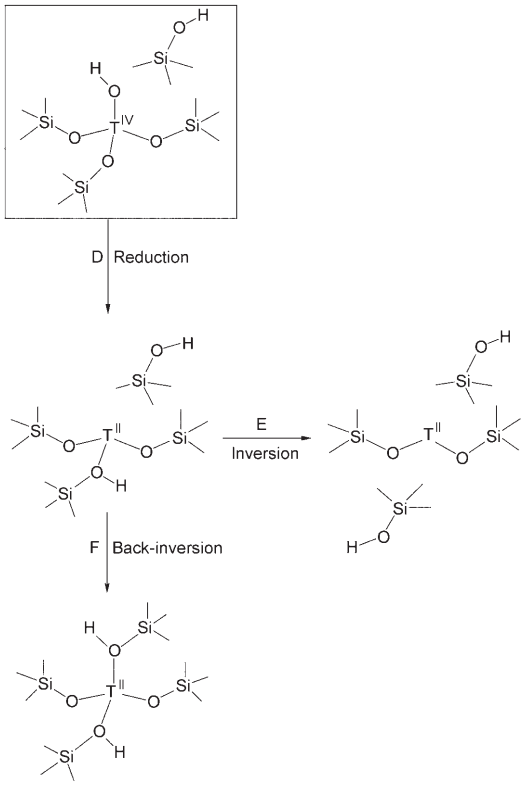



***Figure 5.*** Reduction of $T^{IV}_{tri}$ centers to $T^{II}_{tri}$, and structural reorganization of the $T^{II}_{tri}$ sites; T = Sn, Pb. See text for full details.

Both reduction reactions lead to the formation of a divalent center in a distorted trigonal-pyramidal configuration (which is tripodal, with two T–O–Si and one T–OH–Si bridges) and are calculated to be exothermic.

Considering alternative configurations, silanol inversion in the tripodal structure results in a bipodal structure, as shown in step E [Eq. (9)], whilst back-inversion leads to a tetrapodal structure, as shown in step F [Eq. (10)].

$$(SiO)_2T^{II}_{tri}OHSi + Si_{tri}OH \rightarrow (SiO)_2T^{II}_{bi} + 2\,Si_{tri}OH \quad (9)$$

$$(SiO)_2T^{II}_{tri}OHSi + Si_{tri}OH \rightarrow (SiO)_2T^{II}(OHSi)_2 \quad (10)$$

The formation of a $Sn^{II}$ center in a tetrapodal configuration is highly endothermic, as it is for the trivalent centers. However, the order of stability of the different structures containing $Sn^{II}$ centers is different: tripodal > bipodal > tetrapodal.

The $Pb^{II}$ center appears to be a special case. In agreement with X-ray absorption near-edge structure (XANES) and FT-EXAFS measurements on $Pb^{II}$/ZSM-5, our results indicate that triply coordinated $Pb^{II}$ species are preferred within the zeolite framework.[5] In fact, a $Pb^{II}$ center in a tetrapodal configuration was not found, because the atom is too big to retain the tetrahedral coordination. Instead, optimization starting from a tetrapodal configuration produced a structure similar to the tripodal configuration, but without silanol inversion. When we compared the energies of the two structurally different tripodal configurations, we found that the structure containing the inverted silanol group was more stable by 23 kJ mol$^{-1}$. This result provides further evidence that the inversion of silanol groups is significant in helping to relieve the structural strain associated with larger heteroatoms.

In summary, we predict that the tetravalent-heteroatom sites preferentially adopt tripodal configurations, particularly in the presence of water. The hydrolysis of T–O–Si bridges, which occurs with rearrangement of the local structure, helps to relieve lattice strain and to stabilize the structure. On the other hand, we find that the trivalent-heteroatom sites are most stable in bipodal configurations, whereas $Sn^{II}$ and $Pb^{II}$ sites prefer to adopt tripodal structures. Thus, hydrolysis and inversion play fundamental roles in the stabilization of heteroatom-based active sites in zeolites. The present study has concentrated on Group 4 and 14 elements, but the mechanisms identified are expected to be general. Studies in progress on zeolites containing other early transition metals will be reported elsewhere.

Received: August 23, 2005
Revised: September 27, 2005
Published online: January 30, 2006

**Keywords:** computer chemistry · hydrolysis · reduction · titanium · zeolites

[1] a) M. Taramasso, G. Perego, B. Notari, US Pat. 4,410,501, **1983**; b) B. Notari, *Stud. Surf. Sci. Catal.* **1987**, *47*, 413.
[2] a) N. K. Mal, A. Bhaumik, V. Ramaswamy, A. A. Belhekar, A. V. Ramaswamy, *Stud. Surf. Sci. Catal.* **1995**, *94*, 37; b) N. K. Mal, A. V. Ramaswamy, *J. Mol. Catal. A* **1996**, *105*, 149; c) B. Rakshe, V. Ramaswamy, S. G. Hegde, R. Vetrivel, A. V. Ramaswamy, *Catal. Lett.* **1997**, *45*, 41.
[3] a) R. Fricke, H. Kosslick, V. A. Tuan, I. Grohmann, W. Pilz, W. Storek, G. Walther, *Stud. Surf. Sci. Catal.* **1994**, *83*, 57; b) Y.

 © 2006 Wiley-VCH Verlag GmbH & Co. KGaA, Weinheim 

Nagakawa, C. Dartt, PCT Int. Appl. WO 9634827A1, **1996**; c) M. E. Davis, C. B. Dartt, PCT Int. Appl. WO 9724286A1, **1997**.
[4] N. U. Zhanpeisov, W. S. Ju, M. Anpo, *J. Mol. Struct. (Theochem)* **2002**, *592*, 155.
[5] N. U. Zhanpeisov, W. S. Ju, K. Iino, M. Matsuoka, M. Anpo, *Res. Chem. Intermed.* **2003**, *29*, 407.
[6] a) F. Geobaldo, S. Bordiga, A. Zecchina, E. Giamello, *Catal. Lett.* **1992**, *16*, 109; b) D. Sacrano, A. Zecchina, S. Bordiga, F. Teobaldo, G. Spoto, G. Petrini, G. Leofanti, M. Padovan, G. Tozzola, *J. Chem. Soc. Faraday Trans.* **1993**, *89*, 4123.
[7] a) P. Ratnasamy, D. Srinivas, H. Knozinger, *Adv. Catal.* **2004**, *48*, 1; b) T. Maschmeyer, F. Rey, G. Sankar, J. M. Thomas, *Nature* **1995**, *378*, 159; c) J. M. Thomas, G. Sankar, *Acc. Chem. Res.* **2001**, *34*, 571.
[8] C. J. Brinker, G. W. Sherer in *Sol-Gel Science: The Physics and Chemistry of Sol-Gel Processing*, Academic Press, New York, **1990**.
[9] a) J. K. Rudra, W. B. Fowler, *Phys. Rev. B* **1987**, *35*, 8223; b) K. C. Snyder, W. B. Fowler, *Phys. Rev. B* **1993**, *48*, 13238.
[10] a) A. A. Sokol, C. R. A. Catlow, J. M. Garcés, A. Kuperman, *J. Phys. Chem. B* **1998**, *102*, 10647; b) A. A. Sokol, C. R. A. Catlow, J. M. Garcés, A. Kuperman, *J. Phys. Chem. B* **2002**, *106*, 6163.
[11] P. E. Sinclair, G. Sankar, C. R. A. Catlow, J. M. Thomas, T. Maschmeyer, *J. Phys. Chem. B* **1997**, *101*, 4232.
[12] G. Ricchiardi, A. de Mann, J. Sauer, *Phys. Chem. Chem. Phys.* **2000**, *2*, 2195.
[13] a) A. Damin, S. Bordiga, A. Zecchina, C. Lamberte, *J. Chem. Phys.* **2002**, *117*, 226; b) E. Fois, A. Gamba, E. Spano, *J. Phys. Chem. B* **2004**, *108*, 154.
[14] C. M. Barker, D. Gleeson, N. Kaltsoyannis, C. R. A. Catlow, G. Sankar, J. M. Thomas, *Phys. Chem. Chem. Phys.* **2002**, *4*, 1228.
[15] a) A. Labouriau, K. C. Ott, J. Rau, W. L. Earl, *J. Phys. Chem. B* **2000**, *104*, 5890.
[16] R. Bal, K. Chaudhari, D. Srinivas, S. Sivasanker, P. Ratnasamy, *J. Mol. Catal. A* **2000**, *162*, 199.
[17] a) M. D. Fryzuk, M. Mylvaganam, M. J. Zaworotko, R. MacGillirray, *Polyhedron* **1996**, *15*, 689; b) W. R. Long, T. M. Brown, *Abstr. Pap. Am. Chem. Soc.* **1986**, *191*, 163.
[18] a) P. Sherwood, A. H. de Vries, M. F. Guest, G. Schreckenbach, C. R. A. Catlow, S. A. French, A. A. Sokol, S. T. Bromley, W. Thiel, A. J. Turner, S. Billeter, F. Terstegen, S. Thiel, J. Kendrick, S. C. Rogers, J. Casci, M. Watson, F. King, E. Karlsen, M. Sjøvoll, A. Fahmi, A. Schäfer, Ch. Lennartz, *J. Mol. Struct. (Theochem.)* **2003**, *632*, 1; b) P. Sherwood, A. H. de Vries, S. J. Collins, S. P. Greatbanks, N. A. Burton, M. A. Vincent, I. H. Hillier, *Faraday Discuss.* **1997**, *106*, 79.
[19] C. A. Hijar, R. M. Jacubinas, J. Eckert, N. J. Henson, P. J. Hay, K. C. Ott, *J. Phys. Chem. B* **2000**, *104*, 12157.
[20] D. Gleeson, G. Sankar, C. R. A. Catlow, J. M. Thomas, G. Spano, S. Bordiga, A. Zecchina, C. Lamberti, *Phys. Chem. Chem. Phys.* **2000**, *2*, 4812.
[21] M. F. Guest, J. M. H. Thomas, P. Sherwood, I. J. Bush, H. J. J. van Dam, *Mol. Phys.* **2005**, *103*, 719.
[22] Y. Zhao, B. J. Lynch, *J. Phys. Chem. A* **2004**, *108*, 6908.
[23] J. To, A. A. Sokol, S. A. French, N. Kaltsoyannis, C. R. A. Catlow, *J. Chem. Phys.* **2005**, *122*, 144704.
[24] a) A. Schäfer, H. Horn, R. Ahlrichs, *J. Chem. Phys.* **1992**, *97*, 2571; b) A. Schäfer, C. Huber, R. Ahlrichs, *J. Chem. Phys.* **1994**, *100*, 5829.
[25] J. R. Hill, J. Sauer, *J. Phys. Chem.* **1995**, *99*, 9536.
[26] W. Smith, C. W. Yong, P. M. Roger, *Mol. Simul.* **2002**, *28*, 385.
[27] M. Dolg, U. Wedig, H. Stoll, H. Preuss, *J. Chem. Phys.* **1987**, *86*, 866.
[28] *CRC Handbook of Chemistry and Physics* (Ed.: D. R. Lide), CRC, London, **2003**.
[29] S. A. French, A. A. Sokol, J. To, C. R. A. Catlow, N. S. Phala, G. Klatt, E. van Steen, *Catal. Today* **2004**, *93*, 535.
[30] K. Chaudhari, R. Bal, D. Srinivas, A. J. Chandwadkar, S. Sivasanker, *Microporous Mesoporous Mater.* **2001**, *50*, 209.
[31] A. M. Prakesh, L. Kevan, *J. Catal.* **1998**, *178*, 586.
[32] V. Ramaswamy, B. Tripathi, D. Srinivas, A. V. Ramaswamy, R. Cattaneo, R. Prins, *J. Catal.* **2001**, *200*, 250.

 © 2006 Wiley-VCH Verlag GmbH & Co. KGaA, Weinheim 

*Tellurium Ligands*

DOI: 10.1002/anie.200503372

# A Molecular Actinide–Tellurium Bond and Comparison of Bonding in $[M^{III}\{N(TeP\textit{i}Pr_2)_2\}_3]$ (M = U, La)**

*Andrew J. Gaunt, Brian L. Scott, and Mary P. Neu**

The coordination chemistry of the f-block elements is dominated by complexes with hard donor atom ligands formed through ionic bonds. Molecular species with covalent interactions were historically considered unlikely because the radial distributions of the valence orbitals are too close to the nucleus to participate in bonding.[1] However, this early assumption has slowly been eroded, beginning with the discovery of complexes such as $[U(cot)_2]$[2] (cot = cyclooctatetraene), in which it was demonstrated that the 5f orbitals overlap with ligand-based orbitals to form a covalent interaction. Complexes of this type have prompted fundamental and intensely debated questions in f-element chemistry: To what extent and generality is covalent bonding important? What are the limits of "hard–soft" interactions? And, crucial to understanding trivalent An/Ln separations, how do these interactions differ between $An^{III}$ and $Ln^{III}$ ions of identical ionic radii (i.e. how do relativistic effects affect coordination chemistry)?[3]

Our approach to addressing these questions, in part, is to synthesize and characterize comparable, isostructural, homoleptic actinide and lanthanide complexes with increasingly "soft" heavier chalcogen donor ligands. Preparing Te-donor complexes is particularly challenging because there is no precedent for molecular actinide tellurides and few suitable

[*] Dr. A. J. Gaunt, Dr. B. L. Scott, Dr. M. P. Neu
Actinide, Catalysis, and Separations (C-SIC)
Chemistry Division
Los Alamos National Laboratory
Los Alamos, New Mexico 87545 (USA)
Fax: (+1) 505-667-9905
E-mail: mneu@lanl.gov

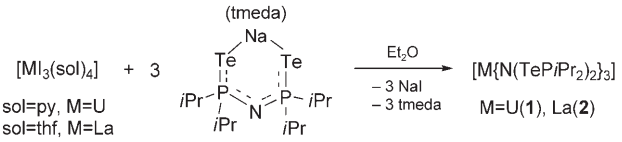
[**] This work was funded by the Heavy Element Chemistry Research Program, Chemical Sciences Division of the Office of Basic Energy Sciences, US Department of Energy, and by the G. T. Seaborg Institute at Los Alamos National Laboratory.

Supporting information for this article is available on the WWW under http://www.angewandte.org or from the author.


WILEY InterScience DISCOVER SOMETHING GREAT
© 2006 Wiley-VCH Verlag GmbH & Co. KGaA, Weinheim

ligand sets have been reported. Ditelluroimidodiphosphinates are ideal candidates, but the P=Te bond is relatively unstable (compared to P=S and P=Se) and these compounds were not available until recently.[4] Our initial attempts to isolate a $U^{III}$ complex by treatment of $[UI_3(thf)_4]$ with $[Na(tmeda)\{N(TePPh_2)_2\}]$ were unsuccessful and resulted in ligand decomposition/rearrangement to $Te^0$ and other products. Replacing the Ph rings with the more electron-donating *i*Pr groups, however, stabilizes the P=Te bond and allows for the synthesis and characterization of $[U\{N(TeP{i}Pr_2)_2\text{-}Te,Te'\}_3]$ (**1**) and $[La\{N(TeP{i}Pr_2)_2\text{-}Te,Te'\}_3]$ (**2**).

Treatment of $[UI_3(py)_4]$ (py = pyridine) and $[LaI_3(thf)_4]$ with three equivalents of $[Na(tmeda)\{N(TeP{i}Pr_2)_2\}]$ in $Et_2O$ yields **1** as a blue-gray solid and **2** as a yellow solid (Scheme 1).




***Scheme 1.*** Syntheses of **1** and **2**.

The by-product of the metathesis reaction, NaI, can be removed by dissolving the compounds in toluene, which allows the isolation of **1** and **2** in 52 and 43% yield, respectively, after filtration and additional of $Et_2O$. Both compounds are air-sensitive, insoluble in $Et_2O$, but soluble in toluene and benzene. The X-ray structures of **1** and **2** (a thermal ellipsoid plot of **1** is shown in Figure 1) were determined for crystals obtained from toluene solution.[5]

The $U^{III}$ and $La^{III}$ complexes are isostructural, homoleptic, and comprised of a six-coordinate metal center bound to three bidentate $[N(TeP{i}Pr_2)_2]^-$ anions in a geometry best described as distorted trigonal-prismatic. The triangular faces of the trigonal prism are defined by one Te atom from each of the $[N(TeP{i}Pr_2)_2]^-$ anions. All three anions bond to the metal through both tellurium atoms, while the nitrogen atoms lie almost 5 Å from the metal ion and do not coordinate. In contrast, $[U\{N(EPPh_2)_2\}_3]$ (E = S, Se) complexes contain tridentate anions that bond through both chalcogen atoms and the nitrogen atom.[6] This difference in denticity is probably due to the increased steric crowding of the *i*Pr groups compared to the Ph rings and the larger size of Te compared to S and Se. The average U–Te distance in **1** is 3.164(2) Å and the average Te–U–Te bite angle is 91.01(3)°. In **2**, the average La–Te distance is 3.224(3) Å and the average Te–La–Te bite angle is 91.06(4)°. The {TePNPTe} moiety is not planar and the twisted conformation of the ligands is described by the average angle between the $MP_2$ (M = U or La) and $MTe_2$ planes of 24.2 and 23.8° for **1** and **2**, respectively. These values are much larger than the twist angles of 5.3 and 6.0° in $[U\{N(SPPh_2)_2\}_3]$ and $[U\{N(SePPh_2)_2\}_3]$, in which the nitrogen atom is coordinated to the metal center.[6] Each ligand has one "shorter" and one "longer" M–Te bond in **1** and **2**. However, a comparison of each equivalent bond in isostructural **1** and **2** shows that all six bonds have a difference of approximately 0.06 Å (Table 1).

***Table 1:*** Metal–tellurium bond lengths [Å] in **1** and **2**.

| **1** | | **2** | | Δ |
|---|---|---|---|---|
| U–Te(1) | 3.1499(7) | La–Te(1) | 3.2074(9) | 0.0575 |
| U–Te(2) | 3.1801(7) | La–Te(2) | 3.2437(10) | 0.0636 |
| U–Te(3) | 3.1362(7) | La–Te(3) | 3.1893(10) | 0.0531 |
| U–Te(4) | 3.1909(7) | La–Te(4) | 3.2559(12) | 0.0650 |
| U–Te(5) | 3.1990(7) | La–Te(5) | 3.2614(11) | 0.0624 |
| U–Te(6) | 3.1270(7) | La–Te(6) | 3.1875(10) | 0.0605 |

The "short" and "long" M–Te bonds in **1** and **2** are probably a result of steric constraints. A disparity in bond lengths has been previously noted in $[Bi\{N(SPPh_2)_2\}_3]$ and suggested to arise from the repulsive influence of the lone pair of electrons on bismuth.[7] However, there is no evidence for this in the isopropyl analogue, which exhibits a single Bi–S bond length.[8]

Molecular compounds with actinide–tellurium bonds have not yet been reported in the literature. A few examples for $Ln^{III}$–Te bonds have been structurally characterized,[9] but these complexes are not homoleptic and most incorporate ancillary stabilizing ligands. Compounds **1** and **2** are the first f-element complexes with ditelluroimidodiphosphinates. The ionic radii of six-coordinate $U^{III}$ and $La^{III}$ are 1.04 and 1.045 Å, respectively, differing by just 0.005 Å.[10] However, the average U–Te distance in **1** is shorter than the average La–Te distance in **2** by 0.060 Å, which is significantly larger than the difference in ionic radii. This experimental observation supports the theory that $An^{III}$ ions have a greater covalent contribution to their bonding than $Ln^{III}$, and that the effect should be more pronounced with "softer" ligands due to increased metal–ligand orbital overlap. To the best of our knowledge, the only other crystallographic observation of $An^{III}/Ln^{III}$ differentiation in isostructural compounds with a chalcogen donor ligand was found in the heteroleptic complexes $[M(9\text{-}aneS_3)I_3(CH_3CN)_2]$ (M = U or La),[3d] in which the U–S bonds are 0.0435–0.0489 Å shorter than the La–S bonds, a difference slightly smaller than for the U/La–Te bonds in **1** and **2**.

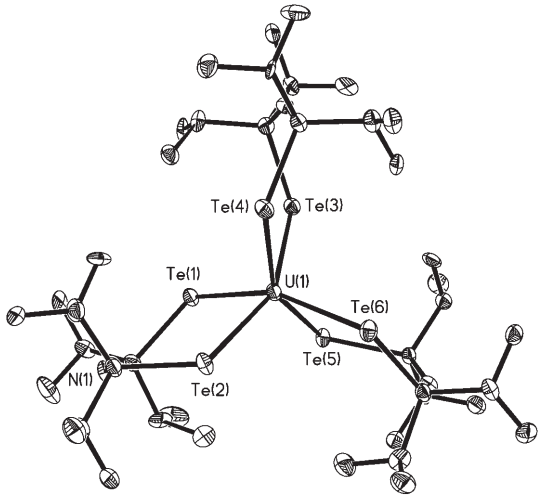



***Figure 1.*** ORTEP representation of the crystal structure of **1** (50% probability ellipsoids). The H atoms have been omitted for clarity.

 © 2006 Wiley-VCH Verlag GmbH & Co. KGaA, Weinheim 

Resonances in the $^{31}P$ NMR spectra of [D$_8$]toluene solutions of **1** and **2** are observed at $\delta = -696.7$ and 29.5 ppm, respectively. The chemical shift for **2** is consistent with those recently reported for complexes of $[N(TeP{i}Pr_2)_2]^-$ with the diamagnetic $Zn^{2+}$, $Cd^{2+}$, $Hg^{2+}$, $Sb^{3+}$, and $Bi^{3+}$ ions,[4b] whereas the high-field shift for **1** is due to the paramagnetic $5f^3$ electronic configuration of $U^{III}$. The UV/Vis/NIR spectrum of a toluene solution of **1** has absorption bands between 480 and 1300 nm attributed to Laporte forbidden 5f–5f transitions and allowed 5f–6d transitions. $La^{III}$ has a $4f^0$ electronic configuration and its complexes are usually colorless. However, **2** is yellow and displays absorption bands at 303 and 378 nm that are not present in the electronic absorption spectrum of the precursor ligand in toluene.

In summary, the isolation of a hitherto unreported molecular compound with actinide–tellurium bonds pushes the boundaries of "hard–soft" interactions in 5f-element chemistry and enables a full and systematic study of $An^{III}$ and $Ln^{III}$ complexes with $[N(EP{i}Pr_2)_2]^-$ ligands over a wide range of donor-atom electronegativities (or "softness") by varying the chalcogen atom. Furthermore, the isolation of an isostructural lanthanide complex has demonstrated a significant difference in the bonding between the similarly sized $U^{III}$ and $La^{III}$, thereby suggesting more covalent character in the U–Te bond than the La–Te bond.

## Experimental Section

All reactions and manipulations were carried out in a helium-filled glovebox. Diethyl ether and toluene were dried by passing through activated alumina columns under argon. Deuterated solvents were purchased in sealed ampoules. All solvents were stored in a glovebox over a 1:1 mixture of 3- and 4-Å molecular sieves before use. All $^1H$ and $^{31}P$ NMR spectra were recorded at room temperature for samples in 4-mm Teflon NMR tube liners inserted into 5-mm glass NMR tubes (to contain the radioactive samples) using a Bruker Avance 300-MHz spectrometer. The $^1H$ NMR spectra were referenced to the residual protio solvent resonances and the $^{31}P$ NMR spectra to external 85% $H_3PO_4$. $[UI_3(py)_4]$ was prepared according to a literature procedure[11] and $[Na(tmeda)\{N(TeP{i}Pr_2)_2\}]$ by modifying a reported synthesis.[4b,12] $[LaI_3(thf)_4]$ was prepared by stirring anhydrous $LaI_3$ in THF overnight and collecting the white solid.

**1**: A suspension of $[UI_3(py)_4]$ (0.0881 g, 0.094 mmol) in $Et_2O$ (5 mL) was treated dropwise with $[Na(tmeda)\{N(TeP{i}Pr_2)_2\}]$ (0.1828 g, 0.283 mmol) in $Et_2O$ (2 mL), resulting in the immediate formation of a gray-blue suspension, which was stirred at room temperature for 20 min. The solid was allowed to settle, the solvent pipetted away, and the solid dried in vacuo to give a dark gray-blue powder. This powder was dissolved in toluene (7 mL), the solution filtered, $Et_2O$ added (7 mL), and the solution stored at −35 °C to yield a microcrystalline dark gray-blue solid (0.0856 g, 52%). C,H,N analysis (%) calcd for $C_{36}H_{84}N_3P_6Te_6U$: C 24.73, H 4.84, N 2.40; found: C 24.96, H 4.94, N 2.40. $^1H$ NMR ([D$_8$]toluene): $\delta = 0.001$, −0.28, −0.74 ppm (s, 84 H; $CH(CH_3)_2$); $^{31}P\{^1H\}$ NMR ([D$_8$]toluene): $\delta = -696.7$ ppm; IR (nujol, KBr plates): $\tilde{\nu} = 472$, 510, 610, 635, 660, 723, 748, 776, 882, 935, 977, 1025, 1078, 1097, 1167, 1227, 1272 cm$^{-1}$; UV/Vis/NIR (toluene solution) $\lambda(\varepsilon) = 483$ (841), 559 (1107), 628 (1269), 948 (876), 1104 (559), 1248 nm (380 M$^{-1}$ cm$^{-1}$).

A dark-blue, rectangular plate crystal ($0.12 \times 0.08 \times 0.02$ mm$^3$) suitable for X-ray diffraction was grown from a toluene solution of **1** after several days at −35 °C.

**2**: A suspension of $[LaI_3(thf)_4]$ (0.060 g, 0.074 mmol) in $Et_2O$ (5 mL) was treated dropwise with $[Na(tmeda)[N(TeP{i}Pr_2)_2]]$ (0.1440 g, 0.223 mmol) in $Et_2O$ (2 mL), resulting in the immediate formation of a yellow suspension, which was stirred at room temperature for 25 min. The solid was isolated as for **1** to give a yellow microcrystalline powder (0.0524 g, 43%). C,H,N analysis (%) calcd for $C_{36}H_{84}LaN_3P_6Te_6$: C 26.22, H 5.13, N 2.55; found: C 26.59, H 4.85, N 2.58. $^1H$ NMR ([D$_6$]benzene): $\delta = 1.98$ (m, 12 H; $CH(CH_3)_2$), 1.22 ppm (m, 72 H; $CH(CH_3)_2$); $^{31}P\{^1H\}$ NMR ([D$_8$]toluene): $\delta = 29.5$ ppm; IR (nujol, KBr plates): $\tilde{\nu} = 470$, 510, 609, 635, 660, 723, 775, 882, 932, 976, 1019, 1077, 1097, 1159, 1171, 1228, 1279 cm$^{-1}$; UV/Vis/NIR (toluene solution) $\lambda(\varepsilon) = 303$ (23 764), 378 nm (11 109 M$^{-1}$ cm$^{-1}$).

A yellow-orange, rectangular plate crystal ($0.24 \times 0.08 \times 0.02$ mm$^3$) suitable for X-ray diffraction was grown from a toluene solution of **2** by allowing the solvent to evaporate slowly.

NMR, IR, and UV/Vis spectra are included in the Supporting Information.

Received: September 22, 2005
Published online: February 6, 2006

**Keywords:** actinides · chalcogens · coordination modes · lanthanides · uranium

[1] See, for example: a) S. Cotton in *Comprehensive Coordination Chemistry II*, Vol. *3* (Eds.: J. A. McCleverty, T. J. Meyer), Elsevier Pergamon, Amsterdam, **2004**, p. 93; b) C. J. Burns, M. P. Neu, H. Boukhalfa, K. E. Gutowski, N. J. Bridges, R. D. Rogers, in *Comprehensive Coordination Chemistry II*, Vol. *3* (Ed.: J. A. McCleverty, T. J. Meyer), Elsevier Pergamon, Amsterdam, **2004**, p. 189; c) J. J. Katz, G. T. Seaborg, L. R. Morss, *The Chemistry of the Actinide Elements*, Vols. *1 and 2*, 2nd ed., Chapman and Hall, New York, **1986**.

[2] A. Streitwieser, U. Müller-Westerhoff, *J. Am. Chem. Soc.* **1968**, *90*, 7364.

[3] a) G. R. Choppin, *J. Alloys Compd.* **2002**, *344*, 55; b) G. R. Choppin, K. L. Nash, *Radiochim. Acta* **1995**, *70–71*, 225; c) M. P. Jensen, A. H. Bond, *Radiochim. Acta* **2002**, *90*, 205; d) L. Karmazin, M. Mazzanti, J. Pécaut, *Chem. Commun.* **2002**, 654; e) T. Mehdoui, J.-C. Berthet, P. Thuéry, M. Ephritikhine, *Chem. Commun.* **2005**, 2860; f) J. G. Brennan, S. D. Stults, R. A. Andersen, A. Zalkin, *Organometallics* **1988**, *7*, 1329; g) F. Nief, *Coord. Chem. Rev.* **1998**, *178–180*, 13.

[4] a) G. G. Briand, T. Chivers, M. Parvez, *Angew. Chem.* **2002**, *114*, 3618; *Angew. Chem. Int. Ed.* **2002**, *41*, 3468; b) T. Chivers, D. J. Eisler, J. S. Ritch, *Dalton Trans.* **2005**, 2675.

[5] Crystal data for **1**: $C_{36}H_{84}N_3P_6Te_6U$, $M_r = 1748.51$, monoclinic, space group $P2_1/c$, $a = 22.3600(18)$, $b = 13.7678(11)$, $c = 20.6919(17)$ Å, $\beta = 113.405(2)°$, $V = 5845.8(8)$ Å$^3$, $Z = 4$, $T = 141(1)$ K, $\mu = 5.901$ mm$^{-1}$, reflections collected/independent = 45 125/9364 ($R$(int) = 0.1090), $R_1(I>2\sigma(I)) = 0.0383$, and $wR_2(I>2\sigma(I)) = 0.0643$. Crystal data for **2**: $C_{36}H_{84}LaN_3P_6Te_6$, $M_r = 1649.39$, monoclinic, space group $P2_1/c$, $a = 22.456(6)$, $b = 13.866(4)$, $c = 20.828(5)$ Å, $\beta = 113.295(3)°$, $V = 5957(3)$ Å$^3$, $Z = 4$, $T = 141(1)$ K, $\mu = 3.784$ mm$^{-1}$, reflections collected/independent = 54 148/10 952 ($R$(int) = 0.1071), $R_1(I>2\sigma(I)) = 0.0544$, and $wR_2(I>2\sigma(I)) = 0.1285$. The crystals were mounted in a nylon cryoloop from Paratone-N oil under an argon gas flow. The data were collected on a Bruker SMART APEX II CCD diffractometer, with a KRYO-FLEX liquid nitrogen vapor cooling device. The instrument was equipped with a graphite-monochromated $Mo_{K\alpha}$ X-ray source ($\lambda = 0.71073$ Å), with MonoCap X-ray source optics. A hemisphere of data was collected using $\omega$-scans, with 5-s frame exposures and 0.3° frame-widths. Data collection and initial indexing and cell refinement were handled using APEX II[13] software. Frame integration, including Lorentz-polarization corrections and final cell parameter calcula-

 © 2006 Wiley-VCH Verlag GmbH & Co. KGaA, Weinheim 

tions, were carried out using SAINT+[14] software. The data were corrected for adsorption using the SADABS[15] program. Decay of reflection intensity was monitored by analysis of redundant frames. The structure was solved by direct methods and difference Fourier techniques. All hydrogen atom positions were idealized as riding on the atom they are attached to. All non-hydrogen atoms were refined anisotropically. Structure solution, refinement, graphics, and creation of publication materials were performed using SHELXTL.[16] CCDC-283264 (**1**) and -283265 (**2**) contain the supplementary crystallographic data for this paper. These data can be obtained free of charge from The Cambridge Crystallographic Data Centre via www.ccdc.cam.ac.uk/data_request/cif.

[6] A. J. Gaunt, B. L. Scott, M. P. Neu, *Chem. Commun.* **2005**, 3215.

[7] D. J. Williams, C. O. Quicksall, K. M. Barkigia, *Inorg. Chem.* **1982**, *21*, 2097.

[8] J. Waters, D. Crouch, J. Raftery, P. O'Brien, *Chem. Mater.* **2004**, *16*, 3289.

[9] a) D. J. Berg, R. A. Andersen, A. Zalkin, *Organometallics* **1988**, *7*, 1858; b) A. Kornienko, D. Freedman, T. J. Emge, J. G. Brennan, *Inorg. Chem.* **2001**, *40*, 140; c) A. Recknagel, M. Noltemeyer, D. Stalke, U. Pieper, H. G. Schmidt, F. T. Edelmann, *J. Organomet. Chem.* **1991**, *411*, 347; d) W. J. Evans, G. W. Rabe, J. W. Ziller, R. J. Doedens, *Inorg. Chem.* **1994**, *33*, 2719; e) D. Freedman, T. J. Emge, J. G. Brennan, *Inorg. Chem.* **2002**, *41*, 492; f) A. C. Hillier, S. Y. Liu, A. Sella, M. R. J. Elsegood, *Inorg. Chem.* **2000**, *39*, 2635; g) D. R. Cary, J. Arnold, *J. Am. Chem. Soc.* **1993**, *115*, 2520.

[10] R. D. Shannon, C. T. Prewitt, *Acta Crystallogr. Sect. B* **1970**, *26*, 1046 (revised effective ionic radii).

[11] L. R. Avens, S. G. Bott, D. L. Clark, A. P. Sattelberger, J. G. Watkin, B. D. Zwick, *Inorg. Chem.* **1994**, *33*, 2248.

[12] We thank Professor Tristram Chivers at the University of Calgary, Canada, for a personal communication providing further details of the synthesis of [Na(tmeda){N(TeP*i*Pr$_2$)$_2$}] given in reference [4b].

[13] APEX II 1.08, **2004**, Bruker AXS, Inc., Madison, Wisconsin 53719.

[14] SAINT+ 7.06, **2003**, Bruker AXS, Inc., Madison, Wisconsin 53719.

[15] SADABS 2.03, **2001**, G. Sheldrick, University of Göttingen, Germany.

[16] SHELXTL 5.10, **1997**, Bruker AXS, Inc., Madison, Wisconsin 53719.

 © 2006 Wiley-VCH Verlag GmbH & Co. KGaA, Weinheim 

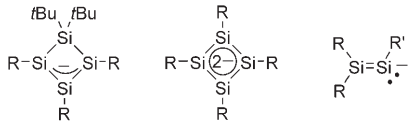
*Low-Valent Silicon Compounds*

DOI: 10.1002/anie.200503975

# An Unsaturated α,ω-Dianionic Oligosilane**

*Kai Abersfelder, Deniz Güclü, and David Scheschkewitz**

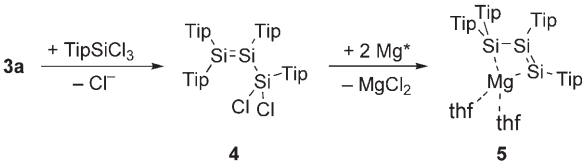
Silyl anions are widely applied as reagents in organic and inorganic chemistry.[1] In this context, interest in α,ω-dianionic oligosilanes as precursors for cyclic and acyclic homo- and heterosilanes has been considerable.[2] Curiously, whereas the chemistry of low-valent silicon compounds is otherwise highly developed,[3] only two anionic compounds with a low-valent silicon backbone had been reported until recently: the cyclobutenide analogue **1**[4] and the cyclobutadiene dianion analogue **2** (Scheme 1).[5]




***Scheme 1.*** Anionic low-valent silicon compounds; **1**, **2**: R = SiMe*t*Bu$_2$; **3a**: R = R′ = Tip = 2,4,6-*i*Pr$_3$C$_6$H$_2$; **3b**: R = SiMe*t*Bu$_2$, R′ = 2,4,6-Me$_3$C$_6$H$_2$.

In 2004, we and Sekiguchi et al. independently succeeded in the isolation of the monoanionic disilenides **3a** and **3b**, which are disila analogues of vinyl anions.[6] These disilenides were expected to combine the reactivity of the Si=Si double bond with the nucleophilicity of silyl anions. Derivative **3a** had been previously proposed by Weidenbruch et al. as an intermediate in the synthesis of their tetrasilabutadiene.[7] In the meantime, further applications of **3a** as a ligand in a zirconium complex[8] and as a building block for a silicon cluster with a "naked" vertex have emerged.[9]

Herein, we report the synthesis and isolation of the first α,ω-dianionic unsaturated oligosilane. Reaction of the lithium salt of disilenide **3a** with an equimolar amount of TipSiCl$_3$ (Tip = 2,4,6-triisopropylphenyl) in tetrahydrofuran (THF) yielded the moderately air- and moisture-sensitive (dichlorosilyl)disilene **4**, quantitatively (Scheme 2). Although single crystals could not be obtained, comparison of the characteristic $^{29}$Si NMR spectrum of **4** ($\delta$ = 99.1, 54.7, and 11.7 ppm) with that of the related compound Tip$_2$Si=Si(Tip)SiMe$_3$[6a] allowed unambiguous identification of **4**. Reduction of **4** with an excess of active magnesium (Mg*)[10] in THF then afforded the magnesium salt **5** of the trisilene-1,3-diide in 42% yield after repeated crystallizations, as very air-sensitive, but thermally highly stable (m.p. 209 °C) orange blocks (Scheme 2).




***Scheme 2.*** Preparation of **5**.

The dianion of **5** was characterized by means of multinuclear NMR and UV/Vis spectroscopy. The $^{29}$Si NMR spectrum shows three signals of equal intensity at $\delta$ = 143.9, 134.5, and −44.4 ppm. The 2D Si–H correlation gave the first indication that the double bond in **5** is shifted with respect to its position in **4**. Whereas the two lowfield resonances (assignable to the Si=Si double bond) couple to only one Tip group each, the signal at $\delta$ = −44.4 ppm shows cross peaks to two such groups. Another prominent feature of the otherwise complex $^1$H and $^{13}$C NMR spectra is the appearance of two distinct, albeit broad, signals ($^1$H NMR: $\delta$ = 3.67, 3.19 ppm; $^{13}$C NMR: $\delta$ = 70.16, 69.36 ppm) for the methylene groups bonded to the oxygen atoms of the two coordinating THF molecules, indicating the presence of a contact ion pair in [D$_6$]benzene solution.

In the UV/Vis spectrum of **5** in pentane, the absorption with the highest wavelength occurs at $\lambda_{max}$ = 415 nm ($\varepsilon$ = 3200 L mol$^{-1}$ cm$^{-1}$), whereas in **3a** the corresponding absorption occurs at $\lambda_{max}$ = 417 nm.[6a] The lack of a significant red shift suggests that not only the vinylic, but also the allylic charges in **5** are essentially localized on the respective silicon atoms. The Coulomb repulsion between the two negative charges should certainly disfavor delocalization. However, the monoanionic cyclotetrasilenide **1** reported by Sekiguchi et al. also has a strictly localized, albeit fluxional, electronic structure.[4]

An X-ray structure determination for a single crystal of **5**·0.5 C$_5$H$_{12}$ confirmed that the trisilene-1,3-diide forms a contact ion pair with the Mg$^{2+}$ counterion (Figure 1).[11] The Si1, Si2, Si3, and Mg1 atoms form an almost perfectly planar array (largest deviation from the least-squares plane: 3.7 pm for Si2). Whereas the Mg1–Si3 distance (262.5(1) pm) is comparable to values usually found for magnesium silanides,[12] the Mg1–Si1 distance (255.2(1) pm) is significantly shorter, which we tentatively attribute to the formal sp$^2$ hybridization of Si1. To our knowledge the Mg1–Si1 bond is the shortest Mg–Si contact observed to date. The coordination sphere of the Mg$^{2+}$ ion is completed by the oxygen atoms of two molecules of THF. The Si1=Si2 double-bond length of 219.8(1) pm in **5** is similar to that in **3a** (219.2(1) pm), and the Si2–Si3 bond (236.2(1) pm) is somewhat longer than usual Si–Si single bonds (234 pm),[13] which reflects the steric congestion in **5** and corroborates the absence of any

[*] K. Abersfelder, D. Güclü, Dr. D. Scheschkewitz
Institut für Anorganische Chemie
Bayerische Julius-Maximilians-Universität Würzburg
Am Hubland, 97074 Würzburg (Germany)
Fax: (+49) 931/888-4623
E-mail: scheschkewitz@mail.uni-wuerzburg.de

[**] This work was funded by the DFG (Sche 906/3-1) and the University of Würzburg. The authors thank Dr. R. Bertermann and M. Schäfer for NMR measurements, Dr. C. Burschka for the X-ray data collection, and Prof. H. Braunschweig for generous support.

Supporting information for this article is available on the WWW under http://www.angewandte.org or from the author.

 © 2006 Wiley-VCH Verlag GmbH & Co. KGaA, Weinheim 

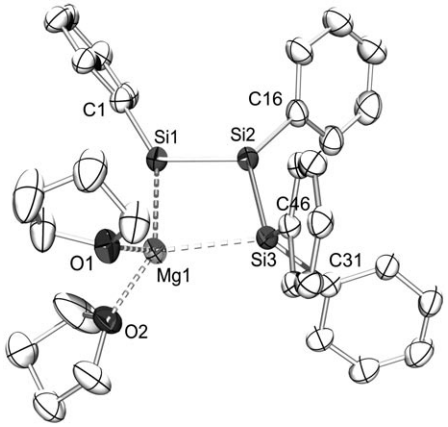
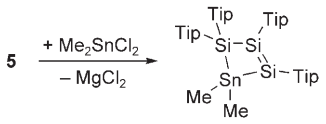



***Figure 1.*** Structure of **5** in the solid state. Thermal ellipsoids set at 50% probability. Hydrogen atoms, isopropyl groups, and the minor disorder component of one of the THF molecules (O2) are omitted for clarity. Selected bond lengths [pm] and angles [°]: Si1–Si2 219.8(1), Si2–Si3 236.2(1), Si1–C1 191.5(2), Si2–C16 191.7(2), Si3–C31 193.4(2), Si3–C46 194.4(2), Si1–Mg1 255.2(1), Si3–Mg1 262.5(1), Mg1–O1 205.1(2), Mg1–O2 203.4(2); Si1-Si2-Si3 102.52(4), C1-Si1-Si2 120.98(7), Si1-Si2-C16 127.83(7), C16-Si2-Si3 129.48(7).

delocalization of the negative charges across the three silicon atoms. The slight elongation of the bonds between Si3 and the *ipso* carbon atoms (Si3–C31: 193.4(2); Si3–C46: 194.4(2) pm) is probably also due to the bulkiness of the Tip substituents.

To test its suitability as a precursor for unsaturated heterocyclic oligosilanes, we treated **5** with $Me_2SnCl_2$ in [$D_6$]benzene. The reaction proceeded smoothly to afford the four-membered ring **6** (Scheme 3), which was unambiguously




**6**

***Scheme 3.*** Preparation of **6**.

identified by multinuclear NMR spectroscopy. As expected, the $^{29}$Si NMR spectrum of **6** consists of three signals at $\delta =$ 105.2, 92.5, and −26.2 ppm, all of which show $^{117/119}$Sn satellites ($\delta(^{119}\text{Sn}) = -39.3$ ppm). Although the silicon atoms adjacent to tin formally differ in hybridization, the coupling constants are quite similar ($sp^2$: $^1J(^{29}\text{Si},^{119}\text{Sn}) = 479$ Hz, $sp^3$: $^1J(^{29}\text{Si},^{119}\text{Sn}) = 497$ Hz). Even the coupling to the central silicon atom is remarkably large ($^2J(^{29}\text{Si},^{119}\text{Sn}) = 228$ Hz). In the $^1$H and $^{13}$C NMR spectra of **6**, two different signals are observed for the methyl groups bonded to tin, which could be due to a lowering of the $C_s$ symmetry through a distortion of the four-membered ring from planarity or a less-symmetric arrangement of the Tip substituents.

The successful synthesis of **6** leads to the expectation that a variety of new unsaturated homo- and heterocyclic silanes might be accessible starting from **5**. The reactivity of **5** towards other main-group and transition-metal electrophiles is currently under investigation.

## *Experimental Section*

All manipulations were carried out under a protective atmosphere of argon, using Schlenk techniques or in a glove box.

**4**: At −196 °C, THF (20 mL) was condensed onto the lithium salt of **3a**[6a] (5.40 g, 6.33 mmol) and $TipSiCl_3$[14] (2.14 g, 6.33 mmol). The mixture was slowly brought to room temperature (30 min) and then stirred for 15 h. All volatiles were removed under high vacuum, and the orange residue was dissolved in hexane (50 mL). Solid LiCl was removed by filtration, and the clear orange solution was concentrated to dryness, affording **4** as an orange solid (6.07 g, 99%). The product was used for the subsequent reactions without further purification. $^1$H NMR (500 MHz, [$D_6$]benzene, 25 °C): $\delta = 7.09$, 7.07, 7.01, 6.94 (s, 8H, Ar-*H*), 4.37, 4.31 (hept, 4H, *i*Pr-C*H*), 4.03 (br, 2H, *i*Pr-C*H*), 3.59 (hept, 2H, *i*Pr-C*H*), 2.72, 2.63 (hept, 4H, *i*Pr-C*H*), 1.41, 1.22, 1.14, 1.13, 1.08, 1.07, 0.89 ppm (d, 72H, *i*Pr-C$H_3$); $^{13}$C NMR (125 MHz, [$D_6$]benzene, 25 °C): $\delta = 156.60$, 155.97, 155.23, 154.03, 152.42, 151.74, 151.23, 151.03, 135.00, 134.12, 130.50, 130.13 (Ar-*C*), 122.67, 122.55, 122.36 (Ar-*C*H), 39.15, 38.37, 37.84, 34.74, 34.65, 34.45, 34.39, 34.22 (*i*Pr-*C*H), 25.49, 25.18, 24.42, 24.31, 23.99, 23.95, 23.88, 22.69 ppm (*i*Pr-*C*$H_3$); $^{29}$Si NMR (99 MHz, [$D_6$]benzene, 25 °C): $\delta = 99.1$, 54.7, 11.7 ppm.

**5**: At −196 °C, THF (20 mL) was added by vacuum transfer to **4** (5.90 g, 6.09 mmol) and Mg* (0.65 g, 24.3 mmol), prepared by the thermal decomposition of magnesium anthracene.[10] While the suspension was brought to room temperature, it gradually darkened until it appeared almost black after 1 h. All volatiles were then removed under high vacuum, and the solid residue was extracted with toluene (50 mL). Following filtration, the solution was concentrated to approximately 5 mL, and pentane (50 mL) was added. The solution was kept at −30 °C overnight, leading to the precipitation of 5.10 g of an orange–red solid. After three recrystallizations, **5** was isolated as orange blocks (2.81 g, 42%). M.p. 209 °C (minimal decomposition); $^1$H NMR (300 MHz, [$D_6$]benzene, 25 °C): $\delta = 7.25$, 7.15 (d, 2H, Ar-*H*), 7.05 (s, 2H, Ar-*H*), 7.02, 6.99, 6.94, 6.84 (d, 4H, Ar-*H*), 4.88, 4.68, 4.37, 4.10, 4.09 (hept, 7H, *i*Pr-C*H*), 3.67 (br, 4H, THF), 3.45 (hept, 1H, *i*Pr-C*H*), 3.19 (br, 4H, THF), 2.88, 2.81, 2.76 (hept, 4H, *i*Pr-C*H*), 1.77, 1.60, 1.59, 1.53, 1.51, 1.42, 1.40, 1.32, 1.31, 1.25, 1.24, 1.23, 1.21, 1.19, 1.06, 0.89, 0.87, 0.69, 0.63, 0.58 ppm (d, 72H, *i*Pr-C$H_3$); $^{13}$C NMR (75 MHz, [$D_6$]benzene, 25 °C): $\delta = 156.01$, 153.85, 153.83, 153.42, 152.89, 152.26, 151.78, 148.15, 147.27, 147.24, 147.11, 145.96, 144.32, 143.65, 142.52 (Ar-*C*), 122.47, 122.13, 121.23, 121.02, 120.55, 120.33, 120.30 (Ar-*C*H), 70.16 (br, THF), 69.36 (br, THF), 37.28, 36.38, 36.19, 36.01, 35.90, 35.56, 34.93, 34.82, 34.73, 34.50, 33.25 (*i*Pr-*C*H), 27.30, 26.60, 26.43, 26.34, 26.06, 25.59, 25.41, 25.09, 24.78, 24.65, 24.58, 24.56, 24.49, 24.46, 24.36, 24.32, 24.24, 24.12, 23.94 ppm (*i*Pr-*C*$H_3$); $^{29}$Si NMR (60 MHz, [$D_6$]benzene, 25 °C): $\delta = 143.9$, 134.5, −44.4 ppm. UV/Vis (pentane): $\lambda_{max}(\varepsilon)$ 415 nm (3200 L mol$^{-1}$ cm$^{-1}$).

**6**: In a glove box, **5** (100 mg, 0.091 mmol) and $Me_2SnCl_2$ (21 mg, 0.095 mmol) were placed in an NMR tube and dissolved in [$D_6$]benzene (0.5 mL). The initially orange solution changed rapidly to yellow. After centrifugation of the NMR tube to deposit precipitated $MgCl_2$, NMR spectra were recorded. $^1$H NMR (300 MHz, [$D_6$]benzene, 25 °C): $\delta = 7.22$, 7.20 (d, 2H, Ar-*H*), 7.03, 6.99 (s, 4H, Ar-*H*), 6.96, 6.87 (d, 2H, Ar-*H*), 4.69, 4.14, 4.06, 4.01, 3.64, 3.48, 2.85–2.61 (hept, 12H, *i*Pr-C*H*), 1.72, 1.63, 1.53, 1.52, 1.47, 1.42 (br), 1.36, 1.30, 1.28, 1.24–1.08, 1.01, 0.88, 0.86 (d, 60H, *i*Pr-C$H_3$), 0.80 (s, 3H, $^2J(^1\text{H},^{117/119}\text{Sn}) = 45$ Hz, SnC$H_3$), 0.73, 0.64, 0.48, 0.45 ppm (d, 12H, *i*Pr-C$H_3$), 0.23 ppm (s, 3H, $^2J(^1\text{H},^{117/119}\text{Sn}) = 43$ Hz, SnC$H_3$); $^{13}$C NMR (75 MHz, [$D_6$]benzene, 25 °C): $\delta = 155.65$, 154.73, 154.71, 154.59, 153.59, 152.23, 152.05, 151.14, 150.85, 149.69, 149.10, 136.92, 136.89, 136.67, 133.51 (Ar-*C*), 122.46, 122.36, 121.91, 121.48, 121.17, 120.77 (Ar-*C*H), 38.02, 37.64, 37.48, 36.90, 36.62, 35.99, 34.83, 34.79, 34.74, 34.46 (*i*Pr-*C*H), 27.76, 26.98, 26.81, 25.90, 25.67 (br), 24.82, 24.75, 24.44, 24.34, 24.23, 24.16, 24.09, 23.96, 21.77 (*i*Pr-*C*$H_3$), −4.08 (Sn*C*$H_3$), −6.48 ppm (Sn*C*$H_3$); $^{29}$Si NMR (60 MHz, [$D_6$]benzene, 25 °C): $\delta = 105.2$ ($^1J(^{29}\text{Si},^{117/119}\text{Sn}) = 458/479$ Hz, Si=*Si*TipSn), 92.5 ($^2J(^{29}\text{Si},^{117/119}\text{Sn}) = 218/228$ Hz, Si=*Si*TipSi), −26.2 ppm ($^1J(^{29}$Si,

 © 2006 Wiley-VCH Verlag GmbH & Co. KGaA, Weinheim 

$^{117/119}$Sn) = 476/497 Hz, Sn*Si*Tip$_2$Si); $^{119}$Sn NMR (112 MHz, [D$_6$]benzene, 25 °C): $\delta = -39.3$ ppm ($^1J(^{119}\text{Sn},^{29}\text{Si}) = 479$, 497 Hz, $^2J(^{119}\text{Sn},^{29}\text{Si}) = 228$ Hz).

Received: November 9, 2005
Published online: February 7, 2006

**Keywords:** anions · Group 14 elements · magnesium · silicon · stannanes

[1] Recent reviews on silyl anions: a) H.-W. Lerner, *Coord. Chem. Rev.* **2005**, *249*, 789; b) A. Sekiguchi, V. Y. Lee, M. Nanjo, *Coord. Chem. Rev.* **2000**, *210*, 11; c) J. Belzner, U. Dehner in *The Chemistry of Organic Silicon Compounds, Vol. 2*, *Part 1* (Eds.: Z. Rappoport, Y. Apeloig), Wiley, Chichester, **1998**, p. 779; d) P. D. Lickiss, C. M. Smith, *Coord. Chem. Rev.* **1995**, *145*, 75; e) K. Tamao, A. Kawachi, *Adv. Organomet. Chem.* **1995**, *38*, 1.

[2] a) H. Gilman, D. J. Peterson, A. W. Jarvie, H. J. S. Winkler, *J. Am. Chem. Soc.* **1960**, *82*, 2076; b) J. Belzner, U. Dehnert, D. Stalke, *Angew. Chem.* **1994**, *106*, 2580; *Angew. Chem. Int. Ed. Engl.* **1994**, *33*, 2450; c) Y. Apeloig, G. Korogodsky, D. Bravo-Zhivotovskii, D. Bläser, R. Boese, *Eur. J. Inorg. Chem.* **2000**, 1091; d) C. Kayser, G. Kickelbick, C. Marschner, *Angew. Chem.* **2002**, *114*, 1031; *Angew. Chem. Int. Ed.* **2002**, *41*, 989; e) R. Fischer, D. Frank, W. Gaderbauer, C. Kayser, C. Mechtler, J. Baumgartner, C. Marschner, *Organometallics* **2003**, *22*, 3723; f) J. Markow, R. Fischer, H. Wagner, N. Noormofidi, J. Baumgartner, C. Marschner, *Dalton Trans.* **2004**, 2166; g) R. Fischer, T. Konopa, J. Baumgartner, C. Marschner, *Organometallics* **2004**, *23*, 1899.

[3] Recent reviews on low-valent silicon: a) V. Y. Lee, A. Sekiguchi, *Organometallics* **2004**, *23*, 2822; b) M. Weidenbruch, *Angew. Chem.* **2003**, *115*, 2322; *Angew. Chem. Int. Ed.* **2003**, *42*, 2222; c) A. Sekiguchi, V. Y. Lee, *Chem. Rev.* **2003**, *103*, 1429; d) M. Weidenbruch, *Organometallics* **2003**, *22*, 4348; e) R. West, *Polyhedron* **2002**, *21*, 467; f) M. Weidenbruch, *J. Organomet. Chem.* **2002**, *646*, 39; g) M. Kira, *Pure Appl. Chem.* **2000**, *72*, 2333.

[4] T. Matsuno, M. Ichinohe, A. Sekiguchi, *Angew. Chem.* **2002**, *114*, 1645; *Angew. Chem. Int. Ed.* **2002**, *41*, 1575.

[5] a) V. Y. Lee, K. Takanashi, T. Matsuno, M. Ichinohe, A. Sekiguchi, *J. Am. Chem. Soc.* **2004**, *126*, 4758; b) K. Takanashi, V. Y. Lee, T. Matsuno, M. Ichinohe, A. Sekiguchi, *J. Am. Chem. Soc.* **2005**, *127*, 5768.

[6] a) D. Scheschkewitz, *Angew. Chem.* **2004**, *116*, 3014; *Angew. Chem. Int. Ed.* **2004**, *43*, 2965; b) M. Ichinohe, K. Sanuki, S. Inoue, A. Sekiguchi, *Organometallics* **2004**, *23*, 3088; c) S. Inoue, M. Ichinohe, A. Sekiguchi, *Chem. Lett.* **2005**, *34*, 1564.

[7] M. Weidenbruch, S. Willms, W. Saak, G. Henkel, *Angew. Chem.* **1997**, *109*, 2612; *Angew. Chem. Int. Ed. Engl.* **1997**, *36*, 2503.

[8] T. Nguyen, D. Scheschkewitz, *J. Am. Chem. Soc.* **2005**, *127*, 10174.

[9] D. Scheschkewitz, *Angew. Chem.* **2005**, *117*, 3025; *Angew. Chem. Int. Ed.* **2005**, *44*, 2954.

[10] B. Bogdanovic, S. T. Liao, R. Mynott, K. Schlichte, U. Westeppe, *Chem. Ber.* **1984**, *117*, 1378.

[11] Crystal structure determination of **5**·0.5 $C_5H_{12}$: orange blocks from pentane; $C_{70.5}H_{114}MgO_2Si_3$, $M_r = 1102.2$, monoclinic, space group $P2_1/n$; $a = 1206.4(2)$, $b = 2641.9(5)$, $c = 2216.5(4)$ pm, $\beta = 99.08(3)°$, $V = 6976(2) \times 10^{-30}$ m$^3$; $Z = 4$, $\rho_{calcd} = 1.049$ g cm$^{-3}$, crystal dimensions: $0.60 \times 0.50 \times 0.50$ mm; diffractometer: STOE IPDS, $Mo_{K\alpha}$ radiation, 173 K, $2\theta_{max} = 52.74°$, 71353 reflections, 13390 independent ($R_{int} = 0.0520$); direct methods; semiempirical absorption correction ($\mu = 1.17$ cm$^{-1}$); refinement (against $F_o^2$) with SHELXTL (version 5.1) and SHELXL-97,[15] 779 parameters, 0 restraints, $R_1 = 0.0510$ ($I > 2\sigma$), $wR_2 = 0.1362$ (all data), GooF = 1.031, max/min residual electron density = $0.679/-0.263 \times 10^{30}$ e m$^{-3}$. CCDC-288946 contains the supplementary crystallographic data for this paper. These data can be obtained free of charge from The Cambridge Crystallographic Data Centre via www.ccdc.cam.ac.uk/data_request/cif.

[12] a) A. R. Claggett, W. H. Ilsley, T. J. Anderson, M. D. Glick, J. P. Oliver, *J. Am. Chem. Soc.* **1977**, *99*, 1797; b) D. W. Goebel, Jr., J. L. Hencher, J. P. Oliver, *Organometallics* **1983**, *2*, 746; c) R. Goddard, C. Krüger, N. A. Ramadan, A. Ritter, *Angew. Chem.* **1995**, *107*, 1107; *Angew. Chem. Int. Ed. Engl.* **1995**, *34*, 1030; d) J. D. Farwell, M. F. Lappert, C. Marschner, C. Strissel, T. D. Tilley, *J. Organomet. Chem.* **2000**, *603*, 185; e) H.-W. Lehner, S. Scholz, M. Bolte, N. Wiberg, H. Nöth, I. Krossing, *Eur. J. Inorg. Chem.* **2003**, 666.

[13] M. Weidenbruch, *The Chemistry of Organic Silicon Compounds, Vol. 3* (Eds.: Z. Rappoport, Y. Apeloig), Wiley, Chichester, UK, **2001**, chap. 5.

[14] C. N. Smit, F. Bickelhaupt, *Organometallics* **1987**, *6*, 1156.

[15] G. M. Sheldrick, SHELXTL Version 5.1, Bruker AXS, Madison, **1998**; G. M. Sheldrick, SHELXL-97, Universität Göttingen, Germany, **1997**.

 © 2006 Wiley-VCH Verlag GmbH & Co. KGaA, Weinheim 

*Miniemulsions*

DOI: 10.1002/anie.200502854

# Enantioselective Enzymatic Reactions in Miniemulsions as Efficient "Nanoreactors"**

*Harald Gröger,* Oliver May, Hendrik Hüsken, Sandrine Georgeon, Karlheinz Drauz, and Katharina Landfester**

The application of enzyme-catalyzed syntheses is of high industrial interest for the manufacture of enantiomerically pure compounds.[1] The well-known high selectivity, in particular enantioselectivity, of enzymes represents a particular advantage; however, conducting enzymatic reactions at

[*] Dr. H. Gröger, Dr. O. May, Dipl.-Ing. (FH) H. Hüsken, Dipl.-Ing. (FH) S. Georgeon
Degussa AG
Service Center Biocatalysis
P.O. Box 1345, 63403 Hanau (Germany)
Fax: (+49) 6181-592961
E-mail: harald.groeger@degussa.com
Prof. Dr. K. Landfester
University of Ulm
Organic Chemistry III/Macromolecular Chemistry
Albert-Einstein-Allee 11, 89081 Ulm (Germany)
Fax: (+49) 731-50-22883
E-mail: katharina.landfester@chemie.uni-ulm.de
Prof. Dr. K. Drauz
Degussa AG
Corporate Center Innovation Management
P. O. Box 1345, 63403 Hanau (Germany)

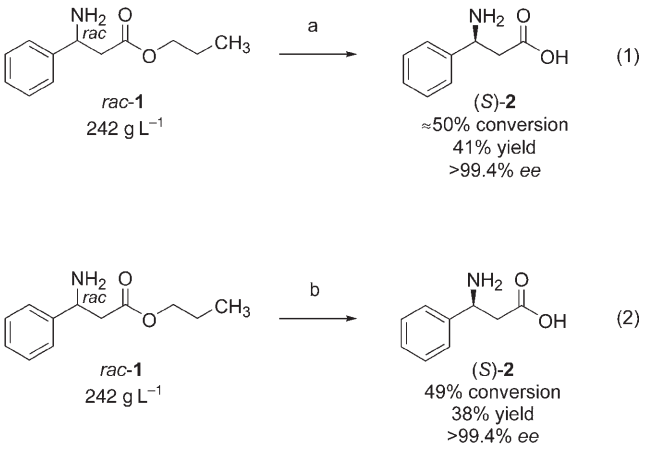
[**] We thank Dr. F.-R. Kunz and Dr. M. Janik and their teams (Degussa, AQura GmbH) for carrying out the chiral HPLC analyses and the NMR-spectroscopic measurements.


© 2006 Wiley-VCH Verlag GmbH & Co. KGaA, Weinheim
WILEY InterScience DISCOVER SOMETHING GREAT

high substrate concentrations—a key criterion for technical applications—often proves difficult.[2] A proven methodology for the accomplishment of (enzymatic) reactions at high substrate concentrations significantly exceeding the solubility limit and preferably in the range of $>100\,g\,L^{-1}$ is the use of enzyme-compatible two-phase solvent systems, consisting of an aqueous phase and an organic solvent. This concept has been applied successfully for many enzymatic reactions.[3,4] Besides high substrate concentrations and engineering advantages, in addition an increase of activity has been often observed when interface-active enzymes are used.

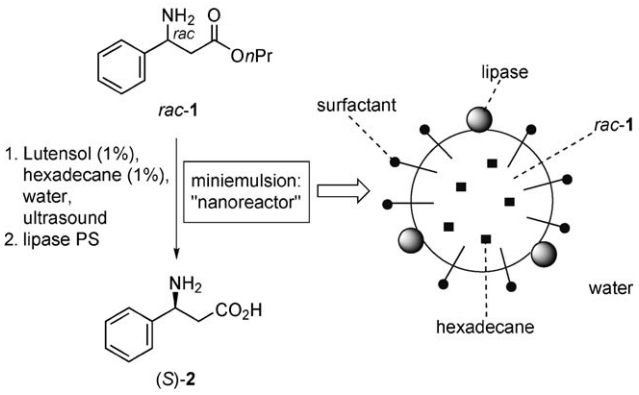
Nevertheless, alternative concepts to the "classic" two-phase solvent system are desirable that would result in increased homogeneity of the reaction mixture, increased overall interface area, and improvement of stirrability. These issues may be addressed by stable miniemulsions, homogenous mixtures in which the organic phase is dispersed in the form of very small "nanodroplets" with diameters in the range of 50–500 nm.[5a] The suitability of these liquid "nanoreactors",[5c] the stable droplets in miniemulsions, for enzymatic transformations in general has been demonstrated recently by Landfester and co-workers for the polymerization of lactones.[6] Here, we report the first enantioselective enzymatic reactions in minemulsions and the suitability of this concept for the preparation of optically active α- and β-amino acids at very high substrate concentrations of $\approx 500$ to $>800\,g\,L^{-1}$.

As a benchmark for comparison of the reaction characteristics of miniemulsions with those of the "classic" two-phase system, we chose the industrially established lipase-catalyzed hydrolysis of racemic β-amino acid *n*-propyl esters in methyl *tert*-butyl ether (MTBE)/water for the preparation of enantiomerically pure β-amino acids.[7,8] When racemic β-phenylalanine *n*-propyl ester, *rac*-**1**, was used as a substrate under standard conditions in the two-phase solvent system, a conversion of $\approx 50\,\%$ was obtained within 15 h at a high substrate concentration of $242\,g\,L^{-1}$ [Scheme 1, Eq. (1)].[7] The reaction proceeds enantioselectively with an *E* value of $>100$, and the resulting optically active β-amino acid (*S*)-β-phenylalanine, (*S*)-**2**, was obtained with an enantiomeric excess of $>99.4\,\%$ *ee*.[9]




***Scheme 1.*** Reaction in a two-phase solvent system [Eq. (1)] and in a miniemulsion [Eq. (2)], both at a substrate concentration of $242\,g\,L^{-1}$. Reaction conditions: a) lipase from *Pseudomonas cepacia* (Lipase PS "Amano", $9\,g\,L^{-1}$), $H_2O$/MTBE 1:1; 15 h, pH 8.2, 20 °C; b) lipase from *Pseudomonas cepacia* (Lipase PS "Amano", $9\,g\,L^{-1}$), $H_2O$, surfactant (1 %), hexadecane (1 %), ultrasound; 6 h, pH 8.2, 20 °C.

The analogous enantioselective enzymatic reaction in a miniemulsion as a nanoreactor required a stable miniemulsion of the racemic β-amino acid *n*-propyl ester, *rac*-**1**, in aqueous media (Scheme 2). The miniemulsion was prepared by initial addition of a surfactant (Lutensol AT 50, 1 %) and a hydrophobic compound (hexadecane, 1 %) to avoid dissolution of the nanodroplets under formation of a "normal" two-phase system as a result of aggregation and Ostwald ripening. Subsequent treatment of this mixture with ultrasound gave a stable miniemulsion, which contained nanodroplets of a defined size[6] (typical diameter of 100–150 nm). This stable miniemulsion was then used as a reaction mixture for the desired enzymatic reactions.




***Scheme 2.*** Concept for the formation of miniemulsions for enzymatic reactions for the preparation of the (*S*)-β-amino acid (*S*)-**2**.

When the miniemulsion was used as reaction media, the enantioselective lipase-catalyzed hydrolysis was significantly faster with a conversion of 49 % after a reaction time of only 6 h. After (nonoptimized[10]) workup the desired product (*S*)-**2** was obtained in 38 % yield and with an enantiomeric excess of $>99.4\,\%$ *ee* [Scheme 1, Eq. (2)]. This accelerated reaction course also implies that the reaction can be conducted with smaller amounts of enzymes. When the reaction time was prolonged to 17 h, the same conversion as that of the benchmark process was obtained with only 50 % of the original amount of enzyme. In general, the lipase was added after treatment of the reaction mixture with ultrasound. Surprisingly, the reaction also proceeded when the enzyme was added prior to the ultrasound treatment, although the conversion was somewhat lower (42 % versus 47 % after a reaction time of 17 h).

The reaction mixture is significantly more homogeneous than the two-phase system. The high homogeneity of the miniemulsion is underlined by a visual comparison (Figure 1). In comparison with the reaction mixture prior to the formation of the miniemulsion (left photo), consisting of the two clearly separated phases water and substrate, just one "visible" phase with a high degree of homogeneity remains after formation of the miniemulsion (right photo). In this connection, the stability of the miniemulsion, in spite of the precipitation of the desired product (*S*)-**2** during the reaction

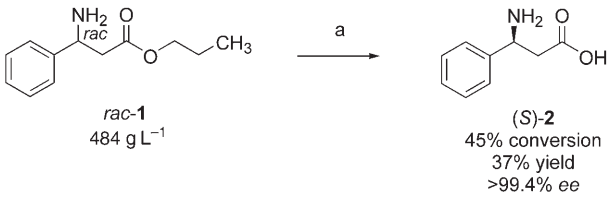
 © 2006 Wiley-VCH Verlag GmbH & Co. KGaA, Weinheim 



***Figure 1.*** Homogeneity of the stable miniemulsion (right) in comparison to the reaction mixture prior to formation of the miniemulsion (left) from the separated phases water and substrate.

(which is subsequently isolated by filtration), is a surprising effect. Thus, the presence of a solid product that precipitates during the reaction does not have a negative impact on the reaction course in the miniemulsion.

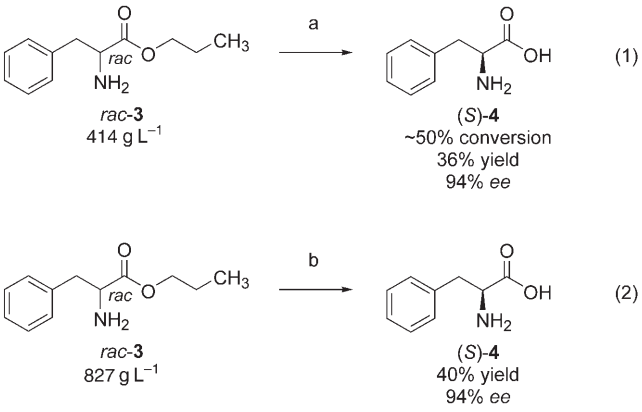
The high degree of homogeneity and excellent stirring properties of the reaction solution prompted us to further increase the substrate concentration. We were pleased to find that the enzymatic synthesis of (*S*)-β-phenylalanine (*S*)-**2** proceeds with high efficiency even at a substrate concentration of 484 g L$^{-1}$ (≈2.3 M) with a conversion of 45% after 17 h. In addition, a (nonoptimized[10]) yield of 37% was obtained, and the enantiomeric excess of the desired (*S*)-β-phenylalanine (*S*)-**2** was also >99.4% *ee* (Scheme 3). To our knowledge, this is one of the highest substrate concentrations reported for enantioselective enzymatic reactions so far.[11] A further increase of the substrate concentration up to 605 g L$^{-1}$, however, resulted in somewhat lower conversion (42% after 24 h).




***Scheme 3.*** Enzymatic synthesis of the (*S*)-β-amino acid (*S*)-**2** in a miniemulsion at a substrate concentration of 484 g L$^{-1}$. Reaction conditions: a) lipase from *Pseudomonas cepacia* (Lipase PS "Amano", 9 g L$^{-1}$), $H_2O$, surfactant (1%), hexadecane (1%), ultrasound; 17 h, pH 8.2, 20 °C.

Subsequently, we extended this approach to the synthesis of analogous α-amino acids at high substrate concentrations. We chose as a model reaction the enzymatic hydrolysis of racemic phenylalanine esters, which was carried out previously at a substrate concentration of 20 g L$^{-1}$ in the presence of a lipase from porcine pancreas (PPL).[12] In our experiments we used the corresponding *n*-propyl ester *rac*-**3**.[13]

Initial experiments with and without miniemulsions at a substrate concentration of 2.0 M (414 g L$^{-1}$) were studied with respect to their reaction rates (pH 7, room temperature, 1 g of a commercial PPL enzyme preparation per L). Once again a higher reaction rate was found for the reaction carried out in a miniemulsion. The reaction rate was 2.4 times higher than that in the corresponding experiment without the miniemulsion. After subsequent process development, this PPL-catalyzed hydrolysis of *rac*-phenylalanine *n*-propyl ester in a minemulsion proceeded at a substrate concentration of 414 g L$^{-1}$ with a conversion of ca. 50% after a reaction time of 22 h. After workup, the desired α-amino acid L-phenylalanine, (*S*)-**4**, was obtained with an enantiomeric excess of 94% *ee* and in a yield of 36% [Scheme 4, Eq. (1)]. Thus, enantioselective enzymatic reactions in miniemulsions at high substrate concentrations of >400 g L$^{-1}$ can be carried out not only for the synthesis of optically active β-amino acids, but also for the synthesis of the analogous α-amino acids. In a further step the substrate concentration was increased up to 4.0 M *rac*-**3** (827 g per L of aqueous solvent). The reaction also proceeded efficiently and gave the product L-phenylalanine (*S*)-**4** in 40% yield and with an enantiomeric excess of 94% *ee* [Scheme 4, Eq. (2)].




***Scheme 4.*** Enzymatic syntheses of L-phenylalanine (*S*)-**4** in a miniemulsion. Reaction conditions: a) lipase from porcine pancreas (Lipase PPL, Sigma, 1 g L$^{-1}$), $H_2O$, surfactant (1%), hexadecane (1%), ultrasound; 22 h, pH 7.0, RT; b) lipase from porcine pancreas (Lipase PPL, Sigma, 5.6 g L$^{-1}$), $H_2O$, surfactant (1%), hexadecane (1%), ultrasound; 21 h, pH 7.0, RT.

In summary, we have carried out the first enantioselective enzymatic reactions in miniemulsions as efficient nanoreactors. The methodology proved to be suitable for the preparation of α-amino acids as well as β-amino acids with high enantiomeric excesses of up to >99% *ee*. A specific key feature of these reactions, which proceed with high conversions, are the high substrate concentrations of ≈500 to >800 g L$^{-1}$, which are among the highest substrate concentrations reported so far for enantioselective enzymatic reactions. We are currently extending this technique to the reactions of other substrates and addressing its technical-scale application. Since the re-use of the biocatalyst is also conceivable in principle, the evaluation of such a biocatalyst recycling will also be a research topic in the future.

## Experimental Section

Lipase-catalyzed enantioselective hydrolysis in miniemulsions (exemplified for the hydrolysis of *rac*-**1** at a substrate concentration of 484 g L$^{-1}$): A mixture of 1.21 g of the lipase PS "Amano" (lipase from *Pseudomas cepacia*; purchased from Amano Enzymes, Inc.) in 40 mL of a surfactant solution was filtered in order to separate the enzyme

 © 2006 Wiley-VCH Verlag GmbH & Co. KGaA, Weinheim 

solution from the nonsoluble solid, thus resulting in the enzyme concentrate. In parallel, a miniemulsion consisting of *rac*-**1** (65.2 g), hexadecane (1.37 g), and 96 mL of a 1 % surfactant solution (Lutensol AT 50, BASF AG) was prepared by stirring these components with an ultrasound tip (4 min at 200 W). Subsequently, the enzyme concentrate and the miniemulsion were mixed. In addition, the pH was adjusted to pH 8.2 and maintained at this value by automated titration with a 1M aqueous solution of sodium hydroxide. The reaction temperature was 20 °C, and the reaction time was 17 h. During the reaction, a white precipitate consisting of the desired product (*S*)-**2** forms. After the reaction, 160 mL of acetone were added in order to complete the precipitation, and the resulting mixture was stirred for a further 45 min. The solid material was filtered and washed with a small amount of acetone and 100 mL of MTBE. At a reaction time of 17 h, a conversion of ca. 45 % was achieved. The product (*S*)-**2** was isolated after work-up in a yield of 37 % and with an enantiomeric excess of $>99.4\,\%$ *ee*.

Received: August 11, 2005
Published online: February 7, 2006

**Keywords:** biphasic catalysis · emulsions · enantioselectivity · enzyme catalysis · hydrolysis

[1] *Enzyme Catalysis in Organic Synthesis, Vol. 1–3, 2nd ed.* (Eds.: K. Drauz, H. Waldmann), Wiley-VCH, Weinheim **2002**.
[2] For a review, see: P. S. J. Cheetham, *J. Biotechnol.* **1998**, *66*, 3 – 10.
[3] For selected examples of commercial biotransformations in two-phase solvent systems, see: a) M. Kataoka, K. Kita, M. Wada, Y. Yasohara, J. Hasegawa, S. Shimizu, *Appl. Microbiol. Biotechnol.* **2003**, *62*, 437 – 445; b) N. M. Shaw, K. T. Robins, A. Kiener in *Asymmetric Catalysis on Industrial Scale* (Eds.: H. U. Blaser, E. Schmidt), Wiley-VCH, Weinheim, **2004**, pp. 105 – 115; c) P. Poechlauer, W. Skranc, M. Wubbolts in *Asymmetric Catalysis on Industrial Scale* (Eds.: H. U. Blaser, E. Schmidt), Wiley-VCH, Weinheim, **2004**, pp. 151 – 164; d) Ref. [7].
[4] A further interesting concept is the use of water-in-oil microemulsions; for selected contributions, see: a) B. Orlich, H. Berger, M. Lade, R. Schomäcker, *Biotechnol. Bioeng.* **2000**, *70*, 638 – 646; b) H. Stamatis, A. Xenakis, F. N. Kolisis, *Biotechnol. Adv.* **1999**, *17*, 293 – 318; c) K. Holmberg, *Adv. Colloid Interface Sci.* **1994**, *51*, 137 – 174.
[5] a) K. Landfester, M. Antonietti in *Colloids and Colloid Assemblies* (Ed.: F. Caruso), Wiley-VCH, Weinheim, **2004**, chap. 6, pp. 175 – 215; b) The expression "nanoreactors" describes stable droplets on the nanometer scale in miniemulsions, in which or at which the desired reaction occurs; for this concept of "nanoreactors" also see: K. Landfester, *Abstracts of Papers, 224th ACS National Meetings*, Boston, MA, USA, August 18 – 22, 2002 and Ref. [5a].
[6] A. Taden, M. Antonietti, K. Landfester, *Macromol. Rapid Commun.* **2003**, *24*, 512 – 516.
[7] H. Gröger, H. Werner (Degussa AG), US Patent 6869781, **2005**.
[8] For previous, selected contributions to the hydrolase-catalyzed resolution of *rac*-β-amino acid esters and corresponding N-acylated derivatives, see: a) S. G. Cohen, S. Y. Weinstein, *J. Am. Chem. Soc.* **1964**, *86*, 725 – 728; b) M. Prashad, D. Har, O. Repic, T. J. Blacklock, P. Giannousis, *Tetrahedron: Asymmetry* **1998**, *9*, 2133 – 2136; c) S. Katayama, N. Ae, R. Nagata, *Tetrahedron: Asymmetry* **1998**, *9*, 4295 – 4299; d) S. J. Faulconbridge, K. E. Holt, L. G. Sevillano, C. J. Lock, P. D. Tiffin, N. Tremayne, S. Winter, *Tetrahedron Lett.* **2000**, *41*, 2679 – 2681.
[9] For the definition of the terms "*E* value" and "*ee* value " for the quantification of the enantioselectivity and enantiomeric excess, respectively, see e.g.: K. Faber, *Biotransformations in Organic Chemistry, 4th ed.*, Springer, Berlin, **2000**, chap. 2.1.1, pp. 28 – 52.
[10] The workup was analogous to that described for the reaction in the two-phase solvent system, see Ref. [7]. The development of a workup protocol specifically for reactions in miniemulsions is the subject of future work.
[11] Further examples for biocatalytic reactions at high substrate concentrations are described, e.g., in: a) A. Liese, K. Seelbach, C. Wandrey, *Industrial Biotransformations*, Wiley-VCH, Weinheim **2000**; b) D. R. Yazbeck, C. A. Martinez, S. Hu, J. Tao, *Tetrahedron: Asymmetry* **2004**, *15*, 2757 – 2763; c) M. Kataoka, K. Kita, M. Wada, Y. Yasohara, J. Hasegawa, S. Shimizu, *Appl. Microbiol. Biotechnol.* **2003**, *62*, 437 – 445; d) M. Schmidt, H. Griengl, *Top. Curr. Chem.* **1999**, *200*, 193 – 226.
[12] J.-Y. Houng, M.-L. Wu, S.-T. Chen, *Chirality* **1996**, *8*, 418 – 422.
[13] The *n*-propyl ester of *rac*-phenylalanine, *rac*-**3**, is considerably more stable than the corresponding methyl ester, which undergoes a nonenzymatic hydrolysis to a significant extent.

 © 2006 Wiley-VCH Verlag GmbH & Co. KGaA, Weinheim 

*Host–Guest Systems*

DOI: 10.1002/anie.200503766

# Two Chloride Ions as a Template in the Formation of a Cyclic Hexaurea**

*Denys Meshcheryakov, Volker Böhmer,* Michael Bolte, Véronique Hubscher-Bruder, Françoise Arnaud-Neu, Haiko Herschbach, Alain Van Dorsselaer, Iris Thondorf, and Werner Mögelin*

The NH groups of dialkyl or diaryl urea (or thiourea) derivatives are strong hydrogen bond donors, a property which has been widely used for the development of self-

[*] D. Meshcheryakov, Dr. V. Böhmer
Fachbereich Chemie, Pharmazie und Geowissenschaften
Abteilung Lehramt Chemie
Johannes Gutenberg-Universität Mainz
Duesbergweg 10–14, 55099 Mainz (Germany)
Fax: (+49) 6131-392-5419
E-mail: vboehmer@mail.uni-mainz.de

Dr. M. Bolte
Institut für Anorganische Chemie
Johann Wolfgang Goethe-Universität Frankfurt
Marie-Curie-Strasse 11, 60439 Frankfurt/Main (Germany)

Dr. V. Hubscher-Bruder, Dr. F. Arnaud-Neu, H. Herschbach, Dr. A. Van Dorsselaer
UMR 7512 (CNRS-ULP), ECPM
25 rue Becquerel, 67087 Strasbourg Cedex 2 (France)

Dr. I. Thondorf, Dr. W. Mögelin
Martin-Luther-Universität Halle-Wittenberg
Fachbereich Biochemie/Biotechnologie
Kurt-Mothes-Strasse 3, 06099 Halle/Saale (Germany)

[**] Financial support from the Deutsche Forschungsgemeinschaft (Bö523/17-1,2 and TH 520/6-1,2) and the CNRS is gratefully acknowledged. We thank Dr. Sabine Gebauer for valuable discussions.

Supporting information for this article is available on the WWW under http://www.angewandte.org or from the author.


WILEY InterScience DISCOVER SOMETHING GREAT
© 2006 Wiley-VCH Verlag GmbH & Co. KGaA, Weinheim

assembled structures[1] and for the construction of anion receptors.[2] The presence of several urea functions within a single molecule and their cooperative interaction with the anion sometimes lead to remarkable selectivities. Examples of anion receptors containing two or more urea functions include linear[3] and branched molecules (podands),[4] as well as macrocyclic[5] molecules.

The cyclic arrangement of three urea subunits should be advantageous for planar anions with $C_3$ symmetry, such as nitrate or carbonate.[6] Computer simulations suggested that the linkage of such anions by three rigid structural elements of the xanthene type would be very promising. Since receptor properties in general are determined by a delicate balance between the prearrangement of ligating functions ("rigidity") and the ability to adapt to the target guest ("flexibility") we decided to partly replace the xanthene units by the more flexible diphenyl ether unit.

The cyclic triurea **3** was obtained in 62% yield by reaction of the diamine **1** with the diisocyanate **2** in acetonitrile (Scheme 1). The cyclic hexamer **4** is also formed (up to 20% yield) together with **3** if the reaction is carried out in dichloromethane. Hexamer **4** forms single crystals when crystallized from a dichloromethane/chloroform/ethanol mixture in the presence of tetrabutylammonium chloride (**5**).[7] Figure 1 shows the remarkable structure of $[\mathbf{4}(Cl)_2]^{2-}$-$[Bu_4N]^+_2$, and typical distances and angles are collated in Table 1.

The macrocyclic hexaurea wraps around two chloride ions (Cl···Cl distance 6.029 Å) in a way which allows three adjacent urea functions to interact with one chloride ion (N···Cl distances between 3.18 and 3.34 Å). The shape of the macrocycle may be described as an "eight",[8] which is additionally slightly folded in the middle to leave only a (noncrystallographic) $C_2$ axis perpendicular to the plane of the original "eight". Two tetrabutylammonium cations lie on one side close to the two chloride ions, which sit in the loops of the "eight".

The conformation of hexamer **4** in solution is determined by various intra- and/or intermolecular hydrogen bonds between urea functions and result in a broad and unassignable $^1$H NMR spectrum (Figure 2a). The addition of increasing amounts of tetrabutylammonium chloride (**5**) results in a single set of sharp signals with increasing intensity appearing until a ratio $n(\mathbf{5})/n(\mathbf{4}) = 2:1$ is reached. Further addition of **5** does not result in any further change in the spectrum (Figure 2b).[9] The set of signals (two singlets for the *tert*-butyl and methyl groups, two pseudotriplets and two pseudodoublets (*o* coupling only) for the aromatic protons of the diphenyl ether units, and four *m*-coupled doublets for the aromatic protons of the xanthene units, as well as three singlets for the urea protons, all in the expected ratio) clearly corresponds to an assembly with (dynamic) $D_2$ symmetry and can be explained by the formation of a 1:2 complex between **4** and chloride, in which the two chloride ions are bound as in the crystalline state.[10] A similar spectrum with slightly different chemical shifts is found in the presence of bromide (Figure 2c), although no saturation is reached at the ratio of 1:2.

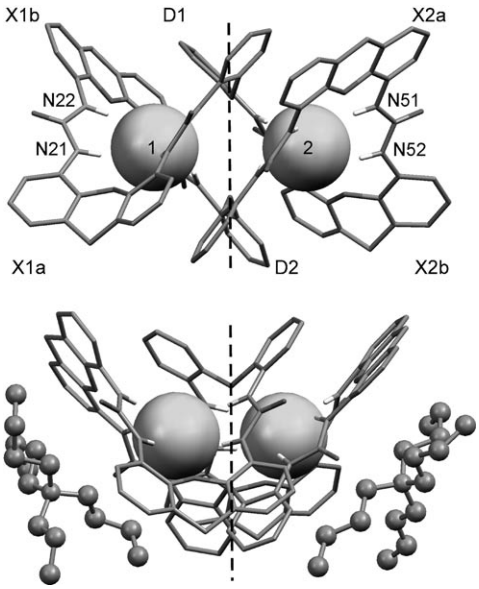
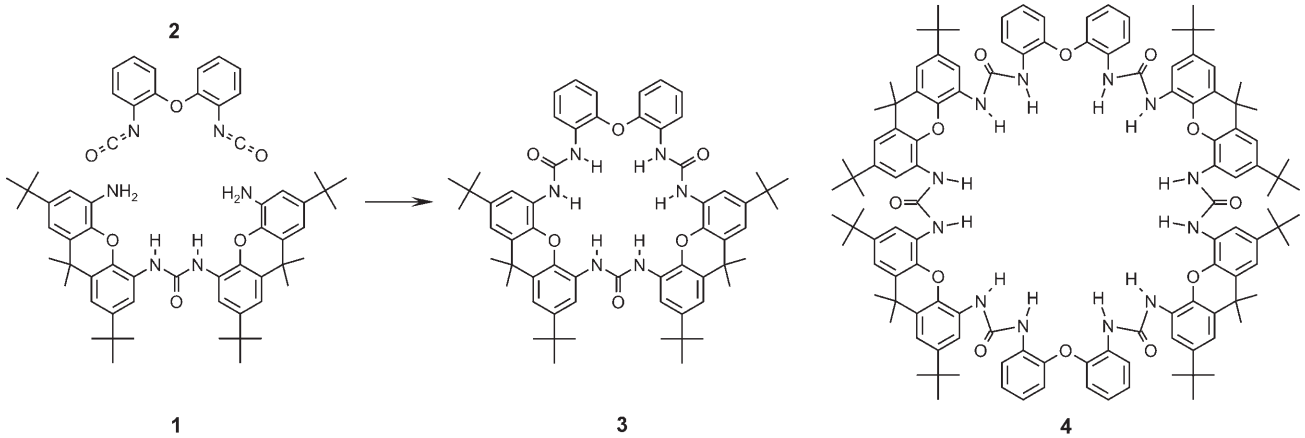



***Figure 1.*** Crystal structure of the 1:2 complex of hexamer **4** with tetrabutylammonium chloride. In the bottom view the structure is turned by 45° around the (noncrystallographic) pseudo-$C_2$ axis (dashed line) to show the tetrabutylammonium cations (ball and stick models). Non-urea hydrogen atoms, solvent molecules, *tert*-butyl, and methyl groups of the xanthene units and tetrabutylammonium cations (in the top view) are omitted for clarity.




***Scheme 1.*** Formation of cyclic oligoureas.

 © 2006 Wiley-VCH Verlag GmbH & Co. KGaA, Weinheim 

***Table 1:*** Typical distances [Å] and angles [°] found in the X-ray structure of $[\mathbf{4}(Cl)_2]^{2-}[Bu_4N]^+_2$ in comparison with averaged values from MD simulations (last two columns). For the numbering of units see Figure 1.

| Atoms | Distance | Atoms | Distance | Calculated for Cl[a] | Calculated for Br[a] |
|---|---|---|---|---|---|
| Cl1-N11[b] | 3.341 | Cl2-N41 | 3.246 | 3.06 | 3.32 |
| Cl1-N12[b] | 3.299 | Cl2-N42 | 3.760 | 3.18 | 3.40 |
| Cl1-N21 | 3.180 | Cl2-N51 | 3.225 | 3.06 | 3.27 |
| Cl1-N22 | 3.227 | Cl2-N52 | 3.420 | 3.06 | 3.26 |
| Cl1-N31 | 3.233 | Cl2-N61 | 3.268 | 3.14 | 3.37 |
| Cl1-N32 | 3.252 | Cl2-N62 | 3.070 | 3.05 | 3.33 |
| Cl1-N300[c] | 5.070 | Cl2-N200[c] | 5.535 | 5.59 | 5.69 |
| Cl1-Cl2 | 6.029 | | | 7.04 | 6.34 |

Interplanar angles for aromatic rings within xanthene (X) and diphenyl ether (D) units

| Unit | Angle | Unit | Angle | Calculated for Cl[a] | Calculated for Br[a] |
|---|---|---|---|---|---|
| D1 | 88.38 | D2 | 74.36 | 67 | 84 |
| X1a | 12.20 | X2a | 0.70 | ca. 0[d] | ca. 0[d] |
| X1b | 37.51 | X2b | 36.70 | ca. 0[d] | ca. 0[d] |

Angles between the averaged planes of the urea units (U) and the adjacent phenyl rings of units X and D

| Units | Angle | Units | Angle | Calculated for Cl[a] | Calculated for Br[a] |
|---|---|---|---|---|---|
| D1-U1-X1a | 13.9/22.0 | D2-U4-X2a | 6.2/36.0 | 38/44 | 26/43 |
| X1a-U2-X1b | 30.1/30.4 | X2a-U5-X2b | 39.1/22.7 | 44/33 | 43/39 |
| X1b-U3-D2 | 33.9/3.5 | X2b-U6-D1 | 29.6/17.5 | 33/38 | 39/26 |

[a] Only one calculated value or pair of values as a result of the dynamic $D_2$ symmetry of the time-averaged structure. [b] Nitrogen atoms of the urea U1 (between D1 and X1a) have numbers N11 and N12, etc. [c] $Bu_4N^+$ ion. [d] All four xanthene units are equivalent and planar in the time-averaged structure.

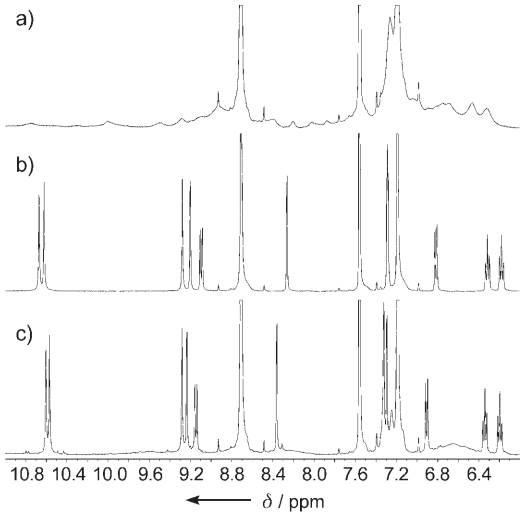



***Figure 2.*** Section of the $^1$H NMR spectra (400 MHz, [D$_5$]pyridine) of the cyclic hexamer **4** ($c = 0.1$ mM) alone (a); with 4 equivalents of tetrabutylammonium chloride (b); and with 4 equivalents of tetrabutylammonium bromide (c).

ESI-MS studies of **4** (negative mode) in acetonitrile/THF (3:1 v/v) show a signal for $[\mathbf{4}+2\,Cl]^{2-}$ ($m/z$ 1018.7) as the base peak (>95%), even if no chloride is added. Clearly ubiquitous traces of chloride are sufficient to form this complex. The addition of increasing amounts of bromide up to a ratio of 1:2 leads only to weak signals for $[\mathbf{4}+Cl+Br]^{2-}$ ($m/z$ 1041.1) and $[\mathbf{4}+Br]^-$ ($m/z$ 2046.5); a similar picture is found for fluoride. Competition experiments involving equimolar concentrations of **4**, $Cl^-$, and $Br^-$ show the preferential formation of the chloride complexes. The signals of $[\mathbf{4}+Br]^-$ and $[\mathbf{4}+Cl+Br]^{2-}$ are present with intensities of $<0.5\%$ and $<2.5\%$ respectively, while $[\mathbf{4}+2\,Br]^{2-}$ was not detected. Spectra acquired from the precipitates obtained from **4** with either $Bu_4NCl$ or $Bu_4NBr$ confirm these findings.

The addition of chloride ions to a solution of **4** in acetonitrile/THF (3:1 v/v) leads to changes in the UV spectrum between 240 and 310 nm which allowed the determination of the stability constants.[11] Values of $\log\beta_{11} = 5.6 \pm 0.5$ and $\log\beta_{12} = 11.2 \pm 0.7$ have been found with $Bu_4NCl$ for $[\mathbf{4}Cl]^-$ and $[\mathbf{4}(Cl)_2]^-$, respectively.[12]

Microcalorimetric titrations with $Bu_4NCl$ confirmed the spectroscopically determined stability constants (Table 2).

***Table 2:*** Thermodynamic parameters [kJ mol$^{-1}$] for the complexation of chloride by **4**.[a]

| Reaction | $\log\beta$ | $-\Delta G$ | $-\Delta H$ | $T\Delta S$ |
|---|---|---|---|---|
| $L + Cl^- \rightarrow LCl^-$ | 6.16 | 35.1 | 23.4 | 11.7 |
| $LCl^- + Cl^- \rightarrow (LCl_2)^{2-}$ | 5.25 | 29.9 | 43.6 | −13.6 |
| $L + 2\,Cl^- \rightarrow (LCl_2)^{2-}$ | 11.4 | 65.1 | 67.0 | −1.9 |

[a] Acetonitrile/THF (1:3 v/v), $Bu_4NCl$, 25 °C.

Overall the complexation is enthalpically driven. A positive $T\Delta S$ value for the first step can be explained by the release of solvent molecules from the solvation shells, while the strong negative value for the second step reflects the high order assumed by the macrocycle in the final complex, where the most perfect interaction (negative $\Delta H$) between the urea functions and the chloride ions is reached.

Molecular dynamics (MD) simulations in a box of chloroform or acetonitrile molecules starting from the X-ray structure did not show significant conformational changes during the simulation period of 9 ns. The time-averaged structure displays approximately $D_2$ symmetry, and thus is in agreement with the $^1$H NMR data. In contrast to the complex, the empty host is flexible and the urea units participate in an extended dynamic system of intramolecular hydrogen bonds. The replacement of the two chloride ions in the complex by bromide does not alter the conformation of the macrocycle. However, the distances between the anions and the surrounding urea units are slightly longer. In agreement with the measurements, the chloride complex is more stable than the bromide complex ($\Delta\Delta E = -113.5$ kJ mol$^{-1}$), mainly because of more favorable interactions between the chloride ions and the macrocycle. The tetrabutylammonium ions are also bound somewhat more strongly in the chloride complex ($\Delta\Delta E = -21.8$ kJ mol$^{-1}$), because of closer contacts to the π-electron-rich aromatic rings. In both complexes the binding of the pair of anions requires a significant reorganization of the host **4** ($\Delta E = 331.6$ and 268.0 kJ mol$^{-1}$ for the chloride and bromide complexes, respectively). Clearly the macrocyclic skeleton is more strained in the chloride complex ($\Delta\Delta E =$

 © 2006 Wiley-VCH Verlag GmbH & Co. KGaA, Weinheim 

63.6 kJ mol$^{-1}$), but this is overcompensated by the "perfect" fit of the urea units around the chloride ions.

The strong complexation of chloride ions suggested that the yield of the hexamer **4** could be increased if the cyclization reaction between **1** and **2** was carried out in the presence of anions. In fact not only is the reaction affected by the polarity of the solvent, but also by the addition of certain tetrabutylammonium salts. The molar ratio between the trimer **3** and the hexamer **4**, as determined by NMR spectroscopy, in the crude product is 5:1 for reactions carried out in dichloromethane. The ratio changes drastically to 1:5 when 2 equivalents of tetrabutylammonium chloride are present in the reaction mixture and to 1:3 in the presence of bromide, while iodide has no influence. The finding that even the presence of bromide anions (less tightly bound than chloride as shown above) leads to an increase in the amount of hexamer **4** can perhaps (partly) also be explained by the fact that the formation of the cyclic trimer **3** is disfavored by bromide ions.

The tight binding of two chloride ions (at a short distance of 6.03 Å)[13] by a macrocyclic hexaurea molecule is a striking example of an "induced fit" of the host molecule by the guest, which becomes possible because of the combination of rigid and flexible units in one molecule. The macrocyclization reaction can also benefit from the complexation of two halide anions. Such a template effect by two anions,[14] or more generally by two spherical particles, is unprecedented to the best of our knowledge in the synthesis of large and hence flexible macrocycles. It is especially remarkable since, unlike templation by transition-metal cations, no geometrical requirements exist for the complexation. We are currently trying to synthesize larger cyclic (and linear) oligoureas which might wrap similarly in a helical way around three or more (chloride) anions.

## Experimental Section

Trimer **3**: A solution of diisocyanate **2** (42 mg, 0.164 mmol) in acetonitrile (15 mL) was added dropwise over 30 min with vigorous stirring under nitrogen to a solution of diamine **1** (120 mg, 0.164 mmol) in acetonitrile (25 mL). The white precipitate was filtered off after 12 h to yield **3** (100 mg, 62 %); m.p. > 280 °C (decomp). $^1$H NMR (400 MHz, [D$_6$]DMSO): $\delta$ = 8.71 (s, 2H, NH), 8.59 (s, 2H, NH), 8.36 (s, 2H, NH), 8.16 (d, $^4J$(H,H) = 2.0 Hz, 2H, ArH$_{xan}$), 8.13 (dd, $^3J$(H,H) = 7.8 Hz, 2H, ArH$_{diph}$), 7.30 (d, $^4J$(H,H) = 2.0 Hz, 2H, ArH$_{xan}$), 7.24 (d, $^4J$(H,H) = 2.0 Hz, 2H, ArH$_{xan}$), 7.15 (d, $^4J$(H,H) = 2 Hz, 2H, ArH$_{xan}$), 7.12 (t, $^3J$(H,H) = 7.6 Hz, 2H, ArH$_{diph}$), 7.02 (t, $^3J$(H,H) = 7.0 Hz, 2H, ArH$_{diph}$), 6.92 (d, $^3J$(H,H) = 7.8 Hz, 2H, ArH$_{diph}$), 1.61 (s, 12H, CCH$_{3xan}$), 1.29 (s, 18H, *t*Bu), 1.21 ppm (s, 18H, *t*Bu). MS (ESI, THF/MeOH): *m*/*z* (%) 1005.6 (100) [*M* + Na]$^+$.

Hexamer **4**: A solution of diisocyanate **2** (42 mg, 0.164 mmol) in dichloromethane (15 mL) was added dropwise over 30 min with vigorous stirring under nitrogen to a solution of diamine **1** (120 mg, 0.164 mmol) and tetrabutylammonium chloride (92 mg, 0.33 mmol) in dichloromethane (20 mL). The solvent was removed under reduced pressure after 12 h. The residue was triturated with ethyl acetate (10 mL) and the white solid was filtered off to yield 88 mg of the 1:2 complex of hexamer **4** with tetrabutylammonium chloride. The white powder was dissolved in dichloromethane (50 mL) and water (50 mL) and the organic layer was washed with water (2 × 50 mL), dried over MgSO$_4$, and evaporated to yield **4** (66 mg, 41 %) as a white solid; m.p. 254–256 °C. The following $^1$H NMR data refer to a solution of **4** with tetrabutylammonium chloride (1:2) since the spectrum of hexamer **4** alone could not be interpreted. $^1$H NMR (400 MHz, [D$_5$]pyridine): $\delta$ = 10.69 (s, 4H, NH), 10.64 (s, 4H, NH), 9.29 (s, 4H, NH), 9.22 (d, $^4J$(H,H) = 2.0 Hz, 4H, ArH$_{xan}$), 9.11 (dd, $^3J$(H,H) = 8.2 Hz, $^4J$(H,H) = 1.2 Hz, 4H, ArH$_{diph}$), 8.27 (d, $^4J$(H,H) = 2.0 Hz, 4H, ArH$_{xan}$), 7.29 (d, $^4J$(H,H) = 2.7 Hz, 4H, ArH$_{xan}$), 7.28 (d, $^4J$(H,H) = 2.4 Hz, 4H, ArH$_{xan}$), 6.83 (dd, $^3J$(H,H) = 7.8 Hz, $^4J$(H,H) = 1.2 Hz, 4H, ArH$_{diph}$), 6.32 (td, $^3J$(H,H) = 7.8 Hz, $^4J$(H,H) = 1.2 Hz, 4H, ArH$_{diph}$), 6.18 (td, $^3J$(H,H) = 7.4 Hz, $^4J$(H,H) = 1.4 Hz, 4H, ArH$_{diph}$), 3.28 (m, NCH$_2$, 16H), 1.86 (s, 12H, CCH$_{3xan}$), 1.83 (s, 12H, CCH$_{3xan}$), 1.78 (s, 36H, *t*Bu), 1.65 (m, 16H, NCH$_2$*CH$_2$*), 1.31 (s, 36H, *t*Bu), 1.29 (m, 16H, *CH$_2$*CH$_3$), 0.83 ppm (t, $^3J$(H,H) = 7.4 Hz, 24H, CH$_2$*CH$_3$*). MS (ESI, THF/MeOH): *m*/*z* (%) 1989.2 (100) [*M* + Na]$^+$.

X-ray structure analysis of [**4**(Cl)$_2$]$^{2-}$[Bu$_4$N]$^+_2$: C$_{122}$H$_{140}$N$_{12}$O$_{12}$·2 Cl$^-$·2 [C$_{16}$H$_{36}$N]$^+$·1.25 CHCl$_3$·1.25 CH$_2$Cl$_2$, colorless block, 0.36 × 0.28 × 0.24 mm$^3$, 173 K, orthorhombic, space group $P2_12_12_1$, $a$ = 17.0189(11), $b$ = 17.7753(11), $c$ = 52.633(4) Å, $V$ = 15922(2) Å$^3$, $Z$ = 4, $\mu$ = 0.206 mm$^{-1}$, $\rho_{calcd}$ = 1.159 g cm$^{-1}$, STOE-IPDS-II-two-circle diffractometer, Mo$_{K\alpha}$ radiation (0.71073 Å), $\omega$ scans, $\theta$ range = 1.21–25.75°, 104218 reflections collected, 28175 independent reflections ($R_{int}$ = 0.122), 1730 parameters, empirical absorption correction (MULABS),[15] structure solution with SHELXS-90,[16] refinement on $F^2$ with SHELXL-97,[17] $R1$ = 0.125, $wR2$ = 0.254, Flack-x parameter 0.04(9), H atoms were geometrically positioned and refined using a riding model, max electron density = 1.32 e Å$^{-3}$. CCDC-286528 contains the supplementary crystallographic data for this paper. These data can be obtained free of charge from the Cambridge Crystallographic Data Centre via www.ccdc.cam.ac.uk/data request/cif.

Received: October 24, 2005
Published online: February 2, 2006

**Keywords:** anions · host–guest systems · macrocycles · oligoureas · template synthesis

[1] J. Rebek, Jr., *Chem. Commun.* **2000**, 637–643.
[2] For comprehensive reviews on anion recognition, see: a) P. D. Beer, P. A. Gale, *Angew. Chem.* **2001**, *113*, 502–532; *Angew. Chem. Int. Ed.* **2001**, *40*, 486–516; b) K. Choi, A. D. Hamilton, *Coord. Chem. Rev.* **2003**, *240*, 101–110; c) P. A. Gale, *Coord. Chem. Rev.* **2003**, *240*, 191–221; anions as templates: R. Vilar, *Angew. Chem.* **2003**, *115*, 1498–1516; *Angew. Chem. Int. Ed.* **2003**, *42*, 1460–1477.
[3] R. Varghese, S. J. George, A. Ajayaghosh, *Chem. Commun.* **2005**, 593–595.
[4] P. Bühlmann, S. Nishizawa, K. P. Xiao, Y. Umezawa, *Tetrahedron* **1997**, *53*, 1647–1654.
[5] R. Herges, A. Dikmans, U. Jana, F. Köhler, P. G. Jones, I. Dix, T. Fricke, B. König, *Eur. J. Org. Chem.* **2002**, 3004–3014.
[6] B. P. Hay, M. Gutowski, D. A. Dixon, J. Garza, R. Vargas, B. A. Moyer, *J. Am. Chem. Soc.* **2004**, *126*, 7925–7934.
[7] In fact the crystals used for the X-ray analysis were obtained from a sample of **3** "contaminated" with about 15 % of **4**.
[8] A regular "eight-shaped" macrocycle would have $D_2$ symmetry, which is in agreement with the solution NMR data.
[9] A stability constant cannot be derived from these data, since the difference $n$(tetrabutyl) − 2 × $n$(complex) (= the amount of free chloride) as determined by the integration of various signals is zero for $n$(**5**)/$n$(**4**) < 2 and increases linearly with $n$(tetrabutyl) for $n$(**5**)/$n$(**4**) > 2. Assuming that a difference of 5 % could be detected at $c$(**4**) = 0.5 mM and $c$(**5**) = 1 mM, this leads to a lower limit of $K = 2 \times 10^8$ M$^{-2}$.
[10] An analogous behavior is observed for other chlorides, for example, NaCl in [D$_6$]DMSO.

 © 2006 Wiley-VCH Verlag GmbH & Co. KGaA, Weinheim 

[11] In the case of bromide, significant spectral changes are only observed with a large excess of $Bu_4NBr$ (ca. 50 fold). The best interpretation of the sprectral changes is obtained by a 1:2 complex of **4**:$Br^-$ with $\log\beta_{12} = 7.7$.
[12] Distinctly higher values of $\log\beta_{11} = 7.4$ and $\log\beta_{12} = 12.9$ with $Na^+$ complexed by [2.2.2]cryptand as the counterion indicate the influence of the cation. Clearly the separation of the ion pairs is less costly in the latter case.
[13] A short distance of 5.52 Å between two chloride ions (additionally bridged by two water molecules) was also found in the nearly planar complex with a cyclic octalactam: A. Szumna, J. Jurczak, *Helv. Chim. Acta* **2001**, *84*, 3760 – 3765.
[14] For examples of preorganization around anions see: a) Y. H. Kim, J. Calabrese, C. McEwen, *J. Am. Chem. Soc.* **1996**, *118*, 1545 – 1546; b) G. M. Hübner, J. Gläser, C. Seel, F. Vögtle, *Angew. Chem.* **1999**, *111*, 395 – 398; *Angew. Chem. Int. Ed.* **1999**, *38*, 383 – 386; c) E. Alcalde, S. Ramos, L. Pérez-García, *Org. Lett.* **1999**, *1*, 1035 – 1038; d) M. R. Sambrook, P. D. Beer, J. A. Wisner, R. L. Paul, A. R. Cowley, *J. Am. Chem. Soc.* **2004**, *126*, 15364 – 15365; e) E. A. Katayev, G. Dan Pantos, M. D. Reshetova, V. N. Khrustalev, V. M. Lynch, Y. A. Ustynyuk, J. L. Sessler, *Angew. Chem.* **2005**, *117*, 7552 – 7556; *Angew. Chem. Int. Ed.* **2005**, *44*, 7386 – 7390.
[15] R. Blessing, *Acta Crystallogr. Sect. A* **1995**, *51*, 33 – 38.
[16] G. M. Sheldrick, *Acta Crystallogr. Sect. A* **1990**, *46*, 467 – 473.
[17] G. M. Sheldrick, SHELXL-97, A Program for the Refinement of Crystal Structures, University of Göttingen, Germany, **1997**.

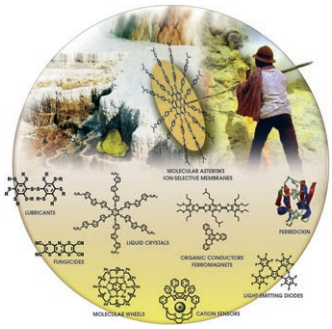
 © 2006 Wiley-VCH Verlag GmbH & Co. KGaA, Weinheim 

# Cover Picture

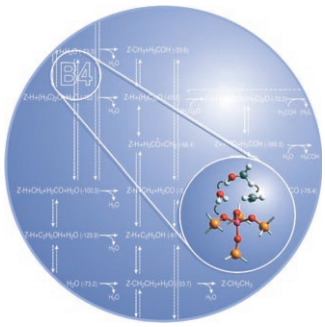



**Yong Yu, Andrew D. Bond, Philip W. Leonard, K. Peter C. Vollhardt,* and Glenn D. Whitener**

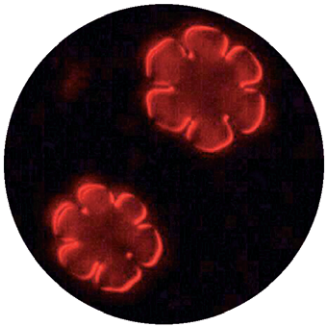
**True artistry** is not limited to the fine arts. Penta(ferrocenyl)cyclopentadienyl complexes like that shown display intriguing structures and reactivity. In their Communication on page 1794 ff., K. P. C. Vollhardt et al. describe penta(ferrocenyl)cyclopentadienyl compounds that have ramifications for materials science, catalysis, and fundamental chemistry. (Background for the cover illustration is the painting "Untitled" by the French artist Marie Sat; graphics prepared by P. W. Leonard.)



***Supramolecular Chemistry***
Persulfurated arenes can be applied in diverse materials such as redox sensors, organic conductors, and liquid crystals. In their Review on page 1686 ff., M. Gingras and co-workers describe the synthesis, structures, and properties of persulfurated arenes.



***Zeolite Catalysis***
In their Communication on page 1714 ff., M. Waroquier and co-workers discuss a detailed theoretical study of the methanol-to-olefin process and show that a direct reaction cannot give the initial carbon–carbon bond.



***Liquid Crystals***
H. Bock and co-workers report in their Communication on page 1783 ff. the synthesis of the first soluble derivatives of ovalenes and their self-assembly into a stable columnar mesophase.

# Contents

**VIP** ***The following Communications have been judged by at least two referees to be "very important papers" and will be published online at www.angewandte.org soon:***


*D. Curran,* G. Moura-Letts, M. Pohlman*
**Solution-Phase Mixture Synthesis with Fluorous Tagging En Route: Total Synthesis of an Eight-Member Stereoisomer Library of Passifloricins**

*H. Zhang, H. Xia,* G. He, T. B. Wen, L. Gong, G. Jia**
**Synthesis and Characterization of Stable Ruthenabenzenes**

*X. Mo, Y. An, C.-S. Yun, S. Yu**
**Nanoparticle-Assisted Visualization of Binding Interactions between Collagen Mimetic Peptide and Collagen Fibers**

*M. Harney, Y. Zhang, L. Sita**
**Discrete, Multiblock Isotactic–Atactic Stereoblock Polypropene Microstructures of Differing Block Architectures by Programmable Stereomodulated Living Ziegler–Natta Polymerization**

*Y. Weizmann, Z. Cheglakov, V. Pavlov, I. Willner**
**Autonomous Fueled Mechanical Replication of Nucleic Acid Templates for the Amplified Optical Detection of DNA**

*B. Botta, F. Caporuscio, D. Subissati, A. Tafi,* M. Botta, A. Filippi, M. Speranza**
**Flattened-Cone 2,8,14,20-Tetrakis(L-valinamido)[4]resorcinarene: Enantioselective Allosteric Receptors in the Gas Phase**


## News


Organometallic Chemistry: A. Fürstner Awarded — **1676**

Biological Chemistry: A. Skerra Receives Prize — **1676**

Structure and Dynamics: F. Kremer Honored — **1676**


## Books


Microwaves in Organic and Medicinal Chemistry — C. Oliver Kappe, Alexander Stadler — *reviewed by N. E. Leadbeater* — **1677**

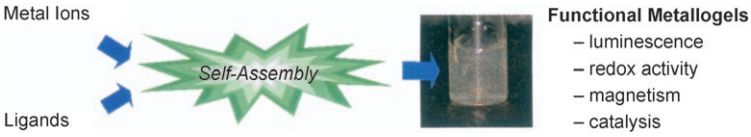
Microwave Assisted Organic Synthesis — J. P. Tierney, P. Lidström — *reviewed by N. E. Leadbeater* — **1678**


## Highlights

### Gels


F. Fages* — **1680 – 1682**

Metal Coordination To Assist Molecular Gelation

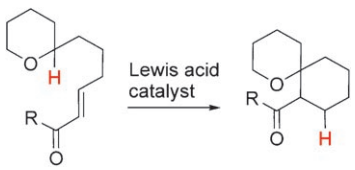




**Gelling together**: Molecular gels are a class of nanoscale materials based on the self-assembly of low-molecular-weight compounds. The manipulation of metal–ligand interactions offers novel opportunities to fabricate highly processable and stimuli-responsive metallogels that capitalize on the rich properties of the metal complexes (see picture).

### C–H Activation


M. Tobisu, N. Chatani* — **1683 – 1684**

A Catalytic Approach for the Functionalization of C($sp^3$)–H Bonds

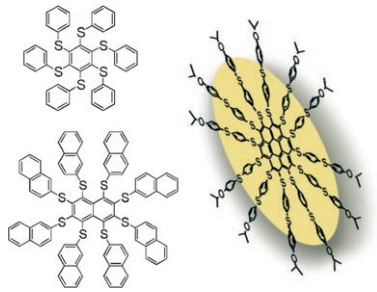




**Access allowed**: A Lewis acid catalyzed 1,5-hydride shift is the key step in the direct functionalization of sterically congested C($sp^3$)–H bonds. This new method complements the existing transition-metal-mediated reactions that are limited to the functionalization of more accessible C–H bonds.



InterScience
© 2006 Wiley-VCH Verlag GmbH & Co. KGaA, Weinheim

# Reviews



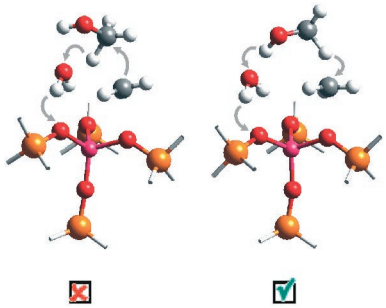
**Underexploited** despite their mild and high-yielding syntheses, persulfurated arenes have been known for about 50 years. The Review describes the structure and properties of the title compounds and derived materials such as supramolecular assemblies, redox sensors, ion-selective membranes, clathrates, organic conductors, liquid crystals, coordination polymers, and bioinorganic systems.

***Supramolecular Chemistry***

M. Gingras,* J.-M. Raimundo, Y. M. Chabre _____ **1686 – 1712**

Persulfurated Aromatic Compounds

# Communications

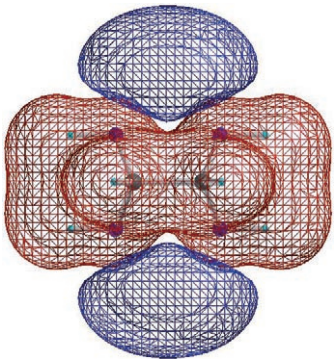


**You are the weakest link, goodbye!** Many individual steps of the direct mechanisms in the methanol-to-olefin process are tied together in an integrated scheme, allowing a simple identification of the weakest links. Calculations show that a combined pathway from methanol directly to ethylene does not exist and no C—C bond can be formed directly.

***Zeolites***

D. Lesthaeghe, V. Van Speybroeck, G. B. Marin, M. Waroquier* **1714 – 1719**

Understanding the Failure of Direct C—C Coupling in the Zeolite-Catalyzed Methanol-to-Olefin Process



**Basic principles**: The use of simple topological principles permits the design of small molecules with very high proton affinities. According to DFT calculations, 3,6,7,8-tetraazatricyclo[3.1.1.1$^{2,4}$]octane and its analogues behave as superbases, and show important structural deviations from known proton sponges. Their electrostatic potential maps show a characteristic very compact region at the protonation site (blue regions in the picture).

***Density Functional Calculations***

E. Estrada,* Y. Simón-Manso _____ **1719 – 1721**

Rational Design and First Principles Studies Toward the Discovery of a Small and Versatile Proton Sponge

**For the USA and Canada:**
ANGEWANDTE CHEMIE International Edition (ISSN 1433-7851) is published weekly by Wiley-VCH PO Box 191161, D 69451 Weinheim, Germany. Air freight and mailing in the USA by Publications Expediting Inc. 200 Meacham Ave., Elmont, NY 11003. Periodicals postage paid at Jamaica NY 11431. US POSTMASTER: send address changes to *Angewandte Chemie*, Wiley-VCH, 111 River Street, Hoboken, NJ 07030. Annual subscription price for institutions: US$ 5685/5168 (valid for print and electronic / print or electronic delivery); for individuals who are personal members of a national chemical society prices are available on request. Postage and handling charges included. All prices are subject to local VAT/sales tax.


© 2006 Wiley-VCH Verlag GmbH & Co. KGaA, Weinheim

# Masthead

A Journal of the Gesellschaft Deutscher Chemiker

**Angewandte International Edition Chemie**

## Editorial Board

*Chairman:*
François Diederich, *Eidgenöss. Techn. Hochschule (Zürich, Switzerland)*

Michael Dröscher, *Degussa AG (Düsseldorf)*
Wolfgang A. Herrmann, *Technische Universität München*
Martin Jansen, *Max-Planck-Institut für Festkörperforschung (Stuttgart)*
Horst Kessler, *Technische Universität München*
Stefan Marcinowski, *BASF AG (Ludwigshafen)*
Rainer Metternich, *Schering AG (Berlin)*
Hartmut Michel, *Max-Planck-Institut für Biophysik (Frankfurt)*
Rolf Mülhaupt, *Albert-Ludwigs-Universität (Freiburg)*
Martin Quack, *Eidgenöss. Techn. Hochschule (Zürich, Switzerland)*
Manfred T. Reetz, *Max-Planck-Institut für Kohlenforschung (Mülheim)*
Hans Ulrich Stilz, *Sanofi Aventis (Frankfurt)*
Rolf Thauer, *Max-Planck-Institut für terrestrische Mikrobiologie (Marburg)*
Walter Thiel, *Max-Planck-Institut für Kohlenforschung (Mülheim)*
Hartmut Wiezer, *Clariant International AG (Muttenz, Switzerland)*
Otto S. Wolfbeis, *Universität Regensburg*

## International Advisory Board

Lia Addadi, *Weizmann Institute of Science (Rehovot, Israel)*
Chun-Li Bai, *Institute of Chemistry, CAS (Beijing, P. R. China)*
Scott Biller, *Novartis Institutes for BioMedical Research (Cambridge, USA)*
Peter B. Dervan, *California Institute of Technology (Pasadena, USA)*
Frans C. De Schryver, *Catholic University of Leuven (Heverlee, Belgium)*
Richard R. Ernst, *Eidgnöss. Techn. Hochschule (Zürich, Switzerland)*
Sir Alan R. Fersht, *Cambridge University (Great Britain)*
Jean M. J. Fréchet, *University of California (Berkeley, USA)*
Roald Hoffmann, *Cornell University (Ithaca, USA)*
Andrew B. Holmes, *University of Melbourne (Melbourne, Australia)*
Robert Langer, *Massachusetts Institute of Technology (Cambridge, USA)*
Yuan-Tseh Lee, *Academia Sinica (Taipei, Taiwan)*
Jean-Marie Lehn, *Université Louis Pasteur (Strasbourg, France)*
Richard A. Lerner, *The Scripps Research Institute (La Jolla, USA)*
Shengming Ma, *Shanghai Institute of Organic Chemistry, CAS (Shanghai, P. R. China)*
Stephen Mann, *University of Bristol (Great Britain)*
E. W. "Bert" Meijer, *Eindhoven University of Technology (Netherlands)*
Bernard Meunier, *Laboratoire de Chimie de Coordination du CNRS (Toulouse, France)*
Chad Mirkin, *Northwestern University (Evanston, USA)*
Klaus Müller, *F. Hoffmann-La Roche Ltd (Basel, Switzerland)*
Eiichi Nakamura, *The University of Tokyo (Tokyo, Japan)*
Kyriacos C. Nicolaou, *The Scripps Research Institute (La Jolla, USA)* and *University of California, San Diego (La Jolla, USA)*
Ryoji Noyori, *Nagoya University (Japan) and RIKEN (Tokyo, Japan)*
Luis Oro, *Universidad de Zaragoza – CSIC (Zaragoza, Spain)*
Seiji Shinkai, *Kyushu University (Fukuoka, Japan)*
J. Fraser Stoddart, *University of California (Los Angeles, USA)*
George M. Whitesides, *Harvard University (Cambridge, USA)*
Richard N. Zare, *Stanford University (USA)*

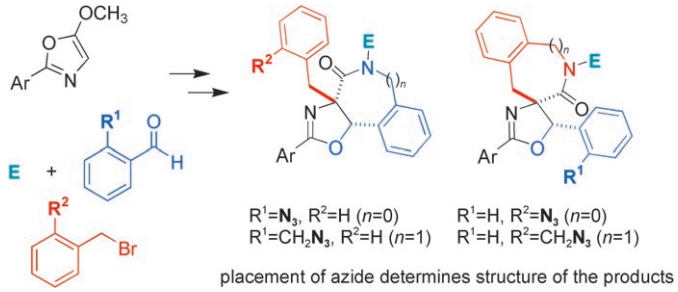
| | |
|---|---|
| **Editor:** | Peter Gölitz |
| **Deputy Editors:** | Neville A. Compton, Haymo Ross |
| **Senior Associate Editors:** | Frank Maaß, José Oliveira, Guy Richardson, Diane Smith |
| **Associate Editors:** | Jens Ackermann, Anjum Dadabhoy, Andrea Dallas, Volker Jacob, Rachel Schmidt-Radde, Elisabeth Weber Mario Müller (Senior Web-Editor) |
| **Assistants:** | Kylie Clayton, Margarete Dostal, Ralf Kempf, Brendan Macpherson, Allison Mills, Heidrun Sigmund, Christiane Walter |
| **Production:** | Margitta Schmitt, Silke Lautenschläger |
| **Secretariat:** | Isabelle Honé, Stefanie Eberle, Corina Pfenning |
| **Manuscript Submission & Personal Homepage:** | manuscriptXpress http://www.manuscriptxpress.com |
| **Telephone:** | (+ 49) 62 01-606-315 |
| **Fax:** | (+ 49) 62 01-606-331 or -328 |
| **E-mail:** | angewandte@wiley-vch.de |
| **Courier services:** | Boschstrasse 12 69469 Weinheim (Germany) |
| **Regular mail:** | Postfach 10 11 61 69451 Weinheim (Germany) |
| **Marketing:** | Claudia Barzen (ext. 458, fax: ext. 328; cbarzen@wiley-vch.de) |
| **Publishers:** | WILEY-VCH Verlag GmbH & Co. KGaA Postfach 10 11 61 69451 Weinheim (Germany) (+ 49) 62 01-606-0 (Tel.) (+ 49) 62 01-606-328 (fax) http://www.wiley-vch.de/ |
| **Publisher:** | Eva-E. Wille |
| **Publication:** | weekly |

WILEY InterScience® DISCOVER SOMETHING GREAT

**Full Text:** www.interscience.wiley.com
**Homepage:** www.angewandte.org

Further masthead information follows before the reviews.

© 2006 WILEY-VCH Verlag GmbH & Co. KGaA, Weinheim

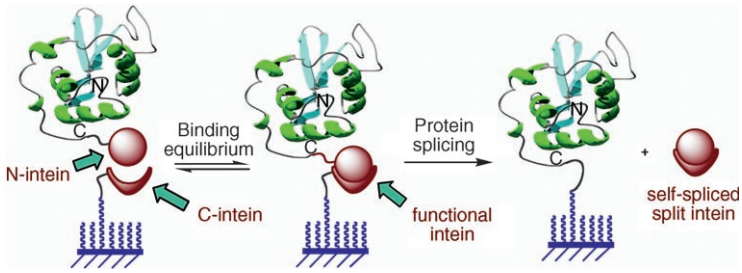



**A short, linear sequence** for the synthesis of complex small polycyclic lactams (see picture) is presented. The sequence, which is applied to the synthesis of a library of 529 compounds, is based on a catalytic, enantioselective cycloaddition between an oxazole and an aldehyde, so that the resultant compounds are enantiomerically pure and readily prepared in either stereochemical series.

## Combinatorial Chemistry

J. M. Mitchell, J. T. Shaw* — **1722 – 1726**

A Structurally Diverse Library of Polycyclic Lactams Resulting from Systematic Placement of Proximal Functional Groups

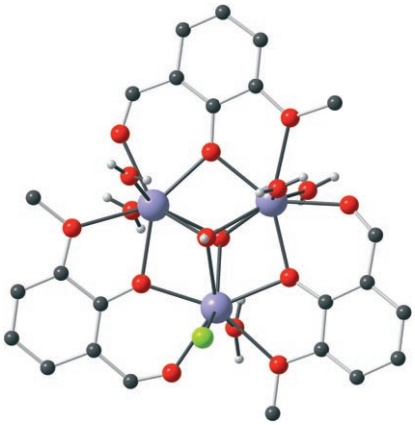



**Without a trace**: The immobilization of biologically active proteins onto a solid support through split-intein-mediated protein trans-splicing reactions requires only very dilute samples. Not only is this process traceless but it does not require purification of the protein, thereby making possible the direct immobilization of proteins from complex mixtures such as cell lysates.

## Immobilization

Y. Kwon, M. A. Coleman, J. A. Camarero* — **1726 – 1729**

Selective Immobilization of Proteins onto Solid Supports through Split-Intein-Mediated Protein Trans-Splicing



**Roll the Dy's**: Two aggregates made up of dysprosium triangles (one example is shown) display a vanishing susceptibility at low temperature, unprecedented in systems comprising an odd number of unpaired electrons. Despite having a near non-magnetic ground state, behavior typical of a single-molecule magnet is observed for the thermally populated excited state.

## Molecular Magnetism

J. Tang, I. Hewitt, N. T. Madhu, G. Chastanet, W. Wernsdorfer, C. E. Anson, C. Benelli, R. Sessoli, A. K. Powell* — **1729 – 1733**

Dysprosium Triangles Showing Single-Molecule Magnet Behavior of Thermally Excited Spin States

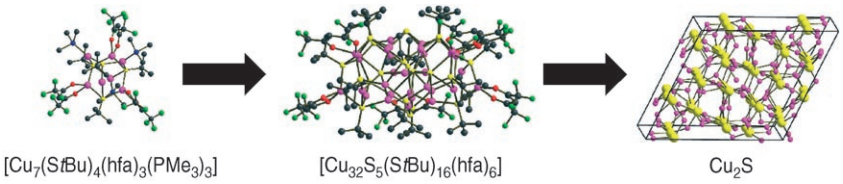

© 2006 Wiley-VCH Verlag GmbH & Co. KGaA, Weinheim

# Contents


## C–S Bond Cleavage

S. Schneider, J. A. S. Roberts, M. R. Salata, T. J. Marks* ——— **1733 – 1736**

Mixed Diketonate Thiolate Copper(I) Precursors for Materials Synthesis: Control of $Cu_2S$-Forming Thermolysis Pathways by Manipulating Lewis Acid and Base Cluster Building Blocks

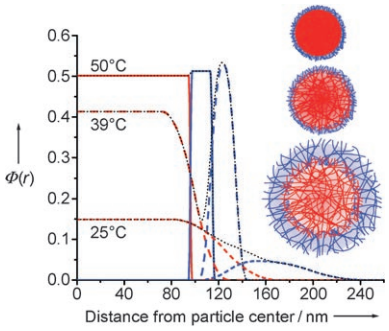



**Scission precision**: The combination of Lewis acidic and Lewis basic building blocks in copper(I) thiolate clusters enables control of the thermal decomposition pathway in the design of new molecular precursors for $Cu_2S$ formation. After C–S bond scission, large clusters with cuprous sulfide cores are isolated as intermediates and are structurally characterized (see scheme; hfa = hexafluoroacetylacetonate).

## VIP Nanoparticles

I. Berndt, J. S. Pedersen, W. Richtering* ——— **1737 – 1741**

Temperature-Sensitive Core–Shell Microgel Particles with Dense Shell

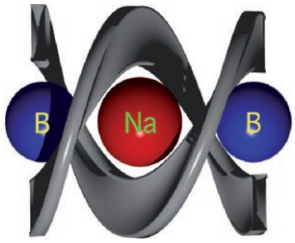



**Cores and effect**: Using different temperature-sensitive polymers a core–shell microgel is prepared, which at intermediate temperatures has a shell with a higher segment density $\Phi$ than the core (see radial density profiles: core (red), shell (blue)). More detailed information is obtained from small-angle neutron scattering. A new form-factor model describes the experimental scattering curves at different temperatures.

## VIP Helical Structures

H. Katagiri, T. Miyagawa, Y. Furusho,* E. Yashima* ——— **1741 – 1744**

Synthesis and Optical Resolution of a Double Helicate Consisting of *ortho*-Linked Hexaphenol Strands Bridged by Spiroborates

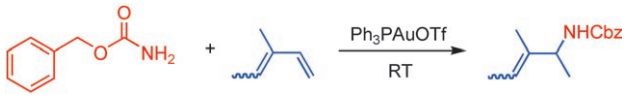



**Double Twist:** The first spiroborate-based helicate was synthesized and shown to be stable in the solid state as well as in solution. The double-stranded structure (see picture) was characterized by $^1$H NMR spectroscopy, ESI MS, and X-ray crystallographic studies. The racemic helicates were resolved by the formation of a diastereomeric, optically active ammonium salt.

## Hydroamination

C. Brouwer, C. He* ——— **1744 – 1747**

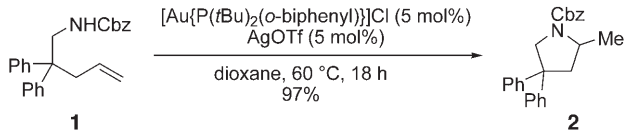
Efficient Gold-Catalyzed Hydroamination of 1,3-Dienes




**The Midas touch**: 1,3-Dienes undergo hydroamination with carbamates and sulfonamides in the presence of $Ph_3PAuOTf$ catalyst under mild conditions (see scheme). The carbobenzyloxy (Cbz) group is readily removed from the product, and the reaction is thus an efficient method to prepare allylic amines.



© 2006 Wiley-VCH Verlag GmbH & Co. KGaA, Weinheim

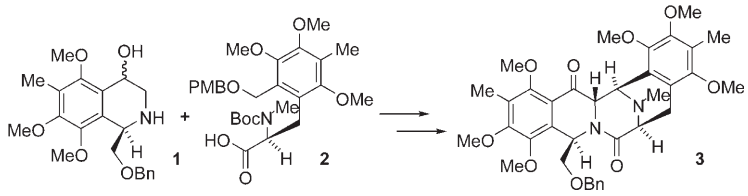



**Gold for rings**: Reaction of alkenyl carbamates such as **1** in the presence of [Au{P(*t*Bu)$_2$(*o*-biphenyl)}]Cl and AgOTf led to nitrogen heterocycles (e.g. **2**). This Au$^{I}$-catalyzed intramolecular hydroamination tolerates a range of labile carbamates and substitution patterns and can be applied to the synthesis of bicyclic carbamates and protected piperidines. Cbz = benzyloxycarbonyl.

## Hydroamination (2)

X. Han, R. A. Widenhoefer* . **1747 – 1749**

Gold(I)-Catalyzed Intramolecular Hydroamination of Alkenyl Carbamates

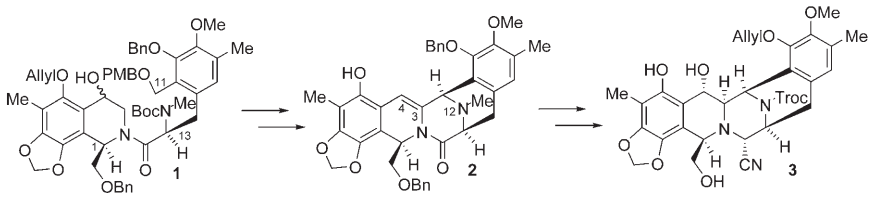



**Facile construction** of subunits **1** and **2** allowed the rapid assembly of the pentacyclic ring system **3** of the cytotoxic tetrahydroisoquinoline alkaloids. A surprising participation reaction was discovered, which necessitated revision of the stereochemical assignments of key intermediates en route to **3**.

## Alkaloid Synthesis

C. Chan, S. Zheng, B. Zhou, J. Guo, R. M. Heid, B. J. D. Wright, S. J. Danishefsky* _____ **1749 – 1754**

The Solution to a Deep Stereochemical Conundrum: Studies toward the Tetrahydroisoquinoline Alkaloids



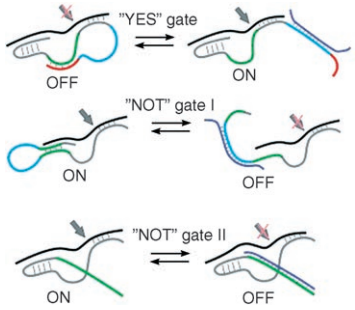

**A new strategy** was designed for the construction of the pentacyclic ring system of ecteinascidin 743. Key features include highly concise routes to the enantiopure, configurationally matched subunit **1**, a novel vinylogous Pictet–Spengler cyclization to **2**, and a stereospecific epoxidation and regioselective reduction sequence of the C3–C4 enamide to secure **3**.

## Natural Products

S. Zheng, C. Chan, T. Furuuchi, B. J. D. Wright, B. Zhou, J. Guo, S. J. Danishefsky* _____ **1754 – 1759**

Stereospecific Formal Total Synthesis of Ecteinascidin 743

**A logical conclusion**: DNA logic gates constructed by using a $Cu^{2+}$-dependent DNA-cleaving deoxyribozyme are as efficient as the relatively unstable ribonucleotide-containing systems. The inputs (effectors), gates (deoxyribozymes), and outputs (substrates) are represented by chemically robust DNA oligonucleotides, which perform logic operations including "YES", "NOT", and "AND(A,NOT(B),NOT(C))" (see picture).




## Molecular Devices

X. Chen, Y. Wang, Q. Liu, Z. Zhang,* C. Fan,* L. He* _____ **1759 – 1762**

Construction of Molecular Logic Gates with a DNA-Cleaving Deoxyribozyme

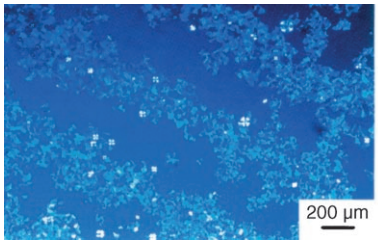

© 2006 Wiley-VCH Verlag GmbH & Co. KGaA, Weinheim

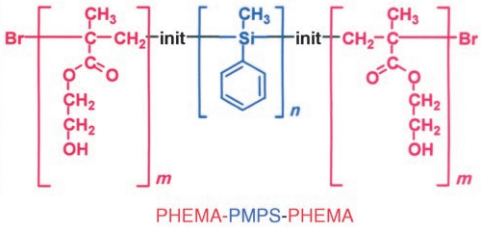
# Contents


## Bioinorganic Chemistry

D. C. Popescu, E. N. M. van Leeuwen, N. A. A. Rossi, S. J. Holder, J. A. Jansen, N. A. J. M. Sommerdijk* ____ **1762 – 1767**

Shaping Amorphous Calcium Carbonate Films into 2D Model Substrates for Bone Cell Culture



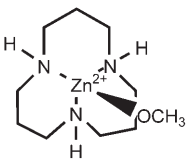




**Boning up on patterning**: Patterned calcium carbonate films with dimensions of 200–400 μm were obtained using the photolithographic properties of a polysilane-based ABA block copolymer, PHEMA-PMPS-PHEMA. These patterns may serve as a 2D model system for $CaCO_3$ biomaterials in which both the $CaCO_3$ resorption by osteoclasts and the calcium phosphate deposition by osteoblasts can be monitored using optical microscopy.

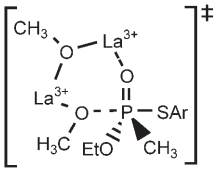
## Metal-Ion Catalysis

S. A. Melnychuk, A. A. Neverov, R. S. Brown* ____ **1767 – 1770**

Catalytic Decomposition of Simulants for Chemical Warfare V Agents: Highly Efficient Catalysis of the Methanolysis of Phosphonothioate Esters



**1**



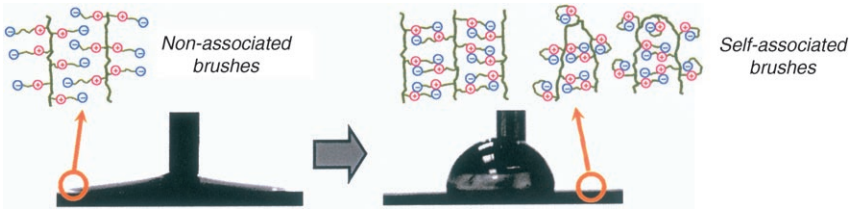
**2**

**As good as the original**: Extremely effective methanolysis of phosphonothioates using metal-containing systems (e.g., **1**) was achieved. The catalytic methanolysis of a $SCH_2CH_2NEt_2$ derivative, an analogue of the organophosphorus chemical warfare material VX, was predicted, and the catalyzed methanolysis of *S*-(3,5-dichlorophenyl) *O*-ethyl methylphosphonothioate was shown to involve a concerted displacement of the aryl thioate (transition state **2**).

## Polymer Brushes

O. Azzaroni, A. A. Brown, W. T. S. Huck* ____ **1770 – 1774**

UCST Wetting Transitions of Polyzwitterionic Brushes Driven by Self-Association



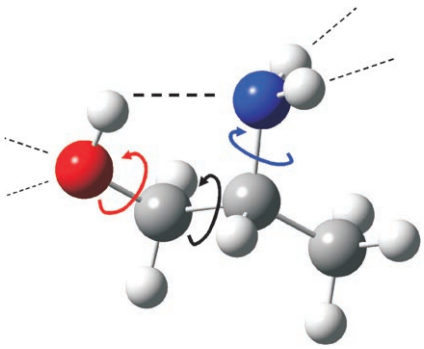

**A sweeping success**: The surface-initiated, atom-transfer radical polymerization of [2-(methacryloyloxy)ethyl]dimethyl(3-sulfopropyl)ammonium hydroxide (MEDSAH) on silicon and gold surfaces leads to homogeneous and patterned brushes of poly-MEDSAH. The association state of the zwitterionic side-groups is determined (see picture; wettability of thin (left) and thick (right) brushes).

## Spectroscopic Techniques

G. Tarczay,* G. Magyarfalvi,* E. Vass* ____ **1775 – 1777**

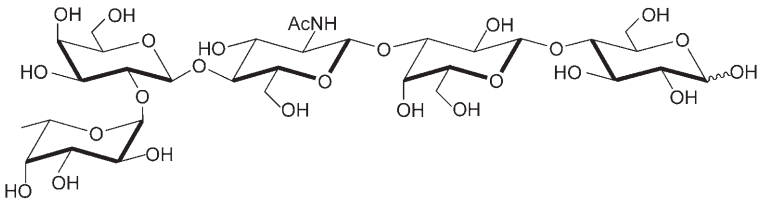
Towards the Determination of the Absolute Configuration of Complex Molecular Systems: Matrix Isolation Vibrational Circular Dichroism Study of (*R*)-2-Amino-1-propanol

**Molecular freeze-frame**: (*R*)-2-Amino-1-propanol was used as an example to show that matrix isolation vibrational circular dichroism spectroscopy is a useful method for the determination of the absolute configuration of molecules with multiple conformers that are capable of strong intermolecular interactions, especially hydrogen bonds.





© 2006 Wiley-VCH Verlag GmbH & Co. KGaA, Weinheim

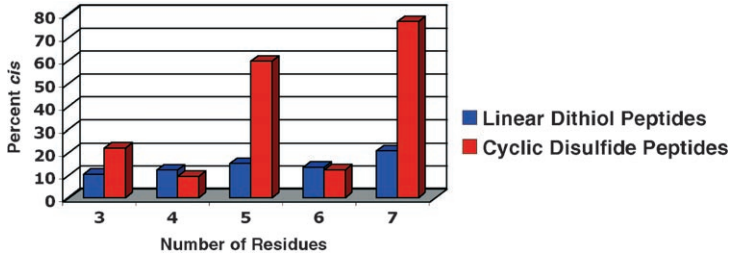


**Sugar production**: A microbiological method has been developed for the production of fucosyl α1,2-linked carbohydrates from lactose. The syntheses of 2′-fucosyllactose and lacto-*N*-neofucopentaose-1 (see structure), which contain the H-2 antigen (Fucα-2Galβ-4R), were achieved by cultivating *Escherichia coli* strains that overexpressed the appropriate heterologous genes.


**Oligosaccharide Synthesis**

S. Drouillard,* H. Driguez, E. Samain ——— **1778 – 1780**

Large-Scale Synthesis of H-Antigen Oligosaccharides by Expressing *Helicobacter pylori* α1,2-Fucosyltransferase in Metabolically Engineered *Escherichia coli* Cells

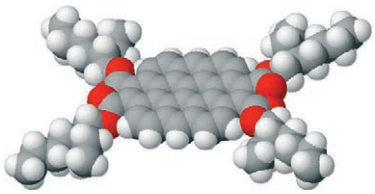

***cis* persists**: The population of the *cis* conformation of the Cys–Pro imide bond of the cyclic disulfide form of peptides of the sequence Ac-Cys-Pro-$(Xaa)_m$-Cys-$NH_2$ (Xaa = Phe, Ala) ranges from 9.3 to 76.9% and shows a striking periodic dependence on the number of residues in the peptide.


**Cyclic Peptides**

T. Shi, S. M. Spain, D. L. Rabenstein* ——— **1780 – 1783**

A Striking Periodicity of the *cis*/*trans* Isomerization of Proline Imide Bonds in Cyclic Disulfide-Bridged Peptides


**The extremely persistent** self-assembly of ovalene tetraesters (see picture) into liquid-crystalline columns from below room temperature to over 375 °C gives these first soluble derivatives of "circumnaphthalene", one of the most stable mesophases known. The close contact of the large π systems within the columnar stacks and their good solubility makes these flexible disks promising tools for organic electronics.

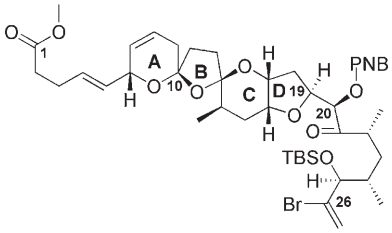



**Self-Assembly**

S. Saïdi-Besbes, É. Grelet, H. Bock* ——— **1783 – 1786**

Soluble and Liquid-Crystalline Ovalenes


**North–South divide**: An efficient synthesis of the entire C1–C26 (northern) portion of azaspiracid-1 is disclosed (see picture). Key transformations include the formation of a bis-spiroketal, the oxidation of a sulfone at C10 to form a β,γ-unsaturated ketone, a tandem Wadsworth–Emmons/hetero-Michael addition to construct ring D, and the highly selective hydroxylation at C20.





**Natural Product Synthesis**

X.-T. Zhou, R. G. Carter* ——— **1787 – 1790**

Synthesis of the C1–C26 Northern Portion of Azaspiracid-1: Kinetic versus Thermodynamic Control of the Formation of the Bis-spiroketal



© 2006 Wiley-VCH Verlag GmbH & Co. KGaA, Weinheim

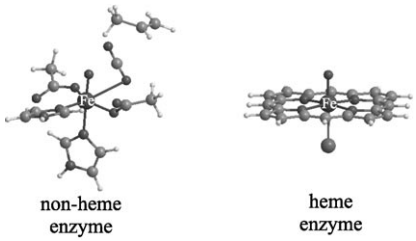
# Contents


## Oxo–Iron Enzymes

S. P. de Visser* ——— 1790 – 1793

Differences in and Comparison of the Catalytic Properties of Heme and Non-Heme Enzymes with a Central Oxo–Iron Group

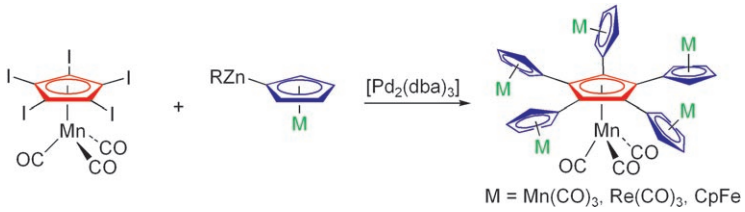
**Why so aggressive?** Density functional calculations on the oxo–iron active species of dioxygenase and monooxygenase enzyme models show that the former ones are more aggressive catalysts with low reaction barriers. The differences are assigned to electronic factors, such as the electron transfer into a σ* anti-bonding Fe–O orbital and the reduction of the metal to an $Fe^{III}$ center in the rate-determining step.




## Oligocyclopentadienyl Complexes

Y. Yu, A. D. Bond, P. W. Leonard, K. P. C. Vollhardt,* G. D. Whitener ——— 1794 – 1799

Syntheses, Structures, and Reactivity of Radial Oligocyclopentadienyl Metal Complexes: Penta(ferrocenyl)cyclopentadienyl and Congeners



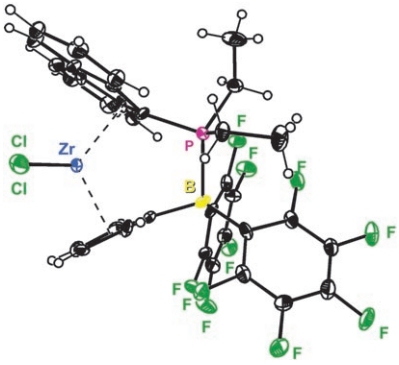

**"Supra"Cp**: Fivefold Negishi coupling of pentaiodocymantrene resulted in radial oligocyclopentadienyl metal complexes (see scheme). These complexes show fascinating conformational and chemical behavior, including M–M and Cp–Cp bond formation and the liberation of the novel supraligand penta(ferrocenyl)cyclopentadiene. dba = dibenzylideneacetone.

## Polymerization Catalysts

K. A. Ostoja Starzewski,* B. S. Xin, N. Steinhauser, J. Schweer, J. Benet-Buchholz ——— 1799 – 1803

Donor–Acceptor Metallocene Catalysts for the Production of UHMW-PE: Pushing the Selectivity for Chain Growth to Its Limits

**Plastic fantastic!** Donor–acceptor zirconocenes with a donor (P)-substituted fluorenyl ligand and an acceptor (B)-substituted cyclopentadienyl ligand (see structure) are highly active ethylene polymerization catalysts that reveal an ultrahigh selectivity for chain propagation even at high temperatures, giving access to ultrahigh-molecular-weight polyethylenes (viscosity-average molecular weights $M_\eta > 1 \times 10^6\ g\,mol^{-1}$).

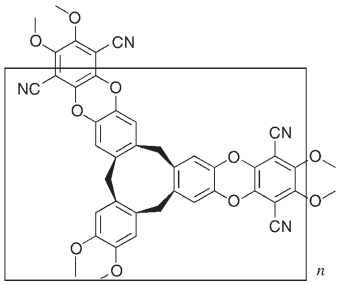



## Microporous Polymers

N. B. McKeown,* B. Gahnem, K. J. Msayib, P. M. Budd,* C. E. Tattershall, K. Mahmood, S. Tan, D. Book, H. W. Langmi, A. Walton ——— 1804 – 1807

Towards Polymer-Based Hydrogen Storage Materials: Engineering Ultramicroporous Cavities within Polymers of Intrinsic Microporosity

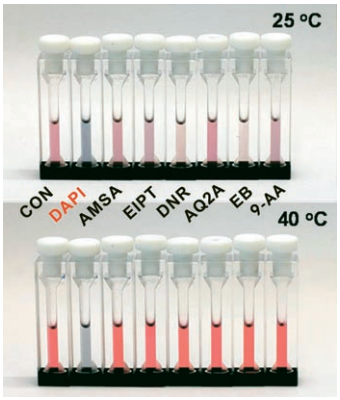
**Three structurally diverse** polymers of intrinsic microporosity reversibly adsorb significant quantities of hydrogen (1.4–1.7% by mass at 77 K) and represent the first examples of a new type of purely organic hydrogen storage material, which can be tailored to meet the specific requirements of hydrogen physisorption.






© 2006 Wiley-VCH Verlag GmbH & Co. KGaA, Weinheim

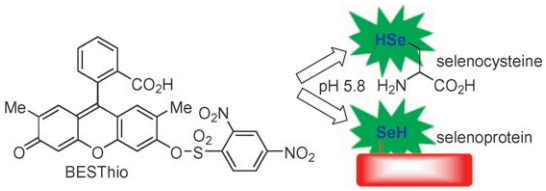
**Nanoparticle assemblies** interconnected with DNA can be used to screen for DNA-binding molecules colorimetrically. The melting temperature of the nanoparticle assembly increases in the presence of strong-DNA-binding molecules. Thus, the strength of the DNA binding can be determined by the change in this sharp melting transition, which is observable by a blue-to-red color change (see picture).




## Colorimetric Sensors

M. S. Han, A. K. R. Lytton-Jean, B.-K. Oh, J. Heo, C. A. Mirkin* ——— **1807 – 1810**

Colorimetric Screening of DNA-Binding Molecules with Gold Nanoparticle Probes




**Simply the BESThio**: The fluorescein derivative BESThio (see scheme) operates as a thiol probe at pH 7.4 and functions as a selenol probe at pH 5.8, and can thus be selectively applied to the rapid quantification of selenocysteine and the determination of the selenocysteine content in selenoproteins such as glutathione peroxidase and thioredoxin reductase with high sensitivity.

## Fluorescent Probes

H. Maeda,* K. Katayama, H. Matsuno, T. Uno ——— **1810 – 1813**

3′-(2,4-Dinitrobenzenesulfonyl)-2′,7′-dimethylfluorescein as a Fluorescent Probe for Selenols

**Looking for outstanding employees?**

**Do you need another expert for your excellent team?**
**... Chemists, PhD Students, Managers, Professors, Sales Representatives...**

Place an advert in the printed version and have it made available online for 1 month, free of charge!

***Angewandte Chemie International Edition***
**Advertising Sales Department: Marion Schulz**
**Phone: 0 62 01 - 60 65 65**
**Fax: 0 62 01 - 60 65 50**
**E-Mail: MSchulz@wiley-vch.de**

## Service

*Keywords* ——— *1814*

*Authors* ——— *1815*

*Angewandte's Sister Journals* ——— *1816 – 1817*

*Preview* ——— *1819*




***For more information on ChemMedChem see www.chemmedchem.org***


© 2006 Wiley-VCH Verlag GmbH & Co. KGaA, Weinheim

# Corrigendum

The $[Ga_2(C_5Me_5)]^+$ Ion: Bipyramidal Double-Cone Structure and Weakly Coordinated, Monovalent $Ga^+$

B. Buchin, C. Gemel, T. Cadenbach, R. Schmid, R. A. Fischer* ____ **1074–1076**

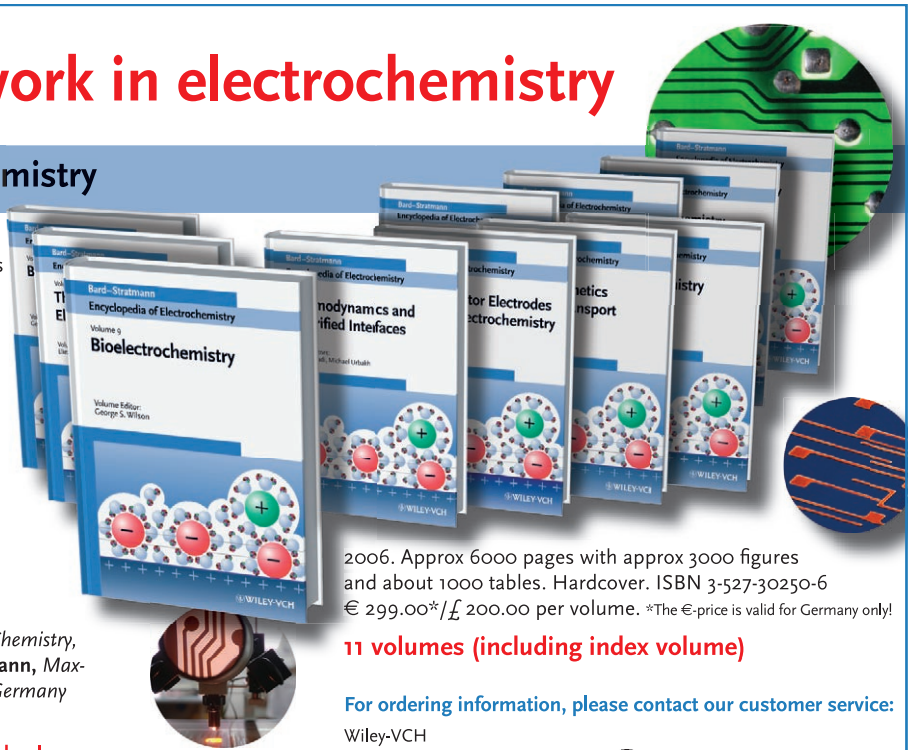
*Angew. Chem. Int. Ed.* **2006**, *45*

DOI 10.1002/anie.200503028

In this Communication three relevant papers which report on the synthesis and characterization of the cation $[In_2(C_5Me_5)]^+$, the indium analogue to the title compound, escaped the authors' attention and should have been cited: A. H. Cowley, C. L. B. Macdonald, J. S. Silverman, J. D. Gorden, A. Voigt, *Chem. Commun.* **2001**, 175; J. N. Jones, C. L. B. Macdonald, J. D. Gorden, A. H. Cowley, *J. Organomet. Chem.* **2003**, *666*, 3; A. H. Cowley, *Chem. Commun.* **2004**, 2369. The authors apologize for this oversight.

The definitive work in electrochemistry

Encyclopedia of Electrochemistry



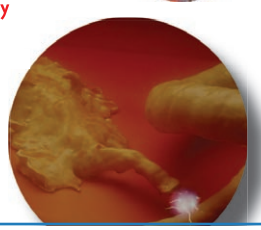

Available Volumes:
1: Thermodynamics and Electrified Interfaces
2: Interfacial Kinetics and Mass Transport
3: Instrumentation and Electroanalytical Chemistry
4: Corrosion and Oxide Films
6: Semiconductor Electrodes and Photoelectrochemistry
8: Organic Electrochemistry
9: Bioelectrochemistry

Forthcoming Volumes *(completed Fall 2006)*:
5: Electrochemical Engineering
7: Inorganic Electrochemistry
10: Modified Electrodes
11: Index

Editors-in-Chief: **Allen J. Bard,** *Department of Chemistry, University of Texas, Austin, USA*/ **Martin Stratmann,** *Max-Planck-Institute for Iron Research, Duesseldorf, Germany*

Stay up-to-date in electrochemistry
- a total of 11 volumes makes this the first and only complete reference on electrochemistry
- covering all aspects, from fundamental research to applications in industry
- easy access to electrochemical topics

www.wiley-vch.de/bard/eoe



2006. Approx 6000 pages with approx 3000 figures and about 1000 tables. Hardcover. ISBN 3-527-30250-6
€ 299.00*/£ 200.00 per volume. *The €-price is valid for Germany only!

11 volumes (including index volume)

For ordering information, please contact our customer service:

Wiley-VCH
E-Mail: service@wiley-vch.de
www.wiley-vch.de

John Wiley & Sons, Inc.
E-Mail: custserv@wiley.com
www.wiley.com

John Wiley & Sons, Ltd.
E-Mail: cs-books@wiley.co.uk
www.wiley.com

WILEY-VCH
WILEY
WILEY InterScience® DISCOVER SOMETHING GREAT

1872504_gu

 © 2006 Wiley-VCH Verlag GmbH & Co. KGaA, Weinheim 



## Awarded...

### A. Fürstner Receives Bayer Prize and Mukaiyama Award

The Otto Bayer Prize 2006 was awarded to Alois Fürstner (Max Planck Institute for Coal Research, Mülheim/Ruhr). Fürstner was honored with the €50000 prize for his pioneering work at the interface between organometallic chemistry and organic synthesis, and particularly for his contributions to alkene and alkyne metathesis and its application to the total synthesis of complex natural products such as macrolides, alkaloids, and glycoconjugates. The title of his award lecture was "*About Splitting and Combining: Notes on Metathesis*". He is also the first recipient of the Mukaiyama Award of the Japanese Society of Synthetic Organic Chemistry. Fürstner received his PhD in 1987 at the Technical University of Graz with H. Weidmann, and following a postdoctoral fellowship with W. Oppolzer (University of Geneva) he completed his habilitation at Graz in 1992. He joined the Max Planck Institute (Mülheim) as a group leader in 1993 and is a director there since 1998. His review on roseophilin and prodigiosin alkaloids in *Angewandte Chemie* in 2003 was also highlighted on the cover of the same issue.[1a] He recently also described the unusual structure and reactivity of a homoleptic super-ate complex of iron.[1b] Fürstner is a member of the editorial board of *Advanced Synthesis & Catalysis* and *ChemMedChem*, among others.



A. Fürstner

### A. Skerra and F. Kremer Receive Beckurts Prize

The Karl Heinz Beckurts Award, which has been presented by the foundation of the same name since 1989 following an initiative of the Helmholtz Association of National Research Centers (Germany), was awarded in 2005 to A. Skerra (Technical University of Munich) and F. Kremer (University of Leipzig), among others. The prize is worth €30000 and is awarded annually for outstanding research work that has spawned industrial innovation.



A. Skerra

**Arne Skerra** studied chemistry at the Technical University of Darmstadt and completed his PhD in 1989 at the Ludwig Maximilians University in Munich working with A. Plückthun and E.-L. Winnacker. In 1990 he joined G. Winter at the Laboratory of Molecular Biology of the Medical Research Council in Cambridge (UK) as a postdoctoral fellow. He then joined the Max Planck Institute for Biophysics in Frankfurt as a group leader, working with Nobel Laureate H. Michel. He completed his habilitation in 1995 at the University of Frankfurt am Main. In 1994 he was appointed professor of protein chemistry at the Technical University of Darmstadt, and in 1998 he moved to the Weihenstephan campus of the Technical University of Munich as a professor of biological chemistry. Skerra was honored for his innovative work in the area of molecular biotechnology and protein design, especially for the development of the artificial receptor proteins, the anticalins. Recently, he reported the construction of an anticalin based on human apolipoprotein D in *ChemBioChem*.[2] In 2001, Skerra founded the company Pieris Proteolab, a biopharmaceutical company focused on the development and commercialization of anticalins for therapeutic use in a variety of diseases, particularly in cancer and cardiovascular diseases.

**Friedrich Kremer** was recognized for his work on the dynamics of condensed matter and particularly for the further development of broadband dielectric spectroscopy in the GHz range. This technology was developed into a fully automated measuring system in collaboration with the company Novocontrol. Kremer recently discussed the dielectric relaxation of side-chain liquid-crystalline ionomers that contain alkaline metal ions.[3] Besides dielectric spectroscopy, his research group also employs NMR and (time-resolved) IR spectroscopy as well as optical and scanning probe methods to investigate the structure and dynamics of supramolecular systems, for example, near glass transitions. They also study the interactions between individual biomolecules with the aid of optical tweezers as microscopic sensors and actuators. Kremer studied physics at the University of Munich and biology at the University of Freiburg, where he completed his PhD with B. Hassenstein in 1977. He then joined L. Genzel at the Max Planck Institute for Solid-State Physics in Stuttgart, and in 1985 he joined E. W. Fischer at the Max Planck Institute for Polymer Research in Mainz, where he carried out his habilitation in 1991–1992. A year later, he was appointed as professor of experimental physics at the University of Leipzig. Kremer serves on the editorial boards of *Macromolecular Chemistry and Physics* and *Macromolecular Rapid Communications*, among others.



F. Kremer


[1] a) A. Fürstner, *Angew. Chem.* **2003**, *115*, 3706; *Angew. Chem. Int. Ed.* **2003**, *42*, 3582; b) A. Fürstner, H. Krause, C. W. Lehmann, *Angew. Chem.* **2006**, *118*, 454; *Angew. Chem. Int. Ed.* **2006**, *45*, 440.

[2] M. Vogt, A. Skerra, *ChemBioChem* **2004**, *5*, 191.

[3] N. A. Nikonorova, E. B. Barmatov, D. A. Pebalk, R. Diaz-Calleja, F. Kremer, *Macromol. Chem. Phys.* **2005**, *206*, 1630.


DOI: 10.1002/anie.200600522


WILEY InterScience DISCOVER SOMETHING GREAT
© 2006 Wiley-VCH Verlag GmbH & Co. KGaA, Weinheim

Gels

DOI: 10.1002/anie.200503704

# Metal Coordination To Assist Molecular Gelation

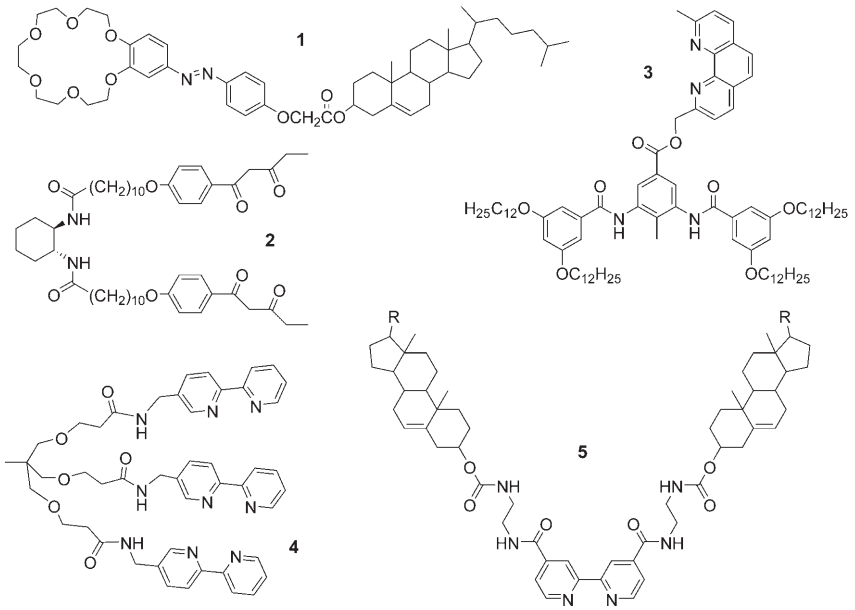
*Frédéric Fages**

**Keywords:**
coordination chemistry · gels · materials science · self-assembly · supramolecular chemistry

Molecular gels have recently evolved as a fascinating class of smart and functional nanoscale materials with high potential for a wide range of advanced applications.[1] Their formation stems from the spontaneous but controlled self-assembly of low-molecular-weight compounds into fibrous architectures, which, in turn, form entangled three-dimensional networks entrapping solvent molecules. In contrast to the case of their polymeric counterparts, molecular gels involve discrete molecular components with well-defined chemical structures. As a consequence, slight changes in the chemical composition of the backbone of the gelator allow the morphology, chirality, and size of the aggregates, and ultimately the macroscopic properties of the gel, to be exquisitely controlled and tuned. As such, the formation of molecular gels represents an elegant bottom-up approach for fabricating nanoscale materials.

So far, there exists a rich variety of organo- and hydrogelator molecular structures that are able to immobilize organic fluids or water, respectively, at extremely low concentrations.[1] Such systems are characterized by a strong propensity to self-assemble unidirectionally through a combination of multiple noncovalent bonds. Dispersion forces, π–π stacking, electrostatic interactions, and mainly hydrogen bonding have been largely exploited. Despite the major role that metal coordination plays in supramolecular chemistry,[2] it is surprising that the use of metal–ligand interactions in the area of molecular gels has been somewhat neglected until very recently. Metal complexes of fatty acids,[3] porphyrins,[4] and phthalocyanins[5] have been long known to produce gels, but these examples represent a rather narrow selection from the huge library of ligand structures available to date. In the last two years, there has been a surge of interest in the use of coordination chemistry as a rational design route toward self-assembled gels with unusual functional properties.

Binding of a metal ion to a gelator molecule containing an appended ligand site can affect self-aggregation modes and allow the gelation ability to be finely tuned. An early example of such metal-responsive organogelators was provided by the cholesterol-based gelator **1**, which contains a crown ether moiety. Indeed, the gelation temperature of **1** in methylcyclohexane/benzene was shown to depend on the concentration of alkali metal cations added.[6] Compound **2**, which has two β-diketonate ligands linked to a bis(amido)cyclohexane gelating scaffold through long alkyl chains, formed weak gels in methanol that became robust upon addition of divalent transition-metal ions.[7] It was suggested that the formation of bis(β-diketonato)copper(II) units served to cross-link the self-assembled fibers. Metal complexation can instead induce the complete loss of gelation ability, as observed in the case of gelators that contain either phenanthroline **3**[8a] or 2,2′-bipyridine **4**[8b] moieties. Gelation by the free ligands requires the establishment of extended arrays of intermolecular hydrogen bonds between amide groups. Upon metal complexation, the latter become associated intramolecularly, which inhibits the formation of intermolecular networks and thereby gelation. In con-




[*] Prof. Dr. F. Fages
GCOM2 UMR CNRS 6114
Université de la Méditerranée
Faculté des Sciences de Luminy, Case 901
13288 Marseille Cedex 9 (France)
Fax: (+33) 4-9182-9580
E-mail: fages@luminy.univ-mrs.fr


WILEY InterScience DISCOVER SOMETHING GREAT
© 2006 Wiley-VCH Verlag GmbH & Co. KGaA, Weinheim

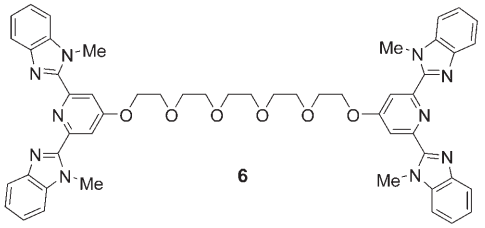
trast, both the bis(cholesteryl) derivative of 2,2′-bipyridine **5** and the homoleptic complex $[Cu^{I}(\mathbf{5})_2]$ function as gelators in 1-butyronitrile. Outstandingly, here it is a change in the redox state of the coordination center that allows the sol–gel phase transition to be reversibly controlled.[9] When a gel of $[Cu^{I}(\mathbf{5})_2]$ was exposed to the oxidant $NOBF_4$ and heated, it was converted into a sol. Conversely, addition of ascorbic acid into a solution of the nongelating copper(II) complex of **5** was followed by the reduction of the metal center and consequent gelation of the solution.

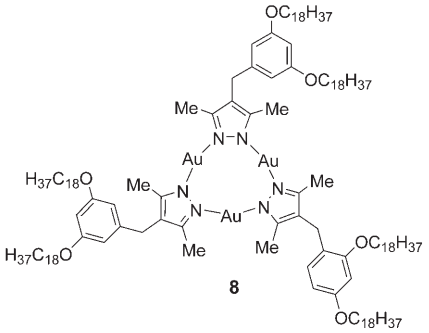
The manipulation of metal–ligand interactions is one of the most widely used construction principles for the generation of complex metallosupramolecular architectures.[2] Metallogelators are systems in which both the ligand and metal ion act as complementary constituent elements in a hierarchical self-assembly process. One of the major attractions of using this metallosupramolecular chemistry approach is the possibility to endow the self-assembled superstructures with the outstanding physicochemical properties of transition-metal ions. The ability of the 2,6-bis(benzimidazolyl)pyridine (BIP) unit to form complexes of specific composition and lability depending on the chemical nature of the metal ion has been elegantly exploited in the case of the bis-BIP compound **6**.[10] Indeed $Co^{II}$ or $Zn^{II}$ ions form 2:1 BIP/metal complexes and thus serve to extend the coordination polymer chains, while $La^{III}$ or $Eu^{III}$ ions act as cross-linking components as they form branched coordination centers with 3:1 stoichiometry. As a result, gelation of acetonitrile was only observed when **6** was combined with both divalent transition-metal and lanthanide ions. Preferential disruption of the lanthanide ion–BIP interactions was suggested to account for the thermochromic sol–gel transition and the thixotropic behavior. Furthermore the **6**:Zn/Eu gels exhibited light-emitting properties that were switched off in the presence of the formate anion as a competing ligand for europium(III). As such, the use of a combination of metal ions in conjunction with the ditopic ligand **6** opened access to metallogels that are responsive to multiple stimuli.

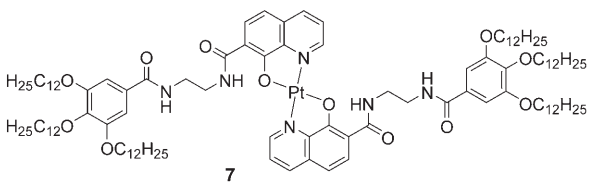
Metal chelates often reveal long-lived excited triplet states that emit strongly in the visible region and thus render them attractive in luminescence-based technologies, photovoltaics, and photocatalysis. A major drawback is their inherent sensitivity to quenching by dioxygen. Recently, an 8-quinolinolatoplatinum(II) complex **7** was shown to gelate a variety of organic solvents at very low concentrations. The main driving force of self-aggregation into fibrous structures has been attributed to a strong π interaction between the chelate moieties. Confocal laser scanning microscopy allowed the phosphorescence emission originating from the nanofibers to be directly visualized, and as a result of the self-assembling effect in the gel the red luminescence was found *not* to be sensitive to quenching by dioxygen.[11] Similarly, room temperature phosphorescence emission could be recorded in the gel state of the trinuclear $Au^{I}$ pyrazolate metallacycle **8**, which self-assembles through aurophilic interactions.[12a] Remarkably, the sol–gel transition coupled with doping/dedoping of $Ag^{I}$ induced a reversible switching of red–green–blue luminescence. Related $Cu^{I}$ pyrazolate systems were used as self-assembling components of security inks for the preparation of rewritable phosphorescent paper.[12b]

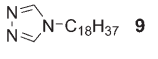
Compounds **9** and **10** are very simple structures in which the 1,2,4-triazole unit carries a long lipophilic chain.[13] Their complexes with divalent transition-metal ions self-assemble into linear polymeric structures to produce organogels with unusual functions. The alkane gels of the **9**/iron(II) system were shown to combine a unique set of magnetic, optical, and thixotropic properties.[13a] For the use of these soft materials in information storage devices, the observation of a spin-crossover transition in the gel state is of paramount interest. In addition, the cobalt(II) complex of the related ligand **10** exhibited a distinct behavior.[13b] Upon heating a solution of **10** in chloroform, the soluble octahedral species were converted into tetrahedral complexes that aggregated into coordination polymeric chains, inducing gelation. The thermochromic transition was observed to be fully reversible. In contrast to the case of conventional organogels, which dissolve upon heating, the reverse effect was indeed observed here as a result of a thermally induced change in the coordination mode.

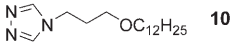
The examples discussed above were selected to illustrate the outstanding contribution of coordination chemistry




 © 2006 Wiley-VCH Verlag GmbH & Co. KGaA, Weinheim 

in the field of self-assembled gels. In recent work, other intrinsic properties of metal centers were also implemented in metallogels. Palladium(II)-containing supramolecular networks were shown to catalyze the oxidation of benzyl alcohol to benzaldehyde.[14] Catalytic metallogels represent a promising approach in supramolecular catalysis.[15] Binding of the paramagnetic metal ion $Gd^{III}$ to the tetraazamacrocyclic moiety of a gelling peptidic scaffold led to biocompatible supramolecular structures that are useful for clinical and biological applications based on magnetic resonance imaging.[16] Counteranion exchange was elegantly used to control the conformation of $Ag^{I}$-containing coordination polymers in water, and, thereby, the sol–gel transition.[16] Finally, it is worth noting that the first demonstration of instant control of gelation using sonication was made using a coordination compound as gelator.[18]

In conclusion, metallogels are a highly promising area of research at the frontier between supramolecular chemistry, coordination chemistry, molecular tectonics, and materials science. The examples described herein illustrate how their well-defined structures can capitalize on the unique richness of the spectroscopic, magnetic, catalytic, and redox attributes of coordination centers. Especially exciting is the possibility to impart collective properties that are usually observed in the crystalline state, such as magnetism, to highly processable gel-phase materials. Furthermore, an important feature common to almost all of the metallogels reported to date is their stimuli-responsive behavior. Far-reaching perspectives are expected in advanced applications of smart metallogels.


[1] a) P. Terech, R. G. Weiss, *Chem. Rev.* **1997**, *97*, 3133 – 3159; b) D. J. Abdallah, R. G. Weiss, *Adv. Mater.* **2000**, *12*, 1237 – 1247; c) L. A. Estroff, A. D. Hamilton, *Chem. Rev.* **2004**, *104*, 1201 – 1217; d) J. H. van Esch, B. L. Feringa, *Angew. Chem.* **2000**, *112*, 2351 – 2354; *Angew. Chem. Int. Ed.* **2000**, *39*, 2263 – 2266; e) N. M. Sangeetha, U. Maitra, *Chem. Soc. Rev.* **2005**, *34*, 821 – 836; f) Special issue: "Low Molecular Mass Gelators. Design, Self-Assembly, Function" (Ed.: F. Fages): *Top. Curr. Chem.* **2005**, *256*; g) *Molecular Gels: Materials with Self-Assembled Fibrillar Networks* (Eds.: R. G. Weiss, P. Terech), Kluwer Academic Publishers, Dordrecht, **2005**; h) M. de Loos, B. L. Feringa, J. H. van Esch, *Eur. J. Org. Chem.* **2005**, 3615 – 3631.

[2] J.-M. Lehn, *Supramolecular Chemistry: Concepts and Perspectives*, VCH, Weinheim, **1995**.

[3] a) D. Lopez, J.-M. Guenet, *Macromolecules* **2001**, *34*, 1076 – 1081; b) G. Mieden-Gundert, L. Klein, M. Fischer, F. Vögtle, K. Heuzé, J.-L. Pozzo, M. Vallier, F. Fages, *Angew. Chem.* **2001**, *113*, 3266 – 3267; *Angew. Chem. Int. Ed.* **2001**, *40*, 3164 – 3166.

[4] a) P. Terech, G. Gebel, R. Ramasseul, *Langmuir* **1996**, *12*, 4321 – 4323; b) T. Ishi-i, R. Iguchi, E. Snip, M. Ikeda, S. Shinkai, *Langmuir* **2001**, *17*, 5825 – 5833.

[5] M. Kimura, T. Muto, H. Takimoto, K. Wada, K. Ohta, K. Hanabusa, H. Shirai, N. Kobayashi, *Langmuir* **2000**, *16*, 2078 – 2082, and references therein.

[6] K. Murata, M. Aoki, T. Nishi, A. Ikeda, S. Shinkai, *J. Chem. Soc. Chem. Commun.* **1991**, 1715 – 1718.

[7] K. Hanabusa, Y. Maesaka, M. Suzuki, M. Kimura, H. Shirai, *Chem. Lett.* **2000**, 1168 – 1169.

[8] a) R. Ziessel, G. Pickaert, F. Camerel, B. Donnio, D. Guilon, M. Cesario, T. Prangé, *J. Am. Chem. Soc.* **2004**, *126*, 12403 – 12413; b) J.-E. Sohna Sohna, F. Fages, *Chem. Commun.* **1997**, 327 – 328.

[9] S.-i. Kawano, N. Fujita, S. Shinkai, *J. Am. Chem. Soc.* **2004**, *126*, 8592 – 8593.

[10] J. B. Beck, S. J. Rowan, *J. Am. Chem. Soc.* **2003**, *125*, 13922 – 13923.

[11] M. Shirakawa, N. Fujita, T. Tani, K. Kaneko, S. Shinkai, *Chem. Commun.* **2005**, 4149 – 4151.

[12] a) A. Kishimura, T. Yamashita, T. Aida, *J. Am. Chem. Soc.* **2005**, *127*, 179 – 183; b) A. Kishimura, T. Yamashita, K. Yamaguchi, T. Aida, *Nat. Mater.* **2005**, *4*, 546 – 549.

[13] a) O. Roubeau, A. Colin, V. Schmitt, R. Clérac, *Angew. Chem.* **2004**, *116*, 3345 – 3348; *Angew. Chem. Int. Ed.* **2004**, *43*, 3283 – 3286; b) K. Kuroiwa, T. Shibata, A. Takada, N. Nemoto, N. Kimizuka, *J. Am. Chem. Soc.* **2004**, *126*, 2016 – 2021.

[14] a) B. Xing, M.-F. Choi, B. Xu, *Chem. Eur. J.* **2002**, *8*, 5028 – 5032; b) J. F. Miravet, B. Escuder, *Chem. Commun.* **2005**, 5796 – 5798.

[15] G. Bühler, M. C. Feiters, R. J. M. Nolte, K. H. Dötz, *Angew. Chem.* **2003**, *115*, 2599 – 2602; *Angew. Chem. Int. Ed.* **2003**, *42*, 2494 – 2497.

[16] S. R. Bull, M. O. Guler, R. E. Bras, T. J. Meade, S. I. Stupp, *Nano Lett.* **2005**, *5*, 1 – 4.

[17] H.-J. Kim, J.-H. Lee, M. Lee, *Angew. Chem.* **2005**, *117*, 5960 – 5964; *Angew. Chem. Int. Ed.* **2005**, *44*, 5810 – 5814.

[18] T. Naota, H. Koori, *J. Am. Chem. Soc.* **2005**, *127*, 9324 – 9325.


 © 2006 Wiley-VCH Verlag GmbH & Co. KGaA, Weinheim 

C–H Activation

DOI: 10.1002/anie.200503866

# A Catalytic Approach for the Functionalization of C(sp$^3$)–H Bonds

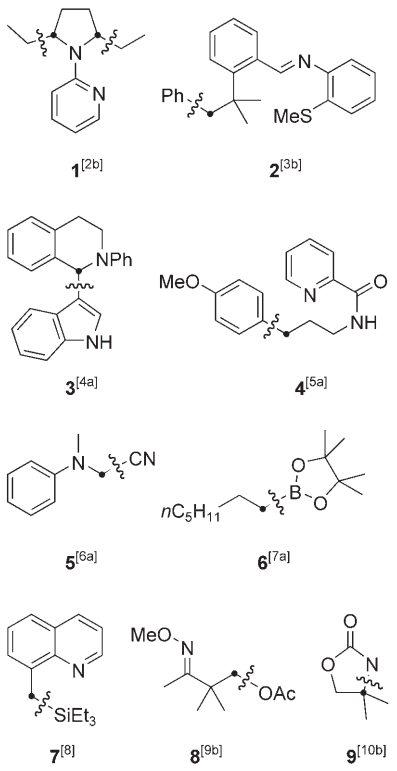
*Mamoru Tobisu and Naoto Chatani**

**Keywords:**
1,5-hydride shift · C–H activation · catalysis · Lewis acids

The development of methodology for the direct functionalization of relatively unreactive C–H bonds has now become a major topic of research.[1] The recent rapid growth of this area is not surprising, since such methodology facilitates the direct formation of C–C and C–Z bonds (Z = O, N, B, Si, etc.) without utilizing prefunctionalized C–X bonds (X = halogens, OTf ($F_3CSO_3^-$), etc.). Although the pioneering studies on the activation of inert C–H bonds by stoichiometric amounts of transition-metal complexes appeared in the early 1960s, it was more than 20 years later that *catalytic* reactions involving the cleavage of C–H bonds were achieved.[1a]

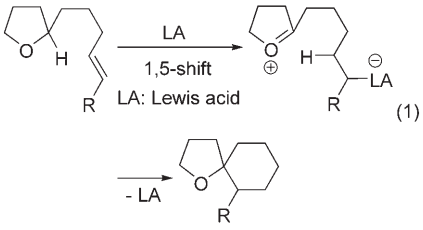
Since these ground-breaking discoveries, a number of catalytic C–H bond functionalization processes have been reported. Until recently, the majority of the catalytic processes reported were applicable to only C(sp$^2$)–H bonds. The functionalization of C(sp$^3$)–H bonds is still a particularly difficult challenge owing to the strength of C(sp$^3$)–H bonds. However, in the last few years, some promising catalytic systems for the selective functionalization of C(sp$^3$)–H bonds have been developed (Scheme 1).[2–10]

Since these processes require the direct interaction between the metal catalyst and the C–H bond to be activated, the steric environment around the reaction center is a critical factor in determining whether the process is feasible. Indeed, the compounds shown in Scheme 1 were synthesized through the functionalization of less hindered primary or secondary C(sp$^3$)–H bonds with the exception of oxazolidinone **9**, which was formed by the metal–nitrenoid insertion into a tertiary C–H bond.[10]

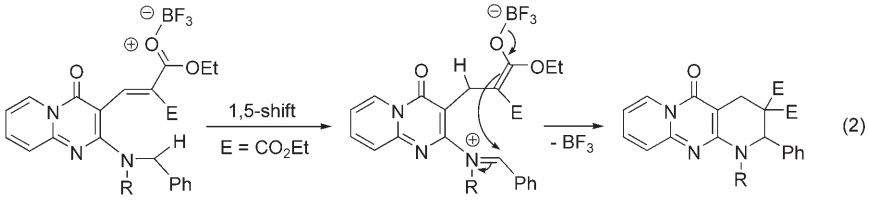



***Scheme 1.*** Selected examples of catalytic functionalization of C(sp$^3$)–H bonds.

The transition-metal-mediated activation of unreactive C–H bonds proceeds by several mechanisms, which include oxidative addition to low-valent metal centers, substitution by electrophilic metal complexes, and metal–carbenoid insertion.[11] A new approach was recently reported by Sames and co-workers.[12] Their proposal includes the initial activation of the unsaturated moiety by an electrophilic metal catalyst, cleavage of a C–H bond in the context of a 1,5-hydride shift, and subsequent ring closure [Eq. (1)].[13] This strategy eliminates the metal-mediated C–H bond-activation step and thus may be applicable to sterically hindered C-(sp$^3$)–H bonds. Although Lewis acid catalyzed and thermal cyclizations based on a similar concept have already been reported, the applicable substrates are limited to those that contain an extended π system [Eq. (2)].[14]




(1)



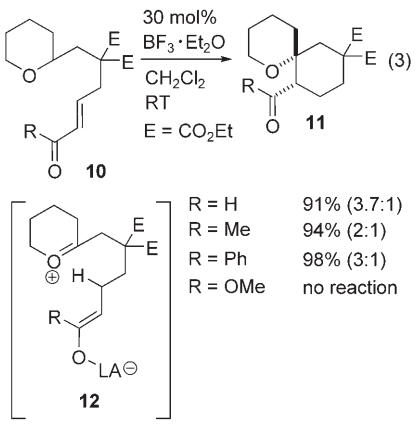

(2)

[*] Dr. M. Tobisu, Prof. Dr. N. Chatani
Department of Applied Chemisry
Osaka University
Suita, Osaka 565-0871 (Japan)
Fax: (+81) 6-6879-7396
E-mail: chatani@chem.eng.osaka-u.ac.jp

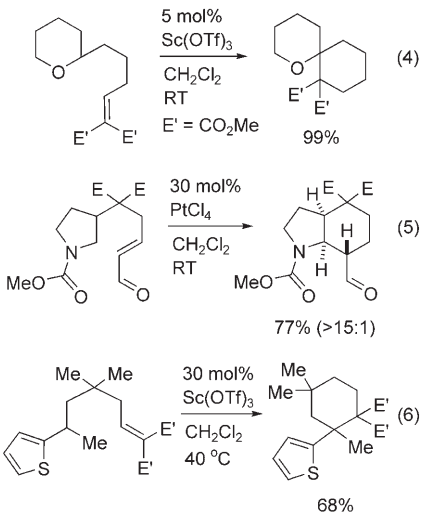


© 2006 Wiley-VCH Verlag GmbH & Co. KGaA, Weinheim

Sames and co-workers realized the concept shown in Equation (1) by utilizing well-designed tetrahydropyran-based substrates **10**, which, in the presence of a catalytic amount of $BF_3{\cdot}Et_2O$, afforded the expected spirocycles **11** [Eq. (3)]. The reaction presumably proceeds via the zwitterionic intermediate **12**, which is formed by a 1,5-hydride shift. α,β-Unsaturated aldehydes and ketones were suitable as hydride acceptors in this conversion, while α,β-unsaturated esters were not reactive under the reaction conditions. Although other Lewis acids, such as $Sc(OTf)_3$, $GaCl_3$, $TiF_4$, and $PtCl_4$, were also active for the reaction of **10**, undesired by-products resulted for this particular substrate.




In contrast, the reactions of α,β-unsaturated malonates proceeded effectively under the influence of the $Sc(OTf)_3$ catalyst [Eq. (4)]. The reaction can be applied not only to tertiary C–H bonds but also to secondary C–H bonds that are adjacent to heteroatoms such as nitrogen or oxygen [Eq. (5)]. A pseudobenzylic $C(sp^3)$–H bond lacking an α-heteroatom can also participate in the catalytic reaction [Eq. (6)]. The current limitation of the reaction is the requirement of a 1,5-relationship between the C–H bond and the electrophilic site.




The new approach for $C(sp^3)$–H bond functionalization reported by Sames et al. represents a potentially powerful method for constructing a quaternary center directly from a tertiary C–H bond in a catalytic manner. Although the underlying concepts are the classical Lewis acid activation of α,β-unsaturated carbonyl compounds, a 1,5-hydride shift, and enolate alkylation, the use of well-designed substrates leads to an unprecedented methodology for the functionalization of sterically congested $C(sp^3)$–H bonds. The methodology is currently limited to substrates containing a $C(sp^3)$–H bond adjacent to a heteroatom or a tertiary benzylic C–H bond as a hydride donor and an electron-deficient alkene as a hydride acceptor. Further applications of this methodology can be expected.[15]


[1] Recent reviews: a) F. Kakiuchi, N. Chatani, *Adv. Synth. Catal.* **2003**, *345*, 1077; b) V. Ritleng, C. Sirlin, M. Pfeffer, *Chem. Rev.* **2002**, *102*, 1731.

[2] a) N. Chatani, T. Asaumi, T. Ikeda, S. Yorimitsu, Y. Ishii, F. Kakiuchi, S. Murai, *J. Am. Chem. Soc.* **2000**, *122*, 12882; b) N. Chatani, T. Asaumi, S. Yorimitsu, T. Ikeda, F. Kakiuchi, S. Murai, *J. Am. Chem. Soc.* **2001**, *123*, 10935.

[3] a) B. D. Dangel, J. A. Johnson, D. Sames, *J. Am. Chem. Soc.* **2001**, *123*, 8149; b) B. Sezen, R. Franz, D. Sames, *J. Am. Chem. Soc.* **2002**, *124*, 13372; c) B. DeBoef, S. J. Pastine, D. Sames, *J. Am. Chem. Soc.* **2004**, *126*, 6556; d) B. Sezen, D. Sames, *J. Am. Chem. Soc.* **2005**, *127*, 5284.

[4] a) Z. Li, C.-J. Li, *J. Am. Chem. Soc.* **2005**, *127*, 6968; b) Z. Li, C.-J. Li, *J. Am. Chem. Soc.* **2005**, *127*, 3673; c) Z. Li, C.-J. Li, *Org. Lett.* **2004**, *6*, 4997; d) Z. Li, C.-J. Li, *J. Am. Chem. Soc.* **2004**, *126*, 11810.

[5] a) V. G. Zaitsev, D. Shabashov, O. Daugulis, *J. Am. Chem. Soc.* **2005**, *127*, 13154; b) D. Shabashov, O. Daugulis, *Org. Lett.* **2005**, *7*, 3657.

[6] a) S.-I. Murahashi, N. Komiya, H. Terai, *Angew. Chem.* **2005**, *117*, 7091; *Angew. Chem. Int. Ed.* **2005**, *44*, 6931; b) S.-I. Murahashi, N. Komiya, H. Terai, T. Nakae, *J. Am. Chem. Soc.* **2003**, *125*, 15312.

[7] a) H. Chen, S. Schlecht, T. C. Semple, J. F. Hartwig, *Science* **2000**, *287*, 1995; b) S. Shimada, A. S. Batsanov, J. A. K. Howard, T. B. Marder, *Angew. Chem.* **2001**, *113*, 2226; *Angew. Chem. Int. Ed.* **2001**, *40*, 2168.

[8] F. Kakiuchi, K. Tsuchiya, M. Matsumoto, E. Mizushima, N. Chatani, *J. Am. Chem. Soc.* **2004**, *126*, 12792.

[9] a) D. Kalyani, N. R. Deprez, L. V. Desai, M. S. Sanford, *J. Am. Chem. Soc.* **2005**, *127*, 7330; b) L. V. Desai, K. L. Hull, M. S. Sanford, *J. Am. Chem. Soc.* **2004**, *126*, 9542; c) A. R. Dick, K. L. Hull, M. S. Sanford, *J. Am. Chem. Soc.* **2004**, *126*, 2301; d) R. Giri, X. Chen, J.-Q. Yu, *Angew. Chem.* **2005**, *117*, 2150; *Angew. Chem. Int. Ed.* **2005**, *44*, 2112; e) R. Giri, J. Riang, J.-G. Lei, J.-J. Li, D.-H. Wang, X. Chen, I. C. Naggar, C. Guo, B. M. Foxman, J.-Q. Yu, *Angew. Chem.* **2005**, *117*, 7586; *Angew. Chem. Int. Ed.* **2005**, *44*, 7420.

[10] a) J. L. Liang, S.-X. Yuan, J.-S. Huang, W.-Y. Yu, C.-M. Che, *Angew. Chem.* **2002**, *114*, 3615; *Angew. Chem. Int. Ed.* **2002**, *41*, 3465; b) C. G. Espino, J. Du Bois, *Angew. Chem.* **2001**, *113*, 618; *Angew. Chem. Int. Ed.* **2001**, *40*, 598; c) P. M. When, J. Du Bois, *J. Am. Chem. Soc.* **2002**, *124*, 12950; d) P. M. When, J. Lee, J. Du Bois, *Org. Lett.* **2003**, *5*, 4823; e) J. J. Fleming, K. W. Fiori, J. Du Bois, *J. Am. Chem. Soc.* **2003**, *125*, 2028; f) K. W. Fiori, J. J. Fleming, J. Du Bois, *Angew. Chem.* **2004**, *116*, 4449; *Angew. Chem. Int. Ed.* **2004**, *43*, 4349; g) C. G. Espino, K. W. Fiori, M. Kim, J. Du Bois, *J. Am. Chem. Soc.* **2004**, *126*, 15378.

[11] a) A. D. Ryabov, *Chem. Rev.* **1990**, *90*, 403; b) C. Jia, T. Kitamura, Y. Fujiwara, *Acc. Chem. Res.* **2001**, *34*, 633.

[12] S. J. Pastine, K. M. McQuaid, D. Sames, *J. Am. Chem. Soc.* **2005**, *127*, 12180.

[13] Iminium ion intermediates have been proposed also in several late transition metal catalyzed reactions for the functionalization of C–H bonds.[2,4,6]

[14] M. Noguchi, H. Yamada, T. Sunagawa, *J. Chem. Soc. Perkin Trans. 1* **1998**, 3327; see also references cited in reference [12].

[15] During the preparation of this manuscript, another application of the methodology was reported: S. J. Pastine, D. Sames, *Org. Lett.* **2005**, *7*, 5429.


 © 2006 Wiley-VCH Verlag GmbH & Co. KGaA, Weinheim 

Supramolecular Chemistry

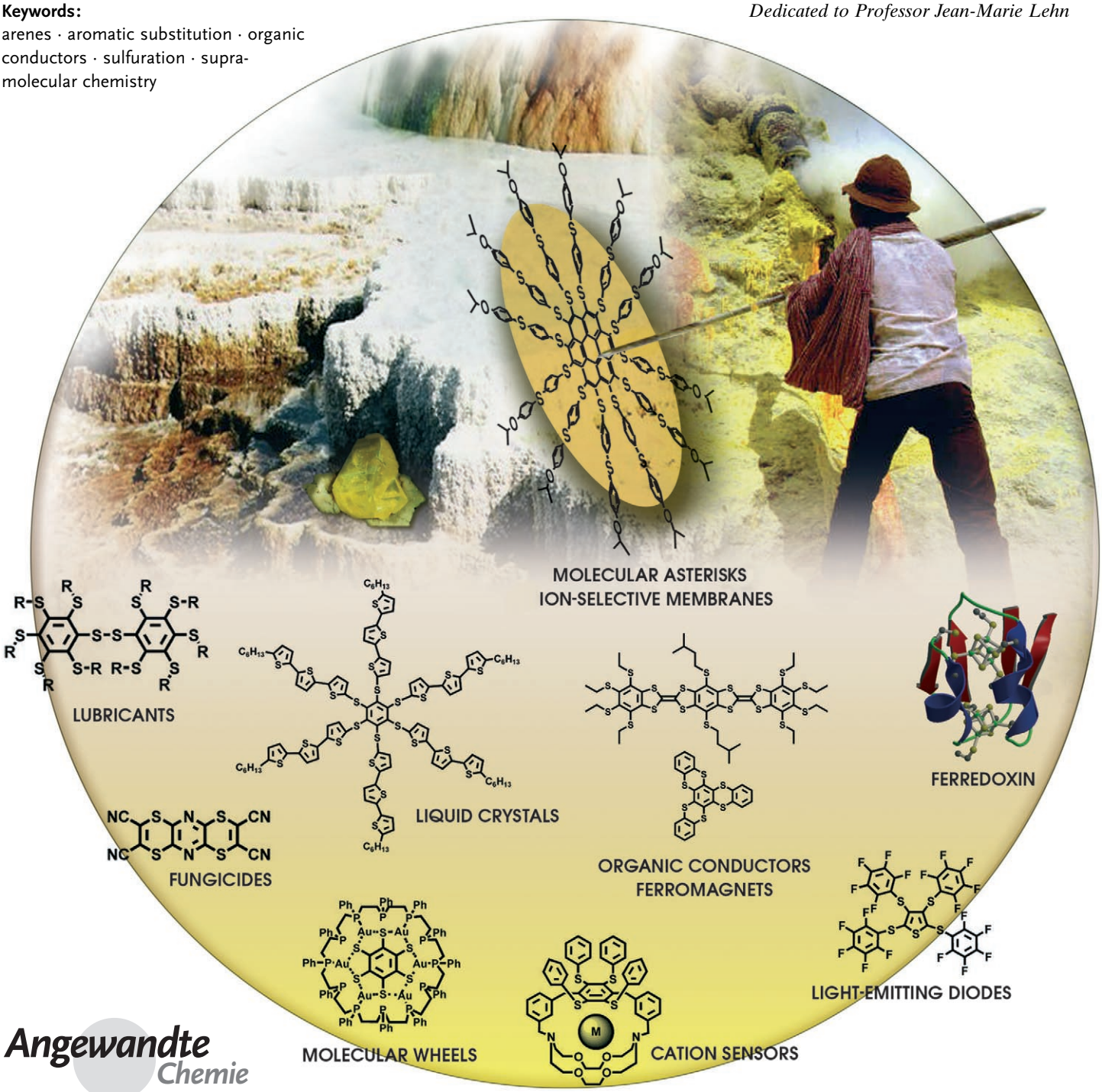
DOI: 10.1002/anie.200500032

# Persulfurated Aromatic Compounds

*Marc Gingras,* Jean-Manuel Raimundo, and Yoann M. Chabre*

**Keywords:**
arenes · aromatic substitution · organic conductors · sulfuration · supramolecular chemistry

*Dedicated to Professor Jean-Marie Lehn*






© 2006 Wiley-VCH Verlag GmbH & Co. KGaA, Weinheim

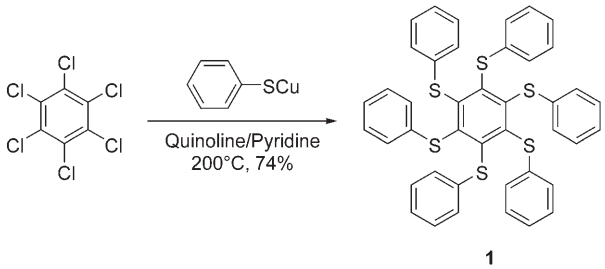
*Persulfurated arenes have been known for about 50 years but they were underexploited in chemistry in spite of facile, mild, and high-yielding syntheses. Their properties (redox potentials, UV/Vis absorption, conductivity, nonlinear optical properties, etc.) are mainly due to the aromaticity of the ring with $sp^2$-hybridized carbon atoms and to the electronic contribution from numerous divalent sulfur ligands, which also stabilize negative or positive charges. The characteristic conformational patterns of the sulfur ligands often facilitate preorganization in supramolecular assemblies, with or without thiophilic metal cations, for designing redox sensors, ion-selective membranes, clathrates, organic conductors, nonlinear optical materials, liquid crystals, coordination polymers, and bioinorganic systems. A new class of supramolecules with various molecular shapes such as asterisks, chains, wheels, and windmills were reported.*

**From the Contents**


| | |
|---|---|
| 1. Introduction and Historical Aspects | 1687 |
| 2. Synthesis, Scope, and Mechanistic Insight | 1688 |
| 3. Conformation and X-Ray Crystallography | 1695 |
| 4. Supramolecular Chemistry and Organometallic Assemblies | 1699 |
| 5. Advanced Organic Materials | 1703 |
| 6. Lubricants and Polymer Stabilizers | 1709 |
| 7. Biocides and Other Industrial Applications | 1709 |
| 8. Conclusion | 1709 |


## 1. Introduction and Historical Aspects

Aromatic rings persubstituted with sulfur ligands (thioethers) are intriguing and underexploited in chemistry. They have raised fundamental questions from theoretical, mechanistic, supramolecular, photophysical, and synthetic points of view because of their interesting physical organic properties (redox potentials, UV/Vis absorption, conductivity, liquid crystallinity, etc.), which are sometimes unexpected. For instance, they are electron acceptors in spite of a rich electronic density; their intense color and absorbance in the visible spectrum, their luminescence, their exothermicity and reactivity in the persulfuration of perhalogenated aromatic compounds are also noteworthy. The rich history behind the development of persulfurated arenes is worth mentioning, primarily because of important solvent issues that led to surprising results. For instance, in 1956 the first study of hexachlorobenzene with "mercaptides" in pyridine indicated that a reaction took place readily, but astonishingly, no persubstituted product was mentioned.[1] Three years later, an article entitled: "Reactions of Hexachlorobenzene with Mercaptides" did not report hexakis(alkylthio)benzene, but tetra- and disubstituted sulfurated products, from an "exothermic process" in ethanol.[2] After another 13 years, a Canadian team investigated the reactivity of perfluoroaromatic compounds toward thiolates in ethylene glycol/pyridine and obtained similar results.[3] Those disappointing results led to a serendipitous discovery through a temporary synthetic route. Hexakis(phenylthio)benzene (**1**) was the first reported compound in this series and was obtained by the reaction of hexachlorobenzene with phenylthiocuprate in a quinoline/pyridine mixture at $>200\,^{\circ}C$ (Scheme 1).[4] The goal of the study was to create Ar–S bonds, but the authors did not realize the importance of persulfurated arenes. Moreover,




**1**

***Scheme 1.*** First synthesis of hexakis(phenylthio)benzene (**1**).

there was "no need for $Cu^I$ catalyst" because most reactions could be run at 20 °C in polar solvents.

It took almost 20 years to find that polar aprotic solvents such as DMF (*N*,*N*-dimethylformamide), HMPA (hexamethylphosphoramide), or DMI (1,3-dimethyl-2-imidazolidinone) would have led to persubstituted arenes. In 1976, a Russian team carried out the persulfuration of perfluorinated biphenyl in DMF.[5] Peach and Musial reported nucleophilic substitutions of hexabromobenzene.[6] This chemistry was definitively launched following a plethora of publications on "hexa-hosts"[7,8] and from reports by Beck et al.[9a] and Peach and Rayner.[9b] The last two groups emphasized the need for polar solvents (DMF, THF/HMPA), but Beck et al. investigated for the first time persubstitution at room temperature. Finally, Tiecco and co-workers published a procedure with HMPA in 1980[10] and Peach and Crowell continued inves-

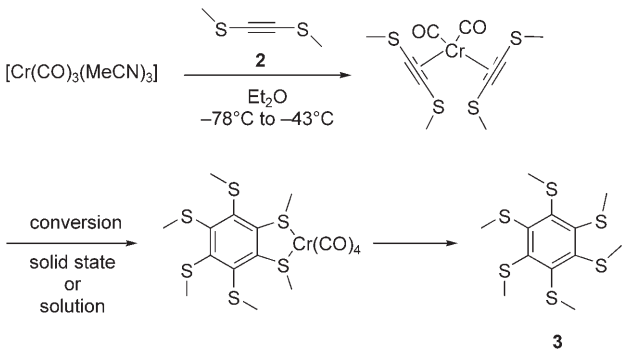
[*] Prof. Dr. M. Gingras, Dr. J.-M. Raimundo, Y. M. Chabre
Chemistry Laboratory of Organic and Metallic Materials (CMOM)
Faculty of Sciences, University of Nice-Sophia Antipolis
28 Av. Valrose, 06108 Nice Cedex 2 (France)
Fax: (+33) 4-9207-6578
E-mail: gingras@unice.fr

 © 2006 Wiley-VCH Verlag GmbH & Co. KGaA, Weinheim 

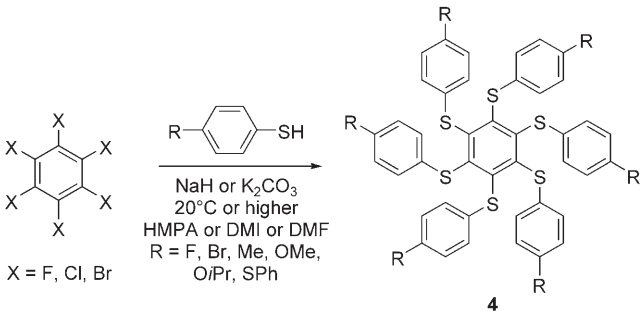
tigations into the "size effect of the thiolate anion".[11] Later on, persulfurated arenes were extensively studied by X-ray crystallography in host–guest chemistry by MacNicol and coworkers. His contribution to this field has been significant.

Interestingly, industrial investigations from the 1960s led the way to early applications of the biocide properties of hexakis(alkylthio)benzene and hexakis(arylthio)benzene.[12] In 1967, a patent entitled "Hexakis Thioethers" was filed with claims for new herbicides, insecticides, additives to lubricating oils, intermediates in dyestuffs and biologically active materials.[13,14] Several applications are known in supramolecular chemistry (self-assemblies, cryptands, etc.), in materials science (liquid crystals, conductive materials, ion-selective membranes, and asterisks), in physical organic chemistry (oxido-reduction, fluorescence, UV/Vis absorption, etc.), in some bioinorganic studies, and in newer industrial applications (lubricants, antioxidants for oil, etc.).

This Review focuses on persulfurated arenes in a broad sense, including their synthesis, properties, and applications. As "hexa-hosts" (clathrates, inclusion compounds) have already been reviewed,[15] this Review does not cover that field, and only persulfurated/persubstituted aromatic cores surrounded by divalent sulfur ligands (thioethers) will be discussed. Compounds incorporating only one or two heteroatoms in common persulfurated heteroaromatic cores will also be discussed.




***Scheme 2.*** Trimerization of **2** and generation of hexakis(methylthio)-benzene (**3**).




***Scheme 3.*** Nucleophilic aromatic substitutions of perhalogenated arenes.

## 2. Synthesis, Scope, and Mechanistic Insight

### 2.1. Synthesis

Until 1978, the use of thiocuprate in a quinoline/pyridine mixture at 200 °C was a common synthetic route to persulfurated arenes.[16] Two uncommon methods relied on the nucleophilic displacement of halogenated nitro substrates with thiolates[9] or on the trimerization of bis(methylthio)acetylene (**2**) in a chromium carbonyl complex to give hexakis(methylthio)benzene (**3**; Scheme 2).[17a]

Later on, two other strategies became predominant: nucleophilic aromatic substitution of perhalogenated arenes by thiolates (Scheme 3) and the formation of hexasodium benzenehexathiolate by reduction of hexakis(isopropylthio)-benzene (**5**) or hexakis(benzylthio)benzene (**6**) with $Na/NH_3$ or Na/HMPA and further alkylations, additions, or complexation with metals (Scheme 4).[18,19] The latter reduction strictly requires oxygen-free conditions because of the extremely facile oxidation of the product.

In nucleophilic substitution, the reaction time, temperature, and product distribution are dependent on the solvent. For example, hexachlorobenzene reacts with $CH_3SLi$ in DMF to produce hexakis(methylthio)benzene in 97 % yield[5] and with *i*PrSNa in DMF at 100 °C for 15 min to give hexakis(isopropylthio)benzene (**5**) in 93 % yield.[20] In less-polar solvents such as polyglycol ethers, the reactions of thiophenolate or ethanethiolate ions at 128 °C for 24 h generated persulfurated benzene in only 23 % yield.[21] The reaction of

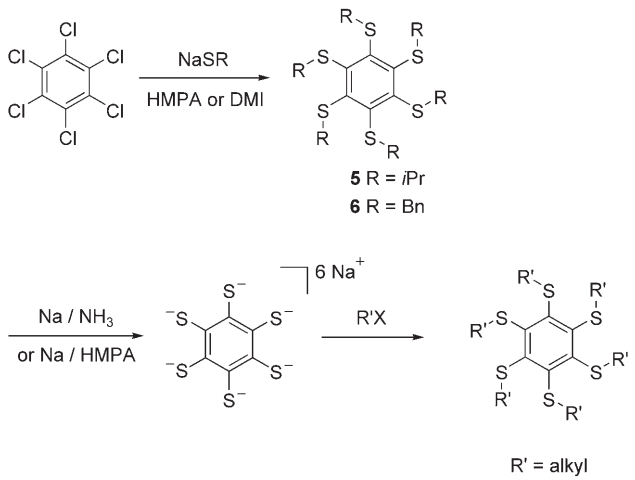


*Marc Gingras was born in Québec, Canada (1962). He obtained his BSc at the University of Sherbrooke (1984) and his PhD at Mc Gill University (Montréal). After postdoctoral studies at the Univ. of Wisconsin-Madison with Prof. Edwin Vedejs (1989–1991, synthetic methods) and with Prof. Laura L. Kiessling (1992–1993, glycochemistry/metathesis), he joined the group of Prof. Jean-Marie Lehn, Strasbourg (1993–1995, supramolecular chemistry). After a stay in Brussels (Belgium), he was appointed professor at the Univ. of Nice-Sophia Antipolis (France) in 1999.*



*Yoann M. Chabre was born in 1979 in Nice. He received his Master's degrees at the Univ. of Nice-Sophia Antipolis (France). He is currently completing his PhD under the guidance of Prof. Marc Gingras at the same university. His research interests are in the fields of organic synthesis, sulfur chemistry, and supramolecular chemistry.*

 © 2006 Wiley-VCH Verlag GmbH & Co. KGaA, Weinheim 




***Scheme 4.*** Generation and alkylation of hexasodium benzenehexathiolate.

$C_6F_6$ and $C_6Cl_6$ with alkylthiolates in pyridine, EtOH, or ethylene glycol provided mainly 2,3,5,6-tetrasubstituted products.[1–3] It was clear that protic solvents slowed down the reaction. HMPA was the best solvent for producing persulfurated benzene derivatives in a few hours from hexachloro- or hexafluorobenzene at only 20 or 0 °C.[19] In 1982, MacNicol described hexakis(β-naphthylthio)benzene and other persulfurated compounds by using DMI as a substitute for toxic HMPA.[22] Most publications now refer to DMI as solvent.

### 2.2. Nucleophiles

Thiolate anions were the most studied nucleophiles, and the reactivity of many perhalogenated arenes was confirmed in highly polar solvents at room temperature or below (e.g. $C_6F_6$, $C_6Cl_6$, and $C_6Br_6$).[19,22] Importantly, most alkyl- or arylthiolate anions efficiently react with perhalogenated arenes. However, high temperatures and reaction times of several days were usually required to prepare hexakis(aryloxy)benzene compounds,[23] and yields were often poor to modest. Beside thiolates, aryl and alkyl selenide anions can be used successfully.

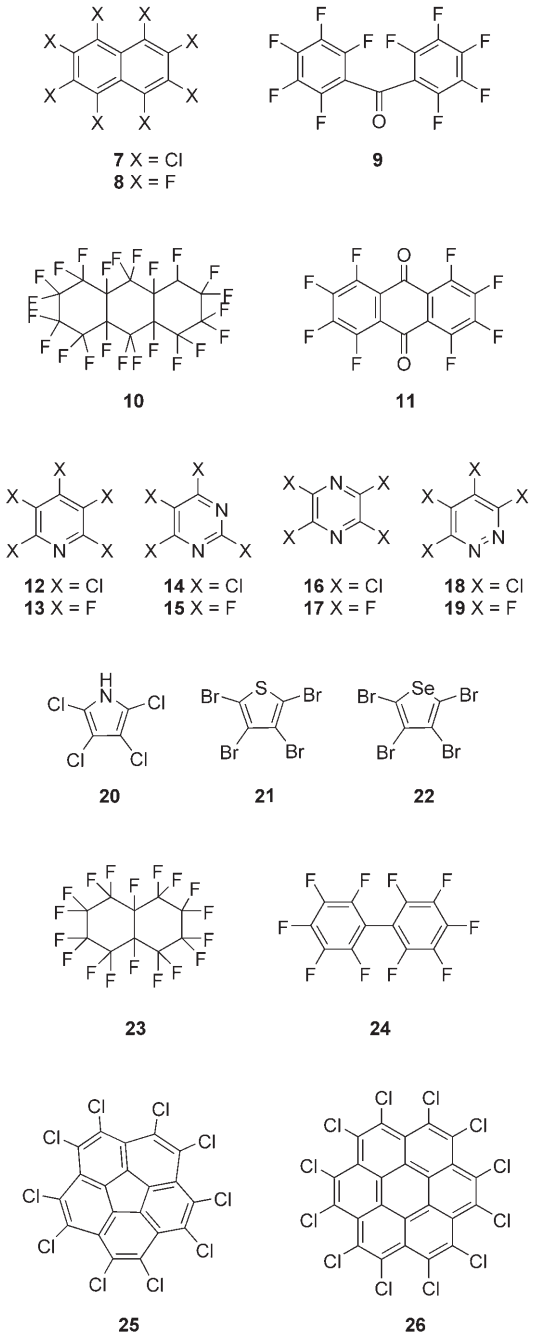


*Jean-Manuel Raimundo was born in Redon, France (1973). He obtained a BSc (biochemistry) at the Univ. of Rennes and a PhD at the Univ. of Angers (France) with Dr. Jean Roncali (1999; organic materials for optoelectronic devices). After postdoctoral studies with Prof. François Diederich (ETH, Zürich, 2000), he took up a one-year academic position at the Univ. of Angers (2001). After further postdoctoral studies at Angers (collaboration with TotalFina Elf; 2002), he was appointed Maître de Conférences at the Univ. of Nice (2003). His research involves supramolecular chemistry and organic synthesis and materials.*

### 2.3. Perhalogenated Non-Benzene Arenes and Heteroarenes

Scheme 5 lists common perhalogenated monocyclic, heterocyclic, and polycyclic aromatic compounds used in aromatic persulfuration with thiolate anions. These nucleophilic persubstitutions belong to a broad family of mild reactions, with a somewhat wide scope of thiolate anions and perhalogenated arenes.

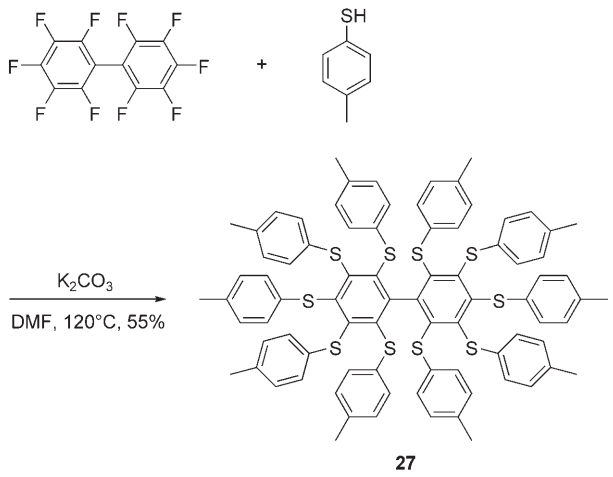
Among early reports, it was mentioned in 1976 that perfluorinated biphenyl reacted with *p*-thiocresol and $K_2CO_3$ in DMF at 120 °C to form persulfurated biphenyl derivatives.




***Scheme 5.*** Perchlorinated arenes and perfluorinated cores used in the persulfuration.

 © 2006 Wiley-VCH Verlag GmbH & Co. KGaA, Weinheim 

It was the first example with polycyclic arenes (Scheme 6).[5] Later, octakis(phenylthio)naphthalene (**31**) was recrystallized in two forms (see Section 3).[24] The use of octafluoronaphthalene (**8**) demonstrated a reaction under mild conditions at

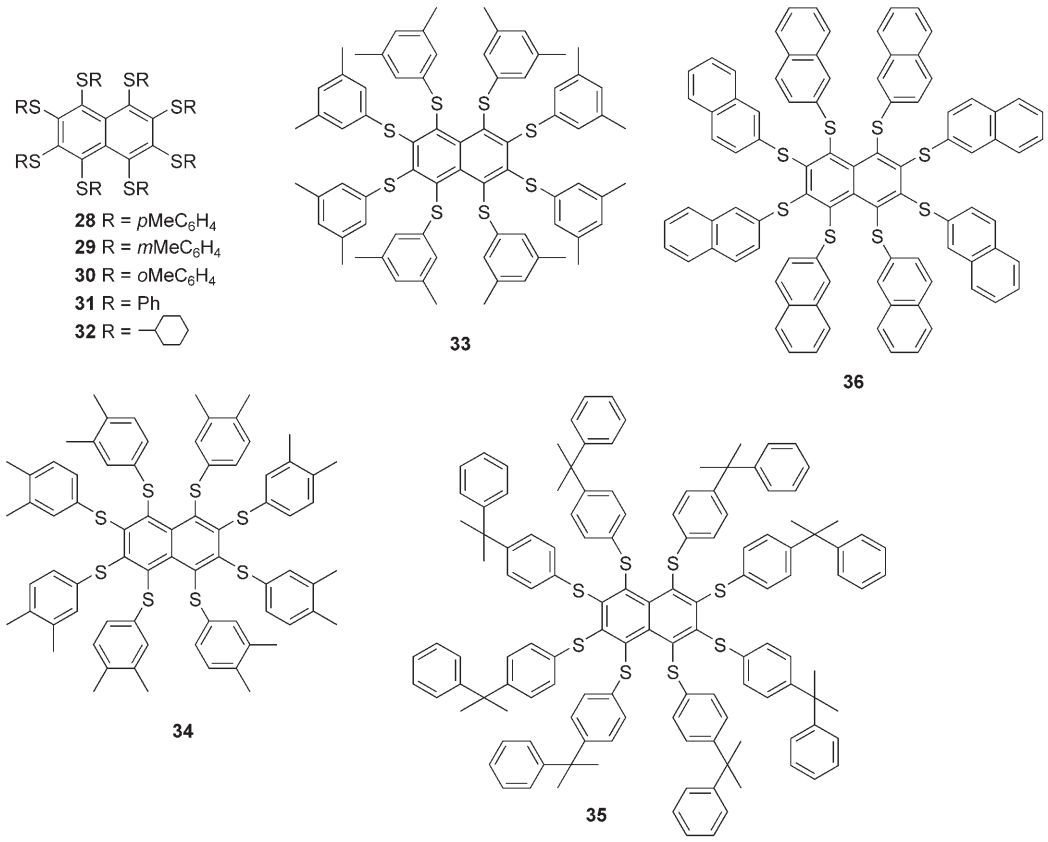



***Scheme 6.*** First persulfuration of polycyclic arenes.

20 °C in DMI with thiophenolate anions. Pressure-induced color and conformational changes are noteworthy. Hoping to find a new class of liquid crystals, some octakis(alkylthio)-naphthalenes with $C_5$, $C_{12}$, or $C_{16}$ alkyl chains were prepared, but no mesogenic phase was found.[25] Several other derivatives were produced for conformational and structural analysis by X-ray crystallography.[26] Other derivatives were also synthesized from octachloronaphthalene (**7**) in DMF.[27] An extensive study on nucleophilic substitutions of perchloro- and perfluoronaphthalene described the effect of several reaction parameters (thiolate/perhalogenated naphthalene ratio, solvent, temperature, thiolate, etc.) on the substitution pattern, regioselectivity, and number of halogen atoms displaced.[28]

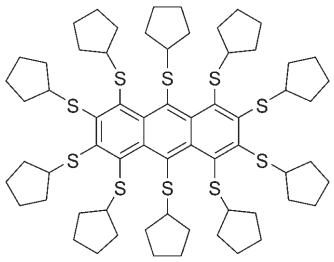
It was also shown that perfluorodecalin (**23**; Scheme 5) reacted with arylthiolates at 60–70 °C to produce octakis-(arylthio)naphthalenes through an unexpected reactivity of polyfluoroalkanes.[29] It was highly intriguing, as perfluoalkanes are generally chemically inert. Related work reported a photosensitized defluorination to unsaturated perfluorocarbons, followed by a reaction with phenylthiolate anions in DMI at room temperature.[30] Scheme 7 shows some known persulfurated naphthalene compounds. Following the same trend, decakis(cyclopentylthio)anthracene (**37**) was prepared from perfluoroperhydroanthracene (**10**), and conformational studies were carried out (see Section 3).[31]

In 1988, MacNicol and co-workers published the first synthesis of dodecachlorocoronene (**26**) under efficient chlorination conditions with $AlCl_3/S_2Cl_2$ in $SO_2Cl_2$ in more than 95 % yield.[32] This important preparation opened new routes toward highly functionalized derivatives in a minimum number of synthetic steps. For instance, persulfuration with



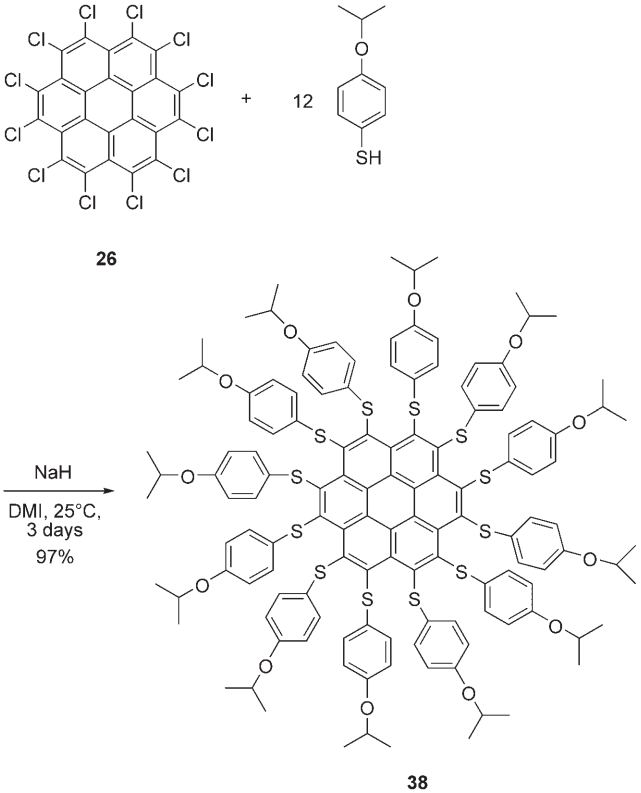

***Scheme 7.*** Some persulfurated naphthalene derivatives.

 © 2006 Wiley-VCH Verlag GmbH & Co. KGaA, Weinheim 



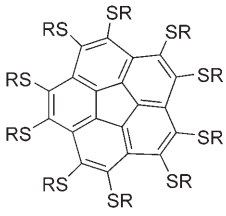
37

various arylthiolates (24 equiv) in DMI generated persubstituted coronene derivatives in excellent yields at 20 °C. Further work was published by the same group[33] and by Lehn et al. in 1997.[34] In 1998 and 2004, Gingras and co-workers introduced the concept of templated coronene functionalization for making "molecular asterisks"; they optimized the procedure by decreasing the excess of thiolate anions (to 14.4 equiv) and obtained, in some cases, an almost quantitative yield of products with 12 consecutive substitutions, each averaging 99.98 % yield (Scheme 8).[35] Some physical organic properties were determined, including UV/Vis absorption and spectroelectrochemical behavior, by using cyclic voltammetry coupled with UV absorption measurements.

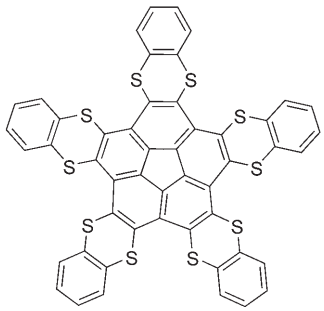



***Scheme 8.*** Persulfuration of dodecachlorocoronene (**26**).

Recently, another aromatic system included nonplanar decachlorocorannulene (**25**),[36] which was persulfurated at about 20 °C in DMI.[37] Various decakis(alkylthio)corannulenes **39**–**41** and pentakis(1,4-benzodithiino)corannulene (**42**)



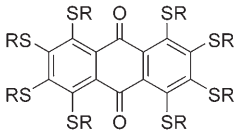

**39** R = $nC_3H_7$
**40** R = $nC_6H_{13}$
**41** R = $nC_{12}H_{25}$



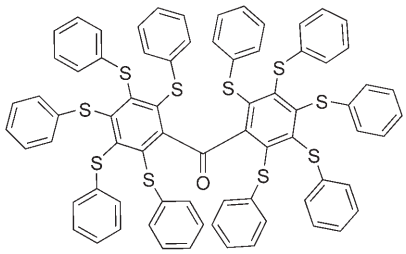
**42**

were prepared for studying complexation of fullerenes with concave aromatic hosts as molecular bowls with multiple arms and flaps. The possibility of making discotic liquids crystals was mentioned.

Per(alkylthio)-substituted 9,10-anthraquinones **43**–**46** were prepared from octafluoroanthraquinone (**11**) in the



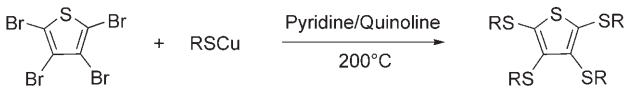

**43** R = $nC_8H_{17}$
**44** R = $nC_{12}H_{25}$
**45** R = $nC_{16}H_{33}$
**46** R = $SO_2C_{12}H_{25}$



**47**

presence of alkylthiolates in DMI.[38] An interesting aspect would have been their redox properties, knowing that anthraquinone systems were popular redox units. Similarly, octakis(phenylthio)benzophenone (**47**) was also produced as a host molecule for clathrate formation.[39]

Persubstituted alkylthiothiophenes **49**–**52** (Scheme 9) were described as biocides or as donor-type organic con-




**48**

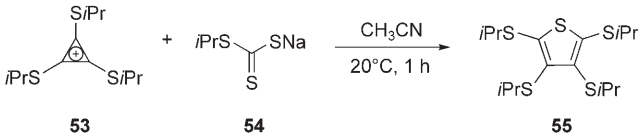
**49** R = $iC_3H_7$
**50** R = $nC_4H_9$
**51** R = $nC_{12}H_{25}$
**52** R = $nC_{24}H_{50}$

***Scheme 9.*** Synthesis of tetrakis(alkylthio)thiophene.

ductors (Section 5.1). The first preparations involved the reaction of tetrabromothiophene (**48**) with mercaptocuprates in a quinoline/pyridine mixture at high temperatures.[40] Tetrakis(isopropylthio)thiophene was also generated in 89 % yield from the cyclopropenyl cation **53** in the presence of the thionocarbonate **54** (Scheme 10).[41]

The reaction of bis(methylthio)acetylene (**2**) with $S_2Cl_2$/$AlCl_3$ generated the radical cation of tetrakis(methylthio)-

 © 2006 Wiley-VCH Verlag GmbH & Co. KGaA, Weinheim 

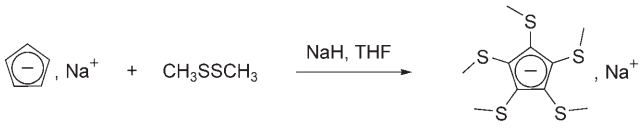



53 54 55

***Scheme 10.*** Synthesis of tetrakis(isopropyl)thiophene (**55**).

thiophene,[42] from which ethylenedithio-substituted thiophene systems were prepared by electrophilic substitution with 1,2-ethanedisulfenyl chloride.[43] Further discussions are presented in Section 5.1 on organic conductors and TTF-type (TTF = tetrathiafulvalene) donors.[44] Direct electrophilic thiomethylation of thiophene with clays and dimethyl disulfide produced tetrakis(thiomethyl)thiophene in 50% yield.[45] Later on, similar methods with montmorillonite clays were used for the formation of Ar–S bonds.[46] Tetrakis(trifluoromethylthio)thiophene was also prepared from bis(trifluoromethylthio)acetylene with sulfur at 120 °C[47] and by photolysis.[48] Persulfurated selenophene was reported for the first time in 1995 in some tetrathiafulvalene (TTF) units fused to selenophene for investigating conductive charge-transfer complexes.[49]

Charged persulfurated aromatic compounds include the cyclopentadienyl anion and the cyclopropenyl cation. In an attempt to prepare organic conductors, pentakis(methylthio)cyclopentadiene anions were produced in 1981[50] by reacting sodium cyclopentadienyl with NaH and dimethyl disulfide (Scheme 11). Other substituted cyclopentadienes with methylthio- or arylthio- groups were also reported.[51] However, most studies involved metallocene complexes with Mn, Ru, Rh, etc.[52]



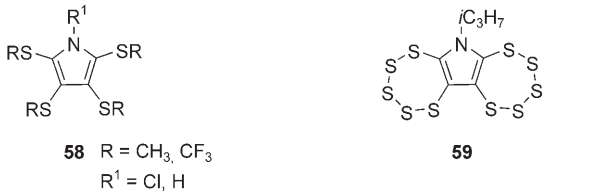

56 57

***Scheme 11.*** Synthesis of the pentakis(methylthio)cyclopentadienyl anion **57**.

Persulfurated cyclopropenyl cations (tris(*tert*-butylthio)- and tris(isopropylthio)cyclopropenyl) were first reported in 1992 in the preparation of nitrogen-containing heterocycles.[53]

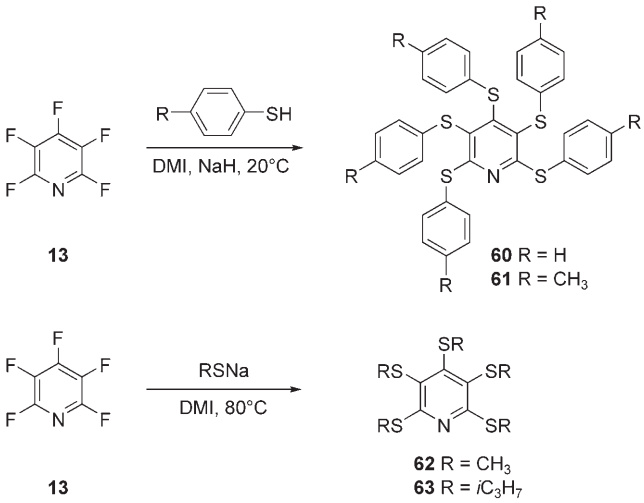
Persulfurated aromatic N-heterocycles include pyrrole, pyrazine, pyridazine, pyrimidine, and pyridine. Nitrogen-containing polycyclic arenes with a persulfurated structure are rare. Our search for monocycles were limited to those containing one or two nitrogen atoms in the ring. N-substituted tetrakis(trifluoromethylthio)pyrroles,[54] N-substituted tetrakis(methylthio)pyrrole,[55] and other N-substituted derivatives[56] **58** were described as potent agrobiochemicals (fungicides, herbicides, insecticides). Most syntheses relied on electrophilic sulfenylation of pyrrole.

Treatment of *N*-isopropyl pyrrole with sulfur monochloride led to **59**, which contains two pentathiepins fused with a pyrrole core.[57] As shown in Scheme 12, pentakis-




**58** R = $CH_3$, $CF_3$; $R^1$ = Cl, H

**59**




**13**

**60** R = H
**61** R = $CH_3$

**13**

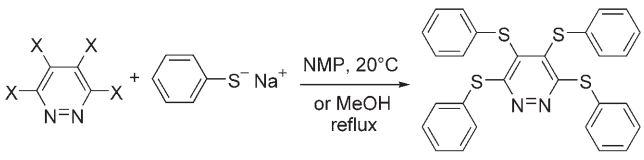
**62** R = $CH_3$
**63** R = $iC_3H_7$

***Scheme 12.*** Synthesis of persulfurated pyridine derivatives.

(arylthio)pyridines **60–61** were prepared from pentafluoropyridine (**13**) and arylthiolates in DMI at room temperature and evaluated in clathrate formation[58] and in electroreduction.[34] Another study described high-yield preparations of pentakis(methylthio)pyridine (**62**) and pentakis(isopropylthio)pyridine (**63**) from pentafluoropyridine (**13**) in DMF at 80 °C (Scheme 12).[59] Pentachloropyridine (**12**) was described as less reactive than pentafluoropyridine (**13**) toward methanethiolate anions,[57] but the reaction conditions used in the comparison were not identical.[9a]

The preparation and properties of tetrakis(trifluoromethylthio)pyrimidines were also reported.[60] Persulfurated pyridazine derivatives were prepared from tetrafluoropyridazine (**18**).[61] Patents described the preparation of pesticides by treating perfluoro- (**18**) or perchloropyridazine (**19**) with sodium thiophenolate or sodium alkylthiolates, either at room temperature in *N*-methyl-2-pyrrolidinone or in boiling MeOH (Scheme 13).[62]

Research on persubstituted pyrazines with sulfur ligands was directed toward new organic conductors and semiconductors (Section 5.1). Of special interest were pyrazine-fused bis-TTF, bis-*p*-dithino, and thianthrene-type systems. Poly-



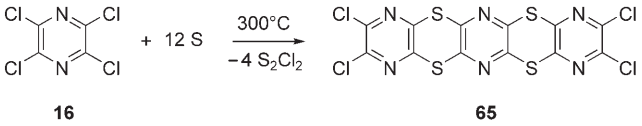

**18** or **19**

**64**

***Scheme 13.*** Synthesis of persulfurated pyridazines. NMP = *N*-methyl-2-pyrrolidinone.

 © 2006 Wiley-VCH Verlag GmbH & Co. KGaA, Weinheim 

cyano-*p*-dithiino pyrazine compounds were described as fungicides and bactericides.[63] Syntheses and persulfurations of tetrachlorotetraazathianthrene and higher homologues were also reported in a patent (Scheme 14).[64]

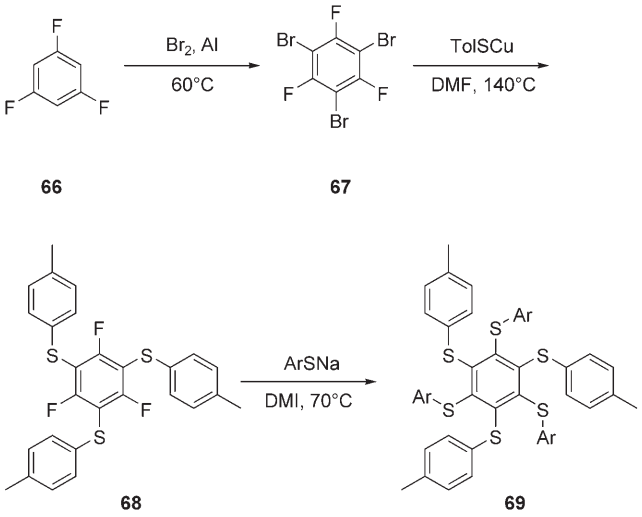



16 65

***Scheme 14.*** Example of the preparation of tetrachlorotetraazathianthrene derivatives.

### *2.4. Persulfurated Arenes with Mixed Sulfur Ligands*

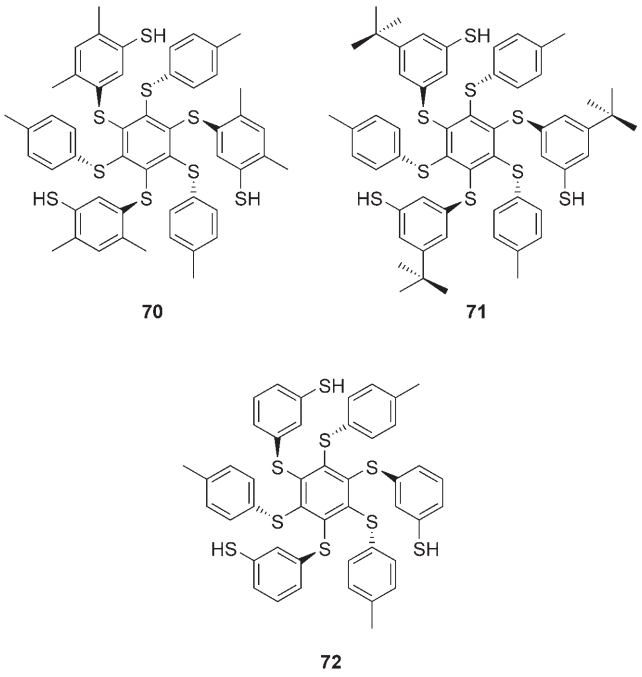
There are only a few examples of mixed persulfurated aromatic derivatives incorporating two different divalent sulfur ligands. Three strategies dealt with a benzene core. During a first bioinorganic and biomimetic study of iron–sulfur protein clusters, the preparation of a convergent tridentate tris-sulfanylated ligand required *p*-tolylthio groups at C1, C3, and C5 of the benzene ring and the remaining sulfanylated ligands at C2, C4, and C6.[65] The key intermediate, 1,3,5-tribromo-2,4,6-trifluorobenzene (**67**),[66] was prepared by bromination ($Al/Br_2$) of 1,3,5-trifluorobenzene (**66**). The chemoselectivity of Br versus F substituents toward *p*-tolylthiocuprate was exploited in the selective displacement of Br substituents to afford 1,3,5-trifluoro-2,4,6-tris(*p*-tolylthio)benzene (**68**). Reaction of the latter compound with appropriate thiolate anions generated mixed persulfurated benzene derivatives **69** (Scheme 15). Several other compounds of this type, **70**–**72**, were prepared in 1990.




66 67 68 69

***Scheme 15.*** Strategy for the synthesis of mixed persulfurated benzene compounds.

A second strategy was used for making a reducible macrobicyclic ligand with a benzene core with different arylthio groups.[67] The method relied on the selective formation of 1,4-difluoro-2,3,5,6-tetraphenylthiobenzene



70 71 72

(**76**) and selective nucleophilic displacement of fluorine atoms by arylthio groups (Scheme 16).

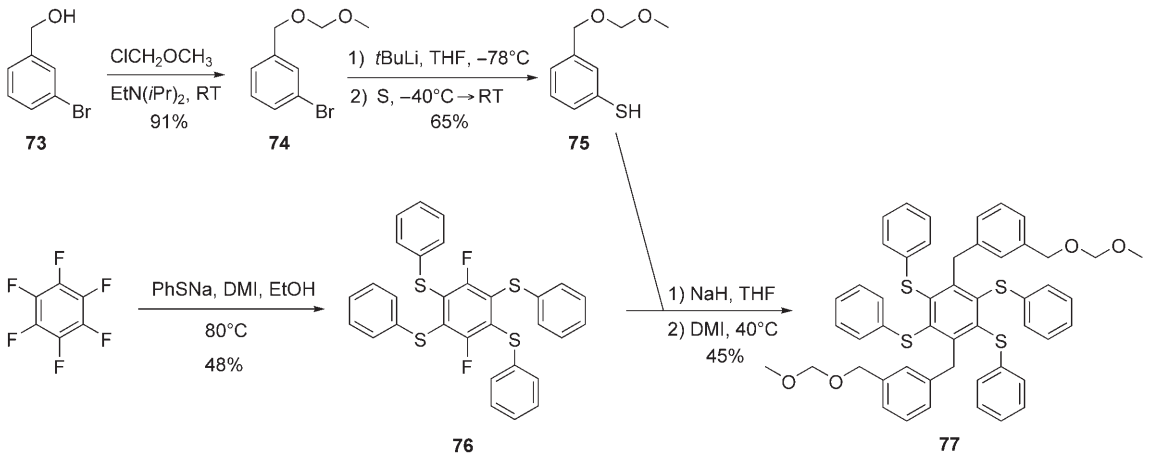
Several other examples in which hexasodium benzenehexathiolate, benzenehexathiol, or derivatives served as precursors for introducing different sulfur ligands in a stepwise manner, especially in the work by Fanghänel and co-workers, are known for making donor-type conductors (Section 5.1). In the dealkylation of hexakis(alkylthio)benzene, it was possible to introduce SH and SR groups onto a benzene core.[10] In the case of naphthalene, several derivatives incorporating mixed SH, SR, SR′ groups were described.[28]

### *2.5. Mechanistic Insight*

Until now, few detailed mechanistic studies were reported for the persulfuration of arenes by nucleophilic displacement, but a rich compilation of data toward persulfurated benzene derivatives suggested a specific sequence of reactivity and regioselectivity. An important observation is that disubstituted 1,4-bis(mercapto)benzene (**79**), tetrasubstituted 2,3,5,6-tetrakis(mercapto)benzene (**81**), and hexakis(mercaptobenzene) (**83**), are usually the main products isolated; the same results are obtained with aryl- or alkylthiolates (Scheme 17).

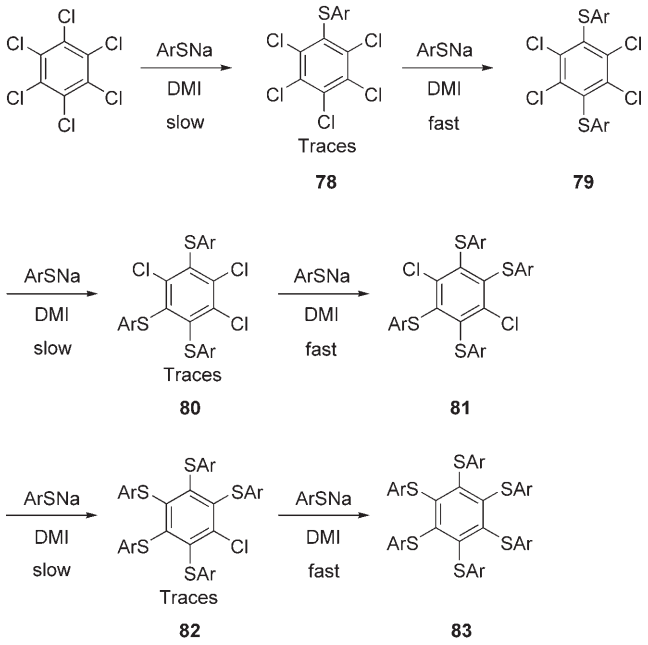
Sulfur substituents are *para* directing, and only traces of products from mono-, tri-, or pentasubstitutions were observed; **78**, **80**, and **82** are thus usually produced as minor components. It was also noticed that chloro, alkylthio-, or arylthio groups accelerated nucleophilic aromatic substitutions. The most sulfur-substituted compounds required milder conditions. No study delineated the mechanism by which each consecutive substitution occurs. As the number of alkyl or arylthio substituents increases, combined with the negative-charge-stabilizing effect of sulfur atoms and the relatively low

 © 2006 Wiley-VCH Verlag GmbH & Co. KGaA, Weinheim 



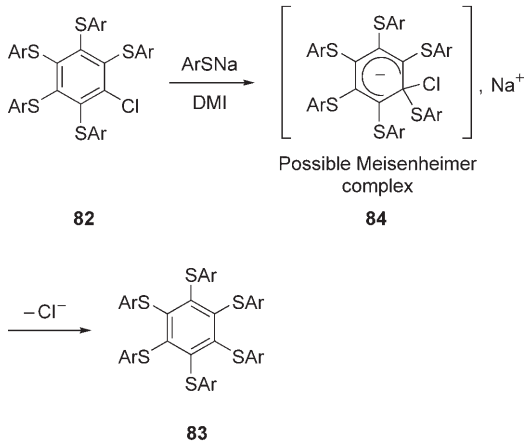

**73** **74** **75** **76** **77**

***Scheme 16.*** Synthetic strategy for the preparation of **77**.



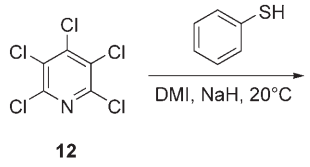

**78** **79** **80** **81** **82** **83**

***Scheme 17.*** Hypothetical mechanism for the persulfuration of hexachlorobenzene.

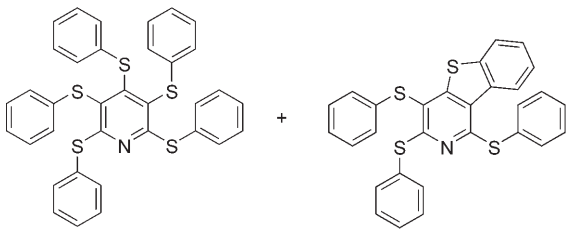



**82** **84** **83**

***Scheme 18.*** Hypothetical $S_NAr$ mechanism in the last step of persulfuration.




**12**



**60** **85**

***Scheme 19.*** Persulfuration of pentachloropyridine. By-product **85** suggests a radical mechanism.

reduction potentials of persulfurated arenes, it would not be unreasonable that a stabilized Meisenheimer complex could be formed, as is usual in an $S_NAr$ mechanism (Scheme 18), but it could also be suggested that a change to a radical or an electron-transfer mechanism ($S_{RN}$) could operate, taking into account difficulties in the preparation of hexakis(*p*-nitrophenylthio)benzene.[68] Nitrobenzene derivatives are known to inhibit $S_{RN}$ mechanism (for example, *p*- or *m*-dinitrobenzene were used as inhibitors of $S_{RN}$). For instance, MacNicol et al. reported the inhibition of persulfuration of pentachloropyridine with thiophenolate anions in the presence of *m*-dinitrobenzene. In another experiment, the ratio of a by-product was dependent on light conditions; low yields were obtained in the dark (Scheme 19).[58]

Additionally, because disulfide by-products are often obtained (from the oxidation of thiolate anions), in the presence or absence of air, it was also indicative of a possible electron-transfer process and oxidation. Another interesting observation was arylthiolate ligand exchange onto a benzene

 © 2006 Wiley-VCH Verlag GmbH & Co. KGaA, Weinheim 

core from hexakis(arylthio)benzene in the presence of other thiolate salts, which resembles a "sulfur dance" around a benzene core.[34] A report on the reactivity and regioselectivity of the sulfuration of octafluoronaphthalene was among rare publications in the field of persulfurated arenes, and several reaction parameters were studied: thiolate ion, temperature, solvent, and stoichiometry.[30]

## 3. Conformation and X-Ray Crystallography

Crystallographic analyses were carried out mostly on persubstituted arylthio arenes, and little data is available for their alkylthio analogues. In 1976, one of the first studies was reported for hexakis(phenylthio)benzene (**1**; Scheme 1).[7a] Its conformational preference in the solid state showed an up and down alternating pattern of the thiophenyl groups, above (*a*) and below (*b*) the plane of the central benzene ring (*ababab*; Figure 1). A torsion angle of 56° between C1 and C3 allows orbital overlap between a lone pair of electrons on the sulfur atom and the central aromatic π system. Recent studies confirmed this preferred conformation.[69]

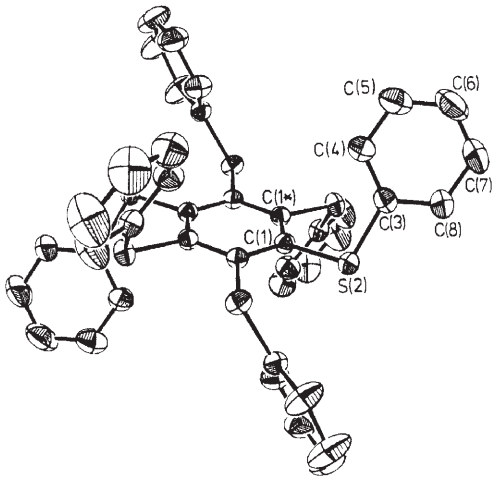



***Figure 1.*** Hexakis(phenylthio)benzene (**1**). Reproduced, with permission, from reference [15].

Overall, most persulfurated benzene compounds retain the alternating up and down substitution pattern,[15] although some exceptions exist: hexakis(β-naphthylthio)benzene (**86**) (Figure 2; *aabbab*)[22] or hexakis(2-methylphenylthio)benzene (*aabbab*).[70]

Hexakis(methylthio)benzene (**3**; Scheme 2) showed an *aaabbb* pattern in the solid state[71] but a sharp singlet for $CH_3$ groups in the $^1H$ or $^{13}C$ NMR spectra at −75 °C, indicating a structure of high symmetry, probably an *ababab* pattern in solution (Figure 3).[9b] However, the free energy difference between various conformers is probably low according to some calculations[68] and $^{13}C$ NMR spectroscopic studies,[72] in such a way that crystal-packing effects are probably responsible for those exceptions. Studies approximated an energy barrier of 3–4 kJ mol$^{-1}$ in favor of an *ab* pattern for *ortho* SMe groups.

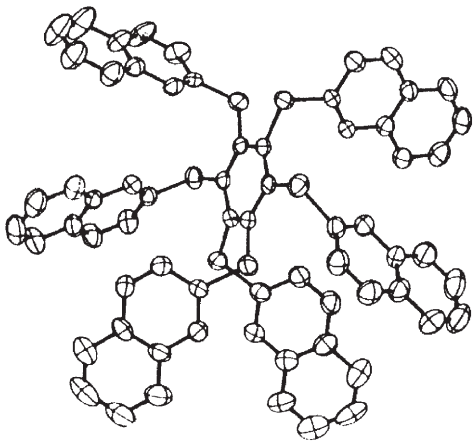


***Figure 2.*** Hexakis(β-naphthylthio)benzene (**86**) in its 1,4-dioxane channel-type inclusion compound with *aabbab* conformation. Reproduced, with permission, from reference [22].

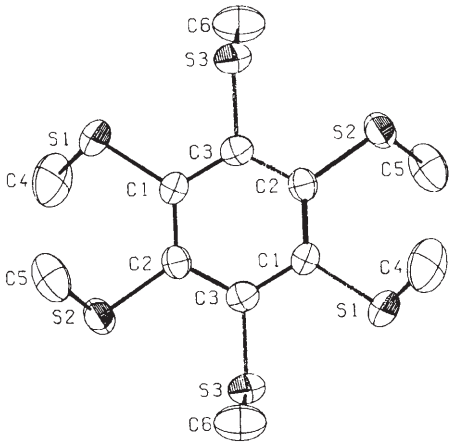



***Figure 3.*** ORTEP plot (50% probability) of the molecule $C_6(SCH_3)_6$ (**3**) in the solid state viewed perpendicular to the $C_6$ plane. Reproduced, with permission, from reference [71].

On the basis of ESR studies on hexakis(*iso*propylthio)benzene (**5**), the authors suggested significant conjugative interaction between the π system of the benzene core and the lone pairs of electrons of the sulfur atoms.[73] In another context, a Pummerer-type rearrangement was proposed in a σ-delocalized hexakis(methylthio)benzene dication in the presence of a strong acid; calculations at the RHF/3-21G* and then at the B3LYP/6-31G* level indicated the most stable conformation to be *ababab*.[74] Bis(tetrakis(methylthio)-benzo)[*c*,*g*] (1,2,5,6)-tetrathiocin (**87**) was analyzed by X-ray diffraction and indicated for each benzene ring an alternating pattern *ababba*, but disulfide bridges modified the expected conformation at these positions (Figure 4).[75]

MM3 calculations of more-complex structures, such as second- and third-generation thiophene-based molecular asterisks (Section 4.1), indicated an *ababab* pattern of the thiophene arms. A similar conformation was also found in X-ray crystal-structure analysis of hexakis(*p*-hydroxyphenoxy)-benzene, an oxygenated asterisk analogue.[76] Although compounds **88** and **89** are not persulfurated arenes, it is note-


© 2006 Wiley-VCH Verlag GmbH & Co. KGaA, Weinheim

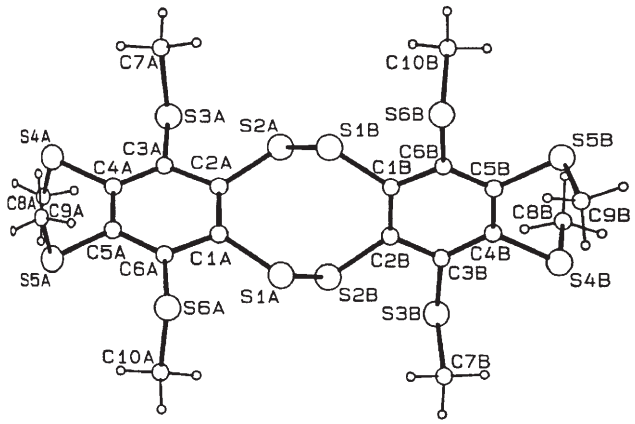



***Figure 4.*** Bis tetrakis(methylthio)benzo[*c*,*g*] (1,2,5,6)-tetrathiocin (**87**) with an alternating *ababba* pattern. Reproduced, with permission, from reference [75].

worthy that pentakis(phenylthio)benzene units adopt *abbba* (as in **88**) or *ababa* (as in **89**) conformations in more-complex structures (Figures 5 and 6).[77]

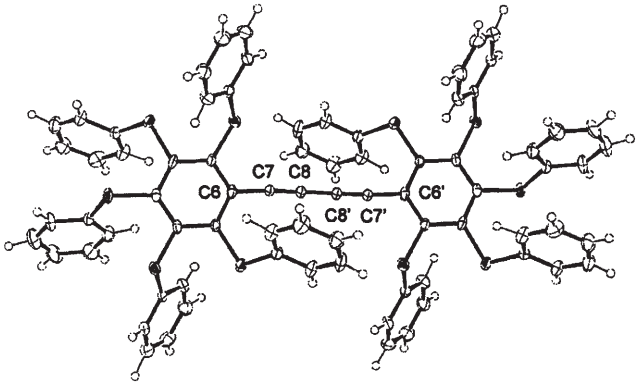



***Figure 5.*** 1,4-Di(penta(*p*-tertiobutylthiophenyl))phenyl-buta-1,3-diyne (**88**) and its *abbba* conformation. Reproduced, with permission, from reference [77].

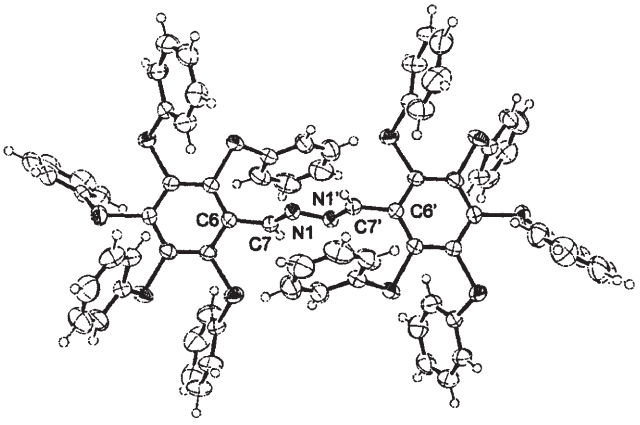



***Figure 6.*** *trans*,*trans*-Decathiophenylbenzaldehyde azine (**89**) and its *ababa* conformation. Reproduced, with permission, from reference [77].

Theoretical calculations and X-ray crystal-structure analysis of benzene hexathiolate $(C_6S_6)Li_6$ recently revealed that the hexaanion exhibited pronounced aromaticity and electron delocalization in the central benzene ring, with a preference for a minimum with $D_{6h}$ symmetry.[78]

Holm et al. cleverly utilized the cavitand concept and the *ababab* conformation to prepare a series of biomimetic iron–sulfur protein clusters (Figure 7). A conformationally con-

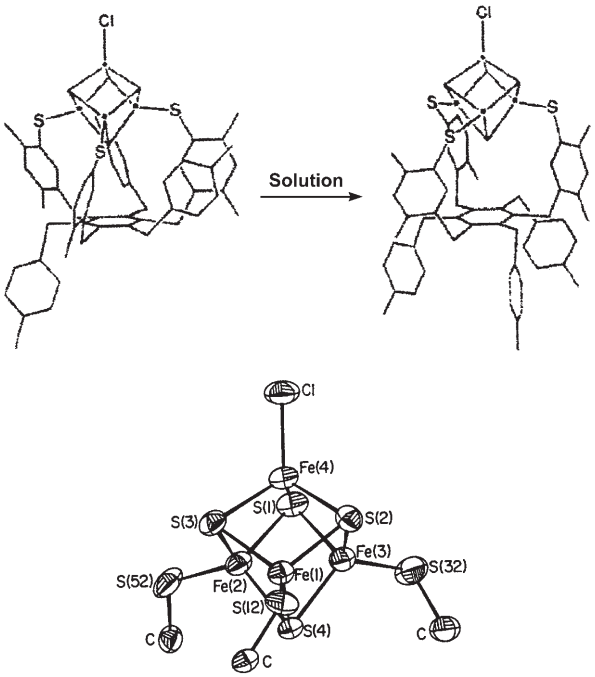


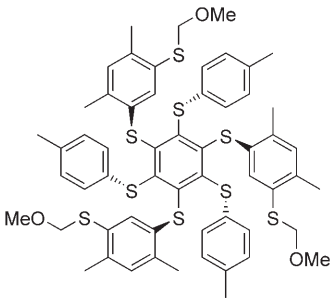

***Figure 7.*** Conformation and X-ray crystal structure of biomimetic iron–sulfur cubane-type clusters. Reproduced, with permission, from references [65, 79].

trolled and semirigid tridentate ligand with three convergent sulfanyl groups acts as a tripodal ligand above the plane of the benzene core. This tridentate ligand originated from C1, C3, and C5 of the benzene ring and "dummy" *p*-tolylthio substituents were located at the remaining C2, C4, and C6 positions. "Dummy ligands" helped to preorganize the tridentate ligand for making electroactive and specific iron–sulfur cubane-type clusters.

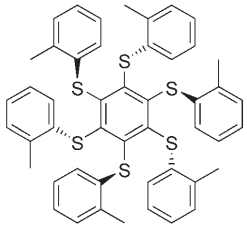
In the solid state, complexes showed an unprecedented *aaaaab* conformation[79] but in solution, $^1$H and $^{13}$C NMR spectroscopic data indicated the usual *ababab* conformer.[65,70,80] Conformations of free tridentate ligands in **90** (*abbabb*)[65] and in **91** (*bbaaab* and *baabab*)[70] represent other exceptions to the *ababab* pattern; however, in solutions at temperatures above 210 K, $^1$H and $^{13}$C NMR spectra suggest a probable *ababab* pattern. Crystal-packing effects are probably again responsible for this behavior.

The first X-ray crystal-structure studies of naphthalene derivatives were those of octakis(β-naphthylthio)naphthalene (**36**) and octakis(phenylthio)naphthalene (**31**).[24] The polymorph **31** crystallized under two unsolvated forms: red and yellow, the interconversion of which is dependent on pressure (Figure 8). Red crystals are achiral and showed an almost

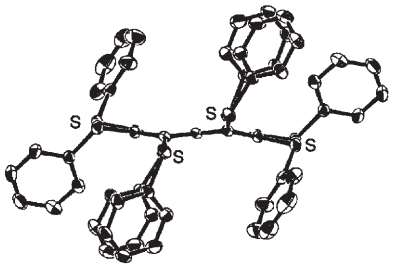
 © 2006 Wiley-VCH Verlag GmbH & Co. KGaA, Weinheim 



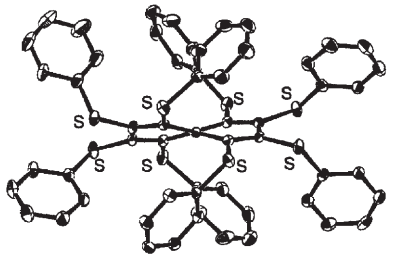
90



91



Red form



Yellow form

***Figure 8.*** X-ray crystal structures of two unsolvated forms of polymorphic compound **31**. Reproduced, with permission, from reference [81].

planar naphthalene core with an *aababbab* pattern of substituents relative to the mean plane of the core. The yellow crystals are chiral, and the naphthalene ring is severely twisted by 31° around the bond at the ring fusion. Adjacent arms alternate as up and down pairs around the core (*aabbaabb*). Thermochemical studies confirmed polymorphism and indicated a first melting temperature ($T_{m1}$) of the yellow form at 174.5 °C and a second of the red form at 201.3 °C ($T_{m2}$).[81]

It was later found that derivatives of octakis(phenylthio)naphthalenes could exist under different conformations. For instance, octakis(*p*-tolylthio)naphthalene (**28**; Figure 9) showed an *abbabaab* pattern, whereas **29** (*aabbaabb*, Figure 10), **33** (*abbaabab*, Figure 11),[82] **34** (*aabbaabb*, Figure 12),[83] and **35** (*abbbabbb*, Figure 13)[84] presented different patterns. Low activation energy between conformers was suggested by AM1 calculations[85] and crystal-packing effects probably contributed to those results.

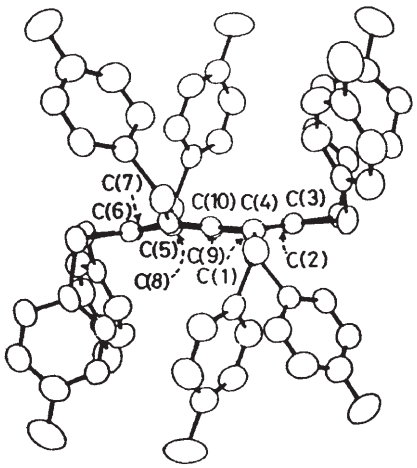



***Figure 9.*** Octakis(*p*-tolylthio)naphthalene (**28**) in its dioxane-solvated form with conformation *abbabaab*. Reproduced, with permission, from reference [26].

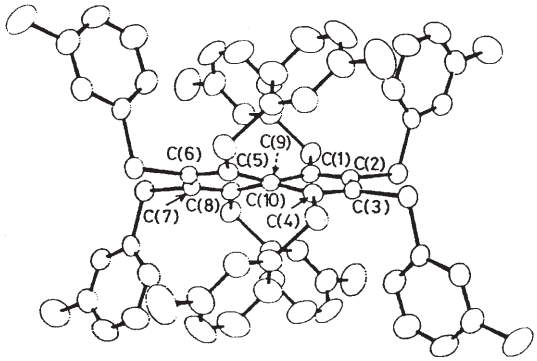



***Figure 10.*** Edge-on view of octakis(*m*-tolylthio)naphthalene (**29**) in the unsolvated crystal (conformation *aabbaabb*). Reproduced, with permission, from reference [26].

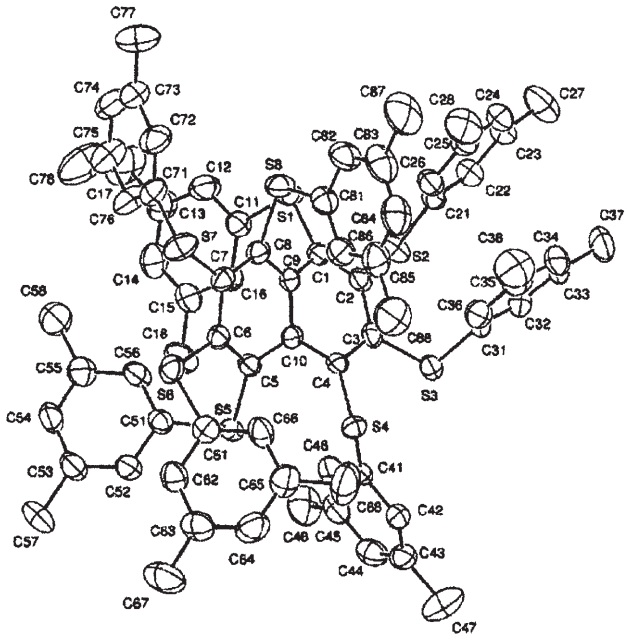


***Figure 11.*** Structure of octakis(3,5-dimethylphenylthio)naphthalene (**33**) in its unsolvated crystal with conformation *abbaabab*. Reproduced, with permission, from reference [82].

 © 2006 Wiley-VCH Verlag GmbH & Co. KGaA, Weinheim 

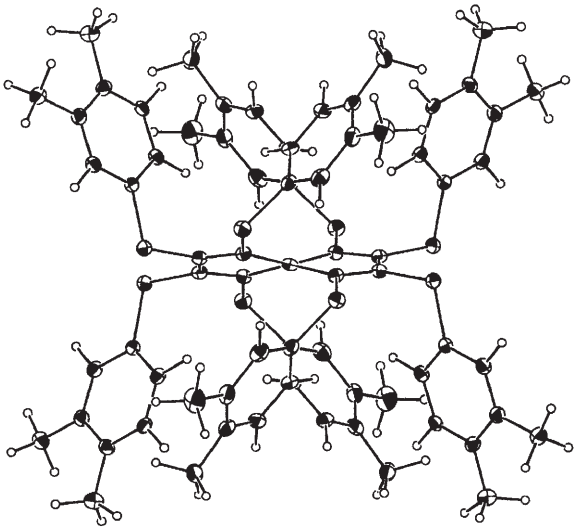


*Figure 12.* Structure of octakis(3,4-dimethylphenylthio)naphthalene (**34**) in its $Et_4Pb$ clathrate with conformation *aabbaabb* ($D_2$-symmetric conformation). Reproduced, with permission, from reference [83].

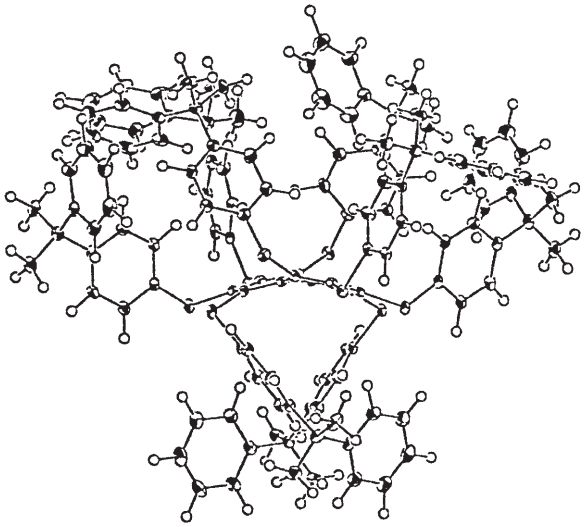


*Figure 13.* Octakis(4-(2-phenylpropan-2-yl)phenylthio)naphthalene (**35**) with conformation *abbbabbb* (its adduct with acetone (1:1) is triclinic). Reproduced, with permission, from reference [84].

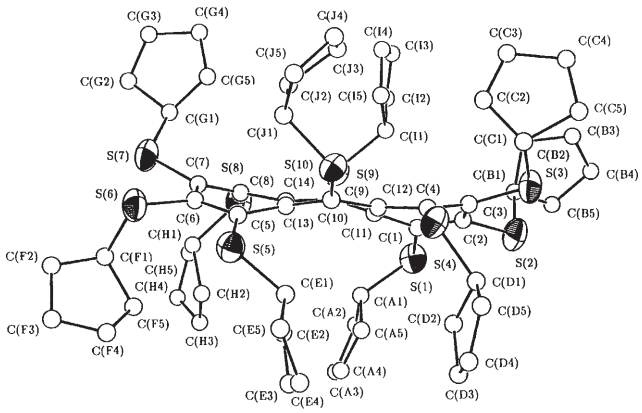



*Figure 14.* Decakis(cyclopentylthio)anthracene (**37**) as its 1,4-dioxane inclusion compound with conformation *abbabaabab*. Reproduced, with permission, from reference [84].

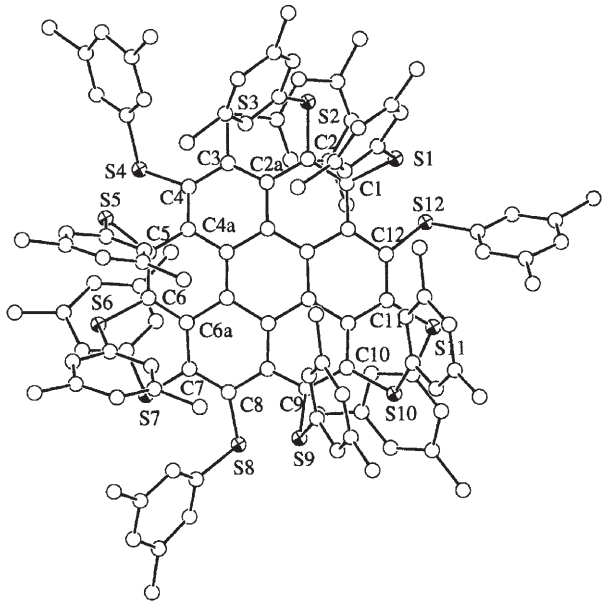



*Figure 15.* Dodecakis(3,5-dimethylphenylthio)coronene (**92**) in its 1,4-dioxane adduct with conformation *aabbaabbaabb*. Reproduced, with permission, from reference [33].

Decakis(cyclopentylthio)anthracene (**37**) was the only persulfurated anthracene compound prepared to date (Figure 14).[31] Purple crystals analyzed by X-ray crystallographic analysis indicated sulfur substituents with an *abbabaabab* conformation. The *peri* interactions caused a deviation from planarity, and lead to a twist-boat conformation for each anthracene ring.

Persulfurated coronene derivatives were also examined in 1994,[33] after preliminary studies for dodecachlorocoronene in 1988.[86] The sulfur ligands are alternately arranged pairwise above and below the mean plane of coronene (Figure 15; *aabbaabbaabb*). However, the coronene core was markedly nonplanar according to the authors. One of the main interests in persubstituted coronene derivatives is the possibility for π stacking of coronene discs toward supramolecular columnar assemblies.

X-ray crystallographic studies of decakis(phenylthio)benzophenone (**47**) were reported.[39] For 1,2,3-tris(*tert*butylthio)-4-dimethylamino-thiophene, X-ray crystallographic studies showed an *ababa* pattern, which could possibly lead to a similar conclusion as for tetrakis(isopropylthio)thiophene (**55**).[41] Complex bis(tetrakis(trifluoromethylthio)pyrrole)-$Hg^{II}$ was also studied by X-ray diffraction studies.[87] Interestingly and unexpectedly, the pentakis(methylthio)cyclopentadienyl anion (**57**) exhibited an *aaaab* pattern (Figure 16).[50]

In summary, many persulfurated arenes exhibit alternating up and down sulfur substituents in the solid state, in a pattern and sequence that depends on the aromatic core. In a few cases, the conformation in solution may be different from that in the solid state, probably owing to crystal packing

 © 2006 Wiley-VCH Verlag GmbH & Co. KGaA, Weinheim 

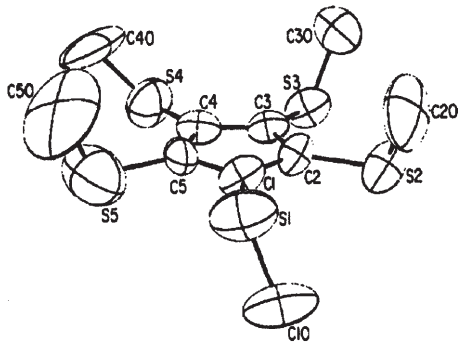



***Figure 16.*** ORTEP plot of the pentakis(thiomethyl)cyclopentadienyl anion (**57**; 50% probability ellipsoids for thiomethyl groups). Reproduced, with permission, from reference [50].

effects. However, because of the low activation energy required for conformer interconversion, an up and down pattern would probably be the most representative stable conformation in solution. This statement is in agreement with a few calculations and NMR spectroscopic data.

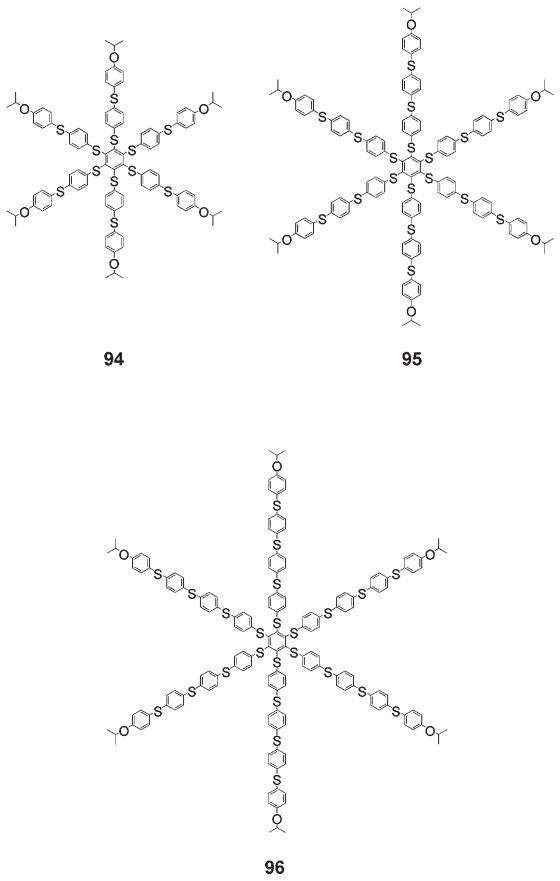
## 4. Supramolecular Chemistry and Organometallic Assemblies

### 4.1. Molecular Asterisks

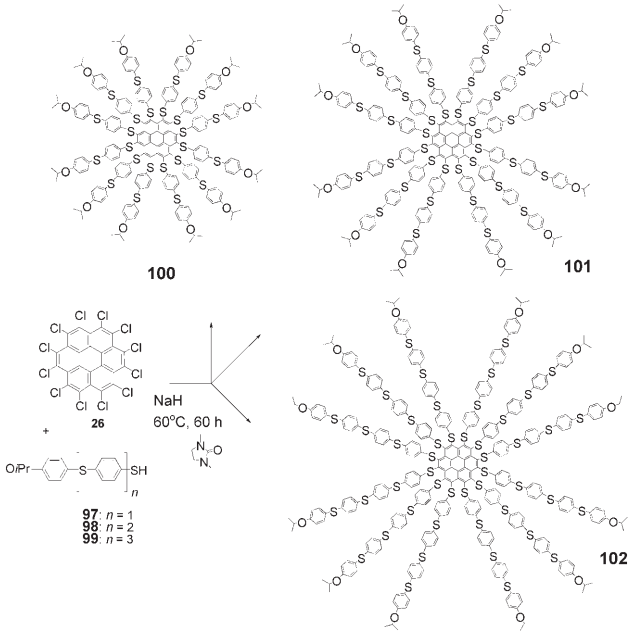
In 1967, star-shaped molecules incorporating a persulfurated benzene core were reported in a patent describing the synthesis of hexakis(*p*-(phenylthio)phenylthio)benzene (**93**) and other branched derivatives.[13] Some questions were raised because of the low solubility in most solvents, which was in contrast to authentic samples reported later. Emphasis on the development and properties of molecular asterisks or star-shaped supramolecules containing a persulfurated aromatic core (benzene or coronene) was reported in 1998.[35a] The convergent assembly relied on the facile persulfuration of hexachlorobenzene or dodecachlorocoronene with poly(*p*-phenylene) sulfide oligomers having a terminal sulfydryl group. First- to fourth-generation asterisks (corresponding to 1 to 4 phenyl groups in the PPS chain, e.g., **94**–**96**) were prepared in order to study some properties by cyclic voltammetry and UV/Vis spectroscopy (Scheme 20). Recent spectroelectrochemical studies of coronene derivatives provided further information (Scheme 21).[35b]

PPS molecular asterisks are electron acceptors,[34] and electron delocalization may occur over the whole supramolecule (hypothesis), as suggested by the easier reduction and red shifts in the UV/Vis spectra as the length of the PPS arms increases (from first- to fourth-generation). However, further data is required before such a conclusion can be reached. They might be supramolecules with a possible three-dimensional electron network in which delocalization may involve thioether bridges.

Our work inspired another study for making water-soluble asterisks: peripheral hydrophilic groups (OH, $NaOPO_3$) were installed at the ends of the PPS arms, which were connected to



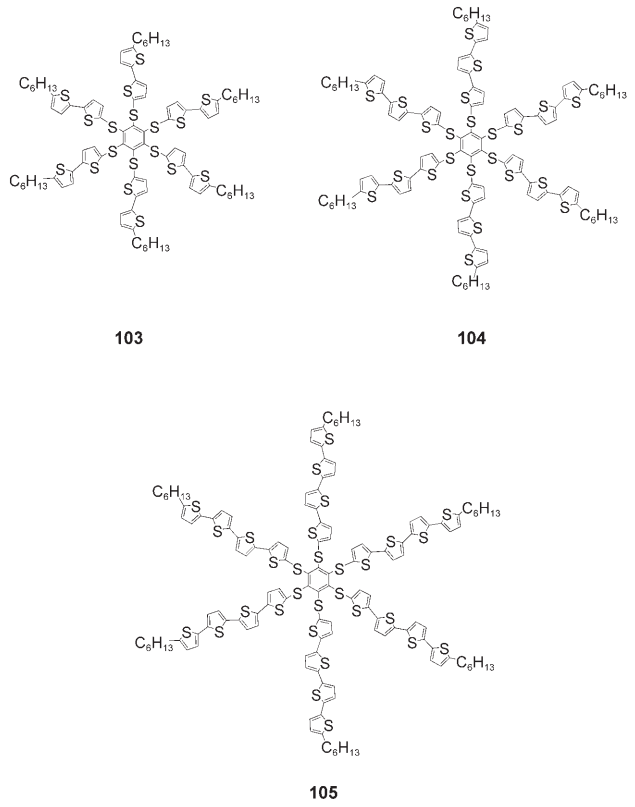

***Scheme 20.*** *p*-Phenylene sulfide molecular asterisks with a benzene core.




***Scheme 21.*** Synthesis of *p*-phenylene sulfide molecular asterisks **100**–**102** with a coronene core.

 © 2006 Wiley-VCH Verlag GmbH & Co. KGaA, Weinheim 

a benzene core.[88] Colloidal properties in water were investigated by UV/Vis, fluorescence, and NMR spectroscopy, DSC, light scattering, and surface tensiometry. In short, there is no clear evidence for self-assembly in aqueous solutions according to DSC (no cooperative phase transition), spin-Echo NMR, dynamic light scattering, tensiometry and UV/Vis studies (no deviation from the Beer–Lambert linearity). Fluorescence was also observed, as reported earlier. They behave more or less like monomolecular species in water. Another group prepared asterisks (up to third-generation) by connecting sulfanylated poly(thiophene)sulfide oligomers to a benzene core (Scheme 22, **103**–**105**).[89] A liquid-crystalline state was observed, as discussed in Section 5.7.



**103** **104**

**105**

***Scheme 22.*** Liquid-crystalline polythiophene molecular asterisks with a benzene core.

### *4.2. Molecular Wheels*

Since the discovery of crown ethers[90] and cryptands[91] much research has been dedicated to cyclic ligands with specific cation- and anion-binding abilities. Over the years, more-complex macrocycles have been prepared in which nitrogen, sulfur, oxygen, and phosphorus atoms were incorporated in the backbone.[92] Generally, large ring compounds require preorganization of reactants prior to macrocycle assembly. This can often be accomplished by using metal ions as templates which often determines the number of heteroatoms and the size of the resulting macrocycle. The resulting supermolecules incorporating metal ions resemble molecular wheels.

When using a similar synthetic strategy by building the wheel inward to outward, Schmidbaur and co-workers[93] demonstrated that a "golden wheel" **106** is formed when 6 equivalents of $(Ph_3P)AuCl$ react with benzenehexathiol and triethylamine in dichloromethane (Figure 17). X-ray crystal-structure determination of hexanuclear (triphenylphosphine)gold benzene hexathiolate, $[(Ph_3P)Au]_6(C_6S_6)^{6-}$ showed that arene carbon, sulfur, gold, and phosphorus atoms are nearly coplanar, with a slight puckering of gold–sulfur pentagons.

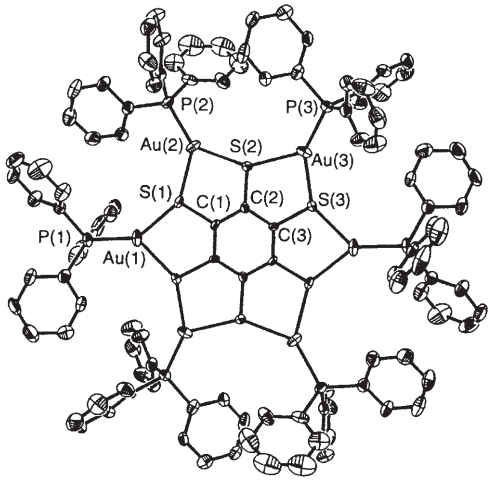
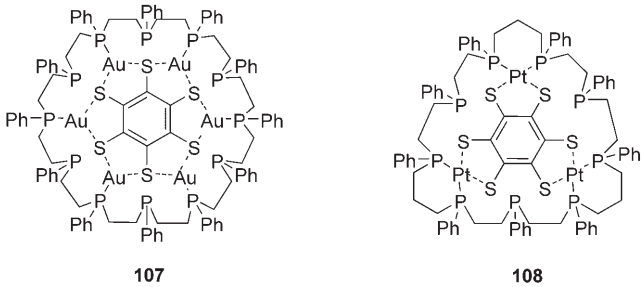



***Figure 17.*** "Golden wheel" **106** from supramolecular assemblies. Reproduced, with permission, from reference [93].

Angelici and Harnisch used a similar strategy to generate a large phosphine macrocycle,[94] with twelve phosphorus atoms in the ring. In their approach, they made a (divinyl)-(phenyl)phosphine gold complex of benzene hexathiolate, precursor to the "golden wheel" **107**, followed by cascade macrocyclization reactions of the neighboring vinyl groups with $PhPH_2$ in presence of azobis(isobutyronitrile) (AIBN) (Scheme 23).[95] However, the yield was not reported, and the X-ray crystal structure has yet to be determined. Besides that example, they proposed $Pt^{II}$ derivatives, but the synthesis of a precursor failed and the macrocycle **108** could not be prepared. Homogeneous catalysis and colloid chemistry seemed a logical extension to those investigations.



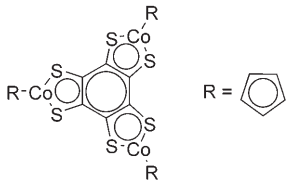
**107** **108**

***Scheme 23.*** "Golden wheel" **107** and hypothetical "Pt wheel" **108** through supramolecular assemblies.

 © 2006 Wiley-VCH Verlag GmbH & Co. KGaA, Weinheim 

### 4.3. Molecular Windmills

"Windmill molecules" made from hexakis(methylthio)-benzene (**3**) and metal carbonyl complexes were first proposed in 1982, but could not be synthesized then.[71] However, the first syntheses of windmill complexes involved benzene hexathiolate anions in the form of trinuclear cobaltocene complexes (e.g. **109**).[96] Electrochemical, EPR,




**109**

optical, and magnetic properties were investigated. In summary, it was shown that charge delocalization in the mixed-valence states is considerably influenced by the counterion and surrounding solvent. A larger solvated cation delocalized the negative charge more significantly, resulting in larger separation of redox potentials and stronger intervalence-transfer bands observed for the two mixed valences. This also leads to a change in the magnetic properties of the trivalent anion.

Tetrakis(trifluoromethylthio)pyrrole was also used in some $Ag^{I}$ and $Hg^{II}$ complexes in which N–Hg and N–Ag σ bonds were observed.[54]

### 4.4. Coordination Polymers and Supramolecular Self-Assemblies with Metal Salts

Because $Ag^{I}$, $Cu^{I}$, $Ni^{II}$, and $Zn^{II}$ ions have a high affinity for sulfur, many of the following supramolecular self-assemblies are amenable to X-ray crystallographic analysis. A zigzag polymeric chain was demonstrated by complexing a silver ion with hexakis(*p*-tolylthio)benzene (Figure 18).[97] An $Ag^{I}$ cation with square-planar coordination geometry served as a bridge between two persulfurated benzene molecules. X-ray crystallographic analysis showed that the *p*-tolylthio groups are almost perpendicular to the benzene core, in an alternating up and down pattern (*abababa*).

In another study, hexakis(phenylthio)benzene was self-assembled in the presence of $Ag^{I}$ salts to produce either a three-dimensional network coordination polymer with pocket structures or linear chains, depending on the counterion used.[98] In the presence of $PF_6^-$, a coordination polymer with pockets was obtained (Figure 19), whereas $NO_3^-$ generated a linear coordination polymer (Figure 20). Thus, a subtle change in the molecular topology was obtained by a specific choice of anion.

The coordination of hexakis(methylthio)benzene (**3**) with $Ag^{I}$ and $Cu^{I}$ salts was also studied (Figure 21).[99] With $Cu^{I}$, orthogonal repeating units incorporating one $Cu^{I}$ ion for every two persulfurated aromatic molecules in a tetrahedral arrangement around $Cu^{I}$ with four sulfur ligands was

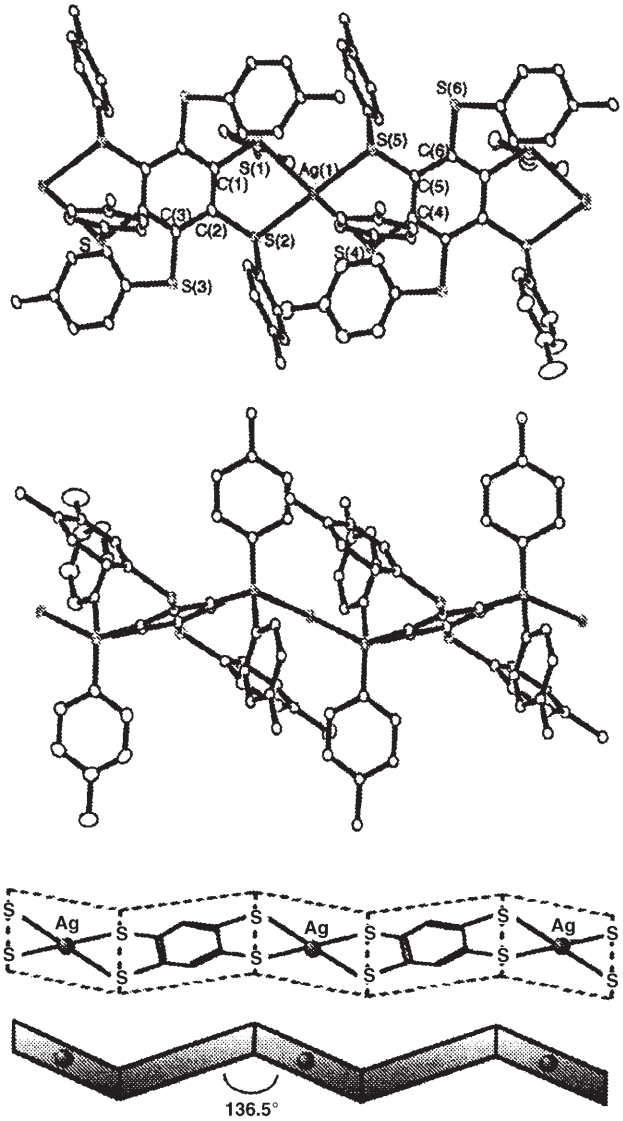



***Figure 18.*** Zigzag coordination polymer by complexing $Ag^{I}$ ion with hexakis(*p*-tolylthio) benzene. Reproduced, with permission, from reference [97].

obtained. Overall, a linear chain structure (coordination polymer) was formed with thiomethyl groups alternating in an up and down arrangement around the benzene core (*abababa*). In the case of $Ag^{I}$, almost the same coordination and geometry were found, but the *bbbaba* conformation probably favored a tridimensional network.

Polymeric membranes for ion-selective electrodes based on *p*-phenylene sulfide molecular asterisks were reported and the selectivity for various metal salts was studied ($Ag^{+}$, $Cu^{2+}$, $Pb^{2+}$, $Ca^{2+}$, $Na^{+}$, $K^{+}$, $Cs^{+}$, $Hg^{2+}$).[100] Second-generation coronene asterisks had the maximum selectivity for $Ag^{+}$ ions, despite the high thiophilicity of $Hg^{2+}$, $Cu^{2+}$, and $Pb^{2+}$. The affinity for $Ag^{+}$ reflects the above results on coordination polymers, with possible coordination of thioethers and cation–π complexes of $Ag^{+}$ with aromatic rings.

Finally, an X-ray crystallographic study of the coordination of $Ag^{I}$ with octakis(cyclohexanylthio)naphthalene

 © 2006 Wiley-VCH Verlag GmbH & Co. KGaA, Weinheim 

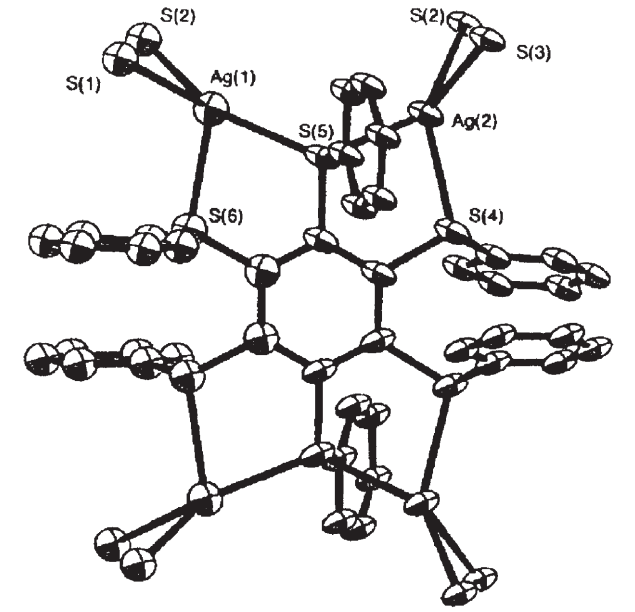



***Figure 19.*** X-ray crystal structure of the coordination polymer of hexakis(phenylthio)benzene and $AgPF_6$. Reproduced, with permission, from reference [98].

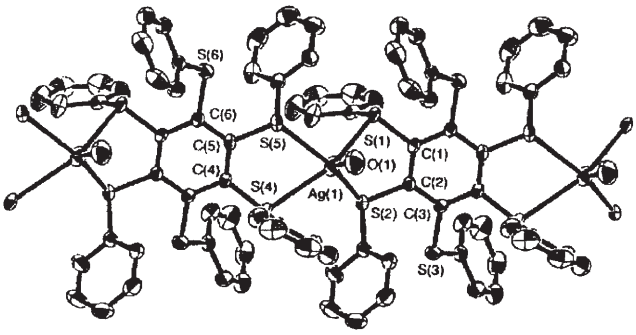



***Figure 20.*** ORTEP plot of the complex [Ag(hexakis(phenylthio)benzene)]$(NO_3)$. Reproduced, with permission, from reference [98].

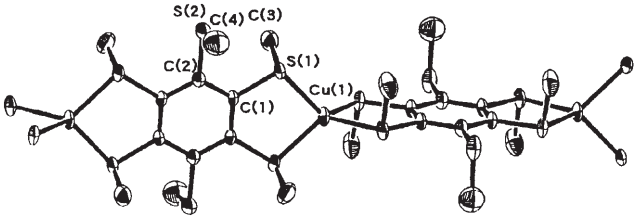



***Figure 21.*** Coordination polymers of hexakis(methylthio)benzene with $CuPF_6$ or $AgPF_6$. Reproduced, with permission, from reference [99a].

(**32**)[101] showed a two-dimensional sheet structure with cavities. The $Ag^I$ ions are coordinated to two adjacent sulfur ligands on the naphthalene core and two oxygenated ligands from a counteranion in a tetrahedral arrangement. The sulfur ligands are almost perpendicular to the core, and adopt a *baababba* pattern; overall, four pairs of sulfur ligands are coordinated to four $Ag^I$ ions.

Other organometallic complexes described were those incorporating $Ni^{II}$, $Zn^{II}$, and $Ti^{IV}$ cations. Polymeric $Ni^{II}$ complexes originally derived from benzenehexathiolate and then from 4,8-bis(alkylthio)-1,3,5,7-tetrathia-s-indacene-2,6-dithiones were synthesized in an attempt to discover new mono-, di-, and polydithiolene organic conductors (Section 5.1).[102] In a similar way, dithione precursors were hydrolyzed and converted into alkylthio-substituted bis(benzene-1,2-dithiolato)zincates.[75] Selective formation of 1,3-dithiole-2-thiones from sodium benzenehexathiolate followed by basic hydrolysis of the thionocarbonate group and addition of titanocene dichloride led to mononuclear titanocene complexes based on benzenehexathiolate derivatives. Interestingly, a trinuclear tris(titanocene) complex was obtained from benzenehexathiolate.[103]

### *4.5. Bioinorganic and Biomimetic Systems*

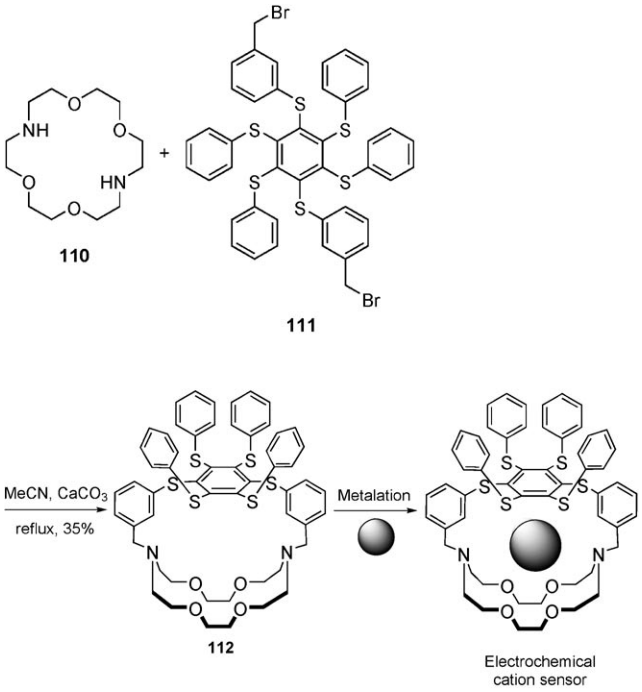
The elegant and leading work of Holm and co-workers with persulfurated benzene derivatives toward bioinorganic and biomimetic systems is worth mentioning, as well as a single publication by Evans et al.[104] In 1987, Holm and co-workers first reported the preparation of analogues of iron–sulfur protein clusters, which are of importance in many biological electron-transfer sites (e.g. ferredoxins and rubredoxins).[79] Their strategy relied on the cavitand concept with alternating up and down sulfurated arms surrounding a benzene core, ready to wrap an iron cluster in a tripodlike structure (Figure 7). This well-thought preorganization of the stereochemistry surrounding a benzene ring helped in the synthesis of semirigid tridentate ligands in which three terminal sulfanyl groups form part of a $Fe_4$–$S_4$ cubanelike iron cluster with two types of iron subsites. The up and down alternating pattern *abababa* of the substituents in persubstituted benzene derivatives was exploited in solution. Synthesis of mixed sulfur ligands on a benzene core was previously discussed (Section 2.4) and was of prime importance in this case. The best relative positions of the convergent sulfanylated arms on the benzene ring were in *meta* positions. Several new tripodlike tridentate ligands were prepared and analyzed by X-ray crystallography, by electrochemistry, and by NMR and UV/Vis spectroscopy.[70,65] Other works described more-complex double cubane clusters, EPR and electrochemical studies,[80,105] as well as Mössbauer measurements.[106] Mixed Fe–Mo and Fe–V clusters were prepared, and regiospecific reactions at a vanadium site were demonstrated.[107] Redox properties were modulated by modification with chelating ligands[108] as well as with isonitrile ligands.[109] Biomimetic systems related to sulfite reductase, nitrogenase, and biotin synthase were reported.[110] Incorporation of metal ions and diverse reactions of cuboidal $Fe_3S_4$ clusters were published.[111]

### *4.6. Cryptands and Redox Sensors*

Persulfurated arenes are electron acceptors.[34,112] The combination of a reducible hexakis(phenylthio)benzene derivative **111** with a persulfurated benzene core with mixed

 © 2006 Wiley-VCH Verlag GmbH & Co. KGaA, Weinheim 

sulfur ligands and a cation-coordinating macrobicyclic structure (tetraoxadiazamacrocycle **110**) was described as a new type of cryptand **112** for some applications as cation sensors with electrochemical detection (Scheme 24).[67] A shift of 170 mV (relative to the uncomplexed state) was found in the reduction potential of the cryptand complexed with a potassium ion. A stability constant of approximately $4000\,\text{M}^{-1}$ for potassium ions was evaluated by $^1$H NMR titration.




***Scheme 24.*** Synthesis of a reducible macrobicyclic cation sensor.

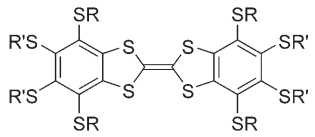
## 5. Advanced Organic Materials

### 5.1. Organic Conductors

#### 5.1.1. TTF Derivatives

Since the discovery in the early 1970s of the metal-like electrical conductivity of organic charge-transfer complexes[113] with segregated columns of donor and acceptor molecules, much effort was devoted to the development of novel organic architectures toward highly conducting and superconducting organic crystalline materials. They could be prepared as mixed-valence compounds by the reaction of donors and acceptors with moderate ionization potentials. Electrocrystallization of a donor radical cation with an acceptor or doping of a donor–acceptor CT complex led to conductive crystals. Particular attention was paid to tetrachalcogenafulvalene derivatives, especially to tetrathiafulvalene (TTF),[114] and led to a series of donor molecules for quasi-one-dimensional electronic conductors[115] in the hope of optimizing electrical conductivity. Several tailor-made sulfur-containing compounds were synthesized with increase TTF donor ability to improve molecular stacking, to shorten S–S distances in and between stacks, to stabilize charges in the doped state, to increase the polarizability, and to decrease Coulombic repulsion in multicharged species.[116,115] With those objectives in mind, many strategies will be described below.

Fanghänel and co-workers developed per(alkylthio)dibenzo-TTFs **113a–n**.[117] Their redox properties were deter-




**113 a-n**

**a** R = R' = $CH_3$
**b** R = R' = $C_2H_5$
**c** R = R' = $nC_5H_{11}$
**d** R = R' = $iC_5H_{11}$
**e** R = R' = $nC_{12}H_{25}$
**f** R = R' = 4,5-Di-*tert*-butyl-1-benzyl
**g** R = $CH_3$, R' = $C_2H_5$
**h** R = $CH_3$, R' = $nC_5H_{11}$
**i** R = $CH_3$, R' = $iC_5H_{11}$
**j** R = $CH_3$, R' = $nC_{12}H_{25}$
**k** R = $CH_3$, R' = -$CH_2$-$CH_2$-
**l** R = $iC_5H_{11}$, R' = $CH_3$
**m** R = $nC_5H_{11}$, R' = -CO-
**n** R = $CH_3$, R' = -CO-

mined by cyclic voltammetry (Table 1). Electrical conductivities (pressed pellets) were measured for some of these compounds after doping by chemical oxidation of the TTF

***Table 1:*** Half-wave oxidation potentials of organic donor components **113**.[a]

| Donor | $E^1_{1/2}$ [V] | $E^2_{1/2}$ [V] |
|---|---|---|
| **113a** | 0.74 | 1.09 |
| **113b** | 0.71 | 1.09 |
| **113c** | 0.74 | 1.11 |
| **113g** | 0.71 | 1.06 |
| **113h** | 0.74 | 1.09 |
| **113j** | 0.74 | 1.12 |
| **113k** | 0.62 | 0.97 |

[a] Measured in 1,2-dichloroethane or 1,2-dichlorobenzene with tetrabutylammonium perchlorate (TBAP) (0.1 M or 0.05 M); 100 $\text{mV s}^{-1}$ vs. SCE.

cores. The oxidation was strongly dependent on substituents. For instance, **113a** was readily oxidized by iodine, bromine, or antimony pentachloride ($SbCl_5$), whereas **113k** was only oxidized by bromine or antimony pentachloride (Table 2). The best conductivity ($7.2\times10^{-2}\,\text{S cm}^{-1}$) was exhibited by **113k** in a charge-transfer complex with $TCNQF_4$, whereas most systems led to semiconducting behavior in the conductivity range $10^{-3}$–$10^{-6}\,\text{S cm}^{-1}$. These derivatives cannot compete with the best conductivities already obtained with TTF salts.

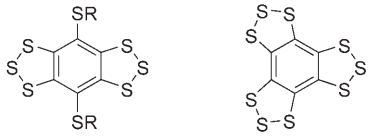
In another investigation, 1,2,3-trithiole rings were annellated to dibenzo-TTF,[118] leading to derivatives **114**–**117**. Benzo-1,2,3-trithiole were chosen owing to their stability and ability to form stable radical cations by oxidation. Benzo-1,2,3-trithioles are weaker electron donors than TTF and are only oxidized by strong oxidants, such as antimony pentachloride ($SbCl_5$). Depending on the amount of $SbCl_5$ added to **117**, the TTF unit is first oxidized, followed by the benzo-


© 2006 Wiley-VCH Verlag GmbH & Co. KGaA, Weinheim

*Table 2:* Measured conductivities $\sigma_{RT}$ of selected derivatives **113**.

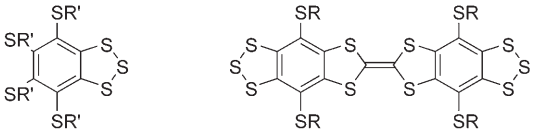
| Donor | Anion or Acceptor[a] | Stoichiometry | $\sigma_{RT}$ [S cm$^{-1}$] |
|---|---|---|---|
| **113a** | $I^-$ | 1:1 | $2.0\times10^{-5}$ |
| **113a** | $Br^-$ | 1:1 | $2.0\times10^{-4}$ |
| **113a** | $SbCl_6^-$ | 2:1 | $2.0\times10^{-6}$ |
| **113g** | $TCNQF_4$ | 1:1 | $4.8\times10^{-3}$ |
| **113h** | $TCNQF_4$ | 1:1 | $3.8\times10^{-3}$ |
| **113j** | $TCNQF_4$ | 1:1 | $8.0\times10^{-4}$ |
| **113k** | $TCNQF_4$ | 3:1 | $7.2\times10^{-2}$ |

[a] $TCNQF_4$ = perfluoro-7,7,8,8-tetracyano-*p*-quinodimethane.



**114a** R = $nC_6H_{13}$
**114b** R = $CH_3$

**115**

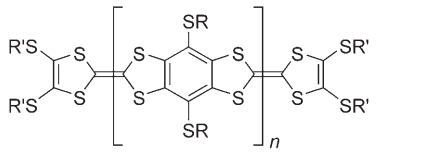


**116** R = $CH_3$ **117** R = $iC_5H_{11}$

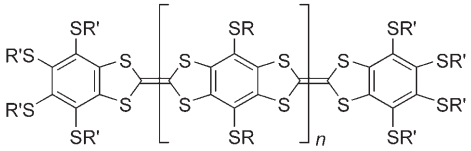
1,2,3-trithiole moieties. Conductivity measurements for **114**–**117** (pressed pellets) indicated weakly conducting compounds with values ranging from $9.3\times10^{-3}$ to $9.6\times10^{-4}$ S cm$^{-1}$.

At the same time, Müllen and co-workers developed another approach based on the synthesis of oligomeric structures containing fully conjugated TTF units, or TTF units linked by saturated spacers.[119] Per(thioalkyl)oligomeric TTF derivatives **118**–**123** were synthesized with the aim of producing extended donors with multiple redox centers in a well-defined spatial arrangement.[120] In this manner, the "dimensionality" within the crystal structure would be increased and shorter S···S distances would be obtained in and between stacks.

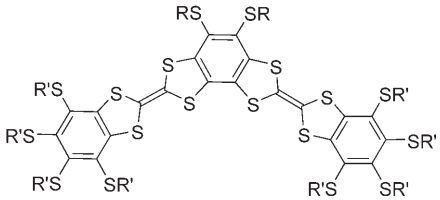
In each case, expansion of the π systems by using rigid covalent bridges resulted in a decrease in solubility, which complicated characterization, but on the other hand, led to an increase in conductivity. Attachment of flexible S-alkyl side chains to the central and at the terminal benzene rings led to an increase in solubility. It was also assumed that S-alkyl substituents could enhance polarizability of the molecule. As for derivatives **120**–**123**, S-alkyl substitution on the outer benzene subunit increased stabilization of the cationic states relative to unsubstituted analogues. However, S-alkyl substitution on the inner benzene ring did not increase stabilization, in spite of an increase in the +M effect from S-alkyl groups relative to their O-alkyl analogues. For all derivatives, the first oxidation step occurred on the terminal TTF subunits of the molecule and depended on the overall number of TTF units. Oxidation led to the formation of more-positively charged cations. Those cations could even reach the hexacationic oxidation state, as was observed for **119**. As for angular derivative **123**, higher values for the first two oxidation steps were measured. Nevertheless, dark charge-transfer complexes were obtained in many cases with DDQ (1:2 stoichiometry) or $TCNQF_4$ (1:2; for **120** 2:3). Conductivity data listed in Table 3 were obtained by using two-probe measurements. It was found that **120** (linear) and **123** (angular) could reach a similar conductivity of $10^{-2}$ S cm$^{-1}$ with $TCNQF_4$ complexes.



$n$ = 1 **118** R = $iC_5H_{11}$ R' = $C_6H_{13}$
$n$ = 2 **119**



$n$ = 1 **120** R = $iC_5H_{11}$ R' = $C_2H_5$
$n$ = 1 **121** R = $iC_5H_{11}$ R' = $CH_3$
$n$ = 2 **122** R = $iC_5H_{11}$ R' = $CH_3$



**123** R = $CH_3$ R' = $C_2H_5$

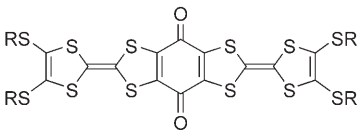
*Table 3:* Half-wave oxidation potentials (in V) and measured conductivities $\sigma_{RT}$ (in S cm$^{-1}$) of **120** and **123**.[a]

| Donor | $E^1_{1/2}$ | $E^2_{1/2}$ | $E^3_{1/2}$ | $E^4_{1/2}$ | DDQ[b] | | TCNQF$_4$ | |
|---|---|---|---|---|---|---|---|---|
| | | | | | D/A[a] | $\sigma_{RT}$ | D/A | $\sigma_{RT}$ |
| **120** | 0.41 | 0.63 | 1.06 | 1.22 | 1:2 | $4\times10^{-3}$ | 1:2 | $7\times10^{-2}$ |
| **123** | 0.54 | 0.69 | 1.06 | 1.22 | 1:2 | $8\times10^{-6}$ | 2:3 | $2\times10^{-2}$ |

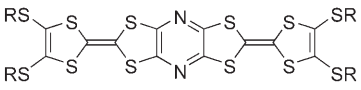
[a] $TBAPF_6$ in $CH_2Cl_2$; 100 mV s$^{-1}$ vs. SCE. [b] DDQ = 2,3-dichloro-5,6-dicyano-1,4-benzoquinone. [c] Stoichiometry donor (D)/acceptor (A).

As the majority of charge-transfer complexes contain segregated donor (D) and acceptor (A) molecules, it was proposed that molecules in which D and A are covalently coupled (e.g. D-A-D or A-D-A triads) could be used as organic conductors.[121] For instance, **124** and **125**[122] as well as **126** and **127**[123] were analyzed by electrochemical techniques. The first oxidation potential (a two-electron-transfer step) in **124** and **125** occurred at higher potentials than that of analogue **118** because of a destabilization of the radical cation owing to an electron-withdrawing effect of the inner benzene

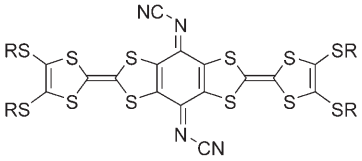
 © 2006 Wiley-VCH Verlag GmbH & Co. KGaA, Weinheim 



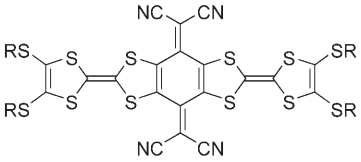
**124** R = $nC_4H_9$
**125** R = $nC_6H_{13}$



**126** R = $CH_3$
**127** R = $nC_6H_{13}$



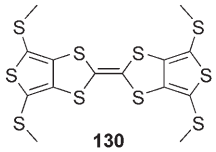
**128** R = *n*-alkyl



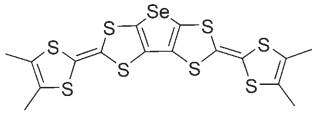
**129** R = *n*-alkyl

ring. Compounds **124** and **125** were also precursors to compounds **128** and **129**.[124]

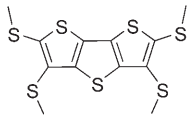
Finally, persulfurated thiophene, selenophene, and more-extended fused thiophene derivatives were also described as new TTF-type donors such as **130**–**135**.[125]



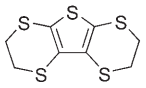
**130**



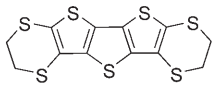
**131**



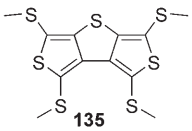
**132**



**133**



**134**

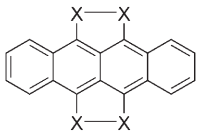


**135**

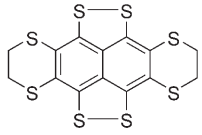
Despite much effort and many synthetic strategies for enhancing the conductivities of persulfurated aromatic TTF derivatives, the best systems provided conductivities in the order of $10^{-2}$ S cm$^{-1}$ and they are classified as semiconductors. They could not compete with TTF conductors and surely not with conducting polymers that exhibit conductivities greater than $10^{2}$ S cm$^{-1}$ (e.g. PPS, polythiophene).[126]

### 5.1.2. *Other Derivatives*

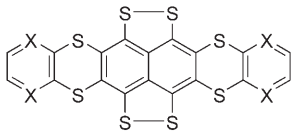
Some tetrachalcogenatetracene derivatives **136** (TTT) and **137** (TSeT), for example, $TTT_2I_3$ and $TSeT_2Br$, proved to be good organic conductors.[127] To understand factors



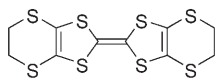
**136** TTT (X = S)
**137** TSeT (X = Se)



**138** EDNA



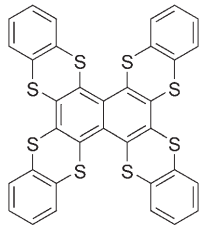
**139** DBDTTTN (X = CH)
**140** DBDTTTN (X = N)



**141** BEDT-TTF

governing superconductivity better, peripheral hydrocarbon groups were replaced by ethylenedithio groups, for example, in BEDT-TTF (**141**; BEDT = bis(ethylenedithio)tetrathiafulvalene). That change favored donor–anion interactions and improved conductivity. Only a few examples of such compounds were found in the literature, for example, **138** (EDNA), **139** and **140** (DBDTTTN),[128] and their selenide or telluride analogues.

Conductivity measurements were usually performed on a single crystal doped with halogen (generally with iodine) or by dissolving donor species into a nonconducting polymer. The formation of charge-transfer complexes was confirmed by changes in the UV/Vis spectra and by an increase in electrical conductivity after doping. In many cases, the conductivity of the films was lower than that of single crystals which could be attributed to the low crystallinity of thin films and to the non-homogeneous coating of a surface. For instance, conductivity of undoped DBDTTN (**139**) in thin films was $7.6 \times 10^{-6}$ S cm$^{-1}$, whereas in a charge-transfer complex (crystal) a value of $3.0 \times 10^{-1}$ S cm$^{-1}$ was found.



**142** NBDT

Those results stimulated the synthesis of novel persulfurated conjugated compounds, for example, naphthatetrakis(benzodithiine) **142** (NBDT).[129] Radical cation salts of **142** were generated by electrocrystallization with $BF_4^-$ or $TCNQ^{\bullet-}$ as counterions to afford air- and moisture-stable crystals. The latter salts were analyzed by EPR, cyclic voltammetry, and conductivity measurements. Cyclic voltammetry data in $CH_2Cl_2$ showed weak reduction (−1.0 V) and oxidation signals (1.0 V) owing to poor solubility. EPR measurements indicated paramagnetism for both NBDT/TCNQ and NBDT/$BF_4$ pairs with a high *g* factor value owing to strong spin-orbit interactions with sulfur atoms. Finally, electrical measure-

 © 2006 Wiley-VCH Verlag GmbH & Co. KGaA, Weinheim 

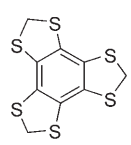
ments indicated a temperature dependence on conductivity. Below 300 K, an increase in conductivity was found up to 250 K; conductivity values then indicated semiconducting behavior at lower temperatures.

Finally, it was proposed that persulfurated cyclopentadienyl derivatives could lead to neutral radical organic conductors with high conductivities (see Section 2.3).[50] Compound **57** (Scheme 11) was previously synthesized and its structure was carefully analyzed by X-ray diffraction to check if dimerization could occur in the solid state. Such phenomena are crucial to reach high conductivity values owing to strong intermolecular interactions in the solid state. Additionally, cyclic voltammetry studies on **57** provided extremely low oxidation potentials in solution ($E_{1/2} = -0{,}03$ and 0.83 V vs SCE in $CH_3CN$).

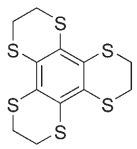
In summary, to date it has not been possible to attain conductivities higher than $10^{-2}$ S cm$^{-1}$ with TTF derivatives or non-TTF compounds. A wide variety of organic semiconductors were prepared (powders or crystals), including some structures with persulfurated arenes. Many systems showed a temperature dependence typical of semiconductors. Solubilizing alkyl groups were often needed for film processing (spin-coating) and characterization, but led to different conducting properties. Encapsulation in a matrix (polymers), Langmuir–Blodgett techniques, and other techniques were proposed to increase molecular organization and to help in processing. Problems related to aging, oxidation, and constant properties over time still need to be overcome for most organic conducting systems. However, the field is still open to the discovery of new light-weight conducting materials as industrial demand is great for their application in many fields and electronic devices.

### 5.2. Organic Ferromagnets

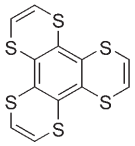
Organic ferromagnets are a representative class of organic materials that evolved after a better understanding of organic conductors and supraconductors. Ferromagnetism is a special electronic state of spin alignment throughout the bulk material. On the basis of theoretical[130] and experimental considerations, two main strategies emerged for the design of organic ferromagnets. The first was based on a mixed stack of charge-transfer complexes from donor and acceptor molecules,[131] the second relied on two segregated stacks incorporating only donor or only acceptor molecules, as commonly found in conducting radical ion salts.[132] To exhibit ferromagnetic behavior, donor or acceptor components need to occupy at least one pair of degenerate highest occupied (HOMO) or lowest unoccupied (LUMO) molecular orbitals, respectively. Preliminary work predicted that molecules with $C_3$ or higher symmetry would be good candidates to reach a triplet ground state and, hence, ferromagnetic behavior. This triplet ground state is often associated with diradical or dicationic molecular species. On the basis of this strategy, $C_3$-symmetric hexathio-substituted benzenes **143**–**146**[133] or naphthalene compounds **142** were prepared as potential organic ferromagnets. Some of these compounds exhibited unique magnetic behavior at low temperatures (**144** and **145**), whereas in other compounds a



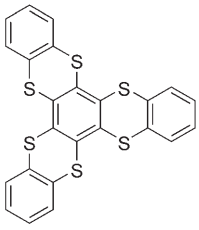
**143**



**144**



**145**

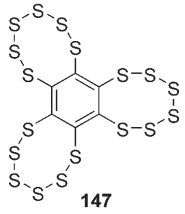


**146**

Jahn–Teller distortion precluded the formation of a triplet state and, hence, ferromagnetic behavior.

### 5.3. Batteries and Electron-Accepting Supramolecules

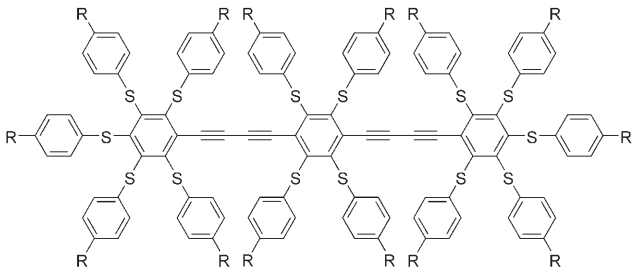
The development of electrical portable devices has become increasingly important in the last decades and emphasized the need for creating new generations of high performance batteries. Miniaturization of such devices also promoted the development of light-weight, high-energy batteries. High-capacity batteries require electrode-active materials that exhibit sufficient ionic conductivity, a highly reversible redox process, and excellent thermal and chemical stability. With these objectives in mind, several companies have already developed organosulfur[134] species as cathode-active materials. For instance, Polyplus Battery Co. used $(R(S)_y)_n$ derivatives in which R is an organic group, and Moltech Corporation used $(CS_x)_n$ or $(C_2S_x)_n$. Persulfurated benzene derivatives **147** could also be utilized as cathode-active materials, and are easily prepared by the reaction of sulfur and hexabromobenzene in the presence of ammonia.[135] Batteries made from organopolysulfides showed an efficient charge capacity of approximately 675 mAh g$^{-1}$ and a 0.5-C discharge capacity of 610 mAh g$^{-1}$.



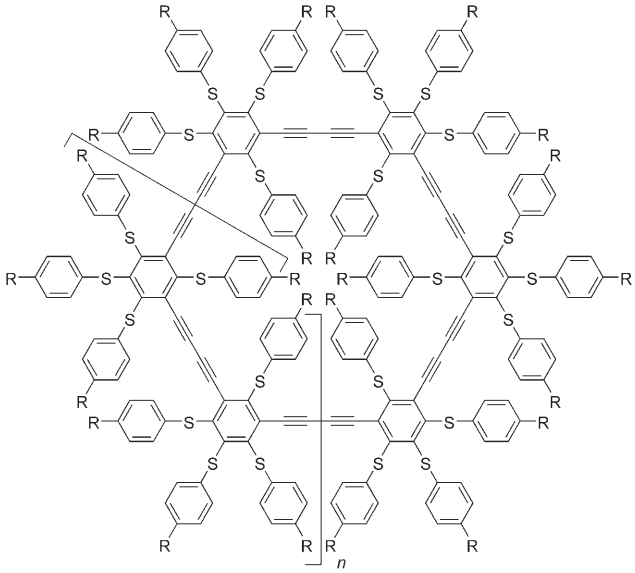
**147**

Electron-accepting supramolecular architectures and molecular wires have attracted attention toward molecular electronics and nanotechnology. Novel architectures with low reduction potentials, called "electron reservoirs",[136] could be used as electronic and photonic devices at the molecular level (or as bulk materials, such as cathode-active materials in batteries). Based on a preliminary demonstration that persulfurated arenes are electron acceptors,[34] Lehn et al. described polysulfurated rodlike structures as reducible molecular wires **148**[137,77] and polysulfurated macrocycles **149** as "molecular batteries", because of their ability to store several electrons.[138] In the first case, by linking two reducible

 © 2006 Wiley-VCH Verlag GmbH & Co. KGaA, Weinheim 



**148** R = *t*Bu



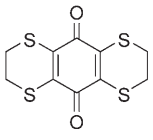
**149** R = *t*Bu
*n* = 1–4

persulfurated substructures with various spacers, they investigated the ability of that bridge to promote electron transfers between individual compartments of a molecular wire. The diacetylene spacer allows electronic communication between reducible pentakis(thiophenyl)benzene end groups, as determined by spectroelectrochemical analysis. In contrast, *p*-divinylbenzene spacers isolate the reducible subunits. Longer, linear, rodlike structures containing up to four reducible substructures were also synthesized and allow delocalization of negative charges over the whole structure. Finally, persulfurated and reducible nanosized macrocycles that contain four, six, eight, or ten reducible substructures connected through diacetylene units accepted several electrons at similar reduction potentials.

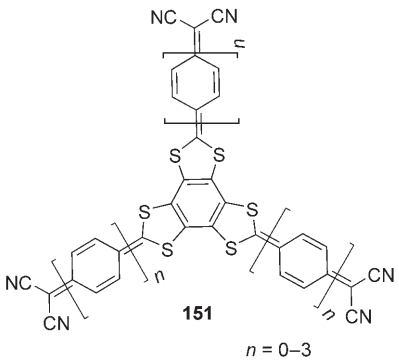
In summary, supramolecular electron acceptors could be made from polysulfides and polysulfurated arenes in which multiple sulfur ligands on an aromatic ring decrease the reduction potentials by stabilizing negative charges. In some cases, the potentials varied by as much as 1.0 V from that of their parent aromatic compounds. The importance of sulfur ligands in materials science is not only of importance for the stabilization of cations or radical cations, but also of radical anions, anions, and multiply charged species.

### 5.4. Materials for Nonlinear Optics

Since the discovery of lasers early in the 1960s, nonlinear optics became a popular research field. Molecules with intramolecular charge-transfer transitions generally exhibit large second- and third-order nonlinear optical responses. These properties were used for applications in optical data storage, laser scanning and control functions, information processing, etc. The most classic approach involved one-dimensional donor–acceptor (D–A) molecules in a molecular array system. In the last few years, multidimensional systems with $T_d$-, $D_{3h}$-, or $C_{3v}$-symmetric groups[139] appeared as new candidates for improving optical responses. In this context, novel sulfur-containing architectures, such as persulfurated arenes, were developed as potential multidimensional NLO materials. However, only a few persulfurated compounds, such as **150** or **151**, have been described to date.[140,141] For



**150**



**151**
*n* = 0–3

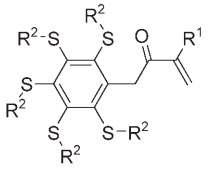
instance, AM1 calculations for derivatives **151** suggested γ-hyperpolarizability ranging from 150 to $86517 \times 10^{-36}$ esu. In general, persulfurated aromatic compounds exhibited γ values comparable to those from other octupolar molecules[142] or from some polymers.[143] With these preliminary encouraging results, more persulfurated aromatic compounds might be investigated in order to optimize the efficiency–transparency trade-off, by varying π-conjugated spacers or end groups.

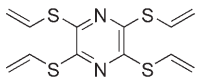
### 5.5. Optical Materials

Materials used for making optical components are of great interest for the development of new technologies. The fields covered by these materials include refractive materials for lenses, prisms, mirrors, optical waveguides, fiber optics, solid light pipes, radiographic screens, etc. Colorless, transparent polymers associated with a high refractive index are good candidates for new optical components. It was found that sulfur-containing compounds exhibit a higher refractive index than those without sulfur. Similar results were obtained for aromatic groups incorporated into organic materials. An interesting point is that some organic polymers could change their refractive index with temperature. The ability to modulate a polymer refractive index by a variation of temperature could be extremely useful for making thermally tunable devices incorporating light-transmitting elements.

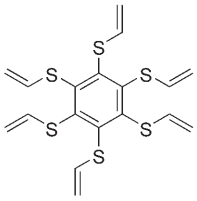
 © 2006 Wiley-VCH Verlag GmbH & Co. KGaA, Weinheim 

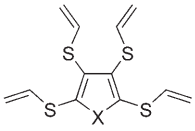
A few examples of polymers based on persulfurated derivatives are known in industry.[144] The aromatic cores used in such polymers were benzene (e.g. **152**, **153**, **155**)[145] pyrazine (e.g. **155**), thiophene (e.g. **156**), and furan (e.g. **157**).[146] In most cases, polymers were prepared in situ by photopolymerization of the appropriate monomer.





**152** $R^1$ = H, $R^2$ = alkyl or aryl **154**
**153** $R^1$ = $CH_3$, $R^2$ = alkyl or aryl

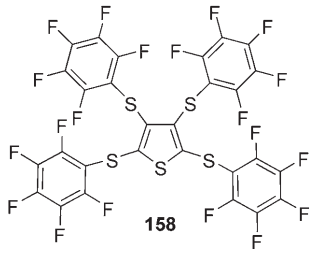




**155** **156** X= S
**157** X= O

### 5.6. Electrophotographic Materials

Some polyfluorinated/polysulfurated compounds were prepared for the creation of electrophotographic or electroluminescent devices.[147] In this context, persulfurated derivatives such as **158** have been used as electron-transporting

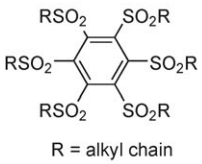


**158**

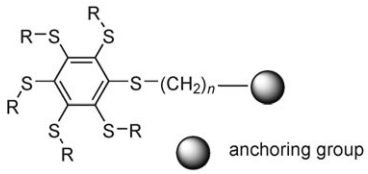
materials in the hole-blocking layer and in the electron injection/transport layer of electrophotographic photoreceptors and of electroluminescent diodes. Devices made from **158** have shown excellent electrical properties and high performance in light-emitting diodes (LEDs) combined with long lifetimes.

### 5.7. Liquid Crystals

Liquid crystals are considered to be a distinct state of matter in which supramolecular interactions lead to an ensemble of molecules with a directional but not a positional order. Among possible mesogenic phases are those called nematic, smectic, cholesteric (or chiral nematic), and discotic. Phase transitions can often be characterized by polarized light, X-ray diffraction, and differential scanning calorimetry (DSC). A typical molecular motif for discotic liquid crystals usually involves a disklike core (a more or less flat aromatic core such as benzene, truxene, and triphenylene) to which peripheral alkyl chains are covalently attached, either directly or by means of a heteroatom bridge. This molecular pattern represents one of the most popular at this time because of the possibility or orienting molecules in discrete ordered columns, while favoring charge transfers within the stack. Persulfurated benzene derivatives such as **159** were investigated as a



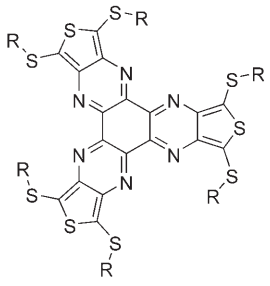
R = alkyl chain
**159**



anchoring group
**160**

promising new class of liquid crystals.[148] However, the corresponding sulfones were selected in most cases because of their superior stacking ability in order to form columns.[149]

The mesogenic discotic phase is important for optoelectronic devices,[150] for liquid-crystal display (LCD) technologies, and for improving charge-transport properties in organic photoconductive systems (LEDs, FETs) or photovoltaic cells.[151] To optimize the performance of devices, the conductivity, and the interface contacts between bulk material and electrodes, two common chemical systems were developed: one used extensive mesogenic π-conjugated systems attached to the desired core (e.g. polythiophene asterisks **103**–**105**; Section 4.1.)[89] and the other utilized extended π-conjugated rings (with a deficient or an electron-rich core) with lateral mesogenic chains (e.g. **161**).[152] Both systems were tested with persulfurated arenes for their properties as discotic liquid crystals.



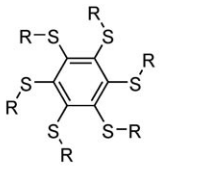
**161**

Other persulfurated arenes were used as mesogenic groups in the preparation of polymer **160**, which exhibits liquid-crystalline phases.[153] They were directly bound to the polymer backbone with or without an acyclic chain as a spacer. They were also utilized for improving the multiplexing properties of liquid crystals in LCD elements.[154]

 © 2006 Wiley-VCH Verlag GmbH & Co. KGaA, Weinheim 

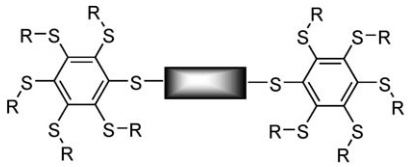
## 6. Lubricants and Polymer Stabilizers

Manufacturers are interested in the development of new lubricants to reduce wear and power loss caused by friction, for example, in gears. It was shown that some persulfurated compounds could be useful additives to improve the properties of lubricating oils, especially for mechanical stress under high pressure and temperature.[155,40] Persulfurated compounds were also used as stabilizers for organic polymeric materials against oxidative, thermal, and UV degradation. Doping organic materials with persulfurated compounds retarded their decomposition, loss of physical properties, and change in color.[14] Compounds **162**–**164** are examples of additives based on persulfurated benzene or thiophene derivatives.

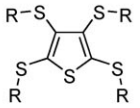


**162**

R = alkyl chain or cycloalkyl



**163**



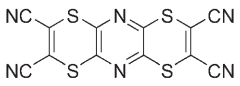
**164**



– α,ω-alkylene groups (2–18 C atoms) in which 1 to 3 $CH_2$ groups may also be replaced by O or S atoms
– 1,4-cyclohexanedimethyl group
– single bond

## 7. Biocides and Other Industrial Applications

Industrial research has long focused on biological applications of persulfurated arenes as insecticides, herbicides, fungicides, and bactericides. They were good algaecides and fungal spore inhibitors with low toxicity towards animals. For example, derivatives of **165** were employed to fight leaf-attacking fungi and seed-attacking organisms.[63] When employed as the sole toxic agent in agar nutrient, they completely destroyed *Staphylococcus aureus*, *Candida albicans*, *Bacillus subtilis*, *Aspergillus terreus*, and many other colonies. Finally, they were useful intermediates in the preparation of dyes for textiles, ink, synthetic detergents, and biologically active materials.[12–14]



**165**

## 8. Conclusion

Although persulfurated arenes have been known since 1957,[4] after the preparation of hexakis(phenylthio)benzene it took almost 20 years to report them in inclusion chemistry, and almost 40 years to demonstrate some examples in supramolecular chemistry (such as molecular asterisks, organometallic assemblies, coordination polymers, and redox sensors), in materials science (liquid crystals, organic conductors, reducible materials, nonlinear optical materials, electrographic materials, and ferromagnets), and in bioorganic chemistry. However, their applications as biocides, dyes, and lubricants, as described in many industrial patents, preceded most academic reports by almost 30 years ago. Even though a limited number of patents have appeared, continued industrial interest is expected owing to the simplicity and efficiency of their preparation. However, more fundamental studies need to be carried out, for example, many physical organic properties of persulfurated arenes are still underexplored (UV/Vis absorption, fluorescence, electrochemical behavior, ESR spectroscopy, liquid crystallinity, metal complexation, ionophore and NLO properties, etc.).[156]

Received: January 5, 2005
Revised: September 13, 2005

[1] A. L. Rocklin, *J. Org. Chem.* **1956**, *21*, 1478–1480.
[2] M. Kulka, *J. Org. Chem.* **1959**, *24*, 235–237.
[3] a) K. R. Langille, M. E. Peach, *J. Fluorine Chem.* **1972**, *1*, 407–414; b) M. E. Peach, A. M. Smith, *J. Fluorine Chem.* **1974**, *4*, 341–344; c) M. E. Peach, A. M. Smith, *J. Fluorine Chem.* **1974**, *4*, 399–408.
[4] a) R. Adams, A. Ferretti, *J. Am. Chem. Soc.* **1959**, *81*, 4927–4931; b) R. Adams, W. Reifschneider, M. D. Nair, *Croat. Chem. Acta* **1957**, *29*, 277–285.
[5] L. P. Robota, B. F. Malichenko, *J. Org. Chem. USSR* **1976**, *12*, 236.
[6] B. C. Musial, M. E. Peach, *Phosphorus Sulfur Relat. Elem.* **1977**, *3*, 41–42.
[7] a) D. D. MacNicol, D. R. Wilson, *J. Chem. Soc. Chem. Commun.* **1976**, 494–495; b) D. D. MacNicol, A. D. U. Hardy, D. R. Wilson, *Nature* **1977**, *266*, 611–612; c) D. D. MacNicol, D. R. Wilson, *Chem. Ind.* **1977**, 84–85.
[8] a) A. D. U. Hardy, D. D. MacNicol, D. R. Wilson, *J. Chem. Soc. Perkin Trans. 2* **1979**, 1011–1019.
[9] a) J. R. Beck, J. A. Yahner, *J. Org. Chem.* **1978**, *43*, 2048–2052; b) M. E. Peach, E. S. Rayner, *J. Fluorine Chem.* **1979**, *13*, 447–454.
[10] a) L. Testaferri, M. Tingoli, M. Tiecco, *J. Org. Chem.* **1980**, *45*, 4376–4380; b) F. Maiolo, L. Testaferri, M. Tingoli, *J. Org. Chem.* **1981**, *46*, 3070–3073.
[11] T. R. Crowell, M. E. Peach, *J. Fluorine Chem.* **1982**, *21*, 469–477.
[12] a) W. Reifschneider (Dow Chemicals Co.), US 3,100,802, **1963** [*Chem. Abstr.* **1964**, *60*, 2951]; b) W. Reifschneider (Dow chemicals Co.), US 3,206,467, **1965** [*Chem. Abstr.* **1965**, *63*, 98005].
[13] W. Reifschneider (Dow Chemicals Co.), US 3,311,664, **1967** [*Chem. Abstr.* **1967**, *67*, 402893].
[14] J. D. Spivack (Ciba-Geigy AG), DE 2819882, **1978** [*Chem. Abstr.* **1978**, *90*, 88309z].
[15] D. D. MacNicol in *Inclusion Compounds, Vol. 2* (Eds.: J. L. Atwood, J. E. D. Davies, D. D. MacNicol), Academic Press, London, **1984**, chap. 5.

 © 2006 Wiley-VCH Verlag GmbH & Co. KGaA, Weinheim 

[16] Another publication appeared in 1985 with trifluoromethanethiocuprate: N. V. Kondratenko, A. A. Kolomeytsev, V. I. Popov, L. M. Yagupolskii, *Synthesis* **1985**, 667 – 669.

[17] a) J. A. Connor, G. A. Hudson, *J. Organomet. Chem.* **1975**, *97*, C43 – C45; b) M. E. Peach, *J. Fluorine Chem.* **1977**, *10*, 319 – 321.

[18] A. M. Richter, V. Engels, N. Beye, E. Fanghänel, *Z. Chem.* **1989**, *29*, 444 – 445.

[19] F. Maiolo, L. Testaferri, M. Tiecco, M. Tingoli, *J. Org. Chem.* **1981**, *46*, 3070 – 3073.

[20] L. Testaferri, M. Tiecco, M. Tingoli, D. Chianelli, M. Montanucci, *Synthesis* **1983**, 751 – 755.

[21] S. D. Pastor, E. T. Hessell, *J. Org. Chem.* **1985**, *50*, 4812 – 4815.

[22] D. D. MacNicol, P. R. Mallinson, A. Murphy, G. J. Sym, *Tetrahedron Lett.* **1982**, *23*, 4131 – 4134.

[23] C. J. Gilmore, D. D. MacNicol, A. Murphy, M. A. Russell, *Tetrahedron Lett.* **1983**, *24*, 3269 – 3272.

[24] R. H. Barbour, A. A. Freer, D. D. MacNicol, *J. Chem. Soc. Chem. Commun.* **1983**, 362 – 363.

[25] W. Poules, K. Praefcke, *Chem.-Ztg.* **1983**, *107*, 373 – 374.

[26] D. D. MacNicol, P. R. Mallinson, C. D. Robertson, *J. Chem. Soc. Chem. Commun.* **1985**, 1649 – 1651.

[27] R. Lang, R. Mayer, D. Decker, T. Kniess, *Z. Chem.* **1990**, *30*, 404 – 405.

[28] H. R. Cremer, P. Sartori, *Chem.-Ztg.* **1989**, *113*, 305 – 314.

[29] a) D. D. MacNicol, C. D. Robertson, *Nature* **1988**, *332*, 52 – 61; b) D. D. MacNicol (University of Glasgow), WO 89/01931, **1989** [*Chem. Abstr.* **1989**, *111*, 96868].

[30] N. A. Kaprinidis, N. J. Turro, *Tetrahedron Lett.* **1996**, *37*, 2373 – 2376.

[31] C. S. Frampton, W. M. McGregor, D. D. MacNicol, P. R. Mallinson, R. G. Plevey, S. J. Rowan, *Supramol. Chem.* **1994**, *3*, 223 – 226.

[32] T. Baird, J. H. Gall, D. D. MacNicol, P. R. Mallinson, C. R. Michie, *J. Chem. Soc. Chem. Commun.* **1988**, 1471 – 1473.

[33] G. A. Downing, C. S. Frampton, D. D. MacNicol, P. R. Mallinson, *Angew. Chem.* **1994**, *106*, 1653 – 1655; *Angew. Chem. Int. Ed. Engl.* **1994**, *33*, 1587 – 1589.

[34] J. H. R. Tucker, M. Gingras, H. Brand, J.-M. Lehn, *J. Chem. Soc. Perkin Trans. 2* **1997**, 1303 – 1307.

[35] a) M. Gingras, A. Pinchart, C. Dallaire, *Angew. Chem.* **1998**, *110*, 3338 – 3341; *Angew. Chem. Int. Ed.* **1998**, *37*, 3149 – 3151; b) M. Gingras, A. Pinchart, C. Dallaire, T. Mallah, E. Levillain, *Chem. Eur. J.* **2004**, *10*, 2895 – 2904.

[36] S. Samdal, L. Hedberg, K. Hedberg, A. D. Richardson, M. Bancu, L. T. Scott, *J. Phys. Chem. A* **2003**, *107*, 411 – 417.

[37] M. Bancu, A. K. Rai, P. Cheng, R. D. Gilardi, L. T. Scott, *Synlett* **2004**, 173 – 176.

[38] W. Poules, K. Praefcke, *Chem.-Ztg.* **1984**, *108*, 369 – 370.

[39] R. K. Henderson, D. D. MacNicol, K. L. McCormack, S. J. Rowan, D. S. Yufit, *Supramol. Chem.* **1998**, *10*, 27 – 32.

[40] W. Reifschneider (Dow Chemical Co.), US 3,250,787, **1966** [*Chem. Abstr.* **1966**, *65*, 3928].

[41] H. Kojima, K. Nakamura, K. Yamamoto, H. Inoue, *Synthesis* **1996**, 1193 – 1195.

[42] H. Bock, P. Rittmeyer, *Z. Naturforsch. B* **1988**, *43*, 419 – 426.

[43] F. Allared, J. Blid, J. Hellberg, T. Remonen, M. Svensson, *Synth. Met.* **2001**, *120*, 1061 – 1062.

[44] K. Kobayashi, *Chem. Lett.* **1985**, *9*, 1423 – 1424.

[45] P. D. Clark, S. Mesher, T. E. Shaun, A. Primak, *Phosphorus Sulfur Silicon Relat. Elem.* **1996**, *114*, 99 – 108.

[46] a) With $ZnCl_2$: P. D. Clark, S. T. E. Mesher, A. Primak, H. Yao, *Phosphorus Sulfur Silicon Relat. Elem.* **1997**, *120*, 413 – 414; b) With $Mn^{II}$: P. D. Clark, S. T. E. Mesher, A. Primak, H. Yao, *Catal. Lett.* **1997**, *48*, 79 – 82.

[47] A. Haas, C. Klare, H. U. Kraechter, *J. Heterocycl. Chem.* **1985**, *22*, 1631 – 1633.

[48] A. Haas, H. U. Kraechter, *Chem. Ber.* **1988**, *121*, 1833 – 1840.

[49] C. Wang, A. Ellern, J. Y. Becker, J. Bernstein, *Adv. Mater.* **1995**, *7*, 644 – 646.

[50] F. Wudl, D. Nalewajek, F. J. Rotella, E. Gebert, *J. Am. Chem. Soc.* **1981**, *103*, 5885 – 5890.

[51] a) K. Hartke, K. H. Lee, W. Massa, B. Schwarz, *Liebigs Ann. Chem.* **1991**, *3*, 243 – 251; b) K. Hartke, K. H. Lee, *Liebigs Ann. Chem.* **1992**, *4*, 413 – 414.

[52] a) K. N. Seneviratne, C. H. Winter, *Organometallics* **1997**, *16*, 2498 – 2499; b) K. Suenkel, D. Motz, *Angew. Chem.* **1988**, *100*, 970 – 971; *Angew. Chem. Int. Ed. Engl.* **1988**, *27*, 939 – 941; c) K. Suenkel, A. Blum, *Z. Naturforsch. B* **1995**, *50*, 413 – 414; d) K. Suenkel, A. Blum, K. Polborn, E. Lippmann, *Chem. Ber.* **1990**, *123*, 1227 – 1231; e) K. Suenkel, D. Steiner, *Chem. Ber.* **1989**, *122*, 609 – 614.

[53] H. Kojima, Y. Kazuhiko, Y. Kinoshita, H. Inoue, *J. Heterocycl. Chem.* **1992**, *29*, 1473 – 1476.

[54] S. Dorn, P. Eggenberg, M. R. C. Gerstenberger, A. Haas, U. Niemann, P. Zobrist, *Helv. Chim. Acta* **1979**, *62*, 1442 – 1450.

[55] H. M. Gilow, C. S. Brown, J. N. Copeland, K. E. Kelly, *J. Heterocycl. Chem.* **1991**, *28*, 1025 – 1034.

[56] a) M. R. C. Gerstenberger, A. Hass, F. Liebig, *J. Fluorine Chem.* **1982**, *19*, 461 – 474; b) M. R. C. Gerstenberger, A. Hass, B. Kirste, C. Krueger, H. Kurreck, *Chem. Ber.* **1982**, *115*, 2540 – 2547; c) D. M. Ceacareanu, M. R. C. Gerstenberger, A. Haas, *Chem. Ber.* **1983**, *116*, 3325 – 3331; d) A. Haas, F. Weiss, *Z. Anorg. Allg. Chem.* **1984**, *518*, 234 – 240; e) A. Haas, A. Kolasa, *Chem. Ber.* **1984**, *117*, 1896 – 1899; f) A. Haas, C. Klare, *Chem. Ber.* **1985**, *118*, 4588 – 4596; g) A. Haas, T. Maciej, *Z. Anorg. Allg. Chem.* **1985**, *524*, 33 – 39; h) K. Cibura, A. Haas, *Rev. Roum. Chim.* **1986**, *31*, 927 – 933; i) A. Haas, C. Klare, *J. Fluorine Chem.* **1989**, *42*, 265 – 278.

[57] L. S. Konstantinova, O. A. Rakitin, C. W. Rees, *Chem. Commun.* **2002**, 1204 – 1205.

[58] C. J. Gilmore, D. D. MacNicol, A. Murphy, M. A. Russell, *Tetrahedron Lett.* **1984**, *25*, 4303 – 4306.

[59] L. Testaferri, M. Tiecco, M. Tingoli, D. Bartoli, A. Massoli, *Tetrahedron* **1985**, *41*, 1373 – 1384.

[60] A. Haas, M. Lieb, *J. Heterocycl. Chem.* **1986**, *23*, 1079 – 1084.

[61] R. D. Chambers, J. A. H. McBride, W. K. R. Musgrave, *J. Chem. Soc. C* **1968**, *16*, 2116 – 2119.

[62] a) R. D. Chambers, J. A. H. McBride, W. K. R. Musgrave (Imperial Smelting Corporation), GB 1,163,582, **1969** [*Chem. Abstr.* **1969**, *71*, 124495]; b) D. E. Bublitz, R. H. Rigterink (Dow Chemical Co.), US. 3,560,498, **1971** [*Chem. Abstr.* **1971**, *75*, 20424].

[63] N. H. Kurihara, D. E. Bublitz (Dow Chemical Co.), US 3,761,475, **1973** [*Chem. Abstr.* **1973**, *79*, 137199].

[64] G. Beck, R. Braden, H. Holtschmidt (Bayer AG), DE 2229163, **1974** [*Chem. Abstr.* **1974**, *80*, 83076].

[65] T. D. P. Stack, J. A. Weigel, R. H. Holm, *Inorg. Chem.* **1990**, *29*, 3745 – 3760.

[66] R. Bolton, J. P. B. Sandall, *J. Chem. Soc. Perkin Trans. 2* **1978**, 137 – 141.

[67] M. Mayor, J.-M. Lehn, *Helv. Chim. Acta* **1997**, *80*, 2277 – 2285.

[68] M. Gingras, C. Dallaire, T. Mallah, A. Pinchart, F. Volatron, unpublished results.

[69] a) L. Pang, F. Brisse, E. A. C. Lucken, *Can. J. Chem.* **1995**, *73*, 351 – 361; b) D. Michalski, M. A. White, P. K. Bakshi, T. S. Cameron, I. Swainson, *Can. J. Chem.* **1995**, *73*, 513 – 521.

[70] T. D. P. Stack, R. H. Holm, *J. Am. Chem. Soc.* **1988**, *110*, 2484 – 2494.

[71] M. E. Peach, C. Burschka, *Can. J. Chem.* **1982**, *60*, 2029 – 2037.

[72] H. Lumbroso, C. Liégeois, L. Testaferri, M. Tiecco, *J. Mol. Struct.* **1986**, *144*, 121 – 133.

[73] A. Alberti, G. F. Pedulli, M. Tiecco, L. Testaferri, M. Tingoli, *J. Chem. Soc. Perkin Trans. 2* **1984**, 975 – 979.


 © 2006 Wiley-VCH Verlag GmbH & Co. KGaA, Weinheim 

[74] K. Kobayashi, O. Takahashi, K. Namatame, O. Kikuchi, N. Furukawa, *Chem. Lett.* **1998**, 515 – 516.
[75] E. Fanghänael, R. Hermann, J. Bierwisch, H. Hartung, U. Baumeister, G. Maier, H. P. Reisenauer, *J. Prakt. Chem. Chem. Ztg.* **1994**, *336*, 444 – 451.
[76] A. A. Freer, D. D. MacNicol, P. R. Mallinson, I. Vallance, *Tetrahedron Lett.* **1992**, *33*, 261 – 264.
[77] M. Mayor, M. Büschel, K. M. Fromm, J.-M. Lehn, *Chem. Eur. J.* **2001**, *7*, 1266 – 1272.
[78] Z. Chen, L. R. Sutton, D. Moran, A. Hirsch, W. Thiel, P. v. R. Schleyer, *J. Org. Chem.* **2003**, *68*, 8808 – 8814.
[79] T. D. P. Stack, R. H. Holm, *J. Am. Chem. Soc.* **1987**, *109*, 2546 – 2547.
[80] T. D. P. Stack, M. J. Carney, R. H. Holm, *J. Am. Chem. Soc.* **1989**, *111*, 1670 – 1676.
[81] Y. Suenaga, A. Ueda, T. Kuroda-Sowa, M. Maekawa, M. Munakata, *Thermochim. Acta* **2003**, *34*, 87 – 94.
[82] G. A. Downing, D. D. MacNicol, P. R. Mallinson, P. K. Milligan, *Acta Crystallogr. Sect. C* **1996**, *52*, 2887 – 2889.
[83] G. A. Downing, C. S. Frampton, J. H. Gall, D. D. MacNicol, *Angew. Chem.* **1996**, *108*, 1643 – 1645; *Angew. Chem. Int. Ed. Engl.* **1996**, *35*, 1547 – 1549.
[84] G. A. Downing, C. S. Frampton, D. D. MacNicol, *Chem. Commun.* **1998**, 2085 – 2086.
[85] X. Qiao, M. A. Padula, D. M. Ho, N. J. Vogelaar, C. E. Schutt, R. A. Pascal, Jr., *J. Am. Chem. Soc.* **1996**, *118*, 741 – 745.
[86] T. Baird, J. H. Gall, D. D. MacNicol, P. R. Mallinson, C. R. Michie, *J. Chem. Soc. Chem. Commun.* **1988**, 1471 – 1473.
[87] D. J. Brauer, *Acta Crystallogr. Sect. B* **1979**, *35*, 1770 – 1773.
[88] F. M. Menger, V. A. Azov, *J. Am. Chem. Soc.* **2002**, *124*, 11 159 – 11 166.
[89] a) S. Inoue, S. Nishiguchi, S. Murakami, Y. Aso, T. Otsubo, V. Vill, A. Mori, S. Ujiie, *J. Chem. Res. Synop.* **1999**, 596 – 597; b) S. Inoue, S. Nishiguchi, S. Murakami, Y. Aso, T. Otsubo, V. Vill, A. Mori, S. Ujiie, *J. Chem. Res. Miniprint* **1999**, 2546 – 2551.
[90] C. J. Pederson, *J. Am. Chem. Soc.* **1967**, *89*, 7017 – 7036.
[91] J.-M. Lehn in *Supramolecular Chemistry, Concepts and Perspectives*, VCH, Weinheim, **1995**, and references therein.
[92] R. M. Izatt, K. Pavilak, J. S. Bradshaw, R. L. Bruening, *Chem. Rev.* **1995**, *95*, 2529 – 2586.
[93] H. K. Hip, A. Schier, J. Riede, H. Schmidbaur, *J. Chem. Soc. Dalton Trans.* **1994**, *15*, 2333 – 2334.
[94] J. A. Harnisch, R. J. Angelici, *Inorg. Chim. Acta* **2000**, *300–302*, 273 – 279.
[95] B. N. Diel, R. C. Haltiwanger, A. D. Norman, *J. Am. Chem. Soc.* **1982**, *104*, 4700 – 4701.
[96] a) M. Okumo, K. Aramaki, S.-I. Nakajima, T. Watanabe, H. Nishihara, *Chem. Lett.* **1995**, 585 – 586; b) J. Chen, K. Aoki, *J. Electroanal. Chem.* **1996**, *402*, 189 – 193; c) M. Okumo, K. Aramaki, H. Nishihara, *J. Electroanal. Chem.* **1997**, *438*, 79 – 83; d) H. Nishihara, M. Okumo, N. Akimoto, N. Kogawa, K. Aramaki, *J. Chem. Soc. Dalton Trans.* **1998**, 2651 – 2656.
[97] Y. Suenaga, K. Kitamura, T. Kuroda-Sowa, M. Maekawa, M. Munakata, *Inorg. Chim. Acta* **2002**, *328*, 105 – 110.
[98] Y. Suenaga, T. Kuroda-Sowa, M. Maekawa, M. Munakata, *J. Chem. Soc. Dalton Trans.* **2000**, 3620 – 3623.
[99] a) Y. Suenaga, T. Kuroda-Sowa, M. Munakata, M. Maekawa, H. Morimoto, *Polyhedron* **1999**, *18*, 429 – 436; b) Y. Suenaga, T. Kuroda-Sowa, M. Munakata, M. Maekawa, H. Morimoto, *Acta Crystallogr. Sect. C* **1998**, *54*, 1566 – 1569.
[100] R. D. Johnson, A. Pinchart, I. H. A. Badr, M. Gingras, L. G. Bachas, *Electroanalysis* **2002**, *13*, 1419 – 1425.
[101] Y. Suenaga, H. Konaka, K. Kitamura, T. Kuroda-Sowa, M. Maekawa, M. Munakata, *Inorg. Chim. Acta* **2003**, *351*, 379 – 384.
[102] E. Fanghänel, J. Bierwisch, A. M. Richter, N. Beye, *Synth. Met.* **1992**, *47*, 87 – 93.
[103] E. Fanghänel, J. Bierwisch, A. Ullrich, A. Herrmann, *Chem. Ber.* **1995**, *128*, 1047 – 1049.
[104] D. J. Evans, G. Garcia, G. J. Leigh, M. S. Newton, M. D. Santana, *J. Chem. Soc. Dalton Trans.* **1992**, 3229 – 3234.
[105] J. Huang, S. Mukerjee, B. M. Segal, H. Akashi, J. Zhou, R. H. Holm, *J. Am. Chem. Soc.* **1997**, *119*, 8662 – 8674.
[106] J. A. Weigel, R. H. Holm, K. K. Surerus, E. Münck, *J. Am. Chem. Soc.* **1989**, *111*, 9246 – 9247.
[107] S. Ciurli, R. H. Holm, *Inorg. Chem.* **1989**, *28*, 1685 – 1690.
[108] S. Ciurli, M. Carrié, J. A. Weigel, M. J. Carney, T. D. P. Stack, G. C. Papaefthymiou, R. H. Holm, *J. Am. Chem. Soc.* **1990**, *112*, 2654 – 2664.
[109] J. A. Weigel, K. K. P. Srivastava, E. P. Day, E. Münck, R. H. Holm, *J. Am. Chem. Soc.* **1990**, *112*, 8015 – 8023.
[110] a) L. Cai, R. H. Holm, *J. Am. Chem. Soc.* **1994**, *116*, 7177 – 7188; b) C. J. A. Daley, R. H. Holm, *J. Inorg. Biochem.* **2003**, *97*, 287 – 298; c) I. Harvey, R. W. Strange, R. Schneider, C. A. Gormal, C. D. Garner, S. S. Hasnain, R. L. Richards, B. E. Smith, *Inorg. Chim. Acta* **1998**, *275–276*, 150 – 158; d) L. Cai, J. A. Weigel, R. H. Holm, *J. Am. Chem. Soc.* **1993**, *115*, 9289 – 9290; e) C. Zhou, L. Cai, R. H. Holm, *Inorg. Chem.* **1996**, *35*, 2767 – 2772.
[111] a) J. Zhou, R. H. Holm, *J. Am. Chem. Soc.* **1995**, *117*, 11 353 – 11 354; b) J. Zhou, Z. Hu, E. Münck, R. H. Holm, *J. Am. Chem. Soc.* **1996**, *118*, 1966 – 1980; c) J. W. Raebiger, C. A. Crawford, J. Zhou, R. H. Holm, *Inorg. Chem.* **1997**, *36*, 994 – 1003; d) C. Zhou, R. H. Holm, *Inorg. Chem.* **1997**, *36*, 4066 – 4077; e) J. Zhou, J. W. Raebiger, C. A. Crawford, R. H. Holm, *J. Am. Chem. Soc.* **1997**, *119*, 6242 – 6250; f) C. Zhou, J. W. Raebiger, B. M. Segal, R. H. Holm, *Inorg. Chim. Acta* **2000**, *300–302*, 892 – 902.
[112] N. Gueguen-Simonet, J. Simonet, L. J. Klein, D. G. Peters, *J. Electrochem. Soc.* **2002**, *149*, E389 – E393.
[113] J. Ferraris, D. O. Cowan, V. V. Walatka, J. H. Perlstein, *J. Am. Chem. Soc.* **1973**, *95*, 948 – 949.
[114] a) F. Wudl, G. Smith, E. J. Hufnagel, *J. Chem. Soc. D* **1970**, 1453 – 1454; b) S. Hünig, G. Kiesslich, D. Scheutzow, R. Zahradnik, P. Carsky, *Int. J. Sulfur Chem. Part C* **1971**, 109.
[115] a) M. Adam, K. Müllen, *Adv. Mater.* **1994**, *6*, 439 – 459; b) T. Jørgensen, T. K. Hansen, J. Becher, *Chem. Soc. Rev.* **1994**, *23*, 41 – 51.
[116] F. B. Bramwell, R. C. Haddon, F. Wudl, M. L. Kaplan, J. H. Marshall, *J. Am. Chem. Soc.* **1978**, *100*, 4612 – 4614.
[117] a) A. M. Richter, N. Beye, E. Fanghänel, *Sulfur Lett.* **1987**, *6*, 135 – 138; b) E. Fanghänel, N. Beye, A. M. Richter, *Tetrahedron* **1990**, *46*, 1553 – 1556; c) A. M. Richter, N. Beye, E. Fanghänel, *Synthesis* **1990**, 1149 – 1151; d) N. Beye, R. Wegner, A. M. Richter, E. Fanghänel, *Tetrahedron Lett.* **1991**, *32*, 479 – 482; e) E. Fanghänel, R. Wegner, N. Beye, K. Peters, K. Müllen, *J. Prakt. Chem. Chem.-Ztg.* **1995**, *337*, 299 – 306.
[118] E. Fanghänel, R. Hermann, H. Naarmann, *Tetrahedron* **1995**, *51*, 2533 – 2542.
[119] a) P. Wolf, K. Müllen, M. Przybylski, *Chimia* **1986**, *40*, 200 – 201; b) P. Wolf, H. Naarmann, K. Müllen, *Angew. Chem.* **1988**, *100*, 290 – 291; *Angew. Chem. Int. Ed. Engl.* **1988**, *27*, 288 – 299; c) M. Adam, H.-J. Räder, J. Röhrich, U. Scherer, P. Wolf, K. Müllen, *Synth. Met.* **1991**, *41–43*, 1623 – 1626; d) S. Frenzel, M. Baumgarten, K. Müllen, *Synth. Met.* **2001**, *118*, 97 – 103.
[120] a) R. Wegner, N. Beye, E. Fanghänel, U. Scherer, R. Wirschem, K. Müllen, *Synth. Met.* **1993**, *53*, 353 – 363; b) M. Adam, E. Fanghänel, K. Müllen, Y.-J. Shen, R. Wegner, *Synth. Met.* **1994**, *66*, 275 – 283.
[121] See for example a) J. Y. Becker, J. Bernstein, S. Bittner, J. A. R. P. Sarma, S. S. Shaik, *Chem. Mater.* **1989**, *1*, 412 – 420; b) M. P. Le Paillard, A. Robert, *Bull. Soc. Chim. Fr.* **1992**, *129*, 205 – 208.
[122] S. Frenzel, K. Müllen, *Synth. Met.* **1996**, *80*, 175 – 182.

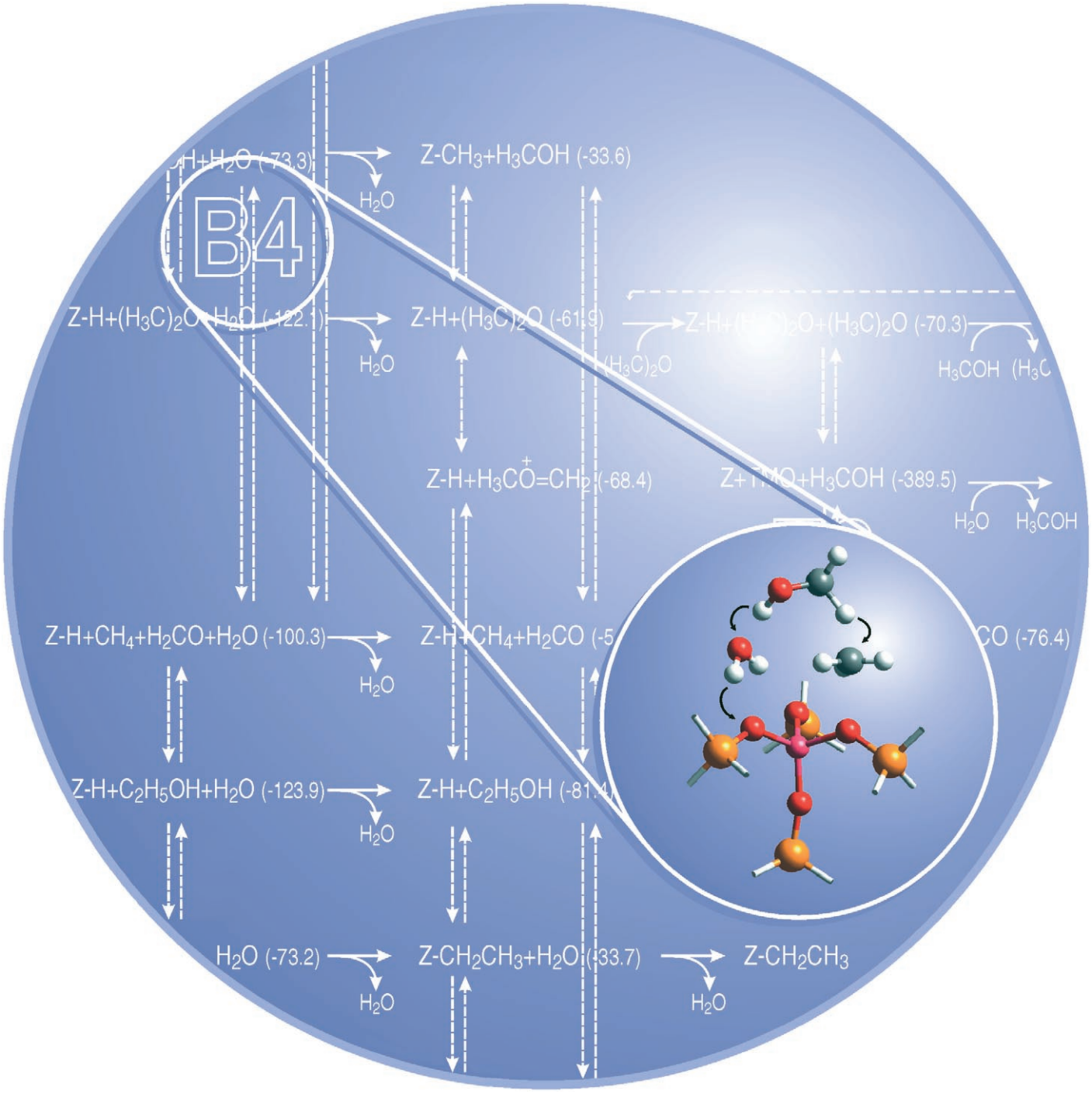
 © 2006 Wiley-VCH Verlag GmbH & Co. KGaA, Weinheim 

[123] a) K. Lahlil, A. Moradpour, C. Merienne, C. Bowlas, *J. Org. Chem.* **1994**, *59*, 8030 – 8033; b) K. Lahlil, A. Moradpour, C. Bowlas, F. Menou, P. Cassoux, J. Bonvoisin, J.-P. Launay, G. Dive, D. Dehareng, *J. Am. Chem. Soc.* **1995**, *117*, 9995 – 10002.
[124] S. Hünig, P. Erk, *Adv. Mater.* **1991**, *3*, 225 – 236.
[125] a) K. Kobayashi, *Chem. Lett.* **1985**, *9*, 1423 – 1424; b) F. Iwasaki, H. Mikami, K. Kobayashi, *Acta Crystallogr. Sect. C* **1990**, *46*, 2152 – 2154; c) C. Wang, A. Ellern, J. Y. Becker, J. Bernstein, *Adv. Mater.* **1995**, *7*, 644 – 646; d) T. Remonen, J. Helberg, J.-U. von Schuïz, *Synth. Met.* **1997**, *86*, 1851 – 1852; e) F. Allared, J. Bild, J. Helberg, T. Remonen, M. Svensson, *Synth. Met.* **2001**, *120*, 1061 – 1062.
[126] P. Bäuerle, *Adv. Mater.* **1993**, *5*, 879.
[127] R. P. Shibaeva in *Extended Linear Chain Compounds, Vol. 2* (Ed.: J. S. Miller), Plenum, New York, **1982**, pp. 435 – 467.
[128] a) K. P. Starkey, L. K. Montgomery, J. C. Huffman, M. J. Samide, D. G. Peters, *Synth. Met.* **1999**, *102*, 1741 – 1742; b) Y. Mori, H. Nakanishi, B. Hilti, C. W. Mayer, G. Rihs, *J. Appl. Phys.* **1991**, *69*, 1475 – 1478; c) J. Finter, B. Hilti, C. W. Mayer, E. Minder, J. Pfeiffer (Ciba-Geigy Corporation), EP 0285564, **1988** [*Chem. Abstr.* **1989**, *110*, 155481].
[129] A. Bartl, J. Fröhner, T. Kniess, G. Domschke, R. Mayer, S. Roth, *Synth. Met.* **1992**, *51*, 115 – 119.
[130] a) H. M. McConnell, *J. Chem. Phys.* **1963**, *39*, 1910; b) T. P. Radhakishman, Z. G. Soos, H. Endres, L. J. Azevedo, *J. Chem. Phys.* **1986**, *85*, 1126 – 1130; c) J. S. Miller, A. J. Epstein, *J. Am. Chem. Soc.* **1987**, *109*, 3850 – 3855; d) J. S. Miller, A. J. Epstein, W. M. Reiff, *Chem. Rev.* **1988**, *88*, 201 – 220; e) J. S. Miller, A. J. Epstein, W. M. Reiff, *Sciences* **1988**, *240*, 40 – 47; f) J. S. Miller, A. J. Epstein, W. M. Reiff, *Acc. Chem. Res.* **1988**, *21*, 114 – 120.
[131] R. Breslow, *Pure Appl. Chem.* **1982**, *54*, 927 – 938.
[132] a) E. Dormann, M. J. Nowak, K. A. Williams, R. O. Angus, Jr., F. Wudl, *J. Am. Chem. Soc.* **1987**, *109*, 2594 – 2599; b) J. B. Torrance, S. Oostra, A. Nazzal, *Synth. Met.* **1987**, *19*, 709 – 714.
[133] a) R. Lapouyade, J. P. Morand, *J. Chem. Soc. Chem. Commun.* **1987**, 223 – 224; b) R. Lapouyade, J. P. Morand, D. Chasseau, J. Amiell, P. Delhaes, *Synth. Met.* **1986**, *16*, 385 – 390; c) J. P. Morand, L. Brzezinski, R. Lapouyade, C. Garrigou-Lagrange, J. Amiell, P. Delhaes, *Mol. Cryst. Liq. Cryst.* **1989**, *176*, 241 – 248; d) T. Nakai, M. Kozaki, K. Sato, D. Shiomi, T. Takui, K. Itoch, K. Okada, *Chem. Lett.* **1998**, 933 – 934.
[134] a) M.-Y. Chu (Polyplus Battery Co., INC), US 5,686,201, **1997** [*Chem. Abstr.* **1997**, *128*, 24927]; b) M.-Y. Chu (Polyplus Battery Co., INC), US 5,582,823, **1996** [*Chem. Abstr.* **1996**, *126*, 106535]; c) T. A. Skotheim, B. Trofimov, A. G. Malkina, I. P. Koralev (Moltech Corporation), US 5,529,860, **1996** [*Chem. Abstr.* **1996**, *125*, 119533].
[135] D.-Y. Seung, W.-C. Jung, C.-H. Do, S.-I. Moon (The Law Offices of Eugene M Lee, PLLC), US 2002/055039, **2002** [*Chem. Abstr.* **2002**, *136*, 343388].
[136] D. Astruc, *Acc. Chem. Res.* **1986**, *19*, 377 – 383.
[137] a) M. Mayor, J.-M. Lehn, K. M. Fromm, D. Fenske, *Angew. Chem.* **1997**, *109*, 2468 – 2471; *Angew. Chem. Int. Ed. Engl.* **1997**, *36*, 2370 – 2372.
[138] M. Mayor, J. M. Lehn, *J. Am. Chem. Soc.* **1999**, *121*, 11231 – 11232.
[139] a) I. Ledoux, J. Zyss, J. S. Stegel, J. Brienne, J. M. Lehn, *Chem. Phys. Lett.* **1990**, *172*, 440 – 444; b) J. Zyss, *J. Chem. Phys.* **1993**, *98*, 6583 – 6599.
[140] M. Matsuoka, A. Oshida, A. Mizoguchi, Y. Hattori, A. Nishimura, *MCLCS&T Sect. B: Nonlinear Optics* **1995**, *10*, 109 – 114.
[141] D. R. Greve, T. Geisler, J. C. Petersen, T. Bjørnholm, *Synth. Met.* **1999**, *102*, 1533 – 1534.
[142] Among other examples: B. Derkowska, J. C. Mulatier, I. Fuks; B. Sahraoui, X. Nguyen Phu, C. Andraud, *J. Opt. Soc. Am. B* **2001**, *18*, 610.
[143] J.-M. Raimundo, S. Lecomte, M. J. Edelmann, S. Concilio, I. Biaggio, C. Bosshard, P. Guenter, F. Diederich, *J. Mater. Chem.* **2004**, *14*, 292 – 295.
[144] D. P. Warren, (Eastman Kodak Co.), US 4,606,864, **1986** [*Chem. Abstr.* **1986**, *106*, 5588].
[145] V. I. Gostevskaya, G. M. Gavrilova, A. V. Afonin, S. V. Amosova, *Russ. J. Org. Chem.* **2001**, *37*, 388 – 389.
[146] T. M. Leslie, H. Samson, (Corning INC), US 2004/0044251, **2004** [*Chem. Abstr.* **2004**, *140*, 235488].
[147] F. Takahiro, T. Masatoshi, K. Hirotoshi, O. Atsuo (Mitsui Chemicals INC) JP2003267975, **2003** [*Chem. Abstr.* **2003**, *139*, 261164].
[148] K. Praefcke, W. Poules, R. Eidenschink, B. Scheuble (Merck Patent GMBH) DE 3332955, **1985** [*Chem. Abstr.* **1985**, *103*, 160215].
[149] a) W. Poules, K. Praefcke, *Chem.-Ztg.* **1983**, *107*, 310 – 311; b) K. Praefcke, W. Poules, B. Scheuble, R. Poupko, Z. Luz, *Z. Naturforsch. B* **1984**, *39*, 950 – 956.
[150] a) K. Ichimura, *Chem. Rev.* **2000**, *100*, 1847 – 1874; b) D. L. Gin, W. Gu, B. A. Pindzola, W.-J. Zhou, *Acc. Chem. Res.* **2001**, *34*, 973 – 980, and references therein.
[151] a) D. Adam, P. Schuhmacher, J. Simmerer, L. Häussling, K. Siemensmeyer, K. H. Etzbach, H. Ringsdorf, D. Harer, *Nature* **1994**, *371*, 141 – 143; b) P. G. Schouten, J. M. Warman, M. P. de Haas, M. A. Fox, H.-L. Pan, *Nature* **1991**, *353*, 736 – 737; c) V. Percec, M. Glodde, T. K. Bera, Y. Miura, I. Shiyanovskaya, K. D. Singer, V. S. K. Balagurusamy, P. A. Heiney, I. Schnells, A. Rapp, H.-W. Spiess, S. D. Hudson, H. Duan, *Nature* **2002**, *419*, 384 – 387, and references therein.
[152] M. Lehmann, V. Lemaur, J. Cornil, J. L. Brédas, S. Goddard, I. Grizzi, Y. Geerts, *Tetrahedron* **2004**, *60*, 3283 – 3291.
[153] K. Praefcke, B. Kohne, E. Poetsch, C. P. Herz (Merck Patent GMBH) DE 3430482, **1985** [*Chem. Abstr.* **1985**, *130*, 161007].
[154] B. Scheuble, R. Eidenschink, G. Weber, (Merck Patent GMBH) DE 3401338, **1985** [*Chem. Abstr.* **1985**, *104*, 159747].
[155] a) W. Reifschneider (Dow Chemicals Co.), US 3,231,585, **1966** [*Chem. Abstr.* **1966**, *64*, 59809]; b) R. Eidenschink, H. Kretzschmann (Nematel Dr. Rudolf Eidenschink), EP 798366A2, **1997** [*Chem. Abstr.* **1997**, *127*, 320732]; c) H. Kretzschmann, R. Eidenschink (Nematel Dr. Rudolf Eidenschink), DE 19850532A1, **2000** [*Chem. Abstr.* **2000**, *132*, 296005].
[156] During the corrections of this Review, we became aware of the following important article: J. N. Lowe, D. A. Fulton, S.-H. Chiu, A. M. Elizarov, S. J. Cantrill, S. J. Rowan, J. F. Stoddart, *J. Org. Chem.* **2004**, *69*, 4390 – 4402

 © 2006 Wiley-VCH Verlag GmbH & Co. KGaA, Weinheim 

# Communications

DOI: 10.1002/anie.200503824




An unprecedented number of possible direct reaction steps from methanol to ethylene are tied together in a single integrated scheme. Calculations show that every imaginable combination of direct reactions fails completely in the formation of the initial carbon–carbon bond. For more details, see the Communication by M. Waroquier and co-workers on the following pages.


WILEY InterScience DISCOVER SOMETHING GREAT
© 2006 Wiley-VCH Verlag GmbH & Co. KGaA, Weinheim

Zeolites

DOI: 10.1002/anie.200503824

# Understanding the Failure of Direct C–C Coupling in the Zeolite-Catalyzed Methanol-to-Olefin Process**

*David Lesthaeghe, Veronique Van Speybroeck, Guy B. Marin, and Michel Waroquier**

The mechanism of the methanol-to-olefin (MTO) process on zeolite H-ZSM-5 has been the source of significant debate by both industrial and academic researchers. Much still remains uncertain, and the literature is replete with diverse and often conflicting propositions. A crucial step is the formation of the first carbon–carbon bond, for which more than 20 distinct mechanistic proposals exist.[1] Early research focused mainly on mechanisms based on the direct formation of small olefins from only methanol and methanol derivatives. Advanced theoretical calculations on these "direct mechanisms" are fragmented throughout the literature, and straightforward comparison is cumbersome owing to the large array of methods employed. Only a handful of papers suggest and compare multiple direct routes,[2,3] but these are limited to low levels of theory calculations on extremely small 1T/3T zeolite clusters.

Recent developments suggest, however, that direct mechanisms might not be responsible for the observed boost in hydrocarbon synthesis.[4] A plausible alternative is given by the "hydrocarbon pool" model,[4,5] in which impurities in the mixture undergo repeated methylation and subsequent olefin elimination. This latter proposal is consistently gaining experimental and theoretical support, which advocates methylbenzenes and methylcyclopentenyl cations as key species.[6,7] Because of an observed kinetic induction period preceding the hydrocarbon formation, the hydrocarbon pool model implies that reactions occurring during this induction period need not necessarily be similar to those on a working catalyst. It is still unresolved, though, which—if any—induction reactions give rise to the hydrocarbon pool.

As the literature currently stands, two important questions regarding direct mechanisms remain unanswered: 1) From a theoretical viewpoint it is still unclear why the numerous proposed direct mechanisms should fail in consistent production of ethylene. 2) From a more practical perspective, it is still unknown what role certain directly formed intermediates might play both during the induction period and during hydrocarbon synthesis. Although experimental methods are often incapable of evaluating individual reaction steps, DFT-based calculations can provide these answers.

An extensive scheme is proposed, tying together a large variety of possible direct reactions, which include several previously overlooked, parallel pathways. On the basis of calculated adsorption energies, reaction barriers (at 0 K), and rate coefficients (at 720 K), it is possible to deduce whether ethylene can be produced from only methanol, and which stable intermediates might be formed directly to finally enhance our understanding of the first carbon–carbon bond formation.

Our aim was to integrate a whole range of reactions in an orderly and concise manner, as shown in Scheme 1. The adsorbed species form the main building blocks, with the total adsorption energy (in $kJ\,mol^{-1}$) shown in brackets. Horizontal movement between these species corresponds to adsorption or desorption of a required molecule. Vertical arrows represent an elementary reaction step for which both forward and reverse intrinsic energy barrier heights at 0 K (in $kJ\,mol^{-1}$) as well as rate coefficients at 720 K (in $s^{-1}$) are included. For simple referencing purposes, each reaction step is identified by a specific code. The starting point (top left corner) is a single methanol molecule adsorbed near the acid site Z-H, leading finally to the creation of ethylene (bottom row). For clarity, we omit connections for which both the forward and reverse reactions are highly activated ($\Delta E_0 > 200\ kJ\,mol^{-1}$) and which are therefore unlikely to proceed in either direction.

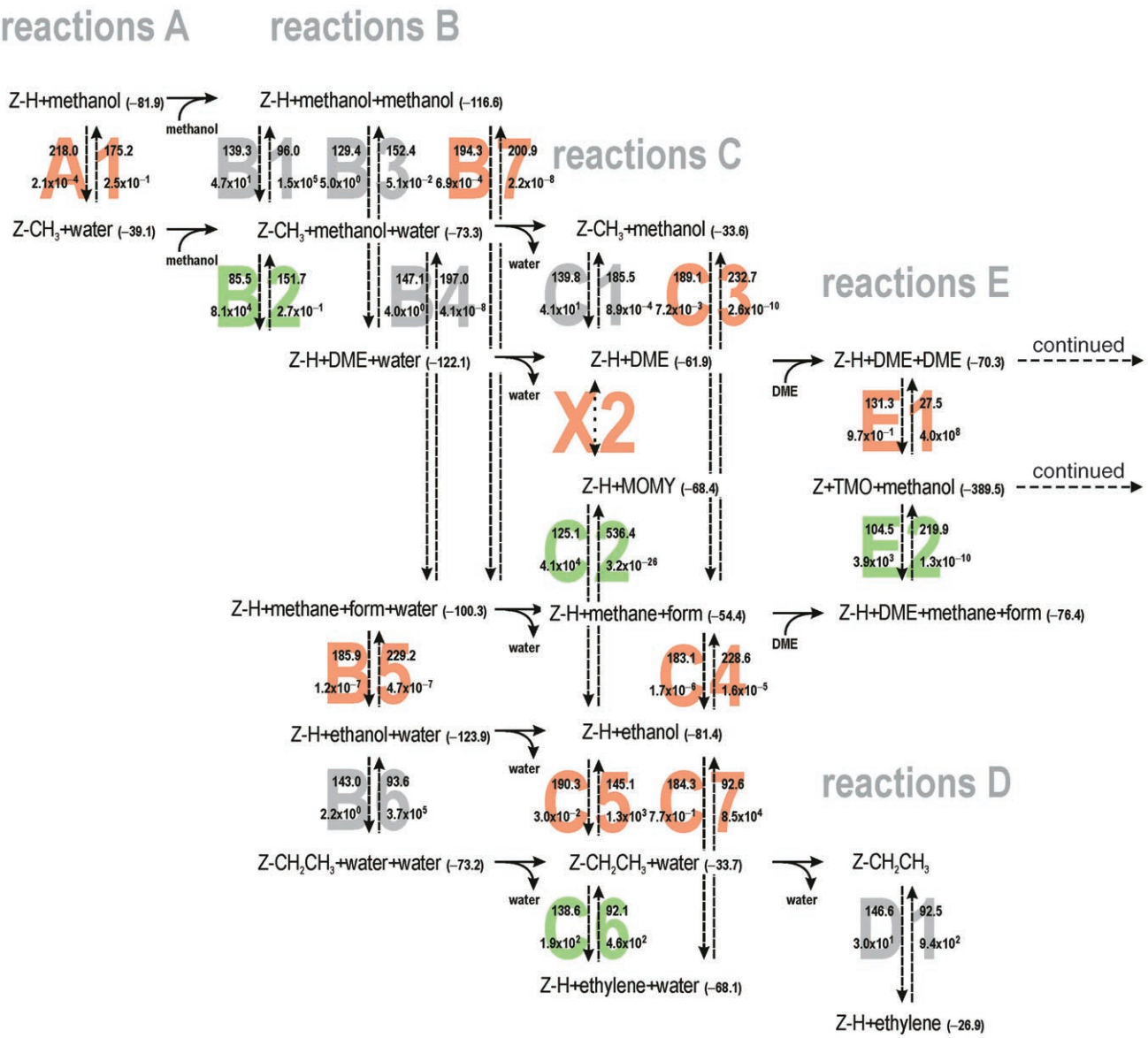
The conversion of methanol is known to start with rapid dehydration to dimethyl ether (DME). This proceeds either via an intermediate methoxide species Z-$CH_3$ (reactions coded A1/B1/B2/C1),[8] or through co-reaction of a methanol dimer (B3). The two-step pathway B1/B2 is facilitated by methanol/water successively lowering the reaction barriers as "assisting molecules", allowing more-favorable transition-state geometries. This first preequilibrium phase in the methanol-to-olefin process is theoretically well documented, ranging from small clusters[9–11] to fully periodic DFT calculations,[12–14] which all lead to similar conclusions.

From this initial mixture, the direct formation of the trimethyl oxonium ion (TMO) has been proposed through nucleophilic attack by adsorbed DME on a framework-bound methoxide species (G1).[15] Alternatively, TMO can also be formed through co-reaction of two DME molecules (E1) or DME and methanol (F1). Owing to the extremely low reverse reaction barriers, one would at first glance expect TMO to be an exceptionally short-lived intermediate. However, positively charged TMO forms an ion pair with the negative aluminum defect, and therefore cannot be adequately described in the small cluster approach. Our previous ONIOM calculations, however, have shown that TMO is additionally stabilized by the zeolite framework,[16] a similar result to that obtained through periodic calculations in chabazite,[17] and that TMO remains an important product formed directly from the equilibrium mixture.

[*] Ir. D. Lesthaeghe, Dr. Ir. V. Van Speybroeck, Prof. Dr. M. Waroquier
Center for Molecular Modeling
Ghent University
Proeftuinstraat 86, 9000 Gent (Belgium)
Fax: (+32) 9-264-6697
E-mail: michel.waroquier@ugent.be
Prof. Dr. Ir. G. B. Marin
Laboratorium voor Petrochemische Techniek
Ghent University
Krijgslaan 281-S5, 9000 Gent (Belgium)

[**] This work was supported by the Fund for Scientific Research–Flanders (FWO) and the Research Board of Ghent University.

 © 2006 Wiley-VCH Verlag GmbH & Co. KGaA, Weinheim 




***Scheme 1.*** Direct routes in the methanol-to-olefin process. Horizontal arrows correspond to an adsorption/desorption step, vertical arrows denote a reaction step. Intrinsic energy barriers at 0 K are shown in kJ mol$^{-1}$, rate coefficients at 720 K are expressed in s$^{-1}$.

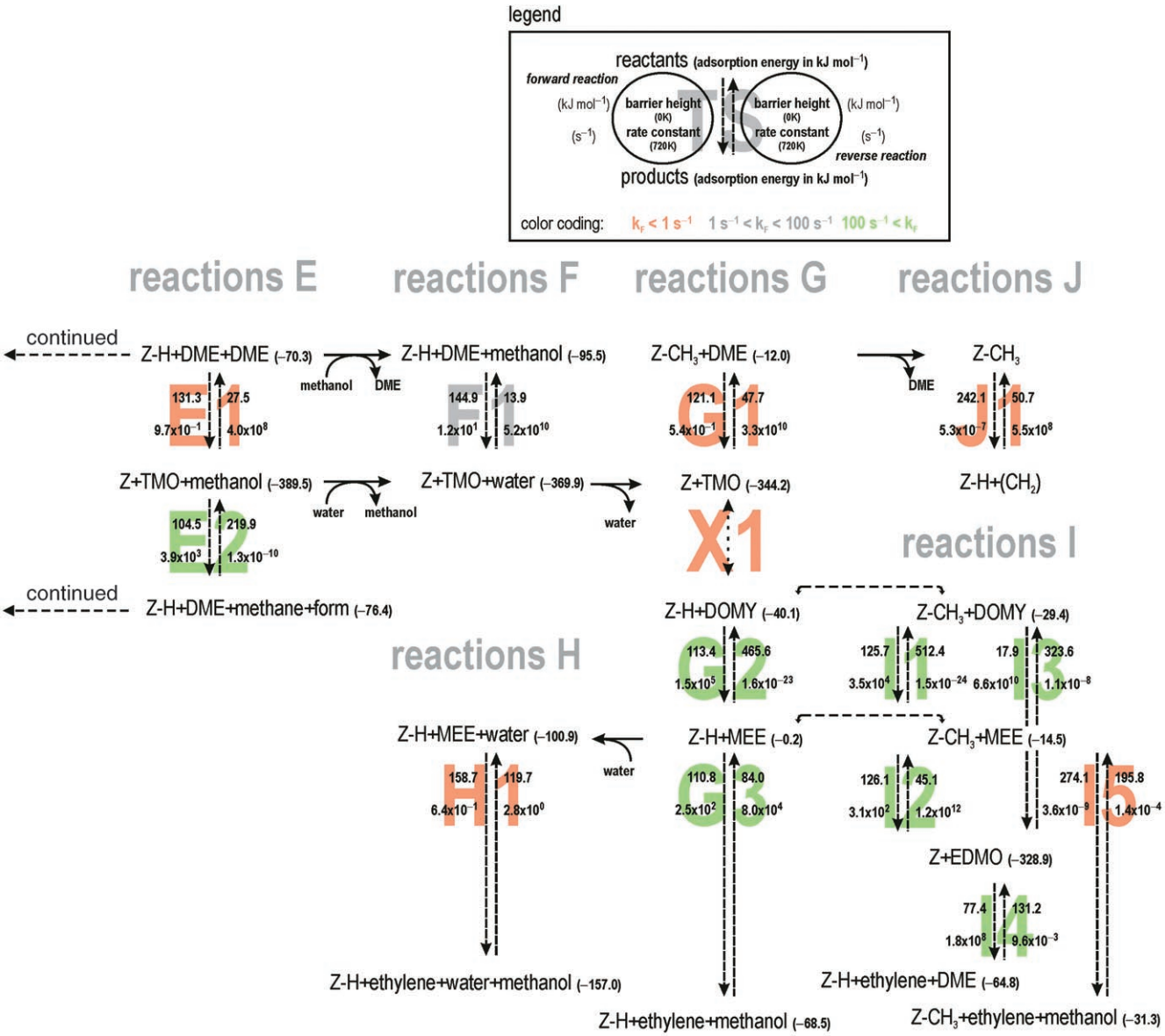
Once TMO is successfully formed, it might be deprotonated by an adjacent basic site (reaction step X1) to form dimethyl oxonium methylide (DOMY).[15] The next step is an intramolecular Stevens rearrangement (G2/I1) to methyl ethyl ether (MEE) or an intermolecular methylation (I2/I3) to form the ethyl dimethyl oxonium ion (EDMO). EDMO readily undergoes β elimination to form ethylene and dimethyl ether (I4). From MEE, several alternative pathways lead directly to ethylene (H1/G3/I5). However, our previous work has shown that there is no possible route from TMO to DOMY (X1).[16] Moreover, the zeolite framework does not offer any supplementary stabilization, which results in DOMY being a highly energetic species.

Alternatively, methyl oxonium methylide (MOMY) has been proposed as a possible intermediate.[18] Adsorbed dimethyl ether could form a dimethyl oxonium ion (DMO), after which it would be deprotonated to MOMY (X2). A Stevens-type rearrangement would lead to ethanol (C2), thus forming the required carbon–carbon bond. Yet again, we have found this step to be non-existent and MOMY to be highly unstable.[16] An altogether different ylide, incorporated into the framework, can be formed by deprotonation of a framework-bound methyl group (J1).[19] This step was found to be highly activated as well.

Generally speaking, the oxygen bridge seems to be insufficiently basic to form the desired ylides. We also state that alternative pathways based on oxonium ylides are highly improbable owing to the high instability of these species. The instability of the ylides consequently rules out the role of MEE as a crucial intermediate as well as the pathway through EDMO.

There are several routes to methane and formaldehyde (form), starting from two methanol molecules (B7),[3] from a surface methoxy species and methanol (B4/C3), or from TMO

 © 2006 Wiley-VCH Verlag GmbH & Co. KGaA, Weinheim 




***Scheme 1.*** (Continued).

jointly adsorbed with methanol (E2). Once formed, however, only extremely high reaction barriers (B5/C4) allow the formation of ethanol. From ethanol, ethylene could be immediately formed (C7), but the fastest routes would be through the formation of a framework-bound ethoxide species (B6/C5) and subsequent ethylene production (C6/D1).

As mentioned earlier, conversions showing both forward and reverse barriers larger than 200 kJ mol$^{-1}$ are not shown in Scheme 1, and a closer investigation of the omitted reaction steps is necessary. In Figure 1 (blue arrows) we show a model representing the steps that were too highly activated to be incorporated, as they all follow a similar concerted reaction mechanism: hydrogen abstraction from a methanol/DME methyl group by a zeolite basic oxygen bridge (alternatively assisted by a water "vehicle molecule") combined with the formation of a carbon–carbon bond with a methanol/DME/

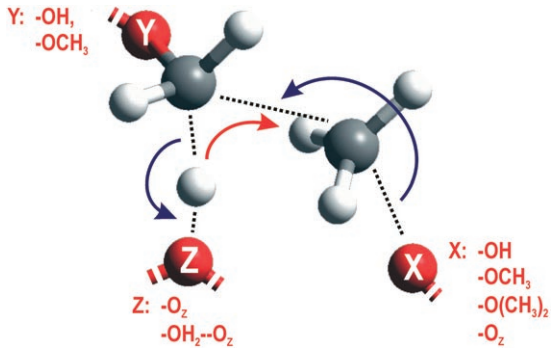



***Figure 1.*** Highly activated reactions corresponding to concerted C–C bond formation and C–H bond breaking by zeolite basic oxygen $O_z$ (blue arrows). Protonation of the methyl group to form methane (red arrow) is observed instead.

 © 2006 Wiley-VCH Verlag GmbH & Co. KGaA, Weinheim 

TMO/framework-bound methyl group. The unprotonated oxygen bridge apparently lacks the strong basic character needed to break the highly covalent C–H bond. An equally strong C–H bond is preferably formed, which is why the system evolves to a nearby transition state, thus leading to methane instead (red arrow in Figure 1). This is similar to observations in molecular-dynamics simulations.[20,21] These concerted reactions form the main bottleneck of the direct mechanism proposal, whereas currently suggested hydrocarbon pool reactions avoid similar concerted steps through the formation of an intermediate carbenium ion.

In conclusion, a large set of direct mechanisms (>80 stationary points) in the MTO process was studied theoretically, providing both rate coefficients at 720 K and reaction barriers at 0 K. Direct comparisons allowed the qualitative evaluation of which steps are likely to proceed. The crucial reaction steps were identified, into which further research is currently underway.

We failed to find a successive pathway from methanol leading all the way to ethylene (or to any intermediate containing a C–C bond), which is in accordance with methanol/DME not being noticeably reactive on H-ZSM-5 in the absence of organic impurities that provide a primordial hydrocarbon pool.[22] From our results, two bottlenecks can be clearly identified: on the one hand the instability of the ylide intermediates and on the other hand the high energy barriers for the often proposed concerted C–C bond-formation reactions, both of which are a direct result of the weak basic character of the zeolite oxygen bridge. It is also possible to define clearly which intermediate species are likely to be directly formed and may consequently interact with the hydrocarbon pool. These intermediates are not limited solely to the mixture of methanol with well-known condensation products DME and water but also TMO, which might act as a viable source of methyl groups, together with methane and formaldehyde.

Summarizing our conclusions, we have tied the numerously proposed reaction mechanisms together to find that not a single combination of direct reaction steps can link methanol to ethylene. This theoretical conclusion provides strong additional support for alternative proposals,[4–7] which bypass the highly activated concerted steps.

## Methods Section

Geometry optimizations were performed on pentatetrahedral (5T) clusters with the Gaussian 03 package[23] at the B3LYP/6-31g(d) level of theory.[24–26] The cluster selection was motivated by the large amount of species taken into account (more than 80 distinctly different stationary points). Moreover, our recent study using ONIOM calculations on extended 30T and 46T clusters showed that the energy profile is only significantly altered in the case of adsorbed ion pairs.[16] Initial interpretation on the 5T level allowed us to evaluate which reactions require further detailed investigation. The cluster was left unconstrained to verify the true nature of stationary points, and zero-point energy (ZPE) corrections were included. Starting from transition-state geometries, the quasi-IRC approach allowed the product geometries to be acquired.[27] Rate coefficients were obtained by using transition-state theory (TST) by calculating the partition functions at 720 K. As elementary reaction steps were considered separately from adsorption/desorption requirements, only intrinsic energy barriers are shown (in kJ mol$^{-1}$): $\Delta E_0 = E_0$(transition state)$-E_0$(adsorbed reactants). Additionally, each elementary reaction was modeled assuming prior adsorption of necessary reagents, resulting in intrinsic rate coefficients (in s$^{-1}$).

Received: October 28, 2005
Revised: November 29, 2005
Published online: February 14, 2006

**Keywords:** ab initio calculations · C–C coupling · heterogeneous catalysis · methanol-to-olefin process · zeolites

[1] M. Stöcker, *Microporous Mesoporous Mater.* **1999**, *29*, 3–48.
[2] S. R. Blaszkowski, R. A. van Santen, *J. Am. Chem. Soc.* **1997**, *119*, 5020–5027.
[3] N. Tajima, T. Tsuneda, F. Toyama, K. Hirao, *J. Am. Chem. Soc.* **1998**, *120*, 8222–8229.
[4] W. Song, D. M. Marcus, H. Fu, J. O. Ehresmann, J. F. Haw, *J. Am. Chem. Soc.* **2002**, *124*, 3844–3845.
[5] I. M. Dahl, S. Kolboe, *J. Catal.* **1994**, *149*, 458–464.
[6] J. F. Haw, J. B. Nicholas, W. Song, F. Deng, Z. Wang, T. Xu, C. S. Heneghan, *J. Am. Chem. Soc.* **2000**, *122*, 4763–4775.
[7] B. Arstad, J. B. Nicholas, J. F. Haw, *J. Am. Chem. Soc.* **2004**, *126*, 2991–3001.
[8] W. Wang, A. Buchholz, M. Seiler, M. Hunger, *J. Am. Chem. Soc.* **2003**, *125*, 15260–15267.
[9] C. M. Zicovich-Wilson, P. Viruela, A. Corma, *J. Phys. Chem.* **1995**, *99*, 13224–13231.
[10] P. E. Sinclair, C. R. A. Catlow, *J. Chem. Soc. Faraday Trans.* **1997**, *93*, 333–345.
[11] S. R. Blaszkowski, R. A. van Santen, *J. Phys. Chem. B* **1997**, *101*, 2292–2305.
[12] E. Sandre, M. C. Payne, J. D. Gale, *Chem. Commun.* **1998**, 2445–2446.
[13] M. Hytha, I. Stich, J. D. Gale, K. Terakura, M. C. Payne, *Chem. Eur. J.* **2001**, *7*, 2521–2527.
[14] M. C. Payne, M. Hytha, I. Stich, J. D. Gale, K. Terakura, *Microporous Mesoporous Mater.* **2001**, *48*, 375–381.
[15] G. A. Olah, H. Doggweiler, J. D. Felberg, S. Frohlich, M. J. Grdina, R. Karpeles, T. Keumi, S. I. Inaba, W. M. Ip, K. Lammertsma, G. Salem, D. C. Tabor, *J. Am. Chem. Soc.* **1984**, *106*, 2143–2149.
[16] D. Lesthaeghe, V. Van Speybroeck, G. B. Marin, M. Waroquier, *Chem. Phys. Lett.* **2006**, *417*, 309–315.
[17] R. Shah, J. D. Gale, M. C. Payne, *J. Phys. Chem. B* **1997**, *101*, 4787–4797.
[18] O. Dewaele, V. L. Geers, G. F. Froment, G. B. Marin, *Chem. Eng. Sci.* **1999**, *54*, 4385–4395.
[19] P. E. Sinclair, C. R. A. Catlow, *J. Phys. Chem. B* **1997**, *101*, 295–298.
[20] C. Lo, C. A. Giurumescu, R. Radhakrishnan, B. L. Trout, *Mol. Phys.* **2004**, *102*, 281–288.
[21] C. S. Lo, R. Radhakrishnan, B. L. Trout, *Catal. Today* **2005**, *105*, 93–105.
[22] J. F. Haw, D. M. Marcus in *Handbook of Zeolite Science and Technology* (Eds.: S. M. Auerbach, K. A. Carrado, P. K. Dutta), Marcel Dekker, New York, **2003**, pp. 833–866.
[23] Gaussian 03, Revision B.03, M. J. Frisch, G. W. Trucks, H. B. Schlegel, G. E. Scuseria, M. A. Robb, J. R. Cheeseman, J. A. Montgomery, Jr., T. Vreven, K. N. Kudin, J. C. Burant, J. M. Millam, S. S. Iyengar, J. Tomasi, V. Barone, B. Mennucci, M. Cossi, G. Scalmani, N. Rega, G. A. Petersson, H. Nakatsuji, M. Hada, M. Ehara, K. Toyota, R. Fukuda, J. Hasegawa, M. Ishida, T. Nakajima, Y. Honda, O. Kitao, H. Nakai, M. Klene, X. Li, J. E. Knox, H. P. Hratchian, J. B. Cross, V. Bakken, C. Adamo, J. Jaramillo, R. Gomperts, R. E. Stratmann, O. Yazyev, A. J.

 © 2006 Wiley-VCH Verlag GmbH & Co. KGaA, Weinheim 

Austin, R. Cammi, C. Pomelli, J. W. Ochterski, P. Y. Ayala, K. Morokuma, G. A. Voth, P. Salvador, J. J. Dannenberg, V. G. Zakrzewski, S. Dapprich, A. D. Daniels, M. C. Strain, O. Farkas, D. K. Malick, A. D. Rabuck, K. Raghavachari, J. B. Foresman, J. V. Ortiz, Q. Cui, A. G. Baboul, S. Clifford, J. Cioslowski, B. B. Stefanov, G. Liu, A. Liashenko, P. Piskorz, I. Komaromi, R. L. Martin, D. J. Fox, T. Keith, M. A. Al-Laham, C. Y. Peng, A. Nanayakkara, M. Challacombe, P. M. W. Gill, B. Johnson, W. Chen, M. W. Wong, C. Gonzalez, J. A. Pople, Gaussian, Inc., Wallingford CT, **2003**.

[24] A. D. Becke, *J. Chem. Phys.* **1993**, *98*, 5648 – 5652.

[25] S. A. Zygmunt, R. M. Mueller, L. A. Curtiss, L. E. Iton, *J. Mol. Struct.* **1998**, *430*, 9 – 16.

[26] D. Lesthaeghe, V. Van Speybroeck, M. Waroquier, *J. Am. Chem. Soc.* **2004**, *126*, 9162 – 9163.

[27] S. Svelle, B. Arstad, S. Kolboe, O. Swang, *J. Phys. Chem. B* **2003**, *107*, 9281 – 9289.

 © 2006 Wiley-VCH Verlag GmbH & Co. KGaA, Weinheim 

*Density Functional Calculations*

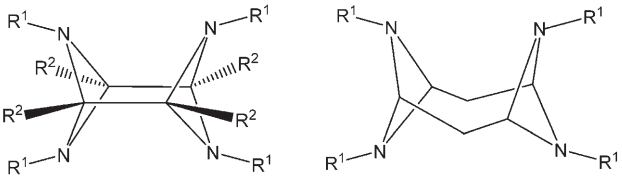
DOI: 10.1002/anie.200503254

# Rational Design and First Principles Studies Toward the Discovery of a Small and Versatile Proton Sponge**

*Ernesto Estrada* and Yamil Simón-Manso*

More than 30 years ago, Alder et al.[1] challenged our classical view of acid–base properties with their discovery of a simple organic compound that showed a basicity ten million times higher than typical organic bases. This superbase, 1,8-bis(dimethylamino)naphthalene (DMAN), is known as "proton sponge" because of its high thermodynamic basicity combined with a kinetic inactivity to deprotonation that resembles the affinity of a sponge for water.[2] Since then, many families of proton sponges have been created and they are finding a growing number of interesting applications.[2–5] Quantum chemical studies have shed some light on the structural factors influencing the high basicity of proton sponges.[6–10] Their abnormally high basicity is accepted to be produced by strong crowding of unshared electron pairs on nitrogen atoms, a strong intramolecular hydrogen bond in the protonated form, and relief of steric strain upon protonation. These characteristics are usually achieved by anchoring two nitrogen atoms sufficiently close in a rigid framework of condensed phenyl rings.[2–5] Furthermore, hydrophobic substituents on the nitrogen atoms confer kinetic stability.

Herein we report the design of a new molecular framework that differs significantly from the traditional topology of proton sponges. We began with the simplest structure in which two nitrogen atoms are about 250 pm apart and have their lone pairs of electrons facing each other, namely, the boat conformation of piperazine. To enforce the boat conformation, we integrated this unit into the minimal framework provided by the structure of 3,6,7,8-tetraazatricyclo[3.1.1.1$^{2,4}$]octane (**1**; Scheme 1). This molecule has two pairs of nitrogen atoms fixed in a configuration that should guarantee acid–base properties similar to those of proton sponges. The geometries and proton affinities of **1**, and its 3,6,7,8-tetramethyl (**2**), 1,2,3,4-tetramethyl (**3**), and 1,2,3,4,5,6,7,8-octamethyl (**4**) derivatives, as well as of DMAN and 1,6-diazabicyclo[4.4.4]tetradecane (BDDT), were calculated by using density functional theory (DFT). The last compound has the highest proton affinity (PA) value among all the aliphatic proton sponges studied by Howard.[11]



**1**: $R^1 = R^2 = H$; **2**: $R^1 = CH_3$, $R^2 = H$
**3**: $R^1 = H$, $R^2 = CH_3$; **4**: $R^1 = R^2 = CH_3$

**5**: $R^1 = H$; **6**: $R^1 = CH_3$

***Scheme 1.*** Structures of 3,6,7,8-tetraazatricyclo[3.1.1.1$^{2,4}$]octane (**1**) and 4,8,9,10-tetraazatricyclo[5.1.1.1$^{3,5}$]decane (**5**) as well as their methylated derivatives.

Compounds **1**–**4** have two equivalent protonation sites, one above and another below the plane formed by the carbon atoms. Consequently, we first calculated the PA for the first protonation site with the second site in the deprotonated state and then for the second site keeping the first one protonated. Some of the principal geometrical parameters of the neutral and protonated optimized structures **1**–**4** are given in Table 1. The N···N distances are about 50 pm lower than the average experimental value of 282.6 pm obtained for 20 proton sponges.[5] The calculated N···N distances in DMAN and BDDT are 279.2 pm and 292.34 pm, respectively. The former value is in full agreement with the experimental value obtained by X-ray diffraction studies (279.2 pm).[5] In general, the N···N$^+$ distance decreases upon protonation. However, this decrease is almost negligible in **1**–**4**, particularly for **2** and **3**. An unexpected increase in the N···N$^+$ distance is observed in **1** and **2** upon adding a second proton. This increment is not observed in **4**. The N–H···N hydrogen-bonding angles in singly protonated **1**–**4** range from 103 to 130° and are much

[*] Dr. E. Estrada
Complex Systems Research Group, X-Ray Unit
RIAIDT, Edificio CACTUS
University of Santiago de Compostela
15782 Santiago de Compostela (Spain)
Fax: (+34) 981-547-077
E-mail: estrada66@yahoo.com
Dr. Y. Simón-Manso
INEST Group, PM-USA and
Center for Theoretical and Computational Nanosciences
National Institute of Standards & Technology (NIST)
100 Bureau Drive, Stop 8380, Gaithersburg, MD 20899-8380 (USA)

[**] We thank Dr. Karl Irikura for his assistance in the preparation of the manuscript. E.E. thanks program "Ramón y Cajal", Spain, for partial financial support.

 © 2006 Wiley-VCH Verlag GmbH & Co. KGaA, Weinheim 

***Table 1:*** Ab initio (B3PW91/6-311++g**) gas-phase geometrical parameters of the proton sponges and associated cations.

| Sponge | Cation 1 | | | | Cation 2 | | |
|---|---|---|---|---|---|---|---|
| | $r$(N···N) [pm] | $r$(N···N$^+$) [pm] | $r$(N···H) [pm] | N–H···N [°] | $r$(N···N$^+$) [pm] | $r$(N···H) [pm] | N–H···N [°] |
| **1** | 239.2 | 233.3 | 103.7 | 103.0 | 237.3 | 103.2 | 96.9 |
| **2** | 235.6 | 233.1 | 105.7 | 116.5 | 236.9 | 104.4 | 112.1 |
| **3** | 237.2 | 232.1 | 103.5 | 103.5 | 231.5 | 104.0 | 102.9 |
| **4** | 234.8 | 226.2 | 125.0 | 129.5 | 226.2 | 120.4 | 139.9 |
| **5** | 286.0 | 254.8 | 107.4 | 137.3 | 269.4 | 103.7 | 124.6 |
| **6** | 279.8 | 257.2 | 108.0 | 141.3 | 269.4 | 104.6 | 132.9 |
| DMAN | 279.2 | 260.3 | 112.0 | 159.2 | – | – | – |
| BDDT | 292.3 | 257.3 | 141.8 | 178.1 | – | – | – |

lower than those reported for proton sponges. According to the X-ray data compiled by Llamaz-Saiz et al.,[5] proton sponges generally have angles between 150 and 180°, with the exceptions of tetraamine[2$^6$]adamanzane and vinamidine proton sponge, which have values of 123.1 and 131.2°, respectively. To summarize, the geometrical parameters for both the bases and the cations of **1**–**4** are significantly different from those of known proton sponges.

***Table 2:*** Ab initio (B3PW91/6-311++g**) gas-phase proton affinities at 273 K and estimated p$K_a$ values in water for the protonation of the proton sponges.

| | PA [kJ mol$^{-1}$] | | | | | |
|---|---|---|---|---|---|---|
| | gas phase | | aqueous phase | | p$K_a$ (Water)[a] | |
| | 1[b] | 2[b] | 1[b] | 2[b] | 1[b] | 2[b] |
| **1** | 1001.93 | 554.41 | 1240.01 | 1207.97 | 15.7 | 10.3 |
| **2** | 1072.96 | 643.18 | 1285.93 | 1224.27 | 23.4 | 13.0 |
| **3** | 1044.54 | 633.94 | 1241.37 | 1201.74 | 15.9 | 9.2 |
| **4** | 1103.11 | 697.74 | 1287.27 | 1250.15 | 23.6 | 17.4 |
| **5** | 1044.66 | 609.35 | 1260.35 | 1222.92 | 19.1 | 12.8 |
| **6** | 1073.84 | 671.86 | 1268.12 | 1226.67 | 20.4 | 13.4 |
| DMAN | 1037.39[c] | – | 1218.75 | – | 12.1[d] | – |
| BDDT | 1082.75 | – | 1294.33 | – | 24.8[e] | – |

[a] Estimated by the linear regression model: p$K_a$ = 0.1684 PA(aq) − 193.14. [b] First and second protonation are designed as 1 and 2, respectively. [c] Experimental value: 1030.1 kJ mol$^{-1}$. [d] Experimental value: 12.1 kJ mol$^{-1}$. [e] Experimental value: 25 kJ mol$^{-1}$.

According to our DFT calculations, **1**–**4** have gas-phase proton affinities that equal or even exceed those of some proton sponges, such as DMAN and BDDT. In particular, the octamethylated compound **4** has a calculated PA that is 20 kJ mol$^{-1}$ higher than that calculated for BDDT (Table 2). Proton affinities for the second protonation of compounds **1**–**4** are, in all cases, very small. Howard has expressed gas-phase PA in terms of the changes in the N···N distance and the hydrogen-bonding angle on protonation.[11] Our calculations do not reproduce these correlations for **1**–**4**. However, the gas-phase proton affinities of **1**–**4** increase as the N···N distance in the base decreases. This is not necessarily a direct cause-and-effect relationship: in particular, methylation of compound **1**, which decreases the N···N separation, also tightens and deepens the electrostatic potential in the region between the nitrogen atoms, which makes the proton more stable there. The electrostatic potentials of compounds **1** and **2** are shown in Figure 1 a,b. The two protonation sites (in blue) are more localized in the case where the amine groups are methylated. This kind of region has been described previously as a hydrophobic environment at the nitrogen atoms, to which the "sponge effect" is attributed.[2]

The most striking geometrical difference between the new proton sponges **1**–**4** and classical sponges such as DMAN and BDDT is the closeness of the nitrogen atoms in the new sponges. The N···N distances in **1**–**4** are not only atypical compared to other proton sponges, but also compared to intra- and intermolecular N$^+$–H···N hydrogen bonds in general. In the data of the 150 crystals compiled and analyzed

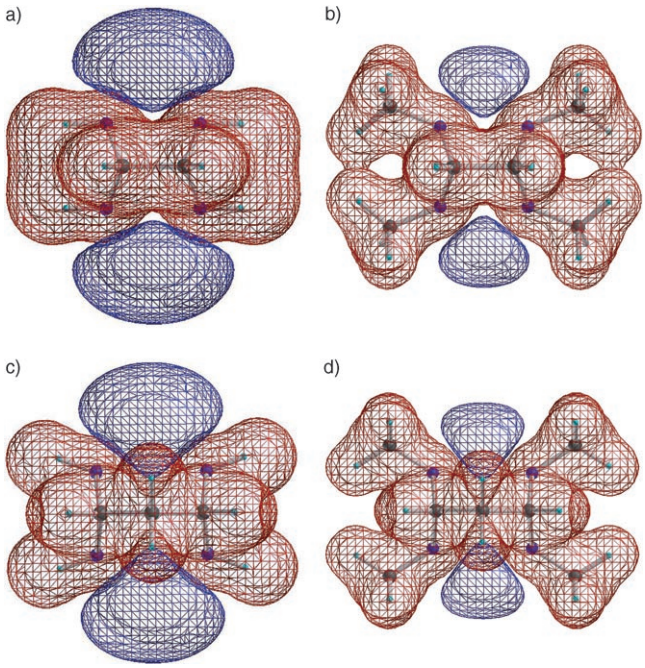



***Figure 1.*** Molecular electrostatic potentials (MEP) of the proton sponges (3D isopotential contours at $|V(\mathbf{r})| = 1.5$ a.u.): a) **1**, b) **2**, c) **5**, and d) **6**.

 © 2006 Wiley-VCH Verlag GmbH & Co. KGaA, Weinheim 

by Llamas-Saiz et al.[5] this distance is never below 250 pm, which is in contrast to the values obtained here for **1**–**4** which are under 240 pm. To investigate the effect of the nitrogen–nitrogen distance we considered separating the nitrogen atoms by four instead of three bonds, thus resulting in 4,8,9,10-tetraazatricyclo[5.1.1.1$^{3,5}$]decane (**5**) and its methylated derivative **6**, namely 4,8,9,10-tetramethyl-4,8,9,10-tetraazatricyclo[5.1.1.1$^{3,5}$]decane (Scheme 1). In contrast to **1**–**4**, the geometrical parameters calculated for **5** and **6** (Table 1) show a close resemblance with those reported for conventional proton sponges. The calculated PA for **5** is 1044.66 kJ mol$^{-1}$, which is more than 40 kJ mol$^{-1}$ higher than that of **1**. The electrostatic potentials of **5** and **6** are similar to those observed for **1** and **2** (Figure 1 c,d) in that they show a more compact potential between the nitrogen atoms in the methylated compounds. Indeed, **6** has a gas-phase PA very similar to that of **2** despite the different geometrical parameters (Table 2). In fact, **5** and **6** do not follow the same relationship between inter-nitrogen separation in the base and gas-phase PA value which is observed for **1**–**4**. As shown in Table 2, all these compounds are predicted to behave as strong proton sponges at both sites of protonation in an aqueous phase according to both the PA values and the estimated p$K_a$ values (see Methods Section).

In summary, the current findings show that the derivatives of 3,6,7,8-tetraazatricyclo[3.1.1.1$^{2,4}$]octane can be used as a prototype of a new proton sponge. We hope that this information will stimulate chemists to develop a synthetic method for this new family of proton sponges.

## Methods Section

All calculations were performed with the Gaussian 98 suite of programs.[12] Becke's "hybrid" three-parameter exchange and the Perdew-Wang correlation functional (B3PW91) have been used in conjunction with the split-valence, polarized, diffuse functions basis set 6-311++g(d,p).[13] Harmonic vibrational frequency calculations were used to confirm that the optimized structures were minima, as characterized by positive frequencies. Zero-point vibrational energies were obtained from these calculations without scaling; we take these values to represent an upper limit to the true values. We assume that basis set superposition error (BSSE) is negligible at the present level of calculation for the species considered here, as previously observed for B3PW91.[14] The optimized geometries were used to evaluate solvation energies, molecular electrostatic potentials (MEP), and other properties at the same level of theory. Solvation energies were calculated by the Self-Consistent Reaction Field (SCRF) using the isodensity model (IPCM) for the cavity.[15] The p$K_a$ values were estimated by a linear regression model of the experimental p$K_a$ data reported by Peräkylä[6] and following an approach reported by Kovačević and Maksić.[16] The linear regression model obtained here is p$K_a$ = 0.1684 PA(aq) − 193.14 with $R > 0.99$.

Received: September 13, 2005
Revised: December 12, 2005
Published online: February 10, 2006

[1] R. W. Alder, P. S. Bowman, W. R. Steele, D. R. Winterman, *Chem. Commun.* **1968**, 723 – 724.
[2] A. F. Pozharskii, *Russ. Chem. Rev.* **1998**, *67*, 1 – 24.
[3] H. A. Staab, T. Saupe, *Angew. Chem.* **1988**, *100*, 895 – 909; *Angew. Chem. Int. Ed. Engl.* **1988**, *27*, 865 – 879.
[4] R. W. Alder, *Chem. Rev.* **1989**, *89*, 1215 – 1223.
[5] A. L. Llamas-Saiz, C. Foces-Foces, J. Elguero, *J. Mol. Struct.* **1994**, *328*, 297 – 323.
[6] M. Peräkylä, *J. Org. Chem.* **1996**, *61*, 7420 – 7425.
[7] P. R. Mallinson, K. Woźniak, G. T. Smith, K. L. McCormack, *J. Am. Chem. Soc.* **1997**, *119*, 11502 – 11509.
[8] J. A. Platts, S. T. Howard, K. Woźniak, *J. Org. Chem.* **1994**, *59*, 4647 – 4651; S. T. Howard, J. A. Platts, R. W. Alder, *J. Org. Chem.* **1995**, *60*, 6085 – 6090; J. A. Platts, S. T. Howard, *J. Org. Chem.* **1996**, *61*, 4480 – 4482; S. T. Howard, J. A. Platts, *J. Org. Chem.* **1998**, *63*, 3568 – 3571; S. T. Howard, I. A. Fallis, *J. Org. Chem.* **1998**, *63*, 7117 – 7119.
[9] D. B. DuPré, *J. Phys. Chem. A* **2003**, *107*, 10142 – 10148.
[10] G. Bucher, *Angew. Chem.* **2003**, *115*, 4174 – 4175; *Angew. Chem. Int. Ed.* **2003**, *42*, 4039 – 4042.
[11] S. T. Howard, *J. Am. Chem. Soc.* **2000**, *122*, 8238 – 8244.
[12] Gaussian 98 (Revision A.7), M. J. Frisch, G. W. Trucks, H. B. Schlegel, G. E. Scuseria, M. A. Robb, J. R. Cheeseman, V. G. Zakrzewski, J. A. Montgomery, R. E. Stratmann, J. C. Burant, S. Dapprich, J. M. Millam, A. D. Daniels, K. N. Kudin, M. C. Strain, O. Farkas, J. Tomasi, V. Barone, M. Cossi, R. Cammi, B. Mennucci, C. Pomelli, C. Adamo, S. Clifford, J. Ochterski, G. A. Petersson, P. Y. Ayala, Q. Cui, K. Morokuma, D. K. Malick, A. D. Rabuck, K. Raghavachari, J. B. Foresman, J. Cioslowski, J. V. Ortiz, B. B. Stefanov, G. Liu, A. Liashenko, P. Piskorz, I. Komaromi, R. Gomperts, R. L. Martin, D. J. Fox, T. Keith, M. A. Al-Laham, C. Y. Peng, A. Nanayakkara, C. Gonzalez, M. Challacombe, P. M. W. Gill, B. G. Johnson, W. Chen, M. W. Wong, J. L. Andres, M. Head-Gordon, E. S. Replogle, J. A. Pople, Gaussian, Inc., Pittsburgh, PA, **1998**.
[13] A. D. Becke, *J. Chem. Phys.* **1993**, *98*, 5648 – 5652.
[14] N. X. Wang, K. Venkatesh, A. K. Wilson, *J. Phys. Chem. A* **2006**, *110*, 779 – 784.
[15] J. B. Foresman, T. A. Keith, K. B. Wiberg, J. Snoonian, M. J. Frisch, *J. Phys. Chem.* **1996**, *100*, 16098 – 16104.
[16] B. Kovačević, Z. Maksić, *Org. Lett.* **2001**, *3*, 1523 – 1526.

**Keywords:** basicity · density functional calculations · proton sponges · rational design

 © 2006 Wiley-VCH Verlag GmbH & Co. KGaA, Weinheim 

Combinatorial Chemistry

DOI: 10.1002/anie.200503341

# A Structurally Diverse Library of Polycyclic Lactams Resulting from Systematic Placement of Proximal Functional Groups**

*Judith M. Mitchell and Jared T. Shaw**

The chemical synthesis of small molecules en masse has emerged as a powerful tool to facilitate discoveries in biology and medicine.[1] Screening in chemical biology often involves the discovery of new cellular processes without prior knowledge of the protein targets. As such, libraries of small molecules that contain extensive skeletal and stereochemical diversity will offer the greatest opportunity for discovery across a variety of biological screens. Combinatorial techniques using split/pool chemistry[2] have been widely employed for the synthesis of small molecules, while advances in chemical automation and other new techniques have enabled the synthesis of large numbers of compounds in a parallel fashion.[3] Despite many advances in library synthesis, the efficient preparation of compounds with different core-atom connectivity within the same library remains an important challenge.[4]

We have addressed the challenge of synthesizing structurally diverse small molecules by designing efficient linear synthetic sequences that rely on the strategic manipulation of a single functional group to determine the three-dimensional array of the library members (Figure 1 B). Synthetic approaches that employ branching pathways[5] and "libraries from libraries" (Figure 1 A) have proven to be extremely useful for the synthesis of complex libraries employing a variety of interesting transformations.[6] Our linear strategy (Figure 1 B) was developed to produce libraries of comparable complexity by using fewer chemical manipulations. Furthermore, our strategy complements "folding" processes[7] by producing compounds with a comparable level of structural diversity from a single solid-phase starting material.

To demonstrate the efficacy of this strategy, we designed a short, linear sequence that exploits a key bond construction between proximal functional groups (Scheme 1). The first step employs an enantioselective variant of the addition of a methoxy-substituted oxazole to an aromatic aldehyde. In this step, the aldehyde may be substituted at the *ortho* position with an azido or azidomethyl substituent. Next, the oxazoline products are alkylated at the position α to the carbonyl group, thus offering a second opportunity to incorporate an azido substituent. The substrates bearing pendant azides are subjected to a Staudinger-type reduction that results in spontaneous cyclization to the corresponding spirocyclic or fused lactams. N-alkylation of the various lactams in a split/pool manner affords the final products. In addition to the four distinct structures produced by the divergent cyclization, we envisioned the conversion of methyl ester **5** into a series of amides **8** to produce a variety of structures that complement the complexity of **7a–d**.

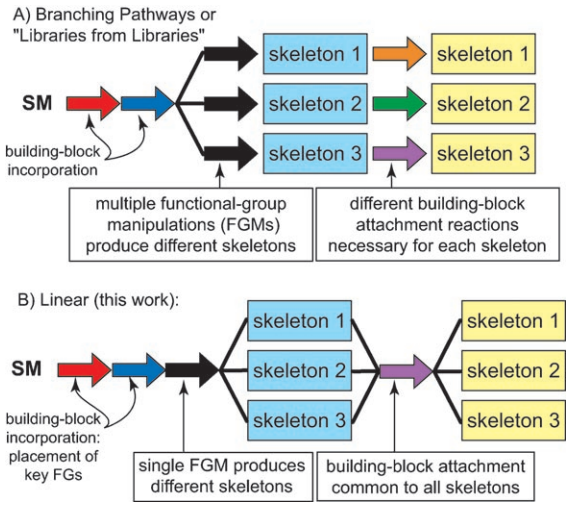



***Figure 1.*** Schematic diagram that compares two strategies for the production of structurally complex libraries.

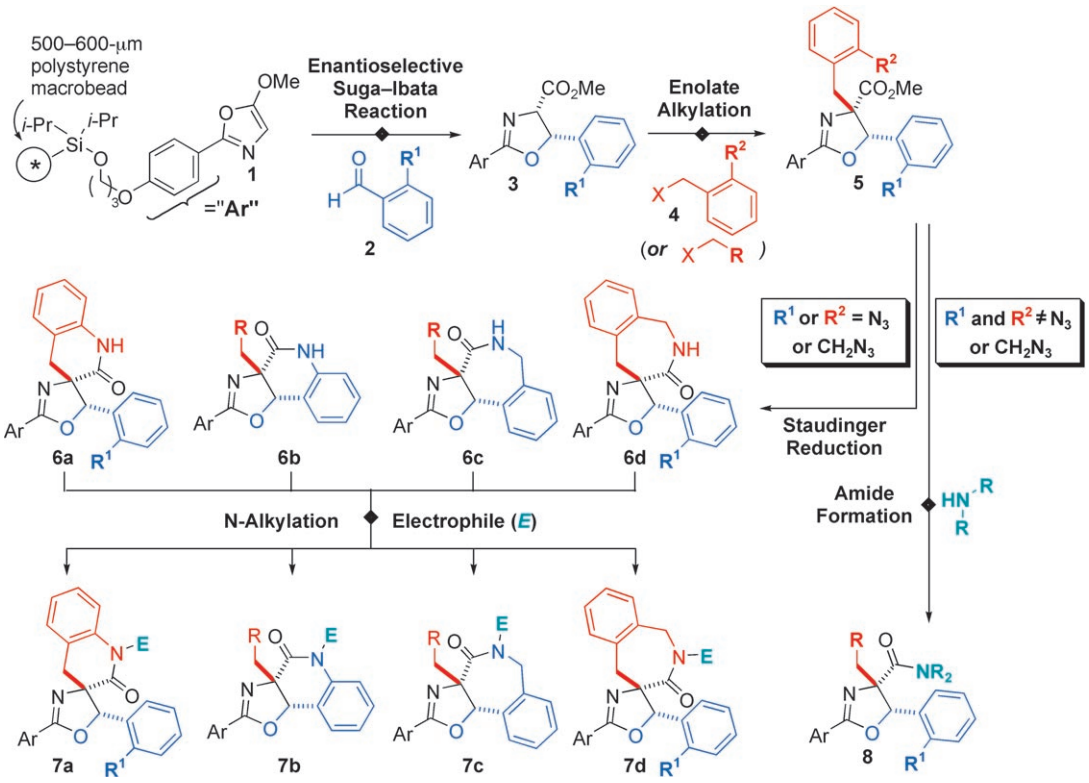
Since many biological screening experiments are often conducted without prior knowledge of the protein target, the best chance for discovery emanates from libraries that present a high level of structural diversity.[8] The importance of three-dimensional shape on "biorelevant" structural diversity has been predicted statistically[9] and demonstrated in a comparison of cyclic and acyclic structures derived from carbohydrates.[10] To assess the overall structural diversity of the structures in our library, we examined a scatter plot of the two variable dihedral angles of the PM5-minimized structures of **7** and **8** (Figure 2). For each compound, the two dihedral angles $\psi$ and $\phi$ of the oxazoline substituents are plotted on $x$ and $y$ axes, respectively. Enantiomers are scored with equal and opposite signs for $\psi$ and $\phi$ to account for the differential interactions that might occur with a biological target. Although **7** and **8** possess two stereocenters, only one diastereomer is produced by our synthetic sequence.

The incorporation of acyclic **8**, fused **7b**,**c**, and spirocyclic **7a**,**d** products in this library results in wide coverage of three-dimensional space. The boatlike conformation adopted by seven-membered ring lactams **7c** and **7d** results in significantly different dihedral angles $\psi$ and $\phi$ relative to their six-membered ring analogues **7a** and **7b**. In the cases of the

[*] Dr. J. M. Mitchell, Dr. J. T. Shaw
Department of Chemical Biology
Broad Institute of Harvard and MIT
320 Bent Street, Cambridge, MA 02141 (USA)
Fax: (+1) 617-324-9601
E-mail: shaw@broad.harvard.edu

[**] This work was conducted under the aegis of the Harvard Center for Methodology and Library Development (NIGMS P50 GM069721). J.T.S. thanks Amgen Pharmaceuticals for a New Faculty Award. We thank Prof. Nabi Magomedov (Rochester University), Dr. Jacob Janey (Merck), Prof. Timothy J. Mitchison (Harvard Medical School), and Professor Stuart Schreiber (Broad Institute) for insightful discussions. The authors thank Max Narovlyansky for the preparation of the solid support, Dr. Nicola J. Tolliday (Broad Institute) for facilitation of screening, and Dr. Ralph Mazitschek (Broad Institute) for assistance with molecular modeling.


InterScience
© 2006 Wiley-VCH Verlag GmbH & Co. KGaA, Weinheim




***Scheme 1.*** Summary of the synthetic pathway that produces a library of complex products from oxazole **1**. (—•—) indicates a split/pool step in which multiple building blocks are incorporated.

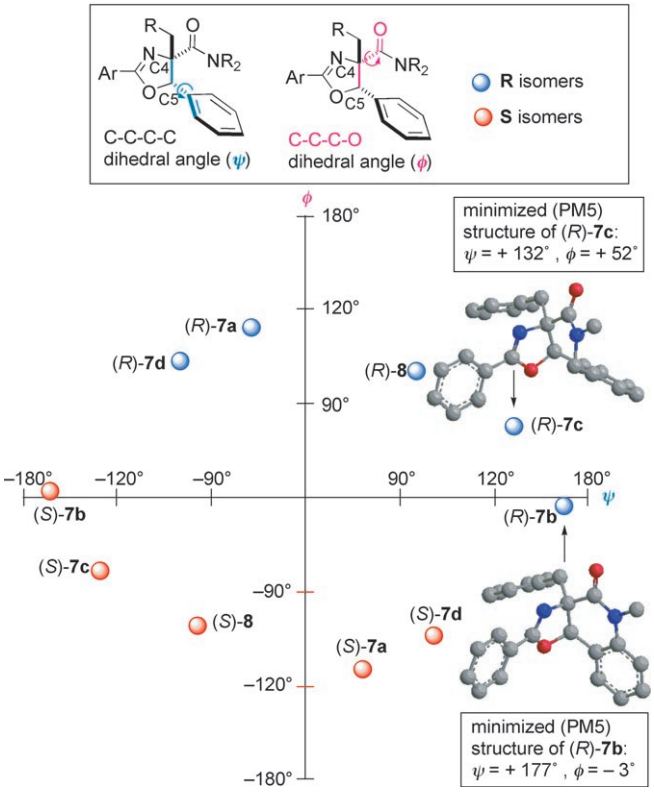



***Figure 2.*** Structural diversity of compounds **7** and **8** as revealed by a scatter plot that compares the dihedral angles $\psi$ and $\phi$ of (*R*)- and (*S*)-**7a–d** and **8**.

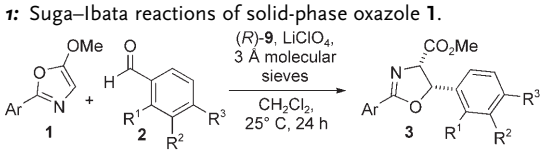
acyclic **8** and spirocyclic **7a**, **d** compounds, free rotation about the C5–phenyl bond is restricted by the dense substitution at C4 of the oxazoline ring.[11] Although a small molecule may not bind to its target in the ground-state conformation, these molecules are all sufficiently rigid that the comparison of the dihedral angles $\psi$ and $\phi$ provides a starting point for the evaluation of their structural diversity. Based on the broad range of biological activities observed for oxazolines and polycyclic lactams,[12] we expect this library of structurally complex compounds to provide interesting results in a variety of biological screens.[13]

Our efforts commenced with development of a solid-phase[14] variant of the Suga–Ibata reaction (Table 1).[15] Several aluminum complexes were examined, and triflate (OTf) complex **9** offered the best overall performance. While the analogous $SbF_6^-$ complex employed by Evans and others[15,16] is more reactive, a study of the temperature profile[17] of this catalyst suggests that it degrades under the higher reaction temperatures that are required for the solid-phase reaction. The reactions of several standard substrates (entries 1 and 4–6) and two azido aldehydes (entries 2 and 3) proceeded in high yield and selectivity. The modest diastereoselectivity (d.r.) of this reaction is alleviated in the subsequent alkylation step (see below). Although our preliminary studies were conducted with (*R*)-**9**, production of the final library employs each enantiomer of this catalyst to maximize the diversity of the products.

Alkylation of the oxazoline intermediates was achieved in high yield and diastereoselectivity using strong, neutral phosphazene bases (BEMP or BTPP) and reactive electro-

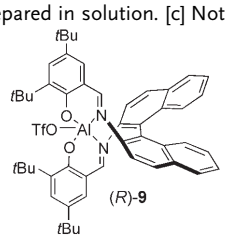
 © 2006 Wiley-VCH Verlag GmbH & Co. KGaA, Weinheim 

***Table 1:*** Suga–Ibata reactions of solid-phase oxazole **1**.



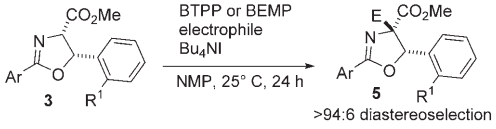

| Entry | $R^1$ | $R^2$ | $R^3$ | Conversion [%][a] | *ee* [%][b] | dr |
|---|---|---|---|---|---|---|
| 1 | H | H | H | 100 | 99 | 91:9[b] |
| 2 | $N_3$ | H | H | 100 | 97 | 88:12[b] |
| 3 | $CH_2N_3$ | H | H | 100 | 95 | 86:14[b] |
| 4 | Br | H | H | 100 | –[c] | 84:16[a] |
| 5 | Cl | H | Cl | 100 | –[c] | 88:12[a] |
| 6 | H | $OCH_3$ | H | 100 | –[c] | 88:12[a] |

[a] Based on LCMS. [b] Based on chiral HPLC comparison to a racemic reference compound prepared in solution. [c] Not determined.



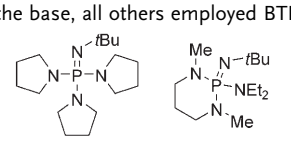

philes (see Table 2).[18] Allylic and benzylic halides both exhibit high conversion rates. Michael-type additions were possible with phenyl vinyl sulfone or *tert*-butyl acrylate, while 2-nitrostyrene was not suitable. In all cases, >94% diastereoselection was observed, and the conditions were suitable for both oxazoline and electrophile substrates containing the azido or azidomethyl substituent.

***Table 2:*** Alkylation of oxazoline **3** with various electrophiles.[a]

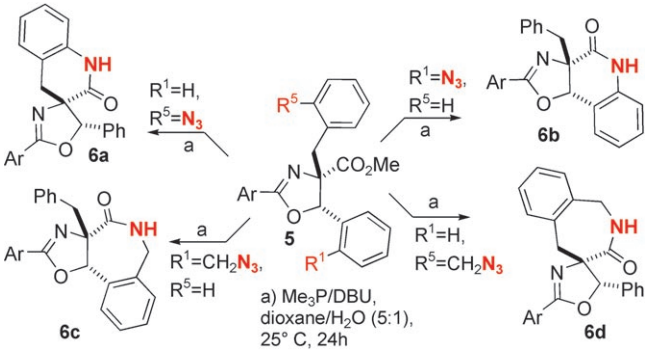



| Entry | Conversion [%] | $R^1$, $R^4$, $R^5$ | E |
|---|---|---|---|
| 1[a] | 100 | $R^1$ = H, $R^4$ = H, $R^5$ = H | |
| 2[a] | 80 | $R^1$ = H, $R^4$ = H, $R^5$ = Br | |
| 3 | 100 | $R^1$ = H, $R^4$ = Br, $R^5$ = H | |
| 4 | 100 | $R^1$ = H, $R^4$ = H, $R^5$ = $N_3$ | |
| 5 | 100 | $R^1$ = H, $R^4$ = H, $R^5$ = $CH_2N_3$ | |
| 6 | 100 | $R^1$ = $N_3$, $R^4$ = H, $R^5$ = H | |
| 7 | 100 | $R^1$ = $CH_2N_3$, $R^4$ = H, $R^5$ = H | |
| 8[a] | 100 | $R^1$ = H, $R^4$ = H | |
| 9 | 86 | $R^1$ = H, $R^4$ = Ph | |
| 10 | 100 | $R^1$ = H, $R^4$ = H, $R^5$ = $SO_2Ph$ | |
| 11 | 100 | $R^1$ = H, $R^4$ = H, $R^5$ = $CO_2tBu$ | |
| 12 | <5 | $R^1$ = H, $R^4$ = Ph, $R^5$ = $NO_2$ | |

[a] BEMP used as the base, all others employed BTPP.




A cyclization reaction between the strategically placed azide and ester functional groups establishes the core-atom connectivity of the final products. This key reduction/cyclization sequence was achieved under Staudinger-type conditions with added base to facilitate ring closure (Scheme 2).[19] A

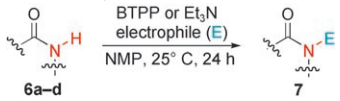



***Scheme 2.*** Cyclization of azido esters. Conversion of >95% (LCMS) is observed in all cases. DBU = 1,8-diazabicyclo[5.4.0]undec-7-ene.

single set of conditions was developed that produced all of the possible fused and spirocyclic lactams in >95% conversion.

The full potential of our strategy was realized by employing the diverse lactam products **6a–d** in a mix-and-split alkylation of the amide NH functionality presented by all of the core structures (Table 3). Once again, we found that the

***Table 3:*** N-Acylation and alkylation of lactams **6a–d**.[a]



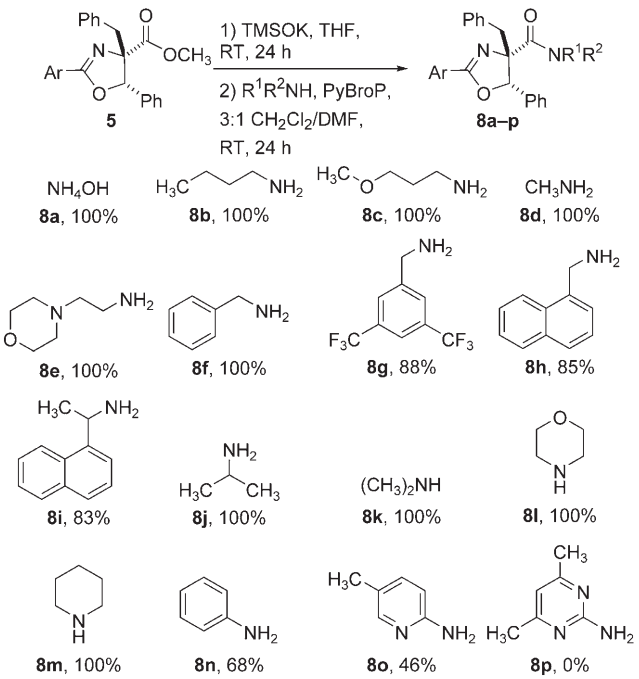

| Electrophile | Lactam[a] 6a | 6b | 6c | 6d |
|---|---|---|---|---|
| $Ac_2O$[b] | 50 | – | 75 | 100 |
| PhCOCl[b] | 100 | 62 | 100 | 100 |
| $PhCH_2Br$ | 100 | 100 | 100 | 100 |
|  | 100 | 100 | 100 | 76 |
| $CH_3I$ | 60 | 100 | 21 | 10 |
| *n*PrBr | 100 | 100 | 8 | 10 |
|  | 100 | 100 | 100 | 100 |

[a] Conversion (%) based on LCMS. [b] Base = $Et_3N$, all others used BTPP (see Table 2). NMP = 1-methyl-2-pyrrolidone.

neutral phosphazene bases were optimal for lactam alkylation, whereas more traditional conditions that employed triethylamine were useful for acylation.[20] While each of the four core structures exhibits a range of reactivity in the alkylation and acylation reactions, successful reactions were observed in 21 out of the 28 possible lactam/electrophile combinations.[21]

While the bulk of the structural complexity of this library results from systematic placement of an azide substituent, the esters **5** lacking an azide could be converted into a series of amides in high yield (Scheme 3). The methyl ester was cleanly

 © 2006 Wiley-VCH Verlag GmbH & Co. KGaA, Weinheim 




***Scheme 3.*** Conversion of ester (*R*)-**5** into a variety of amides. Conversions based on LCMS.

saponified with potassium trimethylsilanolate (TMSOK) and the product employed in an amide coupling reaction with a variety of primary and secondary amines. Although the solid-phase acid intermediate is quite hindered, we were able to use excess reagents to achieve high yields for many primary and secondary amines. Aryl and heteroaryl substrates were less effective. This transformation yields compounds that complement the structural diversity of lactams **7a–d**.

In conclusion, we have demonstrated that a linear synthetic sequence can incorporate a single functional-group manipulation to produce four different core structures. We have applied this sequence to the synthesis of a pilot library of 529[22] complex compounds that result from both enantioselective pathways that will be employed in a series of biological screens. Preliminary screening experiments indicate that the compounds in this library modulate the cellular process of both yeast and human cancer (HeLa) cells.[23] A full account of our synthetic studies and screening experiments will be disclosed shortly.

Received: September 20, 2005
Published online: February 15, 2006

**Keywords:** asymmetric synthesis · combinatorial chemistry · lactams · synthetic methods

[1] a) D. S. Tan, *Nat. Chem. Biol.* **2005**, *1*, 74–84; b) B. R. Stockwell, *Nature* **2004**, *432*, 846–854; c) C. M. Dobson, *Nature* **2004**, *432*, 824–828; d) R. L. Strausberg, S. L. Schreiber, *Science* **2003**, *300*, 294–295; e) K. S. Lam, M. Lebl, V. Krchnak, *Chem. Rev.* **1997**, *97*, 411–448.

[2] a) A. Furka, F. Sebestyen, M. Asgedom, G. Dibo, *Int. J. Pept. Protein Res.* **1991**, *37*, 487–493; b) R. A. Houghten, C. Pinilla, S. E. Blondelle, J. R. Appel, C. T. Dooley, J. H. Cuervo, *Nature* **1991**, *354*, 84–86.

[3] a) B. A. Bunin, J. A. Ellman, *J. Am. Chem. Soc.* **1992**, *114*, 10997–10998; b) L. A. Thompson, J. A. Ellman, *Chem. Rev.* **1996**, *96*, 555–600; c) H. E. Blackwell, L. Perez, R. A. Stavenger, J. A. Tallarico, E. Cope Eatough, M. A. Foley, S. L. Schreiber, *Chem. Biol.* **2001**, *8*, 1167–1182; d) P. A. Clemons, A. N. Koehler, B. K. Wagner, T. G. Sprigings, D. R. Spring, R. W. King, S. L. Schreiber, M. A. Foley, *Chem. Biol.* **2001**, *8*, 1183–1195; e) D. G. Hall, S. Manku, F. Wang, *J. Comb. Chem.* **2001**, *3*, 125–150; f) T. U. Mayer, *Trends Cell Biol.* **2003**, *13*, 270–277; g) S. M. Khersonsky, Y.-T. Chang, *Comb. Chem. High Throughput Screening* **2004**, *7*, 645–652; h) L. Burdine, T. Kodadek, *Chem. Biol.* **2004**, *11*, 593–597; i) D. R. Spring, *Chem. Soc. Rev.* **2005**, *34*, 472–482.

[4] M. D. Burke, S. L. Schreiber, *Angew. Chem.* **2004**, *116*, 48–60; *Angew. Chem. Int. Ed.* **2004**, *43*, 46–58.

[5] a) E. M. Gordon, M. A. Gallop, D. V. Patel, *Acc. Chem. Res.* **1996**, *29*, 144–154; b) M. A. Marx, A.-L. Grillot, C. T. Louer, K. A. Beaver, P. A. Bartlett, *J. Am. Chem. Soc.* **1997**, *119*, 6153–6167; c) M. R. Spaller, M. T. Burger, M. Fardis, P. A. Bartlett, *Curr. Opin. Chem. Biol.* **1997**, *1*, 47–53.

[6] A. Nefzi, J. M. Ostresh, J. Yu, R. A. Houghten, *J. Org. Chem.* **2004**, *69*, 3603–3609.

[7] a) M. D. Burke, E. M. Berger, S. L. Schreiber, *Science* **2003**, *302*, 613–618; b) H. Oguri, S. L. Schreiber, *Org. Lett.* **2005**, *7*, 47–50.

[8] a) S. Shang, D. S. Tan, *Curr. Opin. Chem. Biol.* **2005**, *9*, 248–258; b) S. Fergus, A. Bender, D. R. Spring, *Curr. Opin. Chem. Biol.* **2005**, *9*, 304–309; c) R. Breinbauer, I. R. Vetter, H. Waldmann, *Angew. Chem.* **2002**, *114*, 3002–3015; *Angew. Chem. Int. Ed.* **2002**, *41*, 2878–2890.

[9] W. H. B. Sauer, M. K. Schwarz, *J. Chem. Inf. Comput. Sci.* **2003**, *43*, 987–1003.

[10] Y.-k. Kim, M. A. Arai, T. Arai, J. O. Lamenzo, E. F. Dean III, N. Patterson, P. A. Clemons, S. L. Schreiber, *J. Am. Chem. Soc.* **2004**, *126*, 14740–14745.

[11] Use of semiempirical calculations (PM5) to generate an energy map for rotation about this bond indicates that 180° rotation requires at least 10 kcal mol$^{-1}$ (see the Supporting Information).

[12] 2-Aryl oxazolines analogous to **5** occur as siderophore, antitumor natural products, and synthetic inhibitors of lipid-1 biosynthesis; see: a) T. Peterson, J. B. Neilands, *Tetrahedron Lett.* **1979**, 4805–4808; b) M. Tsukamoto, *J. Antibiot.* **1997**, *50*, 815–821; and c) M. C. Pirrung, L. N. Tumey, A. L. McClerren, C. R. H. Raetz, *J. Am. Chem. Soc.* **2003**, *125*, 1575–1586; quinolones related to **7a** and **7b** exhibit broad bioactivity and also occur naturally, see: d) I. Jarak, M. Kralj, L. Suman, G. Pavlovic, J. Dogan, I. Piantanida, M. Zinic, K. Pavelic, G. Karminski-Zamola, *J. Med. Chem.* **2005**, *48*, 2346–2360; e) B. Baruah, K. Dasu, B. Vaitilingam, A. Vanguri, S. R. Casturi, K. R. Yeleswarapu, *Bioorg. Med. Chem. Lett.* **2004**, *14*, 445–448; f) I.-S. Chen, S.-J. Wu, I.-L. Tsai, T.-S. Wu, J. M. Pezzuto, M. C. Lu, H. Chai, N. Suh, C.-M. Teng, *J. Nat. Prod.* **1994**, *57*, 1206–1211; 2-benzazepine-3-ones related to **7c** and **7d** act as μ-opioid antagonists, see: g) I. Van den Eynde, G. Laus, P. W. Schiller, P. Kosson, N. N. Chung, A. W. Lipkowski, D. Tourwe, *J. Med. Chem.* **2005**, *48*, 3644–3648.

[13] For a recent example of a natural-product-like library, see: a) Z. Gan, P. T. Reddy, S. Quevillon, S. Couve-Bonnaire, P. Arya, *Angew. Chem.* **2005**, *117*, 1390–1392; *Angew. Chem. Int. Ed.* **2005**, *44*, 1366–1368; for a review, see: b) A. Reayi, P. Arya, *Curr. Opin. Chem. Biol.* **2005**, *9*, 240–247.

[14] The diisopropylsilyl linker used for this study was developed by Schreiber and co-workers: a) J. A. Tallarico, K. M. Depew, H. E. Pelish, N. J. Westwood, C. W. Lindsley, M. D. Shair, S. L. Schreiber, M. A. Foley, *J. Comb. Chem.* **2001**, *3*, 312–318; two variants of this linker were recently described which feature

 © 2006 Wiley-VCH Verlag GmbH & Co. KGaA, Weinheim 

complementary levels of stability: b) G. L. Thomas, M. Ladlow, D. R. Spring, *Org. Biomol. Chem.* **2004**, *2*, 1679 – 1681; c) C. M. DiBlasi, D. E. Macks, D. S. Tan, *Org. Lett.* **2005**, *7*, 1777 – 1780; d) oxazole **1** is prepared in seven steps (see the Supporting Information).

[15] a) D. A. Evans, J. M. Janey, N. Magomedov, J. S. Tedrow, *Angew. Chem.* **2001**, *113*, 1936 – 1940; *Angew. Chem. Int. Ed.* **2001**, *40*, 1884 – 1888; b) H. Suga, K. Ikai, T. Ibata, *J. Org. Chem.* **1999**, *64*, 7040 – 7047.

[16] a) L. Hunter, M. D. McLeod, C. A. Hutton, *Org. Biomol. Chem.* **2005**, *3*, 732 – 773; b) A. M. Sawayama, H. Tanaka, T. J. Wandless, *J. Org. Chem.* **2004**, *69*, 8810 – 8820.

[17] J. M. Janey, PhD thesis, Harvard University (USA), **2003**.

[18] a) M. J. O'Donnell, F. Delgado, C. Hostettler, R. Schwesinger, *Tetrahedron Lett.* **1998**, *39*, 8775 – 8778; employing amide bases under traditional conditions was unsuccessful; see: b) D. Seebach, J. D. Aebi, M. Gander-Coquoz, R. Naef, *Helv. Chim. Acta* **1987**, *70*, 1194 – 1216; c) S. Jaroch, R. T. Matsuoka, L. E. Overman, *Tetrahedron Lett.* **1999**, *40*, 1273 – 1276; the recently reported phase-transfer conditions provided the desired product in high yield and diastereoselectivity in model solution studies, but failed in the solid phase, see: d) S.-s. Jew, Y.-J. Lee, J. Lee, M. J. Kang, B.-S. Jeong, J.-H. Lee, M.-S. Yoo, M.-J. Kim, S.-h. Choi, J.-M. Ku, H.-g. Park, *Angew. Chem.* **2004**, *116*, 2436 – 2439; *Angew. Chem. Int. Ed.* **2004**, *43*, 2382 – 2385.

[19] J. T. Lundquist, J. C. Pelletier, *Org. Lett.* **2002**, *4*, 3219 – 3221.

[20] W. L. Scott, J. Alsina, M. J. O'Donnell, *J. Comb. Chem.* **2003**, *5*, 684 – 692.

[21] Use of the Irori (Discovery Partners International) Kan system allowed for the exclusion of low-yielding combinations (see the Supporting Information).

[22] Produced in quantities of 5–10 mg using Discovery Partners X-microkans filled with 35 mg of resin **1** (loading of 1.2 mmol $g^{-1}$); nine out of 12 compounds sampled were $>80\%$ pure; structures were based on **7a**–**d** (92 compounds), **8** (324), and related structures (113), which will be described in a full account of this study (see the Supporting Information). Use of Irori Kans has proven useful for split/pool solid-phase synthesis of libraries without using chemical encoding; for an example of a library synthesized with X-nanoKans (which hold 1 mg of resin), see: a) K. C. Nicolaou, J. A. Pfefferkorn, H. J. Mitchell, A. J. Roecker, S. Barluenga, G. Q. Cao, R. L. Affleck, J. E. Lillig, *J. Am. Chem. Soc.* **2000**, *122*, 9954 – 9967; previously, 500–600-μm macrobeads were encoded using technology described by Still et al., see: b) M. H. J. Ohlmeyer, R. N. Swanson, L. Dillard, J. C. Reader, G. Asouline, R. Kobayashi, M. Wigler, W. C. Still, *Proc. Natl. Acad. Sci. USA* **1993**, *90*, 10922 – 10926.

[23] Several compounds were found to promote the growth of yeast, while a structurally distinct set were cytotoxic to HeLa cells in a dose-dependent manner (see the Supporting Information).

 © 2006 Wiley-VCH Verlag GmbH & Co. KGaA, Weinheim 

Immobilization

DOI: 10.1002/anie.200503475

# Selective Immobilization of Proteins onto Solid Supports through Split-Intein-Mediated Protein Trans-Splicing**

*Youngeun Kwon, Matthew A. Coleman, and Julio A. Camarero**

Protein microarrays, in which proteins are immobilized onto a solid surface, are in principle ideal reagents for high-throughput experiments as they require a very small amount of analyte. During the last few years, protein microarrays ("protein chips") have started to become very promising tools in proteomics as they promise to allow large-scale analysis of protein interactions.[1]

Although a variety of approaches are available for the attachment of proteins onto solid surfaces, most of them rely on nonspecific adsorption methods or on the reaction of chemical groups within proteins (mostly amines and carboxylic acids) with complementary reactive groups on the surface.[9] In both cases, the corresponding proteins are attached to the surface at random orientations.[1d] The use of recombinant affinity tags addresses the orientation issue. In most cases, however, the tag interactions are reversible and are either not stable over the course of subsequent assays or they require large mediator proteins.[2] Direct site-specific immobilization of proteins has also been accomplished by using various chemoselective-ligation reactions.[3] However, these methods rely on bimolecular chemical reactions and therefore their efficiency depends strongly on the concentration of the protein to be immobilized.[3c–d] One way to overcome this limitation is to use an affinity capture ligand approach.[4a] Several groups have successfully used this method for the site-specific immobilization of proteins onto surfaces.[4b–d] In all cases, however, the capture proteins

[*] Dr. Y. Kwon, Dr. J. A. Camarero
Chemical Biology and Nuclear Science Division
Lawrence Livermore National Laboratory
University of California
7000 East Avenue, Livermore, CA 94550 (USA)
Fax: (+1) 925-422-3160
E-mail: camarero1@llnl.gov
Dr. M. A. Coleman
Biosciences Directorate
Lawrence Livermore National Laboratory
University of California
7000 East Avenue, Livermore, CA 94550 (USA)

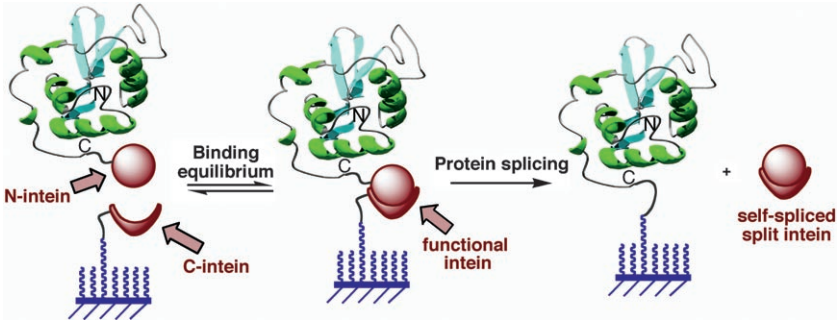
[**] We would like to thank Dr. Alexander R. Mitchell for help and useful discussions during the course of this work. We also thank Professor Xiang-Qin Liu, Dalhousie University, Halifax, Canada, for kindly providing a sample of DNA containing the naturally split DnaE intein. This work was performed under the auspices of the U.S. Department of Energy by the University of California, Lawrence Livermore National Laboratory under contract No. W-7405-Eng-48.

Supporting information for this article is available on the WWW under http://www.angewandte.org or from the author.


WILEY InterScience DISCOVER SOMETHING GREAT
© 2006 Wiley-VCH Verlag GmbH & Co. KGaA, Weinheim

(usually enzymes) remain attached to the surface after the immobilization process is completed.

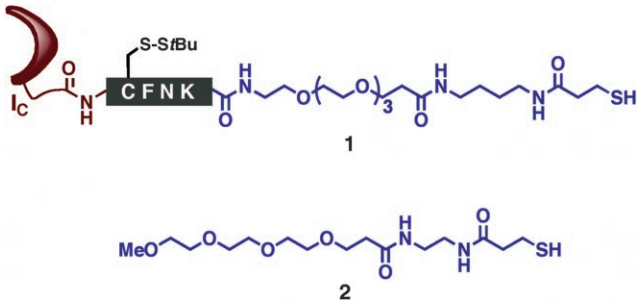
Herein, we report a new traceless capture ligand approach for the selective immobilization of proteins through their C-termini onto a modified-glass surface (Scheme 1).[11] Our approach is based on the use of protein trans-splicing,[5] which is a naturally occurring process similar to protein splicing[6] with the difference that the intein self-processing domain is split into two fragments (N-intein and C-intein). These two intein fragments are inactive individually, however, under appropriate conditions they can bind to each other with high specificity to form a functional protein-splicing domain. In our approach, the C-intein fragment is covalently immobilized onto a glass surface through a PEGylated-peptide (PEG = polyethylene glycol) linker, whereas the N-intein fragment is fused to the C-terminus of the protein that is intended to be attached to surface. When both intein fragments interact, they form an active intein domain, which ligates the protein of interest to the surface. At the same time, the split intein is spliced out into solution (Scheme 1).




***Scheme 1.*** Site-specific immobilization of proteins onto a solid support through split-intein-mediated protein trans-splicing.

The key to our approach is the use of the naturally split DnaE intein from *Synechocystis sp.* PCC6803.[5a] The C- and N-intein fragments of the DnaE intein are able to self-assemble spontaneously ($K_d = 0.1$–$0.2\ \mu M$[7]) and as such do not require any refolding steps.[8] The intein-mediated trans-splicing reaction for DnaE is also very efficient under physiological-like conditions ($\tau_{1/2} \approx 4$ h, trans-splicing yields range from 85% to almost quantitative).[12] To test the suitability of protein trans-splicing for selective protein immobilization onto solid surfaces, we used two model proteins, maltose binding protein (MBP) and enhanced green fluorescent protein (EGFP). Both proteins were modified at the DNA level to append the DnaE N-intein fragment ($I_N$; residues 1–123 of the DnaE intein) at their C-termini. The two fusion proteins (MBP-$I_N$ and EGFP-$I_N$) were readily expressed in *E. coli* and purified by affinity chromatography. To enable the site-specific attachment of the $I_N$ fusion proteins onto a glass surface, an amine-functionalized glass slide was first treated with maleimidopropionic acid *N*-hydroxysuccinimide ester (MPS) and then reacted with a mixture of PEGylated thiol linkers **1** and **2** in a molar ratio of 3:97, respectively (Scheme 2). Both linkers contain a PEG moiety that prevents nonspecific interactions and also acts as a hydrophilic spacer, therefore minimizing any detrimental interaction between the attached protein and the glass surface.[3c]

Linker **1** contains the DnaE C-intein fragment ($I_C$; residues 124–159 of the DnaE intein) followed by the corresponding C-extein sequence CFNK. The Cys residue in the C-extein sequence was protected with an S-*t*Bu protecting group. This was required to ensure that the $I_C$-containing linker was selectively immobilized through its PEGylated terminal thiol onto the maleimido-coated glass surface (Scheme 2). Linker **2** was used as a diluent to control the density of reactive sites on the modified glass surface. When the derivatization was complete, the S-*t*Bu protecting group on the Cys residue was removed with 50% β-mercaptoethanol in *N*,*N*-dimethylformamide (DMF) for 2 h. The surface was washed and immediately used for spotting.[13] Different concentrations of pure EGFP-$I_N$ and MBP-$I_N$ fusion proteins were spotted onto $I_C$-coated glass slides (Figure 1). As a control, a solution of EGFP with no $I_N$ fragment was spotted onto the same slide (Figure 1a). Also, a solution of MBP-$I_N$ was spotted onto a glass slide derivatized with only the nonfunctional linker **2** (Figure 1b). The trans-splicing reaction was incubated for 16 h in a humidified chamber at 37 °C. As shown in Figure 1, only the proteins that contain the $I_N$ polypeptide were observed to specifically immobilize onto the $I_C$-containing glass surfaces. No fluorescent signal was detected from the control protein EGFP, which lacks the $I_N$ polypeptide, after washing (Figure 1a). Furthermore, MBP binding was minimal when the trans-splicing active MBP-$I_N$ fusion protein was spotted onto a control glass slide coated with the nonfunctional linker **2** (Figure 1b, top panel). The trans-splicing mediated attachment of EGFP and MBP, in both cases, was efficient over a range of concentrations (Figure 1). It is interesting to note that the attached EGFP retained its characteristic green fluorescence, indicating that its tertiary structure was unaffected by the attachment to the PEGylated glass surface. The covalent nature of the new bond formed between the C-terminus of the protein and the modified surface was confirmed by washing a glass slide that contained immobi-




***Scheme 2.*** Structures of linkers **1** and **2** that were used for the derivatization of glass slides.

 © 2006 Wiley-VCH Verlag GmbH & Co. KGaA, Weinheim 

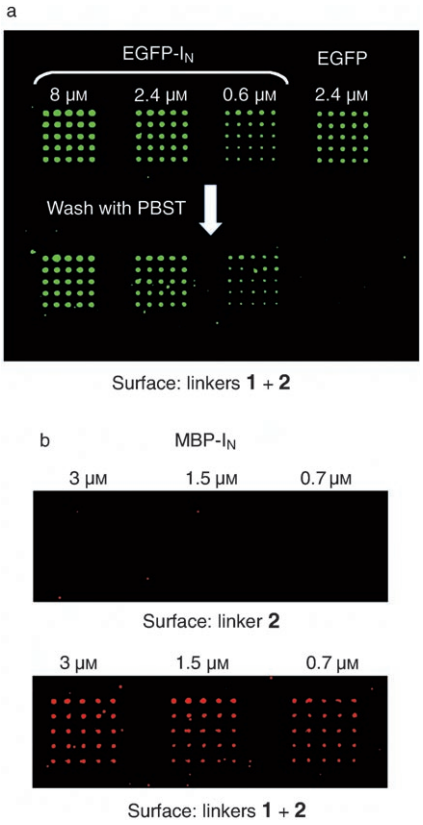



***Figure 1.*** Selective attachment of EGFP-$I_N$ (green) and MBP-$I_N$ (red) onto derivatized glass slides. a) Epifluorescence image of an $I_C$-coated glass slide after the spotting of different concentrations of EGFP-$I_N$ and EGFP (top) and after buffer washes (bottom). b) Different concentrations of MBP-$I_N$ were spotted onto a PEG- (top) and $I_C$-coated (bottom) glass slides. After washing, the immobilized MBP was detected by immunofluorescence. PBST = phosphate-buffered saline/tween (sodium phosphate (50 mM), NaCl (500 mM), and Triton X-100 (0.2%); pH 7.2).

lized MBP with a 2% sodium dodecyl sulfate (SDS) solution (SDS solutions above the critical micelle concentration have been previously used to desorb nonspecifically adsorbed proteins[10] as well as to disrupt specific protein–protein interactions[4d]). Once the stringent wash was complete and the glass slide was restained to allow detection of the remaining attached MBP, no significant loss of fluorescence was detected. This result confirms that the immobilization of the proteins to the surface proceeds mostly through the formation of a stable covalent bond and not through a transient affinity interaction.

The ability to selectively immobilize $I_N$-containing fusion proteins from complex mixtures through protein trans-splicing was also explored. Hence, MPB and MBP-$I_N$ fusion proteins were overexpressed in *E. coli*, and the corresponding soluble cellular fractions were spotted onto $I_C$-coated glass slides as described above. As before, immobilization of the MBP protein, which contains the $I_C$ polypeptide, was extremely selective and exhibited minimal background adsorption (Figure 2a). Encouraged by these results, we investigated the possibility of interfacing this new immobilization technique with cell-free expression systems. Thus,

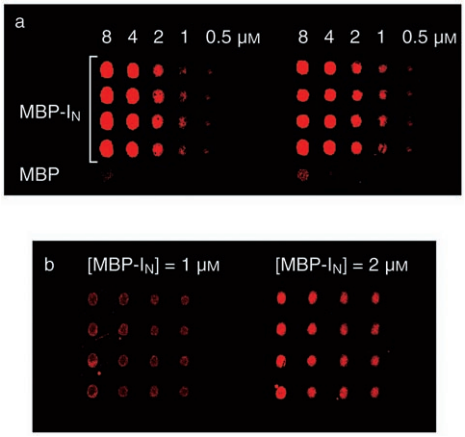



***Figure 2.*** Selective immobilization of MBP-$I_N$ from complex mixtures. a) Soluble cellular fraction of *E. coli* cells overexpressing MBP-$I_N$. b) MBP-$I_N$ expressed in vitro by using a cell-free system. Protein concentrations in the cell lysate and IVT crude reaction were estimated by Western Blotting. In both cases, MBP was detected by immunofluorescence after washing. The level of nonspecific background can be seen at the bottom of the slide when MBP with no DnaE N-intein was spotted.

MBP-$I_N$ was expressed by using an *E. coli*-based in vitro transcription/translation (IVT) system. The crude IVT reaction was spotted without further treatment and was processed as described above. As previously stated, the MPB protein was selectively attached to the $I_C$-coated glass surface (Figure 2b). In both cases, the amount of immobilized protein was shown to be similar.

In summary, we have demonstrated a new strategy for the site-specific immobilization of proteins onto solid supports by protein trans-splicing. The immobilization of the protein is highly specific and efficient, thus eliminating the need for the purification and/or reconcentration of the proteins prior to the immobilization step. More importantly, once the protein is immobilized onto the surface, both intein fragments are spliced out into solution thereby providing a completely traceless method of attachment. Finally, this methodology can be easily interfaced with cell-free protein expression systems, allowing for rapid access to the high-throughput production of protein chips.[14]

Received: October 1, 2005
Revised: December 6, 2005
Published online: February 9, 2006

**Keywords:** bioorganic chemistry · biosensors · immobilization · protein engineering · proteomics

[1] a) K. Tomizaki, K. Usui, H. Mihara, *ChemBioChem* **2005**, *6*, 782–799; b) E. Phizicky, P. I. Bastiaens, H. Zhu, M. Snyder, S. Fields, *Nature* **2003**, *422*, 208–215; c) H. Zhu, M. Snyder, *Curr. Opin. Chem. Biol.* **2003**, *7*, 55–63; d) H. Zhu, M. Bilgin, R. Bangham, D. Hall, A. Casamayor, P. Bertone, N. Lan, R. Jansen, S. Bidlingmaier, T. Houfek, T. Mitchell, P. Miller, R. A. Dean, M. Gerstain, M. Snyder, *Science* **2001**, *293*, 2101–2105; e) H. Zhu, J. F. Klemic, S. Chang, P. Bertone, A. Casamayor, K. G. Klemic,

 © 2006 Wiley-VCH Verlag GmbH & Co. KGaA, Weinheim 

D. Smith, M. Gerstein, M. A. Reed, M. Snyder, *Nat. Genet.* **2000**, *26*, 283 – 289.
[2] a) J. Yin, F. Liu, X. Li, C. T. Walsh, *J. Am. Chem. Soc.* **2004**, *126*, 7754 – 7755; b) R. Y. Lue, G. Y. Chen, Y. Hu, Q. Zhu, S. Q. Yao, *J. Am. Chem. Soc.* **2004**, *126*, 1055 – 1062.
[3] a) M. B. Soellner, K. A. Dickson, B. L. Nilsson, R. T. Raines, *J. Am. Chem. Soc.* **2003**, *125*, 11790 – 11791; b) M. Kohn, R. Wacker, C. Peters, H. Schroder, L. Soulere, R. Breinbauer, C. M. Niemeyer, H. Waldmann, *Angew. Chem.* **2003**, *115*, 6010 – 6014; *Angew. Chem. Int. Ed.* **2003**, *42*, 5830 – 5834; c) J. A. Camarero, Y. Kwon, M. A. Coleman, *J. Am. Chem. Soc.* **2004**, *126*, 14730 – 14731; d) A. Girish, H. Sun, D. S. Yeo, G. Y. Chen, T. K. Chua, S. Q. Yao, *Bioorg. Med. Chem. Lett.* **2005**, *15*, 2447 – 2451.
[4] a) A. J. Chmura, M. S. Orton, C. F. Meares, *Proc. Natl. Acad. Sci. USA* **2001**, *98*, 8480 – 8484; b) C. D. Hodneland, Y. S. Lee, D. H. Min, M. Mrksich, *Proc. Natl. Acad. Sci. USA* **2002**, *99*, 5048 – 5052; c) M. Kindermann, N. George, N. Johnsson, K. Johnsson, *J. Am. Chem. Soc.* **2003**, *125*, 7810 – 7811; d) Y. Kwon, Z. Han, E. Karatan, M. Mrksich, B. K. Kay, *Anal. Chem.* **2004**, *76*, 5713 – 5720.
[5] a) H. Wu, Z. Hu, X. Q. Liu, Proc. *Natl. Acad. Sci. USA* **1998**, *95*, 9226 – 9231; b) F. B. Perler, *Trends Biochem. Sci.* **1999**, *24*, 209 – 211; c) I. Giriat, T. W. Muir, *J. Am. Chem. Soc.* **2003**, *125*, 7180 – 7181.
[6] a) C. J. Noren, J. Wang, F. B. Perler, *Angew. Chem.* **2000**, *112*, 458 – 476; *Angew. Chem. Int. Ed.* **2000**, *39*, 450 – 466; b) F. B. Perler, E. Adam, *Curr. Opin. Biotechnol.* **2000**, *11*, 377 – 383; c) H. Paulus, *Annu. Rev. Biochem.* **2000**, *69*, 447 – 496; d) E. C. Schwartz, T. W. Muir, A. B. Tyszkiewicz, *Chem. Commun.* **2003**, 2087 – 2090; e) M. Q. Xu, T. C. Evans, *Curr. Opin. Biotechnol.* **2005**, *16*, 440 – 446.
[7] For similar $K_d$ values that have been recently reported, see J. Shi, T. W. Muir, *J. Am. Chem. Soc.* **2005**, *127*, 6198 – 6206.
[8] D. D. Martin, M. Q. Xu, T. C. Evans, *Biochemistry* **2001**, *40*, 1393 – 1402.
[9] a) J. Eppinger, D. P. Funeriu, M. Miyake, L. Denizot, J. Miyake, *Angew. Chem.* **2004**, *116*, 3894 – 3898; *Angew. Chem. Int. Ed.* **2004**, *43*, 3806 – 3810; Corrigendum: J. Eppinger, D. P. Funeriu, M. Miyake, L. Denizot, J. Miyake, *Angew. Chem.* **2004**, *116*, 4489; *Angew. Chem. Int. Ed.* **2004**, *43*, 4389; b) C. Bock, M. Coleman, B. Collins, J. Davis, G. Foulds, L. Gold, C. Greef, J. Heil, J. S. Heilig, B. Hicke, M. N. Hurst, G. M. Husar, D. Miller, R. Ostroff, H. Petach, D. Schneider, B. Vant-Hull, S. Waugh, A. Weiss, S. K. Wilcox, D. Zichi, *Proteomics* **2004**, *4*, 609 – 618.
[10] G. B. Sigal, M. Mrksich, G. M. Whitesides, *J. Am. Chem. Soc.* **1998**, *120*, 3464 – 3473.
[11] The term "traceless" is used to emphasize that when the corresponding protein-$I_N$ fusion is attached to an $I_C$-coated surface through protein trans-splicing, the $I_N$ and $I_C$ intein fragments involved in the immobilization process are cleanly removed away.
[12] The effect of pH and temperature on trans-splicing mediated by the naturally split DnaE intein from *Synechocystis sp.* PCC6803 has been extensively studied by Evans et al.[8] The optimal pH for trans-splicing has found to be 7.0, however, the trans-splicing reaction was also relatively efficient at pH values ranging from 5 to 8.
[13] Dried $I_C$-coated glass slides could be stored for several months at −20 °C before being used. To increase the stability of the $I_C$ polypeptide, however, the dried $I_C$-coated glass should be stored with the protected C-extein Cys residue (first residue of the DnaE C-extein fragment).
[14] Our results show that the split-intein-mediated protein trans-splicing reaction for DnaE can be used to generate protein microarrays in about 24 h (2 h: 2-mercaptoethanol deprotection, 6–8 h: protein spotting and 14–16 h protein trans-splicing reaction).

 © 2006 Wiley-VCH Verlag GmbH & Co. KGaA, Weinheim 

*Molecular Magnetism*

DOI: 10.1002/anie.200503564

# Dysprosium Triangles Showing Single-Molecule Magnet Behavior of Thermally Excited Spin States**

*Jinkui Tang, Ian Hewitt, N. T. Madhu, Guillaume Chastanet, Wolfgang Wernsdorfer, Christopher E. Anson, Cristiano Benelli, Roberta Sessoli, and Annie K. Powell**

*Dedicated to Professor Dante Gatteschi on the occasion of his 60th birthday*

The study of paramagnetic metal-ion aggregates has been of increasing interest since the observation that such molecules can exhibit magnetic memory effects.[1–3] Termed single-molecule magnets or SMMs, the important factors leading to such properties derive from the combination of a large ground-state spin and a large magnetic anisotropy of the Ising (easy-axis) type. Studies have largely been based on transition-metal compounds since they typically exhibit both of the aforementioned features. The incorporation of lanthanides into these complexes has been investigated to take advantage of the potentially large number of unpaired f-electrons available.[4–7] However, very little work has been done to date on purely lanthanide-based systems.[8,9] The origin of SMM behavior in lanthanide-containing compounds is more complicated than that of d-block transition-metal ions since there is likely to be a significant orbital component. In the lanthanide-containing phthalocyanine complexes reported in the literature the ligand environment induces a large splitting of the ground *J* manifold, whereas in SMMs large-spin ground states arising from magnetic interactions between the metal centers of the cluster can enhance the weaker single-ion

[*] Dr. J. Tang, Dr. I. Hewitt, Dr. N. T. Madhu, Dr. C. E. Anson, Prof. A. K. Powell
Institut für Anorganische Chemie
Universität Karlsruhe
Engesserstrasse Geb. 30.45, 76128 Karlsruhe (Germany)
Fax: (+49) 721-608-8142
E-mail: powell@chemie.uni-karlsruhe.de
Dr. G. Chastanet, Prof. C. Benelli, Prof. R. Sessoli
Department of Chemistry
University of Florence
Via della Lastruccia 3, 50019 Sesto Fiorentino (Italy)
Dr. W. Wernsdorfer
Laboratoire Louis Néel—CNRS
BP 166, 25 Avenue des Martyrs, 38042 Grenoble Cedex 9 (France)

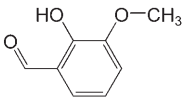
[**] This work was supported by the DFG (SPP1137 and the Center for Functional Nanostructures), QuEMolNa (MRTN-CT2003-504880) and MAGMANet (NMP3-CT-2005-515767). Dr. Patrick Rosa is gratefully acknowledged for his assistance with the ac-magnetic measurements.

Supporting information for this article is available on the WWW under http://www.angewandte.org or from the author.


© 2006 Wiley-VCH Verlag GmbH & Co. KGaA, Weinheim

anisotropies. Given that such aggregates are almost exclusively oxo-bridged systems, and noting that dysprosium(III) shows manifold magnetic behavior and was the first known example of the so called "spin ice" effect,[10] we decided to explore the possibility of obtaining oxo-bridged $Dy^{III}$ aggregates.

Herein we report the synthesis, structures, and preliminary magnetic studies of two similar triangular dysprosium compounds, $[Dy_3(\mu_3\text{-}OH)_2L_3Cl_2(H_2O)_4][Dy_3(\mu_3\text{-}OH)_2L_3Cl(H_2O)_5]Cl_5\cdot 19\,H_2O$ (**1**) and $[Dy_3(\mu_3\text{-}OH)_2L_3Cl(H_2O)_5]Cl_3\cdot 4\,H_2O\cdot 2\,MeOH\cdot 0.7\,MeCN$ (**2**) (where HL = *o*-vanillin, Scheme 1), which display a complex and unprecedented magnetic behavior.




***Scheme 1.*** *o*-Vanillin (2-hydroxy-3-methoxybenzaldehyde).

The crystal structure of **1** consists of triangles of dysprosium centers capped by two $\mu_3$-hydroxo centers (Figure 1 a). This motif has previously been reported for the gadolinium analogue.[11] Along each side of the triangle, a deprotonated *o*-vanillin ligand bridges by its phenoxo group. Aldehyde and methoxy groups also coordinate to the dysprosium center. Two water molecules coordinate to Dy(1) and Dy(2) above and below the plane of the triangle, but for Dy(3) these sites are occupied by a chloride ion above the plane and below a chloride or a water molecule with a 50:50 disorder. Each of the dysprosium centers is eight-coordinate and displays a distorted geometry. The irregular coordination can be described as being based on a pentagonal bipyramid but where one site in the pentagonal plane is vacant; instead there are the two $\mu_3$-hydroxo sites above and below it. The pentagon is defined for Dy(1) thus: methoxy of a ligand O(5), phenolate from the same ligand O(3), which also bridges to Dy(2), O(9) from the phenolate of a neighboring ligand bridging to Dy(3), O(10) from the aldehyde of this bridging ligand, O(1) and O(2) from the bridging $\mu_3$-hydroxo groups above and below the fifth site. The coordination sphere is completed by two water ligands above and below this plane, or, in the case of Dy(3), a chloride ligand and either a chloride or water ligand. Attempts were made to refine the structure in acentric space groups taking into account the possibility of twinning, however, no evidence for an ordered structure involving the chloride and water ligands was found. We conclude that these two ligands are essentially disordered, or at best display only short-range order.

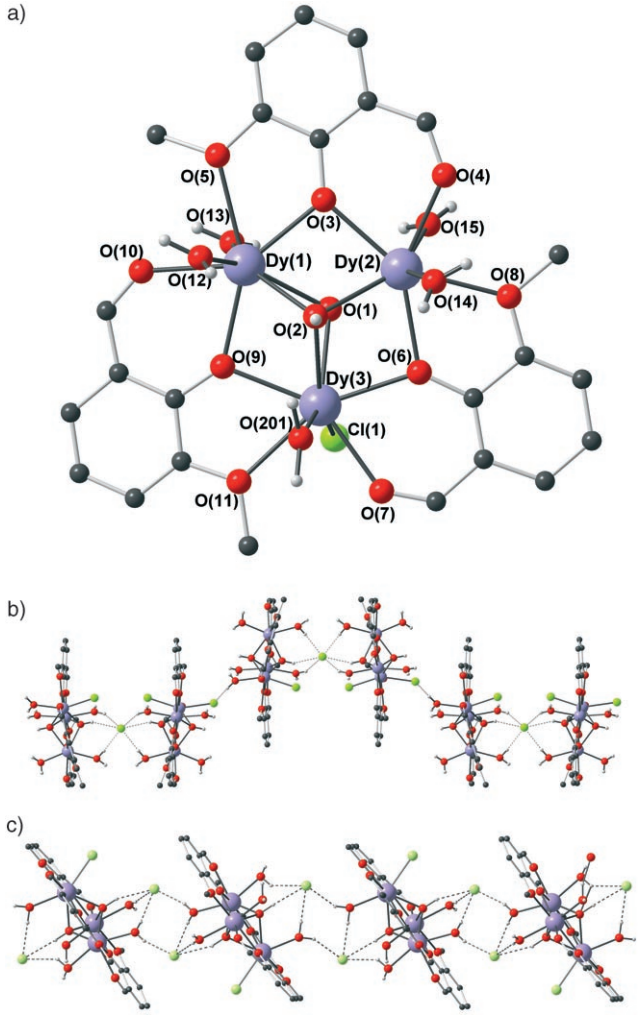



***Figure 1.*** a) Structure of the triangular units in **1** and **2** with numbering scheme. In **1** there is 50:50 disorder of Cl and $H_2O$ at O(201) as described in the text. Intratriangle Dy···Dy distances: **1** 3.50–3.53 Å; **2** 3.51–3.54 Å. The hydrogen bonding is highlighted between trinuclear units in **1** (b) and **2** (c). Color scheme: blue $Dy^{III}$, red O, green Cl, dark gray C, white H.[18]

Pairs of such triangular units are linked by a chloride counterion Cl(3) which is hydrogen bonded to two water ligands (Cl(3)–O($H_2O$) 3.06 Å) and a capping hydroxide (Cl(3)–O(OH) 3.21 Å) from each unit. The resulting pairs of triangles are linked into a chain (Figure 1 b) through hydrogen bonds between the disordered chloride/water ligands on the Dy(3) (Cl(2)–O($H_2O$) 3.12 Å). These show the shortest intertriangle Dy···Dy distances at 7.48 Å. There are π–π effects between these chains. Each of the triangular pairs along the chain is interleaved by a phenyl ring from a unit in the neighboring chain, giving a side-on phenyl carbon C(12)–Cl(3) distance of 3.84 Å. This phenyl is also placed between two other phenyl groups on a neighboring chain at about 3.7 Å. Through these interactions and because of the hydrogen bonding along the chains, they converge through the π-effects and then diverge to create a criss-cross pattern with channels running in the [110] direction with side entrances in the [001] direction (see Supporting Information).

Compound **2** crystallizes to give solely the mono-chloride form of the dysprosium triangles observed in compound **1**. For each triangular unit there are hydrogen bonds to the two chloride counterions, Cl(2) and Cl(3), through the five water ligands and the capping hydroxide. Furthermore, the molecules are linked into chains (Figure 1 c) through this hydrogen bonding between the chloride counterions and water ligands with the shortest interactions, Cl(2)···O(12) (3.07 Å) and Cl(3)···O(16) (3.02 Å), and with the closest intertriangle distance of 6.80 Å. In contrast to **1** there are no direct hydrogen bonds between donor atoms coordinated to $Dy^{III}$ ions of different trimers present in **2**. We also note that the arrangement of chlorides as either ligands or counterions differs in both **1** and **2** from that of the nitrates in the gadolinium analogue.[11] There are also π–π effects in the packing arrangement, but in this case because the linking of

 © 2006 Wiley-VCH Verlag GmbH & Co. KGaA, Weinheim 

the molecules into chains is simpler only the interleaving is important. Each triangle has π–π interactions to five nearest neighbors, although none of the interactions are as strong as those in the structure of **1**.

The static magnetic moment of polycrystalline samples of both **1** and **2** were measured using a SQUID magnetometer in the temperature range 1.8 to 300 K at 0.1 T (Figure 2). The

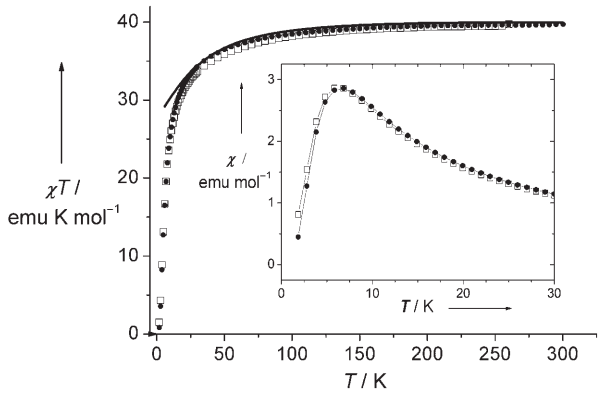



***Figure 2.*** Temperature dependence of the $\chi T$ product (per trimeric unit) for **1** (□) and **2** (●). The solid line represents the calculated value for three uncorrelated $Dy^{III}$ ions (see text). Inset: low-temperature susceptibility $\chi$.

microcrystals of both compounds tend to orientate in the magnetic field and were fixed by either pressing into a pellet or freezing with nujol. The two compounds show an identical behavior with the margin of error produced by a small residual orientation. The room-temperature $\chi T$ value of 40.5 emu K $mol^{-1}$ is in good agreement with that expected for three uncoupled $Dy^{III}$ ions ($J = 15/2$, $g = 4/3$)[12] and decreases almost to zero at low temperature. The susceptibility (inset of Figure 2) goes through a maximum around 6.5 K. Crystal-field effects are expected to reduce the susceptibility, and indeed down to 30 K the observed behavior can be modeled by taking into account the splitting of the $J =$ 15/2 of non-interacting $Dy^{III}$ ions, as shown in Figure 2. In order to reduce the number of parameters an idealized $C_{2v}$ symmetry has been assumed, introducing even terms up to the sixth order in Stevens' operators.[13] The detailed analysis of the crystal field is not the aim of this Communication and would require single-crystal data on this system as well as on the dysprosium-doped diamagnetic analogue to define unambiguously a set of parameters. It is, however, interesting to note that, even by allowing the nine crystal-field parameters to vary freely, the pronounced decrease of $\chi T$ below 30 K cannot be reproduced, and therefore the presence of some significant intratrimer antiferromagnetic interactions can be postulated as, indeed, observed in the gadolinium analogue.[11] The vanishing susceptibility at low $T$ is, however, totally unexpected for a system comprising an odd number of centers with half-integer $J$ value. The magnetization versus field data of a polycrystalline sample confirms the presence of antiferromagnetic interactions as the slope is less steep at low field and increases around $H = 0.95$ T for both compounds (Figure 3). Above this field the magnetization increases

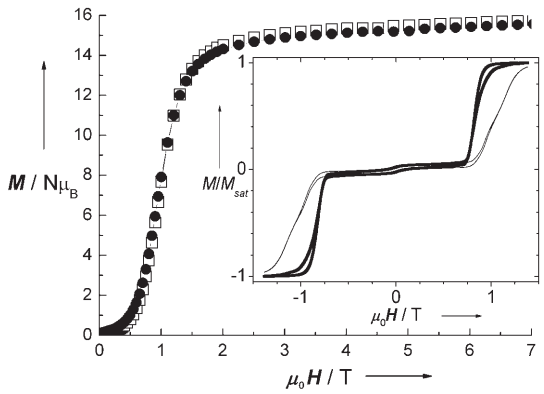



***Figure 3.*** Molar magnetization $M$ versus applied field $\mu_0 H$ measured at $T = 1.8$ K on a polycrystalline sample of **1** (□) and **2** (●). Inset: micro-SQUID measurements at 0.1 K and 28 $mT s^{-1}$ on a single crystal of **2** applying the magnetic field in the plane (light) and perpendicular to the plane (bold) of the $Dy^{III}$ ions.

slowly reaching at 7 T the value of 15.6 $\mu_B$. This value is consistent with that calculated for three uncorrelated $Dy^{III}$ magnetic moments ($3 \times 5.23$ $\mu_B$), assuming the crystal-field parameters are the same as those used to reproduce the $\chi T$ versus $T$ curve of Figure 2. This implies the presence of considerable ligand-field effects. The application of a field stronger than 2 T apparently overcomes all antiferromagnetic interactions.

Single crystals of both **1** and **2** were studied further using the microSQUID technique,[14] and again were found to produce an identical and rather surprising behavior (inset of Figure 3). The curves show a step behavior, in agreement with the higher temperature data, but the position of the step, $H_c$, depends on the orientation of the magnetic field with respect to the plane of the dysprosium triangle. However, the absolute value of the magnetization is not accessible with this technique and each curve has been rescaled to the value measured at the largest field. The initial susceptibility is not exactly zero even at 0.1 K, and a first saturation to a value of 0.05 $M_{sat}$ is observed, as well as a small hysteresis both below and above $H_c$.

To investigate the dynamics of the magnetization further, ac-susceptibility studies were undertaken for **1** and **2**. For both compounds the temperature dependence of the complex susceptibility behavior shows a strong frequency dependence below 20 K. On decreasing the frequency the $\chi'$ versus $T$ curve approaches the static one and shows a maximum around 6.5 K. The out-of-phase component, $\chi''$, when plotted against $T$, shows maxima, the positions of which are frequency-dependent as typically observed for SMMs. However, the peaks are quite distorted with a shoulder structure (see Figure 4 and Supporting Information). In order to extract the temperature dependence of the relaxation time in the presence of complex behavior like non-monotonic equilibrium susceptibility, we have plotted the $\chi''$ data against the logarithm of the frequency (Figure 4), because the average relaxation time can be easily extracted from the frequency at which a maximum in $\chi''$ occurs, being $\tau = 1/(2\pi\nu)$.[15]

Plotting the relaxation time versus the inverse temperature reveals that the behavior is only linear at very high

 © 2006 Wiley-VCH Verlag GmbH & Co. KGaA, Weinheim 

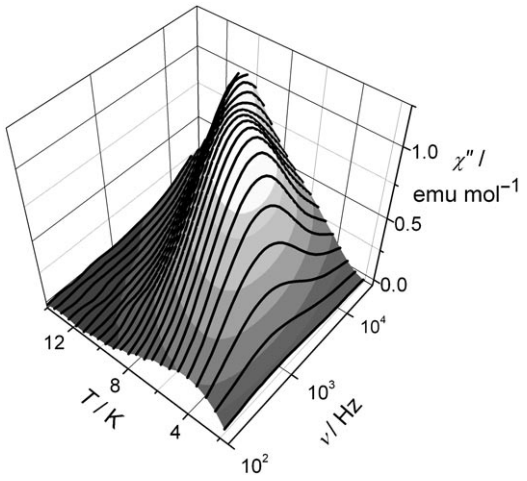



***Figure 4.*** Out-of-phase ac-susceptibility $\chi''$ versus frequency $\nu$ in logarithmic scale for a polycrystalline sample of **2** in the temperature range 1.5–14 K.

temperature with $\tau = 2.2 \times 10^{-8} \exp(61.7\,T^{-1})$, while at low temperature the relaxation time saturates (Figure 5).

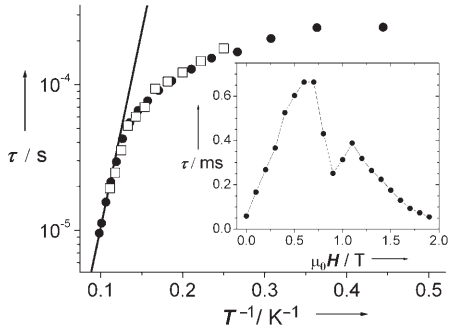



***Figure 5.*** Relaxation time $\tau$ of the magnetization for **1** (□) and **2** (●) versus inverse temperature. The solid line is a fit of the Arrhenius law to the high temperature data of **2**. Inset: the field dependence of the relaxation time for **2** at $T = 7.15$ K.

In order to explore the dynamic behavior even further the frequency dependence of $\chi''$ for **2** has been investigated as a function of the applied field at $T = 7.15$ K, the point at which $\tau$ starts to saturate (see Supporting Information). The field dependence of $\tau$, shown in the inset of Figure 5, is strongly reminiscent of resonant quantum tunneling as it shows a minimum in zero field.[16] A second minimum is observed around 0.9 T, the field at which a step in the magnetization curve is observed.

Both the static and dynamic magnetic properties of these trimeric $Dy^{III}$ species are unprecedented. The observation of a non-magnetic state for a system carrying an odd number of unpaired electrons could be explained by the presence of intercluster interactions. Whereas the presence in **1** and **2** of a hydrogen-bonded network could give rise to antiferromagnetic interactions, these interactions should be very weak. On the contrary, both the temperature of the maximum in $\chi$ and the critical field in the $M$ versus $H$ curve are compatible with an interaction in the order of the Kelvin, that is, of the same order of magnitude of the intratriangle interaction observed in the gadolinium analogue, and of that found in $Dy(OH)_3$.[11,17] Moreover, **1** and **2** have a virtually identical magnetic behavior even in the presence of very different hydrogen-bonding networks. In particular, a significantly weaker intercluster interaction is expected for **2** as no direct hydrogen bonds between donor atoms are observed. Thus, the vanishing susceptibility at low $T$ seems to be a feature of the triangular arrangement of the spins and is possibly related to the anisotropic nature of the intratrimer exchange interaction. The anisotropy axes of each $Dy^{III}$ ion are not expected to be collinear and this further complicates the analysis. The step in the magnetization observed at $H_c$ could be explained by field-induced level crossing between the first excited magnetic state and the almost non-magnetic ground state. More detailed studies, such as ESR spectroscopy of a diamagnetic analogue doped with dysprosium, could provide information on the local anisotropy and allow a rationalization of the observed behavior.

Beyond the unprecedented static properties, the compounds show the unusual coexistence of slow relaxation of the magnetization and an almost diamagnetic ground state. The slow dynamics observed in the ac susceptibility between 2 and 20 K could be associated with the excited state, and interestingly show strong deviation from the Arrhenius law as this state depopulates. The sharp decrease of $\tau$ at zero field and at $H_c$ suggests that an additional relaxation pathway shortcutting the energy barrier is active as predicted at level crossings when resonant quantum tunneling is observed.

The two dysprosium triangles we have investigated here show a vanishing susceptibility at low temperature, which is unprecedented in systems comprising an odd number of unpaired electrons. In spite of the almost non-magnetic ground state, features typical of SMM behavior are observed for the thermally populated excited state, suggesting that a resonant under-barrier relaxation process is also active. This observation is strongly relevant to molecular nanomagnetism because the presence of a large spin ground state appears not to be a necessary condition to observe slow relaxation of the magnetization.

Received: October 7, 2005
Revised: December 23, 2005

**Keywords:** dysprosium · hysteresis · lanthanides · single-molecule magnets

[1] R. Sessoli, H. L. Tsai, A. R. Schake, S. Sheyi, J. B. Vincent, K. Folting, D. Gatteschi, G. Christou, D. N. Hendrickson, *J. Am. Chem. Soc.* **1993**, *115*, 1804.
[2] A. Caneschi, D. Gatteschi, R. Sessoli, A.-L. Barra, L. C. Brunel, M. Guillot, *J. Am. Chem. Soc.* **1991**, *113*, 5873.
[3] R. Sessoli, D. Gatteschi, A. Caneschi, M. A. Novak, *Nature* **1993**, *365*, 141.
[4] S. Osa, T. Kido, N. Matsumoto, N. Re, A. Pochaba, J. Mrozinski, *J. Am. Chem. Soc.* **2004**, *126*, 420.
[5] C. M. Zaleski, E. C. Depperman, J. W. Kampf, M. L. Kirk, V. L. Pecoraro, *Angew. Chem.* **2004**, *116*, 4002; *Angew. Chem. Int. Ed.* **2004**, *43*, 3912.

 © 2006 Wiley-VCH Verlag GmbH & Co. KGaA, Weinheim 

[6] A. Mishra, W. Wernsdorfer, K. A. Abboud, G. Christou, *J. Am. Chem. Soc.* **2004**, *126*, 15648.
[7] A. Mishra, W. Wernsdorfer, S. Parsons, G. Christou, E. K. Brechin, *Chem. Commun.* **2005**, 2086.
[8] L. G. Westin, M. Kritikos, A. Caneschi, *Chem. Commun.* **2003**, *8*, 1012.
[9] N. Ishikawa, M. Sugita, W. Wernsdorfer, *J. Am. Chem. Soc.* **2005**, *127*, 3650.
[10] A. P. Ramirez, A. Hayashi, R. J. Cava, R. Siddharthan, B. S. Shastry, *Nature* **1999**, *399*, 333.
[11] J.-P. Costes, F. Dahan, F. Nicodème, *Inorg. Chem.* **2001**, *40*, 5285.
[12] C. Benelli, D. Gatteschi, *Chem. Rev.* **2002**, *102*, 2369.
[13] A. Abragam, B. Bleaney, *Electron Paramagnetic Resonance of Transition Ions*, Dover, New York, **1986**.
[14] W. Wernsdorfer, *Adv. Chem. Phys.* **2001**, *118*, 99.
[15] A. H. Morrish, *The Physical Principles of Magnetism*, Wiley, New York, **1966**, pp. 87–101.
[16] D. Gatteschi, R. Sessoli, *Angew. Chem.* **2003**, *115*, 278; *Angew. Chem. Int. Ed.* **2003**, *42*, 268.
[17] C. A. Catanese, H. E. Meissner, *Phys. Rev. B* **1973**, *8*, 2060.
[18] CCDC 284870 (**1**) and CCDC 284871 (**2**) contain the supplementary crystallographic data for this paper. These data can be obtained free of charge from the Cambridge Crystallographic Data Centre via www.ccdc.cam.ac.uk/data_request/cif.

 © 2006 Wiley-VCH Verlag GmbH & Co. KGaA, Weinheim 

C–S Bond Cleavage

DOI: 10.1002/anie.200503691

# Mixed Diketonate Thiolate Copper(I) Precursors for Materials Synthesis: Control of $Cu_2S$-Forming Thermolysis Pathways by Manipulating Lewis Acid and Base Cluster Building Blocks**

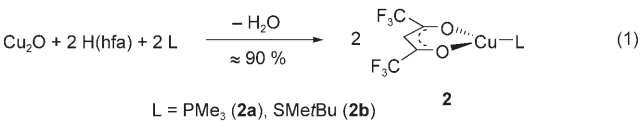
*Sven Schneider, John A. S. Roberts, Michael R. Salata, and Tobin J. Marks**

*Dedicated to Professor Herbert W. Roesky on the occasion of his 70th birthday*

Single-source molecular precursors are of great importance for preparing inorganic powders, nanoparticles, and thin films.[1] The growth temperature, a crucial parameter governing product morphology and optical/electronic properties is severely constrained by the thermolysis characteristics of the precursor. Hence, precursor design strategies that optimize clean decomposition to desired products at tailorable temperatures are of particular interest.

We recently reported the synthesis of the copper(I) thiolate–Lewis base adduct $[(CuS\mathit{t}Bu)_4(PMe_3)_2]$ from polymeric $(CuS\mathit{t}Bu)_n$ (**1**) and its implementation as the first single-source precursor for monoclinic α-$Cu_2S$ (low-chalcocite) thin films, the important $Cu_xS$ phase for photovoltaic applications.[2] Herein we introduce the use of Lewis acidic copper(I) diketonate fragments as a new approach to reducing the nuclearity of the polymeric binary copper thiolate. We further show that thiolate decomposition to $Cu_2S$ can be controlled by combining C–S bond activating Lewis acidic and stabilizing Lewis basic cluster building blocks. Fenske and coworkers pioneered the synthesis and structural chemistry of large phosphine-stabilized copper(I) chalcogenide clusters, utilizing copper salt condensation with the very labile E–Si bonds of silylchalcogenide $E(SiMe_3)_2$ (E = S, Se, Te) reagents.[3] However, $[Cu_{14}S(SPh)_{12}(PPh_3)_6]$ is the only structurally characterized copper sulfide cluster generated by C–S scission but its formation pathway remains unclear.[4] The approach we report herein tunes the thermolysis of the molecular precursors for $Cu_2S$ and yields a new class of large copper(I) clusters with $Cu_2S$ cores. These clusters are intermediates in thiolate C–S bond activation towards $Cu_2S$ and have remarkable solution stabilities.

The hard $Cu^I$ fragment {Cu(hfa)} (hfa = hexafluoroacetylacetonate) was chosen as the Lewis acidic cluster building block because it forms diverse tetrahedral and trigonal-planar complexes. The compounds [Cu(hfa)L] (L = $PMe_3$ (**2a**), SM*e*t*B*u (**2b**)) were prepared in high yield by one-pot syntheses from $Cu_2O$ and H(hfa) in the presence of L, analogous to that for [Cu(hfa)CO] [Eq. (1); see Supporting Information].[5–7]




(1)

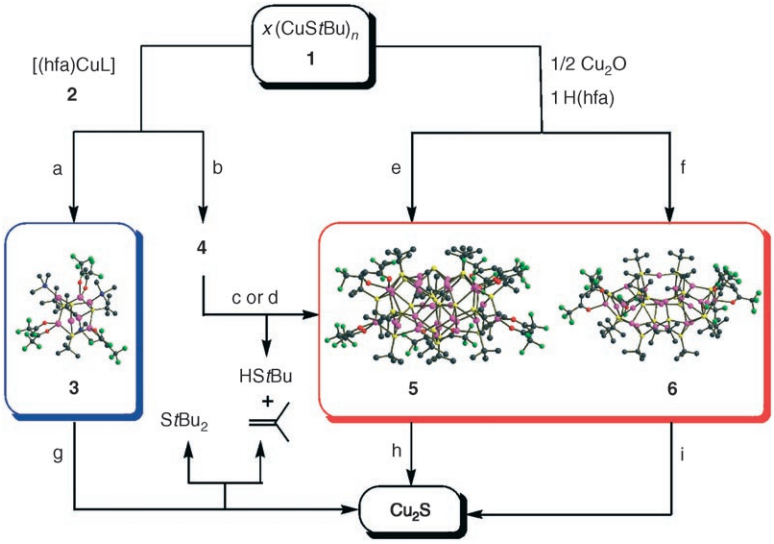
Orange-red blocks of the moderately air-sensitive cluster $[Cu_7(S\mathit{t}Bu)_4(hfa)_3(PMe_3)_3]$ (**3**) are obtained in high yield (> 90%) from an equimolar mixture of **2a** and $(CuS\mathit{t}Bu)_n$ (**1**) in $CH_2Cl_2$ (Scheme 1 and Supporting Information). The integrals in the $^1H$ NMR spectrum and combustion analysis agree with the solid-state molecular structure. At 25 °C, a single set of signals is observed for the three ligands (S*t*Bu, hfa, $PMe_3$) in the $^1H$, $^{13}C$, $^{31}P$, and $^{19}F$ NMR spectra. However, upon cooling to −40 °C, two signals in a 2:1 intensity ratio in the $^{31}P$ and $^{19}F$ NMR spectra indicate the presence of the solid-state $C_s$ symmetry; at least one additional minor species is detected by $^{31}P$ NMR spectroscopy. Rapid ligand positional interchange at room temperature is expected for structurally very diverse, low-coordinate $Cu^I$ thiolates.[8] In the solid state, cluster **3** is bisected by a crystallographic mirror plane containing Cu1, Cu2, Cu4, S1, S2, P1, O1, and O2 (Figure 1).[9] The core of the spherical $Cu_7S_4$ cage features a

[*] Dr. S. Schneider, J. A. S. Roberts, M. R. Salata, Prof. Dr. T. J. Marks
Department of Chemistry and
the Materials Research Center
Northwestern University
2145 Sheridan Rd., Evanston, IL 60208-3113 (USA)
Fax: (+1) 847-491-2990
E-mail: t-marks@northwestern.edu

[**] We thank the NSF MRSEC program for financial support (DMR-0076097) and C. L. Stern for single-crystal X-ray diffraction data acquisition. S.S. thanks the DFG for a postdoctoral fellowship under the Emmy Noether Programm.

Supporting information for this article is available on the WWW under http://www.angewandte.org or from the author.

 © 2006 Wiley-VCH Verlag GmbH & Co. KGaA, Weinheim 




***Scheme 1.*** Syntheses of mixed Cu$^{I}$ thiolate diketonate clusters and stepwise C–S activation towards $Cu_2S$. Blue box: strong Lewis base stabilization. Red box: weak/no Lewis base stabilization. a) $x=1$, L = $PMe_3$, $CH_2Cl_2$, 98%. b) $x=1$, L = SM*e*t*B*u, toluene, 90%. c) $CD_2Cl_2$, room temperature. d) >40 °C, solid. e) $x=1$, THF, 38%. f) $x=3.5$, THF, 22%. g) >145 °C, solid, $-PMe_3$. h) >125 °C, solid. i) >148 °C, solid. For the structures of **3**, **5**, and **6** see Figures 1 and 3.

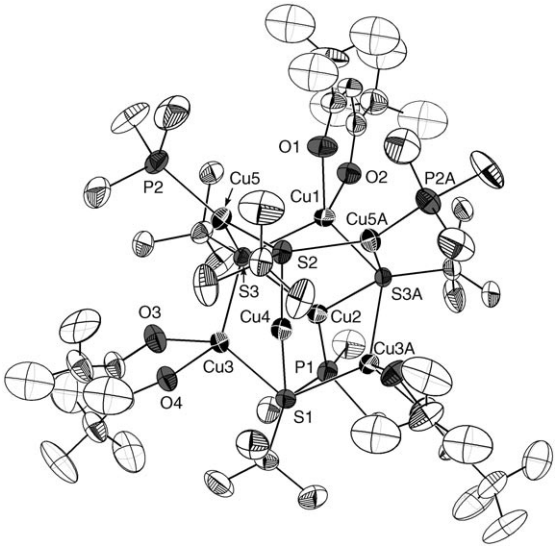



***Figure 1.*** Molecular structure of cluster **3** with thermal ellipsoids drawn at the 50% probability level. Hydrogen atoms and $CH_2Cl_2$ solvent molecules are omitted for clarity. Selected bond lengths [Å] and angles [°]: Cu1–S3 2.3040(9), Cu2–S3 2.4406(9), Cu3–S1 2.3020(8), Cu3–S3 2.2795(10), Cu4–S1 2.1876(14), Cu4–S2 2.1609(14), Cu5–S2 2.2862(8), Cu5–S3 2.2911(9), Cu2–P1 2.2275(13), Cu5–P2 2.2211(11), Cu1–O1 2.096(4), Cu1–O2 2.073(4), Cu3–O3 2.161(3), Cu3–O4 2.074(3); S3-Cu1-S3A 107.63(5), S3-Cu1-O1 110.74(7), S3-Cu1-O2 118.53(5), O1-Cu1-O2 89.13(17), S3-Cu2-S3A 99.28(4), P1-Cu2-S3 129.87(2), S1-Cu3-S3 118.29(4), S1-Cu3-O3 111.24(10), S1-Cu3-O4 112.48(9), S3-Cu3-O3 107.19(9), S3-Cu3-O4 115.90(8), O3-Cu3-O4 87.12(11), S1-Cu4-S2 169.32(6), S2-Cu5-S3 104.82(4), P2-Cu5-S2 125.51(5), P2-Cu5-S3 129.67(4).

$(CuStBu)_4$ unit (Cu3/Cu3A, Cu5/Cu5A) with alternately bridging thiolate ligands above and below the plane defined by the $Cu_4$ rectangle, as in $[(CuStBu)_4(PR_3)_2]$ (R = Me, Et, Ph).[2,10,11] The very rare thiolate ligand $\mu_4$-bridging mode of S3 and S3A, and the distorted tetrahedral geometries around Cu1, Cu3, and Cu3A with relatively short Cu–S bonds[10,12,13] reflect the pronounced {Cu(hfa)} Lewis acidity.[14] The other copper centers exhibit the common linear and trigonal-planar coordination geometries found in copper thiolates.

At 25 °C in the dark, complex **3** is stable in solution ($CD_2Cl_2$, [D$_8$]THF) over several days as assessed by $^1$H NMR spectroscopy. However, at 65 °C, [D$_8$]THF solutions rapidly turn dark red, with diminution in the integral of the S*t*Bu signal in the $^1$H NMR spectrum by approximately 20% over 15 h and the appearance of signals at $\delta = 1.70$ and 4.62 ppm, assignable to 2-methylpropene and indicative of thiolate ligand C–S fragmentation.[15] Thermogravimetric analysis (TGA; Figure 2)

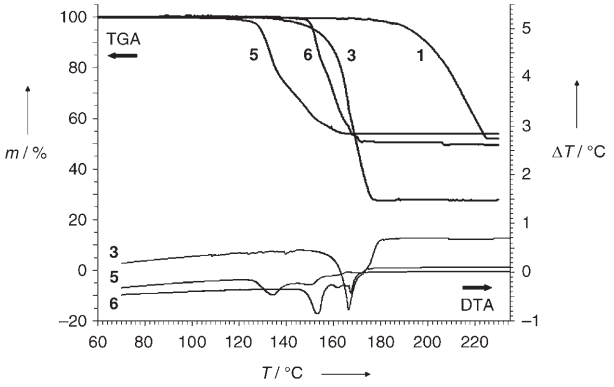



***Figure 2.*** TGA and DTA traces of compounds **3**, **5**, and **6**, and TGA trace of **1**[2] at atmospheric pressure under an $N_2$ flow (100 sccm; temperature ramp, 1 °C min$^{-1}$).

and X-ray diffraction (XRD) analysis of the thermolysis product indicate clean decomposition to α-$Cu_2S$ at temperatures 50 °C lower than the onset of thermolysis in the starting material **1** (198 °C).[16] GC-MS and NMR analyses of the volatiles reveal, in addition to 2-methylpropene and HS*t*Bu, which presumably arise from thiolate β-hydrogen elimination and proton transfer from a hydrosulfide to a thiolate,[10] minor quantities of $StBu_2$. The absence of isobutane and 2,2,3,3-tetramethylbutane argues against intermediate isobutyl radicals in $StBu_2$ formation,[17] while the addition of HS*t*Bu to isobutene by a radical pathway would lead to the anti-Markownikoff product *t*BuS*i*Bu.[18] Therefore, copper Lewis acid catalyzed addition of HS*t*Bu to isobutene appears to be the most likely pathway.[19] Preliminary results show that complex **3** is an excellent single-source precursor for high-quality α-$Cu_2S$ thin-film growth by aerosol-assisted chemical vapor deposition (AACVD) at 200 °C.[10]

To investigate the influence of Lewis base on the C–S scission process, the reaction of **1** and **2b** (1:1) was investigated and found to yield orange product **4** containing a 1:0.8:0.7 ratio of the building blocks {CuS*t*Bu}:{Cu(hfa)}:{SM*e*t*B*u} by $^1$H NMR spectroscopy (Scheme 1; see also Supporting Information). Efforts to grow crystals of

 © 2006 Wiley-VCH Verlag GmbH & Co. KGaA, Weinheim 

**4** for diffractometry were unsuccessful, with recrystallization resulting in SMe*t*Bu loss. Unlike phosphine adduct **3**, the S*t*Bu $^1$H NMR signal of this mixture declines completely over 2 weeks at 25 °C in $CD_2Cl_2$ with concomitant emergence of signals arising from 2-methylpropene. Mixed-sulfide cluster $[Cu_{32}S_5(StBu)_{16}(hfa)_6]$ (**5**) (Scheme 1, Figure 3a,b), which was obtained from the NMR sample as orange blocks, was characterized crystallographically (see below),[9] and by $^1$H NMR spectroscopy, confirming complete SMe*t*Bu ligand loss from **4** and a hfa:S*t*Bu ratio of 6:16 in **5**. Similarly, heating solid **4** in vacuo to about 40 °C overnight results in darkening and isolation of small amounts of **5** after recrystallization from $CH_2Cl_2$, as verified by X-ray diffractometry, and suggesting that C–S activation is triggered by loss of the stabilizing Lewis base L (L = $PMe_3$, SMe*t*Bu). To test this hypothesis, **1** was allowed to react with in-situ generated "{Cu(hfa)}" (Scheme 1 and Supporting Information). At a 1:0.5:1 stoichiometry of **1**:$Cu_2O$:H(hfa), approximately 2/3 of the cuprous oxide undergoes disproportionation to Cu and $[Cu(hfa)_2]$. The remaining material gives a bright orange powder when crystallized from THF/$CH_2Cl_2$ which is identical to **5** by NMR spectroscopy, with elemental (C/H/F/S) and TGA analyses suggesting a stoichiometry closer to $[Cu_{31}S_5(StBu)_{16}(hfa)_5]$. At a 3.5:0.5:1 ratio of **1**:$Cu_2O$:H(hfa), no $Cu^I$ disproportionation is observed, and cluster $[Cu_{24}S_2(StBu)_{16}(hfa)_4]$ (**6**) is isolated in 22 % yield (Scheme 1, Figure 3c,d).[9]

According to the ligand:metal stoichiometries of clusters **5** and **6**, Cu uniformly assumes the +1 oxidation state in all instances, so formal $d^{10}$–$d^{10}$ Cu–Cu bonding can be neglected except through weak correlation effects.[20] Cluster **6** contains two sulfide ions (S1, S2) embedded in a network of cross-linking Cu ions and terminating S*t*Bu$^-$ and hfa$^-$ ligands (Figure 3d) while **5** features, besides three core sulfide ions (S1–S3), two pyramidal $\mu_4$-sulfide units (S4, S5) on the cluster surface (Figure 3b). As in **3**, hfa-bound $Cu^I$ ions exhibit distorted tetrahedral and the others, typical linear and trigonal-planar coordination geometries. All thiolate ligands in **6** are $\mu_3$-bridging, while **5** features five $\mu_4$-thiolates, attributable to the greater Cu(hfa):CuS*t*Bu ratio. In the center of **6**, Cu1 bridges sulfides S1 and S2, while Cu2 and Cu7 covalently connect the $\{Cu_3S_2\}^-$ core with the surrounding CuS*t*Bu scaffold. The remaining Cu–S contacts of distorted square-pyramidal S1 and S2 are considerably longer, resulting in unusual, T-shaped coordination geometries for the metal centers. The cluster core of **5** features a $\{Cu_9S_5\}^-$ cage, having a central, planar $Cu_3S_3$ layer (Cu1–Cu3, S1–S3), sandwiched between two $Cu_3$ layers, Cu5–Cu7 and Cu8–Cu10, respectively, and capping sulfides S4 and S5. This arrangement is reminiscent of the calculated structure of $Cu_{10}S_5$ ($D_{3h}$) if a $Cu^+$ center is added to the middle of the cage in **5**.[20c] Further distortion of the cluster core of **5** results from tightly bound Cu4 and Cu11 which link S4 and S5 covalently to the CuS*t*Bu scaffold. Note also that the high-temperature β-$Cu_2S$ phase can similarly be described as alternately stacked layers of hexagonal CuS sheets and mobile, interstitial Cu ions.[21]

In contrast to **3**, NMR spectra of [D$_8$]THF solutions of **5** and **6** stored in the dark exhibit a significant decline in the S*t*Bu signal and emergent peaks for C–S cleavage byproduct 2-methylpropene after several hours at 25 °C, demonstrating the marked stabilizing effects of the strong Lewis base $PMe_3$ in **3**. TGA and differential thermal analysis (DTA) of **6** (Figure 2) reveal a multistep decomposition process to $Cu_2S$

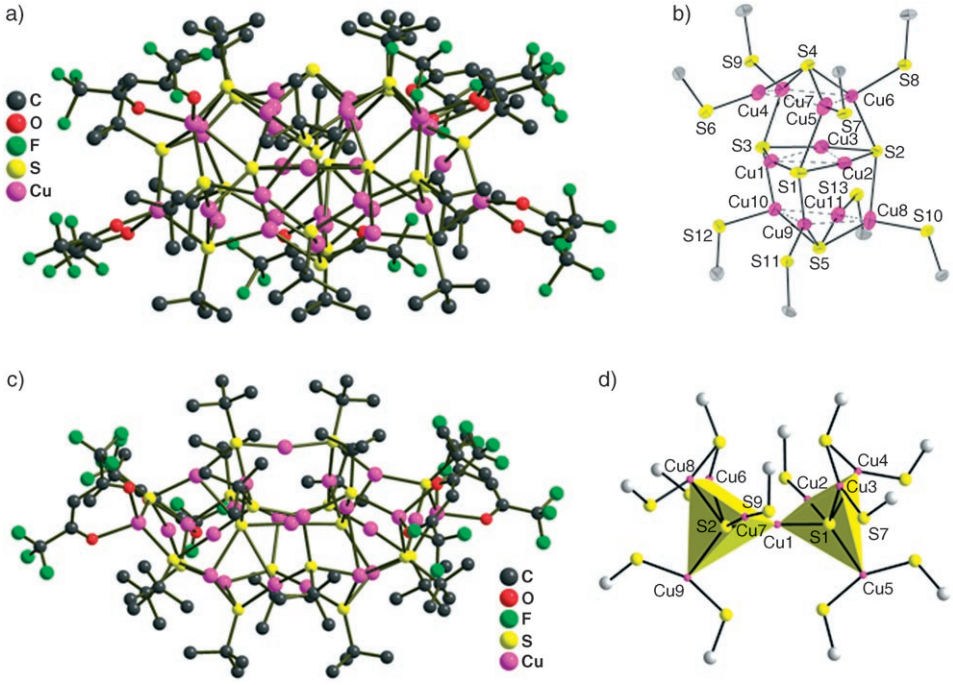



***Figure 3.*** a) Molecular structure of cluster **5**. Hydrogen atoms and $CH_2Cl_2$ solvent molecules are omitted for clarity. b) Cluster core of compound **5** with thermal ellipsoids drawn at the 30 % probability level. Selected bond lengths [Å]: Cu1–S1 2.182(3), Cu1–S3 2.190(3), Cu2–S1 2.182(3), Cu2–S2 2.179(3), Cu3–S2 2.196(3), Cu3–S3 2.191(3), Cu4–S4 2.180(3), Cu4–S6 2.166(3), Cu5–S1 2.653(3), Cu5–S4 2.250(3), Cu5–S7 2.225(3), Cu6–S2 2.370(3), Cu6–S4 2.229(3), Cu6–S8 2.409(3), Cu7–S3 2.410(3), Cu7–S4 2.251(3), Cu7–S9 2.346(3), Cu8–S2 2.616(3), Cu8–S5 2.233(3), Cu8–S10 2.209(3), Cu9–S1 2.395(3), Cu9–S5 2.238(3), Cu9–S11 2.391(3), Cu10–S3 2.358(3), Cu10–S5 2.234(3), Cu10–S12 2.346(3), Cu11–S5 2.186(3), Cu11–S13 2.175(3). c) Molecular structure of cluster **6**. Hydrogen atoms and $CH_2Cl_2$ solvent molecules are omitted for clarity. d) Cluster core of compound **6** with coordination polyhedra around S1 and S2 highlighted. Selected bond lengths [Å]: Cu1–S1 2.173(3), Cu2–S1 2.185(3), Cu3–S1 2.510(3), Cu4–S1 2.502(3), Cu5–S1 2.509(3), Cu1–S2 2.174(3), Cu7–S2 2.164(3), Cu6–S2 2.404(3), Cu8–S2 2.799(3), Cu9–S2 2.568(3).


© 2006 Wiley-VCH Verlag GmbH & Co. KGaA, Weinheim

beginning at approximately 148 °C (**6**) with a strong endotherm at 154 °C (DTA), attributable to C–S activation in the initial step. In the DTA of **3**, this peak is displaced to 167 °C, suggesting that $PMe_3$ dissociation in **3** occurs at higher temperatures than C–S activation in **6**, consistent with the rapid decomposition of **3** to $Cu_2S$ after $PMe_3$ loss. Finally, decomposition of **5** begins as low as 125 °C, this is tentatively explained by the greater average coordination number of the thiolate ligands in **5** than in **6**, which thereby facilitates the C–S activation.

In conclusion, we have shown that C–S scission in $Cu^I$ thiolate clusters can be directed by judiciously combining Lewis acidic building block {Cu(hfa)}, with stabilizing Lewis bases, this is a new approach for $Cu^I$ thiolates. While $PMe_3$ coordination in **3** imparts ideal thermal properties as a single-source precursor for low-temperature $Cu_2S$ growth, the absence of strong Lewis bases L (L = SMe*t*Bu, none) results in synthetically useful Lewis acid assisted C–S bond activation, with clusters **5** and **6** offering new insights regarding pathways from thiolate precursors to bulk $Cu_2S$. Covalent bonding of the cuprous sulfide core to a stabilizing shell matrix imparts remarkable solution control over $Cu_2S$ formation. Further studies will explore this concept for the rational formation of other $Cu^I$ chalcogenide/chalcogenolate clusters, nanoparticles, and thin films.

Received: October 18, 2005
Published online: February 7, 2006

**Keywords:** cleavage reactions · cluster compounds · copper · S ligands

[1] P. O'Brien, N. L. Pickett in *Comprehensive Coordination Chemistry II, Vol. 9* (Eds.: J. A. McCleverty, T. J. Meyer), Elsevier, Oxford, **2004**, pp. 1005.
[2] S. Schneider, Y. Yang, T. J. Marks, *Chem. Mater.* **2005**, *17*, 4286.
[3] S. Dehnen, A. Eichhöfer, D. Fenske, *Eur. J. Inorg. Chem.* **2002**, 279.
[4] K. Tang, T. Xia, X. Jin, Y. Tang, *Polyhedron* **1993**, *12*, 2895.
[5] G. Doyle, K. A. Eriksen, D. Van Engen, *Organometallics* **1985**, *4*, 830.
[6] Spectroscopic data for **2a** agree with the literature, except for the $PMe_3$ disposition.[7] Complex **2a** was suggested to be monomeric based on $^{13}C$ NMR spectroscopy and cryoscopy in 0.040–0.078 M benzene solutions. However, we find a doublet of doublets for the $PMe_3$ signal ($^{13}C$ NMR) in benzene ($c$ = 0.04–1.0 M) which can be explained, for example, by dimer formation with two $PMe_3$ ligands symmetrically bridging two Cu centers. Recently the first crystal structure demonstrating a $\mu^2$-$PMe_3$ ligand was reported: T. Pechmann, C. D. Brandt, H. Werner, *Angew. Chem.* **2000**, *112*, 4069; *Angew. Chem. Int. Ed.* **2000**, *39*, 3909.
[7] K.-M. Chi, H.-K. Shin, K. J. Hampden-Smith, T. T. Kodas, *Inorg. Synth.* **1997**, *31*, 289.
[8] G. Henkel, B. Krebs, *Chem. Rev.* **2004**, *104*, 801.
[9] Crystal structure determination of **3**: $C_{40.5}H_{66}ClCu_7F_{18}O_6P_3S_4$, $M_r$ = 1692.31; orange-red crystals (0.40 × 0.40 × 0.10 mm³), from a saturated $CH_2Cl_2$ solution, $T$ = 153(2) K, $\lambda(Mo_{K\alpha})$ = 0.71073 Å, monoclinic, $P2_1/m$, $a$ = 13.6763(7), $b$ = 16.7478(9), $c$ = 14.8348(8) Å, $\beta$ = 97.1300(10)°, $V$ = 3371.6(3) Å³, $Z$ = 2, $\rho_{calcd}$ = 1.655 g cm$^{-3}$, $2\theta_{max}$ = 57.96°, $\mu$ = 2.486 mm$^{-1}$, $F(000)$ = 1684, 31577 reflections, 8500 unique reflections, 422 parameters, 43 restraints, GOF = 1.057, $R_1$ = 0.0510, w$R_2$ = 0.1605 [$I > 2\sigma(I)$], min./max. residual electron density −1.123/2.494 e Å$^{-3}$. **5**: $C_{95}H_{150}Cl_2Cu_{32}F_{36}O_{12}S_{21}$, $M_r$ = 4945.59; orange crystals (0.16 × 0.11 × 0.06 mm³), from $CH_2Cl_2$, $T$ = 153(2) K, $\lambda(Mo_{K\alpha})$ = 0.71073 Å, triclinic, $P\bar{1}$, $a$ = 18.8516(14), $b$ = 19.1744(15), $c$ = 26.296(2) Å, $\alpha$ = 80.6760(10), $\beta$ = 74.5240(10), $\gamma$ = 73.5350(10)°, $V$ = 8746.5(12) Å³, $Z$ = 2, $\rho_{calcd}$ = 1.878 g cm$^{-3}$, $2\theta_{max}$ = 57.66°, $\mu$ = 4.155 mm$^{-1}$, $F(000)$ = 4876, 81029 reflections, 40866 unique reflections, 1644 parameters, 168 restraints, GOF = 0.957, $R_1$ = 0.0627, w$R_2$ = 0.1592 [$I > 2\sigma(I)$], min./max. residual electron density −1.414/2.399 e Å$^{-3}$. **6**: $C_{85}H_{148}Cl_2Cu_{24}F_{24}O_8S_{18}$, $M_r$ = 3926.97; orange crystals (0.22 × 0.19 × 0.12 mm³), from a $CH_2Cl_2$/THF (1:1), $T$ = 153(2) K, $\lambda(Mo_{K\alpha})$ = 0.71073 Å, triclinic, $P\bar{1}$, $a$ = 14.5907(10), $b$ = 18.7675(13), $c$ = 27.1947(19) Å, $\alpha$ = 92.7680(10), $\beta$ = 98.0640(10), $\gamma$ = 105.4410(10)°, $V$ = 7078.3(8) Å³, $Z$ = 2, $\rho_{calcd}$ = 1.824 g cm$^{-3}$, $2\theta_{max}$ = 50.00°, $\mu$ = 3.875 mm$^{-1}$, $F(000)$ = 3874, 66393 reflections, 33240 unique reflections, 1310 parameters, 247 restraints, GOF = 0.969, $R_1$ = 0.0636, w$R_2$ = 0.1500 [$I > 2\sigma(I)$], min./max. residual electron density −1.616/2.304 e Å$^{-3}$. CCDC-286630, CCDC-286631 and CCDC-286632 contain the supplementary crystallographic data for this paper. These data can be obtained free of charge from The Cambridge Crystallographic Data Centre via www.ccdc.cam.ac.uk/data_request/cif.
[10] S. Schneider, A. Dzudza, J. R. Ireland, M. C. Hersam, T. J. Marks, unpublished results.
[11] I. G. Dance, L. J. Fitzpatrick, D. C. Craig, M. L. Scudder, *Inorg. Chem.* **1989**, *28*, 1853.
[12] I. G. Dance, M. L. Scudder, L. Y. Fitzpatrick, *Inorg. Chem.* **1985**, *24*, 2547.
[13] W. Hirpo, S. Dhingra, M. G. Kanatzidis, *J. Chem. Soc. Chem. Commun.* **1992**, 557.
[14] Only known examples for copper with $\mu_4$-thiolato ligands: a) R. V. Parish, Z. Salehi, R. G. Pritchard, *Angew. Chem.* **1997**, *109*, 276; *Angew. Chem. Int. Ed. Engl.* **1997**, *36*, 251; b) R. G. Prichard, R. V. Parish, Z. Salehi, *J. Chem. Soc. Dalton Trans.* **1999**, 243; c) M. D. Janssen, A. L. Spek, D. M. Grove, G. van Koten, *Inorg. Chem.* **1996**, *35*, 4078; d) H. Xu, J. H. K. Yip, *Inorg. Chem.* **2003**, *42*, 4492.
[15] a) C. Bianchini, I. de los Rios, C. Lopez, M. Peruzzini, A. Romerosa, *J. Organomet. Chem.* **2000**, *593–594*, 485; b) A. Y. Jordan, T. Y. Meyer, *J. Organomet. Chem.* **1999**, *591*, 104.
[16] The small deviation of observed weight loss (28 mass %) from ideal (34 mass %) is attributed to minor loss of highly volatile **2a**.
[17] a) C. J. Thompson, R. A. Meyer, J. S. Ball, *J. Am. Chem. Soc.* **1952**, *74*, 3284; b) J. W. Kraus, J. G. Calvert, *J. Am. Chem. Soc.* **1957**, *79*, 5921.
[18] K. Griesbaum, *Angew. Chem.* **1970**, *82*, 263; *Angew. Chem. Int. Ed. Engl.* **1970**, *9*, 273.
[19] T. Kondo, T. Mitsudo, *Chem. Rev.* **2000**, *100*, 3205.
[20] a) S. Dehnen, A. Schäfer, D. Fenske, R. Ahlrichs, *Angew. Chem.* **1994**, *106*, 786; *Angew. Chem. Int. Ed. Engl.* **1994**, *33*, 746; b) P. Pyykkö, *Chem. Rev.* **1997**, *97*, 597; c) B. Ni, J. R. Kramer, N. H. Werstiuk, *J. Phys. Chem. A* **2003**, *107*, 2890.
[21] R. J. Cava, F. Reidinger, B. J. Wuensch, *Solid State Ionics* **1981**, *5*, 501.

 © 2006 Wiley-VCH Verlag GmbH & Co. KGaA, Weinheim 

Nanoparticles

DOI: 10.1002/anie.200503888

# Temperature-Sensitive Core–Shell Microgel Particles with Dense Shell**

*Ingo Berndt, Jan Skov Pedersen, and Walter Richtering**

Polymeric nanoparticles with core–shell morphology offer promising properties for applications in biomedical as well as industrial fields.[1] Block copolymers which self-assemble into micelles belong to this type of particle. In the micelles, the insoluble blocks form a dense core which is surrounded by a corona of the soluble blocks.[2] Micellar structures, however, lack an intermolecular connection of the unimers and thus may dissolve as a function of, for example, salt concentration, mechanical forces, or simple dilution, which limits their application as "smart" materials. However, block-copolymer micelles with improved stability against dilution could be synthesized by covalently cross-linking core or shell.[3] Other approaches employed dendrimers or hyperbranched polymers.[4] Particles with even more sophisticated properties can be obtained when environmentally responsive polymers are incorporated.[1] Using these species, nanoparticles with spatial separation of regions with different sensitivities on colloidal length scales can be prepared.[5]

Systems with core–shell (or core–corona) morphology mostly display a density profile that decays from the particle center to its periphery. Core–shell nanoparticles where the shell has a denser structure than the core might provide superior properties useful for many applications, as for example, in controlled release or sensors.

Dendrimers were originally assumed to have a structure with a rather open interior region that is surrounded by a denser shell as the number of end groups grows exponentially with the dendrimer generation.[6a] However, the presence of a dense shell could be observed only under very distinct conditions,[6b] and usually dendrimers have a dense core with a monotonically decaying density profile as was demonstrated by means of neutron-scattering investigations and computer simulations.[6c,d]

[*] Dipl.-Chem. I. Berndt, Prof. W. Richtering
Lehrstuhl für Physikalische Chemie II
Institut für Physikalische Chemie
RWTH Aachen
Landoltweg 2, 52056 Aachen (Germany)
Fax: (+49) 241-809-2327
E-mail: richtering@rwth-aachen.de
Prof. J. S. Pedersen
University of Århus
Department of Chemistry
Langelandsgade 140, 8000 Århus C (Denmark)

[**] Financial support by the Deutsche Forschungsgemeinschaft (DFG) and the Fonds der chemischen Industrie is gratefully acknowledged. We thank the Institut Laue-Langevin (ILL), Grenoble, France, for beam time at the D11 instrument and Peter Lindner for local support.

Recently, multiresponsive core–shell microgels have been introduced and investigated by various experimental techniques, such as, fluorescence spectroscopy, calorimetry, and small-angle neutron scattering (SANS). These studies have revealed the mutual influence of core and shell on the temperature-dependent swelling. However, the systems characteristically had a shell density which is lower than that of the core.[5,7]

Since particles with a dense shell have different properties, for example, concerning the release of encapsulated molecules, there is a need for rational synthesis of stimuli-sensitive core–shell particles with a dense shell as well as for techniques that allow the quantitative determination of the density of core and shell.

Herein we present a core–shell microgel consisting of poly-*N*-isopropylacrylamide (PNIPAM) in the shell and poly-*N*-isopropylmethacrylamide (PNIPMAM) in the core. Both polymers display a lower critical solution temperature (LCST) in aqueous solution; in $D_2O$ the transition temperatures are 34 °C for PNIPAM and 44 °C PNIPMAM, whereas in $H_2O$ the transition temperatures are slightly lower. As a consequence, the particle size of the core–shell microgel decreases upon heating in two steps. These doubly temperature-sensitive microgel particles are expected to have a denser shell when the temperature is in between the two LCSTs such that the shell is collapsed but the core is swollen.

The microgel structure has been analyzed by means of SANS and dynamic light scattering (DLS). A core–shell form factor, which has been successfully applied for the analysis of SANS data from core–shell microgels with PNIPAM core and PNIPMAM shell,[7c,d] was used to fit the experimental data. For the current application, modifications of the form factor were required to allow for different widths of the various interfaces of the particles. Radial density profiles revealing the real-space structure have been calculated by Fourier transformation of the scattering amplitude which was obtained from fitting the form factor model to the SANS data.

Core–shell microgels were prepared in two steps. PNIPMAM core particles were synthesized in a similar fashion as PNIPAM microgels by surfactant-aided radical precipitation polymerization[8] and served as nuclei for the subsequent polymerization of the PNIPAM shell. A mixture of NIPAM monomer (0.5 g), cross-linker monomer *N*,*N*′-methylenebisacrylamide (BIS; 9.6 mg, 1.4 mol % with respect to total monomer) and surfactant sodium dodecyl sulfate (SDS; 5.1 mg) in water (25 mL) was added to the core solution (25 mL; 0.5 g microgel) and the polymerization was initiated with potassium peroxodisulfate (12.1 mg). For experimental details see references [5c,7d]. Hydrodynamic radii were determined by DLS from highly diluted samples ($c <$ 0.01 wt %) in heavy water. SANS measurements were carried out at the D11 instrument of the Institut Laue-Langevin (ILL), Grenoble, France, on a 0.2 wt % sample covering a $q$-range from 0.0015 to 0.2 $Å^{-1}$. Data were corrected for background scattering and calibrated on absolute scale by incoherent water scattering according the standard procedures at the ILL.

An expression for the scattering form factor was developed that allows the radial scattering length density distribu-

 © 2006 Wiley-VCH Verlag GmbH & Co. KGaA, Weinheim 

tion $\rho(r)$ of core–shell microgels to be described. A schematic picture of the model's radial density profile is displayed in Figure 1. The center parts of core and shell with homogeneous density are described by $W_{core}$ and $W_{shell}$. The microgel surface

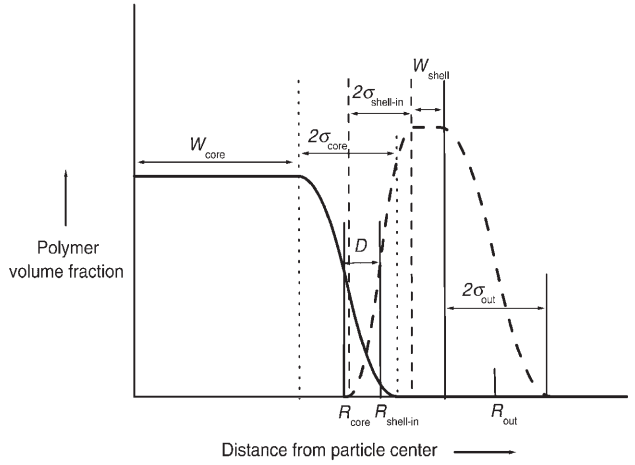



***Figure 1.*** Schematic representation of the radial density profile in core–shell microgels with a "displaced" core–shell interface. See text for details.

is fuzzy because of the inhomogeneous spatial distribution of cross-links within the particle.[9] A profile with a fuzzy surface can be expressed by a parabolic shape with half-width radius $R$ and interface half width $\sigma$ [Eq. (1a)–(1d)].

$$\rho(r) = 1 \text{ if } r \le (R-\sigma) \tag{1a}$$

$$\rho(r) = 1-\frac{1}{2}\frac{[(r-R)+\sigma]}{\sigma^2} \text{ if } (R-\sigma) < r \le R \tag{1b}$$

$$\rho(r) = \frac{1}{2}\frac{[(R-r)+\sigma^2]}{\sigma^2} \text{ if } R < r \le (R+\sigma) \tag{1c}$$

$$\rho(r) = 0 \text{ if } (R+\sigma) < r \tag{1d}$$

The width of central part is given by $W = R-\sigma$ and the volume is $V = 4\pi(R^3/3+R\sigma^2/6)$. The normalized Fourier transformation of this profile can be expressed analytically as Equation (2).

$$\Phi(q,R,\sigma) = \frac{4\pi}{V}[(\frac{R}{\sigma^2}+\frac{1}{\sigma})\frac{\cos(q(R+\sigma))}{q^4} + (\frac{R}{\sigma^2}-\frac{1}{\sigma})\frac{\cos(q(R-\sigma))}{q^4} - \frac{3\sin(q(R+\sigma))}{q^5\sigma^2} - \frac{3\sin(q(R-\sigma))}{q^5\sigma^2} + \frac{2\cos(q,R)}{q^5\sigma^2} + \frac{6\sin(q,R)}{q^5\sigma^2}] \tag{2}$$

The model was further modified such that the interpenetration at the core/shell interface is not necessarily symmetric. This approach allows for having a "depletion" zone between core and shell, that is, a region with a lower polymer volume fraction than in the centers of core and shell. The core part of the particle has radius $R_{core}$, interface width $\sigma_{core}$, volume $V_{core} = 4\pi({R_{core}}^3/3+R_{core}{\sigma_{core}}^2/6)$, and scattering length density $\Delta\rho_{core}$. The outer dimensions of the shell are given by $R_{out}$ and the width of the outer surface profile is $\sigma_{out}$. The inner dimensions of the shell are characterized by $R_{shell\text{-}in}$ and the width of the inner interface is $\sigma_{shell\text{-}in}$. With this the volume of the shell is $V_{shell} = 4\pi[(R^3_{out}/3 + R_{out}\sigma^2_{out}/6) - V_{shell\text{-}in}]$, with $V_{shell\text{-}in} = 4\pi[R^3_{shell\text{-}in}/3 + R_{shell\text{-}in}\sigma^2_{shell\text{-}in}/6]$ and the scattering length density is $\Delta\rho_{shell}$. The parameter $D$, which describes the "displacement" of the core and inner-shell interface can be calculated and it is this parameter that makes it possible to have a displacement of the centers of the two interface profiles; $D = R_{shell\text{-}in} - R_{core}$.

Using these definitions, the scattering amplitude $A(q)$ of a core–shell particle with an asymmetric interface can be expressed as Equation (3).

$$A(q) = \Delta\rho_{shell}V_{shell}\Phi(q,R_{out},\sigma_{out}) - \Delta\rho_{shell}V_{shell\text{-}in}\Phi(q,R_{shell\text{-}in},\sigma_{shell\text{-}in}) + \Delta\rho_{core}V_{core}\Phi(q,R_{core},\sigma_{core}) \tag{3}$$

The half-width radius of the core is $R_{core} = W_{core} + \sigma_{core}$ and the half-width radius of the particle is $R_{out} = R_{core} + D + \sigma_{shell\text{-}in} + W_{shell} + \sigma_{out}$. The resulting form factor is given by the squared scattering length amplitude $P(q) = A^2(q)$. Polydispersity was included in the model using a Gaussian size distribution; a relative size distribution of approximately 10% (typical of such microgels) was obtained thus the sample can be considered as very monodispersed. Finally, the model expression was convoluted by a resolution function, which accounts for instrumental smearing.[10] The model expression was fitted to the experimental data using least-square methods.[11]

Figure 2 displays the influence of temperature on the hydrodynamic radius (in $D_2O$) of the PNIPMAM-core PNIPAM-shell microgel and, for comparison, of the parent PNIPMAM core. Two distinct transitions are observed for the core–shell microgel.

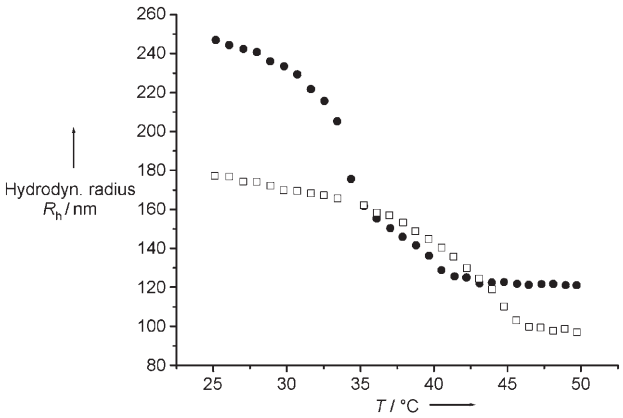



***Figure 2.*** Hydrodynamic radii of the PNIPMAM-core PNIPAM-shell microgel (●) and of the parent PNIPMAM core (□). The core–shell particle is smaller than the core in the intermediate temperature range from 35–41 °C.

The collapsed state at high temperatures can be regarded as a reference state since the synthesis proceeded at 70 °C, which is well above the core LCST and thus the shell is polymerized onto the collapsed core microgel. At temperatures above 45 °C the core–shell particle has a radius that is 13 nm larger than the parent core. A continuous increase of the particle size is observed for the naked core when the

 © 2006 Wiley-VCH Verlag GmbH & Co. KGaA, Weinheim 

temperature is decreased below the LCST of PNIPMAM. However, in the case of the core–shell microgel, the transition is shifted by 4 °C towards lower temperatures and only a slight increase of the hydrodynamic radius is observed when lowering the temperature. The core–shell microgel is smaller than the naked core at temperatures between 35 and 41 °C.

Although DLS can just provide information on the overall particle size, it is evident that the presence of the shell significantly alters the swelling behavior of the core. When the temperature is further decreased below the LCST of PNIPAM a large increase in the hydrodynamic radius is observed and the size of the fully swollen core–shell microgel particle is larger than that of the parent core.

Differential scanning calorimetry and SANS experiments with core–shell microgels that consist of a PNIPAM core and a PNIPMAM shell have shown that a swelling shell exerts an elastic force on the collapsed core that expands the core and shifts the collapse temperatures to higher values.[5d] With the inverse core–shell microgel with PNIPMAM core and PNIPAM shell discussed herein, the situation is opposite: at intermediate temperatures the collapsed shell restricts the core to a more compact structure as it prohibits the swelling of the core.

SANS can provide much more detailed information on the structure of colloidal particles in solution. SANS data obtained with the core–shell microgel are shown in Figure 3. Figure 4 displays the calculated radial density profiles and Table 1 summarizes structural parameters obtained from these fits.

At high temperatures, that is, above both LCSTs, both core and shell are collapsed and the structure is well described by a density profile consisting of two boxes with a narrow interface and a sharp surface with a total width of 3–4 nm (Figure 4). In the high-temperature case, the model could fit the data with a reduced number of parameters and especially $D = 0$ and $\sigma_{\text{shell-in}} = \sigma_{\text{core}}$, that is, a symmetric interface between collapsed core and collapsed shell describes the data. The polymer volume fractions in core and shell are similar at approximately 50%. The parameter

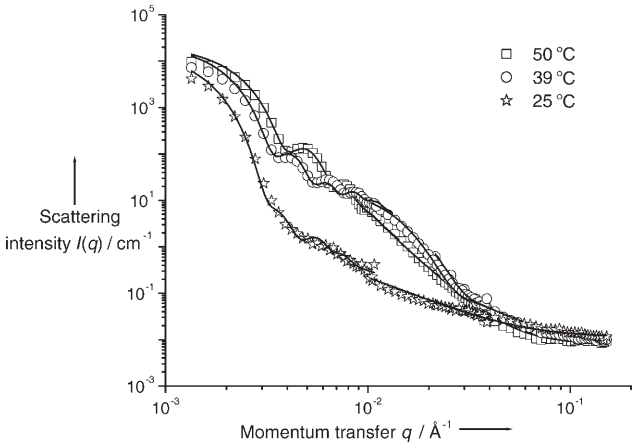



***Figure 3.*** SANS scattering data taken at 25, 39, 50 °C and fit lines according to the model.

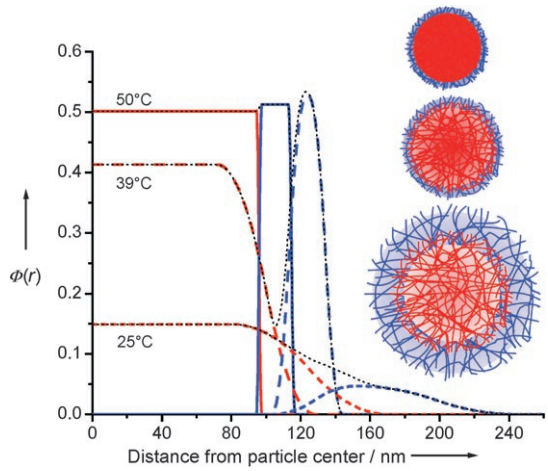



***Figure 4.*** Graph: Radial density profiles calculated from the modeling procedure at 25, 39, and 50 °C; core (red), shell (blue), the black dotted lines show the total density. At the intermediate temperature the shell has a higher density than the swollen core. Also shown are schematic pictures of the density of the core–shell microgels at temperatures 50, 39, and 25 °C (top to bottom).

***Table 1:*** Structural parameters obtained from SANS data analysis.

| $T$ [°C] | $W_{\text{core}}$ [nm] | $\sigma_{\text{core}}$ [nm] | $\Phi_{\text{core}}$ [%] | $\sigma_{\text{shell-in}}$ [nm] | $D$ [nm] | $W_{\text{shell}}$ [nm] | $\sigma_{\text{out}}$ [nm] | $\Phi_{\text{shell}}$ [%] | $R_{\text{SANS}}$ [nm] | $R_{\text{h}}$ [nm] |
|---|---|---|---|---|---|---|---|---|---|---|
| 50 | 95 | 1.5 | 50 | 1.5 | | 15 | 2.0 | 51 | 117 | 121 |
| 39 | 72 | 28 | 41 | 10 | 13 | 1.2 | 9.8 | 53 | 144 | 143 |
| 25 | 80 | 45 | 15 | 23 | 3 | 1.1 | 46 | 4.7 | 244 | 247 |

$R_{\text{SANS}} = R_{\text{core}} + D + \sigma_{\text{shell-in}} + W_{\text{shell}} + 2\sigma_{\text{out}}$ gives the radius at which the shell density goes to zero. $R_{\text{SANS}}$ can be compared directly to the hydrodynamic radius $R_{\text{h}}$ determined by dynamic light scattering and very good agreement is observed.

At 25 °C, both core and shell networks are swollen. The density profile still shows a change in the segment density between core and shell, however, the profile decays constantly from the center to the periphery, as it is common and expected for microgels in the swollen state.[12a,b]

Most interesting is the density profile obtained at 39 °C. The dimensions of the core are increased owing to the swelling of the PNIPMAM at this temperature and the water content in the core increased. Nevertheless, the dimensions of the core at 39 °C ($R_{\text{core}} + \sigma_{\text{core}} = 128$ nm) are still reduced as compared to the pure, naked core at 39 °C, which were determined form SANS measurements to be 148 nm (not shown in the plot in Figure 4). More important, however, the density of the shell is higher than the density inside the core. At this temperature $D_2O$ is already a good solvent for the PNIPMAM core but still a bad solvent for the PNIPAM shell. Apparently, the thermodynamic hydration forces that lead to the swelling of the core are not sufficient to expand the PNIPAM network in the shell. Consequently, a structure is obtained with a shell that is denser than the core.

The total density profiles in Figure 4 provide further information on the particle morphology. At the intermediate

 © 2006 Wiley-VCH Verlag GmbH & Co. KGaA, Weinheim 

temperature of 39 °C a density minimum is observed at around 108 nm. At this temperature, the experimental SANS data could only be fitted with an asymmetric interface between core and shell, that is, $D \neq 0$ and $\sigma_{core} \neq \sigma_{shell\text{-}in}$, this leads to a minimum of the total density.

Static light scattering and SANS investigations of simple (i.e. not core–shell) PNIPAM and PNIPMAM microgels showed that the cross-link density near the particle surface is lower than in the center of the particle when the particles are prepared in a batch polymerization.[12] This inhomogeneous distribution of cross-links is caused by different reaction kinetics of cross-linker and monomer.[9] Such an inhomogeneous cross-link density is also present in the core of the core–shell microgels investigated in this study. Thus the network in the outer region of the PMIPMAM core near the core–shell interface can swell more than the network in the center of the core. It is at first glance surprising that the core is now swollen in such a way that it has an inhomogeneous density. However, it should be kept in mind that the swelling is a result of the system's tendency of maximizing the conformational entropy of the polymer strands between cross-links. Swelling is a more effective way of increasing the entropy in the outer region with low cross density (long strands) compared to that of the more cross-linked (short strands) core center and this is valid also with the gel encapsulated in a constraining shell. The pressure of the swollen core on the collapsed PNIPAM shell leads to a lateral stretching of the shell and a slight increase in the maximum density in the shell compared to what is found at the higher temperature.

An interpenetrating network of core and shell material is formed when the shell is formed on the collapsed core. Referring to results from fluorescence experiments by Lyon and co-workers,[7a,b] we can assume that this interpenetration layer does not penetrate strongly into the core. Consequently, the core network close to the core–shell interface, but not yet inside the interpenetrating network region, is characterized by long strands that can swell strongly at 39 °C. This leads to the segment density minimum shown in Figure 4.

The density profile at the particle surface, that is, the outer profile of the shell, at 39 °C does not decay as sharply as at 50 °C, although the PNIPAM chains at the shell surface should still be in the collapsed state. This could indicate that the surface is slightly rough. As already mentioned above, the swelling core exerts a lateral stretching force on the shell at the core–shell interface which can lead to some buckling of the shell. Since a scattering experiment provides averaged information, the slightly smeared surface profile could be caused by a locally rough surface. At 25 °C the particle surface profile is characterized by a broad decay as it is known from pure PNIPAM microgels.

The data presented herein demonstrate that different temperature-sensitive polymers can be combined in core–shell microgels to tailor and control the density profile in different regions of the particle. The change of density ratio of core and shell with temperature can lead to different uptake and release properties, as compared to core–shell microgels with different chemical functionalities in core and shell. Adding further shells as, for example, grafted chains, can be used to design even more sophisticated nanoparticles.

In conclusion, we present a doubly temperature-sensitive core–shell microgel, which at intermediate temperatures reveals a shell with a higher segment density than the core. The temperature dependence of the hydrodynamic radius already demonstrated that the shell restricts the core swelling at temperatures between the LCSTs of core and shell. More detailed information is obtained from small-angle neutron scattering. A new form-factor model was developed that describes experimental scattering curves at different temperatures. This analysis provides radial density profiles, which clearly show that the shell is denser than the core at intermediate temperatures. Owing to the pronounced temperature sensitivity of core and shell polymers, such core–shell microgels display unique properties that can be tailored by the synthesis and which may be useful in many different applications as for example, encapsulation of active ingredients. In addition the new form-factor model can be applied very generally to particles with core–shell morphology and displaced interfaces.

Received: November 3, 2005
Published online: February 10, 2006

**Keywords:** block copolymers · core–shell nanoparticles · microgels · neutron scattering · temperature sensitivity

[1] a) S. Nayak, L. A. Lyon, *Angew. Chem.* **2004**, *116*, 6874 – 6877; *Angew. Chem. Int. Ed.* **2004**, *43*, 6706 – 6709; b) J. Kim, S. Nayak, L. A. Lyon, *J. Am. Chem. Soc.* **2005**, *127*, 9588 – 9592; c) T. J. V. Prazeres, A. M. Santos, J. M. G. Martinho, *Langmuir* **2004**, *20*, 6834 – 6840; d) Y. Deng, W. Yang, C. Wang, S. Fu, *Adv. Mater.* **2003**, *15*, 1729 – 1732; e) Q. Sun, Y. Deng, *Langmuir* **2005**, *21*, 5812 – 5816.

[2] a) I. W. Hamley, *The Physics of Block Copolymers*, Oxford University Press, Oxford, **1998**; b) J. S. Pedersen, C. Svaneborg, *Curr. Opin. Colloid Interface Sci.* **2002**, *7*, 158 – 166.

[3] a) K. B. Thurmond, T. Kowalewski, K. L. Wooley, *J. Am. Chem. Soc.* **1997**, *119*, 6656 – 6665; K. B. Thurmond, T. Kowalewski, K. L. Wooley, *J. Am. Chem. Soc.* **1996**, *118*, 7239 – 7240; b) T. K. Bronich, P. A. Keifer, L. S. Shlyakhtenko, A. V. Kabanov, *J. Am. Chem. Soc.* **2005**, *127*, 8236 – 8237; c) X.-S. Wang, A. Arsenault, G. A. Ozin, M. A. Winnik, I. Manners, *J. Am. Chem. Soc.* **2003**, *125*, 12686 – 12687.

[4] a) G. E. Oosterrom, J. N. H. Reek, P. C. J. Kamer, P. W. N. M. van Leeuwen, *Angew. Chem.* **2001**, *113*, 1878 – 1901; *Angew. Chem. Int. Ed.* **2001**, *40*, 1828 – 1849; ; b) S. E. Stiriba, H. Kautz, H. Frey, *J. Am. Chem. Soc.* **2002**, *124*, 9698 – 9699; c) R. Haag, *Angew. Chem.* **2004**, *116*, 280 – 284; *Angew. Chem. Int. Ed.* **2004**, *43*, 278 – 282.

[5] a) C. D. Jones, L. A. Lyon, *Macromolecules* **2000**, *33*, 8301 – 8306; b) X. Li, J. Zuo, Y. Guo, X. Yuan, *Macromolecules* **2004**, *37*, 10042 – 10046; c) I. Berndt, W. Richtering, *Macromolecules* **2003**, *36*, 8780 – 8785; d) I. Berndt, C. Popescu, F.-J. Wortmann, W. Richtering, *Angew. Chem.* **2006**, *118*, 1099 – 1102; *Angew. Chem. Int. Ed.* **2006**, *45*, 1081 – 1085.

[6] a) P. G. de Gennes, H. Hervet, *J. Phys. Lett.* **1983**, *44*, L351 – L360; b) S. Rosenfeldt, N. Dingenouts, D. Pötschke, M. Ballauff, A. J. Berresheim, K. Müllen, P. Lindner, *Angew. Chem.* **2003**, *115*, 111 – 114; *Angew. Chem. Int. Ed.* **2003**, *42*, 109 – 112; ; c) D. Boris, M. Rubinstein, *Macromolecules* **1996**, *29*, 7251 – 7260; d) M. Ballauff, C. Likos, *Angew. Chem.* **2004**, *116*, 3060 – 3082; *Angew. Chem. Int. Ed.* **2004**, *43*, 2998 – 3020.

 © 2006 Wiley-VCH Verlag GmbH & Co. KGaA, Weinheim 

[7] a) D. Gan, L. A. Lyon, *J. Am. Chem. Soc.* **2001**, *123*, 8203 – 8209; b) C. D. Jones, J. G. McGrath, L. A. Lyon, *J. Phys. Chem. B* **2004**, *108*, 12 652 – 12 657; c) I. Berndt, J. S. Pedersen, W. Richtering, *J. Am. Chem. Soc.* **2005**, *127*, 9372 – 9373; d) I. Berndt, J. S. Pedersen, P. Lindner, W. Richtering, *Langmuir* **2006**, *22*, 459 – 468.
[8] a) D. Duracher, A. Elaissari, C. Pichot, *Colloid Polym. Sci.* **1999**, *277*, 905 – 913; b) H. Senff, W. Richtering, *J. Chem. Phys.* **1999**, *111*, 1705 – 1711.
[9] X. Wu, R. H. Pelton, A. E. Hamielec, D. R. Woods, W. McPhee, *Colloid Polym. Sci.* **1994**, *272*, 467 – 477.
[10] J. S. Pedersen, D. Posselt, K. Mortensen, *J. Appl. Crystallogr.* **1990**, *23*, 321 – 333.
[11] J. S. Pedersen, *Adv. Colloid Interface Sci.* **1997**, *70*, 171 – 210.
[12] a) M. Stieger, W. Richtering, J. S. Pedersen, P. Lindner, *J. Chem. Phys.* **2004**, *120*, 6197 – 6206; b) S. Meyer, W. Richtering, *Macromolecules* **2005**, *38*, 1517 – 1519; c) I. Berndt, J. S. Pedersen, W. Richtering, unpublished results.

 © 2006 Wiley-VCH Verlag GmbH & Co. KGaA, Weinheim 

Helical Structures

DOI: 10.1002/anie.200504326

# Synthesis and Optical Resolution of a Double Helicate Consisting of *ortho*-Linked Hexaphenol Strands Bridged by Spiroborates

*Hiroshi Katagiri, Toyoharu Miyagawa, Yoshio Furusho,* and Eiji Yashima**

Not surprisingly, the search for new structural motifs for helical architectures has been an intensive research area to date, as the helix is the central structural motif for biomacromolecules in nature.[1] In particular, much effort has recently focused on foldamers, synthetic molecules that fold into an ordered conformation by noncovalent interactions.[1b] For the successful design of foldamers, the structural motifs should be as simple as possible because of the predictability of higher-order structures, the tunability of the structures, etc.

[*] Dr. H. Katagiri, Dr. T. Miyagawa, Dr. Y. Furusho, Prof. E. Yashima
Yashima Superstructured Helix Project
Exploratory Research for Advanced Technology (ERATO)
Japan Science and Technology Agency (JST)
Creation Core Nagoya 101, 2266-22 Anagahora, Shimoshidami,
Moriyama-ku, Nagoya 463-0003 (Japan)
Fax: (+81) 52-739-2081
E-mail: furusho@yp-jst.jp
yashima@apchem.nagoya-u.ac.jp
Prof. E. Yashima
Institute for Advanced Research
Nagoya University
Chikusa-ku, Nagoya 464-8601 (Japan)
Fax: (+81) 52-789-3185

Supporting information for this article is available on the WWW under http://www.angewandte.org or from the author.

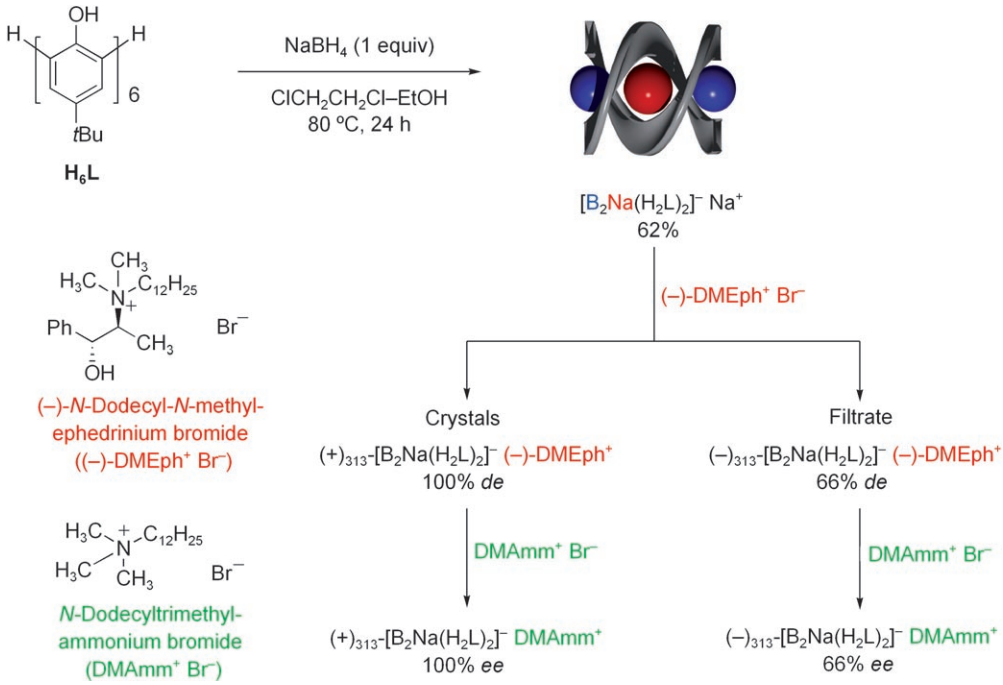
As part of our program to develop synthetic helical polymers and oligomers,[2] we started constructing helical foldamers by utilizing poly-*m*-phenylene as a new key structural motif. The poly- and oligo-*m*-phenylenes are known to adopt the $5_1$-helical conformation in the solid state, but take a random conformation in solution.[3] In studies of the helix induction on 2-hydroxylated oligo-*m*-phenylene derivatives, that is, *ortho*-linked oligophenols,[4] we serendipitously obtained a boron-containing helicate comprised of an *ortho*-linked hexaphenol. In general, helicates are constructed from oligodentate strands and transition metals,[5] and only a few helicates that contain of typical metal cations, such as lithium, sodium, and potassium, are known.[6] However, to the best of our knowledge, boron has never been employed as an assembling center to generate helicates. Boron helicates should be promising for new chiral receptors and asymmetric catalysts owing to the Lewis basic feature of the borate moieties along with their inherent helical chirality.[7,8] We report herein the synthesis and characterization of a double helicate consisting of *ortho*-linked hexaphenol strands bridged by spiroborates and its optical resolution by the formation of a diastereomeric salt.

Single crystals of the boron complex $[B_2Na(H_2L)_2]^-H^+$ suitable for X-ray crystallographic analysis were obtained unexpectedly from a solution of a crude *ortho*-linked hexaphenol $H_6L$ in $CDCl_3$ (Scheme 1)[9] containing a small amount of boric acid and toluene. The X-ray single-crystal analysis revealed the double-stranded helical structure of the complex,[10] which has $D_2$ symmetry with three mutually perpendicular $C_2$ axes. The two strands are $C_2$ symmetric, structurally identical, and are bridged by the spiroborates formed from the terminal biphenol units and the boron atoms (Figure 1).[11] Interestingly, an octacoordinated sodium cation is found at the center of the complex.[12]

Next, we prepared the boron complex $[B_2Na(H_2L)_2]^-Na^+$ by heating a mixture of sodium borohydride and $H_6L$ in 1,2-dichloroethane/ethanol (1:1 *v*/*v*) at 80 °C (Scheme 1). The formation of the boron complex was also confirmed by ESI MS and NMR spectroscopic studies of solution of the complex in acetone.[9] Only one intense peak was observed at *m*/*z* 1819 (negative mode) and 1865 (positive mode), which correspond to the $[B_2Na(H_2L)_2]^-$ and $[B_2Na(H_2L)_2]^-2Na^+$ species, respectively; both spectra agree well with the simulated pattern. The $^1$H NMR spectrum of the complex in [D$_6$]acetone is also consistent with the structure determined by X-ray diffraction analysis in the solid state; each strand is $C_2$ symmetric and the central biphenol units have two free phenolic protons.[13] Moreover, the NOESY spectrum of the complex showed strong negative cross-peaks between the phenol rings A and C (Figure 2). These cross-peaks were attributed to the interstrand NOE interactions (distance $\approx$2.5 Å), thus indicating that the complex adopts a double-stranded helical trinuclear structure in solution.

To date, only a few examples of the optical resolution of racemic helicates have been reported, and they are usually based on the formation of diastereomer ion pairs.[14] The optical resolution of the helicate (±)-$[B_2Na(H_2L)_2]^-Na^+$ was carried out by the formation of a diastereomeric salt (Scheme 1). The cation exchange of the racemate was

 © 2006 Wiley-VCH Verlag GmbH & Co. KGaA, Weinheim 




***Scheme 1.*** Synthesis of the boron complex $[B_2Na(H_2L)_2]^-Na^+$ and subsequent optical resolution by formation of a diastereomeric salt by using (−)-DMEph$^+$Br$^-$ followed by replacement with the achiral ammonium salt DMAmm$^+$Br$^-$.

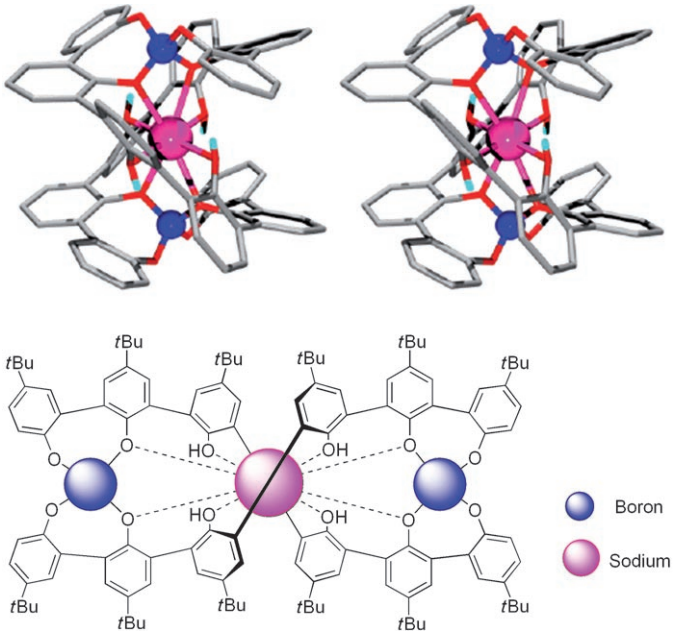



***Figure 1.*** Stereoview of the crystal structure (top) and schematic representation of the boron complex $[B_2Na(H_2L)_2]^-H^+$ (bottom). The hydrogen atoms bonded to carbon atoms, the *tert*-butyl groups, and solvent molecules are omitted for clarity.

performed by adding a tenfold excess of (−)-*N*-dodecyl-*N*-methylephedrinium bromide ((−)-DMEph$^+$Br$^-$) to a solution of the helicate in acetonitrile, and a white microcrystalline solid was precipitated within 24 h. The crystals of $(+)_{313}$-$[B_2Na(H_2L)_2]^-$(−)-DMEph$^+$ were collected by filtration (≈100 % *de* based on $^1$H NMR spectrum ($CD_2Cl_2$, 25 °C)).[9]

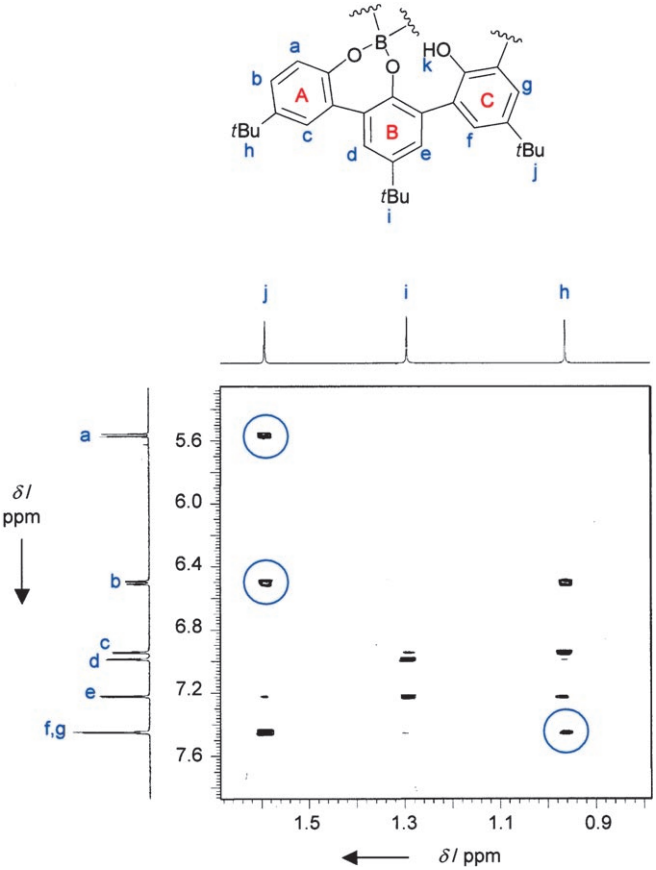



***Figure 2.*** Partial NOESY spectrum of the boron complex $[B_2Na(H_2L)_2]^-Na^+$ in [$D_6$]acetone at 25 °C (mixing time = 500 ms). The cross-peaks attributable to the interstrand NOE interactions are labeled with blue circles.

 © 2006 Wiley-VCH Verlag GmbH & Co. KGaA, Weinheim 

The mother liquor was then evaporated to afford a white solid consisting of the opposite diastereomer $(-)_{313}$-$[B_2Na(H_2L)_2]^-$(−)-DMEph$^+$ as a major component and the excess (−)-DMEph$^+$Br$^-$ (66% *de* based on $^1$H NMR spectrum).[15] The circular dichroism (CD) spectra of both diastereomers showed almost all mirror-image Cotton effects in their patterns in the range of 240–330 nm except for the intensities, because the CD signals due to (−)-DMEph$^+$Br$^-$ are negligibly weak (Figure 3).

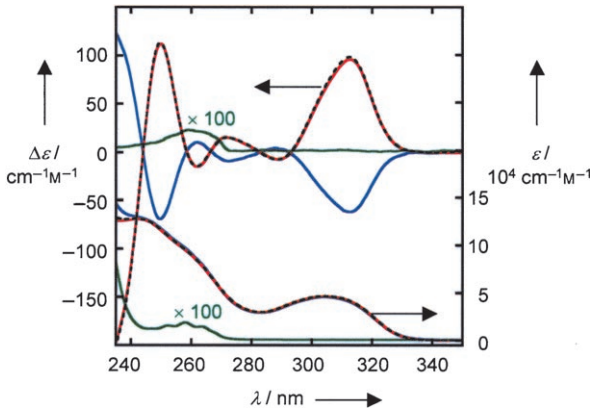



***Figure 3.*** CD and UV/Vis spectra ($CH_3CN$, 25 °C) of the boron complexes of $(+)_{313}$-$[B_2Na(H_2L)_2]^-$(−)-DMEph$^+$ with 100% *de* (red), the corresponding $(+)_{313}$-$[B_2Na(H_2L)_2]^-$DMAmm$^+$ (dashed black line), $(-)_{313}$-$[B_2Na(H_2L)_2]^-$(−)-DMEph$^+$ obtained from the filtrate (blue), and (−)-DMEph$^+$Br$^-$ (green).

Finally, the resulting diastereomeric double-stranded helicates were successfully converted into the corresponding enantiomers when the optically active ammonium cation (−)-DMEph$^+$ was exchanged with dodecyltrimethylammonium bromide (DMAmm$^+$Br$^-$) as the achiral source. Thus, the complex $(+)_{313}$-$[B_2Na(H_2L)_2]^-$DMAmm$^+$, which exhibits helical chirality without any other chiral factors, was obtained. The Cotton effects and UV/Vis spectra were perfectly identical to those of $(+)_{313}$-$[B_2Na(H_2L)_2]^-$(−)-DMEph$^+$, suggesting that the helicate is really stereoinert and enantiomerically pure (Figure 3). The complex $(-)_{313}$-$[B_2Na(H_2L)_2]^-$(−)-DMEph$^+$ (66% *de*). was similarly converted into the complex $(-)_{313}$-$[B_2Na(H_2L)_2]^-$DMAmm$^+$ (66% *de* based on CD spectrum).[9] Furthermore, neither racemization nor decomposition of the complex $(+)_{313}$-$[B_2Na(H_2L)_2]^-$DMAmm$^+$ was observed after heating in acetonitrile at 80 °C for 24 h or in methanol at 60 °C for 12 h.

In summary, we have successfully prepared the first spiroborate-based double-helical complex by using a simple *ortho*-linked hexaphenol as the ligand, and the helicate is stable in the solid state as well as in solution. Both enantiomers of the racemic helicates were resolved by the formation of a diastereomeric, optically active ammonium salt. We believe that various other optically active spiroborate-based double helicates can be prepared by the same strategy. Further applications of the present optically pure helicates to chiral recognition and asymmetric synthesis will be the subject of a forthcoming investigation.

Received: December 6, 2005

**Keywords:** borates · boron · chiral resolution · helical structures · oligophenols

[1] For reviews on artificial helical polymers and oligomers, see: a) M. M. Green, J.-W. Park, T. Sato, A. Teramoto, S. Lifson, R. L. B. Selinger, J. V. Selinger, *Angew. Chem.* **1999**, *111*, 3329–3345; *Angew. Chem. Int. Ed.* **1999**, *38*, 3138–3154; b) D. J. Hill, M. J. Mio, R. B. Prince, T. S. Hughes, J. S. Moore, *Chem. Rev.* **2001**, *101*, 3893–4011; c) T. Nakano, Y. Okamoto, *Chem. Rev.* **2001**, *101*, 4013–4038; d) J. J. L. M. Cornelissen, A. E. Rowan, R. J. M. Nolte, N. A. J. M. Sommerdijk, *Chem. Rev.* **2001**, *101*, 4039–4070; e) L. Brunsveld, B. J. B. Folmer, E. W. Meijer, R. P. Sijbesma, *Chem. Rev.* **2001**, *101*, 4071–4097; f) M. Fujiki, *Macromol. Rapid Commun.* **2001**, *22*, 539–563; g) E. Yashima, K. Maeda, T. Nishimura, *Chem. Eur. J.* **2004**, *10*, 42–51; h) I. Huc, *Eur. J. Org. Chem.* **2004**, 17–29.

[2] For recent examples, see: a) M. Ishikawa, K. Maeda, Y. Mitsutsuji, E. Yashima, *J. Am. Chem. Soc.* **2004**, *126*, 732–733; b) K. Maeda, K. Morino, Y. Okamoto, T. Sato, E. Yashima, *J. Am. Chem. Soc.* **2004**, *126*, 4329–4342; c) K. Maeda, M. Ishikawa, E. Yashima, *J. Am. Chem. Soc.* **2004**, *126*, 15161–15166; d) Y. Tanaka, H. Katagiri, Y. Furusho, E. Yashima, *Angew. Chem.* **2005**, *117*, 3935–3938; *Angew. Chem. Int. Ed.* **2005**, *44*, 3867–3870; e) T. Miyagawa, A. Furuko, K. Maeda, H. Katagiri, Y. Furusho, E. Yashima, *J. Am. Chem. Soc.* **2005**, *127*, 5018–5019, and references therein.

[3] a) D. J. Williams, H. M. Colquhoun, C. A. O'Mahoney, *J. Chem. Soc. Chem. Commun.* **1994**, 1643–1644; b) H. M. Colquhoun, D. J. Williams, *Acc. Chem. Res.* **2000**, *33*, 189–198; c) M.-H. Xu, Z.-M. Lin, L. Pu, *Tetrahedron Lett.* **2001**, *42*, 6235–6238; d) N. Kobayashi, S. Sasaki, M. Abe, S. Watanabe, H. Fukumoto, T. Yamamoto, *Macromolecules* **2004**, *37*, 7986–7991.

[4] H. Goto, Y. Furusho, E. Yashima, *Polym. Prepr. Jpn.* **2005**, *54*, 1484.

[5] For reviews on helicates, see: a) E. C. Constable, *Tetrahedron* **1992**, *48*, 10013–10059; b) J. M. Lehn, *Supramolecular Chemistry: Concepts and Perspectives*, VCH, Weinheim, **1995**; c) C. Piguet, G. Bernardinelli, G. Hopfgartner, *Chem. Rev.* **1997**, *97*, 2005–2062; d) M. Albrecht, *Chem. Rev.* **2001**, *101*, 3457–3497.

[6] a) T. W. Bell, H. Jousselin, *Nature* **1994**, *367*, 441–444; b) E. Psillakis, J. C. Jeffery, J. A. McCleverty, M. D. Ward, *Chem. Commun.* **1997**, 479–480; c) C. Dietrich-Buchecker, J.-P. Sauvage, *Chem. Commun.* **1999**, 615–616; d) M. Capó, J. M. Saá, A. Alvarez, *Chem. Commun.* **2002**, 1982–1983.

[7] For supramolecular receptors, see: a) E. Graf, M. W. Hosseini, R. Ruppert, *Tetrahedron Lett.* **1994**, *35*, 7779–7782; b) Y. Kobuke, Y. Sumida, M. Hayashi, H. Ogoshi, *Angew. Chem.* **1991**, *103*, 1513–1514; *Angew. Chem. Int. Ed. Engl.* **1991**, *30*, 1496–1499.

[8] For synthetic catalysts, see: a) K. Ishihara, H. Yamamoto, *J. Am. Chem. Soc.* **1994**, *116*, 1561–1562; b) H. Yamada, T. Kawate, M. Matsumizu, A. Nishida, K. Yamaguchi, M. Nakagawa, *J. Org. Chem.* **1998**, *63*, 6348–6354; c) D. B. Llewellyn, D. Adamson, B. A. Arndtsen, *Org. Lett.* **2000**, *2*, 4165–4168; d) J. P. Cross, Y. Pérez-Fuertes, M. J. Thatcher, S. Arimori, S. D. Bull, T. D. James, *Tetrahedron: Asymmetry* **2003**, *14*, 1965–1968.

[9] See the Supporting Information for details of the synthesis, structures, and characterization of the ligand $H_6L$ and the boron complex $[B_2Na(H_2L)_2]^-Na^+$ and its optical resolution.

 © 2006 Wiley-VCH Verlag GmbH & Co. KGaA, Weinheim 

[10] The peak corresponding to the countercation could not be located from difference Fourier maps, and the counterproton was missing probably due to the disordered configurations. Crystal data for the complex ($C_{137}H_{164}B_2Cl_9NaO_{14}$): $M_r$ = 2398.45, dimensions $0.20 \times 0.20 \times 0.10$ mm$^3$, monoclinic, space group $C2/c$, $Z = 8$, $\rho_{calcd} = 1.296$ g cm$^{-3}$, $\mu(Mo_{K\alpha}) = 0.363$ mm$^{-1}$, $F(000) = 5624$, $2\theta_{max} = 52.7°$ were $a = 17.9772(8)$, $b = 27.6706(12)$, $c = 27.8814(13)$ Å, $\beta = 96.7810(10)°$, $V = 13772.3(11)$ Å$^3$. A total of 43299 reflections were collected, of which 14091 reflections were independent ($R_{int} = 0.075$). The structure was refined to final $R1 = 0.0800$ for 14091 data [$I > 2\sigma(I)$] with 901 parameters, $wR2 = 0.2482$ for all data, GOF = 0.912, and residual electron density max./min. = 0.94/−0.80 e Å$^{-3}$. CCDC-291892 contains the supplementary crystallographic data for this paper. These data can be obtained free of charge from the Cambridge Crystallographic Data Centre via www.ccdc.cam.ac.uk/data_request/cif.

[11] For spiroborates that comprise 2,2′-biphenol or 2,2′-binaphthol moieties, see: a) M. Periasamy, L. Venkatraman, S. Sivakumar, N. Sampathkumar, C. R. Ramanathan, *J. Org. Chem.* **1999**, *64*, 7643 – 7645; b) S. Green, A. Nelson, S. Warriner, B. Whittaker, *J. Chem. Soc. Perkin Trans. 1* **2000**, 4403 – 4408; c) D. Liu, Z. Shan, F. Liu, C. Xiao, G. Lu, J. Qin, *Helv. Chim. Acta* **2003**, *86*, 157 – 163.

[12] A series of helicates that bear d- or p-block metals and an alkali-metal cation in the center were reported. For examples, see: a) M. Albrecht, O. Blau, R. Frölich, *Chem. Eur. J.* **1999**, *5*, 48 – 56; b) M. Albrecht, M. Schneider, H. Röttele, *Angew. Chem.* **1999**, *111*, 512 – 515; *Angew. Chem. Int. Ed.* **1999**, *38*, 557 – 559; c) M. Albrecht, O. Blau, R. Frölich, *Proc. Natl. Acad. Sci. USA* **2002**, *99*, 3867 – 4872.

[13] The signals were assigned based on COSY, HSQC, and HMBC NMR experiments.[9]

[14] a) R. Krämer, J.-M. Lehn, A. De Cian, J. Fischer *Angew. Chem.* **1993**, *105*, 764 – 767; *Angew. Chem. Int. Ed. Engl.* **1993**, *32*, 703 – 706; b) L. J. Charbonnière, G. Bernardinelli, C. Piguet, A. M. Sargeson, A. F. Williams, *J. Chem. Soc. Chem. Commun.* **1994**, 1419 – 1420; c) G. Rapenne, C. Dietrich-Buchecker, J.-P. Sauvage, *J. Am. Chem. Soc.* **1996**, *118*, 10932 – 10933.

[15] "$(+)_{313}$" and "$(-)_{313}$" denote the signs of the Cotton effect at 313 nm.

 © 2006 Wiley-VCH Verlag GmbH & Co. KGaA, Weinheim 

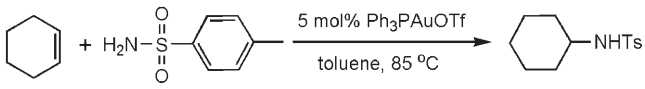
Hydroamination

DOI: 10.1002/anie.200504495

# Efficient Gold-Catalyzed Hydroamination of 1,3-Dienes**

*Chad Brouwer and Chuan He**

Homogenous gold catalysis has proven to be a powerful tool in organic synthesis in recent years.[1,2] Gold(I) and gold(III) are soft and hence carbophilic Lewis acids, which can activate unsaturated C–C bonds toward nucleophilic attack. Despite much success in alkyne activation, the activation of olefins by gold ions has remained relatively unexplored. Our group recently showed that phenols and carboxylic acids can undergo intermolecular addition to inert olefins in the presence of $Ph_3PAuOTf$ (Tf = trifluoromethanesulfonyl).[3] This represents a rare example of carbon–heteroatom bond formation by the gold-catalyzed activation of inert olefins. This method can be extended to the hydroamination of simple alkenes (Scheme 1).[4] These types of transformations have




***Scheme 1.*** Hydroamination of inert olefins with $TsNH_2$. Ts = *p*-toluenesulfonyl.

also been carried out with palladium,[5] platinum,[6] ruthenium,[7] and Brønsted acids.[8,9] However, they are limited in scope, and in the case of palladium, β-hydride elimination occurs to afford unsaturated products. Owing to the ability of gold(I) to activate inert alkenes,[3,4] we envisioned that this method could potentially be used in the addition of nucleophiles to 1,3-dienes as well. 1,3-Dienes are more active than simple alkenes owing to conjugation, thus the addition reaction could be more facile and occur at moderate temperatures.

Reported herein is a gold-catalyzed hydroamination of 1,3-dienes. The resulting allylic amine[10] products are important precursors in organic synthesis and are encountered in many natural products. Transition-metal-catalyzed hydroamination of conjugated dienes is not new: a nickel-catalyzed process was reported as early as 1971.[11] Since then, there have been a few examples in which $Pd^0$, $Rh^I$, $Rh^{III}$, or $Co^{II}$ is

[*] C. Brouwer, Prof. C. He
Department of Chemistry
The University of Chicago
5735 S. Ellis Ave., Chicago, IL 60637 (USA)
Fax: (+1) 773-702-0805
E-mail: chuanhe@uchicago.edu

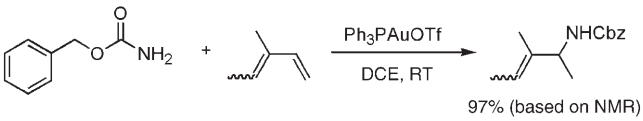
[**] This work was supported by the University of Chicago, a Research Innovation Award (RI1179) from the Research Corporation, and a Research Fellowship from the Alfred P. Sloan Foundation (C.H.). We thank Dr. C.-G. Yang and Dr. J. L. Zhang for helpful discussions.

Supporting information for this article is available on the WWW under http://www.angewandte.org or from the author.


WILEY InterScience DISCOVER SOMETHING GREAT
© 2006 Wiley-VCH Verlag GmbH & Co. KGaA, Weinheim

used.[12] Telomerization often occurs in the palladium- and nickel-catalyzed reactions.[13] Regioselectivity is also difficult to control, and mixtures of 1,2- and 1,4-addition products are often formed. In fact, mild and selective 1,2-hydroamination of dienes is rather rare, in particular, with a 1:1 ratio of nucleophile and diene employed to afford products in high yields. Often excess amounts of dienes must be employed to allow good conversions.

In a series of preliminary screening of nucleophiles, it was found that benzyl carbamate, $CbzNH_2$ (Cbz = benzyloxycarbonyl), was an excellent candidate for hydroamination of 1,3-dienes. The hydroamination of 3-methyl-1,3-pentadiene can be catalyzed by $Ph_3PAuOTf$ at room temperature ($CbzNH_2$/diene 1:1.2) to give the product in almost quantitative yield (by NMR spectroscopy; Scheme 2). As the Cbz group can be




***Scheme 2.*** Hydroamination of 3-methyl-1,3-pentadiene.

readily removed from the product, this reaction offers an efficient method to prepare various allylic amines. Notably, the reaction works almost exclusively for carbamates and sulfonamides; attempts with alkyl and aromatic amines, acetamides, phthalimides, and phosphinamides gave no or only nominal conversions. On the basis of the above-mentioned hydroamination as our model reaction, a series of solvents was screened. We found that coordinating solvents such as 1,4-dioxane and nitromethane tend to shut down the reacting system, whereas noncoordinating solvents such as 1,2-dichloroethane (DCE) and chloroform seem to be ideal.

Using DCE as the solvent, we next set out to find an ideal catalyst system (Table 1). Neither $Ph_3PAuCl$, nor AgOTf by themselves effect the reaction (Table 1, entries 2 and 3). Other counteranions such as $OTs^-$, $NO_3^-$, and $CF_3COO^-$ do not support the hydroamination activity, perhaps due to their binding to the gold(I) ion (Table 1). Noncoordinating anions are required, and $OTf^-$ and $ClO_4^-$ are the best counteranions for the reaction. Gold(III) works (Table 1, entries 14 and 15), but seems to be too active and requires a higher ($\approx$4 equiv) diene loading, perhaps due to oligomerization of the diene. Other metals tested (Table 1, entries 16–18) showed no catalytic activity at all. It is evident that gold(I) is an appropriate catalyst for the hydroamination of conjugated dienes.

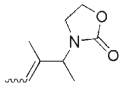
Table 2 illustrates the scope of the hydroamination. Benzyl carbamate **1b** readily adds to diene **1a** to give the product in a very good yield. Other carbamates underwent the transformation; however, the yields varied, depending on the nucleophile employed (Table 2, entries 2–5). Cyclic carbamate **3b** added less readily, and higher temperature was required. The use of 1,3-cyclohexadiene (**7a**) as the substrate also required a higher reaction temperature (Table 2, entry 7). The N-alkylation for these reactions was firmly established by comparison of the product **7c** to the known compound.

***Table 1:*** Catalyst screening for hydroamination of 3-methyl-1,3-pentadiene.[a]

| Entry | Metal salt | Silver salt | Conversion [%][b] |
|---|---|---|---|
| 1 | $Ph_3PAuCl$ | AgOTf | 97 |
| 2 | $Ph_3PAuCl$ | | 0 |
| 3 | | AgOTf | 0 |
| 4 | $Ph_3PAuCl$ | AgOTs | 0 |
| 5 | $Ph_3PAuCl$ | $AgNO_3$ | 0 |
| 6 | $Ph_3PAuCl$ | $AgOOCCF_3$ | 0 |
| 7 | $Ph_3PAuCl$ | $AgSbF_6$ | 60 |
| 8 | $Ph_3PAuCl$ | $AgNTf_2$ | 77 |
| 9 | $Ph_3PAuCl$ | $AgPF_6$ | 89 |
| 10 | $Ph_3PAuCl$ | $AgBF_4$ | 92 |
| 11 | $Ph_3PAuCl$ | $AgClO_4$ | 99 |
| 12 | AuCl | | 0 |
| 13 | AuCl | AgOTf | 90 |
| 14 | $AuCl_3$ | | 29[c] |
| 15 | $AuCl_3$ | AgOTf | 89[c] |
| 16 | $Cu(OTf)_2$ | | 0 |
| 17 | $Sc(OTf)_3$ | | 0 |
| 18 | $Zn(OTf)_2$ | | 0 |

[a] Conditions: 25 °C, overnight, metal salt (5%), silver salt (5%), dichloroethane (2.0 mL), carbamate (1.0 equiv), diene (1.2 equiv). [b] Conversion determined by $^1H$ NMR with dibromomethane as internal standard. [c] Diene: 4.0 equiv.

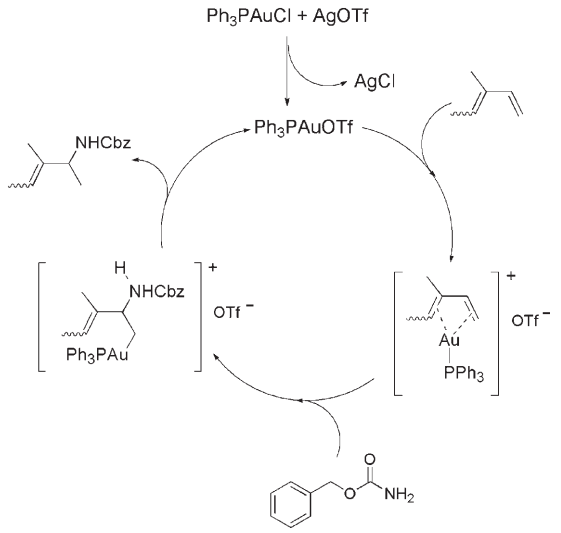
***Table 2:*** Hydroamination of dienes: reaction scope.[a]

| Entry | Olefin | | Nucleophile | | Product | | Yield [%][b] |
|---|---|---|---|---|---|---|---|
| 1 |  | **1a** | $CbzNH_2$ | **1b** |  | **1c** | 86 |
| 2 | | **1a** | $FmocNH_2$ | **2b** |  | **2c** | 33 |
| 3 | | **1a** |  | **3b** |  | **3c** | 63[c] |
| 4 | | **1a** | $MocNH_2$ | **4b** |  | **4c** | 77 |
| 5 | | **1a** | $TsNH_2$ | **5b** |  | **5c** | 81 |
| 6 |  | **6a** | | **1b** |  | **6c** | 86 |
| 7 |  | **7a** | | **1b** |  | **7c** | 87[c] |

[a] Reactions were carried out at room temperature, under $N_2$, in the absence of light, overnight. Typically: diene (1.2 mmol per 1.0 mmol of substrate), $Ph_3PAuOTf$ (0.05 mmol), DCE (2 mL). [b] Yields of isolated products. [c] 50 °C. Fmoc = 9-fluorenylmethoxycarbonyl; Moc = methoxycarbonyl.

Our proposed reaction mechanism is shown in Scheme 3. $Ph_3PAuOTf$, generated by the reaction of $Ph_3PAuCl$ with AgOTf binds to the diene, as supported by $^{31}P$ NMR spectroscopic studies in which the gold(I) catalyst was

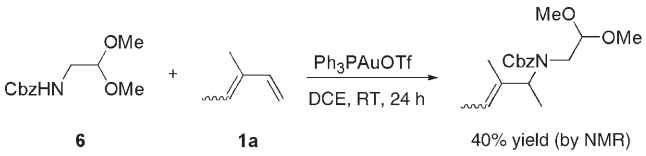
 © 2006 Wiley-VCH Verlag GmbH & Co. KGaA, Weinheim 




***Scheme 3.*** Proposed reaction mechanism.

monitored. Mixing $CbzNH_2$ with $Ph_3PAuOTf$ did not lead to an observable shift of the original $^{31}P$ NMR signal, suggesting no or a weak interaction between the nucleophile and the gold(I) catalyst. Upon addition of the diene substrate, a shift of the $^{31}P$ signal was observed which indicates the formation of a gold(I)–diene complex (Supporting Information). An independent $^{13}C$ NMR spectroscopic study also suggests the coordination of gold(I) ion to the diene, in particular, to the double bond that results in the most stable resonance form (Supporting Information).[14] After the formation of this complex, the nucleophile attacks *anti* to the gold center, as suggested by recent studies.[2,4] The resulting $Au^I$–C bond is then protonated to give the desired product and to regenerate the active catalyst.

This reaction also tolerates certain functional groups. For example, (2,2-dimethoxyethyl)carbamic acid benzyl ester (**6**)[15] retains its dimethyl acetal in the reaction with diene **1a**. (Scheme 4). Gold(I) catalyzes the addition, not only of




***Scheme 4.*** Tolerance to dimethyl acetal.

carbamates and of sulfonamides, but also of alcohols to 1,3-dienes, albeit with lower efficiency (≈30–40% conversion) based on preliminary studies.

To summarize, we report a novel method for the hydroamination of 1,3-dienes in the presence of $Ph_3PAuOTf$ catalyst under mild conditions. A variety of carbamates and sulfonamides add to conjugated dienes to afford protected allylic amines in good to high yields. The use of excess diene is not necessary in this gold-mediated process. We are currently exploring the enantioselective version of the reaction, which will be reported in due time.[16]

## *Experimental Section*

Typical procedure: $Ph_3PAuCl$ (25 mg, 0.050 mmol) and AgOTf (13 mg, 0.050 mmol) were allowed to react in a minivial loaded with benzyl carbamate (0.15 g, 1.0 mmol) in anhydrous 1,2-dichloroethane (2.0 mL) for 5 min. 3-Methyl-1,3-pentadiene (0.14 mL, 1.2 mmol) was then added, and the reaction mixture was stirred overnight under nitrogen at room temperature in the dark. The solvent was evaporated in vacuo, and the residue was purified by flash-column chromatography on silica gel (hexanes/EtOAc 1:0→9:1, $R_f = 0.13$). Product **1c** was isolated in 86% yield (0.20 g, 0.86 mmol) after removal of solvent.

Received: December 18, 2005
Published online: February 2, 2006

**Keywords:** amines · dienes · gold · homogeneous catalysis · hydroamination

[1] a) A. S. K. Hashmi, M. Rudolph, J. P. Weyrauch, M. Woelfle, W. Frey, J. W. Bats, *Angew. Chem.* **2005**, *117*, 2858; *Angew. Chem. Int. Ed.* **2005**, *44*, 2798; b) J. H. Teles, S. Brode, M. Chabanas, *Angew. Chem.* **1998**, *110*, 1475; *Angew. Chem. Int. Ed.* **1998**, *37*, 1415; c) S. Antoniotti, E. Genin, V. Michelet, J.-P. Genêt, *J. Am. Chem. Soc.* **2005**, *127*, 9976; d) C. Nieto-Oberhuber, S. López, M. P. Muñoz, D. J. Cárdenas, E. Buñuel, C. Nevado, A. M. Echavarren, *Angew. Chem.* **2005**, *117*, 6302; *Angew. Chem. Int. Ed.* **2005**, *44*, 6146; e) Z. Shi, C. He, *J. Org. Chem.* **2004**, *69*, 3669; f) Z. Shi, C. He, *J. Am. Chem. Soc.* **2004**, *126*, 5964; g) C. Nieto-Oberhuber, M. P. Muñoz, E. Buñuel, C. Nevado, D. J. Cárdenas, A. M. Echavarren, *Angew. Chem.* **2004**, *116*, 2456; *Angew. Chem. Int. Ed.* **2004**, *43*, 2402; h) A. Arcadi, G. Bianchi, F. Marinelli, *Synthesis* **2004**, 610; i) V. Mamane, T. Gress, H. Krause, A. Fürstner, *J. Am. Chem. Soc.* **2004**, *126*, 8654; j) B. D. Sherry, F. D. Toste, *J. Am. Chem. Soc.* **2004**, *126*, 15978; k) T. Yao, X. Zhang, R. C. Larock, *J. Am. Chem. Soc.* **2004**, *126*, 11164; l) L. Zhang, S. A. Kozmin, *J. Am. Chem. Soc.* **2004**, *126*, 11806; m) B. Guan, D. Xing, G. Cai, X. Wan, N. Yu, Z. Fang, L. Yang, Z. Shi, *J. Am. Chem. Soc.* **2005**, *127*, 18004; n) N. Asao, H. Aikawa, Y. Yamamoto, *J. Am. Chem. Soc.* **2004**, *126*, 7458; o) R.-V. Nguyen, X.-Q. Yao, D. S. Bohle, C.-J. Li, *Org. Lett.* **2005**, *7*, 673; p) A. S. K. Hashmi, *Gold Bull.* **2003**, *36*, 3; q) M. Georgy, V. Boucard, J.-M. Campagne, *J. Am. Chem. Soc.* **2005**, *127*, 14180; r) A. W. Sromek, M. Rubina, V. Gevorgyan, *J. Am. Chem. Soc.* **2005**, *127*, 10500.
[2] A. S. K. Hashmi, J. P. Weyrauch, W. Frey, J. W. Bats, *Org. Lett.* **2004**, *6*, 4391.
[3] C.-G. Yang, C. He, *J. Am. Chem. Soc.* **2005**, *127*, 6966.
[4] J. Zhang, C.-G. Yang, C. He, *J. Am. Chem. Soc.* **2006**, *128*, 1798.
[5] a) S. S. Stahl, *Angew. Chem.* **2004**, *116*, 3480; *Angew. Chem. Int. Ed.* **2004**, *43*, 3400; b) M. Kawatsura, J. F. Hartwig, *J. Am. Chem. Soc.* **2000**, *122*, 9546; c) M. Utsunomiya, J. F. Hartwig, *J. Am. Chem. Soc.* **2003**, *125*, 14286.
[6] H. Qian, X. Han, R. A. Widenhoefer, *J. Am. Chem. Soc.* **2004**, *126*, 9536.
[7] Y. Oe, T. Ohta, Y. Ito, *Chem. Commun.* **2004**, 1620.
[8] B. Schlummer, J. F. Hartwig, *Org. Lett.* **2002**, *4*, 1471.
[9] L. L. Anderson, J. Arnold, R. G. Bergman, *J. Am. Chem. Soc.* **2005**, *127*, 14542.
[10] For a review on allylic amination, see: M. Johannsen, K. A. Jorgensen, *Chem. Rev.* **1998**, *98*, 1689.
[11] R. Baker, D. E. Halliday, T. N. Smith, *Chem. Commun.* **1971**, 1583.
[12] For selected examples, see: a) C. F. Hobbs, D. E. McMackins, *Org. Prep. Proced. Int.* **1972**, *4*, 261; b) J. Pawlas, Y. Nakao, M. Kawatsura, J. F. Hartwig, *J. Am. Chem. Soc.* **2002**, *124*, 3669; c) O. Löber, M. Kawatsura, J. F. Hartwig, *J. Am. Chem. Soc.*

 © 2006 Wiley-VCH Verlag GmbH & Co. KGaA, Weinheim 

**2001**, *123*, 4366; after submission of this Communication, two more examples were published: d) H. Qin, N. Yamagiwa, S. Matsunaga, M. Shibasaki, *J. Am. Chem. Soc.* **2006**, ASAP; e) A. M. Johns, M. Utsunomiya, C. D. Incarvito, J. F. Hartwig, *J. Am. Chem. Soc.* **2006**, ASAP.

[13] S. M. Maddock, M. G. Finn, *Organometallics* **2000**, *19*, 2684.

[14] This has been suggested to occur with the styryl cation: K. Hasegawa, R. Asami, K. Takahashi, *Bull. Chem. Soc. Jpn.* **1978**, *51*, 916.

[15] V. K. Aggarwal, S. Roseblade, R. Alexander, *Org. Biomol. Chem.* **2003**, *1*, 684.

[16] For a related intramolecular hydroamination of alkenyl carbamates, see the following Communication in this issue: X. Han, R. A. Widenhoefer, *Angew. Chem.* **2006**, *118*, 1779; *Angew. Chem. Int. Ed.* **2006**, *45*, 1747, and a related study in reference [4].

 © 2006 Wiley-VCH Verlag GmbH & Co. KGaA, Weinheim 

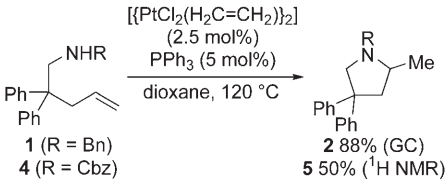
*Hydroamination (2)*

DOI: 10.1002/anie.200600052

# Gold(I)-Catalyzed Intramolecular Hydroamination of Alkenyl Carbamates**

*Xiaoqing Han and Ross A. Widenhoefer**

Intramolecular hydroamination of unactivated olefins has received considerable attention as an attractive and potentially expedient route to the synthesis of functionalized nitrogen heterocycles.[1] However, despite this prolonged focus, a general and efficient procedure has not been realized.[1] In response to this limitation, we recently reported a platinum-catalyzed procedure for the intramolecular hydroamination of unactivated olefins with secondary alkyl amines.[2] As an example, reaction of *N*-benzyl-4-pentenylamine (**1**) with a catalytic 1:2 mixture of $[\{PtCl_2(H_2C{=}CH_2)\}_2]$ and $PPh_3$ at 120 °C for 16 h led to isolation of pyrrolidine **2** in 75% yield (88% by GC) [Eq. (1)].



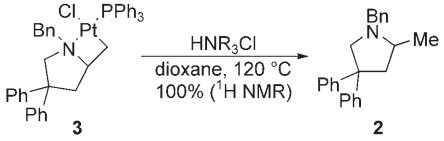

(1)

[*] X. Han, Prof. R. A. Widenhoefer
P. M. Gross Chemical Laboratory
Duke University
Durham, NC 27708-0346 (USA)
Fax: (+1) 919-660-1605
E-mail: rwidenho@chem.duke.edu

[**] We thank the PRF (43636-AC1), administered by the American Chemical Society, the Camille and Henry Dreyfus Foundation, and GlaxoSmithKline for support of this research.

Supporting information for this article is available on the WWW under http://www.angewandte.org or from the author.

Although platinum-catalyzed intramolecular hydroamination displayed good functional-group compatibility, the procedure required reaction temperatures of 120 °C and displayed a limited substrate scope.[2] Preliminary mechanistic experiments pointed to protonolysis of heterobicyclic amine complex **3** with an amine hydrochloride as the turnover-limiting step in the Pt-catalyzed conversion of **1** into **2** [Eq. (2)].[2] On the basis of this insight, we reasoned that




(2)

employment of a less basic amine derivative might lead to a more efficient and more general hydroamination protocol. Indeed, herein we report a mild and effective Au-catalyzed protocol for the intramolecular hydroamination of alkenyl carbamates to form protected nitrogen heterocycles.

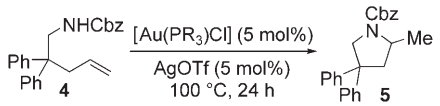
Although tosylamides have been employed to good effect in the catalytic amination of C–C multiple bonds,[3] the strongly reducing conditions required for subsequent deprotection compromises the utility of these transformations.[4,5] For this reason, we targeted benzyl carbamates, which undergo deprotection under mild conditions,[4] as nucleophiles for the catalytic intramolecular hydroamination of unactivated olefins. Selective hydroamination of alkenyl carbamates has previously been achieved only through employment of a stoichiometric amount of $Hg^{II}$ followed by reduction.[6,7] Unfortunately, attempted hydroamination of carbamate **4** employing the catalyst system optimized for the hydroamination of **1** required 120 °C and formed protected pyrrolidine **5** in only 50% yield (determined by $^1$H NMR spectroscopic analysis) [Eq. (1)].[8]

A number of recent reports have documented the utility of cationic $Au^I$–phosphine complexes as catalysts for the addition of carbon[9,10] and oxygen[11–13] nucleophiles to alkenes and alkynes.[14,15] For this reason, we considered that cationic $Au^I$–phosphine complexes might also catalyze the addition of nitrogen nucleophiles to unactivated olefins. An initial experiment was encouraging and treatment of **4** with a catalytic 1:1 mixture of [Au($PPh_3$)Cl] and AgOTf in toluene at 100 °C for 24 h led to **5** in 59% yield ($^1$H NMR; Table 1, entry 1). Subsequent experimentation led to identification of a significantly more active catalyst system for the conversion of **4** into **5** that employed a catalytic 1:1 mixture of [Au{P(*t*Bu)$_2$(*o*-biphenyl)}]Cl (**6**) and AgOTf in dioxane at 100 °C (Table 1, entries 2–8).[16] This catalyst system was also effective at lower temperatures and, in a preparative-scale reaction, treatment of **4** with a catalytic 1:1 mixture of **6** and AgOTf (5 mol%) in dioxane at 60 °C for 18 h led to **5** in 97% yield (Table 2, entry 1). Comparison of P(*t*Bu)$_2$(*o*-biphenyl) and $PMe_2Ph$ as ligands for the $Au^I$-catalyzed hydroamination of **4** suggests that steric rather than electronic factors are responsible for the high efficiency of the former ligand (Table 1, entries 7 and 8).

Neither the rate nor the yield of the $Au^I$-catalyzed conversion of **4** into **5** was affected by the presence of water (1 equiv) (Table 2, entry 2). Gold-catalyzed intramolecular

 © 2006 Wiley-VCH Verlag GmbH & Co. KGaA, Weinheim InterScience 

***Table 1:*** Effect of phosphine and solvent on the $Au^I$-catalyzed hydroamination of **4**.




| Entry | $PR_3$ | Solvent | Yield [%][a] |
|---|---|---|---|
| 1 | $PPh_3$ | toluene | 59 |
| 2 | $PPh_3$ | $CH_3CN$ | 49 |
| 3 | $PPh_3$ | $C_2H_4Cl_2$ | 33 |
| 4 | $PPh_3$ | dioxane | 75 |
| 5 | $P(4\text{-}C_6H_4OMe)_3$ | dioxane | 70 |
| 6 | $P(4\text{-}C_6H_4CF_3)_3$ | dioxane | 23 |
| 7 | $PMe_2Ph$ | dioxane | 7 |
| 8 | $P(t\text{Bu})_2$(*o*-biphenyl) | dioxane | 98 |

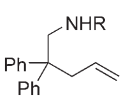
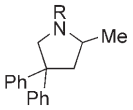
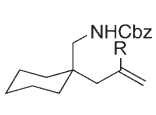
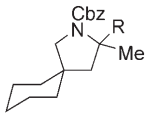
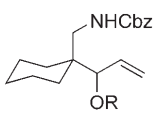
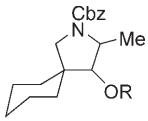
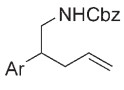
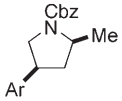
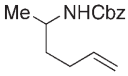
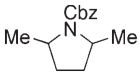
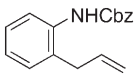
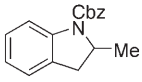
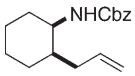
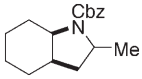
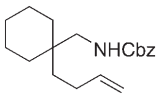
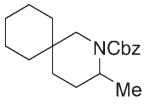
[a] Yield determined by $^1H$ NMR spectroscopic analysis of the crude reaction mixture. Tf = trifluoromethanesulfonyl.

hydroamination was compatible with a range of labile carbamate groups including Boc, Moz, and Fmoc (Table 2, entries 3–5). The protocol tolerates substitution at C1, C2, C3, or C4 of the 4-pentenyl chain, often with encouraging levels of diastereoselectivity (Table 2, entries 6–11). Gold-catalyzed intramolecular hydroamination of alkenyl carbamates is also effective for cyclization of unsubstituted 4-pentenyl derivatives (Table 2, entry 12). Furthermore, $Au^I$-catalyzed hydroamination of alkenyl carbamates can be applied to the synthesis of aromatic and aliphatic heterobicyclic compounds and to the synthesis of piperidine derivatives (Table 2, entries 13–15). Notably, unsubstituted, C1-monosubstituted, and monocyclic 4-pentenylbenzylamines failed to undergo Pt-catalyzed hydroamination; C2-monosubstituted 4-pentenylbenzylamines and 5-hexenylbenzylamines undergo Pt-catalyzed cyclization in modest yield.

Information regarding the mechanisms of the $Au^I$-catalyzed addition of nucleophiles to C–C multiple bonds is limited. Teles et al. proposed an inner-sphere mechanism for the $Au^I$-catalyzed intermolecular addition of alcohols to alkynes on the basis of ab initio calculations.[11] Conversely, stereochemical analysis of the $Au^I$-catalyzed intramolecular addition of alcohols and activated methylene compounds to alkynes were in accord with outer-sphere attack of the nucleophile on a $Au^I$-complexed alkyne.[9,12] On the basis of these latter precedents, we favor a mechanism for the $Au^I$-catalyzed hydroamination of **4** involving outer-sphere attack of the carbamate nitrogen atom on the Au-complexed olefin of **I** coupled with loss of HCl to form the neutral alkyl–gold complex **II** (Scheme 1). Protonolysis of the Au–C bond of **II** would then release pyrrolidine **5** and regenerate the cationic monophosphine gold catalyst.

In summary, we have developed an effective $Au^I$-catalyzed protocol for the intramolecular hydroamination of alkenyl carbamates to form protected nitrogen heterocycles. This protocol allows the intramolecular hydroamination of unactivated olefins under milder conditions and with broader substrate scope than was previously realized with late-transition-metal catalyst systems.[17]

***Table 2:*** Hydroamination of alkenyl carbamates catalyzed by a 1:1 mixture of $Au[P(t\text{Bu})_2$(*o*-biphenyl)$]Cl$ (**6**) and AgOTf (5 mol%) in dioxane.

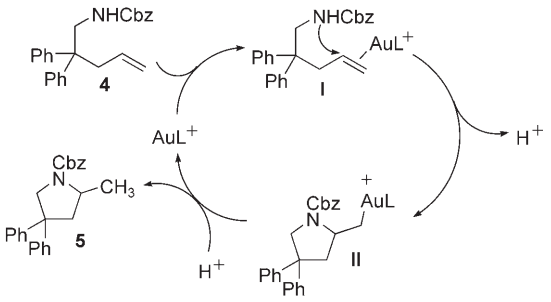
| Entry | Alkene | Heterocycle | Temp [°C] | Time [h] | Yield [%][a] |
|---|---|---|---|---|---|
| |  |  | | | |
| 1 | R = Cbz | | 60 | 18 | 97 |
| 2 | R = Cbz | | 60 | 18 | 96[b] |
| 3 | R = Boc | | 60 | 20 | 96 |
| 4 | R = Moz | | 60 | 16 | 95 |
| 5 | R = Fmoc | | 60 | 24 | 93 |
| |  |  | | | |
| 6 | R = H | | 60 | 23 | 96 |
| 7 | R = Me | | 80 | 40 | 88 |
| |  |  | | | |
| 8 | R = H | | 60 | 22 | 91 (3.6:1) |
| 9 | R = Ac | | 60 | 18 | 63 (3.0:1) |
| 10 |  |  | 100 | 39 | 93 (3.5:1) |
| | Ar = 4-$C_6H_4OMe$ | | | | |
| 11 |  |  | 100 | 55 | 91 (1.5:1)[c] |
| 12 |  |  | 100 | 68 | 87 [c] |
| 13 |  |  | 100 | 47 | 59 [c] |
| 14 |  |  | 100 | 30 | 95 (2.5:1) |
| 15 |  |  | 100 | 26 | 84 |

[a] Isolated material of $\geq 95\%$ purity. [b] Reaction run in the presence of $H_2O$ (1 equiv). [c] Reaction run with 10 mol% of **6**. Cbz = benzyloxycarbonyl, Boc = *tert*-butoxycarbonyl, Moz = *p*-methoxybenzyloxycarbonyl, Fmoc = 9-fluorenylmethyloxycarbonyl.

## *Experimental Section*

**5:** A mixture of **4** (0.17 g, 0.45 mmol), **6** (12 mg, 0.022 mmol), and AgOTf (6 mg, 0.02 mmol) in dioxane (0.45 mL) was degassed by means of one freeze-pump-thaw cycle, pressurized with nitrogen, and stirred at 60 °C for 18 h. The crude reaction mixture was purified by

 © 2006 Wiley-VCH Verlag GmbH & Co. KGaA, Weinheim 




***Scheme 1.*** Proposed mechanism for the $Au^{I}$-catalyzed conversion of **4** into **5**.

chromatography (hexanes/EtOAc 20:1) to give **5** (160 mg, 97%) as a viscous, colorless oil.

Received: January 5, 2006
Published online: February 14, 2006

**Keywords:** alkenes · amines · gold · homogeneous catalysis · hydroamination

[1] M. Beller, A. Tillack, J. Seayad in *Transition metals for Organic Synthesis, 2nd ed.*, Wiley-VCH, Weinheim, **2004**, pp. 403–414.
[2] C. F. Bender, R. A. Widenhoefer, *J. Am. Chem. Soc.* **2005**, *127*, 1070.
[3] a) L. S. Hegedus, J. M. Mckearin, *J. Am. Chem. Soc.* **1982**, *104*, 2444; b) B. Schlummer, J. F. Hartwig, *Org. Lett.* **2002**, *4*, 1471; c) K. Miura, T. Hondo, T. Nakagawa, T. Takahashi, A. Hosomi, *Org. Lett.* **2000**, *2*, 385; d) E. J. Alexanian, C. Lee, E. J. Sorensen, *J. Am. Chem. Soc.* **2005**, *127*, 7690; e) L. M. Lutete, I. Kadota, Y. Yamamoto, *J. Am. Chem. Soc.* **2004**, *126*, 1622.
[4] T. W. Greene, P. G. M. Wuts, *Protective Groups in Organic Synthesis, 3rd ed.*, Wiley, New York, **1999**.
[5] a) S. C. Bergmeier, P. P. Seth, *Tetrahedron Lett.* **1999**, *40*, 6181; b) S. K. Nayak, *Synthesis* **2000**, 1575.
[6] a) K. E. Harding, S. R. Burks, *J. Org. Chem.* **1981**, *46*, 3920; b) S. Danishefsky, E. Taniyama, R. R. Webb, *Tetrahedron Lett.* **1983**, *24*, 11.
[7] A single example of the Pd-catalyzed oxidative amination of an alkenyl carbamate has been reported: S. R. Fix, J. L. Brice, S. S. Stahl, *Angew. Chem.* **2002**, *114*, 172; *Angew. Chem. Int. Ed.* **2002**, *41*, 164.
[8] The remainder of the reaction mixture consisted of benzyl (2,2-diphenyl-3-pentenyl)carbamate.
[9] J. J. Kennedy-Smith, S. T. Staben, F. D. Toste, *J. Am. Chem. Soc.* **2004**, *126*, 4526.
[10] a) S. T. Staben, J. J. Kennedy-Smith, F. D. Toste, *Angew. Chem.* **2004**, *116*, 5464; *Angew. Chem. Int. Ed.* **2004**, *43*, 5350; b) L. Zhang, S. A. Kozmin, *J. Am. Chem. Soc.* **2005**, *127*, 6962.
[11] J. H. Teles, S. Brode, M. Chabanas, *Angew. Chem.* **1998**, *110*, 1475; *Angew. Chem. Int. Ed.* **1998**, *37*, 1415.
[12] Y. Liu, F. Song, Z. Song, M. Liu, B. Yan, *Org. Lett.* **2005**, *7*, 5409.
[13] C.-G. Yang, C. He, *J. Am. Chem. Soc.* **2005**, *127*, 6966.
[14] For recent examples of the $Au^{I}$-catalyzed cyclization of enynes and related substrates, see: a) C. Nieto-Oberhuber, S. Lopez, A. M. Echavarren, *J. Am. Chem. Soc.* **2005**, *127*, 6178; b) M. R. Luzung, J. P. Markham, F. D. Toste, *J. Am. Chem. Soc.* **2004**, *126*, 10858; c) V. Mamane, T. Gress, H. Krause, A. Furstner, *J. Am. Chem. Soc.* **2004**, *126*, 8654; d) C. Nieto-Oberhuber, M. P. Munoz, E. Bunuel, C. Nevado, D. J. Cardenas, A. M. Echavarren, *Angew. Chem.* **2004**, *116*, 2456; *Angew. Chem. Int. Ed.* **2004**, *43*, 2402; e) B. D. Sherry, F. D. Toste, *J. Am. Chem. Soc.* **2004**, *126*, 15978.
[15] For recent examples of the $Au^{III}$-catalyzed addition of carbon and oxygen nucleophiles to alkenes and alkynes, see: a) A. Hoffmann-Röder, N. Krause, *Org. Lett.* **2001**, *3*, 2537; b) A. S. K. Hashmi, L. Schwarz, J.-H. Choi, T. M. Frost, *Angew. Chem.* **2000**, *112*, 2382; *Angew. Chem. Int. Ed.* **2000**, *39*, 2285; c) A. S. K. Hashmi, *Angew. Chem.* **2000**, *112*, 3737; *Angew. Chem. Int. Ed.* **2000**, *39*, 3590; d) X. Yao, C.-J. Li, *J. Am. Chem. Soc.* **2004**, *126*, 6884; e) A. S. K. Hashimi, T. M. Frost, J. W. Bats, *J. Am. Chem. Soc.* **2000**, *122*, 11553; f) T. Yao, X. Zhang, R. C. Larock, *J. Am. Chem. Soc.* **2004**, *126*, 11164.
[16] Treatment of **4** with triflic acid (1 equiv) at 100 °C for 24 h led to complete decomposition of **4** with no detectable formation of **5**. Treatment of **4** with either AgOTf (5 mol%) or **6** (5 mol%) alone in dioxane at 100 °C for 24 led to no detectable consumption of **4**.
[17] For a related intermolecular hydroamination of 1,3-dienes, see the previous Communication in this issue: C. Browder, C. He, *Angew. Chem.* **2006**, *118*, 1776; *Angew. Chem. Int. Ed.* **2006**, *45*, 1744.

 © 2006 Wiley-VCH Verlag GmbH & Co. KGaA, Weinheim 

*Alkaloid Synthesis*

DOI: 10.1002/anie.200503982

# The Solution to a Deep Stereochemical Conundrum: Studies toward the Tetrahydroisoquinoline Alkaloids**

*Collin Chan, Shengping Zheng, Bishan Zhou, Jinsong Guo, Richard M. Heid, Benjamin J. D. Wright, and Samuel J. Danishefsky**

*Dedicated to Professor Thomas Katz*

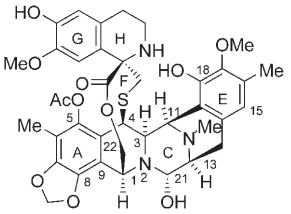
Some years ago we initiated a program directed at the total synthesis of ecteinascidin 743 (**1**),[1] an extremely potent antitumor agent.[2] A total synthesis of **1** was reported by

[*] C. Chan, Dr. S. Zheng, Dr. B. Zhou, Dr. J. Guo, Dr. R. M. Heid, B. J. D. Wright, Prof. S. J. Danishefsky
The Department of Chemistry
Columbia University
Havemeyer Hall, New York, NY 10027 (USA)
Fax: (+1) 212-772-8691
E-mail: s-danishefsky@ski.mskcc.org
Prof. S. J. Danishefsky
The Laboratory for Bioorganic Chemistry
Sloan-Kettering Institute for Cancer Research
1275 York Avenue, New York, NY 10021 (USA)

[**] This work was supported by the National Institutes of Health (Grant HL25848) and by Pharmamar Corporation of Madrid, Spain. We thank Bristol Myers Squibb for the generous fellowship awarded to C.C. B.J.D.W. is grateful for an NSF predoctoral fellowship. We thank Professor Gerard Parkin for X-ray crystallographic analyses and Dr. Yasuhiro Itagaki (Columbia University) for mass spectrometric analyses.

Supporting information for this article is available on the WWW under http://www.angewandte.org or from the author.

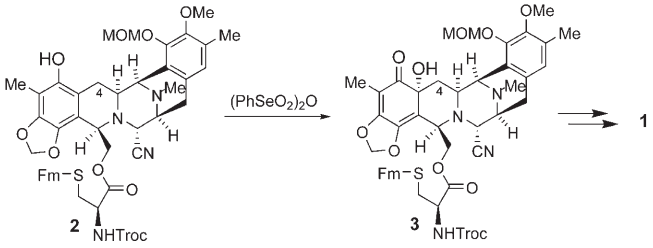

© 2006 Wiley-VCH Verlag GmbH & Co. KGaA, Weinheim



1

E. J. Corey and co-workers in 1996.[3a] A subsequent synthesis of **1** was described by Fukuyama and co-workers.[3b,c] A particularly elegant synthesis of the structurally related saframycin was disclosed by Myers and Kung.[4]

Although there are many fascinating features in the Corey total synthesis, the one that best establishes the context for our work is captured in transformation **2**→**3** (Scheme 1). The

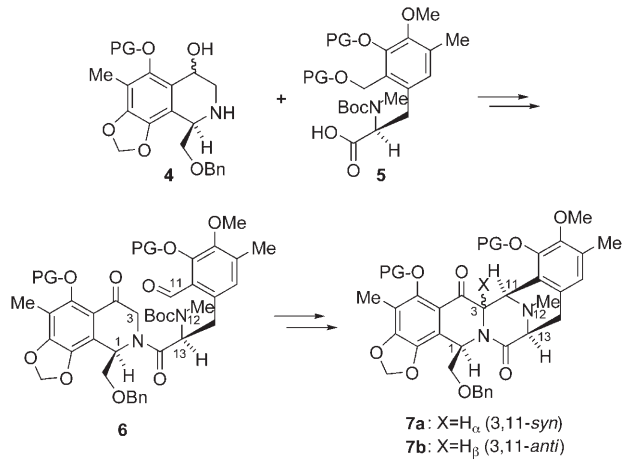


***Scheme 1.*** Corey's oxidation strategy to functionalize C4.

important message in these structures was that Corey and co-workers were able to build the entire saframycin-like[5] platform of **1** without carrying prebuilt functionality at C4. Remarkably, the oxidation with phenylselenenic anhydride shown in Scheme 1 served to functionalize C4 (presumably as the β-carbon atom of an intermediate quinomethide), setting the stage for Michael-like cyclization via the cysteinic sulfur.[6]

Regarding the ecteinascidin total synthesis problem, we focused on a progression in which useful functionality would *already* be in place at C4 as part of the unveiling of the pentacyclic platform. More specifically, the plan we had in mind would feature a lynchpin Mannich cyclization through which an aldehyde function (C11) would be interpolated between N12 and C3 (Scheme 2).[7] In our initial conceptual model, C3 would participate as the β-carbon atom of an enol. For this plan to be practical, the relationship between C1 and C13 would be secured by joining two appropriately matched subunits (cf. **4** and **5**) to reach reactive intermediate **6** and thence pentacyclic product **7**.

Needless to say, two additional stereogenic centers, C3 and C11, would be introduced during the lynchpin Mannich cyclization. The configuration at C11 would be strictly governed by the stereogenicity already in place at C13 (i.e. the 11-H and 13-H necessarily emerge as *syn* in the pentacyclic compound **7**). The configuration likely to emerge at C3 was less predictable. From the matched configurations shown in **6**, there could arise product **7a** corresponding to a *syn* saframycin skeleton, while the alternate possibility **7b** could be termed an *anti* saframycin. At that time, all known saframycins, natural or synthetic,



***Scheme 2.*** Synthetic plan involving key lynchpin Mannich cyclization.

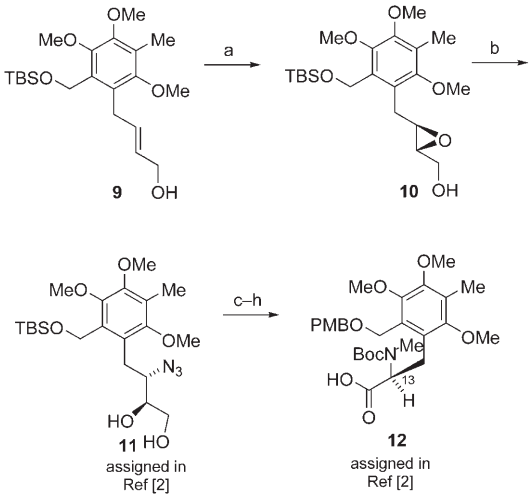
isolated from various sources and synthesized in a variety of different ways, were of the 3,11-*syn* series.[8] On this basis, it was supposed that in the pentacyclic setting, the 3,11-*syn* series is inherently more stable than the corresponding *anti* compounds. We further anticipated that the foregoing logic could be applied either to ecteinascidin 743 or to the broader family of saframycins. In the latter targets, the E-rings are hexasubstituted.

At the time, the AB system housing the future C1 (cf. **8**, Scheme 4) was assembled by asymmetric dihydroxylation.[2] We also attempted the synthesis of *N*-methyltyrosine derivative **12** by reagent-driven asymmetric synthesis (Scheme 3). In particular, compound **9**[2] was converted into epoxide **10** with high enantiomeric excess by Sharpless epoxidation. Azidolysis of this epoxide provided an azidodiol, presumed to be **11**, from which we obtained an *N*-methyl-*N*-*t*-Boc amino acid accordingly formulated as the L-amino acid derivative **12**. (Parenthetically, we had been drawn to this scheme as one that connects the powerful and reliable Sharpless epoxidation reaction with the important goal of synthesizing non-natural amino acids and their derivatives).[9]

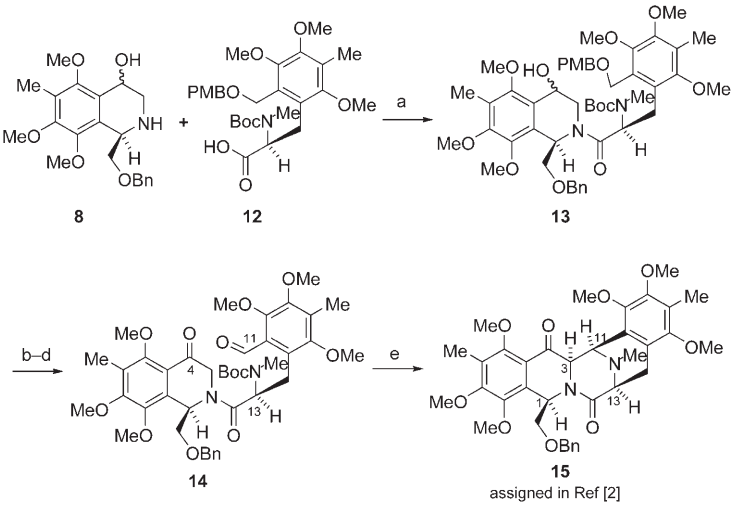
Coupling of **8** with **12** provided an amide, then assigned to be **13** (Scheme 4), which was converted into the presumed aldehyde **14**. Indeed, treatment of this substance, as shown, gave rise to a pentacyclic compound, formulated as **15**. The assignment of *syn* stereochemistry between C3 and C11 followed very closely from the coupling constant between 3-H and 11-H ($J \approx 3.6$ Hz). As 13-H was presumably of the L-amino acid configuration, 11-H was also defined to be α. Given the *syn* relationship between 3-H and 11-H, the former was accordingly assigned as α. At the time, these results seemed rather secure and most promising for our total synthesis program.

We then began investigations to use this chemistry to reach the saframycins as well as their closely related derivatives, most notably ecteinascidin 743. The ultimately successful results of that foray are described in detail in the following manuscript in this issue.[10] However, before the route to the ecteinascidin 743 series was completed, it was necessary to explore the requirements for the lynchpin Mannich cyclization in considerable detail. This study

 © 2006 Wiley-VCH Verlag GmbH & Co. KGaA, Weinheim 




***Scheme 3.*** a) (D)-DET (8%), $Ti(OiPr)_4$ (5.6%), *t*BuOOH (2 equiv), molecular sieves (4 Å), −20°C, 24 h, 98% (95% *ee*); b) $Ti(OiPr)_2(N_3)_2$ (3.5 equiv), benzene, 80°C, 5 h, 76% (single isomer); c) $(MeO)_2CMe_2$/acetone (1:2), cat. *p*-TsOH·$H_2O$, 25°C, 10 min, 100%; d) $H_2$ (1 atm), Pd/C (10%), EtOAc, $(Boc)_2O$ (1.2 equiv), 25°C, 5 h, 100%; e) TBAF (1.5 equiv), THF, 25°C, 1 h, 99%; f) PMBCl (1.2 equiv), NaH (2 equiv), cat. TBAI, THF/DMF (5:1), 0°C→25°C, 5 h, 98%; g) MeI (excess), NaH (5 equiv), THF/DMF (5:1), reflux, 12 h, 93%; h) 1) AcOH (80%), 25°C, 12 h, 2) $KMnO_4$ (0.2 equiv), $NaIO_4$ (4 equiv), $Na_2CO_3$ (0.5 equiv), dioxane/$H_2O$ (2.5:1), 25°C, 10 h, 95%. DET = diethyl tartrate; Ts = *p*-toluenesulfonyl; Boc = *tert*-butoxycarbonyl; TBAF = tetrabutylammonium fluoride; PMB = *p*-methoxybenzyl; TBAI = tetrabutylammonium iodide; DMF = *N*,*N*-dimethylformamide.

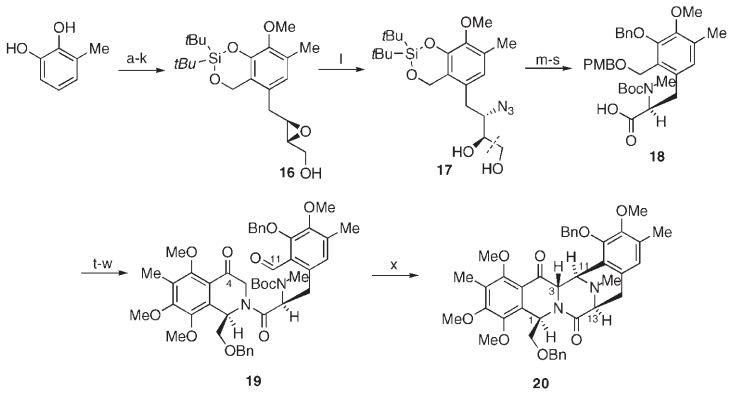



***Scheme 4.*** a) BOPCl (1.1 equiv), $Et_3N$ (2.5 equiv), $CH_2Cl_2$, 25°C, 12 h, 63%; b) DMP (1.5 equiv), $CH_2Cl_2$, 25°C, 30 min, 78%; c) DDQ (1.5 equiv), $CH_2Cl_2$/pH 7.00 buffer solution (18:1), 25°C, 3 h, 84%; d) DMP (1.5 equiv), $CH_2Cl_2$, 25°C, 30 min, 85%; e) formic acid, 100°C, 5 h, 75%. BOPCl = bis(2-oxo-3-oxazolidinyl)phosphinic chloride; DMP = Dess–Martin periodinane; DDQ = 2,3-dichloro-5,6-dicyano-1,4-benzoquinone.

revealed some major unexpected teachings. An account of that learning experience is provided herein.

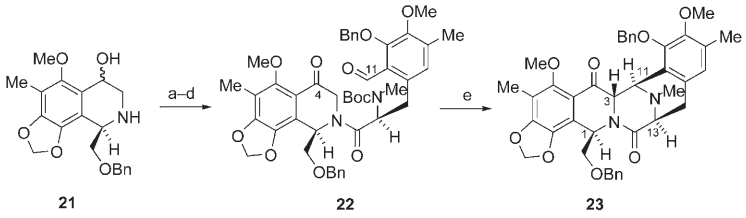
Turning to the ecteinascidin 743 problem, we ultimately required a penta- rather than hexasubstituted E-ring system (such as was the case with **12**). Accordingly, **16** was prepared in much the same fashion as had been previously used to prepare **10** (Scheme 5). Azidolysis of **16** produced **17** and thence, pentasubstituted amino acid **18**. Coupling of **18** with **8** gave an amide, which after suitable processing exposed the required C4 ketone and C11 aldehyde combination (cf. **19**). Cleavage of the Boc group triggered the Mannich closure, giving rise to pentacyclic product **20**. Once again, the configuration at C1 was defined, and we relied on the fixed L-amino acid configuration at C13 to enforce the α stereochemistry at C11. Thus, it was most surprising that the $^1H$ NMR spectrum of this compound indicated it to be of the 3,11-*anti* type ($J_{3\text{-H–}11\text{-H}} = 0$ Hz). Accordingly, 3-H in the pentacyclic product is β, as shown in **20**, rather than α (cf. **15**). Needless to say, we were quite surprised at this outcome. Further serving to deepen the mystery was that the results were strikingly clean. No 3,11-*anti* compound was found starting from **12**, whereas no 3,11-*syn* compound was found starting from **18**.

The cyclizations of potential ecteinascidin precursors were also studied (Scheme 6). It was found that coupling of **21**, prepared in the same manner as **8**, and pentasubstituted amino acid **18**, on further processing produced C4/C11 keto/aldehyde precursor **22**. Again, Mannich closure gave rise to *anti* pentacyclic compound **23**.

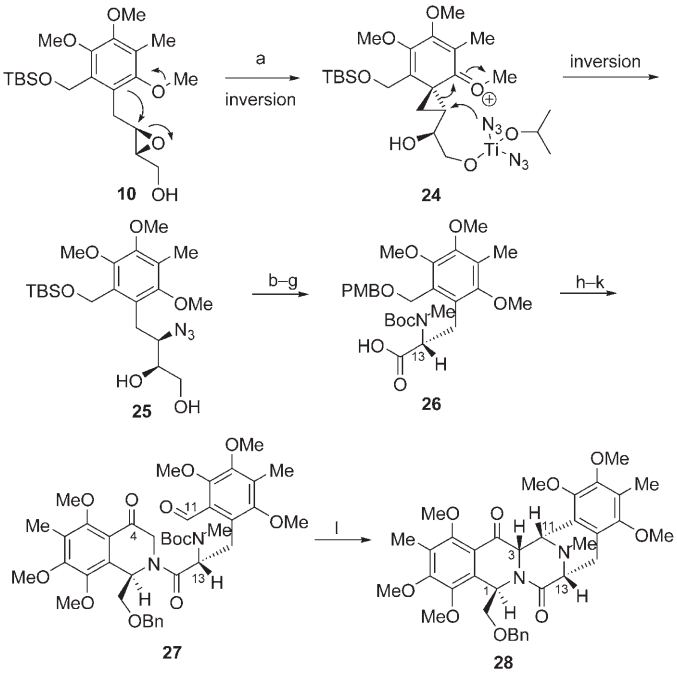



***Scheme 5.*** a) MOMCl (1.2 equiv), DIPEA (1.5 equiv), $CH_2Cl_2$, 25°C, 12 h, 80%; b) $BrCH_2CH{=}CHCH_2OTBS$ (1.1 equiv), $K_2CO_3$ (1.5 equiv), $CH_3CN$, 80°C, 5 h, 95%; c) $Me_2NPh$ (1.1 equiv), toluene, 210°C, 12 h, 96%; d) MeI (excess), $K_2CO_3$ (1.5 equiv), $CH_3CN$, 80°C, 12 h, 87%; e) TBAF (1.5 equiv), THF, 25°C, 1 h, 99%; f) PivCl (1.1 equiv), pyridine/$CH_2Cl_2$ (1:20), 25°C, 3 h, 99%; g) HCl (3 N), THF/IPA (2:1), 25°C, 12 h, 99%; h) $Et_2AlCl$ (3 equiv), $(CH_2O)_n$ (excess), $CH_2Cl_2$, 0°C→25°C, 12 h, 96%; i) $(tBu_2)Si(OTf)_2$ (1.2 equiv), 2,6-lutidine (1.5 equiv), $CHCl_3$, 0°C, 3 h, 85%; j) DIBAL-H (2.5 equiv), $CH_2Cl_2$, −78°C, 30 min, 94%; k) (D)-DET (8%), $Ti(OiPr)_4$ (5.6%), *t*BuOOH (2 equiv), molecular sieves (4 Å), −20°C, 24 h, 98% (95% *ee*); l) $Ti(OiPr)_2(N_3)_2$ (3.5 equiv), benzene, 80°C, 5 h, 76% (single isomer); m) $(MeO)_2CMe_2$/acetone (1:2), cat. *p*-TsOH·$H_2O$, 25°C, 10 min, 100%; n) $H_2$ (1 atm), 10% Pd/C, EtOAc, $(Boc)_2O$ (1.2 equiv), 25°C, 5 h, 100%; o) TBAF (1.5 equiv), THF, 25°C, 1 h, 99%; p) BnBr (1.2 equiv), $K_2CO_3$ (1.5 equiv), $CHCl_3$/MeOH (2:1), 25°C, 12 h, 83% q) PMBCl (1.2 equiv), NaH (2 equiv), cat. TBAI, THF/DMF (5:1), 0°C→25°C, 5 h, 98%; r) MeI (excess), NaH (5 equiv), THF/DMF (5:1), reflux, 12 h, 93%; s) 1) 80% AcOH, 25°C, 12 h, 2) $KMnO_4$ (0.2 equiv), $NaIO_4$ (4 equiv), $Na_2CO_3$ (0.5 equiv), dioxane/$H_2O$ (2.5:1), 25°C, 10 h, 95%; t) **8** (1.2 equiv), BOPCl (1.1 equiv), $Et_3N$ (2.5 equiv), $CH_2Cl_2$, 25°C, 12 h, 63%; u) DMP (1.5 equiv), $CH_2Cl_2$, 25°C, 30 min, 78%; v) DDQ (1.5 equiv), $CH_2Cl_2$/pH 7.00 buffer solution (18:1), 25°C, 3 h, 84%; w) DMP (1.5 equiv), $CH_2Cl_2$, 25°C, 30 min, 85%; x) formic acid, 100°C, 5 h, 75%. MOM = methoxymethyl; DIPEA = diisopropylethylamine; TBS = *tert*-butyldimethylsilyl; Piv = pivaloyl; IPA = isopropyl alcohol; Tf = trifluoromethanesulfonyl; DIBAL-H = diisobutylaluminum hydride; Bn = benzyl.

 © 2006 Wiley-VCH Verlag GmbH & Co. KGaA, Weinheim 



***Scheme 6.*** a) **18** (1.2 equiv), BOPCl (1.1 equiv), $Et_3N$ (2.5 equiv), $CH_2Cl_2$, 25 °C, 24 h, 85%; b) DMP (1.5 equiv), $CH_2Cl_2$, 25 °C, 30 min, 83%; c) DDQ (1.5 equiv), $CH_2Cl_2$/pH 7.00 buffer solution (18:1), 25 °C, 3 h, 90%; d) DMP (1.5 equiv), $CH_2Cl_2$, 25 °C, 30 min, 94%; e) formic acid, 100 °C, 10 min, 70%.



***Scheme 7.*** a) $Ti(OiPr)_2(N_3)_2$ (3.5 equiv), benzene, 80 °C, 5 h, 76% (single isomer); b) $(MeO)_2CMe_2$/acetone (1:2), cat. *p*-TsOH·$H_2O$, 25 °C, 10 min, 100%; c) $H_2$ (1 atm), Pd/C (10%), EtOAc, $(Boc)_2O$ (1.2 equiv), 25 °C, 5 h, 100%; d) TBAF (1.5 equiv), THF, 25 °C, 1 h, 99%; e) PMBCl (1.2 equiv), NaH (2 equiv), cat. TBAI, THF/DMF (5:1), 0 °C→25 °C, 5 h, 98%; f) MeI (excess), NaH (5 equiv), THF/DMF (5:1), reflux, 12 h, 93%; g) 1) AcOH (80%), 25 °C, 12 h, 2) $KMnO_4$ (0.2 equiv), $NaIO_4$ (4 equiv), $Na_2CO_3$ (0.5 equiv), dioxane/$H_2O$ (2.5:1), 25 °C, 10 h, 95%; h) **8**, BOPCl (1.1 equiv), $Et_3N$ (2.5 equiv), $CH_2Cl_2$, 25 °C, 12 h, 63%; i) DMP (1.5 equiv), $CH_2Cl_2$, 25 °C, 30 min, 78%; j) DDQ (1.5 equiv), $CH_2Cl_2$/pH 7.00 buffer solution (18:1), 25 °C, 3 h, 84%; k) DMP (1.5 equiv), $CH_2Cl_2$, 25 °C, 30 min, 85%; l) formic acid, 100 °C, 5 h, 75%.

Taking the seemingly incontrovertible data at face value, one would be obliged to conclude that the stereochemical outcome of the cyclization reactions (i.e. whether the relationship between 3-H and 11-H emerges as *syn* or *anti*) is somehow a function of the degree of substitution of the remote E-ring. Unlikely as this situation would be, this is where the data first took us. Accordingly, we pursued the matter in considerable detail. A variety of seco-aldehydes with pentasubstituted E-rings were prepared and examined. They all led to 3,11-*anti* compounds. At no point could we enter the required 3,11-*syn* series with any compounds in which the E-ring was pentasubstituted.

Of course, the heart of the anomaly rests on the implicit assumption that the relationships between 1-H and 13-H (anticipating ecteinascidin 743 numbering) are the same in **14** and **19**. This assumption seemed justified enough, as we synthesized the two compounds by identical routes. Indeed the AB precursor **8**, bearing the *R* configuration at C1, is identical in the sequences leading to **14** and **19**. As the routes to the two non-identical amino acid derivatives **12** and **18** were the same, it seemed reasonable to assume that these compounds were identically configured at the future C13 center. The solution to the conundrum required abandoning of this seemingly reasonable, but in the end incorrect, assumption.

Specifically, to solve the problem we continued to assume the correctness of the original supposition (i.e. that in the case of the pentasubstituted E-ring compounds such as **16**, azidolysis of the epoxide was the *sole* inversion event). This indeed progressed to the L-amino acid precursor, as previously formulated (cf. **18**). By contrast, in the hexasubstituted case, we now postulated that a "hidden" inversion took place in the context of the azidolysis event, such that the azidolysis reaction had actually produced the D-amino acid derivative (Scheme 7). Thus, the stereochemical assignment at C13 in **14** is not *S*, as shown, but rather *R* (see below).

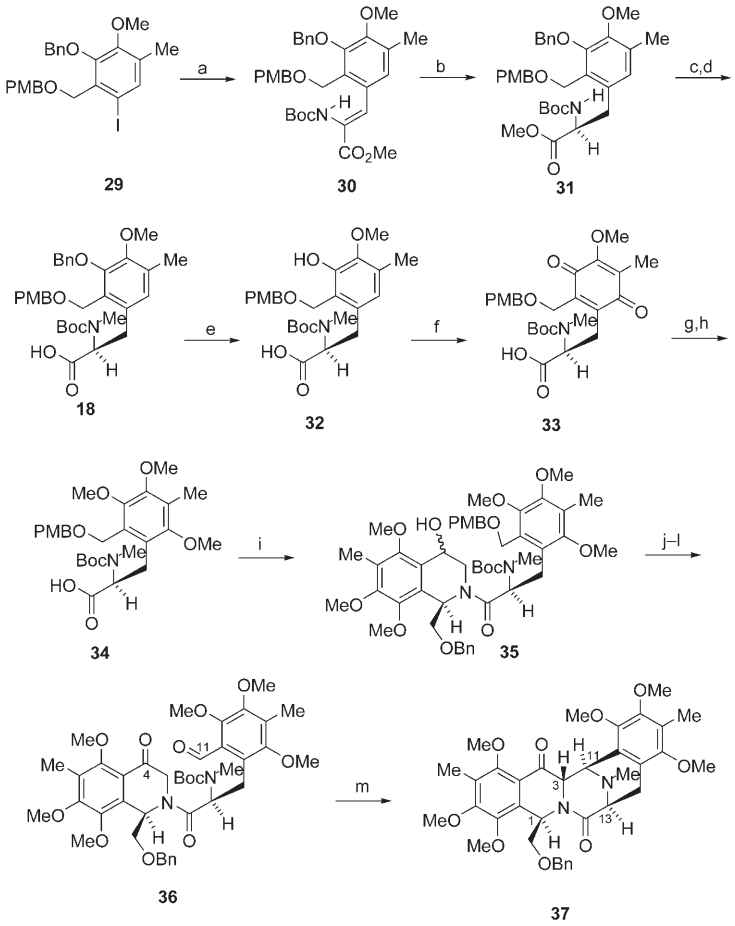
The unusual behavior of the hexasubstituted system could be a consequence of two factors. First, the trajectory for azidolysis is significantly more hindered when the aryl ring is fully substituted. Also, perhaps the additional *ortho*-alkoxy substituent at C15 participates in a precedented but now arcane intramolecular $Ar_1$ participation reaction, generating a methylated spirocyclohexadienone (cf. **24**).[11] This participation results in a hitherto unnoticed *first* inversion around C13. Azidolysis of the activated cyclopropane again with inversion leads then to product **25**, an azido precursor of a D-amino acid (cf. **26**). Ultimately in the hexasubstituted series, eventual processing leads to aldehyde **27**, which bears the *R* stereochemistry (i.e. a D-aminoacyl function) at C13. Cyclization does indeed produce the 3,11-*syn* pentacyclic system, **28**. However, this system is one in which 11-H and 13-H are β, whereas 3-H is also β. In other words, while 3-H and 11-H are indeed *syn*, they, as well as C13, are each of the opposite configuration to that required for the total synthesis of a saframycin. In contrast, in the pentasubstituted epoxide **16**, azidolysis occurred as a single inversion event, as initially assigned, leading ultimately to the L-amino acid aldehydes **19** and **22**, as formulated above en route to the *anti* products **20** and **23**.[12] With this insight, the conundrum would be solved.

We were able to bring very strong support in favor of this hypothesis. The thought was that if one could synthesize a precursor to the lynchpin Mannich cyclization in which the E-ring was hexasubstituted but of the L-amino acid series, one should generate a 3,11-*anti* compound comparable to **20** and **23**. Of course, in principle this could be possible by repeating the sequence that initially produced **26** but using the *ent*-**10** epoxide, which would be available from the Sharpless epoxidation methodology (using the L-tartrate instead of the D-tartrate). However, as has been described, this is a very

 © 2006 Wiley-VCH Verlag GmbH & Co. KGaA, Weinheim 

lengthy route.[2] Thus we had incentive to develop a rather more streamlined approach.

The new route started with iodo aromatic precursor **29** (Scheme 8).[7] This compound was carried through a Jeffery–Heck reaction[13] and a subsequent asymmetric Knowles-type hydrogenation as previously described, leading to the L-amino acid system **18**.[14] In this pentasubstituted E-ring series, the amino acid produced by the Jeffery–Heck/hydrogenation sequence and that from the Sharpless epoxidation/azidolysis sequence were identical in every respect, including optical rotation.[15]




***Scheme 8.*** a) See reference [6]; b) Rh[(cod)-(*S*,*S*)-Et-duphos]$^+$TfO$^-$ (0.008 equiv), $H_2$ (6.8 atm) $CH_2Cl_2$/MeOH (1:1), 25 °C, 72 h, 93%, 99% *ee*; c) LiOH (3 equiv), MeOH/THF/$H_2O$ (1:3:1)), 0 °C→25 °C, 11 h, 93%; d) MeI (2.2 equiv), NaH (3.3 equiv), THF), 0 °C→25 °C, 15 h, 82%; e) $H_2$ (1 atm), Pd/C (10%), EtOAc, 25 °C, 2 h, 99%; f) Fremy salt (10 equiv), $NaH_2PO_4$ (2 M, aqueous), acetone, 25 °C, 75%; g) Zn (400 equiv), AcOH (400 equiv), $CH_2Cl_2$, 25 °C, 95%; h) MeI (5 equiv), $Cs_2CO_3$ (5 equiv), DMF, 25 °C, 75%; i) **8** (1 equiv), BOPCl (1.1 equiv), $Et_3N$ (2.5 equiv), $CH_2Cl_2$, 25 °C, 12 h, 66%; j) DMP (1.5 equiv), $CH_2Cl_2$, 25 °C, 30 min, 78%; k) DDQ (1.5 equiv), $CH_2Cl_2$/pH 7.00 buffer solution (18:1), 25 °C, 3 h, 90%; l) DMP (1.5 equiv), $CH_2Cl_2$, 25 °C, 30 min, 95%; m) formic acid, 100 °C, 5 h, 62%. cod = cycloocta-1,5-diene.

To obtain the hexasubstituted aromatic products by this new technology, we proceeded via pentasubstituted precursors.[16] Removal of the benzyl group of **18** was followed by oxidation to quinone **33** (Scheme 8). The latter, following reductive bismethylation afforded hexasubstituted L-amino acid **34**. An important milestone in substantiating the hypothesis discussed above (Scheme 7) was reached when it was found that **34** was, indeed, the enantiomer of **26**, as shown by optical rotation.[17]

With the groundwork now secure, we next asked the question as to the nature of the lynchpin Mannich cyclization in the case of the properly matched (i.e. (*R*)-C1; (*S*)-C13) hexasubstituted precursor **36** generated in the usual way from amide **35** (Scheme 8). Indeed, when **36** was subjected to the conditions shown, *anti*-**37** was obtained in 62% yield. Thus, the degree of substitution in the E-ring is not determinative in terms of formation of *syn* versus *anti* product. The degree of substitution was only important in determining the stereosense of azidolysis of the relevant epoxides (cf. **10** versus **16**) and thus the eventual handedness of the E-ring amino acid derivatives (cf. **18** versus **26**).

In summary, with the facts now fully documented, the conundrum has been solved. In retrospect, we note a pleasing consistency in the stereochemical sense of the lynchpin Mannich cyclization (see matched precursor **36** and mismatched precursor **27**). In each case cyclization of the iminium species onto the C3–C4 enol occurs from the face opposite to that of the resident C1 benzyloxymethyl group.[18] With the hard-won teachings in hand, we were in a position to focus on a solution aimed at a total synthesis of ecteinascidin 743. These results are described in the subsequent paper in this issue.

Received: November 9, 2005

**Keywords:** antitumor agents · asymmetric synthesis · Mannich cyclization · natural products · total synthesis

[1] a) K. L. Rinehart, T. G. Holt, N. L. Fregeau, J. G. Stroh, P. A. Keifer, F. Sun, L. H. Li, D. G. Martin, *J. Org. Chem.* **1990**, *55*, 4512; b) R. Sakai, K. L. Rinehart, Y. Guan, A. H.-J. Wang, *Proc. Natl. Acad. Sci. USA* **1992**, *89*, 11456.

[2] a) B. Zhou, J. Guo, S. J. Danishefsky, *Org. Lett.* **2002**, *4*, 43; b) B. Zhou, S. Edmondson, J. Padron, S. J. Danishefsky, *Tetrahedron Lett.* **2000**, *41*, 2039; c) B. Zhou, J. Guo, S. J. Danishefsky, *Tetrahedron Lett.* **2000**, *41*, 2043.

[3] Total syntheses of **1**: a) E. J. Corey, D. Y. Gin, R. S. Kania, *J. Am. Chem. Soc.* **1996**, *118*, 9202; b) A. Endo, A. Yanagisawa, M. Abe, S. Tohma, T. Kan, T. Fukuyama, *J. Am. Chem. Soc.* **2002**, *124*, 6552; during the preparation of this manuscript, we became aware of a completed synthesis of **1**: c) J. Chen, X. Chen, M. Bois-Choussy, J. Zhu, *J. Am. Chem. Soc.* **2006**, *128*, 87.

[4] A. G. Myers, D. W. Kung, *J. Am. Chem. Soc.* **1999**, *121*, 10828.

[5] For a review of these compounds, see: J. D. Scott, R. M. Williams, *Chem. Rev.* **2002**, *102*, 1669.

[6] C. Cuevas, M. Pérez, M. J. Martín, J. L. Chicharro, C. Fernández-Rivas, M. Flores, A. Francesch, P. Gallego, M. Zarzuelo, F. de la Calle, J. García, C. Polanco, I. Rodríguez, I. Manzanares, *Org. Lett.* **2000**, *2*, 2545.

[7] For a previous example in the context of a total synthesis, see: C. Chan, R. Heid, S. Zheng, J. Guo, B. Zhou, T. Furuuchi, S. J. Danishefsky, *J. Am. Chem. Soc.* **2005**, *127*, 4596.

[8] For an example of an *anti* renieramycin compound, see: J. W. Lane, Y. Chen, R. M. Williams, *J. Am. Chem. Soc.* **2005**, *127*, 12684.

[9] a) Y. Gao, R. M. Hanson, J. M. Klunder, S. Y. Ko, H. Masamune, K. B. Sharpless, *J. Am. Chem. Soc.* **1987**, *109*, 5765;

 © 2006 Wiley-VCH Verlag GmbH & Co. KGaA, Weinheim 

b) K. B. Sharpless, W. Amberg, Y. L. Bennani, G. A. Crispino, J. Hartung, K.-S. Jeong, H.-L. Kwong, K. Morikawa, Z.-M. Wang, D. Xu, X.-L. Zhang, *J. Org. Chem.* **1992**, *57*, 2768; c) M. Caron, P. R. Carlier, K. B. Sharpless, *J. Org. Chem.* **1988**, *53*, 5185.

[10] See following Communication in this issue: S. Zheng, C. Chan, T. Furuuchi, B. J. D. Wright, B. Zhou, J. Guo, S. J. Danishefsky, *Angew. Chem.* **2006**, *118*, 1786; *Angew. Chem. Int. Ed.* **2006**, *45*, 1754.

[11] S. Winstein, R. Baird, *J. Am. Chem. Soc.* **1957**, *79*, 756.

[12] In light of our current hypothesis, optical rotation data taken for both hexa- and pentasubstituted epoxides (cf. **10** and **16**) and their respective azidodiol products (cf. **11** and **17**) should have, in retrospect, seemed suspicious. Upon azidolysis of pentasubstituted epoxide **16** to azidodiol **17** a sign inversion, from + to − took place [**16**: $[\alpha]_D^{25} = +6.95$ ($CHCl_3$, $c = 1$) and **17**: $[\alpha]_D^{25} = -39.30$ ($CHCl_3$, $c = 0.765$)]. In contrast, in the hexasubstituted series the sign did not change [**10**: $[\alpha]_D^{25} = +1.85$, ($CHCl_3$, $c = 1$) and **11**: $[\alpha]_D^{25} = +25.31$, ($CHCl_3$, $c = 1$)]. However, in the end, unequivocal support of our hypothesis was obtained through a crystal structure of *anti* pentacyclic compound de-Bn-**20**, fully verifying its assigned structure.

[13] a) T. Jeffery, *J. Chem. Soc. Chem. Commun.* **1984**, 1287; b) A. McKillop, R. J. K. Taylor, R. J. Watson, N. Lewis, *Synthesis* **1994**, 31.

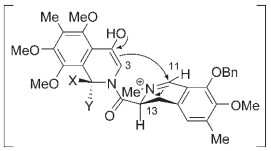
[14] M. J. Burk, J. E. Feaster, W. A. Nugent, R. L. Harlow, *J. Am. Chem. Soc.* **1993**, *115*, 10125.

[15] $[\alpha]_D^{25} = -75.29$ ($c = 1$, $CHCl_3$).

[16] Attempts to perform a Jeffery–Heck reaction on a hexasubstituted precursor of the type **30** were unsuccessful. The chemistry was thus initially done at the pentasubstituted stage, and the sixth substituent was introduced later.

[17] **34**: $[\alpha]_D^{25} = -45.7$ ($CHCl_3$, $c = 1$), **26**: $[\alpha]_D^{25} = +45.9$, ($CHCl_3$, $c = 1$).

[18] Thus, attack at the C11 iminium center necessarily occurs *anti* to 13-H, regardless of whether the latter is α or β. The attack at C3 occurs anti to the benzyloxymethyl group. Thus, if $X = CH_2OBn$, attack occurs on the α face of C3 (3-H β in the product). If $Y = CH_2OBn$, attack occurs at the β face of C3 (leaving the C3 proton α in the product).




 © 2006 Wiley-VCH Verlag GmbH & Co. KGaA, Weinheim 

Natural Products

DOI: 10.1002/anie.200503983

# Stereospecific Formal Total Synthesis of Ecteinascidin 743**

*Shengping Zheng, Collin Chan, Takeshi Furuuchi, Benjamin J. D. Wright, Bishan Zhou, Jinsong Guo, and Samuel J. Danishefsky**

*Dedicated to Professor Ryoji Noyori*

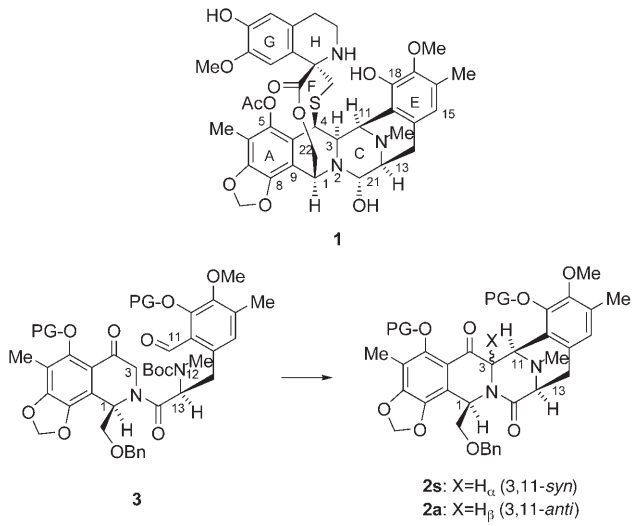
In the preceding communication in this issue, we described a comprehensive study directed at understanding the multifaceted stereochemical issues associated with the cascadelike reaction initiated by cleavage of the urethane function of an *N*-methyl-*N*-Boc ketoaldehyde of the type **3**.[1] Even after extensive experimentation, we could not realize a lynchpin Mannich cyclization of the type **3**→**2s** (**s** = *syn*). Such a cyclization, had it occurred, would have found ready application in the total synthesis of the highly cytotoxic natural product ecteinascidin 743 (**1**; Scheme 1).[2] In practice, it was shown with C1 and C13 matched in their correct relative and absolute configurations as shown in **3** that the product is cleanly the 3,11-*anti* compound **2a** (**a** = *anti*). At no time could we pass from a **2a** to a **2s** compound by epimerization at C3.[3] To attain the relative and absolute stereochemistry at C3, C11, and C13 required to reach **1**, it would be necessary to resort to mismatching at C1 (i.e. (*S*)-C1 rather than (*R*)-C1 configuration). This would in turn necessitate a late-stage and problematic epimerization at C1.[4] In summary, at no stage could we solve the ecteinascidin 743 problem (encompassing C1, C3, C4, C11, and C13) or the saframycin total synthesis problem (encompassing C1, C3, C11, and C13) by direct cyclization of appropriately matched ((*R*)-C1, (*S*)-C13) precursors bearing ketone and aldehyde functions at C4 and C11, respectively (cf. **3**).[5]

[*] Dr. S. Zheng, C. Chan, Dr. T. Furuuchi, B. J. D. Wright, Dr. B. Zhou, Dr. J. Guo, Prof. S. J. Danishefsky
The Department of Chemistry
Columbia University
Havemeyer Hall, New York, NY 10027 (USA)
Fax: (+1) 212-772-8691
E-mail: s-danishefsky@ski.mskcc.org
Prof. S. J. Danishefsky
The Laboratory for Bioorganic Chemistry
Sloan-Kettering Institute for Cancer Research
1275 York Avenue, New York, NY 10021 (USA)

[**] This work was supported by the National Institutes of Health (Grant HL25848) and by Pharmamar Corporation of Madrid, Spain. We thank Dr. Atsushi Endo for many helpful dicussions. B.J.D.W. gratefully acknowledges the NSF for a predoctoral fellowship. We thank Bristol Myers Squibb for the generous fellowship awarded to C.C. We also thank Dr. Yasuhiro Itagaki (Columbia University) for mass spectrometric analyses

Supporting information for this article is available on the WWW under http://www.angewandte.org or from the author.

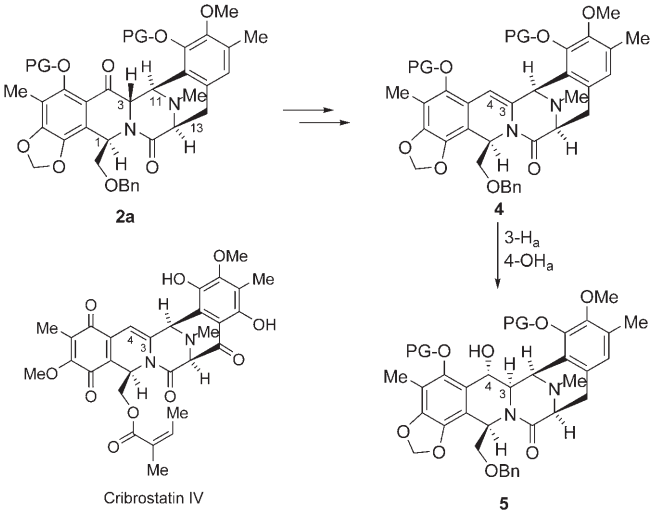

WILEY InterScience DISCOVER SOMETHING GREAT
© 2006 Wiley-VCH Verlag GmbH & Co. KGaA, Weinheim




***Scheme 1.*** Lynchpin Mannich strategy en route to ecteinascidin 743 (**1**). PG = protecting group.

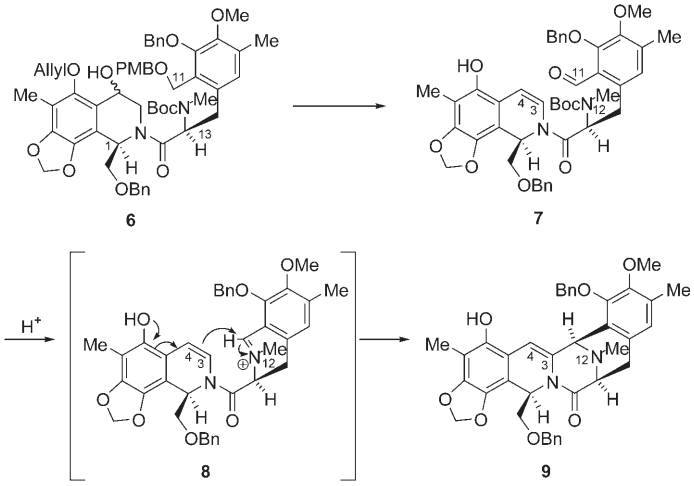
Previously, in connection with our total synthesis of cribrostatin IV, we charted a viable pathway from a **2a**-type compound to a 3,4-dehydro-type compound (cf. **4**).[6] Of course, in cribrostatin IV, the final target we were pursuing contains a 3,4-olefinic linkage. Accordingly, we envisioned an indirect solution to the ecteinascidin 743/saframycin total synthesis problem by reaching a **2a** species that would be converted into a 3,4-dehydro system (cf. **4**).[7] We hoped to reach a key intermediate (cf. **5**) required for the ecteinascidin 743 series from **4** through an overall α-face hydration (i.e. 3-$H_\alpha$, 4-$OH_\alpha$) of the C3–C4 double bond (see **5**, Scheme 2).

On further reflection, a conceptually simpler possibility presented itself. Perhaps direct cyclization of an *ortho*-hydroxystyrene prototype **7** would occur at the styrene double bond, with its regiochemical sense controlled by the hydroxy group of the phenol moiety. The cyclization we envisioned (presumably via the iminium derivative **8**, formed upon cleavage of the Boc group from N12) would produce **9**




***Scheme 2.*** Proposed epimerization strategy at C3.

(Scheme 3). Given the importance of providing access to a broad range of biologically active tetrahydroisoquinoline alkaloids, it seemed prudent to gain reliable and convenient access to the required matched antipodes.[8] Indeed, as will be



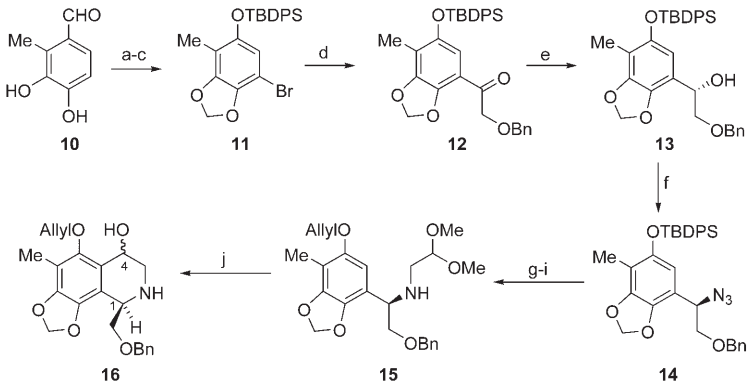

***Scheme 3.*** Construction of the pentacycle through a novel vinylogous Pictet–Spengler cyclization.

described, a new concise plan was devised to reach the configurationally defined tetrahydroisoquinoline moiety ((*R*)-C1). The latter was acylated with the enantiomerically defined L-aminoacyl CDE precursor, bearing the future C11 aldehyde (see compound **6**).[9]

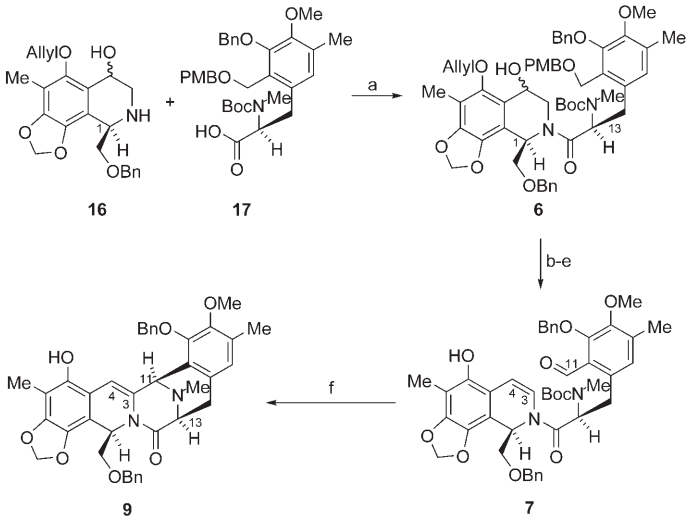
Our synthesis started with a highly regiospecific bromination of the Borchardt catechol **10** (Scheme 4).[10] Engagement of the catechol hydroxyl groups (by methylenation) set the stage for successful Baeyer–Villiger oxidation and hydrolysis. The resultant phenol was protected as its *tert*-butyldiphenylsilyl ether **11**. Lithiation of the bromine function followed by coupling of the organometallic agent with the Weinreb amide of benzyloxyglycolic acid yielded **12**.[11] Asymmetry was introduced by submitting ketone **12** to Noyori transfer-hydrogenation conditions, thereby providing homochiral **13**.[12] A modified Mitsunobu reaction of alcohol **13** with diphenylphosphorylazide gave rise to **14**, with complete inversion of stereochemistry.[13] At this stage, the *R* configuration at C1 was securely fashioned. Catalytic hydrogenation of **14** to the amine was followed by two-carbon-atom homologation, and subsequent deprotection/reprotection of the phenol as its allyl ether gave acetal **15**. The Bobbitt-modified Pomerantz–Fritsch reaction of **15** provided the required tetrahydroisoquinoline **16**, in which the stereochemistry at C1 was correctly defined.[14] That C4 is, at this stage, presented as a mixture of epimers, is an awkwardness rather than an impediment (see below).

Coupling of tetrahydroisoquinoline **16** and the previously described L-tyrosine derivative **17**[6] under the agency of BOPCl afforded amide **6** in excellent yield (Scheme 5). After oxidative cleavage of the PMB group and dehydration of the benzylic alcohol,[15] the primary alcohol was oxidized to the C11 aldehyde.[16] The allyl group was cleaved by treatment with tributyltin hydride in the presence of catalytic

 © 2006 Wiley-VCH Verlag GmbH & Co. KGaA, Weinheim 



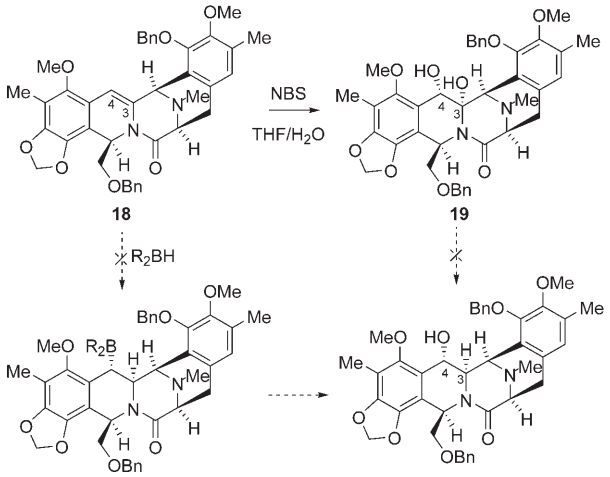
***Scheme 4.*** a) 1) $Br_2$ (1.01 equiv), NaOAc (1.05 equiv), AcOH, 0 °C→25 °C, 12 h; 2) $BrCH_2Cl$ (1.5 equiv), $Cs_2CO_3$ (1.5 equiv), DMF, 105 °C, 12 h, 66%; b) 1) MCPBA (3 equiv), 25 °C→64 °C, 3 h; 2) HCl (0.3 equiv), 0 °C→25 °C, 12 h, 78%; c) TBDPSCl (1.15 equiv), TEA (1.5 equiv), DMAP (0.1 equiv), 25 °C, 12 h, 89%; d) 1) *n*BuLi (1.6 M; 1.1 equiv), toluene/THF (9:1), −78 °C, 20 min; 2) neat Me-(MeO)NC(O)$CH_2$OBn (1.5 equiv), −78 °C, 50 min, 80%; e) Noyori *R,R* catalyst (0.01 equiv), $HCO_2H$ (13.2 equiv), TEA (7.8 equiv), DMF, 0 °C→40 °C, 24 h, 78% (95% *ee*); f) DPPA (2 equiv), DBU (2 equiv), toluene/DMF (9:1), 50 °C, 24 h, 89% (95% *ee*); g) $H_2$ (1 atm), Pd/C (5%), EtOAc, 25 °C, 15 h, 80%; h) 1) $(MeO)_2CHCHO$ (1 equiv), AcOH (4 equiv), $NaCNBH_3$ (1.3 equiv), $MgSO_4$ (6 equiv), MeOH, 0 °C→65 °C, 4 h; 2) TBAF (1.5 equiv), THF, 0 °C, 30 min, 94%; i) allyl bromide (1.15 equiv), NaH (2.8 equiv), DMF, 0 °C→25 °C, 2 h, 84%; j) 7 M HCl (70 equiv), dioxane, 0 °C→25 °C, 72 h, 90%. DMF = *N,N*-dimethylformamide; MCPBA = *m*-chloroperoxybenzoic acid; TBDPS = *tert*-butyldiphenylsilyl; TEA = triethylamine; DMAP = 4-(dimethylamino)pyridine; Bn = benzyl; DPPA = diphenylphosphoryl azide; DBU = 1,8-diazabicyclo[5.4.0]undec-7-ene; TBAF = tetrabutylammonium fluoride.



***Scheme 5.*** a) BOPCl (1.1 equiv), TEA (3 equiv), $CH_2Cl_2$, 0 °C→25 °C, 24 h, 85%; b) DDQ (1.6 equiv), $CH_2Cl_2$/pH 7.00 buffer solution (18:1), 25 °C, 30 min, 90%; c) $Cu(OTf)_2$ (0.2 equiv), benzene, 85 °C, 15 min, 61%; d) DMP (1.5 equiv), $CH_2Cl_2$, 25 °C, 5 h, 94%; e) $[(PPh_3)_2PdCl_2]$ (0.2 equiv), $Bu_3SnH$ (1.2 equiv), AcOH (5 equiv), 0 °C→25 °C, 1 h, 93%; f) $CHF_2CO_2H$ (30 equiv), $MgSO_4$ (4 equiv), benzene, 100 °C, 45 min, 42–58%. BOPCl = bis(2-oxo-3-oxazolidinyl)phosphinic chloride; DDQ = 2,3-dichloro-5,6-dicyano-1,4-benzoquinone; DMP = Dess–Martin periodinane.

$[(Ph_3P)_2PdCl_2]$ to yield cyclization precursor **7**, as hypothesized above.[17] The resulting aldehyde **7** was suited for the crucial intramolecular Pictet–Spengler cyclization. We screened various acidic conditions for achieving the desired cyclization to **9**. In the event, compound **7** successfully underwent cyclization to produce pentacycle **9** upon exposure to 30 equivalents of difluoroacetic acid in benzene. For the moment, the product is obtained in a somewhat disappointing yield of 42–58%.

With a viable route to pentacyclic alkene **9** in hand, we were now faced with the need to functionalize the C3–C4 double bond (Scheme 6). Implementation of this task



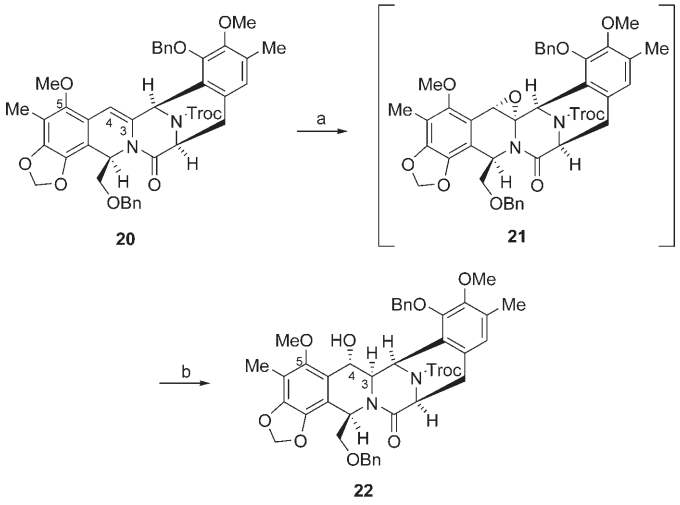
***Scheme 6.*** Unsuccessful attempts to refunctionalize the C3–C4 olefinic linkage. NBS = *N*-bromosuccinimide.

commenced with temporary protection of phenol **9** as its methyl ether derivative **18**. As **18** could be readily obtained in ample quantities, it was used as a model to probe eventual management of the synthesis in a fully updated system. In our first attempts to functionalize the C3–C4 double bond, we took recourse to hydroboration reagents such as BTHF, BMS, $BH_3$·Py, $Br_2BH$, and catecholborane. Remarkably, such attempts uniformly resulted only in recovery of **18**.[18] By contrast, the double bond of **18** could be dihydroxylated with *N*-bromosuccinimide in aqueous THF, leading to a diol assigned as **19** in which the dihydroxylation was presumed to occur from the less-hindered α face.[19] However, attempted reductive removal of the now extraneous angular 3-OH group of **19** with a variety of reducing agents resulted in the recovery of starting material.

Given these results, we concluded that to be successful, a highly reactive oxidizing agent would be needed to attack the double bond. We also needed functionality at C3, which would be more reactive than a simple hydroxy group to allow introduction of the required 3-$H_\alpha$ group. Accordingly, we first explored the use of peracid agents for the epoxidation of the C3–C4 olefin linkage. However, at this stage *N*-oxide formation of the N–Me tertiary amine group became a potential problem. Accordingly, we conducted a McCluskey reaction to afford *N*-Troc urethane **20**.[20] Unfortunately, attempts at various epoxidizing conditions with peracids were unsuccessful (possibly owing to the slowness of the desired reaction in the context of the highly oxidizable aromatic sectors). With our options rapidly narrowing, it was fortunate

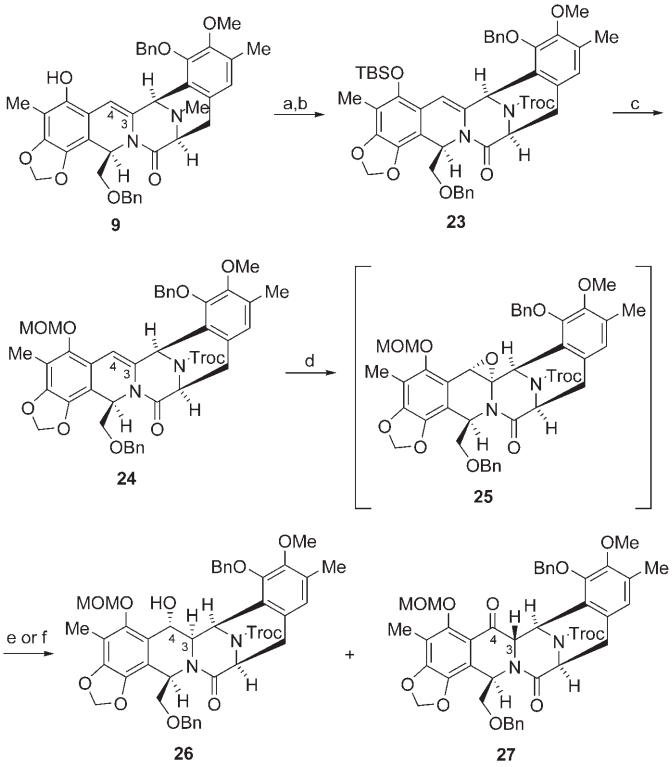
 © 2006 Wiley-VCH Verlag GmbH & Co. KGaA, Weinheim 

that reaction of **20** with 2,2-dimethyldioxirane (DMDO) did occur, giving rise to material formulated as the C3–C4 α-epoxide **21** (Scheme 7).[2d] Treatment of **21** with sodium cyanoborohydride provided the required 3-$H_\alpha$, 4-$OH_\alpha$ hydration product **22**. Greater insight into this fascinating reductive cleavage of the novel enamide epoxide (*cf.* **21**) was gained in the MOM ether series (see below, compound **25**).

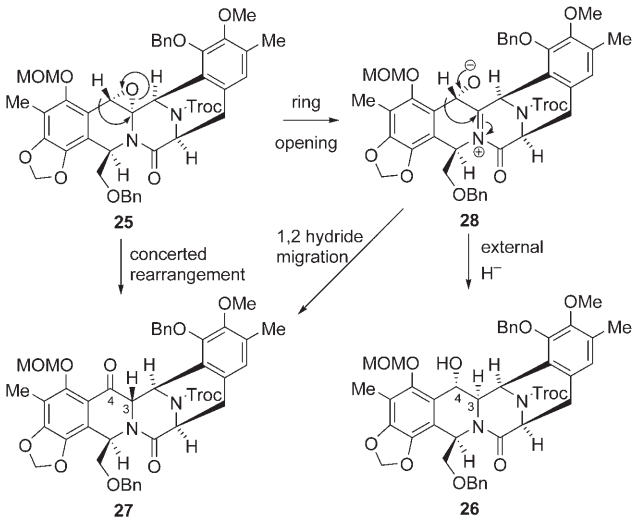



***Scheme 7.*** a) DMDO (1.5 equiv), $CH_2Cl_2$, 0 °C→25 °C, 30 min; b) $NaCNBH_3$ (5 equiv), 10 min, 75 %. DMDO = dimethyl dioxirane.

On the basis of our experiences in this series, we could not be confident that a compound such as **22**, containing a methyl ether at C5 could be advanced to conclude the synthesis. Moreover, in the same vein, it was decided to confirm our various assignments by connecting our series with a previously synthesized intermediate, from which ecteinascidin 743 could definitely be reached. Accordingly, we defined **32** as our milestone target, which is an advanced intermediate in the Fukuyama total synthesis of ecteinascidin 743.[2d] Phenol **9** was first converted into its *tert*-butyldimethylsilyl ether derivative (Scheme 8). This step was followed by a McCluskey reaction of the N–Me amine, thereby providing **23**. Deprotection of the TBS ether with TBAF, followed by addition of MOMCl and Hünig base, led to **24** in good yield.[21] Treatment of this compound with DMDO led, as before (cf. **20**), to epoxidation of the C3–C4 double bond, thus affording the presumed **25**. When this compound was treated with 5 equivalents of sodium cyanoborohydride the major product obtained was a ketone assigned as shown in **27**, although small amounts of **26** were also obtained. Two mechanistic hypotheses were entertained to account for the formation of the ketone (Scheme 9). One could envision a concerted rearrangement with hydride migration, from C4 to C3, to afford ketone **27**. Alternatively, the nitrogen atom of the lactam opens the epoxide to produce amidonium alkoxide **28**. This intermediate can undergo 1,2-hydride migration to give **27** or competitive reduction by an external hydride to provide **26**. Apparently this duality is, in fact, operative, since recourse to a large excess of sodium cyanoborohydride does afford **26** as the predominant product.[22]



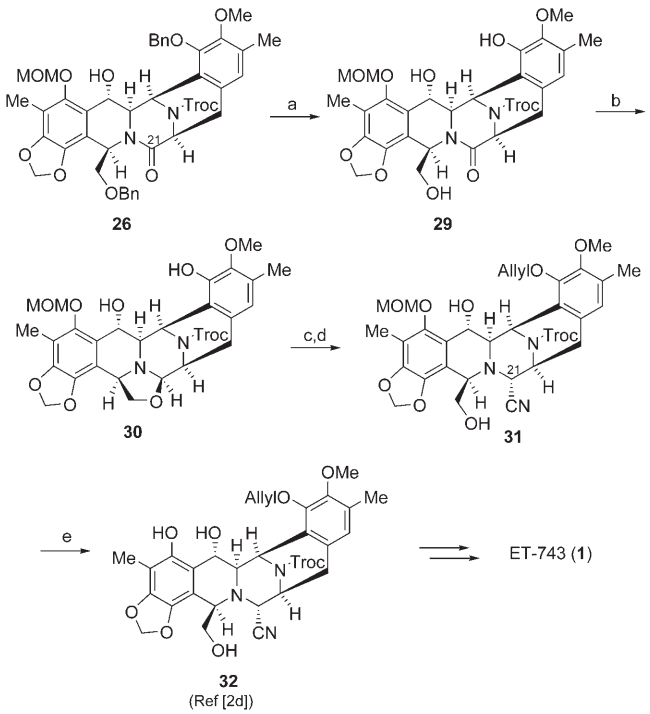

***Scheme 8.*** a) TBSOTf (2.5 equiv), TEA (3 equiv), $CH_2Cl_2$, 0 °C, 30 min, 100 %; b) TrocCl (20 equiv), TBAI (3 equiv), toluene, 110 °C, 3 h, 92 %; c) 1) TBAF (3 equiv), $CH_2Cl_2$, 0 °C, 2 min; 2) MOMCl (3 equiv), Hünig base (5 equiv), 30 min, 79 %; d) DMDO (2 equiv), $CH_2Cl_2$, 0 °C→25 °C, 1.5 h; e) $NaCNBH_3$ (5 equiv), 10 min, **27**/**26** 60 %:10 %; f) $NaCNBH_3$ (50 equiv), 10 min, (**26**) 78 %. TBS = *tert*-butyldimethylsilyl; Tf = trifluoromethanesulfonyl; Troc = 2,2,2-trichloroethoxycarbonyl; TBAI = tetrabutylammonium iodide; MOM = methoxymethyl.




***Scheme 9.*** Mechanistic proposals for the reduction of epoxide **25** to alcohol **26** and ketone **27**.

At this juncture, we faced only the installation of the cyano function at C21 (Scheme 10). Toward this end, the two benzyl protecting groups were removed, thereby giving rise to

 © 2006 Wiley-VCH Verlag GmbH & Co. KGaA, Weinheim 




***Scheme 10.*** a) $H_2$ (1 atm), Pd/C (10%), EtOAc, 25°C, 3 h, 77%; b) DIBAL-H/BuLi (1:1; 40 equiv), THF, 0°C, 5 h, 78%; c) allyl bromide (20 equiv), Hünig base (25 equiv), $CH_2Cl_2$, 50°C, 16 h, 66%; d) KCN (9 equiv), AcOH, 25°C, 4 h, 79%; e) TFA (1 equiv), $CH_2Cl_2$, −20°C, 30 min, 54%. DIBAL-H = diisobutylaluminum hydride; TFA = trifluoroacetic acid.

triol **29**. The latter, upon treatment with a 1:1 ate complex of BuLi and DIBAL-H,[23] underwent partial reduction of the lactam to provide oxazolidine **30**. The reduction seemed to be highly dependent on the reactivity of the ate complex, which may differ from batch to batch. It was found that if there was a slight excess of "BuLi" in the ate complex, the Troc protecting group was easily reduced.[24] Fortunately, the phenol hydroxy group was selectively protected as its allyl ether by treatment of oxazolidine **30** with allyl bromide in the presence of Hünig base. Upon exposure to KCN in acetic acid, **30** underwent ring opening and simultaneous introduction of the C21 cyano group to give aminonitrile **31** as a single isomer. The MOM group was cleaved by treatment of **31** with TFA to give the goal compound **32**. As this compound is an advanced intermediate in the Fukuyama total synthesis of **1**,[2d] our work described herein constitutes a formal total synthesis of ecteinascidin 743.

Having validated our routes, we are now in a position to redirect our focus to reaching ecteinascidin 743 by novel and far more concise pathways without necessarily intersecting an existing pathway. We note that several fascinating pieces of chemistry have been developed herein: 1) the very straightforward routes to the matched subunits **16** and **17**, 2) the use of an unusual *o*-hydroxystyrene moiety for the vinylogous Pictet–Spengler cyclization, and 3) exploitation of an unusual enamide epoxide for the hydration of the C3–C4 double bond, in the desired sense, through reductive treatment of **25**. We are currently exploring direct syntheses of ecteinascidin 743 which are enabled by the formal total synthesis described above.

Received: November 9, 2005

**Keywords:** antitumor agents · asymmetric synthesis · natural products · Pictet–Spengler reaction · total synthesis

[1] See the previous Communication in this issue: C. Chan, S. Zheng, B. Zhou, J. Guo, R. M. Heid, S. J. Danishefsky, *Angew. Chem.* **2006**, *118*, 1781; *Angew. Chem. Int. Ed.* **2006**, *45*, 1749.
[2] Isolation of **1**: a) K. L. Rinehart, T. G. Holt, N. L. Fregeau, J. G. Stroh, P. A. Keifer, F. Sun, L. H. Li, D. G. Martin, *J. Org. Chem.* **1990**, *55*, 4512; b) R. Sakai, K. L. Rinehart, Y. Guan, A. H.-J. Wang, *Proc. Natl. Acad. Sci. USA* **1992**, *89*, 11456; total syntheses of **1**: c) E. J. Corey, D. Y. Gin, R. S. Kania, *J. Am. Chem. Soc.* **1996**, *118*, 9202; d) A. Endo, A. Yanagisawa, M. Abe, S. Tohma, T. Kan, T. Fukuyama, *J. Am. Chem. Soc.* **2002**, *124*, 6552; e) J. Chen, X. Chen, M. Bois-Choussy, J. Zhu, *J. Am. Chem. Soc.* **2006**, *128*, 87; semisynthesis of **1**: f) C. Cuevas, M. Pérez, M. J. Martín, J. L. Chicharro, C. Fernández-Rivas, M. Flores, A. Francesch, P. Gallego, M. Zarzuelo, F. de la Calle, J. García, C. Polanco, I. Rodríguez, I. Manzanares, *Org. Lett.* **2000**, *2*, 2545.
[3] For an example of base-induced epimerization at C3, see: J. W. Lane, Y. Chen, R. M. Williams, *J. Am. Chem. Soc.* **2005**, *127*, 12684.
[4] W. Jin, S. Metobo, R. M. Williams, *Org. Lett.* **2003**, *5*, 2095.
[5] a) B. Zhou, J. Guo, S. J. Danishefsky, *Org. Lett.* **2002**, *4*, 43; b) B. Zhou, S. Edmondson, J. Padron, S. J. Danishefsky, *Tetrahedron Lett.* **2000**, *41*, 2039; c) B. Zhou, J. Guo, S. J. Danishefsky, *Tetrahedron Lett.* **2000**, *41*, 2043.
[6] C. Chan, R. Heid, S. Zheng, J. Guo, B. Zhou, T. Furuuchi, S. J. Danishefsky, *J. Am. Chem. Soc.* **2005**, *127*, 4596.
[7] X. Chen, J. Chen, M. De Paolis, J. Zhu, *J. Org. Chem.* **2005**, *70*, 4397.
[8] For an excellent review of the tetrahydroisoquinoline alkaloids, see: J. D. Scott, R. M. Williams, *Chem. Rev.* **2002**, *102*, 1669.
[9] For a previous example of the connection of the subunits by amide bond formation to a secondary amine, see: E. J. Martinez, E. J. Corey, *Org. Lett.* **2000**, *2*, 993.
[10] A. K. Sinhababu, A. K. Ghosh, R. T. Borchardt, *J. Med. Chem.* **1985**, *28*, 1273.
[11] R. M. Williams, P. P. Ehrlich, W. Zhai, J. Hendrix, *J. Org. Chem.* **1987**, *52*, 2615.
[12] A. Fujii, S. Hashiguchi, N. Uematsu, T. Ikariya, R. Noyori, *J. Am. Chem. Soc.* **1996**, *118*, 2521.
[13] A. S. Thompson, G. R. Humphrey, A. M. DeMarco, D. J. Mathre, E. J. Grabowski, *J. Org. Chem.* **1993**, *58*, 5886.
[14] a) J. M. Bobbitt, J. C. Sih, *J. Org. Chem.* **1968**, *33*, 856; b) J. M. Bobbitt, T. E. Moore, *J. Org. Chem.* **1968**, *33*, 2958.
[15] K. Laali, R. J. Gerzina, C. M. Flajnik, C. M. Geric, A. M. Dombroski, *Helv. Chim. Acta* **1987**, *70*, 607.
[16] D. B. Dess, J. C. Martin, *J. Am. Chem. Soc.* **1982**, *104*, 902.
[17] P. Four, F. Guibe, *Tetrahedron Lett.* **1982**, *23*, 1825.
[18] For a related example, see: M. J. Martin-Lopez, F. Bermejo-Gonzalez, *Tetrahedron Lett.* **1994**, *35*, 8843.
[19] E. J. Corey, J. Das, *Tetrahedron Lett.* **1982**, *23*, 4217.
[20] J. D. Hobson, J. G. McCluskey, *J. Chem. Soc.* **1967**, 2015.
[21] Direct McCluskey reaction of a MOM derivative of the type **9** failed owing to undesired reactivity at the MOM ether protecting group.
[22] For a related rearrangement versus selective reduction of an enamide epoxide, see: L. A. Mitscher, H. Gill, J. A. Filppi, R. L. Wolgemuth, *J. Med. Chem.* **1986**, *29*, 1277.

 © 2006 Wiley-VCH Verlag GmbH & Co. KGaA, Weinheim 

[23] S. Kim, K. H. Ahn, *J. Org. Chem.* **1984**, *49*, 1717.
[24] The use of $LiAlH_2(OEt)_2$, $LiAlH_3(OEt)$, and Red-Al gave intractable reaction products. Along these lines, $LiAlH(OtBu)_3$ reduced lactam **29** to oxazolidine **30**, however, in low conversion (10%), whereas boranes afforded the corresponding amine by exhaustive reduction of the lactam.

 © 2006 Wiley-VCH Verlag GmbH & Co. KGaA, Weinheim 

*Molecular Devices*

DOI: 10.1002/anie.200502511

# Construction of Molecular Logic Gates with a DNA-Cleaving Deoxyribozyme**

*Xi Chen, Yifei Wang, Qiang Liu, Zhizhou Zhang,* Chunhai Fan,* and Lin He**

Logic gates are devices that perform the basic logic operations AND, NOT, and OR, as well as their combinations. It is well-known that electronic logic gates form the basis of conventional silicon computer microprocessors. By analogy, molecular logic gates are crucial for the development of molecular-scale computers, which have attracted significant research interest.[1] In particular, nucleic acids (DNA and RNA) have proven to be highly useful building blocks for the construction of molecular logic gates and computational devices.[2–8] Herein, we report the construction of molecular logic gates that are made entirely of DNA molecules. As examples, we demonstrate the performance of logic operations including "YES", "NOT", and a three-input gate "AND(A,NOT(B),NOT(C))" through the recognition and catalytic properties of DNA. Notably, the combination of the "NOT" gate and the "AND(A,NOT(B),NOT(C))" gate can, in principle, make a universal operator set.

Artificially designed DNA or RNA sequences can fold into well-ordered, three-dimensional structures that either recognize corresponding ligands (aptamers)[9] or catalyze specific chemical reactions (deoxyribozymes or ribozymes).[10–21] In their pioneering work, Stojanovic and co-workers constructed molecular logic gates based on in vitro selected RNA-cleaving deoxyribozymes (DNAzymes) by exploiting allosteric regulation.[6–8] In their system, the activities of deoxyribozymes were allosterically regulated by specific effectors, which were rationally designed oligonucleotides containing complementary sequences to target deoxyribozymes. Either the presence or the absence of effectors was employed as the input, while intact or cleaved substrates were regarded as outputs. The same group later constructed complex systems based on this elegant strategy, such as a molecular-scale half-adder[7] and a MAYA automaton that could play a tic-tac-toe game with a human adversary.[8]

Despite the elegance of this strategy, these logic gates remain to be improved. In particular, as they are based on RNA-cleaving deoxyribozymes, the corresponding substrates must be either RNA or chimeric DNA (a piece of oligodeoxynucleotide containing at least one ribonucleotide base).[6–8] This prerequisite leads to high synthesis costs and susceptibility to oligonucleotide degradation. In view of this fact, it is highly desirable to develop ribonucleotide-free molecular logic gates. Herein, we employ a $Cu^{2+}$-dependent DNA-cleaving deoxyribozyme as the building block for the construction of robust molecular logic gates that are based on DNA only. Our inputs (effectors), gates (deoxyribozymes), and outputs (substrates) are all inexpensive, chemically stable DNA oligonucleotides (Figure 1). The $Cu^{2+}$-dependent DNA-cleaving deoxyribozyme, which was first isolated by Breaker and co-workers,[22] can catalytically cleave DNA substrates by oxidative modification of DNA, which involves the generation of hydroxyl radicals through metal-ion-mediated redox reactions.[22–24]

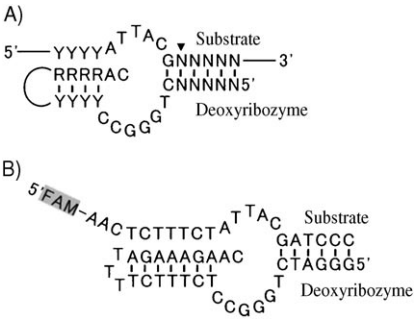



***Figure 1.*** The $Cu^{2+}$-dependent deoxyribozyme and logic gates. A) Structure and consensus sequence of $Cu^{2+}$-dependent deoxyribozyme for DNA substrate cleavage. R, Y, and N represent purine, pyrimidine, and any nucleotide, respectively. The triangle identifies the cleavage site of the substrate. B) Deoxyribozyme as the building block of logic gates and its corresponding substrate. FAM = fluorescein dye.

[*] X. Chen, Y. Wang, Q. Liu, Prof. Dr. Z. Zhang, Prof. Dr. C. Fan, Prof. Dr. L. He
Bio-X Life Science Research Center
Shanghai Jiao Tong University, Shanghai 200030 (China)
Fax: (+86) 21-6282-2491
E-mail: zhangzz@sjtu.edu.cn
fchh@sinap.ac.cn
helin@sjtu.edu.cn
Prof. Dr. C. Fan
Shanghai Institute of Applied Physics
Chinese Academy of Sciences, Shanghai 201800 (China)
Fax: (+86) 21-5955-6902
Prof. Dr. Z. Zhang
Tianjin University of Science and Technology
Tianjin 300040 (China)
Fax: (+86) 22-6027-2071

[**] This work was supported by Shanghai Municipal Commission for Science and Technology (Grant Nos. 03DZ14025, 02JC14029, 0452m068, 60537030), the Shanghai Rising-Star Program, National Natural Science Foundation (20404016), the National "863" Project (Grant No. 2003AA226011), the Key Projects of the Ministry of Education (No. 03066), and the Chinese Academy of Sciences.

Supporting information for this article is available on the WWW under http://www.angewandte.org or from the author.

 © 2006 Wiley-VCH Verlag GmbH & Co. KGaA, Weinheim 

We first constructed a "YES" gate (positive sensor) by employing a deoxyribozyme, DNAzyme_X, with a positive-regulation module (Figure 2, top left). In this design, two modules (oligonucleotides) were appended to either the 3′ or

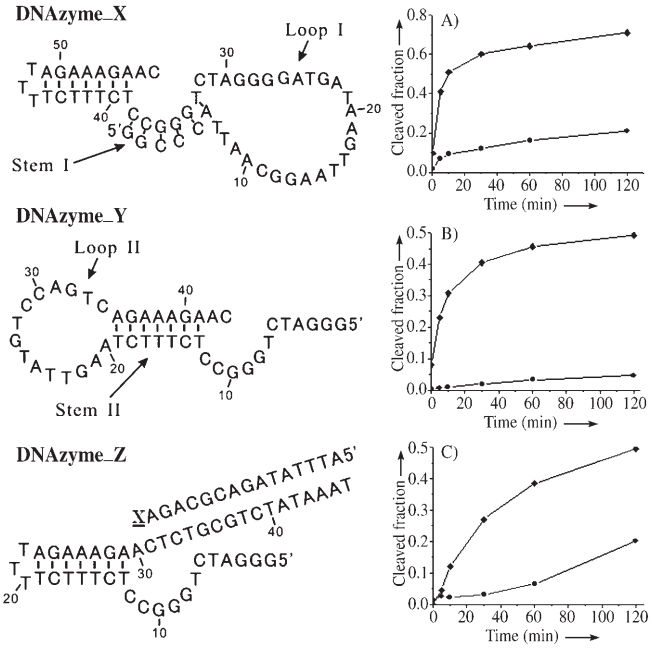



***Figure 2.*** Left: Secondary structures of DNAzymes: DNAzyme_X ("YES" gate), DNAzyme_Y ("NOT" gate I), and DNAzyme_Z ("NOT" gate II). Schematic drawings and detailed descriptions of the transition between the "ON" and "OFF" states for these three gates are shown in the Supporting Information. Right: Plots of the reaction time versus fraction of cleaved products ("ON" (●), "OFF" (◆); the corresponding PAGE pictures are shown in the Supporting Information). A) DNAzyme_X ("YES" gate); B) DNAzyme_Y ("NOT" gate I); C) DNAzyme_Z ("NOT" gate II).

5′ end of the hammerhead-like deoxyribozyme (see Supporting Information). The distal module was complementary to the catalytic core while the proximal module served as the flexible loop (loop I). In the absence of the effector EX, which contained a complementary sequence to loop I (T7–G26), the distal module formed a stem (stem I) with the catalytic core. This stem formation disrupted the structure of the catalytic core and set DNAzyme_X at the "OFF" state. In the presence of the effector EX, the binding of EX to loop I prevented the formation of stem I, thus turning the DNAzyme_X to the "ON" state. As demonstrated in Figure 2A and in the Supporting Information, the activity of DNAzyme_X was effectively regulated by the effector EX, with the apparent catalytic reaction rate constant $k_{obs}$ at ca. 0.1 $min^{-1}$ of the "ON" state and ca. 0.01 $min^{-1}$ of the "OFF" state (ON/OFF ratio 10:1). This ON/OFF ratio, while already sufficient for demonstration of the "YES" gate effect, might be further improved by appending distal modules to both ends, which should significantly reduce the $k_{obs}$ value of the "OFF" state.[25] Notably, the effector binds to the catalytic core in this "YES" gate design, instead of to the substrate-recognition region, which makes it feasible to realize multiple turnovers. This important feature should be applicable to the design of other molecular logic gates, and might lead to significant improvement in the $k_{obs}$ value of the "ON" state.

We then constructed a "NOT" gate (negative sensor) by using DNAzyme_Y (Figure 2, center left) which contained a negative-regulation module (loop II, A20–C34). Note that the triplex-forming stem-loop was essential for DNAzyme_Y (see Supporting Information).[23,24] In the absence of the effector EY, the deoxyribozyme was active ("ON" state) as the triplex was intact. In contrast, in the presence of the effector, EY bound to loop II, which competitively opened stem II and disrupted triplex formation. This process effectively inhibited the enzyme activity and set the DNAzyme_Y at the "OFF" state. With this "NOT" gate, we observed that the $k_{obs}$ of the "ON" state was ca. 0.05 $min^{-1}$, whereas that of the "OFF" state was ca. 0.001 $min^{-1}$, which indicates that the ON/OFF ratio of this "NOT" gate reached 50:1 (Figure 2B and Supporting Information).

The "NOT" gate can also be constructed by introducing a "pistol-like" structure of the deoxyribozyme (Figure 2, bottom left). It was reported that the two deoxyribonucleotide moieties of the 3′ terminus, "AC", were conserved during in vitro selection,[23] which suggests that these two deoxyribonucleotides are crucial for catalysis. In spite of this, partially truncated deoxyribozymes (in the absence of 3′-terminal C) were reported to be active in the presence of both $Cu^{2+}$ ions and ascorbate.[24] We then designed a deoxyribozyme, DNAzyme_Z, which had an extended sequence at the 3′ terminus (see Supporting Information). We employed five potential effectors, each being partially complementary to DNAzyme_Z (EZ: T32–T46, EZ-G: C31–T46, EZ-GT: A30–T46, EZ-GTT: A29–T46, and EZ-GAA: C31–T46). By individually analyzing the deoxyribozyme activity in the presence of both $Cu^{2+}$ and ascorbate, we observed that pairing of the effector with C31 had little effect on the catalytic activity, pairing with both C31 and A30 reduced the catalytic activity to some extent, and pairing with C31, A30, and A29 strongly inhibited the deoxyribozyme (data not shown). Therefore, we selected the strongest inhibitor EZ-GTT as the effector for the "NOT" gate. Interestingly, when DNAzyme_Z was treated with EZ-GTT, the initial $k_{obs}$ value was close to zero. However, we observed that the rate increased with the incubation time (Figure 2C and Supporting Information). Given that the effector was located at the catalytic core of DNAzyme_Z, the increase of $k_{obs}$ might be caused by the destruction of the effector and/or the negative-regulation module. In spite of this apparent time-dependent change of activity at the "OFF" state, the signal-to-noise ratio in the first 20 minutes of the reaction was sufficient for its function as a "NOT" gate (ON/OFF ratio 10:1), that is, DNAzyme_Z was at the "ON" state in the absence of the effector EZ-GTT and at the "OFF" state in the presence of the effector.

On the basis of this "NOT" gate with the pistol-like structure, we further designed an $A \wedge \neg B \wedge \neg C$ gate (A ANDNOT B ANDNOT C, or in the prefix form, AND-(A,NOT(B),NOT(C))). As far as we know, such a DNA-based logic gate has not been previously reported. By definition, the logic gate $A \wedge \neg B \wedge \neg C$ is at the "ON" state when and only when input A is "1", input B is "0", and

 © 2006 Wiley-VCH Verlag GmbH & Co. KGaA, Weinheim 

input C is "0". We then proposed that DNAzyme_XYZ (Figure 3A) could function as the logic gate $A \wedge \neg B \wedge \neg C$ by defining the presence of effectors as input 1 and their absence as input 0. We examined the catalytic activity of DNAzyme_XYZ in either the absence or presence of one or several of the three effectors ($2^3 = 8$ combinations). As expected, after 20 min reaction time the cleaved product was only observed when the deoxyribozyme was treated with EX, while the absence of both EY and EZ-GTT induced substrate cleavage (Figure 3B). We thus successfully demonstrated the construction of a DNA-based three-input logic gate based on simple, basic logic gates. Importantly, this novel gate may form the basis of completely DNA-based half-adders[7] or automata.[8]

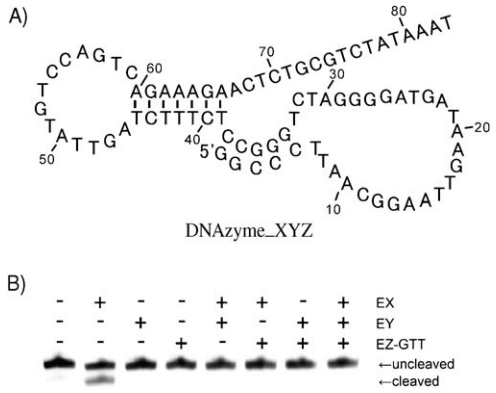



***Figure 3.*** Three-input logic gate $A \wedge \neg B \wedge \neg C$. A) Secondary structure of DNAzyme_XYZ. B) Products and precursors were analyzed by 12% denatured PAGE after 20 min reaction. The employed effectors are the same as those described in Figure 2. The symbols + and − stand for the presence (input 1) and absence (input 0) of effectors, respectively. "Uncleaved" and "cleaved" indicate intact and cleaved products, respectively. Note that the cleaved product (output) is only observed in the presence of EX and in the absence of both EY and EZ-GTT.

The proposed logic gate system based on DNA-cleaving deoxyribozyme has several inherent advantages. First, in contrast to RNA or chimeric DNA, the synthesis of DNA oligonucleotides is fairly inexpensive. Second, unlike chimeric DNA that can only be chemically synthesized, DNA strands might be produced by the PCR, which is much more convenient in molecular biology laboratories. Third, our system is completely DNA-based, thus obviating the special precautions required in the use of RNase which may induce unexpected substrate degradation. Fourth, the speed of our system matches or even exceeds that of the previously reported sequence-specific nucleic acid sensing systems based on RNA-cleaving deoxyribozymes ($k_{obs} > 0.01\ min^{-1}$ at the "ON" state). In addition, this $Cu^{2+}$-dependent deoxyribozyme might inspire many other interesting applications. For example, products of oxidative cleavage carry 3′-terminal-modified phosphates, which are resistant to 3′ to 5′ exonucleases.[24] This means that these products are potentially insusceptible to the restriction–modification system in living organisms. This feature may allow the design of a programmed DNA modification system in which the modification ability comes from the oxidative cleavage activity of deoxyribozymes.

In view of these advantages of our logic-gate system, the sequences of the deoxyribozymes involved remain to be further optimized. Notably, the gate activities of oligonucleotides with minor sequence differences can vary by as much as several orders of magnitude. Other possible disadvantages are as follows: First, the optimal conditions for the oxidative cleavage reaction of deoxyribozymes are different from physiological conditions,[24] and thus the logic gates described herein are not expected to work in vivo in their present form. Second, deoxyribozymes are known to undergo self-cleavage. The self-cleavage rate is significantly lower than that of substrate cleavage,[24] but this still makes it difficult to achieve multiturnover, which is a useful feature for the design of biosensors with amplified signals. These problems still remain to be explored.

In summary, we have described the construction of DNA-based molecular logic gates through modular design. In contrast to all previously reported ribonucleotide-containing systems, the employment of a $Cu^{2+}$-dependent DNA-cleaving deoxyribozyme enabled us to design the highly robust logic gates "YES", "NOT", and $A \wedge \neg B \wedge \neg C$ solely with DNA molecules. This strategy should be potentially useful for the construction of any DNA-based molecular logic gates and computing devices that are essentially free from RNase digestion.

## Experimental Section

Oligonucleotides and reagents: The oligonucleotides were obtained from Bioasia (Shanghai) and purified by high-pressure liquid chromatography (HPLC). Stock solutions of oligonucleotides (10–40 μM) were stored at −20 °C. The sequences of the effectors EX and EY were 5′-CTACTATTCAATTCCGTTAA and 5′-CACTGGACATAACTT, respectively. The sequences of the other oligonucleotides are shown in the figures. The secondary structures of the oligonucleotides were examined by using Zuker and Turner's "mfold" DNA-folding site (http://www.bioinfo.rpi.edu/applications/mfold/old/dna/). The concentrations of the oligonucleotides were measured by UV absorption at 260 nm. L-Ascorbate (Ameresco) was stored in aliquots (100 μM) at −20 °C.

Reaction conditions: Reactions were carried out at 23 °C in the presence of 5′-FAM tagged substrate (250 nM), deoxyribozyme (250 nM), effector (10 μM), HEPES buffer (50 mM, pH 7.0), NaCl (0.3 M), $CuCl_2$ (10 μM), and L-ascorbate (10 μM). Note that although this deoxyribozyme exhibits significant catalytic activity in the presence of $Cu^{2+}$ as the only cofactor,[23] the co-existence of $Cu^{2+}$ and ascorbate further facilitates the DNA cleavage reaction.[24] Before starting the catalytic reaction, deoxyribozymes and effectors (if used) were mixed in the reaction buffer, heated to 90 °C for 1 min, and then slowly cooled to room temperature during a 30-min period. The substrates were then added to the solution and the reaction was initiated by the addition of both $CuCl_2$ and L-ascorbate.

Kinetic analysis: Aliquots were removed at appropriate intervals and quenched with the stop buffer (40 mM EDTA, 8 M urea, 89 mM Tris base, 89 mM boric acid, 20% sucrose, and 0.5% bromophenol blue). Gel electrophoresis was carried out with a Bio-Rad Mini-Protean II cell, and a fluorescence image was obtained and quantified by a Kodak Image Station 2000 MM with ImageQuant (Molecular

 © 2006 Wiley-VCH Verlag GmbH & Co. KGaA, Weinheim 

Dynamics). The $k_{obs}$ value was determined from the slope of initial values in plots of cleaved fraction versus time.

Received: July 19, 2005
Revised: November 21, 2005
Published online: February 10, 2006

**Keywords:** biosensors · DNA · molecular devices · ribozymes · RNA

[1] A. Saghatelian, N. H. Volcker, K. M. Guckian, V. S.-Y. Lin, M. R. Ghadiri, *J. Am. Chem. Soc.* **2003**, *125*, 346.
[2] L. M. Adleman, *Science* **1994**, *266*, 1021.
[3] Q. Liu, L. Wang, A. G. Frutos, A. E. Condon, R. M. Corn, L. M. Smith, *Nature* **2000**, *403*, 175.
[4] Y. Benenson, T. Paz-Elizur, R. Adar, E. Keinan, Z. Livneh, E. Shapiro, *Nature* **2001**, *414*, 430.
[5] A. Okamoto, K. Tanaka, I. Saito, *J. Am. Chem. Soc.* **2004**, *126*, 9458.
[6] M. N. Stojanovic, T. E. Mitchell, D. Stefanovic, *J. Am. Chem. Soc.* **2002**, *124*, 123.
[7] M. N. Stojanovic, D. Stefanovic, *J. Am. Chem. Soc.* **2003**, *125*, 6673.
[8] M. N. Stojanovic, D. Stefanovic, *Nat. Biotechnol.* **2003**, *21*, 1069.
[9] S. E. Osborne, A. D. Ellington, *Chem. Rev.* **1997**, *97*, 349.
[10] K. Kruger, P. J. Grabowski, A. J. Zaug, J. Sands, D. E. Gottschling, T. R. Cech, *Cell* **1982**, *31*, 147.
[11] C. Guerrier-Takada, K. Gardiner, T. Marsh, N. Pace, S. Altman, *Cell* **1983**, *35*, 849.
[12] J. Tang, R. R. Breaker, *Chem. Biol.* **1997**, *4*, 453.
[13] G. A. Soukup, R. R. Breaker, *Curr. Opin. Struct. Biol.* **2000**, *10*, 318.
[14] M. P. Robertson, A. D. Ellington, *Nat. Biotechnol.* **1999**, *17*, 62.
[15] M. P. Robertson, A. D. Ellington, *Nucleic Acids Res.* **2000**, *28*, 1751.
[16] M. Araki, Y. Okuno, Y. Hara, Y. Sugiura, *Nucleic Acids Res.* **1998**, *26*, 3379.
[17] D. Y. Wang, B. H. Lai, A. R. Feldman, D. Sen, *Nucleic Acids Res.* **2002**, *30*, 1735.
[18] D. H. Burke, N. D. Ozerova, M. Nilsen-Hamilton, *Biochemistry* **2002**, *41*, 6588.
[19] Y. Komatsu, S. Yamashita, N. Kazama, K. Nobuoka, E. Ohtsuka, *J. Mol. Biol.* **2000**, *299*, 1231.
[20] T. Kuwabara, M. Warashina, K. Taira, *Trends Biotechnol.* **2000**, *18*, 462.
[21] M. N. Stojanovic, P. de Prada, D. W. Landry, *ChemBioChem* **2001**, *2*, 411.
[22] N. Carmi, L. A. Shultz, R. R. Breaker, *Chem. Biol.* **1996**, *3*, 1039.
[23] N. Carmi, S. R. Balkhi, R. R. Breaker, *Proc. Natl. Acad. Sci. USA* **1998**, *95*, 2233.
[24] N. Carmi, R. R. Breaker, *Bioorg. Med. Chem.* **2001**, *9*, 2589.
[25] V. Saksmerprome, D. H. Burke, *Biochemistry* **2003**, *42*, 13879.

 © 2006 Wiley-VCH Verlag GmbH & Co. KGaA, Weinheim 

Bioinorganic Chemistry

DOI: 10.1002/anie.200502602

# Shaping Amorphous Calcium Carbonate Films into 2D Model Substrates for Bone Cell Culture**

*Daniela C. Popescu, Ellen N. M. van Leeuwen, Nicholas A. A. Rossi, Simon J. Holder, John A. Jansen, and Nico A. J. M. Sommerdijk**

Bone is a highly organized composite material that has the capacity to heal and remodel itself. During the remodeling process, bone is resorbed by osteoclasts (bone-resorbing cells), which subsequently undergo apoptosis or return to the non-resorbing stage. Their place is taken by osteoblasts (bone-producing cells), which synthesize the new mineralized matrix.[1,2] Nevertheless, the self-repair of bone is limited to small bone defects, and its ability to regenerate decreases with age and is affected by diseases. Amongst other materials, biogenic calcium carbonate, for example, coral skeletons and sea urchin spines, has been developed as a promising material for bone replacement and regeneration as it is easily resorbed by osteoclasts and replaced by native bone. Moreover, nacre (present in mollusk shells) shows bone-conductive properties, that is, it stimulates the activity of osteoblasts and induces the formation of new bone. Synthetic, bio-inspired organic–inorganic composites are currently emerging as new materials for bone regeneration, and offer more possibilities to tune

[*] D. C. Popescu, E. N. M. van Leeuwen, Dr. N. A. J. M. Sommerdijk
Laboratory of Macromolecular and Organic Chemistry
Eindhoven University of Technology
P.O. Box 513, 5600 MB, Eindhoven (The Netherlands)
Fax: (+31) 402451036
E-mail: N.Sommerdijk@tue.nl

Dr. N. A. A. Rossi, Dr. S. J. Holder
The Functional Materials Group, School of Physical Sciences
University of Kent, Canterbury CT2 7NR, Kent (UK)

Prof. Dr. J. A. Jansen
Department of Periodontology and Biomaterials
Radboud University Nijmegen Medical Center
P.O. Box 9101, 6500 HB Nijmegen (The Netherlands)

[**] We thank Marijke Siebers and Anja de Ruiter (Radboud University Nijmegen) for providing us with rat BMSC and cell-culture protocols, Otto L. G. van Asselen (Eindhoven University of Technology) for help with the FTIR measurements, Marco R. M. Hendrix and Yuanqiang Q. Li (Eindhoven University of Technology) for the PXRD measurements, Peter C. Thüne (Eindhoven University of Technology) for the XPS studies, Philippe E. L. G. Leclère (Université de Mons-Hainaut) for help with the AFM measurements, and Waldo J. E. Beek (Eindhoven University of Technology) for the surface profilometry. We are grateful to E. W. Meijer (Eindhoven University of Technology) for his critical review of the manuscript and we thank the NWO-CW and the EPSRC (Grant no. GR/R37463) for financial support.

Supporting information for this article (including experimental details) is available on the WWW under http://www.angewandte.org or from the author.


WILEY InterScience DISCOVER SOMETHING GREAT
© 2006 Wiley-VCH Verlag GmbH & Co. KGaA, Weinheim

biocompatibility, biodegradability, and mechanical properties.[3,4]

Bone cell–substrate interactions play an important role in the integration of the biomimetic scaffolds into the natural bone tissue.[5] The development of 2D models is desirable to monitor the interactions of bone cells with scaffold materials, as well as the remodeling process. In vitro model systems can provide valuable information for the design of new biomaterials with a controlled bone–biomaterial interface.[6] A substrate consisting of alternating mineral and nonmineralized lanes can be seen in a cross-section through a 3D porous inorganic scaffold (Figure 1 a), which would allow unlimited transport of nutrients and the live observation of cells during their development (for example, by optical microscopy). Furthermore, 2D patterned substrates consisting of alternating mineralized and nonmineralized regions would also in principle offer the possibility to compare the behavior of the cells in regions with different concentrations of mineral ions (such as $Ca^{2+}$). It is known, for example, that the extracellular concentration of calcium ions controls the proliferation, differentiation, and function of osteoblasts,[7,8] and it has been suggested that the gradual dissolution of biomaterials such as hydroxyapatite, which releases $Ca^{2+}$ ions, might be responsible for their osteoconductive properties.[7,9]

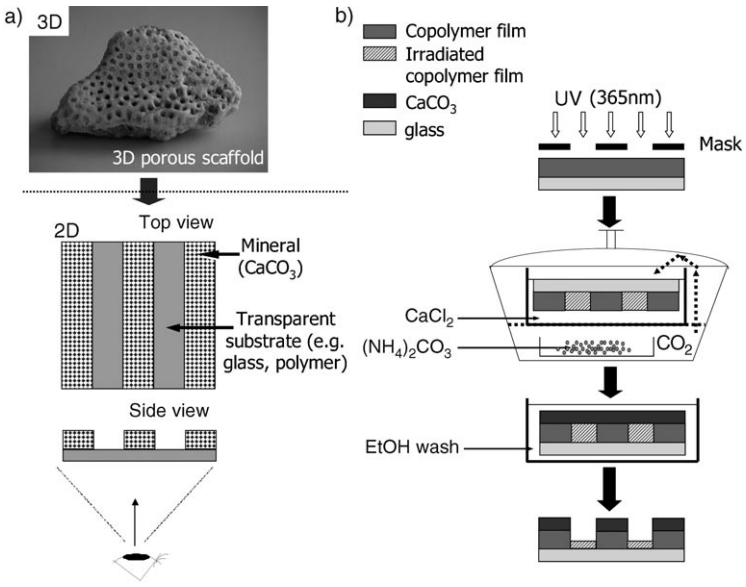


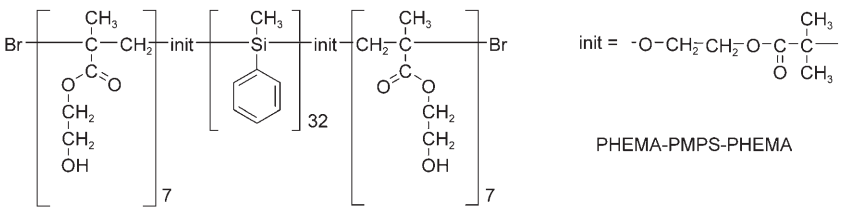

***Figure 1.*** Schematic representation of a) a 2D model substrate consisting of alternating lanes of mineral ($CaCO_3$) and nonmineralized lanes (bottom), which can be seen as a cross-section through a 3D porous inorganic scaffold, such as the piece of coral shown in the top image, and b) of the experimental procedure for the generation of patterns of $CaCO_3$. Dimensions are not to scale.

Patterned self-assembled monolayers (SAMs) have been instrumental in obtaining ordered arrays of minerals,[10–13] patterned single crystals of calcite,[14] as well as patterned continuous mineral films.[13,15–19] The $CaCO_3$ patterns generally are produced by the method developed by Aizenberg et al. which is based on diffusion-limited crystal nucleation and growth.[10–12,15,19] However, the application of SAMs is in principle limited to a small number of substrates. Materials and simple methods that are more generally applicable to the generation of 2D mineral patterns on a variety of substrates are highly desirable.

In nature many organisms make use of amorphous calcium carbonate (ACC) as a transient intermediate for the production of single crystals of calcite and aragonite with elaborate shapes. Being isotropic, ACC can be deposited in any desired shape and, in addition, can sustain mechanical deformations from all directions.[20,21] Although the ACC is normally unstable and transforms immediately into one of the crystalline forms in a synthetic environment, it has been shown to play a crucial role as a precursor phase in the preparation of crystalline $CaCO_3$ films.[22–27] Thin films of $CaCO_3$ can be obtained in the presence of soluble acidic macromolecules, such as poly(acrylic acid) (PAA), poly(aspartic acid), and poly(glutamic acid).[22–33] In some cases, the amorphous phase is temporarily stabilized by these macromolecules during the mineralization process.

We report herein the generation of patterned calcium carbonate films with dimensions of several hundreds of micrometers using the photolithographic properties of an amphiphilic ABA block copolymer—poly(hydroxyethyl methacrylate-*block*-methylphenylsilane-*block*-hydroxyethyl methacrylate) (PHEMA-PMPS-PHEMA)—and the possibility to shape calcium carbonate in its amorphous state. We further show that these patterns serve as 2D model systems for $CaCO_3$ biomaterials. Although several systems have been used before for the guidance of bone cells,[34,35] the present system is, to our knowledge, the first example of mineral patterns consisting of alternating mineralized and nonmineralized regions that were designed as a 2D model substrate for studying the interaction of bone cells with the mineral.

Polysilane-derived polymers show good photolithographic properties as a result of the photochemical lability of the Si–Si bonds in the σ-conjugated Si backbone.[36] We recently reported on the formation and stability of thin films of different amphiphilic poly(methylphenylsilane)-based ABA block copolymers in aqueous media.[37] Cho and co-workers recently demonstrated that hydroxy-modified surfaces were particularly suited for the formation of thin films of $CaCO_3$[38] and so we selected the PHEMA-PMPS-PHEMA copolymer ($M_n = 6600$, $M_w/M_n = 1.5$), which consists of two hydrophilic biocompatible segments (PHEMA)[39] and one apolar polymer block (PMPS; Scheme 1). Thin films of




***Scheme 1.*** Structure of the PHEMA-PMPS-PHEMA copolymer.

 © 2006 Wiley-VCH Verlag GmbH & Co. KGaA, Weinheim 

this polymer were demonstrated to be stable in aqueous media and may be expected to expose some of the OH groups at the polymer–water interface.[37]

PHEMA-PMPS-PHEMA was spin cast from a 5 mg mL$^{-1}$ solution in THF onto glass substrates to yield thin films with a thickness of approximately 30 nm, as demonstrated by AFM. Continuous films of $CaCO_3$ were grown on this polymer layer by immersing them in an aqueous $CaCl_2$ solution containing poly(acrylic acid) (PAA) and allowing $CO_2$ vapor from $(NH_4)_2CO_3$ to diffuse into these solutions. Surface profilometry showed that the average thickness of the $CaCO_3$ films was approximately 1 μm. Optical microscopy studies with cross-polarizers revealed that the as-prepared films did not display birefringence, except for a few spherical domains (Figure 2a), thus indicating that the films were amorphous

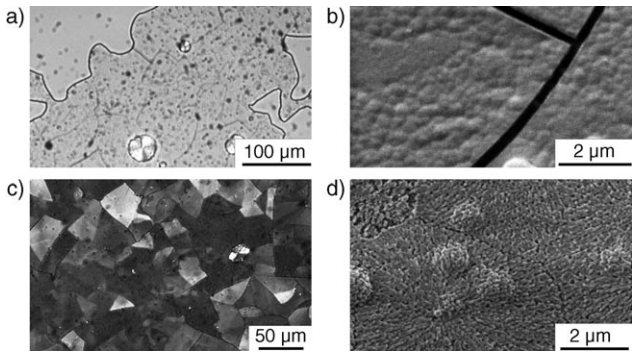



***Figure 2.*** Optical micrographs under cross-polarized light of: a) a $CaCO_3$ film (amorphous) within 2 h of preparation and c) a $CaCO_3$ film (crystalline) 24 h after preparation. Scanning electron micrographs of the above films within: b) 2 h and d) 24 h of preparation.

with few embedded crystalline spherulites. The FTIR spectrum of the freshly prepared $CaCO_3$ films showed vibrations characteristic of amorphous calcium carbonate at 1489 and 1408 cm$^{-1}$ (double carbonate vibration), at 1076 cm$^{-1}$, and two broad bands at 874 cm$^{-1}$ and 710 cm$^{-1}$ (see the Supporting Information).[21,23] Moreover, SEM studies revealed that the freshly prepared films consisted of spherical particles with diameters smaller than 0.5 μm, which are characteristic of ACC (Figure 2b).[22]

The films crystallized upon standing, as demonstrated by the observation, under the cross-polarizers, of a characteristic mosaic structure resulting from the birefringence of the crystals (Figure 2c).[23,24,26] The presence of crystallites with dimensions of 300–400 nm was also observed by SEM (Figure 2d), and the FTIR spectrum was dominated by peaks characteristic of calcite at 1796, 1416, 876, and 713 cm$^{-1}$ (see the Supporting Information).[21] A shoulder on the peak at 1416 cm$^{-1}$ and a very small peak around 1083 cm$^{-1}$ indicated that some vaterite was also present in the crystalline film. Powder X-ray diffraction (PXRD) studies showed the presence of Bragg peaks consistent with a film composed of calcite and vaterite (see the Supporting Information), similar to the observations of Cho and co-workers.[24,38] The relative intensities of the XRD peaks for the two polymorphs were close to those of a calcite and vaterite powder reference sample, thus indicating that the film did not show a preferred crystallographic orientation, as expected for substrates without a preorganized array of functional groups at the surface.[23]

To obtain patterns the neat copolymer films were irradiated with UV light through a mask with dimensions of 200 μm (covered lanes) and 400 μm (irradiated lanes) for two hours. The dimensions of the patterns were chosen such that they exceeded the size of bone cells, which in the case of osteoclasts can reach sizes of 50–100 μm. The degradation of the PMPS block as a function of time of exposure to UV light was monitored by following the decrease in its characteristic fluorescence peak around 365 nm (see the Supporting Information). Surface profilometry showed that after subsequent developed by treatment with ethanol, a pattern of polymer lanes approximately 200 μm wide and 30 nm high was obtained. When these patterned films were subjected to the mineral film formation process, amorphous $CaCO_3$ was deposited both on the polymer lanes and on the areas from which the polymer had been removed, and no pattern formation could be observed. However, when the mineral was deposited onto a pre-exposed, but undeveloped polymer film, the amorphous $CaCO_3$ layer grown on the irradiated lanes could be selectively removed upon immersion of the film into ethanol, which resulted in the formation of a patterned $CaCO_3$ film (Figures 1b and 3a). The selective

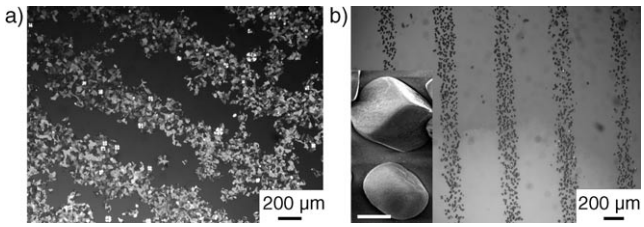



***Figure 3.*** Optical micrographs under cross-polarized light of a) a patterned crystalline $CaCO_3$ film prepared in the presence of PAA and b) of a pattern of discrete calcite and vaterite crystals, obtained in the absence of PAA. Inset in (b): SEM image showing a calcite (top) and a vaterite (bottom) crystal (scale bar: 10 μm).

removal of the $CaCO_3$ only occurred when it existed as an amorphous film; after the film had crystallized, its removal by washing in ethanol proved impossible.

The above results imply that the stabilization of the amorphous phase is crucial for the patterning procedure. Whereas the nonpatterned $CaCO_3$ films (that is, continuous mineral films obtained on the pristine copolymer coatings without UV irradiation and EtOH treatment) were observed to crystallize within 1 h by optical microscopy, the patterned films stayed amorphous for 2—3 h under ambient conditions and were only completely crystalline after 24 h (Figure 3a). This result is probably a consequence of the use of ethanol in the patterning procedure, which was recently demonstrated to stabilize ACC.[40] A further stabilization was achieved by increasing the concentration of PAA from 28 to 65 μg mL$^{-1}$. This extended the lifetime of the amorphous phase to approximately 72 h, but did not further enhance the efficiency of the patterning process.

 © 2006 Wiley-VCH Verlag GmbH & Co. KGaA, Weinheim 

Recently Cho and co-workers also reported the formation of thin films of calcium carbonate in the absence of PAA.[38] However, in the present case only the formation of discrete $CaCO_3$ crystals rather than a continuous mineral film was observed in the absence of PAA (Figure 3b). PXRD studies on these crystals showed Bragg peaks characteristic of calcite and vaterite (see the Supporting Information). The orientation of crystals was random, with a slight preference of the calcite crystals (20–25%) for a (00.1) orientation, as evidenced by the increased intensity of the (00.6) peak relative to the XRD pattern corresponding to a randomly oriented calcite powder reference sample.[11,41] SEM investigation revealed that the samples consisted of about 60% calcite crystals and about 40% vaterite crystals (see the Supporting Information).

When these crystals were grown on irradiated polymer films, development in ethanol was not enough to achieve selective removal of the crystals, however, and an extra step involving peeling of the crystals with adhesive tape was required to obtain a 2D pattern of crystals (Figure 3b). This selective removal of crystals only from the irradiated polymer lanes implies a strong attachment of the crystals to the pristine PHEMA-PMPS-PHEMA films. The removed crystals all possessed smooth flat basal planes with which they had been adhered to the polymer film (see the Supporting Information).

In general, templating surfaces containing OH functionalities usually lead to the formation of calcite expressing the thermodynamically most stable {10.4} faces.[11,42–44] However, SEM images clearly demonstrate that many crystals have not nucleated from the {10.4} faces. The slight preference for (00.1)-oriented crystals as indicated by PXRD implies that the polymer may play an active role in crystal nucleation. Nevertheless, no preferred orientation was observed for the crystalline $CaCO_3$ films. This argues for a role of the amorphous phase, which mediates the formation of the thin films, but does not play an apparent role in the formation of discrete crystals. Furthermore, the fact that ACC films can be removed from the irradiated copolymer lanes by development in ethanol, and that the crystalline $CaCO_3$ films and the discrete crystals cannot implies that there is also a difference in the adhesion of the crystalline and amorphous materials. It may be speculated that the crystalline material acts as a "cross-linker" between the PHEMA-rich copolymer fragments (formed by UV irradiation), thus hindering their dissolution in EtOH and hence the removal of the crystals from the irradiated regions. Nevertheless, the nature of the interaction between the copolymer film and the mineral remains unknown at this stage.

AFM and XPS investigation of the patterned mineral substrates revealed that the lanes where the mineral was removed were still covered with a thin layer rich in PMPS fragments (see the Supporting Information), which have previously been shown to have poor cell adhesive properties.[45] Preliminary cell-culture experiments were performed to test whether these mineral/polymer patterns were suitable for the study of bone-cell–substrate interactions.[46] To this end, rat bone marrow stromal cells (BMSC) were cultured and induced to develop into osteoblast-like (that is, mineral-producing) cells with the aim of monitoring the deposition of new biogenic minerals. These experiments were performed separately on continuous crystallized $CaCO_3$ films and on films of the PHEMA-PMPS-PHEMA copolymer coating after UV irradiation and development to also facilitate the quantitative determination of the alkaline phosphatase (ALP-ase) activity—a marker of early cell differentiation—at different time points. Tissue culture polystyrene (TCPS) was used as a positive control to test whether the cells developed normally in the experimental conditions used.

Phase-contrast microscopy showed that the cells could attach and spread well on crystalline $CaCO_3$ films (comparable to TCPS), while on the developed PHEMA-PMPS-PHEMA regions the cells were less spread and had the tendency to cluster (Figure 4a,b, and see also the Supporting Information). The ALP-ase activity of the cells cultured on

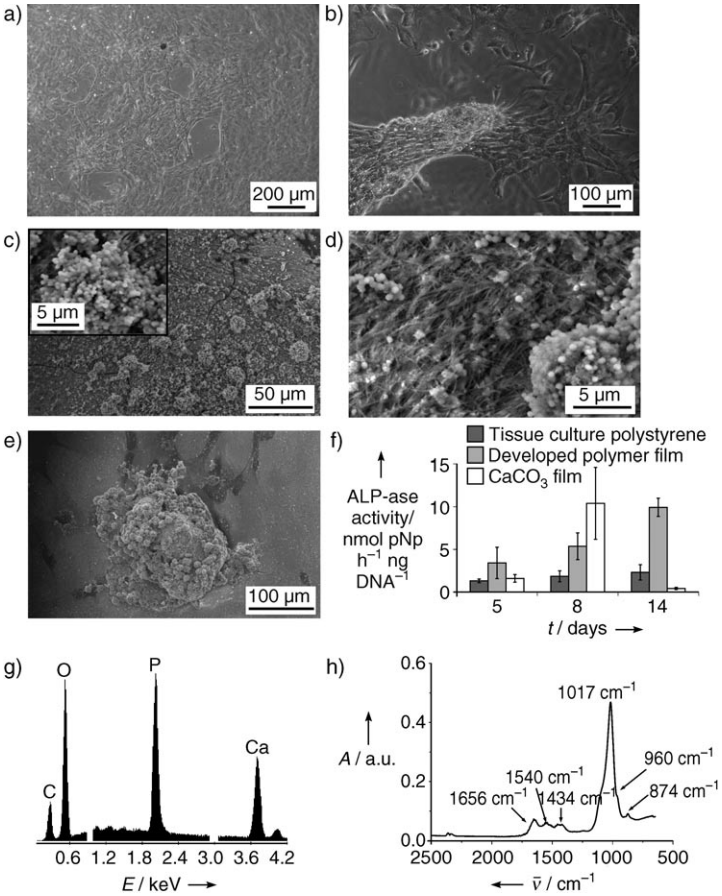



***Figure 4.*** Optical micrographs showing the attachment of rat bone marrow stromal cells (day 5) on: a) a $CaCO_3$ film and b) a developed PHEMA-PMPS-PHEMA polymer film. The cells attached and spread well on $CaCO_3$ films, except for a few holes in the $CaCO_3$ films where cells did not attach. ESEM images showing new mineral deposition by the osteoblast-like cells after 15 days of culture on: c,d) $CaCO_3$ film (inset in c: higher magnification) and e) on the UV-irradiated polymer film. In (d) round bulbs of calcium phosphate, together with collagen fibers can be observed.[50] f) ALP-ase activity of the osteoblast-like cells. The ALP-ase activity was defined as the amount of *p*-nitrophenol (pNp) formed per hour (see the Supporting information) and was normalized to the total DNA concentration. g) Spectral output from the EDX analysis of the mineral bulbs shown in (c). h) FTIR spectrum of the mineral produced by the osteoblast-like cells cultured on $CaCO_3$ films.

 © 2006 Wiley-VCH Verlag GmbH & Co. KGaA, Weinheim 

the $CaCO_3$ film reached a maximum earlier than the activity of the cells cultured on the developed polymer film (Figure 4 f). This observation suggests that the cells on the $CaCO_3$ substrate showed osteogenic differentiation at an earlier point in time than on the polymer substrate.[47] However, the strongest indication of osteoblast differentiation is considered to be the deposition of new mineralized matrix.[48] Indeed, extensive and homogeneous mineral deposition in the form of characteristic small round bulbs of calcium phosphate deposited in between collagen fibers[49] was observed on $CaCO_3$ films (Figure 4 c–d), as demonstrated by SEM and optical microscopy (see the Supporting Information), in combination with energy dispersive X-ray (EDX) and FTIR analysis.[50] Moreover, the characteristic phosphate (at 1017 and 960 $cm^{-1}$) and carbonate (874 $cm^{-1}$) peaks in the FTIR spectrum of the bulbs revealed that the mineral formed was carbonated apatite.[51,52] In contrast, the mineral was formed in scattered clusters on the UV-irradiated polymer film (Figure 4 e).

To explore the possibility of also monitoring the degradation of the calcium carbonate films as a result of bone-cell activity, BMSC were cultured on the patterned crystalline mineral films in the presence of 1α,25-dihydroxyvitamin D3, which is known to induce cell differentiation in osteoclast-like (bone-resorbing) cells.[53] It has been previously shown that osteoclast activity is characterized by an alternation of two phases: mineral resorption and migration of the cell along the mineral surface.[54] Optical microscopy and SEM investigations revealed the presence of large multinucleated cells on the $CaCO_3$ films.[55] Some of these cells were found in lacunae with roughened edges on the otherwise smooth mineral film (Figure 5). These were tentatively interpreted as resorption pits in which osteoclast-like cells had degraded the mineral film. Moreover the system allowed the migration of one of these cells over the calcium carbonate film to be monitored using optical microscopy over a period of 33 days (Figure 5).

The results of these cell-culture experiments suggest that the $CaCO_3$ substrates support rat bone marrow stromal cell attachment and differentiation into osteoblast- and osteoclast-like cells. The ability to monitor the action of bone cells on these patterns, or their components in situ with optical microscopy, indicates that patterns of continuous $CaCO_3$ films have the potential to be developed as 2D model substrates for bone-cell cultures.

Furthermore, the patterning method presented here is not restricted only to glass substrates. In principle, our method would allow for the generation of patterns of $CaCO_3$ on a variety of substrates, including, for example, conducting polymers.[56] This possibility would offer the possibility to fabricate bone-biocompatible devices for the enhancement of the healing of bone fractures by electrical stimulation.[57]

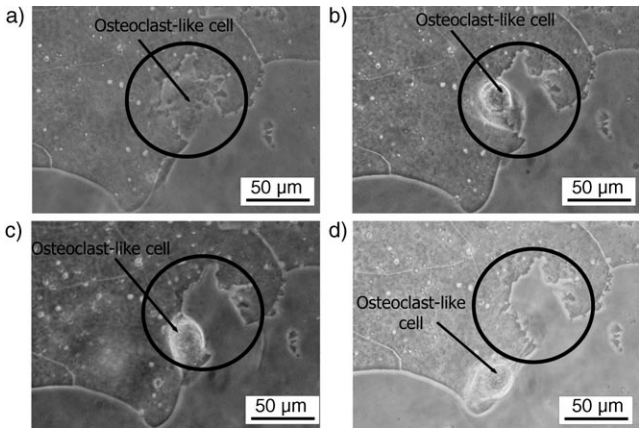



***Figure 5.*** Phase-contrast optical micrographs illustrating a resorption pit on the $CaCO_3$ film (encircled region) and an osteoclast-like cell during the migration phase after: a) day 27, b) day 29, c) day 30, and d) day 33 in the culture medium.

Received: July 25, 2005
Revised: November 6, 2005
Published online: February 10, 2006

**Keywords:** biomimetic synthesis · block copolymers · bone cells · photolithography · thin films

[1] S. L. Teitelbaum, *Science* **2000**, *289*, 1504.
[2] P. Ducy, T. Schinke, G. Karsenty, *Science* **2000**, *289*, 1501.
[3] D. Green, D. Walsh, S. Mann, R. O. C. Oreffo, *Bone* **2002**, *30*, 810.
[4] D. Green, D. Walsh, X. Yang, S. Mann, R. O. C. Oreffo, *J. Mater. Chem.* **2004**, *14*, 2206.
[5] H. Shin, S. Jo, A. G. Mikos, *Biomaterials* **2003**, *24*, 4353.
[6] R. O. C. Oreffo, J. T. Triffitt, *J. Mater. Sci. Mater. Med.* **1999**, *10*, 607.
[7] Y.-L. Chang, C. M. Stanford, J. C. Keller, *J. Biomed. Mater. Res.* **2000**, *52*, 270.
[8] M. M. Dvorak, A. Siddiqua, D. T. Ward, D. H. Carter, S. L. Dallas, E. F. Nemeth, D. Riccardi, *Proc. Natl. Acad. Sci. USA* **2004**, *101*, 5140.
[9] J. A. Jansen, J. P. van de Waerden, J. G. Wolke, K. de Groot, *J. Biomed. Mater. Res.* **1991**, *25*, 973.
[10] J. Aizenberg, A. J. Black, G. M. Whitesides, *Nature* **1999**, *398*, 495.
[11] J. Aizenberg, A. J. Black, G. M. Whitesides, *J. Am. Chem. Soc.* **1999**, *121*, 4500.
[12] J. Aizenberg, *Adv. Mater.* **2004**, *16*, 1295.
[13] B. C. Bunker, P. C. Rieke, B. J. Tarasevich, A. A. Campbell, G. E. Fryxell, G. L. Graff, L. Song, J. Liu, J. W. Virden, G. L. McVay, *Science* **1994**, *264*, 48.
[14] J. Aizenberg, D. A. Muller, J. L. Grazul, D. R. Hamann, *Science* **2003**, *299*, 1205.
[15] I. Lee, S. W. Han, S. J. Lee, H. J. Choi, K. Kim, *Adv. Mater.* **2002**, *14*, 1640.
[16] Y. K. Hwang, S. Y. Woo, J. H. Lee, D.-Y. Jung, Y.-U. Kwon, *Chem. Mater.* **2000**, *12*, 2059.
[17] K. Koumoto, S. Seo, T. Sugiyama, W. S. Seo, *Chem. Mater.* **1999**, *11*, 2305.
[18] F. C. Meldrum, J. Flath, W. Knoll, *Thin Solid Films* **1999**, *348*, 188.
[19] C. Lu, L. Qi, J. Ma, H. Cheng, M. Zhang, W. Cao, *Langmuir* **2004**, *20*, 7378.
[20] Y. Politi, T. Arad, E. Klein, S. Weiner, L. Addadi, *Science* **2004**, *306*, 1161.
[21] L. Addadi, S. Raz, S. Weiner, *Adv. Mater.* **2003**, *15*, 959.
[22] X. Xu, J. T. Han, K. Cho, *Langmuir* **2005**, *21*, 4801.
[23] D. Volkmer, M. Harms, L. B. Gower, A. Ziegler, *Angew. Chem.* **2005**, *117*, 645; *Angew. Chem. Int. Ed.* **2005**, *44*, 639.
[24] J. T. Han, X. Xu, D. H. Kim, K. Cho, *Adv. Funct. Mater.* **2005**, *15*, 475.

 © 2006 Wiley-VCH Verlag GmbH & Co. KGaA, Weinheim 

[25] E. DiMasi, V. M. Patel, M. Sivakumar, M. J. Olszta, Y. P. Yang, L. B. Gower, *Langmuir* **2002**, *18*, 8902.
[26] L. B. Gower, D. J. Odom, *J. Cryst. Growth* **2000**, *210*, 719.
[27] G. Xu, N. Yao, I. A. Aksay, J. T. Groves, *J. Am. Chem. Soc.* **1998**, *120*, 11977.
[28] T. Kato, A. Sugawara, N. Hosoda, *Adv. Mater.* **2002**, *14*, 869.
[29] A. Sugawara, T. Ishii, T. Kato, *Angew. Chem.* **2003**, *115*, 5457; *Angew. Chem. Int. Ed.* **2003**, *42*, 5299.
[30] A. Kotachi, T. Miura, H. Imai, *Chem. Mater.* **2004**, *16*, 3191.
[31] P. K. Ajikumar, R. Lakshminarayanan, S. Valiyaveettil, *Cryst. Growth Des.* **2004**, *4*, 331.
[32] H. Wakayama, S. R. Hall, S. Mann, *J. Mater. Chem.* **2005**, *15*, 1134.
[33] S. Zhang, K. E. Gonsalves, *Langmuir* **1998**, *14*, 6761.
[34] S. Lenhert, L. Zhang, J. Mueller, H. P. Wiesmann, G. Erker, H. Fuchs, L. Chi, *Adv. Mater.* **2003**, *15*, 619.
[35] J. Tan, W. M. Saltzman, *Biomaterials* **2004**, *25*, 3593.
[36] R. D. Miller, J. Michl, *Chem. Rev.* **1989**, *89*, 1359.
[37] D. C. Popescu, N. A. A. Rossi, C.-T. Yeoh, G. G. Durand, D. Wouters, P. E. L. G. Leclère, P. C. Thüne, S. J. Holder, N. A. J. M. Sommerdijk, *Macromolecules* **2004**, *37*, 3431.
[38] X. Xu, J. T. Han, K. Cho, *Chem. Mater.* **2004**, *16*, 1740.
[39] G. Peluso, O. Petillo, J. M. Anderson, L. Ambrosio, L. Nicolais, M. A. B. Melone, F. O. Eschbach, S. J. Huang, *J. Biomed. Mater. Res.* **1997**, *34*, 327.
[40] H. S. Lee, T. H. Ha, K. Kim, *Mater. Chem. Phys.* **2005**, *93*, 376.
[41] Joint Committee on Powder Diffraction Standards—International Center for Diffraction Data, **1999**, PCPDFWIN version 2.02 (calcite).
[42] P. J. J. A. Buijnsters, J. J. J. M. Donners, S. J. Hill, B. R. Heywood, R. J. M. Nolte, B. Zwanenburg, N. A. J. M. Sommerdijk, *Langmuir* **2001**, *17*, 3623.
[43] J. Künther, R. Seshadri, W. Knoll, W. Tremel, *J. Mater. Chem.* **1998**, *8*, 641.
[44] S. Rajam, B. R. Heywood, J. B. A. Walker, S. Mann, R. J. Davey, J. D. Birchall, *J. Chem. Soc. Faraday Trans.* **1991**, *87*, 727.
[45] D. C. Popescu, R. Lems, N. A. A. Rossi, C.-T. Yeoh, J. Loos, S. J. Holder, C. V. C. Bouten, N. A. J. M. Sommerdijk, *Adv. Mater.* **2005**, *17*, 2324.
[46] We have also performed an LDH cytotoxicity test, which indicated that within a concentration range of 7–42 $\mu g\,mL^{-1}$, PAA had no adverse effect on 3T3 cell viability, when compared to the viability of cells cultured in media not containing PAA. In addition, the LDH test produced similar results for the cells cultured on crystalline $CaCO_3$ films and tissue-culture polystyrene, thus suggesting that the mineral films are not toxic to the cells (for details see the Supporting Information).
[47] M.-O. Montjovent, N. Burri, S. Mark, E. Federici, C. Scaletta, P.-Y. Zambelli, P. Patrick Hohlfeld, P.-F. Leyvraz, L. L. Applegate, D. P. Dominique P. Pioletti, *Bone* **2004**, *35*, 1323.
[48] A. L. Boskey, *Connect. Tissue Res.* **1996**, *35*, 357.
[49] J. van den Dolder, P. H. M. Spauwen, J. A. Jansen, *Tissue Eng.* **2003**, *9*, 315.
[50] The observation of the vibrations at 1400–1650 $cm^{-1}$ in the FTIR spectra is consitent with the presence of collagen (see also reference [52] and S. J. Gadaleta, N. P. Camacho, R. Mendelsohn, A. L. Boskey, *Calcif. Tissue Int.* **1996**, *58*, 17).
[51] Z. Meleti, I. M. Shapiro, C. S. Adams, *Bone* **2000**, *27*, 359.
[52] A. L. Boskey, B. D. Boyan, Z. Schwartz, *Calcif. Tissue Int.* **1997**, *60*, 309.
[53] N. Takahashi, N. Udagawa, M. Takami, T. Suda in *Principles of Bone Biology, Vol. 1*, 2nd ed. (Eds.: J. Bilezikian, L. Raisz, G. Rodan), Academic Press, New York, **2002**, p. 109.
[54] J. Kanehisa, J. N. Heersche, *Bone* **1988**, *9*, 73.
[55] Large multinucleated cells with a similar appearance were identified both on the $CaCO_3$ films and on control tissue-culture polystyrene (TCPS). These cells were positively stained on TCPS for the expression of tartrate-resistant acid phosphatase (TRAP), which is a marker of the development of osteoclastic properties (see reference [53]). The TRAP staining could however not be applied to the cells on $CaCO_3$ films, since the mineral films were completely damaged during the staining procedure (see also the Supporting Information).
[56] Patterns of PHEMA-PMPS-PHEMA on polyethyleneterephthalate (PET) substrates covered with a layer of conducting poly(3,4-ethylenedioxythiophene)/polystyrene sulfonic acid (PEDOT/PSS) have been obtained and they will be part of a forthcoming publication.
[57] P. R. Supronowicz, P. M. Ajayan, K. R. Ullmann, B. P. Arulanandam, D. W. Metzger, R. Bizios, *J. Biomed. Mater. Res.* **2002**, *59*, 499.

 © 2006 Wiley-VCH Verlag GmbH & Co. KGaA, Weinheim 

*Metal-Ion Catalysis*

DOI: 10.1002/anie.200503182

# Catalytic Decomposition of Simulants for Chemical Warfare V Agents: Highly Efficient Catalysis of the Methanolysis of Phosphonothioate Esters**

*Stephanie A. Melnychuk, Alexei A. Neverov, and R. Stan Brown**

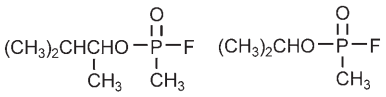
Among the most noxious materials made by man are the organophosphorus chemical-warfare materials, such as the phosphonofluoridate G agents soman (**1**) and sarin (**2**) and the phosphonothioate V agents, such as VX (**3**).[2] The latter is particularly toxic[3] because it is N-protonated at physiological pH and is therefore well accommodated by the acetylcholine esterase active site, which it inhibits through irreversible phosphonyl transfer to an essential serine hydroxy group. Numerous strategies for destroying such materials are available especially with hydrolysis and oxidation.[2,4] Base hydrolysis of V agents and some simulants of these give products that comprise approximately 75–90% of the desired P–SR cleavage products ($R'OP(CH_3)(=O)(O^-) + {}^-SR$) and

[*] S. A. Melnychuk, A. A. Neverov, Dr. R. S. Brown
Department of Chemistry
Queen's University
Kingston, Ontario, K7L3N6 (Canada)
Fax: (+1) 613-533-6669
E-mail: rsbrown@chem.queensu.ca

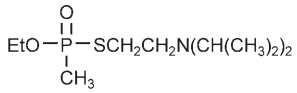
[**] The authors gratefully acknowledge the financial assistance of the Natural Sciences and Engineering Research Council of Canada, the Canada Foundation for Innovation, Queen's University, and the United States Department of the Army, Army Research Office (Grant No. W911NF-04-1-0057) and the Defense Threat Reduction Agency, Joint Science and Technology Office (06012384BP).[1] S.A.M. thanks the Natural Sciences and Engineering Council of Canada for an Undergraduate Summer Research Award at Queen's University.

Supporting information for this article is available on the WWW under http://www.angewandte.org or from the author.

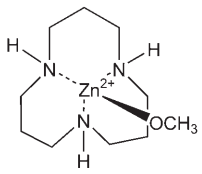

© 2006 Wiley-VCH Verlag GmbH & Co. KGaA, Weinheim



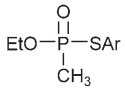
1 2

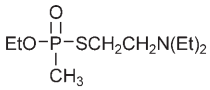


3



$[Zn(OCH_3)(\mathbf{4})]^+$





**5a** Ar = 3,5-dichlorophenyl
**b** Ar = 4-chlorophenyl
**c** Ar = 4-fluorophenyl
**d** Ar = phenyl
**e** Ar = 4-methoxyphenyl

**6**

10–25% of the undesired P–OEt cleavage products ($R'OH + {}^{-}OP(CH_3)(=O)(SR)$).[5,6] The latter are anionic and resist further base-promoted hydrolysis but nevertheless are extremely toxic. However, the methoxide reaction of these same VX simulants was shown to proceed with >93% P–SR cleavage and yield (the other 7%) a new, neutral transesterified methoxylated starting material, which subsequently can be methanolyzed to benign products.[6,7]

Recently, we reported the methanolysis of phosphate and phosphorothioate triesters[8] as well as a series of aryloxy methylphosphonate esters[9] catalyzed by $La^{3+}$ and the complex $[Zn(OCH_3)(\mathbf{4})]^+$. Each is capable of very large accelerations of the methanolysis process at ambient temperature and essentially neutral ${}^{s}_{s}$pH values[10] in methanol. Herein, we report that both metal-containing systems are extremely effective in promoting the methanolysis of phosphonothioates **5a–e**, the only identifiable product being the corresponding *O*-ethyl *O*-methyl methylphosphonate. Based on the results, we predict that the corresponding $-SCH_2CH_2NEt_2$ derivative **6**, a very close analogue of VX, should be catalytically methanolyzed with a $t_{1/2}$ value of $<1$ s at ${}^{s}_{s}$pH 9.1 in the presence of 1 mM of $La^{3+}$-containing catalyst at 25 °C.

The second-order rate constants for the methanolysis of **5a–e** promoted by methoxide, $La^{3+}$, and $[Zn(OCH_3)(\mathbf{4})]^+$ are given in Table 1, the latter two systems being buffered at ${}^{s}_{s}$pH 9.1 in methanol. The kinetic data for each substrate were determined in duplicate under pseudo first-order conditions of excess catalyst relative to substrate at $\geq 5$ equivalents [metal catalyst] and 3 equivalents [methoxide]. The $k_2^{catalyst}$ values in Table 1 were obtained as the gradients of the plots of $k_{obs}$ versus [catalyst]. The Brønsted plots shown in Figure 1 for the $\log k_2^{catalyst}$ constants versus the experimentally determined ${}^{s}_{s}pK_a$ values of the corresponding thiophenols give straight lines described by Equations (1)–(3). The gradients of

$$\log k_2^{OMe} = (6.39 \pm 1.12) - (0.65 \pm 0.10)\ {}^{s}_{s}pK_a{}^{HSAr} \quad r^2 = 0.930 \qquad (1)$$

$$\log k_2^{\mathbf{4}:Zn(OMe)} = (7.89 \pm 0.41) - (0.66 \pm 0.04)\ {}^{s}_{s}pK_a{}^{HSAr} \quad r^2 = 0.990 \qquad (2)$$

$$\log k_2^{La} = (10.51 \pm 0.10) - (0.75 \pm 0.01)\ {}^{s}_{s}pK_a{}^{HSAr} \quad r^2 = 0.999 \qquad (3)$$

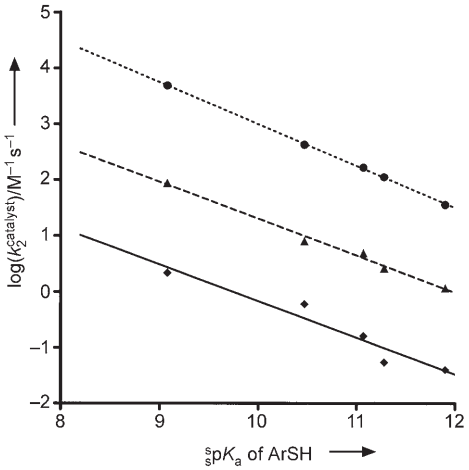



***Figure 1.*** Brønsted plots for $\log k_2^{catalyst}$ versus the ${}^{s}_{s}pK_a$ of aryl thiol; ●, $[\{La^{3+}({}^{-}OCH_3)\}_2]$; ▲, $[Zn(OCH_3)(\mathbf{4})]^+$; ◆, ${}^{-}OCH_3$.

***Table 1:*** Second-order rate constants for the methanolysis of phosphonates **5a–e** catalyzed by methoxide, $[\{La^{3+}({}^{-}OCH_3)\}_2]$, and $[Zn(OCH_3)(\mathbf{4})]^+$ in methanol at $T = 25$ °C.

| Phosphonothioate | ${}^{s}_{s}pK_a$ of thiol (methanol)[a] | $k_2^{OMe}$ [$M^{-1}s^{-1}$] | $k_2^{\mathbf{4}:Zn(OMe)}$ [$M^{-1}s^{-1}$][b] | $k_2^{La}$ [$M^{-1}s^{-1}$][c] |
|---|---|---|---|---|
| **5a** | 9.08 ± 0.04 | 2.17 ± 0.03 (1.96 ± 0.03)[d] | 95.2 ± 1.4 (75.7 ± 4.6)[d] | (4.84 ± 0.09) × $10^3$ |
| **5b** | 10.47 ± 0.01 | 0.60 ± 0.01 | 7.85 ± 0.25 | (4.25 ± 0.12) × $10^2$ |
| **5c** | 11.07 ± 0.03 | 0.16 ± 0.01 | 4.83 ± 0.11 | (1.64 ± 0.07) × $10^2$ |
| **5d** | 11.28 ± 0.14 | 0.054 ± 0.002 | 2.60 ± 0.06 | (1.10 ± 0.02) × $10^2$ |
| **5e** | 11.98 ± 0.08 | 0.040 ± 0.006 | 1.16 ± 0.03 | (3.55 ± 0.17) × $10^1$ |
| **6** | 9.54 ± 0.04 | [e] | 38.02 ± 0.04[f] | (2.06 ± 0.09) × $10^3$ [f] |

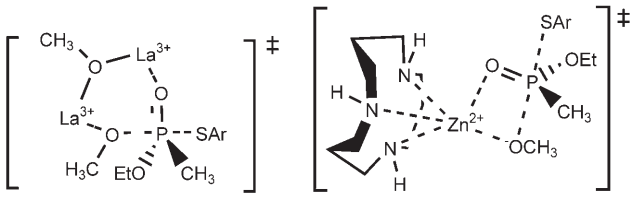
[a] Experimental values from 2 mM solutions titrated in methanol according to procedures in ref. [10]. [b] Catalyst was prepared in situ by adding 1 equivalent of each of $Zn(OTf)_2$ and the triaza ligand along with 0.5 equivalents of tetrabutylammonium hydroxide in methanol to self-buffer the solution at ${}^{s}_{s}$pH 9.1 as the ${}^{s}_{s}pK_a$ of $[Zn^{2+}(HOMe)(\mathbf{4})]$ is 9.1;[8,11] the kinetics were determined in duplicate at 5 [catalyst] concentrations ranging from 0.4 to 2.0 mM. [c] Catalyst was prepared in situ by adding a stock solution of $La(OTf)_3$ in methanol to a 17 mM *N*-ethylmorpholine with perchloric acid in a 4:1 ratio to buffer the solution at ${}^{s}_{s}$pH 9.1; the kinetics were determined in duplicate at 5 $[La^{3+}]_{total}$ concentrations ranging from 0.4 to 2.4 mM. [d] In $[D_1]$methanol. [e] Number predicted to be approximately $2 \times 10^{-3}\ M^{-1}s^{-1}$ under highly basic conditions based on comparison with data for VX and *O*-ethyl *S*-ethyl methylphosphonothioate given in ref. [6]. [f] Predicted $k_2^{catalyst}$ value computed using Equations (2) and (3).

 © 2006 Wiley-VCH Verlag GmbH & Co. KGaA, Weinheim 

the lines are all substantially negative and suggest extensive cleavage of the P–SAr bond in the transition state (TS) for the reaction. The reactions of methoxide and $[Zn(OCH_3)(\mathbf{4})]^+$ with **5a** exhibit solvent kinetic isotope effects of $k_H/k_D = 1.11 \pm 0.03$ and $1.26 \pm 0.10$, respectively; these low values are most consistent with nucleophilic rather than general base-promoted methanolysis.[11]

A turnover experiment was conducted in solution with methanol, the concentrations were 3.62 mM for **5a** and 0.36 mM for $La(OTf)_3$ (Tf = trifluoromethylsulfonyl) buffered with *N*-ethyl morpholine at ${}^{s}_{s}$pH 9.1, in which the dominant catalytically active form in solution was probably the bis-(methoxy)-bridged dimer $[\{La^{3+}(^{-}OCH_3)\}_2]$, which we had shown earlier makes a contribution of $>90\,\%$ toward the catalysis of phosphate ester methanolysis at that ${}^{s}_{s}$pH value.[8a,b] None of the starting material, which has a $^{31}$P NMR signal at $\delta = 50.37$ ppm, was evident within the five minutes required to obtain the spectrum: only a single peak at $\delta = 30.6$ ppm, which corresponds to *O*-ethyl *O*-methyl methylphosphonate, was observed. These data indicate that the catalyst performs at least 20 turnovers in that time, although it is probably far more active than is revealed by this NMR technique.[12]

Several pieces of information allow us to propose a mechanism for the metal-catalyzed reactions of **5a–e** that appears to be a common one for the neutral phosphate, phosphorothioate, and phosphonate esters.[8,9,11] As both metal systems are more active than methoxide for a given substrate ($\approx$30–40-fold for $[Zn(OCH_3)(\mathbf{4})]^+$ and $\approx$1000-fold for $[\{La^{3+}(^{-}OCH_3)\}_2]$), the mechanism likely involves a dual role for the metal ion as a Lewis acid activator of a transiently bound substrate followed by intramolecular nucleophilic delivery of a metal-coordinated methoxide. The skie data and Brønsted slopes with large negative values are consistent with associative mechanisms via TS structures **7** and **8**, in




**7** **8**

which nucleophilic delivery of the methoxide species is coupled with a concerted departure of the leaving group. In the case of $[\{La^{3+}(^{-}OCH_3)\}_2]$, we envision that a methoxide species bridged between two electropositive $La^{3+}$ ions is not nucleophilic enough to attack the bound substrate, so one of the O–$La^{3+}$ bonds is broken in the TS to reveal a bifunctional catalyst containing both the Lewis acid and nucleophilic $La^{3+}$-coordinated methoxide. The $Zn^{2+}$ ion in **8** is five-coordinate, and the intramolecular delivery is accomplished through a direct four-membered TS.

It is of interest to utilize the present correlations to predict the rates of the reactions for a substrate containing an $(R)_2NCH_2CH_2S^-$ group which would be a close analogy of VX without having to handle such a dangerous material. Titration of (*N*,*N*-diethylamino)ethanethiol in methanol gives two macroscopic ${}^{s}_{s}pK_a$ values of $9.54 \pm 0.04$ and $13.3 \pm 0.07$, the low value for the thiol is due to the zwitterionic stabilization of the thiolate anion by the internal ammonium group [Eq. (4)].

$$HS(CH_2)_2\overset{+}{N}(Et)_2H \overset{{}^{s}_{s}pK_a\ 9.54}{\rightleftharpoons} {}^{-}S(CH_2)_2\overset{+}{N}(Et)_2H \overset{{}^{s}_{s}pK_a\ 13.3}{\rightleftharpoons} {}^{-}S(CH_2)_2N(Et)_2 \quad (4)$$

The fact that putative phosphonothioate **6** would be substantially N-protonated in methanol[13] at ${}^{s}_{s}$pH 9.1, the value at which the metal-catalyzed reactions are run, makes the thiolate in $EtO(CH_3)P(=O)SCH_2CH_2N^+(Et)_2H$ a much better leaving group than if the amino group were deprotonated, as it would be under the highly basic conditions required to effect the methoxide reaction in a reasonable time. By analogy, lyoxide-catalyzed decomposition of the related V agents also suffers from this leaving-group retardation at high pH values and proceeds much more slowly[14] than if the decomposition could be done at neutral pH, the value at which the amine is protonated, as is the case with our metal systems. The predicted $k_2^{catalyst}$ values computed with Equations (2) and (3)[15] are given in Table 1 and suggest that a solution of 1 mM $[Zn(OCH_3)(\mathbf{4})]^+$ or $[\{La^{3+}(^{-}OCH_3)\}_2]$ should methanolyze **6** with respective $t_{1/2}$ values of 18 and 0.33 s.

We have described a highly efficient, truly catalytic methodology for the decomposition of phosphonothioates to benign products based on metal-catalyzed methanolysis under essentially neutral conditions. The Brønsted correlation of a well-defined series of simulants allows prediction of the reactivity of more deadly substrates by simple determination of the ${}^{s}_{s}pK_a$ values of the thiol leaving group. The results indicate this approach could be attractive for the decomposition of the real V agents which will not suffer from the known problems of base-catalyzed hydrolysis under highly basic conditions. One can envision that anchoring metal-binding ligands to solid supports may provide effective heterogeneous methods for organophosphate decomposition by alcoholysis, a project under current investigation.

## Experimental Section

**Caution**: all the phosphonothioates are potentially serious neurotoxins and should be handled with extreme care.

All the phosphonothioates were prepared by the following general route from methylphosphonic dichloride via (*S*)-aryl methylphosphonochloridate. Thiophenol (5 mmol) was added to a solution of methylphosphonic dichloride (5 mmol) in dry THF (10 mL) under nitrogen. The mixture was cooled in an ice bath and 1,8-diazabicyclo-[5.4.0]undec-7-ene (DBU; 5 mmol, neat) was added dropwise. The reaction mixture was allowed to stir in an ice bath for 30 min and at room temperature for 24 h. Following this period, $Na_2CO_3$ (1 g) in ethanol (10 mL) was added to the reaction mixture, which was stirred under $N_2$ for 30 minutes. The reaction mixture was filtered, the volatiles removed, and the crude product purified by flash chromatography on silica gel using a Biotage SP1 purification system with ethyl acetate/hexanes (1:1) as the eluent. The non-optimized yields of the isolated products were approximately 20 %. The physical data for **5a–e** are given in the Supporting Information.

 © 2006 Wiley-VCH Verlag GmbH & Co. KGaA, Weinheim 

Kinetic data for the methanolysis of **5a–e** were obtained by UV/Vis methods, as described earlier for phosphates, phosphorothioates, and phosphonates.[8,9,11] The reactions were run under pseudo first-order conditions of excess catalyst in duplicate with a substrate concentration of 0.2 mM. Pseudo first-order rate constants were evaluated by fitting traces of the absorbance versus time to a standard exponential, and the second-order rate constants were evaluated as the gradients of the plots of $k_{obs}$ versus [catalyst].

The turnover experiment was conducted with 3.62 mM **5a** in 0.6 mL of methanol buffered with 17 mM *N*-ethylmorpholine and perchloric acid in a 4:1 ratio to achieve a $^{s}_{s}$pH value of 9.1. $La(OTf)_3$ and tetrabutylammonium hydroxide were added to this reaction mixture so that the final concentration of each was 0.36 mM and 0.09 mL of [$D_1$]methanol. The reaction was followed using $^{31}$P NMR spectroscopic analysis on a 400-MHz machine.

Titrations were performed in duplicate on 2 mM solutions of thiol in methanol under nitrogen at 25 °C using standardized 20 mM $NaOCH_3$ as the titrant. The $^{s}_{s}pK_a$ values were obtained by fitting the titration data using the program Hyperquad 2000 (version 2.1 NT).[16]

Received: September 7, 2005

**Keywords:** chemical warfare · lanthanum · methanolysis · phosphorus · zinc

[1] The content of the information discussed herein does not necessarily reflect the position or the policy of the federal government of the United States of America, and no official endorsement should be inferred.

[2] a) Y.-C. Yang, J. A. Baker, J. R. Ward, *Chem. Rev.* **1992**, *92*, 1729; b) Y.-C. Yang, *Acc. Chem. Res.* **1999**, *32*, 109; c) Y.-C. Yang, *Chem. Ind.* **1995**, 334.

[3] *The Merck Index*, 11th ed., Merck and Co., Rahway, NJ, **1989**; the toxicity of VX in rabbits is given as $LD_{50}^{s.c.} = 15.4\ \mu g\,kg^{-1}$.

[4] H. Morales-Rojas, R. A. Moss, *Chem. Rev.* **2002**, *102*, 2497, and references therein.

[5] N. B. Munro, S. S. Talmage, G. D. Griffin, L. C. Waters, A. P. Watson, J. F. King, V. Hauschild, *Environ. Health Perspect.* **1999**, *107*, 933.

[6] Y.-C. Yang, F. J. Berg, L. L. Szafraniec, W. T. Beaudry, C. A. Bunton, A. Kumar, *J. Chem. Soc. Perkin Trans. 2* **1997**, 607.

[7] Yang et al. also showed[5] that the $HOO^-$ ion reacts with phosphoniothioates to give exclusive P–S cleavage, although these reactions are not catalytic and are carried out under alkaline conditions.

[8] a) J. S. Tsang, A. A. Neverov, R. S. Brown, *J. Am. Chem. Soc.* **2003**, *125*, 7602; b) T. Liu, A. A. Neverov, J. S. W. Tsang, R. S. Brown, *Org. Biomol. Chem.* **2005**, *3*, 1525; c) J. S. W. Tsang, A. A. Neverov, R. S. Brown, *Org. Biomol. Chem.* **2004**, *2*, 3457; d) W. Desloges, A. A. Neverov, R. S. Brown, *Inorg. Chem.* **2004**, *43*, 6752.

[9] R. E. Lewis, A. A. Neverov, R. S. Brown, *Org. Biomol. Chem.* **2005**, *3*, 4082.

[10] For the designation of "pH" in methanol and measurement thereof, see: G. T. T. Gibson, A. A. Neverov, R. S. Brown, *Can. J. Chem.* **2003**, *81*, 495; the autoprotolysis constant of methanol is $10^{-16.77}\,M^2$ so neutral $^{s}_{s}$pH in methanol is 8.4; E. Bosch, F. Rived, M. Rosés, J. Sales, *J. Chem. Soc. Perkin Trans. 1* **1999**, *2*, 1953.

[11] C. Maxwell, A. A. Neverov, R. S. Brown, *Org. Biomol. Chem.* **2005**, *3*, 4329.

[12] In actuality, the turnover experiment for the $La^{3+}$-catalyzed methanolysis of **5a** must be essentially complete early in the NMR experiment because if it were not the summation of the 256 scans over five minutes would have revealed the presence of starting material in the first few scans.

[13] A referee rightly points out that the ammonium ion in **6** does not have the zwitterionic stabilization of $^-SCH_2CH_2N^+(H)Et_2$, so the $^{s}_{s}pK_a$ value will not be as high as 13.3; while true, we note that the $^{s}_{s}pK_a$ value of triethylamine is 10.78, thus indicating that the nitrogen atom in **6** will still be substantially protonated at $^{s}_{s}$pH 9.1.

[14] The methoxide-promoted methanolysis of VX and *O*-ethyl *S*-ethyl methylphosphonothioate at 22 °C and 0.25–0.3 M concentrations of base have $k_2$ values of $1.85\times10^{-3}$ and $1.70\times10^{-3}\,M^{-1}s^{-1}$[5], which is similar to that expected for **6** under highly basic conditions; however, the methoxide reaction on **6** at any $^{s}_{s}$pH value at which the nitrogen atom is protonated is computed by Equation (1) to be 1000-fold faster at $1.28\pm0.10\,M^{-1}s^{-1}$.

[15] The predicted rate constants assume that the Brønsted relationships of Equations (2) and (3), which are derived for aryl thiols, are followed by a primary alkyl thiol. Previous studies indicate that methanolysis and hydrolysis of carboxylate esters bearing aryloxy groups are up to tenfold less reactive than those bearing primary alkoxyl groups, presumably because of steric effects; see: a) N. E. Sunderland, A. A. Neverov, R. S. Brown, *Org. Biomol. Chem.* **2005**, *3*, 65; b) J. F. Kirsch, W. P. Jencks *J. Am. Chem. Soc.* **1964**, *86*, 837.

[16] P. Gans, A. Sabatini, A. Vacca, *Talanta* **1996**, *43*, 1739.

 © 2006 Wiley-VCH Verlag GmbH & Co. KGaA, Weinheim 

Polymer Brushes

DOI: 10.1002/anie.200503264

# UCST Wetting Transitions of Polyzwitterionic Brushes Driven by Self-Association**

*Omar Azzaroni, Andrew A. Brown, and Wilhelm T. S. Huck**

The chemical modification of solid substrates with zwitterionic functionalities has been the subject of intensive research in industry and in academia. The main reason for this interest lies in the potential technological applications of these systems. For example, self-assembled monolayers bearing zwitterionic terminal groups are currently used for designing efficient protein-resistant substrates,[1,2] and surface-immobilized polymers containing zwitterionic side-groups[3,4] have proved to be beneficial in the creation of biocompatible surfaces,[5,6] in providing control over electro-osmotic flow in

[*] Dr. O. Azzaroni, A. A. Brown, Dr. W. T. S. Huck
Melville Laboratory for Polymer Synthesis
Department of Chemistry, University of Cambridge
Lensfield Road, Cambridge CB21EW (UK)
Fax: (+44) 1223-334-866
E-mail: wtsh2@cam.ac.uk

[**] This research was supported financially by the EPSRC (GR/T11555/01), a Marie Curie Research Fellowship (O.A.), and Faraday Partnership–Unipath Ltd. (A.A.B.). UCST = upper critical solubility temperature.

Supporting information for this article is available on the WWW under http://www.angewandte.org or from the author.


WILEY InterScience DISCOVER SOMETHING GREAT
© 2006 Wiley-VCH Verlag GmbH & Co. KGaA, Weinheim

microfluidics,[7] and as the stationary phase in electrostatic ion chromatography.[8] The extremely high dipole moment of zwitterionic groups (around 23 D in the case of sulfobetaines[9,10]) gives rise to a range of unique properties as a consequence of strong inter- and intramolecular dipolar interactions that lead to (reversible) self-association of the polymer chains.[11] Experimentally, a reversible self-association is observed in certain polyzwitterionic hydrogels that display an upper critical solubility temperature (UCST),[12] that is, only at sufficiently high temperatures are the dipolar interactions broken to yield isolated polymer chains that are completely solvated.

Despite many detailed studies on the properties of zwitterionic polymers in solution or bulk,[13–24] it is not well understood how dense layers of these polymers behave on surfaces. Herein, we present a study of the fundamental processes that occur when polyzwitterionic brushes are grown from solid surfaces. We observe the generation of an ionically cross-linked, superdense conformation driven by an avalanche-type self-association process. This conformation, known as the supercollapsed state, and its formation have been predicted in theoretical studies.[25] Consequently, these studies are a crucial step toward the translation of polyzwitterionic solution behavior to surfaces to exploit their diverse properties in the development of new, smart, responsive coatings.

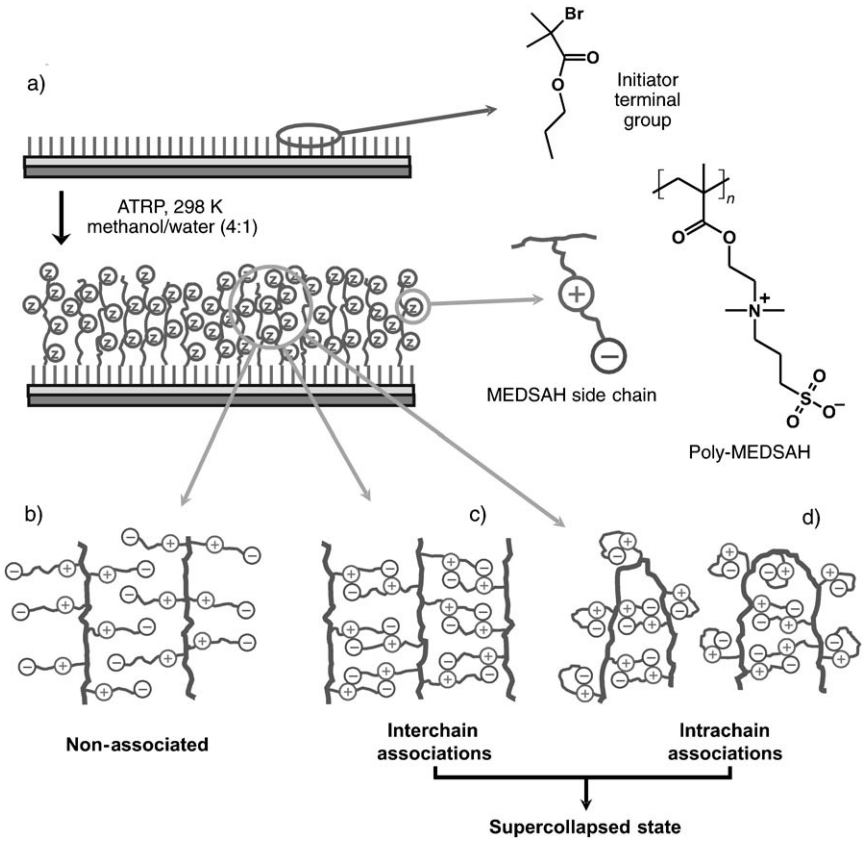



***Figure 1.*** Synthesis of the polyzwitterionic brushes (a) and their different possible conformational states: b) non-associated, c) interchain associations, and d) intrachain associations.

We have synthesized homogeneous and patterned brushes from [2-(methacryloyloxy)ethyl]dimethyl(3-sulfopropyl)ammonium hydroxide (MEDSAH). The synthetic route to these brushes involves the surface-initiated, atom-transfer radical polymerization (ATRP) of MEDSAH on silicon and gold surfaces (Figure 1), adapted from a system previously reported by our group for growing polymer brushes.[26] Emphasis is placed on elucidating the properties of these brushes, and particularly the association states of the zwitterionic side-groups,[27,28] that is, non-associated, interchain associated, or intrachain associated (into a supercollapsed state). We interpreted the results and concluded that all the unique properties ascribed to these zwitterionic brushes arise from these association states and further show that they can be exploited to create "smart" surfaces.

The first and obvious parameter to vary is the thickness ($h$) of the polymer-brush layers and hence the molecular weight of the polymers. It is well known from bulk or solution behavior that the magnitude and characteristics of the interactions leading to a self-associated state are dependent on the nature of the electrostatic environment and the molecular weight of the polyzwitterionic chains.[18,20,21]

For this study, Poly-MEDSAH (PMEDSAH) brushes with thicknesses between 5 and 200 nm were synthesized and analyzed. Figure 2 shows the dependence of the advancing water contact angle ($\theta_{AW}$) on $h$. Clearly, the presence of two well-defined regimes can be observed. Thin brushes ($h <$ 50 nm) display a very hydrophilic surface with a nearly constant $\theta_{AW}$ of about 12°. Thicker brushes ($h$ up to 100 nm) show a surprising and more or less linear increase in hydrophobicity with increase in brush thickness. We will refer to the first and second regimes as the "non-associated regime" and the "self-associated regime", respectively.

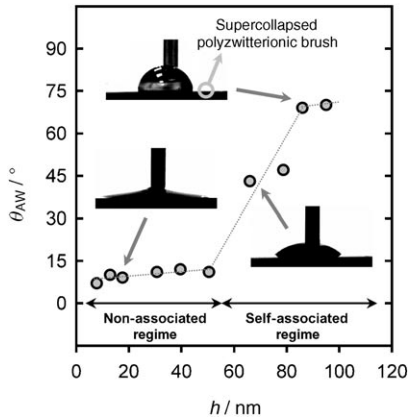



***Figure 2.*** Representation of the advancing water contact angle ($\theta_{AW}$) as a function of polyzwitterionic brush thickness ($h$). The non-associated and self-associated regimes are indicated by arrows. The insets correspond to pictures showing the water contact angles of PMEDSAH brushes in the different regimes. Dotted gray lines are incorporated as a guide for the eye.

 © 2006 Wiley-VCH Verlag GmbH & Co. KGaA, Weinheim 

It is reasonable to suppose that grafted polymer chains bearing high-dipole-moment side-groups will permanently exist in a self-associated conformation. Electrostatic considerations would suggest that opposite charges would be as close as possible to each other, leading to interchain and/or intrachain ionic crosslinks and loops, respectively.[29] However, in water, solvation counteracts the electrostatic effect and forces the anionic and cationic moieties further apart. In addition, electrostatic interactions are dominated by the dielectric characteristics of the medium. In the presence of a solvent of high dielectric constant ($\varepsilon$), like water ($\varepsilon \approx 80$), the electrostatic attraction between the opposite charges should be reduced even more.[30] Lastly, the hydration layer around the charges increases excluded-volume effects, leading to swelling of the brushes. Ion-pairing and self-association would require water to be removed from the charges and will only occur when the electrostatic energy is larger than the energy required for dehydration.[31] To investigate this trade-off between hydration and swelling versus self-association and dehydration, we studied the brushes under water by tapping-mode atomic force microscopy (AFM). Figure 3a shows a 50-nm-thick patterned PMEDSAH brush in air. Under water (Figure 3b), the brushes swell significantly to a thickness of about 150 nm. This swelling is in accordance with the hydrophilic characteristics previously observed by contact-angle goniometry of the homogeneous PMEDSAH-modified substrates. In contrast, Figures 3c and 3d clearly show that thicker PMEDSAH brushes ($h =$ 90 nm in air) essentially do not swell under water ($h = 96$ nm). Although PMEDSAH brushes in the hydrophilic, non-associated regime experience a 200% increase in $h$ when placed in water, the corresponding brushes in the hydrophobic, self-associated regime only experience a 7% increase under similar conditions.

This radical change in wettability upon increasing the brush thickness reflects reorganization processes within the macromolecular film. These changes were observed by analysis of the outermost layers of the PMEDSAH brushes by Auger electron spectroscopy (AES). AES is a surface chemical analysis technique that is capable of detecting elements at concentrations above 0.5–1 atom% in the outer region ($\approx 2$ nm) of the surface layer (Figure 4a).[32] This technique is commonly used to probe the surface composition of polymer surfaces[33] and it has recently been successfully employed to elucidate the chemical composition of the topmost layer of polymer brushes.[34] We monitored the elemental composition of S (due to the $SO_3^-$ moieties), N (due to the quaternary ammonium moieties), and O (due to both $SO_3^-$ moieties and COO ester groups; Figure 4b). AES characterization of PMEDSAH films with different thicknesses revealed a quite sensitive decrease in S composition with increasing film thickness, as determined by the decrease in the Auger signal ratio between S and O ($I_S/I_O$; Figure 4c). However, the N composition remained nearly constant for polymer films of varying thickness ($I_N/I_O \approx 0.4$). This fact could imply a reorganization process leading to a new conformation where the $SO_3^-$ moieties (hydrophilic character) could be preferentially buried in the macromolecular film.

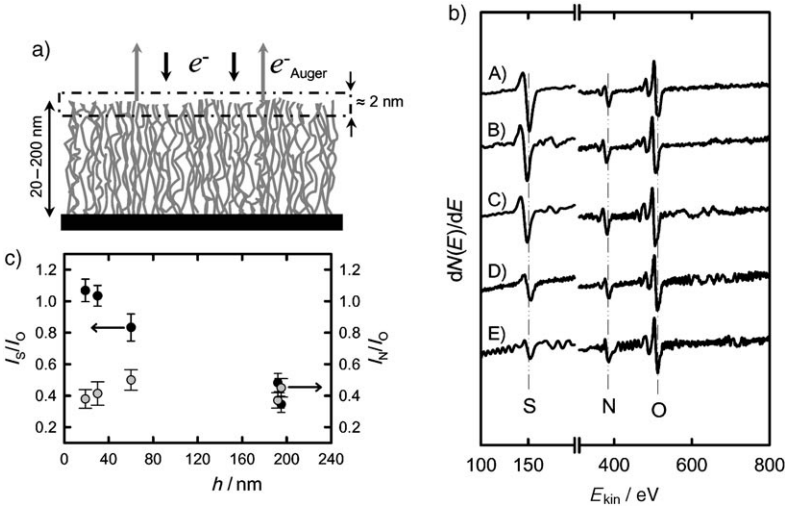



***Figure 4.*** a) Simplified scheme depicting a brush layer bombarded by an electron beam. The Auger electrons generated are collected and measured from the outmost layers. b) Broad AES spectra corresponding to PMEDSAH samples with different thicknesses: A) 19 nm, B) 30 nm, C) 65 nm, D) 192 nm, E) 195 nm. The Auger signals for S (LVV, 152 eV), N (KLL, 380 eV), and O (KLL, 506 eV) are shown. c) Dependence of the Auger signal ratio with thickness for S ($I_S/I_O$, ●) and N ($I_N/I_O$, ●). $E_{kin}$ = kinetic energy.

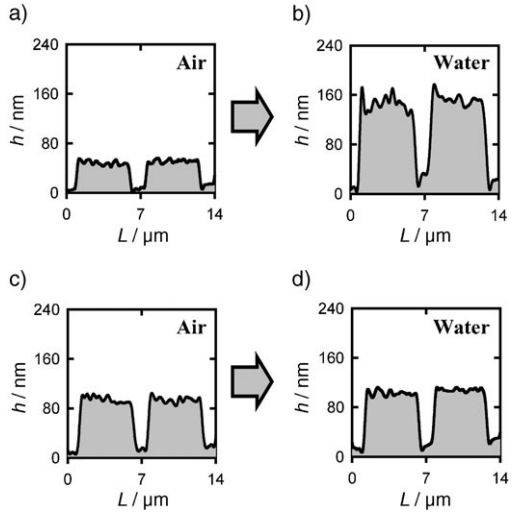



***Figure 3.*** AFM cross-sectional analysis of patterned PMEDSAH brushes: a) 50-nm-thick brushes imaged in air and b) the same brushes imaged under water; c) 90-nm-thick brushes imaged in air and d) the same brushes imaged under water. $L$ = length.

To summarize, the difference between thin, hydrophilic, swollen brushes and thick, hydrophobic, collapsed brushes can be explained as follows: The presence of a hydrophilic regime is determined by a number of factors. For instance,

 © 2006 Wiley-VCH Verlag GmbH & Co. KGaA, Weinheim 

1) the high dipole moment of the bearing groups must be stabilized by a high $\varepsilon$ solvent like water, 2) there is a more favorable interaction of the sulfonate groups with water than with the quaternary ammonium groups, and 3) steric factors related to the polymer backbone and the hydrated charged groups hinder the formation of ion pairs.[29–31] When the brushes are considerably thicker, all these factors change. The electrostatic characteristics (and, as a consequence, the number of ion pairs) depend strongly on the value of the dielectric constant $\varepsilon$ of the medium. As suggested by various authors working within a theoretical framework, i.e. "theoreticians", the dielectric characteristics of the polymer environment are quite sensitive to the polymer conformation.[35–37] In other words, the effective $\varepsilon$ affecting the electrostatic conditions is dependent on the microenvironment of the grafted chains. As a consequence, the inner environment of the brush can suffer a drastic change in $\varepsilon$ after changing from a swollen to a collapsed conformation. The polymer volume fraction in the swollen state is low, and $\varepsilon$ is close to that corresponding to the pure solvent (in our case water, $\varepsilon \approx 80$). However, in the collapsed state there is a significant increase in the polymer volume fraction, which results in a much smaller value for $\varepsilon$ ($\varepsilon \approx 4$ for the dry polymer).[37] Increasing the thickness (i.e. chain length) of the PMEDSAH brushes involves an increase in the number of zwitterionic groups or "stickers" per grafting site.[38] This implies that by increasing $h$ the probability of ion-pairing events or self-association between zwitterionic moieties becomes higher. It must be noted that ion pairing leads to an increase in polymer volume fraction and a decrease in $\varepsilon$. Thus, after reaching a critical $h$ where the first ion-pairing events start, the self-association becomes more favorable and leads to a rapid collapse of the chains. This process has been described theoretically by Khokhlov and co-workers[36,37] as a "supercollapsed state" of charged polymer chains, and corresponds to a very dense conformation where practically all charged functionalities in bearing groups form intra and/or interchain ion pairs.[27,28] The self-associated state of the brush is the first experimental evidence of the supercollapsed state in surface-grafted polymers.

As explained in the introduction, sulfobetaines like MEDSAH exhibit an upper critical solution temperature (UCST).[18] Translating the UCST characteristics of sulfobetaines to our PMEDSAH brushes should allow us to create a thermoresponsive brush with a hydrophobic-to-hydrophilic transition when raising the temperature above the sulfobetaines' UCST (around 30 °C). To corroborate this behavior we measured the contact angles of 180-nm-thick, hydrophobic PMEDSAH brushes at room temperature and at 52 °C. Figure 5 shows the variation in wetting properties (from $\theta_{AW} \approx 79°$ to $\theta_{AW} \approx 58°$) when the temperature is increased from 22 °C to 52 °C, thus supporting the predicted thermoresponsive behavior of PMEDSAH brushes. It must be noted that in the case of our polysulfobetaine brushes the UCST is slightly higher (approx. 40–50 °C) than other values reported in the literature.[18] This fact could be attributed to the presence of traces of inorganic ions remaining in the brush from the polymerization solution, as described in detail by Laschewsky and co-workers.[39] None of our brushes showed levels of impurities above the detection limit of Auger spectroscopy (0.5 atom %), which indicates that any effect due to these trace metal ions will be similar for every surface.

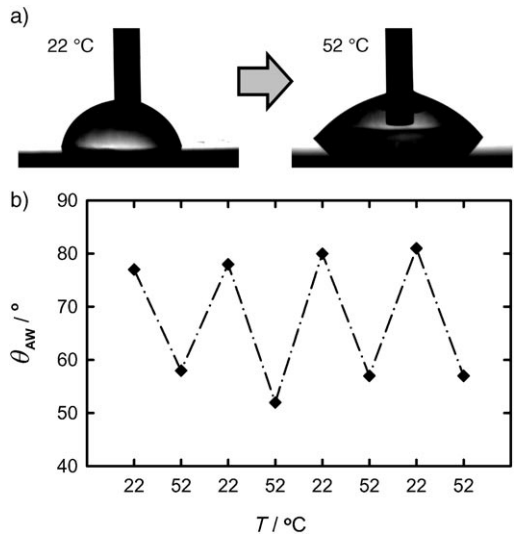



***Figure 5.*** a) Change of the wetting characteristics of thick, supercollapsed PMEDSAH brushes ($h \approx 180$ nm) after increasing the temperature from 22 °C to 52 °C. b) Representation of the advancing contact angle in water ($\theta_{AW}$) as a function of temperature ($T$), depicting the reversible thermoresponsive behavior of PMEDSAH brushes after repeated cycles between 22 °C and 52 °C.

This thermally responsive wettability is completely reversible, as indicated by repeated temperature cycling (Figure 5b). Similar experiments performed after a few months gave identical results, thus confirming the stability of the films and their thermoresponsive characteristics. This system represents, to the best of our knowledge, the first example of a thermoresponsive brush exploiting the UCST properties of the polymer chains. The magnitude of the effect ($\Delta\theta_{AW} \approx 20$–$25°$) is similar to the well-known polyacrylamide-based brushes[40] and hydrogels,[41] but with an inverse thermoresponsive behavior.

In conclusion, we have found that the bulk or solution behavior of sulfobetaines has its counterpart in the surface domain through the thickness- and temperature-dependent characteristics of the brush-like layer. This dependence is evidenced by a pronounced transition in the wetting characteristics that is related to the polyzwitterionic brush forming a completely collapsed self-associated state, which has a significant impact on the wetting characteristics. After passing through the hydrophilic, non-associated regime with $\theta_{AW} \approx 12°$, the self-associated regime develops hydrophobic surface characteristics until it reaches $\theta_{AW} \approx 75°$, thus indicating that in the collapsed state water becomes a poor solvent (poor wetting). This sharp difference in the interaction between the water and the two states was also observed in the swelling behavior. Finally, we have shown that the self-associated state can be reversed by increasing the temperature, leading to a hydrophobic-to-hydrophilic switch that closely resembles the UCST characteristics observed for the same polyzwitterion in solution. This reversible switching of the brushes is ideally suited for applications in microfluidic devices where control

 © 2006 Wiley-VCH Verlag GmbH & Co. KGaA, Weinheim 

over liquids wetting or not wetting channels will greatly aid the design of more complex device layouts.

## Experimental Section

Patterned gold samples were prepared by microcontact printing (μCP) of a thiol initiator (ω-sulfanylundecylbromobutyrate) onto clean gold substrates. For brushes grown on $Si/SiO_2$, 2-bromo-2-methylpropionic acid 3-trichlorosilanylpropyl ester was used to prepare the initiator-modified substrates. MEDSAH was purchased from Aldrich (97% purity) and was used as received. Analytical Reagent grade methanol (99.99%) was purchased from Fisher Scientific and used as received. Deionized water with a resistance of 18.2 MΩ cm was obtained from a Millipore Simplicity 185 system. The polymerization solution was prepared as follows: MEDSAH (30 g, 107 mmol) was dissolved in Milli-Q water (20 mL) and MeOH (80 mL) at 20 °C and deoxygenated by passing a continuous stream of dry $N_2$ through the solution whilst stirring (20 min). 2,2′-Dipyridyl (840 mg, 5.37 mmol), CuCl (212 mg, 2.15 mmol), and $CuCl_2$ (29 mg, 0.21 mmol) were added to this solution. The mixture was then stirred whilst deoxygenating with a stream of dry $N_2$ (15 min). Initiator-modified samples ($\approx 1\ cm^2$ each) were sealed in Schlenk tubes, deoxygenated (four high-vacuum-pump/$N_2$ refill cycles), and left at 20 °C under $N_2$. The polymerization solution was then transferred into each Schlenk tube by means of a syringe, adding enough solution to submerge each sample completely. After various polymerization times, the samples were removed, washed with warm Milli-Q water (60 °C), and dried under a stream of $N_2$. Contact-angle goniometry was performed by using a homemade stage with a computer-controlled microsyringe and digital camera. Infusion and withdrawal rates of 4 $\mu L\,min^{-1}$ were used. Advancing water contact angles ($\theta_{AW}$) were recorded. Surface elemental analyses by AES (INIFTA–La Plata) were carried out by using a single-pass cylindrical mirror analyzer (CMA, Physical Electronics). All spectra were recorded in the differential mode $dN(E)/dE$. Multi-point analysis across each sample was performed in order to obtain an average estimation of surface composition. AFM experiments were carried out in a liquid cell by using a MacMode PicoSPM magnetically driven dynamic force microscope (Molecular Imaging). Images were taken by using commercially available type II MAClevers with a nominal force constant of $2.8\ N\,m^{-1}$ at a driving frequency of 19 Hz in the liquid environment.

Received: September 14, 2005
Revised: November 2, 2005
Published online: February 10, 2006

**Keywords:** ion pairs · polymers · surface chemistry · thin films · zwitterions

[1] R. E. Holmlin, X. Chen, R. G. Chapman, S. Takayama, G. M. Whitesides, *Langmuir* **2001**, *17*, 2841 – 2850.
[2] S. Chen, J. Zheng, L. Li, S. Jiang, *J. Am. Chem. Soc.* **2005**, *127*, 14473 – 14474.
[3] B. S. Heinz, A. Laschewsky, E. D. Rekai, E. Wischerhoff, T. Zacher in *Stimuli-Responsive Water Soluble and Amphiphilic Polymers* (Ed.: C. L. McCormick), American Chemical Society, Washington, **2001**, chap. 10, pp. 162 – 180.
[4] G. Zhai, W. H. Yu, E. T. Kang, K. G. Neoh, C. C. Huang, D. J. Liaw, *Ind. Eng. Chem. Res.* **2004**, *43*, 1673 – 1680.
[5] Y. Jiang, B. Rongbing, T. Ling, S. Jian, L. Sicong, *Colloids Surf. B* **2004**, *36*, 27 – 33.
[6] S. L. West, J. P. Salvage, E. J. Lobb, S. P. Armes, N. C. Billingham, A. L. Lewis, G. W. Hanlon, A. W. Lloyd, *Biomaterials* **2004**, *25*, 1195 – 1204.
[7] W. Jiang, J. N. Awasum, K. Irgum, *Anal. Chem.* **2003**, *75*, 2768 – 2774.
[8] W. Hu, P. N. Haddad, *Trends Anal. Chem.* **1998**, *18*, 73 – 79.
[9] J. L. Brédas, R. R. Chance, R. Silbey, *Macromolecules* **1988**, *21*, 1633 – 1639.
[10] M. Galin, A. Chapoton, J.-C. Galin, *J. Chem. Soc. Perkin Trans. 2* **1993**, 545 – 553.
[11] M. Rubinstein, A. Dobrynin, *Curr. Opin. Colloid Interface Sci.* **1999**, *4*, 83 – 87.
[12] S. Moelbert, P. De Los Rios, *Macromolecules* **2003**, *36*, 5845 – 5853.
[13] V. M. Monroy Soto, J.-C. Galin, *Polymer* **1984**, *25*, 121 – 128.
[14] J. C. Salamone, W. Volksen, A. P. Olson, S. C. Israel, *Polymer* **1978**, *19*, 1157 – 1162.
[15] W.-F. Lee, G.-Y. Huang, *Polymer* **1996**, *37*, 4389 – 4395.
[16] J. Cardoso, O. Manero, *J. Polym. Sci., Part B* **1991**, *29*, 539 – 647.
[17] A. Lowe, C. L. McCormick, *Chem. Rev.* **2002**, *102*, 4177 – 4189.
[18] D. N. Schulz, D. G. Peiffer, P. K. Agarwal, J. Larabee, J. J. Kaladas, L. Soni, B. Handwerker, R. T. Garner, *Polymer* **1986**, *27*, 1734 – 1742.
[19] R. Knoesel, M. Ehrmann, J.-C. Galin, *Polymer* **1993**, *34*, 1925 – 1932.
[20] M. B. Huglin, M. A. Radwan, *Makromol. Chem.* **1991**, *192*, 2433 – 2445.
[21] M. B. Huglin, M. A. Radwan, *Polym. Int.* **1991**, *24*, 97 – 104.
[22] P. Köberle, A. Laschewsky, *Macromolecules* **1994**, *27*, 2165 – 2173.
[23] T. Kato, A. Takahashi, *Ber. Bunsen-Ges. Phys. Chem.* **1996**, *100*, 784 – 787.
[24] H. Wang, T. Hirano, M. Seno, T. Sato, *Eur. Polym. J.* **2003**, *39*, 2107 – 2114.
[25] A. R. Khokhlov, E. Y. Kramarenko, *Macromol. Theory Simul.* **1994**, *3*, 45 – 59.
[26] D. M. Jones, A. A. Brown, W. T. S. Huck, *Langmuir* **2002**, *18*, 1265 – 1269.
[27] G. Georgiev, A. Tzoneva, L. Lyutov, S. Iliev, I. Kamenova, V. Georgieva, E. Kamenska, A. Bund, *Macromol. Symp.* **2004**, *210*, 393 – 401.
[28] G. S. Georgiev, Z. P. Mincheva, V. T. Georgieva, *Macromol. Symp.* **2001**, *164*, 301 – 311.
[29] R. G. Laughlin, *Langmuir* **1991**, *7*, 842 – 847.
[30] Y. Chevalier, P. Le Perchec, *J. Phys. Chem.* **1990**, *94*, 1768 – 1774.
[31] J. G. Weers, J. F. Rathman, F. U. Axe, C. A. Crichlow, L. D. Foland, D. R. Scheuing, R. J. Wiersema, A. G. Zielske, *Langmuir* **1991**, *7*, 854 – 867.
[32] L. E. Davies, N. C. MacDonald, P. W. Palmberg, G. E. Riachy, R. E. Weber, *Handbook of Auger Electron Spectroscopy*, 2nd ed., Physical Electronics, Eden Prairie, MN, **1976**.
[33] S. Süzer, *Pure Appl. Chem.* **1997**, *69*, 163 – 168.
[34] M. C. LeMieaux, Y.-H. Lin, P. C. Cuong, H.-S. Ahn, E. R. Zubarev, V. V. Tsukruk, *Adv. Funct. Mater.* **2005**, *15*, 1529 – 1540.
[35] E. Yu. Kramarenko, I. Y. Erukhimovich, A. R. Khokhlov, *Macromol. Theory Simul.* **2002**, *11*, 462 – 471.
[36] E. Yu. Kramarenko, A. R. Khokhlov, K. Yoshikawa, *Macromol. Theory Simul.* **2000**, *9*, 249 – 256.
[37] S. B. Moldakarimov, E. Y. Kramarenko, A. R. Khokhlov, S. E. Kudaibergenov, *Macromol. Theory Simul.* **2001**, *10*, 780 – 788.
[38] D. Gersappe, M. Fasolka, A. Balacz, S. H. Jacobson, *J. Chem. Phys.* **1994**, *100*, 9170 – 9174.
[39] P. Köberle, A. Laschewsky, T. D. Lomax, *Makromol. Chem. Rapid Commun.* **1991**, *12*, 427 – 433.
[40] T. Sun, G. Wang, L. Feng, B. Liu, Y. Ma, L. Jiang, D. Zhu, *Angew. Chem.* **2004**, *116*, 361 – 364; *Angew. Chem. Int. Ed.* **2004**, *43*, 357 – 360.
[41] E. Wischerhoff, T. Zacher, A. Laschewsky, E. D. Rekai, *Angew. Chem.* **2000**, *112*, 4771 – 4773; *Angew. Chem. Int. Ed.* **2000**, *39*, 4602 – 4604.

 © 2006 Wiley-VCH Verlag GmbH & Co. KGaA, Weinheim 

*Spectroscopic Techniques*

DOI: 10.1002/anie.200503319

# Towards the Determination of the Absolute Configuration of Complex Molecular Systems: Matrix Isolation Vibrational Circular Dichroism Study of (*R*)-2-Amino-1-propanol**

*György Tarczay,* Gábor Magyarfalvi,* and Elemér Vass**

After a few decades of development, vibrational circular dichroism (VCD) spectroscopy has become one of the most powerful tools for the determination of the absolute configuration of chiral molecules.[1,2] The VCD technique has numerous advantages over electronic circular dichroism (CD) spectroscopy. First, the investigated chiral molecule does not need to have any chromophoric groups. Second, VCD spectra have richer structural content, thus the determination of the absolute configuration can be based on more assigned bands. Third, in the case of flexible molecules, the higher resolution allows the simultaneous determination of configuration and conformation.[1] Finally, ab initio calculations of VCD spectra can be carried out much more accurately,[3] hence the probability of an incorrect assignment is much smaller than in the case of electronic CD spectroscopy.

However, the limits of the VCD technique can be reached when studying molecules with multiple conformers capable of strong intermolecular interactions, especially hydrogen bonds. Because many of these substances cannot be dissolved in desirable concentration or aggregate in apolar solvents, one has to record the spectra of neat liquids or solutions in a polar solvent. In this case, the strong intermolecular interactions result in broad spectral features. Furthermore, VCD signs are sensitive to the torsional coordinates; consequently the corresponding VCD bands of different conformers often have opposite signs. These two effects together can lead to blurry, featureless spectra with low information content. Another difficulty is that theoretical modeling of these spectra is much more complicated and less accurate, as the intermolecular interactions and/or the solvent effects would need to be taken into account. Notably, these interactions not only can shift the band positions but can change the intensities and, more importantly, can alter the conformer distribution. In such cases, determination of the absolute configuration by comparison of experimental and calculated VCD spectra is difficult if not completely impossible.

As suggested earlier by Suhai et al.[4] and is demonstrated in the study herein, the combined use of VCD with matrix isolation (MI–VCD) enables the determination of the absolute configuration in the complicated cases mentioned above. To the best of our knowledge MI–VCD has, until now, been applied only to a rigid, single-conformer molecule, α-pinene.[5,6] Although these early studies reported a notable increase in the absolute intensity and much better resolved VCD spectra than the condensed-phase VCD, the MI–VCD technique did not gain widespread application owing to its technical difficulties.[7]

Besides the reported improvements, MI–VCD has numerous further benefits. First, the noble-gas matrix allows an almost interaction-free environment; hence the calculated frequencies and IR and VCD intensities can be compared directly with experiment. Second, when an effusive, direct sample-inlet source is used, the intermolecular complexes are likely to decompose at reduced pressure; if not earlier, then upon entering the high vacuum chamber. Furthermore, diffusion is prevented in low-temperature matrices. Thus, one does not need to consider aggregates during the analysis of spectra. Third, the Boltzmann distribution of the conformers at the temperature of the effusive inlet source is preserved as the molecules adhere rapidly to the cold surface. The conformer ratios can be changed by using a variable-temperature (heatable) inlet source, and this fact can significantly help the assignment of spectral features to the different conformers. Finally, comparison of the MI–VCD spectrum with the calculated VCD strengths can also help the assignments of the matrix-isolation infrared (MI–IR) spectra. As the signs of the VCD bands are usually calculated more definitely than the IR intensities, vibrational transitions with similar IR intensities but with opposite VCD signs can be assigned unambiguously.

To show the above-mentioned benefits of the method, we chose a multiconformer molecular system, (*R*)-2-amino-1-propanol ((*R*)-alaninol). A former computational and MI–IR study by Fausto et al.[8] has shown that alaninol has 25 conformers, five of which were identified in the MI–IR spectra. The VCD spectra of (*S*)-alaninol have been measured as a neat sample[9] and in solution.[10] Both spectra had broad, unresolved, low-intensity features. Owing to broadening and rotameric averaging, the theoretical calculations did not correlate well with the observed spectrum.[10] The MI–VCD technique can be used to eliminate these problems. Comparing the VCD spectrum of the neat liquid sample, the VCD spectrum of the solution, and the MI–VCD spectrum (Figure 1), it is clear, especially in the O–H and N–H stretching region, that the MI–VCD spectra have much better resolution and more information. Furthermore, the absolute intensity and even the signal-to-noise ratio are an

[*] Dr. G. Tarczay, Dr. G. Magyarfalvi, Dr. E. Vass
Institute of Chemistry, Eötvös University
P.O. Box 32, 1518 Budapest 112 (Hungary)
Fax: (+36) 1-372-2909
E-mail: tarczay@chem.elte.hu
gmagyarf@chem.elte.hu
evass@chem.elte.hu

[**] This work was funded by the Hungarian Ministry of Education (FKFP 0131/2001) and the Hungarian Scientific Research Fund (OTKA F042722 and T047186). G.T. acknowledges support from the Foundation for Hungarian Higher Education (Zoltán Magyary fellowship). E.V. was supported by the János Bolyai Research Scholarship of the Hungarian Academy of Sciences. The authors thank Professor Attila G. Császár and Professor Géza Fogarasi for useful suggestions.

Supporting information for this article is available on the WWW under http://www.angewandte.org or from the author.

 © 2006 Wiley-VCH Verlag GmbH & Co. KGaA, Weinheim 

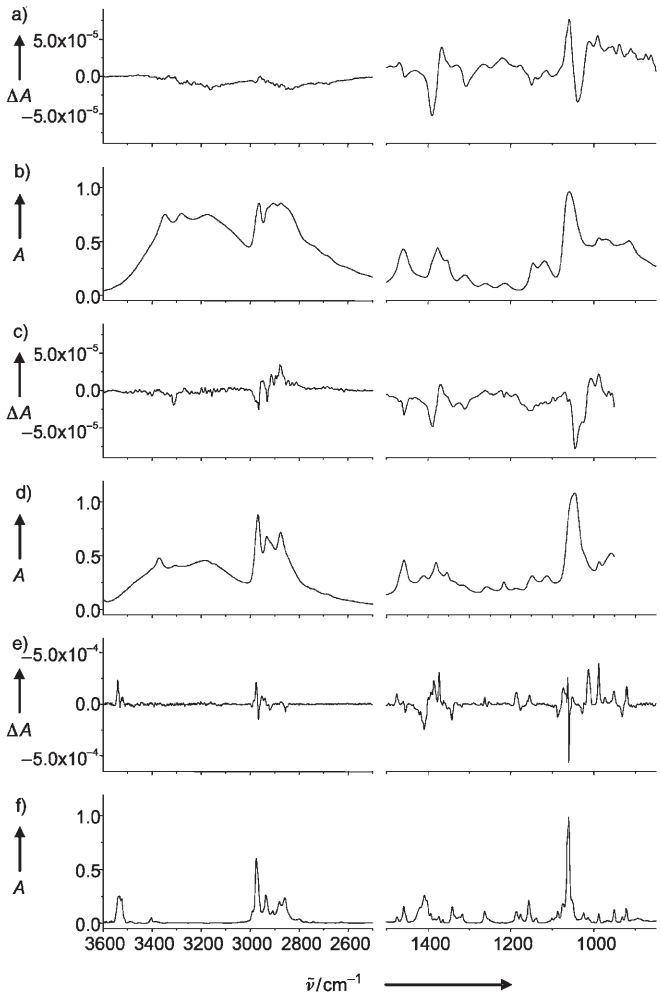



***Figure 1.*** Spectra of (*R*)-alaninol. a) VCD spectrum, neat film; b) IR spectrum, neat film; c) VCD spectrum of a sample in solution in $CDCl_3$; d) IR spectrum of a sample in solution in $CDCl_3$, e) MI–VCD spectrum; f) MI–IR spectrum.

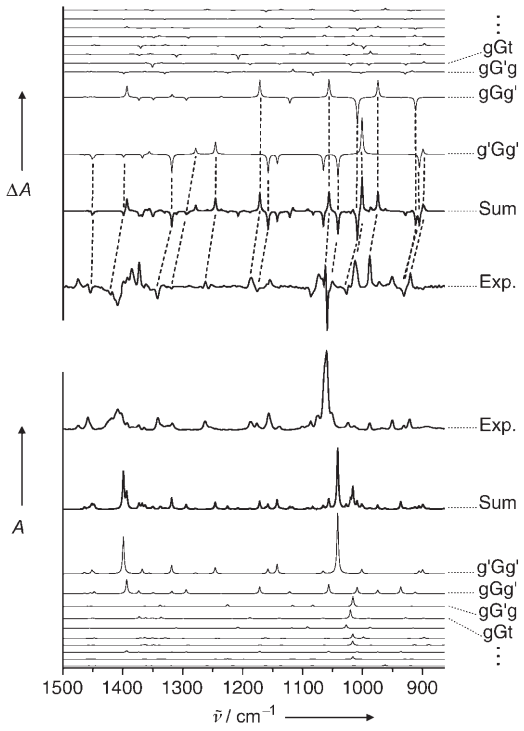



***Figure 2.*** Experimental (Ar matrix) and calculated (BPW91/TZ2P) IR (bottom traces) and VCD (top traces) spectra of (*R*)-alaninol. Labeling of conformers is consistent with reference [8]. Some of the assignments are shown by dashed lines. (See Supporting Information for details.)

order of magnitude larger in the case of MI–VCD spectra. To compare theoretical predictions with experimental data, the Gibbs energy at 298 K ($G_{298}$) was calculated for each conformer, within the framework of the Gaussian 2 (G2) procedure (see the Supporting Information).[11] From these values, the Boltzmann populations of the conformers were determined. Vibrational frequencies and IR and VCD intensities were calculated at the BPW91[12,13]/TZ2P[14] level of theory. All these calculations were carried out by using the Gaussian 98 program package.[15] The final theoretical spectra were obtained from the unscaled frequencies by using 3-$cm^{-1}$ half-width Lorentzian band shapes, summing up the 10 most abundant conformers (appropriately scaling intensities by populations), which were predicted to have populations of at least 1.5 % at 298 K. The reasonably good match (Figure 2) of the theoretical and the MI–VCD spectra of (*R*)-alaninol demonstrates that the absolute configuration of similarly complicated multiconformer systems can be unambiguously determined in this manner. This is in contrast to the neat film and solution VCD spectra, which show broader features and somewhat different band patterns. The latter are very likely caused by a different conformer distribution due to intermolecular interactions. For the analysis of these spectra, one should consider and calculate the VCD spectra of different aggregates and sample·solvent complexes. The advantage of the concerted assignments of the MI–IR and MI–VCD spectra can also be demonstrated by this case study. As an example, the band at $\tilde{\nu} = 1316\ cm^{-1}$ was assigned originally[8] to the γ-CH transition of the g′Gg′ conformer; however, the calculated VCD rotatory strength of this transition and the observed VCD band have opposite signs. On the basis of the calculations and the observed MI–VCD spectrum, this band—at least partly—belongs to the δ-COH transition of the gG′g conformer. (For details and more examples see the Supporting Information.)

In spite of its strengths, the MI–VCD technique might have three major limitations. It can be limited by the maximum size of the molecule that can be evaporated, by the maximum size of the molecule for which quantum-chemical calculations are feasible, and finally by possible VCD artifacts. The first of these limitations can be overcome by using a Knudsen inlet source or laser evaporation. (Recent examples include evaporated small model peptides.[16–18]) Moreover, in contrast to gas-phase measurements, the matrix-isolation technique has the advantage that (assuming a perfect vacuum seal) the sample stream can be arbitrarily slow—only the noble-gas stream and the deposition time have to be adjusted. Computational costs are continuously decreas-

 © 2006 Wiley-VCH Verlag GmbH & Co. KGaA, Weinheim 

ing; furthermore, parallel and hybrid quantum-mechanical/molecular-mechanical codes could be used to calculate VCD spectra. The major problem is caused by the possible artifacts, including those due to dichroism arising from stressed CsI windows and/or nonparallel alignment of the windows, and those caused by the possible inhomogeneities in the matrix. These problems can be reduced by finding better window materials, and by using slow, fully automated, matrix deposition. Baseline problems could be reduced either by recording a background of a pure Ar matrix (whose thickness is exactly the same as that of the sample/Ar mixture) or by the use of a dual polarization modulation VCD spectrometer.[19]

Finally, it is interesting that the method could also be used to investigate reactive chiral molecules (e.g. reaction intermediates, radicals), chiral·chiral (chiral recognition studies) or chiral·achiral molecular complexes (prepared either by annealing the matrix or by the use of a supersonic jet inlet). In such complexes, not only the vibrations of the chiral molecule, but also the intermolecular vibrations and the vibrations of the complexed achiral molecule have nonzero rotational strength. Thus, with the help of the MI–VCD method, it may be possible to differentiate complexes differing only in the steric alignment of the complexed achiral species. (For an example, see the Supporting Information for the computed IR and VCD spectra of two conformers of (*R*)-alaninol·$H_2O$.)[20]

## Experimental Section

A mixture of (*R*)-alaninol (Aldrich, 98% pure, without further purification) and Ar (Messer, 99.996%) (1:1000, 298 K, 0.5–0.1 bar) was deposited at a rate of 0.1 mmol $min^{-1}$ on a CsI plate cooled to 9–12 K by a CTI Cryogenics closed-cycle cryostat. The deposition was continued until reaching $A \approx 1$ for the most intense infrared transition of the investigated spectral ranges. (The intensities in different ranges were renormalized afterwards on the basis of the complete IR spectrum.) After completing the deposition, the cold head was inserted into a Bruker PMA 37 unit equipped with a ZnSe photoelastic modulator (calibrated with a CdS stress plate) and coupled with an Equinox 55 FTIR spectrometer. To minimize artifacts in the VCD spectra, the cold head was aligned in such a way that both the CsI plate and the KBr windows of the head were perpendicular to the IR beam. To improve the signal-to-noise ratio, the spectra were recorded in two spectral ranges using quartz (2200–3600 $cm^{-1}$) and broad-band (830–1830 $cm^{-1}$) optical filters. A HgCdTe detector and a lock-in amplifier were used for signal processing. The acquisition time was 6–9 h; the spectral resolution was set to 2 $cm^{-1}$. After data processing, the baseline of the raw VCD spectra was corrected by fitting a polynomial onto points with zero absorbance, as determined by the corresponding MI–IR spectrum. For comparison, the VCD spectra of (*R*)-alaninol as a neat liquid film ($\approx$12 μm between $BaF_2$ windows) and in solution (35 mg $mL^{-1}$) in $CDCl_3$ (Aldrich, 99.8%) in a 250-μm NaCl cuvette were also recorded.

Received: September 19, 2005
Revised: November 21, 2005
Published online: February 14, 2006

**Keywords:** circular dichroism · configuration determination · conformation analysis · matrix isolation · vibrational spectroscopy

[1] T. B. Freedman, X. Cao, R. K. Dukor, L. A. Nafie, *Chirality* **2003**, *15*, 743.
[2] T. A. Keiderling in *Circular Dichroism and the Conformational Analysis of Biomolecules* (Ed.: G. D. Fasman), Plenum, New York, **1996**, pp. 555–598.
[3] P. J. Stephens, F. J. Devlin, *Chirality* **2000**, *12*, 172.
[4] K. J. Jalkanen, S. Suhai, *Chem. Phys.* **1996**, *208*, 81.
[5] D. W. Schlosser, F. Devlin, K. Jalkanen, P. J. Stephens, *Chem. Phys. Lett.* **1982**, *88*, 286.
[6] D. O. Henderson, P. L. Polavarapu, *J. Am. Chem. Soc.* **1986**, *108*, 7110.
[7] P. J. Stephens, M. A. Lowe, *Annu. Rev. Phys. Chem.* **1985**, *36*, 213.
[8] R. Fausto, C. Cacela, M. L. Duarte, *J. Mol. Struct.* **2000**, *550–551*, 365.
[9] N. T. Cheok, P. Bour, T. A. Keiderling, *J. Am. Chem. Soc.* **1997**, *119*, 7061.
[10] X. Qu, M. Citra, N. Ragunathan, T. B. Freedman, L. A. Nafie, *Proceedings of the 9th International Conference on Fourier Transform Spectroscopy*, SPIE Vol. 2089, **1993**, p. 142.
[11] L. A. Curtiss, K. Raghavachari, G. W. Trucks, J. A. Pople, *J. Chem. Phys.* **1991**, *94*, 7221.
[12] A. D. Becke, *Phys. Rev. A* **1998**, *38*, 3098.
[13] J. P. Perdew, K. Burke, Y. Wang, *Phys. Rev. B* **1996**, *54*, 16533.
[14] T. H. Dunning, P. J. Hay in *Methods of Electronic Structure Theory, Vol. 2*, Plenum, New York, **1977**.
[15] Gaussian 98 (Revision A.11.3), M. J. Frisch, G. W. Trucks, H. B. Schlegel, G. E. Scuseria, M. A. Robb, J. R. Cheeseman, V. G. Zakrzewski, J. A. Montgomery, R. E. Stratmann, J. C. Burant, S. Dapprich, J. M. Millam, A. D. Daniels, K. N. Kudin, M. C. Strain, O. Farkas, J. Tomasi, V. Barone, M. Cossi, R. Cammi, B. Mennucci, C. Pomelli, C. Adamo, S. Clifford, J. Ochterski, G. A. Petersson, P. Y. Ayala, Q. Cui, K. Morokuma, D. K. Malick, A. D. Rabuck, K. Raghavachari, J. B. Foresman, J. Cioslowski, J. V. Ortiz, B. B. Stefanov, G. Liu, A. Liashenko, P. Piskorz, I. Komaromi, R. Gomperts, R. L. Martin, D. J. Fox, T. Keith, M. A. Al-Laham, C. Y. Peng, A. Nanayakkara, C. Gonzalez, M. Challacombe, P. M. W. Gill, B. G. Johnson, W. Chen, M. W. Wong, J. L. Andres, M. Head-Gordon, E. S. Replogle, J. A. Pople, Gaussian, Inc., Pittsburgh, PA, **1998**.
[16] C. Unterberg, A. Gerlach, T. Schrader, M. Gerhards, *J. Chem. Phys.* **2003**, *118*, 8296.
[17] H. Fricke, A. Gerlach, C. Unterberg, P. Rzepcki, T. Schrader, M. Gerhards, *Phys. Chem. Chem. Phys.* **2004**, *6*, 4636.
[18] W. Chin, J.-P. Dognon, C. Canuel, F. Piuzzi, I. Dimicoli, M. Mons, I. Compagnon, G. v. Helden, G. Meijer, *J. Chem. Phys.* **2005**, *122*, 054317.
[19] L. A. Nafie, *Appl. Spectrosc.* **2000**, *54*, 1634.
[20] Note added in proof: After submission of this Communication, a study was published on the VCD spectra of D-lactic acid–water complexes. In agreement with the work discussed herein, the authors concluded that upon complexation, the chiral water molecule acquires significant rotational strength. The sign and magnitude of these VCD lines depend strongly on the geometry of the complex: J. Sadlej, J. C. Dorowolski, J. E. Rode, M. H. Jamróz, *Phys. Chem. Chem. Phys.* **2006**, *8*, 101.

 © 2006 Wiley-VCH Verlag GmbH & Co. KGaA, Weinheim 

Oligosaccharide Synthesis

DOI: 10.1002/anie.200503427

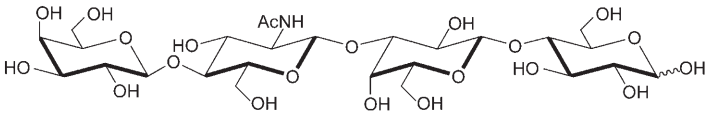
# Large-Scale Synthesis of H-Antigen Oligosaccharides by Expressing *Helicobacter pylori* α1,2-Fucosyltransferase in Metabolically Engineered *Escherichia coli* Cells**

*Sophie Drouillard,* Hugues Driguez, and Eric Samain*

The H antigen is defined by the terminal disaccharide structure Fucα-2Gal. This motif constitutes the basis of the human AB0 histo-blood group system, the A and B antigens being formed by the additional transfer of a Gal or GalNAc residue to the H(0) antigen. In the type 1 and type 2 series, the H antigen is attached to a GlcNAc residue with a β1,3- and a β1,4-linkage (H-1 and H-2 antigens, respectively), whereas it is bound to GalNAc by a β1,3-linkage in the type 3 and type 4 series.[1] The ABH antigens are found on red blood cells, but are also widely distributed in various tissues and secretion fluids. In particular, they are abundant in the intestinal epithelium in which they can serve as receptors for pathogens.[2] *Campylobacter jejuni*, which is the most common cause of bacterial diarrhea, binds to the H-2 antigen[3] and the Norwalk virus, which has been responsible for large outbreaks of gastroenteritis, has been shown to use the H-1 antigen as its primary receptor.[4] Breast feeding protects infants against these infections, which was proven to be a consequence of the presence of large quantities of H-antigen oligosaccharides in human milk. These molecules act as soluble receptors that compete with epithelial ligands, and it has been suggested that synthetic H-antigen oligosaccharides could be used as anti-infective agents.[5]

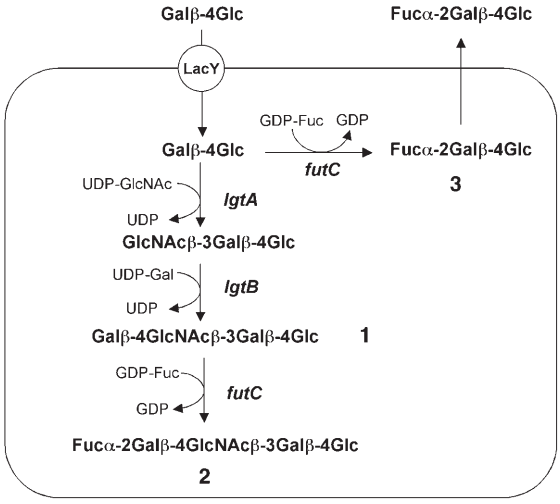
Human milk is unique in containing large quantities of fucosylated oligosaccharides,[6] and these molecules cannot readily be purified from alternative natural sources. Chemical[7,8] and enzymatic[9,10] syntheses of the Fucα-2Gal motif have been achieved, but the methods used are not applicable to the large-scale production of H-antigen structures. Oligosaccharide synthesis by metabolically engineered *Escherichia coli* strains that overexpress heterologous glycosyltransferase genes is a powerful new technique that makes the low-cost production of large amounts of complex carbohydrates possible.

Recently, we have developed an efficient method for the conversion of lactose into lacto-*N*-neotetraose (LNnT; **1**), by



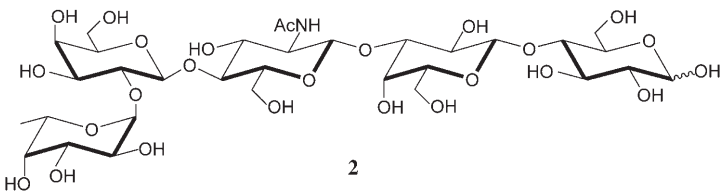
**1**

using a strain which overexpressed *Neisseria meningitidis lgtA* and *lgtB* genes for β1,3-*N*-acetylglucosaminyltransferase and β1,4-galactosyltransferase.[11] As illustrated in Scheme 1, this




***Scheme 1.*** In vivo biosynthesis pathway for **2** and **3** from lactose in engineered *E. coli* cells. Lactose is internalized by the β-galactoside permease LacY and cannot be degraded because of total *lacZ* inactivation. It is glycosylated by β1,3-GlcNAcT and β1,4-GalT encoded by the *N. meningitidis lgtAB* genes. The main final product **1** and lactose are possible acceptors for α1,2-fucosyltransferase encoded by the *H. pylori futC* gene using GDP-Fuc available in the bacterium by overexpressing the *rcsA* gene and by inactivating the *wcaJ* gene.

concept could be used for the first synthesis of lacto-*N*-neofucopentaose-1 (LNnF-1, **2**), an H-2 antigen oligosaccharide, by additionally expressing an α1,2-fucosyltransferase gene in a strain engineered to overproduce GDP-fucose, as already described for the synthesis of Lewis$^x$ structures.[12] Unfortunately, neither of the two mammalian genes *fut1* and *fut2* has been reported to be functionally expressed in *E. coli*. Two bacterial α1,2-fucosyltransferase genes have been cloned from *Helicobacter pylori* (*futC*)[13] and *E. coli* O86 (*wbnK*).[14] However, in vitro assays indicated that the WbnK protein



**2**

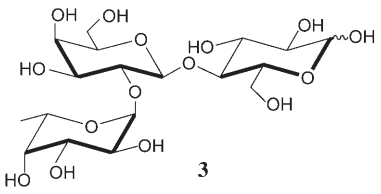
[*] Dr. S. Drouillard, Dr. H. Driguez, Dr. E. Samain
CERMAV-CNRS
BP 53, 38041 Grenoble Cedex 9 (France)
Fax: (+33) 4-7654-7203
E-mail: sophie.drouillard@cermav.cnrs.fr

[**] CERMAV-CNRS is affiliated with the Université Joseph Fourier and is a member of the ICMG (Institut de Chimie Moléculaire de Grenoble).

Supporting information for this article is available on the WWW under http://www.angewandte.org or from the author.


InterScience
© 2006 Wiley-VCH Verlag GmbH & Co. KGaA, Weinheim

only fucosylated the Galβ-3GalNAc motif,[15] and that FutC had the highest activity on type 1 precursors but was almost inactive on type 2 structures unless they contained an α1,3-linked fucose (Lewis$^X$ antigen).[16] The FutC protein was later shown to be a great deal more active when produced as a fusion protein and was successfully used to enzymatically synthesize 2′-fucosyllactose (**3**) at the milligram scale.[9] We



**3**

therefore investigated the use of *futC* for the production of **2**, and we first assessed its expression as a fusion gene under the control of different promoters.

The *futC* gene was amplified by the polymerase chain reaction (PCR) using genomic DNA from *H. pylori* (strain 26695) as a template. The gene contained a 14C tract, which caused a translational frame shift which led to the production of an inactive truncated form.[13] Using PCR splicing by overlap extension[17] (see the Supporting Information), the 14C tract was replaced by the 12-nucleotide sequence CCACCACCACCC to restore the reading frame, eliminate three consecutive rare CCC codons, and prevent potential high-frequency mutations that occur in homopolymeric tracts. The *futC* gene was cloned into the pET-21a and pET-32a plasmids under the control of the T7 promoter and in the pEXT20 and pGEX-6P-3 plasmids under the control of the tac promoter (see the Supporting Information). In vitro assays were performed with lacto-*N*-tetraose (LNT) as an acceptor (Table 1). The results showed that similar fucosyltransferase activities were observed with both promoters and that the expression of *futC* as a fusion gene in the pET-32a and pGEX-6P-3 plasmids did not improve the activity. No significant activity could be detected with lactose, *N*-acetyllactosamine, or LNnT (**1**) as the substrates, which confirmed the previous observations that *futC* was almost inactive on type 2 acceptors.[16]

***Table 1:*** In vitro fucosyltransferase assays.[a]

| Strain | Plasmid | Host | Promoter | Fusion protein | Activity [%][b] |
|---|---|---|---|---|---|
| SD1 | pET-21a*futC* | RIL | T7 | no | 100 |
| SD2 | pEXT20*futC* | JM109 | tac | no | 90 |
| SD3 | pET-32a*futC* | RIL | T7 | thioredoxine | 18 |
| SD4 | pGEX*futC* | JM109 | tac | GST | 32 |

[a] The enzymatic assays were performed at 37 °C for 2 h in a final volume (50 μL) containing Tris–HCl (50 mM, pH 7.0), $MnCl_2$ (20 mM), NaCl (100 mM), $MgCl_2$ (35 mM), ATP (1 mM), bovine serum albumin (5 mg mL$^{-1}$), lacto-*N*-tetraose (1.5 mM) as acceptor, GDP-Fuc (50 mM), $^{14}$C-GDP-Fuc (1.5 μM, 323 mCi mmol$^{-1}$, Amersham), and proteic French extract (5 μL). Reactions were stopped by adding Dowex 1X8-400 chloride anion-exchange resin (500 μL, 0.25 g mL$^{-1}$ in water). After centrifugation, the supernatant was added to liquid scintillation cocktail (4 mL, Amersham) to quantify incorporated radioactivity. [b] The relative activity is expressed as a percentage of the SD1 strain activity (0.13 nmol min$^{-1}$ mg$^{-1}$).

We nevertheless attempted to produce compound **2** in living bacteria. The SD5 strain was constructed by co-transforming the Col1F′ΔlacZ,DE3 host[18] with pET-21a*futC* and the pLNTR plasmid, which harbored both the *N. meningitidis lgtAB* and the *rcsA* genes. The SD5 strain was cultured at high cell density with glucose as the carbon and energy source and fed with lactose (5 g L$^{-1}$). After 22 h of incubation, the lactose was completely consumed and TLC analysis indicated that the intracellular fraction contained two major sugars, which migrated slightly slower than lactose and **1** (see the Supporting Information). Starting from 1 L of culture, 3 g of an oligosaccharide mixture was recovered after purification of the intracellular fraction on activated charcoal. A further purification by chromatography on a Biogel P2 column allowed **2** and **3** to be isolated and identified as main products (57 and 23 %, respectively, in the mixture).

The production of **2** and **3** by the SD5 strain showed that the activity of FutC on type 2 precursors, which was barely detectable in the in vitro experiments, was high enough in living cells to enable a large amount of the H-antigen oligosaccharide to be synthesized. This discrepancy in fucosyltransferase activity could be explained by the previously reported high instability of FutC after cell lysis,[16] but could also be a result of the fact that the cytoplasm of living *E. coli* represents a more appropriate environment for bacterial glycosyltransferase activity than synthetic reaction media. In any case, these results confirmed the advantage of using living bacteria for the production of complex oligosaccharides. The formation of large quantities of **3** in SD5 strain cultures indicated that FutC used lactose efficiently as an acceptor, which resulted in a significant decrease in the expected yield of **2**. It should, however, be possible to improve the yield of **2** by delaying *futC* expression until the tetrasaccharide **1** is already synthesized, to minimize the production of **3** as a side product. On the other hand, **3** is a valuable oligosaccharide that inhibits *Campylobacter* colonization of human intestinal mucosa[3] and is present at high concentrations in human milk.

To produce **3** without **2**, the SD6 strain, which only expresses *futC* and *rcsA*, was constructed and cultured at high cell density as for the SD5 strain in the presence of lactose (5 g L$^{-1}$). After 25 h incubation, lactose was completely consumed and converted into **3**, whose final intra- and extracellular concentrations were colorimetrically quantified and estimated to be 1 and 3 g L$^{-1}$, respectively. By increasing the initial lactose concentration (15 g L$^{-1}$) and the culture time (45 h), these values were improved to 3 and 11 g L$^{-1}$, respectively. Purification on a Biogel P2 column showed that most of the product, after charcoal adsorption, was composed of **3**.

In conclusion, we have developed an efficient method for the production of fucosyl α1,2-linked oligosaccharides by the high-cell-density culture of metabolically engineered *E. coli* strains that overexpress the *H. pylori futC* gene for α1,2-fucosyltransferase. On account of its recognized anti-infective properties, very high yields, and extracellular recovery which facilitates its purification, trisaccharide 2′-fucosyllactose (**3**) could possibly be produced industrially on a multiton scale for nutraceutic applications. The pentasaccharide LNnF-1 (**2**) contains the H-2 antigen structure and could be used as a

 © 2006 Wiley-VCH Verlag GmbH & Co. KGaA, Weinheim 

precursor for the synthesis of other antigens of the ABH histo-blood-group system.

## Experimental Section

The culture process was carried out at 28 °C and pH 6.8 in a 2-L reactor containing mineral culture medium (1 L), as previously described.[19] The procedure consisted first of an exponential growth phase, which started with the inoculation of the fermenter and lasted until exhaustion of glucose (17.5 g) as the carbon substrate. The lactose acceptor was added together with the inducer (isopropyl thio-B-D-galactopyranoside (IPTG), 50 mg $L^{-1}$) at the end of this phase. Then, the fed-batch culture was maintained at a glucose feeding rate of 4.5 g $L^{-1}$ $h^{-1}$ for 5 h and of 2.4 g $L^{-1}$ $h^{-1}$ until consumption of the acceptor. Extracellular oligosaccharides were obtained in the supernatant after centrifugation of the culture (30 min at 7000 *g*). For the intracellular oligosaccharides, bacterial cells of the pellet were suspended and permeabilized by several freeze–thaw cycles. The intracellular oligosaccharides were contained in the supernatant after an additional identical centrifugation. The total fucose of the extra- and intracellular media was quantified colorimetrically after acid hydrolysis by the cysteine chloride reagent method.[20] The oligosaccharides were adsorbed on activated charcoal/celite (1:1, w/w) and eluted with 50% aqueous ethanol. They were separated by size-exclusion chromatography on a Biogel P2 column (1.5 × 200 cm) at 60 °C with water as the mobile phase at a flow rate of 35 mL $h^{-1}$. Pure **2** (13 mg, SD5 culture) and **3** (72 mg, SD6 culture) were isolated from 100 mg of the charcoal-adsorbed fraction for characterization. ESI mass spectra were recorded on a ZQ Waters micromass spectrometer (capillary: 3.5 kV; cone voltage: 80 V). $^1$H and $^{13}$C NMR spectra were obtained with a 300-MHz Bruker AVANCE spectrometer.

**2**: ESI MS: *m*/*z* 876 $[M+Na]^+$; $^1$H NMR ($D_2O$, 303 and 323 K): $\delta = 5.30$ (H-1‴″, d, $J = 2$ Hz, 1H), 5.22 (H-1α, d, $J = 3.4$ Hz, 0.4H), 4.73 (H-1″, d, $J = 7.8$ Hz, 1H), 4.66 (H-1β, d, $J = 7.8$ Hz, 0.6H), 4.54 (H-1‴, d, $J = 7.8$ Hz, 1H), 4.44 (H-1′, d, $J = 7.8$ Hz, 1H), 4.22 (H-5‴″, q, $J = 6.8$ Hz, 1H), 4.14 (H-4′, d, $J = 3$ Hz, 1H), 3.28 (H-2β, m, $J =$ 7.8 Hz, 0.6H), 2.04 ($COCH_3$, s, 3H), 1.23 ppm (H-6‴″, d, $J = 6.8$ Hz, 3H); $^{13}$C NMR ($D_2O$, 303 K): $\delta = 176.1$ (CO), 104.1, 103.9 (C-1′, C-1″), 101.5 (C-1‴), 100.6 (C-1‴″), 97.0 (C-1β), 93.1 (C-1α), 83.2 (C-3′), 56.6 (C-2″), 23.5 ($CH_3$), 16.5 ppm (C-6‴″). **3**: ESI MS: *m*/*z* 511 $[M+Na]^+$; NMR spectra were in agreement with previously reported assignments.[9]

Received: September 28, 2005
Published online: February 14, 2006

**Keywords:** antigens · biosynthesis · gene technology · oligosaccharides · transferases

[1] S. Marionneau, A. Cailleau-Thomas, J. Rocher, B. Le Moulhac-Vaidye, N. Ruvoën, M. Clément, J. Le Pendu, *Biochimie* **2001**, *83*, 565 – 573.
[2] S. M. Henry, *Transfus. Clin. Biol.* **2001**, *8*, 226 – 230.
[3] G. M. Ruiz-Palacios, L. E. Cervantes, P. Ramos, B. Chavez-Munguia, D. S. Newburg, *J. Biol. Chem.* **2003**, *278*, 14112 – 14120.
[4] J. Le Pendu, *Adv. Exp. Med. Biol.* **2004**, *554*, 135 – 143.
[5] D. S. Newburg, *J. Nutr.* **1997**, *127 (Suppl. 5)*, 980S – 984S.
[6] C. Kunz, S. Rudloff, W. Baier, N. Klein, S. Strobel, *Annu. Rev. Nutr.* **2000**, *20*, 699 – 722.
[7] R. U. Lemieux, H. Driguez, *J. Am. Chem. Soc.* **1975**, *97*, 4069 – 4075.
[8] R. K. Jain, R. D. Locke, K. L. Matta, *Carbohydr. Res.* **1991**, *212*, C1 – C3.
[9] C. Albermann, W. Piepersberg, U. F. Wehmeier, *Carbohydr. Res.* **2001**, *334*, 97 – 103.
[10] A. M. Scheppokat, H. Bretting, J. Thiem, *Carbohydr. Res.* **2003**, *338*, 2083 – 2090.
[11] B. Priem, M. Gilbert, W. W. Wakarchuk, A. Heyraud, E. Samain, *Glycobiology* **2002**, *12*, 235 – 240.
[12] C. Dumon, B. Priem, S. L. Martin, A. Heyraud, C. Bosso, E. Samain, *Glycoconjugate J.* **2001**, *18*, 465 – 474.
[13] G. Wang, D. A. Rasko, R. Sherburne, D. E. Taylor, *Mol. Microbiol.* **1999**, *31*, 1265 – 1274.
[14] J. Shao, M. Li, Q. Jia, Y. Lu, P. G. Wang, *FEBS Lett.* **2003**, *553*, 99 – 103.
[15] W. Yi, J. Shao, L. Zhu, M. Li, M. Singh, Y. Lu, S. Lin, H. Li, K. Ryu, J. Shen, H. Guo, Q. Yao, A. Bush, P. G. Wang, *J. Am. Chem. Soc.* **2005**, *127*, 2040 – 2041.
[16] G. Wang, P. G. Boulton, N. W. C. Chan, M. M. Palcic, D. E. Taylor, *Microbiology* **1999**, *145*, 3245 – 3253.
[17] R. M. Horton, Z. L. Cai, S. N. Ho, L. R. Pease, *Biotechniques* **1990**, *8*, 528 – 535.
[18] C. Dumon, E. Samain, B. Priem, *Biotechnol. Prog.* **2004**, *20*, 412 – 419.
[19] E. Samain, S. Drouillard, A. Heyraud, H. Driguez, R. A. Geremia, *Carbohydr. Res.* **1997**, *302*, 35 – 42.
[20] Z. Dische, L. B. Shettles, *J. Biol. Chem.* **1948**, *175*, 595 – 603.

 © 2006 Wiley-VCH Verlag GmbH & Co. KGaA, Weinheim 

Cyclic Peptides

DOI: 10.1002/anie.200503470

# A Striking Periodicity of the *cis*/*trans* Isomerization of Proline Imide Bonds in Cyclic Disulfide-Bridged Peptides**

*Tiesheng Shi, Stephen M. Spain, and Dallas L. Rabenstein**

Many peptide hormones and peptide toxins contain one or more intramolecular disulfide bonds that are essential for biological activity. Intramolecular disulfide bonds are also used in the de novo design of peptides and peptidomimetic compounds to confer structural constraints that increase bioactivity and selectivity and to improve bioavailability,[1] and disulfide-bridged peptides are used as scaffolds in the development of new drug leads, through combinatorial or phage-display peptide libraries.[2,3]

The disulfide-bridged peptide rings often contain one or more proline residues.[4] Proline can facilitate the formation of β-turns[5] and increase structural diversity as a result of *cis*/

[*] Dr. T. Shi, Dr. S. M. Spain, Prof. Dr. D. L. Rabenstein
Department of Chemistry
University of California
Riverside, CA 92521 (USA)
Fax: (+1) 951-827-4713
E-mail: dlrab@ucrac1.ucr.edu

[**] This work was supported in part by National Institutes of Health grant GM 37000.


WILEY InterScience DISCOVER SOMETHING GREAT
© 2006 Wiley-VCH Verlag GmbH & Co. KGaA, Weinheim

*trans* isomerization across the Xaa–Pro peptide bond (where Xaa is any amino acid). Because interchange between the *cis* and *trans* isomers by rotation around the Xaa–Pro peptide bond is slow on the NMR spectroscopy time scale, both isomers can be observed directly in NMR spectra of proline-containing peptides. The population of the *cis* conformation is typically 5–20% for linear proline-containing peptides.[6–8] However, structural constraints imposed by disulfide bond(s) can force Xaa–Pro peptide bonds located within disulfide-bridged ring(s) to be predominantly or even completely in the normally less-favored *cis* conformation (cf. sea anemone polypeptide anthopleurin,[9] $\delta$-conotoxin EVIA,[10] and sunflower trypsin inhibitor SFTI-1, a 14 amino acid peptide with a disulfide bridge between cysteine 3 and cysteine 11[11,12]). Thus, knowledge of the structural and dynamic properties of Xaa–Pro peptide bonds embedded within disulfide-bridged peptide rings will contribute to the insightful design of new bioactive peptides or peptidomimetic compounds. Herein, we report, for the first time, a striking periodicity of the *cis/trans* isomerization of the Cys–Pro peptide bond in the cyclic disulfide-bridged form of peptides of the sequence Ac-Cys-Pro-(Xaa)$_m$-Cys-NH$_2$. Knowledge of this effect provides a new design feature for increasing and controlling the structural diversity of peptide libraries.

Table 1 lists the (reduced) linear dithiol (***n*R**) and (oxidized) cyclic disulfide (***n*O**) peptides synthesized and studied in the present work, where ***n*** is the number of amino acid residues. The parent peptides **4R** and **4O** are model compounds for the reduced and oxidized forms of the active site of the thiol-disulfide oxidoreductase enzyme glutaredoxin (thioltransferase);[13] other peptides in Table 1 are derived from **4R** and **4O**, conferring a variation in ring size for the oxidized form of the peptide. The room-temperature $^1$H NMR spectra of both the reduced and oxidized forms of each peptide listed in Table 1 show two sets of resonances. Using methods described previously,[14,15] the two sets of resonances were assigned to peptides having the *cis* and *trans* conformations across the Cys–Pro peptide bond on the basis of Cys$^1$–C$_\alpha$H/Pro–C$_\alpha$H, and Cys$^1$–C$_\alpha$H/Pro–C$_\delta$H$_2$ cross peaks, respectively, in 2D ROESY spectra. Equilibrium constants for *cis/trans* isomerization ($K = [trans]/[cis]$) were determined from resonance intensities at 25 °C. Rate constants for *cis*-to-*trans* isomerization, $k_{ct}$, (in cases where the *trans* conformation is the more abundant) and for *trans*-to-*cis* isomerization, $k_{tc}$, (in cases where the *cis* conformation is the more abundant) were determined by the inversion magnetization-transfer method.[15–17] Rate constants $k_{tc}$ and $k_{ct}$ were calculated from $k_{ct}$ and $k_{tc}$, respectively, and $K$. The values determined for equilibrium constants and for rate constants and their activation parameters are summarized in Table 2.

***Table 1:*** Synthesized and characterized peptides.[a]

| Peptide | Sequence | Monoisotopic mass: theoretical (found)[b] | NMR resonances for kinetic study[c] |
|---|---|---|---|
| **3R** | Ac-Cys-Pro-Cys-NH$_2$ | 362.1 (362) | Cys$^1$ NH |
| **3O** | Ac-Cys-Pro-Cys-NH$_2$ | 360.1 (360) | [d] |
| **4R**[e] | Ac-Cys-Pro-Phe-Cys-NH$_2$ | 509.2 (509) | Acetyl CH$_3$ |
| **4O**[e] | Ac-Cys-Pro-Phe-Cys-NH$_2$ | 507.2 (507) | Acetyl CH$_3$ |
| **5R** | Ac-Cys-Pro-Phe-Ala-Cys-NH$_2$ | 580.2 (580) | Acetyl CH$_3$ |
| **5O** | Ac-Cys-Pro-Phe-Ala-Cys-NH$_2$ | 578.2 (578) | Acetyl CH$_3$ |
| **6R** | Ac-Cys-Pro-Phe-Ala-Ala-Cys-NH$_2$ | 651.3 (651) | Acetyl CH$_3$ |
| **6O** | Ac-Cys-Pro-Phe-Ala-Ala-Cys-NH$_2$ | 649.1 (649) | Phe NH |
| **7R** | Ac-Cys-Pro-Phe-Ala-Ala-Ala-Cys-NH$_2$ | 722.3 (722) | [f] |
| **7O** | Ac-Cys-Pro-Phe-Ala-Ala-Ala-Cys-NH$_2$ | 720.3 (720) | Acetyl CH$_3$ |

[a] Peptides larger than **7R** and **7O** were not studied because of low solubility in water. [b] Measured either by fast atom bombardment (FAB-MS) or by matrix-assisted laser desorption/ionization mass spectrometry (MALDI-MS). [c] The pair of resonances for the *cis* and *trans* isomers used in magnetization-transfer NMR experiments. [d] Peptide **3O** isomerizes in aqueous solution to a reaction mixture that was not characterized; **3O** also is extremely hygroscopic. [e] Data from ref. [8]. [f] No suitable *cis/trans* pair of resonances could be found for the inversion magnetization-transfer experiments.

The *cis* isomers of the Cys–Pro peptide bond are the least abundant for the linear dithiol peptides, as expected, varying from 10% to 20%. However, the population of the *cis* isomers of the cyclic disulfide peptides varies over a much wider range (9.3% to 76.9%) and shows a striking dependence on the size of the disulfide-bridged ring (Figure 1); formation of the disulfide bond causes a significant increase in the *cis* population for peptides with an odd number of amino acids in the ring (from 10.3% to 21.7% for peptide **3**, from 14.9% to 59.5% for peptide **5**, and from 20.4% to 76.9% for

***Table 2:*** Equilibrium constants, rate constants, and activation parameters for *cis/trans* isomerization of the Cys–Pro imide bond.[a,b]

| Peptide | $K$[c] | % *cis* | $k_{ct}$ [s$^{-1}$][d] | $k_{tc}$ [s$^{-1}$][d] | $\Delta H^{\ddagger}_{ct}$ [kcal mol$^{-1}$] | $\Delta S^{\ddagger}_{ct}$ [cal K$^{-1}$ mol$^{-1}$] | $\Delta G^{\ddagger}_{ct}$ [kcal mol$^{-1}$] |
|---|---|---|---|---|---|---|---|
| **3R** | 8.7 ± 0.2 | 10.3 | $3.9\times10^{-2}$[e] | $4.4\times10^{-3}$[e] | 21.1 ± 0.5 | 2 ± 2 | 20.5 ± 0.5 |
| **3O**[f] | 3.6 ± 0.3 | 21.7 | | | | | |
| **4R**[g] | 7.3 ± 0.3 | 12.0 | $4.3\times10^{-2}$[e] | $6.0\times10^{-3}$[e] | 21.3 ± 1.2 | 6 ± 4 | 19.5 ± 1.5 |
| **4O**[g] | 9.8 ± 0.2 | 9.3 | $4.2\times10^{-1}$ | $4.3\times10^{-2}$ | 18.6 ± 0.7 | 2 ± 2 | 18.0 ± 1.1 |
| **5R** | 5.7 ± 0.5 | 14.9 | $4.9\times10^{-2}$[e] | $8.7\times10^{-3}$[e] | 20.8 ± 1.3 | 6 ± 1 | 19.0 ± 1.5 |
| **5O** | 0.68 ± 0.05 | 59.5 | $1.4\times10^{-1}$ | $2.0\times10^{-1}$ | 17.9 ± 0.7 | −2 ± 2 | 18.6 ± 0.9 |
| **6R** | 6.5 ± 0.5 | 13.3 | $6.1\times10^{-2}$[e] | $9.4\times10^{-3}$[e] | 20.9 ± 0.2 | 6 ± 1 | 19.1 ± 0.2 |
| **6O** | 7.2 ± 0.2 | 12.2 | $8.1\times10^{-2}$[e] | $1.1\times10^{-2}$[e] | 23.1 ± 0.7 | 14 ± 2 | 18.9 ± 0.7 |
| **7R**[h] | 3.9 ± 0.1 | 20.4 | | | | | |
| **7O** | 0.30 ± 0.01 | 76.9 | $4.4\times10^{-3}$[e] | $1.7\times10^{-2}$[e] | 21.9 ± 1.7 | 4 ± 5 | 20.6 ± 2.3 |

[a] In 90% $H_2O$/10% $D_2O$ at pH 3.0. [b] The rate and equilibrium constants and values of $\Delta G^{\ddagger}_{ct}$ refer to 25 °C. [c] $K = [trans]/[cis]$. [d] Average uncertainty of rate constants is ± 10%. [e] Values were obtained by extrapolating to 25 °C using the activation parameters determined from the rate data measured at higher temperatures. [f] It was not possible to characterize the *cis/trans* isomerization kinetics because of the instability of the peptide over the time required to measure the kinetic data by the inversion magnetization-transfer method. [g] Data from ref. [8]. [h] No suitable *cis/trans* pair of resonances could be found for the inversion magnetization-transfer experiments.


© 2006 Wiley-VCH Verlag GmbH & Co. KGaA, Weinheim

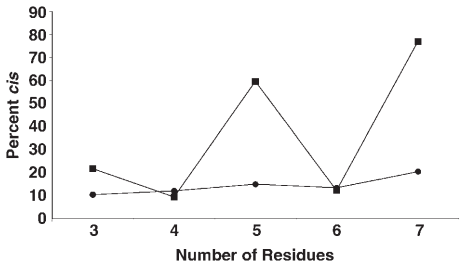



***Figure 1.*** Percent *cis* conformation of the Xaa–Pro imide bond as a function of the number of residues in the linear dithiol peptides (●) and cyclic disulfide peptides (■).

peptide **7**), but a slight decrease for peptides with an even number of amino acids in the ring (from 12.1% to 9.3% for peptide **4** and from 13.3% to 12.2% for peptide **6**). Because structural constraints might be expected to decrease as the ring-size increases, the finding that the *cis* isomer is the dominant species for peptides **5O** and **7O** is unexpected, as is the periodic change in *cis* and *trans* populations (Figure 1). To our knowledge, this is the first observation that the *cis* and *trans* populations of Xaa–Pro peptide bonds periodically change with the size of the ring for disulfide-bridged peptides. It is interesting, however, that a periodic sequence-length dependence was reported for the β-sheet content of cyclic peptide homologues of gramicidin S containing 6, 8, 10, 12, 14, and 16 residues (cyclized by peptide bonds rather than disulfide bridges).[18]

The *cis* and *trans* conformations are in equilibrium, and their relative populations are determined by their relative rates of interchange by rotation around the Cys–Pro peptide bond. The rate constants for *cis*-to-*trans* and for *trans*-to-*cis* interchange are all within narrow ranges for the linear peptides **3R**–**6R**: 0.039–0.061 $s^{-1}$ for $k_{ct}$ and 0.0044–0.0094 $s^{-1}$ for $k_{tc}$, whereas they cover much wider ranges for the cyclic peptides **4O**–**7O**: 0.0044–0.42 $s^{-1}$ for $k_{ct}$ and 0.011–0.20 $s^{-1}$ for $k_{tc}$. It was expected that the rate constants would decrease upon formation of the disulfide bonds owing to steric constraints and reduced flexibility of the peptide backbones in the ring structures. However, we made the unexpected discovery in a previous study that $k_{ct}$ and $k_{tc}$ for **4O** are 10 and 7 times larger, respectively, than the corresponding rate constants for **4R**.[7] This rate enhancement was found to be general for model cyclic disulfide-containing peptides for the active sites of other thiol/disulfide oxidoreductase enzymes.[8] The significantly increased rates for **4O** and for similar model peptides were interpreted in terms of an intramolecular catalysis mechanism in which a hydrogen bond is formed between the pyramidalized imide nitrogen atom of proline and the NH hydrogen of the Pro–Xaa peptide bond in the transition state, resulting in a lowering of the energy barrier for rotation around the Cys–Pro peptide bond.[7,8] This intramolecular catalysis mechanism appears to be substantiated by a recent crystal-structure study of a mutant of the enzyme DsbA.[19]

The results in Table 2 demonstrate that the rate enhancement is also observed for **5O** as compared to **5R**; $k_{ct}$ is increased by a factor of 2.9 ($k_{ct}$(**5O**)/$k_{ct}$(**5R**)) while $k_{tc}$ is increased by an even larger factor of 23. Indeed, the rate enhancement for *trans*-to-*cis* isomerization for **5O** is so large that $k_{tc}$ is actually larger than $k_{ct}$, with the result that the *cis* conformation is the kinetically favored and more abundant conformation for **5O**. However, when the ring size is increased from five to six amino acids (**6O**), there is essentially no rate acceleration for either *cis*-to-*trans* or *trans*-to-*cis* isomerization. We cannot compare the rate constants for **7R** and **7O** because rate constants could not be measured for **7R**. However, $k_{ct}$ for **7O** is at least a factor of 8 smaller than $k_{ct}$ for all the other peptides in Table 2, including both the linear and the disulfide-bridged peptides, while $k_{tc}$ is within a factor of 2 of $k_{tc}$ for the linear peptides and for **6O**. The exceptionally small value for $k_{ct}$ indicates a large increase in the kinetic stability of the *cis* conformation of the Cys–Pro peptide bond in **7O**, with the result that the *cis* conformation is the more abundant.

The use of disulfide bonds to form cyclic peptides features prominently in the drug discovery process:[2,3] cyclic peptides have a higher bioavailability, they have a decreased conformational flexibility, they are less prone to enzymatic degradation and the surface loops of proteins and bioactive peptides have often been implicated in peptide–protein binding.[3] The results of the present work suggest two implications for the use of disulfide bonds in the design of bioactive peptides: 1) conformational diversity can be increased by incorporation of the Cys–Pro dipeptide sequence in the disulfide-bridged loop and 2) the distribution between the two conformations of the Cys–Pro peptide bond can be controlled through the number of amino acids in the loop.[20] Studies are in progress in this direction. Also, studies are in progress to elucidate the molecular basis for the periodicity of the *cis*/*trans* isomerization reported herein.

## Experimental Section

Linear reduced peptides ***n*R** (***n*** = **3–7**) were assembled on a Millipore model 9050 Plus peptide synthesizer using standard solid-phase peptide synthesis methods based on (9H-fluoren-9-ylmethoxy)carbonyl (Fmoc) chemistry, starting with peptide amide resin PS-PEG-PAL (PS = polystyrene, PEG = poly(ethylene glycol), PAL = 5-(4-aminomethyl-3,5-dimethoxyphenoxy)valeric acid. Reagent B with a composition of 88% trifluroacetic acid, 2% triisopropylsilane, 5% phenol and 5% water was used for peptide cleavage. Pure peptides were separated by semi-preparative HPLC and characterized by mass spectrometry, see Table 1. The disulfide peptides ***n*O** were prepared by oxidation of the crude reduced peptides ***n*R** with *trans*-$[Pt(CN)_4Cl_2]^{2-}$ or *trans*-$[Pt(en)_2Cl_2]^{2+}$ by procedures described previously.[21] 2–10 mM peptide solutions in 90% $H_2O$/10% $D_2O$ at pH 3.0 were prepared as NMR spectroscopy samples; samples of reduced peptides contained 20–30 mM deuterated 1,4-dithiothreitol. 1D and 2D-TOCSY and 2D-ROESY spectra were recorded on a 500 MHz Varian Unity-Inova spectrometer using standard NMR pulse sequences with suppression of the water signal and were assigned by methods described earlier.[14,15] Rate constants were determined by the inversion magnetization-transfer method[8,15–17] using the *cis*/*trans* resonance pairs given in Table 1.

Received: September 30, 2005
Published online: February 10, 2006

 © 2006 Wiley-VCH Verlag GmbH & Co. KGaA, Weinheim 

**Keywords:** disulfide peptides · isomerization · NMR spectroscopy · peptides · proline


[1] P. Li, P. P. Roller, J. Xu, *Curr. Org. Chem.* **2002**, *6*, 411 – 440.

[2] a) P. K. Pallaghy, R. S. Norton, *Biopolymers* **2000**, *54*, 173 – 179; b) J. D. McBride, H. N. Freeman, R. J. Leatherbarrow, *J. Pept. Sci.* **2000**, *6*, 446 – 452; c) N. C. Wrighton, F. X. Farrell, R. Chang, A. K. Kashyap, F. P. Barbone, L. S. Mulcahy, D. L. Johnson, R. W. Barrett, L. K. Jolliffe, W. J. Dower, *Science* **1996**, *273*, 458 – 463; d) W. J. Fairbrother, H. W. Chrisinger, A. G. Cochran, G. Fuh, C. J. Keenan, C. Quan, S. K. Shriver, J. Y. K. Tom, J. A. Wells, B. C. Cunningham, *Biochemistry* **1998**, *37*, 17754 – 17764; e) J. L. Chagnaud, D. Moynet, D. Londos-Gagliardi, J. H. Bezian, P. Vincendeau, H. Fleury, B. Guillemain, *Lett. Pept. Sci.* **2002**, *9*, 95 – 106; f) S. J. Russell, T. Blandl, N. J. Skelton, A. G. Cochran, *J. Am. Chem. Soc.* **2003**, *125*, 388 – 395; g) M. S. Dennis, C. Eigenbrot, N. J. Skelton, M. H. Ultsch, L. Santell, M. A. Dwyer, M. P. O'Connell, R. A. Lazarus, *Nature* **2000**, *404*, 465 – 470; h) N. J. Skelton, Y. M. Chen, N. Dubree, C. Quan, D. Y. Jackson, A. Cochran, K. Zobel, K. Deshayes, M. Baca, M. T. Pisabarro, H. B. Lowman, *Biochemistry* **2001**, *40*, 8487 – 8498.

[3] A. G. Cochran, R. T. Tong, M. A. Starovasnik, E. J. Park, R. S. McDowell, J. E. Theaker, N. J. Skelton, *J. Am. Chem. Soc.* **2001**, *123*, 625 – 632.

[4] a) E. C. Jimenez, B. M. Olivera, W. R. Gray, L. J. Cruz, *J. Biol. Chem.* **1996**, *271*, 28002 – 28005; b) M. Wu, R. E. W. Hancock, *J. Biol. Chem.* **1999**, *274*, 29 – 35; c) Y. F. Hallock, R. C. Sowder II, L. K. Pannell, C. B. Hughes, D. G. Johnson, R. Gulakowski, J. H. Cardellina II, M. R. Boyd, *J. Org. Chem.* **2000**, *65*, 124 – 128; d) X.-H. Wang, M. Connor, R. Smith, M. W. Maciejewski, M. E. H. Howden, G. M. Nicholson, M. J. Christie, G. F. King, *Nat. Struct. Biol.* **2000**, *7*, 505 – 512; e) K. P. Sai, M. V. Jagannadham, M. Vairamani, N. P. Raji, A. S. Devi, R. Nagaraj, N. Sitaram, *J. Biol. Chem.* **2001**, *276*, 2701 – 2707; f) A. L. Salmon, L. J. M. Cross, A. E. Irvine, T. R. J. Lappin, M. Dathe, G. Krause, P. Canning, L. Thim, M. Beyermann, S. Rothemund, M. Bienert, C. Shaw, *J. Biol. Chem.* **2001**, *276*, 10145 – 10152.

[5] W.-J. Zhang, A. Berglund, J. L.-F. Kao, J.-P. Couty, M. C. Gershengorn, G. R. Marshall, *J. Am. Chem. Soc.* **2003**, *125*, 1221 – 1235.

[6] G. Fischer, *Chem. Soc. Rev.* **2000**, *29*, 119 – 127.

[7] D. L. Rabenstein, T. Shi, S. Spain, *J. Am. Chem. Soc.* **2000**, *122*, 2401 – 2402.

[8] T. Shi, S. M. Spain, D. L. Rabenstein, *J. Am. Chem. Soc.* **2004**, *126*, 790 – 796.

[9] M. J. Scanlon, R. S. Norton, *Protein Sci.* **1994**, *3*, 1121 – 1124.

[10] L. Volpon, H. Lamthanh, J. Barbier, N. Gilles, J. Molgo, A. Menez, J.-M. Lancelin, *J. Biol. Chem.* **2004**, *279*, 21356 – 21366.

[11] S. Luckett, R. S. Garcia, J. J. Barker, Al. V. Konarev, P. R. Shewry, A. R. Clarke, R. L. Brady, *J. Mol. Biol.* **1999**, *290*, 525 – 533.

[12] J. D. McBride, E. M. Watson, A. B. Brauer, A. M. Jaulent, R. J. Leatherbarrow, *Biopolymers* **2002**, *66*, 79 – 92.

[13] A. Holmgren, F. Åslund, *Methods Enzymol.* **1995**, *252*, 283 – 292.

[14] C. K. Larive, L. Guerra, D. L. Rabenstein, *J. Am. Chem. Soc.* **1992**, *114*, 7331 – 7337.

[15] C. K. Larive, D. L. Rabenstein, *J. Am. Chem. Soc.* **1993**, *115*, 2833 – 2836.

[16] G. Robinson, B. E. Chapman, P. W. Kuchel, *Eur. J. Biochem.* **1984**, *143*, 643 – 649.

[17] S. V. S. Mariappan, D. L. Rabenstein, *J. Magn. Reson.* **1992**, *100*, 183 – 188.

[18] A. C. Gibbs, L. H. Kondejewski, W. Gronwald, A. M. Nip, R. S. Hodges, B. D. Sykes, D. S. Wishart, *Nat. Struct. Biol.* **1998**, *5*, 284 – 288.

[19] E. Ondo-Mbele, C. Vives, A. Kone, L. Serre, *J. Mol. Biol.* **2005**, *347*, 555 – 563.

[20] H. Weisshoff, K. Frost, W. Brandt, P. Henklein, C. Mügge, C. Frömmel, *FEBS Lett.* **1995**, *372*, 203 – 209.

[21] a) T. Shi, D. L. Rabenstein, *J. Org. Chem.* **1999**, *64*, 4590 – 4595; b) T. Shi, D. L. Rabenstein, *J. Am. Chem. Soc.* **2000**, *122*, 6809 – 6815; c) T. Shi, D. L. Rabenstein, *Tetrahedron Lett.* **2001**, *42*, 7203 – 7206; d) T. Shi, D. L. Rabenstein, *Bioorg. Med. Chem. Lett.* **2002**, *12*, 2237 – 2240.


 © 2006 Wiley-VCH Verlag GmbH & Co. KGaA, Weinheim 

*Self-Assembly*

DOI: 10.1002/anie.200503601

# Soluble and Liquid-Crystalline Ovalenes**

*Salima Saïdi-Besbes, Éric Grelet, and Harald Bock**

*Dedicated to Dr. Nguyen Huu Tinh on the occasion of his 65th birthday*

Large polycyclic organic π systems of high symmetry, such as acenes,[1] rylenes,[2] and fullerenes,[3] are not only exciting objects of synthesis and of great fundamental interest, but are also gaining more and more importance as electronically and optically active components in devices such as field-ffect transistors[4] and solar cells.[5]

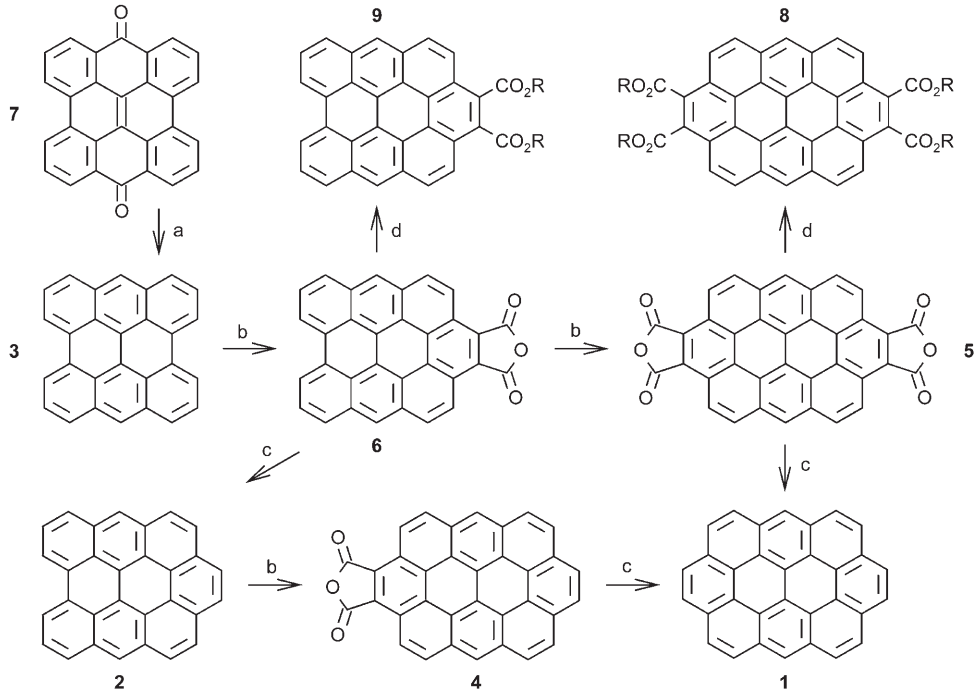
In 1948, Clar reported the synthesis of the orange compound **1**, which he called ovalene, which he obtained by treating either 1,14-benzobisanthene (**2**) or bisanthene (**3**) with maleic anhydride under oxidative conditions to obtain the corresponding carboxylic anhydrides **4** and **5**, respectively, followed by decarboxylation (Scheme 1).[6] Geometrically, ovalene may be regarded as a two-dimensional analogue of fullerene $C_{70}$, since their cross-sections are approximately equivalent, just as coronene corresponds in shape to a cross-section of $C_{60}$.

There have been no reports of soluble ovalene-di- or -tetracarboxylic acid derivatives derived from **4** or **5** in the literature since Clar's first synthesis of the insoluble parent hydrocarbon and the carboxylic anhydrides. Clar reported that **5** was dark brown, while **4** was dark red. Their large aromatic systems, which promise good orbital overlap between neighboring molecules in the solid state, makes ovalene derivatives interesting candidates for organic opto-electronics, provided that they can be processed, namely are

[*] Dr. S. Saïdi-Besbes, Dr. É. Grelet, Dr. H. Bock
Centre de Recherche Paul Pascal
CNRS/Université Bordeaux I
115, Av. Schweitzer, 33600 Pessac (France)
Fax: (+33) 5-5684-5600
E-mail: bock@crpp-bordeaux.cnrs.fr

[**] We are grateful to the Région Aquitaine and to the Association Universitaire de la Francophonie for financial support.


© 2006 Wiley-VCH Verlag GmbH & Co. KGaA, Weinheim



***Scheme 1.*** Synthesis of **1** and **2** and of their carboxylic ester derivatives **8** and **9**: a) 1. Zn, pyridine, acetic acid; 2. chloranil; b) maleic anhydride, nitrobenzene; c) soda lime, 400 °C; d) RBr, ROH, DBU.

soluble and film-forming. The elliptical shape of the aromatic core means that the introduction of solubilizing substituents may lead to columnar liquid-crystalline (LC) self-assembled systems with an associated efficient transport of excitons and charge along the columns.[7,8]

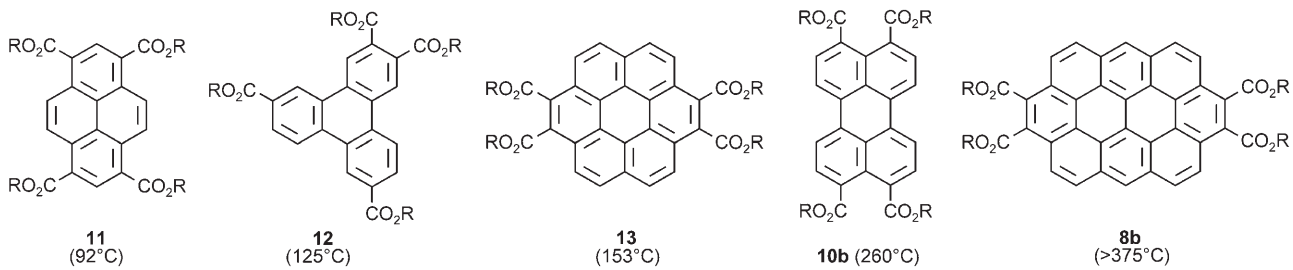
We therefore set out to prepare a soluble and columnar liquid-crystalline form of **5**, which is completely insoluble in organic solvents and hard to purify. The synthetic approach starting from **3** should also lead to soluble derivatives of the violet benzobisanthene dicarboxylic anhydride (**6**), which is obtained, instead of **5**, from the reaction of **3** and maleic anhydride in refluxing nitrobenzene if the reaction time is reduced to minutes instead of hours.[9]

We synthesized **5** starting from naphthadianthrone (**7**, which is obtained by photocyclization of commercial bianthrone).[10] To avoid isolation of the very unstable **3**, we followed the procedure developed by Brockmann and Randebrock. Treatment of **7** with zinc dust and acetic acid in pyridine gave a mixture of dihydro- and higher hydrogenated bisanthenes,[11,12] which we used directly in the benzogenic oxidative Diels–Alder reaction to give **6** and **5**, without attempting to prepare **3** by oxidation with chloranil.[11] Blue, fully aromatized bisanthene (**3**) is regenerated in situ during heating in nitrobenzene and adds maleic anhydride upon reaching reflux temperature.

To obtain esters **8** and **9**, we then faced the synthetic challenge of esterifying efficiently the quite unreactive insoluble anhydrides with long and branched alcohols, in particular 2-ethylhexanol, which we had used on other aromatic cores to induce high solubility as well as columnar liquid-crystalline self-assembly at room temperature.[13,14]

We had found previously that large aromatic dianhydrides such as perylene-3,4,9,10-tetracarboxylic dianhydride (PTCDA), reported by other research groups as being difficult to esterify,[15] react with a mixture of propanol and bromopropane in the presence of potassium carbonate to give the tetrapropylester **10a** (R = *n*-propyl) in good yield.[13] However, this method is less efficient with longer, less-polar alcohols and bromoalkanes such as 2-ethylhexanol and 1-bromo-2-ethylhexane and gave only low yields after exceedingly long reaction times (on the order of a week). By modifying a procedure reported for the esterification of phthalocyanine-2,3,6,7,10,11,14,15-octacarboxylic acid[16] we succeeded in obtaining high yields of the 2-ethylhexyl esters **10b** and **8b** (Scheme 2, R = 2-ethylhexyl) overnight by esterification with 2-ethylhexanol and 1-bromo-2-ethylhexane in acetonitrile in the presence of the strong soluble base 1,8-diazabicyclo[5.4.0]undec-7-ene (DBU).

As expected, X-ray diffraction studies on **8b** showed the presence of a hexagonal columnar liquid-crystalline phase at room temperature, with a column-to-column distance of 22 Å and a disk-to-disk spacing of 3.5 Å (Figure 1). The mesophase is stable over a very large range of temperatures, and no



***Scheme 2.*** Room-temperature liquid-crystalline arene tetracarboxylic tetra-2-ethylhexyl esters (R = 2-ethylhexyl). The transition temperatures from the columnar mesophase to the isotropic liquid are given in parentheses. **11** and **13** show subambient melting points of −28 °C and +12 °C, respectively. No transition to a crystalline phase was detected in **12**, **10b**, and **8b** by differential scanning calorimetry down to −60 °C.

 © 2006 Wiley-VCH Verlag GmbH & Co. KGaA, Weinheim 

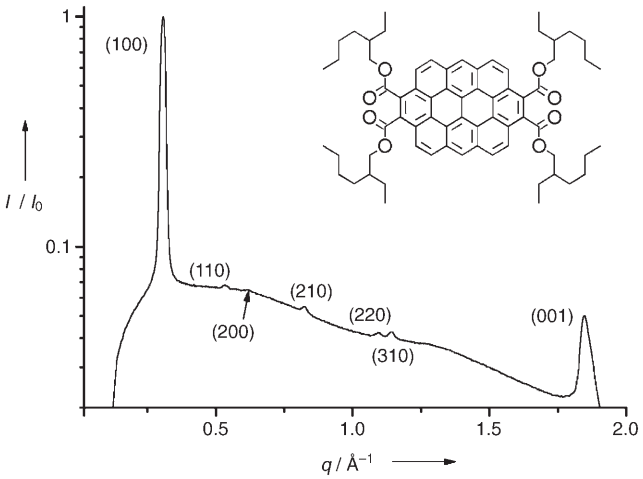



***Figure 1.*** Room-temperature powder X-ray diffractogram of **8b**.

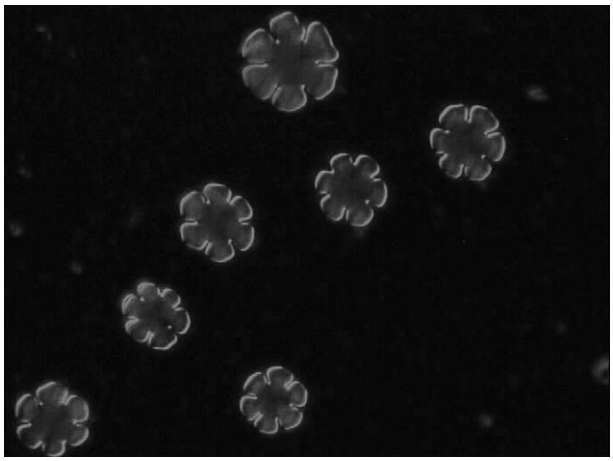


***Figure 2.*** Growth of homeotropically aligned hexagonal columnar domains of **8c** upon cooling through the liquid-to-mesophase transition. The image was taken by differential interference contrast (DIC) microscopy in the reflection mode (350 μm × 450 μm) of a thin film between a silicon wafer and a glass slide.

transition to an isotropic liquid phase could be observed up to our experimental limit of 375 °C.

This very wide temperature range of the columnar phase is in agreement with the evolution of liquid crystallinity as the core size increases in arene tetracarboxylates: the clarification temperature of the room-temperature liquid-crystalline pyrene, triphenylene, and coronene tetra(2-ethylhexyl) esters **11**, **12**, and **13** increases with core size from the pyrene (92 °C)[13] to the triphenylene (125 °C)[17] to the coronene ester (153 °C).[17] The perylene derivative **10b**[13] is an exception to the rule, as it has a higher clearing temperature (260 °C) than the coronene ester although it has four carbon atoms less, because stacking of rotated perylene moieties allows excellent space filling without interference from the out-of-plane carboxylate groups.[18]

In order that the LC-to-liquid transition occurred at an accessible temperature, we replaced half of the 2-ethylhexyl groups by using 2-decyltetracan-1-ol as well as 2-ethylhexyl bromide in the esterification. The resulting mixed ester (**8c** with one R group on each side being 2-ethylhexyl and the other 2-decyltetradecyl) shows a mesophase-to-liquid transition at 220 °C, and cooling through this temperature yields the typical six-petaled flowerlike domains of a hexagonal columnar phase growing in homeotropic alignment (that is, columns perpendicular to substrates; Figure 2).

To obtain a soluble ovalene derivative with only small non-absorbing alkyl substituents, we treated **5** with propanol and 1-bromopropane to yield the tetrapropyl ester **8a** (R = *n*-propyl). Ester **8a** melts above 375 °C and is highly soluble in common organic solvents (> 5 % in chloroform). Ovalene tetraesters **8** are dark brown in the solid state, and their orange solutions in chloroform show a main absorption maximum at 359 nm, which is shifted by 15 nm with respect to unsubstituted ovalene (**1**: maximum at 344 nm; Figure 3).

In the same manner as ovalene tetraesters **8** are formed from **5**, soluble benzobisanthene diesters **9** are obtained efficiently from **6** by reaction with 1-bromoalkane, 1-alkanol, and DBU. They are dark violet solids that give pinkish red solutions in chloroform with a main absorption maximum at the same wavelength as ovalene (359 nm) and strong long-

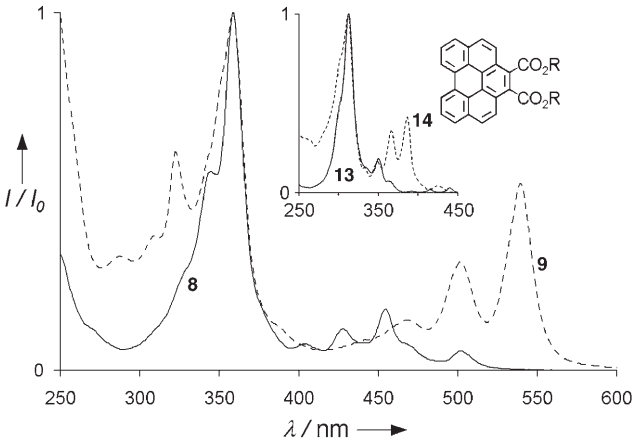



***Figure 3.*** Normalized absorption spectra in chloroform of **8** and **9** and, for comparison, of their shortened homologues **13** and **14**.

wavelength absorptions at 539 and 501 nm. The identical wavelength of the main absorption peaks of **8** and **9** illustrate that the two chromophores are electronically related. No corresponding peak is found for solutions of bisanthene (**3**),[19] whereas coronene tetraester **13** and the corresponding benzo[ghi]perylene diester **14** show the same relationship (main absorption peak at 313 nm, shifted by 8 nm with respect to unsubstituted coronene; inset in Figure 3).

In summary, soluble ovalene and benzobisanthene dyes are readily accessible by an optimized approach from naphthadianthrone (**7**) and an efficient esterification procedure. Furthermore, the appropriate choice of the alkyl substituents leads to ovalene esters that undergo columnar self-assembly at room temperature over extremely large temperature ranges. Very few other mesogens, in particular, hexasubstituted hexabenzocoronenes[8,20] and octasubstituted phthalocyanines,[16,21] are known to self-assemble into columns over temperature ranges of over 350 °C.

 © 2006 Wiley-VCH Verlag GmbH & Co. KGaA, Weinheim 

Besides improving considerably their synthetic accessibility, we have thus dramatically increased the physical versatility of the ovalene and bisanthene chromophores by rendering them soluble and strongly self-organizing.

## Experimental Section

**8b**: Four portions of zinc powder (4 × 6 g) and 80% acetic acid (4 × 10 mL) were added in 30-minute intervals to a refluxing suspension of **7** (2 g) in pyridine (200 mL). The yellow suspension became green, then brown. After 5 h, the solution was cooled to room temperature, the zinc powder filtered off, and water (1 L) added. The precipitate thus formed was filtered off and dried under vacuum to yield 1.6 g of a yellow insoluble solid (crude, partially hydrogenated **3**). This solid was heated at reflux for 12 h with maleic anhydride (5 g) in nitrobenzene (60 mL). A color change from greenish yellow via blue and violet to brown was observed during warming and the first 30 minutes at reflux. Chloroform was added to the cooled solution, and the insoluble solid filtered off, washed with chloroform, and dried under vacuum to yield crude dianhydride **5** (2.9 g). The dianhydride was suspended in acetonitrile (150 mL), then 2-ethylhexyl bromide (0.1 mol, 19.3 g), 2-ethylhexanol (0.1 mol, 13.0 g), and DBU (80 mmol, 12.2 g) added, and the mixture refluxed for 16 h. The solvent was evaporated, and methanol added to precipitate the product, which was purified by column chromatography (silica gel, dichloromethane) and reprecipitation from butanol. Yield: 2.79 g of a brown (dark orange-red) waxy solid (52% with respect to naphthodianthrone). $^1$H NMR (400 MHz, $CDCl_3$): $\delta = 8.59$ (d, $J = 9$ Hz, 4H, ArH), 8.01 (d, $J = 9$ Hz, 4H, ArH), 7.98 (s, 2H, ArH), 4.90–4.77 (m, 8H, $CH_2O$), 2.22–2.13 (m, 4H, CH), 1.91–1.48 (m, 32H, $CH_2$), 1.25 (t, $J = 7$ Hz, 12H, $CH_3$), 1.07 ppm (t, $J = 7$ Hz, 12H, $CH_3$); $^{13}$C NMR (400 MHz, APT, $CDCl_3$): $\delta = 169.2$ ($CO_2$), 127.8 ($C_{Ar}H$), 126.8 ($C_{Ar}$), 126.1 ($C_{Ar}$), 123.8 ($C_{Ar}H$), 123.5 ($C_{Ar}$), 123.0 ($C_{Ar}H$), 118.8 ($C_{Ar}$), 116.3 ($C_{Ar}$), 115.6 ($C_{Ar}$), 69.2 ($CH_2O$), 39.3 (CH), 30.8 ($CH_2$), 29.3 ($CH_2$), 24.2 ($CH_2$), 23.4 ($CH_2$), 14.4 ($CH_3$), 11.3 ppm ($CH_3$). Elemental analysis calcd for $C_{68}H_{78}O_8$: C 79.81, H 7.68%; found: C 79.99, H 7.82%

**9a** (R = *n*-propyl): In the same way as described above, crude monoanhydride **6** (2.5 g) was obtained if the reflux with maleic anhydride in nitrobenzene was stopped after 15 min. The anhydride was esterified with propyl bromide, propanol, and DBU as above and purified by column chromatography (silica gel, dichloromethane) and recrystallization from butanol. Yield: 1.29 g of dark red/violet crystals (45% with respect to naphthodianthrone). M.p. 315 °C. $^1$H NMR (400 MHz, $CDCl_3$): $\delta = 7.94$ (d, $J = 8$ Hz, 2H, ArH), 7.82 (d, $J = 9$ Hz, 2H, ArH), 7.51 (d, $J = 8$ Hz, 2H, ArH), 7.45 (s, 2H, ArH), 7.40 (t, $J = 8$ Hz, 2H, ArH), 7.36 (d, $J = 9$ Hz, 2H, ArH), 4.59 (t, $J = 7$ Hz, 4H, $CH_2O$), 2.01 (sext, $J = 7$ Hz, 4H, $CH_2$), 1.19 ppm (t, $J = 7$ Hz, 6H, $CH_3$); $^{13}$C NMR (400 MHz, APT, $CDCl_3$): $\delta = 168.8$ ($CO_2$), 128.8 ($C_{Ar}$), 128.0 ($C_{Ar}H$), 127.8 ($C_{Ar}$), 127.3 ($C_{Ar}$), 125.4 ($C_{Ar}H$), 124.9 ($C_{Ar}$), 124.8 ($C_{Ar}$), 124.4 ($C_{Ar}H$), 123.5 ($C_{Ar}H$), 122.8 ($C_{Ar}H$), 121.0 ($C_{Ar}$), 120.7 ($C_{Ar}$), 119.8 ($C_{Ar}$), 118.3 ($C_{Ar}H$), 118.0 ($C_{Ar}$), 67.6 ($OCH_2$), 22.3 ($CH_2$), 10.9 ppm ($CH_3$). Elemental analysis calcd for $C_{38}H_{26}O_4$: C 83.50, H 4.79%; found: C 83.88, H 5.06%.

Received: October 12, 2005
Published online: February 9, 2006

**Keywords:** cycloadditions · electron transfer · liquid crystals pi interactions · self-assembly

[1] a) T. Takahashi, M. Kitamura, B. Shen, K. Nakajima, *J. Am. Chem. Soc.* **2000**, *122*, 12 876; b) J. E. Anthony, J. S. Brooks, D. L. Eaton, S. R. Parkin, *J. Am. Chem. Soc.* **2001**, *123*, 9482; c) S. H. Chan, H. K. Lee, Y. M. Wang, N. Y. Fu, X. M. Chen, Z. W. Cai, H. N. C. Wong, *Chem. Commun.* **2005**, 66; d) H. Yamada, Y. Yamashita, M. Kikuchi, H. Watanabe, T. Okujima, H. Uno, T. Ogawa, K. Ohara, N. Ono, *Chem. Eur. J.* **2005**, 11, 6212.

[2] a) F. Würthner, C. Thalacker, S. Diele, C. Tschierske, *Chem. Eur. J.* **2001**, *7*, 2245; b) S.-W. Tam-Chang, W. Seo, I. K. Iverson, S. M. Casey, *Angew. Chem.* **2003**, *115*, 925; *Angew. Chem. Int. Ed.* **2003**, *42*, 897; c) H. Langhals, J. Büttner, P. Blanke, *Synthesis* **2005**, *3*, 0364; d) F. Nolde, J. Qu, C. Kohl, N. G. Pschirer, E. Reuther, K. Müllen, *Chem. Eur. J.* **2005**, *11*, 3959; e) H. Langhals, O. Krotz, K. Polborn, P. Mayer, *Angew. Chem.* **2005**, *117*, 2479; *Angew. Chem. Int. Ed.* **2005**, *44*, 2427.

[3] a) J. C. Hummelen, B. W. Knight, F. LePeq, F. Wudl, J. Yao, C. L. Wilkins, *J. Org. Chem.* **1995**, *60*, 532; b) C. Thilgen, F. Diederich, *Top. Curr. Chem.* **1999**, *199*, 135; c) M. M. Wienk, J. M. Kroon, W. J. H. Verhees, J. Knol, J. C. Hummelen, P. A. van Hal, R. A. J. Janssen, *Angew. Chem.* **2003**, *115*, 3493; *Angew. Chem. Int. Ed.* **2003**, *42*, 3371.

[4] a) A. Kraft, *ChemPhysChem* **2001**, *2*, 163; b) S. Jung, Z. Yao, *Appl. Phys. Lett.* **2005**, *86*, 083505; c) M. M. Payne, S. R. Parkin, J. E. Anthony, C.-C. Kuo, T. N. Jackson, *J. Am. Chem. Soc.* **2005**, *127*, 4986.

[5] a) C. W. Tang, *Appl. Phys. Lett.* **1986**, *48*, 183; b) D. Désilets, P. M. Katzmayer, R. A. Burt, *Can. J. Chem.* **1995**, *73*, 319; c) S. Yoo, B. Domercq, B. Kippelen, *Appl. Phys. Lett.* **2004**, *85*, 5427.

[6] a) E. Clar, *Nature* **1948**, *161*, 238; b) E. Clar, *Chem. Ber.* **1949**, *82*, 55.

[7] a) M. O'Neill, S. M. Kelly, *Adv. Mater.* **2003**, *15*, 1135; b) D. Adam, P. Schuhmacher, J. Simmerer, L. Häussling, K. Siemensmeyer, K. H. Etzbach, H. Ringsdorf, D. Haarer, *Nature* **1994**, *371*, 141; c) L. Schmidt-Mende, A. Fechtenkötter, K. Müllen, E. Moons, R. H. Friend, J. D. MacKenzie, *Science* **2001**, *293*, 1119.

[8] A. M. van de Craats, J. M. Warman, A. Fechtenkötter, J. D. Brand, M. A. Harbison, K. Müllen, *Adv. Mater.* **1999**, *11*, 1469.

[9] R. Scholl, K. Meyer, *Ber. Dtsch. Chem. Ges.* **1934**, *67*, 1229.

[10] S. M. Arabei, T. A. Pavich, *J. Appl. Spectrosc.* **2000**, *67*, 236.

[11] H. Brockmann, R. Randebrock, *Chem. Ber.* **1951**, *84*, 533.

[12] K. Wolkenstein, J. H. Gross, T. Oeser, H. Schöler, *Tetrahedron Lett.* **2002**, *43*, 1653.

[13] T. Hassheider, S. A. Benning, H.-S. Kitzerow, M.-F. Achard, H. Bock, *Angew. Chem.* **2001**, *113*, 2119; *Angew. Chem. Int. Ed.* **2001**, *40*, 2060.

[14] S. Alibert-Fouet, S. Dardel, H. Bock, M. Oukachmih, S. Archambeau, I. Seguy, P. Jolinat, P. Destruel, *ChemPhysChem* **2003**, *4*, 983.

[15] R. H. Mitchell, M. Chaudhary, R. V. Williams, R. Fyles, J. Gibson, M. J. Ashwood-Smith, A. J. Fry, *Can. J. Chem.* **1992**, *70*, 1015.

[16] L. Dulog, A. Gittinger, *Mol. Cryst. Liq. Cryst.* **1992**, *213*, 31.

[17] H. Bock, M. Rajaoarivelo, E. Grelet, unpublished results.

[18] I. Seguy, P. Jolinat, P. Destruel, R. Mamy, H. Allouchi, C. Courseille, M. Cotrait, H. Bock, *ChemPhysChem* **2001**, *2*, 448.

[19] E. Clar, *Polycyclic Hydrocarbons, Vol. 2*, Academic Press & Springer, **1964**, p. 99.

[20] a) P. Herwig, C. W. Kayser, K. Müllen, H. W. Spiess, *Adv. Mater.* **1996**, *8*, 510; b) K. Müllen, A. C. Grimsdale, *Angew. Chem.* **2005**, *117*, 5732; *Angew. Chem. Int. Ed.* **2005**, *44*, 5592.

[21] W. T. Ford, L. L. Sumner, W. M. Zhu, Y. H. Chang, P. J. Um, K. H. Choi, P. A. Heiney, N. C. Maliszewsky, *New J. Chem.* **1994**, *18*, 495.

 © 2006 Wiley-VCH Verlag GmbH & Co. KGaA, Weinheim 

*Natural Product Synthesis*

DOI: 10.1002/anie.200503733

# Synthesis of the C1–C26 Northern Portion of Azaspiracid-1: Kinetic versus Thermodynamic Control of the Formation of the Bis-spiroketal**

*Xiao-Ti Zhou and Rich G. Carter**

*Dedicated to Professor James D. White on the occasion of his 70th birthday*

Azaspiracid-1, a toxin found in European shellfish, was first observed in the mid-1990s when several individuals became ill from eating mussels harvested off the coast of Western Ireland. Considerable synthetic attention has been directed toward this compound by our group[1] and others.[2] Additional excitement was generated by the revelation that the initial structure of azaspiracid-1 (**1**) had been misassigned (Figure 1).[3] The genesis of the error was believed to be in the ABCDE northern portion of the molecule. Recently, the revised structure **2** was determined in an impressive series of publications by Nicolaou et al.[4] Independently and concurrently, we also converged on the same stereochemical conclusion.[5] Herein, we disclose our successful synthesis of the C1–C26 northern portion of the revised structure of azaspiracid-1 (**2**).

Our retrosynthetic analysis, as shown in Scheme 1, involved disconnection of **3** at the C19–20 linkage to provide the tetracycle **5** and the previously reported keto-phosphonate **6**.[5] The bis-spiroketal could be accessed from the ketone **7**, which would, in turn, be available from the sulfone **8** and the known aldehyde **9**.[5] It is important to note that the revised structure of azaspiracid **2** contains a new challenge in its synthetic architecture: the bisallylic carbon–oxygen bond at C6. We hypothesized that attempted formation of the bis-spiroketal in the presence of this labile functionality might prove problematic, particularly under acidic conditions. On the basis of this assumption, care was taken not to incorporate both alkenes in this region until the bis-spiroketal had been formed.

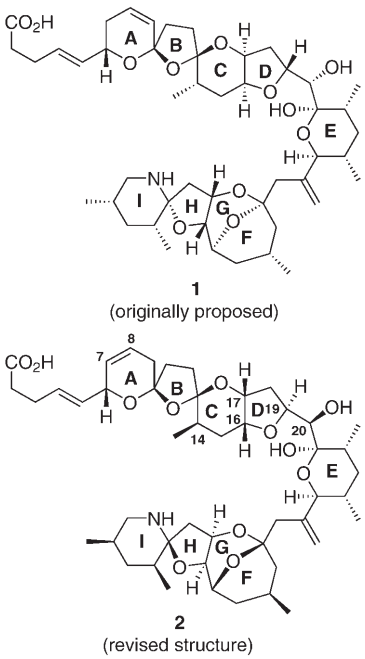
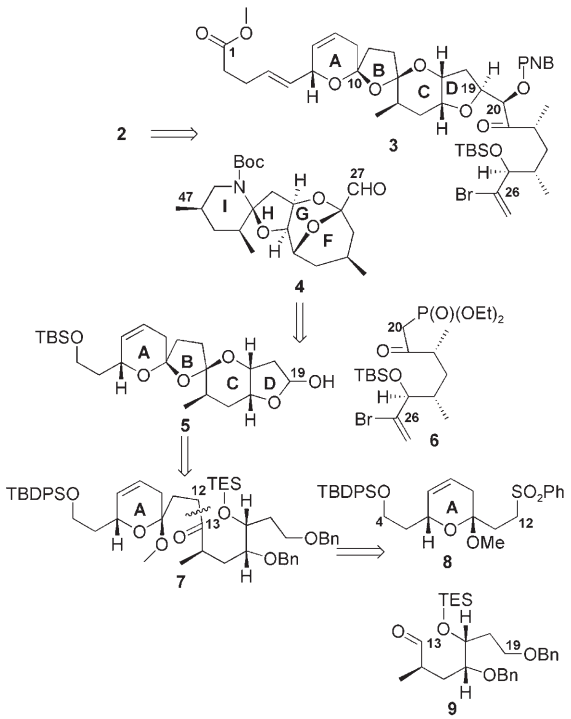



***Figure 1.*** Original (**1**) and revised (**2**) structures of azaspiracid-1.



***Scheme 1.*** Retrosynthetic analysis of azaspiracid-1 (**2**). PNB = *para*-nitrobenzoate; TBS = *tert*-butyldimethylsilyl; Boc = *tert*-butyloxycarbonyl; TBDPS = *tert*-butyldiphenylsilyl; TES = triethylsilyl; Bn = benzyl.

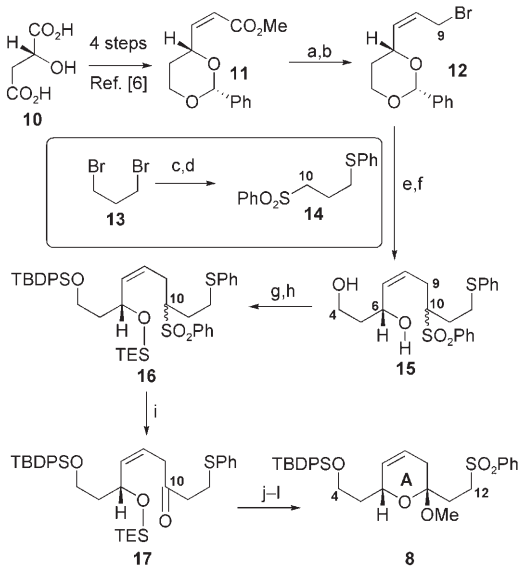
Synthesis of the sulfone fragment commenced with the commercially available maleic acid **10** (Scheme 2). Following a known four-step protocol,[6] the *cis*-unsaturated ester **11** was constructed. Subsequent reduction of the carbonyl moiety

[*] Dr. X.-T. Zhou, Prof. Dr. R. G. Carter
Department of Chemistry
Oregon State University
Corvallis, OR 97331 (USA)
Fax: (+1) 541-737-9486
E-mail: rich.carter@oregonstate.edu

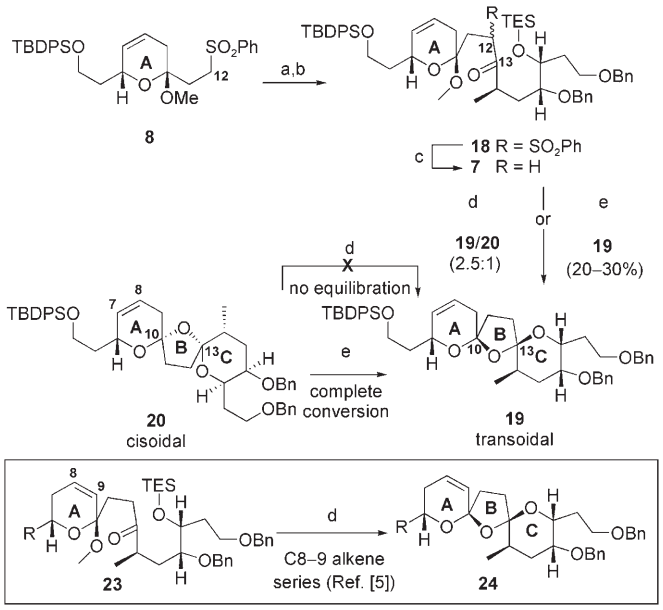
[**] Financial support was provided by the National Institutes of Health (GM63723). This publication was made possible in part by grant number P30 ES00210 from the National Institute of Environmental Health Sciences, NIH. The authors would also like to thank Professor Max Deinzer (OSU) and Dr. Jeff Morré (OSU) for mass spectral data, Rodger Kohnert (OSU) and Dr. Clemens Anklin (Brüker Biospin) for NMR assistance, Damien Kuiper (OSU) for synthetic assistance with sulfone **14** and aldehyde **9**, and Dr. Roger Hanselmann (Rib-X Pharmaceuticals) for helpful discussions.

Supporting information for this article is available on the WWW under http://www.angewandte.org or from the author.

 © 2006 Wiley-VCH Verlag GmbH & Co. KGaA, Weinheim 



***Scheme 2.*** Synthesis of the sulfone. Reagents and conditions: a) DIBAL-H, $CH_2Cl_2$, −78 °C, 98%; b) $Ph_3P$, $CBr_4$, MeCN, 92%; c) NaH, PhSH, DMF, 0 °C, 73%; d) $NaSO_2Ph$, DMF, 86%; e) *n*BuLi, **14** (2.6 equiv), THF, −78 °C; f) 2 N HCl, MeCN, 58% (over two steps); g) TBDPSCl, imid., $CH_2Cl_2$, 92%; h) TESOTf, 2,6-lutidine, $CH_2Cl_2$, 95%; i) NaHMDS, THF then $(TMSO)_2$, 72% (BORSM); j) $NH_4F$, MeOH/$CH_2Cl_2$ (4:1); k) PPTS, MeOH, 68% (over two steps, BORSM); l) TPAP, NMO, MeCN, 40 °C, 88%. DIBAL-H = diisobutylaluminum hydride; DMF = *N*,*N*-dimethylformamide; imid = imidazole; TESOTf = triethylsilyl triflate; HMDS = hexamethyldisilazide; TMS = trimethylsilyl; PPTS = pyridinium *p*-toluenesulfonate; TPAP = tetra-*n*-propylammonium perruthenate; NMO = *N*-methylmorpholine-*N*-oxide. BORSM = based on recovered starting material.



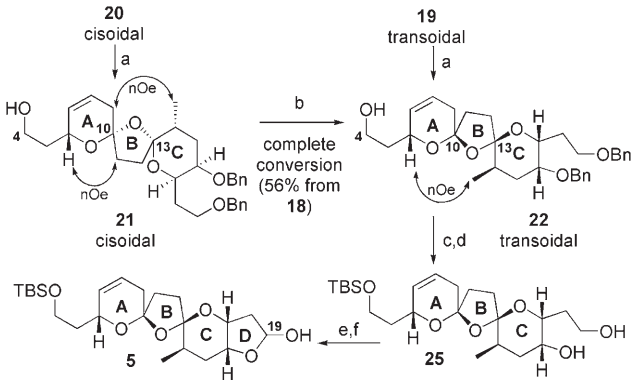
***Scheme 3.*** Synthesis and equilibration of bis-spiroketals. Reagents and conditions: a) 2,2,6,6-tetramethylpiperidine, *n*BuLi, THF then **9**; b) TPAP, NMO, $CH_2Cl_2$, M.S., 92% over two steps; c) Na/Hg, $Na_2HPO_4$, THF, $H_2O$, 86%; d) PPTS, THF/$H_2O$ (4:1), 18 h; e) CSA, *t*BuOH/PhMe (1:1), 18 h. M.S. = molecular sieves; CSA = camphorsulfonic acid.

followed by conversion into the allylic bromide provided **12**. Coupling of this electrophile with the readily available sulfone **14** (synthesized from the commercially available sodium salt of benzenesulfinic acid, thiophenol, and 1,3-dibromopropane (**13**)) and deprotection of the acetal gave the diol **15** as a mixture of stereoisomers at C10. Sequential protection at C4 and C6 provided the bis-silyl species **16**. After careful optimization, we found that the sulfone **16** could be cleanly converted into the β,γ-unsaturated ketone **17** using sodium hexamethyldisilizane and bis(trimethylsilyl) peroxide.[7] Despite our fears of the possible instability of **17**, this compound proved to be remarkably robust (stable to chromatography and prolonged storage in the freezer). Subsequent conversion into the methoxy ketal followed by oxidation of the sulfone[8] using Ley's TPAP reagent[9] yielded the coupling partner **8**.

With the sulfone subunit **8** in hand, we embarked on the combination of the subunits **8** and **9** (Scheme 3). Julia coupling of **8** and **9** with LDA proved problematic; however, use of the more hindered lithium base derived from 2,2,6,6-tetramethylpiperidine nicely addressed this issue. Subsequent oxidation with TPAP provided the ketosulfone species **18** in excellent yield (92%) over the two steps. Desulfonylation of **18** using Na/Hg amalgam followed by the formation of the bisspiroketal of **7** under our second-generation conditions (PPTS, THF/$H_2O$)[5] led cleanly to the desired transoidal bis-spiroketal **19** with the corresponding cisoidal bis-spiroketal **20** as the minor product (2.5:1 **19**/**20**). This result is in stark contrast to the C8–9 series in which ketone **23** gave solely the transoidal bis-spiroketal **24**.[5] Interestingly, resubmission of the cisoidal bis-spiroketal **20** to the same reaction conditions did not lead to formation of any transoidal bis-spiroketal **19**. On the basis of these results, the location of the alkene in the A ring at the C8–9 position (allylic to C10) appears to be a catalyst for the unraveling and subsequent equilibration at C10. Even more intriguing, treatment of the TBDPS-protected cisoidal bis-spiroketal **20** under our first-generation conditions (CSA, *t*BuOH/PhMe)[1d–f] led to complete equilibration to the transoidal bis-spiroketal **19**. It would appear from these experiments that the use of PPTS in THF/$H_2O$ leads to formation of the bis-spiroketal under kinetic control, whereas with CSA in *t*BuOH/PhMe the reaction proceeds under thermodynamic control. Additional support for this conclusion can be found in the exclusive formation of transoidal bis-spiroketal **19** from **7** upon treatment with CSA in *t*BuOH/PhMe. Note that decomposition appears to be a significant contributor to the low yield (20–30%) in the formation of the spiroketal from **7** using the first-generation conditions. The second-generation conditions were optimal for the initial formation of the bis-spiroketal of **7**, whereas the first-generation conditions were preferred for the equilibration of **20**.

Removal of the C4-silyl protecting group on **20** revealed additional information (Scheme 4). Treatment of **21** under the first-generation conditions once again leads to complete conversion into the transoidal bis-spiroketal **22**. Interestingly, use of our second-generation conditions also led to slow formation of the transoidal bis-spiroketal **22** (1:1 ratio of bis-spiroketals **21**/**22** after 72 h). Decomposition became a com-

 © 2006 Wiley-VCH Verlag GmbH & Co. KGaA, Weinheim 

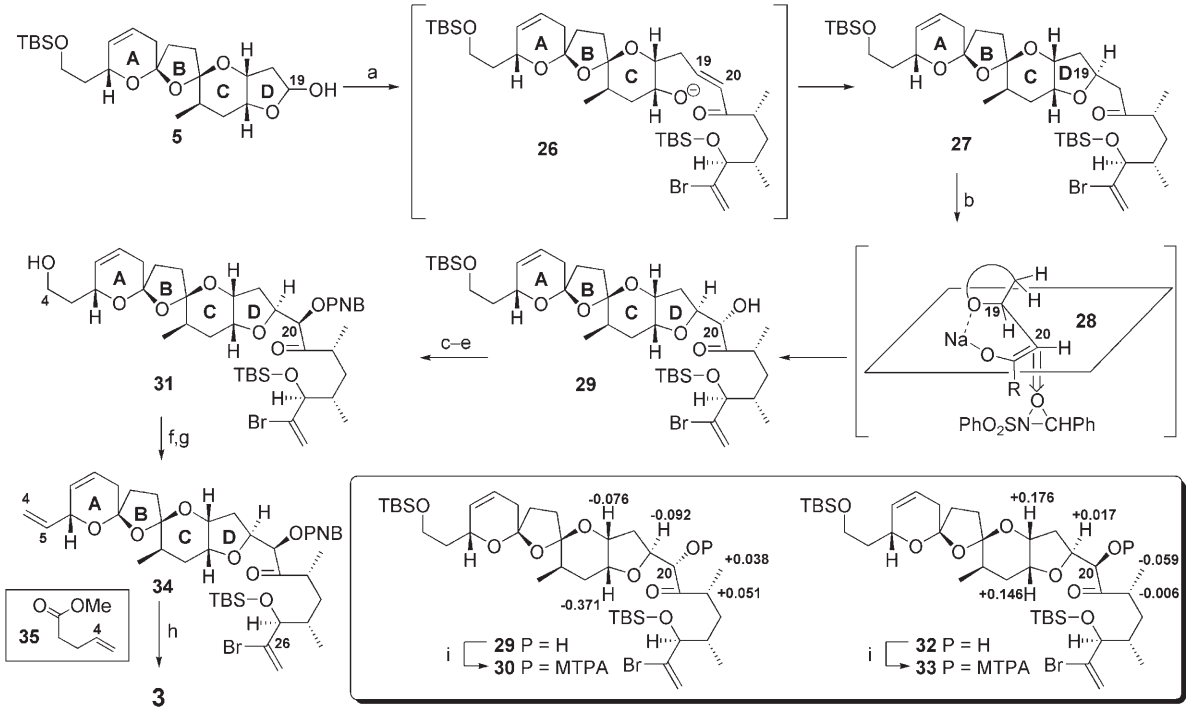


***Scheme 4.*** Equilibration of C4-hydroxy bis-spiroketals. Reagents and conditions: a) TBAF, THF; b) CSA, *t*BuOH/PhMe (1:1), 18 h; c) TBSOTf, 2,6-lutidine, $CH_2Cl_2$, −78 °C, 99%; d) LiDBB, THF, −78 °C, 95%; e) TPAP, NMO, $CH_2Cl_2$, M.S.; 67%; f) DIBAL-H, $CH_2Cl_2$, 90%. TBAF = tetra-*n*-butylammonium fluoride; DBB = lithium 4,4–di-*tert*-butylbiphenylide.

petitive pathway upon extended reaction times, making complete conversion of **21** into **22** under the second-generation conditions not feasible. The hydroxy group at C4 would appear to assist in the ionization of the bis-spiroketals, presumably through increasing the acidity of the local environment and/or a hydrogen-bonding interaction. Finally, debenzylation and oxidation/reduction at C19 provided the tetracycle **5** (Scheme 4).

Completion of the northern portion of azaspiracid-1 (**2**) is shown in Scheme 5. Wadsworth–Emmons coupling of **5** and **6** using KHMDS with in situ, intramolecular hetero-Michael addition yielded **27** with single stereochemistry at C19 of the furan D ring. Deprotonation using NaHMDS followed by a large excess of the Davis oxaziridine provided the hydroxyketone **29** as a single stereoisomer. Mosher ester analysis[10] confirmed that **30** displayed the undesired α stereochemistry. The stereochemical outcome in the hydroxylation can be explained through chelation of the sodium *Z*-enolate **28** to the oxygen atom of the furan D ring. Initial attempts to invert the stereochemistry at C20 using Mitsunobu-type conditions proved unsuccessful. Fortunately, triflation followed by displacement using the potassium salt of *p*-nitrobenzoic acid in DMF cleanly provided the desired β stereochemistry. The stereochemistry of **31** was once again confirmed by means of Mosher ester analysis. Desilylation using CSA followed selenation, and oxidation/elimination using TPAP yielded the reactive bisallylic pyran **34**. To the best of our knowledge, the TPAP-mediated oxidation of selenium has not been previously reported.[11] Attempted oxidation of the selenide using traditional conditions (e.g. $H_2O_2$, THF)[12] led to multiple products. Finally, selective olefin metathesis with **35** using the second-generation Grubbs catalyst[13] gave the target **3**.

In summary, an efficient approach to the entire C1–C26 northern portion of azaspiracid-1 has been described (27 steps from known ester **12**). We have unearthed novel controlling factors for formation of the bis-spiroketal under kinetic versus



***Scheme 5.*** Completion of the northern portion of azaspiracid-1 (**2**). Reagents and conditions: a) **6**, KHMDS, THF, −78 °C→RT, 84%; b) NaHMDS, THF, then Davis oxaziridine, 70%, >20:1 d.r.; c) $Tf_2O$, 2,6-lutidine, $CH_2Cl_2$, −78 °C, 88%; d) $KO_2C$-*p*-$NO_2$-$C_6H_4$ (20 equiv), DMF, 90%; e) CSA, MeOH/$CH_2Cl_2$, 93%; f) *o*-$NO_2C_6H_4SeCN$, $Bu_3P$, THF 93%; g) TPAP, NMO, $Et_3N$, $CH_2Cl_2$, 66%; h) second-generation Grubbs catalyst, **35**, $CH_2Cl_2$, 95% (BORSM), >10:1 *E*/*Z*; i) (*R*)/(*S*)-Mosher acid chloride, DMAP, $CH_2Cl_2$. MTPA = α-methoxy-α-trifluoromethylphenylacetic acid (Mosher); DMAP = 4-(dimethylamino)pyridine. The stereochemistry at C20 was confirmed by Mosher ester analysis. Representative data points for the difference in the chemical shift values [(*S*)-Mosher ester−(*R*)-Mosher ester (in ppm); $CDCl_3$, 300 or 400 MHz] are shown for structures **30** and **33**.

 © 2006 Wiley-VCH Verlag GmbH & Co. KGaA, Weinheim 

thermodynamic control. The proper choice of substitution patterns and acidic media allows for the tuning of the equilibration of the bis-spiroketal. In addition, key steps in this synthetic sequence include the oxidation of a sulfone at C10 to form the β,γ-unsaturated ketone, tandem Wadsworth–Emmons/intramolecular hetero-Michael addition to construct ring D, Davis oxidation to incorporate the hydroxy moiety at C20, and selective olefin metathesis to incorporate the sidearm at C5. Application of this strategy to the total synthesis of azaspiracid-1 will be reported in due course.

Received: October 21, 2005
Revised: November 17, 2005
Published online: February 10, 2006

**Keywords:** azaspiracid-1 · fused-ring systems · natural products · spiro compounds

[1] a) R. G. Carter, D. J. Weldon, *Org. Lett.* **2000**, *2*, 3913 – 3916; b) R. G. Carter, D. J. Weldon, T. C. Bourland, *221st National ACS Meeting*, **2001**, San Diego, ORG-479; c) R. G. Carter, D. E. Graves, *Tetrahedron Lett.* **2001**, *42*, 6035 – 6039; d) R. G. Carter, T. C. Bourland, D. E. Graves, *Org. Lett.* **2002**, *4*, 2177 – 2179; e) R. G. Carter, D. E. Graves, M. A. Gronemeyer, G. S. Tschumper, *Org. Lett.* **2002**, *4*, 2181 – 2184; f) R. G. Carter, T. C. Bourland, X.-T. Zhou, M. A. Gronemeyer, *Tetrahedron* **2003**, *59*, 8963 – 8974.

[2] a) A. B. Dounay, C. J. Forsyth, *Org. Lett.* **2001**, *3*, 975 – 978; b) J. Aiguade, J. Hao, C. J. Forsyth, *Org. Lett.* **2001**, *3*, 979 – 982; c) J. Aiguade, J. Hao, C. J. Forsyth, *Tetrahedron Lett.* **2001**, *42*, 817 – 820; d) J. Hao, J. Aiguade, C. J. Forsyth, *Tetrahedron Lett.* 2001, 42, 821 – 824; e) K. C. Nicolaou, P. M. Pihko, N. Diedrichs, N. Zou, F. Bernal, *Angew. Chem.* **2001**, *113*, 1302 – 1305; *Angew. Chem. Int. Ed.* **2001**, *40*, 1262 – 1265; f) K. R. Buszek, *221st National ACS Meeting*, **2001**, San Diego, ORGN-570; g) C. J. Forsyth, J. Hao, J. Aiguade, *Angew. Chem.* **2001**, *113*, 3775 – 3779; *Angew. Chem. Int. Ed.* **2001**, *40*, 3663 – 3667; h) K. C. Nicolaou, W. Qian, F. Bernal, N. Uesaka, P. M. Pihko, J. Hinrichs, *Angew. Chem.* **2001**, *113*, 4192 – 4195; *Angew. Chem. Int. Ed.* **2001**, *40*, 4068 – 4071; i) M. Sasaki, Y. Iwamuro, J. Nemoto, M. Oikawa, *Tetrahedron Lett.* **2003**, *44*, 6199 – 6201; j) K. R. Buszek, T. S. Gibson, B. C. Reinhardt, J. R. Sunde, *226th ACS National Meeting*, **2003**, New York, ORGN-179; k) Y. Ishikawa, S. Nishiyama, *Tetrahedron Lett.* **2004**, *45*, 351 – 354; l) Y. Ishikawa, S. Nishiyama, *Heterocycles* **2004**, *63*, 539 – 565; m) Y. Ishikawa, S. Nishiyama, *Heterocycles* **2004**, *63*, 885 – 893; n) L. K. Geisler, S. Nguyen, C. J. Forsyth, *Org. Lett.* **2004**, *6*, 4159 – 4162.

[3] a) K. C. Nicolaou, Y. Li, N. Uesaka, T. V. Koftis, S. Vyskocil, T. Ling, M. Govindasamy, W. Qian, F. Bernal, D. Y.-K. Chen, *Angew. Chem.* **2003**, *115*, 3771 – 3776; *Angew. Chem. Int. Ed.* **2003**, *42*, 3643 – 3648; b) K. C. Nicolaou, D. Y.-K. Chen, Y. Li, W. Qian, T. Ling, S. Vyskocil, T. V. Koftis, M. Govindasamy, N. Uesaka, *Angew. Chem.* **2003**, *115*, 3777 – 3781; *Angew. Chem. Int. Ed.* **2003**, *42*, 3649 – 3653.

[4] a) K. C. Nicolaou, S. Vyskocil, T. V. Koftis, Y. M. A. Yamada, T. Ling, D. Y.-K. Chen, W. Tang, G. Petrovic, M. O. Frederick, Y. M. Satake, *Angew. Chem.* **2004**, *116*, 4412 – 4418; *Angew. Chem. Int. Ed.* **2004**, *43*, 4312 – 4318; b) K. C. Nicolaou, T. V. Koftis, S. Vyskocil, G. Petrovic, T. Ling, Y. M. A. Yamada, W. Tang, M. O. Frederick, *Angew. Chem.* **2004**, *116*, 4418 – 4424; *Angew. Chem. Int. Ed.* **2004**, *43*, 4318 – 4324.

[5] X.-T. Zhou, R. G. Carter, *Chem. Commun.* **2004**, 2138 – 2140.

[6] a) O. Flögel, M. G. O. Amombo, H.-U. Reißig, G. Zahn, I. Brüdgam, H. Hartl, *Chem. Eur. J.* **2003**, *9*, 1405 – 1415; b) B. Herradon, *Tetrahedron: Asymmetry* **1991**, *2*, 191 – 194.

[7] J. R. Hwu, *J. Org. Chem.* **1983**, *48*, 4432 – 4433.

[8] K. R. Guertin, A. S. Kende, *Tetrahedron Lett.* **1993**, *34*, 5369 – 5372.

[9] S. V. Ley, J. Norman, W. P. Griffith, S. P. Marsden, *Synthesis* **1994**, 639 – 666.

[10] a) I. Ohtani, T. Kusumi, Y. Kashman, H. Kakisawa, *J. Am. Chem. Soc.* **1991**, *113*, 4092 – 4096; b) J. A. Dale, H. S. Mosher, *J. Am. Chem. Soc.* **1973**, *95*, 512 – 519; c) G. R. Sullivan, J. A. Dale, H. S. Mosher, *J. Org. Chem.* **1973**, *38*, 2143 – 2147.

[11] For the first example of a metal-catalyzed oxidation of aryl allylic selenides, see: a) R. G. Carter, T. C. Bourland, *Chem. Commun.* **2000**, 2031 – 2032; b) T. C. Bourland, R. G. Carter, A. F. T. Yokochi, *Org. Biomol. Chem.* **2004**, *2*, 1315 – 1329.

[12] P. A. Grieco, S. Gilman, M. Nishizawa, *J. Org. Chem.* **1976**, *41*, 1485 – 1486.

[13] A. K. Chatterjee, T.-L. Choi, D. P. Sanders, R. H. Grubbs, *J. Am. Chem. Soc.* **2003**, *125*, 11 360 – 11 370.

 © 2006 Wiley-VCH Verlag GmbH & Co. KGaA, Weinheim 

*Oxo–Iron Enzymes*

DOI: 10.1002/anie.200503841

# Differences in and Comparison of the Catalytic Properties of Heme and Non-Heme Enzymes with a Central Oxo–Iron Group**

*Sam P. de Visser**

Many enzymes contain transition-metal ions, such as iron, in their active form, which are bound through one or several of the ligands to the protein environment. Two typical complex types have been identified in transition-metal-coordinated enzymes: one type contains a central heme group, the other has no heme group.[1,2] Heme enzymes are a large family of enzymes involved in a variety of important bioprocesses ranging from oxygen transport by hemoglobin to the biosynthesis of hormones and detoxification mechanisms as done for instance by cytochrome P450 (P450) enzymes.[2] The latter group of enzymes are monooxygenase enzymes that utilize molecular oxygen of which one oxygen atom is transferred to the substrate whereas the other oxygen atom leaves the

[*] Dr. S. P. de Visser
The Manchester Interdisciplinary Biocentre and
the School of Chemical Engineering and Analytical Science
The University of Manchester
Sackville Street, PO Box 88, Manchester M60 1QD (UK)
Fax: (+44) 161-306-4399
E-mail: sam.devisser@manchester.ac.uk

[**] The research was supported by a grant for CPU time of the Computational Chemistry Working Party (CCWP).

Supporting information for this article is available on the WWW under http://www.angewandte.org or from the author.


WILEY InterScience DISCOVER SOMETHING GREAT
© 2006 Wiley-VCH Verlag GmbH & Co. KGaA, Weinheim

process as water. Some pentacoordinated, non-heme iron complexes, by contrast, are able to utilize both oxygen atoms of molecular oxygen and therefore work as dioxygenases.[3]

Nevertheless, the active intermediate of monooxygenase and dioxygenase enzymes appears to be a central oxo–iron group, which in P450 and horseradish peroxidase (HRP) enzymes is also called Compound I (Cpd I). For simplicity, we will use this terminology as well for the dioxygenase models although there are electronic differences as will be pointed out below. One particular dioxygenase and the topic of the studies presented here is α-ketoglutarate dioxygenase (αKG), which is a class of enzymes that are involved in the synthesis of collagen in mammals and antibiotics in microbes as well as in DNA base repair.[4–7] Herein, we will describe the fundamental differences between heme and non-heme oxo–iron complexes and the electronic factors that distinguish their catalytic properties as based on density functional theory (DFT) studies of model complexes.

αKG during the catalytic cycle binds molecular oxygen of which one atom is used to convert α-ketoglutarate into succinate and $CO_2$, thereby creating an oxo–iron complex.[5–7] In the case of the taurine/αKG system, which we use as a model here, the oxo–iron complex hydroxylates taurine and is linked to the peptide backbone through interactions with two histidine and one aspartate ligand. Thus, the active hydroxylating species of dioxygenase and monooxygenase enzymes, like P450 and HRP, contains a central oxo–iron group. The major difference between the two enzyme classes, however, is that the dioxygenases do not require a cofactor during the catalytic cycle, nevertheless, they are able to hydroxylate substrates fairly easily.[5–7] What then are the differences between the active species of dioxygenase and monooxygenase enzymes and how does their catalytic behavior differ? In order to find an answer to these tantalizing questions we have performed density functional calculations on enzyme models of the oxo–iron species of αKG and P450 enzymes and calculated their reactivity patterns with respect to a typical substrate, namely propene. Earlier work on heme-type oxo–iron porphyrin models for P450 and HRP systems showed that the regioselectivity of propene epoxidation versus methyl group hydroxylation is dependent on small environmental perturbations.[8,9]

The electronic ground state of Cpd I of the heme enzymes P450 and HRP is a set of nearly degenerate quartet and doublet spin states,[10] which creates two-state reactivity patterns with competing reaction mechanisms on the two spin state surfaces.[11] In particular, the doublet spin state leads to product formation via a short-lived intermediate, whereas from the quartet spin state a long-lived intermediate is reached, which makes side-reactions leading to by-products possible.[12] Therefore, the population of the doublet and quartet spin states of Cpd I of heme enzymes influences the product distributions, rate coefficients and kinetic isotope effects.[12] By contrast, αKG Cpd I has a quintet ground state, which is well separated from other spin states.[7,13]

The optimized geometry of the Cpd I (αKG) in the quintet spin state as a long-range complex with propene, is shown in Figure 1 with critical bond lengths identified. The calculated oxo–iron bond of αKG Cp I is 1.653 Å and is of

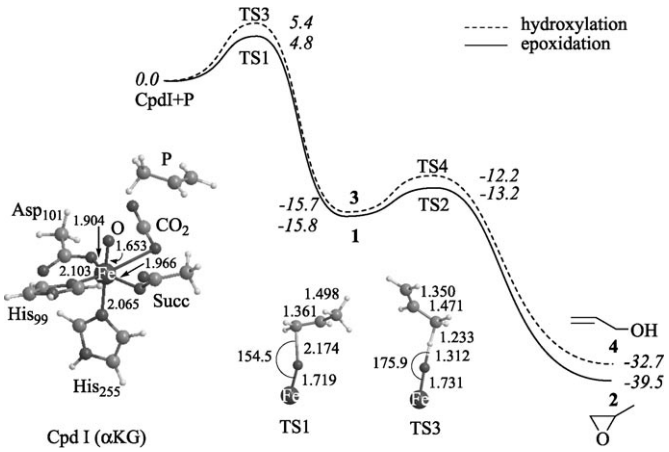



***Figure 1.*** Optimized geometry (with critical bond lengths [Å]) of the model of αKG Cpd I (left), and the potential-energy profile for the mechanisms of the competitive hydroxylation and epoxidation of propene (P) as obtained with UB3LYP/LACV3P++* with zero-point corrections at the LACVP level of theory. All energies are in kcal mol$^{-1}$ relative to the reactant complex (Cpd I + P). Also shown are extracts of the geometries (with bond lengths [Å] and angles [°]) of the rate-determining transition states along the epoxidation (TS1) and hydroxylation (TS3) surfaces.

comparable length with heme-type oxo–iron bonds as in P450 models (1.651 Å) or HRP models (1.621 Å),[14] while the experimentally obtained Fe–O distance of HRP Cpd I is 1.7 Å.[15] The iron–imidazole linkage (2.065 Å) is similar to that observed for HRP (2.173 Å).[14] Thus, our model calculations on oxo–iron systems in either heme or non-heme environments give similar geometric features so that the differences in properties between the two model systems do not arise from geometric factors but will have an electronic origin. However, as shown before, factors[8] such as the protein environment and hydrogen-bonding interactions may change the geometries, so that a full quantum mechanical/molecular mechanical (QM/MM) treatment will be required.

Subsequently, we investigated the activation of propene by αKG Cpd I. Upon propene activation two reaction mechanisms are possible, namely C=C double-bond epoxidation and methyl C–H hydroxylation. The epoxidation reaction is initiated with a C–O bond-activation step via a barrier TS1 to form a radical intermediate (**1**), which after a ring-closure barrier (TS2) produces the epoxide product complex (**2**). The hydroxylation mechanism starts with an initial hydrogen-abstraction step (via barrier TS3) to form a hydroxo–iron complex with a nearby allene radical (intermediate **3**), which subsequently rebounds (via barrier TS4) to form the propenol complex **4**. The potential energy profiles for the reactions are displayed in Figure 1 as well as highlights of the geometries of the rate-determining transition states TS1 and TS3.

We also calculated the reaction mechanisms at the triplet and septet spin states, but all structures were found to be much higher-lying than the corresponding quintet spin states. The reaction mechanism closely resembles the one obtained with P450 Cpd I, where also close-lying hydroxylation and epoxidation mechanisms via radical intermediates (**1** and **3**)

 © 2006 Wiley-VCH Verlag GmbH & Co. KGaA, Weinheim 

were identified.[8] On both surfaces the intermediates are separated by a small barrier of 2.6 (TS2) or 3.5 (TS4) kcal $mol^{-1}$ toward products. The rate-determining steps, however, are the initial C–O formation step via TS1 or the hydrogen abstraction via TS3, and are only 0.6 kcal $mol^{-1}$ apart. Therefore, our calculations predict competitive hydroxylation and epoxidation reactions in the gas phase. The absolute barriers of propene activation by αKG Cpd I are substantially lower than the ones obtained with P450 or HRP Cpd I models, which were 8.5 and 12.3 kcal $mol^{-1}$, respectively, via doublet spin TS1 using the same methods and basis sets. Thus, the αKG Cpd I model as used here is a much stronger oxygenation catalyst than the heme-type enzymes P450 and HRP and will be much more reactive and might even be able to hydroxylate very strong C–H bonds. This result is in line with DFT calculations on synthetic non-heme Fe=O catalysts versus oxo–iron porphyrin models.[16] Moreover, αKG shows a single-state reactivity on a dominant quintet spin surface, whereas heme enzymes generally give multi-state reactivity on competing doublet and quartet spin surfaces.

Since the reactivity differences between αKG and P450 originate from the electronic structure of the two different Cpd I species, we show in Figure 2 the high-lying occupied and low-lying virtual orbitals of Cpd I of αKG (top) and P450 (bottom). Both sets of orbitals are characterized by the iron 3d-block orbitals, which split into the typical three-below-two ($t_{2g}$, $e_g$) pattern. In addition, P450 has a high-lying heme orbital ($a_{2u}$), which is partially occupied and gives the system an extra oxidizing equivalent. Of similar shape and value in the two Cpd I systems are the anti-bonding orbitals along the Fe–O bond ($\pi^*_{xz}$, $\pi^*_{yz}$, and $\sigma^*_{z^2}$), although the orbital lobes of the penta-coordinated system are somewhat shifted due to the location of the ligands. The major differences between P450 Cpd I and αKG Cpd I, however, arise due to the fact that heme is a tetradentate ligand, which distorts the $t_{2g}$ ($\pi^*$) set of orbitals into a one-below-two ($\delta$, $\pi^*$) subset. This extra stabilization converts an anti-bonding orbital ($\pi^*_{x^2-y^2}$) into a low-lying non-bonding $\delta$ orbital with double occupation. Thus, while P450 Cpd I in the *xy* plane of symmetry contains two electrons in a non-bonding orbital ($\delta$), in αKG Cpd I these two electrons are both located in anti-bonding orbitals ($\pi^*_{x^2-y^2}$, $\sigma^*_{xy}$). This implies that heme is a stronger ligand than the corresponding histidine and aspartate ligands that are in the *xy* plane in αKG Cpd I.

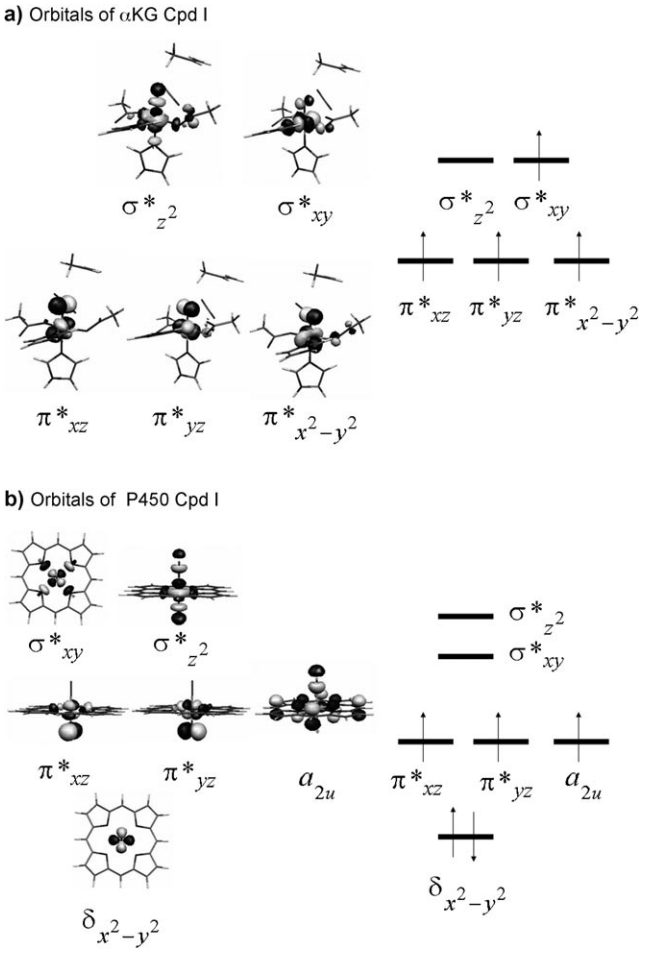



***Figure 2.*** High-lying occupied and low-lying virtual orbitals of a) αKG and b) P450.

Both the epoxidation and hydroxylation reactions, that is, via TS1 or TS3, are accomplished with a simultaneous electron-transfer process leading to a radical site on the substrate ($\varphi_S$), namely an allene radical in the hydroxylation process and a secondary carbon radical in the epoxidation reaction. In the case of P450, it was shown that the electron is preferentially transferred into the $a_{2u}$ orbital thereby creating radical intermediates (**1** and **3**) with orbital occupation $\pi^*_{xz}{}^1\pi^*_{yz}{}^1a_{2u}{}^2\varphi_S{}^1$ with the metal in the formal oxidation state IV.[8] Thus, the heme ligand shuttles electrons away from the process but the total number of unpaired electrons and the oxidation state of the metal stay the same.

By contrast, in the case of αKG, the electron transfer process in TS1 and TS3 fills the empty anti-bonding $\sigma^*_{z^2}$ orbital, whereby a situation is created with the complete metal 3d-block orbitals singly occupied plus a radical center on the substrate, that is, the occupation of the intermediates **1** and **3** is: $\pi^*_{x^2-y^2}{}^1\pi^*_{xz}{}^1\pi^*_{yz}{}^1\sigma^*_{z^2}{}^1\sigma^*_{xy}{}^1\varphi_S{}^1$ (Figure 3), with all metal 3d-block orbitals occupied with one α-spin electron and the $\varphi_S$ orbital with one β-spin electron. Therefore, during the hydroxylation and epoxidation reaction processes in αKG the system gains radical character by creating an intermediate complex with six unpaired electrons with the metal 3d-block orbitals extra stabilized due to exchange stabilization. Moreover, in the case of αKG, the metal center in TS1 and TS3 is

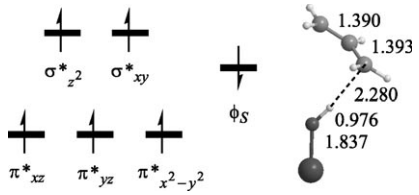



***Figure 3.*** Orbital occupation of intermediate complexes **1** and **3** (left), and the optimized geometry (with interatomic distances [Å]) of **3** (right) from the reaction of propene with αKG Cpd I.

 © 2006 Wiley-VCH Verlag GmbH & Co. KGaA, Weinheim 

reduced to a formal oxidation state III and one electron is transferred into an anti-bonding orbital along the Fe–O axis, that is, $\sigma^*_{z^2}$. This weakens the Fe–O bond and hence lowers the reaction barrier considerably. Indeed, the geometric features of the transition state show the attack of the substrate along the *z* axis of the system (Figure 1) and filling of the $\sigma^*_{z^2}$ orbital. The Fe-O-H angle in TS3 is almost linear (175.9°) and the Fe-O-C angle in TS1 is 154.5°, both imply the overlap of the $\sigma^*_{z^2}$ orbital of Cpd I with the substrate moiety.

In conclusion, pentacoordinate oxo–iron complexes, as they appear in various enzymes, are shown to be efficient catalysts which can hydroxylate alkyl groups and epoxidize C=C bonds with small reaction barriers. By contrast, heme enzymes are more gentle catalysts and therefore probably easier to control in biosystems. So it may very well be that nature has chosen catalysts with a heme ligand for substrate-specific processes. The reactivity patterns of non-heme and heme enzymes show some critical differences which originate from electronic factors. Moreover, while in heme enzymes the reaction is initiated with the electron transfer into a partially filled heme orbital ($a_{2u}$), the non-heme complexes transfer the first electron to an empty $\sigma^*_{z^2}$ orbital that weakens the Fe–O bond. As a result, the initial reaction barrier leads to a large open-shell system with six unpaired electrons, which is exchange-stabilized due to single occupancy of the complete 3d-metal block orbitals.

## Theoretical Methods

All calculations were performed using the Jaguar 5.5 program package[17] and utilized the UB3LYP hybrid density functional method.[18] Geometries were fully optimized (without constraints) using the double-ζ-quality LACVP basis set and subsequent single-point calculations with the triple-ζ-type LACV3P+* basis set were performed.[19] The nature of the critical points was verified with an analytical frequency calculation in Gaussian 98.[20] All energies reported here use the LACV3P+* data with ZPE corrections at the LACVP level of theory. We used a model based on the 1OS7 pdb[5] in which the histidine ligands were replaced by imidazole, and the aspartate and succinate ligands by acetic acid. We used propene as a substrate since this is the smallest model in which competitive alkyl hydroxylation and C=C bond epoxidation mechanisms can be studied.[8,9]

Received: October 31, 2005
Published online: February 10, 2006

**Keywords:** density functional calculations · enzyme catalysis · enzyme models · epoxidation · hydroxylation

[1] a) M. Costas, M. P. Mehn, M. P. Jensen, L. Que, Jr., *Chem. Rev.* **2004**, *104*, 939–986; b) M. L. Neidig, E. I. Solomon, *Chem. Commun.* **2005**, 5843–5863.
[2] *Cytochrome P450: Structure, Mechanisms and Biochemistry* (Ed.: P. R. Ortiz de Montellano), Plenum Press/Kluwer Publishers, New York, **2005**.
[3] a) T. D. H. Bugg, *Tetrahedron* **2003**, *59*, 7075–7101; b) J. M. Bollinger, Jr., J. C. Price, L. M. Hoffart, E. W. Barr, C. Krebs, *Eur. J. Inorg. Chem.* **2005**, 4245–4254.
[4] S. C. Trewick, T. F. Henshaw, R. P. Hausinger, T. Lindahl, B. Sedgwick, *Nature* **2002**, *419*, 174–178.
[5] J. R. O'Brien, D. J. Schuller, V. S. Yang, B. D. Dillard, W. N. Lanzilotta, *Biochemistry* **2003**, *42*, 5547–5554.
[6] J. C. Price, E. W. Barr, L. M. Hoffart, C. Krebs, J. M. Bollinger, Jr., *Biochemistry* **2005**, *44*, 8138–8147.
[7] C. Krebs, J. C. Price, J. Baldwin, L. Saleh, M. T. Green, J. M. Bollinger, Jr., *Inorg. Chem.* **2005**, *44*, 742–757.
[8] a) S. P. de Visser, F. Ogliaro, P. K. Sharma, S. Shaik, *Angew. Chem.* **2002**, *114*, 2027–2031; *Angew. Chem. Int. Ed.* **2002**, *41*, 1947–1951; b) S. P. de Visser, F. Ogliaro, P. K. Sharma, S. Shaik, *J. Am. Chem. Soc.* **2002**, *124*, 11809–11826.
[9] D. Kumar, S. P. de Visser, P. K. Sharma, E. Derat, S. Shaik, *J. Biol. Inorg. Chem.* **2005**, *10*, 181–189.
[10] D. L. Harris, *Curr. Opin. Chem. Biol.* **2001**, *5*, 724–735.
[11] S. Shaik, S. P. de Visser, F. Ogliaro, H. Schwarz, D. Schröder, *Curr. Opin. Chem. Biol.* **2002**, *6*, 556–567.
[12] a) S. P. de Visser, F. Ogliaro, S. Shaik, *Angew. Chem.* **2001**, *113*, 2955–2958; *Angew. Chem. Int. Ed.* **2001**, *40*, 2871–2874; ; b) S. P. de Visser, D. Kumar. S. Shaik, *J. Inorg. Biochem.* **2004**, *98*, 1183–1193; c) D. Kumar, S. P. de Visser, S. Shaik, *Chem. Eur. J.* **2005**, *11*, 2825–2835.
[13] A. Bassan, T. Borowski, P. E. M. Siegbahn, *Dalton Trans.* **2004**, 3153–3162.
[14] a) S. P. de Visser, S. Shaik, P. K. Sharma, D. Kumar, W. Thiel, *J. Am. Chem. Soc.* **2003**, *125*, 15779–15788; b) S. P. de Visser, *J. Phys. Chem. A* **2005**, *109*, 11050–11057.
[15] G. I. Berglund, G. H. Carlsson, A. T. Smith, A. Hendriksen, J. Hajdu, *Nature* **2002**, *417*, 463–468.
[16] a) A. Decker, E. I. Solomon, *Angew. Chem.* **2005**, *117*, 2292–2295; *Angew. Chem. Int. Ed.* **2005**, *44*, 2252–2255; b) D. Kumar, H. Hirao, L. Que, Jr., S. Shaik, *J. Am. Chem. Soc.* **2005**, *127*, 8026–8027.
[17] Jaguar 5.5, Schrödinger Inc., Portland, OR, USA, **2000**.
[18] a) A. D. Becke, *J. Chem. Phys.* **1993**, *98*, 5648–5652; b) C. Lee, W. Yang, R. G. Parr, *Phys. Rev. B* **1988**, *37*, 785–789.
[19] J. P. Hay, W. R. Wadt, *J. Chem. Phys.* **1985**, *82*, 299–310.
[20] Gaussian 98 (Revision A.9): M. J. Frisch et al., see Supporting Information.

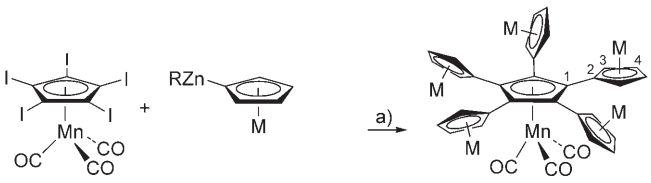
 © 2006 Wiley-VCH Verlag GmbH & Co. KGaA, Weinheim 

Oligocyclopentadienyl Complexes

DOI: 10.1002/anie.200504047

# Syntheses, Structures, and Reactivity of Radial Oligocyclopentadienyl Metal Complexes: Penta(ferrocenyl)cyclopentadienyl and Congeners**

*Yong Yu, Andrew D. Bond, Philip W. Leonard, K. Peter C. Vollhardt,* and Glenn D. Whitener*




***Scheme 1.*** a) $[Pd_2(dba)_3]$ (25%), THF, 65 °C, 18 h. dba = dibenzylideneacetone.

Among the oligocyclopentadienyl metal complexes,[1] the radial or "starburst" version based on the [5]radialene core[2] has been elusive. Such permetalated pentacyclopentadienylated cyclopentadienyls (Cps) are of latent interest as novel tunable dendritic molecules,[3] unusual electronic and magnetic materials,[4] hexametallic "minisurfaces" with potential in catalysis,[5] extremely bulky "supra"Cps,[6] cyclic pentadecker "Ferris wheel" metallocenes,[7] and circumferential annealing precursors to the corresponding unknown semibuckminsterfullerene $C_{30}H_{10}$,[8] the cap of the (5,5)nanotube, or its metalated form.[9] We report the syntheses, structures, and properties of the first examples of this class of compounds, in addition to some transformations that pertain to the preceding premises.

We had succeeded previously in the preparation of $[(CpH)_5CpMn(CO)_3]$ and its pentaanion by the fivefold Pd-catalyzed coupling of $[C_5I_5Mn(CO)_3]$ **1** with $CpSnBu_3$ (or $Cp^-$),[10] generating what was anticipated to be a ready ligand for permetalation. This expectation proved completely fallacious, conditions normally conducive to reaction[1,6] leading only to decomposition.[11] We therefore turned to a direct metallacyclopentadienylation strategy and, after extensive experimentation with cross-coupling reagents,[12] a Negishi protocol.[13] Gratifyingly, exposure of **1** to 5 equivalents of the Zn species **2**[13d] gave the desired sexicyclopentadienyl metal complexes **3** (Scheme 1, see the Experimental Section), in addition to the partly reduced tetra- (Mn, Re, Fe) and triCp-metalated (Mn) systems, as well as some fulvalene dimetal products derived from oxidative coupling of **2**; all of these were isolated after a sequence of three chromatographic separations on silica gel, eluting with varying mixtures of hexanes, $CH_2Cl_2$, and EtOAc.[14] Considering that fivefold coupling to **1** has occurred in these transformations, furnishing extraordinarily crowded frames, the yields, especially that of **3c**, are admirable. Remarkable is that, despite the encumbered environment, the CpM substituents are sufficiently mobile at ambient temperature to equilibrate the pairs of α and β hydrogens, respectively, on the NMR timescale, providing simple spectra. On cooling to −60 °C, the corresponding signals for **3a** and **3b** decoalesce to a single, fully resolved ABCD pattern (1:1:1:1), quantified by variable-temperature NMR and EXSY: $\Delta H^{\ddagger} = 12.1\ (\pm 1.4)$ kcal mol$^{-1}$, $\Delta S^{\ddagger} = -2.1\ (\pm 6)$ e.u. (**3a**), $\Delta H^{\ddagger} = 12.8\ (\pm 0.8)$ kcal mol$^{-1}$, $\Delta S^{\ddagger} = -2.6\ (\pm 3)$ e.u. (**3b**), while those of **3c** only broaden at the limits of solubility. The data are consistent with a chiral ligand with fivefold symmetry at low temperature and its presumably ungeared enantiomerization on coalescence.[15]

Mobility is also suggested by the X-ray structural features of these molecules, for example, **3a** and **3c** (Figure 1),[14] in which the radial Cp substituents are oriented at various angles relative to the central ring (from nearly coplanar 20.2° (CpFe1) to nearly perpendicular 75.9° (CpMn5)) and the appended metals are located either *syn* or *anti* to Mn1, without a pronounced preference, but in both molecules oriented in the same sense around the periphery. Signs of strain are found in distortions from ideal geometry, namely elongated substituent $Cp_{quat}$–M bonds in the direction of $\eta^1,\eta^4$ bonding[16] (average bond lengths (long/short, Å): 2.21/2.14 (**3a**); 2.12/2.04 (**3c**)), pyramidalization[6,17] of the carbons of the central Cp ring directing the radial bonds away from Mn1 (average angle $Cp_{centroid}(Mn1)$-$C_{quat}$-$C_{quat}$ 172.0° (**3a**) and 172.2° (**3c**)), similar nonlinearity along $C_{quat}$-$C_{quat}$-$Cp_{centroid}(M)$ (average 170.0 (**3a**) and 168.7° (**3c**)), increased $Cp_{centroid}$–Mn1 distances (1.792, 1.796 Å), relative to the parent $[CpMn(CO)_3]$ (1.766 Å),[18] and bent ferrocenyls in **3c** (average value 173.2°).[19] The lack of coplanarity of the sexicyclopentadienyl core seemingly attenuates but does not obviate intermetallic communication, as indicated by the only slightly perturbed electronic spectra of **3a** and **3c** (compared to those of the component chromophores)[20] and, more diagnostically, preliminary cyclic voltammetry data recorded for **3c**, $E_{1/2} = 5$ (1e), 169 (2e), and 282 (2e) mV ($CH_2Cl_2$, $NBu_4PF_6$, versus

[*] Dr. Y. Yu, P. W. Leonard, Prof. K. P. C. Vollhardt, Dr. G. D. Whitener
Center for New Directions in Organic Synthesis
Department of Chemistry
University of California at Berkeley
and
Chemical Sciences Division
Lawrence Berkeley National Laboratory
Berkeley, CA 94720-1460 (USA)
Fax: (+1) 510-643-5208
E-mail: kpcv@berkeley.edu
Dr. A. D. Bond
Department of Chemistry
University of Southern Denmark
Campusvej 55, 5230 Odense M (Denmark)

[**] This work was supported by the Director, Office of Energy Research, Office of Basic Energy Sciences, Chemical Sciences Division, of the US Department of Energy, under Contract DE-AC02-05CH11231. The Center for New Directions in Organic Synthesis is facilitated by Bristol-Myers Squibb as a Sponsoring Member and Novartis as a Supporting Member. P.W.L. was an NSF Fellow. G.D.W. was supported by NSF and Bayer-Miles predoctoral fellowships.


WILEY InterScience DISCOVER SOMETHING GREAT
© 2006 Wiley-VCH Verlag GmbH & Co. KGaA, Weinheim

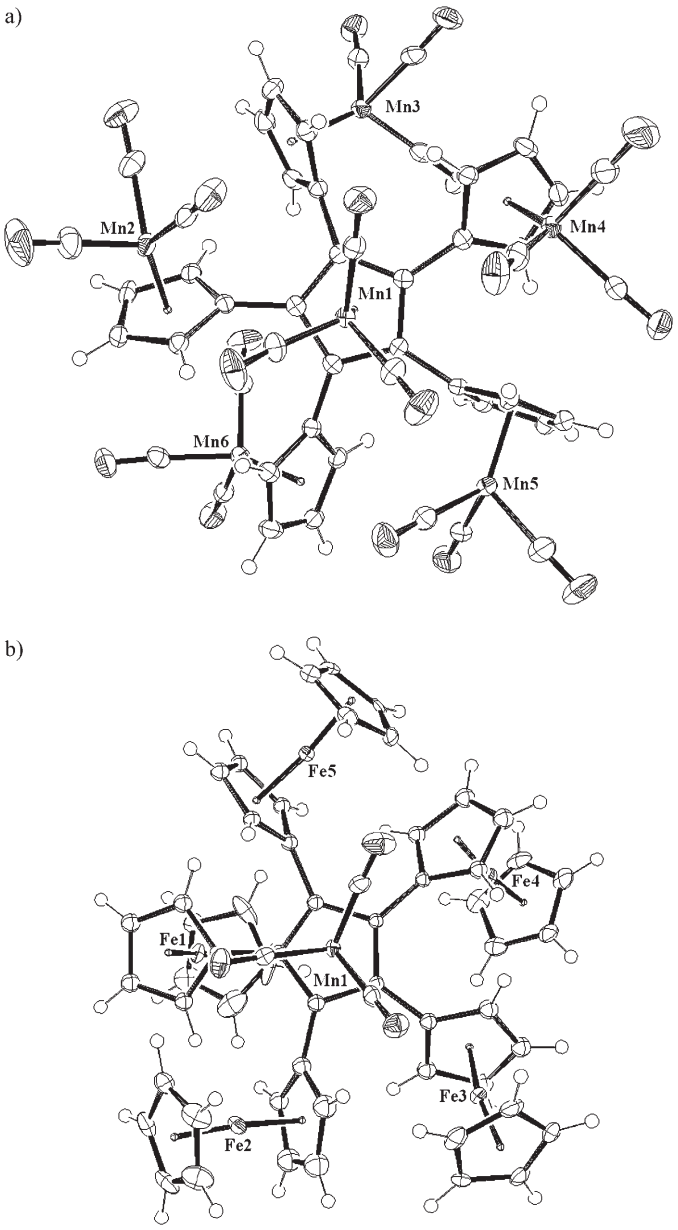



***Figure 1.*** Complexes **3a** (a) and **3c** (b) in the solid; displacement ellipsoids at 50% probability.

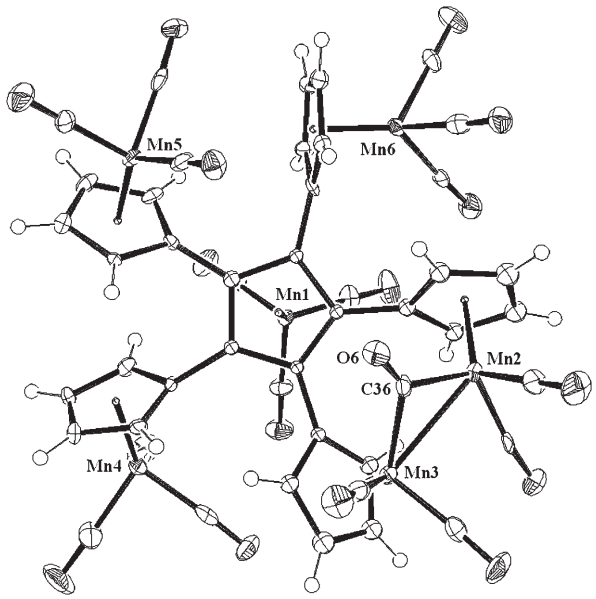
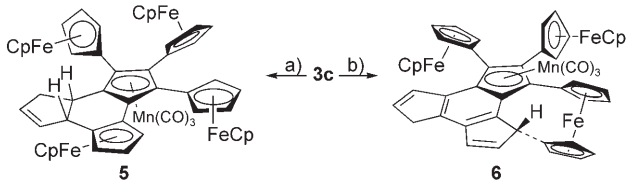



***Figure 2.*** Complex **4** in the solid; displacement ellipsoids at 50% probability. Selected bond lengths [Å] and angles [°]: Mn2–Mn3 2.754(1), Mn2–C36 1.998(6), Mn3–C36 1.959(6), C36–O6 1.186(7); Mn2-Mn3-C36 45.3(2), Mn3-Mn2-C36 46.5(2), Mn2-C36-Mn3 88.2(2).

$[Cp_2Fe]^0/[Cp_2Fe]^+$, referenced to internal $[Cp^*_2Fe]^0/[Cp^*_2Fe]^+$, −466 mV; $Cp^* = C_5Me_5$).[4,21]

To test the potential for cluster formation of these systems, **3a** was irradiated (450 W Hg lamp, THF) for 130 seconds to furnish the very sensitive, black-purple, monodecarbonylated **4** (Figure 2)[14] in 32% yield. The successful isolation of the dinuclear bridging-carbonyl species is remarkable in light of the only fleeting existence of the parent $[Cp_2Mn_2(CO)_5]$[22] and highlights the steric encumbrance in **3a**, substantially relieved in **4**, and the chelating qualities of the ligand.

First attempts toward annealing the pendant Cp ligands were executed with the relatively robust pentaferrocenyl complex **3c**. In an unprecedented process, subjection to TsOH gave the monocoupled product **5**, in which one ring had been demetalated (Scheme 2, Figure 3).[14,23] Fe4 is *syn* to Mn1, and the *cis* stereochemistry at C46–C47 suggests

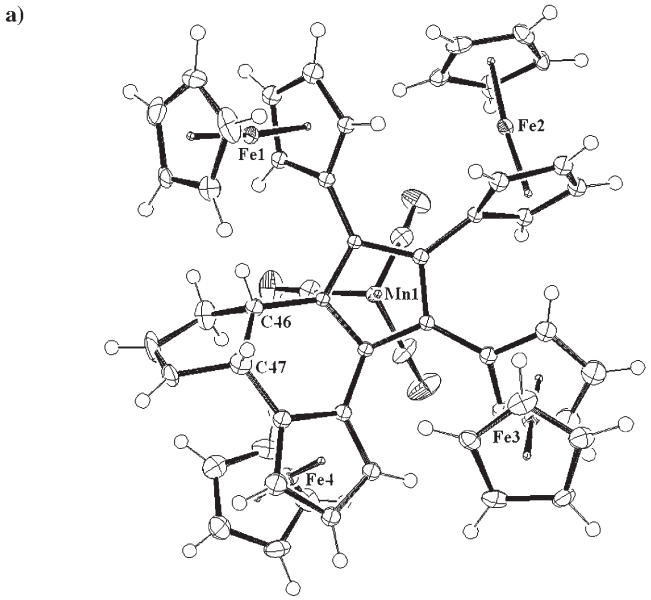



***Scheme 2.*** a) $TsOH{\cdot}H_2O$ (20 equiv), THF, 65 °C, 16 h, 66%; b) $[Cu(OTf)_2]$ (26 equiv), THF, 65 °C, 1.6 h, 31%. Ts = toluene-4-sulfonyl, Tf = trifluoromethanesulfonyl.

possibly *exo* electrophilic attack on the original ferrocene unit with Fe5 located *anti*. Turning to ultimately more desirable oxidative coupling conditions using $Cu^{2+}$[24] resulted in the remarkable dehydrogenative double Cp union embedded in **6** (Scheme 2, Figure 3).[14] While one C–C bond was formed as desired between C10 and C11, a second occurred to the unsubstituted Cp of Fe3, between C7 and C41, assembling a 1,1′-ferrocenotriindene frame. This outcome indicates that steric blocking of the "dangling" Cps in **3c** may be required to enforce the desired regiochemistry of annealing. Noteworthy in the $^1$H NMR spectrum of **6** is the unusually deshielded resonance at $\delta = 8.73$ ppm, tentatively assigned to H14, positioned close to Fe1 (3.00 Å in the crystal) and its deshielding cone.[25]

The penta(ferrocenyl)cyclopentadienyl ligand in **3c**, if it could be liberated, would constitute a unique, electronically tunable supraCp.[6] Indeed, irradiation[26] of **3c** in the presence of 1-heptyne provided **7** in excellent yield (Scheme 3, Figure 4).[14] Compared to **3c**, the molecule is much relieved

 © 2006 Wiley-VCH Verlag GmbH & Co. KGaA, Weinheim 



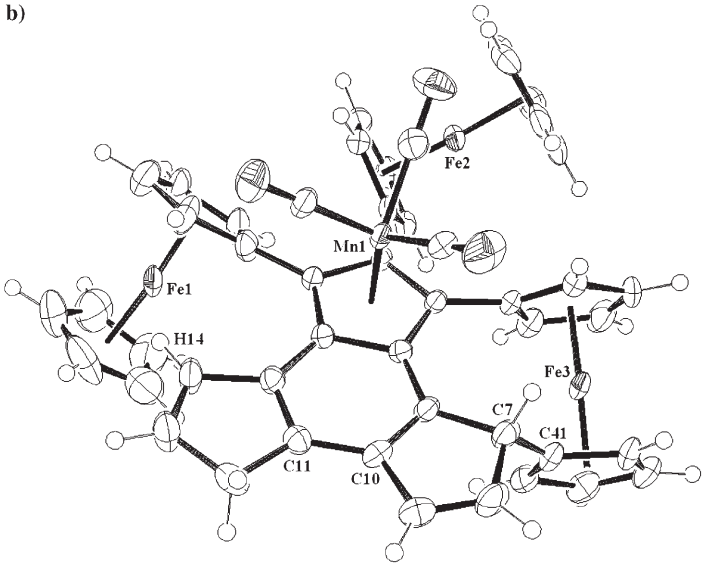
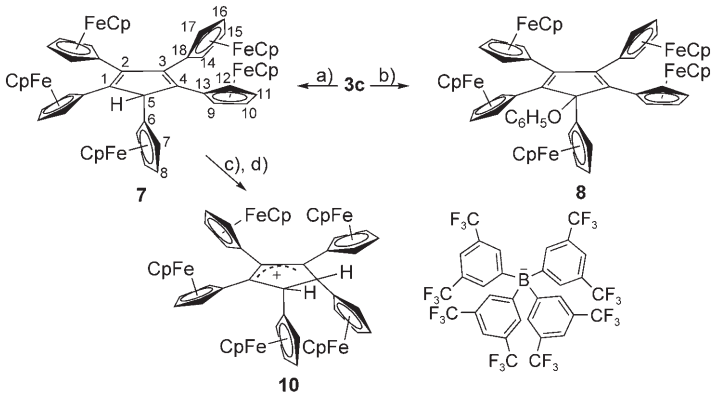




*Figure 3.* Complexes **5** (a) and **6** (b) in the solid; displacement ellipsoids at 50% probability.




***Scheme 3.*** a) *hν*, 1-heptyne (100 equiv), THF, 2 h, 88%; b) *hν*, phenol (20 equiv), THF, 10 h, 31%; c) $(C_6H_5)_3CPF_6$ (1.1 equiv), $CH_2Cl_2$, 0°C, 0.5 h, then 23°C, 1.5 h, 60%; d) $NaBAr^F{}_4$, $CH_2Cl_2$, 23°C, 2 h, 83%. $Ar^F{}_4 = B(C_6H_3(CF_3)_2)_4$.

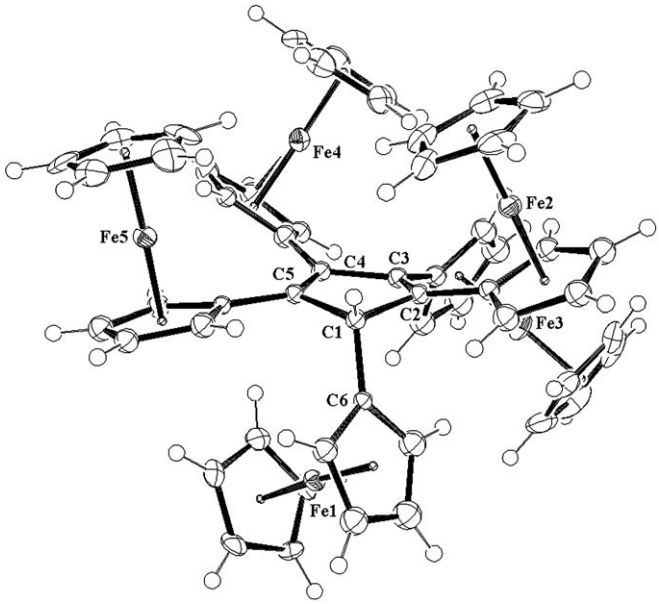



***Figure 4.*** Complex **7** in the solid; displacement ellipsoids at 50% probability. Selected bond lengths [Å] and angles [°]: C1–C2 1.525(8), C2–C3 1.361(9), C3–C4 1.499(8), C1–C5 1.520(9), C1–C6 1.548(9); C2-C1-C6 117.3(5), C5-C1-C6 104.9(5), C1-C2-C3-C4 1.2(2), C2-C3-C4-C5 −10.8(2), C3-C4-C5-C1 15.5(2), C4-C5-C1-C2 −14.4(2).

of strain, as evidenced by attenuation of all the bond distortions described above for the periphery of **3c**. Nevertheless, the bulk of the Fe1 substituent widens the angle C5-C1-C6, in turn enforcing a near-planar C3-C4-C5-C1 cyclopentadiene frame, with C2 located above it, delineating an envelope with an angle of 162.8°. Comparison of the cyclic voltammogram with that of **3c** ($E_{1/2} = -114$ (1e), 170 (2e), and 330 mV (2e)) reveals clearly the effect of removing the electron-withdrawing $Mn(CO)_3$ moiety[27] and isolating Fe1 electronically from the remainder of the molecule.

Surprisingly, an attempt to generate **7** from **3c** in the presence of phenol resulted in the "umpolung" product **8** (Scheme 3),[14] possibly indicative of the intermediacy of penta(ferrocenyl)cyclopentadienyl cation (or the occurrence of a radical pathway[28]). Consideration of the former seemed reasonable, in view of the known ability of the ferrocenyl substituent to stabilize a positive charge.[29] The Cp cation system has a rich history as an antiaromatic species with potential applications in electronic materials,[30] and the isolation of a stabilized derivative might provide the opportunity for a first X-ray structural analysis. Independent support for the possible existence of such a species was obtained in cyclic voltammetry experiments with the corresponding symmetrical, ruby-red penta(ferrocenyl)cyclopentadienyl anion **9** (see the Experimental Section), obtained from **3c** by deprotonation with NaH in DMSO/THF (1:6). This anion reveals *three* reversible oxidation steps at $E_{1/2} = -1.25$, 0.20, and 1.20 V (THF/DMSO, 4:1), interpreted as reflecting the transitions from anion→radical→cation (pos-

 © 2006 Wiley-VCH Verlag GmbH & Co. KGaA, Weinheim 

sibly ferrocene centered)→dication. These results boded well for bulk stepwise oxidations in the future, but more immediately suggested an approach to the cation by hydride abstraction from **3c**. In the event, protonation to the deep-green **10** occurred, the *cis*-dihydro structure of which was made certain by a synchrotron radiation analysis.[14] This result parallels that observed in the attempted synthesis of the Cp* cation by the same method.[31] Compound **10** is fluxional, providing only broad and inconclusive signals in its NMR spectra at room temperature. At −35 °C, a static and unsymmetrical structure is observed, probably the result of hindered mobility of the substituents around the allyl unit. Thus, relative to comparable bonds in **3c**, the allylic C–C bonds are shortened, as are its terminal linkages to the appended ferrocenyls. At higher temperatures, H shifts may contribute to the observed line broadening.[32] The quest for the penta(ferrocenyl)cyclopentadienyl cation is continuing, relying on the potential of **8** and **9** to function as suitable precursors.

In summary, we have synthesized the first radial oligocyclopentadienyl metal complexes and have made preliminary explorations of their reactivity, which also led to the synthesis of a unique supracyclopentadienyl ligand, **7**. The methodology should be amenable to the preparation of other permetalated systems and give rise to novel structures of interest in organic, organometallic, and materials chemistry.

## Experimental Section

**3a**: Pale-yellow crystals; m.p. 255–257 °C (decomp); $^1$H NMR (300 MHz, [D$_8$]THF), 55 °C): $\delta = 5.26$ (t, $J = 2.1$ Hz, 10 H, H3), 5.03 ppm (t, $J = 2.1$ Hz, 10 H, H4); $^{13}$C{$^1$H} NMR (100 MHz, $CD_2Cl_2$): $\delta = 225.0$, 223.2, 100.2 (C2), 99.5 (C1), 91.1 (C3), 82.4 ppm (C4); UV/Vis ($CH_2Cl_2$): $\lambda_{max}$ (lg$\varepsilon$) 346 nm (3.93); IR (KBr): $\tilde{\nu}_{(CO)} =$ 2021, 1925 cm$^{-1}$; MS (FAB): *m*/*z* (%): 1214 (4) [$M^+$], 1186 (3), 1158 (4), 1130 (100) [$M^+$−3 CO]; HRMS (FAB): calcd for $C_{48}H_{20}O_{18}Mn_6$: 1213.6933; found: 1213.6954. Elemental analysis calcd for $C_{48}H_{20}Mn_6O_{18}$: C 47.48, H 1.66; found: C 47.55, H, 1.81.

**3b**: Colorless crystals; m.p. 296–298 °C (decomp); $^1$H NMR (300 MHz, [D$_6$]acetone): $\delta = 5.98$ (t, $J = 2.2$ Hz, 10 H, H3), 5.72 ppm (t, $J = 2.2$ Hz, 10 H, H4); $^{13}$C{$^1$H} NMR (125 MHz, [D$_6$]acetone): $\delta =$ 222.8 (Mn-CO), 195.5 (Re-CO), 103.7 (C2), 99.8 (C1), 95.1 ppm (2 C; C3,4); IR (KBr): $\tilde{\nu}_{(CO)} = 2023$, 1915 cm$^{-1}$; MS (FAB): *m*/*z* (%): 1872 (20) [$M^+$], 1844 (40), 1786 (100) [$M^+$−3 CO]; HRMS (FAB): calcd for $C_{48}H_{20}O_{18}MnRe_5$: 1873.7818; found: 1873.7818. Elemental analysis calcd for $C_{48}H_{20}MnO_{18}Re_5$: C 30.82, H 1.08; found: C 30.81, H 0.98.

**3c**: Red crystals; m.p. 298–300 °C (decomp); $^1$H NMR (400 MHz, [D$_8$]THF, 54 °C): $\delta = 5.24$ (t, $J = 1.9$ Hz, 10 H, H3), 4.39 (t, $J = 1.9$ Hz, 10 H, H4), 4.14 ppm (s, 25 H, Cp); $^{13}$C{$^1$H} NMR (75 MHz, [D$_8$]THF): $\delta = 227.3$, 103.3 (C1), 84.8 (C2), 76.0 (C3), 71.1 (C4), 67.8 ppm (Cp); UV/Vis ($CH_2Cl_2$): $\lambda_{max}$ (log$\varepsilon$) 275 (sh, 4.54), 343 (sh, 3.85), 469 nm (3.42); IR (KBr): $\tilde{\nu}_{(CO)} = 2000$, 1920 cm$^{-1}$; MS (FAB): *m*/*z* (%): 1124 (80) [$M^+$], 1040 (40) [$M^+$−3 CO], 307 (100); HRMS (FAB): calcd for $C_{58}H_{45}O_3Fe_5Mn$: 1123.9496; found: 1123.9497. Elemental analysis calcd for $C_{58}H_{45}Fe_5MnO_3$: C 61.67, H 4.03; found: C 61.91, H, 4.15.

**4**: Black-purple crystals; m.p. 228–230 °C (decomp); $^1$H NMR (300 MHz, $CD_2Cl_2$): $\delta = 5.22$ (br s, 4 H), 4.84 (m, 10 H), 4.78 (m, 4 H), 4.60 ppm (br s, 2 H); $^{13}$C{$^1$H} NMR (100 MHz, $CD_2Cl_2$): $\delta = 95.8$, 95.5, 94.6, 91.0, 89.5, 87.2, 83.1, 82.5, 82.0, 81.7 ppm ($C_{quat}$ could not be located before compound decomposed); IR (KBr): $\tilde{\nu}_{(CO)} = 2021$, 1934, 1736 cm$^{-1}$; MS (FAB): *m*/*z* (%): 1187 (10) [$M$H$^+$], 1129 (100) [$M$H$^+$−2 CO]. Elemental analysis calcd for $C_{47}H_{20}Mn_6O_{17}$: C 47.59, H 1.70; found: C 47.57, H 1.79.

**5**: Yellow crystals; m.p. 100 °C (decomp); $^1$H NMR (300 MHz, [D$_8$]THF): $\delta = 6.39$ (m, 1 H), 6.33 (m, 1 H), 4.53 (m, 1 H), 4.50 (m, 1 H), 4.47 (m, 1 H), 4.41 (m, 3 H), 4.36 (m, 2 H), 4.28 (m, 2 H), 4.24 (s, 5 H), 4.22 (s, 5 H), 4.16 (m, 4 H), 4.06 (m, 1 H), 3.88 (s, 5 H), 3.82 (s, 5 H), 2.49 ppm (br s, 4 H); $^{13}$C{$^1$H} NMR (100 MHz, $CD_2Cl_2$): $\delta =$ 227.0, 133.8, 132.2, 103.7, 90.7, 82.0, 81.0, 80.5, 76.4, 75.8, 75.7, 73.9, 72.4, 71.9, 71.8 (Cp), 70.7, 70.6, 70.54, 70.48 (Cp), 70.4, 70.1 (Cp), 69.6 (Cp), 68.6, 68.5, 68.0, 67.8, 67.7, 67.2, 66.8, 66.5, 65.4, 64.0, 44.5, 43.8, 38.9 ppm; IR (KBr): $\tilde{\nu}_{(CO)} = 2000$, 1919, 1914 cm$^{-1}$; MS (FAB): *m*/*z* (%): 1004 (100) [$M^+$], 920 (55) ([$M^+$−3 CO)]; HRMS (FAB): calcd for $C_{53}H_{41}Fe_4MnO_3$: 1003.9834; found: 1003.9834. Elemental analysis calcd for $C_{53}H_{41}Fe_4MnO_3$: C 63.39, H 4.12; found: C 63.65, H 4.22.

**6**: Yellow crystals; m.p. 100 °C (decomp); $^1$H NMR (500 MHz, $CDCl_3$): $\delta = 8.73$ (m, 1 H), 6.89 (dd, $J = 5.5$, 2.0 Hz, 1 H), 6.77 (br d, $J =$ 6.3 Hz, 1 H), 6.71 (dd, $J = 5.5$, 2.0 Hz, 1 H), 4.91 (br s, 1 H), 4.80 (br s, 1 H), 4.69 (m, 3 H), 4.47 (br s, 2 H), 4.40 (m, 2 H), 4.30 (br s, 2 H), 4.14 (m, 1 H), 4.13 (br s, 2 H), 4.07 (s, 5 H), 3.99 (br s, 7 H), 3.81 (br s, 1 H), 3.62 (d, $J = 22$ Hz, 1 H), 3.46 ppm (d, $J = 22$ Hz, 1 H); IR (KBr): $\tilde{\nu}_{(CO)} = 2004$, 1927, 1918 cm$^{-1}$; MS (FAB): *m*/*z* (%): 880 (100) [$M^+$], 796 (95) ([$M^+$−3 CO)]; HRMS (FAB): calcd for $C_{48}H_{33}Fe_3MnO_3$: 879.9858; found: 879.9841.

**7**: Orange-red crystals; m.p. 308–309 °C; $^1$H NMR (500 MHz, $CDCl_3$): $\delta = 4.98$ (m, 2 H, H14 or 17), 4.91 (m, 2 H, H9 or 12), 4.61 (m, 2 H, H9 or 12), 4.53 (m, 2 H, H14 or 17), 4.44 (s, 1 H, H5), 4.38 (m, 2 H, H7), 4.36 (m, 2 H, H10 or 11), 4.35 (m, 2 H, H10 or 11), 4.32 (m, 2 H, H15 or 16), 4.26 (s, 10 H, Cp), 4.25 (m, 2 H, H15 or 16), 4.11 (m, 2 H, H8), 4.05 (s, 10 H, Cp), 3.88 ppm (s, 5 H, Cp); $^{13}$C{$^1$H} NMR (100 MHz, $CD_2Cl_2$): $\delta = 110.6$ (C2 or 4), 109.4 (C2 or 4), 93.3 (C6), 86.7 (C13), 85.6 (C18), 74.5 (C14 or 17), 74.2 (C14 or 17), 72.1 (C9 or 12), 71.6 (C7), 71.5 (C9 or 12), 71.3 (Cp), 71.0 (Cp), 70.9 (Cp), 70.3 (C10 or 11), 69.5 (C10 or 11), 68.9 (C15 or 16), 68.4 (C15 or 16), 67.7 (C8), 60.0 ppm (C5); MS (FAB): *m*/*z* (%): 986 (100) [$M^+$]; HRMS (FAB): calcd for $C_{55}H_{46}Fe_5$: 986.0346; found: 986.0349. Elemental analysis calcd for $C_{55}H_{46}Fe_5$: C 66.98, H 4.70; found: C 67.15, H 4.79.

**8**: Red crystals; m.p. 175 °C (decomp); $^1$H NMR (500 MHz, $CDCl_3$): $\delta = 7.43$ (t, $J = 7.5$ Hz, 2 H), 7.23 (br d, $J = 7.0$ Hz, 2 H), 6.99 (t, $J = 7.0$ Hz, 1 H), 5.35 (br s, 2 H), 5.31 (br s, 2 H), 5.01 (br s, 2 H), 4.72 (br s, 2 H), 4.38 (br s, 2 H), 4.35 (br s, 2 H), 4.33 (br s, 2 H), 4.32 (br s, 2 H), 4.27 (br s, 2 H), 4.11 (s, 10 H), 4.03 (br s, 2 H), 3.90 (s, 5 H), 3.78 ppm (s, 10 H); $^{13}$C{$^1$H} NMR (125 MHz, $CDCl_3$): $\delta = 157.7$, 143.3, 137.3, 129.2, 120.8, 117.3, 96.5, 93.6, 84.0, 81.7, 73.0, 72.7, 70.4, 69.6, 69.5, 69.4, 68.8, 68.4, 67.6, 67.5, 67.0, 65.9, 65.7 ppm; MS (FAB): *m*/*z* (%): 1078 (100) [$M^+$], 1002 (60), 985 (70) [$M^+$−$C_6H_5O$]; HRMS (FAB): calcd for $C_{61}H_{50}Fe_5O$: 1078.0609; found: 1078.0624. Elemental analysis calcd for $C_{61}H_{50}Fe_5O$: C 67.95, H 4.67; found: C 68.03, H 4.87.

**9**: $^1$H NMR (400 MHz, [D$_6$]DMSO): $\delta = 4.69$ (br s, 10 H), 4.03 (br s, 10 H), 3.88 ppm (s, 20 H); $^{13}$C{$^1$H} NMR (100 MHz, [D$_8$]THF): $\delta =$ 118.1, 94.8, 70.8, 68.5, 63.6 ppm.

**10**: Deep green crystals; m.p. 133–135 °C (decomp); $^1$H NMR (500 MHz, $CD_2Cl_2$, −35 °C): $\delta = 7.77$ (s, 8 H, $Ar^F_4$), 7.60 (s, 4 H, $Ar^F_4$), 5.71 (br s, 1 H), 5.54 (br s, 1 H), 5.42 (br s, 1 H), 5.12 (br s, 1 H), 4.71 (br s, 1 H), 4.53 (br s, 7 H), 4.46 (br s, 2 H), 4.44 (br s, 1 H), 4.32 (br s, 6 H), 4.28 (br s, 7 H), 4.23 (br s, 1 H), 4.18 (br s, 1 H), 4.11 (br s, 6 H), 3.99 (br s, 6 H), 3.91 (br s, 1 H), 3.86 (br s, 1 H), 3.64 (br s, 1 H), 3.59 (br s, 1 H), 2.83 ppm (br s, 1 H); $^{13}$C{$^1$H} NMR (125 MHz, $CD_2Cl_2$, −35 °C): $\delta =$ 186.3 (allyl), 185.7 (allyl), 161.7 (q, $J = 50$ Hz, $Ar^F_4$), 141.7 (allyl), 134.7 ($Ar^F_4$), 128.6 (q, $J = 28$ Hz, $Ar^F_4$), 124.5 (q, $J = 273$ Hz, $Ar^F_4$), 117.5 ($Ar^F_4$), 88.0, 85.3 (br), 84.9, 82.9 (br, 3C), 79.8 (br), 79.4, 79.2 (br), 78.4, 77.2, 76.7 (br), 74.1 (Cp), 73.8 (Cp), 73.6 (br), 73.2 (br), 72.3 (br), 71.4, 71.2, 70.3 (Cp), 69.8 (Cp), 69.7, 69.1 (Cp), 68.4, 67.9 (br), 66.7, 66.2, 59.6 ($C_{sp^3}$), 56.6 ($C_{sp^3}$) ppm, several carbon signals could not be identified with certainty; MS (FAB): *m*/*z* (%): 987 (100) [$M^+$ cation]; HRMS (FAB): calcd for $C_{55}H_{47}Fe_5$: 987.0425; found:

 © 2006 Wiley-VCH Verlag GmbH & Co. KGaA, Weinheim 

987.0426. Elemental analysis calcd for $C_{87}H_{59}BF_{24}Fe_5$: C 56.47, H 3.21; found: C 56.49, H 3.16.

Received: November 15, 2005
Published online: February 10, 2006

**Keywords:** carbocations · cyclopentadienyl ligands · metal–metal interactions · palladium · radialenes

[1] For a review, see: C. G. de Azevedo, K. P. C. Vollhardt, *Synlett* **2002**, 1019.

[2] For a review, see: H. Hopf, G. Maas, *Angew. Chem.* **1992**, *104*, 953; *Angew. Chem. Int. Ed. Engl.* **1992**, *31*, 931.

[3] For recent discourses on the subject, see: a) W.-L. Jia, R.-Y. Wang, D. Song, S. J. Ball, A. B. McLean, S. Wang, *Chem. Eur. J.* **2005**, *11*, 832; b) B. Stulgies, P. Prinz, J. Magull, K. Rauch, K. Meindl, S. Rühl, A. de Meijere, *Chem. Eur. J.* **2005**, *11*, 308, and references therein.

[4] a) For a recent example, see: C. Elschenbroich, O. Schiemann, O. Burghaus, K. Harms, *Chem. Commun.* **2005**, 2149; b) for selected pertinent reviews, see: H. Nishihara, M. Murata, *J. Inorg. Organomet. Polym. Mater.* **2005**, *15*, 147; c) A. Ceccon, S. Santi, L. Orian, A. Bisello, *Coord. Chem. Rev.* **2004**, *248*, 683; d) S. Barlow, D. O'Hare, *Chem. Rev.* **1997**, *97*, 637.

[5] See, for example, *Catalysis by Di- and Polynuclear Metal Cluster Complexes* (Eds.: R. D. Adams, F. A. Cotton), Wiley-VCH, New York, **1998**.

[6] For reviews, see: a) C. Janiak, H. Schumann, *Adv. Organomet. Chem.* **1991**, *33*, 291; b) J. Okuda, *Top. Curr. Chem.* **1991**, *160*, 97. The term "supra" was adopted from ref. [6a], although a referee suggested "super" instead, a notion to which we cannot object.

[7] For a recent review of multiple-decker complexes, see: V. Beck, D. O'Hare, *J. Organomet. Chem.* **2004**, *689*, 3920.

[8] a) F. Geneste, A. Moradpour, G. Dive, D. Peeters, J. Malthête, J.-F. Sadoc, *J. Org. Chem.* **2002**, *67*, 605; b) W.-L. Zhu, C. M. Puah, K. C. Ng, H.-L. Jiang, X.-J. Tan, K.-X. Chen, *J. Chem. Soc. Perkin Trans. 2* **2001**, 233, and references therein.

[9] For some recent related literature, see: a) Y. Zhao, Y.-H. Kim, A. C. Dillon, M. J. Heben, S. B. Zhang, *Phys. Rev. Lett.* **2005**, *94*, 5504; b) E. Nakamura, *J. Organomet. Chem.* **2004**, *689*, 4630; c) K. Lee, H. Song, J. T. Park, *Acc. Chem. Res.* **2003**, *36*, 78; d) A. L. Chistyakov, I. V. Stankevich, *Russ. Chem. Bull. Int. Ed.* **2003**, *52*, 1027.

[10] R. Boese, G. Bräunlich, J.-P. Gotteland, J.-T. Hwang, C. Troll, K. P. C. Vollhardt, *Angew. Chem.* **1996**, *108*, 1100; *Angew. Chem. Int. Ed. Engl.* **1996**, *35*, 995.

[11] See comments in: a) W. Steffen, M. Laskoski, J. G. M. Morton, U. H. F. Bunz, *J. Organomet. Chem.* **2004**, *689*, 4345; b) K. Sünkel, *Chem. Ber.* **1997**, *130*, 1721; for an early unsuccessful attempt to generate penta(ferrocenyl)cyclopentadiene, see: M. Rosenblum, N. Brawn, B. King, *Tetrahedron Lett.* **1967**, *8*, 4421.

[12] a) *Metal-Catalyzed Cross-Coupling Reactions*, 2nd ed. (Eds.: A. de Meijere, F. Diederich), Wiley-VCH, Weinheim, **2004**; b) *Handbook of Organopalladium Chemistry for Organic Synthesis, Vol. 1 and 2* (Eds.: E. Negishi, A. de Meijere), Wiley-Interscience, New York, **2002**.

[13] For related applications, see: a) L. V. Dinh, J. A. Gladysz, *Chem. Commun.* **2004**, 998; b) V. Mamane, I. Ledoux-Rak, S. Deveau, J. Zyss, O. Riant, *Synthesis* **2003**, 455; c) H. Yao, R. N. Grimes, *Organometallics* **2003**, *22*, 4539; d) M. Enders, G. Kohl, H. Pritzkow, *J. Organomet. Chem.* **2001**, *622*, 66; e) R. D. A. Hudson, B. M. Foxman, M. Rosenblum, *Organometallics* **2000**, *19*, 469, and references therein.

[14] All new compounds gave satisfactory analytical and spectroscopic data (see the Experimental Section) and were (except for anion **9**) subjected to X-ray crystallographic analysis. The structure of **3b** is very similar to that of **3a** and will be reported in connection with other ongoing work. **3a**: $C_{48}H_{20}Mn_6O_{18}\cdot 2(CH_3)_2CO$, crystal size $0.40\times0.32\times0.20$ mm$^3$, space group $P2_1/c$, scan range $3.0<2\theta<50.4°$, $T=154(2)$ K, $a=21.8294(3)$, $b=11.2973(2)$, $c=22.1502(3)$ Å, $\beta=109.592(1)°$, $V=5146.3(1)$ Å$^3$, $Z=4$, $\rho_{calcd}=1.717$ g cm$^{-3}$, $\mu(Mo_{K\alpha})=1.509$ mm$^{-1}$, 9126 unique reflections, of which 6332 were taken as observed $[I>3\sigma(I)]$, $R=0.032$, $R_w=0.040$. **3c**: $C_{58}H_{45}Fe_5MnO_3$, crystal size $0.26\times0.20\times0.13$ mm$^3$, space group $P\bar{1}$, scan range $3.0<2\theta<51.0°$, $T=140(2)$ K, $a=11.3590(3)$, $b=13.6829(2)$, $c=15.3923(4)$ Å, $\alpha=96.307(1)$, $\beta=110.155(1)$, $\gamma=99.502(1)°$, $V=2178.81(9)$ Å$^3$, $Z=2$, $\rho_{calcd}=1.713$ g cm$^{-3}$, $\mu(Mo_{K\alpha})=1.950$ mm$^{-1}$, 6951 unique reflections, of which 4590 were taken as observed $[I>3\sigma(I)]$, $R=0.040$, $R_w=0.042$. **4**: $C_{47}H_{20}Mn_6O_{17}\cdot 2CH_2Cl_2$, crystal size $0.26\times0.15\times0.10$ mm$^3$, space group $P\bar{1}$, scan range $3.0<2\theta<51.1°$, $T=137(2)$ K, $a=13.3789(11)$, $b=14.3484(11)$, $c=14.4646(11)$ Å, $\alpha=113.958(1)$, $\beta=104.846(1)$, $\gamma=90.015(1)°$, $V=2435.6(3)$ Å$^3$, $Z=2$, $\rho_{calcd}=1.849$ g cm$^{-3}$, $\mu(Mo_{K\alpha})=1.803$ mm$^{-1}$, 7783 unique reflections, of which 5250 were taken as observed $[I>2\sigma(I)]$, $R(F^2)=0.053$, $wR(F^2)=0.133$ (all data). **5**: $C_{53}H_{41}Fe_4MnO_3\cdot CH_2Cl_2$, crystal size $0.15\times0.12\times0.08$ mm$^3$, space group $P\bar{1}$, scan range $3.0<2\theta<51.3°$, $T=140(2)$ K, $a=11.7988(9)$, $b=11.9163(9)$, $c=16.877(1)$ Å, $\alpha=87.124(2)$, $\beta=88.289(1)$, $\gamma=65.960(2)°$, $V=2164.2(3)$ Å$^3$, $Z=2$, $\rho_{calcd}=1.671$ g cm$^{-3}$, $\mu(Mo_{K\alpha})=1.762$ mm$^{-1}$, 6915 unique reflections, of which 4040 were taken as observed $[I>3\sigma(I)]$, $R=0.047$, $R_w=0.051$. **6** (synchrotron radiation, Station 9.8, SRS Daresbury): $C_{48}H_{33}Fe_3MnO_3$, crystal size $0.60\times0.01\times0.01$ mm$^3$, space group $I2/a$, scan range $6.8<2\theta<44.7°$, $T=220(2)$ K, $a=25.418(3)$, $b=7.5321(12)$, $c=37.026(6)$ Å, $\beta=91.525(7)°$, $V=7086.2(18)$ Å$^3$, $Z=8$, $\rho_{calcd}=1.650$ g cm$^{-3}$, $\mu(\lambda=0.6850$ Å$)=1.599$ mm$^{-1}$, 5062 unique reflections, of which 3686 were taken as observed $[I>2\sigma(I)]$, $R(F^2)=0.047$, $wR=0.121$ (all data). **7**: $C_{55}H_{46}Fe_5$, crystal size $0.19\times0.10\times0.04$ mm$^3$, space group $P\bar{1}$, scan range $3.0<2\theta<51.0°$, $T=113(2)$ K, $a=11.2529(3)$, $b=12.7063(3)$, $c=15.3914(5)$ Å, $\alpha=99.989(2)$, $\beta=109.098(1)$, $\gamma=98.480(2)°$, $V=1998.1(1)$ Å$^3$, $Z=2$, $\rho_{calcd}=1.639$ mm$^{-1}$, $\mu(Mo_{K\alpha})=1.811$ mm$^{-1}$, 6430 unique reflections, of which 3610 were taken as observed $[I>3\sigma(I)]$, $R=0.046$, $R_w=0.050$. **7**·dichlorobenzene: $C_{55}H_{46}Fe_5\cdot C_6H_4Cl_2$, Crystal size $0.23\times0.08\times0.06$ mm$^3$, space group $P2_1/c$, scan range $3.00<2\theta<51.2°$, $T=160(2)$ K, $a=19.734(1)$, $b=11.3912(6)$, $c=21.809(1)$ Å, $\beta=107.846(1)°$, $V=4666.6(4)$ Å$^3$, $Z=4$, $\rho_{calcd}=1.613$ g cm$^{-3}$, $\mu(Mo_{K\alpha})=1.673$ mm$^{-1}$, 8310 unique reflections, of which 3752 were taken as observed $[I>3\sigma(I)]$, $R=0.045$, $R_w=0.048$. **8**: $C_{61}H_{50}Fe_5O\cdot 2CH_2Cl_2$, crystal size $0.27\times0.15\times0.11$ mm$^3$, space group $P\bar{1}$, scan range $3.0<2\theta<51.1°$, $T=122(2)$ K, $a=11.4335(1)$, $b=11.6544(2)$, $c=19.4721(5)$ Å, $\alpha=89.393(1)$, $\beta=84.396(1)$, $\gamma=83.449(1)°$, $V=2565.41(8)$ Å$^3$, $Z=2$, $\rho_{calcd}=1.616$ g cm$^{-3}$, $\mu(Mo_{K\alpha})=1.633$ mm$^{-1}$, 8224 unique reflections, of which 5086 were taken as observed $[I>3\sigma(I)]$, $R=0.049$, $R_w=0.056$. **10** (synchrotron radiation, Lawrence Berkeley Laboratory): $[C_{55}H_{47}Fe_5][B(C_6H_3(CF_3)_2)_4]$, crystal size $0.13\times0.07\times0.03$ mm$^3$, space group $P\bar{1}$, scan range $2.6<2\theta<43.3°$, $T=173(2)$ K, $a=14.0742(7)$, $b=16.1664(9)$, $c=18.5486(7)$ Å, $\alpha=111.064(3)$, $\beta=101.068(3)°$, $\gamma=97.727(2)°$, $V=3768.5(3)$ Å$^3$, $Z=2$, $\rho_{calcd}=1.631$ g cm$^{-3}$, $\mu(\lambda=0.7749$ Å$)=1.318$ mm$^{-1}$, 6596 unique reflections, of which 4936 were taken as observed $[I>2\sigma(I)]$, $R(F^2)=0.087$, $wR=0.242$. CCDC-289381–289388 contain the supplementary crystallographic data for this paper. These data can be obtained free of charge from The Cambridge Crystallographic Data Centre via www.ccdc.cam.ac.uk/data_request/cif.

[15] For a review of related organometallic molecular propellers, see: S. Brydges, L. E. Harrington, M. J. McGlinchey, *Coord. Chem. Rev.* **2002**, *233–234*, 75.

[16] K. Sünkel, C. Stramm, M. Lang, W. Kempinger, J. Hofmann, *Inorg. Chim. Acta* **1998**, *269*, 111, and references therein.

 © 2006 Wiley-VCH Verlag GmbH & Co. KGaA, Weinheim 

[17] M. Elian, M. M. L. Chen, D. M. P. Mingos, R. Hoffmann, *Inorg. Chem.* **1976**, *15*, 1148.
[18] P. J. Fitzpatrick, Y. L. Page, J. Sedman, I. S. Butler, *Inorg. Chem.* **1981**, *20*, 2852.
[19] For a review, see: J. C. Green, *Chem. Soc. Rev.* **1998**, *27*, 263.
[20] G. L. Geoffroy, M. S. Wrighton, *Organometallic Photochemistry*, Academic, New York, **1979**.
[21] For a recent pertinent study, see: D. Obendorf, H. Schottenberger, K. Wurst, N. Schuler, G. Laus, *J. Organomet. Chem.* **2005**, *690*, 811, and references therein.
[22] a) T. E. Bitterwolf, K. A. Lott, A. J. Rest, J. Mascetti, *J. Organomet. Chem.* **1991**, *419*, 113; b) B. S. Creaven, A. J. Dixon, J. M. Kelly, C. Long, M. Poliakoff, *Organometallics* **1987**, *6*, 2600; (fulvalene)dimanganese(hexacarbonyl) photodecarbonylates without Mn–Mn bond formation: c) P. E. Bloyce, R. H. Hooker, A. J. Rest, T. E. Bitterwolf, N. J. Fitzpatrick, J. E. Shade, *J. Chem. Soc. Dalton Trans.* **1990**, 833; d) W. A. Herrmann, D. Andrejewksi, E. Herdtweck, *J. Organomet. Chem.* **1987**, *319*, 183; for a calculated structure of $[Cp_2Mn_2(CO)_5]$, see: e) A. W. Ehlers, E. J. Baerends, F. M. Bickelhaupt, U. Radius, *Chem. Eur. J.* **1998**, *4*, 210.
[23] For demetalation pathways of ferrocenes, see, inter alia: a) O. J. Curnow, G. M. Fern, M. L. Hamilton, A. Zahl, R. van Eldik, *Organometallics* **2004**, *23*, 906; b) R. Prins, A. R. Korswagen, A. G. T. G. Kortbeek, *J. Organomet. Chem.* **1972**, *39*, 335; c) R. M. Golding, L. E. Orgel, *J. Chem. Soc.* **1962**, 363.
[24] M. D. Watson, A. Fechtenkötter, K. Müllen, *Chem. Rev.* **2001**, *101*, 1267.
[25] H. L. Lentzner, W. E. Watts, *Tetrahedron* **1971**, *27*, 4343.
[26] Patterned after: S. Top, E. B. Kaloun, S. Toppi, A. Herrbach, M. J. McGlinchey, G. Jaouen, *Organometallics* **2001**, *20*, 4554. Under the literature conditions, the yields were poor and irreproducible. The role of the alkyne in these decomplexations is under investigation.
[27] A. N. Nesmeyanov, S. P. Gubin, I. B. Zlotina, S. A. Smirnova, *Izv. Akad. Nauk SSSR Ser. Khim.* **1969**, 1405.
[28] The generation of phenoxy radical on photolysis of phenol has been demonstrated. See: C.-M. Tseng, Y. T. Lee, C.-K. Ni, *J. Chem. Phys.* **2004**, *121*, 2459, and references therein.
[29] See, inter alia: a) L. E. Harrington, I. Vargas-Baca, N. Reginato, M. J. McGlinchey, *Organometallics* **2003**, *22*, 663, and references therein; b) 1,3-diferrocenylallyl cation: S. Barlow, L. M. Henling, M. W. Day, W. P. Schaefer, J. C. Green, T. Hascall, S. R. Marder, *J. Am. Chem. Soc.* **2002**, *124*, 6285, and references therein; c) tri(ferrocenyl)cyclopropenyl cation: I. Agranat, E. Aharon-Shalom, *J. Am. Chem. Soc.* **1975**, *97*, 3829.
[30] a) R. Haag, A. de Meijere in *Modern Arene Chemistry* (Ed.: D. Astruc), Wiley-VCH, Weinheim, **2002**, pp. 32–52; b) A. D. Allen, T. T. Tidwell, *Chem. Rev.* **2001**, *101*, 1333.
[31] a) M. Otto, D. Scheschkewitz, T. Kato, M. M. Midland, J. B. Lambert, G. Bertrand, *Angew. Chem.* **2002**, *114*, 2379; *Angew. Chem. Int. Ed.* **2002**, *41*, 2275; b) T. Müller, *Angew. Chem.* **2002**, *114*, 2380; *Angew. Chem. Int. Ed.* **2002**, *41*, 2276; c) J. N. Jones, A. H. Cowley, C. L. B. Macdonald, *Chem. Commun.* **2002**, 1520.
[32] H shifts may occur along the carbon frame, see: a) D. M. Brouwer, J. A. van Doorn, *Recl. Trav. Chim. Pays-Bas* **1970**, *89*, 333; and may also involve protonated ferrocene units, see: M. Bühl, S. Grigoleit, *Organometallics* **2005**, *24*, 1516, and references therein.

 © 2006 Wiley-VCH Verlag GmbH & Co. KGaA, Weinheim 

Polymerization Catalysts

DOI: 10.1002/anie.200504173

# Donor–Acceptor Metallocene Catalysts for the Production of UHMW-PE: Pushing the Selectivity for Chain Growth to Its Limits**

*K. Aleksander Ostoja Starzewski,* Bruce S. Xin, Norbert Steinhauser, Johannes Schweer, and Jordi Benet-Buchholz*

*Dedicated to Professor Hans H. Brintzinger and Professor Max Herberhold on the occasion of their 70th birthdays*

The properties of metallocenes are often described with respect to their catalysis of the polymerization of ethylene or propylene.[1,2] It is well documented that the catalytic activity of especially homogeneous zirconocene catalysts activated with methylaluminoxane (MAO) can be outstanding, with turnover numbers being reminiscent of enzymic catalysis.[2a,i] The selectivity of metallocene catalysts, discussed prominently with respect to the catalytic cycle of the polymerization of propylene with a special focus on stereo- and regioselectivity, is also exceptional.[2e] However, another important selectivity of an olefin-activating catalyst lies in its ability to choose olefin insertion, and thus C–C bond-forming chain growth, over several competing reaction paths that terminate the growth of the chain. The efficiency of this selection accounts for the differences between catalysts for isomerization, dimerization, oligomerization, and polymerization processes. The performance of the catalyst strongly depends

[*] Prof. Dr. K. A. Ostoja Starzewski
Lanxess Deutschland GmbH
Building Q18, 51369 Leverkusen (Germany)
Fax: (+49) 214-30-81836
E-mail: aleksander.ostojastarzewski@lanxess.com
Dr. B. S. Xin[+]
Bayer AG
Leverkusen (Germany)
Dr. N. Steinhauser
Lanxess Deutschland GmbH
Dormagen (Germany)
Dr. J. Schweer, Dr. J. Benet-Buchholz[++]
Bayer Industry Services GmbH & Co OHG
Leverkusen (Germany)
[+] Present address:
Mitsubishi Chemical Corp.
Yokohama (Japan)
[++] Present address:
Institut Catalan d'Investigacio Quimica
Tarragona (Spain)

[**] For previous publications on donor–acceptor metallocene polymerization catalysts, see Reference [1]. UHMW-PE = ultrahigh-molecular-weight polyethylene.

Supporting information for this article is available on the WWW under http://www.angewandte.org or from the author.


© 2006 Wiley-VCH Verlag GmbH & Co. KGaA, Weinheim

on the monomer and the reaction conditions (in particular, the polymerization temperature), and is determined by the transition metal, its ligand field,[3a] and the co-catalyst, and in heterogeneous reactions also by the supporting material.

Zirconocenes, when activated with MAO, are known to predominantly catalyze the *polymerization* of ethylene whereas many of these catalyze the *oligomerization* of propylene.[3i] In other words, chain propagation is strongly favored over chain termination with ethylene in the presence of zirconocenes.[3j] The number of uninterrupted chain-growth steps followed by one "error"—the alternative elementary steps described in Reference [3j]—defines the selectivity of the catalytic process. A single-site catalyst that makes on average one "error" in 100 catalytic cycles does not produce a high-molecular-weight polyethylene (PE). If, for example, one β-H transfer occurs after 99 ethylene insertions (99% selectivity), a low-molecular-weight PE (number-average molecular weight $M_n \approx 2.8 \times 10^3\ g\,mol^{-1}$) soft wax is formed with a polydispersity $M_w/M_n$ of approximately 2 ($M_w$ = weight-average molecular weight). On the other hand, 99.9% selectivity results in the formation of a hard wax ($M_n \approx 2.8 \times 10^4\ g\,mol^{-1}$), whereas 99.99% selectivity results in high-molecular-weight PE (e.g. one β-H transfer after 9999 ethylene insertions gives $M_n \approx 2.8 \times 10^5\ g\,mol^{-1}$). In the idealized extreme case, a catalyst selectivity of 100% would generate the scenario of a living polymerization.[4] In such a situation, no competing reactions take place. Each macromolecule remains bound to one transition-metal complex and grows as long as there are monomer molecules available. If all the catalyst molecules are structurally and conformationally identical and start and stop to polymerize precisely at the same time, the molecular weight distribution $M_w/M_n$ will have a value of 1.

Whereas polyethylenes with molecular weights on the order of $10^5\ g\,mol^{-1}$ are easily accessible with a variety of metallocene catalysts, PEs with molecular weights on the order of $10^6\ g\,mol^{-1}$ are difficult to obtain. Catalysts that display ultrahigh selectivity for chain growth (propagation) are required for the production of the so-called ultrahigh-molecular-weight polyethylenes (UHMW-PEs), which cover a molecular-weight range of approximately $10^6$–$10^7\ g\,mol^{-1}$. Such catalysts have to perform between approximately 35000 and 350000 insertions without any "errors".

A few zirconocenes have been reported to generate UHMW-PEs at ambient or lower polymerization temperatures.[5] By slowing down all possible reactions, the lowest-energy reaction path becomes strongly favored. However, elevated polymerization temperatures of 50°C or above (typically 60–90°C or even higher) are preferred for economic reasons in industrial processes. However, at higher temperatures, higher-energy reaction paths may become more accessible thus reducing the selectivity. In addition, the highly efficient co-catalyst MAO may complicate matters as it can act as a chain-transfer agent, more or less severely depending on the metallocene structure. To promote high catalyst activity as well as high degrees of polymerization, the structure of the catalyst has to be optimized to enhance the energy difference between the transition state for ethylene insertion and the other transition states on the reaction hypersurface. The search for highly active catalysts, which efficiently suppress side reactions at high temperatures, is an important but difficult task.

UHMW-PE has outstanding material properties in terms of chemical, photochemical, and biological stability and biocompatibility; it also exhibits high impact toughness and high resistance against abrasion. It is used accordingly in heavy-duty, high-durability parts and in high-end medical applications, for example, as artificial implants in hip replacements. However, drawbacks stem from a difficult processability of the material as well as material failure due to inhomogeneities in the formed parts. Substituting the currently used heterogeneous Ziegler–Natta catalyzed polymerization process[6] with a process based on well-defined metallocene catalysts could help to overcome these problems, as the latter catalytic systems can be better tailored to optimize the material and processing properties of the polymeric product.

The polymerization of ethylene in the temperature range 60–90°C has been performed with representative zirconocene catalysts in combination with MAO by us as well as by others.[7–9] A broad survey of the results obtained in polymerizations in pentane at 60°C with approximately 100 different metallocenes was presented by Alt and Köppl.[2a] PEs with molecular weights that lie well below the borderline of $10^6\ g\,mol^{-1}$ (which corresponds to a targeted intrinsic viscosity, $[\eta]$, for UHMW-PE of at least $7.9\ dL\,g^{-1}$, as measured in *o*-dichlorobenzene at 140°C) were typically obtained. Further data obtained between 70°C and 90°C are provided in Table 1 for comparison. One advanced metallocene catalyst that shows high activities and is suitable for the preparation of

***Table 1:*** Metallocene/MAO-catalyzed ethylene polymerizations.[a]

| Entry | Metallocene | Al/Zr | Solvent | $T_o$ [°C] | $T_p$ [°C] | $A$ [t $(mol_M)^{-1}\,h^{-1}$] | $[\eta]$ [$dL\,g^{-1}$] | Reference |
|---|---|---|---|---|---|---|---|---|
| 1 | $[(Cp)_2ZrCl_2]$ | 5000 | Hex | | 80 | 26 | 1.9 | [7] |
| 2 | $[(Cp)_2ZrCl_2]$ | 10000 | Tol | | 80 | 52 | 2.2 | this work |
| 3 | $[(MeCp)_2ZrCl_2]$ | 12000 | Hex | | 80 | 91 | 2.6 | [7] |
| 4 | $[(Me_5Cp)_2ZrCl_2]$ | 5000 | Hex | | 80 | 25 | 3.2 | [7] |
| 5 | *rac*-$[Me_2Si(H_4Ind)_2ZrCl_2]$ | 10000 | Tol | 80 | 90 | 75 | 3.4 | this work |
| 6 | *rac*-$[C_2H_4(H_4Ind)_2ZrCl_2]$ | 10000 | Tol | 80 | 86 | 98 | 3.3 | this work |
| 7 | *rac*-$[Me_2Si(Ind)_2ZrCl_2]$ | 10000 | Tol | 80 | 90 | 180 | 1.5 | this work |
| 8 | *rac*-$[C_2H_4(Ind)_2ZrCl_2]$ | 10000 | Tol | 80 | 88 | 195 | 1.2 | this work |
| 9 | *rac*-$[C_2H_4(Ind)_2ZrCl_2]$ | 5000 | Hex | | 80 | 81 | 1.6 | [7] |
| 10 | *rac*-$[C_2H_4(4,7\text{-}Me_2Ind)_2ZrCl_2]$ | 10000 | Hex | | 80 | 142 | 2.7 | [7] |
| 11 | $[(4,7\text{-}Me_2Ind)_2ZrCl_2]$ | 5000 | Hex | | 80 | 138 | 5.9 | [7] |
| 12 | *meso*-$[C_2H_4(4,7\text{-}Me_2Ind)_2ZrCl_2]$ | 5000 | Hex | | 70 | 37 | 13.9 | [7] |
| 13 | $[Me_2C(Flu)(Cp)ZrCl_2]$ | 10000 | Tol | 80 | 89 | 48 | 1.5 | this work |

[a] Results were obtained with unbridged and with covalently bridged *ansa*-zirconocenes. Cp = cyclopentadienyl; Ind = indenyl; Flu = fluorenyl; MAO = methylaluminoxane; $T_o$ = temperature at start of polymerization; $T_p$ = polymerization temperature; $[\eta]$ = intrinsic viscosity measured in *o*-dichlorobenzene (ODCB) at 140°C; Tol = toluene; Hex = hexane; ethylene pressure = 10 bar.

 © 2006 Wiley-VCH Verlag GmbH & Co. KGaA, Weinheim 

UHMW-PE was reported by Resconi et al.[7] The covalently bridged *meso*-ethylene-bis(4,7-dimethyl-1-indenyl)zirconium dichloride (*meso*-[EBDMIZrCl$_2$]) was reported to yield the highest-molecular-weight PE of all the zirconocenes tested so far. Under MAO activation at 70 °C it generates a molecular weight of $2\times10^6$ g mol$^{-1}$ ($[\eta]=13.9$ dL g$^{-1}$) with a high activity of 37 $t_{PE}\,(mol_{Zr})^{-1}\,h^{-1}$ (Table 1, entry 12).

Most classical unbridged zirconocenes and covalently bridged *ansa*-zirconocenes in combination with MAO are unsuitable for the production of UHMW-PE at the relevant process temperatures. The few exceptions, however, suggest that the target ultrahigh ($1–10\times10^6$ g mol$^{-1}$) molecular-weight range may be reached and, therefore, encourage the design of more advanced high-activity metallocene structures for this purpose.[7–9]

Recently, we have identified and developed a new class of metallocene polymerization catalysts, the so-called donor–acceptor metallocenes (Figure 1). These are characterized by the co-existence of donor (D) and acceptor (A) groups in complex sandwich structures, which may be D–A bridged or unbridged. Highly polar dative transannular D–A interactions in bridged states and Lewis basic and Lewis acidic functionalities in unbridged states are the resulting features. The modular D–A principle opens easy synthetic access to a broad range of novel metallocene structures, in which the well-known cyclopentadienyl (Cp), indenyl (Ind), fluorenyl (Flu), or heterocyclic ligands are now situated within a D–A metallocene environment to result in sometimes surprising catalytic features.[1] Herein, we report on simple structural variations based on the D–A metallocene lead structure that result unexpectedly in highly efficient polymerization catalysts for the synthesis of UHMW-PE.

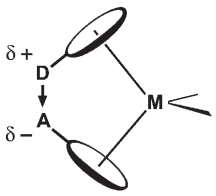



***Figure 1.*** Bridged structure of the donor–acceptor metallocenes. D = donor, A = acceptor, M = metal.

[(Cp)Me$_2$PBCl$_2$(Cp)ZrCl$_2$] (**1**) for HDPE

[(Cp)Et$_2$PB(C$_6$F$_5$)$_2$(Cp)ZrCl$_2$] (**2**) for HDPE

[(Flu)Et$_2$PB(C$_6$F$_5$)$_2$(Cp)ZrCl$_2$] (**3**) for UHMW-PE

[(Flu)Et$_2$PBPh$_2$(Cp)ZrCl$_2$] (**4**) for UHMW-PE

The simple D–A metallocene **1** is a bis(cyclopentadienyl)zirconium dichloride that carries a dimethylphosphino donor substituent on one Cp ring and a dichloroboranyl acceptor substituent on the other Cp ring. In the presence of MAO it forms a highly active and thermally robust homogeneous catalyst for ethylene polymerization, with a maximum activity of 118 $t_{HDPE}\,(mol_{Zr})^{-1}\,h^{-1}$ (HDPE = high-density PE) at approximately 105 °C.[1d] In polymerizations with the reference system [(Cp)Me$_2$PBCl$_2$(Cp)ZrCl$_2$] (**1**) at temperatures between 20 °C and 100 °C, the viscosity-average molecular weight ($M_\eta$) of the PE obtained decreases from approximately $7\times10^5$ to $1\times10^5$ g mol$^{-1}$.

The excellent catalytic properties of **1** are further improved with catalyst **2**. The [(Cp)Et$_2$PB(C$_6$F$_5$)$_2$(Cp)ZrCl$_2$]/MAO system is even more active and promotes higher molecular weights of PE (Table 2). At 72 °C and 10 bar ethylene, it produces 148 $t_{HDPE}\,(mol_{Zr})^{-1}\,h^{-1}$ with $M_\eta=3.23\times10^5$ g mol$^{-1}$. Both D–A metallocenes **1** and **2** activated with MAO are two to three times more-active than the highly active benchmark catalyst [(Cp)$_2$ZrCl$_2$] (Table 1) but are likewise unsuitable for use in the temperature range required for the production of UHMW-PE.

***Table 2:*** Metallocene/MAO-catalyzed ethylene polymerizations.[a]

| Metallocene | | $T_o$ [°C][b] | $T_p$ [°C] | $A$ [t $(mol_{Zr})^{-1}\,h^{-1}$] | $[\eta]$ [dL g$^{-1}$][c] | $M_\eta$ [g mol$^{-1}$][d] |
|---|---|---|---|---|---|---|
| [(Cp)Me$_2$PBCl$_2$(Cp)ZrCl$_2$] | **1** | 80 | 86 | 96 | 2.5 | $1.93\times10^5$ |
| | | 60 | 65 | 90 | 3.1 | $2.64\times10^5$ |
| [(Cp)Et$_2$PB(C$_6$F$_5$)$_2$(Cp)ZrCl$_2$] | **2** | 80 | 86 | 124 | 2.7 | $2.19\times10^5$ |
| | | 60 | 72 | 148 | 3.6 | $3.23\times10^5$ |
| [(Flu)Et$_2$PB(C$_6$F$_5$)$_2$(Cp)ZrCl$_2$] | **3** | 80 | 88 | 58 | 7.9 | $1.00\times10^6$ |
| | | 60 | 66 | 52 | 13.3 | $2.11\times10^6$ |
| [(Flu)Et$_2$PBPh$_2$(Cp)ZrCl$_2$] | **4** | 80 | 81 | 25 | 15.2 | $2.56\times10^6$ |
| | | 60 | 66 | 28 | 17.6 | $3.16\times10^6$ |
| | | 40 | 48 | 40 | 20.3 | $3.89\times10^6$ |

[a] Results were obtained using D–A zirconocenes in toluene; ethylene pressure = 10 bar; Al/Zr = 10000; polymerization time = 30 minutes. [b] $T_o$ = temperature at start of polymerization. [c] Intrinsic viscosity was measured in ODCB at 140 °C. [d] Calculated viscosity-average molecular weight.

Surprisingly, a simple variation of the parent structure through the exchange of the donor Cp ligand by a donor fluorenyl ligand to give [(Flu)Et$_2$PB(C$_6$F$_5$)$_2$(Cp)ZrCl$_2$] **3** (Figure 2)[10] brings about a dramatic enhancement in the selectivity in favor of chain growth versus chain-transfer and -termination reactions. Even at a polymerization temperature of 88 °C, UHMW-PE with $M_\eta=1.0\times10^6$ g mol$^{-1}$ is formed. By lowering the polymerization temperature to 66 °C, the calculated molecular weight is $2.1\times10^6$ g mol$^{-1}$ (Table 2). The donor–acceptor fluorenyl–cyclopentadienyl zirconocene **3** does not resemble the homogeneous unbridged fluorenyl zirconocene catalysts, which suffer from thermal lability (catalyst deactivation) probably as a result of ring slippage,[2a,11] nor does it resemble the isopropylidene (one carbon atom) bridged Razavi (Flu)(Cp)zirconocene[2f] in its catalytic behavior (Table 1, entry 13) or the dimethylsilylene (one silicon atom) bridged[2g] or the ethylene (two carbon atom) bridged[2a,8] (Flu)(Cp)zirconocenes. Instead, **3** is thermally robust and displays high catalytic activity (comparable to Kaminsky's complex [(Cp)$_2$ZrCl$_2$], Table 1, entry 2), and in addition shows highly advanced capabilities of attaining ultrahigh molecular weights.

The absolute molecular weights of the PE obtained with **3** must be even higher than those calculated from intrinsic viscosities, because under the experimental conditions chosen the macromolecular structure obtained is long-chain branched, as concluded from high-temperature gel permeation chromatography (HT-GPC)/viscosimetry coupling

 © 2006 Wiley-VCH Verlag GmbH & Co. KGaA, Weinheim 

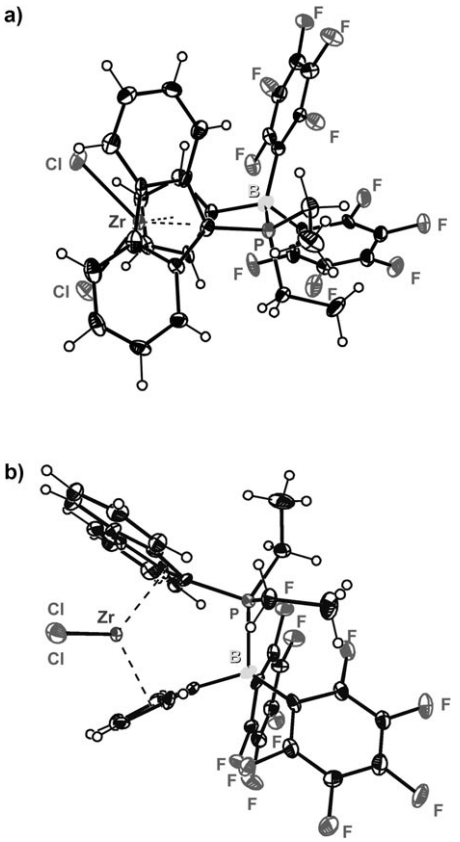



***Figure 2.*** Top (a) and side (b) views of the structure of [(Flu)$Et_2$PB-$(C_6F_5)_2$(Cp)$ZrCl_2$] (**3**) from preliminary single-crystal X-ray data.[10]

experiments, which show significant deviations from the linear $[\eta]/M$ correlation.[12] From the HT-GPC/viscosimetry coupling data in the polymerization experiment performed at 66 °C with D–A metallocene **3**, it may be estimated that the weight-average molecular weight $M_w$ is close to $11 \times 10^6\ g\,mol^{-1}$. It is thus clear that the necessary molecular-weight range for all UHMW-PE applications can be covered by using D–A metallocene catalysis. The molecular-weight distributions become broader with increasing polymerization temperature; at 20 °C $M_w/M_n = 3$, whereas $M_w/M_n = 16$ at over 100 °C. The polyethylene formed at 103 °C is still a very high-molecular-weight PE with $M_w = 8.34 \times 10^5\ g\,mol^{-1}$.

By varying the structure of the catalyst, it is possible to obtain PEs with even higher molecular weights. The selectivity of the catalyst was further improved by changing the strongly electron-withdrawing pentafluorophenyl substituents on the boron acceptor in D–A metallocene **3** to simple phenyl substituents in **4**. Table 2 shows the further enhanced intrinsic viscosities of 15.2 and $17.6\ dL\,g^{-1}$ obtained at polymerization temperatures of 81 °C and 66 °C, respectively, from which viscosity-average molecular weights of $M_\eta = 2.6 \times 10^6$ and $3.2 \times 10^6\ g\,mol^{-1}$ were calculated. Polymerization at 48 °C led to an increase in the viscosity to $20.3\ dL\,g^{-1}$, corresponding to a calculated molecular weight for the PE of $3.9 \times 10^6\ g\,mol^{-1}$. More physical studies of the polymers are necessary to obtain the absolute values for the molecular weights of the PE obtained using **4** and to quantify the degree of long-chain branching.

In summary, outstanding catalytic properties originate from the combination of fluorenyl- and cyclopentadienyl ligands within the donor–acceptor metallocene catalyst framework. This D–A metallocene subclass gives access to ultrahigh-molecular-weight polyethylenes. Mechanical properties, which depend strongly on the molecular weight, can now be tailored as a result of this near-perfectly improved controllable selectivity for chain growth.

There is evidence for long-chain-branched polyethylene architectures (LCB-PE). Long-chain branching is known to improve processability. In addition, processability can be improved by bimodal or by broadened molecular-weight distributions.[13a,b] These can be tailored by using two D–A metallocenes within the same reactor, preselected according to the molecular weights of the PE obtained with the individual catalysts at the same temperature, or by taking advantage of the temperature-dependent molecular-weight distribution obtained with **3**. With these additional tools in hand, it should be possible to overcome at least some of the drawbacks associated with the current UHMW-PEs and to tailor improved and novel types of UHMW-PE for various high-end applications.

The subclass of (Flu)(Cp) D–A metallocenes has also been applied successfully to other homo- and copolymerizations. Significant progress has been made in tailoring the molecular weight of elastomeric polypropylene (e-PP) and in the areas of ethylene-propylene (EPM) and ethylene-propylene-diene elastomers (EPDM), where metallocene-based polymers have suffered traditionally from limited molecular weights[13c,d] and thus a limited application range. These advanced D–A metallocenes have been successfully used as catalysts for the living olefin polymerization, and the results of these studies will be published in due course.

Received: November 23, 2005
Published online: February 10, 2006

**Keywords:** donor–acceptor systems · homogeneous catalysis · metallocenes · polymerization · zirconium

[1] a) K. A. Ostoja Starzewski, *Macromol. Symp.* **2004**, *213*, 47; b) K. A. Ostoja Starzewski, N. Steinhauser, PCT WO 029065, **2004**; c) K. A. Ostoja Starzewski, B. S. Xin, PCT WO 76999, **2002**, US Patent 6 657027; d) K. A. Ostoja Starzewski, W. M. Kelly, A. Stumpf, D. Freitag, *Angew. Chem.* **1999**, *111*, 2588; *Angew. Chem. Int. Ed.* **1999**, *38*, 2439.

[2] Reviews: a) H. G. Alt, A. Köppl, *Chem. Rev.* **2000**, *100*, 1205; b) N. E. Grimmer, N. J. Coville, *S. Afr. J. Chem.* **2001**, *54*, 7; c) L. Resconi, L. Cavallo, A. Fait, F. Piemontesi, *Chem. Rev.* **2000**, *100*, 1253; d) H. H. Brintzinger, D. Fischer, R. Mülhaupt, B. Rieger, R. Waymouth, *Angew. Chem.* **1995**, *107*, 1255; *Angew. Chem. Int. Ed. Engl.* **1995**, *34*, 1843; e) W. Spalek, M. Antberg, M. Aulbach, B. Bachmann, V. Dolle, S. Haftka, F. Küber, J. Rohrmann, A. Winter in *Ziegler Catalysts* (Eds.: G. Fink, R. Mülhaupt, H. H. Brintzinger), Springer, Berlin, **1995**, pp. 83 – 97; f) A. Razavi, D. Vereecke, L. Peters, K. D. Dauw, L. Nafpliotis, J. L. Atwood in *Ziegler Catalysts* (Eds.: G. Fink, R. Mülhaupt, H. H. Brintzinger), Springer, Berlin, **1995**, pp. 111 – 147; see also: g) Y. Chen, M. D. Rausch, J. C. W. Chien, *J. Organomet. Chem.* **1995**, *497*, 1; h) W. Kaminsky, K. Külper, H. H. Brintzinger, F. R. W. P. Wild, *Angew. Chem.* **1985**, *97*, 507; *Angew. Chem. Int.*

 © 2006 Wiley-VCH Verlag GmbH & Co. KGaA, Weinheim 

*Ed. Engl.* **1985**, *24*, 507; i) H. Sinn, W. Kaminsky, H. J. Vollmer, R. Woldt, *Angew. Chem.* **1980**, *92*, 396; *Angew. Chem. Int. Ed. Engl.* **1980**, *19*, 390.

[3] Nickel catalysts, for example, are well known for their preference for the dimerization, oligomerization, and isomerization of olefins.[3g,h] However, nickel catalysts can be converted into olefin polymerization catalysts by suitable ligand environments.[3a–f] Nickel ylide catalysts are known to even produce UHMW-PE.[3a,b] UHMW-PE with $M_\eta = 1.237 \times 10^6\ g\,mol^{-1}$ was synthesized using a nickel ylide catalyst at 70 °C in the absence of a co-catalyst.[3a] a) Late Transition-Metal Polymerization Catalysis: K. A. Ostoja Starzewski in *Nickel Polymerization Catalysts with Ylide Steering Ligands* (Eds.: B. Rieger, L. Baugh, S. Kacker, S. Striegler), Wiley-VCH, Weinheim, **2003**, pp. 1–26; b) K. A. Ostoja Starzewski, J. Witte, *Angew. Chem.* **1987**, *99*, 76; *Angew. Chem. Int. Ed. Engl.* **1987**, *26*, 63; for other nickel polymerization catalysts, see, for example: c) J. Kukral, A. Abele, G. Müller, B. Rieger in *Late Transition Metal Polymerization Catalysis* (Eds.: B. Rieger, L. Baugh, S. Kacker, S. Striegler), Wiley-VCH, Weinheim, **2003**, pp. 27–58; d) G. A. Luinstra, J. Queisser, B. Bildstein, H.-H. Gortz, C. Amort, M. Malaun, A. Krajete, G. Werne, M. O. Kristen, N. Huber, C. Gernert, *Late Transition Metal Polymerization Catalysis* (Eds.: B. Rieger, L. Baugh, S. Kacker, S. Striegler), Wiley-VCH, Weinheim, **2003**, pp. 59–99; e) S. D. Ittel, L. K. Johnson, M. Brookhart, *Chem. Rev.* **2000**, *100*, 1253–1345; f) C. Wang, S. Friedrich, T. R. Younkin, R. T. Li, R. H. Grubbs, D. A. Bansleben, M. W. Day, *Organometallics* **1998**, *17*, 3149; for oligomerization catalysts, see, for example: g) W. Keim, *Angew. Chem.* **1990**, *102*, 251; *Angew. Chem. Int. Ed. Engl.* **1990**, *29*, 235; h) G. Wilke, *Angew. Chem.* **1988**, *100*, 189; *Angew. Chem. Int. Ed. Engl.* **1988**, *27*, 186; i) In a simple heuristic view, a zirconocene is alkylated and ionized by MAO. The catalytic cycle starts with a zirconocenium cation as the active 14-electron species, with a Zr–Me group as the starting point of the growing chain. The electron-deficient species coordinates ethylene to form a π complex (16-electron species), which rearranges to form a four-membered metallacyclic transition state. This transition state opens the way to a migratory insertion, thereby regenerating an active metallocenium cation now with a Zr–Pr group as the grown chain. The multifold repetition of this sequence of elementary steps leads to the PE macromolecule; j) Important alternative reactions stop the chain growth, while the activity of the catalyst is retained: 1) β-H transfer to the active metal center (also called β-H elimination), 2) β-H transfer to the monomer, and 3) chain transfer to aluminum (i.e. to the co-catalyst). The activity-retaining reaction paths 1–3 (above), which hinder the increased molecular weight of the products, lead to terminated chains with vinyl end-groups and either a) active Zr–H moieties (by β-H transfer to the metal), b) active Zr–Et moieties (by β-H transfer to the monomer), or c) the active Zr–Me species and PE macromolecules attached to Al (by chain transfer to MAO and simultaneous methyl transfer from MAO to Zr). There are other side reactions that deactivate the catalyst.

[4] For a review on living olefin polymerizations, see: a) G. W. Coates, P. D. Hustad, S. Reinartz, *Angew. Chem.* **2002**, *114*, 2340; *Angew. Chem. Int. Ed.* **2002**, *41*, 2236.

[5] a) Review: W. Kaminsky, *Macromol. Chem. Phys.* **1996**, *197*, 3907, and Table 1 therein; b) W. Kaminsky, R. Engehausen, K. Zoumis, W. Spalek, J. Rohrmann, *Macromol. Chem.* **1992**, *193*, 1643; c) F. Zhang, Y. Mu, J. Wang, Z. Shi, W. Bu, S. Hu, Y. Zhang, S. Feng, *Polyhedron* **2000**, *19*, 1941; d) B. Liang, Y. Li, G. Xie, *Macromol. Rapid Commun.* **1996**, *17*, 193; a divalent samarocene also was reported to produce UHMW-PE at room temperature with very low activity; see: e) H. Yasuda, E. Ihara, M. Morimoto, M. Nodono, S. Yoshioka, M. Furo, *Macromol. Symp.* **1995**, *95*, 203; non-metallocene bis(phenoxyimine)zirconium catalysts also have been used to prepare UHMW-PE at 25 °C; see: f) H. Makio, N. Kashiwa, T. Fujita, *Adv. Synth. Catal.* **2002**, *344*, 477.

[6] M. Velikova, *Eur. Polym. J.* **2001**, *37*, 1255.

[7] L. Resconi, U. Giannini, T. Dall'Occo in *Metallocene-Based Polyolefins* (Eds.: J. Scheirs, W. Kaminsky), Wiley, New York, **2000**, pp. 69–101. Even higher molecular weights but lower catalyst activities were obtained at lower temperatures and with different co-catalysts, which presumably hinder chain transfer to aluminum.

[8] The database[2a] covers unbridged as well as one-, two-, and three-atom covalently bridged structures with simple as well as with substituted cyclopentadienyl, indenyl, and fluorenyl ligands. A heterogeneous silica-supported unbridged fluorenyl zirconocene, $(Flu)_2ZrCl_2/MAO/SiO_2$, yielded at 60 °C a PE with a molecular weight of $1 \times 10^6\ g\,mol^{-1}$. A homogeneous $C_2$-bridged $(Flu)_2HfCl_2$/MAO catalyst system with a hexenyl-substituted ethylene bridge yielded a PE with a molecular weight of $1.6 \times 10^6\ g\,mol^{-1}$ at 58 °C, with a catalyst activity of 3 $t_{PE}\,(mol_{Hf})^{-1}\,h^{-1}$: H. G. Alt, M. Jung, *J. Organomet. Chem.* **1999**, *580*, 1.

[9] Homogeneous zirconocene catalysts such as *ansa*-(3-Me-Ind)(Cp)$ZrCl_2$/MAO and *ansa*-(3-Et-Ind)(Cp)$ZrCl_2$/MAO, in which a one-carbon-atom bridge is part of a methyl-phenyl-substituted pentalene structure, yield at 75 °C PEs with molecular weights of $1.5 \times 10^6$ and $1.2 \times 10^6\ g\,mol^{-1}$ with low catalyst activities of 3 and 4 $t_{PE}\,(mol_{Zr})^{-1}\,h^{-1}$, respectively: W. Kaminsky, F. Müller, O. Sperber, *Macromol. Mater. Eng.* **2005**, *290*, 347.

[10] K. A. Ostoja Starzewski, J. Benet-Buchholz, unpublished results.

[11] a) H. G. Alt, private communication; b) H. G. Alt, E. Samuel, *Chem. Soc. Rev.* **1998**, *27*, 323; c) M. A. Schmid, H. G. Alt, W. Milius, *J. Organomet. Chem.* **1997**, *541*, 3; d) M. A. Schmid, H. G. Alt, W. Milius, *J. Organomet. Chem.* **1996**, *525*, 15; e) M. A. Schmid, H. G. Alt, W. Milius, *J. Organomet. Chem.* **1996**, *525*, 9; f) M. A. Schmid, H. G. Alt, W. Milius, *J. Organomet. Chem.* **1995**, *501*, 101.

[12] M. Hoffmann, H. Krömer, R. Kuhn in *Polymeranalytik, Vol. 1*, Georg Thieme, Stuttgart, **1977**, p. 324.

[13] a) Rheology and Processing of Metallocene-Based Polymers: *Metallocene-Based Polyolefins, Vol. 2* (Eds.: J. Scheirs, W. Kaminsky), Wiley, New York, **2000**, pp. 378–459; see also: b) H. Knuuttila, A. Lehtinen, H. Salminen in *Metallocene-Based Polyolefins, Vol. 2* (Eds.: J. Scheirs, W. Kaminsky), Wiley, New York, **2000**, pp. 365–378; c) M. Galimberti, F. Piemontesi, O. Fusco in *Metallocene-Based Polyolefins, Vol. 1* (Eds.: J. Scheirs, W. Kaminsky), Wiley, New York, **2000**, pp. 309–343; d) A. Tynys, T. Saarinen, K. Hakala, T. Helaja, T. Vanne, P. Lehmus, B. Löfgren, *Macromol. Chem. Phys.* **2005**, *206*, 1043.

 © 2006 Wiley-VCH Verlag GmbH & Co. KGaA, Weinheim 

Microporous Polymers

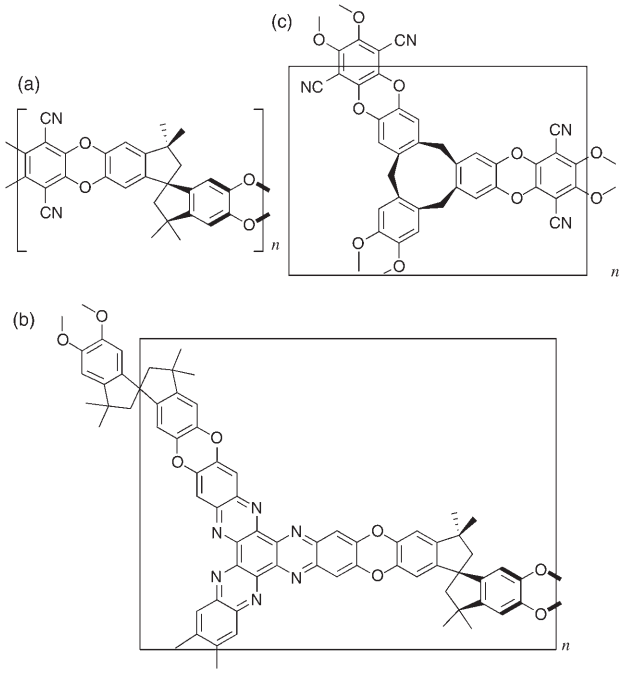
DOI: 10.1002/anie.200504241

# Towards Polymer-Based Hydrogen Storage Materials: Engineering Ultramicroporous Cavities within Polymers of Intrinsic Microporosity**

*Neil B. McKeown,* Bader Gahnem, Kadhum J. Msayib, Peter M. Budd,* Carin E. Tattershall, Khalid Mahmood, Siren Tan, David Book, Henrietta W. Langmi, and Allan Walton*

A major technical obstacle to the widespread use of hydrogen ($H_2$) as a nonpolluting fuel for cars is the lack of a safe and efficient system for on-board storage.[1] Of the many potential solutions being investigated,[2] an attractive possibility is a system based on the reversible adsorption of $H_2$ on the internal surface of a microporous material such as a zeolite,[3] carbon,[4] or metal-organic framework (MOF).[5,6] At present, the quantity of $H_2$ that can be adsorbed onto any type of microporous material falls below the requirements of a practical $H_2$ storage system. Hence, there is an urgency to develop materials which can be tailored to provide a structure[7,8] and chemical composition[9] suitable for the specific demands of $H_2$ physisorption.

Previously, organic polymers have not been considered as materials for the storage of hydrogen because polymers generally have enough conformational and rotational freedom to pack space efficiently and thus do not offer high surface areas. However, the recently reported polymers of intrinsic microporosity (PIMs) are composed wholly of fused-ring subunits designed to provide highly rigid and contorted macromolecular structures that pack space inefficiently. Hence they form solids with large amounts of interconnected free volume, providing accessible internal surface areas in the range 500–900 $m^2 g^{-1}$.[10,11] PIMs are prepared by using a benzodioxane formation reaction between suitable monomers, one of which must contain a site of contortion such as a spiro-center or a rigid nonplanar unit. A PIM can be prepared either as an insoluble network or as a soluble polymer, suitable for solution-based processing, depending upon the number of catechol and aromatic *ortho*-dihalide groups possessed by the monomers. For example, a soluble PIM (PIM-1) is prepared from the reaction between 5,5′,6,6′-tetrahydroxy-3,3,3′,3′-tetramethyl-1,1′-spirobisindane and tetrafluoroterephthalonitrile, whereas, a network-PIM (HATN-network-PIM) is formed from the reaction between the same readily available spiro-cyclic bis(catechol) monomer and hexachlorohexaazatrinaphthylene (Scheme 1).[11,12] PIM-1




***Scheme 1.*** Structure of the PIMs used in this study: a) PIM-1, b) HATN-network-PIM, and c) CTC-network-PIM.

can be cast from solution to form robust microporous self-standing films that show excellent promise for gas[13] and solution phase membrane separations.[11] The HATN-network-PIM has in-built ligands for metal complexation and the $Pd^{II}$-loaded material is proving an excellent heterogeneous catalyst for Suzuki aryl–aryl coupling reactions.[12]

In the context of hydrogen adsorption, we believe that PIMs may offer an attractive combination of properties including low intrinsic density (they are composed of only light elements—C, H, N, O—a real advantage over MOF materials),[14] chemical homogeneity (an advantage over carbons), thermal and chemical stability, and synthetic reproducibility. Of particular interest is the potential to tailor the micropore structure by choice of monomer precursors, for example, by the use of monomers that contain pre-formed cavities to provide sites of an appropriately small size for hydrogen adsorption. To investigate this possibility, the bowl-shaped receptor monomer, cyclotricatechylene (CTC),[15] was incorporated within a network-PIM by using

[*] Prof. N. B. McKeown, Dr. B. Gahnem, Dr. K. J. Msayib
School of Chemistry
Cardiff University
Cardiff, CF10 3AT (UK)
Fax: (+44) 29-2087-4030
E-mail: mckeownnb@cardiff.ac.uk
Dr. P. M. Budd, Dr. C. E. Tattershall, Dr. K. Mahmood, S. Tan
Organic Materials Innovation Centre
School of Chemistry
University of Manchester
Manchester, M13 9PL (UK)
Fax: (+44) 161-275-4273
E-mail: peter.budd@manchester.ac.uk
Dr. D. Book, Dr. H. W. Langmi, Dr. A. Walton
Department of Metallurgy and Materials
School of Engineering
University of Birmingham
Birmingham, B15 2TT (UK)

[**] We thank the EPSRC and the Higher Education Commission of Pakistan (K.M.) for funding.


InterScience
© 2006 Wiley-VCH Verlag GmbH & Co. KGaA, Weinheim

the benzodioxane-forming reaction between CTC and tetrafluoroterephthalonitrile. The gas-adsorption properties of the resulting material, designated CTC-network-PIM (Scheme 1), were compared to those of the previously prepared PIM-1 and HATN-network-PIM. For each material used in the study, the structure was confirmed by elemental analysis, IR spectroscopy, and, in the case of PIM-1, solution $^{1}H$ and $^{13}C$ NMR spectroscopy. The weight-average molar mass of the PIM-1 sample was estimated as 230 000 g mol$^{-1}$ by using gel permeation chromatography as calibrated against polystyrene standards.

The BET surface area of each PIM is in the region of 800 m$^2$ g$^{-1}$ (Table 1) as measured by nitrogen adsorption at 77 K (Figure 1 a). Analysis of the low-pressure nitrogen adsorption data by the Horvath–Kawazoe method[16] indicates that in each case the pore size distribution is strongly biased towards pores in the range 0.6–0.7 nm (Figure 1 b)—that is, they are predominantly ultramicroporous.[17] The particularly marked concentration of micropores of 0.6 nm diameter for the CTC-network-PIM appears related to the internal dimensions of the bowl-shaped CTC subunit and suggests that pore size distribution within PIMs can be tuned by the choice of monomer precursor.

***Table 1:*** Gas adsorption data for the PIMs.

| PIM | BET area [m$^2$ g$^{-1}$][a] | % mass $H_2$ (1 bar, 77 K)[b] | % mass $H_2$ (10 bar, 77 K)[c] | $H_2$ per fused ring[c] |
|---|---|---|---|---|
| PIM-1 | 760 | 1.04 | 1.44 | 0.5 |
| HATN | 820 | 1.37 | 1.56 | 0.43 |
| CTC | 830 | 1.43 | 1.70 | 0.56 |

[a] From volumetric $N_2$ isotherm. [b] From volumetric $H_2$ isotherm. [c] From gravimetric $H_2$ isotherm.

The measurement of $H_2$ sorption is technically demanding and can be prone to errors.[18] The classical volumetric method can give false high values due to $H_2$ leaks, whereas gravimetric analysis may exaggerate $H_2$ adsorption greatly due to contamination with molecules of greater mass (e.g. $H_2O$). Hence, complementary sorption isotherms for each of the PIMs were obtained for ultrapure, dry $H_2$ at 77 K by using both gravimetric analysis (Hiden IGA-1), over the pressure range 0 to 20 bar, and volumetric analysis (Micromeritics ASAP 2020), over the range 0 to 1 bar. For the gravimetric analysis, the buoyancy correction required to take into account the mass of hydrogen displaced by the sample at a given pressure was calculated using a density of 1.4 g mL$^{-1}$, which was based upon helium pyconometry measurements. For both methods of analysis, consistent results were obtained as shown in Figure 2 and listed in Table 1. In addition, for both types of measurement the adsorption is rapid and completely reversible, which is consistent behavior with that expected for the physisorption of $H_2$ on a microporous material. The isotherms show that the three PIMs each adsorb significant quantities of $H_2$ (maximum 1.4–1.7 % by mass) at relatively low pressures with saturation being reached at less than 10 bar

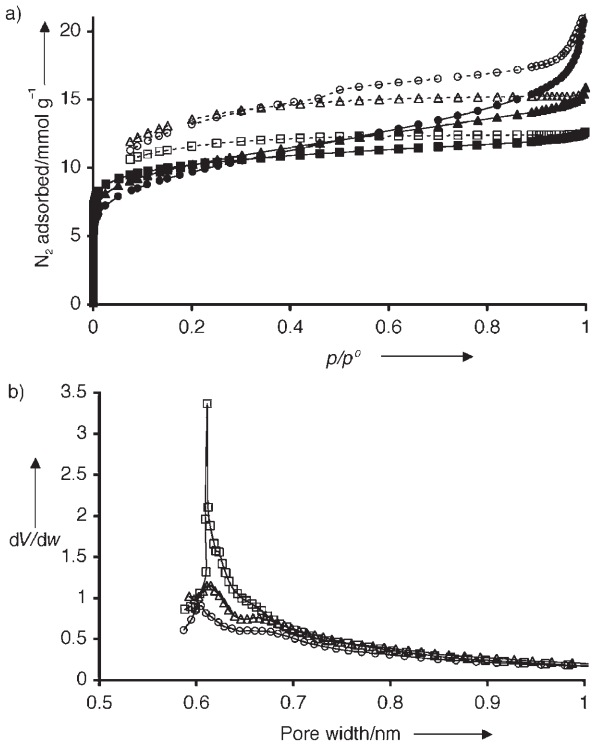



***Figure 1.*** a) Nitrogen adsorption (filled symbols) and desorption isotherms (open symbols) at 77 K; b) apparent micropore size distributions (d$V$/d$w$; the unit is mL g$^{-1}$ nm$^{-1}$) calculated by the Horvath–Kawazoe method (carbon slit-pore model) for PIM-1 (○), HATN-network-PIM (△), and CTC-network-PIM (□).

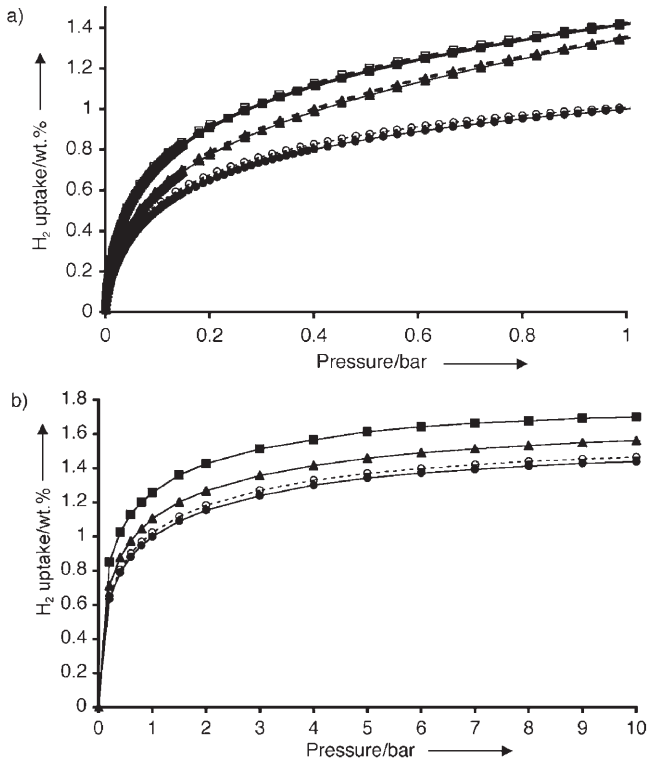



***Figure 2.*** The $H_2$ adsorption (filled symbols) and desorption isotherms (open symbols) at 77 K for PIM-1 (○), HATN-network-PIM (△) and CTC-network PIM (□), obtained using a) volumetric and b) gravimetric analysis.

 © 2006 Wiley-VCH Verlag GmbH & Co. KGaA, Weinheim 

pressure and with most of the adsorption taking place below 1 bar.

It is of interest that the order of PIMs based on the efficiency of $H_2$ uptake at 77 K and 1 bar is: CTC-network > HATN-network > PIM-1, which is the reverse of that for nitrogen adsorption under the same conditions (Figure 1 a). Calculations show that the maximum number of hydrogen molecules adsorbed per fused-ring of the polymeric repeat unit (Scheme 1) is approximately 0.5 $H_2$ per ring. However, the spread of values from 0.43 (HATN-network), 0.5 (PIM-1) to 0.56 (CTC-network) suggests that the greater predominance of ultramicropores, resulting from the bowl-shaped CTC subunit, enhances $H_2$ adsorption.

The results show that these PIMs adsorb comparable amounts of $H_2$ to that of the best examples of zeolites[3] and MOFs[5,19] and, although their performance falls short of some very high surface area carbons, they adsorb similar quantities of $H_2$ to carbons of similar surface area.[4,7] However, to attain practical hydrogen storage materials from PIMs, it will be necessary to engineer examples with larger accessible surface areas ($>2000\ m^2g^{-1}$) whilst maintaining a predominately ultramicroporous structure to retain the beneficial multi-wall interactions with $H_2$ molecules. This is a similar goal to that of many researchers investigating nanoporous carbons[7] and MOFs.[8] For PIMs, microporosity results from the association of the macromolecules during precipitation from solvent. Therefore, control over the resulting pore structure will be achieved by the design of the macromolecular structure by choice of appropriate monomer precursors; for example, by the addition of larger substituents to frustrate polymer chain packing further, by the optimization of the distance between the sites of contortion (e.g. spiro-centers) or by the use of monomers with predefined cavities as illustrated by the CTC-network-PIM. In addition, unlike all other types of microporous materials, the structures of PIMs are not necessarily constrained by a fixed network structure and may be dissolved in suitable solvents and swollen by suitable non-solvents. This will allow established methods of polymer structural manipulation to be applied to help optimize $H_2$ adsorption; for example, the rapid removal of solvent from a swollen PIM could generate additional free volume and thus provide greater accessible surface area.[20] With many synthetic and processing aspects to explore, we believe that the optimization of PIMs for $H_2$ adsorption presents additional opportunities towards achieving the US Department of Energy's ambitious 2010 target of a practical storage system that holds 6.0 % $H_2$ by mass.[21]

## Experimental Section

The preparations of PIM-1[11] and HATN-network-PIM[12] were as previously described.

CTC-network-PIM: To a stirred solution of tetrafluoroterephthalonitrile (0.47 g, 2.349 mmol) and cyclotricatechylene (0.574 g, 1.566 mmol) in dry DMF (50 mL) was added finely ground anhydrous potassium carbonate (2.6 g, 18.84 mmol). The reaction mixture was then heated at 120 °C for 12 h under nitrogen. On cooling, the reaction mixture was added to 300 mL of stirred distilled water and the solid product collected by filtration and washed with water and MeOH. Purification was achieved by refluxing the product with MeOH, acetone, and THF. The yellow network polymer was then ground and dried in a vacuum oven at 120 °C (0.8 g, 93 % yield). IR (KBr $cm^{-1}$): $\nu = 3060$, 3010, 2956, 2870 (C-H), 2235 (CN), 1610 (C-$C_{Ar}$), 1170, 1250 $cm^{-1}$ (C-O). Elemental analysis (%) found: C 61.64, H 3.78, N 7.29, F 0.91 %; ideal polymer structure $C_{33}H_{12}N_3O_6$ requires C 72.53, H 2.21, N 7.69, F 0.00 %). TGA shows loss of approximately 5 % water below 100 °C with significant ash residue obtained during combustion analysis. Surface area (BET) = 830 $m^2g^{-1}$.

Gas adsorption studies**:** Volumetric $N_2$ and $H_2$ sorption studies were undertaken using a Micromeritics Instrument Corporation (Norcross, Georgia) Accelerated Surface Area and Porosimetry (ASAP) 2020 system. Before sorption analysis, the sample was subjected to the degas vacuum system under ultra high vacuum ($10^{-9}$ bar) at a temperature of 120 °C overnight. The sample was backfilled with nitrogen and transferred to the analysis system. The sample was then again degassed under ultrahigh vacuum ($10^{-9}$ bar) at a temperature of 100 °C for a period of at least 6 h, and kept at ultra high vacuum until analysis. Sorption analysis was carried out at liquid-nitrogen temperature (77 K). Helium was used for the freespace determination, after sorption analysis, both at ambient temperature and at 77 K. Apparent surface areas were calculated from $N_2$ adsorption data by multi-point BET analysis. Apparent micropore distributions were calculated from $N_2$ adsorption data by the Horvath–Kawazoe method, assuming a slit-pore geometry and the original H–K carbon–graphite interaction potential. Similar results are obtained using cylinder pore geometry with a Ross–Olivier carbon–graphite interaction potential.

Gravimetric $H_2$ sorption studies were undertaken by using a Hiden Isochema (Warrington, England) Intelligent Gravimetric Analyser (IGA), which incorporates a microbalance capable of measuring weights with a resolution of $\pm 0.2$ μg, and can operate over a pressure range from ultrahigh vacuum to 20 bar. Before sorption analysis, the sample was degassed under ultrahigh vacuum ($10^{-9}$ bar) at a temperature of 120 °C for a period of at least 6 h. Sorption and desorption analysis was carried out at liquid nitrogen temperature (77 K). Measured masses were corrected for buoyancy. The density values for buoyancy corrections (ca. 1.4 $gmL^{-1}$) was obtained by helium pycnometry in the IGA.

Received: November 29, 2005
Published online: February 10, 2006

**Keywords:** hydrogen storage · microporous materials · nanostructures · polymers

[1] R. F. Service, *Science* **2004**, *305*, 958 – 961.
[2] L. Schlapbach, A. Zuttel, *Nature* **2001**, *414*, 353 – 358.
[3] a) A. Zecchina, S. Bordiga, J. G. Vitillo, G. Ricchiardi, C. Lamberti, G. Spoto, M. Bjorgen, K. P. Lillerud, *J. Am. Chem. Soc.* **2005**, *127*, 6361 – 6366; b) C. O. Arean, M. R. Delgado, G. T. Palomino, M. T. Rubio, N. M. Tsyganenko, A. A. Tsyganenko, E. Garrone, *Microporous Mesoporous Mater.* **2005**, *80*, 247 – 252; c) H. W. Langmi, A. Walton, M. M. Al-Mamouri, S. R. Johnson, D. Book, J. D. Speight, P. P. Edwards, I. Gameson, P. A. Anderson, I. R. Harris, *J. Alloys Compd.* **2003**, *356–357*, 710 – 715.
[4] a) M. G. Nijkamp, J. Raaymakers, A. J. van Dillen, K. P. de Jong, *Appl. Phys. A* **2001**, *72*, 619 – 623; b) H. G. Schimmel, G. J. Kearley, M. G. Nijkamp, C. T. Visserl, K. P. de Jong, F. M. Mulder, *Chem. Eur. J.* **2003**, *9*, 4764 – 4770; c) B. Panella, M. Hirscher, S. Roth, *Carbon* **2005**, *43*, 2209 – 2214.
[5] J. L. C. Rowsell, A. R. Millward, K. S. Park, O. M. Yaghi, *J. Am. Chem. Soc.* **2004**, *126*, 5666 – 5667.
[6] a) N. L. Rosi, J. Eckert, M. Eddaoudi, D. T. Vodak, J. Kim, M. O'Keeffe, O. M. Yaghi, *Science* **2003**, *300*, 1127 – 1129; b) B. Panella, M. Hirscher, *Adv. Mater.* **2005**, *17*, 538 – 541.

 © 2006 Wiley-VCH Verlag GmbH & Co. KGaA, Weinheim 

[7] Y. Gogotsi, R. K. Dash, G. Yushin, T. Yildirim, G. Laudisio, J. E. Fischer, *J. Am. Chem. Soc.* **2005**, *127*, 16006 – 16007.
[8] H. Chun, D. N. Dybtsev, H. Kim, K. Kim, *Chem. Eur. J.* **2005**, *11*, 3521 – 3529.
[9] O. Hubner, A. Gloss, M. Fichtner, W. Klopper, *J. Phys. Chem. A* **2004**, *108*, 3019 – 3023.
[10] a) P. M. Budd, B. S. Ghanem, S. Makhseed, N. B. McKeown, K. Msayib, C. E. Tattershall, *Chem. Commun.* **2004**, 230 – 231; b) P. M. Budd, N. B. McKeown, D. Fritsch, *J. Mater. Chem.* **2005**, *15*, 1977 – 1986; c) N. B. McKeown, P. M. Budd, K. J. Msayib, B. S. Ghanem, H. J. Kingston, C. E. Tattershall, S. Makhseed, K. J. Reynolds, D. Fritsch, *Chem. Eur. J.* **2005**, *11*, 2610 – 2620; d) N. B. McKeown, S. Hanif, K. Msayib, C. E. Tattershall, P. M. Budd, *Chem. Commun.* **2002**, 2782 – 2783; e) N. B. McKeown, S. Makhseed, P. M. Budd, *Chem. Commun.* **2002**, 2780 – 2781.
[11] P. M. Budd, E. S. Elabas, B. S. Ghanem, S. Makhseed, N. B. McKeown, K. Msayib, C. E. Tattershall, D. Wang, *Adv. Mater.* **2004**, *16*, 456 – 459.
[12] P. M. Budd, B. Ghanem, K. Msayib, N. B. McKeown, C. Tattershall, *J. Mater. Chem.* **2003**, *13*, 2721 – 2726.
[13] P. M. Budd, K. J. Msayib, C. E. Tattershall, B. S. Ghanem, K. J. Reynolds, N. B. McKeown, D. Fritsch, *J. Membr. Sci.* **2005**, *251*, 263 – 269.
[14] It is notable that one of the pioneering groups in the MOF area has recently reported ordered "covalent organic frameworks" (COFs) with the aim of enhancing gravimetric hydrogen capacity, see A. P. Coté, A. I. Benin, N. W. Ockwig, M. O'Keeffe, A. J. Matzger, O. M. Yaghi, *Science* **2005**, *310*, 1166 – 1170.
[15] A. S. Lindsay, *J. Chem. Soc.* **1965**, 1685 – 1692.
[16] G. Horvath, K. Kawazoe, *J. Chem. Eng. Jpn.* **1983**, *16*, 470 – 475.
[17] By IUPAC definition, pores of dimensions less than 2 nm are micropores (see D. H. Everett, *Pure Appl. Chem.* **1972**, *44*, 577 – 638), however, micropores are increasing subdivided into ultramicropores (less than 0.7 nm) and supermicropores 0.7–2.0 nm (see J. Rouquerol, F. Rouquerol, K. S. W. Sing, *Adsorption by Powders and Porous Solids*, Academic Press, London, **1999**).
[18] A. Anson, M. Benham, J. Jagiello, M. A. Callejas, A. M. Benito, W. K. Maser, A. Zuttel, P. Sudan, M. T. Martinez, *Nanotechnology* **2004**, *15*, 1503 – 1508.
[19] a) K. W. Chapman, P. D. Southon, C. L. Weeks, C. J. Kepert, *Chem. Commun.* **2005**, 3322 – 3324; b) B. L. Chen, N. W. Ockwig, A. R. Millward, D. S. Contreras, O. M. Yaghi, *Angew. Chem.* **2005**, *117*, 4823 – 4827; *Angew. Chem. Int. Ed.* **2005**, *44*, 4745 – 4749; c) M. Dinca, J. R. Long, *J. Am. Chem. Soc.* **2005**, *127*, 9376 – 9377; d) L. Pan, M. B. Sander, X. Y. Huang, J. Li, M. Smith, E. Bittner, B. Bockrath, J. K. Johnson, *J. Am. Chem. Soc.* **2004**, *126*, 1308 – 1309.
[20] Y. Tsujita, *Prog. Polym. Sci.* **2003**, *28*, 1377 – 1401.
[21] *Basic Research Needs for the Hydrogen Economy*, Office of Basic Energy Sciences, US Department of Energy, **2004**.

 © 2006 Wiley-VCH Verlag GmbH & Co. KGaA, Weinheim 

Colorimetric Sensors

DOI: 10.1002/anie.200504277

# Colorimetric Screening of DNA-Binding Molecules with Gold Nanoparticle Probes**

*Min Su Han, Abigail K. R. Lytton-Jean, Byung-Keun Oh, Jungseok Heo, and Chad A. Mirkin**

Combinatorial chemistry is a powerful tool that enables scientists to synthesize many compounds within a short time period.[1] This ability to synthesize large libraries of compounds has enabled the development of many potential anticancer drugs.[2] However, one of the bottlenecks in drug discovery is the selection of drug candidates from the many compounds within these libraries.[3] To overcome this problem, high-throughput screening methods are used to screen large libraries of potential drug candidates for biological activity.[4] Many anticancer drugs, such as doxorubicine, daunorubicin, and amsacrine, are known to interact reversibly with DNA to form a drug/DNA complex.[5] Generally, the strength of binding between the anticancer drug and DNA correlates with the biological activity of the drug and is therefore an important piece of information in the screening process.[6] In the past, typical screening processes have included mass spectrometry, nuclear magnetic resonance (NMR) spectroscopy, light scattering, and electrochemistry.[7] Unfortunately, these methods are not applicable to high-throughput screening. Fluorescence screening compatible with high-throughput protocols have been developed only recently.[8]

Herein, we describe a colorimetric assay for determining the binding affinities between potential DNA-binding molecules and duplex DNA by using networks of Au nanoparticles interconnected with duplex DNA.[9] The colorimetric readout can be visualized with the naked eye without requiring additional instrumentation. DNA-functionalized Au nanoparticles have been used previously to detect DNA, proteins, and metal ions.[10] To the best of our knowledge, this is the first example where DNA-functionalized Au nanoparticles are used to determine relative binding affinities of molecules to duplex DNA. This capability is applicable to screening libraries for drug candidates in a high-throughput fashion. This method utilizes the aggregation-induced, red-to-blue

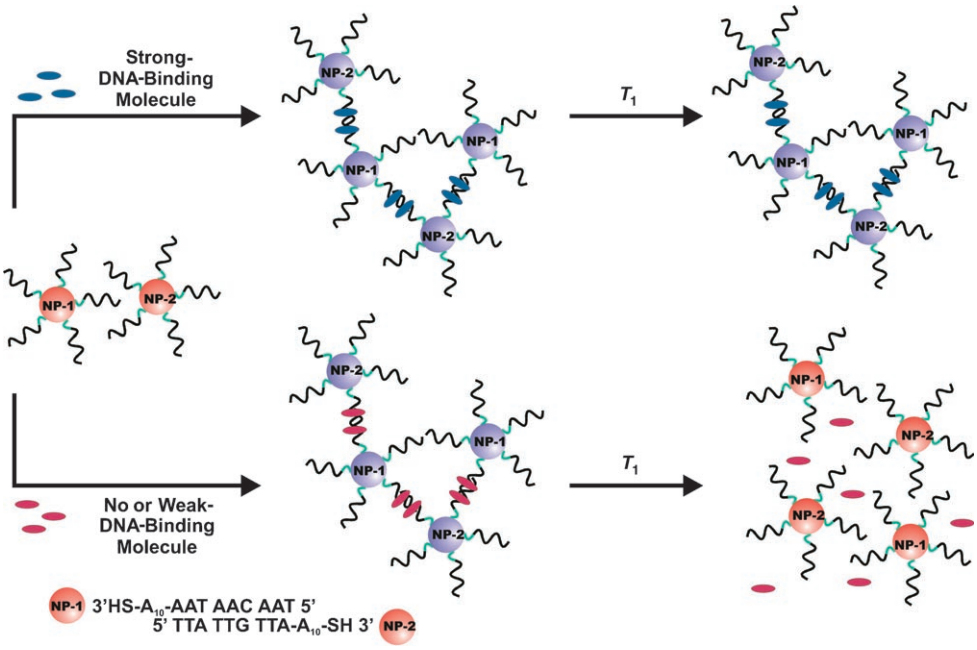
[*] M. S. Han, A. K. R. Lytton-Jean, B.-K. Oh, J. Heo, Prof. C. A. Mirkin
Department of Chemistry and
The Institute for Nanotechnology
2145 Sheridan Road, Evanston, IL, 60208-3113 (USA)
Fax: (+1) 847-467-5123
E-mail: chadnano@northwestern.edu

[**] This work was supported by the NIH through a Director's Pioneer Award to C.A.M., the NCI through a CCNE, the NSF, and the AFOSR. M.S.H. is grateful for a fellowship from the Korea Research Foundation (MOEHRD, Basic Research Promotion Fund) (Grant no. M01-2003-000-10140-0).

Supporting information for this article is available on the WWW under http://www.angewandte.org or from the author.

 © 2006 Wiley-VCH Verlag GmbH & Co. KGaA, Weinheim 

color change associated with 13-nm Au nanoparticles. Gold nanoparticles were functionalized with one of two complementary thiol-modified oligonucleotide strands and are denoted NP-1 and NP-2. When NP-1 and NP-2 are combined, they form aggregates through a reversible DNA-hybridization process. This process results in a red-to-blue color change caused by a red-shifting and dampening of the nanoparticle plasmon resonance.[9] Increasing the temperature above the melting temperature ($T_m$) of the DNA reverses the process, and the particles dissociate with a concomitant blue-to-red color change. The melting transition occurs over a very narrow temperature range with the first derivative of the transition exhibiting a full width at half maximum (fwhm) of 1–2 °C. This transition is significantly more narrow than the transition associated with a nanoparticle-free duplex of identical length and sequence (fwhm ≈ 10–12 °C)[10a] and is characteristic of nanoparticle and polymer probes heavily functionalized with oligonucleotide strands.[11] When NP-1 and NP-2 are combined in the presence of any of the known duplex DNA-binding molecules in Table 1, duplexes form between the Au nanoparticles that




***Scheme 1.*** Schematic representation of the structural and color change of nanoparticle/DNA-binding-molecule assemblies at a specific temperature ($T_1$).

***Table 1:*** Melting temperatures ($T_m$) of nanoassemblies and duplex DNA in the presence of DNA-binding molecules.

| Compound | $T_m$[a] [°C] | $T_m$[b] [°C] |
|---|---|---|
| no DNA binder | 26.4 | 19.1 |
| DAPI | 50.4 | 27.8 |
| DNR | 38.4 | 25.4 |
| EB | 37.8 | 21.8 |
| EIPT | 29.2 | 20.5 |
| AMSA | 27.2 | 19.5 |
| AQ2A | 28.5 | 19.4 |
| 9-AA | 30.9 | 19.3 |

[a] Conditions: NP-1 and NP-2 (each 1.5 nM) in sodium phosphate buffer (10 mM; pH 7.0) containing sodium chloride (100 mM). [b] Conditions: DNA-1 and DNA-2 (each 2.0 μM) in sodium phosphate buffer (10 mM; pH 7.0) containing sodium chloride (300 mM).

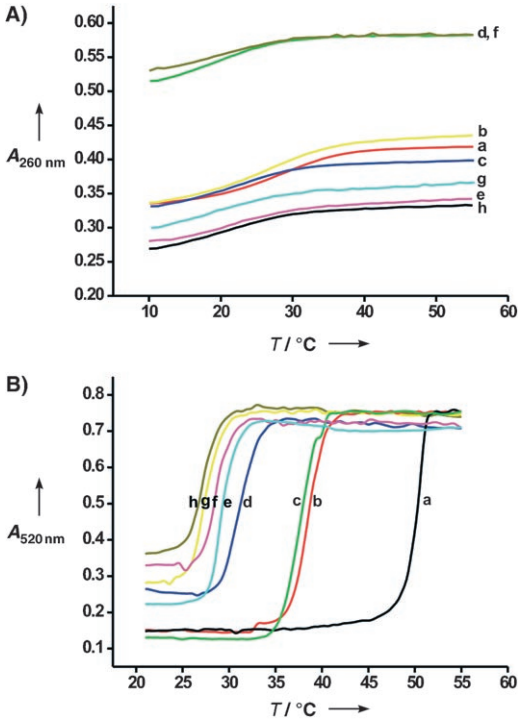



***Figure 1.*** Melting curves of A) DNA-1 and DNA-2 (no nanoparticles) and B) NP-1 and NP-2 assemblies in the absence (h) and presence of DNA-binding molecules DAPI (a), DNR (b), EB (c), 9-AA (d), EIPT (e), AQ2A (f), and AMSA (g).

are more stable than those in the absence of the DNA-binding molecules (Scheme 1). This increased stability is reflected by an increase in the melting temperature. Note that the shape and width of the transition is almost independent of the DNA-binding molecule (Figure 1). Therefore, by monitoring the blue-to-red color transition of hybridized oligonucleotide-modified Au nanoparticles in the presence of different compounds, we can determine the relative binding strength of DNA-binding molecules with the naked eye. It is assumed that any effect on DNA-binding affinity caused by increased temperature will be similar for all DNA-binding molecules because of the similar DNA-binding interactions (π–π stack-

 © 2006 Wiley-VCH Verlag GmbH & Co. KGaA, Weinheim 

ing, electrostatic, and hydrogen bonding) between DNA binders and duplex DNA.

The assay is initiated by mixing NP-1 and NP-2 (each at 1.5 nM) in a 1:1 molar ratio in 10 mM phosphate-buffered saline (PBS) buffer (0.1M NaCl; pH 7.0). The melting temperatures of the nanoassemblies (NP-1 and NP-2) were then determined in the presence of 4′,6-diamidino-2-phenylindole (DAPI), ellipticine (EIPT), amsacrine (AMSA), daunorubicin (DNR), anthraquinone-2-carboxylic acid (AQ2 A), ethidium bromide (EB), and 9-aminoacridine (9-AA) (5 μM), respectively. UV/Vis melting profiles were measured by monitoring the absorbance at 520 nm with increasing temperature (scan rate 0.5 °C $min^{-1}$). The melting temperatures were determined by taking the maxima of the first derivative of the melting curves. Control experiments were run by determining the melting temperatures of unmodified duplex DNA at 260 nm (DNA-1: 5′-TAACAATAA-3′, DNA-2: 5′-TTATTGTTA-3′) in the presence of all seven DNA-binding molecules (Table 1).

The strength of binding between anticancer drugs and DNA generally correlates with the biological activity of the drug [6] and is reflected in an increased melting temperature for the DNA.[12] Therefore, we can screen for the relative binding affinities of molecules for a particular DNA sequence that links the nanoparticle assembly by monitoring the color change as a function of temperature with all other conditions kept constant. The trends in the melting temperatures of the nanoparticles and the unmodified control duplex (with and without DNA-binding molecules) are similar (Table 1 and Figure 1). The addition of a known binder results in an enhanced $T_m$ value. The $T_m$ values depend on many factors, including salt concentration, DNA concentration, and binding affinity of the particle for complementary DNA. Indeed, in this regard, the nanoparticle assemblies provide several substantial advantages over direct detection of DNA binding by UV/Vis spectroscopy. The melting transition for the DNA-interlinked assemblies occurs over a very narrow temperature range compared to the broad melting transitions of nanoparticle-free duplex DNA (Figure 1 A). This allows a more precise analysis of the change in melting temperature of the nanoparticle assemblies (Figure 1 B). Furthermore, the presence of the DNA-binding molecule induces a more substantial temperature increase in the nanoparticle system relative to the nanoparticle-free duplex system (Table 1), which allows us to identify and differentiate between weak-, intermediate-, and strong-DNA-binding molecules more easily. For example, the $T_m$ value monitored by UV/Vis spectroscopy is 19.1 °C for duplex DNA without DAPI and 27.8 °C in the presence of DAPI ($\Delta = 8.7$ °C). However, the $T_m$ value of the same sequences attached to nanoparticle assemblies shifts from 26.4 to 50.4 °C ($\Delta = 24$ °C) upon introduction of DAPI. The dramatic increase in the melting temperature of the nanoparticle aggregates in the presence of DNA-binding molecules is due, in part, to an extremely high ratio of DNA-binding molecules to nanoparticle DNA (Figure 1 B, ratio = 33:1) relative to the nanoparticle-free case (Figure 1 A, ratio = 5:2). Such a high ratio is possible because the nanoparticles absorb light much more strongly (at 260 and 520 nm) than the DNA, which allows us to work at very low concentrations of nanoparticle probe while maintaining a high concentration of DNA-binding molecules. It is impossible to work at this high DNA-binding-molecule/DNA ratio when using nanoparticle-free DNA because many DNA-binding molecules absorb light at the same wavelength as DNA and thus interfere with the signal of the oligonucleotides at 260 nm. Also, the absorbance of some DNA-binding molecules at 260 nm is sensitive to environmental changes (temperature, binding, dielectric) and interferes with melting measurements made by monitoring the absorbance of DNA at 260 nm.[13] Note that melting transitions for the nanoparticle aggregates were monitored at 520 nm (corresponding to the gold plasmon resonance) and those for duplex DNA were monitored at 260 nm.

In general, assay methods that can detect drug candidates with the naked eye without resorting to any instrumentation are convenient, and, for this reason, an assay that could screen for drug candidates on the basis of DNA-binding strength would be of great interest. At present, there are no colorimetric assays that provide this capability. The use of DNA-functionalized Au nanoparticles for this purpose is demonstrated in Figure 2. As the temperature increases, the color changes from blue to red at specific temperatures. All eight cells (one control and seven DNA-binding molecules) appear light blue/purple at 25 °C. At 30 °C, the nanoassemblies containing the control and weak-DNA-binding molecules turn red; only the nanoassemblies containing DAPI, DNR, and EB remain blue/purple. Increasing the temperature to 40 °C causes all of the samples except the nanoassembly containing DAPI—a strong-DNA-binding molecule—to turn red. These results show the discrimination between weak, intermediate, and strong-DNA-binding molecules by an easily identified color change. The trend of the binding affinities for DNA was determined to be DAPI > DNR ≈ EB > other DNA-binding molecules, which is consistent with the control experiments involving serial analysis of each DNA-binding molecule with nanoparticle-free duplex DNA.

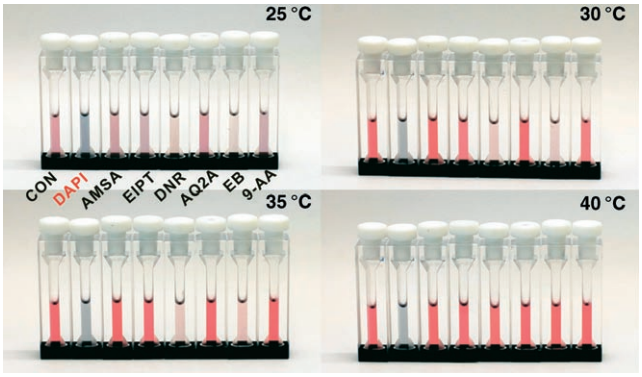



***Figure 2.*** The color change of the nanoassembly (NP-1 and NP-2, each 1.5 nM) in the absence (CON) and presence of DNA-binding molecules (5 μM) specific temperatures.

In summary, we have developed a colorimetric assay for determining the relative binding strengths of molecules to duplex DNA by monitoring the color of nanoparticle network

 © 2006 Wiley-VCH Verlag GmbH & Co. KGaA, Weinheim 

materials exposed to the DNA binders with increasing temperature. The assay has a number of advantages over conventional systems that monitor molecule–DNA interactions directly or with molecular fluorophore probes. The sharp melting transition associated with network materials made from DNA-interlinked gold nanoparticles, their strong absorbance at 520 nm, and the large perturbations in the $T_m$ values upon analyte binding allow significantly better discrimination between weak, intermediate, and strong-DNA-binding molecules. Furthermore, the simplicity of this assay should make it more convenient than other methods that rely on mass spectrometry, NMR spectroscopy, light scattering, electrochemistry, and fluorometry. Finally, this assay can be adapted easily to high-throughput screening methods, which can be used to determine potential anticancer agents from large combinatorial libraries on the basis of their duplex DNA-binding affinity.

Received: December 1, 2005
Published online: February 15, 2006

**Keywords:** DNA · gold · high-throughput screening · nanostructures · sensors

[1] a) L. A. Thompson, J. A. Ellman, *Chem. Rev.* **1996**, *96*, 555 – 600; b) F. Balkenhohl, C. von dem Bussche-Hünnefeld, A. Lansky, C. Zechel, *Angew. Chem.* **1996**, *108*, 2436 – 2487; *Angew. Chem. Int. Ed. Engl.* **1996**, *35*, 2288 – 2337.
[2] a) D. L. Boger, B. E. Fink, M. P. Hedrick, *J. Am. Chem. Soc.* **2000**, *122*, 6382 – 6394; b) V. Nesterenko, K. S. Putt, P. J. Hergenrother, *J. Am. Chem. Soc.* **2003**, *125*, 14672 – 14673.
[3] M. J. A. Walker, T. Barrett, L. J. Guppy, *Targets* **2004**, *3*, 208 – 215.
[4] a) P. A. Johnston, P. A. Johnston, *Drug Discovery Today* **2002**, *7*, 353 – 363; b) D. L. Boger, J. Desharnais, K. Capps, *Angew. Chem.* **2003**, *115*, 4270 – 4309; *Angew. Chem. Int. Ed.* **2003**, *42*, 4138 – 4176; c) S. Wang, T. B. Sim, Y.-S. Kim, Y.-T. Chang, *Curr. Opin. Chem. Biol.* **2004**, *8*, 371 – 377.
[5] a) X.-L. Yang, A. H.-J. Wang, *Pharm. Therap.* **1999**, *83*, 181 – 215; b) C. Bailly, W. A. Denny, L. E. Mellor, L. P. G. Wakelin, M. J. Waring, *Biochemistry* **1992**, *31*, 3514 – 3524.
[6] a) D. Řeha, M. Kabeláč, F. Ryjáček, J. Šponer, J. E. Šponer, M. Elstner, S. Suhai, P. Hobza, *J. Am. Chem. Soc.* **2002**, *124*, 3366 – 3376; b) I. Antonini, P. Polucci, T. C. Jenkins, L. R. Kelland, E. Menta, N. Pescalli, B. Stefanska, J. Mazerski, S. Martelli, *J. Med. Chem.* **1997**, *40*, 3749 – 3755.
[7] a) S. A. Hofstadler, R. H. Griffey, *Chem. Rev.* **2001**, *101*, 377 – 390; b) H. Robinson, W. Priebe, J. B. Chaires, A. H.-J. Wang, *Biochemistry* **1997**, *36*, 8663 – 8670; c) R. F. Pasternack, C. Bustamante, P. J. Collings, A. Giannetto, E. J. Gibbs, *J. Am. Chem. Soc.* **1993**, *115*, 5393 – 5399; d) C.-Z. Li, Y. Liu, H. T. Luong, *Anal. Chem.* **2005**, *77*, 478 – 485.
[8] D. L. Boger, B. E. Fink, S. R. Brunette, W. C. Tse, M. P. Hedrick, *J. Am. Chem. Soc.* **2001**, *123*, 5878 – 5891.
[9] C. A. Mirkin, R. L. Letsinger, R. C. Mucic, J. J. Storhoff, *Nature* **1996**, *382*, 607 – 609.
[10] a) R. Elghanian, J. J. Storhoff, R. C. Mucic, R. L. Letsinger, C. A. Mirkin, *Science* **1997**, *277*, 1078 – 1080; b) L. He, M. D. Musick, S. R. Nicewarner, F. G. Salinas, S. J. Benkovic, M. J. Natan, C. D. Keating, *J. Am. Chem. Soc.* **2000**, *122*, 9071 – 9077; c) D. J. Maxwell, J. R. Taylor, S. Nie, *J. Am. Chem. Soc.* **2002**, *124*, 9606 – 9612; d) T. Niazov, V. Pavlov, Y. Xiao, R. Gill, I. Willner, *Nano Lett.* **2004**, *4*, 1683 – 1687; e) V. Pavlov, Y. Xiao, B. Shlyahovsky, I. Willner, *J. Am. Chem. Soc.* **2004**, *126*, 11768 – 11769; f) J. Liu, Y. Lu, *J. Am. Chem. Soc.* **2003**, *125*, 6642 – 6643.
[11] K. J. Watson, S.-J. Park, J.-H. Im, S. T. Nguyen, C. A. Mirkin, *J. Am. Chem. Soc.* **2001**, *123*, 5592 – 5593.
[12] J. Joseph, E. Kuruvilla, A. T. Achuthan, D. Ramaiah, G. B. Schuster, *Bioconjugate Chem.* **2004**, *15*, 1230 – 1235.
[13] S. Tanaka, Y. Baba, A. Kagemoto, *Makromol. Chem.* **1981**, *182*, 1475 – 1480.

 © 2006 Wiley-VCH Verlag GmbH & Co. KGaA, Weinheim 

*Fluorescent Probes*

DOI: 10.1002/anie.200504299

# 3′-(2,4-Dinitrobenzenesulfonyl)-2′,7′-dimethylfluorescein as a Fluorescent Probe for Selenols**

*Hatsuo Maeda,* Kohei Katayama, Hiromi Matsuno, and Tadayuki Uno*

Selenium is a biologically essential element for cellular redox balance, immune responses, cancer prevention, and inflammation protection.[1–3] In mammalian tissues, selenocysteine (SeCys), genetically encoded as the 21st amino acid, appears to be the predominant chemical form of selenium, and is specifically incorporated into selenoproteins (SePs). Therefore, the functions of SeP are of great interest in elucidating the pathogenesis of some disorders.[1–4] Approximately 35 SePs have been identified in mammals such as humans and mice.[1,3] Some SePs, such as glutathione peroxidase (GPx)[5] and thioredoxin reductase (TrxR),[6] are well-characterized enzymes, while others with biologically important functions have not been fully elucidated.[1–4] A better understanding of the roles of SePs requires a sensitive and rapid method for the identification and measurement of SePs or SeCys, and especially for the determination of the SeCys content in SePs. This is not only because SeCys residues are essential for the enzymatic or biological activity of SePs but also because the loss of selenium is often observed in isolated SePs such as TrxR[7] and selenoprotein P,[8] although their origin still remains unclear. Assays that utilize fluorescent probes meet these requirements. However, no probes for selenol have been developed; instead, chromatographic methods coupled

[*] Prof. H. Maeda, K. Katayama, H. Matsuno, Prof. T. Uno
Division of Analytical Chemistry
Graduate School of Pharmaceutical Sciences
Osaka University
1-6 Yamada-oka, Suita, Osaka 565-0871 (Japan)
Fax: (+81) 6-6879-8206
E-mail: h-maeda@phs.osaka-u.ac.jp

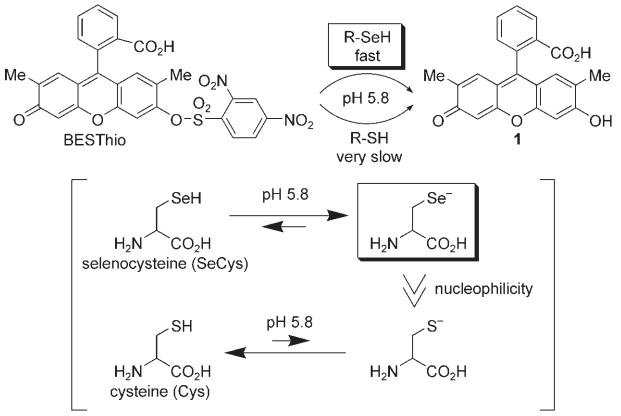
[**] This work was supported in part by a Grant-in-Aid for Scientific Research (B, 15390012) from the Ministry of Education, Culture, Sports, Science, and Technology of Japan.

Supporting information for this article is available on the WWW under http://www.angewandte.org or from the author.


WILEY InterScience DISCOVER SOMETHING GREAT
© 2006 Wiley-VCH Verlag GmbH & Co. KGaA, Weinheim

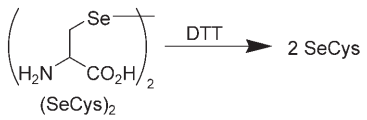
with fluorometric or mass spectrometric detection are used for the determination of SeCys.[9–13]

Recently, 3′-(2,4-dinitrobenzenesulfonyl)-2′,7′-dimethylfluorescein (BESThio; Scheme 1) was reported as a fluorescent probe for thiols that was useful for the fluorometric analysis of cholinesterases.[14] The fluorogenic reaction of BESThio occurs through deprotection into **1** through aromatic nucleophilic substitution[15] by thiolate anions. This mechanism indicates that the degree of thiol dissociation is important for BESThio to function as a thiol probe. The quantification of glutathione ($pK_a(SH) = 8.5$) with BESThio was unsuccessful in media at pH values less than 7.0, which indicates that careful selection of the reaction pH would allow BESThio to discriminate between selenols and thiols. This selectivity is possible not only because the $pK_a$(SeH) value of SeCys is 5.2, which is much lower than the $pK_a$(SH) value of 8.3 of its thiol counterpart cysteine (Cys), but also because selenols behave as stronger nucleophiles than thiols (see Scheme 1).[16] An attempt based on a similar concept failed to confer specific probing ability toward selenols with existing fluorescent thiol probes such as monobromobimane, 7-fluoro-4-nitrobenzo-2-oxa-1,3-diazole, *N*-(1-pyrene)maleimide, and *N*-(7-dimethylamino-4-methylcoumaryl)maleimide.[9] In contrast to these probes, BESThio was found to exert Janus-faced functions switched by a proper choice of the pH of the media (Scheme 1). Herein, we describe that at pH 5.8 BESThio works as a probe for selenol and is useful for the quantification of SeCys and the determination of the selenol content of GPx and mammalian TrxR in the presence of dithiothreitol (DTT).




***Scheme 1.*** The fluorescent probe BESThio and its discrimination between selenols and thiols.

The fluorescent responses of BESThio toward SeCys ($I_{SeH}$) were compared with those toward a thiol ($I_{SH}$) in sodium phosphate buffer in the pH range 5.8–7.4 in a 96-well microtiter plate. The reducing reagent DTT as well as Cys were examined as the thiols. The addition of DTT is essential not only because SeCys must be reductively generated from selenocysteine $(CysSe)_2$ [Eq. (1)] but also because the analysis of SePs is preferably performed under reductive conditions. Thus, $I_{SeH}$ was recorded 10 min after incubating a mixture of BESThio (final concentration: 22.5 μM), $(CysSe)_2$ (5 μM), and DTT (5 μM) at 37 °C, while $I_{SH}$ was measured after the reaction of BESThio with only Cys or DTT (10 μM). Figure 1 shows the pH dependency of the $I_{SeH}/I_{SH}$ ratio. As expected, $I_{SeH}/I_{SH}$ values increased with the acidity of the medium. The optimal discriminating ability of BESThio toward SeCys over Cys or DTT was observed in phosphate buffer at pH 5.8, resulting in an $I_{SeH}/I_{SH}$ value of over 200. Although $I_{SeH}$ decreased with the acidity of the medium, a reasonable sensitivity of BESThio toward SeCys was observed even at pH 5.8 with $I_{SeH} = 1.2 \times 10^4$ au for 1.0 nmol SeCys, compared to pH 7.4 where the value was reduced to only 9% of this value. Note that BESThio displayed no fluorescent response toward amines and alcohols such as ethylamine, piperidine, glucose, and catechol over the pH range 5.8–7.4. Colorimetry with 5,5′-dithio-bis(2-nitrobenzoic acid) (DTNB) was not a specific method for measuring SeCys over Cys or DTT, even in phosphate buffer at pH 5.8 (see Supporting Information), although DTNB has been used not only for the quantification of thiols[17] but also for the determination of the thiol content of proteins.[18]




(1)

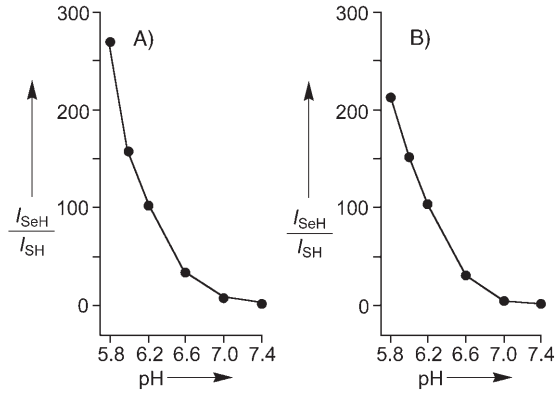



***Figure 1.*** pH-Dependent changes in the selectivity ($I_{SeH}/I_{SH}$) of BESThio (final concentration: 22.5 μM) toward SeCys (10 μM), generated by the reaction of $(CysSe)_2$ (5 μM) with DTT (5 μM) over A) Cys or B) DTT (10 μM each), observed after incubation in phosphate buffer at 37 °C for 10 min.

Excitation and emission spectra were recorded at several intervals during the reaction of BESThio, $(CysSe)_2$, and DTT at 37 °C in phosphate buffer at pH 5.8 (Figure 2). Immediately upon addition of $(CysSe)_2$ to a mixture of BESThio and DTT, the excitation and emission peaks of **1** appeared in the spectra resulting from its generation from BESThio upon reaction with SeCys. The intensity of the peaks increased rapidly until 5 min after the addition of $(CysSe)_2$ at which point the intensity stabilized. The estimated values for the rate constant ($k_{obsd}$) for the reaction of BESThio with SeCys, Cys, or DTT at pH 5.8 and 37 °C were $7.4 \times 10^2$, 0.4, or 0.7 $M^{-1} s^{-1}$, respectively. Thus, a selenol SeCys moiety transformed BESThio into **1**

 © 2006 Wiley-VCH Verlag GmbH & Co. KGaA, Weinheim 

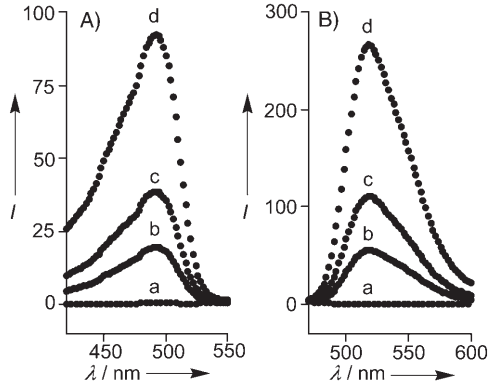



*Figure 2.* A) Excitation ($\lambda_{em}$, 580 nm) and B) emission ($\lambda_{ex}$, 450 nm) spectra for BESThio (final concentration: 5 μM) in 0.1 M phosphate buffer at pH 5.8 (3 mL, containing 0.1% EtOH as cosolvent) at 37°C, measured: a) immediately after the addition of DTT (5 μM), or at b) 0.5, c) 1, and d) 5 min after the further addition of $(CysSe)_2$ (5 μM).

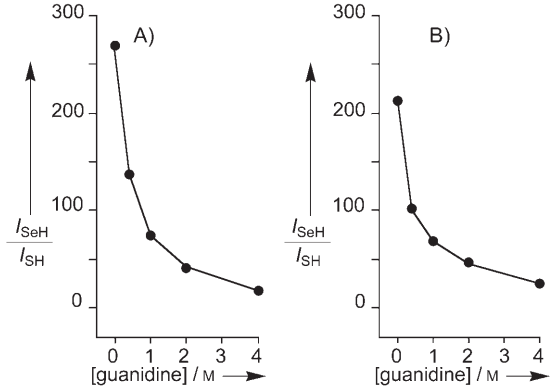



*Figure 3.* Effects of the concentration of guanidine upon the selectivity ($I_{SeH}/I_{SH}$) of BESThio (final concentration: 22.5 μM) toward SeCys (10 μM) generated from the reaction of $(CysSe)_2$ (5 μM) with DTT (5 μM) over A) Cys or B) DTT (10 μM each), observed after incubation in phosphate buffer at pH 5.8 at 37°C for 10 min.

more than 1000-times faster than did Cys and DTT at pH 5.8 in phosphate buffer. A microtiter plate assay with BESThio (25 μM, 180 μL) and DTT (100 μM, 10 μL) in phosphate buffer at pH 5.8 allowed the quantification of SeCys generated from $(CysSe)_2$ (10 μL). The detection limit was 0.8 pmol/well, when estimated as the lowest concentration that afforded a three-fold greater fluorescence emission than the standard deviation of blank responses. A linear calibration curve for SeCys was obtained over the range 1–1000 pmol/well.

This SeCys assay was applied to the analysis of the SeCys content of commercially available GPx (from bovine erythrocytes) and TrxR (from rat liver). However, BESThio provided no fluorescent augmentation at all toward these proteins probably because the SeCys residues in these SePs are buried too deeply to react with BESThio. These results indicated that pretreatment of SePs with a denaturating reagent is inevitable for the present determination of the SeCys content of SePs. The determination of the SeCys content with BESThio was thus carried out as follows: The SePs were incubated at 37°C for 30 min in the presence of guanidine or urea, then the denaturated SePs were mixed with DTT and solutions of the probe prepared in phosphate buffer at pH 5.8 containing 4 M guanidine or 5 M urea. After incubation of the resulting mixtures at 37°C for 10 min, the fluorescence was measured. On the basis of the observed fluorescent responses, guanidine worked well for denaturating the SePs under these conditions while urea did not. However, the presence of guanidine at a markedly high concentration (e.g. 4 M) seemed to militate against the highly specific determination of SeCys with BESThio over Cys or DTT. Thus, the effects of the concentration of guanidine on the discriminating ability of BESThio toward SeCys over Cys or DTT were evaluated in detail (Figure 3). The $I_{SeH}/I_{SH}$ values decreased with the guanidine concentration in phosphate buffer at pH 5.8. Guanidine at 4 M markedly attenuated the original specificity of BESThio as a selenol probe. However, phosphate buffer containing 0.4 M guanidine led to a discrimination of BESThio toward SeCys from Cys or DTT by a factor of more than 100. These results suggested that the analysis of SePs with BESThio should be performed in the presence of guanidine at concentrations of less than 0.4 M.

With these results in hand, the analysis of GPx and TrxR was performed as follows: A mixture of solutions of SeP and 8 M guanidine (10 μL each) was incubated at 37°C for 30 min in a 96-well microtiter plate. BESThio (25 μM, 220 μL) in phosphate buffer at pH 5.8 and either an aqueous solution of DTT (0.1 M) or $H_2O$ (10 μL) were added to the solution of denatured SeP. Through this procedure, the concentration of guanidine was diluted to 0.32 M, allowing BESThio to work as a selenol probe. After incubation at 37°C for 20 min, the increase in fluorescence in each well was measured. The calibration curve was obtained from the same microtiter plate. The measurements were performed for GPx at 20.7, 82.8, and 207.1 μg mL$^{-1}$, and for TrxR at 62.8, 157.1, and 314.1 μg mL$^{-1}$, yielding a mean value ($n = 3$) for the estimated SeCys content per subunit for each SeP (see Table 1).

***Table 1:*** Determination of the SeCys content in selenoproteins (SePs) glutathione peroxidase (GPx) and thioredoxin reductase (TrxR) by fluorometric assay with BESThio.

| Entry | SeP | DTT | SeCys per subunit[a] |
|---|---|---|---|
| 1 | GPx | added | 1.03 ± 0.14 |
| 2 | GPx | none | 0.91 ± 0.11 |
| 3 | TrxR | added | 1.09 ± 0.19 |
| 4 | TrxR | none | 1.02 ± 0.30 |

[a] Mean value ± standard deviation ($n = 3$).

GPx is a homotetramer (84.5 kDa), while TrxR is a homodimer. The molecular weight of the commercially available TrxR was not certified. TrxR from rat liver should consist of TrxR1 (111 kDa) and TrxR2 (102 kDa), and the former seems more abundant in these tissues than the latter.[19] Therefore, the molecular weight of the examined TrxR was assumed to be 111 kDa. Each subunit of these SePs contains only one SeCys residue in theory. The estimated number for SeCys residues per subunit for each of the SePs was near the theoretical value of 1. The measurements

 © 2006 Wiley-VCH Verlag GmbH & Co. KGaA, Weinheim 

without the addition of DTT underestimated the SeCys content, the degree of which was only about 10% (Table 1, entries 2 and 4). Thus, it was demonstrated that the fluorometric method with BESThio as a selenol probe works well for the analysis of the SeCys content in SePs. It should be mentioned here that the influence of the Cys residues in GPx and TrxR on the present assay was negligible. For example, GPx at 24.5 pmol (207.1 $\mu g\,mL^{-1}$, 10 $\mu L$) theoretically contains 490 pmol Cys residues as well as 98 pmol SeCys residue. Under essentially the same conditions, 1000 pmol Cys, which was greater than the theoretical Cys content, resulted in a minute fluorescent response, which was estimated to correspond to only 1.7 pmol SeCys.

In summary, BESThio displays a Janus-faced ability to probe thiols or selenols, and functions as the first probe for selenol by merely changing the pH value of the medium from 7.4 to 5.8. The use of slightly acidic media does not limit the application of BESThio as a selenol probe. Thus, this BESThio assay provides a useful tool for the identification and measurement of unknown as well as known selenoproteins with unique chemical and biological properties.

Received: December 3, 2005
Published online: February 10, 2006

**Keywords:** analytical methods · fluorescent probes · proteins · selenium

[1] M. P. Rayman, *Lancet* **2000**, *356*, 233 – 241.
[2] J. Chen, M. J. Berry, *J. Neurochem.* **2003**, *86*, 1 – 12.
[3] L. Schomburg, U. Schweizer, J. Köhrle, *Cell. Mol. Life Sci.* **2004**, *61*, 1988 – 1995.
[4] D. M. Driscoll, P. R. Copeland, *Annu. Rev. Nutr.* **2003**, *23*, 17 – 40.
[5] J. R. Arthur, *Cell. Mol. Life Sci.* **2000**, *57*, 1825 – 1835.
[6] D. Mustacich, G. Powis, *Biochem. J.* **2000**, *346*, 1 – 8.
[7] L. Zhong, E. S. J. Arnér, J. Ljung, R. Åslund, A. Holmgren, *J. Biol. Chem.* **1998**, *273*, 8581 – 8591.
[8] S. Ma, R. M. Caprioli, K. E. Hill, R. F. Burk, *J. Am. Soc. Mass Spectrom.* **2003**, *14*, 593 – 600.
[9] W. C. Hawkes, M. A. Kutnink, *J. Chromatogr.* **1992**, *576*, 263 – 270.
[10] J. Zheng, Y. Shibata, N. Furuta, *Talanta* **2003**, *59*, 27 – 36.
[11] J. R. Encinar, D. Schaumlöffel, Y. Ogra, R. Lobinski, *Anal. Chem.* **2004**, *76*, 6635 – 6642.
[12] B. Iscioglu, E. Henden, *Anal. Chim. Acta* **2004**, *505*, 101 – 106.
[13] J. L. Gómez-Ariza, M. A. Caro de la Torre, I. Giráldez, E. Morales, *Anal. Chim. Acta* **2004**, *524*, 305 – 314.
[14] H. Maeda, H. Matsuno, M. Ushida, K. Katayama, K. Saeki, N. Itoh, *Angew. Chem.* **2005**, *117*, 2982 – 2985; *Angew. Chem. Int. Ed.* **2005**, *44*, 2922 – 2925.
[15] G. Bartoli, P. E. Todesco, *Acc. Chem. Res.* **1977**, *10*, 125 – 132.
[16] C. Jacob, G. I. Giles, N. M. Giles, H. Sies, *Angew. Chem.* **2003**, *115*, 4890 – 4907; *Angew. Chem. Int. Ed.* **2003**, *42*, 4742 – 4758.
[17] G. L. Ellman, K. D. Courtney, V. Andres, Jr., R. M. Featherstone, *Biochem. Pharmacol.* **1961**, *7*, 88 – 95.
[18] G. L. Ellman, *Arch. Biochem. Biophys.* **1959**, *82*, 70 – 77.
[19] S.-R. Lee, J.-R. Kim, K.-S. Kwon, H. W. Yoon, R. L. Levine, A. Ginsburg, S. G. Rhee, *J. Biol. Chem.* **1999**, *274*, 4722 – 4734.

 © 2006 Wiley-VCH Verlag GmbH & Co. KGaA, Weinheim 

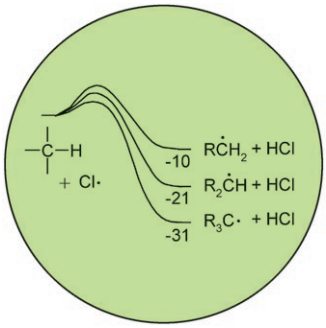
# Cover Picture



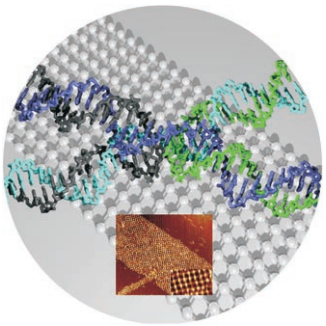

## Harald Tlatlik, Paul Simon, Agnieszka Kawska, Dirk Zahn, Rüdiger Kniep,*

## Paul Simon, Dirk Zahn, Hannes Lichte, and Rüdiger Kniep*

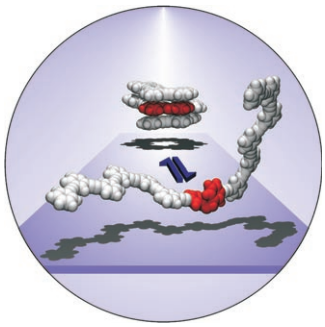
***Form development*** during growth of fluorapatite–gelatine nanocomposites is effected by pre-structuring of gelatine matrices by ion impregnation. The cover picture shows the hierarchical fractal aggregate (background), structural details of a fanlike aggregate, and a simulation of the "stiffening" effect on a protein molecule of $Ca^{2+}$ ion incorporation. This effect is discussed by R. Kniep and co-workers in their Communication on page 1905 ff. A second paper on page 1911 ff. deals with the effect of intrinsic electric dipole fields on the form development of the nanocomposite materials.




***Reactivity and Selectivity***
In their Minireview on page 1844 ff., H. Mayr and A. R. Ofial challenge the widely accepted reactivity–selectivity principle for organic reactions: Reactivity and selectivity of a species should exhibit opposite behavior—but it's not as easy as it sounds!



***Nanoscience***
DNA molecules are excellent building blocks for the construction of complex superstructures. Construction principles as well as possible applications of such assemblies are described by U. Feldkamp and C. M. Niemeyer in their Review on page 1856 ff.



***Photoresponsive Materials***
A first step towards the design of intelligent delivery vehicles is presented by S. Hecht and co-workers in their communication on page 1878 ff., which describes the unfolding of the hollow helical secondary structure of a foldamer upon irradiation.

# Contents

**VIP** *The following Communications have been judged by at least two referees to be "very important papers" and will be published online at www.angewandte.org soon:*


*D. Curran,* G. Moura-Letts, M. Pohlman*
**Solution-Phase Mixture Synthesis with Fluorous Tagging En Route: Total Synthesis of an Eight-Member Stereoisomer Library of Passifloricins**

*H. Zhang, H. Xia,* G. He, T. B. Wen, L. Gong, G. Jia**
**Synthesis and Characterization of Stable Ruthenabenzenes**

*X. Mo, Y. An, C.-S. Yun, S. Yu**
**Nanoparticle-Assisted Visualization of Binding Interactions between Collagen Mimetic Peptide and Collagen Fibers**

*M. Harney, Y. Zhang, L. Sita**
**Discrete, Multiblock Isotactic–Atactic Stereoblock Polypropene Microstructures of Differing Block Architectures by Programmable Stereomodulated Living Ziegler–Natta Polymerization**

*Y. Weizmann, Z. Cheglakov, V. Pavlov, I. Willner**
**Autonomous Fueled Mechanical Replication of Nucleic Acid Templates for the Amplified Optical Detection of DNA**

*B. Botta, F. Caporuscio, D. Subissati, A. Tafi,* M. Botta, A. Filippi, M. Speranza**
**Flattened-Cone 2,8,14,20-Tetrakis(L-valinamido)[4]resorcinarene: Enantioselective Allosteric Receptors in the Gas Phase**


## News


Chemiedozententagung 2006: Awards to B. Giese and M.-J. Crawford; ADUC Prizes ——— **1836**


## Books


Chemistry and Technology of Emulsion Polymerisation — Alex M. van Herk — *reviewed by P. M. Cunningham* ——— **1837**

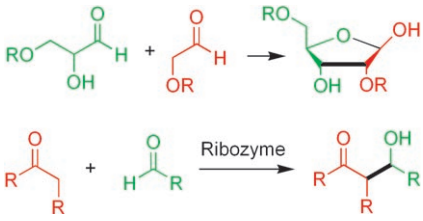

## Highlights

### Chemical Evolution


M. Rueping* ——— **1838 – 1840**

Aldol Reactions within the RNA World

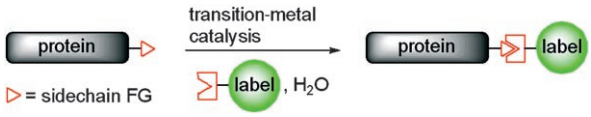

**Keep the fire burning**: It is hard to find new aspects to the aldol reaction, as a wealth of diastereoselective and enantioselective examples with a range of catalysts are known. However, recent work on template-mediated cross-aldol reactions and ribozyme-catalyzed aldol reactions show that this topic is still hot. Both reports are relevant to the theory of the RNA world.




### Protein Modification


J. H. van Maarseveen,* J. N. H. Reek, J. W. Back ——— **1841 – 1843**

Transition-Metal Catalysis as a Tool for the Covalent Labeling of Proteins


**They make a good couple**: Protein modification the transition-metal catalysis enables the selective labeling of proteins and has been demonstrated in complex mixtures. Current examples of such coupling reactions are the Ir-catalyzed reductive amination of lysine residues and the alkylation of tryptophan residues by Rh carbenes in proteins under aqueous conditions (see scheme).



InterScience


© 2006 Wiley-VCH Verlag GmbH & Co. KGaA, Weinheim

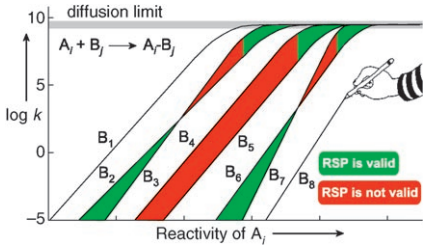
# Minireviews


**Reaction Kinetics**

H. Mayr,* A. R. Ofial _____ **1844 – 1854**

The Reactivity–Selectivity Principle: An Imperishable Myth in Organic Chemistry


**Fact or Myth?** Selectivity is the distance between the correlation lines for two substrates $B_j$. You may confirm by trial that it is impossible to draw a large number of non-intersecting correlation lines on this graph, all of which converge when going from left to right, as required by the still widely accepted reactivity–selectivity principle (RSP).

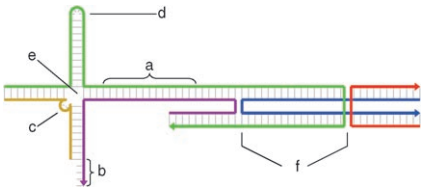



# Reviews


**Nanoscience**

U. Feldkamp,*
C. M. Niemeyer* _____ **1856 – 1876**

Rational Design of DNA Nanoarchitectures


**In the past 20 years**, DNA has been established as a powerful material for molecular constructions at the nanometer scale. The ability to design building blocks from DNA containing well-defined secondary structure motifs (a–f, in the scheme) allows the assembly of large supramolecular arrays, scaffolds, and even mechanical and logical nanodevices.

# Communications


**Foldamers**

A. Khan, C. Kaiser, S. Hecht* **1878 – 1881**

Prototype of a Photoswitchable Foldamer





**Know where to fold 'em**: A foldamer exhibiting a light-induced helix–coil transition (see scheme) can be constructed by introducing a photochromic azobenzene moiety (red) into the center of an amphiphilic phenylene ethynylene backbone (blue). This system gives insight into folding and unfolding mechanisms and promises applications in photoresponsive (bio)materials and "smart" delivery devices based on photoresponsive dynamic receptors.

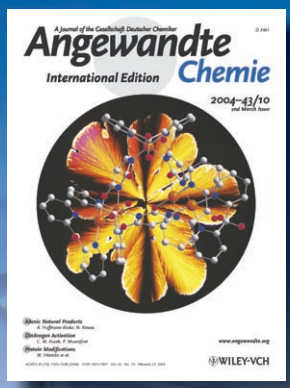

**For the USA and Canada:**
ANGEWANDTE CHEMIE International Edition (ISSN 1433-7851) is published weekly by Wiley-VCH PO Box 191161, D 69451 Weinheim, Germany. Air freight and mailing in the USA by Publications Expediting Inc. 200 Meacham Ave., Elmont, NY 11003. Periodicals postage paid at Jamaica NY 11431. US POSTMASTER: send address changes to *Angewandte Chemie*, Wiley-VCH, 111 River Street, Hoboken, NJ 07030. Annual subscription price for institutions: US$ 5685/5168 (valid for print and electronic / print or electronic delivery); for individuals who are personal members of a national chemical society prices are available on request. Postage and handling charges included. All prices are subject to local VAT/sales tax.



© 2006 Wiley-VCH Verlag GmbH & Co. KGaA, Weinheim

# The best in chemistry –

## for more than a hundred years




A Journal of the Gesellschaft Deutscher Chemiker

**Angewandte**
International Edition **Chemie**

**www.angewandte.org**

**1888:** ***The beginning of a success story***

### Constant Innovations

**1962:** *First issue of the International Edition*
**1976:** *Graphical abstracts*
**1979:** *Cover pictures*
**1988:** *Centenary of Angewandte*
**1989:** *Routine use of color*
**1991:** *New section: Highlights*
**1992:** *Computerized editorial tracking system*
**1995:** *Internet service for readers*
**1998:** *Regular press service; full-text online*
**2000:** *New section: Essays; EarlyView: Communications available online ahead of the printed version*
**2001:** *New section: Minireviews*
**2002:** *Online submission of manuscripts*
**2003:** *Weekly publication; new section: News; new layout*
**2004:** *Backfiles (1962-1997); ManuscriptXpress: Online system for authors and referees*



### Angewandte's advisors...

***François Diederich***
*ETH Zürich*

»***Angewandte Chemie*** *has proven over the past two decades to be the most innovative of all chemical journals, taking leadership in both quality and presentation of the published material. Rapid, high visibility of important scientific work is readily ensured. It is a true privilege to serve on the Editorial Board.*«

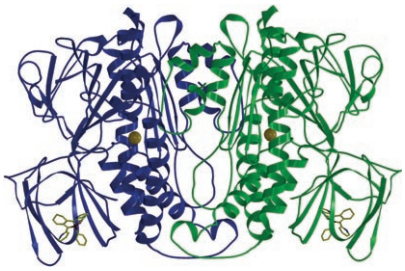
***Angewandte Chemie International Edition*** *is a journal of the German Chemical Society (GDCh)*

GDCh

WILEY InterScience® DISCOVER SOMETHING GREAT

WILEY-VCH

1811404_gu



**Redox-based chemotherapy**: The irreversible inhibition of human glutathione reductase results in a unique S-Au$^{I}$-S coordination, which was determined crystallographically. The chemotherapeutic potential of phosphine–metal complexes was probed by kinetic analysis of the fast and effective inhibition of redox enzymes as well as by DNA-interaction studies and cell-proliferation tests.

***Enzyme Inhibitors***

S. Urig, K. Fritz-Wolf, R. Réau, C. Herold-Mende, K. Tóth, E. Davioud-Charvet, K. Becker* _____ **1881 – 1886**

Undressing of Phosphine Gold(I) Complexes as Irreversible Inhibitors of Human Disulfide Reductases

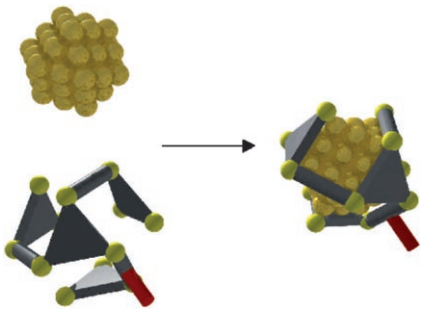


**Like a Russian doll**: In the nanomolecule $Sc_{24}C_{10}I_{30}$, an outer $I_{30}$ envelope (pink) surrounds a $Sc_{20}$ T3 supertetrahedron (blue), which is filled by a $C_{10}$ T2 supertetrahedron (gray), which, in turn, is filled by a $Sc_4$ T1 tetrahedron (light gray), containing two electrons in a four-center, two-electron bond.

***Iodine Supertetrahedra***

L. Jongen, A.-V. Mudring,* G. Meyer* _____ **1886 – 1889**

The Molecular Solid $Sc_{24}C_{10}I_{30}$: A Truncated, Hollow T4 Supertetrahedron of Iodine Filled with a T3 Supertetrahedron of Scandium That Encapsulates the Adamantoid Cluster $Sc_4C_{10}$

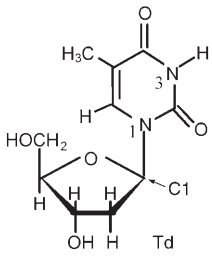


**Get a grip**: A tailor-made ligand bearing 12 thioether groups can act as a "gripper" for the $Au_{55}$ cluster to give thermally stable, monofunctionalized labels for biomolecules (see scheme). Conjugates of the gold cluster with DNA strands can act as efficient fluorescence quenchers and can survive the harsh thermal conditions of PCR experiments.

***DNA Nanotechnology***

W. M. Pankau, S. Mönninghoff, G. von Kiedrowski* _____ **1889 – 1891**

Thermostable and Monoconjugable Gold Clusters with a Dodecadentate Thioether Ligand Gripper




**The damage to biological systems** by high-energy quanta occurs mainly through secondary species created in the ionization path. Interaction of the low-energy (0–3 eV) electrons with thymidine (Td) in the gas phase was investigated. These electrons induce loss of hydrogen from the N3 position and scission of the N1–C1 bond. The transfer of excess electrons, initially localized on thymine, to the sugar moiety was not observed.

***DNA Strand Breaks***

S. Ptasińska, S. Denifl, S. Gohlke, P. Scheier, E. Illenberger,* T. D. Märk _____ **1893 – 1896**

Decomposition of Thymidine by Low-Energy Electrons: Implications for the Molecular Mechanisms of Single-Strand Breaks in DNA

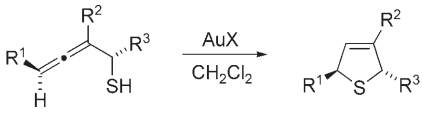

© 2006 Wiley-VCH Verlag GmbH & Co. KGaA, Weinheim

# Contents


## Gold Catalysis

N. Morita, N. Krause* ____ **1897 – 1899**

The First Gold-Catalyzed C–S Bond Formation: Cycloisomerization of α-Thioallenes to 2,5-Dihydrothiophenes

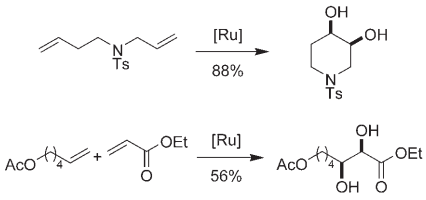



**One good ring deserves another**: A highly efficient and stereoselective cycloisomerization of α-thioallenes to 2,5-dihydrothiophenes is the first example of a gold-catalyzed carbon–sulfur bond formation (see scheme, X = Cl, I). Both gold(I) and gold(III) salts can be used as the pre-catalyst, with AuCl and AuI giving the best yields. The method is of interest for the stereoselective synthesis of biologically active 2,5-disubstituted dihydro- or tetrahydrothiophenes.

## Synthetic Methods

S. Beligny, S. Eibauer, S. Maechling, S. Blechert* ____ **1900 – 1903**

Sequential Catalysis: A Metathesis/Dihydroxylation Sequence

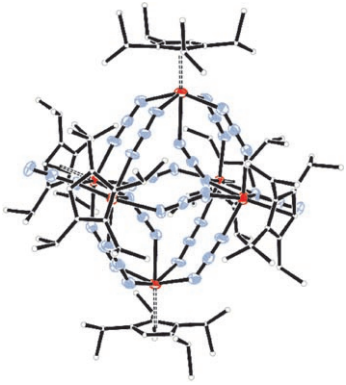



**A real step-saver:** A single ruthenium–carbene complex catalyzes a sequence of two reactions, namely, a metathesis reaction (ring-closing or cross metathesis) and subsequent dihydroxylation of the newly formed double bond. A variety of cyclic and acyclic *cis*-diols were prepared in good yields (see scheme). This new methodology provides an interesting alternative to the pinacol coupling.

## Azides

M. D. Walter, F. Weber, G. Wolmershäuser, H. Sitzmann* ____ **1903 – 1905**

A Hexanuclear Ytterbium Complex Anion with Fourteen Azido Ligands

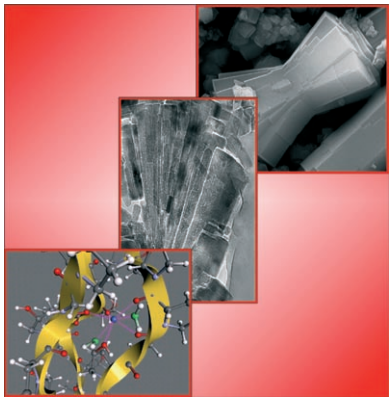


**Bridge to ytterbium**: In the hexanuclear cluster ion $[(^4CpYb)_6(N_3)_{14}]^{2-}$ ($^4Cp = C_5H(CHMe_2)_4$), the $Yb^{3+}$ centers are arranged in a distorted octahedron (see Figure; Yb red, N blue, C white). The twelve edges of the octahedron are bridged by ten $\mu_{1,3}$-$N_3$ and two $\mu_{1,1}$-$N_3$ ligands. Two additional azido ligands located within the cluster cavity act as $\mu_{1,1,3}$-$N_3$ bridges.

## Morphogenesis (1)

H. Tlatlik, P. Simon, A. Kawska, D. Zahn, R. Kniep* ____ **1905 – 1910**

Biomimetic Fluorapatite–Gelatine Nanocomposites: Pre-Structuring of Gelatine Matrices by Ion Impregnation and Its Effect on Form Development

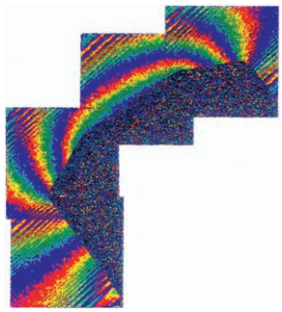


**Form follows the ion**: The morphogenesis of fluorapatite–gelatine nanocomposites is studied from both electron microscopy and atomistic simulation revealing ion impregnation effects on the growth mechanisms. Depending on the ionic species used for pre-treatment of the organic component dramatic changes of the mesoscopic structuring are observed.



© 2006 Wiley-VCH Verlag GmbH & Co. KGaA, Weinheim

**The seeder of the pack**: The electrical potential distribution (see phase image of an electron hologram) around the basal plane close to the prism faces of a hexagonal fluorapatite–gelatine nanocomposite seed influences the growth of the nanocomposite. The seed consists of elementary dipoles on the nanometer scale, which all have the same orientation along the *c* axis of the composite seed. Further form development of the seed leads to fractal patterns.



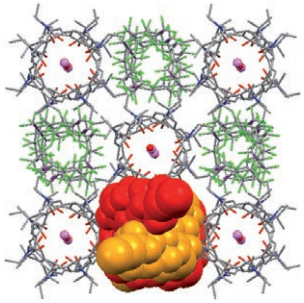
***Morphogenesis (2)***

P. Simon, D. Zahn, H. Lichte, R. Kniep* ——— **1911 – 1915**

Intrinsic Electric Dipole Fields and the Induction of Hierarchical Form Developments in Fluorapatite–Gelatine Nanocomposites: A General Principle for Morphogenesis of Biominerals?

---

**Beauty is in the I of the beholder**: Metal-ion coordination and I···I halogen bonding direct the self-assembly of achiral starting materials (a calix[4]arene tetraamide, $BaI_2 \cdot 2\,H_2O$, and 1,8-diiodoperfluorooctane) into a homochiral supramolecular complex containing double helices (see structure; Ba light purple, I purple, F green, O red, N blue, C gray; one double helix in red and yellow).

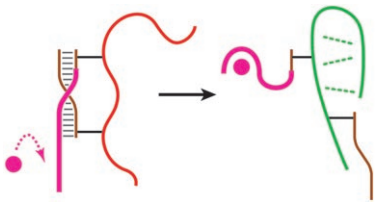


***Supramolecular Chemistry***

A. Casnati, R. Liantonio, P. Metrangolo,* G. Resnati,* R. Ungaro, F. Ugozzoli* ——— **1915 – 1918**

Molecular and Supramolecular Homochirality: Enantiopure Perfluorocarbon Rotamers and Halogen-Bonded Fluorous Double Helices

---



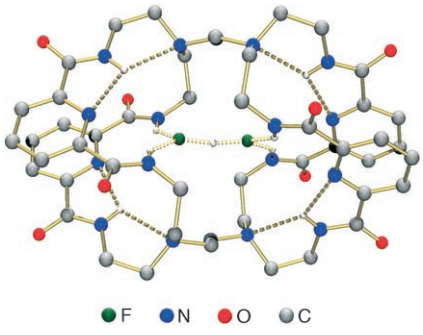
**Taking control with DNA**: Covalently attached double-stranded DNA constraints can control the conformations of other macromolecules. A variety of approaches (including competitive ligand–aptamer interactions) were used to modulate the effects of such constraints on the structure of a large RNA molecule.

***DNA Nanotechnology***

C. V. Miduturu, S. K. Silverman* ——— **1918 – 1921**

Modulation of DNA Constraints That Control Macromolecular Folding

---




**The quest is over**: A tricyclic amide-based anion receptor has been synthesized by connecting two monocyclic precursors. The receptor is highly selective for the binding of the elusive bifluoride anion $HF_2^-$, and the adduct represents the first structural example of an encapsulated bifluoride. The bifluoride lies midway between the two macrocycles making up the tricycle and is held by four hydrogen-bonding contacts with the macrocyclic amides.

***Anion Sensor***

S. O. Kang, D. Powell, V. W. Day, K. Bowman-James* ——— **1921 – 1925**

Trapped Bifluoride

---

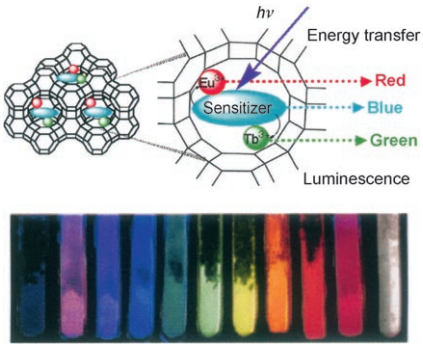

© 2006 Wiley-VCH Verlag GmbH & Co. KGaA, Weinheim

# Contents


## Lanthanide Luminescence

Y. Wada,* M. Sato,
Y. Tsukahara ——— **1925 – 1928**

Fine Control of Red–Green–Blue Photoluminescence in Zeolites Incorporated with Rare-Earth Ions and a Photosensitizer

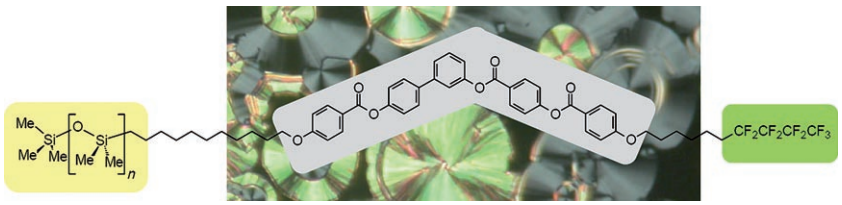



**All the colors of the rainbow** can be observed upon excitation of a zeolite crystal incorporated with varying quantities of $Eu^{3+}$ and $Tb^{3+}$ ions as well as a sensitizer molecule (benzophenone or 4-acetylbiphenyl) in its framework structure (see picture). The colors can be fine-tuned by varying the amounts of the three components as well as the excitation wavelength and temperature.

## Liquid Crystals

R. A. Reddy, G. Dantlgraber,
U. Baumeister,
C. Tschierske* ——— **1928 – 1933**

Liquid-Crystalline Quaternary Block Molecules Incorporating Bent-Core Units



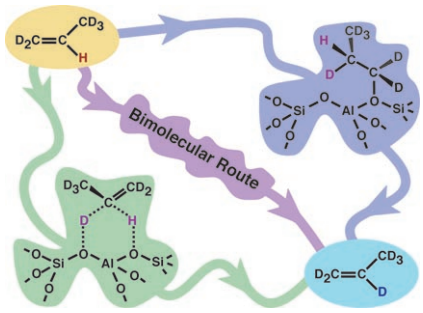

**A flick of a switch**: The combination of fluorinated segments and oligo(dimethylsiloxane) units with bent mesogenic cores leads to new liquid-crystalline materials (see picture) that display a temperature-dependent change from ferroelectric to antiferroelectric switching. Such materials have potential use in, for example, fast-switching electrooptical microdisplays.

## Heterogeneous Catalysis

D. M. Marcus, M. J. Hayman, Y. M. Blau,
D. R. Guenther, J. O. Ehresmann,
P. W. Kletnieks, J. F. Haw* — **1933 – 1935**

Mechanistically Significant Details of the H/D Exchange Reactions of Propene over Acidic Zeolite Catalysts

**Quid pro quo**: Hydrogen–deuterium exchange of propene on solid acid catalysts was studied at 573 and 673 K with a reaction time of 3 s (see scheme). At low partial pressures and temperatures, H/D exchange produced $[D_5]$propene as the main product. Complete deuteration ($[D_6]$propene) was observed only at a higher temperature with the most acidic catalyst.

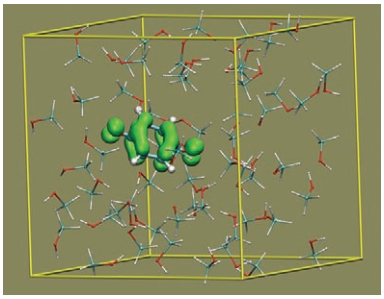



## Marcus Theory

J. VandeVondele,* M. Sulpizi,
M. Sprik ——— **1936 – 1938**

From Solvent Fluctuations to Quantitative Redox Properties of Quinones in Methanol and Acetonitrile

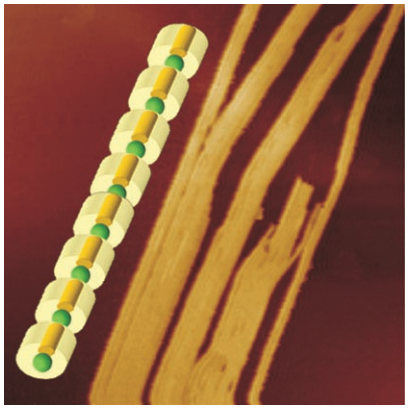
**The effects of substituents** and solvent on the redox properties of quinones were studied within the framework of Marcus theory. The relative redox potentials and reorganization energies in methanol and acetonitrile were computed with a fully atomistic method based on DFT and molecular dynamics (see model of the radical anion of benzoquinone in methanol). Hydrogen bonding contributes 0.2 eV to the reorganization energy in methanol.





© 2006 Wiley-VCH Verlag GmbH & Co. KGaA, Weinheim

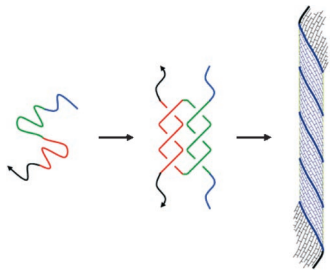
**Second generation** diazadibenzoperylene dendrimers (yellow units) undergo supramolecular polymerization with $Ag^+$ ions (green spheres) to afford rigid-rod coordination polymers, as confirmed by atomic force microscopy studies (see image). Such cylindrical coordination polymers constitute a new class of π-conjugated materials linked by metal centers which may find application in nanoscale electronic devices.



## Coordination Polymers

F. Würthner,* V. Stepanenko, A. Sautter ——— **1939 – 1942**

Rigid-Rod Metallosupramolecular Polymers of Dendronized Diazadibenzoperylene Dyes

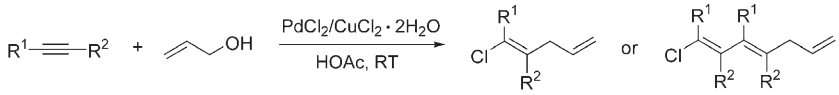


**The long and the short of it**: A short oligonucleotide is designed to self-assemble into micrometer-long nanotubes, which further serve as templates to fabricate metallic nanowires. This study addresses the question: what is the minimum number of DNA strands that are required for self-assembly of well-defined DNA nanostructures?

## DNA

H. Liu, Y. Chen, Y. He, A. E. Ribbe, C. Mao* ——— **1942 – 1945**

Approaching The Limit: Can One DNA Oligonucleotide Assemble into Large Nanostructures?

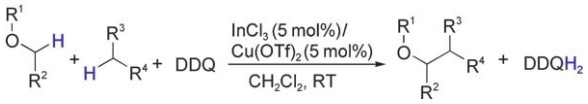



**The direct approach**: The unprecedented result of the title reaction (see scheme) is explained by a mechanism involving competition between π-allylpalladation through cleavage of the C—O bond and the insertion of an alkene. The procedure provides a highly stereo- and regioselective method to construct 1,4-dienes in an economical and environmentally benign manner.

## Reaction Mechanisms

J. Huang, L. Zhou, H. Jiang* **1945 – 1949**

Palladium-Catalyzed Allylation of Alkynes with Allyl Alcohol in Aqueous Media: Highly Regio- and Stereoselective Synthesis of 1,4-Dienes




**An unlikely couple**: C—C bonds can be formed between ethers and methylene compounds by cross-dehydrogenative-coupling (see scheme; DDQ = 2,3-dichloro-5,6-dicyanobenzoquinone). This straightforward reaction employs mild conditions and simple catalysts and allows reasonably high yields.

## Synthetic Methods

Y. Zhang, C.-J. Li* ——— **1949 – 1952**

Highly Efficient Cross-Dehydrogenative-Coupling between Ethers and Active Methylene Compounds

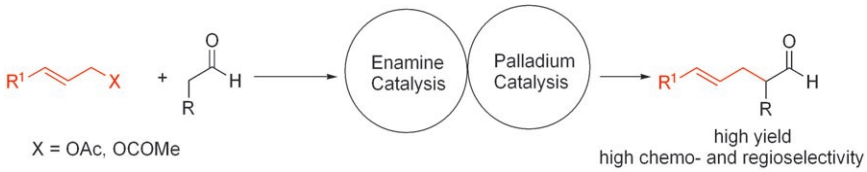

© 2006 Wiley-VCH Verlag GmbH & Co. KGaA, Weinheim

# Contents


## Synthetic Methods

I. Ibrahem, A. Córdova* ____ **1952 – 1956**

Direct Catalytic Intermolecular α-Allylic Alkylation of Aldehydes by Combination of Transition-Metal and Organocatalysis



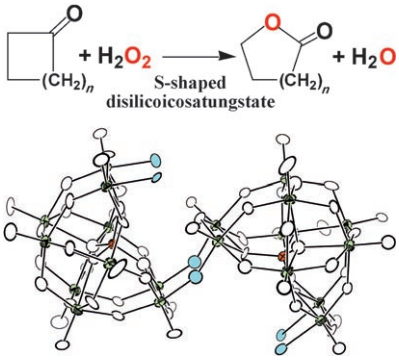

**All in the same pot together**: The direct catalytic α-allylic alkylation of aldehydes and cyclic ketones is achieved by using a simple, unprecedented one-pot procedure. Transition-metal and enamine catalysis are combined so that α-allylic alkylated aldehydes and cyclic ketones are formed in high yield with a direct catalytic chemo- and regioselective method.

## Polyoxometalates

A. Yoshida, M. Yoshimura, K. Uehara, S. Hikichi, N. Mizuno* ____ **1956 – 1960**

Formation of S-Shaped Disilicoicosatungstate and Efficient Baeyer–Villiger Oxidation with Hydrogen Peroxide

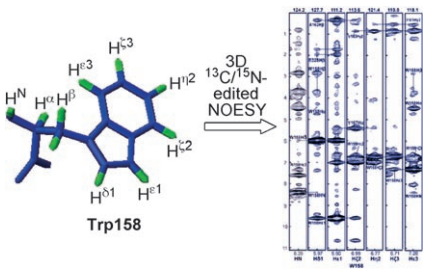
**Partial protonation** of a divacant lacunary Keggin-type silicodecatungstate in an anhydrous organic solvent led to dehydrative condensation and formation of a novel S-shaped disilicoicosatungstate (see picture). The S-shaped cluster efficiently promotes Baeyer–Villiger oxidation of cycloalkanones with high turnover numbers (TONs, ≥1900) and high selectivities (≥90%) for the corresponding lactones.




## Protein-Structure Determination

Z. Lin, Y. Q. Xu, S. Yang, D. W. Yang* ____ **1960 – 1963**

Sequence-Specific Assignment of Aromatic Resonances of Uniformly $^{13}C$,$^{15}N$-Labeled Proteins by Using $^{13}C$- and $^{15}N$-Edited NOESY Spectra

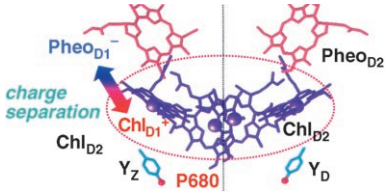



**NOESY neighbors**: A single 3D $^{13}C$- and $^{15}N$-edited NOESY experiment can be used to assign aromatic side-chain resonance signals of $^{13}C$,$^{15}N$-labeled proteins on the basis of prior assignments of the signals of backbone and aliphatic side-chain groups. This strategy will improve the precision of protein structures, especially of large proteins.

## Photosynthesis

H. Ishikita, J. Biesiadka, B. Loll, W. Saenger, E.-W. Knapp* ____ **1964 – 1965**

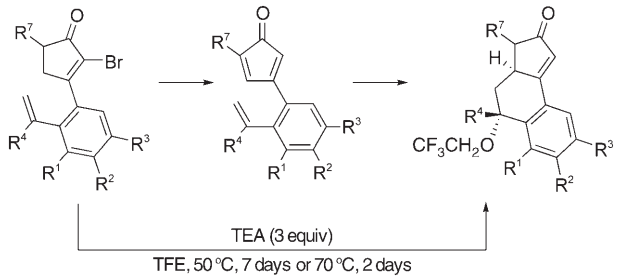
Cationic State of Accessory Chlorophyll and Electron Transfer through Pheophytin to Plastoquinone in Photosystem II




**It must be charged**: The redox potential difference between pheophytin ($Pheo_{D1}$) and primary plastoquinone in the electron transfer in photosystem II from accessory chlorophyll on the D1 branch ($Chl_{D1}$) is consistent with the free-energy difference estimated from kinetic studies only when computed for the cationic state $Chl^{+}_{D1}$. $Y_D$ = symmetry related redox-inactive tyrosine, $Y_Z$ = redox-active tyrosine.



© 2006 Wiley-VCH Verlag GmbH & Co. KGaA, Weinheim

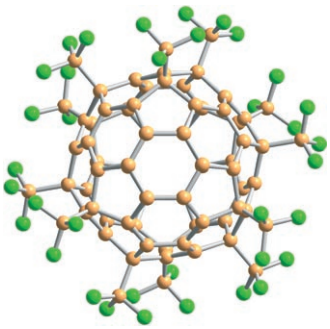



## Cyclizations

M. Harmata,* P. Zheng, P. R. Schreiner,* A. Navarro-Vázquez ——— 1966 – 1971

Deantiaromatization as a Driving Force in an Electrocyclic Reaction

**But how does it smell?** Theory and experiment support the notion that "deantiaromatization" can serve as a driving force in the 8-π-electron electrocyclization of a cyclopentadienone (see scheme; TEA = triethylamine; TFE = trifluoroethanol). The reaction proceeds in synthetically useful yields and could be applicable to the synthesis of the antiviral agent hamigeran B.

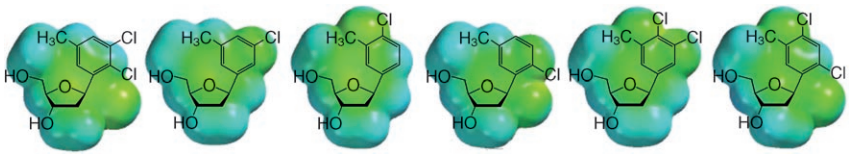


## Fullerenes

S. I. Troyanov,* A. Dimitrov, E. Kemnitz* ——— 1971 – 1974

Selective Synthesis of a Trifluoromethylated Fullerene and the Crystal Structure of $C_{60}(CF_3)_{12}$

**Unexpected selectivity**: [60]Fullerene and $CF_3I$ react selectively at 440 °C to synthesize $C_{60}(CF_3)_{12}$. In the product with $S_6$ symmetry, 12 $CF_3$ groups form a continuous loop of alternating *para*- and *meta*-$C_6(CF_3)_2$ hexagons. In the crystal, the chains of molecules are strengthened owing to stacking interactions and shielding effects from the $CF_3$ groups, thus accounting for the low volatility and solubility of the compound.

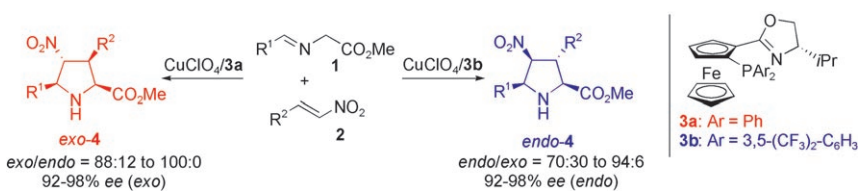


## Enzyme Fidelity

H. O. Sintim, E. T. Kool* ——— 1974 – 1979

Remarkable Sensitivity to DNA Base Shape in the DNA Polymerase Active Site

**Shaping up**: DNA polymerase I can distinguish easily and with high sensitivity between nucleobases that have the same size but differ in shape. The shape, altered through variation in the position of the halogen substituent(s), plays more of a prominent role in base-pairing efficiency and selectivity than other factors.




## Cycloadditions

X.-X. Yan, Q. Peng, Y. Zhang, K. Zhang, W. Hong, X.-L. Hou,* Y.-D. Wu ——— 1979 – 1983

A Highly Enantio- and Diastereoselective Cu-Catalyzed 1,3-Dipolar Cycloaddition of Azomethine Ylides with Nitroalkenes

**Electronic properties of the ligands** switch the diastereoselectivity in the Cu-catalyzed 1,3-dipolar cycloaddition of azomethine ylides to nitroalkenes: *exo*- or *endo*-pyrrolidines were obtained with high diastereo- and enantioselectivities in the presence of different chiral (phosphanylferrocenyl)oxazoline ligands (e.g. **3a**, **b**).


© 2006 Wiley-VCH Verlag GmbH & Co. KGaA, Weinheim

# Contents

WILEY InterScience®
DISCOVER SOMETHING GREAT

"**Hot Papers**" are chosen by the Editors for their importance in a rapidly evolving field of high current interest. A preview with the graphical abstracts of these articles can be found on the *Angewandte Chemie* homepage in Wiley InterScience at www.angewandte.org.

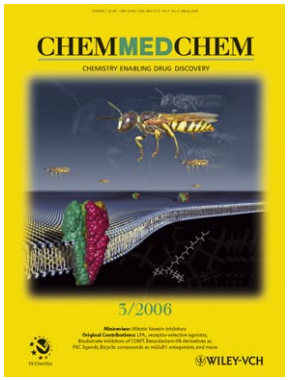
All articles in *Angewandte Chemie* are published online several weeks ahead of print. They are found under the "**EarlyView**" link on the journal's homepage in Wiley InterScience.

## Service

*Keywords* ____ *1984*

*Authors* ____ *1985*

*Preview* ____ *1987*




***For more information on ChemMedChem see www.chemmedchem.org***

# Corrigenda

Molecular Recognition of a Three-Way DNA Junction by a Metallosupramolecular Helicate

A. Oleksy, A. G. Blanco, R. Boer, I. Usón, J. Aymamí, A. Rodger, M. J. Hannon,* M. Coll* ____ **1227–1231**

*Angew. Chem. Int. Ed.* **2006**, *45*

DOI 10.1002/anie.200503822

The correct spelling of the surname of the first author of this Communication is Oleksy, as shown in the author list here.

Transcription and Amplification of Molecular Chirality to Oppositely Biased Supramolecular π Helices

A. Ajayaghosh,* R. Varghese, S. J. George, C. Vijayakumar ____ **1141–1144**

*Angew. Chem. Int. Ed.* **2006**, *45*

DOI 10.1002/anie.200503142

In the cover picture text of Issue 7, page 1005 there are two errors: first, the DNA helix which Janus is holding in his right hand is not left but right-handed—just as it is supposed to be. Second, Janus is in fact a Roman and not a Greek God. The editors and authors apologize for these oversights.

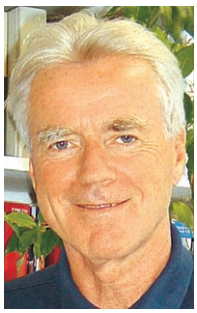

© 2006 Wiley-VCH Verlag GmbH & Co. KGaA, Weinheim



## Awarded...

### Emil Fischer Medal to B. Giese

The Emil Fischer Medal is awarded every two years by the Gesellschaft Deutscher Chemiker (GDCh, German Chemical Society) during the Congress of Chemistry Lecturers (Chemiedozententagung), which takes place on March 19—22, 2006, in Hamburg. This year, Bernd Giese (University of Basel) will receive the medal for his outstanding work in the area of organic radical reactions.[1a,b] He successfully applied such reactions even in natural product synthesis, but the current focus of his research is shifted more towards biochemistry. His research group is interested in the splitting of DNA and lipids using radicals, as well as in the mode of action of ribonucleotide reductase and the mechanism of electron transfer in DNA. Recently, he reported in *Angewandte Chemie* on the direct observation of radical cation intermediates in electron-transfer processes in peptides.[1c]



B. Giese

Born in Hamburg, Giese studied chemistry at the Universities of Heidelberg, Hamburg, and Munich. He completed his PhD in 1969 under the supervision of R. Huisgen and then worked at BASF. In 1971, he joined the group of C. Rüchardt and completed his habilitation at the University of Freiburg in 1976. A year later, Giese accepted a position at the Technical University of Darmstadt and remained there for 12 years before taking up his current position as Professor at the University of Basel.

### Carl Duisberg Award to M.-J. Crawford

The Carl Duisberg Memorial Award is awarded annually by the GDCh to young chemists who have completed their habilitation and excelled in their original research. The award in 2006 will be presented to Margaret-Jane Crawford (Ludwig-Maximilians-Universität, Munich, LMU) at the congress in Hamburg. She receives the prize for her work on the chemistry of uranium. During her habilitation, she studied uranium halides and pseudohalides as well as dioxouranium dihalides. She recently reported on $UN_{21}^{3-}$, a binary actinide heptaazide anion, in *Angewandte Chemie*.[2]



M.-J. Crawford

Crawford studied chemistry at the University of Glasgow and completed her PhD at the LMU with T. M. Klapötke on small, highly reactive molecules such as azide, pseudohalides, and fluorinated compounds. Following a postdoctoral stay at the University of New Brunswick in Canada she returned to the LMU, where she completed her habilitation in 2005 on preparative uranium chemistry.

### ADUC Awards for Young Chemists

The Arbeitsgemeinschaft Deutscher Universitätprofessoren für Chemie (ADUC, Association of German University Professors of Chemistry) annually awards prizes to outstanding young chemists. At the congress in Hamburg, the prizes for 2006 will be presented to:

- **Jörn Schmedt auf der Günne** (LMU Munich) for his work on amorphous solids such as poly(carbonsuboxide),[3]
- **Bernd F. Straub** (LMU Munich) for the rational design of transition-metal catalysts, such as highly efficient reagents for bromine/magnesium exchange,[4] based on theoretical investigations, and
- **Stefan Hecht** (Max Planck Institute for Coal Research, Mülheim/Ruhr) for studies on helical folding and photoswitchable peptides as well as functionalized self-organized nanostructures. He recently reported a prototype of a photoswitchable foldamer in *Angewandte Chemie*.[5]

### Klaus Grohe Prize 2006: Call for Nominations

The Klaus Grohe Foundation, administered by the GDCh, awards the Klaus Grohe Prize to outstanding young scientists (postgraduate students as well as postdoctoral researchers up to three years after completion of their doctorate) working in the field of medicinal chemistry and drug discovery at European research centers. This year, two prizes, each worth €2000, will be presented at the 124th Assembly of the Society of German Researchers and Physicians (GDNÄ), which will take place in Bremen, Germany, in September. The prizewinners will present a lecture on their area of research.

Proposals should include a letter of nomination (personal applications are welcome), curriculum vitae, and a list of publications. Please send applications to: Gesellschaft Deutscher Chemiker, Awards and International Affairs, P.O. Box 900440, 60444 Frankfurt am Main, Germany. The deadline for applications is May 31, 2006.


[1] a) B. Giese, *Angew. Chem.* **1983**, *95*, 771; *Angew. Chem. Int. Ed. Engl.* **1983**, *22*, 753; b) D. P. Curran, N. A. Porter, B. Giese, *Stereochemistry of Radical Reactions*, VCH, Weinheim, **1996**; c) B. Giese, M. Napp, O. Jacques, H. Boudebous, A. M. Taylor, J. Wirz, *Angew. Chem.* **2005**, *117*, 4141; *Angew. Chem. Int. Ed.* **2005**, *44*, 4073.

[2] M.-J. Crawford, A. Ellern, P. Mayer, *Angew. Chem.* **2005**, *117*, 8086; *Angew. Chem. Int. Ed.* **2005**, *45*, 7874.

[3] J. Schmedt auf der Günne, J. Beck, W. Hoffbauer, P. Krieger-Beck, *Chem. Eur. J.* **2005**, *11*, 4429.

[4] A. Krasovskiy, B. F. Straub, P. Knochel, *Angew. Chem.* **2006**, *118*, 165; *Angew. Chem. Int. Ed.* **2006**, *45*, 159.

[5] A. Khan, C. Kaiser, S. Hecht, *Angew. Chem.* **2006**, *118*, 1912; *Angew. Chem. Int. Ed.* **2006**, *45*, 1878.


DOI: 10.1002/anie.200600601


WILEY InterScience DISCOVER SOMETHING GREAT
© 2006 Wiley-VCH Verlag GmbH & Co. KGaA, Weinheim

Chemical Evolution

DOI: 10.1002/anie.200504053

# Aldol Reactions within the RNA World**

*Magnus Rueping**

**Keywords:**
aldol reactions · DNA templates · ribozymes · RNA

The aldol reaction is one of the most important transformations in chemistry and biology. In this reaction a new carbon–carbon bond is formed with concomitant generation of up to two adjacent stereocenters. Hence, the aldol reaction has often been utilized in the construction of essential synthetic building blocks and in the assembly of fragments in the chemical and biological syntheses of complex natural and unnatural products. Numerous methods for diastereo- and enantioselective aldol reactions have been developed, employing, for example, chiral enolates or aldehydes, stoichiometric amounts of chiral additives, and chiral metal-based or metal-free catalysts.[1] In addition, highly selective aldol reactions have been performed with biochemical catalysts such as antibodies and aldolases.[1f,g,2]

In nature, two types of aldolases have been identified and classified according to their reaction mechanism.[3] Class I aldolases, primarily found in mammals and higher plants, activate the donor by forming a Schiff base, which subsequently adds to the acceptor. In contrast, Class II aldolases, found in fungi and bacteria, utilize divalent metal ions as a co-factor which acts as a Lewis acid in the active site.

Despite the wealth of aldol processes reported, two novel approaches have been unveiled, introducing fundamentally new aspects to this reaction type. Joyce and co-workers disclosed a new template-assisted cross-aldol reaction,[4] and Famulok and co-workers discovered the first ribozyme (RNA enzyme) that effectively catalyzes an aldol reaction.[5]

Ribozymes are believed to be part of the evolution of life on earth. It is thought that RNA may have served as both genetic material and the primary enzyme, a hypothesis that is referred to as the "RNA world".[6] In support of this hypothesis a number of ribozymes have been identified that catalyze biologically important chemical reactions—for example, nucleotide synthesis,[7] peptide-bond formation and cleavage,[8] amino acid transfer,[9] Michael reactions,[10] porphyrin metalations,[11] alkylations,[12] redox reactions,[13] and RNA polymerizations[14]—reactions that are indispensable for the development of life.

However, until recently one of the most fundamental reactions in living cells, the aldol reaction, essential for glycolysis, sugar metabolism, and other metabolic pathways, was missing from the list of RNA-catalyzed reactions. Now, Famulok and co-workers have succeeded in finding a ribozyme that catalyzes this important reaction.[15] The authors applied a selection–amplification procedure to identify a ribozyme in an RNA library consisting of $2\times10^{15}$ different sequences. To do so, each member of the library was linked at the 5′-terminus to a levulinic amide aldol donor by means of a photocleavable tag to allow facile characterization of the separated riboyzme after successful aldol reaction (Scheme 1). The acceptor aldehyde was biotinylated so that the RNA aldol product could be separated easily by chromatography on streptavidine agarose gel. The search starting with a pool $2\times10^{15}$ RNAs resulted in one ribozyme that catalyzed the aldol reaction about 4300 times faster than the uncatalyzed background reaction (Scheme 2).

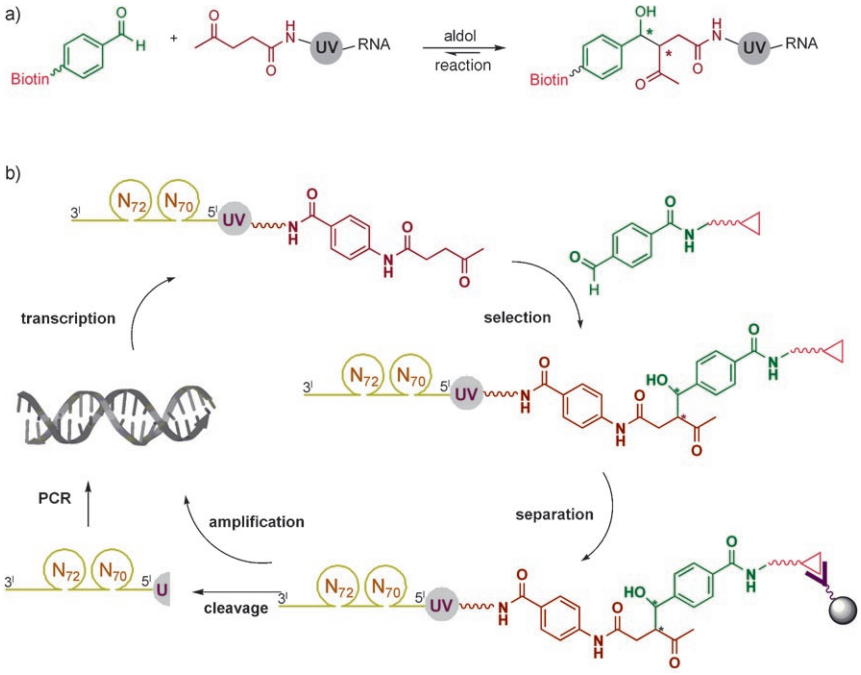
One requirement for this ribozyme to catalyze the aldol reaction, in accordance with contemporary class II aldolases, is the use of $Zn^{2+}$ ions. Without this cofactor no reaction occurred, imposing the general question whether the $Zn^{2+}$ acts as a Lewis acid to activate the aldol donor in aldolase ribozymes or whether it is needed for folding and stability of the ribozyme structure. Additionally one might wonder if any ribozymes exist, or previously existed, that are similar to class I aldolases requiring amine cofactors, and if such ribozymes were able to catalyze the aldol and retro-aldol reactions essential for carbohydrate metabolism.

This raises similarities to the template-assisted aldol reaction reported by Joyce and co-workers. In their work the authors describe the first DNA-templated cross-aldol reaction as a model for the formation of the pentose sugar ribose in the RNA world. Ribose is the substantial component of RNA and can be obtained by the formose reaction, the condensation of formaldehyde under alkaline conditions.[16] However, the amount of ribose thus obtained, among a complex mixture of other $C_3$, $C_4$, $C_5$, and $C_6$ sugar derivatives, is only about 1%.[17] Therefore, it has been speculated that there might be other abiotic pathways to ribose, and indeed several laboratories have described conditions that lead to increased yields of ribose derivatives, such as ribose-2,4-diphosphate.[18]

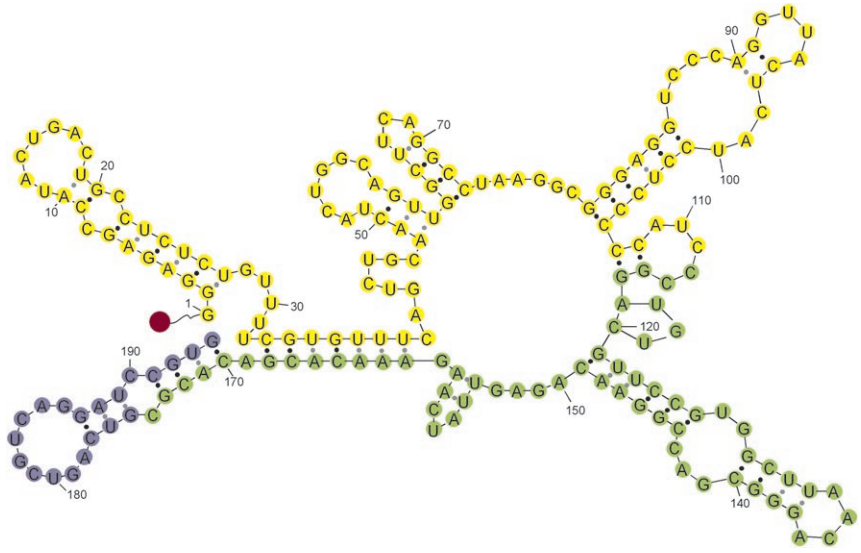
[*] Prof. Dr. M. Rueping
Degussa Endowed Professorship
Institute for Organic Chemistry und Chemical Biology
Johann Wolfgang Goethe University Frankfurt am Main
Marie-Curie-Strasse 11
60439 Frankfurt am Main (Germany)
Fax: (+49) 69-798-29248
E-mail: m.rueping@chemie.uni-frankfurt.de

[**] The author thanks Degussa for generous funding, Prof. Dr. Gerhard Quinkert for stimulating discussions, and the chemistry faculty in Frankfurt for their warm welcome.


InterScience
© 2006 Wiley-VCH Verlag GmbH & Co. KGaA, Weinheim




***Scheme 1.*** a) Aldol reaction of a biotinylated aldehyde with a levulinic amide aldol donor attached to a photocleavable linker and the ribozyme. b) Selection of the aldolase ribozyme from an RNA pool of $2\times10^{15}$ molecules with randomized regions of 70 and 72 nucleotides was achieved by reaction of the modified RNA sequences with a biotinylated aldehyde and subsequent separation of the aldol product by affinity chromatography on streptavidin agarose gel. Upon UV irradiation the biotin tag was cleaved to afford the desired sequences, which were then subjected to polymerase chain reaction with reverse transcriptase (RT-PCR). Alternatively, RT-PCR was performed directly with immobilized sequences. After 11 selection cycles the most abundant and active sequence was isolated and examined further.



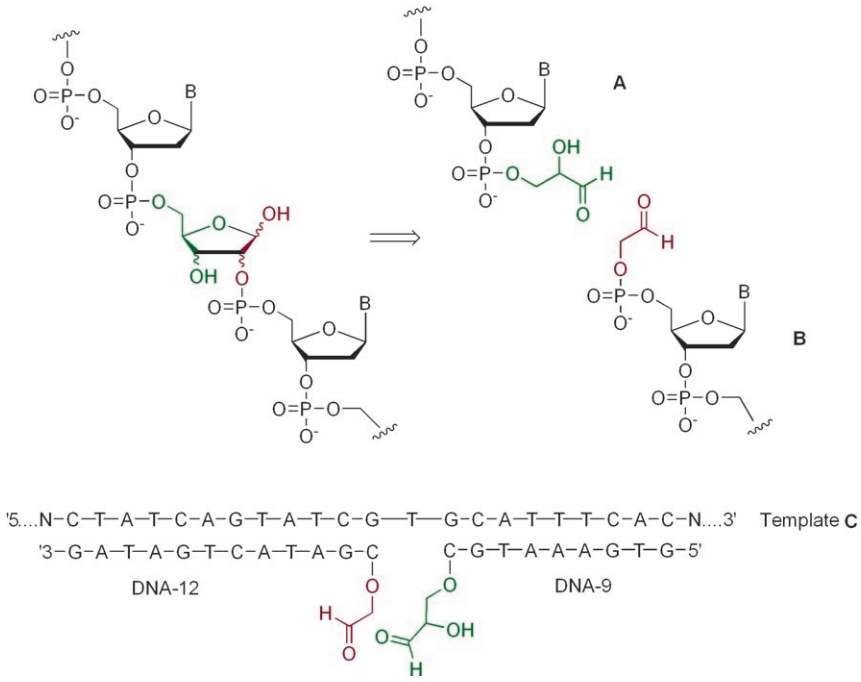
***Scheme 2.*** Proposed secondary structure of the aldolase ribozyme based on data from enzyme studies. The sequence requirement for aldolase activity was obtained by stepwise truncation of the RNA. The nucleotides in yellow are essential for catalytic activity and probably contain the active site, while the nucleotides in blue are irrelevant for catalysis. Truncation of the nucleotides in green from the 3′ end reduce the activity; they are believed to function as the stabilizing element of the aldolase ribozyme.

Joyce and co-workers, attracted by the question of how ribose, which is generally unstable especially when activated, may have been formed in an RNA world, now report a conceptually new approach (Scheme 3). They linked the two aldehydes needed for pentose formation, glyceraldehyde and glycoaldehyde, to two oligonucleotides in such a way that they obtained 5′-glyceryl-DNA and 3′-glycoaldehyde-DNA derivatives, respectively. The modified oligonucleotides were then combined with a complementary DNA template which was recognized by Watson–Crick base pairing.[19] This template was designed in such a way that the two aldehydes were aligned with the optimal orientation for the aldol reaction to occur. Furthermore, the template effect was thought to support the cross-aldol reaction by increasing the effective concentration and suppressing undesired side reactions. By employing this elegant approach, successful cross-aldol reactions were observed at mildly alkaline pH and ambient temperature. No reaction occurred in the absence of the template. Interestingly, reactions performed in the presence of various amine co-factors increased the reaction rate significantly, suggesting an aldolase class I mechanism.

The DNA-templated aldol reaction represents an attractive approach to the construction of pentose sugars, but it can only be seen as a debatable model, because in the RNA world no DNA template would have existed. Hence, if pentose would have been synthesized in a templated fashion, the question arises what such a template would have looked like and how it would have evolved.

The results of the template-assisted pentose synthesis and the newly discovered aldolase ribozyme bring important insights into the viability of sugar, especially ribose, synthesis with regard to the proposed RNA world. Naturally, we will never be able to know if the RNA world ever existed, but suggestions of this kind challenge scientists to think more generally about chemical transformations within the RNA-world scenario and generate experiments to test their ideas. As in any good research project the results presented pose more questions than deliver answers. Questions whether ribozymes are actually able to catalyze

 © 2006 Wiley-VCH Verlag GmbH & Co. KGaA, Weinheim 




***Scheme 3.*** Cross-aldol reaction of a 5′-glyceryl-DNA conjugate **A** and a 3′-glycoaldehyde-DNA derivative **B** on the utilized standard template **C.** Successful reactions were performed in mildly alkaline (pH 8.5) solutions or in the presence of various amine co-factors.

complex aldol and related carbonyl reactions and the role co-factors play might be answered in the near future. Further questions, such as whether it is possible to construct a self-replicating artificial system resembling the RNA world, are more difficult to answer. Thus, there are still many gaps to be filled with regard to both the development and evolution of the RNA world and the progress towards contemporary biology.


[1] Selected reviews: a) T. Mukaiyama, *Org. React.* **1982**, *28*, 203; b) C. H. Heathcock in *Asymmetric Synthesis, Vol. 3* (Ed. J. D. Morrison), Academic Press, New York, **1984**, chap. 2; c) D. A. Evans, J. V. Nelson, T. R. Taber, *Top. Stereochem.* **1982**, 13, 1; d) S. Masamune, W. Choy, J. S. Petersen, L. R. Sita, *Angew. Chem.* **1985**, *97*, 1; *Angew. Chem. Int. Ed. Engl.* **1985**, *24*, 1; e) E. M. Carreira in *Catalytic Asymmetric Synthesis, 2nd ed.* (Ed.: I. Ojima), Wiley-VCH, New York, **2000**; f) T. D. Machajewski, C.-H. Wong, *Angew. Chem.* **2000**, *112*, 1406; *Angew. Chem. Int. Ed.* **2000**, *39*, 1352; g) *Modern Aldol Reactions* (Ed.: R. Mahrwald), Wiley-VCH, Weinheim, **2004**.

[2] a) P. G. Schultz, J. Yin, R. A. Lerner, *Angew. Chem.* **2002**, *114*, 4607; *Angew. Chem. Int. Ed.* **2002**, *41*, 4427; b) M. G. Silvestri, G. Desantis, M. Mitchell, C. H. Wong, *Top. Stereochem.* **2003**, *23*, 267.

[3] a) B. L. Horecker, O. Tsolas, C. Y Lai in *The Enzymes, Vol. VII* (Ed.: P. D. Boyer), Academic Press, New York, **1972**, pp. 213–258; b) W.-D. Fessner, A. Schneider, H. Held, G. Sinerius, C. Walter, M. Hixon, J. V. Schloss, *Angew. Chem.* **1996**, *108*, 2366; *Angew. Chem. Int. Ed. Engl.* **1996**, *35*, 2219.

[4] M. Oberhuber, G. F. Joyce, *Angew. Chem.* **2005**, *117*, 7752; *Angew. Chem. Int. Ed.* **2005**, *44*, 7580.

[5] S. Fusz, A. Eisenführ, S. G. Srivatsan, A. Heckel, M. Famulok, *Chem. Biol.* **2005**, *12*, 941.

[6] *The RNA World, 2nd ed.* (Eds.: R. F. Gesteland, T. R. Cech, J. F. Atkins), Cold Spring Harbor Press, Cold Spring Harbor, **1999**.

[7] P. J. Unrau, D. P. Bartel, *Nature* **1998**, *395*, 260.

[8] a) B. Zhang, T. R. Cech, *Nature* **1997**, *390*, 96; b) X. Dai, A. De Mesmaeker, G. F. Joyce, *Science* **1995**, *267*, 237.

[9] a) P. A. Lohse, J. W. Szostak, *Nature* **1996**, *381*, 442; b) A. Jenne, M. Famulok, *Chem. Biol.* **1998**, *5*, 23.

[10] G. Sengle, A. Eisenführ, P. S. Arora, J. S. Nowick, M. Famulok, *Chem. Biol.* **2001**, *8*, 459.

[11] a) M. M. Conn, J. R. Prudent, P. G. Schultz, *J. Am. Chem. Soc.* **1996**, *118*, 7012; b) Y. Li, D. Sen, *Nat. Struct. Biol.* **1996**, *3*, 743.

[12] a) C. Wilson, J. W. Szostak, *Nature* **1995**, *374*, 777; b) M. Wecker, D. Smith, L. Gold, *RNA* **1996**, *2*, 982.

[13] a) S. Tsukiji, S. B. Pattnaik, H. Suga, *Nat. Struct. Biol.* **2003**, *10*, 713; b) S. Tsukiji, S. B. Pattnaik, H. Suga, *J. Am. Chem. Soc.* **2004**, *126*, 5044.

[14] W. K. Johnston, P. J. Unrau, M. S. Lawrence, M. E. Glasner, D. P. Bartel, *Science* **2001**, *292*, 1319.

[15] For Ribozyme catalyzed Diels-Alder reactions, see: a) T. M. Tarasow, S. L. Tarasow, B. E. Eaton, *Nature* **1997**, *389*, 54; b) B. Seelig, A. Jäschke, *Chem. Biol.* **1999**, *6*, 167.

[16] a) A. Butlerow, *Justus Liebigs Ann. Chem.* **1861**, *120*, 295; b) O. Loew, *J. Prakt. Chem.* **1886**, *33*, 321; c) E. Fischer, *Ber. Dtsch. Chem. Ges.* **1888**, *21*, 988.

[17] P. Decker, H. Schweer, R. Pohlman, *J. Chromatogr.* **1982**, *244*, 281.

[18] a) D. Müller, S. Pitsch, A. Kittaka, E. Wagner, C. E. Wintner, A. Eschenmoser, *Helv. Chim. Acta* **1990**, *73*, 1410; b) S. Pitsch, A. Eschenmoser, B. Gedulin, S. Hui, G. Arrhenius, *Origins Life Evol. Biosphere* **1995**, *25*, 297; c) G. Zubay, *Origins Life Evol. Biosphere* **1998**, *28*, 13; d) A. Ricardo, M. A. Carrigan, A. N. Olcott, S. A. Benner, *Science* **2004**, *303*, 196.

[19] For a review on DNA-templated synthesis, see: X. Li, D. R. Liu, *Angew. Chem.* **2004**, *116*, 4956; *Angew. Chem. Int. Ed.* **2004**, *43*, 4848; For a DNA-templated nitroaldol reaction, see: Z. J. Gartner, M. W. Kanan, D. R. Liu, *Angew. Chem.* **2002**, *114*, 1874; *Angew. Chem. Int. Ed.* **2002**, *41*, 1796.


 © 2006 Wiley-VCH Verlag GmbH & Co. KGaA, Weinheim 

Protein Modification

DOI: 10.1002/anie.200504352

# Transition-Metal Catalysis as a Tool for the Covalent Labeling of Proteins

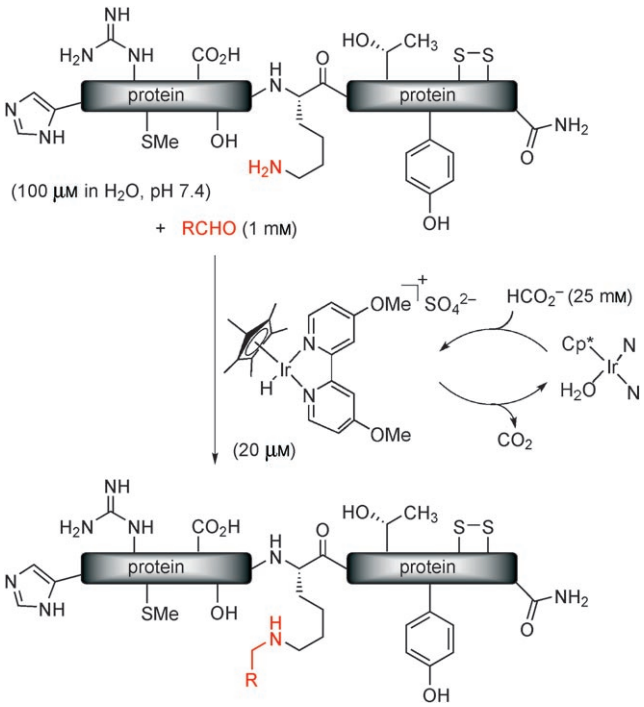
*Jan H. van Maarseveen,* Joost N. H. Reek, and Jaap Willem Back*

**Keywords:**
bioconjugation · protein modifications · transition metals

Chemical approaches that facilitate the analysis and comprehension of complex biological processes play a central role in the emerging field of chemical biology. Selective covalent labeling for tracking biomolecules in complex mixtures is a well-established technique that clearly illustrates the importance of chemistry for biology. However, the mild and selective chemical modification of complex biomolecules such as proteins under physiological conditions remains a huge challenge that underscores the urgent need for new biocompatible reactions.[1] The modification of proteins may take place at specific chemically reactive but metabolically stable nonproteogenic moieties (for example, azides, alkynes, or ketones)[2] that have been introduced by the natural biosynthetic pathway or at reactive moieties present in native proteins.[3] Modifications of the side chains of all the amino acids containing functional groups in proteins have been described; however, the selectivity varies tremendously.

Lysine residues are predominantly present at the periphery of proteins and their accessibility makes them ultimately suitable for functionalization. An example of lysine modification is the use of reductive amination as a technique for the introduction of an array of functionalities and labels at the ε-amino groups whilst retaining the positive charge at a physiological pH value.[4] Primary amines are converted into imines after condensation with aldehydes, which can in turn be converted into stable secondary amines by reduction. Classically, reduction is achieved with high doses of harsh agents such as $NaBH_4$, $NaBH_3CN$, and boranes. A common feature of these reagents is that they are water-sensitive and do not react optimally within the physiological pH range. Moreover, cleavage of disulfide bonds within the proteins may occur in the presence of an excess of reductive agents.

Recently, an iridium-catalyzed hydrogenation protocol was developed by McFarland and Francis for the reductive amination of lysine residues in proteins (Scheme 1).[5] It was found that the electron-rich water-stable complex $[Cp^*Ir(bipy)(H_2O)]SO_4$ ($Cp^* = C_5Me_5$, bipy = 4,4′-dimethoxy-2,2′-bipyridyl) can be transformed into an Ir-H species by using formate as the hydride source. This Ir-H complex is able to reduce imines derived from lysine residues and




***Scheme 1.*** Reductive alkylation of lysine residues by Ir-catalyzed transfer hydrogenation.

[*] Dr. J. H. van Maarseveen,
Prof. Dr. J. N. H. Reek
Van't Hoff Institute for Molecular Sciences
University of Amsterdam
Nieuwe Achtergracht 129
1018 WS Amsterdam
(The Netherlands)
Fax: (+31) 20-525-5670
E-mail: jvm@science.uva.nl
Dr. J. W. Back
Swammerdam Institute of Life Sciences
(Mass Spectrometry group)
University of Amsterdam
Nieuwe Achtergracht 166
1018 WV Amsterdam
(The Netherlands)


© 2006 Wiley-VCH Verlag GmbH & Co. KGaA, Weinheim

several aliphatic and aromatic aldehydes. The new method, in which reduction equivalents (hydrides) are supplied from a metal catalyst that is replenished by a source of formiate, improves on the classical approach, in that the water compatibility of all the components is ensured and the reaction proceeds well at ambient temperature at the physiological pH value of 7.4.

It should be noted, however, that the reactions are still not complete after one day, whereas the classical reductive agents take minutes to a few hours for near-complete conversions. The Ir-catalyzed reductive amination has been tested in several model proteins that contain disulfide bonds (for example, lysozyme, RNAse) and showed no sign of unwanted cleavage of the S–S bonds. To prove the generality of the approach, it needs to be demonstrated that the more-sensitive disulfide-containing proteins also survive this relatively mild treatment. As shown by the authors, an important application of this reaction may be the coupling of proteins in a straightforward manner with polyethyleneglycol for therapeutic or biotechnological purposes.[6] However, the conjugation of aldehydes to complex biomacromolecules may in general give rise to several side products,[7] thus causing significant heterogeneity.

Another recent example of the transition-metal-catalyzed transformation of proteins reported by Antos and Francis is the selective modification of tryptophan residues by a water-compatible rhodium carbene (Scheme 2).[8] Myoglobin, which possesses two tryptophan residues, was doubly modified, and MS/MS analysis of a tryptic digest did not reveal any unwanted modifications. The low abundancy of tryptophan in proteins relative to lysine means that organic probes of the rhodium carbene type are expected to lead to a much more selective modification.

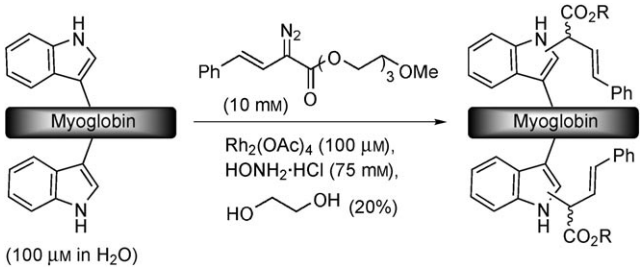
Now that the applicability of transition-metal catalysis has been proven in the field of protein modification by these excellent examples, one might want to speculate on the potential of other metal-catalyzed processes. A prerequisite for the transition-metal catalyst is that it should be sufficiently active and selective under conditions typically used in biochemistry.[9] The best catalyst candidates should indeed work in an aqueous environment and should be highly tolerant of different functional groups.

The huge research efforts towards generating more environmentally friendly catalytic processes have shown that many transition-metal catalysts can indeed be translated to water-soluble analogues.[10] The greatest challenges in the development of these aqueous-phase processes are not related to catalyst activity, but rather to limitations in the solubility of the organic substrates. Functional-group tolerance is also not necessarily a problem, since many transition-metal catalysts that can be used in organic synthesis have been designed to be so.[11] Therefore, several transition-metal-catalyzed coupling reactions are anticipated to be suitable for the selective modification of proteins.

In the literature there are several examples in which transition-metal catalysts are used in conjunction with biomolecules; however, these generally involve chemo-enzymatic dynamic kinetic resolution.[12] In these processes the metal center is generally used as a racemization catalyst and the enzyme is used for asymmetric functionalization, for example, acetylation of one of the enantiomeric forms of an alcohol. Various metal complexes have been used for dynamic kinetic resolution, and various mechanisms are operative under mild conditions. For example, palladium catalysts have been used that racemize through the formation of π-allylpalladium intermediates.[13] Interestingly, the same intermediate is formed in allylic substitution reactions, in which nucleophilic attack at the π-allylpalladium intermediate generates substituted products. It is therefore reasonable to assume that proteins can be functionalized by appropriate π-allylpalladium complexes, thus leading to amination of lysine residues or etherification of serine, threonine, or tyrosine residues.[16] In such approaches, the residue selectivity should be directed by the catalyst.

The Hartwig–Buchwald amination of aryl halides is also an interesting reaction that deserves further exploration in this area.[14] Proper choice of the catalyst can lead to selective arylation of lysine-derived amines that, similarly to the Ir-catalyzed reductive amination protocol or allylic alkylation, should retain their basic character after substitution (although to a lesser extent). The challenge for these novel metal-catalyzed substitution reactions constitutes the development of biocompatible conditions, of which the base required for these reactions will be the biggest obstacle.

It should be underscored, however, that the intrinsic main problem of native protein bioconjugation is to control the extent of functionalization of specific reactive moieties. This is also apparent from the Ir-catalyzed functionalization of lysine residues, which provides mixtures of proteins with several levels of modification (for example, of the six lysine residues present in lysozyme, four were modified at maximum). A partial solution to this problem is the selective modification of low-abundant amino acids such as tryptophan. We envision that bioconjugation mediated by transition-metal catalysis of appropriate non-natural amino acid residues (for example, *para*-iodophenylalanine) that have been introduced during the natural biosynthesis remains the most promising strategy.[2] Transition-metal-catalyzed reactions that seem ultimately suited for bioconjugation by functionalization of *para*-iodophenylalanine are the Buchwald–Hartwig amination,[14] as well




***Scheme 2.*** Selective labeling of tryptophan with a rhodium carbene.

 © 2006 Wiley-VCH Verlag GmbH & Co. KGaA, Weinheim 

as Heck, Sonogashira, and Suzuki coupling reactions.[15]

Overall it is clear that the iridium-catalyzed reductive amination protocol for lysine residues in proteins and the modification of tryptophan residues by rhodium carbenes as developed by Antos and Francis shows the potential of transition-metal catalysis in chemical biology research.

Published online: February 22, 2006


[1] J. A. Prescher, C. R. Bertozzi, *Nat. Chem. Biol.* **2005**, *1*, 13.

[2] a) J. H. van Maarseveen, J. W. Back, *Angew. Chem.* **2003**, *115*, 6106; *Angew. Chem. Int. Ed.* **2003**, *42*, 5926; b) M. E. Hahn, T. W. Muir, *Trends Biochem. Sci.* **2005**, *30*, 26; c) L. Wang, P. G. Schultz, *Angew. Chem.* **2005**, *117*, 34; *Angew. Chem. Int. Ed.* **2005**, *44*, 34; d) N. Budisa, *Angew. Chem.* **2004**, *116*, 6586; *Angew. Chem. Int. Ed.* **2004**, *43*, 6426.

[3] a) *Chemistry of Protein Conjugation and Cross-Linking* (Ed.: S. S. Wong), CRC, Boca Raton, FL, **1991**; b) *Bioconjugate techniques* (Ed.: G. T. Hermanson), 1st ed., Academic Press, San Diego, **1996**.

[4] G. E. Means, R. E. Feeney, *Anal. Biochem.* **1995**, *224*, 1.

[5] J. M. McFarland, M. B. Francis, *J. Am. Chem. Soc.* **2005**, *127*, 13490.

[6] a) M. J. Roberts, M. D. Bentley, J. M. Harris, *Adv. Drug Delivery Rev.* **2002**, *54*, 459; b) F. M. Veronese, G. Pasut, *Drug Discovery Today* **2005**, *10*, 1451.

[7] B. Metz, G. F. A. Kersten, P. Hoogerhout, H. F. Brugghe, H. A. M. Timmermans, W. E. Hennink, D. J. A. Crommelin, W. Jiskoot, A. De Jong, H. Meiring, J. Ten Hove, *J. Biol. Chem.* **2004**, *279*, 6235.

[8] J. M. Antos, M. B. Francis, *J. Am. Chem. Soc.* **2004**, *126*, 10256.

[9] a) *Aqueous-Phase Organometallic catalysis: Concepts and applications*, 2nd ed. (Eds.: B. Cornils, W. A. Herrmann), Wiley-VCH, Weinheim, **2004**; b) K. H. Shaughnessy, R. B. DeVasher, *Curr. Org. Chem.* **2005**, *9*, 585.

[10] *Multiphase Homogeneous Catalysis* (Ed.: B. Cornils), Wiley-VCH, Weinheim, **2005**.

[11] a) K. C. Nicolaou, P. C. Bulger, D. Sarlah, *Angew. Chem.* **2005**, *117*, 4516; *Angew. Chem. Int. Ed.* **2005**, *44*, 4442; b) K. C. Nicolaou, P. C. Bulger, D. Sarlah, *Angew. Chem.* **2005**, *117*, 4564; *Angew. Chem. Int. Ed.* **2005**, *44*, 4490.

[12] For an overview see: O. Pàmies, J.-E. Bäckvall, *Chem. Rev.* **2003**, *103*, 3247.

[13] a) J. V. Allen, J. M. J. Williams, *Tetrahedron Lett.* **1996**, *37*, 1859; b) J. H. Suh, D. Lee, I. T. Lim, J. Y. Junq, M. J. Kim, *J. Org. Chem.* **1999**, *64*, 8423.

[14] Z. Lu, R. J. Twieg, *Tetrahedron Lett.* **2005**, *46*, 2997.

[15] a) K. W. Anderson, S. L. Buchwald, *Angew. Chem.* **2005**, *117*, 6329; *Angew. Chem. Int. Ed.* **2005**, *44*, 6173; b) L. R. Moore, K. H. Shaughnessy, *Org. Lett.* **2004**, *6*, 225; c) M. Dai, C. Wang, J. Chen, Z. Yang, *Org. Lett.* **2004**, *6*, 221.

[16] Note added in proof: A study has been published on the alkylation of tyrosine residues by π-arylpalladium complexes; see S. D. Tilley, M. B. Francis, *J. Am. Chem. Soc.* **2006**, *128*, 1080.



© 2006 Wiley-VCH Verlag GmbH & Co. KGaA, Weinheim

DOI: 10.1002/anie.200503273

Reaction Kinetics

# The Reactivity–Selectivity Principle: An Imperishable Myth in Organic Chemistry**

*Herbert Mayr* and Armin R. Ofial*

**Keywords:**
frontier-orbital effect · Hammond effect · intrinsic barriers · linear free energy relationships · reaction kinetics

*Dedicated to Professor Jürgen Sauer on the occasion of his 75th birthday*

*The reactivity–selectivity principle (RSP), once a tenet of organic chemistry, eroded during the 1970s and was more or less abandoned by 1980. Although it has been clear for more than 25 years that a decrease in selectivity with increasing reactivity can only be expected with certainty if diffusion control is approached, the RSP has survived as an intuitively appealing rule. This Minireview shows why selectivity cannot generally decrease with increasing reactivity and highlights the weaknesses of the theoretical foundations of the RSP.*

## 1. Introduction

Dozens of reviews on the reactivity–selectivity principle (RSP) have been published during the past three decades,[1] most of which agree in the conclusion that one cannot generally expect a decrease in selectivity with increasing reactivity.[2–14] Twenty-five years ago, Arnett summarized:

"The RSP seems to be such a reasonable proposition that there have been a number of attempts to justify it on more or less theoretical grounds and to relate it to the Hammond postulate. However, as the RSP has been subjected to increasing scrutiny, its credibility has eroded steadily. It now seems plain that, *although the concept of the principle is attractive, it is virtually useless in practice as a general rule* since the number of times it does not work is approaching the number of times that it does".[7b]

Since we are in full consent with this statement, the question arises, why another overview?

In spring 2005, the senior author presented an analysis of reactivity–selectivity relationships as part of a lecture "Mythology in Organic Chemistry" at several universities. The succeeding discussions revealed that a majority of chemists still consider the decrease in selectivity with increasing reactivity as a rule, and violations of the RSP as rare exceptions that are only encountered in some special cases.[15–17] We believe that the kinetics of electrophile–nucleophile combinations that we have studied in recent years are ideally suited to correct this view and to clarify why the RSP can only hold in a narrow range. This Minireview highlights some milestones in the rise and the fall of the reactivity–selectivity principle, presents some recent reactivity–selectivity relationships, and concludes with a simple geometrical argument as to why it is impossible that selectivity generally decreases with increasing reactivity.

## 2. Experimental Facts

Typically, the chemistry student first encounters the inverse relationship between reactivity and selectivity when studying the selectivities of radical-initiated halogenations of alkanes. The different selectivities of chlorinations and brominations (Figure 1) can be rationalized by the late, productlike, transition states of hydrogen abstraction by the bromine radical and the early, reactantlike, transition states of hydrogen abstractions by the chlorine radical. The low activation barriers for the hydrogen abstractions by Cl$^{\bullet}$, which are shown in Figure 1, have been determined experimentally.[20]

As fast kinetic methods were not readily available in the 1960s and 1970s, much information about the relative stabilities of reactive intermediates was derived from studies of selectivities under the assumption that low selectivity is generally associated with high reactivity. Investigations by Sneen and co-workers[21] on the selectivities of solvolytically generated carbocations were systematically extended by Raber, Harris, Hall, and Schleyer and seemed to confirm

[*] Prof. Dr. H. Mayr, Dr. A. R. Ofial
Department Chemie und Biochemie
Ludwig-Maximilians-Universität München
Butenandtstrasse 5–13 (Haus F), 81377 München (Germany)
Fax: (+49) 89-2180-77717
E-mail: herbert.mayr@cup.uni-muenchen.de

[**] We thank the Deutsche Forschungsgemeinschaft and the Fonds der Chemischen Industrie for financial support of this work.



InterScience

© 2006 Wiley-VCH Verlag GmbH & Co. KGaA, Weinheim

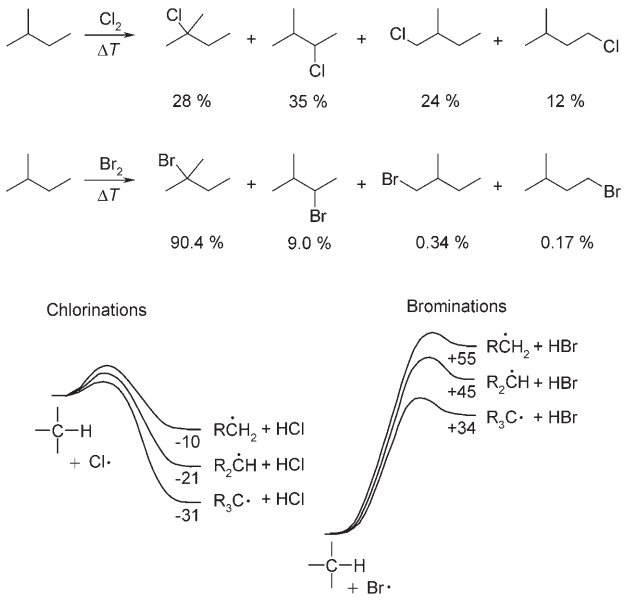



***Figure 1.*** Product ratios[18] for the chlorination and bromination of 2-methylbutane and calculated reaction enthalpies ($\Delta_r H$ in [kJ mol$^{-1}$][19]).

the RSP:[22] When alkyl chlorides were solvolyzed in solutions of sodium azide in aqueous acetone (80%), highly stabilized carbocations, such as the tritylium ion, which are formed rapidly in $S_N1$ reactions, show high selectivities, whereas less-stabilized, more-reactive carbocations, such as the adamantyl cations, which are formed slowly in the solvolysis reactions, show low selectivities (Figure 2).

Only one year later, Ritchie reported a fundamentally different behavior in the reactions of stabilized carbocations and diazonium ions with nucleophiles (Figure 3).[23] More-reactive electrophiles showed the same selectivities as less-reactive electrophiles, leading Ritchie to the formulation of electrophile-independent nucleophilicity parameters $N_+$ and nucleophile-independent electrophilicity parameters log $k_0$ [Eq. (1)].

$$\log (k/k_0) = N_+ \qquad (1)$$

As this finding was in sharp contrast to the reactivity–selectivity principle, which had been considered as a fundamental law, a direct consequence of allegedly "basic principles", that is, of the Bell–Evans–Polanyi principle and the Leffler–Hammond relationship (see Section 3), numerous attempts were made to explain why Ritchie's carbocations did not follow the general rule.[15–17,24] Better solvation of the less-stabilized carbocations was considered as one of the reasons for the unexpected behavior shown in Figure 3.[25]

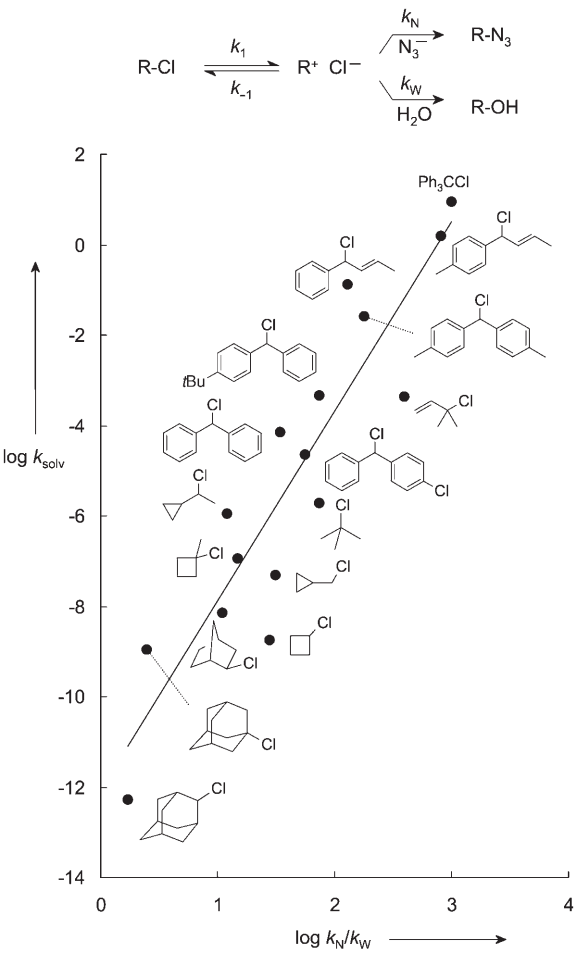
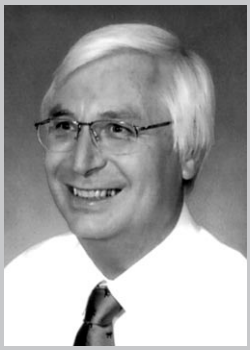



***Figure 2.*** Stability–selectivity ($N_3^-/H_2O$) plot for carbocations derived from solvolysis of alkyl chlorides (25 °C, 80% aqueous acetone, data from reference [22]).



*Herbert Mayr obtained his PhD in 1974 (R. Huisgen; LMU München), and after post-doctoral studies (G. A. Olah; Cleveland), he completed his habilitation in 1980 (P. von R. Schleyer; Erlangen). After professorships in Lübeck and Darmstadt he returned to the LMU München in 1996. In 2003 he became a member of the Bavarian Academy of Sciences. He received the Alexander von Humboldt Honorary Fellowship of the Foundation for Polish Science (2004) and the Liebig Denkmünze (GDCh, 2006). His interests include quantitative approaches to organic reactivity and the theory of polar organic reactions.*



*Armin R. Ofial studied chemistry at the TU Darmstadt with Alarich Weiss and Herbert Mayr (doctoral degree, 1996). Since 1997 he has been a Research Associate at the LMU München. In 2005 he received a postdoctoral fellowship of the Japan Society for the Promotion of Science for a research stay in the group of Shunichi Fukuzumi (Osaka, Japan). His research interests include reactions of iminium ions, electron-transfer processes, and chemical kinetics.*


© 2006 Wiley-VCH Verlag GmbH & Co. KGaA, Weinheim

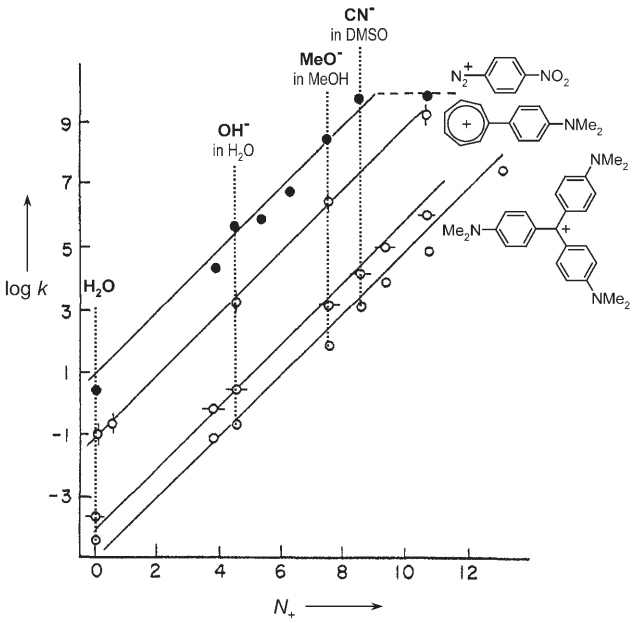



***Figure 3.*** Constant selectivity relationships for the reactions of carbenium and diazonium ions with nucleophiles.[23a]

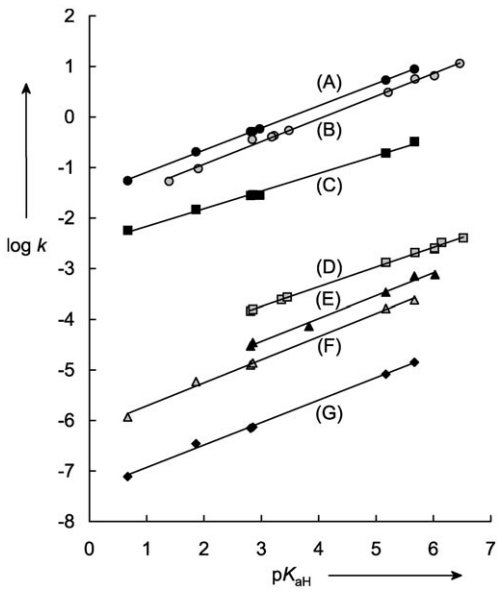



***Figure 4.*** Dependence of the second-order rate constants of $S_N2$ reactions of 3- and 4-substituted pyridines with a variety of reagents on the $pK_{aH}$ value of the pyridines:[26] A) $MeSO_3F$ in 2-nitropropane, 25 °C;[7b] B) $PhSO_2Cl$ in $H_2O$, 25 °C;[27] C) $EtSO_3F$ in 2-nitropropane, 25 °C;[7b] D) allyl bromide in nitromethane, 40 °C;[28] E) methyl iodide in nitrobenzene, 25 °C;[29] F) methyl iodide in 2-nitro-propane, 25 °C;[7b] G) ethyl iodide in 2-nitropropane, 25 °C.[7b]

In retrospect, the astonishment about the Ritchie relationship is amazing, because at that time plenty of other reactivity–selectivity relationships were known which showed a similar behavior as described by Ritchie.[7b,30] Figure 4 shows some examples.

Nowadays hundreds of correlations displaying constant selectivity are known,[31] and an example from our own laboratory is shown in Figure 5:[32–34] The 1-nitroethyl anion, the most reactive carbanion of the series shown, differentiates between a series of quinone methides in the same way as the much less nucleophilic carbanion obtained from dimedone.

Giese's observation that the selectivities of radicals may be inverted by variation of the temperature (Figure 6)[14] cast further doubt on the generality of the reactivity–selectivity principle.

Although the importance of the diffusion-control limit for the interpretation of reactivity–selectivity correlations had already been noted by Kemp and Casey,[35] it was Rappoport and Ta-Shma[13,36] who demonstrated that the change from activation to diffusion control is responsible for the different reactivity–selectivity relationships observed by Ritchie (Figure 3)[23] and by Raber, Harris, Hall, and Schleyer (Figure 2)[22]: The decrease in selectivity with increasing reactivity of the carbocations shown in Figure 2 is due to the fact that $N_3^-$ undergoes diffusion-controlled reactions ($k_{az} = 5 \times 10^9\ M^{-1}\,s^{-1}$) with all carbocations that react with water at a rate faster than $10^5\ s^{-1}$,[37] and the change in selectivity is caused by the variable rate constants $k_w$ for the reactions with water (Figure 7).[37d,38,39]

The azide-clock method, later developed by Jencks and Richard, uses this phenomenon for deriving absolute rate

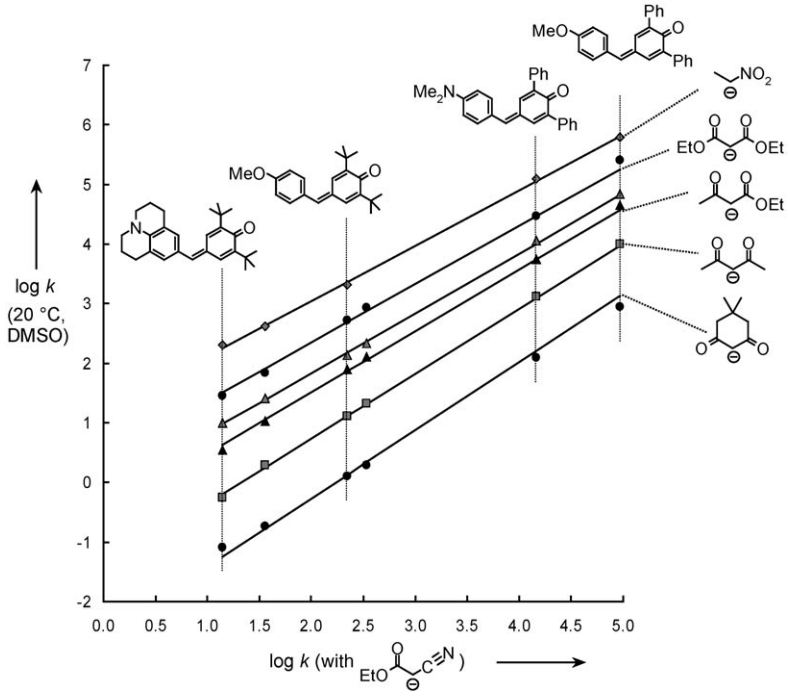



***Figure 5.*** Plot of the reactivities of various carbanions toward quinone methides versus the reactivities of the ethyl cyanoacetate anion toward these electrophiles.[32,34]


© 2006 Wiley-VCH Verlag GmbH & Co. KGaA, Weinheim

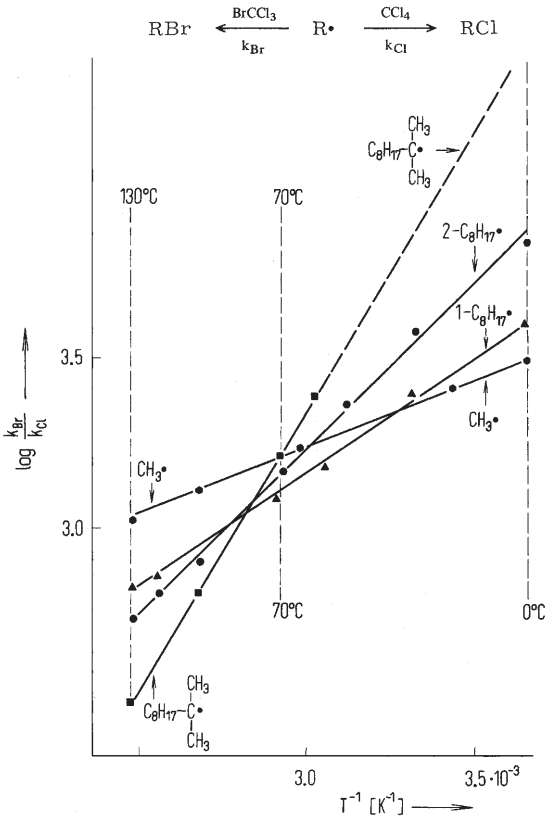



***Figure 6.*** Variation of the reaction temperature causes an inversion of the selectivities of radical reactions (figure taken from reference [14a]).

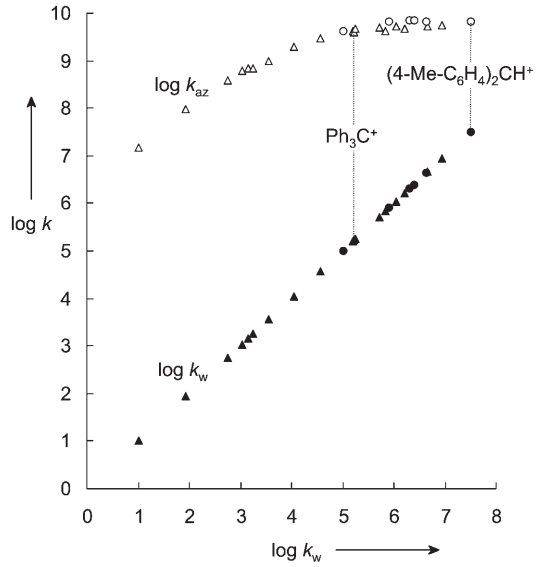



***Figure 7.*** Rate constants $k_{az}$ ([$M^{-1}s^{-1}$], 20°C) for the azide trapping of laser flash photolytically generated tritylium (triangles) and benzhydrylium ions (circles) as a function of $k_w$ ([$s^{-1}$], 20°C), the rate constants for the decay of carbenium ions in acetonitrile/water mixtures ($CH_3CN/H_2O$ 33:67 for tritylium ions;[37d] $CH_3CN/H_2O$ 20:80 for benzhydrylium ions[38]).

constants for the reactions of carbocations with solvents from the ratio of azide-trapped products to solvolysis products (R-$N_3$/R-OSolv).[40–42]

In the late 1980s and early 1990s, the senior author reported a general method to determine rate constants for the reactions of carbocations with π-systems (e.g., alkenes and allyl silanes),[43–47] and it was found that Ritchie's constant selectivity relationship [Eq. (1)] was not sufficient to describe the whole body of data. Excellent correlations were obtained, however, when an additional, nucleophile-specific slope parameter $s$ was introduced.[48,49] In [Eq. (2)] $k$ is the

$$\log k_{20^\circ C} = s(E + N) \qquad (2)$$

second-order rate constant ([$M^{-1}s^{-1}$]), $E$ is a nucleophile-independent electrophilicity parameter, and $N$ is an electrophile-independent nucleophilicity parameter.

The resulting reactivity–selectivity correlations have been discussed previously,[50,51] and Figure 8 illustrates how one might arrive at contradictory conclusions when the RSP is employed to derive relative reactivities of carbocations. Let us assume that we would try to determine the reactivity order of carbenium ions solely from competition experiments towards different allyl silanes:

- By choosing (2-methylallyl)trimethylsilane (**A**) and prenyltrimethylsilane (**C**) as a pair of competing nucleophiles, we observe that selectivity ($S = \log k_A - \log k_C$) decreases from left to right in Figure 8. By utilizing the RSP, we would (correctly) conclude that the reactivities of the carbenium ions *increase* from left to right.
- The choice of the pair prenyltrimethylsilane (**C**) and allylchlorodimethylsilane (**D**) for an analogous series of competition experiments would reveal an increase in selectivity ($S = \log k_C - \log k_D$) from left to right until $k_C$ approaches the diffusion limit. This time, the RSP would lead to the (incorrect) conclusion that the reactivities of the carbenium ions in Figure 8 *decrease* from left to right.
- To complete the confusion, we might consider a series of competition experiments with a third pair of nucleophiles, for example, allyltrimethylsilane (**B**) and prenyltrimethylsilane (**C**). When moving from left to right in Figure 8 we would first observe a decrease in selectivity ($S = \log k_B - \log k_C$), then no selectivity for (4-MeO-$C_6H_4)_2CH^+$, and finally an increase in selectivity ($S = \log k_C - \log k_B$). In this range, application of the reactivity–selectivity principle would again lead to an incorrect order of carbocation reactivities.
- A comparison of **A** and **B** would finally reveal constant selectivity in the range $k < 10^8\,M^{-1}s^{-1}$.

These examples clearly show that changes in selectivity alone do not allow one to derive relative reactivities of the carbenium ions. Reactivity orders can only be derived from competition experiments if one of the competition partners is known to react with diffusion control.[50] Measurements of absolute rate constants are, therefore, needed to determine the correct reactivity order of electrophiles.

Since the publication of the relationships illustrated in Figure 8, Equation (2) has become the basis for the most comprehensive nucleophilicity scales presently available.[52–55] As shown in Figure 9, reactions of carbanions,[33,56,57] amines,[58] alkoxides,[58,59] phosphanes,[60] enamines,[52,61] diazo-

 © 2006 Wiley-VCH Verlag GmbH & Co. KGaA, Weinheim 

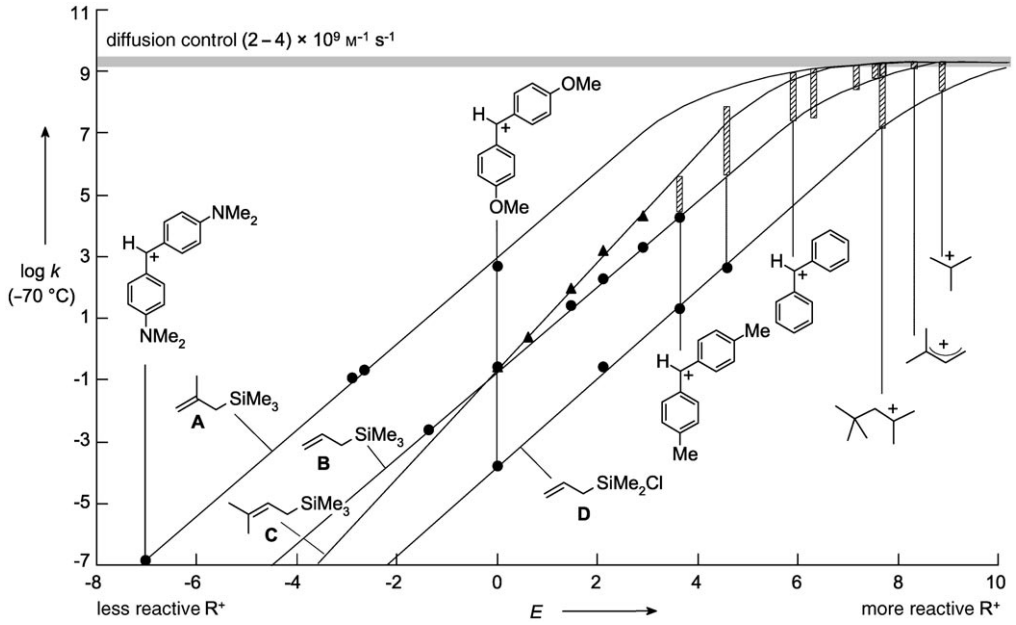



***Figure 8.*** Rate constants for the reactions of carbenium ions with allylsilanes.[50] Dots correspond to directly measured rate constants and shaded bars to the results of competition experiments. Plots versus the electrophilicity parameter *E*, defined by Equation (2).

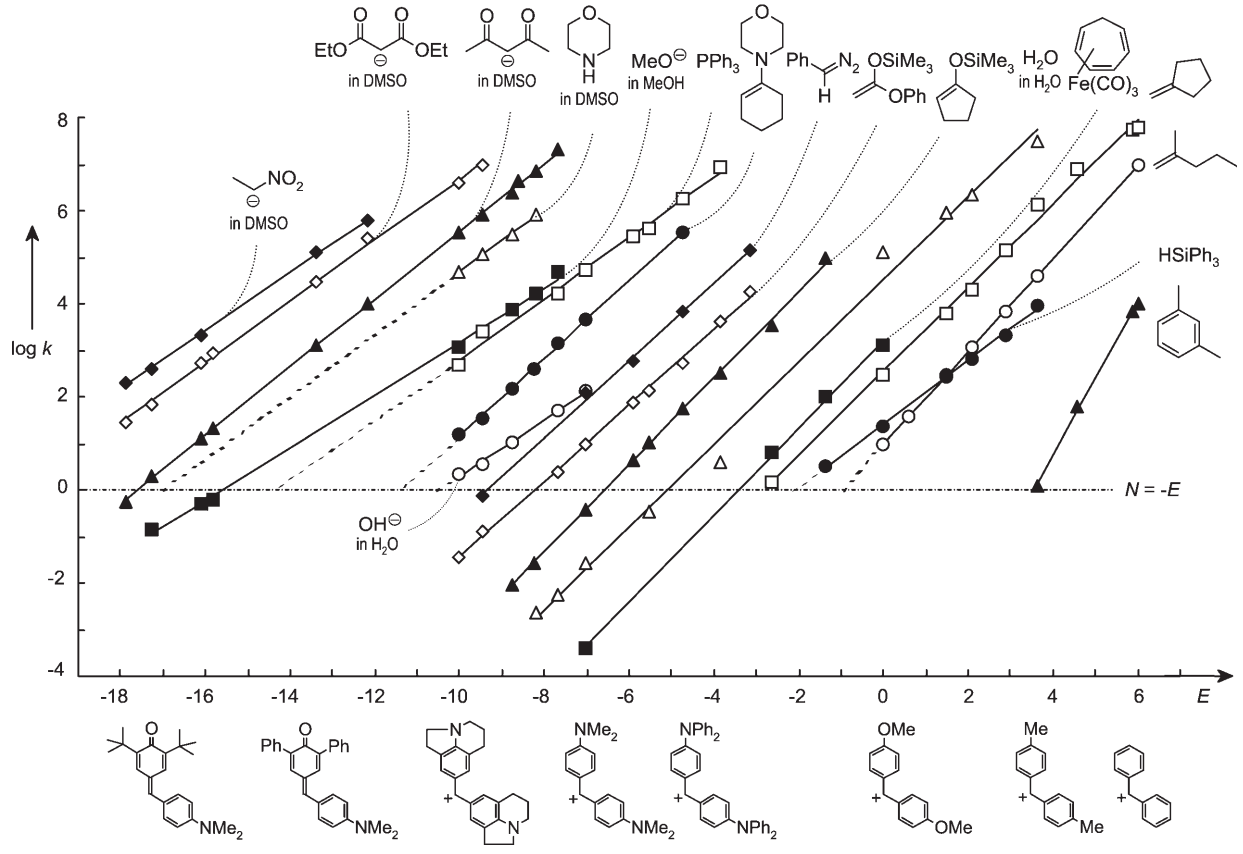



***Figure 9.*** Direct comparison of the reactivities of different classes of nucleophiles (in $CH_2Cl_2$, 20 °C). Plots versus the electrophilicity parameter *E*, defined by Equation (2).

alkanes,[62] ketene acetals,[52,63] enol ethers,[52,64] water,[65] transition metal π-complexes,[52,66] alkenes,[52] hydride donors,[49,67] and arenes[52,68] with benzhydrylium ions follow linear correlations with the electrophilicity parameter *E*. In some cases it has been shown that these correlation lines bend for $k > 10^8\,M^{-1}\,s^{-1}$ and asymptotically approach the diffusion


© 2006 Wiley-VCH Verlag GmbH & Co. KGaA, Weinheim

limit, which is typically at $(2–4)\times10^{9}\,M^{-1}s^{-1}$ for cation–molecule reactions in $CH_3CN$ (20 °C) and at $(2–4)\times10^{10}\,M^{-1}s^{-1}$ for cation–anion combinations in the same solvent.

The abscissa of Figure 9 covers 24 orders of magnitude from very strong electrophiles, such as the unsubstituted benzhydrylium ion on the right, to relatively weak electrophiles such as the amino-substituted quinone methides on the left. Only few of the available data sets have been selected for the construction of Figure 9 in order to avoid extensive crossings. If selectivity were generally to decrease with increasing reactivity, *all* correlation lines of Figure 9 would converge when going from left to right, that is, from low reactivity to high reactivity. For clear geometrical reasons, this is not possible. One cannot even *invent* a scenario in which selectivity generally decreases with increasing reactivity!

The reader can easily verify this statement by trying to draw correlation lines for the reactions of about 100 substrates $B_j$ with reagents $A_i$ of variable reactivity in Figure 10. Whereas it is easy to "invent" correlation lines

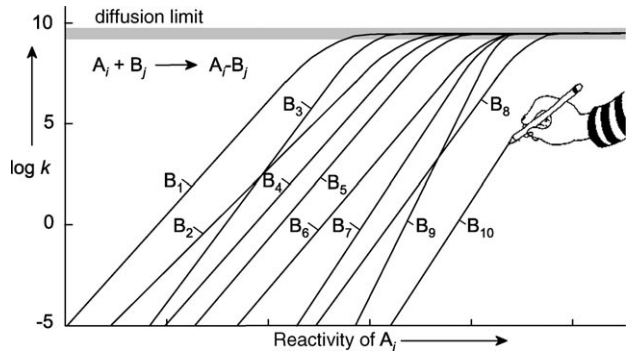



***Figure 10.*** Correlations for the reactions of the substrates $B_j$ with a series of reagents $A_i$ of variable reactivity: Try to formulate the RSP as a general principle!

for about 10 substrates $B_j$, all of which converge when moving towards the right according to the RSP, one will soon get into trouble when constructing more correlation lines without intersections, even if the search is not restricted to linear correlations and takes into account correlation lines of any curvature.

In view of the fact that inverse relationships between reactivity and selectivity cannot even be formulated as a general principle, it may appear curious that the RSP has so long been considered a general rule. The reason is evident: Most early applications were concerned with short-lived intermediates whose reactivities were studied by competition experiments and not by direct rate measurements. If one extrapolates Figure 9 to higher reactivities, one arrives at a picture related to Figure 8. If we only consider the high reactivity part of this figure ($\log k > 6$), one will often find a decrease in selectivity when going from left to right, because now the faster of two parallel reactions is close to diffusion control, while the slower of the two reactions still shows variable rates.

If it is evident that one of two competing reactions is diffusion-controlled, one can rely on a behavior as expected by the RSP and, in addition, derive important information from selectivities determined by competition experiments. In such cases, the diffusion-controlled reaction can be considered as a clock, and product ratios can be utilized for determining rate constants for the reactions of carbocations with solvents[42] or propagation rate constants in ionic polymerizations.[69,70]

## 3. How Solid Are the "Theoretical Foundations" of the Reactivity–Selectivity Principle?

The Bell–Evans–Polanyi principle rationalizes the increasing rates of many reactions with increasing exothermicities by describing the transition states *C* as a blend of reactant and product configurations (Figure 11).[71] Brønsted's catalysis law has been interpreted in the same way.[31]

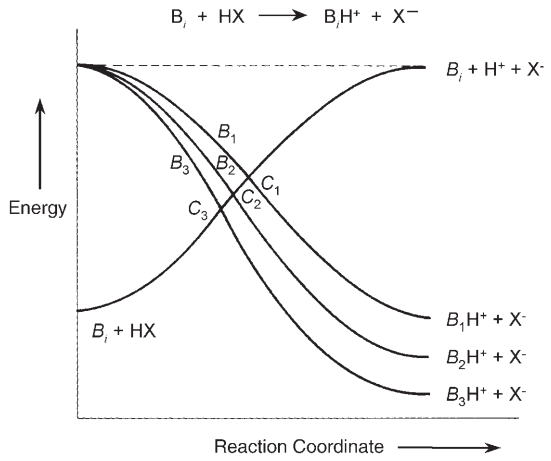



***Figure 11.*** The Bell–Evans–Polanyi principle.[71]

A quantitative relationship between the effects of structural variation on rate and equilibrium constants was given by the Hammond–Leffler $\alpha$ value,[72,73] which was supposed to change from 0 for reactantlike transition states to 1 for productlike transition states and was considered as a measure of the position of the transition states (Figure 12).[5,31,72]

Bordwell's finding of $\alpha = 1.54$ for the deprotonation of nitrotoluenes in water[74] which corresponds to $\alpha = -0.54$ for

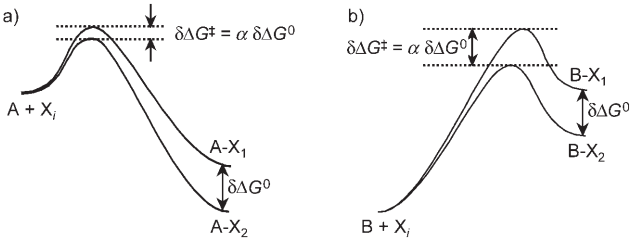



***Figure 12.*** Different positions of a) reactant- and b) productlike transition states.


© 2006 Wiley-VCH Verlag GmbH & Co. KGaA, Weinheim

the reverse reaction (Figure 13) cast doubts on the use of $\alpha$ as an indicator of the position of the transition state, because it was outside the defined range ($0 < \alpha < 1$).

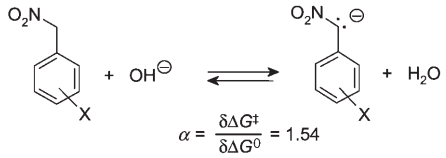



***Figure 13.*** Deprotonation of nitrotoluenes.

The identity reactions depicted in Figure 14 have been reported to be accelerated by electron-donating as well as by electron-accepting substituents X.[75] As $\Delta G^0 = 0$ throughout

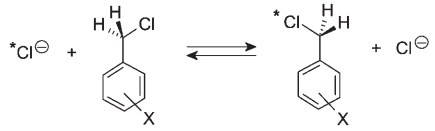



***Figure 14.*** Identity reactions of benzyl chlorides.

these reaction series, a Hammond–Leffler $\alpha$ value of infinity results,[5,76,77] which shows that Bordwell's observation of an unusual $\alpha$ value cannot be a rare exception resulting from special solvation effects.[78] Rather, it becomes clear that $\alpha$ cannot be a measure of the position of the transition state.

As pointed out by Pross and Shaik, the transition state has its own identity,[5,6,77,79] and cannot simply be described as a blend of reactant and product configurations, which is implied in the Bell–Evans–Polanyi and the Leffler–Hammond treatment. The Marcus theory describes this phenomenon by variable intrinsic barriers.[80]

In our work, we have found that the Leffler–Hammond coefficients $\alpha$ in hydride-transfer reactions do not reflect the position of the transition states. Kinetic investigations showed that in hydride abstractions from CH groups by carbocations, modification of $\Delta G^0$ caused by variation of the carbocation has a much stronger effect on $\Delta G^{\neq}$ than an equal change in $\Delta G^0$ which is caused by variation of the hydride donor.[67d]

To rationalize this observation, we performed ab initio quantum chemical calculations for the transfer of an allylic hydrogen atom from substituted propenes to substituted allyl cations (Figure 15).[81] As expected, electron-releasing substituents X and Y in the hydride acceptors diminish the exothermicity (Figure 15a), whereas electron-releasing substituents in the hydride donors increase the exothermicity of the reactions (Figure 15b).

The geometric parameters and the charge distribution in the activated complexes are in line with the Hammond postulate and show that increasing exothermicity shifts the transition states on the reaction coordinate toward reactants. By plotting $\Delta G^{\neq}$ versus $\Delta G^0$, a value of 0.72 is found for the Hammond–Leffler parameter $\alpha = \delta\Delta G^{\neq}/\delta\Delta G^0$ when the hydride acceptor is varied (Figure 15a), and $\alpha = 0.28$ when the hydride donor is varied (Figure 15b). If $\alpha$ were a measure

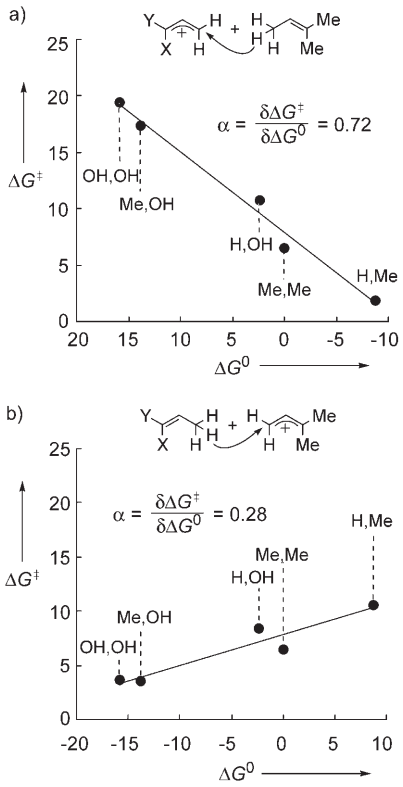
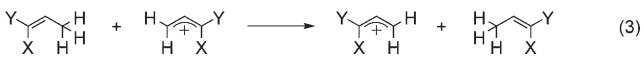



***Figure 15.*** Brønsted plots for the forward and reverse hydride-transfer reactions. a) Variation of the hydride acceptor; b) variation of the hydride donor; energies in [kcal mol$^{-1}$], MP2/6-31+G(d,p)//RHF/6-31+G(d,p).[81]

of the transition state, one would derive late transition states for the reactions in Figure 15a and early transition states for the reactions in Figure 15b. Because the identity reaction ($X = Y = CH_3$) is part of both reaction series, one might come up with an early or a late transition state for the same reaction, depending on the reaction series considered. Thus the Hammond–Leffler $\alpha$ value cannot reflect the position of the transition state.

A solution to this paradox came from a consideration of the degenerate hydride transfers illustrated in Equation (3).[81]




(3)

MP2 calculations indicate that the activation free energies of these reactions, that is, the intrinsic barriers $\Delta G_0^{\neq}$ as defined by the Marcus theory,[80] increase with increasing electron-releasing abilities of X and Y. Therefore, the intrinsic barriers must also be variable in the reaction series of Figure 15. Since substituent variation in the donor (Figure 15b) influences reaction enthalpy and intrinsic barriers in the opposite sense, while substituent variation in the acceptor (Figure 15a) affects both terms in the same sense, the slopes of the two correlations are different, even though identical transition states are involved.[81]


© 2006 Wiley-VCH Verlag GmbH & Co. KGaA, Weinheim

It is well known that the Bell–Evans–Polanyi treatment cannot be employed for explaining the variable reactivities of cycloaddition reactions. Reactions of comparable $\Delta G^0$ (e.g., most Diels–Alder reactions) differ tremendously in rates,[82,83] which can be explained by perturbational MO theory (PMO theory).[82] Since substituent variation has a larger effect on $\Delta G^{\neq}$, the smaller the HOMO–LUMO gap is (Figure 16), in frontier-orbital-controlled reactions selectivity generally increases with increasing reactivity,[14a] in contrast to the postulate of the RSP.

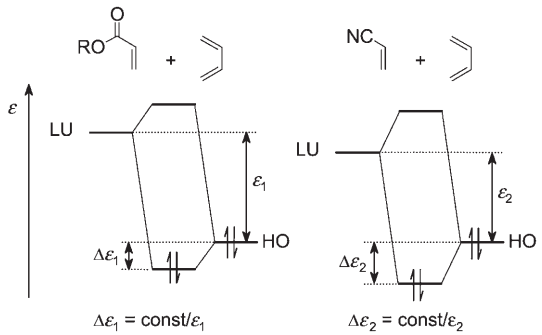



***Figure 16.*** Frontier-orbital interactions in Diels–Alder reactions.

Very often discussions of substituent effects consider only one of these effects, that is, either the Leffler–Hammond (a consequence of Bell–Evans–Polanyi) or the frontier-orbital effect. Such treatments are sufficient if one of the effects clearly dominates. If both terms operate in the same direction, it is even difficult to identify the origin of the experimentally observed effects. Thus, the increase in reactivity from left to right in Figures 8 and 9 may either be explained by a decrease in $\Delta G^0$ (Bell-Evans-Polanyi) or by a lowering of the LUMO energies of the electrophiles.

Both effects will affect the relative reactivities of two nucleophiles to a different degree, however (Figure 17). An increase in electrophilicity shifts the transition states towards reactants and, according to the Bell–Evans–Polanyi treatment, causes a decrease in selectivity (Hammond effect, Figure 17a). A lowering of the LUMO of the electrophile, on the other hand, will increase the rate of the reaction of the more-reactive nucleophile (higher HOMO) to a higher extent and result in an increase in selectivity (frontier-orbital effect, Figure 17b). Though intellectually unsatisfactory, the linear correlations depicted in Figure 9 are explained by a superposition of the curved lines of Figure 17.[84]

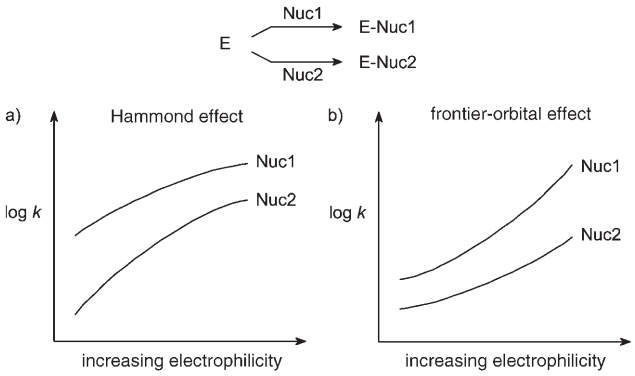



***Figure 17.*** Opposing effects on reactivity–selectivity relationships: a) Hammond effect: effect of the variation of $\Delta G^0$ on the relative reactivities of two nucleophiles; b) frontier-orbital effect: effect of the variation of $\varepsilon_{LUMO}$ on the relative reactivities of two nucleophiles.

If the Hammond effect dominates (Figure 17a) selectivities will decrease with increasing reactivities and if the frontier-orbital term dominates (Figure 17b) selectivities will increase with increasing reactivities. Constant selectivity relationships will result if both effects cancel each other.

Figure 18 illustrates this analysis for the reactions of carbocations with allyltrimethylsilane and prenyltrimethylsilane. Both nucleophiles react at similar rates, even though the

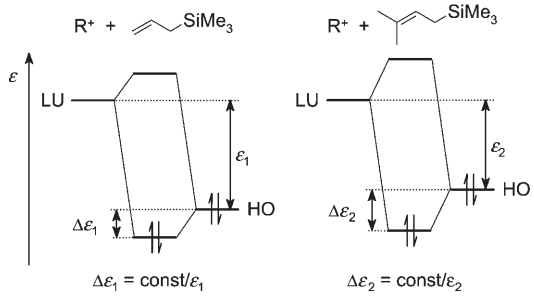



***Figure 18.*** Frontier-orbital interactions for the reactions of carbocations $R^+$ with allyltrimethylsilane and prenyltrimethylsilane.

HOMO of prenyltrimethylsilane is higher than that of allyltrimethylsilane (Figure 8). Probably the more-favorable electronic interaction in the case of prenylsilane is compensated by the stronger steric repulsion. As $\varepsilon_1 > \varepsilon_2$, the order of the second-order perturbation energies is $\Delta\varepsilon_2 > \Delta\varepsilon_1$. A variation in the carbocation, that is, of LU($R^+$), will then affect $\Delta\varepsilon_2$ more than $\Delta\varepsilon_1$ because the HOMO–LUMO gap $\varepsilon_2$ is smaller than $\varepsilon_1$. The higher slopes of π-systems with methyl groups at the position of electrophilic attack can thus be explained.[52,85]

Presently, we feel unable to evaluate the relative importance of the Hammond and the frontier-orbital effects, and for that reason consider it problematic to predict generally slopes of the correlation lines that imply changes in selectivities in the activation-controlled range.[86]

## 4. Conclusion

For geometrical reasons it is impossible to formulate the RSP as a general principle (Figure 10). A general decrease in selectivity with increasing reactivity can only be expected in fast reactions that are close to diffusion control. In reactions with rate constants $k < 10^8\,M^{-1}s^{-1}$, selectivity can decrease, increase, or remain constant when reactivity is increased, and additional information is necessary to predict the effects of structural variation on selectivity.

It is the relative importance of the Hammond effect and the frontier-orbital effects that controls the slopes of the correlations as shown in Figures 4, 5, 8, and 9 and thus

 © 2006 Wiley-VCH Verlag GmbH & Co. KGaA, Weinheim 

accounts for the variable reactivity–selectivity relationships commonly encountered.

Why is RSP, despite its frequently shown failures, still considered as a rule from which only some rare exceptions exist? Why doesn't it follow the typical course of scientific theories that are modified or abandoned when disproved by experiments?[87] We feel that the reactivity–selectivity principle has adopted the status of a myth that is no longer subject to common rules of scientific practice. Chemists like to compare the behavior of molecules with that of living beings, and our intuition is shaped by the experience that the hungry lion shown in Figure 19 is highly (re)active and will unselectively chase the next prey, be it game, man, or rabbit. The satisfied lion, on the other hand, will be selective and not hunt a fast gazelle, but only grab a rabbit that comes within reach. However, this parable is incomplete: Like the Bell–Evans–Polanyi principle and the Leffler–Hammond treatment, this consideration derives the behavior of the lion from the condition of the animal before and after the meal. However, chemical reactivity is not only controlled by the thermodynamic difference between reactants and products but also by transition-state-specific properties (e.g., frontier-orbital interactions), which are included in the Marcus intrinsic barriers. What is the counterpart of this term in Figure 19? Hard to tell how the lion is feeling during the meal, but we definitely know that we enjoy eating a delicious dessert, also if we are not hungry.




***Figure 19.*** A catchy illustration of the reactivity–selectivity principle.[88]

Received: September 15, 2005
Published online: February 7, 2006

[1] a) R. Huisgen, *Angew. Chem.* **1970**, *82*, 783 – 794; *Angew. Chem. Int. Ed. Engl.* **1970**, *9*, 751 – 762; b) W. P. Jencks, *Chem. Rev.* **1985**, *85*, 511 – 527; c) I. Lee, *Chem. Soc. Rev.* **1990**, *19*, 317 – 333; d) R. Taylor, *Electrophilic Aromatic Substitution*, Wiley, Chichester, **1990**.
[2] C. D. Johnson, *Chem. Rev.* **1975**, *75*, 755 – 765.
[3] C. D. Johnson, *Tetrahedron* **1980**, *36*, 3461 – 3480.
[4] a) P. R. Schreiner, D. L. Severance, W. L. Jorgensen, P. von R. Schleyer, H. F. Schaefer III, *J. Am. Chem. Soc.* **1995**, *117*, 2663 – 2664; b) P. R. Schreiner, P. von R. Schleyer, H. F. Schaefer III, *J. Org. Chem.* **1997**, *62*, 4216 – 4228.
[5] A. Pross, *Theoretical and Physical Principles in Organic Reactivity*, Wiley, New York, **1995**.
[6] S. S. Shaik, H. B. Schlegel, S. Wolfe, *Theoretical Aspects of Physical Organic Chemistry-The $S_N2$ Mechanism*, Wiley, New York, **1992**.
[7] a) E. M. Arnett, K. E. Molter, *Acc. Chem. Res.* **1985**, *18*, 339 – 346; b) E. M. Arnett, R. Reich, *J. Am. Chem. Soc.* **1980**, *102*, 5892 – 5902; c) E. M. Arnett, R. Reich, *J. Am. Chem. Soc.* **1978**, *100*, 2930 – 2931; d) E. M. Arnett, C. Petro, *J. Am. Chem. Soc.* **1976**, *98*, 1468 – 1471; e) E. M. Arnett, K. Molter, *J. Phys. Chem.* **1986**, *90*, 383 – 389.
[8] a) F. G. Bordwell, J. C. Branca, T. A. Cripe, *Isr. J. Chem.* **1985**, *25*, 357 – 366; b) F. G. Bordwell, D. L. Hughes, *J. Org. Chem.* **1980**, *45*, 3314 – 3320.
[9] E. Buncel, H. Wilson, *J. Chem. Educ.* **1987**, *64*, 475 – 480.
[10] S. J. Formosinho, *J. Chem. Soc. Perkin Trans. 2* **1988**, 839 – 846.
[11] O. Exner, *J. Chem. Soc. Perkin Trans. 2* **1993**, 973 – 979.
[12] R. Curci, A. Dinoi, M. F. Rubino, *Pure Appl. Chem.* **1995**, *67*, 811 – 822.
[13] R. Ta-Shma, Z. Rappoport, *J. Am. Chem. Soc.* **1983**, *105*, 6082 – 6095.
[14] a) B. Giese, *Angew. Chem.* **1977**, *89*, 162 – 173; *Angew. Chem. Int. Ed. Engl.* **1977**, *16*, 125 – 136; b) B. Giese, *Acc. Chem. Res.* **1984**, *17*, 438 – 442.
[15] a) A. Pross, *Adv. Phys. Org. Chem.* **1977**, *14*, 69 – 132; b) A. Pross, *J. Am. Chem. Soc.* **1976**, *98*, 776 – 778.
[16] a) J. P. Richard, *Tetrahedron* **1995**, *51*, 1535 – 1573; b) J. P. Richard, T. L. Amyes, T. Vontor, *J. Am. Chem. Soc.* **1992**, *114*, 5626 – 5634.
[17] P. Denton, C. D. Johnson, *J. Chem. Soc. Perkin Trans. 2* **1995**, 477 – 481.
[18] Relative rates of alkyl radical formation for primary C–H/secondary C–H/tertiary C–H by chlorine (1:4.3:7.0) and bromine (1:80:1600) radicals can be found in textbooks, for example: a) P. Sykes, *Reaktionsmechanismen der Organischen Chemie, 9th ed.*, Wiley-VCH, Weinheim, **1988**, p. 382; b) P. Y. Bruice, *Organic Chemistry, 4th ed.*, Pearson Education, Upper Saddle River, NJ, **2004**, p. 343; c) M. B. Smith, J. March, *March's Advanced Organic Chemistry, 5th ed.*, Wiley, New York, **2001**, p. 901.
[19] Reaction enthalpies $\Delta_r H$ (at 298 K) were calculated from the following bond dissociation energies (in kJ mol$^{-1}$): a) H–Cl (431.6) and H–Br (87.5): J. Berkowitz, G. B. Ellison, D. Gutman, *J. Phys. Chem.* **1994**, *98*, 2744 – 2765; b) *n*-butane (1-H: 421.3, 2-H: 411.1) and $(CH_3)_3$C-H (400.4): Y.-R. Luo, *Handbook of Bond Dissociation Energies in Organic Compounds*, CRC, Boca Raton, **2003**.
[20] a) S. M. Senkan, D. Quam, *J. Phys. Chem.* **1992**, *96*, 10837 – 10842; b) L. Sheps, A. C. Crowther, C. G. Elles, F. F. Crim, *J. Phys. Chem. A* **2005**, *109*, 4296 – 4302.
[21] R. A. Sneen, J. V. Carter, P. S. Kay, *J. Am. Chem. Soc.* **1966**, *88*, 2594 – 2595.
[22] D. J. Raber, J. M. Harris, R. E. Hall, P. von R. Schleyer, *J. Am. Chem. Soc.* **1971**, *93*, 4821 – 4828.

 © 2006 Wiley-VCH Verlag GmbH & Co. KGaA, Weinheim 

[23] a) C. D. Ritchie, *Acc. Chem. Res.* **1972**, *5*, 348 – 354; b) C. D. Ritchie, *Can. J. Chem.* **1986**, *64*, 2239 – 2250.
[24] C. D. Johnson, B. Stratton, *J. Chem. Soc. Perkin Trans. 2* **1988**, 1903 – 1907.
[25] a) C. D. Ritchie, *Pure Appl. Chem.* **1978**, *50*, 1281 – 1290; b) C. D. Ritchie, P. O. I. Virtanen, *J. Am. Chem. Soc.* **1972**, *94*, 4966 – 4971; c) C. D. Ritchie, P. O. I. Virtanen, *J. Am. Chem. Soc.* **1972**, *94*, 4963 – 4965.
[26] For reaction series (A), (C), (E), (F), and (G) the p$K_{aH}$ values (25 °C, $H_2O$) of pyridines are from: a) A. Fischer, W. J. Galloway, J. Vaughan, *J. Chem. Soc.* **1964**, 3591 – 3596; b) H. C. Brown, X. R. Mihm, *J. Am. Chem. Soc.* **1955**, *77*, 1723 – 1726; c) H. C. Brown, D. H. McDaniel, *J. Am. Chem. Soc.* **1955**, *77*, 3752 – 3755; d) for reaction series (B) the p$K_{aH}$ values ($I = 0.05$ M, 25 °C, $H_2O$) are from reference [27]; e) for reaction series (D) the p$K_{aH}$ values (20 °C, $H_2O$) are given in reference [28].
[27] O. Rogne, *J. Chem. Soc. B* **1970**, 727 – 730.
[28] K. Clark, K. Rothwell, *J. Chem. Soc.* **1960**, 1885 – 1895.
[29] G. Coppens, F. Declerck, C. Gillet, J. Nasielski, *Bull. Soc. Chim. Belg.* **1963**, *72*, 25 – 37.
[30] F. G. Bordwell, D. L. Hughes, *J. Am. Chem. Soc.* **1986**, *108*, 7300 – 7309.
[31] A. Williams, *Free Energy Relationships in Organic and Bio-Organic Chemistry*, The Royal Society of Chemistry, Cambridge, **2003**.
[32] R. Lucius, H. Mayr, *Angew. Chem.* **2000**, *112*, 2086 – 2089; *Angew. Chem. Int. Ed.* **2000**, *39*, 1995 – 1997.
[33] R. Lucius, R. Loos, H. Mayr, *Angew. Chem.* **2002**, *114*, 97 – 102; *Angew. Chem. Int. Ed.* **2002**, *41*, 91 – 95.
[34] T. Lemek, H. Mayr, *J. Org. Chem.* **2003**, *68*, 6880 – 6886.
[35] D. S. Kemp, M. L. Casey, *J. Am. Chem. Soc.* **1973**, *95*, 6670 – 6680.
[36] a) Z. Rappoport, R. Ta-Shma, *J. Org. Chem.* **1982**, *47*, 5207 – 5209; b) R. Ta-Shma, Z. Rappoport, *Tetrahedron Lett.* **1982**, *23*, 781 – 784; c) Z. Rappoport, *Tetrahedron Lett.* **1979**, *20*, 2559 – 2562.
[37] a) R. A. McClelland in *Reactive Intermediate Chemistry* (Eds.: R. A. Moss, M. S. Platz, M. Jones, Jr.), Wiley, **2004**, chap. 1, pp. 3 – 40; b) R. A. McClelland, *Tetrahedron* **1996**, *52*, 6823 – 6858; c) R. A. McClelland, F. L. Cozens, S. Steenken, T. L. Amyes, J. P. Richard, *J. Chem. Soc. Perkin Trans. 2* **1993**, 1717 – 1722; d) R. A. McClelland, V. M. Kanagasabapathy, N. S. Banait, S. Steenken, *J. Am. Chem. Soc.* **1991**, *113*, 1009 – 1014.
[38] R. A. McClelland, V. M. Kanagasabapathy, S. Steenken, *J. Am. Chem. Soc.* **1988**, *110*, 6913 – 6914.
[39] Xanthylium ions react 3 to 10 times faster with azide ions ($CH_3CN/H_2O$ 20:80, 25 °C) than expected from the correlation shown in Figure 7 and are not considered here: R. A. McClelland, N. Banait, S. Steenken, *J. Am. Chem. Soc.* **1989**, *111*, 2929 – 2935.
[40] a) J. P. Richard, W. P. Jencks, *J. Am. Chem. Soc.* **1984**, *106*, 1383 – 1396; b) J. P. Richard, W. P. Jencks, *J. Am. Chem. Soc.* **1984**, *106*, 1373 – 1383; c) J. P. Richard, M. E. Rothenberg, W. P. Jencks, *J. Am. Chem. Soc.* **1984**, *106*, 1361 – 1372; d) J. P. Richard, W. P. Jencks, *J. Am. Chem. Soc.* **1982**, *104*, 4689 – 4691; e) for an analogous sulfite-clock, see: P. R. Young, W. P. Jencks, *J. Am. Chem. Soc.* **1979**, *101*, 3288 – 3294.
[41] W. P. Jencks, *Acc. Chem. Res.* **1980**, *13*, 161 – 169.
[42] a) J. P. Richard, T. L. Amyes, M. M. Toteva, Y. Tsuji, *Adv. Phys. Org. Chem.* **2004**, *39*, 1 – 26; b) J. P. Richard, T. L. Amyes, M. M. Toteva, *Acc. Chem. Res.* **2001**, *34*, 981 – 988.
[43] a) R. Schneider, U. Grabis, H. Mayr, *Angew. Chem.* **1986**, *98*, 94 – 95; *Angew. Chem. Int. Ed. Engl.* **1986**, *25*, 89 – 90; b) R. Schneider, H. Mayr, *Angew. Chem.* **1986**, *98*, 1033 – 1034; *Angew. Chem. Int. Ed. Engl.* **1986**, *25*, 1016 – 1017; c) H. Mayr, R. Schneider, U. Grabis, *Angew. Chem.* **1986**, *98*, 1034 – 1036; *Angew. Chem. Int. Ed. Engl.* **1986**, *25*, 1017 – 1019.
[44] a) H. Mayr, G. Hagen, *J. Chem. Soc. Chem. Commun.* **1989**, 91 – 92; b) G. Hagen, H. Mayr, *J. Am. Chem.* Soc. **1991**, *113*, 4954 – 4961.
[45] a) H. Mayr, R. Schneider, C. Schade, J. Bartl, R. Bederke, *J. Am. Chem. Soc.* **1990**, *112*, 4446 – 4454; b) H. Mayr, R. Schneider, B. Irrgang, C. Schade, *J. Am. Chem. Soc.* **1990**, *112*, 4454 – 4459; c) H. Mayr, R. Schneider, U. Grabis, *J. Am. Chem. Soc.* **1990**, *112*, 4460 – 4467; d) B. Irrgang, H. Mayr, *Tetrahedron* **1991**, *47*, 219 – 228.
[46] H. Mayr, *Angew. Chem.* **1990**, *102*, 1415 – 1428; *Angew. Chem. Int. Ed. Engl.* **1990**, *29*, 1371 – 1384.
[47] J. Bartl, S. Steenken, H. Mayr, *J. Am. Chem. Soc.* **1991**, *113*, 7710 – 7716.
[48] H. Mayr, M. Patz, *Angew. Chem.* **1994**, *106*, 990 – 1010; *Angew. Chem. Int. Ed. Engl.* **1994**, *33*, 938 – 957.
[49] H. Mayr, T. Bug, M. F. Gotta, N. Hering, B. Irrgang, B. Janker, B. Kempf, R. Loos, A. R. Ofial, G. Remennikov, H. Schimmel, *J. Am. Chem. Soc.* **2001**, *123*, 9500 – 9512.
[50] M. Roth, H. Mayr, *Angew. Chem.* **1995**, *107*, 2428 – 2430; *Angew. Chem. Int. Ed. Engl.* **1995**, *34*, 2250 – 2252.
[51] H. Mayr, O. Kuhn, M. F. Gotta, M. Patz, *J. Phys. Org. Chem.* **1998**, *11*, 642 – 654.
[52] H. Mayr, B. Kempf, A. R. Ofial, *Acc. Chem. Res.* **2003**, *36*, 66 – 77.
[53] H. Mayr, A. R. Ofial in *Carbocation Chemistry* (Eds.: G. A. Olah, G. K. S. Prakash), Wiley, Hoboken, NJ, **2004**, chap. 13, pp. 331 – 358.
[54] A. R. Ofial, H. Mayr, *Macromol. Symp.* **2004**, *125*, 353 – 367.
[55] H. Mayr, A. R. Ofial, *Pure Appl. Chem.* **2005**, *77*, 1807 – 1821.
[56] a) T. Bug, H. Mayr, *J. Am. Chem. Soc.* **2003**, *125*, 12 980 – 12 986; b) T. Bug, T. Lemek, H. Mayr, *J. Org. Chem.* **2004**, *69*, 7565 – 7576.
[57] A. A. Tishkov, H. Mayr, *Angew. Chem.* **2005**, *117*, 145 – 148; *Angew. Chem. Int. Ed.* **2005**, *44*, 142 – 145.
[58] S. Minegishi, H. Mayr, *J. Am. Chem. Soc.* **2003**, *125*, 286 – 295.
[59] T. B. Phan, H. Mayr, *Can. J. Chem.* **2005**, *83*, 1554 – 1560.
[60] B. Kempf, H. Mayr, *Chem. Eur. J.* **2005**, *11*, 917 – 927.
[61] a) A. D. Dilman, S. L. Ioffe, H. Mayr, *J. Org. Chem.* **2001**, *66*, 3196 – 3200; b) B. Kempf, N. Hampel, A. R. Ofial, H. Mayr, *Chem. Eur. J.* **2003**, *9*, 2209 – 2218; c) H. Schimmel, A. R. Ofial, H. Mayr, *Macromolecules* **2002**, *35*, 5454 – 5458.
[62] T. Bug, M. Hartnagel, C. Schlierf, H. Mayr, *Chem. Eur. J.* **2003**, *9*, 4068 – 4076.
[63] T. Tokuyasu, H. Mayr, *Eur. J. Org. Chem.* **2004**, 2791 – 2796.
[64] a) J. Burfeindt, M. Patz, M. Müller, H. Mayr, *J. Am. Chem. Soc.* **1998**, *120*, 3629 – 3634; b) A. D. Dilman, H. Mayr, *Eur. J. Org. Chem.* **2005**, 1760 – 1764.
[65] S. Minegishi, S. Kobayashi, H. Mayr, *J. Am. Chem. Soc.* **2004**, *126*, 5174 – 5181.
[66] a) H. Mayr, K.-H. Müller, *Collect. Czech. Chem. Commun.* **1999**, *64*, 1770 – 1779; b) H. Mayr, O. Kuhn, C. Schlierf, A. R. Ofial, *Tetrahedron* **2000**, *56*, 4219 – 4229; c) F. Dulich, K.-H. Müller, A. R. Ofial, H. Mayr, *Helv. Chim. Acta* **2005**, *88*, 1754 – 1768.
[67] a) H. Mayr, N. Basso, G. Hagen, *J. Am. Chem. Soc.* **1992**, *114*, 3060 – 3066; b) H. Mayr, N. Basso, *Angew. Chem.* **1992**, *104*, 1103 – 1105; *Angew. Chem. Int. Ed. Engl.* **1992**, *31*, 1046 – 1048; c) M.-A. Funke, H. Mayr, *Chem. Eur. J.* **1997**, *3*, 1214 – 1222; d) H. Mayr, G. Lang, A. R. Ofial, *J. Am. Chem. Soc.* **2002**, *124*, 4076 – 4083.
[68] M. F. Gotta, H. Mayr, *J. Org. Chem.* **1998**, *63*, 9769 – 9775.
[69] M. Roth, H. Mayr, *Macromolecules* **1996**, *29*, 6104 – 6109.
[70] a) P. De, R. Faust, H. Schimmel, A. R. Ofial, H. Mayr, *Macromolecules* **2004**, *37*, 4422 – 4433; b) L. Sipos, P. De, R. Faust, *Macromolecules* **2003**, *36*, 8282 – 8290; c) M. S. Kim, R. Faust, *Macromolecules* **2002**, *35*, 5320 – 5322; d) H. Schlaad, Y. Kwon, L. Sipos, R. Faust, B. Charleux, *Macromolecules* **2000**, *33*, 8225 – 8232.


© 2006 Wiley-VCH Verlag GmbH & Co. KGaA, Weinheim

[71] M. J. S. Dewar, R. C. Dougherty, *The PMO Theory of Organic Chemistry*, Plenum, New York, **1975**, p. 218.
[72] a) J. E. Leffler, *Science* **1953**, *117*, 340 – 341; b) J. E. Leffler, E. Grunwald, *Rates and Equilibria of Organic Reactions*, Wiley, New York, **1963**.
[73] G. S. Hammond, *J. Am. Chem. Soc.* **1955**, *77*, 334 – 338.
[74] F. G. Bordwell, W. J. Boyle, Jr., *J. Am. Chem. Soc.* **1972**, *94*, 3907 – 3911.
[75] a) J.-i. Hayami, N. Hihara, N. Tanaka, A. Kaji, *Bull. Chem. Soc. Jpn.* **1979**, *52*, 831 – 835; b) for the analogous bromide exchange, see: S. Sugden, J. B. Willis, *J. Chem. Soc.* **1951**, 1360 – 1363.
[76] A. Pross, *Tetrahedron Lett.* **1983**, *24*, 835 – 838.
[77] A. Pross, S. S. Shaik, *New J. Chem.* **1989**, *13*, 427 – 433.
[78] For further examples of untypical Brønsted coefficients, see: F. Terrier, M. Mokhtari, R. Goumont, J.-C. Hallé, E. Buncel, *Org. Biomol. Chem.* **2003**, *1*, 1757 – 1763, and references therein.
[79] A. Pross, S. S. Shaik, *J. Am. Chem. Soc.* **1982**, *104*, 1129 – 1130.
[80] R. A. Marcus, *J. Phys. Chem.* **1968**, *72*, 891 – 899.
[81] E.-U. Würthwein, G. Lang, L. H. Schappele, H. Mayr, *J. Am. Chem. Soc.* **2002**, *124*, 4084 – 4092.
[82] a) K. Fukui, *Angew. Chem.* **1982**, *94*, 852 – 861; *Angew. Chem. Int. Ed. Engl.* **1982**, *21*, 801 – 809; b) I. Fleming, *Frontier Orbitals and Organic Chemical Reactions*, Wiley, Chichester, **1976**; c) R. F. Hudson, *Angew. Chem.* **1973**, *85*, 63 – 84; *Angew. Chem. Int. Ed. Engl.* **1973**, *12*, 36 – 57; d) R. Sustmann, *Pure Appl. Chem.* **1974**,*40*, 569 – 593.
[83] a) J. Sauer, R. Sustmann, *Angew. Chem.* **1980**, *92*, 773 – 801; *Angew. Chem. Int. Ed. Engl.* **1980**, *19*, 779 – 807; b) R. Huisgen in *1,3-Dipolar Cycloaddition Chemistry, Vol. 1* (Ed.: A. Padwa), Wiley-Interscience, New York, **1984**, chap. 1, pp. 1 – 176.
[84] One referee commented: "The statement, that constant selectivity relationships will result when Hammond effects and frontier-orbital effects cancel, is not enough. It would be hard to imagine that these effects accidentally cancel in such an overwhelming number of cases. Is there something else that makes constant selectivity relationships the rule?" We fully agree with this statement. Unfortunately, we cannot give an answer and hope that this Minireview will stimulate theoretical chemists to suggest solutions.
[85] C. Schindele, K. N. Houk, H. Mayr, *J. Am. Chem. Soc.* **2002**, *124*, 11208 – 11214.
[86] S. Shaik, A. Shurki, *Angew. Chem.* **1999**, *111*, 616 – 657; *Angew. Chem. Int. Ed.* **1999**, *38*, 586 – 625.
[87] K. Popper, *Logik der Forschung*, Springer, Wien, **1935**.
[88] Reproduction of photos by courtesy of Ultimate Africa Safaris, Seattle, USA.

 © 2006 Wiley-VCH Verlag GmbH & Co. KGaA, Weinheim 

U. Feldkamp and C. M. Niemeyer

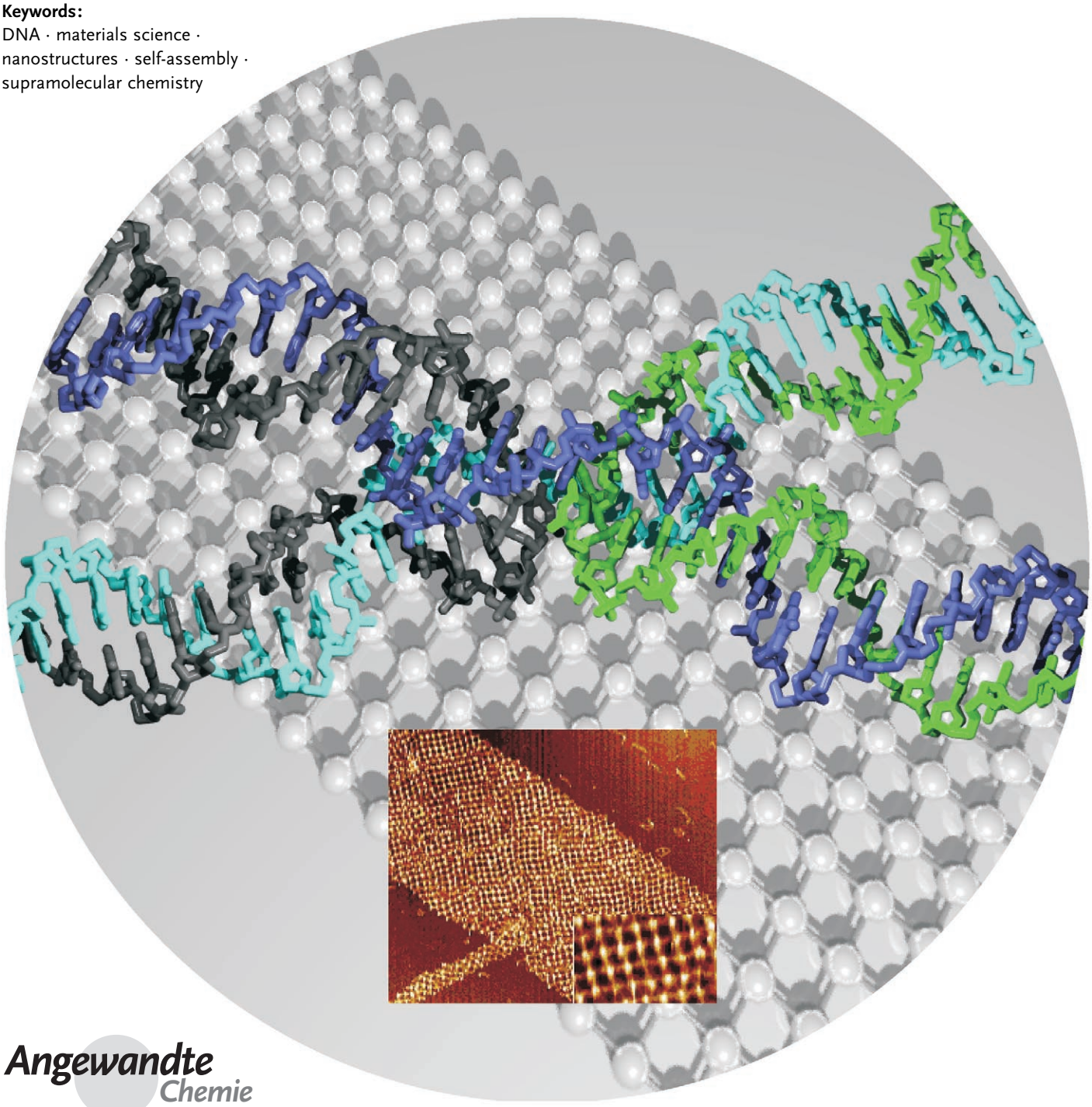
DOI: 10.1002/anie.200502358

Nanoscience

# Rational Design of DNA Nanoarchitectures

*Udo Feldkamp* and Christof M. Niemeyer**

**Keywords:**
DNA · materials science · nanostructures · self-assembly · supramolecular chemistry





© 2006 Wiley-VCH Verlag GmbH & Co. KGaA, Weinheim

*DNA has many physical and chemical properties that make it a powerful material for molecular constructions at the nanometer length scale. In particular, its ability to form duplexes and other secondary structures through predictable nucleotide-sequence-directed hybridization allows for the design of programmable structural motifs which can self-assemble to form large supramolecular arrays, scaffolds, and even mechanical and logical nanodevices. Despite the large variety of structural motifs used as building blocks in the programmed assembly of supramolecular DNA nanoarchitectures, the various modules share underlying principles in terms of the design of their hierarchical configuration and the implemented nucleotide sequences. This Review is intended to provide an overview of this fascinating and rapidly growing field of research from the structural design point of view.*

**From the Contents**

1. Introduction 1857
2. General Considerations of DNA-Sequence Design 1858
3. One-Dimensional DNA Strands for Assembly and Immobilization of Non-Nucleic Acid Compounds 1859
4. Design and Assembly of DNA Motifs 1860
5. Three-Dimensional Structures from DNA 1866
6. Applications of DNA Nanoarchitectures 1868
7. Conclusions and Perspectives 1872

## 1. Introduction

Biomolecules, such as proteins and nucleic acids, possess perfect binding properties which have been optimized over billions of years of evolution. Hence, biomolecules are currently intensively investigated for their use as building blocks and structure-directing components in the so-called "bottom-up" approach to generate materials and devices with precise control at the nanometer length scale. Nucleic acids have preferentially been used in the self-assembly of functional nanomaterials since they are more readily available by synthetic chemical means and are more convenient to handle than proteins.[1–4]

DNA is a particularly promising candidate to serve as a construction material in nanosciences. Despite its simplicity, the outstanding specificity of the A-T and G-C Watson–Crick hydrogen-bonding interaction allows the convenient programming of artificial DNA receptor moieties through the simple four-letter alphabet. The power of DNA as a molecular tool is enhanced by our ability to synthesize virtually any DNA sequence by automated methods,[5] and to amplify any DNA sequence from microscopic to macroscopic quantities by the polymerase chain reaction (PCR).[6] Another very attractive feature of DNA is its memory of chain direction. Although a DNA double helix is actually a flexible polymer, as impressively demonstrated by the very compact shape of chromosomes, this flexibility is negligible for short double strands. The persistence length, that is, the length up to which polymers can be considered essentially rigid and straight, is about 50 nm, which corresponds to 150 base pairs in the double helix.[7] Below this size, double-stranded DNA (dsDNA) behaves as a rather rigid polymer, and can, therefore, be used as a rigid spacer between two tethered functional molecular components at the two ends. On the other hand, single-stranded DNA (ssDNA) is very flexible and is, therefore, capable of forming tight loop structures or even directional turns of about 180°. Hence, the combination of distinct ssDNA and dsDNA elements within an artificial DNA motif allows structural building blocks to be designed with tailored flexibility and rigidity. As we will describe in this Review, the rigidity of artificial DNA motifs can even exceed that of dsDNA.

An additional advantage of using DNA as a construction material is its relatively high physicochemical stability, which is much higher than that of proteins. Hence, nanostructured materials which are constructed from DNA can be synthesized, processed, and stored under a broad range of environmental conditions without the necessity of special precautions to avoid decomposition of this biological material. Moreover, it is particularly noteworthy that nature provides us with a variety of highly specific enzymes which allow the processing of DNA materials with atomic precision and accuracy at the Ångström level. For example, the backbone of DNA molecules produced by either chemical or biological processes can be cleaved specifically at a known site by restriction endonucleases, thereby opening up the possibility to produce monodisperse solutions containing DNA molecules of precisely known size and chemical composition. No other (polymeric) material offers these advantages, which are ideal for molecular constructions in the range of about 5 nanometers up to the micrometer scale. These advantages have already been utilized in the extensive application of DNA for rational constructions on the nanometer length scale,[1] and recent advances have demonstrated its applic-

[*] Dr. U. Feldkamp, Prof. Dr. C. M. Niemeyer
Fachbereich Chemie
Biologisch-Chemische Mikrostrukturtechnik
Universität Dortmund
Otto-Hahn Strasse 6, 44227 Dortmund (Germany)
Fax: (+49) 231-755-7082
E-mail: udo.feldkamp@uni-dortmund.de
christof.niemeyer@uni-dortmund.de

 © 2006 Wiley-VCH Verlag GmbH & Co. KGaA, Weinheim 

ability for fabricating arrays of colloidal components, proteins, and even nanomechanical devices.[1,3,4,8–11]

Further developments in this field, however, require elaborate tools for tailoring sequences of the DNA nucleobases of short synthetic oligonucleotides which encode the primary structure of supramolecular DNA architecture in one, two, and three dimensions. This primary structure determines the ability of an oligonucleotide to hybridize with other (partially) complementary oligomers, thereby allowing the formation of distinct motifs, such as tiles which comprise DNA helices, junctions, crossovers, and loops (Figure 1). These motifs are then used as building blocks which can self-assemble by hybridization of pendent single strands (sticky ends) to form larger, two- and three-dimensional elements. This Review is intended to summarize the construction principles so far applied to the rational fabrication of DNA nanoarchitectures. General construction principles will be discussed as well as the underlying rules for designing the base sequences of the building blocks. Finally, an overview will be presented on the current state-of-the-art and conclusions drawn on future perspectives of DNA-based nanomaterials.

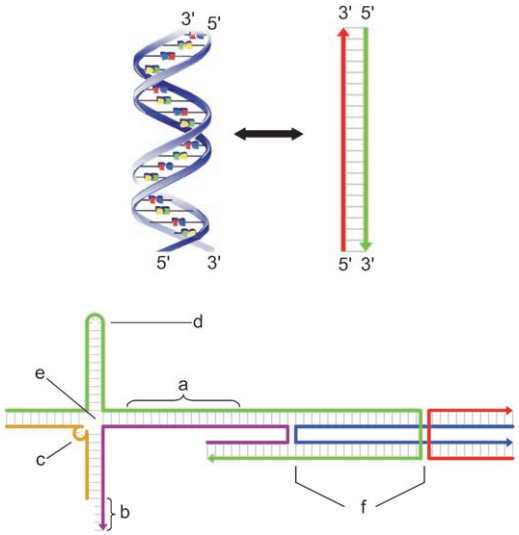



***Figure 1.*** The well-known DNA double helix (top left) is comprised of two antiparallel strands of oligonucleotides which are bound together by specific Watson–Crick hydrogen bonds, represented as the ladder-like structure (top right). The choice of suitable DNA sequences allows the generation of complex motifs which contain a) double-helical regions, b) sticky ends, c) bulge loops, d) hairpin loops, e) junctions, and f) crossovers (see schematic representation at the bottom). Note that three-dimensional information, such as helices, grooves, and angles between helices, are omitted in this schematic representation. The arrowheads indicate the 5′→3′ direction of individual oligonucleotides.

## 2. General Considerations of DNA-Sequence Design

The design and construction process of DNA-based nanoarchitecture comprises several major steps. Firstly, any requirements to be satisfied by the envisioned construct and its potential application should be identified. For example, it may eventually be wished to use the scaffold for the directed attachment of non-nucleic acid components, such as nanoparticles or proteins. In this case it needs to be determined whether the DNA scaffold should be rigid or flexible. The next question might concern whether the construct is to be used as a static scaffold or as a dynamic mechanical device that undergoes reversible or irreversible transitions between distinct and predictable conformations. Depending on the demands, the individual building blocks should then either be comprised of just rigid scaffolding elements or else may contain distinct single-stranded regions, often termed "toe holds", which can hybridize to effector oligomers or act as dynamic elements for strand replacement and, thereby, induce large conformational changes of the motif.

It must also be determined whether symmetric or non-symmetric patterns are to be produced by the assembly of the array, what kind of periodicity is desired, in how many dimensions the scaffold should grow, and whether this growth is to be terminated or potentially infinite.

Depending on these requirements, suitable DNA motifs comprised of junctions, loops, crossovers, and single-stranded binding sites ("sticky ends") need to be selected as building blocks for the desired scaffold architecture. These motifs may also contain additional chemical groups which can enable the attachment of non-nucleic acid components, such as proteins and nanoparticles. As discussed below, biotin-modified loop elements and aptamer sequences have so far been successfully



*Udo Feldkamp is a research assistant at the University of Dortmund (Germany). He was born in Duisburg and studied Computer Science in Kaiserslautern and Dortmund, where he also completed his PhD thesis on computer-aided DNA sequence design under the supervision of Prof. Wolfgang Banzhaf. His research still focuses on DNA-based nanotechnology and DNA computing, but he is also interested in other fields of bioinformatics and in computational intelligence.*



*Christof M. Niemeyer has been Professor of Chemistry (chair of Biological and Chemical Microstructuring) at the University of Dortmund (Germany) since 2002. He studied chemistry at the University of Marburg and completed his PhD on organometallic chemistry at the Max-Planck-Institut für Kohlenforschung in Mülheim/Ruhr with Prof. Manfred T. Reetz. He then did postdoctoral research at the Center for Advanced Biotechnology in Boston (USA) with Prof. Charles R. Cantor, and received his habilitation at the University of Bremen. He is interested in semisynthetic DNA–protein and nanoparticle–conjugates as well as their applications in life sciences, catalysis, and molecular nanotechnology.*

 © 2006 Wiley-VCH Verlag GmbH & Co. KGaA, Weinheim 

applied for this purpose. Aptamers are short stretches of sequences which specifically recognize distinct target structures as a result of complementary three-dimensional conformations.

In addition to the choice of the general type of motif, its particular properties, such as the length (and consequently the number of helical turns) of the DNA strands used and the position of fixed subsequences within the strands, for example, restriction sites for characterization (see below) or other further processing steps, or binding sites for incorporating proteins into the assembly, need to be defined. Importantly, the particular thermodynamic properties, that is, the melting points, of distinct sequence stretches need to be chosen to achieve a homogeneous assembly or to enable clearly separated hybridization steps to be achieved during a stepwise assembly.

The sequences of the individual oligonucleotides then need to be designed according to these requirements. For a reliable self-assembly, the hybridization of complementary DNA strands needs to be as specific as possible, which means that the intended base pairing must occur efficiently and be stable, while all undesired conformations should be highly improbable. Unfortunately, the simple maximization of affinity, for example, by increasing the length and content of G and C base pairs, does not necessarily lead to high specificity, because the two characteristics are not correlated for the hybridization of nucleic acids.[12] Instead, the stability of undesired hybridizations, measured, for example, by the changes in the free energy upon duplex formation, needs to be minimized at the same time as the stability of desired hybridizations is maximized.[13] This can usually be achieved by restricting the similarity between the base sequence and the Watson–Crick complements of all the other strands to which a given (sub)sequence must not hybridize.[14–17] The requirements specified in the previous step, that is, homogeneous stabilities or fixed subsequences, must also be included in this step.

The first sequence-design program SEQUIN was developed by Seeman to facilitate the design of oligonucleotides for construction purposes.[14] The sequences are constructed from short overlapping subsequences of fixed length (usually 3–5 nucleotides) to restrict sequence similarity. Each occurring subsequence must appear only once in all sequences, and its Watson–Crick complement must not be present at all. SEQUIN allows the designer to interactively construct sequences out of such overlapping subsequences by notifying which subsequences have already been used and which are still available. Although this interactive approach still makes the design process a laborious task, because additional requirements, such as certain GC ratios, must be considered manually, SEQUIN has been and is still being used very successfully to design oligomer sequences for complex motifs, such as branched junctions and crossover tiles (see Section 4.2). An alternative software package which also implements the concept of similarity avoidance, but is more user-friendly as a consequence of its automated construction process, has also been described.[15,18] This program can also take into account additional requirements, such as homogeneous melting temperatures or avoidance of guanine repetitions. A good overview of further programs for the design of oligomer sequences based on various concepts of sequence similarity and algorithmic approaches is given in the review by Brenneman and Condon.[16]

Finally, the various different DNA oligomers designed have to be assembled in vitro. Ideally this can be as simple as mixing all the components in a tube to initiate the self-assembly driven by Watson–Crick base pairing. More often, however, reaction conditions and entire protocols have to be carefully planned or empirically determined by a trial-and-error process.[19] For example, single building blocks might be assembled and purified in individual reactions before they are combined to produce the final architecture. A most crucial step in the entire process is that the structural integrity, connectivity, and possibly also the conformation of the resulting supramolecular network need to be characterized by using biochemical methods, such as electrophoresis of reporter strands (Figure 2),[20] restriction analysis, or fragmentation assays,[21] or nowadays by microscopic techniques, such as atomic force microscopy (AFM),[22] transmission electron microscopy (TEM), or cryoelectron microscopy.[23]

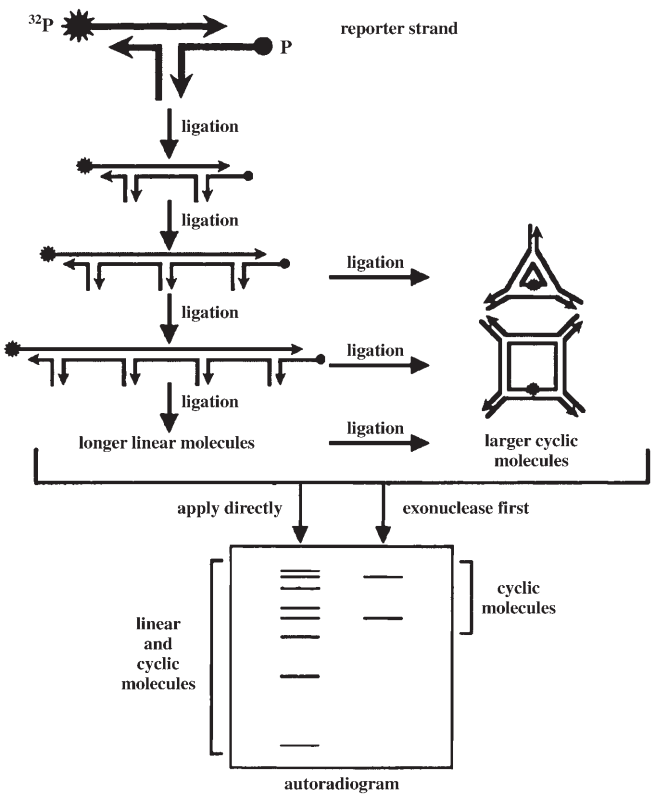



***Figure 2.*** Characterization of DNA nanoarchitectures using reporter strands designed such that their length corresponds to the number of self-assembled tiles, here a three-way DNA junction motif. Reproduced with permission from reference [149].

## 3. One-Dimensional DNA Strands for Assembly and Immobilization of Non-Nucleic Acid Compounds

A comparatively simple task from a construction point-of-view concerns the design of single-stranded DNA (ssDNA)


© 2006 Wiley-VCH Verlag GmbH & Co. KGaA, Weinheim

oligomer sequences for use as a template for the directed assembly of chemical compounds, proteins, or nanoparticles tagged with complementary sequences. Such designs are important for several applications. For example, short ssDNA oligomers, typically 10–25 bases in length, which are immobilized at solid supports can be used as capture probes in the DNA-directed immobilization (DDI) of nanoparticles, proteins, or small molecules tagged with complementary sequences (Figure 3, top). This approach has distinct advantages over

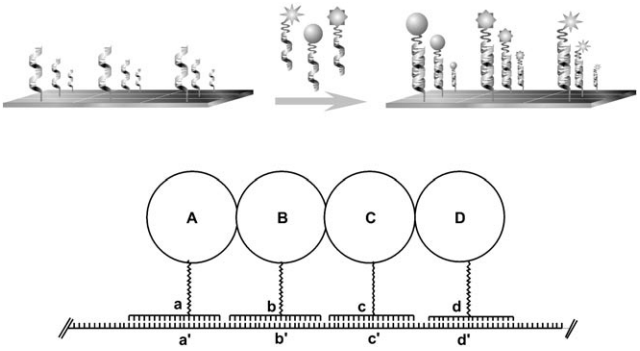



***Figure 3.*** Immobilization and directed assembly of components. Top: DNA-directed immobilization (DDI) of DNA–protein conjugates with surface-bound capture oligomers of a DNA microarray; bottom: schematic representation of DNA-based directional assembly of four different nanoscale building blocks to form a stoichiometrically and spatially defined supramolecular aggregate.[28] The upper section was reprinted with permission from reference [25].

conventional immobilization methods because the attachment is reversible and it occurs under chemically mild conditions. Furthermore, the specificity of Watson–Crick base pairing allows for the simultaneous immobilization of many different components in a single step when an array of capture oligomers is used as the immobilization matrix.[24] Recent applications of the DDI principle have demonstrated that DNA microarrays can be used efficiently as decoding tools in combinatorial chemistry and chemical biology.[25] In addition to this field of research, the heterogeneous hybridization implemented in DDI is also important for DNA computing on surfaces (see Section 6.1).

The hybridization of short complementary DNA oligonucleotides can also be utilized for the assembly of metal and semiconductor nanoparticles tagged with appropriate DNA oligomers. This approach, introduced in 1996 by Mirkin et al.,[26] allows the facile synthesis of three-dimensional nanoparticle materials and has evolved into a comprehensive field of research with a multitude of applications that range from materials research to analytics and biomedical diagnostics.[3,8–10,27]

While the above-mentioned nanoparticle assembly leads, in principle, to infinite growth of the supramolecular assemblies, ssDNA can also be used for the directional nanoscale assembly of various components, each of which is tagged with an individual oligomer sequence (Figure 3, bottom). This approach, initially demonstrated for DNA-tagged proteins,[28] has been extended to the directional assembly of inorganic nanoparticles,[29–31] and was also applied in DNA-templated organic synthesis, where two (or more) reactive chemical groups are held in proximity by means of a DNA scaffold.[32]

From a DNA-sequence design point-of-view, both the DNA-directed immobilization and the directional nanoscale assembly (Figure 3) share the problem of hybridization efficiency and specificity. High efficiency is clearly needed for a high yield of assembled components. Furthermore, the hybridization efficencies must also be homogeneous for all the components to be assembled so as to avoid undesired bias, which could otherwise lead to misinterpretations and false positives, for example, in biochip applications.[18] Unfortunately, calculating molecular properties of oligonucleotides such as melting temperature or free enthalpy of duplex formation is insufficient to allow hybridization efficiency to be predicted reliably, since the latter is also influenced by the formation of secondary structure and kinetic equilibria.[18,33] A most important factor to be taken into account derives from the tendency of single-stranded oligomers to form secondary structures. This problem becomes even more severe when several oligomer-tagged components are assembled on a long carrier strand.[33] Therefore, any applications which involve a large number of short ssDNA oligomers and/or long ssDNA molecules essentially depend on a very careful sequence design which has to consider more than intermolecular dissimilarity, that is, each strand is highly dissimilar to the complement of each other strand. It also has to implement intramolecular dissimilarity, such that no region of a given strand is too similar to the complement of another region of this same strand. Therefore, the sequence-design process has to precisely define what "too similar" means and requires means to enforce the dissimilarity. The most thorough method to prevent formation of secondary structures is based on the prediction of the thermodynamic stabilities of each sequence designed by using programs such as mfold[34] or RNAfold[35,36] and the rejection of sequences for which stable secondary structures are predicted.

## 4. Design and Assembly of DNA Motifs

The simple hybridization of single-stranded oligomers to form linear duplex structures is insufficient to construct more-complex DNA nanoarchitectures in two and three dimensions. In such cases, more-complex motifs are required as building blocks. The higher complexity of these motifs adds new requirements to the sequence design, and therefore, makes it much more challenging. Potential applications of such DNA nanoarchitecture include the use of rigid DNA scaffolds for the positioning of macromolecules with high precision at the nanometer length scale, and the exploitation of the powerful computational properties of DNA molecules.

### 4.1. Junctions and Lattices

In the early 1980s, Seeman conducted pioneering work on the construction of artificial nucleic acid architectures using synthetic DNA branched junction motifs mainly containing three and four arms (motifs **1** and **2** in Figure 4),[37] which are

 © 2006 Wiley-VCH Verlag GmbH & Co. KGaA, Weinheim 

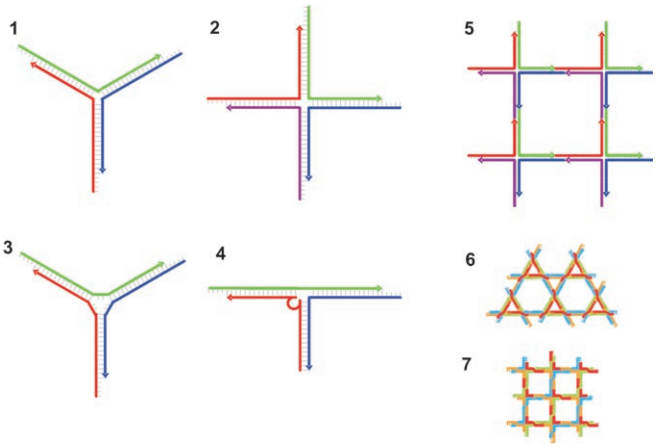



***Figure 4.*** Schematic representation of DNA junctions and lattices. Stable branched DNA junction motifs are three- (**1**) and four-armed (**2**) junctions.[37] Addition of an internal loop of unpaired bases increases mechanical flexibility (**3**),[39] a bulge loop allows for stacking of two arms (**4**), thereby fixing the angle between them to 180°.[40] A sketch of a lattice assembled from four-armed junctions **2** is shown as construct **5**. In fact, the helices of motif **2** do not cross orthogonally, thus allowing the assembly of Kagome lattices (**6**). Insertion of the protein RuvA fixes the angle between the helices to approximately 90°, thus leading to square lattices (**7**).[46] Pictures **6** and **7** were reproduced with permission from reference [46].

comprised of double-stranded DNA (dsDNA) helices. One half of each ssDNA oligomer involved contributes to one arm, while the other half is bound to one of the two neighboring arms. Thus, the helical arms of the juction are connected to each other at a central branching point (Figure 4). Variants with five and six arms were also synthesized by Seeman and co-workers, but these motifs turned out to be less stable.[38] The amount of branch migration, that is, the change between several different conformations, can be controlled by careful choice of the degree of base-pair symmetry around the branch point.[37] In other words, the mobility of the branch point of a given junction can be adjusted by sequence design. The mechanical flexibility of the junction can be increased by inclusion of unpaired bases into the strands such that the branch point now contains an internal loop (motif **3** in Figure 4).[39] The addition of a bulge to only one of the three strands of a three-armed junction (motif **4** in Figure 4) leads to stacking interactions between two arms, and therefore fixes the angle between them to about 180°.[40] The sequence design of such loops requires the search for another subsequence that has a low tendency to cross-hybridize to any other region of the motif. A simple and commonly used sequence stretch consists of only thymine bases, because they do not form structures by themselves (such as G and C, see Section 4.3.1), and it is rather easy to avoid long adenine repetitions in the other parts of the assembly.

Construction of so-called meso- and antijunctions, which are multiarmed motifs in which not all or not even a single helix axis points towards the center of the junction, has also been demonstrated.[41] These motifs are more difficult to assemble than branched junctions because they are less stable than junctions and show a tendency towards indefinite polymerization,[41] which makes them less attractive as components in nanoarchitecture. Nevertheless, antijunctions are automatically formed during the assembly of junctions into lattices (see below), and both antijunctions and mesojunctions have been used in the construction of single-stranded DNA knots.[41] These are cyclic strands that are knotted such that they cannot be disentagled to circles without cutting them.

The DNA junction motifs were designed as building blocks for fabricating repetitive DNA nanoarchitecture, such as lattices and grids (**5** in Figure 4), as well as for the assembly of lattice models of regular bodies (see Section 5.2). Sticky ends at the junctions' arms enable the self-assembly of these motifs into two-dimensional lattices by enzymatic or chemical coupling.[37] These lattices are potentially useful as scaffolds with nanometer-spaced repetitive structural features. However, the assembly of these simple junction motifs led to the formation of highly irregular structures, rather than the repetitive DNA superstructures anticipated. These observations have led to the conclusion that the junction motifs were inappropriate for the assembly of regular gridlike architectures because of their high conformational flexibility.[42]

Nonetheless, junction motifs have recently been used as building blocks for the generation of three-dimensional dendritic structures which can be labeled with distinct mixtures of fluorescent dyes, thereby turning them into "nano bar codes" for the multiplexed detection of nucleic acids.[43,44]

Another application of junction-based lattices concerns the representation of so-called "graphs". These are mathematical constructs consisting of a set of vertices or nodes and a set of edges, each of which connects two vertices (Figure 5a). Graphs are used as computer data structures to model a wide range of systems and processes. For example, various graph-based algorithms have been developed for the optimization of workflows, communication networks, and for applications in life sciences, such as the assembly of short sequenced DNA strands to reconstruct complete genomes.[45]

Recently, a nonplanar graph structure, that is, a graph for which all two-dimensional arrangements contain at least one pair of edges crossing each other (see Figure 5b,c), has been assembled using junction motifs as vertices and duplexes as edges (Figure 5d,e).[39] This graph consisted of five vertices, each of which connects three or four of the, in total, eight edges of this geometric figure. The vertices were formed by either three- or four-armed junctions, while the edges were constructed from linear duplexes and three-armed junctions, the latter of which contained one arm which was closed by a hairpin loop to provide additional structural flexibility. Such a graph is not only interesting as a scaffold for nanoconstruction, but it also holds promise for DNA computing. In this context, this figure might be used for solving standard problems in computer science, such as the Hamilton path problem or the satisfiability problem. Descriptions of these problems can be found in Section 6.1.[39]

A recent study has demonstrated that the shape of a junction within the two-dimensional lattices, in particular, the angles between the arms and the orientation of sticky ends, can be controlled by the addition of the DNA-binding protein RuvA.[46] This protein plays an important role in vivo as part

 © 2006 Wiley-VCH Verlag GmbH & Co. KGaA, Weinheim 

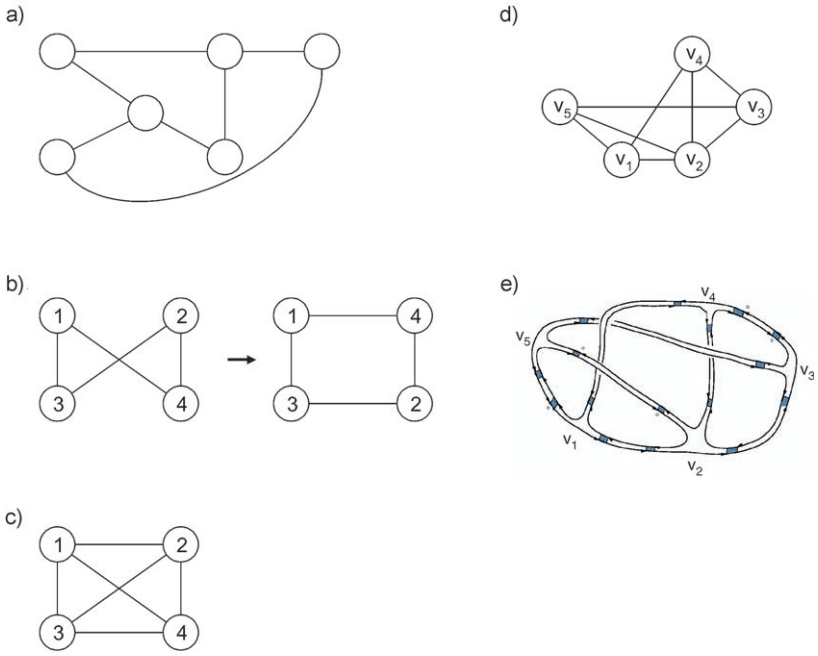



***Figure 5.*** Graphs and their realization as DNA molecules. a) A graph consists of vertices (circles) connected by edges (lines). b) The left graph is planar, since the vertices can be arranged such that no two edges cross each other. c) This graph is not planar, because there are crossing edges for each arrangement of vertices. d) This graph was realized by a DNA structure.[39] e) Sketch of the DNA assembly representing graph (d). Vertices are represented by three- and four-armed branched junctions (motifs **1** and **2** in Figure 4), and edges by double helices. Image (e) was reproduced with permission from reference [39].

of a protein complex processing Holliday junctions during bacterial homologous recombination. Cryoelectron microscopy analysis shows that the presence of RuvA during the assembly of four-armed junctions into regular lattices changes the structure of the lattice from a Kagome-type lattice comprised of hexagons and triangles (without RuvA, see **6** in Figure 4) into a grid comprised of squares (with RuvA, see **7** in Figure 4).[46]

Although three- and four-armed junctions have been demonstrated to be highly flexible building blocks,[42] they can nevertheless be used for constructing more-rigid architectures. One example concerns a motif consisting of four four-armed junctions. Although the schematic representation of motif **2** and assembly **5** in Figure 4 may suggest the helices of a four-armed junction cross perpendicularly, they actually possess an angle of about 60°. Thus, four such junctions form a rhomboidal supramolecular structure, shown as in motif **8** in Figure 6, which is also a more realistic depiction of construct **5**.[47] A set of rhomboids was subsequently assembled into one-dimensional "railroad tracks" (**9** in Figure 6) as well as into two-dimensional lattices (**10** in Figure 6). Remarkably, no cyclic ligation products, such as lattices that roll up to form tubes, were observed. Moreover, AFM analyses showed that the torsion angles between helices are relatively constant throughout the entire lattice (Figure 6).[47] These results clearly demonstrate that the rhomboid motif, if it is assembled directly from ssDNA oligomers without the detour of an initial assembly of junctions which are then assembled into motif **8**, shows less structural flexibility than individual junction motifs (for example, **1** and **2**). In fact, motif **8** can be regarded as a rigid and flat building block.

The introduction of bulged $T_4$ loops into all four helices connecting two adjacent junctions of four four-armed junctions in motif **8** induces a bending of the particular helices and, therefore, opens up a way to generate so-called $4\times4$ tiles (motif **11**, in Figure 7).[48] These motifs are shaped like four-armed "suprajunctions" which contain stretched four-armed junctions as their arms. The tiles **11** were assembled to form linear ribbons and two-dimensional lattices (**12**, in Figure 7).[48] Very recently, He et al. managed to assemble unusually large two-dimensional arrays from motif **11** by employing two new concepts.[49] First, motif **11** was designed to be symmetrical, which means that the base sequences of all four arms were identical. Second, a "corrugation strategy" was used, where adjacent building blocks face up and down alternately, such that small curvatures occurring in the individual motifs cancel each other out instead of cumulating throughout the supramolecular assembly.

Arrays of motif **11** have also been used for a number of applications, including the fabrication of ohmic conductors through metalization of a ribbon-type assembly with silver.[48,50] Moreover, building block **11** was used to generate periodic arrays of the protein streptavidin (STV) by inserting a biotin moiety into one of the $T_4$ bulges (structure **12** and AFM image in Figure 7).[48,51] Various assemblies of motifs similar to **11** (for example, comprising only three four-armed junctions) and of other building blocks such as triangles and rhomboids were also used as a mask for molecular lithography.[52,53] This was achieved by adsorption of the DNA

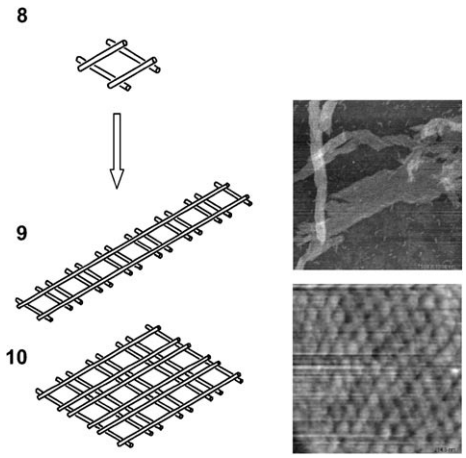



***Figure 6.*** The rhombus motif. The three-dimensional structure of DNA junction motifs results in the assembly of four four-armed junctions **2** containing two closed ends that lead to the formation of a rhombus (**8**), which can be used as a basic component for the self-assembly of linear (**9**) or planar (**10**) superstructures. The AFM images show examples of structure **10** at two different magnifications. Reprinted with permission from reference [47].

 © 2006 Wiley-VCH Verlag GmbH & Co. KGaA, Weinheim 

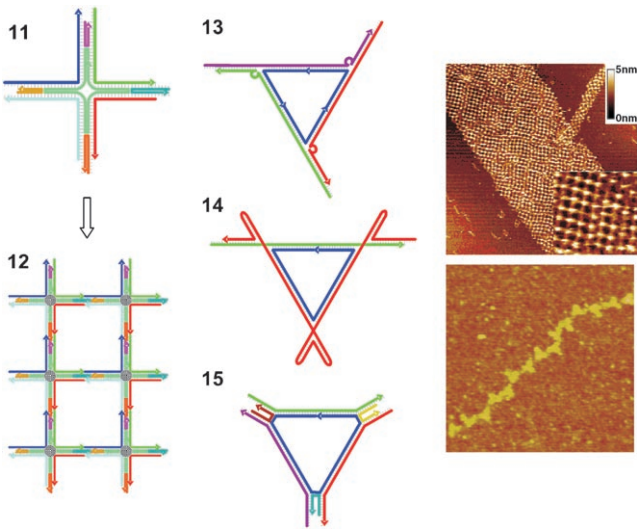



***Figure 7.*** Higher order motifs. The assembly of four four-armed junctions **2**, containing additional bulges, led to the formation of a four-armed suprajunction **11** (a 4×4 tile).[48] Structure **12** represents an example of a lattice comprised of 4×4 tiles that are decorated with streptavidin molecules (black circles) bound to one of the bulges of each tile through incorporated biotin groups.[51] The upper right AFM image shows such a lattice. Several different triangular structures have been constructed from bulged three-armed (**13**)[57] and four-armed junctions (**14** and **15**, respectively).[56,58] Motif **14** was designed for linear assemblies. Replacement of some hairpins with additional sticky ends allows for the building of two-dimensional structures.[56] The lower AFM image shows a linear assembly of **14** with the triangles lying on alternating sides of the connecting helix. The AFM images were reprinted with permission from references [51] (upper) and [56] (lower).

superstructures onto mica and subsequent coverage with a thin layer of gold, thus leading to the formation of a negative imprint of the nanostructure in the metal that could be analyzed by AFM.

DNA triangles (for example, motif **13** in Figure 7) are also promising candidates for the fabrication of so-called tensegrity structures. These are constructs of rigid rods (here DNA duplexes) which are connected by short so-called tendons (here, for example, branch points of DNA junction motifs).[54–56] The balance between the rods pushing the three-dimensional structure outward and the tendons pulling it inward stabilizes the shape of such a structure, even under application of external forces. For example, a tetrahedron of rods and short tendons is stable, while a cubelike structure would collapse under external forces, such as gravity.

The shape of a DNA triangle, or, more precisely, the angles between adjacent arms in the triangle's corners, are defined by the lengths of the helical edges. Therefore, a DNA triangle can be regarded as a two-dimensional tensegrity structure. Clearly, a very precise choice of the lengths of the rods and tendons is essentially important, because tendons that were too long would make the assembled structure too flexible, whereas tendons that were too short or badly chosen lengths of rods may completely prevent the formation of closed structures. Such triangular DNA structures comprised of three bulged three-armed junctions as vertices were designed to be ligated into planar hexamer structures.[57] While two of the junction's arms formed edges, the third arm formed a hairpin loop containing a restriction site which, after digestion with an endonuclease, provided a sticky end for further assembly (motif **13** in Figure 7). The primary ligation products of **13**, however, were found to be cyclic tetramers rather than the cyclic hexamers expected. Since this deviation in the size of the cyclic ligation products could only occur when the triangles were flexible, this experiment demonstrated the lack of rigidity of these building blocks. Similar approaches using four-armed junctions as vertices were more successful. Indeed, these building blocks allowed for the production of large one- and two-dimensional arrays.[56,58] In particular, adjacent triangles were connected by one[56] or two[58] sticky ends (motifs **14** and **15** in Figure 7, respectively), and, therefore, these two motifs assembled into two slightly different 2D patterns. The supramolecular architecture was then analyzed by AFM. A typical image is shown in Figure 7.

### *4.2. Crossover Tiles*

DNA junctions are rather flexible and the assembly of these building blocks often did not yield the regular superstructures desired. To solve this problem, Seeman and coworkers constructed more rigid components, the so-called crossover tiles. Double crossover (DX) tiles consist of two double-stranded helices, which interchange single strands at two crossover points (motifs **16**–**18** in Figure 8).[59] In total, five different structural motifs of DX tiles exist. In three of them (for example, motif **18**, Figure 8), their helical domains are oriented parallel, which means that the minor grooves of both helices meet each other in each turn, as do the major grooves. Consequently, extensive Coulomb repulsion occurs between the two parallel strands and, therefore, these motifs reveal structural instability.[59] The two antiparallel motifs **16** and **17**, where the minor groove of one helix lies in the major groove of the other helix, are more stable because of the decreased Coulomb repulsion. They differ in the number of helical half-turns between the crossover points, being either even (**16**, a so-called DAE motif) or odd (DAO, **17**). Distances between the two crossover points which do not contain multiples of helical half-turns lead to torsional stress within the motif, and therefore such building blocks are less stable and have not as yet been applied for construction purposes. Since a DX tile can be considered as two four-armed junctions connected by two neighboring arms, branch migration is possible. This can be avoided by appropriate choice of the base sequences during the design of such tiles (see Section 4.1). However, because the two crossover points would have to branch-migrate concertedly, this process is less likely to occur than in regular DNA junctions.[59]

DX tiles are usually designed such that they comprise sticky ends at their four arms which can be used for self-assembly. To assemble DX tiles into planar two-dimensional superstructures, the total lengths of the arms (including the sticky ends) must contain multiples of helical half-turns between the crossover points of adjacent tiles. Additional

 © 2006 Wiley-VCH Verlag GmbH & Co. KGaA, Weinheim 

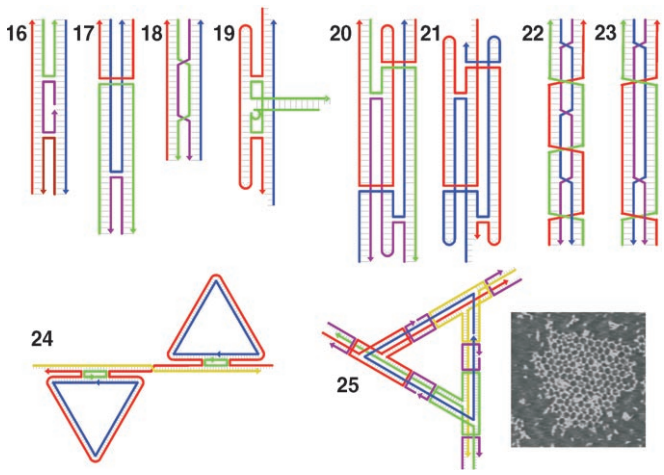



***Figure 8.*** Crossover tiles. The more-stable and thus usually applied double-crossover (DX) tiles are DAE (**16**) and DAO (**17**) with antiparallel helices.[59] The DPE motif (**18**) is an example of a less-stable DX tile with parallel helices. The modified DX motif **19** has an additional three-armed junction which provides a sticky end protruding from the tile plane.[60] The triple-crossover (TX) tile (**20**) can be regarded as being built from two DAO-DX tiles that share the central helix.[59] The positioning of the sticky ends at the central helix (**21**) allows for the lateral helices to lie above and below the plane of the tile assembly.[61] In paranemic crossover (PX) tiles (**22**), the two helices exchange strands wherever possible.[62] Together with its topoisomer $JX_2$ (**23**), the PX tile builds the base of a strand-replacement-driven nanodevice (see Figure 16).[131] The inclusion of one of the helices of a DX tile **16** as an edge into a DNA triangle can be used to generate a linear assembly (**24**).[70] In motif **25**, DX tiles have been connected into a triangular structure, which in turn can assemble into a pseudohexagonal lattice (see AFM image).[72] The AFM image was reprinted with permission from reference [72].

structural features can be engineered into the basic structure of a DX motif. For example, inclusion of a bulged three-armed branched junction (motif **4**) between the crossover points (as shown in motif **19** in Figure 8) allows for the attachment of further molecules protruding from the plane.[60]

Triple crossover (TX) tiles consist of three helices lying in a plane, connected through crossover points.[61] Motif **20** (Figure 8) is a typical example. It was constructed from two DAO-DX tiles (**17**) that share the central helix. This construction allows for the assembly of a reporter strand running through all the tiles of a TX assembly (Figure 2). Furthermore, TX tiles offer the facility to include gaps in shifted arrays and allow the incorporation of components which protrude from the plane of two-dimensional arrays (see below).[61]

Paranemic crossover (PX) molecules comprise another class of DNA motifs (motif **22**, in Figure 8). Similar to parallel DX tiles, PX molecules are composed of two parallel helices; however, PX motifs form crossovers at every point possible. This renders the tiles more stable than the comparable DX molecule.[62] The term "paranemic" here indicates that even if the blue and the green strand of motif **22** were connected by hairpin loops at both ends of the motif (as well as the red and the violet strand), the melting of this motif would result in two seperated cyclic molecules that do not interpenetrate topologically.

While all crossover tiles can be considered as flat and rigid building blocks, the structural variety of individual types offers a large range of options for modulating the spacing and connectivity of the building blocks and of the final superstructure desired. Moreover, crossover motifs can be further modified and expanded to include additional functionalities. For example, the use of a derivative of motif **19**, designed such that the third (unstacked) arm forms a hairpin loop protruding from the tile plane, allowed for the self-assembly of striped crystals with defined spacings between the stripes of hairpin loops.[22,63] These superstructures have been visualized by AFM, and a typical example is shown in Figure 14. Similar striped superstructures were fabricated by self-assembly of TX tiles, where one type of tile had sticky ends only at the central helix (motif **21** in Figure 8).[61] The number of helical turns between these sticky ends and the crossover points were chosen as non-integer multiples. Therefore, ligation of such a tile with other tiles into two-dimensional arrays positions the two lateral helices above and below the array plane, respectively.[61]

The striped arrays described above have been suggested as nanoscale barcodes,[64] and they have already been used as scaffolds for the positioning of gold nanoparticles (see AFM image in Figure 14),[65,66] and even recently to produce alternating rows of two differently sized nanoparticle species.[67] Moreover, one- and two-dimensional positioning of streptavidin and gold nanoparticles has been achieved using nanoarrays of TX tiles which contained hairpin loops in the lateral helices.[68] While most arrays obtained from these simple tiles are potentially infinite in size, the replacement of specific sticky ends in some tiles by blunt ends or hairpin loops terminates the self-assembly process. Thus, these tiles then define the boundaries for the growth of two-dimensional crystals, thus allowing, for example, the generation of V- or X-shaped structures.[69]

Crossover tiles have also been used as building blocks for the generation of larger motifs, which were then used as building blocks themselves. For example, a cyclic double-stranded supramolecular structure which included three flexible bulges was constructed (motif **24** in Figure 8).[70,71] It formed a triangle with the bulges as vertices and the helices between the bulges as edges. One of these edges was actually formed by one helix of a DX motif while the second helix of this DX tile was used for the assembly of a long "carrier" strand by means of ligation of the sticky end. This approach allowed for the fabrication of a chain of the triangles, which were nicely visible by AFM imaging.[70] In a related approach, the carrier strand was equipped with a paranemic crossover motif, which induced a connection between duplex helices that were wrapped around each other without ligation.[71] Moreover, triangles comprised of DX tiles at all three edges that interchange strands at additional crossover points at the vertices (motif **25** in Figure 8) were successfully assembled into pseudohexagonal lattices by ligating the external arms.[72] These assemblies were also characterized by AFM (Figure 8).

In general, the variety of crossover and junction motifs together with more simple elements such as sticky ends, helices, bulges, and loops offer a large set of building blocks for the fabrication of DNA architecture. The combination of

 © 2006 Wiley-VCH Verlag GmbH & Co. KGaA, Weinheim 

these elements in higher-order motifs (for example, **13** and **24**) enriches this set even more. However, this hierarchical approach necessitates an additional decision by the designer, namely how many elements are to be included in a single building block. For example, Mao et al. constructed the rhomboid motif **8** as a small grid comprised of four four-armed junctions **2**.[47] They carried out this "assembly" in the planning step only, but specified motif **8** as an "atomic" building block which was directly assembled in vitro from the respective single-stranded oligomers. Another possible approach would include the initial assembly of the single strands to junctions in vitro and then assemble the junctions to motif **8** and further one- or two-dimensional superstructures. However, the latter way was significantly less promising because individual branched junction motifs show a much higher structural flexibility than motif **8**. Thus, the decision on whether to split higher-order building blocks into smaller elements, and, if so, into which elements they should be split, is of essential importance.

### 4.3. Other Motifs

#### 4.3.1. Guanine Quadruplexes

Guanine-rich stretches of DNA form inter- and intramolecular G quadruplexes in the presence of monovalent cations, such as potassium ions. The G quadruples contain four strands which are aligned into a "bundle" with a square cross-section (motif **26** in Figure 9). Such quadruplexes have

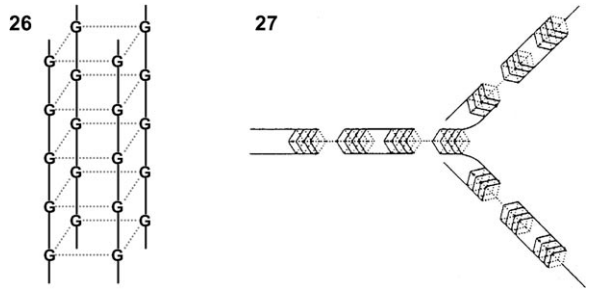



***Figure 9.*** Guanine quadruplexes. Motif **26** consists of four guanine-rich strands that align in the presence of $K^+$ ions into a bundle with a square cross-section. Such motifs can be assembled into branched wirelike structures (**27**). The picture of structure **27** was reproduced with permission from reference [73].

also been used as buildings blocks in the self-assembly of DNA nanoarchitecture to generate linear structures which are more rigid than a regular double helix.[73] Following this concept, so-called frayed wires, which have additional dangling ends at each building block, were produced from G quadruplexes.[74] Networks of frayed wires were then constructed using linker strands that form Watson–Crick and Hoogsteen base pairs with the "fringes". These assemblies were characterized by AFM.[74] The assembly of branched nanowires of guanine quadruplexes has also been demonstrated (**27** in Figure 9).[73]

#### 4.3.2. Tecto-RNA

DNA's close relative RNA has also been used for the rational design of two-dimensional structures. Two hairpin loops are connected by a right-angled structural motif form to give the so-called tectoRNA motif (motif **28** in Figure 10).[75]

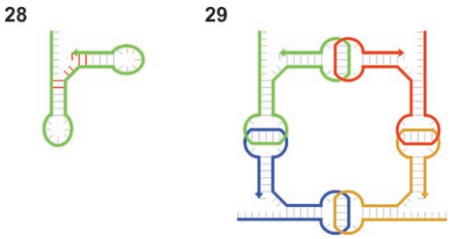



***Figure 10.*** Tecto-RNA. Two hairpin loops connected by a right-angled RNA motif (red bases and base pairs) form a tectoRNA building block **28**.[75] Four species of **28** with complementary loop sequences assemble into square motifs such as **29** which are themselves building blocks for grids or ladderlike structures.

Square-shaped assemblies such as **29** comprised of four tectoRNA motifs connected through hybridization of their loop strands were then used as building blocks for the assembly of larger two-dimensional superstructures. The use of different combinations of the positioning and orientation of the sticky ends in **29** motifs enabled ladderlike structures and several different forms of 2D grids to be assembled.[75] Recently, the one-dimensional, ladderlike assembly of **29** was used for the electrostatic deposition of cationic gold nanoparticles inside the loops of **29**.[76]

#### 4.3.3. Chemical Branch Points and Linkers

Synthetic non-nucleic acid molecules may also serve as linkers or branch points of DNA nanoarchitecture (Figure 11). According to this approach, a synthetic core tethered by two or more DNA oligomers may contribute additional structural or chemical properties while maintaining its capabilities for Watson–Crick base pairing, thus enabling specific supramolecular self-assembly (Figure 11a). As an example, Stewart and McLaughlin have used nickel-centered cyclams as hubs for four DNA oligomers (Figure 11b).[77] Different types of oligomer–cyclam complexes with complementary oligomers were assembled into larger structures. However, because of their characterization only by gel electrophoresis, it is currently unknown whether the superstructures were linear or latticelike. Gothelf et al. attached DNA oligomers to salicylaldehyde groups of two- and three-armed compounds, called linear oligonucleotide-functionalized modules (LOMs; Figure 11c) and tripoidal OMs (TOMs; Figure 11d), respectively.[78] In their approach, the DNA strands guide the self-assembly of linear and branched structures by positioning the branch-point modules in proximity to one another. The actual assembly is then carried out by covalent linkage of the individual compounds and the DNA oligomers can subsequently be removed from the assembled products.[79] Supramolecular assemblies were constructed by von Kiedrowski and co-workers from so-called

 © 2006 Wiley-VCH Verlag GmbH & Co. KGaA, Weinheim 

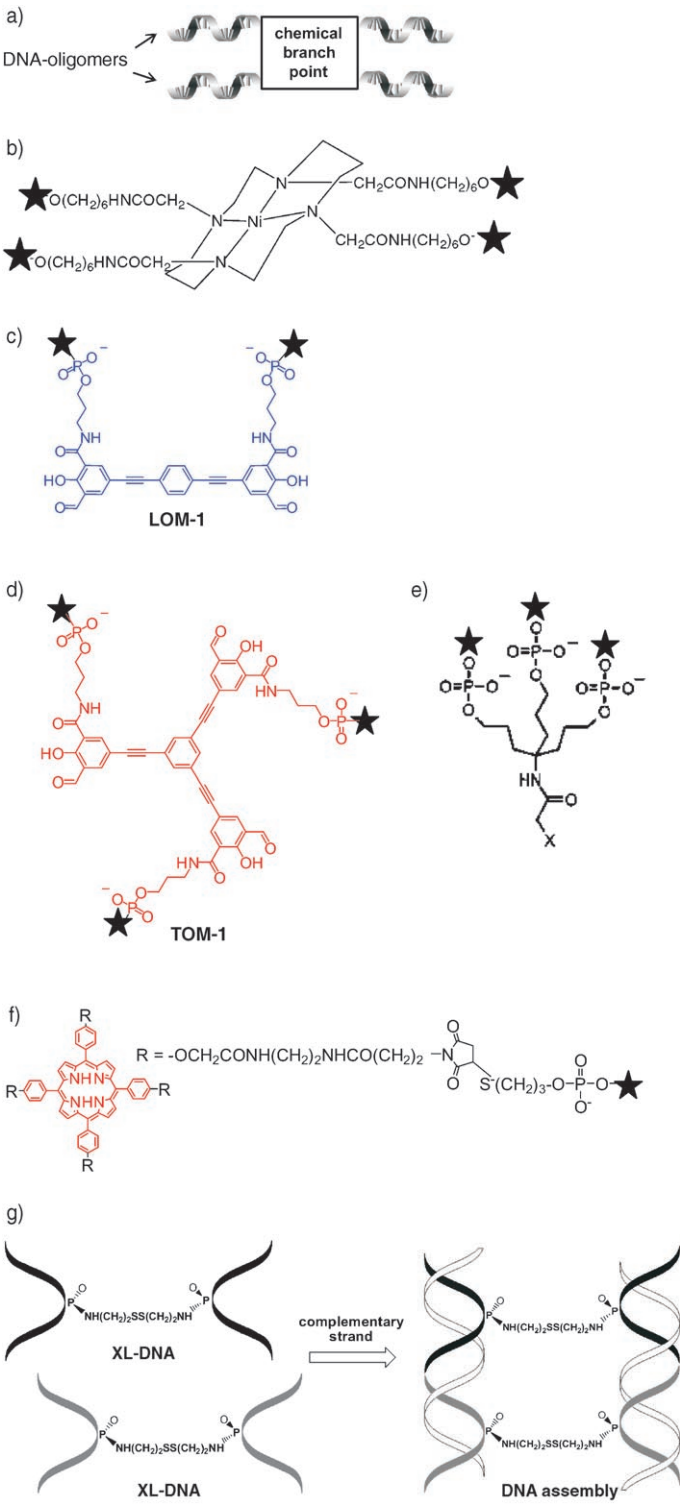



***Figure 11.*** Chemical branch points and linkers. The general scheme depicted in (a) shows a central hub or branch point which connects several DNA oligomers, while the hub itself does not consist of DNA. Examples of chemical branch points are [Ni(cyclam)] (b),[77] compounds with salicylaldehyde groups (c, d),[78] a branched alkane containing a quaternary carbon atom (e),[80] and a porphyrin derivative (f).[85] The stars in images (b–f) mark the attachment points of the DNA oligomers. g) Disulfide cross-linked DNA strands are assembled by hybridization to form long complementary strands.[82] Images (b–g) were adapted with permission from the references cited.

trisoligonucleotides which contained three DNA arms that were connected to each other by a Y-shaped chemical linker (Figure 11 e).[80] These building blocks were used to assemble a superstructure with the connectivity of a tetrahedron.[55] Moreover, this concept permitted the copying of the connectivity of individual motifs on the basis of self-assembly,[81] and, hence, it may open up the doors for self-replication of DNA nanoarchitecture.[55]

Endo and Majima used linker molecules to connect the backbones of two short DNA strands (Figure 11 g).[82] When several different species of this disulfide cross-linked DNA (XL-DNA) were hybridized to long continuous strands, the relative position of the two resulting double helices was determined by several chemical cross-links. The XL-DNA modules were also used as mediators in an oligomer-dependent translation system.[83] Various XL-DNA modules were hybridized along an "input strand" that contained the information. Complementary oligomers were then hybridized to the free strands of the XL mediators, and ligation connected these oligomers to form an "output strand". Such a translator can be useful in DNA computing, for example, for encryption or to map variable inputs as a standard input code.[84] In a joint approach, Endo, Majima, and Seeman were able to hybridize four-way porphyrin connectors coupled covalently to four DNA strands (Figure 11 f), with sticky ends protruding from a two-dimensional DX tile array.[85] The spatial contraints induced by the connector caused the array to roll into a three-dimensional tubular structure.

## 5. Three-Dimensional Structures from DNA

In the majority of the examples described above, it was intended that the tiles assembled into flat two-dimensional structures. However, one of the major goals of Seeman's concept published in the early 1980s was the construction of three-dimensional DNA crystals which might serve as a periodic scaffold for the X-ray crystallographic analysis of guest molecules, such as proteins, that would not form crystals by themselves.[86] It proved to be much more difficult to construct regular 3D architectures than fabricating 2D arrays,[87] and this goal was not realized until 2004 (see Section 5.3).[88] In addition to this recent brakethrough, a number of examples of 3D structures were successfully built from DNA, such as nanotubes and geometric stick-figure objects.

### 5.1. DNA Nanotubes

From a conceptual point-of-view, DNA nanotubes are produced by initially assembling a 2D grid or a ribbon of tiles which then rolls up to form a tubular structure. To this end, building blocks with an inherent tendency to form curved structures were used, which is realized in modified 4 × 4 tiles,[50] DAE-DX tiles (**30** in Figure 12),[89,90] and TX tiles.[91] Interestingly, tubular DNA assemblies which were obtained from motifs **11** and **20**, respectively, were metalized by electroless silver deposition and resulted in the production


© 2006 Wiley-VCH Verlag GmbH & Co. KGaA, Weinheim

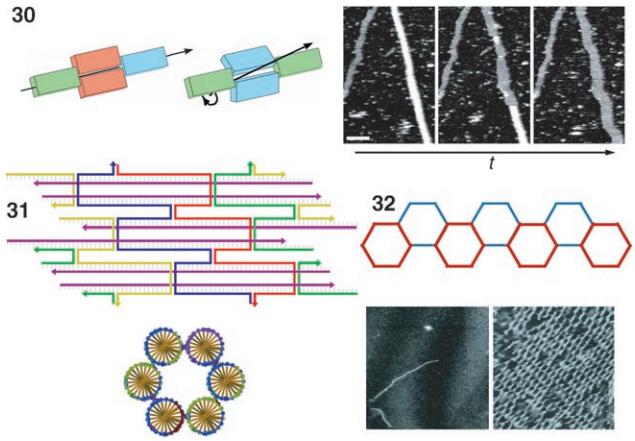



***Figure 12.*** DNA nanotubes. Schematic representation of the rectangular DX tile **30**; the left assembly forms a lattice lying in a plane,[90] while in the right scheme, the spacing and orientation of crossover points encourages a curved assembly, thus allowing for the construction of a tube. The AFM image shows how a nanotube (white linear structure) progressively opens under AFM into a flat lattice (gray structure). The six helices of motif **31** connected by crossover points form a six-helix bundle (6HB).[92] The central axis of the six helices of this motif forms a hexagonal cross-section (see scheme below). An overlapping assembly of 6HB motifs leads to a two-layer lattice (**32**). The two AFM images (bottom right) show a long nanotube of 6HB motifs (left) and a hexagonal lattice (right). All images are reproduced/adapted with permission from references [90] (**30** and upper AFM image) and [92] (6HB scheme and lower AFM image).

constructed supramolecules with the connectivity of a cube (**33** in Figure 13)[94] as well as a truncated octahedron (**34**, Figure 13)[95] by assembling three- and four-armed branched junctions, respectively, which served as vertices. Recently, a tetrahedron was constructed out of four 55-mer ssDNA oligomers by Turberfield and co-workers (**35**, Figure 13).[96]

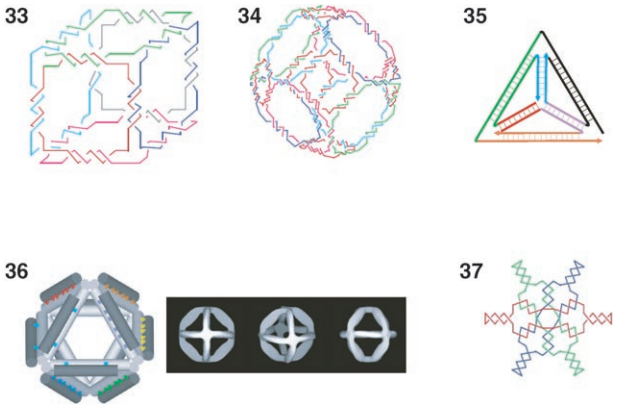



***Figure 13.*** 3D-object wire frames. While constructs **33** and **34** possess only the connectivity, but not the three-dimensional shape, of a cube[94] and a truncated octahedron,[95] respectively, DNA model **35** is most likely a proper tetrahedron because of the rigid tensegrity structure.[96] The three-dimensional shape of octahedron **36** has been proven by cryoelectron microscopy.[23] When one of the three Borromean rings of construction **37** is cut, the other two rings are unlinked.[98] Reprinted from the references cited.

of Ohmic conductors.[50,91] Addition of protruding hairpin loops to motifs of type **16** led to diagonally or perpendicular striped surfaces on the outer tubes, similar to the aforementioned flat, striped arrays (see Section 4.2). The striped patterns were adjustable by careful selection of the sticky ends of the motifs employed.[90] The formation of DNA nanotubes can be assisted by using chemical connectors to induce spacial constraints (see Section 4.3).[85]

Another type of DNA-based nanotube has been built by the assembly of six-helix-bundle (6HB) motifs.[92] The 6HB consisted of crossover tiles comprised of six parallel helices (motif **31** in Figure 12) which were curved around a central axis, parallel to the helical axes, such that the cross-section of the tube tile formed a hexagon with the helix axes as vertices (Figure 12). While a linear array of 6HB motifs formed a nanotube, blocking some of the sticky ends led to a two-dimensional two-layer array of hexagons, similar to slices cut from such a nanotube layed out in a plane (see **32** and the AFM image in Figure 12).[92] A similar motif comprised of only three helices (3HB) did not form tubes with hollow space, but rather produced filaments which might be applicable as templates for the growth of metal nanowires.[93]

### *5.2. Stick-Figure Models of Regular Objects*

A series of DNA stick-figure objects that resemble the wire frame of regular bodies with duplexes as edges have been successfully fabricated from DNA. Seeman and co-workers This object is a more-rigid wire frame than the cube because its triangular sides fulfill the tensegrity concept (see Section 4.1). The conformational stability of the tetrahedron was recently validated through AFM imaging with an ultrasharp tip. Three upper edges were recognizable, and external force could be applied to the tetrahedron using the AFM tip.[97] Another example of a putative DNA tetrahedron containing chemically linked trisoligonucleotides was reported by von Kiedrowski et al. (see Section 4.3.3).[55]

Geometric objects have even been produced from genetically encoded DNA. Shih et al. designed a 1669 nucleotide ssDNA which, after addition of five 40-mer oligonucleotides, readily folded into a connected structure of five DX and seven PX tiles, thereby producing a 3D object with an octahedral shape (**36**, Figure 13).[23] As evident from cryoelectron microscopy analysis (Figure 13), this octahedron revealed a rigid and well-defined three-dimensional shape because of tensegrity resulting from its triangular sides. Tensegrity clearly proves to be a promising tool for the design of 3D DNA nanoarchitecture. Finding base sequences that adopt the intended structure is not much more difficult than in the two-dimensional case, but the major problem is to find structures stable enough to withstand the forces of gravity.

A set of Borromean rings, which are interconnected rings that are all disconnected by cleavage of just a single ring, was also made for DNA (**37**, Figure 13).[98] In this assembly, two three-armed junctions where designed such that only one of them adopts the usual B-DNA conformation while the other one was in the Z-DNA conformation.

 © 2006 Wiley-VCH Verlag GmbH & Co. KGaA, Weinheim 

### 5.3. A Three-Dimensional DNA Lattice

Recently, Seeman and co-workers reported a regular, continuous 3D DNA lattice.[88] The three-dimensional structure was analyzed by X-ray diffraction analysis and shown to consist of three repeating layers of parallel helices. Helices of adjacent layers interchange strands where they cross, thus fixing the layers relative to each other. All the helices within a layer run parallel to each other at a distance of 20 Å and are rotated 60° relative to those of the adjacent layers. As a consequence, solvent channels are formed which run both parallel and perpendicular to the helical axes. Surprisingly, the rather complex construct is comprised of various copies of only a single 13-mer oligonucleotide. Four copies of this oligomer form a three-dimensional building block that consists of two short helical regions connected by strand crossovers. Another striking aspect is that the entire construct is held together by only a few base pairs formed by Watson–Crick complements. The strands are mainly assembled by parallel-stranded homo-base pairing, mainly occurring between guanine and adenine bases, respectively, and the supramolecular structure is additionally stabilized by interstrand stacking between base pairs of different strands. Variable-length insertions between the helical regions and interlayer junctions defined the spacing of the lattice and thus the dimensions of the solvent channels. The authors anticipated that such lattices from DNA might be used as scaffolds which host guest molecules inside the solvent channels, thereby allowing for the X-ray crystallographic analyis of the guests.[88]

## 6. Applications of DNA Nanoarchitectures

The term "application" in the context of DNA nanoarchitecture does not refer to commercial products available on the market, and we assume that these can only be envisioned in the long-term. At present, applications only concern the distinct utilization of structural and functional properties of DNA nanoarchitecture, such as the directed positioning of molecules and nanoparticles using a DNA scaffold, the generation of electrically conducting elements through metalization of DNA architecture, the use of DNA assemblies as mechanical elements, and the utilization of the informational content of DNA constructs for computing. While the first two types of application have already been discussed in the context of the description of structural features in Sections 3–5, we will focus here on DNA nanomechanical devices and DNA computing.

### 6.1. DNA Computing

In 1994 Adleman demonstrated that DNA can be used for computationally solving a small example of a standard problem in computer science.[99] Since this initial example, a large number of publications have followed that describe various approaches to exploit the parallel reaction of large numbers of molecules for highly parallel computing in very small spaces. Since excellent reviews on the topic of DNA computing are already available,[100,101] we will limit this Review to approaches for DNA computing which are based on regular assemblies of DNA motifs as building blocks. However, we will initially describe an example where the biochemical manipulations are rather basic so as to introduce the general concepts of DNA computing, the type of problems that can be addressed, and how logic calculations can be carried out by means of biochemical techniques.

The simplest type of DNA assembly, that is, the hybridization of a single-stranded oligonucleotide with its Watson–Crick complement, represents an efficient method of employing molecular recognition and extraction of information. This approach was applied to surface-based DNA computing, where capture oligomers were immobilized on a solid surface to solve a satisfiability problem of Boolean functions, which is a computationally hard, standard problem in computer science.[102] A Boolean function takes vectors $(x_1, \ldots, x_n)$ of $n$ bits $x_i$, each of which can take the values 0 or 1, as arguments and delivers a 0 or 1 as a result. Such a function can be described by a term consisting of the variables $x_i$ and Boolean operators NOT, AND, and OR. NOT turns a 0 into a 1 and vice versa, AND results in 1 only if all arguments equal 1, and OR results in 1 if at least one of its arguments equals 1 (Table 1). In the satisfiability problem, this term is comprised of so-called clauses linked by AND operators. Each clause consists of variables and negations of variables linked by the operator OR. For example, "$(x_1$ OR $x_2)$ AND $(x_1$ OR NOT $x_3$ OR $x_4)$" would be a valid function description. The problem is to decide whether there is at least one argument vector $(x_1, \ldots, x_n)$ such that the given function maps this vector to the result 1. For the function to result in 1 (to be "satisfied") for an argument vector, each clause has to result in 1.

**Table 1:** Boolean operators.[a]

| $x$ | $y$ | NOT $x$ | $x$ AND $y$ | $x$ OR $y$ | $x$ XOR $y$ |
|---|---|---|---|---|---|
| 0 | 0 | 1 | 0 | 0 | 0 |
| 0 | 1 | 1 | 0 | 1 | 1 |
| 1 | 0 | 0 | 0 | 1 | 1 |
| 1 | 1 | 0 | 1 | 1 | 0 |

[a] $x$ and $y$ are the arguments which can take the values 0 or 1; the four columns on the right-hand side show the results of the four operators NOT, AND, OR, and XOR for each argument combination.

In the surface-based DNA computing experiment[102] a set of DNA oligonucleotides representing each of the $2^n$ possible vectors were immobilized. The strands encoding for vectors which did not satisfy the given function were removed from the surface by iteration of the following process: one clause was regarded in each cycle. To this end, complementary oligomers representing arguments that satisfied the currently regarded clause were hybridized to the vector strands. These complementary strands were selected by hand, which is a major weakness of this method because this step can become very laborious for large numbers of variables. Digestion of immobilized oligomers that were still single-stranded removed invalid vector candidates (which did not satisfy this clause) from the surface. The duplexes were then melted

 © 2006 Wiley-VCH Verlag GmbH & Co. KGaA, Weinheim 

and the complementary oligomers were removed by washing. The parallel hybridization of several different oligomer species protected several different vector-encoding strands from digestion simultaneously, and hence, the digestion represented a logical OR operation. The iteration of the hybridization, digestion, melting, and washing steps, each time for a different clause of the given function, resulted in a progressively narrowing selection of argument vectors, and thus, a logical AND operation. Finally, only strands representing argument vectors that satisfied all the clauses and thus the whole function were left on the surface as a result of the logic computation.

One major drawback of this approach concerns the general problem shared by all DNA computing models for solving hard computational problems. Even though the time needed for the computation grows only polynomially with the number of variables, instead of exponentially as is the case for conventional computers, this advantage is paid for with an exponentially growing number of DNA strand species required to carry out the computation. Furthermore, the time required for this approach only grows polynomially if one only counts the steps described above. One step, namely, the selection of complementary oligomers for hybridization, will, however, grow exponentially, because the number of different oligomer species to be selected depends exponentially on the number of variables.[103] Furthermore, this selection step is actually a part of the calculation and should not be left to the human operator, but should be executed by the molecular computer itself.

With respect to an approach where complete computations are executed just by the assembly of DNA motifs and without human interaction, Winfree et al. described the similarity of DNA crossover tiles to Wang tiles—a mathematical model of two-dimensional geometrical shapes with colored edges.[104,105] Two such tiles only assemble if the joint edges have the same color (Figure 14). The assembly of Wang tiles can be used to simulate a cellular automaton. This is a theoretical model of a computer which can, in principle, execute any calculation done with a conventional computer. By simulating the Wang tiles with DX motifs and edge colors with sticky end complementarity (see Figure 14), Winfree et al. showed that a two-dimensional self-assembly of DAE-DX tiles (**16**) can also be used to execute arbitrary computations. As an example, they designed a set of DX tiles capable of solving a small example of the Hamilton-path problem. This is a computationally difficult standard problem in computer science, where the task is to search for paths along edges through the graph such that every vertex is visited exactly once.[104]

Recently, Jonoska et al. suggested that transducers, another theoretical model for computers, can be simulated by the assembly of TX tiles, such as **20**.[106] This molecular computing model is called algorithmic self-assembly. This approach is elegant because the complete computation (except the read-out of the result) is executed through hybridization and ligation. No other laborious steps, such as PCR, gel electrophoresis, or oligomer extraction with magnetic beads, which were used in Adleman's pioneering work, are needed. Therefore, algorithmic self-assembly is a very promising step towards energy- and time-efficient molecular computing. It is also very interesting from a designer's point of view, because it can be applied to noncomputational applications as well. Similar to the choice of a set of simple rules and instructions determining an entire computation, the corresponding sticky-end complementarity of the crossover tiles determines the assembly. Therefore, these rules can be used as a high-level design language for the self-assembly of tiles which must be translated to base sequences for the sticky ends. The authors anticipated that, similar to a relative small computer program which is capable of executing a rather complex computation, a small set of different tiles might be sufficient to predetermine the structure of complex self-assemblies.

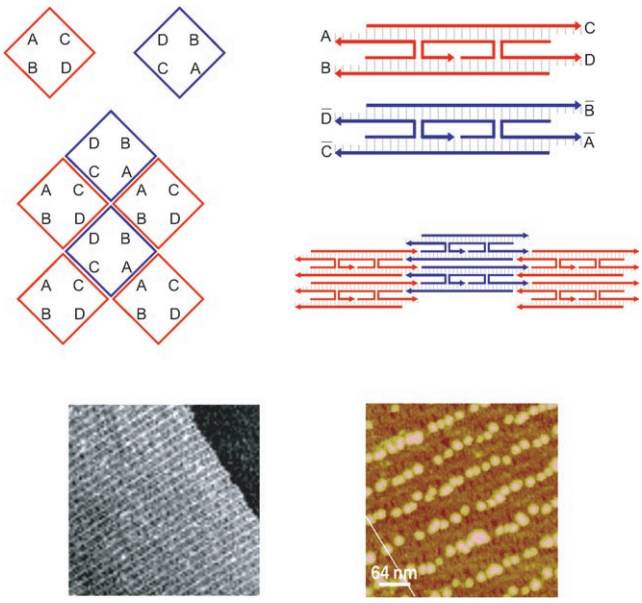



***Figure 14.*** Computational assembly of the DNA tile motifs. Tiles with color-coded edges (Wang tiles, top left; colors represented by letters) can be assembled according to the edge codes (bottom left), thereby executing computations.[104] When such tiles are represented by examples of DX motifs, such as **16**, and the edge code is mapped to sticky-end complementarity (top right), the computation can also be executed by self-assembly of the DX tiles into a two-dimensional array (bottom right). The left AFM image shows such an assembly. The protruding hairpins of two tile species, constructed in an analogous manner to motif **19**, produce clearly visible stripes.[63] In the AFM image on the right, gold nanoparticles were attached to the hairpins.[66] AFM images are reproduced with permission from references [63] (left) and [66] (right).

The concept of algorithmic self-assembly was impressively demonstrated by Rothemund et al., who assembled DX tiles, such as **16** and **17**, into Sierpinski triangles.[107] These are symmetric triangular structures which represent the iteration of XOR calculations of neighboring binary digit bits in a vector. The first row of the assembly stands for the input vector, has one digit set to 1, and all other digits set to 0. In each following row, a tile is attached to sticky ends of two neighboring tiles in the preceding row which encode the value of the represented digits. The XOR operation of two binary digits results in 1 if, and only if, one digit equals 1 and the

 © 2006 Wiley-VCH Verlag GmbH & Co. KGaA, Weinheim 

other digit equals 0 (Table 1). Each attached tile represents this operation by its combination of sticky ends. It presents sticky ends encoding 1 to the next row if, and only if, the two sticky ends connecting it to the preceding row encode a 0 and a 1. The marking with a protruding hairpin loop (as in motif **19**) of tiles that represent XOR operations resulting in 1 results in a symmetric triangular pattern of loops (the result of the corresponding XOR operation = 1) and no loops (result = 0). Although relatively high rates of incorrect hybridization of up to 10% occurred during the assembly, the authors were able to demonstrate by virtue of AFM analysis that this strategy led to the production of large crystals of the Sierpinski triangle.[107] These examples demonstrate that the concept of algorithmic self-assembly, in principle, works and can, in practice, be applied for solving some small problems. However, it has not yet been applied to the assembly of highly aperiodic superstructures comprised of larger numbers of tile species. This would be needed to compute problems of interesting size or to construct, for example, complex circuits.

If TX tiles are constructed such that they are comprised of two DAO-DX tiles which share the central helix (see, for example, motif **20** in Figure 8), a reporter strand is available. Hence, the ligation of self-assembled TX tiles produces a single DNA strand that runs through the entire set of tiles of the array (see, for example, the green strand in **20**). Since reporter strands are used in DNA nanoconstruction to prove that the tiles are, indeed, assembled into the expected structure (Figure 2), this method can also be used as an output of a computation which is executed by the self-assembly process.

Mao et al. used the one-dimensional self-assembly of TX tiles to calculate a binary arithmetic function, namely cumulative XOR of a 4-bit binary number.[108] The XOR operation is described above. Cumulative XOR takes a series of input digits ($x_1, x_2, \ldots, x_n$) and calculates a series of output digits ($y_1, y_2, \ldots, y_n$). The first output digit $y_1$ is initialized with $x_1$, and each following output digit $y_i$ (with $1 < i \leq n$) is the result of the calculation $y_{i-1}$ XOR $x_i$. The cumulative XOR is calculated by assembling two parallel rows of tiles (Figure 15). The rows start with special initiation tiles, one of which provides a sticky end encoding for $y_1 = 0$, and the other a sticky end complementary to one sticky end of the $x_1$ tile. Thus, a complete row of the input-encoding tiles can be assembled (the blue tiles in Figure 15), connected by sticky ends that represent position information (symbolized by $S_i$). Each of these tiles offers a sticky end that encodes the value of digit $x_i$ to the second row. As can be seen in the Wang tile example in Figure 15, two edges (sticky ends) encoding the values of $x_i$ and $y_{i-1}$ determine which species of XOR tile (red) can bind to these edges. The correct tile species carries an edge encoding the correct value of $y_i$ for attachment of the next XOR tile. The final result $y_n$ is encoded in the last, free sticky end of the XOR tile row. Subsequent to the assembly reaction, the complete computation and the solutions can be reproduced by reading out the reporter strand by using hybridization-based assays or DNA sequencing.

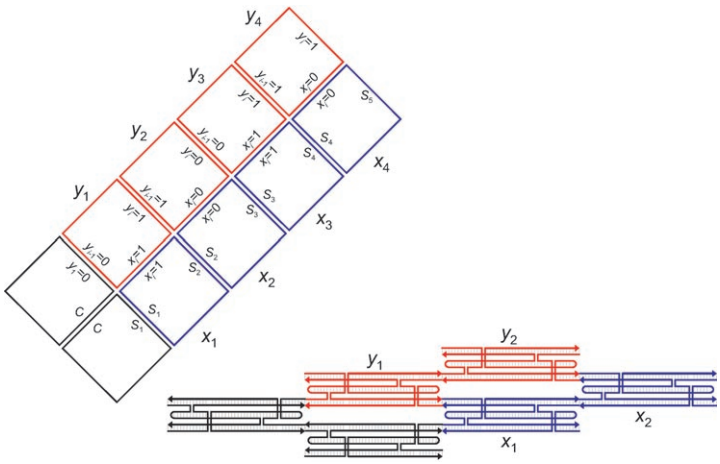



***Figure 15.*** Cumulative XOR calculation through assembly of DNA tiles.[108] The two black tiles initiate the self-assembly process; they are connected through an edge/sticky end marked with *C* and offer sticky ends for the attachment of the $x_1$ and $y_1$ tiles. The blue tiles represent the values of the $x_i$ digits, which offer sticky ends complementary to those of the $y_i$ tiles. The $x_i$ tiles are connected through position-encoding sticky ends labeled $S_i$. The red tiles represent the values of $y_i$ attached to the assembly depending on the sticky ends encoding $y_{i-1}$ and $x_i$. Edges with no labels represent blunt ends. The bottom drawing shows an implementation of the tile self-assembly with TX motifs **20**.

Crossover tiles containing four helices, constructed in a similar manner to the basic motifs **17** and **20**, were suggested to be potential building blocks for the assembly, from a topological point-of-view, of three-dimensional graphs to solve Hamilton-cycle problems.[109] These are another class of computationally hard standard problems in computer sciences related to the Hamilton-path problem described above, but here the starting vertex must also be the ending vertex. The in vitro realization of this approach, however, has not yet been demonstrated.

Multilayered arrays of DNA tiles, in principle, offer the possibility to separate the function to be calculated from the input, output, and intermediate results of the computation. Based on this concept, Carbone and Seeman proposed a simulation of Boolean circuits.[110] These are circuits of logic gates which can be used to calculate arbitrary functions of binary arithmetics by mapping input vectors of binary digits to single-result digits. Each such function is represented by a triangular circuit comprised of two types of gates. One type calculates the binary NAND operation on two binary digits which results in 1 if, and only if, both digits equal 0. Each binary function can be formulated using only NAND operations. The other gate type represents the identity function, which simply passes on its input. The identity gates are only used for closing gaps to gain a triangular structure of the circuit. Such a circuit, in turn, can be implemented by a triangular self-assembly of TX tiles, in which the different species of tile motifs define where to position NAND gates and identity gates.

The distances between sticky ends and crossover points in the gate-coding DNA tiles were chosen such that, after self-assembly, the lateral helices (here called pawns) protrude roughly perpendicular above and below the plane of the tiles, similar to the situation described above for the generation of

 © 2006 Wiley-VCH Verlag GmbH & Co. KGaA, Weinheim 

striped patterns (see motif **21** in Figure 8). The pawns can then be used to attach a second layer on top of the first one. In this second layer the actual calculation of the function for a specific input vector is executed, whereas the first layer defines the function for arbitrary input vectors. A first row of TX tiles, which are attached to the pawns of the first row of the first layer of tiles, encodes the binary input vector. Each sticky end oriented toward the second row encodes one bit. In the second and all the following rows, operation tiles representing elemental binary operations are ligated to the preceding row. There is a tile species for each possible combination of input bits (encoded by the sticky ends connecting the tile to the preceding row) and operation (NAND or identity, encoded by protruding sticky ends complementary to the appropriate pawn of the first layer). The result of the represented elemental operation is encoded by the tile's sticky end oriented towards the next row. These operation tiles hybridize to the input bit combinations provided by the preceding row and to the pawn of the first layer whose species defines the operation type. They then offer sticky ends to the output bit (the intermediate results) for further hybridization of the next row. The final row contains only one tile (the tip of the triangle) whose output sticky ends represent the final result. The authors also suggested a method involving PX-JX tiles to render the circuit layer programmable (and thus reusable) after self-assembly (see Section 6.2). Since this approach basically employs three-dimensional self-assembly, its experimental realization appears to be particularly difficult and has not yet been demonstrated in vitro.

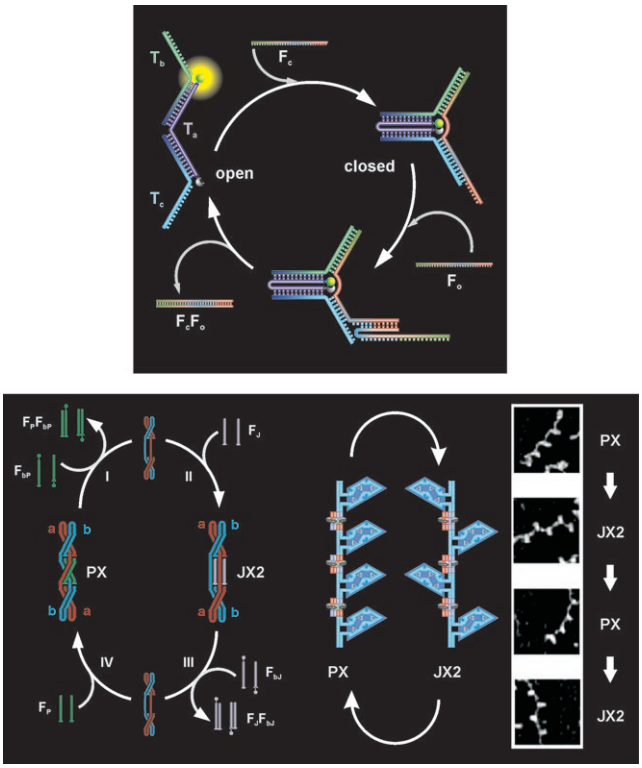



***Figure 16.*** Strand replacement and nanomachines. The strand replacement mechanism is demonstrated with the DNA tweezers from Yurke et al. (top).[121] The tweezers consist of two arms $T_b$ and $T_c$ connected through a hinge strand $T_a$. Hybridization of a fuel strand $F_c$ containing regions complementary to the single-stranded regions of both arms closes the complex. Another fuel strand $F_o$ that is the perfect complement of $F_c$ hybridizes to the single-stranded toe hold of $F_c$. Branch migration leads to formation of a perfect duplex of $F_c$ and $F_o$, thus opening the structure again. The bottom image shows a schematic drawing of how this method is used in the PX/$JX_2$ nanomachine to change between conformations **22** and **23**. The AFM images show an experimentally realized example, where the orientation of half hexagons along a linear array is switched through PX-$JX_2$ transition of the connecting tiles. The images are reprinted with permission from reference [111].

### *6.2. DNA Nanomechanical Devices*

DNA is not only useful for the construction of static scaffolds but it can also be used for the fabrication of dynamic assemblies.[111,112] Distinct base pairing can be switched by the addition of thermodynamically more favorable binding partners and conformational changes of the nucleic acid molecule as a consequence of environmental changes. These conformational changes offer a large number of possible actuation principles for dynamic DNA devices, which then may actually perform mechanical work. Such environmental changes include the variation of salt concentrations that control supercoiling,[113,114] the transition between the B and Z conformation of a DNA double helix,[115] the reversible formation of a G quadruplex with $K^+$ ions,[116] as well as the formation of C-quadruplex motifs[117] and triple helical structures[118–120] by alteration of the pH value. All these structural changes are reversible and, hence, the direction of the transition can be inverted by oscillating the ionic strength of the environment.

Another method, called strand replacement, which results in the selective formation of duplexes by hybridization (Figure 16), can also be made reversible by the simple addition of a well-designed DNA oligonucleotide. If one strand of a duplex has a dangling end (in this context often called "toe hold"), the perfect Watson–Crick complement of the strand can hybridize to this toe hold. Since the additional base pairs along the toe hold make the perfect duplex energetically more favorable than the shorter already-existing duplex, and the duplex is also more stable than the intermittent branched three-stranded structure, the perfect complement replaces the shorter strand through branch migration. This principle has been used in several DNA nanomachines, as demonstrated by the research groups of Yurke, Turberfield, and Simmel. The mechanical devices constructed from DNA included tweezers,[121] scissors,[122] and actuators,[123] where strand replacement opens and closes the arms of these devices, as well as a number of expansions and combinations of these three approaches.[118,124–127]

The extension and contraction of DNA molecules can be achieved simply by the opening and closing of hairpin loops,[128] or, more elaborately, by the transition between a G quadruplex and duplex conformation.[127,129] Simmel and co-workers employed the latter method in an outstanding step towards a real-world application.[127] They opened and closed

 © 2006 Wiley-VCH Verlag GmbH & Co. KGaA, Weinheim 

a G-quadruplex-shaped thrombin-binding aptamer by strand replacement. This process allowed the release or binding of a thrombin molecule in the presence of a specific DNA sequence. Xiao et al. modified this approach to develop a thrombin detector.[130] They immobilized the aptamer on a gold electrode and labeled it with methylene blue (MB). In the absence of thrombin, the aptamer is in a conformational equilibrium between the G quadruplex and the unfolded state such that the MB labels of unfolded aptamers may enable efficient electron transfer with the electrode. The presence of thrombin shifts this equilibrium towards the thrombin-binding G-quadruplex conformation, thus altering the electron-tunneling distance and thus inhibiting electron transfer.

Seeman and co-workers have fabricated more-complex devices from crossover tiles which are capable of changing between the PX conformation and its topoisomer $JX_2$. As depicted in Figure 16, the replacement of strands involved in the central crossover induced the rotation of pairs of sticky ends within the PX motif.[131] This constructional concept has recently been extended to create a DNA nanomechanical device which can produce specific DNA polymers from short oligonucleotides. To this end, a linear array of pairs of diamond-shaped motifs was connected by PX/$JX_2$ units.[84] Here, the conformational state of each unit (PX or $JX_2$) determines which of the two diamond motifs of a pair lies on which side of the DNA array. Additional DX motifs were hybridized to sticky ends provided by the diamond motifs. Further hybridization and ligation resulted in the formation of two linear assemblies parallel to the diamond-pair–PX/$JX_2$ array, one on each side. Since the presence or absence of switching oligomers which induce strand replacement determines the sequence of the diamond motifs on each side of the array, they also determine the series of sticky ends provided for the attachement of DX tiles. Therefore, the order in which the DX motifs are assembled can be precisely adjusted. The devices align a number of DX tiles in a specific order in response to the DNA signals (the "set strands") and then they can be fused together by ligation. Since there is no transcriptional relationship between the set strands and the product strand, this device has potential applications in the synthesis of DNA polymers, encryption of information, and as a variable-input device for DNA computing.[84]

Another device which can produce a stimulus-sensitive response is the "molecular finite state machine" developed by Shapiro and co-workers.[132,133] The computational model of the finite state machine processes a sequence of input symbols in succession, while its molecular analogue processes an elaborately designed DNA duplex. This is achieved by iteratively cutting the DNA duplex with the restriction enzyme FokI and ligating "software duplexes" to the newly produced sticky end, thereby defining the position of the following cut. Similar to the model that recognizes input sequences of certain properties by assuming an accepting state, the DNA equivalent could be used to recognize a combination of RNA transcripts and release a terminating molecule that effects the expression of genes.[134]

Other examples of DNA nanomechanical devices include walking and rolling DNA constructs,[135–138] molecular gears,[139] the reversible aggregation and dispersion of gold nanoparticles,[140] and a game computer that never loses a match of tic-tac-toe.[141]

From a design point-of-view, the basic elements of nanodevices and the sequences of their oligonucleotide building blocks are often very similar to those used for static assemblies; only the precise role of the elements may change: double helices can be levers instead of scaffolding rods, and bulges or other single-stranded elements can serve as hinges, not only as tendons. The overall design of nanodevices, however, is clearly more complex than that of static assemblies, because one not only needs to consider the single conformational state desired, but at least two or even more.

## 7. Conclusions and Perspectives

The large increase in relevant publications in this field clearly indicates that the design and fabrication of DNA nanoarchitectures is far more than an intellectually fascinating game. In particular, recent advances in the utilization of comparatively simple symmetrical structures (for example, **9** and **10** in Figure 6 or **12** in Figure 7) have generated promising ways for real-life applications that are based on the directional positioning of proteins and nanoparticles or of nanoscale electron-conducting elements. However, many other applications, such as scaffolds for the assembly of more-complex arrays comprised of various different proteins and nanoparticles, or the computational solution of problem instances on a mathematically relevant scale, will essentially depend on the design of highly asymmetric, large-scale self-assembling architectures. Although DNA has clearly been proven to be a most promising construction material for such applications, significant problems in terms of scaling-up the process need to be solved in the future.

### 7.1. Scalability and Sequence Design

As already discussed above, the design of DNA sequences for applications in nanoscience needs to take into account, in particular, the avoidance of unintended hybridization of the sequences selected. This can be achieved by minimizing sequence symmetry. One serious problem that future developments in DNA nanotechnology are likely to face concerns scale, that is, the ability to render DNA nanoarchitectures such that larger and/or more-complex patterns are formed, which will demand the integration of more different addressable sites, and therefore, more unique sticky ends. This increasing number of sticky ends consequently requires increasing lengths of DNA sequences, which may lead to a loss of unique subsequences, that is, the number of subsequences appearing more than once in the set of all sequences will grow. This, again, increases the likelihood of unwanted cross-hybridizations, and therefore, decreases the yield of the desired assembly products.

This general problem can partly be circumvented by hierarchical construction. The building blocks (for example, junctions or tiles) are first produced in separate reactions and are then assembled into higher order structures in a second

 © 2006 Wiley-VCH Verlag GmbH & Co. KGaA, Weinheim 

step. In addition, proper sticky ends can be incoporated subsequently into building block synthesis in an intermediate step, for example, by restriction of stem-loop structures using endonucleases.[142] If the building blocks are sufficiently stable and inert against strand invasion, only the specific binding of the sticky ends of the building blocks need to be considered in the second step. Another successful attempt to use strands economically is the application of symmetry to motif design, that is, the multiple usage of the same strand for different parts of a motif, for example, for different arms of a 4 × 4 tile.[49] However, these strategies postpone, but do not solve, the problem of scale. In the majority of the existing studies, the sticky ends had lengths between four and eight nucleotides. If a particular application demands a large number of different tile species, for example, to assemble extended and highly asymmetric arrays, sticky ends have to be comprised of more nucleotides to enable specific discrimination during hybridization. Also, longer "toe holds" for strand replacement might be needed to improve strand exchange kinetics.[143] The requirement of long sticky ends also necessitates the incorporation of more helical turns and larger spaces between the junctions and binding sites (for example, proteins), thereby increasing the minimal size of such constructions.

As a possible solution, Winfree and Bekbolatov proposed to complement error prevention (the avoidance of cross-hybridization) with error correction (the repair of cross-hybridization after its occurrence).[144] To this end, each tile of a two-dimensional assembly is separated into four tiles which assemble into the complete tile through unique internal sticky ends. Cooperative binding stabilizes correct connections, but an incorrect hybridization only results in the self-assembly process continuing with additional errors, thereby further destabilizing this unwanted conformation. The introduction of error correction may prove to be a valuable addition to DNA nanoarchitectures, but it aggravates the scaling problem of sequence design because an even larger number of unique sticky ends need to be provided. Hence, applications of DNA nanoarchitecture on a larger scale and with a significantly higher complexity than the examples currently reported essentially require the development of sophisticated computer programs for the design and selection of DNA sequences.[14–16]

### 7.2. Outlook

A number of exciting developments in the near future may be anticipated from the designs, constructions, and experimental results reported in this Review. Addressable regular DNA arrays for the attachment of molecular and colloidal components for sensing and screening may soon become reality and may have the potential to be a standard laboratory technique. Hence, this approach appears to be promising for commercial applications. However, to facilitate mass production, one must not only be able to characterize the structural integrity of the self-assembly products, but one also needs to systematically quantify the yields of correctly assembled structures. To this end, suitable analytical assays need to be developed, which are likely to combine biochemical and imaging techniques.

With respect to nanoelectronics, the successful production of conducting nanowires by means of DNA templating has already been demonstrated,[145] and the next steps for the construction of more-complex electronic components and circuits will require the development of original and innovative concepts for tailoring the structural diversity and connectivity of DNA architectures.[146,147] An additional critical point concerns the production processes, that is, the self-assembly, which should be performed under physiological aqueous conditions, and the post-assembly processing, which usually requires harsh chemical conditions or even dry-state manufacturing.

The most challenging goals probably concern the development of nanomechanical and self-replicating devices, which may open the door to autonomous machines. To this end, the mechanical work performed by DNA devices will have to be exploited for a sensible, productive use, for example, be incorporated into a larger DNA scaffold. Such architectures might be capable of conducting a logic computation as a reply to certain stimuli. First examples in this direction have already been described,[127,134] and they might be considered as very initial steps towards the fabled autonomous nanorobots (nanobots) that heal wounds and perform surgery inside a living organism. Although the development of efficient methodologies for sequence design will be mandatory for the realization of these perspectives in the future, we would like to emphasize that the number of contributions to this young field is steadily increasing.[150] Therefore, one may anticipate that novel and nonconventional approaches will emerge to solve the problems currently existing. To end this Review, we would, therefore, like to cite the pioneer of DNA nanoconstruction Nadrian Seeman: "As with any craft material, the structural applications of DNA are limited only by the imagination".[148]

*We acknowledge financial support of our work by the Deutsche Forschungsgemeinschaft (DFG), the European Union (NUCAN project, STREP 013775), and by the research program "Molecular Basics of Biosciences" of the University of Dortmund. We thank Kersten Rabe for help with the artwork of the frontispiece.*

Received: July 6, 2005
Revised: November 30, 2005
Published online: February 10, 2006

[1] N. C. Seeman, *Nature* **2003**, *421*, 427.
[2] C. A. Mirkin, *Inorg. Chem.* **2000**, *39*, 2258.
[3] C. M. Niemeyer, *Angew. Chem.* **2001**, *113*, 4254; *Angew. Chem. Int. Ed.* **2001**, *40*, 4128.
[4] C. M. Niemeyer, C. A. Mirkin in *NanoBiotechnology: Concepts, Methods and Applications*, Wiley-VCH, Weinheim, **2004**.
[5] M. H. Caruthers, *Science* **1985**, *230*, 281.
[6] K. B. Mullis, *Angew. Chem.* **1994**, *106*, 1271; *Angew. Chem. Int. Ed. Engl.* **1994**, *33*, 1209.
[7] J. F. Marko, S. Cocco, *Phys. World* **2003**, *16*, 37.
[8] E. Katz, I. Willner, *Angew. Chem.* **2004**, *116*, 6166; *Angew. Chem. Int. Ed.* **2004**, *43*, 6042.

 © 2006 Wiley-VCH Verlag GmbH & Co. KGaA, Weinheim 

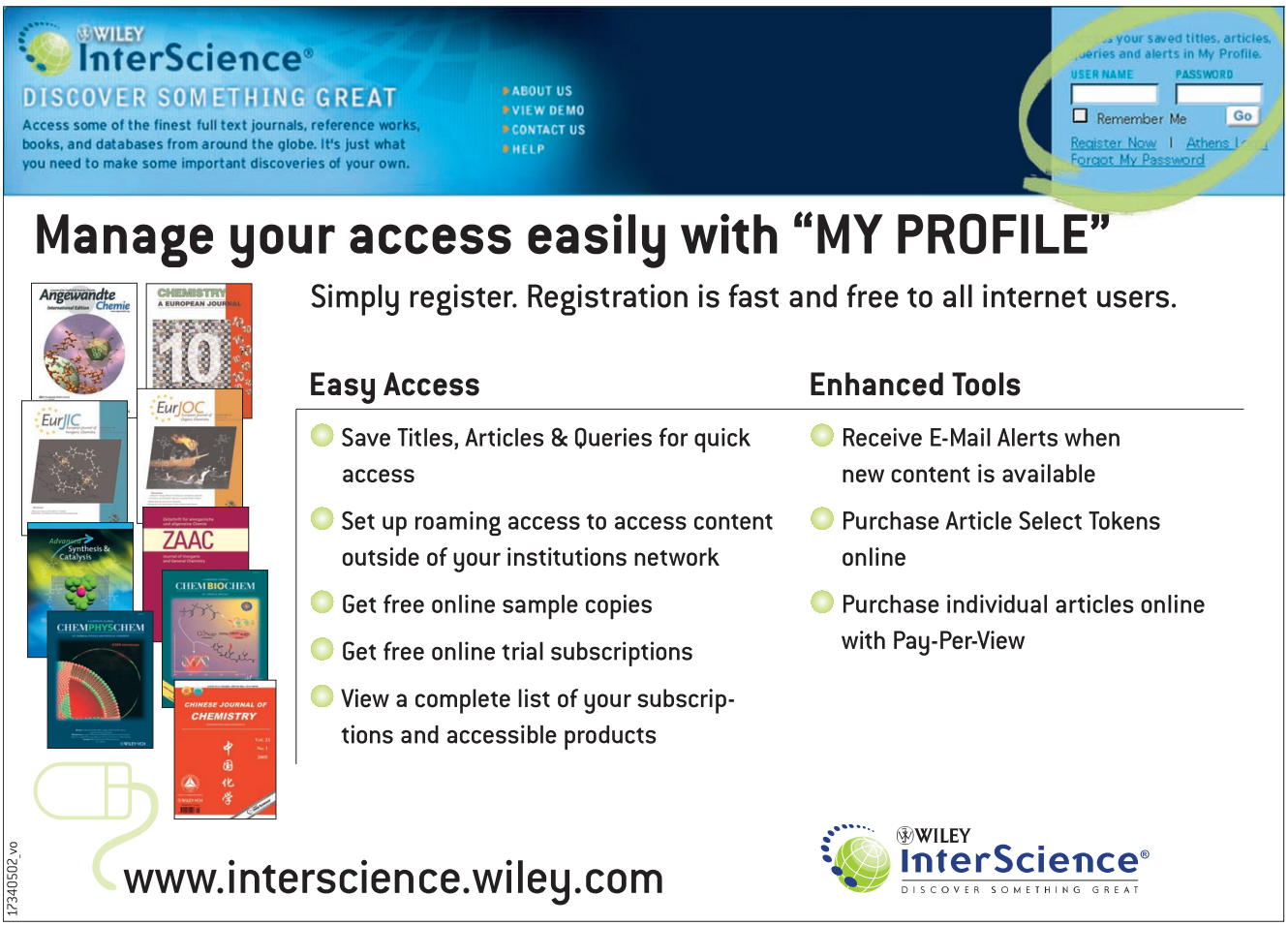
[9] M. C. Daniel, D. Astruc, *Chem. Rev.* **2004**, *104*, 293.
[10] N. L. Rosi, C. A. Mirkin, *Chem. Rev.* **2005**, *105*, 1547.
[11] K. V. Gothelf, T. H. LaBean, *Org. Biomol. Chem.* **2005**, *3*, 4023.
[12] V. V. Demidov, M. D. Frank-Kamenetskii, *Trends Biochem. Sci.* **2004**, *29*, 62.
[13] J. Ackermann, F.-U. Gast, *Z. Naturforsch. A* **2003**, *58*, 157.
[14] N. C. Seeman, *J. Biomol. Struct. Dyn.* **1990**, *8*, 573.
[15] U. Feldkamp, H. Rauhe, W. Banzhaf, *Genetic Programming and Evolvable Machines* **2003**, *4*, 153.
[16] A. Brenneman, A. E. Condon, *Theoret. Comput. Sci.* **2002**, *287*, 39.
[17] R. M. Dirks, M. Lin, E. Winfree, N. A. Pierce, *Nucleic Acids Res.* **2004**, *32*, 1392.
[18] U. Feldkamp, R. Wacker, W. Banzhaf, C. M. Niemeyer, *ChemPhysChem* **2004**, *5*, 367.
[19] N. C. Seeman, H. Wang, B. Liu, J. Qi, X. Li, X. Yang, F. Liu, W. Sun, Z. Shen, R. Sha, C. Mao, Y. Wang, S. Zhang, T.-J. Fu, S. Du, J. E. Mueller, Y. Zhang, J. Chen in *Proceedings of the Second Annual Meeting on DNA Based Computers* (Princeton University, June 10–12, 1996), American Mathematical Society, **1999**, p. 215.
[20] N. C. Seeman, H. Wang, X. Yang, F. Liu, C. Mao, W. Sun, L. Wenzler, Z. Shen, R. Sha, H. Yan, M. H. Wong, P. Sa-Ardyen, B. Liu, H. Qiu, X. Li, J. Qi, S. M. Du, Y. Zhang, J. E. Mueller, T.-J. Fu, Y. Wang, J. Chen, *Nanotechnology* **1998**, *9*, 257.
[21] N. C. Seeman, *Annu. Rev. Biophys. Biomol. Struct.* **1998**, *27*, 225.
[22] E. Winfree, F. Liu, L. A. Wenzler, N. C. Seeman, *Nature* **1998**, *394*, 539.
[23] W. M. Shih, J. D. Quispe, G. F. Joyce, *Nature* **2004**, *427*, 618.
[24] C. M. Niemeyer, *Curr. Opin. Chem. Biol.* **2000**, *4*, 609.
[25] M. Lovrinovic, C. M. Niemeyer, *Angew. Chem.* **2005**, *117*, 3241; *Angew. Chem. Int. Ed.* **2005**, *44*, 3179.
[26] C. A. Mirkin, R. L. Letsinger, R. C. Mucic, J. J. Storhoff, *Nature* **1996**, *382*, 607.
[27] J. J. Storhoff, C. A. Mirkin, *Chem. Rev.* **1999**, *99*, 1849.
[28] C. M. Niemeyer, T. Sano, C. L. Smith, C. R. Cantor, *Nucleic Acids Res.* **1994**, *22*, 5530.
[29] A. P. Alivisatos, K. P. Johnsson, X. Peng, T. E. Wilson, C. J. Loweth, M. P. Bruchez, Jr., P. G. Schultz, *Nature* **1996**, *382*, 609.
[30] C. M. Niemeyer, W. Bürger, J. Peplies, *Angew. Chem.* **1998**, *110*, 2391; *Angew. Chem. Int. Ed.* **1998**, *37*, 2265.
[31] C. J. Loweth, W. B. Caldwell, X. Peng, A. P. Alivisatos, P. G. Schultz, *Angew. Chem.* **1999**, *111*, 1925; *Angew. Chem. Int. Ed.* **1999**, *38*, 1808.
[32] X. Li, D. R. Liu, *Angew. Chem.* **2004**, *116*, 4956; *Angew. Chem. Int. Ed.* **2004**, *43*, 4848.
[33] C. M. Niemeyer, L. Boldt, B. Ceyhan, D. Blohm, *J. Biomol. Struct. Dyn.* **1999**, *17*, 527.
[34] M. Zuker, D. H. Mathews, D. H. Turner in *RNA Biochemistry and Biotechnology* (Ed.: B. F. C. Clark), Kluwer, Dordrecht, **1999**, p. 11.
[35] I. L. Hofacker, *Nucleic Acids Res.* **2003**, *31*, 3429.
[36] I. L. Hofacker, W. Fontana, P. F. Stadler, L. S. Bonhoeffer, M. Tacker, P. Schuster, *Chem. Mon.* **1994**, *125*, 167.
[37] N. C. Seeman, *J. Theor. Biol.* **1982**, *99*, 237.
[38] Y. Wang, J. E. Mueller, B. Kemper, N. C. Seeman, *Biochemistry* **1991**, *30*, 5667.
[39] P. Sa-Ardyen, N. Jonoska, N. C. Seeman in *DNA Computing: 8th International Workshop on DNA-Based Computers*, DNA8 (Sapporo, Japan, June 10–13, 2002), Revised Papers, Vol. 2568 (Ed.: A. Ohuchi), Springer, **2003**, p. 1.
[40] B. Liu, N. B. Leontis, N. C. Seeman, *Nanobiology* **1994**, *3*, 177.
[41] S. M. Du, S. Zhang, N. C. Seeman, *Biochemistry* **1992**, *31*, 10955.
[42] N. C. Seeman, Y. Zhang, J. Chen, *J. Vac. Sci. Technol. A* **1994**, *12*, 1895.
[43] Y. Li, Y. D. Tseng, S. Y. Kwon, L. d'Espaux, J. S. Bunch, *Nat. Mater.* **2004**, *3*, 38.
[44] Y. Li, Y. T. H. Cu, D. Luo, *Nat. Biotechnol.* **2005**, *23*, 885.
[45] J. C. Setubal, J. Meidanis, *Introduction to Computational Molecular Biology*, PWS, Boston, **1997**.
[46] J. Malo, J. C. Mitchell, C. Vénien-Bryan, J. R. Harris, H. Wille, D. J. Sherratt, A. J. Turberfield, *Angew. Chem.* **2005**, *117*, 3117; *Angew. Chem. Int. Ed.* **2005**, *44*, 3057.
[47] C. Mao, W. Sun, N. C. Seeman, *J. Am. Chem. Soc.* **1999**, *121*, 5437.
[48] H. Yan, S. H. Park, G. Finkelstein, J. H. Reif, T. H. LaBean, *Science* **2003**, *301*, 1882.
[49] Y. He, Y. Tian, Y. Chen, Z. Deng, A. E. Ribbe, C. Mao, *Angew. Chem.* **2005**, *117*, 6852; *Angew. Chem. Int. Ed.* **2005**, *44*, 6694.
[50] S. H. Park, H. Yan, J. H. Reif, T. H. LaBean, G. Finkelstein, *Nanotechnology* **2004**, *15*, S525.
[51] S. H. Park, P. Yin, Y. Liu, J. H. Reif, T. H. LaBean, H. Yan, *Nano Lett.* **2005**, *5*, 729.
[52] Z. Deng, C. Mao, *Angew. Chem.* **2004**, *116*, 4160; *Angew. Chem. Int. Ed.* **2004**, *43*, 4068.
[53] Y. He, Y. Chen, H. Liu, A. E. Ribbe, C. Mao, *J. Am. Chem. Soc.* **2005**, *127*, 12202.
[54] R. B. Fuller, *Synergetics*, Macmillan, New York, **1975**.
[55] G. von Kiedrowski, L.-H. Eckardt, K. Naumann, W. M. Pankau, M. Reimold, M. Rein, *Pure Appl. Chem.* **2003**, *75*, 609.
[56] D. Liu, M. Wang, Z. Deng, R. Walulu, C. Mao, *J. Am. Chem. Soc.* **2004**, *126*, 2324.
[57] J. Qi, X. Li, X. Yang, N. C. Seeman, *J. Am. Chem. Soc.* **1996**, *118*, 6121.
[58] N. Chelyapov, Y. Brun, M. Gopalkrishnan, D. Reishus, B. Shaw, L. Adleman, *J. Am. Chem. Soc.* **2004**, *126*, 13924.
[59] T.-J. Fu, N. C. Seeman, *Biochemistry* **1993**, *32*, 3211.
[60] X. Li, Y. Xiaoping, Q. Jing, N. C. Seeman, *J. Am. Chem. Soc.* **1996**, *118*, 6131.
[61] T. H. LaBean, H. Yan, J. Kopatsch, F. Liu, E. Winfree, J. H. Reif, N. C. Seeman, *J. Am. Chem. Soc.* **2000**, *122*, 1848.
[62] Z. Shen, H. Yan, T. Wang , N. C. Seeman, *J. Am. Chem. Soc.* **2004**, *126*, 1666.
[63] F. Liu, R. Sha, N. C. Seeman, *J. Am. Chem. Soc.* **1999**, *121*, 917.
[64] H. Yan, T. H. LaBean, L. Feng, J. H. Reif, *Proc. Natl. Acad. Sci. USA* **2003**, *100*, 8103.
[65] S. Xiao, F. Liu, A. E. Rosen, J. F. Hainfeld, N. C. Seeman, K. Musier-Forsyth, R. A. Kiehl, *J. Nanopart. Res.* **2002**, *4*, 313.
[66] J. D. Le, Y. Pinto, N. C. Seeman, K. Musier-Forsyth, T. A. Taton, R. A. Kiehl, *Nano Lett.* **2004**, *4*, 2343.
[67] Y. Y. Pinto, J. D. Le, N. C. Seeman, K. Musier-Forsyth, T. A. Taton, R. A. Kiehl, *Nano Letters* **2005**, *5*, 2399.
[68] H. Li, S. H. Park, J. H. Reif, T. H. LaBean, H. Yan, *J. Am. Chem. Soc.* **2004**, *126*, 418.
[69] R. Schulman, S. Lee, N. Papadakis, E. Winfree in *DNA Computing: 9th International Workshop on DNA Based Computers*, DNA9 (Madison, USA, June 1–3, 2003), Revised Papers, Vol. 2943 (Eds.: J. Chen, J. Reif), Springer, **2004**, p. 108.
[70] X. Yang, L. A. Wenzler, J. Qi, X. Li, N. C. Seeman, *J. Am. Chem. Soc.* **1998**, *120*, 9779.
[71] X. Zhang, H. Yan, Z. Shen, N. C. Seeman, *J. Am. Chem. Soc.* **2002**, *124*, 12940.
[72] B. Ding, R. Sha, N. C. Seeman, *J. Am. Chem. Soc.* **2004**, *126*, 10230.
[73] C. Zhou, Z. Tan, C. Wang, Z. Wei, Z. Wang, C. Bai, J. Qin, E. Cao, *J. Biomol. Struct. Dyn.* **2001**, *19*, 807.
[74] M. A. Batalia, E. Protozanova, R. B. Macgregor, D. A. Erie, *Nano Lett.* **2002**, *2*, 269.
[75] A. Chworos, I. Severcan, A. Y. Koyfman, P. Weinkam, E. Oroudjev, H. G. Hansma, L. Jaeger, *Science* **2004**, *306*, 2068.
[76] A. Y. Koyfman, G. Braun, S. Magonov, A. Chworos, N. O. Reich, L. Jaeger, *J. Am. Chem. Soc.* **2005**, *127*, 11886.


 © 2006 Wiley-VCH Verlag GmbH & Co. KGaA, Weinheim 

[77] K. M. Stewart, L. W. McLaughlin, *J. Am. Chem. Soc.* **2004**, *126*, 2050.
[78] K. V. Gothelf, A. Thomsen, M. Nielsen, E. Cló, R. S. Brown, *J. Am. Chem. Soc.* **2004**, *126*, 1044.
[79] K. V. Gothelf, R. S. Brown, *Chem. Eur. J.* **2005**, *11*, 1062.
[80] M. Scheffler, A. Dorenbeck, S. Jordan, M. Wüstefeld, G. von Kiedrowski, *Angew. Chem.* **1999**, *111*, 3513; *Angew. Chem. Int. Ed.* **1999**, *38*, 3311.
[81] L. H. Eckardt, K. Naumann, W. M. Pankau, M. Rein, M. Schweitzer, N. Windhab, G. von Kiedrowski, *Nature* **2002**, *420*, 286.
[82] M. Endo, T. Majima, *J. Am. Chem. Soc.* **2003**, *125*, 13654.
[83] M. Endo, S. Uegaki, T. Majima, *Chem. Commun.* **2005**, 3153.
[84] S. Liao, N. C. Seeman, *Science* **2004**, *306*, 2072.
[85] M. Endo, N. C. Seeman, T. Majima, *Angew. Chem.* **2005**, *117*, 6228; *Angew. Chem. Int. Ed.* **2005**, *44*, 6074.
[86] N. C. Seeman, *DNA Cell Biol.* **1991**, *10*, 475.
[87] N. C. Seeman, *Curr. Opin. Struct. Biol.* **1996**, *6*, 519.
[88] P. J. Paukstelis, J. Nowakowski, J. J. Birktoft, N. C. Seeman, *Chem. Biol.* **2004**, *11*, 1119.
[89] A. Ekani-Nkodo, A. Kumar, D. K. Fygenson, *Phys. Rev. Lett.* **2004**, *93*, 268301.
[90] P. W. K. Rothemund, A. Ekani-Nkodo, N. Papadakis, A. Kumar, D. K. Fygenson, E. Winfree, *J. Am. Chem. Soc.* **2004**, *126*, 16344.
[91] D. Liu, S. H. Park, J. H. Reif, T. H. LaBean, *Proc. Natl. Acad. Sci. USA* **2004**, *101*, 717.
[92] F. Mathieu, S. Liao, J. Kopatsch, T. Wang, C. Mao, N. C. Seeman, *Nano Lett.* **2005**, *5*, 661.
[93] S. H. Park, R. Barish, H. Li, J. H. Reif, G. Finkelstein, H. Yan, T. H. LaBean, *Nano Lett.* **2005**, *5*, 693.
[94] J. Chen, N. C. Seeman, *Nature* **1991**, *350*, 631.
[95] Y. Zhang, N. C. Seeman, *J. Am. Chem. Soc.* **1994**, *116*, 1661.
[96] R. P. Goodman, R. M. Berry, A. J. Turberfield, *Chem. Commun.* **2004**, 1372.
[97] R. P. Goodman, I. A. T. Schaap, C. F. Tardin, C. M. Erben, R. M. Berry, C. F. Schmidt, A. J. Turberfield, *Science* **2006**, *310*, 1661.
[98] C. Mao, W. Sun, N. C. Seeman, *Nature* **1997**, *386*, 137.
[99] L. M. Adleman, *Science* **1994**, *266*, 1021.
[100] M. H. Garzon, R. J. Deaton, *IEEE Trans. Evol. Comput.* **1999**, *3*, 236.
[101] A. J. Ruben, L. F. Landweber, *Nat. Rev. Mol. Cell Biol.* **2000**, *1*, 69.
[102] Q. Liu, L. Wang, A. G. Frutos, A. E. Condon, R. M. Corn, L. M. Smith, *Nature* **2000**, *403*, 175.
[103] H. Wu, *BioSystems* **2001**, *59*, 1.
[104] E. Winfree, X. Yang, N. C. Seeman in *Proceedings of the Second Annual Meeting on DNA Based Computers* (Princeton University, June 10–12, 1996), American Mathematical Society, **1996**, p. 191.
[105] E. Winfree, T. Eng, G. Rozenberg, in *DNA Computing, 6th International Workshop on DNA-Based Computers, DNA 2000* (Leiden, The Netherlands, June 2000), Revised Papers, Vol. 2054 (Ed.: G. Rozenberg), Springer, **2001**, p. 63.
[106] N. Jonoska, S. Liao, N. C. Seeman in *Aspects of Molecular Computing, Essays Dedicated to Tom Head on the Occasion of His 70th Birthday, Vol. 2950* (Ed.: G. Rozenberg), Springer, **2004**, p. 219.
[107] P. W. K. Rothemund, N. Papadakis, E. Winfree, *PLoS Biol.* **2004**, *2*, e424.
[108] C. Mao, T. H. LaBean, J. H. Reif, N. C. Seeman, *Nature* **2000**, *407*, 493.
[109] N. Jonoska, S. A. Karl, M. Saito in *Proceedings of the 3rd DIMACS Workshop on DNA Based Computers* (University of Pennsylvania, June 23–25, 1997) (Ed.: D. Wood), American Mathematical Society, **1999**, p. 123.
[110] A. Carbone, N. C. Seeman, *Proc. Natl. Acad. Sci. USA* **2002**, *99*, 12577.
[111] C. M. Niemeyer, M. Adler, *Angew. Chem.* **2002**, *114*, 3933; *Angew. Chem. Int. Ed.* **2002**, *41*, 3779.
[112] F. C. Simmel, W. U. Dittmer, *Small* **2005**, *1*, 284.
[113] X. Yang, A. V. Vologodskii, B. Liu, B. Kemper, N. C. Seeman, *Biopolymers* **1998**, *45*, 69.
[114] C. M. Niemeyer, M. Adler, S. Lenhert, S. Gao, H. Fuchs, L. F. Chi, *ChemBioChem* **2001**, *2*, 260.
[115] C. Mao, W. Sun, Z. Shen, N. C. Seeman, *Nature* **1999**, *397*, 144.
[116] R. P. Fahlman, M. Hsing, C. S. Sporer-Tuhten, D. Sen, *Nano Lett.* **2003**, *3*, 1073.
[117] D. Liu, S. Balasubramanian, *Angew. Chem.* **2003**, *115*, 5912; *Angew. Chem. Int. Ed.* **2003**, *42*, 5734.
[118] Y. Chen, C. Mao, *J. Am. Chem. Soc.* **2004**, *126*, 8626.
[119] Y. Chen, C. Mao, *J. Am. Chem. Soc.* **2004**, *126*, 13240.
[120] M. Brucale, G. Zuccheri, B. Samori, *Org. Biomol. Chem.* **2005**, *3*, 575.
[121] B. Yurke, A. J. Turberfield, A. P. Mills, Jr., F. C. Simmel, J. L. Neumann, *Nature* **2000**, *406*, 605.
[122] J. C. Mitchell, B. Yurke in *DNA Computing, 7th International Workshop on DNA-Based Computers, DNA 2001* (Tampa, USA, 10–13 June 2001) (Ed.: N. C. Seeman), Springer, **2002**, p. 258.
[123] F. C. Simmel, B. Yurke, *Phys. Rev. E* **2001**, *63*, 041913.
[124] F. C. Simmel, B. Yurke, *Appl. Phys. Lett.* **2002**, *80*, 883.
[125] A. J. Turberfield, J. C. Mitchell, B. Yurke, A. P. Mills, Jr., M. I. Blakey, F. C. Simmel, *Phys. Rev. Lett.* **2003**, *90*, 118102.
[126] Y. Chen, M. Wang, C. Mao, *Angew. Chem.* **2004**, *116*, 3638; *Angew. Chem. Int. Ed.* **2004**, *43*, 3554.
[127] W. U. Dittmer, E. Reuter, F. C. Simmel, *Angew. Chem.* **2004**, *116*, 3634; *Angew. Chem. Int. Ed.* **2004**, *43*, 3550.
[128] L. Feng, S. H. Park, J. H. Reif, H. Yan, *Angew. Chem.* **2003**, *115*, 4478; *Angew. Chem. Int. Ed.* **2003**, *42*, 4342.
[129] P. Alberti, J.-L. Mergny, *Proc. Natl. Acad. Sci. USA* **2003**, *100*, 1569.
[130] Y. Xiao, A. A. Lubin, A. J. Heeger, K. W. Plaxco, *Angew. Chem.* **2005**, *117*, 5592; *Angew. Chem. Int. Ed.* **2005**, *44*, 5456.
[131] H. Yan, X. Zhang, Z. Shen, N. C. Seeman, *Nature* **2002**, *415*, 62.
[132] Y. Benenson, T. Paz-Elizur, R. Adar, E. Keinan, Z. Livneh, E. Shapiro, *Nature* **2001**, *414*, 430.
[133] Y. Benenson, R. Adar, T. Paz-Elilzur, Z. Livneh, E. Shapiro, *Proc. Natl. Acad. Sci. USA* **2003**, *100*, 2191.
[134] Y. Benenson, B. Gil, U. Ben-Dor, R. Adar, E. Shapiro, *Nature* **2004**, *429*, 423.
[135] J. H. Reif in *DNA Computing: 8th International Workshop on DNA-Based Computers*, DNA8 (Sapporo, Japan, June 10–13, 2002), Revised Papers, Vol. *2568* (Ed.: A. Ohuchi), Springer, **2003**, p. 22.
[136] W. B. Sherman, N. C. Seeman, *Nano Lett.* **2004**, *4*, 1203.
[137] J.-S. Shin, N. A. Pierce, *J. Am. Chem. Soc.* **2004**, *126*, 10834.
[138] P. Yin, H. Yan, X. G. Daniell, A. J. Turberfield, J. H. Reif, *Angew. Chem.* **2004**, *116*, 5014; *Angew. Chem. Int. Ed.* **2004**, *43*, 4906.
[139] Y. Tian, C. Mao, *J. Am. Chem. Soc.* **2004**, *126*, 11410.
[140] P. Hazarika, B. Ceyhan, C. M. Niemeyer, *Angew. Chem.* **2004**, *116*, 6631; *Angew. Chem. Int. Ed.* **2004**, *43*, 6469.
[141] M. N. Stojanovic, D. Stefanovic, *Nat. Biotechnol.* **2003**, *21*, 1069.
[142] F. Liu, H. Wang, N. C. Seeman, *Nanobiology* **1999**, *4*, 257.
[143] B. Yurke, A. P. Mills, Jr., *Genetic Programming and Evolvable Machines* **2003**, *4*, 111.
[144] E. Winfree, R. Bekbolatov in *DNA Computing: 9th International Workshop on DNA Based Computers, DNA9* (Madison, USA, June 1–3, 2003), Revised Papers, Vol. 2943 (Ed.: J. Reif), Springer, **2004**, p. 126.
[145] E. Braun, Y. Eichen, U. Sivan, G. Ben-Yoseph, *Nature* **1998**, *391*, 775.

 © 2006 Wiley-VCH Verlag GmbH & Co. KGaA, Weinheim 

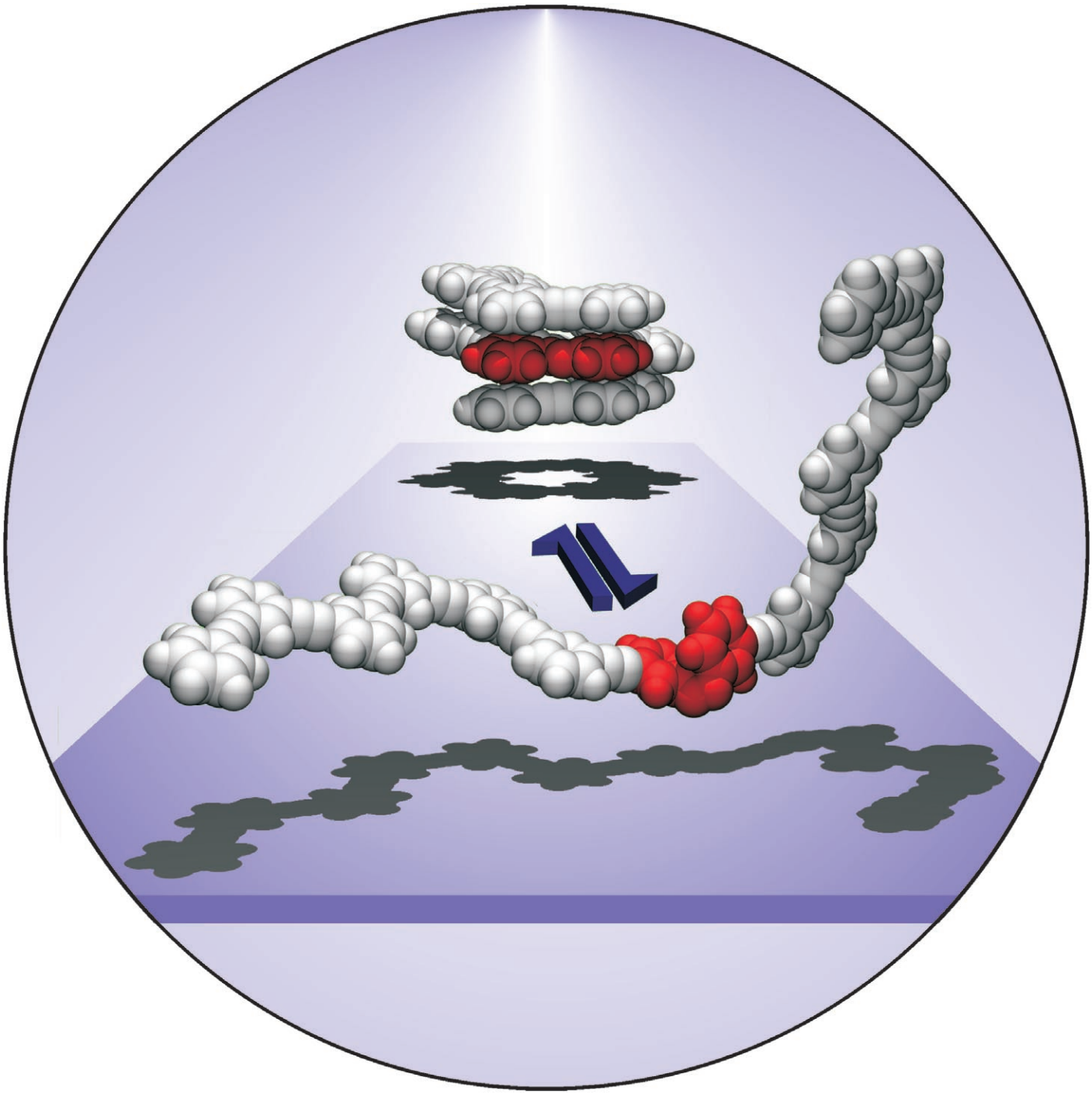
[146] K. Keren, M. Krueger, R. Gilad, G. Ben-Yoseph, U. Sivan, E. Braun, *Science* **2002**, *297*, 72.
[147] K. Keren, R. S. Berman, E. Buchstab, U. Sivan, E. Braun, *Science* **2003**, *302*, 1380.
[148] N. C. Seeman, *Chem. Intell.* **1995**, *1*, 38.
[149] N. C. Seeman, *Angew. Chem.* **1998**, *110*, 3408; *Angew. Chem. Int. Ed.* **1998**, *37*, 3220.
[150] During the production process of this manuscript, further work on DNA nanoarchitecture was published: Park et al. assembled square-shaped arrays of 16 species of $4\times4$ tiles and demonstrated the precise programmability of streptavidin attachment to specific tiles by AFM imaging: S. H. Park, C. Pistol, S. J. Ahn, J. H. Reif, A. R. Lebeck, C. Dwyer, T. H. LaBean, *Angew. Chem.* **2006**, *118*, 749; *Angew. Chem. Int. Ed.* **2006**, *45*, 735). Two-dimensional arrays of different $4\times4$ tiles were also used by Sharma et al. to position gold nanoparticles with variable interparticle spacings, by employing DNA–gold conjugates where each nanoparticle has exactly one DNA strand attached to it: J. Sharma, R. Chhabra, Y. Liu, Y. Ke, H. Yan, *Angew. Chem.* **2006**, *118*, 744; *Angew. Chem. Int. Ed.* **2006**, *45*, 730. Winfree and co-workers have reported on two algorithmic self-assemblies of DNA Wang tiles that mimick a binary counter and copy bit strings, respectively, which represent two important basic computational operations: R. D. Barish, P. W. K. Rothemund, E. Winfree, *Nano Letters*, **2005**, *5*, 2586.




 © 2006 Wiley-VCH Verlag GmbH & Co. KGaA, Weinheim 

# Communications

DOI: 10.1002/anie.200503849



Irradiation of a foldamer bearing a central photochromic azobenzene moiety causes unfolding of the hollow helical secondary structure—a first step towards the design of smart delivery vehicles. For more details, see the communication by S. Hecht and co-workers on the following pages. (Graphic generated by Ragnar S. Stoll.)


WILEY InterScience DISCOVER SOMETHING GREAT
© 2006 Wiley-VCH Verlag GmbH & Co. KGaA, Weinheim

Foldamers

DOI: 10.1002/anie.200503849

# Prototype of a Photoswitchable Foldamer**

*Anzar Khan, Christian Kaiser, and Stefan Hecht**

The formation of secondary structures, for example in proteins, can be mimicked by foldamers,[1] which can adopt stable, usually helical conformations in solution. Research in this area has advanced tremendously in recent years and is of great interest in the bio- and nanosciences. Foldamers are ideally suited for the design of responsive materials because of the dynamic nature of the reversible folding reaction. However, switching between the foldamer conformations typically involves changes in temperature or solvent composition.[1] Alternative stimuli such as pH[2] and metal coordination[3] involve the addition of acid or base and metal cations, respectively, and are therefore associated with the formation of by-products. Clearly, the use of light as a noninvasive stimulus that can be applied with precise control over timing, location, and intensity of exposure would be highly desirable. Photochromic molecules[4] have frequently been utilized to switch a variety of molecular and materials properties,[5] including, for example, photomodulation of the helix–coil equilibrium in linear peptides.[6]

Herein, we report the first example of a photoswitchable foldamer. Our concept is based on the incorporation of a photoisomerizable core into a foldamer strand (Figure 1). Two backbone segments are joined by the photoresponsive core such that the entire strand is long enough to be able to fold into a helical conformation. Irradiation causes a significant geometrical change of the core caused by photoisomerization, which results in denaturation of the helix because each individual backbone segment is too short to adopt a stable helical conformation. Thermal (or photochemical) isomerization reverses the switching process and produces the initial, helically folded state.




***Figure 1.*** Photoswitchable foldamers: Irradiation of the photoisomerizable kinked unit (red) in the middle of a helically folded backbone (blue) induces a reversible helix–coil transition.

Our system is based on amphiphilic oligo(*meta*-phenylene ethynylene) foldamers, which were pioneered by Moore and co-workers.[7] The introduction of a kinked and planar, *meta*-connected *trans*-azobenzene, which closely mimics the structure of a dimeric repeat unit, into the center of a dodecamer leads to target structure **1** (Scheme 1).[8] The lengths of the two oligomer segments were deliberately chosen to allow folding of the entire strand but not the individual parts. The azobenzene core was optimized so that it could be excited selectively, and novel enantiomerically pure (*S*)-α-methyltetra(ethyleneglycol) side chains were introduced to bias the sense of the helical twist and thereby allow monitoring of the conformational transition by means of circular dichroism (CD) spectroscopy.[9]

The folding behavior of oligomer **1** was investigated by using typical solvent-dependent denaturation experiments by monitoring the conformational equilibrium with UV/Vis absorption spectroscopy (Figure 2).[7] The sigmoidal shape of the resultant titration curve is indicative of a cooperative folding process, and detailed analysis reveals a helix stabilization energy in pure acetonitrile of $\Delta G(CH_3CN) = -1.7\ kcal\,mol^{-1}$.[9] Therefore, replacement of the central dimeric phenylene ethynylene unit in the native tetradecamer[7] with the azobenzene core leads to only slight destabilization of the helix; this destabilization is attributed to weaker π,π-stacking interactions caused by the presence of electron-donating methoxy substituents.[10]

Irradiation at 365 nm of the helically folded $\mathbf{1}_{trans}$ to excite selectively the central azobenzene chromophore led to rapid conversion into the corresponding $\mathbf{1}_{cis}$ as monitored by UV/Vis absorption spectroscopy (Figure 3a). A decrease in the π–π* (350–400 nm) absorption, a small increase in the n–π* (400–450 nm) absorption, and an increase in the π–π* (< 265 nm) absorption, as well as two well-defined isosbestic points at 265 and 418 nm are observed. These absorbance changes are indicative of the *trans*→*cis* photoisomerization process.[4] Whereas the photochemical $\mathbf{1}_{trans} \rightarrow \mathbf{1}_{cis}$ conversion takes place within seconds, the thermal $\mathbf{1}_{cis} \rightarrow \mathbf{1}_{trans}$ reversion occurs over the time frame of several hours at room temperature.

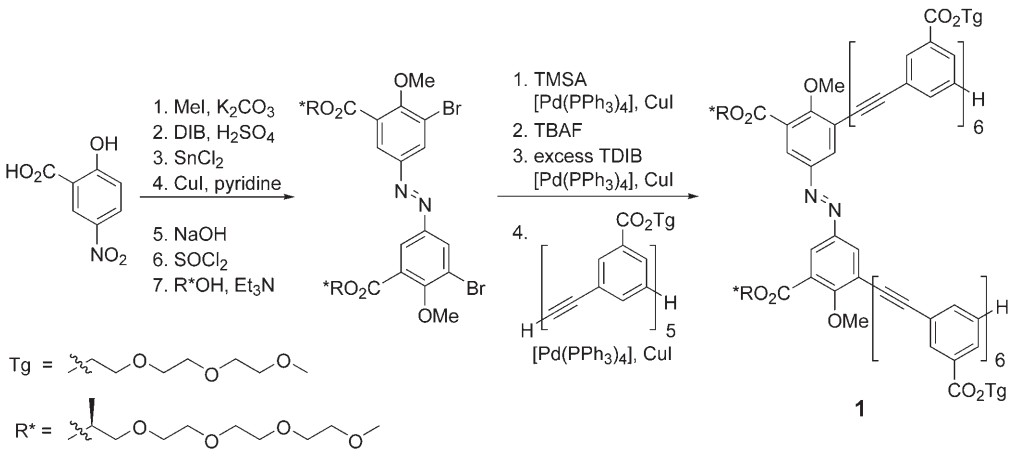
To monitor the conformational changes during both the forward and reverse isomerization processes, CD spectra of solutions of **1** were recorded in solvent mixtures that promote folding (Figure 3b).[11] The CD spectrum of $\mathbf{1}_{trans}$ in aqueous acetonitrile shows a strong positive Cotton effect, which is indicative of the helical conformation, while no CD signal has been observed in denaturing solvents, such as chloroform. The CD signal arises from exciton coupling within the helical backbone and is the result of chirality transfer from the chiral side chains of the core to the helix. Interestingly, the observed spectral shape, which indicates a *P*-helical twist sense, is exactly opposite to that of oligomers carrying side chains with the chiral methyl group in β position.[9] Although irradiation

[*] A. Khan, C. Kaiser, Dr. S. Hecht
Max-Planck-Institut für Kohlenforschung
Kaiser-Wilhelm-Platz 1, 45470 Mülheim an der Ruhr (Germany)
Fax: (+49) 208-306-2979
E-mail: hecht@mpi-muelheim.mpg.de

[**] Synthesis of the chiral side chains was carried out by Christian Kaiser at Freie Universität Berlin. The authors thank Dr. Eckhard Bill (MPI für Bioanorganische Chemie, Mülheim/Ruhr) for the extensive use of the CD spectrometer. Generous support by the Alexander von Humboldt Foundation (Sofja Kovalevskaja Program sponsored by the Federal Ministry of Education and Research and the Program for Investment in the Future (ZIP) of the German government), the German Research Foundation (DFG: SFB 448, GK 788, HE 3675/2-1), and the Max Planck Society (MPG) is gratefully acknowledged.

Supporting information for this article is available on the WWW under http://www.angewandte.org or from the author.

 © 2006 Wiley-VCH Verlag GmbH & Co. KGaA, Weinheim 




***Scheme 1.*** Synthesis of photoswitchable foldamer **1**. DIB = dibromoisocyanuric acid, TMSA = trimethylsilylacetylene, TBAF = tetrabutylammonium fluoride, TDIB = triethyleneglycol 3,5-diiodobenzoate.

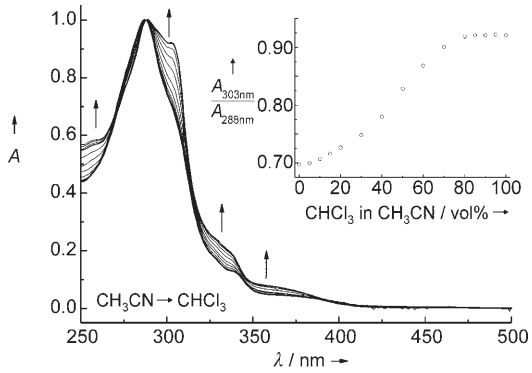



***Figure 2.*** UV/Vis absorption spectra of **1** in acetonitrile ($4.7\times10^{-6}$ M) with increasing chloroform content (100 vol% $CH_3CN$ → 100 vol% $CHCl_3$) at 25 °C. The inset shows the absorbance ratio $A_{303\,nm}/A_{288\,nm}$ as a function of solvent composition.

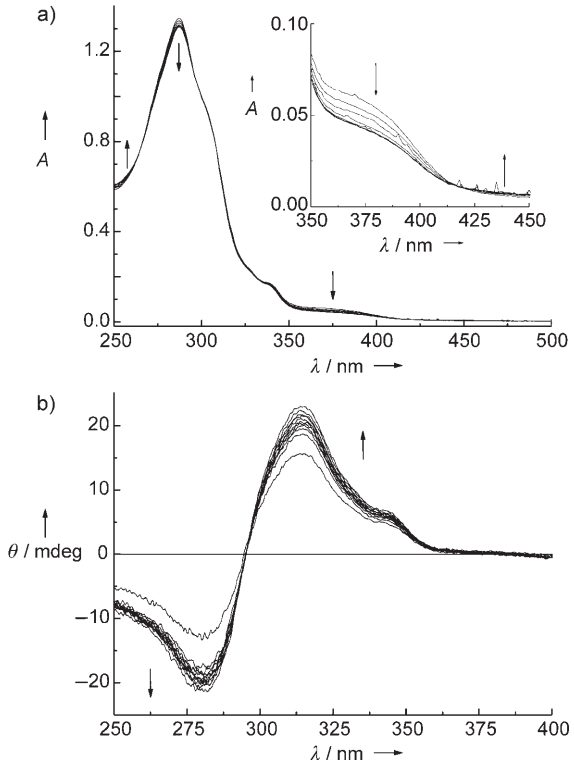



***Figure 3.*** a) UV/Vis absorption spectra obtained during photochemical *trans*→*cis* isomerization of **1** caused by irradiation at 365 nm in acetonitrile ($5.9\times10^{-6}$ M) at 25 °C ($t$ = 0, 1, 3, 7, 15, 31, 63 s). The inset shows a magnification of the decreasing π–π* absorption band of the azobenzene unit. b) CD spectra obtained during thermal *cis*→*trans* isomerization of **1** in 60 vol% $H_2O$ in $CH_3CN$ ($5.7\times10^{-6}$ M) at 22 °C (starting at PSS: $t$ = 0, 1.5, 3, 4.5, 7.5, 10, 48, 53, 72 h).

leads to rapid decrease of the CD signal, which indicates depletion of the helical conformation through unfolding, thermal reversion leads to complete recovery of the initial CD signal intensity, thus indicating refolding of the backbone.[12] The presence of a distinct isodichroic point at 295 nm suggests a clean conversion between the two conformations. Surprisingly, the observed conformational transition is not evident from the band shape of the UV/Vis absorption spectra. The composition of the mixture in the photostationary state (PSS) can be deduced directly from the ratio of the CD signals ($\mathbf{1}_{cis}/(\mathbf{1}_{cis}+\mathbf{1}_{trans}) \approx 40\,\%$).[8] Analysis of the data also provides the rate constant for the thermal *cis*→*trans* isomerization $k_{cis\rightarrow trans}$ at 25 °C of approximately $3.8\times10^{-5}\ s^{-1}$, which corresponds to a half-life $t_{1/2}$ of around 5 h and an activation energy $\Delta G^{\neq}$ of approximately 23.5 kcal mol$^{-1}$; these values are typical for azobenzene-based macromolecules in solution.[13]

We have designed a photochromic foldamer and demonstrated switching of the helix–coil folding transition. Light-triggered systems such as **1** can provide fundamental insight into the folding and unfolding mechanisms by enabling time-resolved measurements[14] and promise applications in photoresponsive (bio)materials[5,15] and smart delivery devices based on photoresponsive dynamic receptors.[16] Our work in progress is focused along these directions, in particular, on the extension of the described system to photoresponsive polymeric folding backbones with increased *cis* content in the PSS.

Received: October 31, 2005
Published online: January 20, 2006

 © 2006 Wiley-VCH Verlag GmbH & Co. KGaA, Weinheim 

**Keywords:** azo compounds · foldamers · helical structures · photochromism


[1] D. J. Hill, M. J. Mio, R. B. Prince, T. S. Hughes, J. S. Moore, *Chem. Rev.* **2001**, *101*, 3893 – 4012.

[2] a) C. Dolain, V. Maurizot, I. Huc, *Angew. Chem.* **2003**, *115*, 2844 – 2846; *Angew. Chem. Int. Ed.* **2003**, *42*, 2738 – 2740; b) E. Kolomiets, V. Berl, I. Odriozola, A.-M. Stadler, N. Kyritsakas, J.-M. Lehn, *Chem. Commun.* **2003**, 2868 – 2869.

[3] a) M. Barboiu, J.-M. Lehn, *Proc. Natl. Acad. Sci. USA* **2002**, *99*, 5201 – 5206; b) M. Barboiu, G. Vaughan, N. Kyritsakas, J.-M. Lehn, *Chem. Eur. J.* **2003**, *9*, 763 – 769; c) R. B. Prince, T. Okada, J. S. Moore, *Angew. Chem.* **1999**, *111*, 245 – 249; *Angew. Chem. Int. Ed.* **1999**, *38*, 233 – 236.

[4] a) *Photochromism—Molecules and Systems* (Ed.: H. Dürr, H. Bouas-Laurent), Elsevier, Amsterdam, **2003**; b) *Molecular Switches* (Ed.: B. L. Feringa), Wiley-VCH, Weinheim, **2001**; c) Special Issue: "Photochromism: Memories and Switches", *Chem. Rev.* **2000**, *100*, 1683 – 1890; d) *Organic Photochromic and Thermochromic Compounds* (Eds.: J. C. Crano, R. J. Guglielmetti), Kluwer Academic/Plenum Publishers, New York, **1999**; e) *Organic Photochromes* (Ed.: A. V. El'tsov), Consultants Bureau, New York, **1990**.

[5] S. Hecht, *Small* **2005**, *1*, 26 – 29, and references therein.

[6] For the side-chain approach, see: a) O. Pieroni, A. Fissi, N. Angelini, F. Lenci, *Acc. Chem. Res.* **2001**, *34*, 9 – 17; for the tether approach, see: b) G. A. Woolley, *Acc. Chem. Res.* **2005**, *38*, 486 – 493; for related polyisocyanates with azobenzene-containing side chains, see: c) S. Mayer, R. Zentel, *Prog. Polym. Sci.* **2001**, *26*, 1973 – 2013.

[7] a) J. C. Nelson, J. G. Saven, J. S. Moore, P. G. Wolynes, P. G. *Science* **1997**, *277*, 1793 – 1796; b) R. B. Prince, J. G. Saven, P. G. Wolynes, J. S. Moore, *J. Am. Chem. Soc.* **1999**, *121*, 3114 – 3121; for a recent review, see: c) C. R. Ray, J. S. Moore, *Adv. Polym. Sci.* **2005**, *177*, 91 – 149.

[8] See the Supporting Information.

[9] For the use of (*S*)-β-methyltri(ethyleneglycol) side chains, see: a) R. B. Prince, L. Brunsveld, E. W. Meijer, J. S. Moore, *Angew. Chem.* **2000**, *112*, 234 – 236; *Angew. Chem. Int. Ed.* **2000**, *39*, 228 – 230; b) R. B. Prince, J. S. Moore, L. Brunsveld, E. W. Meijer, *Chem. Eur. J.* **2001**, *7*, 4150 – 4154.

[10] For related examples, see: a) S. Lahiri, J. L. Thompson, J. S. Moore, *J. Am. Chem. Soc.* **2000**, *122*, 11315 – 11319; b) H. Goto, J. M. Heemstra, D. J. Hill, J. S. Moore, *Org. Lett.* **2004**, *6*, 889 – 892.

[11] Solutions in aqueous acetonitrile were used for the CD experiments to maximize the CD signal as a result of the increased hydrophobic driving force and therefore ensure more accurate kinetic data.

[12] An alternative explanation to account for the CD spectral changes would be a transition to a more loosely packed helical conformation. Although this conformation is rather unlikely because of the inherent strain caused by the incorporation of the nonmatching and nonplanar azobenzene core, it cannot be ruled out at present time. Fluorescence emission spectroscopy, which is a complementary experimental technique for monitoring the helix–coil transition, was found inapplicable in this particular system, and both HPLC and gel permeation chromatography have not been able to completely resolve the $\mathbf{1}_{trans}/\mathbf{1}_{cis}$ mixture.

[13] For example, see: L.-X. Liao, F. Stellacci, D. V. McGrath, *J. Am. Chem. Soc.* **2004**, *126*, 2181 – 2185.

[14] For example, see: W. Y. Yang, R. B. Prince, J. Sabelko, J. S. Moore, M. Gruebele, *J. Am. Chem. Soc.* **2000**, *122*, 3248 – 3249.

[15] For an elegant example, see: a) A. Koçer, M. Walko, W. Meijberg, B. L. Feringa, *Science* **2005**, *309*, 755 – 758; for a recent review, see: b) K. Kinbara, T. Aida, *Chem. Rev.* **2005**, *105*, 1377 – 1400.

[16] R. B. Prince, S. A. Barnes, J. S. Moore, *J. Am. Chem. Soc.* **2000**, *122*, 2758 – 2762.


 © 2006 Wiley-VCH Verlag GmbH & Co. KGaA, Weinheim 

Enzyme Inhibitors

DOI: 10.1002/anie.200502756

# Undressing of Phosphine Gold(I) Complexes as Irreversible Inhibitors of Human Disulfide Reductases**

*Sabine Urig, Karin Fritz-Wolf, Régis Réau, Christel Herold-Mende, Katalin Tóth, Elisabeth Davioud-Charvet, and Katja Becker**

Phosphole-based π-conjugated organic systems are useful for optoelectronic applications since the phosphole ring is weakly aromatic and possesses a central nucleophilic P atom.[1–3] Modification of their nucleophilic heteroatom by coordination to metal centers may render these compounds promising candidates for chemotherapeutic applications.[4] Inhibition of disulfide reductases contributes to the cytotoxic effects of anticancer compounds.[5,6] Here, we report the effects of novel, highly potent, phosphole-containing gold and platinum complexes on human glutathione reductase (hGR), thioredoxin reductase (hTrxR), and DNA, as well as their growth-inhibitory action on tumor cells. To date, hardly any structures of medicinally relevant gold(I)–protein complexes have been reported.[7] Herein, we describe the first crystal structure of modified hGR with almost linear S-$Au^{I}$-S-coordination in the active site.

[*] S. Urig, Prof. Dr. K. Becker
Interdisciplinary Research Center
Justus Liebig University
Heinrich-Buff-Ring 26–32, 35392 Giessen (Germany)
Fax: (+49) 641-99-39129
E-mail: becker.katja@gmx.de

Dr. K. Fritz-Wolf
Department of Biophysics
Max Planck Institute for Medical Research
69120 Heidelberg (Germany)

Prof. Dr. R. Réau
UMR 6509, Institut de Chimie
CNRS-Université de Rennes 1
35042 Rennes Cedex (France)

Dr. C. Herold-Mende
Department of Neurosurgery
University of Heidelberg
69120 Heidelberg (Germany)

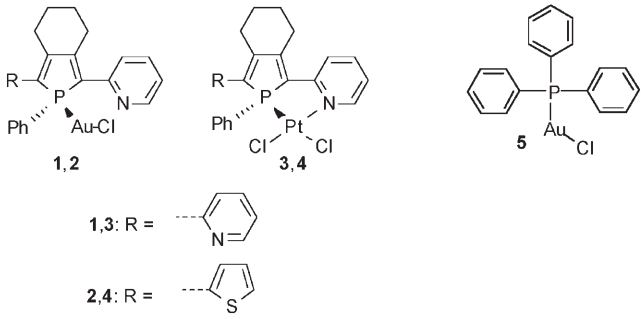
Dr. K. Tóth
Division Biophysics of Macromolecules
German Cancer Research Center
69120 Heidelberg (Germany)

Dr. E. Davioud-Charvet
CNRS UMR 8525, Lille University (France)
and Center of Biochemistry, University of Heidelberg (Germany)

[**] We gratefully acknowledge the DFG (grant BE 1540/6-3 to K.B.) and the CNRS-DFG program (E.D.-C.) for financial support. E.D.-C. is a delegate supported by the Centre National de la Recherche Scientifique, France. The X-ray crystallographic work was performed at the Swiss Light Source, beamline X06SA, Paul Scherrer Institute, Villigen, Switzerland.


© 2006 Wiley-VCH Verlag GmbH & Co. KGaA, Weinheim

The homodimeric flavoenzymes TrxR and GR are associated with many cellular processes such as antioxidant defence, redox balance, regulation of various proteins, and nucleotide metabolism.[8,9] The cysteine thiol functions in the active site as well as the redox-active Sec (selenocysteine) of TrxR are interesting drug targets.[10] We identified as novel and highly potent disulfide reductase inhibitors [1-phenyl-2,5-di(2-pyridyl)phosphole]AuCl **1**[11] as well as three other complexes **2**–**4** bearing 2-pyridyl or 2-thienyl substituents on the phosphole ring and gold(I) (AuCl; **2**) or platinum(II) ($PtCl_2$; **3**, **4**) as the metal center.




Time-dependent inhibition studies with hGR showed that the gold(I)–phosphole complexes **1** and **2** are active in the low nanomolar range (Table 1) and at least two orders of magnitude more active than the corresponding platinum(II) complexes **3** and **4**. The inhibition of hGR by the phosphole complexes can be explained by a competition with the oxidized glutathione (GSSG) followed by an irreversible reaction to yield the covalent product. The competitive inhibition of hGR($E_{red}$) with respect to GSSG was more obvious for **3** ($K_i = 19.7 \pm 0.48$ μM) than for **1** ($K_i = 0.46 \pm 0.06$ μM)[11] (see Figure 1 and [Eq. (1)], thus contributing to the inhibitory effect of the platinum(II) phospholes; this is indicated by $K_i$ values similar to $i_{0.5}$ values[12] and >60% enzyme reactivation after desalting. The gold(I) compounds are very dynamic in solution at room temperature (free rotation around the inter-ring C–C bond),[3] and this flexibility facilitates their access to the glutathione binding site. In contrast, the platinum analogues with a pyridylphosphole ligand form rigid chelates. In addition, because of the high electrophilic affinity of $Au^I$ for S ligands the gold-containing inhibitor is the preferred binding partner for hGR in the presence of the physiological substrate GSSG.

***Table 1:*** Inactivation of reduced hGR, wild-type hTrxR, and mutant hTrxR.[a]

| Enzyme | **1** | **2** | **3** | **4** |
|---|---|---|---|---|
| Wild-type | | | $i_{0.5}$ [nM] | |
| hGR (1.4 nM) | 1 | 2 | 1000 | 400 |
| 100 μM GSSG | | | | |
| wt-hTrxR (24 nM) | 6.9 | 7 | 6.7 | 8 |
| 20 μM hTrxC72S | | | | |
| wt-hTrxR (4.8 nM) | 0.8 | 1 | 2 | 1.1 |
| 3 mM DTNB | | | | |
| Mutants | | | $i_{0.5}$ [μM] | |
| hTrxRSec498Cys (1.8 μM) | 0.9 | 1.9 | 2 | 2.4 |
| 20 μM hTrxC72S | | | | |
| hTrxRSec498Cys (1.8 μM) | 2.5 | 3 | 32.7 | 22 |
| 3 mM DTNB | | | | |
| hTrxR-16 (100 nM) | 1.7 | n.d.[b] | 30 | n.d.[b] |
| 3 mM DTNB | | | | |
| hTrxR-8 (100 nM) | 1 | n.d.[b] | 12.5 | n.d.[b] |
| 3 mM DTNB | | | | |

[a] After 10 min preincubation with **1**–**4**. [b] n.d. = not determined.

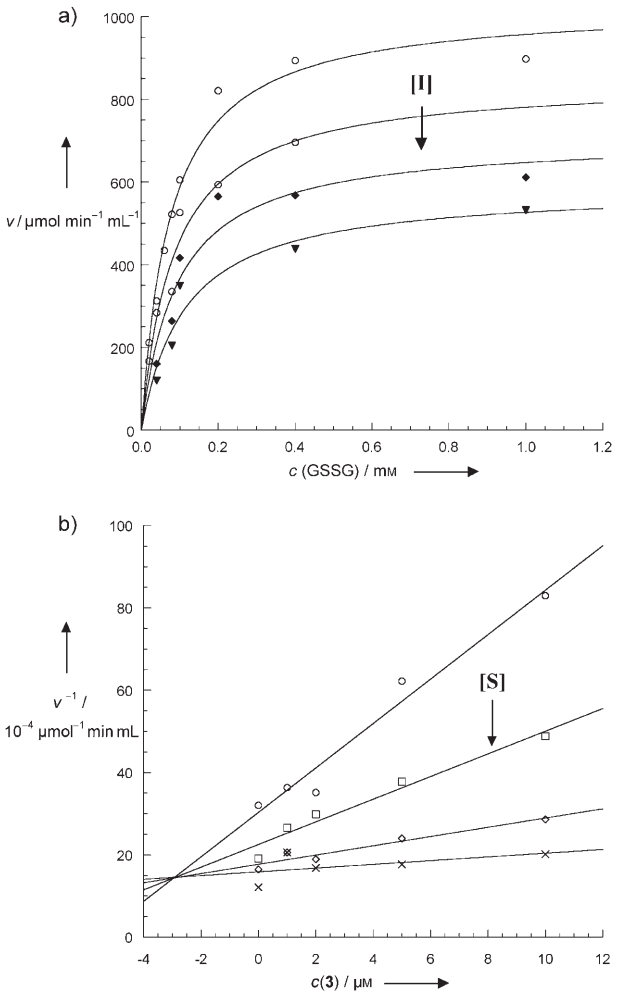



***Figure 1.*** Kinetic analysis of hGR inhibition by **3** (0–10 μM): Michaelis–Menten (a) and Dixon plot (b). Assuming initial competitive inhibition, a $K_i$ value of 19.7 ± 0.48 μM was calculated from a secondary plot ($K_M/K_i$ versus [I]) [Eq. (1)].

$$v = \frac{V_{max}[S]}{K_M(1 + [I]/K_i) + [S]} \quad (1)$$

The effects on TrxR are more complex because of its two distinct active sites located in the FAD domain of the N-terminal part and at the C-terminal extension of each subunit. The two active sites provide two potential binding sites for substrates and inhibitors.[13] Small substrates like 5,5′-dithiobis(2-nitrobenzoic acid) (DTNB) have access to both sides and can thus be reduced at either redox center. In contrast,

 © 2006 Wiley-VCH Verlag GmbH & Co. KGaA, Weinheim 

the 12-kDa protein thioredoxin (Trx) is reduced only at the C-terminal redox center of TrxR.[14] Since most inhibitors as well as small substrates can interact with both active sites, it is often difficult to determine an unambiguous inhibition type.

The inhibitory action of compounds **1**–**4** was analyzed in assays by using Trx or DTNB as substrate (Figure 2). First, the

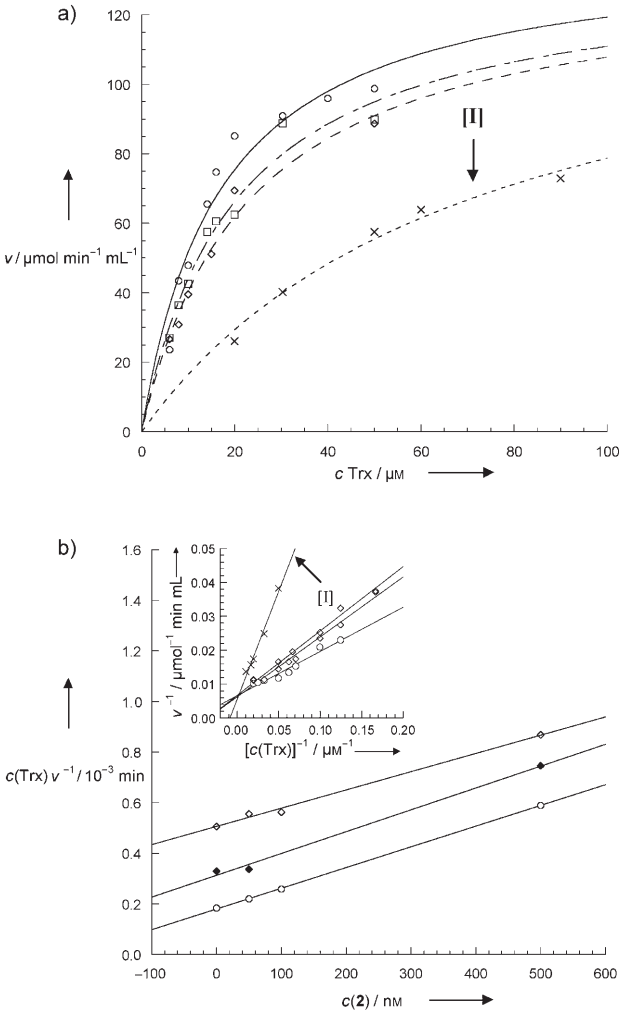



***Figure 2.*** Kinetic analysis of hTrxR inhibition. Inhibition of Trx reduction by **2** (0, 50, 100, 500 nM): a) nonlinear regression ($K_i = 157.6 \pm 9.36$ nM) [Eq. (1)]. b) Cornish–Bowden plot; from lower to upper line: 8, 30, 50 μM Trx. Inset: Lineweaver–Burk plot.

time-dependent inhibitory action of **1**–**4** was studied on wild-type TrxR possessing a Cys-Sec pair at the flexible C-terminal part. Complexes **1**–**4** are extremely efficient with $i_{0.5}$ values in the nanomolar range (Table 1). It is noteworthy that the $i_{0.5}$ values of these complexes are very similar, showing that the phosphole substitution pattern (pyridyl versus thienyl) has only a marginal effect. The gold(I) complex **1** was studied in more detail. Under steady-state conditions the competitive component of hTrxR($E_{red}$) inhibition by **1** was more pronounced with DTNB as substrate ($K_i = 0.52 \pm 0.08$ nM), suggesting that the inhibitor interacts with the N-terminal redox center. Competitive inhibition of TrxR is followed by rapid irreversible inhibition, which cannot be reversed by dilution or desalting. 2,3-Dithiopropanol (British Anti-Lewisite, BAL) could prevent and reverse the inhibition of hTrxR by **1**.[15] It was found that 0.3 equiv of inhibitor **1** led to 50% completely inactive TrxR molecules ($t_{1/2} \leq 0.5$ s). Slightly higher concentrations immediately led to total inactivation of the enzyme.

Studies on TrxR mutants[16] confirmed the Sec residue as the prime target of our compounds (Table 1). The inhibition of the Sec→Cys mutant was two to four orders of magnitude less than that of the wild-type TrxR. The higher $i_{0.5}$ values in the DTNB assay and inhibition of truncated mutants of TrxR[16] confirmed the role of DTNB as a competitor at the N-terminal active site. In conclusion, hTrxR can be very efficiently inhibited by gold(I) phospholes ($k_i \geq 1.5\ s^{-1}$) (S-Au-Se coordination). Platinum(II) phospholes are specific inhibitors of TrxR with a 400-fold higher affinity than for hGR.

To gain more insight into the mechanism of the irreversible inhibition of our novel class of gold inhibitors, we studied the interaction of hGR with **1** by X-ray crystallography. We obtained monoclinic crystals (space group *C*2) in which half of a hGR dimer[17] was contained in the asymmetric unit. Each monomer was modified by one molecule of **1** covalently bound to the surface-exposed Cys284, and surprisingly, one Au atom covalently bound between Cys58 and Cys63 in the active site (Figure 3). Both modifications can be explained by the fact that cysteine S atoms are known to effectively displace $Cl^-$ ligands from gold(I) complexes in solution,[7,18,19] and that the gold(I) complexes have a high affinity for S. The presence of a (pyridylphosphole)gold fragment at the Cys284 suggests that the $Cl^-$ ligand is more easily displaced than the phosphole ligand. Hence our proposed mechanism includes a first attack of inhibitor **1** at the Cys58-thiolate, release of $Cl^-$, and the formation of a (Cys58-S)-Au-phosphole intermediate. In the meantime, another molecule of inhibitor binds to Cys284, forming the (Cys284-S)-Au-phosphole product (Figure 3a). There is a second cysteine (Cys63) close to this intermediate in the active site, thus leading to a nucleophilic attack of the Cys63-thiolate, displacement of the phosphole ligand, and S-Au-S coordination in the inactive GR product (Figure 3b).[11] The S-Au-S coordination shows the almost linear geometry (S-Au-S angle 167.5°) characteristic of gold(I) centers. A related mechanism had been hypothesized previously for the anti-arthritic drug auranofin ([$Au^I(PEt_3)$(thioglucose)]) but was not proved. It was suggested that auranofin might lose both the thioglucose and the triethylphosphine ligands, leading to final gold protein thiol adducts similar to those arising from gold salts.[18]

To study the DNA-binding behavior of the gold(I) complexes, we treated plasmid DNA with **1**. The resulting melting curves (Figure 4a) show strong effects of **1** (1–20 μM) on DNA with loss of characteristic shape at higher inhibitor concentrations (loss of cooperativity (Figure 4b). This can be explained by the binding of **1** to DNA and is consistent with other studies showing DNA interaction with AuCl complexes.[20]

 © 2006 Wiley-VCH Verlag GmbH & Co. KGaA, Weinheim 

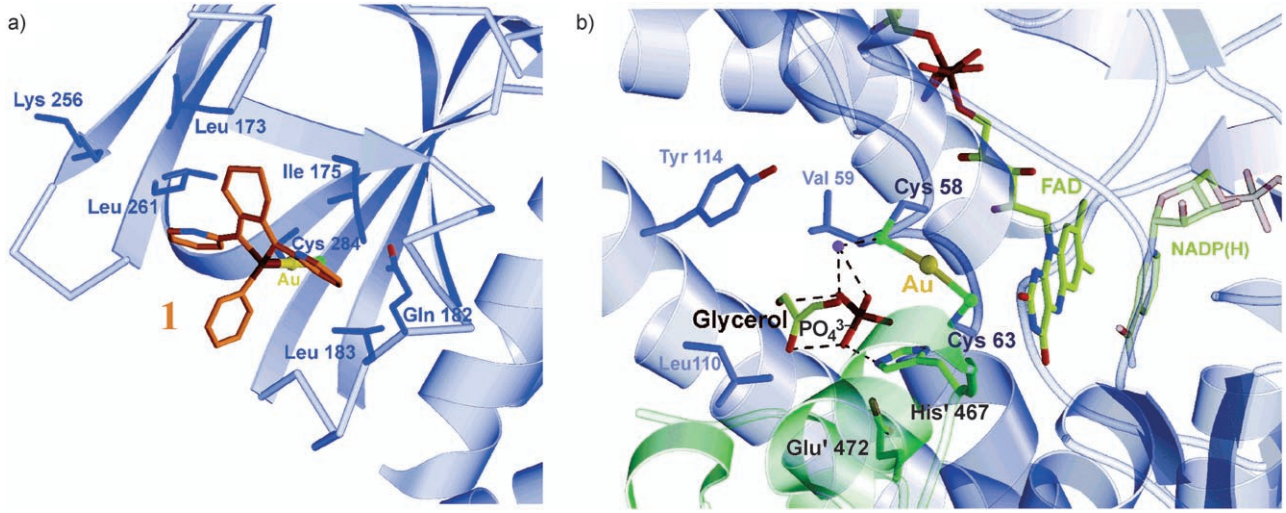



***Figure 3.*** Refined structure of hGR modified by **1**. a) Surface-exposed (Cys284-S)-Au-phosphole. b) Active site: (Cys58-S)-Au-(S-Cys63) as the central unit, $K^+$ ion (electrostatic interaction with Cys58), and $PO_4^{3-}$ group (interaction with $K^+$, glycerol, and His′467 of the symmetry-related monomer). Structure was drawn using MOLSCRIPT and RASTER 3D.[34,35]

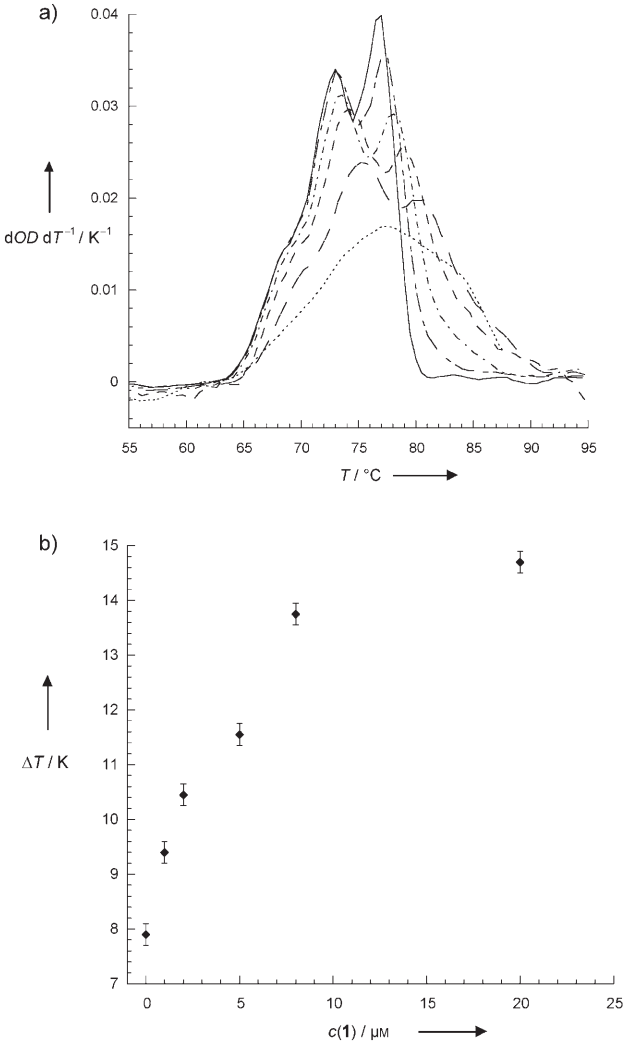



***Figure 4.*** Interaction of **1** with pUC18 plasmid DNA. a) Derivative of the denaturaion curves in order from solid to dotted line: DNA alone, with 1, 2, 5, 8, and 20 μM **1**. b) Loss of cooperativity of the melting process as shown by the increasing $\Delta T$ values.

The chemotherapeutic properties of **1**–**4** were tested on glioblastoma cells and compared to the results with (triphenylphosphine)gold(I) chloride (**5**). The lowest $IC_{50}$ values (5–20 μM) were obtained with gold(I) complexes **1**, **2**, and **5** (Table 2). The presence of either an electron-deficient 2-pyridyl or electron-rich 2-thienyl substituent on the phosphole ligand has only a marginal effect in the cell. The cellular uptake and intracellular distribution of our compounds seem to be similar to the action of auranofin on macrophages.[21] The corresponding sulfhydryl shuttle mechanism through membrane and intracellular spaces could occur with selectivity of the phosphole ligands for certain sulfhydryl groups (lipophilicity for membrane SH groups, affinities of metals for sulfur, steric factors).

***Table 2:*** Antiproliferative effects ($IC_{50}$ [μM]) of compounds **1**–**5** on three different glioblastoma cell lines.

| Cell line | **1** | **2** | **3** | **4** | **5** |
|---|---|---|---|---|---|
| NCH37[a] | 5.4 ± 0.7 | 5.7 ± 0.2 | 33 ± 3.2 | 28.1 ± 0.8 | 6.1 ± 0.2 |
| NCH82[a] | 12.5 ± 0.8 | 7.5 ± 0.04 | 65 ± 6.3 | 81.8 ± 4.1 | 7.2 ± 0.2 |
| NCH89[a] | 10.8 ± 0.8 | 15.2 ± 0.4 | 43 ± 3.7 | 78.4 ± 3.1 | 20.3 ± 0.7 |

[a] Mean $IC_{50}$ value of carmustine (BCNU) in these cell lines: 430 μM. Carmustine is an established nitrosourea drug for the treatment of glioblastoma: 430 μM.

In conclusion, the presented gold(I)– and platinum(II)–phosphole compounds **1**–**4** are the most potent TrxR inhibitors to date, with gold(I) complex **1** previously identified as the best known GR inhibitor. Their inhibitory properties are complemented by high affinity for DNA. Both effects result in toxicity towards glioblastoma cells. An X-ray diffraction study has confirmed that (phosphine)gold chloride complexes act as prodrugs with a stepwise ligand displacement. We are currently focused on in vivo testing as well as further optimization of the complexes as sugar derivatives.

 © 2006 Wiley-VCH Verlag GmbH & Co. KGaA, Weinheim 

## Experimental Section

Recombinant hGR and hTrxR mutants were produced as described.[6,22] Wild-type TrxR was purified from human placenta.[15,23] Compounds **1**–**4** were synthesized according to published procedures and characterized by NMR spectroscopy.[3,24] [AuCl($PPh_3$)] (**5**) was purchased from Sigma, BAL was from Fluka (Germany). CCDC 277831 (**1**) contains the supplementary crystallographic data for this paper. These data can be obtained free of charge from The Cambridge Crystallographic Data Centre via www.ccdc.cam.ac.uk/data_request/cif.

Inhibition studies: The data for the enzyme kinetics were obtained using Hitachi U-2100 and Beckmann DU 650 UV/Vis spectrophotometers. Compounds **1**–**5** were dissolved in DMF. Inactivation of hGR was measured in the GSSG-reduction assay,[25] inactivation of wild-type hTrxR and hTrxR mutants (hTrxRSec498-Cys (a), hTrxR-16, hTrxR-8 (b))[16] was measured in the DTNB assay[26] as well as in the Trx reduction assay.[6] Half-maximal inhibition of the enzymes ($i_{0.5}$)[12] was determined by incubating hGR (1.4 nM), wild-type hTrxR (4.8 nM and 24 nM), or mutant hTrxR (0.1–1.8 μM) (FAD-containing subunits) for 10 min with NADPH (100 or 200 μM) and inhibitor (0.5–500 nM and 1–40 μM, depending on assay conditions) at 25 °C. The enzyme activity was measured by adding GSSG (100 μM), DTNB (3 mM), or hTrx (20 μM) to the mixtures. To determine the type of inhibition by **1**–**4** the reaction was started with NADPH, and $K_M$ values for GSSG, DTNB, and Trx were analyzed (KaleidaGraph, Synergy Software, USA). For analysis of irreversible inhibition, 250 nM wild-type TrxR was incubated with 200 μM NADPH in the absence or presence of 1–10 μM inhibitor for 10 min and subsequently with or without BAL for 20 min. After desalting using Sephadex G-25 columns (Amersham Biosciences, Germany) the fractions were analyzed for residual or restored enzyme activity as described above.

Crystallization: GR (50 $\mu g\,mL^{-1}$), reduced with 100 μM NADPH was incubated with 20 μM **1** for 20 min at 25 °C and then concentrated. Crystals were grown at 30 °C using the hanging-drop vapor-diffusion technique: 10 $mg\,mL^{-1}$ hGR in 120 mM $(NH_4)_2SO_4$/potassium phosphate (100 mM; pH 7.5) was equilibrated against 720 mM $(NH_4)_2SO_4$/potassium phosphate (100 mM; pH 7.5). Prior to the measurements crystals were soaked in mother liquor with 35 % glycerol.

X-ray crystallographic studies: Data were recorded by the rotation method and processed with the program XDS.[27] The data set[28] was collected at 100 K, using synchrotron radiation (SLS, Villigen, Switzerland, beamline X06SA, rotation per image: 1.0°, $\lambda =$ 0.902691 Å, detector CCD, (MARCCD)). Reflection phasing and refinements were carried out using the CNS program suite[29] and model correction using the graphic program O.[30] The structure was solved by molecular replacement using the structure of hGR modified by S-nitrosoglutathione as the search model.[31] An anomalous difference Patterson map was calculated to localize Au atoms. The structure of the complex was refined to 2.6-Å resolution with an overall temperature factor of 37.2 $Å^2$ ($R_{free} = 25.9$ % with a cross-validated coordinate error of 0.37 Å). The configuration was verified by PROCHECK.[32]

DNA interaction: Linearized pUC18 plasmid DNA was incubated with 1–20 μM **1** in degassed phosphate buffer (10 mM; pH 7.0) containing 1 % dioxane (ratio of **1** to number of basepairs 1:20–1:1). Thermal denaturation curves were recorded between 50 and 97 °C (0.5 °C $min^{-1}$) at a wavelength of 260 nm (hyperchromic effect) on a Cary 4 E spectrophotometer (Varian, Mulgrave, Australia). After normalization to absorbance at room temperature and smoothing in five-point intervals, derivative melting curves of the samples were drawn (KaleidaGraph). The cooperativity of the melting procedure was characterized by the halfwidth ($\Delta T$) of the derivative peak.

Proliferation assays: Cells from glioblastoma cell lines NCH37, NCH82, and NCH89 were cultured as described in reference [33]. Proliferation assays were performed as described[33] using the BrdU Labeling and Detection Kit III (Roche Diagnostics, Germany). Cells ($7 \times 10^3$ cells per well) were seeded in replicas in 96-well plates for 24 h. Then, **1**–**5** (1, 5, 10, 20, 50, and 100 μM in DMSO) were added to the wells and 48 h later, BrdU (ad 10 μM) was applied and measured according to the manufacturer's instructions.

Received: August 4, 2005
Revised: December 3, 2005
Published online: February 22, 2006

**Keywords:** enzyme inhibitors · gold · medicinal chemistry · platinum · structure elucidation

[1] C. Hay, M. Hissler, C. Fischmeister, J. Rault-Berthelot, L. Toupet, L. Nyulaszi, R. Réau, *Chem. Eur. J.* **2001**, *7*, 4222.
[2] C. Hay, C. Fave, M. Hissler, J. Rault-Berthelot, R. Réau, *Org. Lett.* **2003**, *5*, 3467.
[3] a) C. Fave, T. Y. Cho, M. Hissler, C. W. Chen, T. Y. Luh, C. C. Wu, R. Réau, *J. Am. Chem. Soc.* **2003**, *125*, 9254; b) H.-C. Su, O. Fadhel, C.-J. Yang, T.-Y. Cho, C. Fave, M. Hissler, C.-C. Wu, R. Réau, *J. Am. Chem. Soc.* **2006**, *128*, 983.
[4] C. K. Mirabelli, R. K. Johnson, D. T. Hill, L. F. Faucette, G. R. Girard, G. Y. Kuo, C. M. Sung, S. T. Crooke, *J. Med. Chem.* **1986**, *29*, 218.
[5] K. Becker, C. Herold-Mende, J. J. Park, G. Lowe, R. H. Schirmer, *J. Med. Chem.* **2001**, *44*, 2784.
[6] A. Irmler, A. Bechthold, E. Davioud-Charvet, V. Hofmann, R. Réau, S. Gromer, R. H. Schirmer, K. Becker, *Flavins Flavoproteins* **2002**, *14*, 803.
[7] J. Zou, P. Taylor, J. Dornan, S. P. Robinson, M. D. Walkinshaw, P. J. Sadler, *Angew. Chem.* **2000**, *112*, 39, 3054; *Angew. Chem. Int. Ed.* **2000**, *39*, 2931.
[8] K. Becker, S. Gromer, R. H. Schirmer, S. Müller, *Eur. J. Biochem.* **2000**, *267*, 6118.
[9] E. S. Arnér, A. Holmgren, *Eur. J. Biochem.* **2000**, *267*, 6102.
[10] S. Gromer, S. Urig, K. Becker, *Med. Res. Rev.* **2004**, *24*, 40.
[11] M. Deponte, S. Urig, L. D. Arscott, K. Fritz-Wolf, R. Réau, C. Herold-Mende, S. Koncarevic, M. Meyer, E. Davioud-Charvet, D. P. Ballou, C. H. Williams, Jr., K. Becker, *J. Biol. Chem.* **2005**, *280*, 20628.
[12] A. Cortés, M. Cascante, M. L. Cardenas, A. Cornish-Bowden, *Biochem. J.* **2001**, *357*, 263.
[13] R. Millet, S. Urig, J. Jacob, E. Amtmann, J. P. Moulinoux, S. Gromer, K. Becker, E. Davioud-Charvet, *J. Med. Chem.* **2005**, *48*, 7024.
[14] T. W. Gilberger, B. Bergmann, R. D. Walter, S. Muller, *FEBS Lett.* **1998**, *425*, 407.
[15] S. Gromer, L. D. Arscott, C. H. Williams, Jr., R. H. Schirmer, K. Becker, *J. Biol. Chem.* **1998**, *273*, 20096.
[16] Definition of TrxR mutants: a) penultimate selenocysteine residue replaced by cysteine; b) deletion at the C terminus.
[17] P. A. Karplus, G. E. Schulz, *J. Mol. Biol.* **1987**, *195*, 701.
[18] M. J. Abrams, B. A. Murrer, *Science* **1993**, *261*, 725.
[19] C. F. Shaw, *Chem. Rev.* **1999**, *99*, 2589.
[20] C. K. Mirabelli, C. M. Sung, J. P. Zimmerman, D. T. Hill, S. Mong, S. T. Crooke, *Biochem. Pharmacol.* **1986**, *35*, 1427.
[21] R. M. Snyder, C. K. Mirabelli, S. T. Crooke, *Biochem. Pharmacol.* **1986**, *35*, 923.
[22] A. Nordhoff, U. S. Bucheler, D. Werner, R. H. Schirmer, *Biochemistry* **1993**, *32*, 4060.
[23] S. Gromer, H. Merkle, R. H. Schirmer, K. Becker, *Methods Enzymol.* **2002**, *347*, 382.
[24] F. Leca, C. Lescop, L. Toupet, R. Réau, *Organometallics* **2004**, *23*, 6191.
[25] G. Krohne-Ehrich, R. H. Schirmer, R. Untucht-Grau, *Eur. J. Biochem.* **1977**, *80*, 65.

 © 2006 Wiley-VCH Verlag GmbH & Co. KGaA, Weinheim 

[26] E. S. Arnér, L. Zhong, A. Holmgren, *Methods Enzymol.* **1999**, *300*, 226.
[27] W. Kabsch, *J. Appl. Crystallogr.* **1993**, *26*, 795.
[28] Crystal dimensions: $0.25 \times 0.15 \times 0.10$ mm; crystal system: monoclinic; space group: $C2$; $a = 120.31$, $b = 62.72$, $c = 83.99$ Å, $\alpha = \gamma = 90°$, $\beta = 122.47°$; $2\theta_{max} = 5.2°$; synchrotron radiation, $\lambda = 0.902691$ Å; $T = 100$ K; reflections for refinement (CNS): 16319; $I/\sigma$: 13.1 (5.3); resolution range: 14.98–2.6 (2.76–2.6); 100% completeness; mean redundancy: 3.8 (3.8); $R_{sym}(100\Sigma|I\eta - \langle I\rangle|/\Sigma I\eta) = 8.0$ (25.9)%; $rmsd_{bonds} = 0.007$ Å; $rmsd_{angles} = 1.8$; $R_{cryst}(100\Sigma||F_{obs}| - |F_{calc}||/\Sigma|F_{obs}|) = 20.1\%$; $R_{free}$(3% of randomly chosen unique reflections) = 25.9%; data deposited at the RCSB Protein Data Bank: PDB ID Code 2AAQ.
[29] A. T. Brunger, P. D. Adams, G. M. Clore, W. L. DeLano, P. Gros, R. W. Grosse-Kunstleve, J. S. Jiang, J. Kuszewski, M. Nilges, N. S. Pannu, R. J. Read, L. M. Rice, T. Simonson, G. L. Warren, *Acta Crystallogr. Sect. D* **1998**, *54*, 905.
[30] T. A. Jones, J. Y. Zou, S. W. Cowan, Kjeldgaard, *Acta Crystallogr. Sect. A* **1991**, *47*, 110.
[31] K. Becker, S. N. Savvides, M. Keese, R. H. Schirmer, P. A. Karplus, *Nat. Struct. Biol.* **1998**, *5*, 267.
[32] R. A. Laskowski, M. W. MacArthur, D. S. Moss, J. M. Thornton, *J. Appl. Crystallogr.* **1993**, *26*, 283.
[33] C. Herold-Mende, H. H. Steiner, T. Andl, D. Riede, A. Buttler, C. Reisser, N. E. Fusenig, M. M. Mueller, *Lab. Invest.* **1999**, *79*, 1573.
[34] P. J. Kraulis, *J. Appl. Crystallogr.* **1991**, *24*, 946.
[35] E. A. Merritt, D. J. Bacon, *Methods Enzymol.* **1997**, *277*, 505.

 © 2006 Wiley-VCH Verlag GmbH & Co. KGaA, Weinheim 

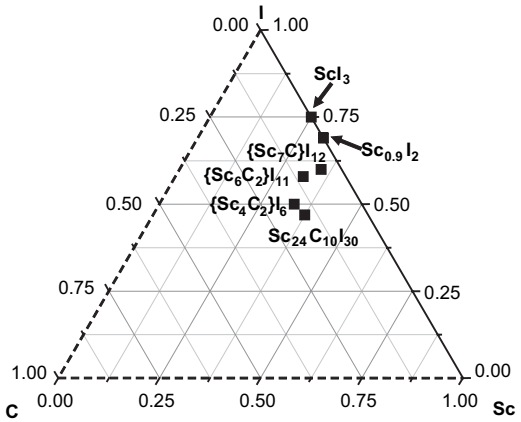



***Figure 1.*** Compounds in the Sc/C/I system (binary C/I and Sc/C compounds are omitted).

*Iodine Supertetrahedra*

DOI: 10.1002/anie.200503914

# The Molecular Solid $Sc_{24}C_{10}I_{30}$: A Truncated, Hollow T4 Supertetrahedron of Iodine Filled with a T3 Supertetrahedron of Scandium That Encapsulates the Adamantoid Cluster $Sc_4C_{10}$**

*Liesbet Jongen, Anja-Verena Mudring,* and Gerd Meyer**

*Dedicated to Professor John D. Corbett on the occasion of his 80th birthday*

There are two iodides of scandium (Figure 1), the rather trivial insulator $ScI_3$ and the scandium-deficient compound $Sc_{0.9}I_2$,[1] which is metallic above and insulating below approximately 100 K. At low temperatures, the excess electrons (according to $9 \times Sc_{0.89}I_2 = (Sc^{3+})_8\square_1(I^-)_{18}(e^-)_6$ for a hypothetical ninefold superstructure) are localized in scandium 3d states, resulting in the presence of some divalent scandium ($Sc^{2+}$), as revealed by the compound's well-resolved ESR spectrum.[2] Excess electrons may also be used for Sc–Sc bonding, as evidenced by the rather short Sc–Sc distance of 328 pm in $NaSc_2I_6$[3] and supported by band-structure calculations.[2,3] The Sc–Sc bonding and Sc–I antibonding interactions must be finely tuned at the Fermi level,[2] which explains the enigmatic scandium deficiencies observed not only in $Sc_{0.9}I_2$, but also in $CsSc_{0.8}I_3$, for example.[2,4]

Excess electrons may not only be delocalized, as in metallic $Sc_{0.9}I_2$, or localized at the atoms ($Sc^{2+}$, paramagnetic) or in bonds, but may also be used by a third partner. This is, at least in a simple (ionic) model, the case in $Sc_4C_2I_6 = (Sc^{3+})_4(C_2^{6-})(I^-)_6$.[5] In this compound, in addition to Coulombic $Sc^{3+}$–$I^-$ interactions, there are also strong covalent Sc–C and Sc–Sc interactions, as revealed by the short Sc–Sc and Sc–C distances of 302 and 200 pm, respectively. A similar picture holds for $Sc_6C_2I_{11}$,[5] which bears one excess electron in this model.

In an attempt to produce $Sc_6C_2I_{11}$ in pure form for physical measurements, we have now obtained $Sc_{2.4}CI_3$,[6] a slightly more scandium-rich carbide iodide than $Sc_4C_2I_6 \mathrel{\hat{=}} Sc_2CI_3$ (Figure 1).[5] The new compound is better formulated as $Sc_{24}C_{10}I_{30}$, as its solid-state structure is built from molecules of this composition. The large cubic unit cell ($V = 16.943(3)$ nm$^3$ at 293 K) contains eight crystallographically equivalent $Sc_{24}C_{10}I_{30}$ molecules.[7] As one eighth of the unit-cell volume is 2.12 nm$^3$, and if a space filling of 70% is assumed, each molecule has a volume of 1.48 nm$^3$ and a diameter of 1.42 nm (if it were spherical).

The "nanomolecule" $Sc_{24}C_{10}I_{30}$ has an outer envelope of 30 iodine atoms (Figure 2). A T4 supertetrahedron would consist of 35 iodine atoms (according to $\Sigma\text{atoms} = [{}^1\!/_6(n+1)(n+2)(n+3)]$, for a T$n$ supertetrahedron, with $n = 4$), but as it is hollow ($-1$ iodine atom) and truncated at the four corners ($-4$ iodine atoms), there are only 30 iodine atoms in the outer shell. This truncated, hollow T4* supertetrahedron surrounds a T3 supertetrahedron of 20 scandium atoms, which is filled

[*] Dr. L. Jongen, Dr. A.-V. Mudring, Prof. Dr. G. Meyer
Institut für Anorganische Chemie
Universität zu Köln
Greinstrasse 6, 50939 Köln (Germany)
Fax: (+49) 221-470-5083
E-mail: a.mudring@uni-koeln.de
gerd.meyer@uni-koeln.de

[**] This work has been supported by the Deutsche Forschungsgemeinschaft (SFB 608 "Komplexe Übergangsmetallverbindungen mit Spin- und Ladungsfreiheitsgraden und Unordnung") and by the Alexander von Humboldt Stiftung (postdoc stipend to L.J.).

 InterScience © 2006 Wiley-VCH Verlag GmbH & Co. KGaA, Weinheim 

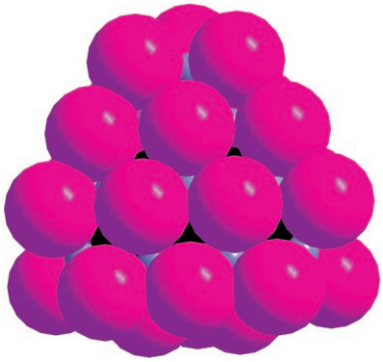


***Figure 2.*** Space-filling model of the $Sc_{24}C_{10}I_{30}$ molecule. Sc blue, C black, I pink.

by a T2 supertetrahedron of 10 carbon atoms, which, in turn, is filled by a T1 tetrahedron of four scandium atoms (Figure 3). Therefore, the molecular structure of $Sc_{24}C_{10}I_{30}$, which can be described as $Sc_4C_{10}Sc_{20}I_{30} = T1 + T2 + T3 + T4^*$, is reminiscent of a Russian doll, or, in other words, the molecule has an onion-like structure.

In the $Sc_{24}C_{10}I_{30}$ molecule, the 20 scandium atoms of the T3 supertetrahedron form 10 tetrahedra, which share common vertices and are filled with single carbon atoms. Each of the octahedral interstices of the T3 supertetrahedron is occupied by one of the vertices of the inner $Sc_4$ T1 tetrahedron. The 10 carbon atoms have the same arrangement as the carbon atoms in adamantane ($C_{10}H_{16}$); both structures can be interpreted as fragments of the diamond lattice. They also have the same topology as the oxygen atoms in $P_4O_{10}$, which encapsulate a $P_4$ tetrahedron. Thus, the $P_4O_{10}$ molecule and the $Sc_4C_{10}$ fragment are isostructural. The shortest Sc–Sc distance in $Sc_{24}C_{10}I_{30}$ is only 276 pm, much shorter than that in $Sc_4C_2I_6$ (302 pm). Additionally, the Sc–C interactions of 200–210 pm in the $Sc_4C$ tetrahedra of $Sc_{24}C_{10}I_{30}$ must be regarded as strong, when compared with the Sc–C distances of approximately 230 pm observed in the $Sc_6C$ octahedra of $Sc\{Sc_6C\}I_{12}$.[8]

In the cubic unit cell ($Pa\bar{3}$), the $Sc_{24}C_{10}I_{30}$ molecules are arranged in the same way as the nitrogen atoms in solid nitrogen.[9] Pairs of $Sc_{24}C_{10}I_{30}$ molecules are oriented with their triangular faces towards each other; the distance between the centers of the molecules is 1190 pm (Figure 4).

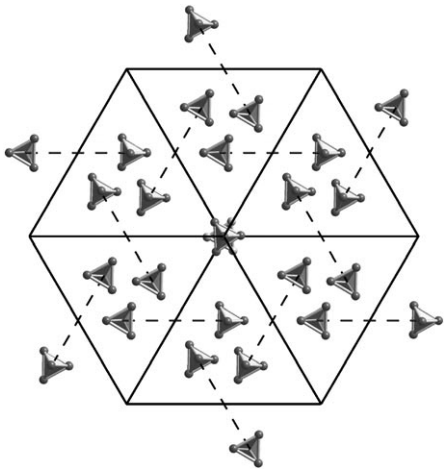


***Figure 4.*** Spatial arrangement of the inner $Sc_4$ T1 tetrahedra, which are representative of the complete $Sc_{24}C_{10}I_{30}$ molecules, as viewed down the [111] direction. The similarity between the structures of $Sc_{24}C_{10}I_{30}$ and solid nitrogen is highlighted by the dashed lines, which indicate pairs of molecules, as described in the text.

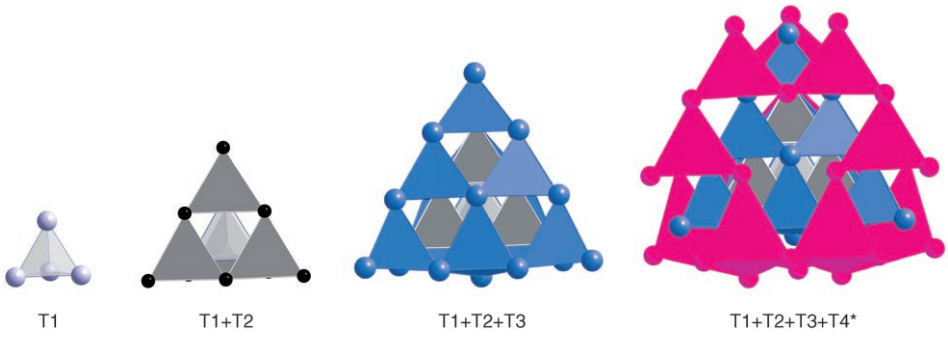



***Figure 3.*** Structure of the $Sc_{24}C_{10}I_{30}$ molecule: $Sc_4 = T1$; $Sc_4C_{10} = T1 + T2$; $Sc_4C_{10}Sc_{20} = T1 + T2 + T3$; $Sc_4C_{10}Sc_{20}I_{30} = T1 + T2 + T3 + T4^*$ ($T4^*$ is the truncated, hollow T4 supertetrahedron). Sc blue, C black, I pink.

Of course, unlike the nitrogen atoms in the $N_2$ molecules, the $Sc_{24}C_{10}I_{30}$ molecules are only held together by van der Waals interactions.

The $Sc_{20}$ T3 supertetrahedron of the $\{Sc_4C_{10}Sc_{20}\}^{30+}$ ion in its $\{I_{30}\}^{30-}$ envelope has the same structure as the recently discovered $Au_{20}$ supertetrahedron.[10] A filled supertetrahedral anion was also found in $Cs_8[Sn_{10}O_4S_{20}](H_2O)_{13}$, for example.[11] Supertetrahedra are by no means uncommon in chalcogenide chemistry,[12] although the first oxidic T5 supertetrahedron was only recently observed in $Na_{26}Mn_{39}O_{55}$.[13]

In $Sc_{24}C_{10}I_{30}$ (with $C^{4-}$ and $I^{1-}$), scandium has an oxidation state of slightly less than +3 (+2.92), if a purely ionic model is considered. Hence, there are two excess electrons per molecule, according to $(Sc^{3+})_{24}(C^{4-})_{10}(I^-)_{30}(e^-)_2$. These electrons can be expected to reside in the empty $Sc_4$ tetrahedron, in analogy to the 20 electrons that occupy 10 bonding orbitals (four-center, two-electron (4c–2e) bonds) in the naked $Au_{20}$ cluster.[10] Indeed, extended Hückel molecular orbital (EHMO) calculations for $\{Sc_4\}^{10+}$, as well as for $\{Sc_4C_{10}Sc_{20}\}^{30+}$ reveal similar bonding pictures.[14] In both cases, the HOMO is a 4c–2e orbital (Figure 5). Of course, the empty $Sc_4$ tetrahedron could also be filled with two hydrogen atoms, which would consume the two electrons. Although the

 © 2006 Wiley-VCH Verlag GmbH & Co. KGaA, Weinheim 

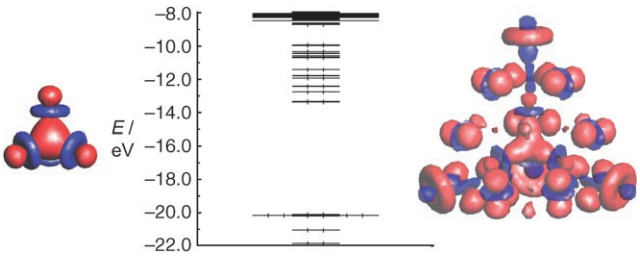



***Figure 5.*** The HOMOs for the $\{Sc_4\}^{10+}$ tetrahedron (left) and the $\{Sc_4C_{10}Sc_{20}\}^{30+}$ cluster (right), as well as the molecular orbital diagram for $\{Sc_4C_{10}Sc_{20}\}^{30+}$, obtained from EHMO calculations.

hydrogen atoms in related compounds usually occupy octahedral sites, which are displaced away from the center towards a triangular face of the octahedron, the possibility that hydrogen atoms occupy the $Sc_4$ tetrahedron cannot be completely ruled out. However, the yield was not enhanced when hydrogen was deliberately added to the reaction, either as $ScH_2$ or as hydrogen gas, which diffuses through the tantalum container at the chosen reaction temperature.

In the Sc/C/I system (Figure 1), $Sc_7CI_{12} = (Sc^{3+})\{(Sc^{3+})_6(C^{4-})(e^-)_5\}(I^-)_{12}$, in which single carbon atoms occupy the centers of scandium octahedra, is certainly the most stable compound.[8] In $Sc_6C_2I_{11}$ and $Sc_4C_2I_6$, $C_2$ (ethanide) units occupy the scandium octahedra.[5] In $Sc_4C_2I_6$, the octahedra share *trans* edges to form chains. Every second octahedron is distorted in such a way that it can also be described as two tetrahedra sharing a common edge. As mentioned above, $Sc_{24}C_{10}I_{30}$ is only slightly more reduced than $Sc_4C_2I_6 \mathrel{\hat{=}} Sc_{20}C_{10}I_{30}$. Thus, it can be argued that the incorporation of an empty $Sc_4$ tetrahedron stabilizes the $Sc_{24}C_{10}I_{30}$ oligomer. Oligomers are rather uncommon in the chemistry of interstitially stabilized rare-earth-metal halide clusters. With scandium, the bromides $Sc_{19}Z_4Br_{28}$ (Z = Mn, Fe, Ru, Os) are known.[15] These compounds contain the $R_{16}Z_4X_{20}$ oligomer (R = rare-earth metal, X = halogen) first observed for $Y_4RuI_5$.[16] The component $R_{16}Z_4$ cluster consists of four edge-sharing $R_6Z$ octahedra. Carbon atoms in tetrahedral interstices are known from $RbPr_5C_2Cl_{10}$.[17] In this compound, two $Pr_4C$ tetrahedra share a common face to form a $Pr_5$ trigonal bipyramid, which encapsulates a $C_2$ unit.

The crystal structure of $Sc_{24}C_{10}I_{30}$ consists of molecules of the same composition, which are packed in the same way as the nitrogen atoms in solid nitrogen. The molecules have an onion- or Russian-doll-like structure, $(e^-)_2Sc_4C_{10}Sc_{20}I_{30}$, and contain two excess electrons, which reside in the inner $Sc_4$ tetrahedron and occupy a 4c–2e orbital.

Received: November 4, 2005
Published online: February 17, 2006

**Keywords:** carbon · electronic structure · iodine · scandium · supertetrahedra

[1] a) B. C. McCollum, J. D. Corbett, *Chem. Commun.* **1968**, 1666; b) B. C. McCollum, D. S. Dudis, A. Lachgar, J. D. Corbett, *Inorg. Chem.* **1990**, *29*, 2030.

[2] G. Meyer, L. Jongen, A.-V. Mudring, A. Möller, *Inorg. Chem. Focus* **2005**, *2*, 105.

[3] A. Lachgar, D. S. Dudis, P. K. Dorhout, J. D. Corbett, *Inorg. Chem.* **1991**, *30*, 3321.

[4] G. Meyer, J. D. Corbett, *Inorg. Chem.* **1981**, *20*, 2627.

[5] D. S. Dudis, J. D. Corbett, *Inorg. Chem.* **1987**, *26*, 1933.

[6] Synthesis: $Sc_{2.4}CI_3 \mathrel{\hat{=}} Sc_{24}C_{10}I_{30}$ was obtained as a by-product in an attempt to synthesize $Sc_6C_2I_{11}$, starting from $ScI_3$, scandium, and graphite (molar ratio 1:1:1). $ScI_3$ was synthesized from the elements and sublimed under high vacuum at 1193 K. Scandium-metal pieces and graphite were used as purchased. All starting materials and products were stored and manipulated in an argon-filled glove box (MBraun, Garching). The reaction was carried out in a sealed tantalum container, jacketed with a fused-silica tube, at a temperature of 1123 K. After two weeks, the reaction mixture was cooled by turning off the power to the furnace. Good quality blue-black single crystals of $Sc_{24}C_{10}I_{30}$ were obtained, along with a black powder and single crystals of $Sc_6C_2I_{11}$. X-ray powder diffraction at room temperature (transmission mode, Imaging Plate Guinier Camera G670 (Huber, Rimsting)), monochromatic $Mo_{K\alpha}$ radiation) revealed that the product mainly consists of two phases, $Sc_6C_2I_{11}$ and $Sc_4C_2I_6$. $Sc_{24}C_{10}I_{30}$ could not be detected by X-ray powder diffraction at room temperature.

[7] Crystal data and structure refinement: A suitable single crystal ($0.3 \times 0.2 \times 0.2$ mm) was sealed in a glass capillary in an argon-filled glove box. Intensity data were collected at room temperature on an IPDS I diffractometer, and at 130 K on an IPDS II diffractometer (both Stoe, Darmstadt). 130(2) K: cubic, $Pa\bar{3}$ (No. 205); $a = 2551.82(5)$ pm, $V = 16.6169(6)$ nm$^3$; $Z = 8$, $\rho_{calcd} = 4.002$ g cm$^{-3}$; $1.38 < \theta/° < 24.99$; $Mo_{K\alpha}$ radiation ($\lambda = 71.073$ pm); $F(000) = 17232$; $\mu = 12.973$ mm$^{-1}$; 139853 reflections measured, 4879 unique, 3997 observed; $R1 = 0.0281$, $wR2 = 0.0654$ (for $I_o > 2\sigma(I_o)$). 293 K: cubic, $Pa\bar{3}$ (No. 205); $a = 2568.4(3)$ pm, $V = 16.943(3)$ nm$^3$; $Z = 8$, $\rho_{calcd} = 3.925$ g cm$^{-3}$; $2.24 < \theta/° < 23.85$; $Mo_{K\alpha}$ radiation ($\lambda = 71.073$ pm); $F(000) = 17232$; $\mu = 12.723$ mm$^{-1}$; 51375 reflections measured, 4346 unique, 2331 observed; $R1 = 0.0668$, $wR2 = 0.1378$ (for $I_o > 2\sigma(I_o)$). The data were processed with the program SHELX-97 [G. M. Sheldrick, SHELX-97, Universität Göttingen, **1997**]. Scattering factors were taken from: A. J. C. Wilson, International Tables for Crystallography, *Vol. C, Mathematical, Physical and Chemical Tables*, Kluwer, Dordrecht, The Netherlands, **1995**. Numerical absorption corrections were performed after crystal-shape optimization using the programs XRED and XSHAPE [Stoe, XRED 1.01 and XSHAPE 1.01, Darmstadt, **1996**]. Further details on the crystal structure investigations may be obtained from the Fachinformationszentrum Karlsruhe, 76344 Eggenstein-Leopoldshafen, Germany (fax: (+49)7247-808-666; e-mail: crysdata@fizkarlsruhe.de), on quoting the depository numbers CSD-414259 (130 K) and CSD-414260 (293 K).

[8] D. S. Dudis, J. D. Corbett, S.-J. Hwu, *Inorg. Chem.* **1986**, *25*, 3434.

[9] a) J. Donohue, *Acta Crystallogr.* **1961**, *17*, 1000; b) J. A. Venables, C. A. English, *Acta Crystallogr. Sect. B* **1974**, *30*, 929; and references therein.

[10] a) J. Li, H.-J. Zhai, L.-S. Wang, *Science* **2003**, *299*, 864; b) R. B. King, Z. Chen, P. von R. Schleyer, *Inorg. Chem.* **2004**, *43*, 4564.

[11] W. Schiwy, B. Krebs, *Angew. Chem.* **1975**, *87*, 451; *Angew. Chem. Int. Ed. Engl.* **1975**, *14*, 436.

[12] a) H. Li, M. O'Keeffe, O. M. Yaghi, *Science* **1999**, *283*, 1145; b) B. Feng, X. Bu, N. Zheng, *Chem. Eur. J.* **2004**, *10*, 3356.

[13] A. Möller, P. Amann, V. Kataev, N. Schittner, *Z. Anorg. Allg. Chem.* **2004**, *630*, 890.

[14] Theoretical calculations: Semi-empirical EHMO calculations for the molecular clusters $\{Sc_4\}^{10+}$ and $\{Sc_4C_{10}Sc_{20}\}^{30+}$ were performed with the program package CAESAR [J. Ren, W. Liang, M.-H. Whangbo, CAESAR, PrimeColor Software Inc.,

 © 2006 Wiley-VCH Verlag GmbH & Co. KGaA, Weinheim 

Raleigh, NC, USA, **1998**.] with the following parameters (double-zeta functions): $H_{ij}$ [eV], $\zeta_1$, coefficient 1, $\zeta_2$, coefficient 2: Sc: 4s −7.05, 1.5, 0.5172, 0.9, 0.587; 4p −3.98, 1.14, 1.0, 0.0, 0.0; 3d −8.35, 4.4, 0.359, 2.0, 0.766; C: 2s −19.66, 1.98, 0.7931, 1.24, 0.2739; 2p −10.86, 2.2, 0.2595, 0.96, 0.8026.

[15] S. J. Steinwand, J. D. Corbett, J. D. Martin, *Inorg. Chem.* **1997**, *36*, 6413.

[16] M. W. Payne, M. Ebihara, J. D. Corbett, *Angew. Chem.* **1991**, *103*, 842; *Angew. Chem. Int. Ed. Engl.* **1991**, *30*, 856.

[17] G. Meyer, S. Uhrlandt, *Angew. Chem.* **1993**, *105*, 1379; *Angew. Chem. Int. Ed. Engl.* **1993**, *32*, 1318.

 © 2006 Wiley-VCH Verlag GmbH & Co. KGaA, Weinheim 

DNA Nanotechnology

DOI: 10.1002/anie.200502370

# Thermostable and Monoconjugable Gold Clusters with a Dodecadentate Thioether Ligand Gripper**

*Wolf Matthias Pankau, Sven Mönninghoff, and Günter von Kiedrowski**

The Schmid cluster,[1] $[Au_{55}(PPh_3)_{12}Cl_6]$, has stimulated many different areas of technology ranging from catalysis research[2] to the concept of quantum electronics.[3,4] Monofunctionalized water-soluble derivatives of this cluster[5] have become commercially available and found numerous applications.[6–14] Recently, gold clusters have been employed as universal fluorescence quenchers in molecular beacons[15] and as nanoscale antennas for the reception of radio radiation in the GHz frequency region, which causes local and selective inductive heating of cluster-labeled biomolecules.[16] These applications as well as current experiments in DNA nanotechnology[17–23] point to the need for the increased thermostability of these gold clusters. We have shown that replacement of the monopodal triphenylphosphane ligands in such clusters with water-soluble tripodal thioethers based on 1,3,5-tris(thiomethyl)benzene leads to gold clusters with improved stability.[24]

Herein, we report a new generation of biocompatible gold clusters that are surrounded by a single dodecadentate, nanoscale thioether-based "gripper". This method allows nanoparticles to be singly functionalized without the otherwise necessary step of purification of mixtures by HPLC.[25] We demonstrate that "gripped" clusters in oligonucleotide conjugates can survive the temperature conditions of polymerase chain reaction (PCR) and hybridization experiments.

The concept behind our ligand is sketched in Figure 1. The $Au_{55}$ cluster was proposed to possess a cuboctahedral core, the surface of which is composed of eight corner-sharing triangles (111) and six squares (110).[1] Although there is an ongoing debate[26,27] about the cluster geometry, we decided to adopt this proposal as a working hypothesis. $Au_{55}$ is expected to bind four tripodal ligands provided that the binding mode of the ligands is comparable to that of the Schmid cluster, in which the 12 triphenylphosphanes most likely occupy the corners of the cuboctahedron. If the four tripodal ligands are connected by suitable linkers, a dodecadentate ligand will result. The synthesis was also designed so that the final material carries a single functional group to allow conjugation to (bio)molecules.

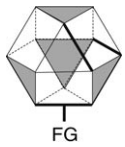



***Figure 1.*** General concept of a gold cluster gripper. Four tripodal units (1,3,5-tris(thiomethyl)benzene groups) occupy four (111) faces of the cuboctahedral cluster. The tripodal units are linked (bold lines) to give a dodecadentate ligand, which also bears a functional group (FG) suitable for conjugation to a biomolecule.

Scheme 1 shows the synthesis of the target ligand **8**. We selected a monomaleimido group as the monoconjugable unit to ensure functional comparability with the commercially available variant of the Schmid cluster. Thioether **2** was generated from trisbromide **1** as a key precursor that allowed the synthesis of **8** by a divergent–convergent route in only six steps with an overall yield of 31%. The gold cluster was synthesized from ligand **8** by phase-transfer synthesis, as previously described for the tristhioether derived from L-cysteine.[24] High-resolution transmission electron microscopy revealed a narrow size distribution of the clusters with a mean diameter of 1.4 nm, which is as expected for $Au_{55}$ particles. The cluster was conjugated with a 5′-thiol-modified 27-mer oligonucleotide, the complement of which was labeled with fluorescein in the 3′ position.

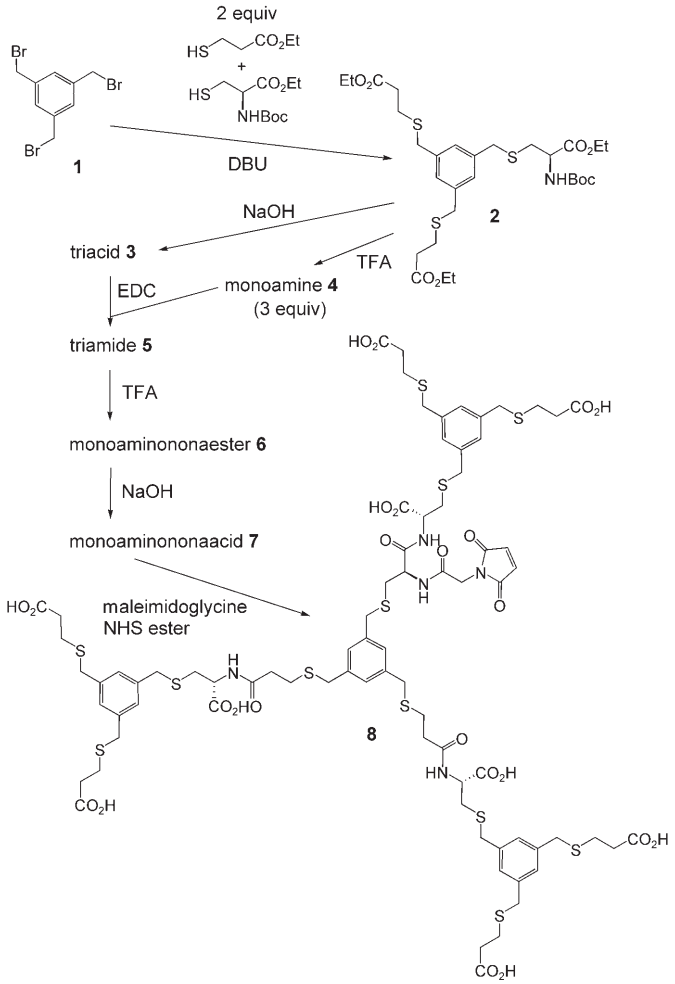
To study the thermostability of the label, a thermal-stress experiment was performed in which the fluorescence signal of a mixture of both oligonucleotides was monitored during 100 cycles of temperature variation. Each cycle consisted of a period of heating from 20 to 95 °C at 10 K min$^{-1}$, a thermal-stress period for 6 min at 95 °C, and a period of cooling at a rate of 20 K min$^{-1}$, which corresponds to an average temperature of 70.5 °C. The process of the temperature cycling experiment is depicted in Figure 2. At low temperatures, the duplex holds the gold cluster and the fluorescent dye within spatial proximity. Quenching of fluorescence takes place, which results in low fluorescence intensity. At high temperatures, the fluorescent oligonucleotide exists in its single-strand form, and an increase in fluorescence signal is observed

[*] Dr. W. M. Pankau, S. Mönninghoff, Prof. Dr. G. von Kiedrowski
Lehrstuhl für Organische Chemie I
Bioorganische Chemie
Ruhr-Universität Bochum
Universitätsstrasse 150, NC 2/173, 44780 Bochum (Germany)
Fax: (+49) 234-32-14355
E-mail: kiedro@ruhr-uni-bochum.de

[**] This work has been supported by the Deutsche Forschungsgemeinschaft and the BMBF. We thank M. Wüstefeld for carrying out the oligonucleotide syntheses, G. Schmid for a sample of $[Au_{55}(PPh_3)_{12}Cl_6]$, and Degussa AG for the generous donation of tetrachloroauric acid.

Supporting information for this article is available on the WWW under http://www.angewandte.org or from the author.

 © 2006 Wiley-VCH Verlag GmbH & Co. KGaA, Weinheim 




***Scheme 1.*** Structure and synthesis of the dodecadentate ligand **8** bearing a monomaleimido functional group. Boc = *tert*-butyloxycarbonyl; DBU = 1,8-diazabicyclo[5.4.0]-7-undecene; EDC = 1-ethyl-3-(3-dimethylaminopropyl)carbodiimide; TFA = trifluoroacetic acid; NHS = *N*-hydroxysuccinimide.

because the gold cluster is no longer in proximity to act as a quencher. If the gold cluster escapes the grip of the ligand during a cycle, or if the conjugation with the complementary strand breaks, no fluorescence quenching will be observed in the following cycle. Thus, kinetic information about the stability of clusters and their oligonucleotide conjugation can be derived from the increase in low-temperature fluorescence as a function of the cycle number (and thus duration of thermal stress). Figure 3 depicts the development of the

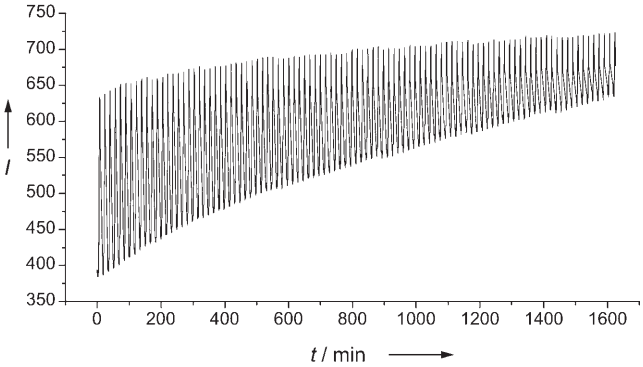



***Figure 3.*** Fluorescence intensity (*I*) during 100 temperature cycles of a solution containing 1 μM 5′-ATGCACCCATTGGACATAACCGGGAAT-3′-FAM, 3 μM 5′-SH-modified complementary oligonucleotide conjugated with a mixture of gold-filled and unfilled grippers **8**, 300 mM NaCl, and 100 mM 3-(*N*-morpholino)propanesulfonic acid (MOPS) at pH 7.5.

temperature-driven fluorescence oscillations as a function of time. Fitting of the fluorescence minima to a model involving first-order decomposition of the cluster yielded a half-life of $\tau_{1/2} = 55 \pm 5$ cycles, which corresponds to 900 min for an average temperature of $T = 70.5\,^{\circ}\mathrm{C}$. The increase of the maxima of fluorescence oscillations in Figure 3 is due to a slight evaporation of water from the cuvette, which could not be avoided completely at the high temperatures employed.

Control experiments (see the Supporting Information) allow us to draw the following conclusions: There is evidence

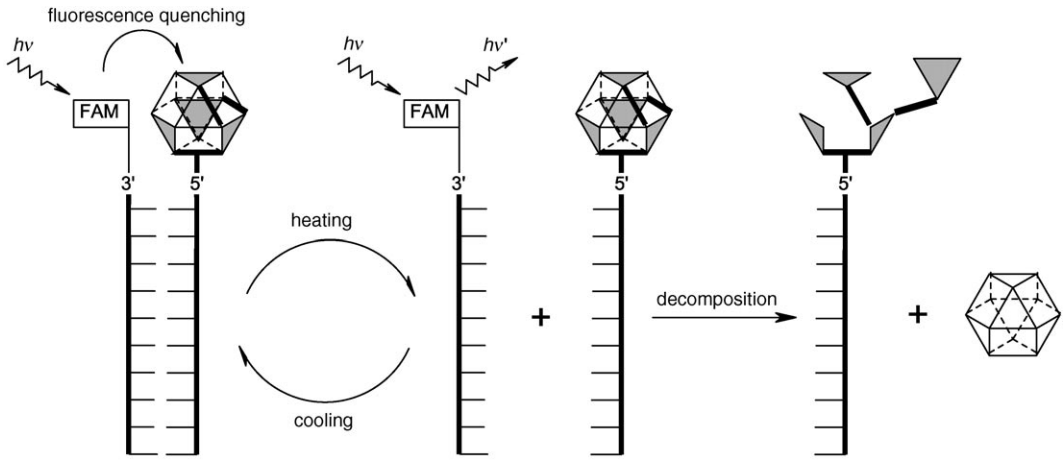



***Figure 2.*** Chemical and physical processes underlying the determination of the cluster stability in the thermal-stress experiment. The fluorescence of the 3′-fluorescein labeled oligonucleotide in the presence of the complementary 5′-gold cluster is measured during the heating/cooling cycles. FAM = fluoroscein amino modifier.

 © 2006 Wiley-VCH Verlag GmbH & Co. KGaA, Weinheim 

from a comparison of experiments involving the empty and the filled gripper that it is the gold cluster rather than the gripper itself that is the responsible for the quenching, which is as expected in view of the UV-absorption properties of the ligand. Moreover, the fluorescence of both the duplex without the gripper and the labeled single strand decreases with the temperature; the latter, however, shows a higher level of fluorescence intensity, which is attributable to the poorer stacking of the 3′-fluorescein with the single strand. The different baseline courses for the single- and double-stranded species also explain why a slight increase in fluorescence is observed at the melting transition for the duplex with the empty gripper.

Any conceivable application of gold clusters in DNA bio- and nanotechnology in which their remarkable properties are employed will require compatibility of the label with at least the basic procedures of molecular biology. To the best of our knowledge, the gripped cluster presented here is the first example of an $Au_{55}$ monolabel surviving the temperature conditions of PCR and hybridization protocols. A typical PCR experiment may be equivalent to around 100 min of the heating experiments described above, considering that the exposure to a temperature of 95 °C lasts for only around 1 min in PCR whereas each of these heating cycles lasted 6 min at 95 °C. The average temperature in our experiment is close to that of PCR, so that one cycle in our experiment may be equivalent to four to six typical PCR cycles. It is evident from Figure 3 that only a small fraction (less than 10 %) of the gold nanocrystals did not survive the first 100 min of treatment. It should be emphasized that the full potential of universal fluorescence quenching (e.g. in multiplexed quantitative PCR of gene sets by employing beacon sets with different dyes in the same tube) and radio-frequency-induced single-molecule heating (e.g. for nanoscale robotics) can only be realized with thermostable cluster materials.[28]

Received: July 7, 2005
Revised: December 12, 2005
Published online: February 22, 2006

**Keywords:** cluster compounds · DNA · fluorescence · gold · nanotechnology

[1] G. Schmid, R. Boese, R. Pfeil, F. Bandermann, S. Meyer, G. H. M. Calis, J. W. A. van der Velden, *Chem. Ber.* **1981**, *114*, 3634 – 3642.
[2] M. Haruta, S. Tsubota, T. Kobayashi, H. Kageyama, M. J. Genet, D. J. Delmon, *J. Catal.* **1993**, *144*, 175 – 192.
[3] G. Schmid, U. Simon, *Chem. Commun.* **2005**, 697 – 710.
[4] Y. Volokitin, J. Sinzig, L. J. de Jongh, G. Schmid, I. I. Moiseev, *Nature* **1996**, *384*, 621 – 623.
[5] J. F. Hainfeld, F. R. Furuya, *J. Histochem. Cytochem.* **1992**, *40*, 177 – 184.
[6] M. Bendayan, *Science* **2001**, *291*, 1363 – 1365.
[7] D. E. Bergles, J. D. B. Roberts, P. Somogyi, C. E. Jahr, *Nature* **2000**, *405*, 187 – 190.
[8] Z. Nusser, N. Hajos, P. Somogyi, I. Mody, *Nature* **1998**, *395*, 172 – 177.
[9] G. Segond von Banchet, B. Heppelman, *J. Histochem. Cytochem.* **1995**, *43*, 821 – 827.
[10] M. Malecki, A. Hsu, L. Truong, S. Sanchez, *Proc. Natl. Acad. Sci. USA* **2002**, *99*, 213 – 218.
[11] R. Shigemoto, A. Kulik, J. D. B. Roberts, H. Ohishi, Z. Nusser, T. Kaneko, P. Somogyi, *Nature* **1996**, *381*, 523 – 525.
[12] C. A. Mirkin, R. L. Letsinger, R. C. Mucic, J. J. Storhoff, *Nature* **1996**, *382*, 607 – 609.
[13] A. P. Alivisatos, X. Peng, T. E. Wilson, K. P. Johnsson, C. J. Loweth, M. P. Bruchez, Jr., P. G. Schultz, *Nature* ***1996***, *382*, 609 – 611.
[14] C. M. Niemeyer, *Angew. Chem.* **2001**, *113*, 4254 – 4287; *Angew. Chem. Int. Ed.* **2001**, *40*, 4128 – 4158.
[15] B. Dubertret, M. Calame, A. J. Libchaber, *Nat. Biotechnol.* **2001**, *19*, 365 – 370.
[16] K. Hamad-Schifferli, J. J. Schwartz, A. T. Santos, S. Zhang, J. M. Jacobson, *Nature* **2002**, *415*, 152 – 155.
[17] L. H. Eckardt, K. Naumann, W. M. Pankau, M. Rein, M. Schweitzer, N. Windhab, G. von Kiedrowski, *Nature* **2002**, *420*, 286.
[18] A. Luther, R. Brandsch, G. von Kiedrowski, *Nature* **1998**, *396*, 245 – 248.
[19] G. von Kiedrowski, L. H. Eckardt, K. Naumann, W. M. Pankau, M. Reimold, M. Rein, *Pure Appl. Chem.* **2003**, *75*, 609 – 619.
[20] N. C. Seeman, *Nature* **2003**, *421*, 427 – 431.
[21] S. Liao, N. C. Seeman, *Science* **2004**, *306*, 2072 – 2074.
[22] S. Xiao, F. Liu, A. E. Rosen, J. F. Hainfeld, N. C. Seeman, K. Musier-Foryth, R. A. Kiehl, *J. Nanopart. Res.* **2002**, *4*, 313 – 317.
[23] R. Elghanian, J. Storhoff, R. C. Mucic, R. L. Letsinger, C. A. Mirkin, *Science* **1997**, *277*, 1078 – 1081.
[24] W. M. Pankau, K. Verbist, G. von Kiedrowski, *Chem. Commun.* **2001**, 519 – 520; a tetrapodal thioether system was reported a short time later: X. M. Li, M. R. de Jong, K. Inoue, S. Shinkai, J. Huskens, D. N. Reinhoudt, *J. Mater. Chem.* **2001**, *11*, 1919 – 1923.
[25] H. Yang, J. E. Reardon, P. A. Frey, *Biochemistry* **1984**, *23*, 3857 – 3862.
[26] H. Rapoport, W. Vogel, H. Cölfen, R. Schlögl, *J. Phys. Chem. B* **1997**, *101*, 4175 – 4183.
[27] N. T. Wilson, R. L. Johnston, *Phys. Chem. Chem. Phys.* **2002**, *4*, 4168 – 4171.
[28] C. M. Niemeyer, M. Adler, *Angew. Chem.* **2002**, *114*, 3933 – 3937; *Angew. Chem. Int. Ed.* **2002**, *41*, 3779 – 3783.

 © 2006 Wiley-VCH Verlag GmbH & Co. KGaA, Weinheim 

DNA Strand Breaks

DOI: 10.1002/anie.200503930

# Decomposition of Thymidine by Low-Energy Electrons: Implications for the Molecular Mechanisms of Single-Strand Breaks in DNA**

*Sylwia Ptasińska, Stephan Denifl, Sascha Gohlke, Paul Scheier, Eugen Illenberger,* and Tilmann D. Märk*

Low-energy electrons decompose gas-phase thymidine (a thymine unit coupled to a sugar unit) through dissociative electron attachment (DEA) involving two low-lying resonances at 1.2 and 1.8 eV and a broad resonant feature located between 5.5 and 12 eV. The peak at 1.2 eV arises from the rupture of the glycosidic N1–C1 bond (observable through the anion of the sugar moiety), whereas the resonance located at 1.8 eV results from the loss of a neutral hydrogen atom from the N3 position of the thymine moiety within thymidine. The broad resonant feature in the energy range 5.5–12 eV is associated with the rupture of the N1–C1 bond, in this case observable through the thymine anion generated. From the analysis of the DEA signatures it follows that excess-electron transfer from the thymine to the sugar unit within thymidine and vice versa is not operative. These findings have significant consequences for the molecular description of DNA damage caused by low-energy electrons. It excludes the possibility of electron migration from low-lying π* MOs of a nucleobase to low-lying σ* MOs of the DNA backbone leading to strand breaks.

The investigation of damage in biological systems, more specifically, in living cells and DNA, induced by high-energy quanta has been the subject of countless investigations over the past decades.[1–3] Such alterations can appear, for example, when human beings are exposed to radioactivity or other sources of high-energy radiation. On the other hand, analogous questions arise in the application of radiosensitizers in tumor therapy. It is well accepted that the main biological effect is usually not produced by the primary interaction of the high-energy quanta with the complex molecular network in a living cell, but rather by the action of the secondary species which are generated along the ionization track.[2] The interaction of these secondary species (ions, electron, or radicals) with DNA and its surroundings can cause mutagenic, genotoxic, and other potentially lethal DNA lesions,[3] such as single-strand breaks (SSBs) and double-strand breaks (DSBs). Electrons are the most abundant of these secondary species having an initial energy distribution extending to about 20 eV.[4] For the understanding of the effects of radiation in cells, it is therefore essential to investigate the action induced by these electrons on vital cellular components such as water and DNA.

So far the effects from high-energy radiation has been investigated for two systems that vary greatly in complexity, namely plasmid DNA and building blocks of DNA in the gas-phase. Experiments on plasmid DNA demonstrated that electrons at subionization energies induce SSBs and DSBs.[5] Recent experiments showed the potential of electrons at even subexcitation energy (0–4 eV) to induce SSBs in plasmid DNA.[1] Although SSBs within double-stranded DNA is not likely to be lethal for the cell, the situation may dramatically change during the process of replication of the nucleic acid, that is, when the double strand separates into two individual strands.

On the other hand, gas-phase studies[6–12] revealed that isolated nucleobases (NBs) undergo dissociative electron attachment (DEA) in the energy range of approximately 6–9 eV and also at subexcitation energies ($<3$ eV, wherein only SSBs are observed). The high-energy feature, however, leads to loss of $H^-$ and further fragment ions associated with the rupture of the ring structure, whereas the low-energy resonance exclusively leads to the loss of neutral hydrogen through the DEA process shown in Equation (1).

$$e^- + NB \rightarrow NB^{-\#} \rightarrow (NB{-}H)^- + H \quad (1)$$

$NB^{-\#}$ is the transitory negative ion (TNI) generated by resonant electron capture and $(NB{-}H)^-$ is the closed-shell anion formed by ejection of a neutral hydrogen radical from $NB^{-\#}$. The reaction is energetically driven by the appreciable electron affinity of the (NB–H) radicals that lie in the range between 3 and 4 eV.[6,10] Further experiments with partly deuterated thymine[9,11] demonstrated that hydrogen abstraction is operative exclusively from the N sites. Moreover, by exactly tuning the electron energy, the loss of H can even be made site selective: although electrons at 1 eV induce H loss at the N1 position (N1–H), the process can be switched, at 1.8 eV, to N3-H.[12]

These last findings were obtained by using thymine and uracil, methylated at one of the N positions. The observation that neither the loss of H from $CH_3$, nor the loss of the entire methyl group takes place when at the corresponding N position H is replaced by $CH_3$. These findings have significant consequences for the molecular description of strand breaks by low-energy electrons. A recent theoretical study[13] (modeling a section of DNA that contained cytosine, the sugar ring, and the (neutralized) phosphate group) predicted a transfer of the electron from the initial π* anion state of the base to a σ* state in the backbone, ultimately leading to rupture of the C–O bond between the phosphate and the sugar. Within DNA the N1 position of T is coupled to the sugar moiety, and

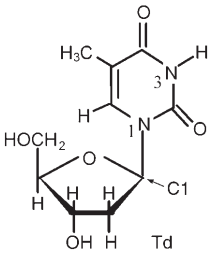
[*] Dipl.-Chem. S. Gohlke, Prof. Dr. E. Illenberger
Institut für Chemie und Biochemie
Physikalische und Theoretische Chemie
Freie Universität Berlin
Takustrasse 3, 14195 Berlin (Germany)
Fax: (+49) 30-838-56612
E-mail: iln@chemie.fu-berlin.de
Mag. S. Ptasińska, Mag. Dr. S. Denifl, Prof. Mag. Dr. P. Scheier, Prof. Dr. T. D. Märk
Institut für Ionenphysik und Angewandte Physik
Leopold Franzens Universität Innsbruck und
Center for Molecular Biosciences Innsbruck (CMBI)
Technikerstrasse 25, A-6020 Innsbruck (Austria)

[**] Financial support from FWF (Wien), EU (Brussels) through the EPIC Network and DFG (Bonn) is gratefully acknowledged.

 © 2006 Wiley-VCH Verlag GmbH & Co. KGaA, Weinheim 

according to the results obtained in the methylated compounds, transfer of energy via the N1 position is inhibited once N1–H is replaced by N1–$CH_3$.

Although the inhibition of energy transfer should also apply if $CH_3$ is replaced by the sugar, one cannot necessarily exclude the transfer of excess charge, initially localized on thymine, through the N1–C1 glycosidic bond to the sugar molecule, particularly when low-lying σ* MOs are accessible. To track this problem, we have studied herein low-energy electron impact to gas-phase thymidine (Td), which represents a thymine coupled to the sugar 2-deoxyribose (DRB) through a condensation reaction. For simplicity, the deoxyribose moiety in Td (DRB–OH) will be assigned as dR throughout this manuscript.




The present investigations were performed in a crossed electron/molecule beams device at the Innsbruck laboratory with a method previously described in detail.[6,14] The electron beam is formed in a custom-built hemispherical electron monochromator, operated at an energy resolution between 110 and 130 meV (full width at half maximum) and an electron current of 5–8 nA. The molecular beam emanates from a source that consists of a temperature-regulated oven and a capillary. Experiments have been performed in the range of 390–426 K to obtain information on the thermal-decomposition behavior of Td. This was an inherent problem in the herein described experiments and as such is discussed below. Negative ions formed in the collision zone of the crossed beams are extracted by a weak electric field towards the entrance of the quadrupole mass spectrometer. The mass-selected negative ions are detected by a channeltron by using a single-pulse counting technique. The intensity of a particular mass-selected negative ion is then recorded as a function of the electron energy.

The electron-energy scale was calibrated by using the known $SF_6^-$ signal near 0 eV. Absolute calibration of the DEA cross sections were established by using the established cross section of $Cl^-/CCl_4$,[15] which yielded measures for the cross sections at an estimated accuracy within one order of magnitude. Thymidine was purchased from Sigma–Aldrich at a stated purity of 99.5%.

Figure 1 shows the energy dependence of negative ions observed from electron impact to the gaseous sample generated at 398 K. The signal at 241 amu can be assigned to $(Td-H)^-$ owing to the loss of a neutral hydrogen atom from thymidine according to Equation (2). This reaction is analogous to that observed in the nucleobases [Eq. (1)] and must proceed on an intact thymidine molecule.

$$Td + e^- \rightarrow Td^{-\#} \rightarrow (Td-H)^- + H \qquad (2)$$

The signal at 125 amu can be assigned to $(T-H)^-$ and that at 115 amu to $(dR-2H)^-$. Under the assumption that the entire signal arises from reactions of intact Td targets, the signals can then be attributed to the scission of the N1–C1 bond with the excess electrons localized on the thymine and

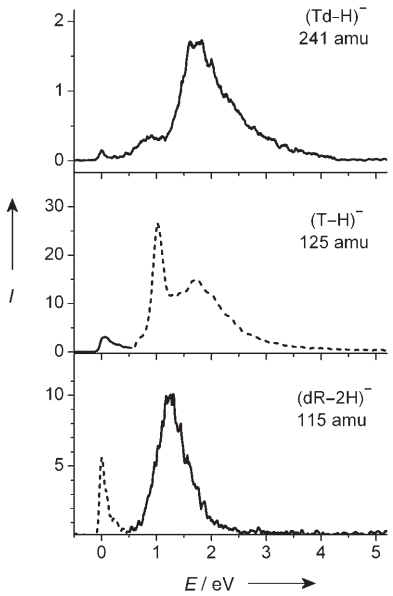



***Figure 1.*** Yields of product ions observed from electron attachment to thymidine (Td, 242 amu) obtained at a temperature of 398 K. T represents thymine and dR the 2-deoxyribose molecule after loss of OH. The numbers on the intensity scale (*I*) correspond to the estimated absolute DEA cross sections in units of $10^{-22}$ $m^2$. The dotted portions of the ion-yield curves are identified to arise from thermally decomposed Td (see the text).

sugar unit. The sugar unit is then further subjected to the loss of two hydrogen atoms. These results are in agreement with a previous study performed at the Berlin Laboratory[16] in which questions were raised with respect to a possible thermal decomposition of Td. A detailed study of that problem revealed that the vast majority of the beam in fact consists of nondecomposed Td molecules. As shown in Figure 1, the dashed portions in the ion yields arise from electron attachment to products of thermally decomposed Td.

Irrespective of the presence of thermal decomposition, the $(Td-H)^-$ signal (241 amu) must arise from intact Td molecules. The site from which the hydrogen atom is abstracted can immediately be identified through comparison with the signal arising from hydrogen loss from thymine methylated at the N1 position (m1T; Figure 2). In m1T, hydrogen loss from the N1 position is blocked,[12] and the ion signal $(M-H)^-$ (M corresponds to the target molecule) is

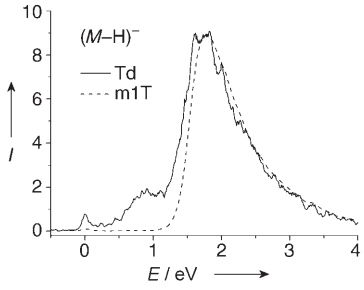



***Figure 2.*** Comparison of the yield of anion $(M-H)^-$ resulting from hydrogen loss in thymidine ($M$ = Td) with that of thymine methylated at the N1 position ($M$ = m1T).

 © 2006 Wiley-VCH Verlag GmbH & Co. KGaA, Weinheim 

consequently owing to hydrogen loss from the N3 position. As the shapes of the two signals in Figure 2 nearly coincide, we can conclude that Td hydrogen abstraction predominantly occurs at the thymine moiety, more precisely, at the N3 position. The small contributions near 1 and 0 eV may be due to H loss from the sugar moiety.

Figure 3 shows the 125-amu signal and the 115-amu signal on an extended energy scale. Although the shape of the low-energy 125-amu signal (1) is very similar to that from isolated

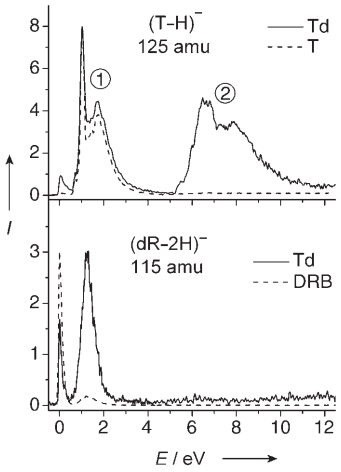



***Figure 3.*** Comparison of negative-ion formation from Td and the isolated building blocks T[6] and 2-deoxyribose (DRB) [17] on an extended energy scale.

T, it differs completely at higher energies (2) in that an additional pronounced contribution in the range 5.5 to 10 eV is observed only from Td. Superficially, from this additional $(T-H)^-$ signal, one could conclude that the beam consists only of nondecomposed Td molecules. The additional signal would then also be evidence of the different probabilities to distribute excess energy, that is, in isolated T, the excess energy must be shared between H and $(T-H)^-$, as the negative ion is unstable with respect to dissociation and autodetachment above 3–4 eV. This therefore makes DEA unlikely. In contrast, in Td the excess energy can be shared between polyatomic fragments of approximately equal size with a correspondingly large number of degrees of freedom resulting in the formation of $(T-H)^-$ at energies above 5 eV.

A careful analysis of the 125-amu signal at different sublimation temperatures, however, revealed that the intensity ratio between features 1 and 2 changes with increasing temperature in favor of the low-energy contribution 1, see Figure 4. This directly indicates that the low-energy $(T-H)^-$ signal arises from thermally decomposed Td (in part or completely). Moreover, the shape of the 115-amu fragment also shows a variation with temperature (not shown here) in that the peak near 0 eV is relatively enhanced until, at 425 K, the shape of the ion yield becomes very close to that from isolated DRB. This also indicates thermal decomposition leading to the 115-amu signal located close to 0 eV (in part or completely).

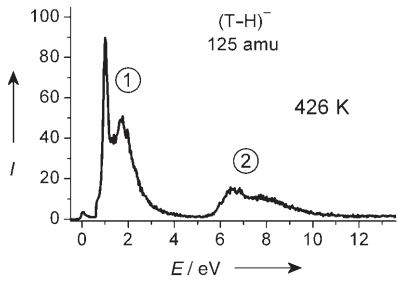



***Figure 4.*** The yield of $(T-H)^-$ from Td at an elevated temperature of 426 K.

The likely thermal-decomposition products are (T–H) and dR (rupture of the glycosidic N1–C1 bond). Electron attachment to neutral (T–H), however, would never lead to a $(T-H)^-$ signal like that shown in Figures 1 and 3.[18] A likely scenario is that the thymine radical (T–H), formed by thermal decomposition, is transformed into T by hydrogen pickup in the course of collisions with the walls of the capillary. Accordingly, the complement dR (117 amu, $C_5H_9O_3$) is transformed into a closed-shell compound of the stoichiometric composition $C_5H_{10}O_3$ and subjected to DEA. The alternate (and probably more likely) scenario is that thymidine decomposes into T + $C_5H_8O_3$ (116 amu); that is, the cleavage of the N1–C1 glycosidic bond is accompanied by hydrogen transfer generating two closed-shell fragments which are subjected to DEA.

Irrespective of the thermal-decomposition products, our data indicate that near 400 K (the temperature at which the spectra of Figure 1 and Figure 3 have been recorded), the vast majority of the molecular beam consists of intact Td molecules. This can be concluded directly from the intensity ratio between feature 1 and feature 2 in the $(Td-H)^-$ signal in Figure 3. As the cross section for DEA has, normally, a general reciprocal dependence with energy,[18] the density of the target creating feature 2 (Td) must be appreciably larger than that creating feature 1. This also follows from the absolute intensity of the $(T-H)^-$ signal, which, from T is more than two orders of magnitude larger than from Td (at a comparable gas pressure). It is in fact likely that the entire low-energy feature of the $(T-H)^-$ signal originates from T (present as a thermal-decomposition product) and not from intact Td. This directly follows from the shape of the ion yield, $(M-H)^-$, owing to the loss of hydrogen from T that is methylated at the N1 position (m1T) (see Figure 2). Methylation at N1 or coupling to the sugar should have the same effect on T with respect to hydrogen loss. We therefore conclude that the low-energy $(T-H)^-$ signal arises from thermal decomposition. Similar arguments apply for the 115-amu signal near 1.2 eV. This leads to the conclusion that the structure near 0 eV is a result of decomposition, whereas the majority of the signal intensity at 1.2 eV can be attributed to the DEA reaction of intact Td. In Figure 1 the dotted part of the ion-yield curve corresponds to contribution from thermal-decomposition products.

To summarize the present findings:

a) At energies above 5.5 eV, electron attachment to thymidine occurs through localization of the excess charge on

 © 2006 Wiley-VCH Verlag GmbH & Co. KGaA, Weinheim 

the thymine part. This is supported by the observation of a similar feature in isolated T (yielding a variety of DEA fragments and characterized as a core excited resonance[6]). The excited transient anion decomposes into $(T-H)^-$ through rupture of the glycosidic N1–C1 bond. The neutral counterpart is $C_5H_9O_3$ (dR), which may further decompose (by loss of $H_2$, $H_2O$, etc.) due to the presence of appreciable excess energy.

b) At subexcitation energies (< 3 eV), Td captures electrons through resonances located at 1.8 eV and at 1.2 eV. The 1.8-eV feature ($(Td-H)^-$ at 241 amu) can be assigned as a shape resonance with π* character, with the excess charge localized on the thymine moiety leading the loss of H from the N3 position. The 1.2-eV resonance ($(dR-2H)^-$ at 115 amu) is linked to electron localization on the sugar moiety (shape resonance of σ* character) leading to the rupture of the glycosidic N1–C1 bond.

We have hence a situation wherein initial capture into σ* MOs at the sugar unit leads to rupture of the σ (N-C) bond, whereas capture into π* MOs of the thymine unit exclusively leads to loss of H from the N3 site. This last reaction is expected to occur through vibronic coupling, that is, a mixing of π* states with repulsive valence σ* states through vibrational motion.[19] Only core excited states of the thymine unit induce cleavage of the glycosidic N–C bond.

We shall now briefly consider the implications of these findings for the molecular mechanism of DNA damage by low-energy electrons. The fact that the 115-amu signal does not carry any signature of electron attachment to the thymine moiety and, accordingly, neither the $(Td-H)^-$ signal (loss of hydrogen from N3) nor the $(T-H)^-$ signal carries any signature of electron attachment to the sugar moiety. It therefore follows that electron transfer between the two units (associated with fragmentation) is inhibited. Rupture of the N1–C1 bond in fact takes place, but only through electron localization on either of the two units.

The present findings directly demonstrate that migration of the excess charge from the π* anions of the nucleobases to the DNA backbone is inhibited and may hence not contribute to SSBs as previously proposed.[13] Instead, attachment of low-energy electrons can lead to loss of H from the N3 position (1.8 eV) and to the rupture of the N1–C1 bond at either 1.2 eV or in the energy range between 5.5 eV and 10 eV. All three processes can be considered as primary events contributing to strand breaks. The first creates a highly mobile and reactive H radical (with its potential to induce further damage in DNA), whereas the latter two induce rupture of the glycosidic bond that can lead to excision of thymine from DNA. It has to be noted that the presence of the phosphate group could in fact modify the charge-transfer behavior with respect to that presently observed in Td.

So far there is little information on the role of the phosphate group. In a very recent study[20] on self-assembled monolayers of DNA with orientations perpendicular and parallel to the surface, the desorption of $OH^-$ following electron bombardment was studied. From the analysis of the data the authors concluded that in the energy range 2–5 eV direct DEA reactions to the phospate unit take place, whereas at higher energy reactive scattering may also contribute to the $OH^-$ desorption signal.

Received: November 6, 2005

**Keywords:** anions · DNA damage · electron attachment · gas-phase reactions · nucleotides

[1] F. Martin, P. D. Burrow, Z. Cai, P. Cloutier, D. Hunting, L. Sanche, *Phys. Rev. Lett.* **2004**, *93*, 068101.
[2] C. von Sonntag, *The Chemical Basis for Radiation Biology, Taylor and Francis*, London **1987**.
[3] J. F. Ward in *Advances in Radiation Biology, Vol. 5* (Eds.: J. T. Lett, H. Adler), Academic Press, New York, **1977**, pp. 181–239.
[4] $5 \times 10^4$ Secondary electrons per deposited MeV quantum primary energy. International Commission on Radiation Units and Measurements, ICRU Report 31 (ICRU, Washington DC, **1979**.
[5] B. Boudaiffa, P. Cloutier, D. Hunting, M. A. Huels, L. Sanche, *Science* **2000**, *287*, 1658.
[6] G. Hanel, S. Denifl, P. Scheier, M. Probst, B. Farizon, M. Farizon, E. Illenberger, T. D. Märk, *Phys. Rev. Lett.* **2003**, *90*, 188104.
[7] S. Denifl, S. Ptasińska, M. Cingel, S. Matejcik, P. Scheier, T. D. Märk, *Chem. Phys. Lett.* **2003**, *377*, 74.
[8] R. Abouaf, J. Pommier, H. Dunet, *Int. J. Mass Spectrom.* **2003**, *226*, 397.
[9] H. Abdoul-Carime, S. Gohlke, E. Illenberger, *Phys. Rev. Lett.* **2004**, *92*, 168103.
[10] S. Denifl, S. Ptasińska, M. Probst, J. Hrusak, P. Scheier, T. D. Märk, *J. Phys. Chem. A* **2004**, *108*, 6562.
[11] S. Ptasińska, S. Denifl, B, Mróz, M. Probst, V. Grill, E. Illenberger, P. Scheier, T. D. Märk, *J. Chem. Phys.* **2005**, *123*, 124302.
[12] S. Ptasińska, S. Denifl, P. Scheier, E. Illenberger, T. D. Märk, *Angew. Chem.* **2005**, *117*, 7101; *Angew. Chem. Int. Ed.* **2005**, *44*, 6941.
[13] J. Berdys, I. Anusiewicz, O. Skurski, J. Simons, *J. Am. Chem. Soc.* **2004**, *126*, 6441.
[14] D. Muigg, G. Denifl, A. Stamatovic, T. D. Märk, *Chem. Phys.* **1998**, *239*, 409.
[15] S. Matejcik, G. Senn, P. Scheier, A. Kiendler, A. Stamatovic, T. D. Märk, *J. Chem. Phys.* **1997**, *107*, 8955.
[16] H. Abdoul-Carime, S. Gohlke, E. Fischbach, J. Scheike, E. Illenberger, *Chem. Phys. Lett.* **2004**, *387*, 267. In this manuscript, the sugar anion was erroneously assigned as $dR^-$ instead of $(dR-2H)^-$.
[17] S. Ptasińska, S. Denifl, P. Scheier, T. D. Märk, *J. Chem. Phys.* **2004**, *120*, 8505.
[18] Associative electron attachment usually leads to a narrow peak close to 0 eV, (if a mass spectrometrically observable negative ion is formed at all), see, for example: "Electron Attachment Processes in Free and Bound Molecules" in *Photoinonization and Photodetachment*, *Part II*: E. Illenberger; *Advanced Series in Physical. Chemistry, Vol. 10 B* (Ed.: C.-Y. Ng), World Scientific, Singapore, **2000**, pp. 1063–1160.
[19] A. M. Scheer, K. Aflatooni, G. A. Gallup, P. D. Burrow, *Phys. Rev. Lett.* **2004**, *92*, 068102.
[20] X. Pan, L. Sanche, *Phys. Rev. Lett.* **2005**, *94*, 198104.

 © 2006 Wiley-VCH Verlag GmbH & Co. KGaA, Weinheim 

Gold Catalysis

DOI: 10.1002/anie.200503846

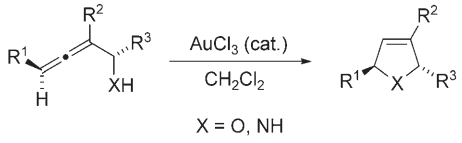
# The First Gold-Catalyzed C–S Bond Formation: Cycloisomerization of α-Thioallenes to 2,5-Dihydrothiophenes**

*Nobuyoshi Morita and Norbert Krause**

*Dedicated to Professor Henning Hopf on the occasion of his 65th birthday*

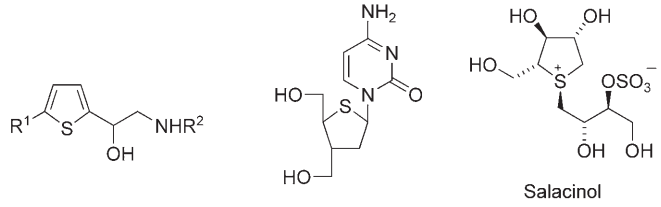
The use of gold catalysts in organic synthesis has received much attention in recent years because they exhibit extraordinary reactivities and selectivities in various transformations such as inter- and intramolecular addition reactions, cyclizations, cycloisomerizations, and rearrangements.[1] To date, these gold-catalyzed reactions have been utilized for the highly efficient formation of C–C, C–O, and C–N bonds. In contrast, there seems to be no precedent for the formation of a carbon–sulfur bond in the presence of a gold catalyst. A rationale for this might be that organosulfur compounds such as thiols, sulfides, and disulfides are known to strongly coordinate to transition metals, especially to gold, which does not render the use of gold catalysts in the presence of these functional groups very promising. This high affinity of gold and sulfur is frequently applied in various fields, for instance in the generation of self-assembled monolayers (SAMs)[2] and the use of gold thiolates as drugs, for example, for the treatment of rheumatoid arthritis.[3]

Recently, we reported the highly efficient gold-catalyzed cycloisomerization of α-hydroxyallenes to 2,5-dihydrofurans,[4] as well as of α-aminoallenes to 3-pyrrolines[5] in good to high yields with complete axis-to-center chirality transfer (that is, chirality transfer from the allenic chirality axis to the newly formed stereogenic center; Scheme 1). The heterocyclic products formed are highly useful for the synthesis of natural products and pharmaceuticals.




***Scheme 1.*** Gold-catalyzed cycloisomerization of α-hydroxyallenes and α-aminoallenes. $R^1$, $R^2$, $R^3$ = H, allyl, aryl.

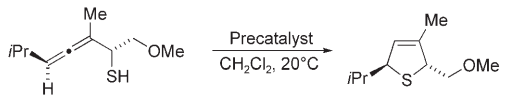
The corresponding, as yet unprecedented, cycloisomerization of α-thioallenes to 2,5-dihydrothiophenes would be highly rewarding as well. For example, oxidation or reduction of the resulting heterocycles smoothly affords thiophenes or tetrahydrothiophenes which are important structural motifs in natural products and biologically active compounds (Scheme 2). These include antihypertensive compounds,[6] potential inhibitors of HIV,[7] glucosidase inhibitors (salacinol, kotalanol),[8] an essential coenzyme (biotin)[9] and a cholecystokinin type-B receptor antagonist (tetronothiodin).[10] Moreover, 2,5-disubstituted tetrahydrothiophenes can be utilized as chiral ligands in enantioselective reactions.[11]




***Scheme 2.*** Biologically active thiophenes and tetrahydrothiophenes.

In spite of the importance of these heterocyclic compounds, the stereocontrolled synthesis of 2,5-disubstituted dihydrothiophenes and tetrahydrothiophenes has received only scant attention.[12] Herein we report the highly efficient synthesis of 2,5-dihydrothiophenes by stereoselective cycloisomerization of α-thioallenes, which is the first example of a gold-catalyzed carbon–sulfur bond formation. We initiated our study with the α-thioallene **1a**[13] which was treated with various coin-metal precatalysts (Au, Ag, Cu; 5–20 mol%) in $CH_2Cl_2$ under argon at room temperature (Table 1).

***Table 1:*** Cycloisomerization of α-thioallene **1a** to 2,5-dihydrothiophene **2a**.




**1a** (d.r. > 99:1) **2a** (d.r. > 99:1)

| Entry | Precatalyst (mol%) | *t* | Yield (**2a**) [%] |
|---|---|---|---|
| 1 | $AuCl_3$ (5) | 3 h | 58[a] |
| 2 | $AuBr_3$ (5) | 20 min | 56[a] |
| 3 | AuCl (5) | 1.5 h | 88 |
| 4 | AuI (5) | 5 min | 88 |
| 5 | AuI (1) | 1.5 h | 64 |
| 6 | $[Ph_3PAuCl]$ (5) | 7 days | trace |
| 7 | $[Ph_3PAuCl]$ (5)/ $AgBF_4$ (10) | 4 h | 52 |
| 8 | $AgBF_4$ (15) | 2 days | trace |
| 9 | AgCl (15) | 2 days | no reaction |
| 10 | CuCl (20) | 1 h | trace |
| 11 | CuI (20) | 2 days | no reaction |

[a] Small amounts of disulfide **3** were formed as side product.

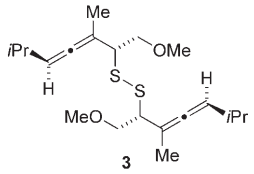
[*] Dr. N. Morita, Prof. Dr. N. Krause
Organic Chemistry II
Dortmund University
Otto-Hahn-Strasse 6, 44227 Dortmund (Germany)
Fax: (+49) 231-755-3884
E-mail: norbert.krause@uni-dortmund.de

[**] Financial Support by the Deutsche Forschungsgemeinschaft, the Fonds der Chemischen Industrie, and the European Community (COST D24/0003/01) is gratefully acknowledged.

Supporting information for this article is available on the WWW under http://www.angewandte.org or from the author.

 © 2006 Wiley-VCH Verlag GmbH & Co. KGaA, Weinheim 

Whereas copper or silver precatalysts afforded no cyclization product or only trace amounts (Table 1, entries 8–11), various gold precatalysts, such as AuCl, AuI, $AuCl_3$, or $AuBr_3$, induced the desired C–S bond formation to furnish the 2,5-dihydrothiophene **2a** in good to excellent yields. Interestingly, the reaction time can be decreased dramatically by changing the halide anion in the order Cl > Br > I (Table 1, entries 1–4). By using the highly active gold(I) iodide, the catalyst loading could be reduced to 1 mol%, giving the desired product with 64% yield (Table 1, entry 5). Not surprisingly, the less Lewis acidic [$Ph_3PAuCl$] does not catalyze the cycloisomerization (Table 1, entry 6), whereas formation of a cationic gold species by combining [$Ph_3PAuCl$] with $AgBF_4$[1] afforded **2a** with 52% yield (Table 1, entry 7). Finally, the use of $AuCl_3$ or $AuBr_3$ led to the formation of the disulfide **3** as side product

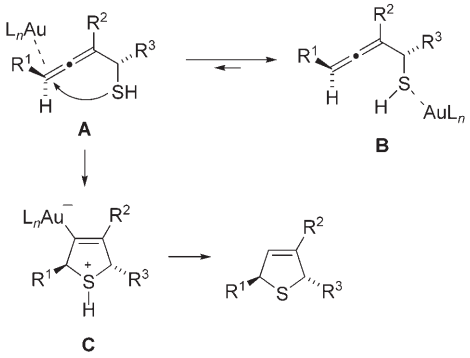



**3**

(Table 1, entries 1, 2), which might indicate a reduction of the gold(III) precatalyst to a gold(I) species by the substrate **1a**. In all cases, after complete consumption of the starting material an insoluble, catalytically inactive residue (possibly metallic gold) formed on the walls of the reaction flask.

Further optimizations of the reaction conditions were carried out with α-thioallenes **1b**–**1e**[13,14] using mainly gold(I) chloride as the precatalyst since this is less hydroscopic and easier to handle than AuI. The corresponding 2,5-dihydrothiophenes were obtained with moderate to high yields and complete axis-to-center chirality transfer (Table 2). The cycloisomerization proceeds smoothly in $CH_2Cl_2$ solution (Table 2, entries 1, 5–8) whereas very slow conversions and low yields were obtained in THF, toluene, or hexane (Table 2, entries 2–4). This situation might be due to coordination of the gold catalyst by THF which decreases its Lewis acidity, and to the low solubility of gold(I) chloride in hydrocarbon solvents. As observed in the cyclization of **1a**, the use of AuI instead of AuCl induced a very fast transformation of α-thioallene **1b** to 2,5-dihydrothiophene **2b** which was isolated with 87% yield after only 5 min reaction time (Table 2, entry 5). The corresponding cycloisomerization of the allenes **1c**–**1e** clearly demonstrates that the method can be applied to substrates with various substituent patterns. Notably, treatment of the α-thioallene **1e**[14] with 5 mol% of AuCl afforded the 2,5-dihydrothiophene **2e** with only 43% yield (Table 2, entry 8). In this case, coordination of the gold catalyst to the olefinic double bond[15] may cause a considerable deactivation.

A plausible mechanistic model of the gold-catalyzed cycloisomerization of α-thioallenes to 2,5-dihydrothiophenes is shown in Scheme 3. Similar to the corresponding reaction of



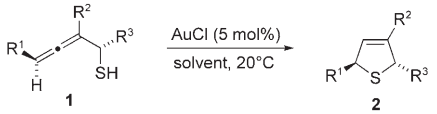

***Scheme 3.*** Proposed mechanism of the gold-catalyzed cycloisomerization of α-thioallenes to 2,5-dihydrothiophenes.

α-hydroxy- and α-aminoallenes,[3,4] coordination of the Lewis acidic, carbophilic gold catalyst[1] to the "terminal" allenic double bond (intermediate **A**) is required for an intramolecular nucleophilic attack of the thiol via an $S_N2$-type transition state to afford the zwitterionic species **C** which upon protodemetalation is transformed into the heterocyclic product with complete axis-to-center chirality transfer. Compared to the other heteroatom-substituted allenes, however, coordination of the gold catalyst to the sulfur atom of the α-thioallenes (complex **B**) is probably more pronounced than its coordination to other heteroatoms, causing a lower reactivity.

At present, the oxidation state of the catalytically active gold species is unknown; the high activity of gold(I) precatalysts, as compared to gold(III) salts (Table 1, entries 3, 4 vs. 1, 2), and the observation of the disulfide **3** as a side product if a gold(III) salt is used as the precatalyst (Table 1, entries 1, 2) may indicate that a gold(I) compound is the catalytically active species in all cases. We are currently trying to clarify this point with the aid of ab initio calculations.

In summary, we have discovered a highly efficient and stereoselective cycloisomerization of α-thioallenes to 2,5-dihydrothiophenes which is the first example for a gold-catalyzed carbon–sulfur bond forma-

***Table 2:*** Scope of the cycloisomerization of α-thioallenes **1** to 2,5-dihydrothiophenes **2**.




**1** **2**

| Entry | **1** | $R^1$ | $R^2$ | $R^3$ | d.r. (**1**) | Solvent | *t* | **2** (Yield) | d.r. (**2**) |
|---|---|---|---|---|---|---|---|---|---|
| 1 | **1b** | *i*Pr | Me | $CH_2OBn$ | 95:5 | $CH_2Cl_2$ | 1.5 h | **2b** (86%) | 95:5 |
| 2 | **1b** | *i*Pr | Me | $CH_2OBn$ | 95:5 | THF | 2 days | **2b** (24%) | 95:5 |
| 3 | **1b** | *i*Pr | Me | $CH_2OBn$ | 95:5 | toluene | 1 days | **2b** (55%) | 95:5 |
| 4 | **1b** | *i*Pr | Me | $CH_2OBn$ | 95:5 | hexane | 2 days | **2b** (trace) | – |
| 5[a] | **1b** | *i*Pr | Me | $CH_2OBn$ | 95:5 | $CH_2Cl_2$ | 5 min | **2b** (87%) | 95:5 |
| 6 | **1c** | *i*Pr | Me | 4-$CF_3C_6H_4OCH_2$ | >99:1 | $CH_2Cl_2$ | 4 h | **2c** (67%) | >99:1 |
| 7 | **1d** | *n*-hexyl | Me | $CH_2OBn$ | >99:1 | $CH_2Cl_2$ | 2 h | **2d** (82%) | >99:1 |
| 8 | **1e** | $H_2C{=}CH(CH_2)_7$ | H | H | – | $CH_2Cl_2$ | 1.5 h | **2e** (43%) | – |

[a] AuI (5 mol%) was used instead of AuCl.

 © 2006 Wiley-VCH Verlag GmbH & Co. KGaA, Weinheim 

tion. Both gold(I) and gold(III) salts can be employed as the precatalyst, with AuCl and AuI giving the highest yields.[16] In contrast to this, copper or silver precatalysts afford no cyclization product or only trace amounts. Application of the method to the synthesis of biologically active 2,5-disubstituted thiophenes, dihydrothiophenes, or tetrahydrothiophenes, as well as experimental and theoretical investigations on the reaction mechanism, are underway.

Received: October 31, 2005
Published online: February 17, 2006

**Keywords:** C–S bond formation · cycloisomerization · gold · heterocycles · homogeneous catalysis · isomerization

[1] a) A. Hoffmann-Röder, N. Krause, *Org. Biomol. Chem.* **2005**, *3*, 387–391; b) A. S. K. Hashmi, *Angew. Chem.* **2005**, *117*, 7150–7154; *Angew. Chem. Int. Ed.* **2005**, *44*, 6990–6993; c) A. S. K. Hashmi, *Gold Bull.* **2004**, *37*, 51–61; d) A. S. K. Hashmi, *Gold Bull.* **2003**, *36*, 3–9; e) A. Arcadi, S. D. Giuseppe, *Curr. Org. Chem.* **2004**, *8*, 795–812; f) G. Dyker, *Angew. Chem.* **2000**, *112*, 4407–4409; *Angew. Chem. Int. Ed.* **2000**, *39*, 4237–4239.

[2] a) A. Ulman, *Chem. Rev.* **1996**, *96*, 1533–1554; b) H. Gronbeck, A. Curioni, W. Andreoni, *J. Am. Chem. Soc.* **2000**, *122*, 3839–3842; c) K. Fujita, N. Nakamura, H. Ohno, B. S. Leigh, K. Niki, H. B. Gray, J. H. Richards, *J. Am. Chem. Soc.* **2004**, *126*, 13954–13961.

[3] a) S. P. Fricker, *Gold Bull.* **1996**, *29*, 53–60; b) S. L. Best, P. J. Sadler, *Gold Bull.* **1996**, *29*, 87–93; c) C. F. Shaw III, *Chem. Rev.* **1999**, *99*, 2589–2600; d) E. R. T. Tiekink, *Gold Bull.* **2003**, *36*, 117–124.

[4] a) A. Hoffmann-Röder, N. Krause, *Org. Lett.* **2001**, *3*, 2537–2538; b) N. Krause, A. Hoffmann-Röder, J. Canisius, *Synthesis* **2002**, 1759–1774.

[5] N. Morita, N. Krause, *Org. Lett.* **2004**, *6*, 4121–4123.

[6] J. F. Bagli, W. D. Mackay, E. Ferdinandi, *J. Med. Chem.* **1976**, *19*, 876–882.

[7] a) J. Wirsching, J. Voss, G. Adiwidjaja, A. Giesler, J. Kopf, *Eur. J. Org. Chem.* **2001**, 1077–1087; b) Y. Yoshimura, K. Kitano, K. Yamada, H. Satoh, M. Watanabe, S. Miura, S. Sakata, T. Sasaki, A. Matsuda, *J. Org. Chem.* **1997**, *62*, 3140–3152; c) J. Mann, A. J. Tench, A. C. Weymouth-Wilson, S. Shaw-Ponter, R. J. Young, *J. Chem. Soc. Perkin Trans. 1* **1995**, 677–681; d) J. Brånalt, I. Kvarnströn, S. C. T. Svensson, B. Classon, B. Samuelsson, *J. Org. Chem.* **1994**, *59*, 4430–4432; e) J. Brånalt, I. Kvarnström, G. Niklasson, S. C. T. Svensson, B. Classon, B. Samuelsson, *J. Org. Chem.* **1994**, *59*, 1783–1788; f) J. A. Secrist III, K. N. Tiwari, J. M. Riordan, J. A. Montgomery, *J. Med. Chem.* **1991**, *34*, 2361–2366.

[8] a) D. A. Kuntz, A. Ghavami, B. D. Johnston, B. M. Pinto, D. R. Rose, *Tetrahedron: Asymmetry* **2005**, *16*, 25–32; b) E. Gallienne, M. Benazza, G. Demailly, J. Bolte, M. Lemaire, *Tetrahedron* **2005**, *61*, 4557–4568; c) A. Ghavami, K. S. Sadalapure, B. D. Johnston, M. Lobera, B. B. Snider, B. M. Pinto, *Synlett* **2003**, 1259–1262; d) A. Ghavami, B. D. Johnston, B. M. Pinto, *J. Org. Chem.* **2001**, *66*, 2312–2317; e) H. Yuasa, J. Tanaka, H. Hashimoto, *Tetrahedron Lett.* **2000**, *41*, 6615–6618; f) M. Yoshikawa, T. Murakami, K. Yashiro, H. Matsuda, *Chem. Pharm. Bull.* **1998**, *46*, 1339–1340; g) M. Yoshikawa, T. Murakami, H. Shimada, H. Matsuda, J. Yamahara, G. Tanabe, O. Muraoka, *Tetrahedron Lett.* **1997**, *38*, 8367–8370.

[9] a) R. A. Volkmann, J. T. Davis, C. N. Meltz, *J. Am. Chem. Soc.* **1983**, *105*, 5946–5948; b) S. Lavielle, S. Bory, B. Moreau, M. J. Luche, A. Marquet, *J. Am. Chem. Soc.* **1978**, *100*, 1558–1563; c) P. N. Confalone, G. Pizzolato, M. R. Uskokovic, *J. Org. Chem.* **1977**, *42*, 1630–1633.

[10] a) P. C. B. Page, H. Vahedi, K. J. Batchelor, S. J. Hindley, M. Edger, P. Beswick, *Synlett* **2003**, 1022–1024; b) J. Watanabe, N. Fujisaki, K. Fujimori, Y. Anzal, S. Oshima, T. Sano, T. Ohtsuka, K. Watanabe, T. Okuda, *J. Antibiot.* **1993**, *46*, 1–10; c) T. Ohtsuka, H. Kotaki, N. Nakayama, Y. Itezono, N. Shimma, T. Kudoh, T. Kuwahara, M. Arisawa, K. Yokose, *J. Antibiot.* **1993**, *46*, 11–17; d) T. Ohtsuka, N. Nakayama, Y. Itezono, N. Shimma, T. Kuwahara, K. Yokose, H. Seto, *J. Antibiot.* **1993**, *46*, 18–24; e) T. Ohtsuka, T. Kudoh, N. Shimma, H. Kotaki, N. Nakayama, Y. Itezono, N. Fujisaki, J. Watanabe, K. Yokose, H. Seto, *J. Antibiot.* **1992**, *45*, 140–143.

[11] a) M. A. Silva, B. R. Bellenie, J. M. Goodman, *Org. Lett.* **2004**, *6*, 2559–2562; b) J. Zanardi, D. Lamazure, S. Miniere, V. Reboul, P. Metzner, *J. Org. Chem.* **2002**, *67*, 9083–9086; c) E. Hauptman, R. Shapiro, W. Marshall, *Organometallics* **1998**, *17*, 4976–4982.

[12] 2,5-Disubstituted dihydrothiophenes: a) W. G. Blenderman, M. M. Joullie, G. Preti, *J. Org. Chem.* **1983**, *48*, 3206–3213; b) W. G. Blenderman, M. M. Joullie, *Synth. Commun.* **1981**, *11*, 881–888; c) J. M. McIntosh, G. M. Masse, *J. Org. Chem.* **1975**, *40*, 1294–1298; 2,5-Disubstituted tetrahydrothiophenes: d) K. Haraguchi, H. Takahashi, H. Tanaka, *Tetrahedron Lett.* **2002**, *43*, 5657–5660; e) F. Lautenschlaeger, *J. Org. Chem.* **1968**, *33*, 2620–2627.

[13] Thioallenes **1a**–**1d** were prepared from the corresponding α-hydroxyallene[4] by Mitsunobu reaction[5] with thioacetic acid, followed by cleavage of the thioester with potassium carbonate (Q. Yao, *Org. Lett.* **2002**, *4*, 427–430).

[14] Thioallene **1e** was prepared from methyl trideca-2,3,12-trienoate (J. A. Marshall, M. A. Wolf, E. M. Wallace, *J. Org. Chem.* **1997**, *62*, 367–371) by reduction to the allenic alcohol (diisobutylaluminum hydride, THF), and subsequent Mitsunobu reaction.[13]

[15] a) C.-G. Yang, C. He, *J. Am. Chem. Soc.* **2005**, *127*, 6966–6967; b) X. Yao, C.-J. Li, *J. Am. Chem. Soc.* **2004**, *126*, 6884–6885.

[16] Typical procedure: AuCl (3 mg, 13 μmol) was added to a stirred solution of α-thioallene **1a** (50 mg, 0.27 mmol) in $CH_2Cl_2$ (5 mL) at room temperature under argon, and the mixture was stirred for 90 min at room temperature (the reaction was monitored by thin-layer chromatography (TLC)). The solvents were removed under reduced pressure. The residue was purified by column chromatography on silica gel with cyclohexane/ethyl acetate (30:1) as eluent to afford 2,5-dihydrothiophene **2a** (44 mg, 88%) as a yellow oil. $^1$H NMR ($CDCl_3$, 400 MHz): $\delta = 5.45$ (br s, 1H), 4.13–4.08 (m, 1H), 4.07–4.01 (m, 1H), 3.64 (dd, $J = 9.3$, 4.8 Hz, 1H), 3.44 (dd, $J = 9.3$, 6.8 Hz, 1H), 3.39 (s, 3H), 1.81–1.73 (m, 1H), 1.79 (s, 3H), 0.94 (d, $J = 6.8$ Hz, 3H), 0.91 ppm (d, $J = 6.8$ Hz, 3H). $^{13}$C NMR ($CDCl_3$, 100 MHz): $\delta = 138.8$, 128.0, 60.7, 59.0, 55.9, 34.3, 26.8, 20.3, 19.2, 15.7 ppm.

 © 2006 Wiley-VCH Verlag GmbH & Co. KGaA, Weinheim 

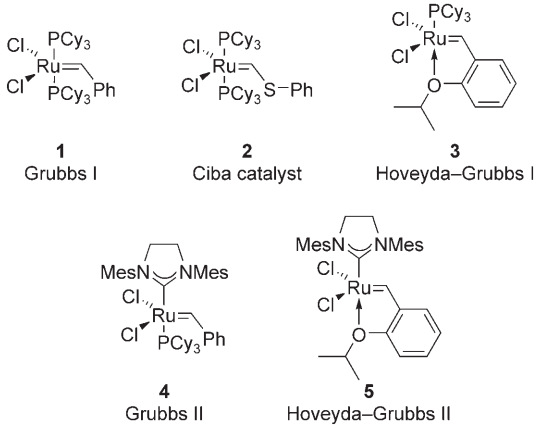
Synthetic Methods

DOI: 10.1002/anie.200503552

# Sequential Catalysis: A Metathesis/Dihydroxylation Sequence**

*Samuel Beligny, Stefan Eibauer, Simon Maechling, and Siegfried Blechert**

During the last years olefin metathesis has become a powerful tool in synthetic organic chemistry.[1] The advent of well-defined catalysts such as the commercially available ruthenium complexes **1**–**5** has allowed chemists to develop a wide range of useful applications (Scheme 1).[2] The utility of some




***Scheme 1.*** Commercially available ruthenium metathesis complexes.

ruthenium–carbene complexes in catalytic processes has been extended beyond olefin metathesis to other synthetic transformations. For example, carbene **1** has been used in the Kharasch addition,[3] and carbenes **1** and **4** were reported to catalyze a variety of hydrogenation processes such as regiospecific ketone and olefin reductions, transfer dehydrogenation of ketones, and dehydrogenative oxidation of alcohols.[4] Complexes **1** and **4** were, in addition, shown to be efficient catalysts for the isomerization of double bonds and also for the deprotection of allylic amines.[5–8]

A common goal in the development of new reactions is not only high catalyst efficiency, but also the use of a single catalyst for more than one chemical transformation in a single synthetic operation. Ultimately this can lead to the use of a single catalyst to mediate two or more reactions that are fundamentally different in nature, so-called sequential catalysis.[9] Such sequential reactions have been demonstrated combining an olefin metathesis step with the processes described above. One of the most striking examples is the one-pot synthesis of (*R*)-(−)-muscone reported by the Grubbs group, in which three steps—ring-closing metathesis (RCM), transfer dehydrogenation, and hydrogenation—are catalyzed by a single ruthenium source.[4] Snapper and coworkers as well as Schmidt have also reported the synthesis of cyclic enols by a tandem RCM/olefin isomerization catalyzed by the Grubbs I catalyst.[10,11] We report herein a sequential metathesis/dihydroxylation sequence involving RCM or cross-metathesis (CM) followed by *cis*-dihydroxylation of the resulting C−C double bond utilizing the same ruthenium source, resulting in the facile synthesis of dihydroxylated products in modest to excellent yields under mild conditions.

A variety of ruthenium sources, such as $RuCl_3$,[12] $RuO_2$,[13] $[RuCl_2(dppp)_2]$ (dppp = 1,3-bis(diphenylphosphanyl)propane),[14] $[RuCl_2(PPh_3)_3]$,[15] $[Ru(acac)_3]$ (acac = acetylacetonate)[15] TPAP (tetrapropylammonium perruthenate),[15] and Ru/C,[15] have been used for the formation of the oxidative species $RuO_4$ in different oxidation reactions.[16] The method of choice for dihydroxylation of olefins is in situ formation from a catalytic amount of $RuCl_3 \cdot 3H_2O$ using $NaIO_4$ as the stoichiometric oxidant.[17] To the best of our knowledge, ruthenium–carbenes have not been used for this purpose. The choice of solvent was found to be critical, and when a 3:3:1 mixture of MeCN/EtOAc/$H_2O$ was employed, a very fast *cis*-dihydroxylation of olefins was observed.[18] Brønsted acids, and especially Lewis acids, have been shown to further accelerate the rate of hydrolysis and minimize side reactions such as over-oxidation.[19] We envisaged that it would be possible to utilize a ruthenium–carbene to perform a metathesis reaction and then oxidize this ruthenium source to conduct a *cis*-dihydroxylation of the newly formed disubstituted olefin in a single reaction vessel.

In our initial studies we examined the utility of ruthenium–carbenes **1**–**5** as precatalysts for the dihydroxylation of tetrahydropyridine **6**. The best results were found when the olefinic substrate was dissolved in a 3:3:1 mixture of MeCN/EtOAc/$H_2O$ at 0 °C in the presence of 10 mol % of $YbCl_3 \cdot 6H_2O$ before 1.5 equivalents of $NaIO_4$ and 1.5 mol % of the ruthenium–carbene were added. Because the reaction mixture was heterogeneous, vigorous stirring was of prime importance for reproducible results. The reaction was quenched with saturated aqueous $Na_2S_2O_3$ when TLC analysis showed complete consumption of the starting material.

All five ruthenium catalysts promoted formation of the vicinal *cis*-diol **7**; however, the Grubbs I catalyst **1**, the Ciba catalyst **2**, and the Hoveyda–Grubbs I catalyst **3** gave the best results (Table 1, entries 1–3) providing the diol in excellent yield and short reaction time. The lower yields and longer reaction times observed for catalysts **4** and **5** are probably a consequence of the strong binding between the N-hetero-

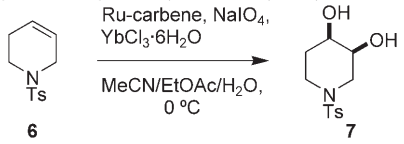
[*] Dr. S. Beligny, S. Eibauer, Dr. S. Maechling, Prof. Dr. S. Blechert
Technische Universität Berlin
Strasse des 17. Juni 135, 10623 Berlin (Germany)
Fax: (+49) 30-314-23619
E-mail: blechert@chem.tu-berlin.de

[**] We are grateful to the Fonds der Chemischen Industrie, the Friedrich-Naumann-Stiftung, and the Graduiertenkolleg "Synthetische, mechanistische und reaktionstechnische Aspekte von Metallkatalysatoren" for financial support.

Supporting information for this article is available on the WWW under http://www.angewandte.org or from the author.


InterScience
© 2006 Wiley-VCH Verlag GmbH & Co. KGaA, Weinheim

***Table 1:*** Comparison of precatalysts for dihydroxylation.




6 7

| Entry | Cat. | *t* [min] | Yield [%][a] |
|---|---|---|---|
| 1 | **1** | 10 | 81 |
| 2 | **2** | 10 | 81 |
| 3 | **3** | 10 | 88 |
| 4 | **4** | 30 | 63 |
| 5 | **5** | 40 | 63 |

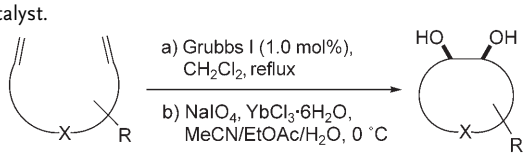
[a] Yields of isolated products.

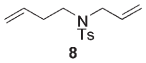
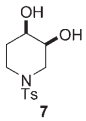
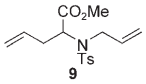
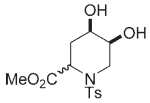
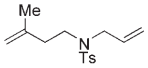
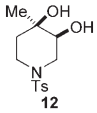
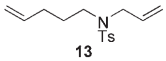
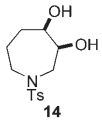
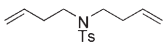
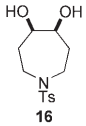
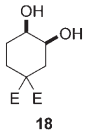
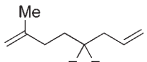
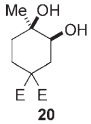
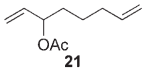
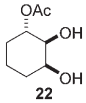
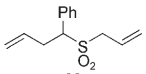
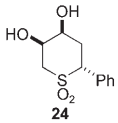
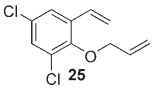
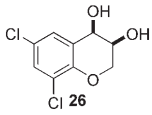
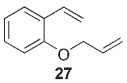
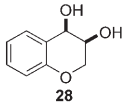
cyclic carbene (NHC) ligand and the ruthenium in these complexes which slows down the formation of the oxidative species.[15]

Following these observations, we attempted a one-pot RCM/dihydroxylation using catalyst **1**. A variety of dienes were treated with 1 mol% of **1** in dichloromethane under reflux conditions. Early studies showed that the presence of small quantities of dichloromethane resulted in low yields in the dihydroxylation step. Therefore, the solvent was removed in vacuo after completion of the RCM step. The crude ring-closed product was dissolved in a 3:3:1 mixture of MeCN/EtOAC/$H_2O$, cooled to 0 °C, and treated with 10 mol% of $YbCl_3{\cdot}6H_2O$ and 1.2–1.6 equivalents of $NaIO_4$. The reaction was generally rapid and gave the desired vicinal diol in modest to excellent yields and was performed in the presence of a variety of functional groups.

$^1$H NMR coupling constants and NOE experiments as well as comparison with analytical data of known compounds showed that the products obtained were, as expected, *cis*-1,2-diols. The overall yield was generally linked to the reaction time of the second step; shorter reaction times gave in most cases better yields. For entries 1 and 4 in Table 2, 1.2 equivalents of $NaIO_4$ were used, whereas for some cases such as entries 2 and 5, up to 1.6 equivalents were required in order to drive the reaction to completion. In the case of entries 10 and 11, the electron density of the double bond appears to influence dihydroxylation, with electron-poor double bonds leading to higher yields. When a stereocenter was already in place after the RCM step, the dihydroxylation occurred with excellent stereoselectivity (24:1 in favor of the *trans* product for entry 8 and 28:1 in favor of the *trans* product for entry 9). These high diastereoselectivities are in line with prior observations.[20] However, with the allylglycine derivative (entry 2) only a 0.8:1 mixture of diastereoisomers was obtained. The low diastereoselectivity observed in this particular case seems to be the result of a low degree of substrate induction rather than of epimerization at the carbon bearing the ester moiety during the course of the dihydroxylation. The diastereoisomeric excess was studied at different reaction times. Regardless of whether the reaction was quenched after 5, 10, 20, or 120 minutes, the same ratio of diastereoisomers was observed. The reaction was also successful with trisubstituted olefins (entry 3 and 7), which widens the scope of the method.

***Table 2:*** RCM/dihydroxylation sequence using ruthenium–carbene **1** as precatalyst.



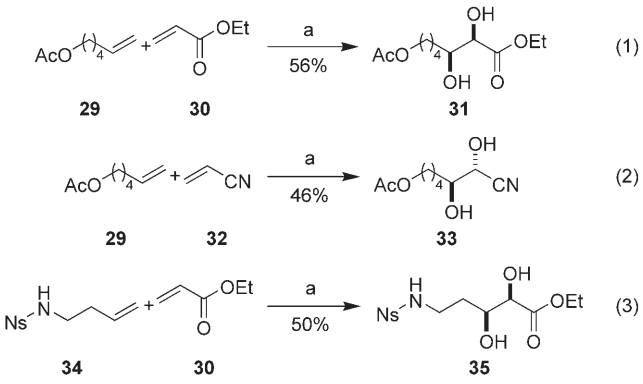

| Entry | Starting cmpd. | Equiv $NaIO_4$ | Product | *t* [min] | Yield [%] |
|---|---|---|---|---|---|
| 1 |  **8** | 1.2 |  **7** | 60/10 | 88 |
| 2 |  **9** | 1.4 |  **10** | 60/20 | 88 |
| 3 |  **11** | 1.3 |  **12** | 60/40 | 70 |
| 4 |  **13** | 1.2 |  **14** | 60/10 | 71 |
| 5 |  **15** | 1.6 |  **16** | 60/40 | 21 |
| 6 |  **17** | 1.4 |  **18** | 60/20 | 74 |
| 7 |  **19** | 1.6 |  **20** | 12 h/40 | 46[a] |
| 8 |  **21** | 1.4 |  **22** | 60/25 | 49 |
| 9 |  **23** | 1.6 |  **24** | 120/20 | 49[a] |
| 10 |  **25** | 1.6 |  **26** | 60/30 | 63 |
| 11 |  **27** | 1.6 |  **28** | 60/35 | 33 |

[a] Reaction was conducted with 2.0 mol% Grubbs I catalyst. [b] Reaction time RCM/dihydroxylation.

We next embarked on the studies of the tandem CM/dihydroxylation. We chose CM partners likely to give both

 © 2006 Wiley-VCH Verlag GmbH & Co. KGaA, Weinheim 

good selectivity and good yield in the CM step.[21] For this reaction the protocol was slightly changed. The Hoveyda–Grubbs II catalyst **5** (2.5–3.0 mol%) was used as it has been shown to be very efficient for CM with electron-deficient olefins.[22] The amount of $YbCl_3{\cdot}6H_2O$ was increased to 15 mol%. A 1:1 mixture of coupling partners was used for reactions (1) and (3) depicted in Scheme 2. Three equivalents




***Scheme 2.*** CM/dihydroxylation sequence using ruthenium–carbene **5** as precatalyst. a) 1. **5** (2.5–3.0 mol%), $CH_2Cl_2$, reflux; 2. $NaIO_4$, $YbCl_3{\cdot}6H_2O$, MeCN/EtOAc/$H_2O$, 0°C.

of acrylonitrile were used in reaction (2), and the excess was removed in vacuo together with the dichloromethane prior to the dihydroxylation step. The dihydroxylated products were successfully obtained, though the overall yields were lower than those for the RCM/dihydroxylation. This is presumably because catalyst **5** promotes the dihydroxylation less effectively (see above). Accordingly, formation of the diol required more time, with up to two hours for reaction (2). Pleasingly, the dihydroxylation [reaction (3)] was finished after 10 minutes. The product of reaction (2) was obtained as a 3:1 mixture of diastereoisomers, which is consistent with literatures precedent showing that the CM of acrylonitrile with similar substrates gives mixtures of geometric isomers in favor of the *Z* isomer.[22a]

In summary, a new process combining a metathesis step and a dihydroxylation step has been developed. Owing to the high tolerance of functional groups, this process has an interesting potential, notably in natural product synthesis. This process also presents an alternative to the pinacol coupling. The combination of two catalytic processes relying on a single ruthenium source, in addition to low catalyst loading make this reaction particularly interesting. Further studies to extend this process with emphasis on the synthesis of natural products are in progress.

## Experimental Section

Typical procedure for RCM/dihydroxylation (Table 2, entry 1): The Grubbs I catalyst (0.005 mmol, 4.1 mg, 1 mol%) was added to a solution of diene **8** (132 mg, 0.5 mmol, 1.0 equiv) in $CH_2Cl_2$ (1 mL). The resulting solution was refluxed at 50°C until the starting diene was completely consumed. $CH_2Cl_2$ was removed by evaporation, and $YbCl_3{\cdot}6H_2O$ (0.05 mmol, 19.4 mg, 10 mol%) was added followed by 2.1 mL of the solvent mixture MeCN/EtOAc/$H_2O$ (3:3:1). After the reaction mixture had been cooled to 0°C, solid $NaIO_4$ (128 mg, 0.6 mmol, 1.2 equiv) was added and the mixture stirred vigorously until the olefin was completely consumed (TLC). The mixture was quenched with 2 mL of saturated aqueous $Na_2S_2O_3$ solution, and the resulting slurry was extracted with methyl *tert*-butyl ether (MTBE; 3×5 mL). The combined organic layers were washed with brine (10 mL) and dried ($Na_2SO_4$). Filtration and concentration in vacuo afforded the crude product. Flash column chromatography on silica eluting with 1% MeOH in $CH_2Cl_2$ gave product **7** as a white solid in 88% yield (120 mg, 0.44 mmol). m.p. 138–140°C; $^1$H NMR (500 MHz, $CDCl_3$): $\delta = 7.64$ (d, 2H, $J = 8.0$ Hz, H-Ar), 7.32 (d, 2H, $J = 8.0$ Hz, H-Ar), 3.86 (m, 1H, H-3), 3.77 (m, 1H, H-4), 3.17 (dd, 1H, $J = 3.0$, 11.5 H-2), 3.09–2.97 (m, 3H, H-2, H-6), 2.47–2.37 (m, 4H, $CH_3$-Ts, OH), 2.23 (brs, 1H, OH), 1.93–1.79 ppm (m, 2H, H-5); $^{13}$C NMR (125 MHz, $CDCl_3$): $\delta = 143.9$ (C-Ar quart.), 133.1 (C-Ar quart.), 129.9 (CH-Ar), 127.7 (CH-Ar), 67.9 (CH-OH, C-3), 67.5 (CH-OH, C-4), 47.9 ($CH_2$, C-2), 42.0 ($CH_2$, C-6), 29.5 ($CH_2$, C-5), 21.6 ppm ($CH_3$-Ts); IR (ATR): $\tilde{\nu} = 3446$, 2928, 1338, 1163 cm$^{-1}$; MS (EI, 70 eV): *m/z* (%) 271 (8) [$M^+$], 184 (26), 155 (30) [$Ts^+$], 116 (100) [$M-Ts^+$], 91 (66) [$Ts-SO_2^+$]; HRMS (EI): calcd for $C_{12}H_{17}NO_4S$ [$M^+$] 271.0878, found 271.0876.

Typical procedure for CM/dihydroxylation (Scheme 2, reaction (1)): Acetate **29** (30 μL, 0.2 mmol, 1.0 equiv) and ester **30** (20.5 μL, 0.2 mmol, 1.0 equiv) were dissolved in $CH_2Cl_2$ (200 μL). The Hoveyda–Grubbs II catalyst **5** (3.1 mg, 0.005 mmol, 2.5 mol%) was added. The resulting solution was refluxed until the starting material was completely consumed (TLC). $CH_2Cl_2$ was removed by evaporation in vacuo, and $YbCl_3{\cdot}6H_2O$ (0.03 mmol, 11.6 mg, 15 mol%) was added followed by 840 μL of the solvent mixture MeCN/EtOAc/$H_2O$ (3:3:1). After the reaction mixture had been cooled to 0°C, $NaIO_4$ (64.2 mg, 0.3 mmol, 1.5 equiv) was added and the mixture was stirred vigorously until the olefin was completely consumed (TLC). The mixture was quenched with 1 mL of saturated aqueous $Na_2S_2O_3$ solution, and the resulting slurry was extracted with MTBE (3×3 mL). The combined organic layers were washed with brine (5 mL) and dried ($Na_2SO_4$). Filtration and concentration in vacuo afforded the crude product. Flash column chromatography on silica eluting with 1% MeOH in $CH_2Cl_2$ gave product **31** in 56% yield (28 mg, 0.11 mmol). $^1$H NMR (500 MHz, $CDCl_3$): $\delta = 4.30$ (q, 2H, $J =$ 7.0 Hz, $CO_2CH_2CH_3$), 4.14–4.06 (m, 3H, H-2, H-7), 3.91–3.86 (m, 1H, H-3), 3.06 (d, 1H, $J = 5.0$ Hz, OH), 2.05 (s, 3H, $OCOCH_3$), 1.94 (d, 1H, $J = 9.5$ Hz, OH), 1.72–1.51 (m, 5H, H-4, H-5, H-6), 1.50–1.40 (m, 1H, H-5), 1.32 ppm (t, 3H, $J = 7.0$ Hz, $CO_2CH_2CH_3$); $^{13}$C NMR (125 MHz, $CDCl_3$): $\delta = 173.6$ (C=O), 171.3 (C=O), 73.1 (CH-OH, C-2), 72.3 (CH-OH, C-3), 64.3 ($CH_2$, C-7), 62.3 ($CO_2CH_2CH_3$), 33.5 ($CH_2$, C-4), 28.5 ($CH_2$, C-6), 22.3 ($CH_2$, C-5), 21.1 ($OCOCH_3$), 14.2 ppm ($CO_2CH_2CH_3$); IR (ATR): $\tilde{\nu} = 3454$, 2942, 1735, 1367, 1240 cm$^{-1}$; MS (EI, 70 eV): *m/z* (%) 115 (18), 104 (100), 85 (78), 76 (76); HRMS (EI): calcd. for $C_{11}H_{21}O_6$ [$MH^+$] 249.1338, found 249.1343.

Received: October 6, 2005
Published online: February 10, 2006

**Keywords:** dihydroxylation · metathesis · ruthenium–carbenes · sequential catalysis

[1] For reviews on catalytic olefin metathesis, see: a) R. H. Grubbs, S. J. Miller, G. C. Fu, *Acc. Chem. Res.* **1995**, *28*, 446; b) H.-G. Schmalz, *Angew. Chem.* **1995**, *107*, 1981; *Angew. Chem. Int. Ed. Engl.* **1995**, *34*, 1833; c) M. Schuster, S. Blechert, *Angew. Chem.* **1997**, *109*, 2124; *Angew. Chem. Int. Ed. Engl.* **1997**, *36*, 2036; d) A. Fürstner, *Top. Catal.* **1997**, *4*, 285; e) S. K. Armstrong, *J. Chem. Soc. Perkin Trans. 1* **1998**, 371; f) R. H. Grubbs, S. Chang, *Tetrahedron* **1998**, *54*, 4413; g) A. Fürstner, *Angew. Chem.* **2000**,

 © 2006 Wiley-VCH Verlag GmbH & Co. KGaA, Weinheim 

*112*, 3140; *Angew. Chem. Int. Ed.* **2000**, *39*, 3012; h) T. M. Trnka, R. H. Grubbs, *Acc. Chem. Res.* **2001**, *34*, 18; i) *Handbook of Olefin Metathesis* (Ed.: R. H. Grubbs), VCH-Wiley, Wienheim, **2003**; j) R. R. Schrock, A. H. Hoveyda, *Angew. Chem.* **2003**, *115*, 4740; *Angew. Chem. Int. Ed.* **2003**, *42*, 4592; k) R. H. Grubbs, *Tetrahedron* **2004**, *60*, 7117.

[2] a) For a review on the synthesis of oxygen- and nitrogen-containing heterocycles by ring-closing olefin metathesis, see: A. Deiters, S. F. Martin, *Chem. Rev.* **2004**, *104*, 2199; b) for the synthesis of phosphorus and sulfur heterocycles by ring-closing olefin metathesis, see: M. D. McReynolds, J. M. Dougherty, P. R. Hanson, *Chem. Rev.* **2004**, *104*, 2239; c) for a review on enyne metathesis, see: S. T. Diver, A. J. Giessert, *Chem. Rev.* **2004**, *104*, 1317; d) for a review on ring-rearrangement metathesis, see: S. Basra, S. Blechert, *Strategies and Tactics in Organic Synthesis*, *Vol. 4*, **2005**, p. 315.

[3] J. A. Tallarico, L. A. Malnick, M. L. Snapper, *J. Org. Chem.* **1999**, *64*, 344.

[4] J. Louie, C. W. Bielawski, R. H. Grubbs, *J. Am. Chem. Soc.* **2001**, *123*, 11312.

[5] S. S. Kinderman, J. H. van Maarseveen, H. E. Shoemaker, H. Hiemstra, F. P. J. T. Rutjes, *Org. Lett.* **2001**, *3*, 2045.

[6] B. Alcaide, P. Almendros, J. M. Alonso, M. F. Aly, *Org. Lett.* **2001**, *3*, 3781.

[7] C. Cadot, P. I. Dalko, J. Cossy, *Tetrahedron Lett.* **2002**, *43*, 1839.

[8] For a review on non-metathetic behavior of ruthenium–carbenes, see: B. Alcaide, P. Almendros, *Chem. Eur. J.* **2003**, *9*, 1258.

[9] A. Ajamian, J. L. Gleason, *Angew. Chem.* **2004**, *116*, 3842; *Angew. Chem. Int. Ed.* **2004**, *43*, 3754.

[10] a) A. E. Sutton, B. A. Seigal, D. F. Finnegan, M. L. Snapper, *J. Am. Chem. Soc.* **2002**, *124*, 13390; b) B. Schmidt, *Eur. J. Org. Chem.* **2003**, 816.

[11] For a review on reaction sequences promoted by a single ruthenium–carbene precatalyst, see: B. Schmidt, *Eur. J. Org. Chem.* **2004**, 1865.

[12] F. A. Khan, J. Dash, N. Sahu, C. Sudheer, *J. Org. Chem.* **2002**, *67*, 3783.

[13] S. Torii, T. Inokuchi, K. Kondo, *J. Org. Chem.* **1985**, *50*, 4980.

[14] L. Gonsalve, I. W. C. E. Arends, R. A. Sheldon, *Chem. Commun.* **2002**, 202.

[15] S. Roth, S. Göhler, H. Cheng, C. B. W. Stark, *Eur. J. Org. Chem.* **2005**, 4109.

[16] For reviews on oxidation with $RuO_4$, see: a) S.-I. Murahashi, N. Komiya in *Ruthenium in Organic Synthesis* (Ed.: S.-I. Murahashi), Wiley-VCH, Weinheim, **2004**, pp. 53–93; b) B. Plietker, *Synthesis* **2005**, 2453.

[17] P. H. Carlsen, T. Katsuki, V. S. Martin, K. B. Sharpless, *J. Org. Chem.* **1981**, *46*, 3936.

[18] T. K. M. Shing, V. W.-F. Tai, E. K. W. Tam, *Angew. Chem.* **1994**, *106*, 2408; *Angew. Chem. Int. Ed. Engl.* **1994**, *33*, 2312.

[19] a) B. Plietker, M. Niggemann, *Org. Lett.* **2003**, *5*, 3353; b) B. Plietker, M. Niggemann, *J. Org. Chem.* **2005**, *70*, 2402.

[20] a) T. K. M. Shing, E. K. W. Tam, V. W.-F. Tai, I. H. F. Chung, Q. Jiang, *Chem. Eur. J.* **1996**, *2*, 50; b) B. Plietker, M. Niggemann, A. Pollrich, *Org. Biomol. Chem.* **2004**, *2*, 1116.

[21] For a review on cross metathesis, see: S. J. Connon, S. Blechert, *Angew. Chem.* **2003**, *115*, 1944; *Angew. Chem. Int. Ed.* **2003**, *42*, 1900.

[22] a) S. Randl, S. Gessler, H. Wakamatsu, S. Blechert, *Synlett* **2001**, 430; b) S. Imhof, S. Randl, S. Blechert, *Chem. Commun.* **2001**, 1692.

 © 2006 Wiley-VCH Verlag GmbH & Co. KGaA, Weinheim 

Azides

DOI: 10.1002/anie.200503986

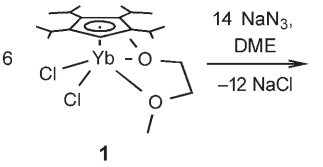
# A Hexanuclear Ytterbium Complex Anion with Fourteen Azido Ligands**

*Marc D. Walter, Frank Weber, Gotthelf Wolmershäuser, and Helmut Sitzmann**

*Dedicated to Professor Herbert Schumann on the occasion of his 70th birthday*

Azides are of fundamental interest for experimental[1–5] and theoretical[6] work. The different coordination modes available to the azido ligand offer great flexibility in the self-assembly of extended networks or interesting clusters, which have been well studied for transition metals.[4,7] However, organolanthanide azides,[8] with the exception of $[Li(thf)_4][Cp_3Sm{-}N_3{-}SmCp_3]$ ($Cp = C_5H_5$),[9] have not been thoroughly investigated.

Herein, we report the first monocyclopentadienyl ytterbium azido complex, which is formed by the slow reaction of the half-sandwich complex $[^4CpYbCl_2(dme)]$ (**1**; $^4Cp = C_5H(CHMe_2)_4$)[10] with sodium azide in dimethoxyethane (DME) at ambient temperature [Eq. (1)]. The red-




(1)

purple product (**2**) is insoluble in aliphatic (such as pentane or *n*-hexane) or aromatic solvents, but moderately soluble in ethers (such as diethyl ether or DME). IR spectra of **2** show three strong absorptions at 2083, 2170, and 2189 $cm^{-1}$, and one absorption of medium intensity at 2127 $cm^{-1}$. These observations are indicative of an oligomeric structure.

Crystals suitable for an X-ray diffraction experiment were grown from a concentrated DME solution at −15 °C. The crystals lose coordinated solvent at 90–150 °C, and their color changes to light blue; however, up to 250 °C no further visible changes take place. No shock-sensitivity was observed (for more information on this topic, see ref. [11]).

The molecular structure of **2** consists of a centrosymmetric aggregate of the type $[Na(dme)_3]_2[^4Cp_6Yb_6(\mu_{1,1'}\text{-}N_3)_2(\mu_{1,3}\text{-}$

[*] Dr. M. D. Walter, Dr. F. Weber, Dr. G. Wolmershäuser, Prof. Dr. H. Sitzmann
Fachbereich Chemie
Technische Universität Kaiserslautern
Erwin-Schrödinger-Strasse, 67663 Kaiserslautern (Germany)
Fax: (+49) 631-205-4676
E-mail: sitzmann@chemie.uni-kl.de

[**] We thank Professor O. J. Scherer for helpful discussions.


© 2006 Wiley-VCH Verlag GmbH & Co. KGaA, Weinheim

$N_3)_{10}(\mu_{1,1',3}\text{-}N_3)_2]$, in which the two $[Na(dme)_3]^+$ ions are positioned between the ytterbium cluster anions. The six {$^4$CpYb} units of the anion describe a slightly distorted octahedron (Figure 1). These units are linked together to give

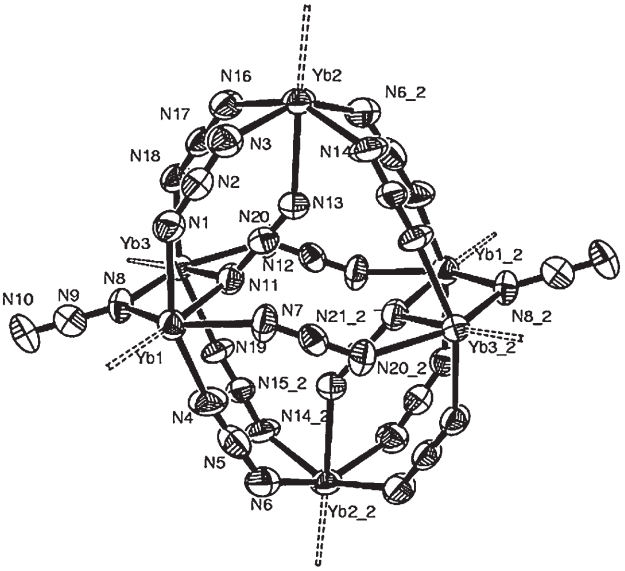



***Figure 1.*** ORTEP diagram of the $[^4Cp_6Yb_6(N_3)_{14}]^{2-}$ ion of **2** (thermal ellipsoids set at 50% probability). $^4$Cp rings are omitted for clarity. Atoms with labels bearing "_2" are generated by the symmetry operation: $-x, -y, -z$. Selected interatomic distances [Å] and angles [°]: N8–N9 1.263(11), N9–N10 1.128(10), N11–N12 1.224(10), N12–N13 1.146(10), Yb1–N1 2.323(8), Yb1–N4 2.265(8), Yb1–N7 2.309(8), Yb1–N8 2.434(7), Yb1–N11 2.405(9), Yb2–N3 2.316(10), Yb2–N6_2 2.319(10), Yb2–N13 2.524(7), Yb2–N14 2.291(9), Yb2–N16 2.366(8), Yb3–N8 2.397(8), Yb3–N11 2.462(8), Yb3–N18 2.328(7), Yb3–N19 2.279(7), Yb3–N20 2.336(8), Yb1···Yb2 5.910(1), Yb1···Yb3 4.032(1), Yb1···Yb1_2 7.526(2), Yb1···Yb3_2 6.476(1), Yb2···Yb3 5.981(1), Yb2···Yb2_2 9.602(1); N1-N2-N3 178.1(11), N4-N5-N6 178.3(12), N8-N9-N10 179.0(12), N11-N12-N13 176.4(10), N14_2-N15_2-N19 178.1(12), N16-N17-N18 178.3(11), N7-N21_2-N20_2 178.1(11).

two vertical sixteen-membered {$Yb_4N_{12}$} rings, which share Yb2 and Yb2_2, and an equatorial twelve-membered {$Yb_4N_8$} ring in a chair conformation (Figure 1). The two {Yb-N-Yb} fragments of the twelve-membered ring are each additionally bridged by the terminal nitrogen atom of another azido ligand, giving rise to two four-membered {$Yb_2N_2$} rings, which are folded at an angle of 173.5° along the Yb3-Yb1 (or Yb3_2-Yb1_2) axis (Figure 2). The edge-defining distances between ytterbium centers in the $Yb_6$ octahedron vary from 4.032(1) to 5.981(1) Å.

In organolanthanide chemistry, hexanuclear complexes with octahedral structures have been observed with 1) chloro bridges, for example, $[Cp_3Yb_3Cl_5(thf)_3]^+[Cp_6Yb_6Cl_{13}]^-$,[12] $[Li(thf)_4]_2[(C_5Me_4SiMe_2t\text{Bu})Yb_6I_8]$,[13] and $[Na(OEt_2)_x][^4Cp_6La_6Cl_{13}]$,[14] 2) selenido bridges, for example, $[(C_5Me_5)_6Sm_6Se_{11}]$,[15] or 3) tetrahydroborato bridges, for example, $[(C_5Me_4n\text{Pr})_6Sm_6(BH_4)_{12}]$.[16]

The Yb–$^4$Cp(centroid) distance of 2.33 Å is identical with that in **1**.[10] The N–N distances within the $\mu_{1,3}$-bridging azido ligands vary from 1.144(11) to 1.204(13) Å, in good agreement with the distances found in $[Li(thf)_4][Cp_3Sm\text{–}N_3\text{–}SmCp_3]$.[9] The variation in these N–N distances is insignificant, considering their standard deviations. However, the $N_\alpha$–$N_\beta$ distances of 1.263(11) and 1.224(10) Å for N8–N9 and N11–N12, respectively, are longer than the $N_\beta$–$N_\gamma$ distances of 1.128(10) and 1.146(10) Å for N9–N10 and N12–N13, respectively. Similar distances have been reported for complexes with terminal azido ligands, for example, $[Ti(N_3)_6]^{2-}$,[17] or $[(1,2,4\text{-}(Me_3C)_3C_5H_2)_2U(N_3)_2]$.[18] In purely ionic azides, the N–N bonds within the azido ligand usually have the same length of approximately 1.18 Å, whereas in covalent azides significantly larger differences between the two N–N distances are observed, typical values for the $N_\alpha$–$N_\beta$ and $N_\beta$–$N_\gamma$ bonds being 1.24 and 1.13 Å, respectively.[19] All of the azido groups in **2** are nearly linear, with an average N-N-N angle of 178(2)°, the expected value for ionic metal azides.[5]

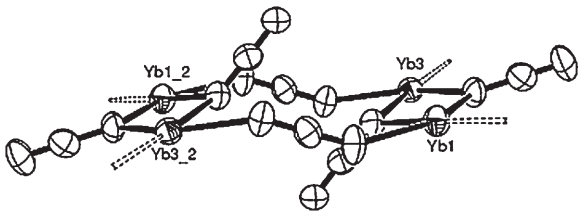



***Figure 2.*** ORTEP diagram of the equatorial ring in the $[^4Cp_6Yb_6(N_3)_{14}]^{2-}$ ion of **2** (thermal ellipsoids set at 50% probability; Yb partially shaded, N open). $^4$Cp rings are omitted for clarity. Atoms with labels bearing "_2" are generated by the symmetry operation: $-x, -y, -z$.

The lighter members of the lanthanide series (to the left of ytterbium), which have larger atomic radii, tend to exhibit similar reactivity to ytterbium. In future work, we will, therefore, perform analogous reactions with the lighter lanthanide metals.

## Experimental Section

**2**: A blue-purple solution of **1**[10](0.85 g, 1.51 mmol) in DME (15 mL) was stirred with sodium azide (0.20 g, 3.07 mmol) for 3 days at ambient temperature. The solvent was removed under vacuum, and the red-purple residue was extracted with diethyl ether (4 × 10 mL). Centrifugation and concentration of the combined extracts gave a dark red-purple solid, which was washed with pentane (2 × 4 mL) and dried under vacuum (0.53 g, 0.147 mmol, 58.2%). Although no shock sensitivity was observed, the compound should be handled with great care. Crystals suitable for X-ray diffraction were grown from a concentrated DME solution at −15 °C. The crystals lose coordinated solvent at 90–150 °C and change color to light blue, but do not melt upon heating to 250 °C. Elemental analysis (%) calcd for $Na_2C_{126}H_{234}O_{12}N_{42}Yb_6$ (3613.74): C 41.88, H 6.53, N 16.28; found: C 41.63, H 5.96, N 17.13. IR (Nujol): $\tilde{\nu}$ = 2189 (s), 2170 (s), 2127 (m), 2083 cm$^{-1}$ (s).

Crystal data for **2**: $C_{126}H_{234}N_{42}Na_2O_{12}Yb_6$, $M_r$ = 3613.74, triclinic, $P\bar{1}$, $a$ = 15.9778(16), $b$ = 16.741(2), $c$ = 17.2818(19) Å, $\alpha$ = 115.426(13), $\beta$ = 91.198(13), $\gamma$ = 94.089(13)°, $V$ = 4157.5(8) Å$^3$ at $T$ = 173(2) K, $Z$ = 1, $\rho_{calcd}$ = 1.443 Mg m$^{-3}$, $\mu(Mo_{K\alpha})$ = 3.407 mm$^{-1}$, $F(000)$ = 1822, 50290 reflections collected, 18438 independent reflections, GOF = 0.759, $R_1$ = 0.0507, $wR_2$ = 0.1089. Hydrogen atoms were refined in idealized positions. All calculations were performed with SHELXS-97 and SHEXL-97.[20] CCDC-288348 contains the supplementary crystallographic data for this paper. These data can be

 © 2006 Wiley-VCH Verlag GmbH & Co. KGaA, Weinheim 

obtained free of charge from The Cambridge Crystallographic Data Centre via www.ccdc.cam.ac.uk/data_request/cif.

Received: November 9, 2005
Published online: February 22, 2006

**Keywords:** azides · cluster compounds · solid-state structures · ytterbium

[1] L. F. Audrieth, *Chem. Rev.* **1934**, *34*, 169.
[2] Z. Dori, R. F. Ziolo, *Chem. Rev.* **1973**, *73*, 247.
[3] O. Reckeweg, A. Simon, *Z. Naturforsch. B* **2003**, *58*, 1097.
[4] F. Karau, W. Schnick, *Z. Anorg. Allg. Chem.* **2005**, *631*, 2315.
[5] I. C. Tornieporth-Oetting, T. M. Klapötke, *Angew. Chem.* **1995**, *107*, 559; *Angew. Chem. Int. Ed. Engl.* **1995**, *34*, 511.
[6] L. Gagliardi, P. Pyykkö, *Inorg. Chem.* **2003**, *42*, 3074.
[7] S. Han, J. L. Manson, J. Kim, J. S. Miller, *Inorg. Chem.* **2000**, *39*, 4182.
[8] H. Schumann, J. A. Meese-Marktscheffel, L. Esser, *Chem. Rev.* **1995**, *95*, 865.
[9] H. Schumann, C. Janiak, J. Pickardt, *J. Organomet. Chem.* **1988**, *349*, 117.
[10] H. Sitzmann, O. Schmitt, F. Weber, G. Wolmershäuser, *Z. Anorg. Allg. Chem.* **2001**, *627*, 12.
[11] A. Kornath, *Angew. Chem.* **2001**, *113*, 3231; *Angew. Chem. Int. Ed.* **2001**, *40*, 3135.
[12] W. P. Kretschmer, J. H. Teuben, S. I. Troyanov, *Angew. Chem.* **1998**, *110*, 92; *Angew. Chem. Int. Ed.* **1998**, *37*, 88.
[13] S. P. Constantine, G. M. De Lima, P. B. Hitchcock, J. M. Keates, G. A. Lawless, *Chem. Commun.* **1996**, 2421.
[14] O. Schmitt, Ph.D. Thesis, Universität Kaiserslautern **2001**.
[15] W. J. Evans, G. W. Rabe, M. A. Ansari, J. W. Ziller, *Angew. Chem.* **1994**, *106*, 2200; *Angew. Chem. Int. Ed. Engl.* **1994**, *33*, 2110.
[16] F. Bonnet, M. Visseaux, D. Barbier-Baudry, A. Hafid, E. Vigier, M. M. Kubicki, *Inorg. Chem.* **2004**, *43*, 3682.
[17] R. Haiges, J. A. Boatz, S. Schneider, T. Schroer, M. Yousufuddin, K. O. Christe, *Angew. Chem.* **2004**, *116*, 3210; *Angew. Chem. Int. Ed.* **2004**, *43*, 3148.
[18] G. Zi, L. Jia, E. L. Werkema, M. D. Walter, J. P. Gottfriedsen, R. A. Andersen, *Organometallics* **2005**, *24*, 4251.
[19] W. Fraenk, T. M. Klapötke in *Inorganic Chemistry Highlights* (Eds.: G. Meyer, D. Naumann, L. Wesemann), Weinheim, Wiley-VCH, **2002**, pp. 259–278.
[20] G. M. Sheldrick, SHELXS-97, Program for crystal structure solution, Universität Göttingen, **1997**; G. M. Sheldrick, SHELXL-97, Program for crystal structure refinement, Universität Göttingen, **1997**.

 © 2006 Wiley-VCH Verlag GmbH & Co. KGaA, Weinheim 

Morphogenesis (1)

DOI: 10.1002/anie.200503610

# Biomimetic Fluorapatite–Gelatine Nanocomposites: Pre-Structuring of Gelatine Matrices by Ion Impregnation and Its Effect on Form Development**

*Harald Tlatlik, Paul Simon, Agnieszka Kawska, Dirk Zahn, and Rüdiger Kniep**

In the course of osteogenesis[1] and dentinogenesis[2] in vertebrates, functional materials such as bone and teeth are formed from apatite and proteins (collagen). The resulting hierarchically structured nanocomposites are dominated by a close orientational relationship between the triple-helical collagen molecules (arranged in form of fibrils) and the apatite nanocrystals which nucleate in the gaps between neighboring protein molecules. In these arrangements, the crystallographic *c* axes of the apatite nanocrystals are oriented parallel to the longitudinal direction of the fibrils.[3,4] In biological systems the mineralization process is controlled by metabolism and cell activity and hence is on a very high level of complexity.[5] To reduce this level of complexity in our experiments, an in vitro setup was chosen without cell activity and insoluble collagen was replaced by soluble gelatine (denatured collagen). The choice of gelatine gel increases the mobility of the proteins which eases rearrangements of protein fibers during the processes of self-organization. The mineral component, apatite, is added to the system in the form of aqueous solutions of the appropriate ions. The biomineralization process is mimicked by a double-diffusion system in which the ions migrate into the gelatine gel from opposite reservoirs containing solutions of calcium and phosphate/fluoride, respectively.

About 10 years ago we first reported a fractal growth mechanism of fluorapatite aggregates synthesized in gelatine matrices by double-diffusion experiments.[6] Subsequently, these aggregates were demonstrated to be structured on the nano-scale.[7] Moreover, the aggregates were identified as an inorganic–organic composite with about 2.3 wt% gelatine,[8] an amount which is also observed in mature tooth enamel.[9] The basic structural unit in the fractal aggregates is represented by an ideal, elongated hexagonal prism with an aspect ratio between 3:1 and 4:1. These hexagonal prisms had already been suggested to be of central significance for the biomimetic morphogenesis[10] and thus motivated TEM investigations which revealed a superstructure within the

[*] Dipl.-Ing. H. Tlatlik, Dr. P. Simon, Dipl.-Chem. A. Kawska, Dr. D. Zahn, Prof. Dr. R. Kniep
Max Planck Institute for the Chemical Physics of Solids
Nöthnitzer Strasse 40, 01187 Dresden (Germany)
Fax: (+49) 351-46-460-3002
E-mail: kniep@cpfs.mpg.de

[**] We gratefully acknowledge the Fonds der Chemischen Industrie for financial support.


© 2006 Wiley-VCH Verlag GmbH & Co. KGaA, Weinheim

fluorapatite–gelatine nanocomposite:[11] Apatite nanocrystals are arranged in a highly mosaic, controlled structure around the central gelatine molecules. The hexagonal (*c*-)axes of the apatite nanocrystals and the long axes of the protein macromolecules are in parallel orientation. A (diffuse) superstructure of about 5 nm (and multiples) periodicity was observed indicating the motif of a closest (rod-) packing of the nanocomposite units. The formation of the composite material is hence controlled by the gelatine molecules which bear the information about the local (nanometer scale) structure. These features allow the fluorapatite/gelatine nanocomposites to be regarded as a model system for the hierarchical growth steps and the formation of real structures during dentino- and osteogenesis.[12]

Phenomenological aspects of the fractal morphogenesis of fluorapatite–gelatine aggregates have been discussed from a materials chemistry point of view.[13] In a recent and interesting work the fluorapatite–gelatine composite and its morphogenesis (form development) were interpreted in terms of the formation and existence of "mesocrystals".[14] To illustrate the overall complexity, self-similarity, and the fractal character of the hierarchically grown fluorapatite–gelatine nanocomposites, a representative half-dumbbell-like aggregate is shown in Figure 1 together with a seed already showing initial stages of splitting. This kind of biomimetic morphogenesis clearly exceeds the form developments already known from pure inorganic minerals, such as sheave-bundles, dumbbells, and spherulites (ontogenesis of minerals),[15] and has its origin in the intrinsic structuring at the nanoscale level.

The experimental conditions for the growth of fluorapatite–gelatine nanocomposites were identical to our previous studies with the double-diffusion technique.[6,8,10,16] Recently, we started to quantify the diffusion of calcium and phosphate ions in gelatine gels and explored the effect of fluoride ions on the morphogenesis of calcium phosphate–gelatine composites.[17] Thereby, we again focused our interest on the periodic zones within the gelatine gel (so-called Liesegang bands) where the composite formation takes place. The Liesegang bands are denoted as P, M, and C, respectively, according to their local appearance in the gelatine plug: P and C bands next to the phosphate and the calcium source, respectively. The M bands (middle bands) are located between P and C. While the fractal growth mechanism (see Figure 1) dominates in the P and M bands, we identified a new, fan-like growth pattern which preferentially occurs in the C bands. Herein the two different growth mechanisms are highlighted in the Figures by blue frames (fractal) and red frames (fan-like). Both principles involve the initial formation of a hexagonal-prismatic seed and develop via dumbbell-like structures to spheres. Distinguishing the two form developments is thus far from trivial and requires the knowledge of specific morphological criteria.

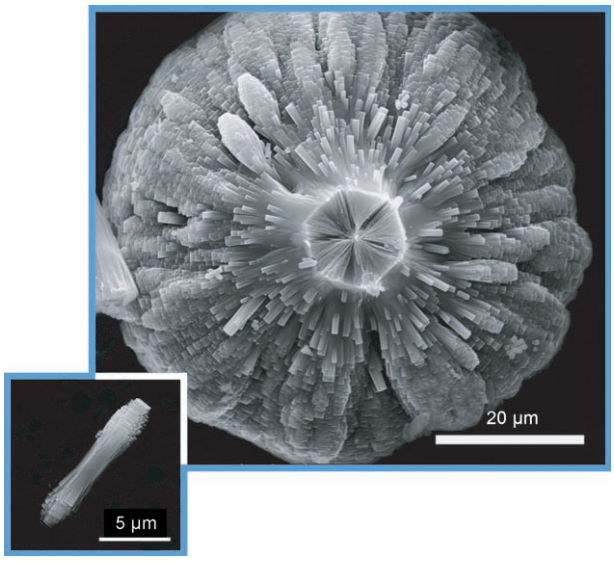



***Figure 1.*** Self-similarity and fractal pattern formation by growth of fluorapatite–gelatine nanocomposites (SEM images). Main picture: half of a dumbbell aggregate viewed along the central seed axis. Inset: Central seed exhibiting tendencies of splitting at both ends ("small" dumbbell). The development from "small" to "large" dumbbells implies a remarkable reduction of shape information, in which only the "club-motif" is transmitted.

In Figure 2 the two different morphogeneses (red: fan-like, C bands; blue: fractal, P and M bands) are illustrated by a series of six successive growth states. The key morphological differences are discussed on the basis of the red (fan-like) series: The central hexagonal prismatic seed has a compressed habit with an aspect ratio of about 2:1. The fan-like development evolves from a common (central) plane perpendicular to the hexagonal axis of the seed. The following structural units have a wedge-like shape with the size of their basal faces increasing during the growth process. The small opening angle of the "prism-faces" against the central axis already indicates an inner structure with a radial arrangement of sub-individuals which is best seen from the TEM pictures discussed later (Figure 4). The individual units growing on or out of the prismatic seed are separated by planar faces and straight edges. Bent shapes as characteristic for biological systems and also observed in the fractal growth series (framed in blue) do not occur. The surfaces of the dumbbells and spheres of the fan-like aggregate are characterized by a coarse hexagonal tiling reflecting the basal faces of the individuals. In the fractal growth series, however, the surface structures of the dumbbells and spheres become smaller and smaller. Both final growth states result in spheres with an equatorial notch. However, while the sphere-aggregates grown by the fractal growth mechanism exhibit a toroidal cavity around the seed,[6,8,10,16,17] the fan-like spheres are completely filled in the vicinity of their "intergrowth" plane. This observation is directly related to the absence of a "free bridge" in the center of the growing fan-like aggregates where as the free bridge is only found in the fractal growth (compare red arrows with the blue double arrows in Figure 2). To summarize all the observations made, the main differences between the fan-like and fractal morphogeneses may be characterized in terms of "crystallographical" (straight, hard) and "biological" (bent, soft), respectively.

The general principles of form developments and the transfer of information for both series of morphogeneses are expected to be already included in the structures of the central seeds and should be well recognized in those

 © 2006 Wiley-VCH Verlag GmbH & Co. KGaA, Weinheim 

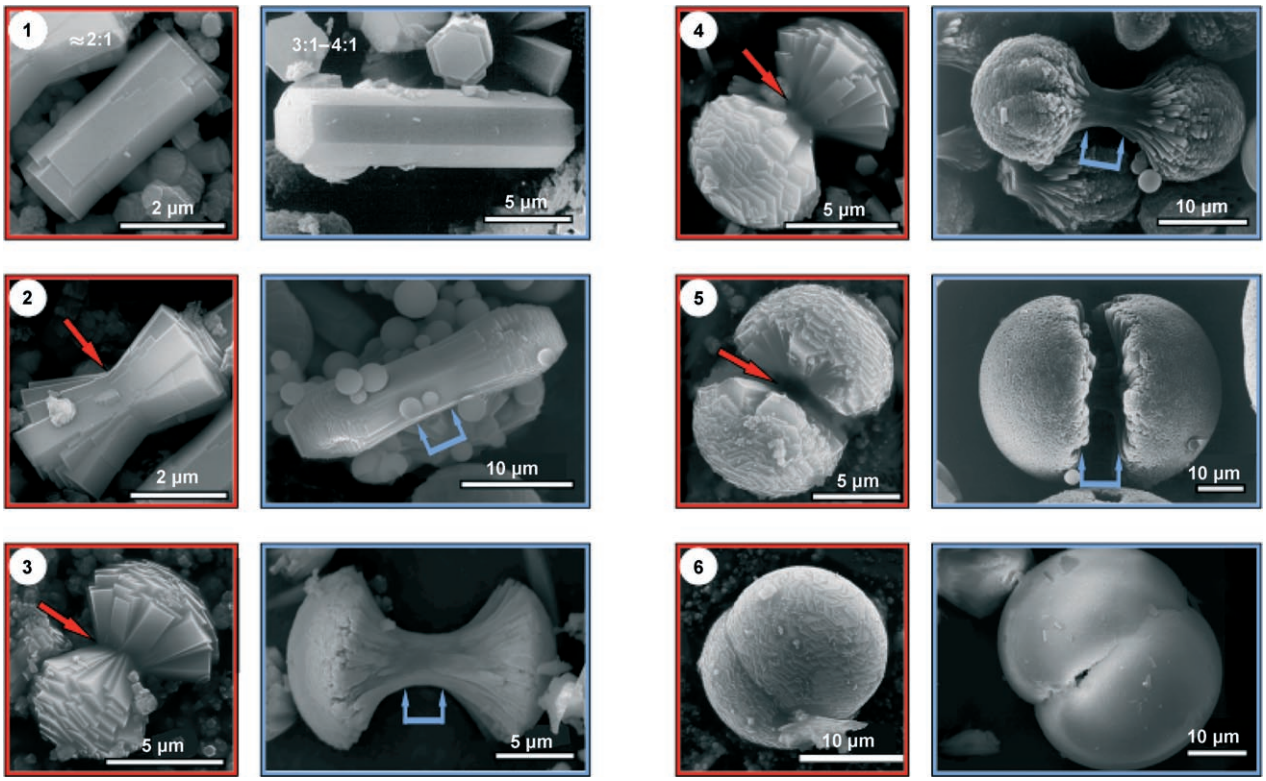



***Figure 2.*** SEM images illustrating subsequent states (1–6) of the morphogeneses of fluorapatite–gelatine nanocomposites for fan-like (red frames) and fractal (blue frames) growth mechanisms. The red and blue arrows indicate the growth plane and the "free bridge" respectively, see text for details.

aggregates which represent the states in which "splitting" begins (see growth states 2 in Figure 2). TEM investigations related to the fractal growth series showed that the origin for the development of the new generation lies deep inside a growing seed, even if the outer shape of the individual reveals only weak indications for beginning "splitting". It became clear from these observations that for the fractal series "splitting" is better described as an outgrowth-phenomenon (instead of "up growth") which is clearly seen in Figure 3 (top right). The "native" seed area (state 1 in Figure 2) is smaller than the central area highlighted in orange (Figure 3 top right) and the developing new generations come out of the core region like a blossom. These bent patterns are correlated with the orientation of gelatine fibers which seem to follow the development directions of the future generations. However, the fractal growth process may also be controlled by gelatine fibers first forming three-dimensional cones. This rearrangement of gelatine fibers would correspond to a new quality of self-organization in terms of hierarchical structuring, that would exceed the intrinsic properties of the hexagonal-prismatic seeds with their nanocomposite-superstructure.[11,12] Intense investigations are currently focused on this subject.

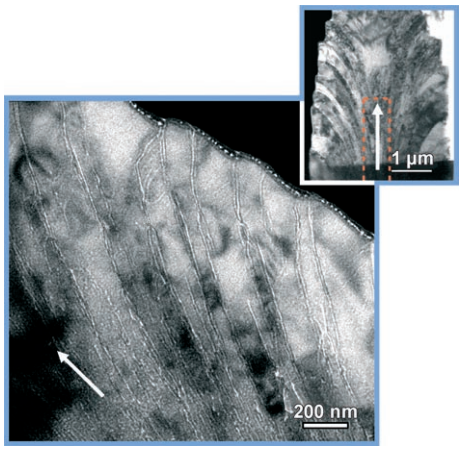



***Figure 3.*** TEM images of a fluorapatite–gelatine nanocomposite showing first tendencies for branching in the fractal growth series (growth state 2 in Figure 2, blue series). Cuts prepared by focused ion beam (FIB). White arrows indicate the direction of the hexagonal *c* axis of the central prismatic seed. Inset: Overview of one half of a prismatic seed with blossom-like development of a new generation, see text for details. Main picture: Gelatine fibrils with bent structures along the growth directions of the new generation.

In contrast to the fractal growth series with the more biological soft and bent motifs the fan-like morphogenesis appears more crystallographic with hard and straight shapes of the individuals. In fact, TEM investigations (Figure 4) indicate stiffness and rigidity of the organic component of the composite. The gelatine fibrils run as straight lines without orientational changes through the composite individuals. Inside each individual the fibrils seem to start from a single common origin and are arranged in a fan-like manner with only small opening angles. Details of this kind of growth mechanism are yet unknown as detailed analyses of the

 © 2006 Wiley-VCH Verlag GmbH & Co. KGaA, Weinheim 




***Figure 4.*** TEM images of a fluorapatite–gelatine nanocomposite individual showing first states of branching in the fan-like growth series (state 2 in Figure 2, red series). Cuts prepared by ultramicrotomy. Inset: Overview of the fan-like grown individual. Main picture: Enlarged section of an aggregate of wedge-like individuals. The dotted straight structures with a small opening angle represent the (calcified) organic component of the composite (gelatine).

structure of the central intergrowth plane are missing. To date, we have identified a pronounced radial structure of the intergrowth plane which is similar to the pattern found in the fracture area of a seed from the fractal growth series.

As the two types of morphogeneses exhibit a close correlation to the local areas of composite formation within the gelatine-gel plug, that is, fan-like (straight and hard) in the C bands and fractal (bent and soft) in the M and P bands, it appears reasonable to assume that this phenomenon is related to pre-structuring effects of the gelatine gels prior to the composite formation in the double diffusion cells. In this picture the different growth mechanisms depend on whether the gelatine gels are impregnated with calcium or phosphate ions first.

Recent atomic force microscopy (AFM) investigations in the formation of microcracks in bone and the corresponding healing processes as well as observations concerning the stress–strain behavior of collagen revealed that the presence of calcium ions accounts for stiffening of the organic matrix.[18–20] This effect was postulated to originate from the formation of ionic bonds between the calcium ions and charged groups of the collagen molecules. As clear evidence for this assumption is missing, we decided to further elucidate this question during our studies in the biomimetic morphogenesis of the fluorapatite–gelatine composites in the C bands. The C bands are located close to the calcium-ion source and are thus also expected to experience a stiffening effect of the gelatine molecules by calcium association. The apparent similarities are also of interest from a conceptional point of view: Confirmation of a stiffening effect would provide further evidence for the suitability of our model system to the study of steps in osteo- and dentinogenesis, that is, the biomineralization of bone and teeth.

We performed atomistic computer simulations to explore the interactions of aqueous solutions of calcium or phosphate ions with a gelatine molecule as well as possible conformational effects on the triple-helical protein. The fiber proteins were described by an all-atom model of three $(Gly\text{-}Pro\text{-}Hyp)_{12}$ polypeptide strands and empirical potential-energy functions were used to model the interactions of the triple helix with the water molecules and the ions.[21,22] Using a recently developed algorithm for the identification of adsorption sites[23,24] we performed a series of 100 independent aggregation experiments for each ionic species. From this series, a small number of characteristic binding positions could be isolated. The binding positions were found to dramatically depend on the associated ion species. The calcium ions form ionic bonds to the oxygen atoms of the carbonyl groups of the polypeptide backbone and to the side-chains of proline and hydroxyproline (Figure 5). Although calcium association may cause opening of some of the hydrogen bonds between the individual peptide strands of the triple-helix, only a marginal effect on the overall fiber structure is observed which causes only small configurational changes of a very local nature. For the phosphate ions we observe a completely different picture. In contrast to the calcium ions, the phosphate ions are preferentially bound outside the triple-helix. This process involves the formation of two to three hydrogen bonds with hydroxyproline side-groups and partially also with amino groups. In case of phosphate binding by only a few hydrogen bonds the fiber structure

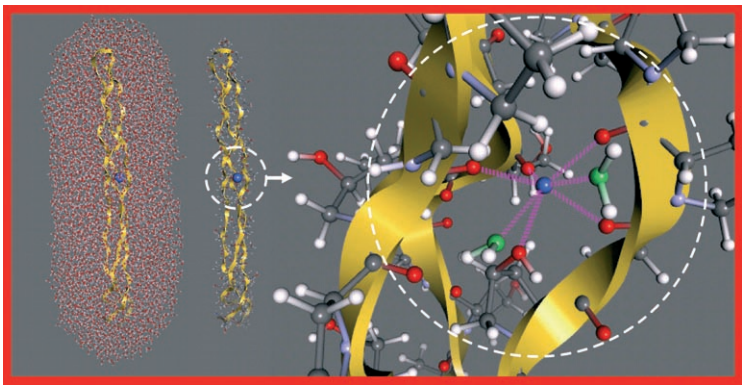


***Figure 5.*** Left: Model of a triple-helical polypeptide including a solvent shell (about 5000 water molecules) of 1.2 nm minimum thickness together with one attached (included) calcium ion. Yellow ribbons represent the backbones of the three peptide strands of the protein fiber. Middle: Same model without solvent molecules. Right: Enlargement of the binding site. Calcium forms ionic bonds (purple dashed lines) to carbonyl oxygen atoms of the protein ($d_{Ca\cdots O} \approx 2.3$ Å). Further ionic interactions involve oxygen atoms (highlighted in green) of neighboring water molecules ($d_{Ca\cdots O} \approx 2.7$ Å). (H white, O red, C gray, N light blue, Ca dark blue).

 © 2006 Wiley-VCH Verlag GmbH & Co. KGaA, Weinheim 

usually remains unaffected. However, in about 50% of our simulation runs phosphate aggregation caused heavy deformations of the polypeptide. Such a situation is illustrated for $[PO_4]^{3-}$ ion association in Figure 6. The protein fiber has a bent structure which originates from the local formation of three hydrogen bonds to the phosphate ion. Such tendencies for bending the polypeptide were also observed for $[HPO_4]^{2-}$ ion aggregation.

Whereas the gelatine molecules in the C bands are closest to the calcium (and chloride) solution, the phosphate ions have to pass the P and M bands before reaching the C band. During our double-diffusion experiments we may therefore expect a large number of calcium ions to be incorporated in the triple-helical structure of the fiber proteins of the C band before the nucleation of nanoapatite starts. This "structural pre-treatment" involves only calcium ions and is not influenced by the chloride ions which are observed to remain in solution.

The electrostatic repulsion of the incorporated calcium ions favors a straight arrangement of the fiber protein in which the binding sites are at maximum separation. The triple-helix thus experiences a stiffening effect. In the P bands an analogous tendency results from the Coulomb repulsion of the phosphate ions associated to the protein fiber. However, this effect competes with the local bending originating from the lateral (external) take up of the phosphate group (Figure 6). We expect this combination of phenomena with opposite effects to considerably increase the conformational complexity of the triple helices. This implies a large number of possible structures for protein fibers impregnated with phosphate ions which may account for an enhanced flexibility.

In analogy to the chloride ions, the sodium ions which act as counterions in the phosphate/fluoride solution do not have a significant effect on the gelatine molecules. While our simulations showed only a weak tendency for the association of sodium or chloride ions, this does not apply to the fluoride ions. The latter are present in the phosphate solution close to the P band. Unlike the phosphate ions, the fluoride ions are found to form only one single contact to the fiber protein, thereby only marginally affecting the local structure of the triple-helix.

The results of our molecular dynamics simulations fully support our experimental observations for the fan-like and the fractal morphogeneses. The form development of the fluorapatite–gelatine composites is controlled by both the self-organized growth of the inorganic (nanoapatite)/organic (gelatine) composite and by the structural pre-treatment of gelatine by ion impregnation. The ion pre-treatment of gelatine may involve two competing effects resulting in various intermediate forms between fan-like and fractal growth as illustrated in Figure 7. Such aggregates are preferentially found in the M bands and depend on the growth state and the local supply of ions (the migration of calcium ions into the gelatine gels is faster than of phosphate ions). A detailed investigation of these issues is yet to come.[25] However, the identification of the "real" origin of the "symmetric" growth mechanism seed→dumbbell→sphere of the fluorapatite–gelatine nanocomposites is a more important task. The latter issue might reflect a general principle of the formation of growth patterns in nanostructured biominerals and is currently under investigation by means of electron holography.[26]

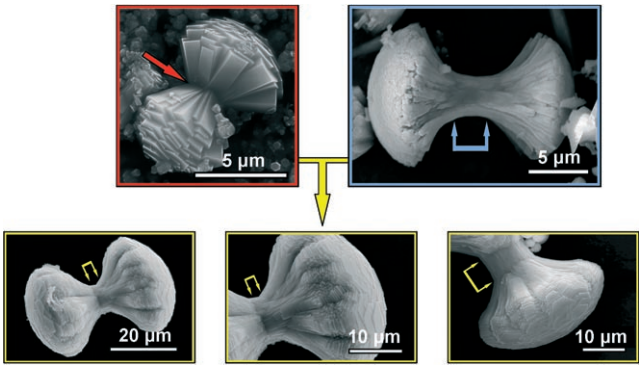



***Figure 7.*** SEM images of fluorapatite–gelatine composites in dumbbell morphology (states 3 in Figure 2). Aggregates formed by the fan-like (red) and the fractal (blue) growth mechanism, respectively. The yellow-framed series represents transitional growth states, resulting from a mixture of both archetypes in various dumbbell developments and surface tillings. The red and blue arrows indicate the growth plane and free bridge, respectively, the yellow arrows indicate these features in the hybrid structures.

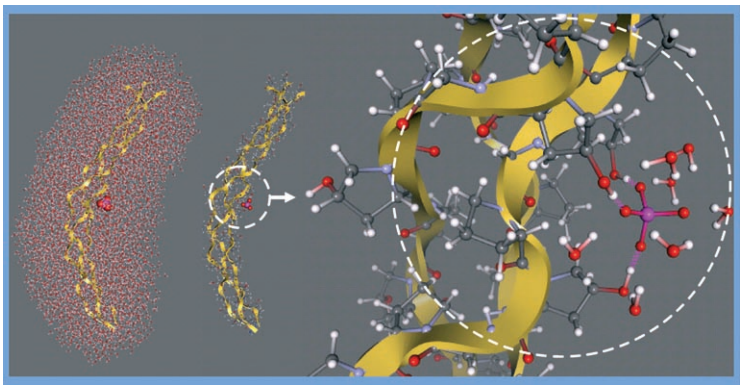


***Figure 6.*** Same as Figure 5, but illustrating the association of a phosphate ion. For clarity only the hydrogen bonds of the phosphate ion to the protein fiber ($d_{O\cdots H} \approx 1.3$ Å) are depicted (dashed purple lines). Though three hydroxyproline–phosphate bonds are formed, only two strands of the triple-helix are involved. This imbalance causes tensile stress to the right side of the fiber, while the left side is less affected. As a consequence, the previously straight polypeptide is bent. (H white, O red, C gray, N light blue, P purple).

Received: October 12, 2005
Revised: November 25, 2005
Published online: February 22, 2006

**Keywords:** biomineralization · composite materials · fluorapatite · molecular dynamics · morphogenesis

 © 2006 Wiley-VCH Verlag GmbH & Co. KGaA, Weinheim 

[1] W. Jahnen-Dechent in *Biomineralization, Progress in Biology, Molecular Biology and Application, 2nd ed.* (Ed.: E. Bäuerlein), Wiley-VCH, Weinheim, **2004**.

[2] K. Reichenmiller, Ch. Klein in *Biomineralization, Progress in Biology, Molecular Biology and Application, 2nd ed.* (Ed.: E. Bäuerlein), Wiley-VCH, Weinheim, **2004**.

[3] B. R. Heywood, N. H. C. Sparks, R. P. Shellis, S. Weiner, S. Mann, *Connect. Tissue Res.* **1990**, *25*, 103 – 119.

[4] W. J. Landis, K. J. Hodgens, J. Arena, M. J. Song, B. F. McEwen, *Microsc. Res. Tech.* **1996**, *33*, 192 – 202.

[5] *Chemistry for the 21st Century* (Eds.: E. Keinan, I. Schlechter), Wiley-VCH, Weinheim, **2001**.

[6] R. Kniep, S. Busch, *Angew. Chem.* **1996**, *108*, 2787 – 2791; *Angew. Chem. Int. Ed. Engl.* **1996**, *35*, 2624 – 2626.

[7] S. Busch, U. Schwarz, R. Kniep, *Chem. Mater.* **2001**, *13*, 3260 – 3271.

[8] S. Busch, U. Schwarz, R. Kniep, *Adv. Funct. Mater.* **2003**, *13*, 189 – 198.

[9] W. E. Harzer in *Die Evolution der Zähne* (Eds.: K. Alt, W. Türp), Quintessenz, Berlin, **1997**.

[10] S. Busch, H. Dolhaine, A. DuChesne, S. Heinz, O. Hochrein, F. Laeri, O. Podebrand, U. Vietze, T. Weiland, R. Kniep, *Eur. J. Inorg. Chem.* **1999**, 1643 – 1653.

[11] P. Simon, W. Carrillo-Cabrera, P. Formanek, C. Göbel, D. Geiger, R. Ramlau, H. Tlatlik, J. Buder, R. Kniep, *J. Mater. Chem.* **2004**, *14*, 2218 – 2224.

[12] P. Simon, U. Schwarz, R. Kniep, *J. Mater. Chem.* **2005**, *15*, 4992 – 4996.

[13] E. Dujardin, S. Mann, *Adv. Mater.* **2002**, *14*, 775 – 788.

[14] H. Cölfen, M. Antonietti, *Angew. Chem.* **2005**, *117*, 5714 – 5730; *Angew. Chem. Int. Ed.* **2005**, *44*, 5576 – 5591.

[15] D. P. Grigor'ev, *Ontongeny of Minerals*, Israel Program for Scientific Translations, Jerusalem, **1965**.

[16] R. Kniep in *Facetten einer Wissenschaft* (Eds.: A. Müller, H. J. Quadbeck-Seeger, E. Diemann), Wiley-VCH, Weinheim, **2004**.

[17] C. Göbel, P. Simon, J. Buder, H. Tlatlik, R. Kniep, *J. Mater. Chem.* **2004**, *14*, 2225 – 2230.

[18] J. B. Thompson, J. H. Kindt, B. Drake, H. G. Hansma, D. E. Morse, P. K. Hansma, *Nature* **2001**, *414*, 773 – 776.

[19] J. Currey, *Nature* **2001**, *414*, 699.

[20] G. E. Fantner, T. Hassenkam, J. H. Kindt, J. C. Weaver, H. Birkedal, L. Pechenik, J. A. Cutroni, G. A. G. Cidade, G. D. Stucky, D. E. Morse, P. K. Hansma, *Nat. Mater.* **2005**, *4*, 612 – 616.

[21] D. Zahn, O. Hochrein, *Phys. Chem. Chem. Phys.* **2003**, *5*, 4004 – 4007.

[22] A. D. MacKerell, D. Bashford, R. L. Bellott, R. L. Dunbrack, J. D. Evanseck, M. J. Field, S. Fischer, J. Gao, H. Guo, S. Ha, D. Joseph-McCarthy, L. Kuchnir, K. Kuczera, F. T. K. Lau, C. Mattos, S. Michnick, T. Ngo, D. T. Nguyen, B. Prodhom, W. E. Reiher, B. Roux, M. Schlenkrich, J. C. Smith, R. Stote, J. Straub, M. Watanabe, J. Wiorkiewicz-Kuczera, D. Yin, D. M. Karplus, *J. Phys. Chem. B* **1998**, *102*, 3586 – 3616.

[23] A. Kawska, J. Brickmann, O. Hochrein, D. Zahn, *Z. Anorg. Allg. Chem.* **2005**, *631*, 1172 – 1176.

[24] A. Kawska, J. Brickmann, R. Kniep, O. Hochrein, D. Zahn, *J. Chem. Phys.* **2006**, 024513.

[25] Migration velocity and diffusion coefficients of calcium and phosphate ions in gelatine gel matrices are currently under examination. The simple double-diffusion setup[6,8,10,16] used does not allow the measurement of spatial and temporal developments of ion concentrations and pH values. For compensation of this problem the reaction parameters are kept constant.

[26] P. Simon, D. Zahn, H. Lichte, R. Kniep, *Angew. Chem.* **2006**, *118*, 1945 – 1949; *Angew. Chem. Int. Ed.* **2006**, *45*, 1911 – 1915.


 © 2006 Wiley-VCH Verlag GmbH & Co. KGaA, Weinheim 

*Morphogenesis (2)*

DOI: 10.1002/anie.200504465

# Intrinsic Electric Dipole Fields and the Induction of Hierarchical Form Developments in Fluorapatite–Gelatine Nanocomposites: A General Principle for Morphogenesis of Biominerals?**

*Paul Simon, Dirk Zahn, Hannes Lichte, and Rüdiger Kniep**

The biomimetic system fluorapatite–gelatine bears strong resemblance to the biosystem hydroxyapatite–collagen which plays a decisive role in the human body as functional material in the form of bone[1] and teeth.[2] In both systems, the hierarchical and self-similar organization of nanocomposite structures is of prominent relevance.[3–6] The morphogenesis of fluorapatite–gelatine nanocomposites offers the advantage of revealing a concise sequence of growth developments, whereas bone and teeth are formed by a much more complex process with involvement of cell activities in a living system. Substitution of the rigid, insoluble collagen by water-soluble gelatine (denatured collagen) provides a high mobility and accessibility and thus enhances the reactivity of the functional groups of the biopolymer derivative.

Fluorapatite–gelatine nanocomposites (about 98 wt% apatite) are grown in buffered aqueous solutions of calcium, phosphate, and fluoride ions, which migrate into a gelatine-gel plug in a double-diffusion cell.[7–14] Within a few days, so-called Liesegang bands are formed consisting of the grown composite aggregates. Depending on the position of the Liesegang bands within the gelatine-gel plug two different kinds of morphogeneses are observed:[14] A fan-like aggregate development close to the calcium source in the double-diffusion cell and a fractal morphogenesis in those bands which are close to the phosphate/fluoride source. It was shown by molecular dynamics simulations[14] that pre-impregnation of gelatine by calcium ions causes stiffening and rigidity of the triple-helical molecules, whereas pre-impregnation by phosphate ions (and protonated variants) keeps the gelatine macromolecules flexible. Herein, we restrict our focus on the fractal growth series with the more flexible organic component which not only allows the formation of straight (linear) but even of bent patterns of gelatine.

Initial stages of the fractal growth comprise micrometer-sized, hexagonal-prismatic composite seeds (marked violet in Figure 1a). These species develop in subsequent growth stages to dumbbells states and complete their development as closed spheres with an equatorial notch (Figure 1a). The morphogenesis can be described in terms of a fractal growth mechanism with a total of about ten generations and a reduction factor of about 0.7 in successive generations.[8,11] The presence of mineralized macromolecules in the fluorapatite–gelatine nanocomposites was shown in earlier works.[12,13] The appearance of dislocations and a resulting superstructure pattern at the nanometer scale observed in transmission electron microscopy (TEM) high-resolution micrographs indicate the presence of incorporated gelatine macromolecules running parallel [001] within the composite seed. The superstructure is visualized in the fast Fourier transform (FFT) of the high-resolution images in form of diffuse streaks around the primary beam with a periodicity of about 5 nm and multiples of this value (Figure 1b).[12] The diffuse streaks are running parallel to the (100) planes of

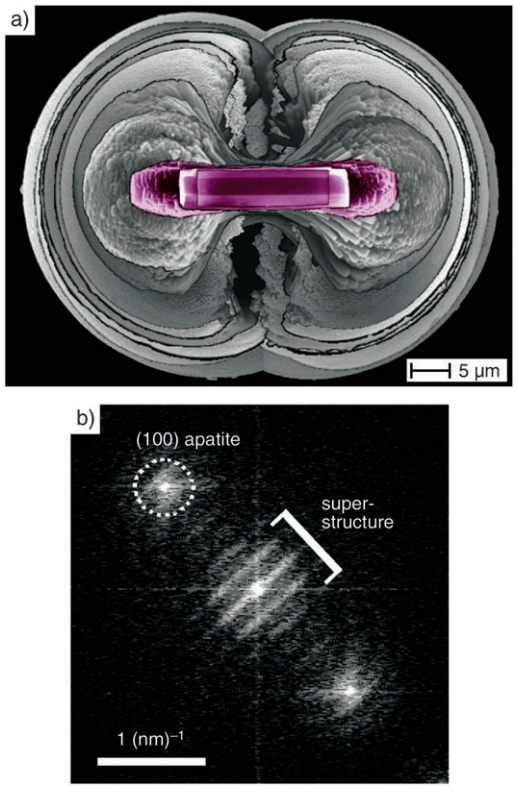



***Figure 1.*** a) Superposition of growth stages of fractal fluorapatite–gelatine nanocomposite aggregates (scanning electron microscopy images). The morphogenesis starts with an elongated hexagonal-prismatic seed, which develops by out-growth areas at both ends (central violet area). Subsequently, the aggregate forms dumbbell shaped structures, and finally ends up with a closed sphere (with an equatorial notch). b) The FFT of TEM high-resolution micrographs showing the superstructure of the central composite seed (caused by mineralized gelatine triple helices) as diffuse streaks around the primary beam corresponding to a periodicity of about 5 nm and multiples of this value. For further details see text.

[*] Dr. P. Simon, Dr. D. Zahn, Prof. Dr. R. Kniep
Max Planck Institute for the Chemical Physics of Solids
Nöthnitzer Strasse 40, 01187 Dresden (Germany)
Fax: (+49) 351-46-460-3002
E-mail: kniep@cpfs.mpg.de
Prof. Dr. H. Lichte
Institute of Structure Physics
Triebenberg Laboratory for High-Resolution Electron Microscopy and Holography
Technical University of Dresden
Zum Triebenberg 50, 01328 Dresden Zaschendorf (Germany)

[**] We thank the Fonds der Chemischen Industrie for generous support. We also thank Dr. W. Carrillo-Cabrera and Dr. P. Formanek for fruitful discussions and experimental help with FIB.

 © 2006 Wiley-VCH Verlag GmbH & Co. KGaA, Weinheim 

apatite, thus showing the ordered intergrowth of the organic and the inorganic components.[13]

In 1999, a possible influence of intrinsic electric fields on the fractal morphogenesis of fluorapatite–gelatine nanocomposite aggregates was discussed.[8,11] Model calculations of the electric fields around simulated (schematic) seed and dumbbell states were carried out, whereas detailed knowledge of the inner structure of these growth stages was not available at that time.[8] A change of morphology could be achieved by applying an external electric field ($E = 5000\ \mathrm{V}\,(1.4\ \mathrm{cm})^{-1}$ DC).[8] Generally, the growth rate was lowered and rounded up-growth regions were observed instead of the prismatic splitting of the seed found without the external field. The influence of electric fields on other relevant biological systems could be also proved. In 1996, Yamashita et al. demonstrated that the growth rate of bone-like layers can be affected by surface polarization of hydroxyapatite (HAp) or ferroelectric $BaTiO_3$ substrates by an applied external electric field.[15] This observation has a potentially large impact for bone implantation because there is interest in inducing apatite mineralization on synthetic substrates and to stimulate bone adhesion on the implant.[16] In addition, the piezoelectric effect of bone was used by applying external electric fields to improve the bone healing processes. Inside bone and tendon, collagen fibrils are arranged parallel to their long axes. The triple-helical molecules exhibit point group 3 and can be both piezo- and pyroelectric. The generation of electric fields caused by mechanical stress is attributed to the piezoelectric effect of collagen, whereas pyroelectricity proved to be low.[17] Fluorapatite features the centrosymmetric crystal class 6/*m*, therefore neither piezo- nor pyroelectricity can be considered. However, Yamashita et al. showed, that in the case of hydroxyapatite, polarizability is caused by a reorientation of the dipole moments of the $OH^-$ ions within the structural channels. In this way, accelerated crystal growth was observed on polarized HAp surfaces.[15]

The influence of an electric field on the mineralization process of polystyrenesulfonate (PSS) by $CaCO_3$ was observed by Cölfen et al.[18] Positive charging of the (001) crystal surface of calcite led to selective adsorption of negatively charged PSS molecules. Composite nanocrystal blocks formed which subsequently aggregated, thus forming "mesocrystals". Theoretical calculations showed that such non-spherical charged objects in an electrolyte solution cause an anisotropic electric potential, giving rise to mutual alignment. Recently, single-molecule manipulation by means of scanning tunneling microscopy on biopolymers was reported by using electrical fields and conductivity switching. The helical structure and molecule length of a peptide bundle could be varied by application of an external field, the variation arose through the interaction of the field with the large dipole moment of the helix.[19]

The results summarized above together with our experimental work on the fluorapatite–gelatine nanocomposites encouraged us to investigate the influence of intrinsic electric fields on the morphogenesis and morphology of these aggregates in more detail. We focused our efforts on the central composite seed (see Figure 1 a), since it represents the initial and thus the fundamental growth step during the morphogenesis. The nanocomposite seed itself already consists of a self-similar and hierarchical inner nanostructure.[13] Our TEM investigations show that mineralized triple helices form a three-dimensional (3D) framework and that these protein macromolecules within the composite seed are in parallel orientation with the long axis of the composite seed which is the crystallographic *c* axis of the highly mosaic-controlled apatite specimen.[12,13,20] We assume, that the triple helices exhibit opposite charges at their ends, and that by adding up all these microscopic dipoles a macroscopic electric dipole of the composite system is formed. This dipole could have an important or even a decisive influence on further growth steps and thus on the fractal morphogenesis.

In this case, we chose electron holography to image the electric fields. This method allows both the phase and amplitude of the image wave to be recorded. The phase holds information which is lost in the amplitude images (corresponding to conventional images). The electrical potential distribution integrated along the beam direction produces a phase shift of the incident electron wave which is registered by means of an interferogram. Thus, electron holography offers the unique opportunity to visualize, for example, electric or magnetic micro- and nanofields.[21,22]

In Figure 2 a, a conventional TEM micrograph of a hexagonal-prismatic seed with the typical aspect ratio close to 3:1 is shown. Only the silhouette of the seed is visible, whereas the phase image (amplified eight-times) clearly shows the electric potential distribution around the seed (Figure 2 b). The observed projected potential strongly resembles a macroscopic dipole. The phase profile (Figure 2 b, inset) shows a gradient of about 1 rad per 300 nm. This finding corresponds to about 0.13 times the polarization observed inside $BaTiO_3$ ($P = 0.26\ \mathrm{C\,m^{-2}}$, $\varepsilon_r \approx 1700$).

We performed calculations to check our assumption that the macroscopic dipole is built up by an assembly of elementary dipoles at the nanometer scale. The model is based on the assumption of all the dipoles being aligned parallel to the *c* axis of the composite seed (Figure 3 a, arrows within the seed). Thereby, we adopt the hypothesis that each triple-helical gelatine molecule shows an idealized protonation state, that is, all the N-termini are completely protonated and all the C-termini are deprotonated. The lengths of the fiber proteins and their vertical spacings were chosen according to TEM micrographs.[12,13] Contour plots of the phase shift, calculated on the base of this structural model, are shown in Figure 3 a, in which each isoline corresponds to a phase shift of $2\pi$. The comparison with experimental data (from Figure 2 b) gives a qualitative and direct agreement to the computer model. Therefore, in principle, the assumption of a nanodipole model seems to be reasonable. However, a quantitative analysis indicates that the phase shift of the model calculations compared with measured values is overestimated by a factor of eight. A possible reason for this could be a deviation from idealized protonation/deprotonation states of the $-NH_3^+$ and $-COO^-$ functional groups. Another source of error could be given by the estimated values for the length of the collagen molecules and the lateral spacing between them.[12,13] Finally, some triple helices may adopt an antiparallel orientation with respect to each other and thus,

 © 2006 Wiley-VCH Verlag GmbH & Co. KGaA, Weinheim 

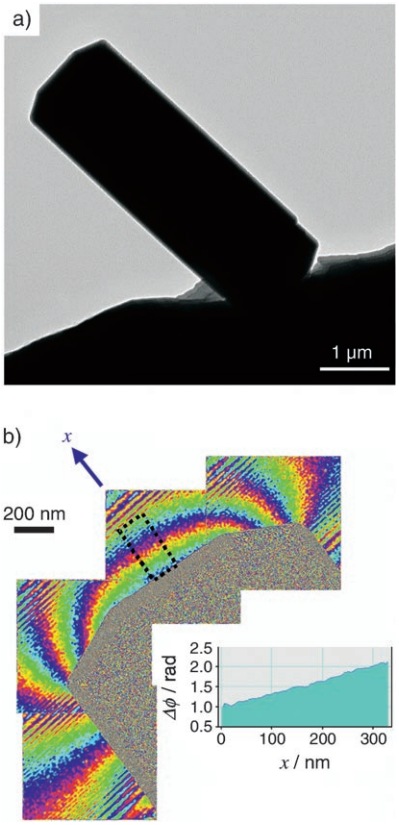



***Figure 2.*** Hexagonal-prismatic fluorapatite–gelatine nanocomposite seed; a) conventional TEM micrograph. b) Retrieved phase image of an electron hologram (amplified eight-times, composed of four single images) shows the electric potential distribution around a seed. Color code denotes a phase shift of 2π from green to green. Fresnel fringes of the interferograms appear as striation patterns at the corners of the phase images. The observed projected potential corresponds to a mesoscopic dipole. Inset: The phase profile (depicted for the rectangle with dotted border in the main picture at the basal plane) reveals a phase increase of about 1 rad per 300 nm.

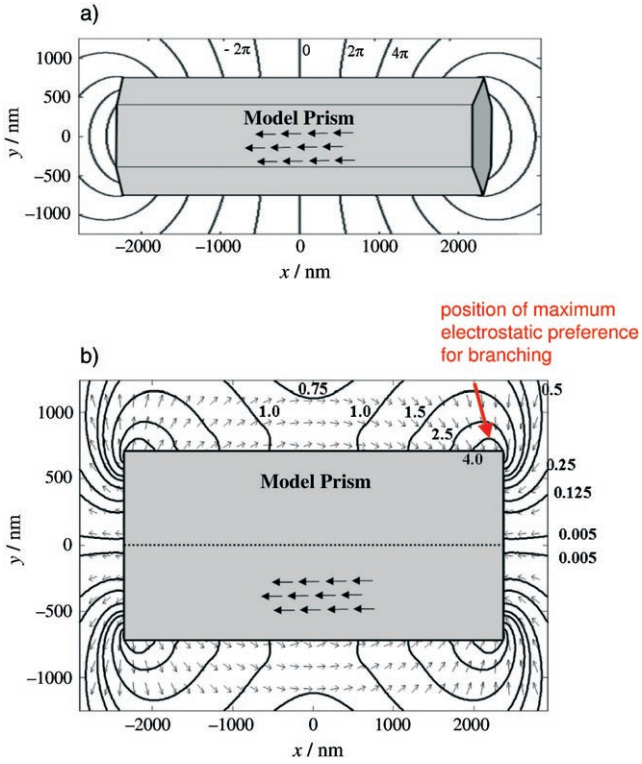



***Figure 3.*** a) Simulation of the phase image around a nanocomposite seed based on an ideal arrangement of nanodipoles. The model is constructed of triple helices in parallel orientation along [001] within the seed. Triple helices represent dipoles and are depicted as arrows. For further details see text. The contour plot of the phase shift shows a good qualitative agreement with the electron holographic experimental data (Figure 2b). b) Calculation of preferred orientation of the triple helices attaching from the gel and of the energy isolines around a composite seed in aqueous solution. The energy isolines (kJ mol$^{-1}$) indicate where and "how" neighboring macromolecules from the gel are attached to the seed (small arrows indicate the preferred orientations of the macromolecules). The largest divergence is produced at the corners, especially at the prism faces near the basal planes of the seed (red arrow). At these positions, there is also the strongest tendency for triple helices from the gel to adopt a different orientation with respect to the hexagonal *c* axis and thus give evidence of preparations for branching at both ends of the seed (beginning of fractal outgrowths).

some electric dipoles may be neutralized. However, these microscopic discrepancies between observed and calculated patterns do not change the qualitative truth of the character of the contour plot at the macroscopic scale. A quantitative agreement can be achieved by a global scaling parameter of 1/8. This factor eliminates microscopic aberrations by averaging and thus, provides a model with mesoscopic resolution which is both quantitatively and quantitatively correct.

Assuming an effective dipole moment of 1/8 e × 300 nm for every triple helix, we constructed an energy profile which displays the local preferred position and orientation of triple helices coupling out of the aqueous gel onto the surface of the seed. Thereby, the dielectric effect of the medium $\varepsilon_r = 78$ (water) was assessed. Certainly, this value features an upper limit since the dielectricity number of apatite of about eight is significantly lower. Small arrows in Figure 3b exhibit the energetically most preferred take-up orientations, exclusively based on Coulomb interactions of the dipole model. The energy difference concerning the orientation and the alignment within the seed is given by means of isopotential lines. Most of the triple helices in solution (in the surrounding gel) prefer a different orientation than those within the seed. This tendency is mostly pronounced at the prism faces in the vicinity of the basal plane. The energy difference between the orientation parallel to [001] and the preferred (new) arrangement amounts to at least 4 kJ mol$^{-1}$. During the formation of the composite the surrounding solvent (water) will be replaced by apatite and hence, the dielectric effect is decreased by a factor of about 1/10 and the energy difference can be estimated up to 40 kJ mol$^{-1}$.

Locations showing the highest probability of electrostatic orientational deviation coincide with the experimentally observed branching positions of a seed. The process of making preparations for branching is already clearly recognized in the mature growth state of the seed (Figure 1a, violet area, and Figure 4). In TEM micrographs (Figure 4a) of samples thinned by the focused ion beam technique (FIB), rolling arcs are observed which start at the initial seed

 © 2006 Wiley-VCH Verlag GmbH & Co. KGaA, Weinheim 

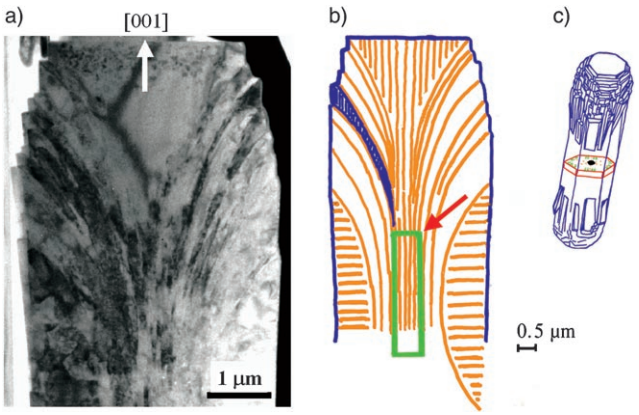



***Figure 4.*** a) TEM overview image of part, (ca. one half) of a "nearly splitting" seed; cut parallel to [001] (white arrow). The outgrowth-area for the next (the 1st) generation is clearly indicated by the contour-steps on the prism-faces near the basal plane. b) Schematic representation of (a) showing the hierarchical arrangement of gelatine triple helices and fibrils (orange) within a mature seed specimen before "real splitting". Central seed: green bordered area. At the corners of the central seed branching is in preparation. The area with highest tendency for branching effects (see Figure 3b) is marked with a red arrow. c) A schematic 3D-representation of the growth state of the nanocomposite ("mature seed"). For further details see text.

(Figure 4b, central green rectangle) and trend outside, whereas the basal plane of the composite seed (as well as its specific nanocomposite structure)[13] continues to grow in direction of the hexagonal *c* axis. The clear orientational change of the macromolecular composite component in the waist region of the mature composite seed (Figure 4b) is not completely understood to date, but it is a general feature and not a unique phenomenon.

Consequently, we could show first clear evidence for a direct correlation between intrinsic fields and the self-organized growth of the biocomposite system fluorapatite–gelatine. These fields are caused by a parallel orientation of triple-helical protein fibers of gelatine and produce, in the case of fluorapatite–gelatine seeds, a mesoscopic dipole field. The model calculations show that the tendency for branching at the ends of the elongated seed is caused by an energetically favored orientation of triple helices significantly off the hexagonal *c*-axis direction. At this point a next higher level of hierarchy occurs by oriented bundling of gelatine macromolecules and formation of microfibrils which stretch out of the volume with bent, conelike patterns (Figure 4b).[23] Thus, the dipole field influences the further growth development of the seed and in this way, it monitors the fractal morphogenesis of the composite aggregate. Our results enable a deeper insight into the growth of biological composite materials, such as bone and teeth, and open up new perspectives to influence or monitor this process by means of (external) electrical fields. Further work will comprise imaging and simulation of the electric fields of succeeding growth stages as well as of isolated triple-helical fiber proteins to understand the influence of electric fields on the hierarchical (fractal) pattern formation. Intrinsic electric dipole fields which take over control of pattern-formation processes in complex self-assembling biocomposite systems may represent a general principle in the transfer of information. We are still far away from clearly stating this causality but there are already many signs and experimental observations pointing in just that direction.

## Experimental Section

Details for preparation of fluorapatite–gelatine nanocomposites are reported elsewhere.[7,8] The composite aggregates were isolated from the gelatine matrix, subsequently washed with water, and finally dried at 40 °C for some hours. The seeds were deposited from an ethanol suspension onto a thin silicon wafer bar to perform holographic measurements. Afterwards, the samples were covered by a thin conductive carbon film (thickness ≈30 nm) from three different directions, thus avoiding charging. By variation of the electron dose used as well as the recording times it was shown that the holograms and the reconstructed phase images did not show any changes. Through this result, charging could be ruled out. The electron holographic experiments were carried out at the Special Laboratory Triebenberg for Electron Holography and High-Resolution Microscopy of the Technical University Dresden. A field emission microscope (FEI company, Eindhoven, NL) CM200 FEG/ST-Lorentz with a holography module (biprism) was used. Holograms were recorded at an acceleration voltage of 200 kV in Lorentz mode. The analysis of the holograms was performed by means of the Digital Micrograph software (Gatan, USA). Fringe periodicity of the interferograms amounted to 4.9 nm corresponding to a resolution of about 14.7 nm, whereas the fringe contrast varied from 11 % to 13 %.

Received: December 15, 2005
Published online: February 22, 2006

**Keywords:** biomineralization · composite materials · electrical dipole fields · electron holography · fluorapatite · morphogenesis

[1] *Bone Formation* (Eds.: F. Bronner, M. Farach-Carson), Springer, Heidelberg, **2003**.
[2] *Development, Function and Evolution of Teeth* (Eds.: M. F. Teaford, M. M. Smith, M. W. J. Ferguson), Cambridge University Press, Cambridge, **2000**.
[3] A. R. Matthew, I. Jasiuk, J. Taylor, J. Rubin, T. Ganey, R. P. Apkarian, *Bone* **2003**, *33*, 270.
[4] H. S. Gupta, W. Wagermaier, G. A. Zickler, D. R. B. Aroush, S. S. Funari, P. Roschger, H. D. Wagner, P. Fratzl, *Nano Lett.* **2005**, *5*, 2108.
[5] R. Tang, L. Wang, C. A. Orme, T. Bonstein, P. J. Bush, G. H. Nancollas, *Angew. Chem.* **2004**, *116*, 2751; *Angew. Chem. Int. Ed.* **2004**, *43*, 2697.
[6] A. Veis, *Science* **2004**, *306*, 419.
[7] R. Kniep, S. Busch, *Angew. Chem.* **1996**, *108*, 2787; *Angew. Chem. Int. Ed. Engl.* **1996**, *35*, 2624.
[8] S. Busch, H. Dolhaine, A. DuChesne, S. Heinz, O. Hochrein, F. Laeri, O. Podebrand, U. Vietze, T. Weiland, R. Kniep, *Eur. J. Inorg. Chem.* **1999**, *10*, 1643.
[9] S. Busch, U. Schwarz, R. Kniep, *Chem. Mater.* **2001**, *13*, 3260.
[10] S. Busch, U. Schwarz, R. Kniep, *Adv. Funct. Mater.* **2003**, *13*, 189.
[11] R. Kniep in *Facetten einer Wissenschaft* (Eds.: A. Müller, H. J. Quadbeck-Seeger, E. Diemann), Wiley-VCH, Weinheim, **2004**.
[12] P. Simon, W. Carrillo-Cabrera, P. Formanek, C. Göbel, D. Geiger, R. Ramlau, H. Tlatlik, J. Buder, R. Kniep, *J. Mater. Chem.* **2004**, *14*, 2218.
[13] P. Simon, U. Schwarz, R. Kniep, *J. Mater. Chem.* **2005**, *15*, 4992.
[14] H. Tlatlik, P. Simon, A. Kawska, D. Zahn, R. Kniep, *Angew. Chem.* **2006**, *118*, 1939–1944; *Angew. Chem. Int. Ed.* **2006**, *45*, 1905–1910.

 © 2006 Wiley-VCH Verlag GmbH & Co. KGaA, Weinheim 

[15] K. Yamashita, N. Oikawa, T. Umegaki, *Chem. Mater.* **1996**, *8*, 2697.
[16] P. Calvert, S. Mann, *Nature* **1997**, *386*, 127.
[17] S. B. Lang, *Nature* **1966**, *212*, 704.
[18] a) H. Cölfen, M. Antonietti, *Angew. Chem.* **2005**, *117*, 5714; *Angew. Chem. Int. Ed.* **2005**, *44*, 5576; b) T. X. Wang, H. Cölfen, M. Antonietti, *J. Am. Chem. Soc.* **2005**, *127*, 3246.
[19] K. Kitagawa, T. Morita, S. Kimura, *Angew. Chem.* **2005**, *117*, 6488; *Angew. Chem. Int. Ed.* **2005**, *44*, 6330.
[20] P. Simon, H. Lichte, A. Valera, W. Carrillo-Cabrera, D. Mönter, W. Reschetilowski, *Z. Anorg. Allg. Chem.* **2005**, *631*, 983.
[21] "Electron Holography: A powerful tool for analysis of nanostructures": H. Lichte, M. Lehmann, *Adv. Imaging Electron Phys.* **2002**, *123*, 225.
[22] H. Lichte, M. Reibold, K. Brand, M. Lehmann, *Ultramicroscopy* **2002**, *93*, 199.
[23] Note that the crystallographic orientation of the nanoapatite collective in principle (besides significant mosaic structuring) remains constant over the whole volume of the mature seed. This, again, is subject of further investigations.

 © 2006 Wiley-VCH Verlag GmbH & Co. KGaA, Weinheim 

Supramolecular Chemistry

DOI: 10.1002/anie.200504459

# Molecular and Supramolecular Homochirality: Enantiopure Perfluorocarbon Rotamers and Halogen-Bonded Fluorous Double Helices**

*Alessandro Casnati, Rosalba Liantonio, Pierangelo Metrangolo,* Giuseppe Resnati,* Rocco Ungaro, and Franco Ugozzoli**

The beautiful examples of helical structures provided by nature have inspired huge efforts in the generation of synthetic helical assemblies.[1] Many of the homochiral supramolecular helical structures that have been described were created through the self-assembly of chiral molecules and polymers.[2] A few reports on the preparation of artificial homochiral helices from achiral components also exist.[3] The generation of double-helical architectures retains a unique fascination, as life itself is encoded within a double-helical structure. Both metal-ion coordination[4] and hydrogen bonding[5] are well-established agents for the self-assembly of double helices.

Herein, we demonstrate how halogen bonding (XB)[6] directs the self-assembly of naked halide anions and long-chain diiodoperfluoroalkanes (diiodo-PFAs), leading to the formation of a new type of artificial molecular double helix. In the homochiral supramolecular complex **4** (Figure 1), the perfluorinated module **3** exclusively adopts a right-handed (*P*) helical conformation (molecular chirality), which translates into chiral and enantiopure fluorous[7] double helices (supramolecular chirality), owing to strong and directional I⁻···I–C halogen bonding.

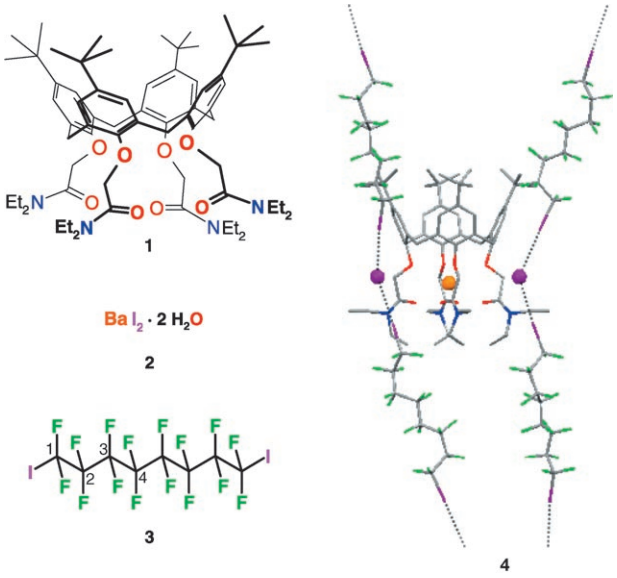



***Figure 1.*** Structural formulas of the individual components **1**–**3**, and a section of the crystal structure of the supramolecular complex **4**. Hydrogen atoms and water molecules are omitted for clarity.

Naked halide anions function as particularly effective halogen-bond acceptors.[8] Ternary mixtures of calixcrown-arenes, KI, and diiodo-PFAs give supramolecular complexes in which the calixarene modules complex the $K^+$ ions, and the naked $I^-$ ions assemble the diiodo-PFAs into infinite fluorous halogen-bonded chains, which segregate the calixarene domains.[8e] We chose 4-*tert*-butylcalix[4]arenetetra-*N*,*N*-diethylacetamide (**1**) for its ability to coordinate alkali and alkaline-earth metal cations, and to form separated ion pairs. Interestingly, calixarene **1** forms a supramolecular complex with KI that is characterized by a columnar stacking of **1**⊂$K^+$ supercations intercalated by naked $I^-$ ions; this arrangement leaves voids parallel to the stacking direction.[9a] When **1** is combined with a divalent cation in **1**⊂$Sr(Pic)_2$ (Pic = picrate),

[*] Dr. R. Liantonio, Prof. P. Metrangolo, Prof. G. Resnati
NFMLab-DCMIC "G. Natta," Politecnico di Milano
Via L. Mancinelli 7, 20131 Milano (Italy)
and
NFMLab-DCMIC, Como Campus of Politecnico di Milano
Via Castelnuovo 7, 22100 Como (Italy)
Fax: (+39) 02-2399-3080
E-mail: pierangelo.metrangolo@polimi.it
giuseppe.resnati@polimi.it
Prof. F. Ugozzoli
Dipartimento di Chimica Generale ed Inorganica
Università degli Studi di Parma
Parco Area delle Scienze 17/a, 43100 Parma (Italy)
Fax: (+39) 0521-905557
E-mail: franco.ugozzoli@unipr.it
Prof. A. Casnati, Prof. R. Ungaro
Dipartimento di Chimica Organica ed Industriale
Università degli Studi di Parma
Parco Area delle Scienze 17/a, 43100 Parma (Italy)

[**] This work was partially supported by the Fondazione Cariplo and the EU (COST D29/0011/03 and D31/0017/08).

Supporting information for this article is available on the WWW under http://www.angewandte.org or from the author.


© 2006 Wiley-VCH Verlag GmbH & Co. KGaA, Weinheim

the picrate anions are segregated in channels parallel to columnar stacks of $\mathbf{1}\subset Sr^{2+}$ ions (see Supporting Information).[9b]

We reasoned that by selecting calixarene **1** for the complexation of alkaline-earth iodide salts in the presence of the diiodo-PFA **3**, the stoichiometry of the system would probably lead to the formation of a supramolecular complex with two **3**–$I^-$ chains in channels parallel to columnar stacks of $\mathbf{1}\subset M^{2+}$ supercations. In fact, the low affinity of PFAs and hydrocarbon (HC) derivatives for one another favors the segregation of the two fluorous halogen-bonded chains in one domain, within which interactions between the chains would be optimized. Moreover, since it has been theorized that the most stable conformation for a dimer of long-chain PFAs is the double helix,[10] it seemed likely that the two fluorous halogen-bonded chains would adopt a double helical arrangement.

The supramolecular complex **4** was prepared by the self-assembly of calixarene **1**, barium dioxide dehydrate (**2**), and 1,8-diiodoperfluorooctane (**3**). X-ray diffraction analysis of single crystals of **4** revealed the supramolecular organization of **1**, **2**, and **3** in the 1:1:2 complex **4** (see Supporting Information). Although composed of intrinsically achiral modules, the supramolecular complex **4** crystallizes in the chiral tetragonal space group *I*422. The supercation $\mathbf{1}\subset Ba^{2+}$ has $C_4$ symmetry: the $Ba^{2+}$ ion, which lies on the fourfold rotation axis, is coordinated by the four amide oxygen atoms at 2.65(1) Å and the four phenol oxygen atoms at 2.74(1) Å, in the form of a square antiprism.[11] The $I^-$ counterions are located outside of the $\mathbf{1}\subset Ba^{2+}$ columns, separated by 6.624(5) Å from the $Ba^{2+}$ ions. The fluorinated modules **3** have $C_2$ symmetry and are linked to the $I^-$ ions by $I^-\cdots I$–C halogen bonds. The geometrical parameters for the halogen bonds are: $I^-\cdots I$ 3.380(2) Å (20% reduction of the sum of the van der Waals and ionic radii (4.14 Å)[12]); $I^-\cdots I$–C 175(1)°, $I\cdots I^-\cdots I$ 136(1)°. The perfectly ordered diiodo-PFA molecule **3** adopts a distorted *gauche* conformation (C1-C2-C3-C4 62(2)°), and most notably, coils into a homochiral arch, which forms a turn of a right-handed (*P*) single helix.[13] Under halogen-bonding control,[8d,14] only one of the two possible rotamers of **3** is incorporated in the homochiral crystal matrix of **4**. Unlike their HC parents, linear PFAs are characterized by a helical distortion of their carbon frameworks, as a consequence of the steric and electrostatic repulsions between adjacent fluorine atoms.[10,15] PFAs thus exist as enantiomers with opposite helicities, which interconvert easily as a function of temperature and pressure. To our knowledge, the formation of homochiral **4** is the first case of a spontaneous resolution of the helical conformation of a long-chain PFA.

In the supramolecular organization of **4**, the $I^-$ ions and the diiodo-PFA modules **3**, which are present in a 1:1 ratio, behave as bidentate halogen-bond acceptors and donors, respectively. Infinite 1D fluorous $\cdots I^-\cdots I$–$(CF_2)_8$–$I\cdots$ chains develop in the form of left-handed (*M*) supramolecular helices, which run along the *c* axis (Figure 2). The $\mathbf{1}\subset Ba^{2+}$ supercations are stacked such that the amide chains and *tert*-butyl groups of the calixarene molecules of adjacent supercations face each other (Figure 3a). The charge of the cation

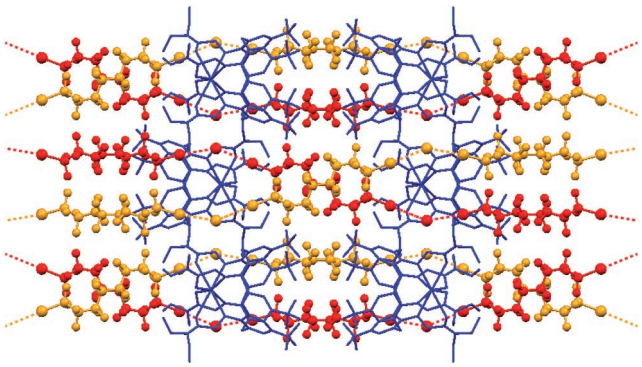


***Figure 2.*** A view down the *b* axis of the crystal structure of the supramolecular complex **4**. The $\mathbf{1}\subset Ba^{2+}$ supercations are shown in blue. Pairs of fluorous **3**–$I^-$ chains, shown in yellow and red, form double helices. Dashed lines indicate halogen bonds. Hydrogen atoms and water molecules are omitted for clarity.

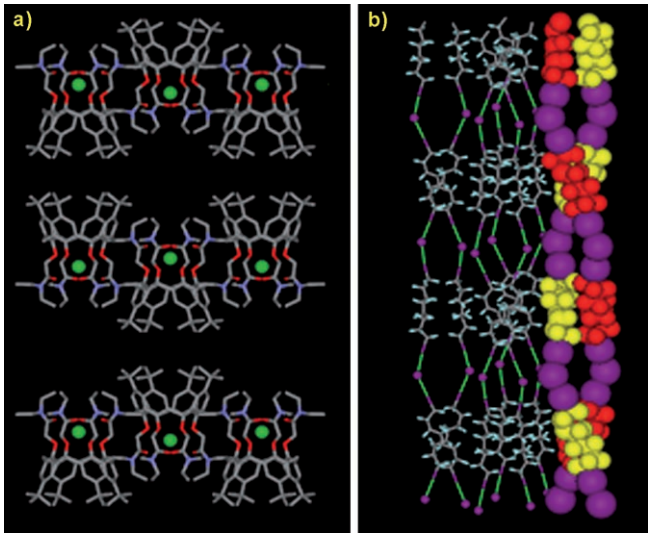



***Figure 3.*** Views orthogonal to the *c* axis of the crystal structure of the supramolecular complex **4**. Ba green, I purple, F light blue, O red, N dark blue, C gray. a) The cationic sublattice. Hydrogen atoms and water molecules are omitted for clarity. b) The anionic sublattice. Green lines indicate halogen bonds. One double helix is represented by van der Waals spheres, with the PFA chains in yellow and red, and the iodine atoms in purple.

determines that two infinite fluorous **3**–$I^-$ helices (Figure 3b) are generated for each column of $\mathbf{1}\subset Ba^{2+}$. These pairs of helices propagate along the $4_2$ screw axes, parallel to the columns of $\mathbf{1}\subset Ba^{2+}$ supercations, which run along the fourfold rotation axes (and introduce the fourfold rotational symmetry into the periodically ordered solid). Thus, four fluorous double helices surround each column of supercations, and vice versa (Figure 4). The tendency of the diiodo-PFA molecules to align themselves next to one another and parallel to the stacked calixarenes is consistent with the segregation frequently observed in related crystal structures,[8c,e] and influences the overall supramolecular organization.

Owing to the identical conformations of the **3**–$I^-$ chains and to the interchain F···F contacts,[16] the pairs of fluorous

 © 2006 Wiley-VCH Verlag GmbH & Co. KGaA, Weinheim 

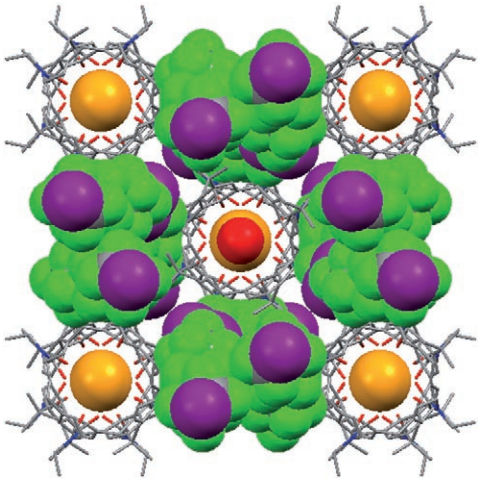


***Figure 4.*** A view down the *c* axis of the crystal structure of the supramolecular complex **4**. Ba orange, I purple, F green, O red, N blue, C gray. The calixarene molecules are represented by capped sticks, and all other components by van der Waals spheres. Hydrogen atoms are omitted for clarity.

helices self-organize into double helices, with a pitch of 71.43(1) Å, which is twice as long as the *c* axis (35.716(5) Å). Although they have been postulated,[10] there are no precedents for homochiral perfluorinated helices or double helices.

In summary, we have described the single-crystal X-ray structure of the homochiral supramolecular complex **4**. The stoichiometry of the complex and halogen bonding both play crucial roles in determining the formation of the double helices in **4**. To our knowledge, the use of halogen bonding as a directing force for the construction of double-helical suprastructures and the use of fluorinated modules are unprecedented. The results described herein open up new possibilities for the assembly of linear molecules into artificial double-helix systems.[1] Moreover, examination of the conformations of PFA chains is of importance in understanding the helical structures of perfluorinated polymers. These relatively simple polymers display a very rich phase behavior, as a result of their helical conformations. The results reported herein indicate that, in the solid state, the helical arrangement of PFA chains can be homochiral, and the double helix can be the most stable conformation for pairs of chains. The use of analogues of calixarene **1** with chiral and enantiopure pendants for the preparation of supramolecular analogues of **4** is currently under study. The chiral calixarene modules should reinforce the tendency of the supramolecular adducts to crystallize in structures containing homochiral double helices.

## *Experimental Section*

For the preparation of 4-*tert*-butylcalix[4]arenetetra-*N*,*N*-diethylacetamide (**1**), see ref. [17]. For the preparation of **1**⊂$BaI_2 \cdot x\,H_2O$, see Supporting Information. The supramolecular complex **4** was prepared starting from **1**⊂$BaI_2 \cdot x\,H_2O$ (0.026 mmol, 40 mg) and 1,8-diiodoperfluorooctane (**3**; 0.078 mmol, 51 mg). The two solids were dissolved in ethanol (2 mL) in a vial at room temperature. The open vial was placed inside a closed bottle containing paraffin oil. The slow evaporation of the solvent at room temperature afforded colorless crystals of **4** (yield 85 %). M.p. 190 °C (decomp.). A single crystal of **4** suitable for X-ray analysis was mounted on a glass rod and cooled to 173 K in a nitrogen stream. Intensity data were collected on an Enraf-Nonius CAD4 diffractometer using graphite-monochromatized $Cu_{K\alpha}$ radiation ($\lambda = 1.54178$ Å) from a fine-focus sealed tube (40 kV, 20 mA). CCDC-292936 (**4**) contains the supplementary crystallographic data for this paper. These data can be obtained free of charge from The Cambridge Crystallographic Data Centre via www.ccdc.cam.ac.uk/data_request/cif.

Received: December 15, 2005
Published online: February 21, 2006

**Keywords:** calixarenes · halogen bonding · helical structures · perfluoro compounds · self-assembly

[1] M. Albrecht, *Angew. Chem.* **2005**, *117*, 6606 – 6609; *Angew. Chem. Int. Ed.* **2005**, *44*, 6448 – 6451, and references therein.
[2] J. L. M. Cornelissen, A. E. Rowan, R. J. M. Nolte, N. A. J. M. Sommerdijk, *Chem. Rev.* **2001**, *101*, 4039 – 4070, and references therein; L. Brunsveld, B. J. B. Folmer, E. W. Meijer, R. P. Sijbesma, *Chem. Rev.* **2001**, *101*, 4071 – 4098, and references therein; T. Giorgi, S. Lena, P. Mariani, M. A. Cremonini, S. Masiero, S. Pieraccini, J. P. Rabe, P. Samorì, G. P. Spada, G. Gottarelli, *J. Am. Chem. Soc.* **2003**, *125*, 14741 – 14749; R.-M. Ho, Y.-W. Chiang, C.-C. Tsai, C.-C. Lin, B.-T. Ko, B.-H. Huang, *J. Am. Chem. Soc.* **2004**, *126*, 2704 – 2705.
[3] X. Yang, L. Chai, X. Chi, Y. Liu, R. Cao, Y. Lu, X. Jiang, H. Tang, T. Li, *Chem. Eur. J.* **1999**, *5*, 1144 – 1149; H. Onouchi, K. Maeda, E. Yashima, *J. Am. Chem. Soc.* **2001**, *123*, 7441 – 7442; M. Inouye, M. Waki, H. Abe, *J. Am. Chem. Soc.* **2004**, *126*, 2022 – 2027; M. Ishikawa, K. Maeda, Y. Mitsutsuji, E. Yashima, *J. Am. Chem. Soc.* **2004**, *126*, 732 – 733; G. Cui, H. Xu, W. Xu, G. Yuan, D. Zhang, L. Jiang, D. Zhu, *Chem. Commun.* **2005**, 277 – 278.
[4] J.-M. Lehn, *Supramolecular Chemistry: Concepts and Perspectives*, VCH, Weinheim, **1995**; *Comprehensive Supramolecular Chemistry, Vol. 9* (Eds.: J.-M. Lehn, J. L. Atwood, J. E. D. Davies, D. D. MacNicol, F. Vögtle) Pergamon, Oxford, **1996**, pp. 213 – 252; C. Piguet, G. Bernardinelli, G. Hopfgartner, *Chem. Rev.* **1997**, *97*, 2005 – 2062; M. J. Hannon, S. Bunce, A. J. Clarke, N. W. Alcock, *Angew. Chem.* **1999**, *111*, 1353 – 1355; *Angew. Chem. Int. Ed.* **1999**, *38*, 1277 – 1278; O. Mamula, A. von Zelewsky, T. Bark, G. Bernardinelli, *Angew. Chem.* **1999**, *111*, 3129 – 3133; *Angew. Chem. Int. Ed.* **1999**, *38*, 2945 – 2948; A. Erxleben, *Inorg. Chem.* **2001**, *40*, 2928 – 2931; K. Tanaka, A. Tengeiji, T. Kato, N. Toyama, M. Shionoya, *Science* **2003**, *299*, 1212 – 1213.
[5] J. Sánchez-Quesada, C. Seel, P. Prados, J. de Mendoza, *J. Am. Chem. Soc.* **1996**, *118*, 277 – 278; S. J. Coles, J. G. Frey, P. A. Gale, M. B. Hursthouse, M. E. Light, K. Navakhun, G. L. Thomas, *Chem. Commun.* **2003**, 568 – 569; Q. Zeng, D. Wu, C. Liu, H. Ma, J. Lu, S. Xu, Y. Li, C. Wang, C. Bai, *Cryst. Growth Des.* **2005**, *5*, 1041 – 1047; M. Du, Z.-H. Zhang, X.-J. Zhao, *Cryst. Growth Des.* **2005**, *5*, 1247 – 1254; Z.-H. Zhou, J.-M. Yang, H.-L. Wan, *Cryst. Growth Des.* **2005**, *5*, 1825 – 1830; Y. Tanaka, H. Katagiri, Y. Furusho, E. Yashima, *Angew. Chem.* **2005**, *117*, 3935 – 3938; *Angew. Chem. Int. Ed.* **2005**, *44*, 3867 – 3870.
[6] P. Metrangolo, H. Neukirch, T. Pilati, G. Resnati, *Acc. Chem. Res.* **2005**, *38*, 386 – 395.
[7] *Handbook of Fluorous Chemistry* (Eds.: J. A. Gladysz, D. P. Curran, I. T. Horwath), Wiley-VCH, Weinheim, **2004**; J. A. Gladysz, D. P. Curran, *Tetrahedron* **2002**, *58*, 3823 – 3825.
[8] a) J. Grebe, G. Geiseler, K. Harms, K. Dehnicke, *Z. Naturforsch. B* **1999**, *54*, 77 – 86; b) R. Weiss, O. Schwab, F. Hampel, *Chem. Eur. J.* **1999**, *5*, 968 – 974; c) R. Liantonio, P. Metrangolo, T. Pilati, G. Resnati, *Cryst. Growth Des.* **2003**, *3*, 355 – 361; d) A. Mele, P.

 © 2006 Wiley-VCH Verlag GmbH & Co. KGaA, Weinheim 

Metrangolo, H. Neukirch, T. Pilati, G. Resnati, *J. Am. Chem. Soc.* **2005**, *127*, 14972–14973; e) G. Gattuso, R. Liantonio, P. Metrangolo, F. Meyer, A. Pappalardo, M. F. Parisi, T. Pilati, I. Pisagatti, G. Resnati, *Supramol. Chem.* **2006**, in press.

[9] a) A. Arduini, E. Ghidini, A. Pochini, R. Ungaro, G. D. Andreetti, G. Calestani, F. Ugozzoli, *J. Inclusion Phenom.* **1988**, *6*, 119–134; b) N. Muzet, G. Wipff, A. Casnati, L. Domiano, R. Ungaro, F. Ugozzoli, *J. Chem. Soc. Perkin Trans. 2* **1996** 1065–1075.

[10] Yu. B. Vysotsky, V. S. Bryantsev, F. L. Boldyreva, V. B. Fainerman, D. Vollhardt, *J. Phys. Chem. B* **2005**, *109*, 454–462, and references therein.

[11] The calixarene cavity also hosts a water molecule, which resides on the fourfold rotation axis, 5.57(8) Å from the $Ba^{2+}$ ion.

[12] http://www.webelements.com.

[13] Other dihedral angles [°] in the diiodo-PFA molecule **3** of the supramolecular complex **4**: C2-C3-C4-C4′ 161(1), C3-C4-C4′-C3′ 161(1).

[14] H. Neukirch, E. Guido, R. Liantonio, P. Metrangolo, T. Pilati, G. Resnati, *Chem. Commun.* **2005**, 1534–1536.

[15] S. Soon Jang, M. Blanco, W. A. Goddard III, G. Caldwell, R. B. Ross, *Macromolecules* **2003**, *36*, 5331–5341, and references therein.

[16] The shortest F···F distance between two facing diiodo-PFA molecules **3** in the supramolecular complex **4** is 2.789 Å (5% reduction of the sum of the van der Waals radii (2.94 Å)[12]).

[17] G. Calestani, F. Ugozzoli, A. Arduini, E. Ghidini, R. Ungaro, *J. Chem. Soc. Chem. Comm.* **1987**, *5*, 344–346.

 © 2006 Wiley-VCH Verlag GmbH & Co. KGaA, Weinheim 

DNA Nanotechnology

DOI: 10.1002/anie.200504124

# Modulation of DNA Constraints That Control Macromolecular Folding**

*Chandrasekhar V. Miduturu and Scott K. Silverman**

We recently reported double-stranded DNA as a constraint to control macromolecular conformation.[1] In these experiments, two short 10- to 20-nucleotide DNA strands were covalently attached through their 5′-termini to specific nucleotides within the autonomously folding 160-nucleotide P4–P6 RNA domain (molecular weight ≈51 000). When the attached DNA strands were complementary, a duplex was formed by Watson–Crick base pairing. If the geometric constraint imposed by the DNA duplex was incompatible with the known RNA tertiary structure,[2] then a competition was established in which either the DNA constraint or the RNA conformation must be compromised (Figure 1).[1] These

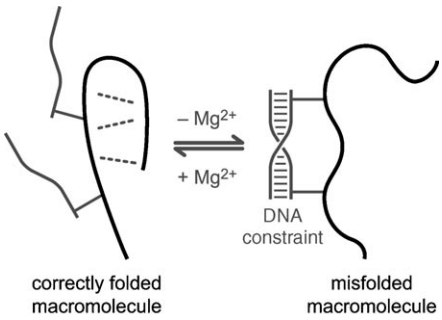



***Figure 1.*** Use of a DNA constraint to control the folding of a macromolecule such as RNA. In the absence of the DNA constraint, RNA folding is characterized by its $[Mg^{2+}]_{1/2}$ value. The DNA constraint suppresses native folding even at $[Mg^{2+}] > [Mg^{2+}]_{1/2}$. Under these conditions, modulation of the constraint, as described herein, switches the RNA folding state from misfolded to correctly folded.

experiments demonstrated a new approach to DNA nanotechnology[3] in which the conformations of other macromolecules are controlled by DNA acting as a dynamic structural element. A fundamental feature of this approach is that the effect of the DNA constraint on macromolecular structure should be modulated by external stimuli. Herein, we show that DNA constraints on macromolecular conformation can indeed be modulated in several ways. The DNA constraint can be destroyed irreversibly by degradation with a nuclease or restriction enzyme. The constraint can also be destroyed with a reducing agent that cleaves a disulfide linkage between the RNA and DNA. The DNA constraint can be modulated reversibly by sequential binding and removal of oligonucleotides. Finally, when one of the DNA constraint strands incorporates an aptamer sequence, the cognate small-molecule ligand can modulate the DNA constraint. This wide range of methods for the modulation of DNA constraints upon macromolecular conformation will expand greatly the applicability of our new approach to DNA nanotechnology.

The stability of RNA tertiary structure depends much more strongly on the presence of $Mg^{2+}$ than does the formation of DNA duplexes.[4] Under typical in vitro folding conditions, such as Tris-borate buffer solution (Tris = tris(hydroxymethyl)aminomethane; pH 8.3) and 35 °C, the structured P4–P6 RNA has an empirical $Mg^{2+}$ concentration termed the $[Mg^{2+}]_{1/2}$ value, which characterizes its folding. A shift in the $[Mg^{2+}]_{1/2}$ value acts as a sensitive probe for thermodynamic perturbations upon RNA structures,[5] including effects due to DNA constraints.[1] A DNA duplex that is structurally compatible with the folded RNA conformation does not affect the $[Mg^{2+}]_{1/2}$ value; in contrast, an incompatible DNA constraint increases $[Mg^{2+}]_{1/2}$ because the DNA duplex must be disrupted for the RNA to fold.[6] The $Mg^{2+}$-dependent folding of P4–P6 is monitored quantitatively by nondenaturing polyacrylamide gel electrophoresis (native

[*] C. V. Miduturu, Prof. S. K. Silverman
Department of Chemistry
University of Illinois at Urbana-Champaign
600 South Mathews Avenue, Urbana, IL 61801 (USA)
Fax: (+1) 217-244-8024
E-mail: scott@scs.uiuc.edu

[**] This research was supported by the Burroughs Wellcome Fund, the March of Dimes, the National Institutes of Health, and the UIUC Department of Chemistry. S.K.S. is a Fellow of the David and Lucile Packard Foundation.

Supporting information for this article is available on the WWW under http://www.angewandte.org or from the author.


InterScience
© 2006 Wiley-VCH Verlag GmbH & Co. KGaA, Weinheim

PAGE).[5,7,8] The $[Mg^{2+}]_{1/2}$ value for unconstrained wild-type P4–P6 is $\approx 0.7$ mM. Owing to the highly cooperative folding transition that has a Hill coefficient of $n \approx 4$ on native PAGE, wild-type P4–P6 is almost completely folded when $[Mg^{2+}] > 1.0$ mM. However, when an incompatible DNA constraint is attached, the $[Mg^{2+}]_{1/2}$ value shifts considerably to the right; for example, to $\approx 12$ mM when a 10-bp constraint is attached at P4–P6 nucleotides U107 and C240, which are too far apart for the DNA constraint to span and yet allow the RNA conformation to be maintained.[1] At a fixed intermediate $Mg^{2+}$ concentration such as 1.5–2.0 mM, at which the wild-type (unconstrained) RNA is entirely folded, the DNA duplex prevents folding of the constrained P4–P6. Modulation of the DNA constraint at the fixed intermediate $Mg^{2+}$ concentration should then switch the unfolded or folded status of the RNA. We took advantage of the native PAGE folding assay and the strong dependence of RNA folding on $Mg^{2+}$ concentration to demonstrate modulation of the DNA-constraint effect in several ways.

First, we established that a DNA constraint could be destroyed irreversibly with enzymes or chemical reagents. This was performed with either deoxyribonuclease (DNase) or exonuclease III, both of which nonspecifically degrade the 20 bp duplex DNA (Figure 2a).[9] Alternatively, the DNA constraint was cleaved sequence specifically with the restriction enzyme BsrBI. In all these cases, the RNA was misfolded at $[Mg^{2+}] = 1.5$ mM with the DNA constraint intact; removal of the constraint by the nuclease allowed the RNA to fold properly. We also modulated the DNA constraint by using the reducing agent dithiothreitol (DTT). For this purpose, one of the two DNA strands was attached to RNA not through reductive amination (N-linked)[1] but instead through disulfide formation (S-linked), by using a DNA strand with a 5′-SH group and an RNA nucleotide with a 2′-$OCH_2CH_2SH$ moiety.[10] Disruption of the S-linked constraint with DTT led to native RNA folding, and the reducing agent tris(2-carboxyethyl)phosphine (TCEP) gave equivalent results (Figure 2b).[11,12]

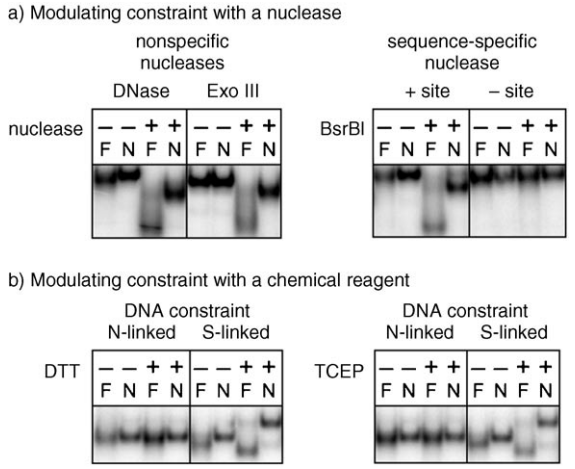



***Figure 2.*** Modulation of the DNA constraint with a nuclease or a chemical reagent, as monitored by native PAGE. a) Modulation of the constraint with nonspecific deoxyribonucleases or with the BsrBI restriction enzyme. The lanes labeled "−site" represent BsrBI treatment of a constraint sequence that lacks the BsrBI recognition site. The $[Mg^{2+}]$ was constant at 1.5 mM ($T = 25\,°C$). F and N denote foldable and nonfoldable versions of P4–P6 RNA, respectively. Without nuclease treatment, both F and N migrate equivalently. With nuclease treatment, F migrates much faster than N, which is the signature of P4–P6 folding.[5] b) Modulation of the constraint by reduction with DTT or TCEP (10 mM). Only after reductive cleavage of the S-linked constraint does F migrate much faster than N.[11] For the N-linked constraint, both DNA strands were joined to RNA by reductive amination.[1] For the S-linked constraint, one strand was joined by reductive amination and the other through a disulfide linkage.

We sought to modulate the DNA constraint reversibly by adding a complementary (C) DNA oligonucleotide that competes for one of the two duplex strands (Figure 3a).[13] The DNA-constraint strand targeted by the complement was extended at its 3′-end to provide an initiation site for strand invasion. Modulation of the DNA constraint was entirely reversible because subsequent addition of a rescue (R) strand restored the initial constrained state. Full restoration of the constraint required tuning of the relative DNA:DNA binding affinities through strategic mutations in the C strand such that R complemented C perfectly, whereas the affinity of C for the constraint strand was weakened slightly.[13c,e]

Integration of fluorescence response into the reversible DNA-constraint modulation would allow simple and rapid detection of macromolecular conformation changes by spectroscopic rather than electrophoretic assays. For this purpose, we appended a pyrene chromophore to the RNA; pyrene is known to report well on $Mg^{2+}$-dependent P4–P6 tertiary folding.[8,14] The RNA folding state was readily monitored through repeated cycles of C and R strand addition (Figure 3b) in accord with the native PAGE experiments.[15]

Modulation of the DNA constraint with a small-molecule ligand instead of an oligonucleotide would be a potentially general method to transduce ligand–aptamer interactions into changes in macromolecular conformation (Figure 4a). Towards this goal, one of the DNA-constraint strands was redesigned to incorporate the aptamer sequence for the ligand hemin (molecular weight 652),[16] such that binding of hemin would compete with formation of the duplex constraint. Exposure of the DNA-constrained RNA to hemin indeed led to modulation of the constraint, as shown by return of the $[Mg^{2+}]_{1/2}$ value to very near to that found for unconstrained P4–P6 (Figure 4b). Importantly, restoration of normal RNA folding upon hemin addition was suppressed by specific DNA mutations[17] that are known to disable aptamer–hemin interactions but do not alter the integrity of the constraint.

In summary, we have demonstrated a variety of approaches for the modulation of duplex DNA constraints on the macromolecular folding of RNA. These experiments provide the fundamental control elements of a new direction in DNA nanotechnology in which the conformations of other macromolecules are dynamically controlled by DNA. Our most generalizable approach is the use of a ligand–aptamer interaction as the control element (Figure 4). Although the present experiments used the previously reported hemin–aptamer combination, in principle it should be feasible to identify aptamers for nearly any small molecules of interest[18] and to integrate these ligand–aptamer combinations into

 © 2006 Wiley-VCH Verlag GmbH & Co. KGaA, Weinheim 

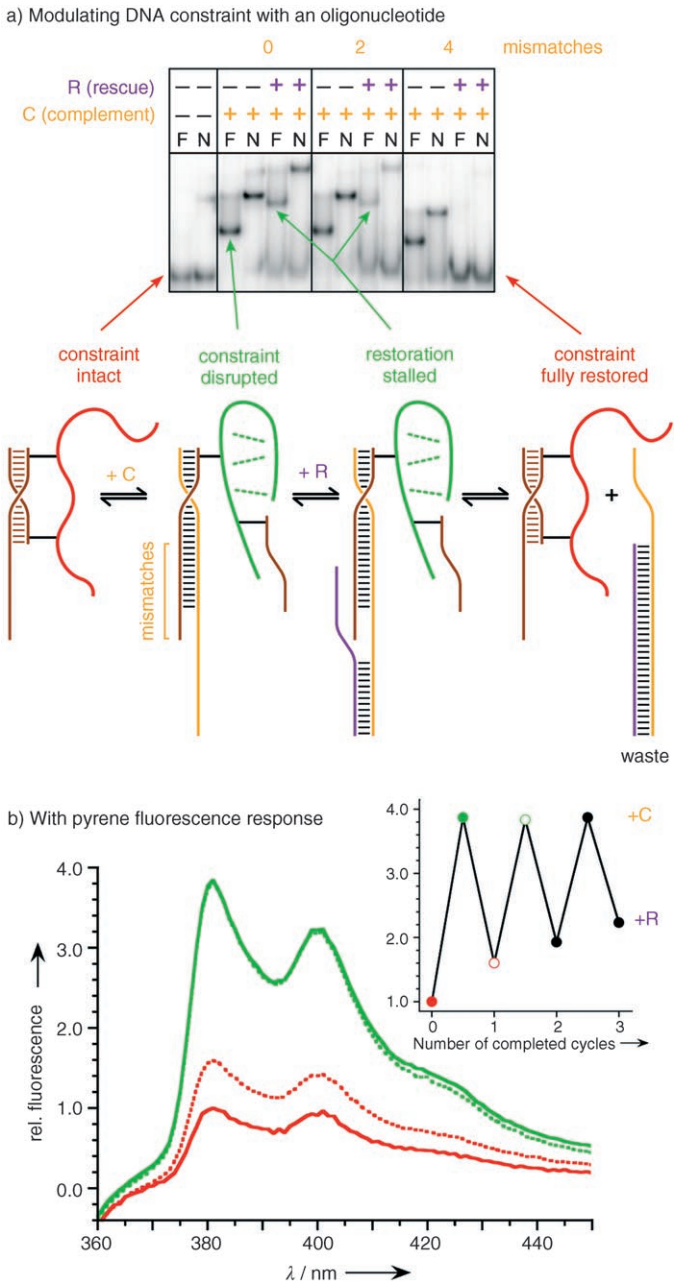



***Figure 3.*** Modulation of the DNA constraint by added oligonucleotides, as monitored by native PAGE or pyrene fluorescence. a) Native PAGE. The [$Mg^{2+}$] was constant at 1.5 mM ($T$ = 35 °C). b) Pyrene fluorescence under similar conditions. The inset shows reversibility over several cycles of complement (C) and rescue (R) strand addition.[15] After each addition, samples were incubated for 1 h, which was sufficient for completion of the fluorescence changes. Other groups have also described duplex exchanges that require minutes or longer.[13]

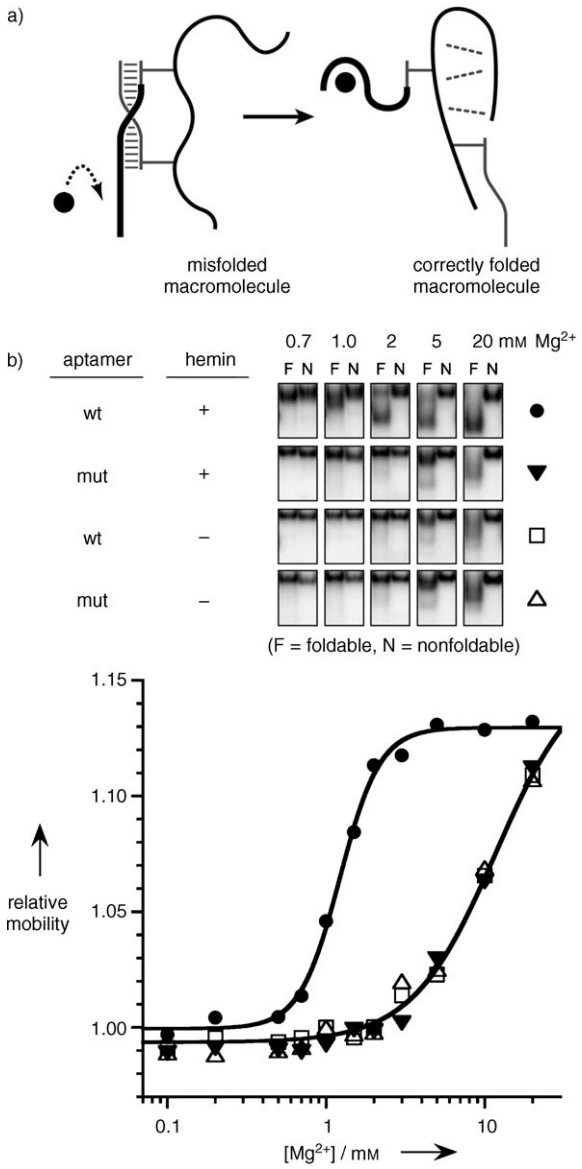



***Figure 4.*** Modulation of the DNA constraint by competing ligand–aptamer interactions. a) Design of the competition. b) Native PAGE data demonstrating experimental validation of the design by using the hemin aptamer ($T$ = 25 °C).[16] Inclusion of hemin decreases the $[Mg^{2+}]_{1/2}$ value from ≈12 mM to 1.2 mM; the latter value is comparable to that of unconstrained wild-type P4–P6 under the same conditions (data not shown). In contrast, when the known single-nucleotide G9A mutation that prevents hemin binding[17] is present in the aptamer sequence, addition of hemin does not affect the $[Mg^{2+}]_{1/2}$ value. wt = wild-type, mut = mutant.

DNA nanotechnology. The present experiments used RNA as the macromolecule whose structure is controlled,[1] although it should be possible to control the structures of other macromolecules,[19] including nonbiological foldamers.[20] In future investigations, the combination of DNA-mediated conformational control with fluorescence detection of structural changes or with changes in RNA catalytic activity should allow creation of sensors whose functions are governed by formation and modulation of DNA constraints.

Received: November 19, 2005
Published online: February 17, 2006

**Keywords:** aptamers · DNA · nanotechnology · RNA · structural constraints

 © 2006 Wiley-VCH Verlag GmbH & Co. KGaA, Weinheim 

[1] C. V. Miduturu, S. K. Silverman, *J. Am. Chem. Soc.* **2005**, *127*, 10144 – 10145.

[2] J. H. Cate, A. R. Gooding, E. Podell, K. Zhou, B. L. Golden, C. E. Kundrot, T. R. Cech, J. A. Doudna, *Science* **1996**, *273*, 1678 – 1685.

[3] a) F. C. Simmel, W. U. Dittmer, *Small* **2005**, *1*, 284 – 299; b) S. H. Lee, C. Mao, *BioTechniques* **2004**, *37*, 517 – 519; c) N. C. Seeman, *Nature* **2003**, *421*, 427 – 431.

[4] a) I. Tinoco, Jr., C. Bustamante, *J. Mol. Biol.* **1999**, *293*, 271 – 281; b) S. Nakano, M. Fujimoto, H. Hara, N. Sugimoto, *Nucleic Acids Res.* **1999**, *27*, 2957 – 2965.

[5] S. K. Silverman, T. R. Cech, *Biochemistry* **1999**, *38*, 8691 – 8702.

[6] A compatible DNA duplex does not decrease the $Mg^{2+}$ requirement for RNA folding, because the duplex is intact in both the unfolded and folded RNA conformations. Therefore, the free-energy change for the unfolded-to-folded RNA interconversion is unchanged by attachment of the DNA duplex.

[7] a) B. T. Young, S. K. Silverman, *Biochemistry* **2002**, *41*, 12271 – 12276; b) S. K. Silverman, M. Zheng, M. Wu, I. Tinoco, Jr., T. R. Cech, *RNA* **1999**, *5*, 1665 – 1674; c) S. K. Silverman, M. L. Deras, S. A. Woodson, S. A. Scaringe, T. R. Cech, *Biochemistry* **2000**, *39*, 12465 – 12475; d) S. K. Silverman, T. R. Cech, *RNA* **2001**, *7*, 161 – 166; e) E. A. Doherty, R. T. Batey, B. Masquida, J. A. Doudna, *Nat. Struct. Biol.* **2001**, *8*, 339 – 343; f) S. Matsumura, Y. Ikawa, T. Inoue, *Nucleic Acids Res.* **2003**, *31*, 5544 – 5551.

[8] S. K. Silverman, T. R. Cech, *Biochemistry* **1999**, *38*, 14224 – 14237.

[9] The DNA sequences are provided in the Supporting Information.

[10] S. Jin, C. V. Miduturu, D. C. McKinney, S. K. Silverman, *J. Org. Chem.* **2005**, *70*, 4284 – 4299.

[11] The altered mobilities observed upon removing the S-linked constraint are due to changes in compactness. See the Supporting Information for full details of all native PAGE experiments and for denaturing PAGE experiments that verify DNA cleavage by the nuclease or reducing agent.

[12] In principle, it should be possible to reverse the removal of the DNA constraint by oxidative restoration of the disulfide linkage, but we have not attempted this process.

[13] a) F. C. Simmel, B. Yurke, *Phys. Rev. E* **2001**, *63*, 041913; b) F. C. Simmel, B. Yurke, *Appl. Phys. Lett.* **2002**, *80*, 883 – 885; c) J. J. Li, W. Tan, *Nano Lett.* **2002**, *2*, 315 – 318; d) A. J. Turberfield, J. C. Mitchell, B. Yurke, A. P. Mills, Jr., M. I. Blakey, F. C. Simmel, *Phys. Rev. Lett.* **2003**, *90*, 118102; e) P. Alberti, J. L. Mergny, *Proc. Natl. Acad. Sci. USA* **2003**, *100*, 1569 – 1573; f) W. U. Dittmer, A. Reuter, F. C. Simmel, *Angew. Chem.* **2004**, *116*, 3634 – 3637; *Angew. Chem. Int. Ed.* **2004**, *43*, 3550 – 3553; g) W. U. Dittmer, F. C. Simmel, *Nano Lett.* **2004**, *4*, 689 – 691.

[14] M. K. Smalley, S. K. Silverman, *Nucleic Acids Res.* **2006**, *34*, 152 – 166.

[15] The imperfect efficiency observed in the Figure 3b inset is similar to inefficiencies observed in independent studies that also rely on DNA oligonucleotides as "fuel" strands.[13c,e,f]

[16] a) Y. Li, C. R. Geyer, D. Sen, *Biochemistry* **1996**, *35*, 6911 – 6922; b) P. Travascio, Y. Li, D. Sen, *Chem. Biol.* **1998**, *5*, 505 – 517.

[17] H.-W. Lee, D. J.-F. Chinnapen, D. Sen, *Pure Appl. Chem.* **2004**, *76*, 1537 – 1545.

[18] a) T. Hermann, D. J. Patel, *Science* **2000**, *287*, 820 – 825; b) J. Liu, Y. Lu, *J. Fluoresc.* **2004**, *14*, 343 – 354.

[19] a) B. Choi, G. Zocchi, S. Canale, Y. Wu, S. Chan, L. J. Perry, *Phys. Rev. Lett.* **2005**, *94*, 038103; b) B. Choi, G. Zocchi, Y. Wu, S. Chan, L. J. Perry, *Phys. Rev. Lett.* **2005**, *95*, 078102.

[20] D. J. Hill, M. J. Mio, R. B. Prince, T. S. Hughes, J. S. Moore, *Chem. Rev.* **2001**, *101*, 3893 – 4012.


 © 2006 Wiley-VCH Verlag GmbH & Co. KGaA, Weinheim 

Anion Sensor

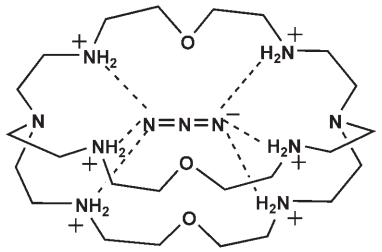
DOI: 10.1002/anie.200504066

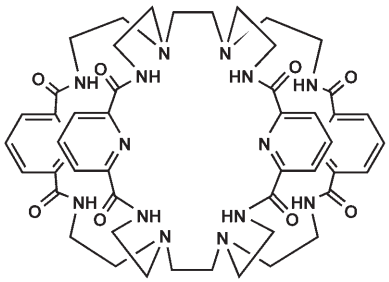
# Trapped Bifluoride**

*Sung Ok Kang, Douglas Powell, Victor W. Day, and Kristin Bowman-James**

*In memory of Bernard Dietrich*

Since Jean-Marie Lehn first reported the structure of an encapsulated triatomic azide in a bicyclic azacryptand known as bis-tren, researchers have sought to do the same for another triatomic anion, bifluoride.[1–3] Lehn, Martell, and co-




workers reported physical data that indicated such an encapsulation in an azacryptand similar to bis-tren;[3] however, crystallographic corroboration has, to our knowledge, remained elusive. We have isolated and structurally characterized a number of fluoride complexes with both monocyclic and bicyclic amine-based[4] and amide-based[5] anion receptors. Despite finding bifluoride in the crystal lattice in a number of the amine-based macrocycles and cryptands, we had not encountered an encapsulated bifluoride. Recently,

[*] Dr. S. O. Kang, Dr. D. Powell, Dr. V. W. Day, Prof. K. Bowman-James
Department of Chemistry
University of Kansas
1251 Wescoe Hall Drive, Lawrence, KS 66045 (USA)
Fax: (+1) 785-864-5396
E-mail: kbjames@ku.edu

[**] We thank the National Science Foundation for support of this work (CHE-0316623) and for purchase of the X-ray diffractometer (CHE-0079282).

Supporting information for this article (including details of the synthesis of the precursors to **1**) is available on the WWW under http://www.angewandte.org or from the author.


© 2006 Wiley-VCH Verlag GmbH & Co. KGaA, Weinheim

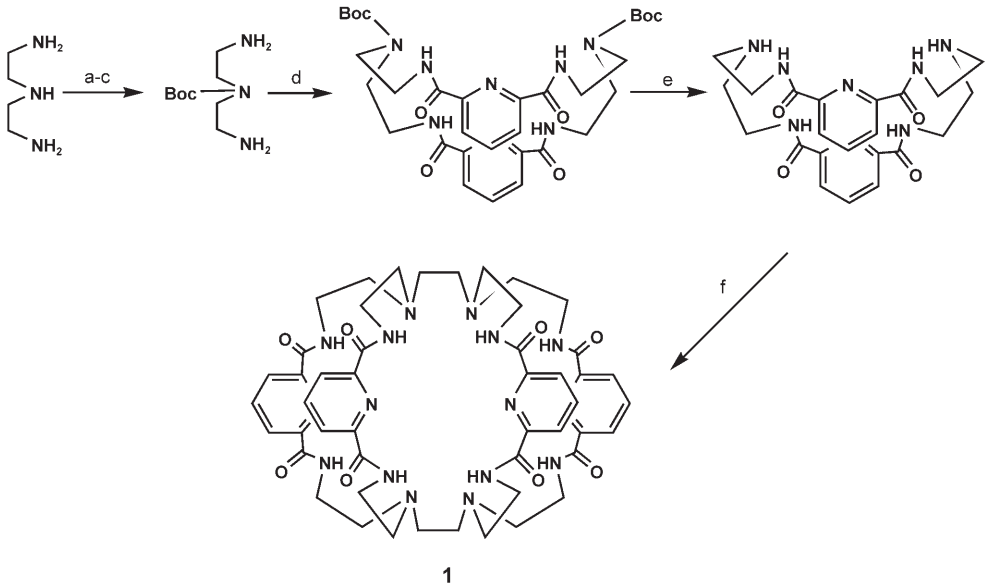
however, in a quest to expand the dimensionality of our anion ligands, we synthesized a tricyclic receptor **1** consisting of two monocyclic macrocycles joined by two bridging ethylene linkages. Our goal was to use this higher-dimensioned ligand as a receptor for ditopic anions. The crystal structure of what we anticipated would be the fluoride complex revealed instead an encapsulated bifluoride ion, thus making this the first example of bifluoride encapsulation within a multicyclic receptor.

The key to the design of this new anion receptor was to link two tetraamido macrocycles at two points, and to explore binding proclivities of the resulting tricycle for ditopic anion guests. The tetraamido ligands chosen are known to be excellent frameworks for binding simple anions,[6] but only a few tricyclic polyamide systems have been reported to date.[7,8] Although these more complex receptors show promise for binding multiatomic and multitopic anions, crystal-structure data have been lacking. Hence, the synthesis and structural characterization of the tricyclic ligand **1** and its bifluoride complex not only open a new area in anion-inclusion chemistry, but also provide much needed crystallographic information. Here we report the synthesis of the new tricyclic receptor **1**, the resulting anion-binding data, and the crystal structures of both the free base and the bifluoride complex, which display amazingly similar structural features.

The tricycle **1** consists of two tetraamido macrocycles bridged by two ethylene spacers. The monocyclic precursor to **1** was synthesized by using selective protection and deprotection techniques. First the terminal amines of diethylenetriamine (dien) were protected with phthaloyl groups, followed by protection of the central secondary amine with di-*tert*-butyldicarbonate (Boc anhydride), and lastly deprotection of the terminal amines (Scheme 1, steps a–c). The macromonocycle was formed by condensation of two Boc-protected triamines with two molecules of pyridine-2,6-dicarbonyl chloride (Scheme 1, step d). After removing the Boc groups, **1** was obtained in 30% yield by coupling two macrocycles at the two unprotected amine sites using dibromoethane (Scheme 1, steps e and f). Crystals of free ligand **1** suitable for X-ray diffraction were grown by slow evaporation from $CHCl_3$. Crystals of the bifluoride complex were grown from a solution of $CH_3CN/CHCl_3$ and **1** in the presence of excess $n Bu_4N^+F^-$.[9]

Although the isolation of a bifluoride complex was not necessarily anticipated, fluoride is known to be a strong base in organic solvents; for example, it abstracts a β-hydrogen atom from anhydrous tetra-*n*-butylammonium salts to yield 1-butene, tri-*n*-butylamine, and tetra-*n*-butylammonium bifluoride.[10] Fluoride has also been observed to abstract hydrogen from amide-based macrocycles[11] and cryptands,[5] as well as urea-,[12] thiourea-,[13] and pyrrole-based[14] acyclic anion hosts, often with the observation of bifluoride in the $^1$H NMR spectra. Even pure tetra-*n*-butylammonium fluoride contains small amounts of bifluoride. Regardless of the source of either the hydrogen ion or bifluoride, the isolation of the bifluoride complex indicates selectivity of **1** for bifluoride over fluoride, at least in the crystalline form.

The bifluoride complex crystallized as the hydrated tetra-*n*-butylammonium salt, $n Bu_4N[\mathbf{1}(FHF)]\cdot 3H_2O$.[9] Although the free-base and bifluoride-complexed forms of tricycle **1** both possess rigorous crystallographic $C_2$ symmetry in their solid-state structures, the conformation of the complexed tricycle approximates quite closely $D_2$ symmetry. The four diamido pyridine groups adopt a pseudo-$S_4$ up-down-up-down arrangement (Figure 1a); this pseudo-$S_4$ axis passes through the two fluorine atoms of the bifluoride anion. The crystallographic $C_2$ axis is perpendicular to this pseudo-$S_4$ axis and passes through the bifluoride hydrogen atom as well as the midpoints of the two ethylene C–C bonds between the tetraamido macrocycles. The macrocycle binds the bifluoride through four amide hydrogen bonds. The remaining four amido protons are involved in intraligand hydrogen bonds. Each of the four diamidopyridine arms of the tricycle contains a three-atom hydrogen bonding network between one of the amide hydrogen atoms and the lone pairs of electrons on its adjacent pyridine and amine nitrogen atoms (N7···H4(N4)···N1 and N16···H19-(N19)···N22 in Table 1). The circle-like pattern resulting from these hydrogen bonds is clearly seen in Figure 1a. Although the constrained geometry makes the N–H···N angles quite acute, the distances are normal for NH···N hydrogen bonds, and this pattern is also present in the solid-state structure of the free base. While these four-atom (3N and 1H) groupings are not required to be coplanar, they are, to within 0.01 Å in the $[\mathbf{1}(FHF)]^-$ complex.




***Scheme 1.*** Synthesis of the tricyclic ligand **1**: a) phthalic anhydride, $CH_3CN$; b) $(Boc)_2O$, $CHCl_3/CH_3CN$; c) $NH_2NH_2\cdot H_2O$, EtOH; d) pyridine-2,6-dicarbonyl chloride, $NEt_3$, $CH_2Cl_2$; e) TFA, $CH_2Cl_2$; f) $BrCH_2CH_2Br$, $K_2CO_3$, $CH_3CN$. Boc = *tert*-butoxycarbonyl, TFA = trifluoroacetic acid.

 © 2006 Wiley-VCH Verlag GmbH & Co. KGaA, Weinheim 

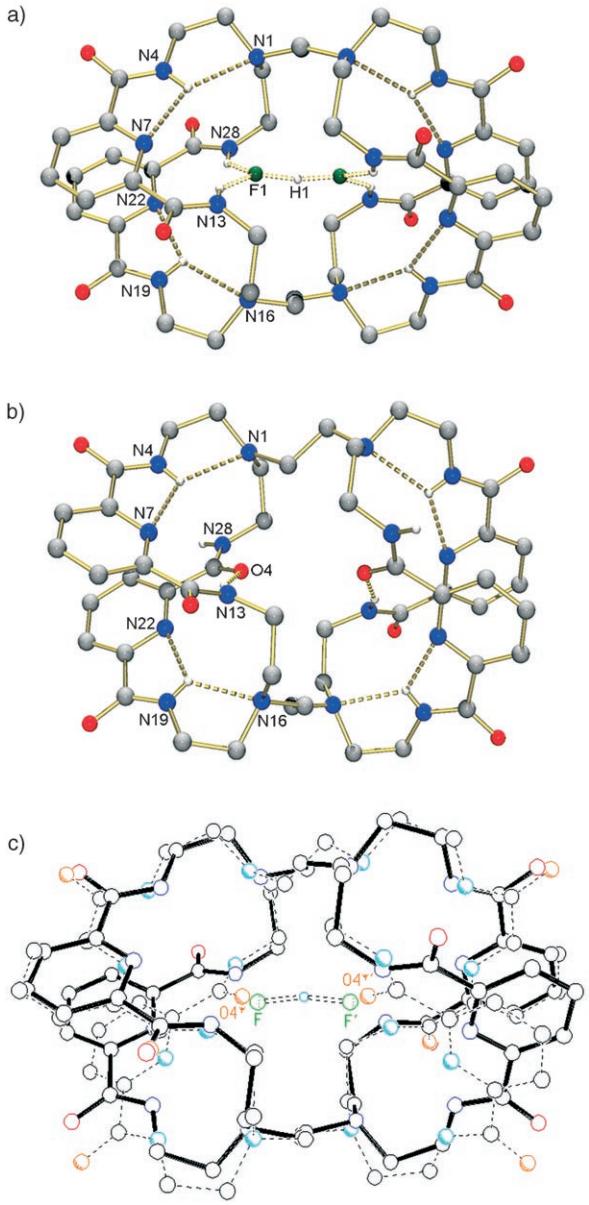



***Figure 1.*** Crystal structures of a) the bifluoride complex of **1**, b) the free base of **1**, and c) the superposition of the bifluoride and free-base structures seen from the same viewpoint. The bifluoride complex in (c) is shown with darker colors and solid bonds, and the free base is shown with lighter colors and dotted bonds. The water molecules of hydration are not shown.

The four remaining amides are hydrogen-bonded to the bifluoride. The F···F separation is 2.475(4) Å with the hydrogen symmetrically situated between the two fluoride ions on the twofold axis. The F···H···F angle is almost linear at 168(4)°.

The free base (**1**) crystallized as the hexahydrate, with six water molecules (three per asymmetric unit) just outside of the cavity (Figure 1b).[9] The tricycle again possesses rigorous crystallographic $C_2$ symmetry with an $S_4$-like arrangement of the diamidopyridine groups. The structural similarities for the tricycle in the hexahydrated free base and complexed forms are quite striking, as shown in the tricycle superposition in Figure 1c. The four three-atom hydrogen-bonding networks

***Table 1:*** Selected hydrogen bond lengths and angles for the bifluoride complex of **1** and free base **1**.

| | [**1**(FHF)]$^-$ | | **1** | |
|---|---|---|---|---|
| D-H···A | *d*(D···A) [Å] | < (DHA) [°] | *d*(D···A) [Å] | < (DHA) [°] |
| N4-H4···N1 | 2.839(2) | 98(2) | 2.814(2) | 104(1) |
| N4-H4···N7 | 2.755(3) | 111(2) | 2.710(2) | 108(1) |
| N19-H19···N16 | 2.896(4) | 114(4) | 2.689(1) | 111(2) |
| N19-H19···N22 | 2.734(4) | 102(3) | 2.576(1) | 115(2) |
| N13-H13···F1 | 2.754(3) | 155(3) | | |
| N28-H28···F1 | 2.724(3) | 154(2) | | |
| N13-H13···O4 | | | 2.905(1) | 159(2) |
| F1-H1···F1[a] | 2.475(4) | 168(4) | | |

[a] Symmetry transformations used to generate equivalent atoms: *x*, $-y+1$, $-z+1$.

between the amide hydrogen atom and the lone pairs of electrons on the adjacent pyridine and amine nitrogen atoms are still observed. The principal difference between the complexed and uncomplexed tricycle involves an approximately 180° rotation of two amide groups, which places the corresponding amide oxygen atoms inside the ligand cavity and enables them to form hydrogen bonds to other amide hydrogen atoms and serve as surrogate anions. The F···O4* separation for the superimposed structures in Figure 1c is 0.75 Å. The proton for each of these two rotated amide groups forms a hydrogen bond to an external water molecule.

The bifluoride complex was further characterized by $^1$H and $^{19}$F NMR spectroscopy, which indicates that the anion remains inside the cavity even in solution (Figure 2). In the $^1$H NMR spectrum recorded in [D$_6$]DMSO, the signal of the encapsulated bifluoride hydrogen atom is seen as a triplet as a result of coupling of the hydrogen atom with the adjacent fluoride ions with $I_F = 1/2$. This signal is shifted 2.1 ppm downfield to $\delta = 17.5$ ppm ($J_{HF} = 128$ Hz) compared to free bifluoride, which occurs at $\delta = 15.4$ ppm in [D$_6$]DMSO (Figure 2a). In the $^{19}$F NMR spectrum, the signal assigned to unbound bifluoride at $\delta = -145.3$ ppm is shifted upfield to $\delta = -152.1$ ppm ($\Delta\delta = 6.8$ ppm) in [**1**(FHF)]$^-$ (Figure 2b).

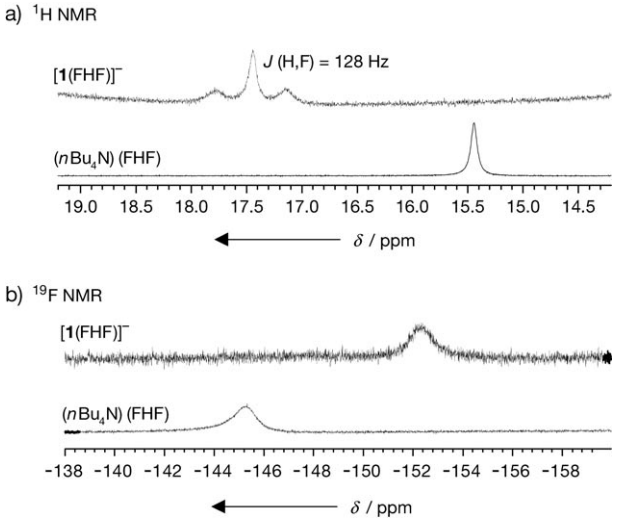



***Figure 2.*** (a) $^1$H NMR and (b) $^{19}$F NMR spectra of $n$Bu$_4$N$^+$FHF$^-$ and [**1**(FHF)]$^-$ in [D$_6$]DMSO.

 © 2006 Wiley-VCH Verlag GmbH & Co. KGaA, Weinheim 

The signal is broad, possibly as a result of unresolved coupling with both the amide and bifluoride hydrogen atoms.

Binding studies of **1** with anions by using $^1$H NMR techniques revealed amazingly selective binding and high affinity for the ditopic $FHF^-$ ion ($K_a = 5500$) followed by $H_2PO_4^-$ (740), $N_3^-$ (340), and $CH_3COO^-$ (100), with negligible binding for $HSO_4^-$, $Cl^-$, $Br^-$, $I^-$, $NO_3^-$, and $ClO_4^-$ ions in [D$_6$]DMSO. The association constant value of **1** for bifluoride in $CDCl_3$ is close to the calculation limit by NMR methods ($K_a$ ca. $10^4$–$10^5$; Figure 3). A complicated titration curve was

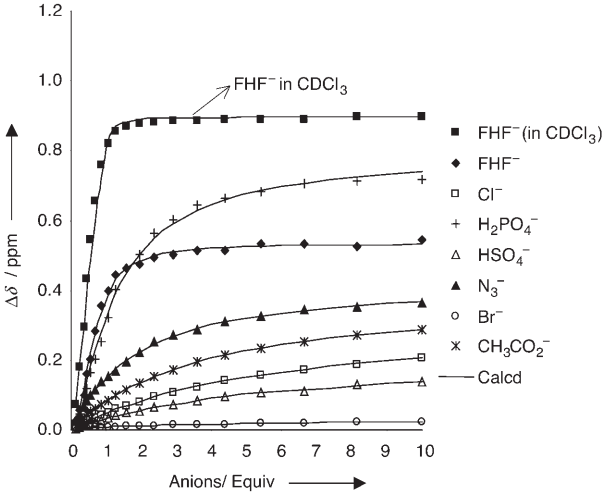



***Figure 3.*** Plot of the chemical shift of the NH protons of **1** (2 mM) upon increasing the concentration of $n$Bu$_4$N$^+$X$^-$ in [D$_6$]DMSO, and comparison to a similar plot of $FHF^-$ binding in $CDCl_3$ (■).

observed when fluoride was added to a solution of **1**, which is probably attributed to both the formation of multiple stoichiometries between fluoride ions and **1** as well as the generation of bifluoride.[10]

In conclusion, the new tricyclic anion receptor results from the successful coupling of two monocyclic receptors through two ethylene linkers. Each tetraamido macromonocycle provides a site for anion binding, which results in a stable, complementary structure for ditopic anions. Not only do the two structures provide the first crystallographic reports for tricyclic amide-based receptors, but the structure of the encapsulated bifluoride complex successfully ends the quest of a number of chemists over three decades for this elusive anion.

## *Experimental Section*

**1**: 1,2-Dibromoethane (1.00 mL, 11.6 mmol) was added to a solution of the deprotected macromonocycle (0.20 g, 0.43 mmol) with $K_2CO_3$ (0.50 g, 3.62 mmol) in $CH_3CN$ (200 mL), and the reaction mixture was refluxed for 2 days. The solvent was evaporated and water (100 mL) was added to the residue. After stirring the mixture for 3 h, the precipitate was isolated by filtration and dried. This crude product was purified by column chromatography (basic $Al_2O_3$, 2% MeOH in $CH_2Cl_2$) to give the pure macrotricycle **1** (30% yield). $^1$H NMR (400 MHz, [D$_6$]DMSO, 23 °C, TMS): $\delta = 8.70$ (br s, 8H; NH), 7.88 (t, $J$(H,H) = 7.0 Hz, 4H; ArH), 7.79 (d, $J$(H,H) = 7.4 Hz, 8H; ArH), 3.35 (m, 16H; $CH_2$), 2.79 ppm (m, 24H; $CH_2$); $^{13}$C NMR (400 MHz, $CDCl_3$) $\delta = 163.8$ (C=O), 149.1, 138.5, 124.6 (Ar), 54.7, 53.0, 38.1 ppm ($CH_2$); FAB MS: $m/z = 989.7$ [$M$H]$^+$. Elemental analysis (%) calcd for $C_{48}H_{60}N_{16}O_8 \cdot CH_2Cl_2 \cdot H_2O$: C 53.89, H 5.91, N 20.52; found: C 53.69, H 5.66, N 20.77.

NMR studies: $^1$H NMR spectra were recorded on a Bruker Avance 400 spectrometer at 400 MHz. Each titration involved 20 measurements in [D$_6$]DMSO at room temperature. Aliquots from a stock solution of the $n$Bu$_4$N$^+$ salts (20 mM) were gradually added to the initial solution of the ligand (2 mM). All proton signals were referred to TMS. The association constants $K_a$ were calculated by EQNMR.[15] $^{19}$F NMR spectra were recorded on a Bruker Avance 400 spectrometer at 376.5 MHz, and the chemical shifts were recorded in ppm relative to aqueous NaF at −122.4 ppm as an external standard. All spectra were recorded at 23 °C.

Received: November 15, 2005
Published online: February 21, 2006

**Keywords:** anion recognition · bifluoride · host–guest systems · supramolecular chemistry · tricyclic receptors

[1] J.-M. Lehn, E. Sonveaux, A. K. Willard, *J. Am. Chem. Soc.* **1978**, *100*, 4914–4916.
[2] R. J. Motekaitis, A. E. Martell, I. Murase, *Inorg. Chem.* **1986**, *25*, 938–944.
[3] R. J. Motekaitis, A. E. Martell, I. Murase, J.-M. Lehn, M. W. Hosseini, *Inorg. Chem.* **1988**, *27*, 3630–3636.
[4] a) S. Mason, J. M. Llinares, M. Morton, T. Clifford, K. Bowman-James, *J. Am. Chem. Soc.* **2000**, *122*, 1814–1815; b) J. A. Aguilar, T. Clifford, A. Danby, J. M. Llinares, S. Mason, E. García-España, K. Bowman-James, *Supramol. Chem.* **2001**, *13*, 405–417; c) M. A. Hossain, J. M. Llinares, S. Mason, P. Morehouse, D. Powell, K. Bowman-James, *Angew. Chem.* **2002**, *114*, 2441–2444; *Angew. Chem. Int. Ed.* **2002**, *41*, 2335–2338; d) M. A. Hossain, P. Morehouse, D. Powell, K. Bowman-James, *Inorg. Chem.* **2005**, *44*, 2143–2149.
[5] a) S. O. Kang, J. M. Llinares, D. Powell, D. VanderVelde, K. Bowman-James, *J. Am. Chem. Soc.* **2003**, *125*, 10152–10153; b) S. O. Kang, D. VanderVelde, D. Powell, K. Bowman-James, *J. Am. Chem. Soc.* **2004**, *126*, 12272–12273; c) S. O. Kang, D. Powell, K. Bowman-James, *J. Am. Chem. Soc.* **2005**, *127*, 13478–13479.
[6] a) M. A. Hossain, J. M. Llinares, D. Powell, K. Bowman-James, *Inorg. Chem.* **2001**, *40*, 2936–2937; b) M. A. Hossain, S. O. Kang, D. Powell, K. Bowman-James, *Inorg. Chem.* **2003**, *42*, 1397–1399.
[7] a) G. Das, P. Tripathi, A Tripathi, P. K. Bharadwaj, *Tetrahedron* **2000**, *56*, 1501–1504; b) P. Lipkowski, D. T. Gryko, J. Jurczak, J. Lipkowski, *Tetrahedron Lett.* **1998**, *39*, 3833–3836.
[8] a) A. P. Davis, R. S. Wareham, *Angew. Chem.* **1998**, *110*, 2397–2401; *Angew. Chem. Int. Ed.* **1998**, *37*, 2270–2273; b) A. P. Davis, R. S. Wareham, *Angew. Chem.* **1999**, *111*, 3160–3179; *Angew. Chem. Int. Ed.* **1999**, *38*, 2978–2996; c) G. Lecollinet, A. P. Dominey, T. Velasco, A. P. Davis, *Angew. Chem.* **2002**, *114*, 4267–4270; *Angew. Chem. Int. Ed.* **2002**, *41*, 4093–4096; d) E. Klein, M. P. Crump, A. P. Davis, *Angew. Chem.* **2004**, *116*, 302–306; *Angew. Chem. Int. Ed.* **2005**, *44*, 298–302.
[9] X-ray data for $n$Bu$_4$N$^+$[**1**(FHF$^-$)]·3H$_2$O: $C_{64}H_{103}F_2N_{17}O_{11}$, $M_r$ = 1324.63, crystal dimensions $0.36 \times 0.30 \times 0.30$ mm$^3$, orthorhombic, space group $C222_1$, $a = 14.611(2)$, $b = 17.121(2)$, $c = 28.675(3)$ Å, $\alpha = \beta = \gamma = 90°$, $V = 7173(2)$ Å$^3$, $Z = 4$, $\rho_{calcd} = 1.227$ g cm$^{-3}$, $T = 100(2)$ K, $F(000) = 2848$, $\mu(Mo_{K\alpha}) = 0.089$ mm$^{-1}$, 10514 ($R_{int} = 0.043$) independent reflections (43041 measured), $R_1$ (unweighted, based on $F$) = 0.074 for 8546 "observed" reflections having $I > 2\sigma(I)$ and $2\theta(Mo_{K\alpha})$

 © 2006 Wiley-VCH Verlag GmbH & Co. KGaA, Weinheim 

$< 60.20°$; $R_1$ (unweighted, based on $F$) = 0.084, $wR_2$ (weighted, based on $F^2$) = 0.221 and GOF (on $F^2$) = 1.020 for all 10514 independent reflections having $2\theta(Mo_{K\alpha}) < 60.20°$. X-ray data for **1**·6 $H_2O$: $C_{48}H_{72}N_{16}O_{14}$, $M_r = 1097.22$, crystal dimensions $0.36 \times 0.34 \times 0.10\ mm^3$, monoclinic, space group $C2/c$, $a = 17.116(2)$, $b = 14.949(2)$, $c = 22.082(3)$ Å, $\alpha = \gamma = 90°$, $\beta = 106.782(3)$, $V = 5409(1)$ $Å^3$, $Z = 4$, $\rho_{calcd} = 1.347\ g\,cm^{-3}$, $T = 100(2)$ K, $F(000) = 2336$, $\mu(Mo_{K\alpha}) = 0.101\ mm^{-1}$, 7867 ($R_{int} = 0.028$) independent absorption-corrected reflections (30720 measured), $R_1$ (unweighted, based on $F$) = 0.049 for 6680 "observed" reflections having $I > 2\sigma(I)$ and $2\theta(Mo_{K\alpha}) < 60.11°$; $R_1$ (unweighted, based on $F$) = 0.057, $wR_2$ (weighted, based on $F^2$) = 0.132 and GOF (on $F^2$) = 1.021 for all 7867 independent absorption-corrected reflections having $2\theta(Mo_{K\alpha}) < 60.11°$. CCDC-289348 and CCDC-289349 contain the supplementary crystallographic data for this paper. These data can be obtained free of charge from The Cambridge Crystallographic Data Centre via www.ccdc.cam.ac.uk/data_request/cif.

[10] a) R. K. Sharma, J. L. Fry, *J. Org. Chem.* **1983**, *48*, 2112 – 2114; b) D. P. Cox, J. Terpinski, W. Lawrynowicz, *J. Org. Chem.* **1984**, *49*, 3216 – 3219; c) K. O. Christe, W. W. Wilson, R. D. Wilson, R. Bau, J. A. Feng, *J. Am. Chem. Soc.* **1990**, *112*, 7619 – 7625; d) F. Y. Fujiwara, J. S. Martin, *J. Am. Chem. Soc.* **1974**, *96*, 7625 – 7631; e) J. S. Martin, F. Y. Fujiwara, *J. Am. Chem. Soc.* **1974**, *96*, 7632 – 7637; f) H. Sun, S. G. DiMagno, *J. Am. Chem. Soc.* **2005**, *127*, 2050 – 2051.

[11] A. M. Costere, M. J. Bañuls, M. J. Aurell, M. D. Ward, S. Argent, *Tetrahedron* **2004**, *60*, 9471 – 9478.

[12] a) D. Esteban-Gómez, L. Fabbrizzi, M. Licchelli, *J. Org. Chem.* **2005**, *70*, 5717 – 5720; b) M. Boiocchi, L. D. Boca, D. E. Gómez, L. Fabbrizzi, M. Licchelli, E. Monzani, *J. Am. Chem. Soc.* **2004**, *126*, 16507 – 16514.

[13] a) T. Gunnlaugsson, P. E. Kruger, P. Jensen, F. M. Pfeffer, G. M. Hussey, *Tetrahedron Lett.* **2003**, *44*, 8909 – 8913; b) F. M. Pfeffer, T. Gunnlaugsson, P. Jensen, P. E. Kruger, *Org. Lett.* **2005**, *7*, 5357 – 5360; c) T. Gunnlaugsson, P. E. Kruger, P. Jensen, J. Tierney, H. D. P. Ali, G. M. Hussey, *J. Org. Chem.* **2005**, *70*, 10875 – 10878.

[14] a) S. Camiolo, P. A. Gale, M. B. Hursthouse, M. E. Light, A. J. Shi, *Chem. Commun.* **2002**, 758 – 759; b) P. A. Gale, K. Navakhun, S. Camiolo, M. E. Light, M. B. Hursthouse, *J. Am. Chem. Soc.* **2002**, *124*, 11228 – 11229; c) S. Camiolo, P. A. Gale, M. B. Hursthouse, M. E. Light, *Org. Biomol. Chem.* **2003**, *1*, 741 – 744.

[15] M. Hynes, *J. Chem. Soc. Dalton Trans.* **1993**, 311 – 312.

 © 2006 Wiley-VCH Verlag GmbH & Co. KGaA, Weinheim 

Lanthanide Luminescence

DOI: 10.1002/anie.200502670

# Fine Control of Red–Green–Blue Photoluminescence in Zeolites Incorporated with Rare-Earth Ions and a Photosensitizer**

*Yuji Wada,* Mutsuko Sato, and Yasunori Tsukahara*

Red–green–blue (RGB) photoluminescent crystals have recently merited considerable attention because of their potential application to optoelectronic devices such as full-color displays.[1–3] Energy transfer has been demonstrated in the photosensitization of metal complexes,[4] dendrimers,[5] phosphors,[6] and electroluminescence devices.[7] However, the control of energy transfer to multiple components for multicolored luminescence[8,9c] has so far been extremely difficult because of the sensitivity of luminescence systems to their chemical environments. Nanohybrid systems using zeolites appear to be good candidates to overcome such difficulties.[9] Herein, we report rare-earth-ion-exchanged zeolites incorporated with a photosensitizer (Figure 1 A) that exhibit successful RGB photoluminescence depending on which rare-earth ions and photosensitizers are used (Figure 1 B). The color can also be finely tuned by varying the temperature and the excitation wavelength.

The sodium form of faujasite-type zeolite, Na-X ($SiO_2/Al_2O_3 = 2.46$, $Na/Al = 1.0$; Tosoh Co.), was stirred in an aqueous solution of $Ln(NO_3)_3{\cdot}6H_2O$ (Ln = Tb, Eu; 0.08 M; $[Tb^{III}]/[Eu^{III}] = 10{:}0$, 10:1, 1:1, and 0:10) for 16 h at 353 K to exchange the sodium ions with $Ln^{III}$ ions. The products were removed by centrifugation, then washed with deionized water, and dried in air at 353 K. The $Ln^{III}$-exchanged zeolites were degassed at 423 K for 1 h for dehydration and were then either exposed to benzophenone (bzp) vapor at 373 K for 16 h or stirred in a solution of 4-acetylbiphenyl (acbp) in ethanol at room temperature for 20 h. The resulting samples were then degassed at room temperature for 5 h. The reaction sequence was carried out on a vacuum line to avoid exposure of the zeolites to the atmosphere.

The percentages of Tb and Eu in the zeolites were determined by inductively coupled plasma techniques (Jobin

[*] Prof. Y. Wada, M. Sato, Y. Tsukahara
Department of Material and Life Science
Graduate School of Engineering
Osaka University
2-1 Yamada-oka Suita, Osaka 565-0871 (Japan)
Fax: (+81) 6-6879-7875
E-mail: ywada@mls.eng.osaka-u.ac.jp

[**] This work was supported by a Grant-in-Aid for Scientific Research on Priority Areas (417, no. 17029038) from the Ministry of Education, Culture, Sports, Science, and Technology (MEXT) of the Japanese Government. We express special thanks to Prof. S. Fukuzumi for critical reading of the manuscript. We thank Mrs. Ayako Morishima at JASCO International Co. Ltd. for measuring quantum yields.

Supporting information for this article is available on the WWW under http://www.angewandte.org or from the author.


© 2006 Wiley-VCH Verlag GmbH & Co. KGaA, Weinheim

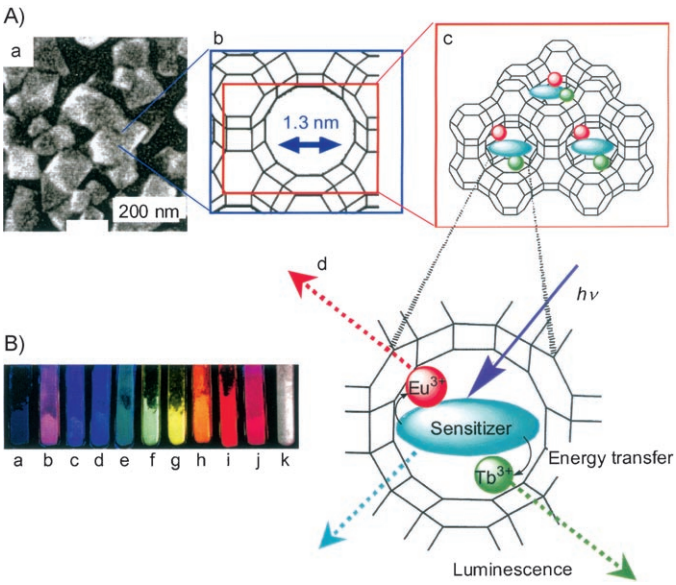



***Figure 1.*** A) a) Scanning electron microscopy image of faujasite zeolite; b, c) views of the framework structure of the zeolite crystal; the sizes of the 12-ring open window and inner cage are 0.7 and 1.3 nm, respectively; d) luminescence from the sensitizer molecule and sensitized emission of $Tb^{III}$ and $Eu^{III}$ ions through energy transfer from the sensitizer molecule. B) Photographs of the photoluminescence from the zeolite samples, with colors varying from violet to red depending on the incorporated amounts of $Tb^{III}$ and $Eu^{III}$ ions, the type of photosensitizer (benzophenone or 4-acetylbiphenyl), and the excitation wavelength. See Table 1 for the composition of the samples.

Yvon ULTIMA2). The amounts of the sensitizers incorporated in the zeolites were determined by combustion chemical (C, N) analysis and ranged between 10–11 molecules in a unit cell, which corresponds to one to two molecules of sensitizer per supercage of the zeolites (see Table 1 and Supporting Information). Emission and excitation spectra were obtained with a SPEX Fluorog-3 (Jobin Yvon), and quantum yields ($\Phi$) were determined by standard procedures using a spectrofluorometer (JASCO FP-6600) equipped with an integrating sphere (JASCO ISF-531).

***Table 1:*** Composition of samples a–k as shown in Figure 1 B.

| | Sample | $\lambda$ [nm][a] | Luminescence component Eu (red)[b] | Tb (green)[b] | Sensitizer (blue)[c] |
|---|---|---|---|---|---|
| a | Zeolite-X | 365 | 0 | 0 | 0 |
| b | Tb31Eu3.2(acbp)-X | 254 | 3.2 | 31 | 11 acbp |
| c | Tb31Eu3.2(acbp)-X | 365 | 3.2 | 31 | 11 acbp |
| d | Tb34(acbp)-X | 365 | 0 | 34 | 10 acbp |
| e | Tb34(acbp)-X | 254 | 0 | 34 | 10 acbp |
| f | Tb34(bzp)-X | 365 | 0 | 34 | 10 bzp |
| g | Tb31Eu3.2(bzp)-X | 365 | 3.2 | 31 | 11 bzp |
| h | Tb15Eu18(bzp)-X | 365 | 18 | 15 | 11 bzp |
| i | Eu32(bzp)-X | 365 | 32 | 0 | 11 bzp |
| j | Tb18Eu15(acbp)-X | 254 | 18 | 15 | 10 acbp |
| k[d] | Tb31Eu3.2(acbp)-X | 254 | 3.2 | 31 | 11 acbp |

[a] Excited using a Handy UV Lamp (AS ONE Co.). [b] Numbers of $Tb^{III}$ and $Eu^{III}$ ions contained in a unit cell of the zeolite crystal. [c] Number of sensitizer molecules in the unit cell; acbp = 4-acetylbiphenyl, bzp = benzophenone. [d] Measured at 77 K.

The samples exhibit photoluminescence as demonstrated in Figure 1 B. The colors obtained varied from violet (b) to red (j) through blue (c, d) and green (e) by changing the amounts of the rare-earth cations and the nature of the sensitizer (4-acetylbiphenyl or benzophenone). 4-Acetylbiphenyl encapsulated in the zeolite cavity gave rise to blue emission besides the red and green colors emitted by $Eu^{III}$ and $Tb^{III}$ ions, respectively, leading to simultaneous RGB photoluminescence (see Supporting Information). On the other hand, benzophenone did not give rise to blue emission and only functioned as a photosensitizer of $Eu^{III}$ and $Tb^{III}$ ions (see Supporting Information).[10] The ratio of the intensities of the red and green emissions increases gradually in the order Tb34(bzp)-X, Tb31Eu3.2(bzp)-X, Tb15Eu18(bzp)-X, and Eu32(bzp)-X (see Table 1 for notation), as shown in Figure 1 B parts f–i.

The rare-earth cations remain in the supercage probably as a result of attractive interactions with the photosensitizer (even after heat treatment),[11] thus the photosensitizer may be located in proximity to the cations. The quantum yields of the photosensitized luminescence were determined (see Table 2), and the absolute values were found to range between 0.007 and 0.28 depending on the photosensitizer. Tb34(bzp)-X exhibits the highest quantum yield with a value of 0.28. The samples that contain bzp as a photosensitizer show higher quantum yields than those that contain acbp; the latter probably suffers from vibronic deexcitation by ethanol molecules that remain in the zeolite following its introduction into the cavity.

***Table 2:*** Quantum yields $\Phi$ of the samples.

| Sample | $\lambda_{ex}$ [nm][a] | $\Phi$ [%][b] |
|---|---|---|
| Tb31Eu3.2(acbp)-X | 280 | 1.92 |
| Tb31Eu3.2(acbp)-X | 300 | 0.87 |
| Tb31Eu3.2(acbp)-X | 360 | 0.67 |
| Tb34(acbp)-X | 300 | 1.29 |
| Tb34(acbp)-X | 360 | 0.27 |
| Tb31Eu3.2(bzp)-X | 342 | 22.4 |
| Tb18Eu15(bzp)-X | 342 | 11.3 |
| Tb34(bzp)-X | 342 | 27.8 |

[a] Excitation wavelength. [b] Absolute quantum yields of luminescence measured at room temperature.

When the excitation wavelength for 4-acetylbiphenyl is changed, the intensity ratio of the colors of the three components is also varied. Figure 2 shows the spectra of photoluminescence obtained at 77 and 293 K (see also Supporting Information). Characteristic sharp bands at 488, 540, 582, and 621 nm are attributed to the f–f transitions of $Tb^{III}$ ($^5D_4$–$^7F_J$, $J = 6, 5, 4, 3$), while the bands at 592 and 610 nm are attributed to those of $Eu^{III}$ ($^5D_0$–$^7F_J$, $J = 1, 2$).[4] The broad band with a maximum at 400–410 nm is attributed to the emission of the 4-acetylbiphenyl chromophore.[12] The green component of the emission increases drastically upon increasing the excitation wavelength from 260 nm to 320 nm but decreases above 320 nm, whereas the other two components increase steadily over the range studied (Figure 2 A b).

There are 11 molecules of acbp in a unit cell of Tb31Eu3.2(acbp)-X, which shows blue luminescence as well

 © 2006 Wiley-VCH Verlag GmbH & Co. KGaA, Weinheim 

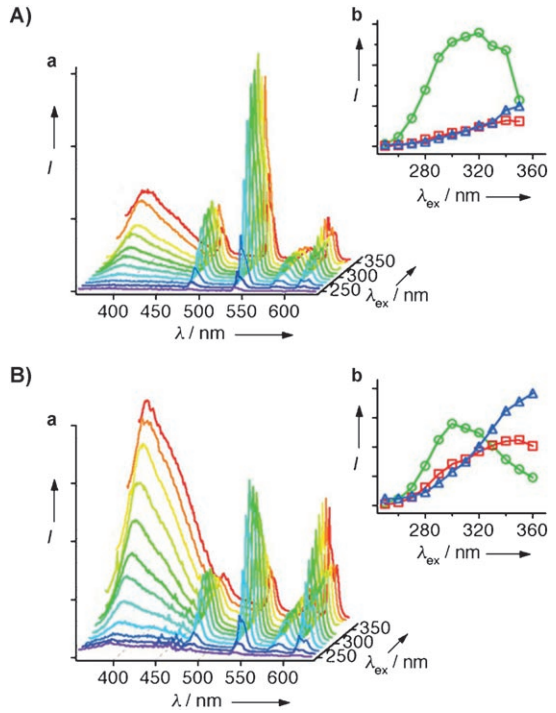



***Figure 2.*** Changes in the photoluminescence of sample Tb31Eu3.2-(acbp)-X with excitation wavelength over the range 250–360 nm, measured at A) 77 K and B) 293 K. a) Photoluminescence spectra of Tb31Eu3.2(acbp)-X at different excitation wavelengths. b) Changes in the emission intensity of the three components ($\lambda_{em}$ = 540 nm for $Tb^{III}$ (green), $\lambda_{em}$ = 610 nm for $Eu^{III}$ (red), and $\lambda_{em}$ = 400 nm for 4-acetylbiphenyl (blue)) at various excitation wavelengths ($\lambda_{ex}$) over the range 250–360 nm.

as the red and green emission resulting from the photosensitization of the rare-earth cations. We found that the blue luminescence at around 410 nm is observed only when the number of acbp molecules is greater than one (see Supporting Information). This result leads us to assume that the changes in the ratio of the colors of the three components depending on the excitation wavelength is related to the configuration of the two acbp molecules located in proximity. The excitation energy can be transferred to the $Eu^{III}$ and $Tb^{III}$ ions through different routes according to the different configurations of the two acbp molecules which probably results in a dependence on the excitation wavelength.

The intensity ratio of the three colored components depends not only on the excitation wavelength but also on the temperature. The emission wavelength of the maximum of the green component is shifted to shorter wavelengths at 293 K (Figure 2 B), while similar changes as shown in Figure 2 A are observed. The temperature dependence of the photoluminescence of Tb31Eu3.2(acbp)-X was examined over the range 77–293 K (see Supporting Information). The green component of the emission (from the $Tb^{III}$ ions) decreases more rapidly than the red and blue components with increasing temperature. This results in a change of the color from white (part k in Figure 1 B) to pink (part b in Figure 1 B). Such a change in the luminescence intensities as a function of the temperature results from a change in the rate of energy transfer from 4-acetylbiphenyl to the $Tb^{III}$ ions, which has a higher energy barrier than, for example, $Eu^{III}$ ions.[13]

If three colored components were mixed in fluid solution, only the emission from the lowest vibration level of the triplet excited state of 4-acetylbiphenyl would be observed, irrespective of the different excitation wavelengths, according to Kasha's rule.[4] Furthermore, changes in the ratio of the three colored components as a function of the excitation wavelength and temperature are attained only by using zeolites as a host. Thus, these systems require further investigation to understand their mechanisms. The zeolite supercage incorporated with various amounts of three colored components provides an ideal environment to control the energy-transfer processes that take place between them as a function of the excitation wavelength and temperature. Zeolites offer the advantage of precisely locating their guests at crystallographic cation sites in nanosized pores. Thus, we can tune the photoluminescence color over a wide range by varying the amounts of the rare-earth cations and the organic photosensitizer at the design stage of the material (parts b–j in Figure 3) as well as by changing the temperature and the excitation wavelength during the utilization (lines A and B in Figure 3), as illustrated in the CIE *x*–*y* chromaticity diagram of the multicolored photoluminescence of the samples.

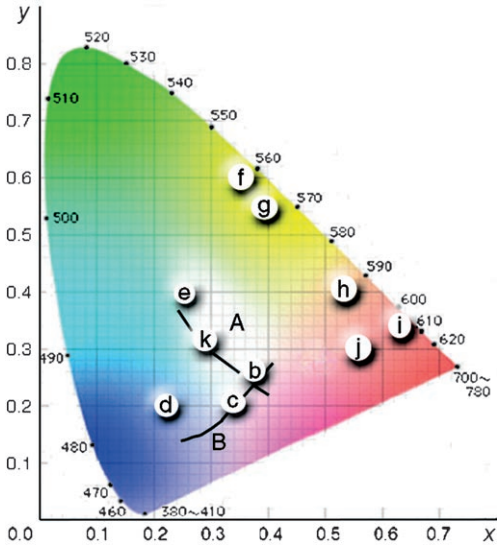



***Figure 3.*** CIE (Commission Internationale de l'Eclairage) *x*–*y* chromaticity diagram showing the location of the multicolored photoluminescence from the samples (b–k, corresponding to the samples shown in Figure 1 B) and changes in the photoluminescence of sample Tb31Eu3.2(acbp)-X at various temperatures from 77 K (k) to 293 K (b) upon excitation at 330 nm (line A) and at different excitation wavelengths from 250 to 360 nm at room temperature (line B).

In conclusion, the use of zeolite supercages provides a promising strategy to develop RGB-photoluminescent materials for nanoscale optoelectronic devices such as thermosensors and full-color displays.[14]

Received: July 29, 2005
Revised: December 8, 2005
Published online: February 17, 2006

 © 2006 Wiley-VCH Verlag GmbH & Co. KGaA, Weinheim 

**Keywords:** host–guest systems · lanthanides · luminescence · sensitizers · zeolites

[1] a) A. Kishimura, T. Yamashita, T. Aida, *J. Am. Chem. Soc.* **2005**, *127*, 179 – 183; b) M. Morimoto, S. Kobatake, M. Irie, *J. Am. Chem. Soc.* **2003**, *125*, 11080 – 11087; c) C. Moreno Castro, M. C. Ruiz Delgado, V. Hernández, Y. Shirota, J. Casado, J. T. López Navarrete, *J. Phys. Chem. B* **2002**, *106*, 7163 – 7170.

[2] a) R. Jin, Y. W. Cao, C. A. Mirkin, K. L. Kelly, G. C. Schatz, J. G. Zheng, *Science* **2001**, *294*, 1901 – 1903; b) Y. Ohko, T. Tatsuma, T. Fuji, K. Naoi, C. Niwa, Y. Kubota, A. Fujishima, *Nat. Mater.* **2003**, *2*, 29 – 31.

[3] a) W. Chen, A. G. Joly, J.-O. Malm, J.-O. Bovin, S. Wang, *J. Phys. Chem. B* **2003**, *107*, 6544 – 6551; b) W. Chen, J.-O. Bovin, A. G. Joly, S. Wang, F. Su, G. Li, *J. Phys. Chem. B* **2004**, *108*, 11927 – 11934.

[4] a) Q. Li, T. Li, J. Wu, *J. Phys. Chem. B* **2001**, *105*, 12293 – 12296; b) S. Quici, G. Marzanni, M. Cavazzini, P. L. Anelli, M. Botta, E. Gianolio, G. Accorsi, N. Armaroli, F. Barigelletti, *Inorg. Chem.* **2002**, *41*, 2777 – 2784.

[5] a) D. L. Jiang, T. Aida, *Nature* **1997**, *388*, 454 – 456; b) P. Furuta, J. Brooks, M. E. Thompson, J. M. J. Fréchet, *J. Am. Chem. Soc.* **2003**, *125*, 13165 – 13172.

[6] E. Danielson, M. Devenney, D. M. Giaquinta, J. H. Golden, R. C. Haushalter, E. W. McFarland, D. M. Poojary, C. M. Reaves, W. H. Weinberg, X. D. Wu, *Science* **1998**, *279*, 837 – 839.

[7] a) Y. Q. Wang, A. Steckl, *J. Appl. Phys. Lett.* **2003**, *82*, 502 – 504; b) S. Welter, K. Brunner, J. W. Hofstraat, L. Cola, *Nature* **2003**, *421*, 54 – 57; c) C. D. Müller, A. Falcou, N. Reckefuss, M. Rojahn, V. Wiederhirn, P. Rudati, H. Frohne, O. Nuyken, H. Becker, K. Meerholz, *Nature* **2003**, *421*, 829 – 833.

[8] a) C. Botta, G. Patrinoiu, P. Picouet, S. Yunus, J.-E. Communal, F. Cordella, F. Quochi, A. Mura, G. Bongiovanni, M. Pasini, S. Desitri, G. Silvestro, *Adv. Mater.* **2004**, *16*, 1716 – 1721; b) J. Hill, S. Heriot, Y. O. Worsfold, T. H. Richardson, A. M. Fox, *Phys. Rev.* **2004**, *69*, 041303 – 1–4; c) P. N. Minoofar, B. S. Dunn, J. I. Zink, *J. Am. Chem. Soc.* **2004**, *126*, 2656 – 2665; d) M. Pauchard, S. Huber, R. Méallet-Renault, H. Maas, R. Pansu, G. Calzaferri, *Angew. Chem.* **2001**, *113*, 2921 – 2924; *Angew. Chem. Int. Ed.* **2001**, *40*, 2839 – 2842; e) W. Chen, R. Sammynaiken, Y. Huang, *J. Appl. Phys.* **2000**, *88*, 1424 – 1431.

[9] a) Y. Wada, T. Okubo, M. Ryo, T. Nakazawa, Y. Hasegawa, S. Yanagida, *J. Am. Chem. Soc.* **2000**, *122*, 8583 – 8584; b) S. Heer, K. Kompe, H.-U. Gudel, M. Haase, *Adv. Mater.* **2004**, *16*, 2102 – 2105; c) L. Fu, Z. Liu, Y. Liu, B. Han, J. Wang, P. Hu, L. Cao, D. Zhu, *J. Phys. Chem. B* **2004**, *108*, 13074 – 13078; d) H. Ow, D. R. Larson, M. Srivastava, B. A. Baird, W. W. Webb, U. Wiesner, *Nano Lett.* **2005**, *5*, 113 – 117; e) L. Wang, C. Yang, W. Tan, *Nano Lett.* **2005**, *5*, 37 – 43.

[10] S. Hashimoto, S. Kirikae, S. Tobita, *Phys. Chem. Chem. Phys.* **2002**, *4*, 5856 – 5862.

[11] S. B. Hong, E. W. Shin, S. H. Moon, C.-H. Pyun, C.-H. Kim, Y. S. Uh, *J. Phys. Chem.* **1995**, *99*, 12274 – 12277.

[12] Y. H. Kim, D. W. Cho, N. W. Song, D. Kim, M. Yoon, *J. Photochem. Photobiol. A* **1997**, *106*, 161 – 167.

[13] a) S. Katagiri, Y. Hasegawa, Y. Wada, S. Yanagida, *Chem. Lett.* **2004**, *33*, 1438 – 1439; b) M. Latva, H. Takalo, V.-M. Mukkala, C. Matachescu, J. C. Rodriguez-Ubis, J. Kankare, *J. Lumin.* **1997**, *75*, 149 – 169; c) J. Yu, *J. Lumin.* **1998**, *78*, 265 – 270.

[14] See Supporting Information for the absorption, photoluminescence, and excitation spectra of Tb31Eu3.1(acbp)-X and Tb31Eu3.2(bzp)-X; for the changes in the photoluminescence of the samples at various temperatures and different wavelengths; for the photoluminescence spectra of Tb32(acbp)11-X and Tb32(acbp)4-X; and for the number of luminescent components in the supercage.

 © 2006 Wiley-VCH Verlag GmbH & Co. KGaA, Weinheim 

Liquid Crystals

DOI: 10.1002/anie.200503402

# Liquid-Crystalline Quaternary Block Molecules Incorporating Bent-Core Units**

*R. Amaranatha Reddy, Gert Dantlgraber, Ute Baumeister, and Carsten Tschierske**

*Dedicated to Professor Siegfried Hünig on the occasion on his 85th birthday*

The design of functional supramolecular systems by the self-organization of single molecules to give complex superstructures is a contemporary challenge. Whereas classical supramolecular chemistry focuses on assemblies formed by a limited number of molecules (host–guest chemistry),[1] the design of self-organized bulk materials with special properties is also an important task. The design of materials with polar order, for example, is of importance for piezoelectric, pyroelectric, and nonlinear optical applications. Polar ordered liquid-crystalline (LC) soft matter, in which the configuration of polar order can be switched by means of electric fields, can be used in fast-switching electrooptical microdisplays and light modulators.

Chiral rodlike molecules organized in a tilted configuration in layers (SmC* phases) were initially used as ferroelectric (FE) and antiferroelectric (AF) switchable liquid-crystalline materials.[2] In the last decade, achiral bent-core molecules were found to provide a novel class of AF switching LC materials.[3–5] Here, the polar order is due to the shape of the molecules which restricts the rotation around the long axis and leads to a spontaneous polarization (P) parallel to the layer planes (see Figure 1 a). In most of these mesophases, the bent direction in adjacent layers is antiparallel so that the layer polarization alternates from layer to layer, which leads to a macroscopic apolar AF structure ($SmCP_A$ phases).[4] More recently, FE switching mesophases ($SmCP_F$) also have been reported for such materials.[6–13] In such cases, the bent direction in adjacent layers is parallel and switching takes place between two energetically equivalent polar structures (see Figure 1 a).

[*] Dr. R. A. Reddy, Dr. G. Dantlgraber, Prof. Dr. C. Tschierske
Institute of Organic Chemistry
Martin-Luther-University Halle-Wittenberg
Kurt-Mothes-Strasse 2, 06120 Halle (Germany)
Fax: (+49) 345-5525-346
E-mail: carsten.tschierske@chemie.uni-halle.de

Dr. U. Baumeister
Institute of Physical Chemistry
Martin-Luther-University Halle-Wittenberg (Germany)

[**] This work was supported by the DFG and the Fonds der Chemischen Industrie. R.A.R. is grateful to the Alexander von Humboldt Foundation for a research fellowship.

Supporting information for this article is available on the WWW under http://www.angewandte.org or from the author.


WILEY InterScience DISCOVER SOMETHING GREAT
© 2006 Wiley-VCH Verlag GmbH & Co. KGaA, Weinheim

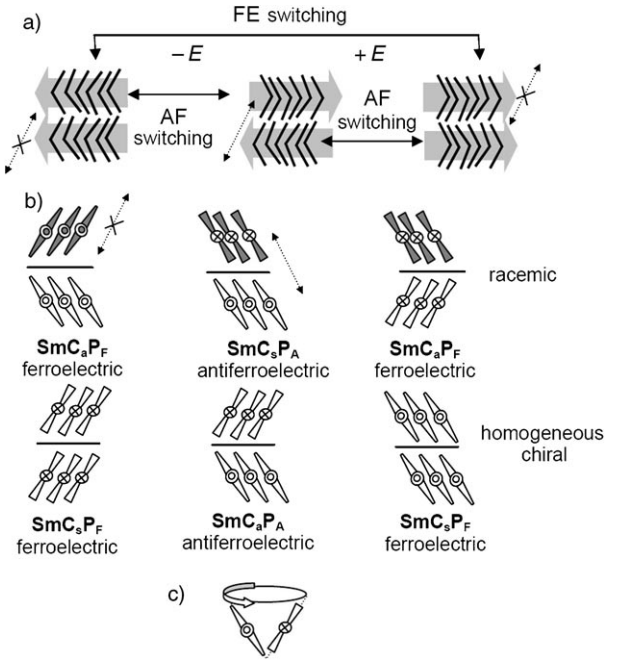



***Figure 1.*** Modes of organization of bent-core molecules in polar smectic LC phases. a) Side views: gray arrows indicate the polar directions; dotted arrows indicate out-of-plane interlayer fluctuations, which are easier in the $SmCP_A$ structure than in the $SmCP_F$ structure.[4] b) Views parallel to the bend direction: subscript s denotes synclinic organization (the tilt direction is the same in adjacent layers); subscript a denotes anticlinic (the tilt direction changes from layer to layer); subscript F denotes ferroelectric (synpolar); subscript A denotes antiferroelectric (antipolar). The chirality of the layers is indicated by the gray or white color of the molecules (see Supporting Information for an explanation of layer chirality). $SmC_aP_F$ and $SmC_sP_A$ represent racemic structures (chirality sense changes in adjacent layers); $SmC_sP_F$ and $SmC_aP_A$ are homogeneous chiral structures (chirality sense is identical in the layers). Dotted arrows indicate out-of-plane interlayer fluctuations, which are easier in the $SmC_sP$ structures than in the $SmC_aP$ structures. c) Switching on a cone changes both the polar and tilt directions, that is, layer chirality is retained.[4]

Note that the molecules are tilted relative to the layer normal in most of these smectic phases which gives rise to chirality in their LC superstructures (the layer normal, tilt direction, and polar axis define a chiral system; see Supporting Information).[4] As with organic molecules where the covalent connection of stereogenic centers leads to diastereomers, the combination of chiral layers in liquid-crystalline phases leads to diastereomeric superstructures. As shown in Figure 1 b, the chirality sense can be either identical in adjacent layers, leading to homogeneously chiral structures ($SmC_sP_F$ and $SmC_aP_A$), or opposite, leading to macroscopic racemic superstructures ($SmC_aP_F$ and $SmC_sP_A$).[4] These structures can be distinguished by means of their distinct optical properties using a polarizing microscope.

As mentioned above, in soft matter systems macroscopic polar structures are unstable and therefore ferroelectric switching materials are rare. One group of compounds that have a pronounced tendency to form such FE switching smectic phases incorporate oligo(dimethylsiloxane)[6,7] or carbosilane units[10] (see, for example, compounds **H*n*** in Figure 2). This observation indicates that a polyphilic molecular structure and the segregation of oligo(dimethylsiloxane) units into separate sublayers is a successful way to generate new bulk properties.[5b,6,7,10] Whereas the majority of bent-core molecules are built up of only two distinct parts, namely, the rigid bent core and the terminal alkyl chains, these oligo(dimethylsiloxane)-substituted molecules are composed of three distinct and incompatible units and therefore represent ternary block molecules (Figure 2).

Herein, we report the first examples of bent-core molecules composed of four distinct units. As shown in Figure 2, these quaternary block molecules **F*n*** combine two different end chains—an oligo(dimethylsiloxane) and a perfluoroalkyl chain—as well as alkyl spacers and aromatic bent-core units. As a result of their special structure, these molecules show interesting properties, such as a temperature-dependent transition from ferroelectric to antiferroelectric switching and a temperature-dependent transition between diastereomeric superstructures. In addition, it is shown for the first time that the switching behavior of diastereomeric mesophase structures can be different, with one being ferroelectric and the other being antiferroelectric.

Compounds **F1, F2**, and **Fi2** were synthesized in an analogous manner as reported for the non-fluorinated oligo(dimethylsiloxane) derivatives **H*n***,[6] by hydrosilylation of the appropriate fluorinated olefinic precursor **F** (see Supporting Information). The properties of these new compounds were determined by polarizing microscopy, X-ray scattering, and electrooptical techniques. The observed mesophase types and transition temperatures are collated in Table 1 and compared with the olefinic precursor **F**. All compounds **F*n*** ($n = 1, 2$) show optically isotropic mesophases

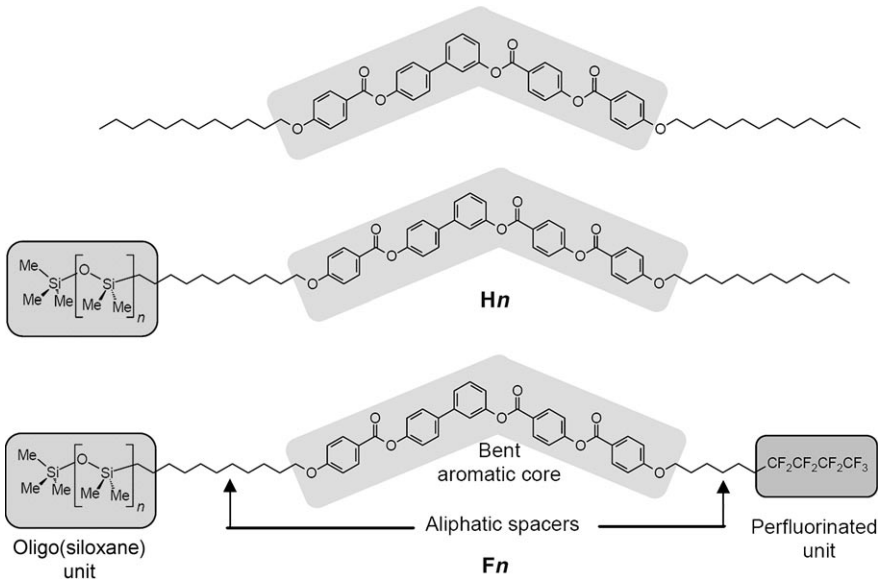
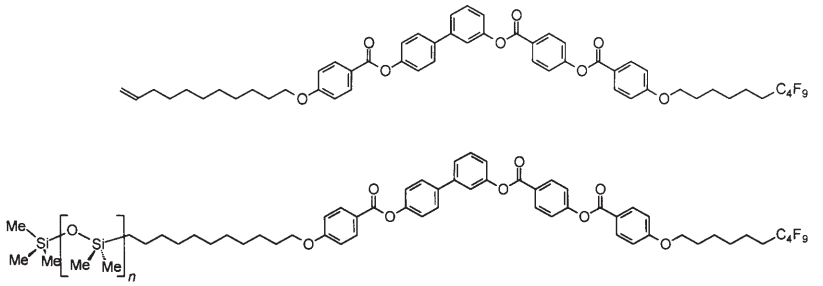



***Figure 2.*** Structures of a classical bent-core molecule (top),[20] ternary bent-core molecules **H*n***,[6] and quaternary bent-core molecules **F*n***.

 © 2006 Wiley-VCH Verlag GmbH & Co. KGaA, Weinheim 

***Table 1:*** Mesophases, transition temperatures, and transition enthalpy values (in brackets) of the fluorinated compounds ***Fn*** in comparison with compound **F**, which lacks an oligo(dimethylsiloxane) group.[a]




| Compound | *n* | *T* [°C] ($\Delta H$ [kJ mol$^{-1}$])[b] |
|---|---|---|
| **F** | – | Cr 111 (29.3) $SmCP_A$ 123 (20.0) Iso |
| **F1** | 1 | Cr 94 (21.0) $SmCP_{A+F}$[*] ≈110 (–) $SmCP_F$[*] 130 (21.1) Iso |
| **F2** | 2 | Cr 104 (22.6) $SmCP_F$[*] 127 (19.2) Iso |
| **Fi2**[c] | 2 | Cr 105 (22.8) $SmCP_F$[*] 127 (20.1) Iso |

[a] Abbreviations: Cr = crystalline solid state; $SmCP_A$ = AF switching polar smectic phase, with tilted arrangement of the molecules; $SmCP_F$[*] = FE switching polar smectic phase, with tilted arrangement of the molecules; superscript [*] indicates the formation of a chiral superstructure, as seen by domains of opposite chirality (see Supporting Information) although the molecules themselves are configurationally achiral; Iso = isotropic liquid state. [b] 10 K min$^{-1}$, first heating scan. [c] In this compound the branched $(Me_3SiO)_2Si(Me)$ group is used instead of the linear $Me_3Si(OSiMe_2)_2$ unit as used in compound **F2**.

composed of domains of opposite chirality sense (see Supporting Information) as also reported for the non-fluorinated analogues ***Hn***.[6,7]

X-ray scattering of the mesophase of compound **F1** (see Figure 3a) indicates a fluid layer structure without in-plane order, as characterized by a layer reflection together with the fourth order.[14] The layer thickness is 4.2 nm, which is much smaller than the calculated molecular length ($l$ = 5.95 nm in the most-extended conformation with all-*trans* alkyl chains, according to CPK models) and is in line with a strongly tilted arrangement of the molecules in a smectic monolayer structure (Figure 4a). This observation also indicates that there is no segregation of the fluorinated and the oligo(dimethylsiloxane) end chains into distinct sublayers which would otherwise lead to a bilayer structure with alternating oligo(siloxane) and perfluoroalkane sublayers (see Figure 4b).[15] Nevertheless, the diffuse scattering in the wide-angle region has a very unsymmetrical profile in which two maxima can be distinguished (see inset in Figure 3a). The maximum at 0.46 nm corresponds to the mean distance between the hydrocarbon parts of the molecules, while the shoulder corresponds to a mean distance of 0.62 nm and is assigned to the mean distance between the nanosegregated pentamethyldisiloxane units. Interestingly, this shoulder is absent in the diffraction pattern of the corresponding non-fluorinated pentamethyldisiloxane derivative **H1**[6] which indicates that although the fluorinated segments do not form their own sublayers they can facilitate the segregation of the oligo(dimethylsiloxane) parts. The mixed sublayers containing the fluorinated chains and aliphatic spacer segments (see Figure 4a) are probably more incompatible with the pentamethyldisiloxane units than the alkyl chains themselves and favor a segregation of these units into separate sublayers.

Switching experiments with compound **F1** (10-μm thick noncoated ITO cell, Figure 3b) indicate only one peak in the switching current curve down to a frequency of 0.1 Hz and point to a FE switching process. However, optical investigations indicated a more complex behavior. Although the shape of the polarization current curve does not change over the whole temperature range, a clear temperature-dependent change of the switching process is seen. Domains with an $SmC_aP_F$ structure[16] were grown under a triangular ac electric field at 100 Hz (see Figure 5b). These domains are characterized by extinction crosses that coincide with the directions of the polarizer and analyzer, indicating an anticlinic organization of the molecules. Under the applied ac field, this $SmC_aP_F$ structure is stable at all temperatures. Upon switching off the field at $T > 110$ °C, there is no change in the orientation of the extinction crosses (see Figure 5a) which means that the structure does not change and remains $SmC_aP_F$ also at zero voltage;

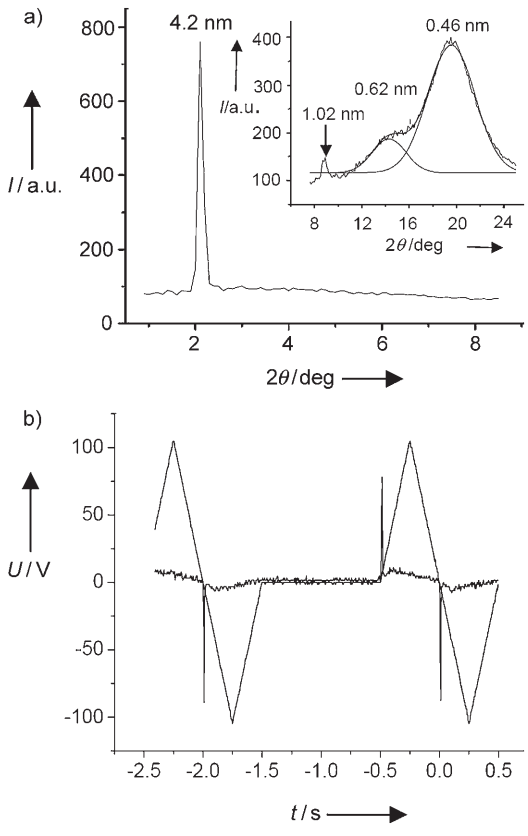



***Figure 3.*** Investigation of compound **F1**: a) X-ray diffraction pattern at $T$ = 110 °C; the inset shows the wide-angle region with two maxima, and the arrow within the inset shows the fourth-order smectic reflection. b) Switching current response at $T$ = 115 °C in a 10-μm thick noncoated indium tin oxide (ITO) cell (EHC, Japan) on applying an alternating normal (1 Hz) and modified triangular-wave voltage.[11]

 © 2006 Wiley-VCH Verlag GmbH & Co. KGaA, Weinheim 

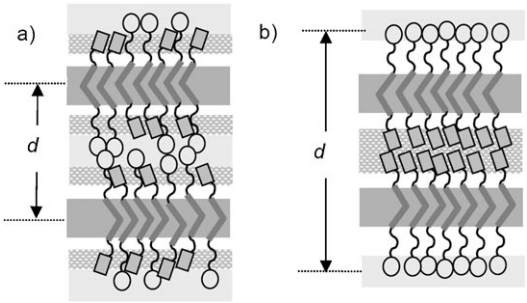



***Figure 4.*** Models of the organization of compounds ***Fn*** in the smectic phases: a) Monolayer structure in which the fluorinated chains and the hydrocarbon chains are organized in common sublayers. b) Bilayer structure in which the fluorinated chains and hydrocarbon chains are organized in different sublayers (not observed for ***Fn***).

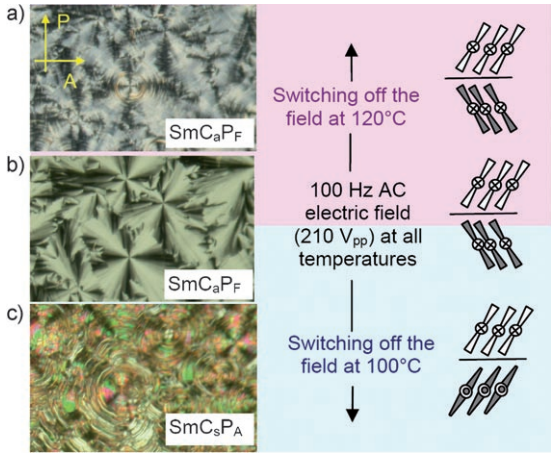



***Figure 5.*** Textures and mesophase structures of compound **F1** in a 10-μm noncoated ITO cell obtained a) at $T>110$ °C after switching off the ac field, b) under the applied ac field ($V_{pp}$ = peak-to-peak voltage), and c) at $T<110$ °C after switching off the field. Yellow arrows show the positions of the polarizer (P) and analyzer (A).

that is, the polar FE state seems to be stable (or long-living metastable) under the experimental conditions. These results indicate a bistable switching process, that is, a direct switching between two different polar FE states without a nonpolar AF state at zero voltage (FE switching).

Switching off the field at $T<110$ °C leads to a different behavior. In this case, the extinction crosses slowly relax at zero voltage to a position that is inclined 45° with respect to polarizer and analyzer and the texture becomes more colored (i.e. the birefringence is increased, see Figure 5c). These observations indicate that the molecules now adopt a synclinic organization, with the molecules tilted by approximately 45° in the layers, achieved by a rotation of the molecules on a cone into the AF SmC$_s$P$_A$ state. There are three stable states (the two polar FE states and the nonpolar AF state) which indicates an antiferroelectric type of switching. Hence, there is a transition from a FE switching process at high temperature to AF switching at lower temperatures. Such a change of the switching type has only rarely been observed for other bent-core molecules,[13] mostly in mixtures[12] or with a reverse sequence.[9]

Besides this temperature dependence, there is a remarkable frequency dependence of the switching process. At lower frequency (<0.5 Hz) or under a dc field, the extinction crosses are only slightly inclined (ca. 15°) with the direction of the polarizer and analyzer (see Figure 6a). This can be explained with a structure in which an anticlinic organization (SmC$_a$P$_F$, extinction crosses would be parallel to the polarizers) is mixed with a synclinic organization (SmC$_s$P$_F$, extinction crosses would be inclined by 45°) on a mesoscopic scale (see models shown in Figure 6a).[17] In other words, two diastereomeric organizations, chiral (SmC$_s$P$_F$) and racemic (SmC$_a$P$_F$), coexist.

Again, a significant change of the switching process can be seen at around 110 °C. At $T>110$ °C the extinction crosses do not change their position after switching off the field (compare Figure 6a and b), but upon application of an electric field with the opposite sign the crosses rotate by about 60°. In this way, the extinction crosses again become inclined with the direction of the polarizer and analyzer by 15° but in the opposite direction (compare Figure 6b and c). This indicates a bistable switching process, that is, a direct switching between two different FE states. Reorganization of the molecules takes place in each layer by a rotation on a cone which reverses the polar direction and the tilt direction in the synclinic as well as in the anticlinic domains (follow the black line in Figure 6 from a to c).

At $T<110$ °C a different behavior is observed (see Figure 6a,c,d). At this temperature the extinction crosses

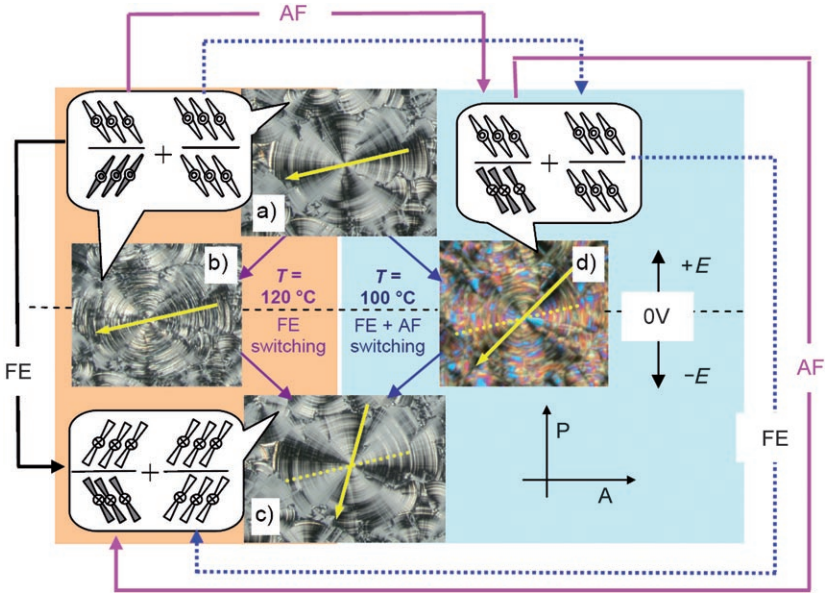



***Figure 6.*** Temperature dependence of the switching process of compound **F1** (10-μm noncoated ITO cell) at low frequency (<0.5 Hz) or under a dc field. Textures seen between crossed polarizers a) under an applied field (35 $V_{dc}$) at 100 °C or at 120 °C, b) after switching off the field at 120 °C, c) after reversal of the applied field at 120 °C or 100 °C, and d) after switching off the field at 100 °C.


© 2006 Wiley-VCH Verlag GmbH & Co. KGaA, Weinheim

relax at zero voltage to a position that is inclined by 45° with respect to the polarizer and analyzer, and the texture becomes more colored (i.e. the birefringence is increased, see Figure 6d). This behavior indicates that at zero voltage all molecules adopt a synclinic organization with the molecules tilted by about 45° in the layers. Hence, it seems that at $T<$ 110 °C only the anticlinic microdomains relax to the synclinic AF state (follow the pink line in Figure 6 from a to d), whereas the synclinic microdomains do not relax (follow the dotted blue line in Figure 6 from a to d). Upon field reversal, the extinction crosses continue rotation to the state shown in Figure 6c, inclined with the polarizers by approximately 15°, indicating that again synclinic and anticlinic microdomains coexist. This is achieved if in the homogeneously chiral microdomains all molecules switch around a cone from one synclinic FE structure to the other synclinic FE structure with an opposite tilt direction and polar direction (follow the dotted blue line in Figure 6 from d to c), whereas in the racemic domains the molecules in every second layer switch around a cone leading to a transition from the synclinic AF structure to the anticlinic FE structure (follow the pink line in Figure 6 from d to c). This means that the chiral synclinic FE microdomains ($SmC_sP_F$) are more stable and retain their polar organization at zero voltage. Only after field reversal do these synclinic FE domains switch to the opposite FE state. The racemic anticlinic FE microdomains ($SmC_aP_F$) are less stable and readily relax to the AF state at zero voltage. Hence at $T<110$ °C there is a coexistence of FE and AF switching microdomains and there is a temperature-dependent change of the switching mechanism from FE to AF only for the anticlinic (racemic) organization, whereas for the synclinic (chiral) organization the FE structure is stable also at zero voltage over the whole temperature range and FE switching is exclusively observed. This is the first time that the observation of such a distinct switching behavior is reported for diastereomeric configurations of a mesophase. However, the AF switching is slow and therefore at all the temperatures only one polarization reversal current peak is found under a triangular wave voltage.

In the case of compounds **F2** and **Fi2**, which have larger nonbranched or branched heptamethyltrisiloxane segments, optical investigations under a dc field indicate a bistable (FE) switching over the whole temperature range (see Supporting Information).[6]

Another remarkable feature of these compounds is seen during the growing process of the domains under an applied ac field (see Figure 7). Whereas for compound **F1** the racemic $SmC_aP_F$ organization was exclusively obtained under these conditions (see Figure 5b), in the case of compound **F2** there is a temperature-dependent reorganization of the molecules. For **F2** a homogeneously chiral synclinic organization (extinction brushes inclined with the polarizers, $SmC_sP_F$) is obtained upon cooling the isotropic liquid state, but on further cooling a slow transition to the (racemic) anticlinic organization (extinction brushes parallel to the polarizers, $SmC_aP_F$) is observed. This means that there is a temperature-dependent change of the diastereomeric superstructures from synclinic FE at high temperature to anticlinic FE at lower temperatures.[19]

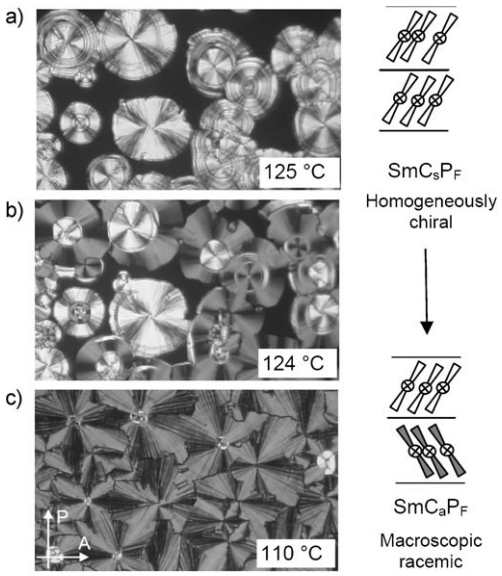



***Figure 7.*** Changes in the molecular organization of compound **F2** as seen upon cooling under a triangular-wave electric ac field (150 $V_{pp}$; 200 Hz; 5-μm noncoated ITO cell): a) Exclusively $SmC_sP_F$ domains; b) Transition from $SmC_sP_F$ to $SmC_aP_F$; c) Nearly complete transition to $SmC_sP_F$ domains (see also Supporting Information).

In summary, the first examples of quaternary four-block bent-core molecules are reported. Compounds **F2** and **Fi2** with large heptamethyltrisiloxane units show exclusively ferroelectric switching, whereas a clear antiferroelectric switching is observed for compound **F**, which lacks a siloxane unit (Table 1). It is thought that the segregation of the siloxane units favors the synpolar organization that leads to FE switching. For compounds **F2** and **Fi2**, the siloxane sublayers are robust and FE switching is observed at all temperatures. However, for compound **F1** with a short pentamethyldisiloxane unit there seems to be a competing influence of the fluorocarbon chains. At lower temperature, the fluorinated segments become more rigid and therefore the out-of-plane interlayer fluctuations between the layers become more important. These fluctuations are entropically favored and can take place more easily across synclinic and antipolar interfaces than across anticlinic and synpolar interfaces (see dotted arrows in Figure 1a,b).[6a,18] For this reason the $SmC_aP_F$ domains, which have both types of unfavorable interfaces, are more strongly destabilized by a decrease in the temperature than the $SmC_sP_F$ domains, which have only one type. This could explain why these domains relax to the $SmC_sP_A$ state at zero voltage (AF switching), whereas the $SmC_sP_F$ domains remain stable (FE switching). Hence, variations in the balance of fluorinated and siloxane end groups lead to interesting bulk properties and allow a fine-tuning of the mesophases of bent-core mesogens.

Received: September 26, 2005
Published online: February 21, 2006

**Keywords:** chirality · electrooptics · liquid crystals · phase transitions

 © 2006 Wiley-VCH Verlag GmbH & Co. KGaA, Weinheim 

[1] J.-M. Lehn, *Supramolecular Chemistry: Concepts and Perspectives*, VCH, Weinheim, **1995**.

[2] H.-S. Kitzerow, C. Bahr, *Chirality in Liquid Crystals*, Springer, New York, **2001**.

[3] T. Niori, T. Sekine, J. Watanabe, T. Furukawa, H. Takezoe, *J. Mater. Chem.* **1996**, *6*, 1231.

[4] D. R. Link, G. Natale, R. Shao, J. E. Maclennan, N. A. Clark, E. Körblova, D. M. Walba, *Science* **1997**, *278*, 1924.

[5] Reviews: a) G. Pelzl, S. Diele, W. Weissflog, *Adv. Mater.* **1999**, *11*, 707; b) R. A. Reddy, C. Tschierske, *J. Mater. Chem.* **2005**, DOI: 10.1039/b504400f.

[6] a) G. Dantlgraber, A. Eremin, S. Diele, A. Hauser, H. Kresse, G. Pelzl, C. Tschierske, *Angew. Chem.* **2002**, *114*, 2514; *Angew. Chem. Int. Ed.* **2002**, *41*, 2408; b) C. Keith, R. A. Reddy, U. Baumeister, A. Hauser, C. Tschierske, *J. Am. Chem. Soc.*, DOI: 10.1021/ja057685t.

[7] G. Dantlgraber, S. Diele, C. Tschierske, *Chem. Commun.* **2002**, 2768; C. Keith, R. A. Reddy, C. Tschierske, *Chem. Commun.* **2005**, 871.

[8] D. M. Walba, E. Körblova, R. Shao, J. E. Maclennan, D. R. Link, M. A. Glaser, N. A. Clark, *Science* **2000**, *288*, 2181; E. Gorecka, D. Pociecha, F. Araoka, D. R. Link, M. Nakata, J. Thisayukta, Y. Takanishi, J. Watanabe, H. Takezoe, *Phys. Rev. E* **2000**, *62*, R4524; R. A. Reddy, B. K. Sadashiva, *J. Mater. Chem.* **2002**, *12*, 2627.

[9] H. Nadasi, W. Weissflog, A. Eremin, G. Pelzl, S. Diele, B. Das, S. Grande, *J. Mater. Chem.* **2002**, *12*, 1316.

[10] G. Dantlgraber, U. Baumeister, S. Diele, H. Kresse, B. Lühmann, H. Lang, C. Tschierske, *J. Am. Chem. Soc.* **2002**, *124*, 14852; C. Keith, R. A. Reddy, H. Hahn, H. Lang, C. Tschierske, *Chem. Commun.* **2004**, 1898.

[11] J. P. Bedel, J. C. Rouillon, J. P. Marcerou, M. Laguerre, H. T. Nguyen, M. F. Achard, *J. Mater. Chem.* **2002**, *12*, 2214.

[12] K. Kumazawa, M. Nakata, F. Araoka, Y. Takanishi, K. Ishikawa, J. Watanabe, H. Takezoe, *J. Mater. Chem.* **2004**, *14*, 157; M. Nakata, D. R. Link, J. Thisayukta, Y. Takanishi, K. Ishikawa, J. Watanabe, H. Takezoe, *J. Mater. Chem.* **2001**, *11*, 2694.

[13] S. Rauch, P. Bault, H. Sawade, G. Heppke, G. G. Nair, A. Jakli, *Phys. Rev. E* **2002**, *66*, 021706.

[14] Second- and third-order reflections are missing probably as a result of the effect of the fluorinated segments upon the electron density distribution.

[15] It seems that segregation of the fluorinated segments is inhibited for steric reasons, because in this case the perfluorinated segments can improve the space filling in the aliphatic sublayers by incorporation between the spacer units that connect the Si units with the bent cores.

[16] For a more detailed discussion of the $SmC_aP_F$ structure, see: C. L. Folcia, J. Ortega, J. Etxebaria, *Liq. Cryst.* **2003**, *30*, 1189; P. Pyc, J. Mieczkowski, D. Pociecha, E. Gorecka, B. Donnio, D. Guillon, *J. Mater. Chem.* **2004**, *14*, 2374.

[17] M. Zennyoji, Y. Takanishi, K. Ishikawa, J. Thisayukta, J. Watanabe, H. Takezoe, *J. Mater. Chem.* **1999**, *9*, 2775.

[18] Y. Lansac, P. K. Maiti, N. A. Clark, M. A. Glaser, *Phys. Rev. E* **2003**, *67*, 011703; A. Jakli, C. Lischka, W. Weissflog, G. Pelzl, S. Rauch, G. Heppke, *Ferroelectrics* **2000**, *243*, 239.

[19] Usually, this phase sequence is the other way around; that is, the chiral organization ($SmC_aP_A$) is obtained by heating from a crystalline or B4[*] phase, whereas on cooling from the isotropic liquid the racemic structure ($SmC_sP_A$) is formed (see ref. [3]).

[20] D. Shen, A. Pegenau, S. Diele, I. Wirth, C. Tschierske, *J. Am. Chem. Soc.* **2000**, *122*, 1593.


 © 2006 Wiley-VCH Verlag GmbH & Co. KGaA, Weinheim 

*Heterogeneous Catalysis*

DOI: 10.1002/anie.200503471

# Mechanistically Significant Details of the H/D Exchange Reactions of Propene over Acidic Zeolite Catalysts**

*David M. Marcus, Miranda J. Hayman, Yoni M. Blau, Darryl R. Guenther, Justin O. Ehresmann, Philip W. Kletnieks, and James F. Haw**

Although H/D exchange is indispensable to the study of reaction mechanisms in solution, they have been underexploited in studies of heterogeneous catalysis. Spectroscopic studies of H/D exchange at low temperatures and long reaction times on solid catalysts have been reported,[1,2] and more realistic temperatures have been used for studies of equivalent exchange sites as in methane.[3] We were drawn to the possibilities of studying mechanisms by observing exchange into structurally distinct sites within the constraints of high temperatures and several-second reaction times used for these reactions in actual practice.[4]

We have found that by careful experimental design of H/D exchange reactions, including appropriate reagent compositions or concentrations, and quantitative fitting of the ion mass distributions of product species,[5] we can sometimes reveal a surprising level of complexity in reactions that at first glance would appear to be simple or even elementary. We have carried out experiments pulsing controlled amounts of protonated reactants onto deuterated catalysts (as shown here) as well as equimolar mixtures of fully protonated and fully deuterated reagents onto half-deuterated catalysts in either pulse or continuous flow mode. As the first contribution from these studies, we report on H/D exchange for propene on three microcrystalline solid acids: the aluminosilicate zeolite DZSM-5, its boron analogue D[B]ZSM-5, and the silico-aluminophosphate DSAPO-34. In every case herein the inventory of exchangeable deuterium atoms in the catalyst beds vastly exceeded that of the hydrogen atoms in the propene reagent pulses by a factor of at least 300 in all cases but one, and in that instance there was still more than a 13-fold excess. Whereas an oversimplified view of olefin H/D exchange would predict that we would observe $[D_6]$propene as the exclusive equilibrium product of this reaction, our observations of incomplete deuteration and

[*] D. M. Marcus, M. J. Hayman, Y. M. Blau, D. R. Guenther, J. O. Ehresmann, P. W. Kletnieks, Prof. J. F. Haw
Department of Chemistry
University of Southern California
Los Angeles, CA 90089-1661 (USA)
Fax: (+1) 213-740-0930
E-mail: jhaw@usc.edu

[**] This work was supported by the US Department of Energy (DOE) Office of Basic Energy Sciences (BES; grant no. DE-FG03-99ER14956).

Supporting information for this article is available on the WWW under http://www.angewandte.org or from the author.


© 2006 Wiley-VCH Verlag GmbH & Co. KGaA, Weinheim

positional selectivity is evidence of products formed through multiple iterations of mechanisms operating in the kinetic regime but still well short of thermodynamic equilibrium.

Figure 1 presents GC-FID chromatograms and propene ion mass distributions ($m/z$ 36–50) from otherwise identical experiments in which either 1 or 100 μL of propene gas at

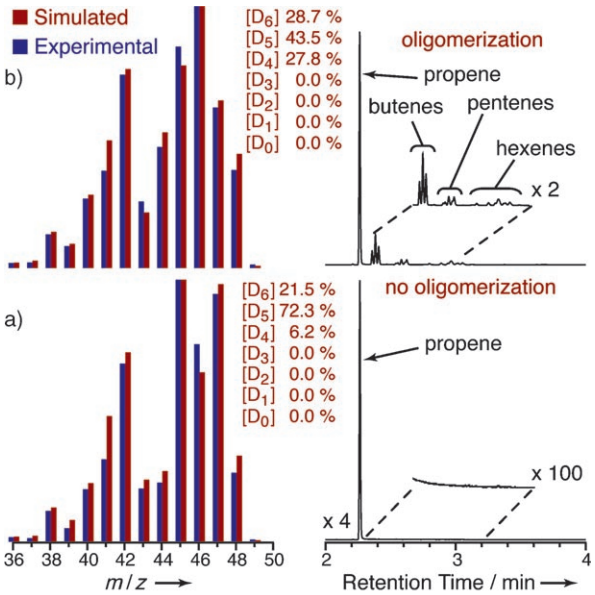



***Figure 1.*** Gas chromatography/flame-ionization detector (GC-FID) chromatograms detailing the products exiting a 300-mg DSAPO-34 catalyst bed following pulses (at 760 Torr) of propene at a volume of either a) 1 μL (>1300-fold excess of exchangeable deuterons to protons) or b) 100 μL (>13-fold excess of deuterons to protons), at 573 K under flowing He carrier gas (600 sccm (standard cubic centimeters per minute)). Also shown are the fitted ion mass distributions from propene exiting the catalyst bed.

room temperature and atmospheric pressure was injected into a He gas flow stream passing over a 300-mg catalyst bed of fully deuterated DSAPO-34 at 573 K. The reaction time was in each case only 3 seconds so as to observe kinetic rather than equilibrium products. Figure 1a shows that the smaller propene pulse produced no volatile products other than propene and that the distribution of propene isotopomers was approximately 6% $[D_4]$propene, 72% $[D_5]$propene, and 22% $[D_6]$propene. The propene isotopomer distribution obtained from the larger propene pulse was substantially and reproducibly different with 28% $[D_4]$propene, 44% $[D_5]$propene, and 29% $[D_6]$propene, and the product distribution included not only propene but also the oligomerization and cracking products, butenes, pentenes, and hexenes.

The fitted data of the isotope distribution patterns and associated isotopomer distributions for three catalysts at either 573 or 673 K are shown in Figure 2. In each case the amount of propene pulsed into the reactor (1 μL at room temperature and atmospheric pressure) was very low, corresponding to one equivalent per several thousand acid sites—the exact value depending on the acid site density. At such low propene loadings we saw almost no oligomerization and cracking products, and a symmetric isotopomer distribution

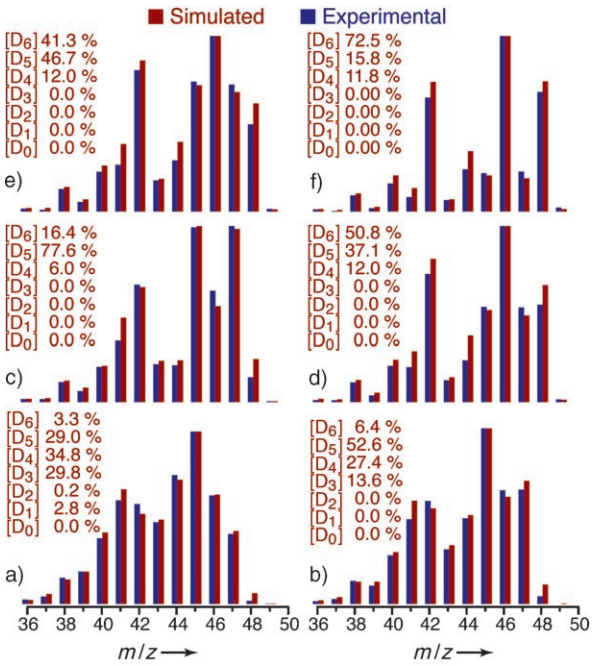
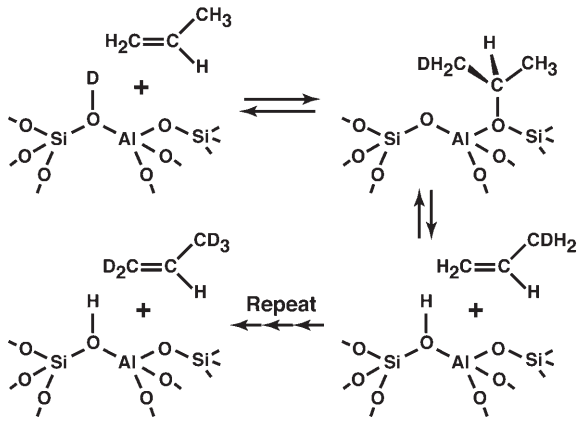



***Figure 2.*** Ion mass distributions and accompanying fits from propene exiting 200-mg catalyst beds following 1-μL pulses of propene (760 torr) under flowing He carrier gas (600 sccm): a) on D[B]ZSM-5 at 573 K (>400-fold excess of exchangeable deuterons to protons); b) on the same bed of D[B]ZSM-5 at 673 K, propene is deuterated to a greater extent but with only a small increase in yield of $[D_6]$propene; c) on DSAPO-34 at 573 K (900-fold excess of deuterons to protons); d) on the same bed of DSAPO-34 at 673 K, a majority of the propene is fully deuterated; e) on DZSM-5 at 573 K (>300-fold excess of deuterons to protons), propene yields mostly $[D_5]$propene and $[D_6]$propene; and f) on the same bed of DZSM-5 at 673 K, the product is predominantly $[D_6]$propene.

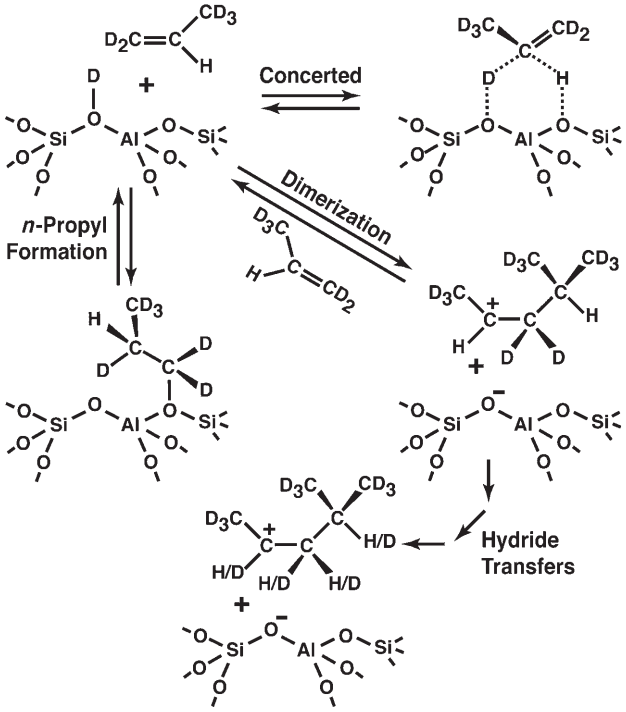
was never observed, as was always the case with much higher propene concentrations at 573 K. Figure 2 shows an increasing extent of propene deuteration at higher temperatures but resistance to deuteration from $[D_5]$propene to $[D_6]$propene. For example, Figure 2b (D[B]ZSM-5 at 673 K) shows that the product is primarily $[D_5]$propene with negligible formation of $[D_6]$propene. Nearly complete deuteration to form $[D_6]$propene in high yield (73%) was achieved only for the catalyst we expected to be the strongest acid (DZSM-5) at the highest temperature studied, 673 K (Figure 2f).

The fine structure that we observed in the propene H/D exchange reaction on solid acid catalysts leads to straightforward and detailed mechanistic proposals that are well-suited to future theoretical modeling studies. Scheme 1 describes the equilibration of free propene with a framework-bound isopropoxy species, shown on DZSM-5 for simplicity. This reaction, for which there is abundant spectroscopic and theoretical evidence,[6,7] eventually leads to H/D exchange in exactly five of the six positions in propene. As seen in Figures 1 and 2, however, exchange of the sixth position does occur, indicating that formation of a framework-bound isopropoxy species is not the only active pathway for H/D exchange. To account for the inhibited exchange of the sixth hydrogen with deuterium we propose three possible pathways, which are outlined in Scheme 2. First, a bimolec-

 © 2006 Wiley-VCH Verlag GmbH & Co. KGaA, Weinheim 




***Scheme 1.*** Propene reacts reversibly on a deuterated aluminosilicate zeolite (e.g. DZSM-5) to form a framework-bound isopropoxy species with selective H/D exchange.




***Scheme 2.*** Potential routes for propene H/D exchange to [$D_6$]propene on a zeolite acid catalyst.

ular mechanism where dimerization of [$D_5$]propene to a branched hexene isomer accompanied by normal H/D exchange and straightforward hydride transfer steps produces a statistical distribution of 25% [$D_4$]propene, 50% [$D_5$]propene, and 25% [$D_6$]propene. This distribution is in excellent agreement with all of our experiments at lower temperatures and higher pressures, such as the result shown in Figure 1b (28% [$D_4$]propene, 44% [$D_5$]propene, and 29% [$D_6$]propene). Even at pressures low enough such that we do not observe the oligomerization and cracking that are indicative of this bimolecular route, [$D_6$]propene is still formed (e.g. Figure 1a). To account for this observation, we propose two reasonable unimolecular pathways involving either the formation of an *n*-propoxy intermediate (analogous to the isopropoxy route in Scheme 1) or a concerted pathway analogous to the established mechanism for H/D exchange in benzene.[8]

## Experimental Section

HSAPO-34 was synthesized using standard procedures,[9] H[B]ZSM-5 (Si/B = 30) was synthesized according to a reported procedure,[10] and HZSM-5 (Si/Al = 40) was purchased from Zeolyst International. All catalysts were calcined overnight at 823 K. Deuterium oxide (*d*, 99.9%) was purchased from Cambridge Isotopes, and 5% propene in He was purchased from Matheson Tri-Gas. The catalysts were pressed into 10–20-mesh pellets without binder or other additives. Catalyst beds were deuterated by treatment with at least 15 equivalents of deuterium oxide at 648 K and maintained at that temperature for 30 mins before being lowered to reaction temperature. NMR spectroscopy confirms that the catalyst beds were not significantly dealuminated or deboronated by treatment with deuterium oxide (see Supporting Information). A schematic of the catalytic flow reactor is also provided in the Supporting Information. Reactor effluent gases were analyzed with an Agilent gas chromatograph (Model 6890) using both mass spectrometric (Agilent 5973 inert mass selective detector) and flame-ionization detectors.

Received: September 30, 2005
Revised: November 22, 2005

**Keywords:** heterogeneous catalysis · isotopic labeling · microporous materials · oligomerization · zeolites

[1] J. Sommer, M. Hachoumy, F. Garin, *J. Am. Chem. Soc.* **1995**, *117*, 1135.
[2] J. N. Kondo, L. Shao, F. Wakabayashi, K. Domen, *J. Phys. Chem. B* **1997**, *101*, 9314.
[3] B. Schoofs, J. A. Martens, P. A. Jacobs, R. A. Schoonheydt, *J. Catal.* **1999**, *183*, 355.
[4] Y. Xiong, P. G. Rodewald, C. D. Chang, *J. Am. Chem. Soc.* **1995**, *117*, 9427.
[5] Standard ion mass distributions measured on our mass spectrometer for propene and [$D_6$]propene, along with statistically simulated distributions for all other isotopomers of propene, are fitted to the experimental ion mass distributions using the solver function of Microsoft Excel 2004.
[6] V. B. Kazansky, *Acc. Chem. Res.* **1991**, *24*, 379.
[7] J. F. Haw, J. B. Nicholas, T. Xu, L. W. Beck, D. B. Ferguson, *Acc. Chem. Res.* **1996**, *29*, 259.
[8] L. W. Beck, T. Xu, J. B. Nicholas, J. F. Haw, *J. Am. Chem. Soc.* **1995**, *117*, 11594.
[9] B. M. Lok, C. A. Messina, R. L. Patton, R. T. Gajek, T. R. Cannan, E. M. Flanigen, US Patent 4,440,871, **1984**.
[10] B. Sulikowski, J. Klinowski *J. Phys. Chem.* **1992**, *96*, 5030.

 © 2006 Wiley-VCH Verlag GmbH & Co. KGaA, Weinheim 

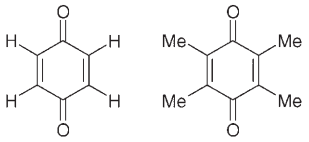
Marcus Theory

DOI: 10.1002/anie.200503581

# From Solvent Fluctuations to Quantitative Redox Properties of Quinones in Methanol and Acetonitrile**

*Joost VandeVondele,* Marialore Sulpizi, and Michiel Sprik*

Electron-transfer (ET) reactions are among the most fundamental chemical processes and are crucial in a number of important biological processes, such as photosynthesis and cell respiration.[1] Nature and chemists alike have been tuning electron-donor and -acceptor sites or their environments to obtain ET rates and relative donor–acceptor stabilities that are optimized for a particular task. Herein, we report an atomistic theoretical approach based on molecular-dynamics simulations and density functional theory to predict quantitatively the effects of such modifications on the parameters that control ET. This work confirms recent experiments[2] that highlight the role of hydrogen-bonding interactions in ET processes. We have investigated the redox properties of substituted quinones in methanol (MeOH) as a prototypical hydrogen-bonding solvent and in acetonitrile (MeCN) as a solvent with similar dielectric properties but without the specific hydrogen-bonding interactions. In view of their biological importance, it is not surprising that quinones are often employed in electrochemical experiments and that the effects of the solvent and substituents on the redox properties have been well characterized.[3–10] We employed 1,4-benzoquinone (BQ) and 2,3,5,6-tetramethylbenzoquinone (duroquinone, DQ) in this study.




BQ DQ

A key step in the understanding of ET reactions was the formulation by Marcus[11,12] of the rate of ET ($k_{ET}$) as a function of the reaction free energy $\Delta G$ and $\lambda$, that is, the sum of the inner ($\lambda_i$) and outer ($\lambda_o$) sphere reorganization energies [Eq. (1)], in which $\kappa$ is a proportionality constant that depends on the donor and acceptor quantum coupling, $T$ the temperature, and $k_B$ the Boltzmann constant. Furthermore, Marcus also derived an approximate expression for $\lambda_o$ that provides insight into the nature of the reorganization energy for simple solutes in a homogeneous environment. Based on continuum theory, it provides the nonspecific solvent reorganization energy $\lambda_s$ as a function of the effective radii of the donor and the acceptor ($r_D$ and $r_A$), their distance of separation $r$, the solvent refractive index $n_D$, and the relative permittivity $\varepsilon_r$ [Eq. (2)]. In this work, we obtain estimates for $\Delta G$ and $\lambda$ beyond the continuum approximation by using atomistic simulations.

$$k_{ET} = \kappa \exp\left(-\frac{(\Delta G + \lambda)^2}{4\lambda k_B T}\right) \quad (1)$$

$$\lambda_s = \frac{e^2}{4\pi\varepsilon_0}\left(\frac{1}{2r_D} + \frac{1}{2r_A} - \frac{1}{r}\right)\left(\frac{1}{n_D^2} - \frac{1}{\varepsilon_r}\right) \quad (2)$$

In simulation, the free-energy difference between the oxidized and reduced states of a system can be computed exactly from ensemble averages on the basis of the vertical ionization energy ($\Delta E$).[13–19] Such an ensemble average can be computed by using molecular-dynamics (MD) simulations. Herein, we have employed a computationally straightforward, but approximate formula for the free-energy difference $\Delta A$. This formula can be derived[13–15] if the atomistic equivalent of the parabolic functions derived from Marcus theory, which depict the assumed harmonic dependence of the free energy on the vertical energy gap, is introduced as an approximation. This atomistic equivalent is the premise that $\Delta E$ fluctuates with Gaussian statistics during the MD simulation. If this premise is satisfied, one rigorously obtains the (Helmholtz) oxidation free energy ($\Delta A$) given in Equation (3), in which $\lambda$ is described by Equation (4), and $\Delta E_O$ and $\sigma_O^2$ denote the mean and variance, respectively, of the distribution of the values of $\Delta E$ as obtained with an MD simulation in the canonical ensemble on the oxidized potential energy surface. $\Delta E_R$ and $\sigma_R^2$ are the corresponding quantities on the reduced surface. Equations (3) and (4) were evaluated in this work with the oxidized and reduced surfaces defined by the energies of a neutral and anionic quinone in solution, respectively. The value of $\lambda$ obtained from Equation (4) is the total reorganization free energy and depends only on the fluctuations of the vertical energy. The solutions are at ambient conditions for the reactions studied herein, and the expected volume changes are small; therefore it is reasonable to assume that Gibbs and Helmholtz free-energy differences will be similar. The average of the two expressions for $\Delta A$ is commonly[17,18] employed as a statistically robust estimate of $\Delta A$, but herein we have exploited the fact that $\Delta A$ can be obtained from a single, sufficiently long simulation in an oxidation state of choice.

$$\Delta A = \Delta E_O + \lambda = \Delta E_R - \lambda \quad (3)$$

$$\lambda = \frac{1}{2k_B T}\sigma_O^2 = \frac{1}{2k_B T}\sigma_R^2 \quad (4)$$

[*] Dr. J. VandeVondele, Dr. M. Sulpizi, Prof. Dr. M. Sprik
Department of Chemistry
University of Cambridge
Lensfield Road, Cambridge CB21EW (UK)
Fax: (+44) 1223-336-362
E-mail: jv244@cam.ac.uk

[**] Computer resources were mostly provided as part of a EPSRC grant to the UKCP consortium by the HPCx facilities at Daresbury Laboratory.


InterScience
© 2006 Wiley-VCH Verlag GmbH & Co. KGaA, Weinheim

To be predictive, simulations evaluating Equations (3) and (4) must be able to compute $\Delta E$ accurately, with converged statistics for the average values and variances. We employ a practical method that aims at balancing these requirements by combining classical and quantum descriptions in a way that retains atomistic detail, a high-level description of the vertical energy, and good statistics. This method is similar to the approach employed in reference [17]. Figure 1 shows the model system we have used. We compute

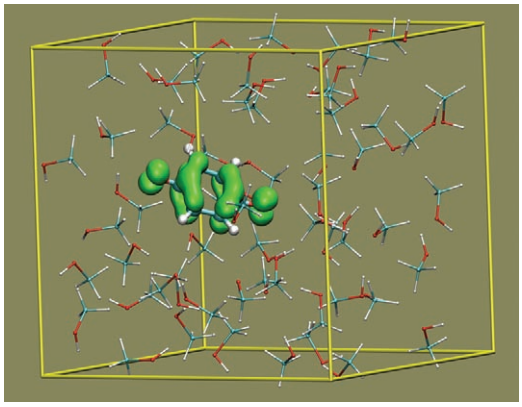


***Figure 1.*** Representative configuration of $BQ^{\bullet-}$ in liquid MeOH as employed in the density functional calculations. The periodically repeated simulation cell, with edges of 15.74 Å, contains 57 solvent molecules. The green isosurface represents the spin density at 0.003 a.u.

several thousand statistically uncorrelated configurations of the system in the oxidized state by using classical molecular dynamics and adopt a DFT description of these configurations for the calculation of the vertical energy. This method combines the strength of classical models (i.e. the accessibility of long time scales and thus the statistical accuracy with which the quantities $\Delta E_O$ and in particular $\sigma_O^2$ can be evaluated) with the accuracy of the more elaborate quantum-mechanical models. Indeed, DFT includes electronic relaxation and thus describes the solvent polarization and changes in strength of hydrogen bonding upon reduction. In this context, the instantaneous polarization, which determines $n_D$ and which is numerically the dominant term in Equation (2), is missing in simple point-charge-based force fields. Since the classical model is only employed in our approach to generate structures of the solvent and the solute in the neutral closed-shell state and not for the more subtle radical-anion state, we expect this simplification to have only a minimal influence on the accuracy of the calculation.

The redox properties of BQ and DQ in MeOH and MeCN, computed with Equations (3) and (4), are summarized in Table 1. MD simulations were continued until the statistical uncertainty in the computed one-electron potentials and solvent reorganization energies was approximately 30 mV, which is similar to the estimated error in the corresponding experimental quantities.[2,7] The convergence of the one-electron potentials is shown in Figure 2 and the results are compared with the experimental values. However, whereas the experimental results[7] are reported against the ferrocene/ferrocenium couple, the computed free energies (Table 1) have a reference potential that is determined by the technique used to compute the electrostatic interactions, by the nature of the solvent, and by the size of the simulation cell. The results shown in Figure 2 are therefore shifted (independently in each of the two solvents) to align the average of the computed potentials with the average of the experimental potentials. The similarity of the shifts (1.197 and 1.108 V in MeOH and MeCN, respectively) indicates that the ferrocene/ferrocenium couple and our reference might have a similar and possibly weak solvent dependence. The potential for the full reaction $DQ^{\bullet-} + BQ \rightarrow DQ + BQ^{\bullet-}$ is independent of the reference electrode, and we obtain values of $0.43 \pm 0.06$ and $0.42 \pm 0.06$ V in MeOH and MeCN, respectively. These values are, within the statistical uncertainties, in good agreement with the experimental values (0.46 and 0.35 V, respectively). A contribution of 100 mV to the substituent-induced shift of the redox potential in both solvents comes from a difference in reorganization free energy (see Table 1). This difference is consistent with the continuum dielectric expression for $\lambda_s$ [Eq. (2)], which predicts a larger reorganization energy for smaller solutes. A quantitative comparison to the $\lambda_s$ values from Equation (2) requires a value for the effective radius of

***Table 1:*** Redox properties of benzoquinone and duroquinone in MeOH and MeCN.[a]

| | $N$[b] | $\Delta E_O$[c] | $\lambda$[d] | $\Delta A$[e] |
|---|---|---|---|---|
| | | | MeOH | |
| BQ | 2680 | −0.341(06) | 1.050(29) | 0.710(31) |
| DQ | 1785 | −0.676(07) | 0.952(30) | 0.277(29) |
| | | | MeCN | |
| BQ | 1252 | −0.462(07) | 0.812(33) | 0.351(32) |
| DQ | 740 | −0.792(07) | 0.719(28) | −0.073(29) |

[a] Obtained from atomistic simulations by using a combination of DFT and classical models. All energies are in eV and the estimated uncertainty in the last two figures is shown in brackets. [b] Number of configurations (sampled at regular 10-ps intervals) employed in the averaging. [c] Average vertical ionization energy. [d] Reorganization free energy. [e] Oxidation free energy of benzoquinone ($BQ^{\bullet-} \rightarrow BQ + e^-$) and duroquinone ($DQ^{\bullet-} \rightarrow DQ + e^-$).

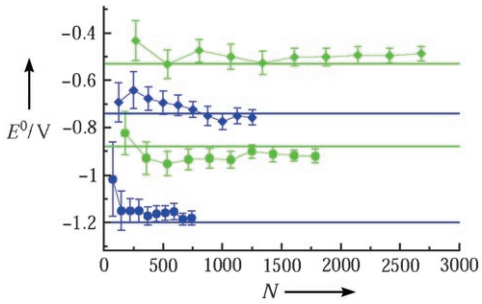



***Figure 2.*** Convergence of the calculated one-electron potentials (diamonds: BQ, circles: DQ) in acetonitrile (blue) and methanol (light green) towards the experimental values from reference [7] (horizontal lines) with respect to the number of employed configurations ($N$). The experimental data are versus the ferrocene/ferrocenium couple and the computed results have been shifted to take into account this difference in reference electrode (see text for details).

 © 2006 Wiley-VCH Verlag GmbH & Co. KGaA, Weinheim 

the solutes, which is not precisely defined and thus uncertain. By using estimated radii of 0.297 nm and 0.358 nm (see Methods Section), we find a reorganization free energy difference of approximately 220 meV, which is larger than the value obtained directly from simulation. For the systems studied herein, we expect no significant effect of the unit-cell size on the reorganization free energy differences, even though the individual terms were not converged with respect to system size. Most of the redox-potential difference can be attributed to the electron-donating effect of the methyl substituents. This effect is predominantly included in the free energy $\Delta A$ through the average vertical energy $\Delta E_O$.

One of the most striking results of our simulations is the effect of the hydrogen bonding on the reorganization energy. Indeed, the results in Table 1 show that the $\lambda$ value of both BQ and DQ is increased by approximately $230 \pm 60$ meV in MeOH relative to MeCN. The tiny difference in the dielectric properties of MeOH and MeCN, which have Pekar factors of 0.538 and 0.529, respectively, can only account for approximately 20 meV of this shift. The major contribution to this shift must therefore be specific interactions with the solvent. Our results are in remarkable quantitative agreement with recent experiments,[2] in which a 0.2-eV shift was measured for the electron-transfer system DQ–1,2,4-trimethoxybenzene in a MeOH/benzonitrile mixture and was attributed to hydrogen bonding to the quinone. Combined with the previous argument regarding the effective size of the solutes, this observation rationalizes the ordering of the reorganization energies $\lambda_{DQ(MeCN)} < \lambda_{BQ(MeCN)} < \lambda_{DQ(MeOH)} < \lambda_{BQ(MeOH)}$.

In summary, we have employed a novel combination of DFT and classical molecular dynamics to provide quantitative values for key parameters of electron-transfer reactions. By using this computational approach, we have been able to rationalize the difference in redox potentials and reorganization energies of quinones caused by chemical substituents and changes in their environments. The new approach is both sufficiently general and efficient to allow, for example, further exploration of the redox properties of systems of biological interest in their native environment.

## Methods Section

Equilibrated configurations of BQ and DQ with 43 and 42 MeCN, and with 57 and 56 MeOH molecules, respectively, were generated by using constant-volume (cubic unit cell with 15.74-Å edges, see Figure 1), constant-temperature (298 K) MD simulations with the Amber program.[20] Configurations sampled at regular 10-ps intervals were retained to compute the distributions of the vertical energies. All atom force fields for MeCN[21] and MeOH[22] are available, and the solutes have been parameterized by using the RESP procedure.[20] The vertical energies were computed from the energy difference between the oxidized and the reduced state by using DFT with periodic boundary conditions. DFT calculations were performed with the freely available CP2K/Quickstep program[23] based on the hybrid Gaussian and plane-wave method[24] using the Becke–Lee–Yang–Parr functional,[25,26] Goedecker–Teter–Hutter pseudo-potentials,[27,28] a Gaussian TZV2P primary basis for all atoms, and a 280Ry auxiliary plane-wave basis for the density.[23] Matrix elements smaller than $10^{-10}$ were neglected, and wavefunctions were optimized with the orbital-transformation method[29] until the electronic gradient was smaller than $10^{-6}$. Estimates of the uncertainties are one σ estimates based on blocked analysis of the data using 16 blocks. The estimated solute radii were chosen to yield volumes equivalent to the molecular volumes for which the electron density is larger than 0.003 a.u.

Received: October 10, 2005
Published online: February 17, 2006

**Keywords:** density functional calculations · electron transfer · hydrogen bonds · molecular dynamics · quinones

[1] R. A. Marcus, N. Sutin, *Biochim. Biophys. Acta* **1985**, *811*, 265–322.
[2] T. Yago, Y. Kobori, K. Akiyama, S. Tero-Kubota, *Chem. Phys. Lett.* **2003**, *369*, 49–54.
[3] J. S. Jaworski, E. Leśniewska, M. K. Kalinowski, *J. Electroanal. Chem.* **1979**, *105*, 329–334.
[4] C. Rüssel, W. Jaenicke, *J. Electroanal. Chem.* **1984**, *180*, 205–217.
[5] J. H. Wilford, M. D. Archer, *J. Electroanal. Chem.* **1985**, *190*, 271–277.
[6] P. Wardman, *J. Phys. Chem. Ref. Data* **1989**, *18*, 1637–1755.
[7] M. Bauscher, W. Mäntele, *J. Chem. Phys.* **1992**, *96*, 11101–11108.
[8] H. Kurreck, M. Huber, *Angew. Chem.* **1995**, *107*, 929–931; *Angew. Chem. Int. Ed. Engl.* **1995**, *34*, 849–866.
[9] N. Gupta, H. Linschitz, *J. Am. Chem. Soc.* **1997**, *119*, 6384–6391.
[10] N. V. Rees, A. D. Clegg, O. V. Klymenko, B. A. Coles, R. G. Compton, *J. Phys. Chem. B* **2004**, *108*, 13047–13051.
[11] R. A. Marcus, *J. Chem. Phys.* **1956**, *24*, 966–978.
[12] R. A. Marcus, *Rev. Mod. Phys.* **1993**, *65*, 599–610.
[13] A. Warshel, *J. Phys. Chem.* **1982**, *86*, 2218–2224.
[14] G. King, A. Warshel, *J. Chem. Phys.* **1990**, *93*, 8682–8692.
[15] M. Tachiya, *J. Phys. Chem.* **1993**, *97*, 5911–5916.
[16] D. W. Small, D. V. Matyushov, G. A. Voth, *J. Am. Chem. Soc.* **2003**, *125*, 7470–7478.
[17] M. H. M. Olsson, G. Hong, A. Warshel, *J. Am. Chem. Soc.* **2003**, *125*, 5025–5039.
[18] Y. Tateyama, J. Blumberger, M. Sprik, I. Tavernelli, *J. Chem. Phys.* **2005**, *122*, 234505.
[19] J. VandeVondele, R. Lynden-Bell, E. J. Meijer, M. Sprik, *J. Phys. Chem. B* **2005**; ASAP DOI: 10.1021/jp054841+.
[20] D. A. Case, T. A. Darden, T. E. Cheatham, III, C. L. Simmerling, J. Wang, R. E. Duke, R. Luo, K. M. Merz, B. Wang, D. A. Pearlman, M. Crowley, S. Brozell, V. Tsui, H. Gohlke, J. Mongan, V. Hornak, G. Cui, P. Beroza, C. Schafmeister, J. W. Caldwell, W. S. Ross, P. A. Kollman, AMBER 8, **2004**, University of California, San Francisco.
[21] X. Grabuleda, C. Jaime, P. A. Kollman, *J. Comput. Chem.* **2000**, *21*, 901–908.
[22] J. W. Caldwell, P. A. Kollman, *J. Phys. Chem.* **1995**, *99*, 6208–6219.
[23] J. VandeVondele, M. Krack, F. Mohamed, M. Parrinello, T. Chassaing, J. Hutter, *Comput. Phys. Commun.* **2005**, *167*, 103–128.
[24] G. Lippert, J. Hutter, M. Parrinello, *Mol. Phys.* **1997**, *92*, 477–487.
[25] A. D. Becke, *Phys. Rev. A* **1988**, *38*, 3098–3100.
[26] C. T. Lee, W. T. Yang, R. G. Parr, *Phys. Rev. B* **1988**, *37*, 785–789.
[27] S. Goedecker, M. Teter, J. Hutter, *Phys. Rev. B* **1996**, *54*, 1703–1710.
[28] C. Hartwigsen, S. Goedecker, J. Hutter, *Phys. Rev. B* **1998**, *58*, 3641–3662.
[29] J. VandeVondele, J. Hutter, *J. Chem. Phys.* **2003**, *118*, 4365–4369.

 © 2006 Wiley-VCH Verlag GmbH & Co. KGaA, Weinheim 

Coordination Polymers

DOI: 10.1002/anie.200503717

# Rigid-Rod Metallosupramolecular Polymers of Dendronized Diazadibenzoperylene Dyes**

*Frank Würthner,* Vladimir Stepanenko, and Armin Sautter*

*Dedicated to Professor Siegfried Hünig on the occasion of his 85th birthday*

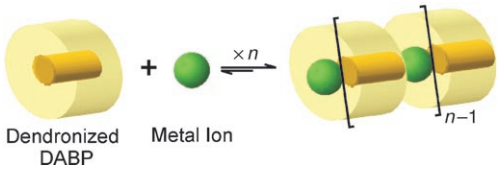
One of the most significant recent highlights in the field of dendrimer chemistry is the development of dendronized polymers,[1] which have become an important class of rigid-rod polymeric materials that display promise in applications such as molecular wires,[2] self-adaptive materials,[3] and as functional scaffolds for catalysis.[4] Three general approaches, namely the "graft-to", "graft-from", and macromonomer strategies, have been applied for the synthesis of dendronized polymers.[1a] The first two strategies comprise coupling of dendrons to preformed polymers, while in the macromonomer strategy, which is of relevance for the present work, dendrons of the desired generations are attached to a polymerizable unit at their focal points and subsequently polymerized. Such polymerization of dendron-equipped monomeric units has been accomplished mainly by conventional polymerization methods.[1a–c] Alternatively, a supramolecular approach using noncovalent interactions such as hydrogen bonding or metal-ion coordination may be applied for this purpose.[5] Despite the fact that a large number of dendronized polymers have been synthesized in the past years by the above-mentioned macromonomer strategy using conventional polymerization methods,[1a–c] and that self-assembly of dendrimers by hydrogen bonding to supramolecular dendronic structures has been explored,[6] as well as the fact that numerous supramolecular metallodendrimers[7] have been reported, only a few studies have addressed the metallosupramolecular polymerization of dendron-equipped monomeric groups to dendronized polymers:[8] Zimmerman and co-workers presented a dendronized tin porphyrin polymer that was used as a precursor for the preparation of novel organic nanotubes,[8a] and Chow et al. synthesized dendronized organoplatinum polymers by functionalizing dendrimer end groups with terminal alkyne units and subsequently reacting these dendrimers with a platinum precursor.[8b]

[*] Prof. Dr. F. Würthner, V. Stepanenko, Dr. A. Sautter
Institut für Organische Chemie
Universität Würzburg
Am Hubland, 97074 Würzburg (Germany)
Fax: (+49) 931-888-4756
E-mail: wuerthner@chemie.uni-wuerzburg.de

[**] We gratefully acknowledge financial support of our work by the Fonds der Chemischen Industrie.

Supporting information for this article is available on the WWW under http://www.angewandte.org or from the author.

Previously, we reported on metal-ion- and hydrogen-bond-directed self-assembly of diazadibenzoperylene (DABP) dyes into cyclic and polymeric architectures.[9] In particular, silver(I) ion mediated self-assembly of these supramolecular building blocks afforded the respective metallosupramolecular coordination polymers.[9e] However, as for the majority of coordination polymers,[5,10] chain growth by metal–ligand coordination was accompanied by strong π–π aggregation, which led to precipitation and the formation of mesophases,[9b,c] while individual polymeric chain molecules could not be observed. To overcome this deficiency, we envisioned that metal-ion-directed self-assembly of dendronized diazadibenzoperylenes may lead to well-defined dendronized coordination polymers (Scheme 1). Herein, we report the synthesis, characterization, and metal-ion-mediated supramolecular polymerization of diazadibenzoperylenes equipped with first to third generation Fréchet-type dendrons.

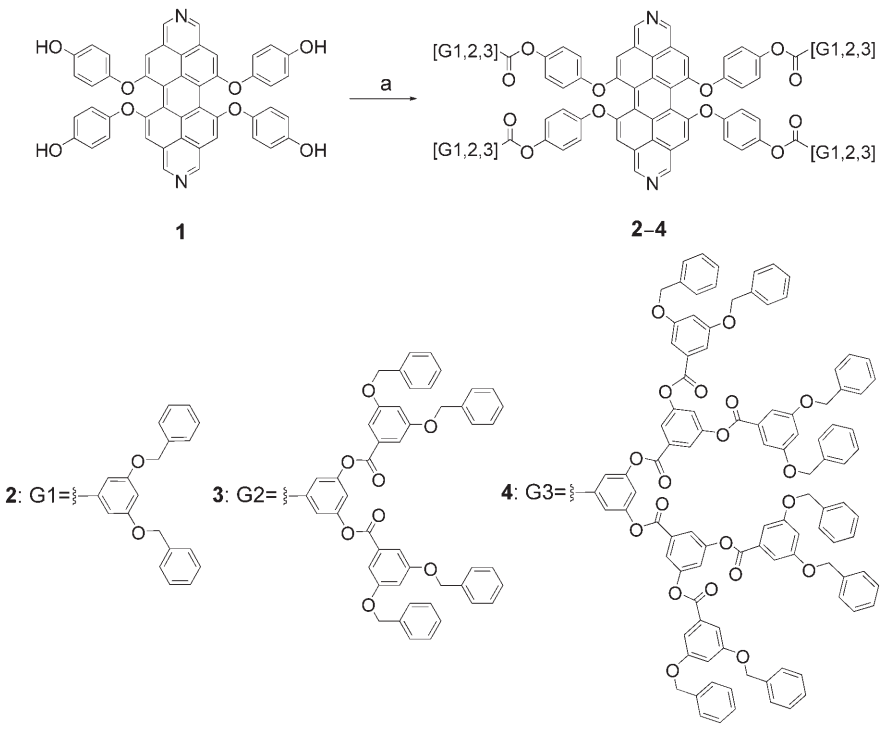



***Scheme 1.*** Concept for the formation of encapsulated rigid-rod coordination polymers by metal-ion-directed self-assembly of dendronized diazadibenzoperylene (DABP) dyes.

The first, second, and third generation dendronized diazadibenzoperylenes **2**–**4** (Scheme 2), respectively, were synthesized by DCC/DPTS-activated esterification of tetra(4-hydroxyphenoxy)diazadibenzoperylene (**1**)[9a,c] with the respective benzoic acid dendrons, which were prepared according to published procedures.[11] The yields of dendritic diazadibenzoperylenes **2**–**4** successively decreased from the first to the third generation (75 to 20%), indicating increasing steric hindrance for the attachment of four dendritic wedges to the 4-hydroxyphenoxy-substituted diazadibenzoperylene **1**. This was also reflected in the reaction times of 2 days for the dendrimers **2** and **3** and 6 days for **4**. Nevertheless, compounds **2**–**4** could be isolated in good to reasonable quantities and high purity and were fully characterized by $^1$H NMR spectroscopy, MALDI-TOF MS, and elemental analysis (see Supporting Information).

The first evidence for successful isolation of the dendronized diazadibenzoperylene chromophore and prevention of π–π aggregation by dendritic substituents was obtained from UV/Vis and fluorescence spectroscopy.[12] Dendrimers **2**–**4** exhibited almost identical absorption spectra in the visible region, showing the typical absorption maxima of the first electronic transition ($S_0 \rightarrow S_1$) of the diazadibenzoperylene chromophore at 495 and 464 nm.[9a,e] On the other hand, an increasing absorption due to the polyester dendrons was observed in the UV region with higher generation numbers. The fluorescence emission spectra showed maxima at 510 and 544 nm that are very close to the values observed for the tetraphenoxy-substituted diazadibenzoperylene chromo-

 © 2006 Wiley-VCH Verlag GmbH & Co. KGaA, Weinheim 




***Scheme 2.*** Synthesis of dendronized diazadibenzoperylenes **2**–**4**: a) Corresponding benzoic acid dendron [G*n*]-COOH ($n=1,2,3$), DCC, DPTS, $CH_2Cl_2$, argon, room temperature, 2–6 days; 75% yield for **2**: 43% yield for **3**; 20% yield for **4**. DCC = dicyclohexyl carbodiimide, DPTS = 4-dimethylaminopyridinium-*p*-toluenesulfonate.

phore,[9e] and the quantum yields of fluorescence in dichloromethane were determined as $\Phi_F = 0.81 \pm 0.03$ (**2**), $0.84 \pm 0.03$ (**3**), and $0.82 \pm 0.03$ (**4**). These results reveal that the dendronization has no effect on the optical properties of the dissolved diazadibenzoperylene chromophore in solutions of dichloromethane. However, as reported previously,[9b,c] π–π aggregation of the diazadibenzoperylene chromophores in less-polar solvents, thin films, or the crystalline state leads to significant changes in the fine structure of the spectra as well as broadening of the bands in the UV/Vis absorption spectra. It is expected that dendronization should result in an encapsulation of the chromophore and thereby hinder π–π aggregation in solution and also in the pristine state. Indeed, UV/Vis spectra of thin films prepared from dendronized diazadibenzoperylenes **2**–**4** showed neither significant band broadening nor a pronounced change in the vibronic fine structure (for an example, see the spectrum for **3** in Figure 1), implying that the aggregation of the dendronized chromophores in the pristine state is negligible.

Metal-ion-mediated polymerization of diazadibenzoperylene dendrimers **2**–**4** was investigated first by NMR spectroscopy in a mixture of $CDCl_3/CD_3OD$ (80:20) using AgOTf as a source of the metal ion with a well-established linear ditopic coordination mode. In particular, in the case of the first and second generation dendrimers **2** and **3** at a 1:1 stoichiometry of the monomeric building block and AgOTf, distinct line broadening in the $^1$H NMR spectra and displacement to higher field of the resonance of the protons at the α position to the nitrogen atoms was observed, for example, from $\delta = 9.23$ to 8.62 ppm for **2** (see Figure 2).[13] Also, the viscosity of the solution increased and gelation was observed upon cooling the sample to 5 °C. These observations can be taken as a clear indication for the formation of coordination polymers.[5]

To further substantiate the formation of dendronized coordination polymers, $^1$H DOSY (diffusion ordered spectroscopy)[14] NMR experiments were carried out. This 2D NMR technique has recently been successfully applied to characterize supramolecular coordination polymers, whose labile and dynamic nature quite often limits the success of conventional techniques for the characterization of polymers.[15] DOSY NMR spectra were measured first for each monomeric dendrimer (**2**–**4**) alone and subsequently after the addition of one equivalent of AgOTf to the solution of the respective monomer. Figure 2a and b display the DOSY NMR spectra for the monomer **2** and for a 1:1 stoichiometric mixture of **2** and AgOTf, respectively, with the corresponding $^1$H NMR spectrum plotted against the logarithm of the diffusion coefficient $D$ [$m^2 s^{-1}$]. Monomeric ligand **2** exhibited a diffusion coefficient of $\log(D/m^2 s^{-1}) = -8.85$, while a significantly lower value ($\log(D/m^2 s^{-1}) = -10.13$) was observed for the 1:1 mixture of **2**

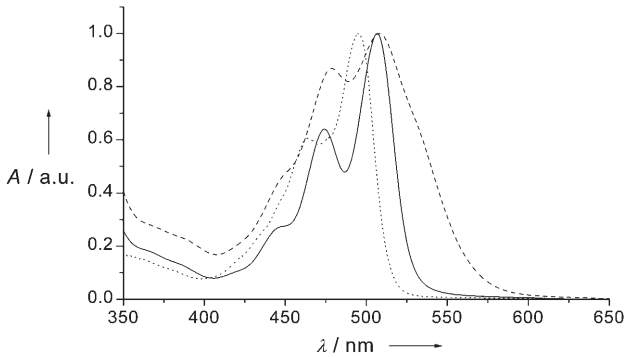



***Figure 1.*** UV/Vis absorption spectrum of a thin film of dendronized diazadibenzoperylene **3** (——) casted from a solution in toluene onto a quartz glass, in comparison with its solution spectrum in dichloromethane (•••••) and the spectrum of a thin film of another diazadibenzoperylene derivative without dendritic substituents (-----).

and AgOTf. This considerable decrease in the diffusion coefficient (more than one order of magnitude) upon addition of an equivalent of $Ag^+$ ion to monomer **2** clearly indicates the formation of the corresponding coordination polymer. As the monomeric dendrimer **3** is itself a large molecule ($M_r = 3833.1\ g\,mol^{-1}$), it shows a smaller diffusion coefficient ($\log(D/m^2 s^{-1}) = -9.49$) compared to that for **2**. However, also in this case the diffusion coefficient was decreased ($\log(D/m^2 s^{-1}) = -10.35$) significantly upon addition of one equivalent of AgOTf, implying the formation of a polymer. In contrast, for the third generation dendronized diazadibenzo-

 © 2006 Wiley-VCH Verlag GmbH & Co. KGaA, Weinheim 

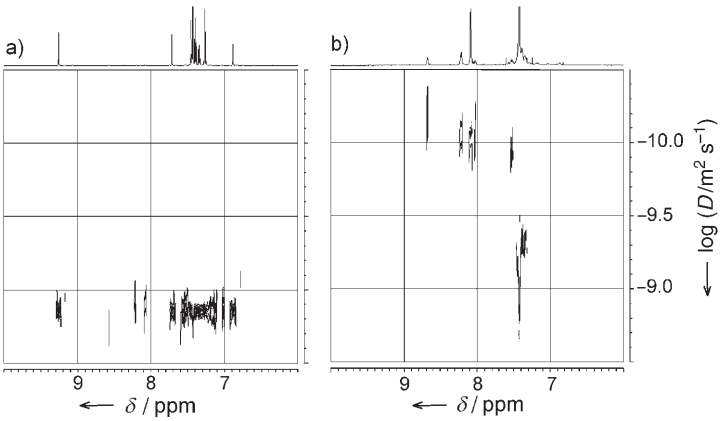



***Figure 2.*** $^1$H DOSY NMR spectra (aromatic region) of a) monomeric dendrimer **2** and b) its coordination polymer, both dissolved in 80:20 mixtures of $CDCl_3$/$CD_3OD$ ($c = 3.5$ mM) at 25 °C. The diffusion coefficients $D$ [$m^2 s^{-1}$] are plotted with a logarithmic scale against the chemical shift $\delta$.

perylene **4** and its 1:1 stoichiometric mixture with AgOTf, almost identical diffusion coefficients of $\log(D/m^2 s^{-1}) = -9.60$ and $-9.64$, respectively, were obtained. Apparently, monomer **4** does not undergo a polymerization by complexation with $Ag^+$ ions owing to the pronounced steric demand of the dendritic wedges that surround the diazadibenzoperylene core, a result that is in accordance with molecular modeling studies (Figure 3).

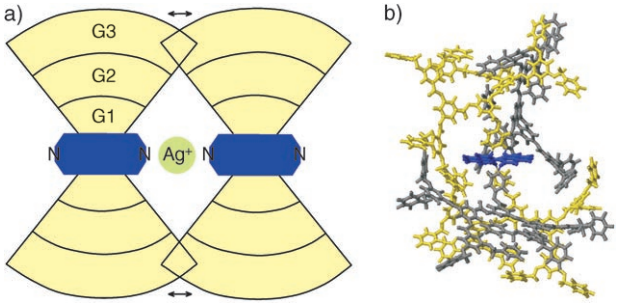



***Figure 3.*** a) Schematic representation of the steric demands of first to third generation (G1–G3) dendritic wedges in $Ag^+$ complexes of dendronized diazadibenzoperylenes. b) Energy-minimized structure of the third generation dendrimer **4** (MD-MM2, CAChe 3.2 program) showing the encapsulation of the chromophore.

To provide further evidence for metal-ion-directed polymerization and to gain insight into the structural features of the desired polymers, atomic force microscopy (AFM) investigations were performed. Figure 4 illustrates the tapping-mode AFM images of samples prepared by spin-coating solutions of monomeric dendrimers **2**–**4** and their 1:1 stoichiometric mixtures with AgOTf in DMF onto highly ordered pyrolytic graphite (HOPG). The AFM images of dendrimers **2** and **3** (Figure 4a and 4c) show small spherical objects that can be attributed to the respective individual dendrimer molecules. In contrast, the image of the sample prepared from a 1:1 stoichiometric mixture of **2** and AgOTf (Figure 4b) reveals the presence of long, slightly bended fibers with an average height of $2.3 \pm 0.3$ nm and lateral width of $5.0 \pm 0.5$ nm. Likewise, the AFM study of the 1:1 stoichiometric mixture of second generation dendrimer **3** and $Ag^+$ ions confirmed the formation of long polymeric structures that adhere to each other. In the AFM images, these structures appear as straight rods (Figure 4d) with an average height of $3.2 \pm 0.3$ nm and lateral width of $5.5 \pm 0.4$ nm as determined by cross-sectional analysis. The third generation dendritic diazadibenzoperylene **4** shows globular structures on the HOPG substrate (Figure 4e), with a diameter of $4.9 \pm 0.3$ nm that is in accordance with the value estimated by molecular modeling studies of ligand **4** (see Figure 3). As expected from the results of the DOSY NMR experiments, no polymeric structures could be seen in the AFM images of the sample prepared from a 1:1 stoichiometric mixture of **4** and AgOTf, but rather globular objects with a diameter of $8.0 \pm 0.5$ nm (approximately twice as large as the monomeric ligand **4**) were observed (Figure 4f). These results suggest the formation of dimeric complexes of **4** which is not very surprising as the polymerization of the third generation dendritic ligands should be disfavored owing to the steric hindrance by the dendrons (see Figure 3).

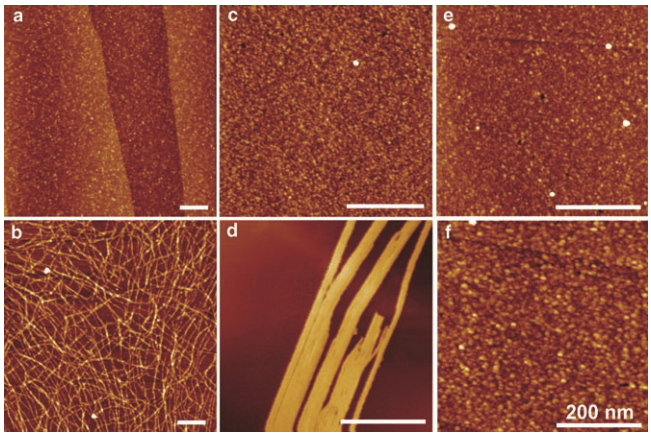



***Figure 4.*** AFM height images of ligands **2** (a), **3** (c), and **4** (e) alone and in the presence of one equivalent of AgOTf (b, d, and f, respectively). The samples were prepared by spin-coating solutions in *N*,*N*-dimethylformamide (DMF; $c = 1.3$ mM for **2** and **3**, $c = 2.0$ mM for **4**) onto HOPG. Scale bar: 200 nm; *z* scale: 12 nm.

Our present results provide clear evidence that dendronized diaza aromatic building blocks can be polymerized by metal-ion coordination to afford defined rigid-rod polymers. The supramolecular polymerization was shown to be highly dependent on the generation number of the attached dendrons; thus, first and second generation dendrimers afforded polymeric materials, while the third generation resisted polymerization as a result of the shielding of the aza coordination site by dendritic wedges. The first and second generation, metal ion/dye-encapsulated rigid-rod polymers constitute an interesting class of π-conjugated materials, whose further investigation is currently underway.

Received: October 20, 2005
Published online: January 30, 2006

 © 2006 Wiley-VCH Verlag GmbH & Co. KGaA, Weinheim 

**Keywords:** dendrimers · dyes/pigments · polymerization · scanning probe microscopy · supramolecular chemistry


[1] a) H. Frauenrath, *Prog. Polym. Sci.* **2005**, *30*, 325 – 384; b) A. D. Schlüter, *Top. Curr. Chem.* **2005**, *245*, 151 – 191; c) A. D. Schlüter, J. P. Rabe, *Angew. Chem.* **2000**, *112*, 860 – 880; *Angew. Chem. Int. Ed.* **2000**, *39*, 864 – 883; d) J. M. J. Fréchet, *Proc. Natl. Acad. Sci. USA* **2002**, *99*, 4782 – 4787; For other approaches towards rigid-rod polymers, see: e) G. Wegner, *Macromol. Chem. Phys.* **2003**, *204*, 347 – 357.

[2] a) W.-S. Li, D.-L. Jiang, T. Aida, *Angew. Chem.* **2004**, *116*, 3003 – 3007; *Angew. Chem. Int. Ed.* **2004**, *43*, 2943 – 2947; b) A. Pogantsch, F. P. Wenzl, E. J. W. List, G. Leising, A. C. Grimsdale, K. Müllen, *Adv. Mater.* **2002**, *14*, 1061 – 1064; c) A. P. H. J. Schenning, R. E. Martin, M. Ito, F. Diedrich, C. Boudon, J.-P. Gisselbrecht, M. Gross, *Chem. Commun.* **1998**, 1013 – 1014.

[3] a) V. Percec, T. K. Bera, M. Glodde, Q. Fu, V. S. K. Balagurusamy, P. A. Heiney, *Chem. Eur. J.* **2003**, *9*, 921 – 935; b) V. Percec, M. Glodde, T. K. Bera, Y. Miura, I. Shiyanovskaya, K. D. Singer, V. S. K. Balagurusamy, P. A. Heiney, I. Schnell, A. Rapp, H.-W. Spiess, S. D. Hudson, H. Duan, *Nature* **2002**, *419*, 384 – 387.

[4] a) C. O. Liang, B. Helms, C. J. Hawker, J. M. J. Fréchet, *Chem. Commun.* **2003**, 2524 – 2525; b) B. M. J. M. Suijkerbuijk, L. Shu, R. J. M. K. Gebbink, A. D. Schlüter, G. van Koten, *Organometallics* **2003**, *22*, 4175 – 4177.

[5] a) J.-M. Lehn, *Polym. Int.* **2002**, *35*, 825 – 839; b) U. S. Schubert, C. Eschbaumer, *Angew. Chem.* **2002**, *114*, 3016 – 3050; *Angew. Chem. Int. Ed.* **2002**, *41*, 2892 – 2926; c) L. Brunsveld, B. J. B. Folmer, E. W. Meijer, R. P. Sijbesma, *Chem. Rev.* **2001**, *101*, 4071 – 4197; for a current overview on metallosupramolecular polymers, see: d) R. Dobrawa, F. Würthner, *J. Polym. Sci. Part A* **2005**, *43*, 4981 – 4995.

[6] a) F. Vögtle, S. Gestermann, R. Hesse, H. Schwierz, B. Windisch, *Prog. Polym. Sci.* **2000**, *25*, 987 – 1041; b) V. Percec, C.-H. Ahn, G. Ungar, D. J. P. Yeardley, M. Möller, S. S. Sheiko, *Nature* **1998**, *391*, 161 – 164; c) W.-D. Jang, D.-L. Jiang, T. Aida, *J. Am. Chem. Soc.* **2000**, *122*, 3232 – 3233; d) Y. Ma, S. V. Kolotuchin, S. C. Zimmerman, *J. Am. Chem. Soc.* **2002**, *124*, 13757 – 13769.

[7] a) G. R. Newkome, E. He, C. N. Moorefield, *Chem. Rev.* **1999**, *99*, 1689 – 1746; b) F. Zeng, S. C. Zimmerman, *Chem. Rev.* **1997**, *97*, 1681 – 1712.

[8] a) Y. Kim, M. F. Mayer, S. C. Zimmerman, *Angew. Chem.* **2003**, *115*, 1135 – 1138; *Angew. Chem. Int. Ed.* **2003**, *42*, 1121 – 1126; b) H.-F. Chow, C.-F. Leung, W. Li, K.-W. Wong, L. Xi, *Angew. Chem.* **2003**, *115*, 5069 – 5073; *Angew. Chem. Int. Ed.* **2003**, *42*, 4919 – 4923.

[9] a) F. Würthner, A. Sautter, J. Schilling, *J. Org. Chem.* **2002**, *67*, 3037 – 3044; b) A. Sautter, C. Thalacker, B. Heise, F. Würthner, *Proc. Natl. Acad. Sci. USA* **2002**, *99*, 4993 – 4996; c) A. Sautter, C. Thalacker, F. Würthner, *Angew. Chem.* **2001**, *113*, 4557 – 4560; *Angew. Chem. Int. Ed.* **2001**, *40*, 4425 – 4428; d) A. Sautter, D. G. Schmid, G. Jung, F. Würthner, *J. Am. Chem. Soc.* **2001**, *123*, 5424 – 5430; e) F. Würthner, A. Sautter, C. Thalacker, *Angew. Chem.* **2000**, *112*, 1298 – 1301; *Angew. Chem. Int. Ed.* **2000**, *39*, 1243 – 1245.

[10] H. W. Roesky, M. Andruh, *Coord. Chem. Rev.* **2003**, *236*, 91 – 119.

[11] C. J. Hawker, J. M. J. Fréchet, *J. Chem. Soc. Perkin Trans. 1* **1992**, 2459 – 2469.

[12] For related work on dendronized perylene bisimide chromophores, see: A. C. Grimsdale, K. Müllen, *Angew. Chem.* **2005**,*117*, 5732 – 5772; *Angew. Chem. Int. Ed.* **2005**, *44*, 5592 – 5629.

[13] The length of supramolecular coordination polymers is dependent on the solvent- and temperature-dependent binding constant and on the exact stoichiometry, as the latter is the case for condensation polymers.

[14] C. S. Johnson, Jr., *Prog. NMR Spectrosc.* **1999**, *34*, 203 – 256.

[15] a) J. M. J. Paulusse, R. P. Sijbesma, *Chem. Commun.* **2003**, 1494 – 1495; b) T. Vermonden, J. van der Gucht, P. de Waard, A. T. M. Marcelis, N. A. M. Besseling, E. J. R. Sudhölter, G. J. Fleer, M. A. Cohen Stuart, *Macromolecules* **2003**, *36*, 7035 – 7044; c) R. Dobrawa, M. Lysetska, P. Ballester, M. Grüne, F. Würthner, *Macromolecules* **2005**, *38*, 1315 – 1325.


 © 2006 Wiley-VCH Verlag GmbH & Co. KGaA, Weinheim 

DNA

DOI: 10.1002/anie.200504022

# Approaching The Limit: Can One DNA Oligonucleotide Assemble into Large Nanostructures?**

*Haipeng Liu, Yi Chen, Yu He, Alexander E. Ribbe, and Chengde Mao**

Herein we address one fundamental question in DNA supramolecular chemistry: what is the minimum number of DNA strands that are required for self-assembly of well-defined DNA nanostructures? Biomacromolecular self-assembly is an important research area for both the basic study of biomacromolecules and the engineering of novel biomaterials. Though the focus of this field is primarily on peptides and proteins,[1] more and more attentions have been paid to DNA in recent years.[2] The main advantage associated with DNA is the simplicity and predictability of the DNA secondary structure. Hence, DNA is an ideal model system to study biomacromolecular self-assembly and an excellent tool for nanoconstruction.[2] Numerous examples have shown that a single-component molecule can self-assemble into well-defined nanostructures.[3] However, no such DNA system has been rationally designed in spite of the excellent programmability of DNA.[4]

Herein, we report the self-assembly of DNA nanotubes from one DNA single-strand, this is the fundamentally minimum requirement for the number of DNA strands to assemble into well-defined geometric structures. This process superficially resembles the self-assembly of natural protein nanofilaments, such as microtubules: a single-component protein self-assembles into one-dimensional nanostructures

[*] H. Liu, Y. Chen, Y. He, A. E. Ribbe, Prof. C. Mao
Department of Chemistry
Purdue University
West Lafayette, IN 47907 (USA)
Fax: (+1) 765-494-0239
E-mail: mao@purdue.edu

[**] This work is supported by NSF (EIA-0323452), DARPA/DSO (MDA 972-03-1-0020), and Purdue University (a start-up fund). AFM study was carried out in the Purdue Laboratory for Chemical Nanotechnology (PLCN).


WILEY InterScience DISCOVER SOMETHING GREAT
© 2006 Wiley-VCH Verlag GmbH & Co. KGaA, Weinheim

many micrometers long. DNA nanotubes have been assembled with various strategies from systems that contain several different DNA strands and require careful ratio calibration. For example, a double crossover (DX) molecule contains four or five DNA strands,[5] a triple crossover (TX) molecules contains four strands,[6] a cross molecule contains nine strands,[7] and a six-helix bundle contains 20 strands.[8] To reduce the number of strands involved and avoid ratio calibration, the key to the molecular design is sequence symmetry.[9] In our study, a double crossover (DX)-like structure is used (Figure 1), which contains two identical,

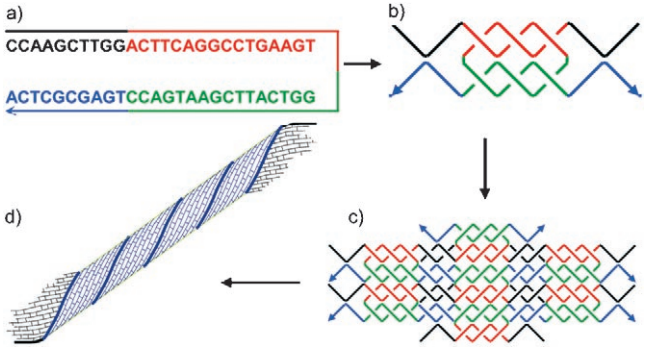



***Figure 1.*** Schematic representation of a DNA nanotube. a) DNA sequence of a single strand containing four palindromic segments, each of which is shown in a different color. The arrow indicates the 3′ end of the DNA strand. As temperature decreases, the DNA strands first form a two-stranded complex (b), these further associate with each other to form two-dimensional sheets (c), and eventually fold into nanotubes (d).

52-nucleotide (nt) long strands. The strand consists of four segments, which are 10, 16, 16, and 10 bases long, respectively. Each segment is a palindrome, thus self-complementary. At native condition, two strands will associate with each other to form a two-stranded complex. The complex contains two duplex domains and four single-stranded overhangs. The complex will further assemble into 2D lattices through hybridization between the single-stranded overhangs. Because many nicks exist at the crossover points, the 2D lattices are not stiff and could fold into tubes. The folding from 2D lattices into tubes is an intracomplex process, whereas the growth from small 2D lattices into large extended 2D lattices is an intercomplex process. At the low DNA concentration (around 1 μM), the tube formation would be kinetically more favorable than formation of large extended 2D lattices. Hence, DNA nanotubes (helical or non-helical) are expected to be primary products from the DNA self-assembly.

Assembled DNA samples were characterized by atomic force microscopy (AFM) by literature methods.[9] After purification, the DNA strand was dissolved in a neutral buffer containing $Mg^{2+}$ ions. Self-assembly was performed by slowly cooling from 95 °C to 4 °C (see Experimental Section for details). Then the samples were absorbed onto mica surfaces for AFM imaging. Long DNA nanotubes can be clearly visualized (Figure 2). They are up to 60 μm long and around 6 nm high. Their width varies between 30–70 nm.

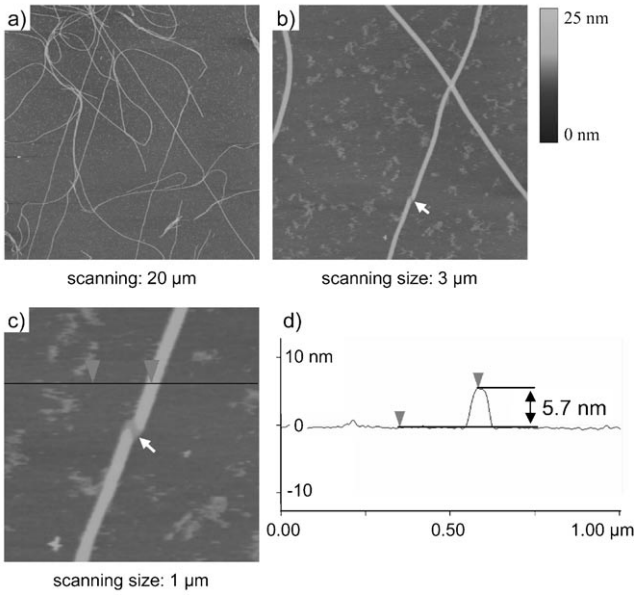



***Figure 2.*** a)–c) AFM analysis of DNA nanotubes. From (a) to (c), the magnification of the images increases. All images have the same height scale, shown on the right. White arrows indicate defects where DNA nanotubes are not completely closed. d) A cross-section profile of the DNA nanotube in (c) taken along the black line, the gray arrows in (c) and (d) mark the same positions.

However, each individual tube has a uniform height and width. This observation might suggest that once a segment of the tube forms, this segment might initiate further rapid assembly of the rest of the nanotube. In rare cases, we have observed random defects along the tubes (as indicated by the white arrows in Figure 2b,c). Although the origins of the defects are not clear, such defects allow clear assignment of the hollow tubular structures of DNA assemblies.

The DNA tubes can also be studied by fluorescence microscopy when the DNA strands are partially conjugated with fluorescein, a green fluorescence dye, at the 5′ ends (Figure 3). These results agree with the AFM data. The advantage of fluorescence imaging is that it is easy and time efficient.[9] In Figure 3, the DNA tubes appear aligned to some extent. The reason is not clear, but is suspected to be due to the liquid flow during the sample preparation.

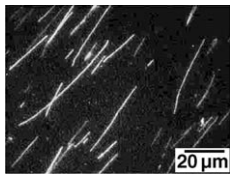



***Figure 3.*** A fluorescence microscopy image of DNA nanotubes.

The DNA nanotubes are robust. After being stored in aqueous solution at room temperature for three months, the DNA nanotubes remain intact as shown by AFM imaging. Thermal-denaturation analysis also indicates the fiber structure is stable, the optical absorption at 260 nm, which is the maximum absorption wavelength of DNA, remain unchanged up to 60 °C. We attribute the nanotube stability to the long single-stranded overhangs, which are 10 bases long and ensure strong cohesions between the dimeric complexes. To our surprise, DNA nanotubes can even be assembled from unpurified synthetic DNA molecules,

 © 2006 Wiley-VCH Verlag GmbH & Co. KGaA, Weinheim 

which contain many shorter strands that result from failed DNA synthesis. This observation further indicates that the nanotubes are robust and can tolerate imperfect DNA strands.

The DNA strand contains palindromic segments. In principle, it could forms many different oligomers other than the desired dimeric complex. However, because the concentration range used is quite low, it is less likely to form alternative oligomeric structures. If they formed, they would randomly aggregate into non-ordered structures containing many unpaired DNA single-stranded regions. Such aggregates are less stable than the ordered DNA nanotubes. Under an equilibrium condition, the random aggregates would dissociate and re-assemble into more stable DNA nanotubes. Our experimental data are consistent with, but can not prove, this speculation.

The DNA nanotubes can serve as templates to fabricate metallic nanowires. We adapted a reported two-step metallization protocol.[10] Briefly, DNA nanotubes were absorbed onto freshly cleaved mica surface, and incubated with a $Pd^{2+}$ ion solution. The $Pd^{2+}$ ions adsorbed on the DNA were then chemically reduced to form metallic nanowires. AFM imaging shows that the metallized nanowires are 30–80 nm wide and up to 30 μm long (Figure 4), slightly wider than their DNA templates but with the same length scale. The height of the Pd nanowires varies between 10–18 nm, significantly higher than bare DNA nanotubes (≈6 nm). Unlike the bare DNA nanotubes which are smooth, the Pd nanowires consist of grains of 30–60 nm diameter compactly deposited along the DNA tube skeletons. From the AFM images, the Pd grains appear to be in contact with each other and form continuous wires without apparent gaps.

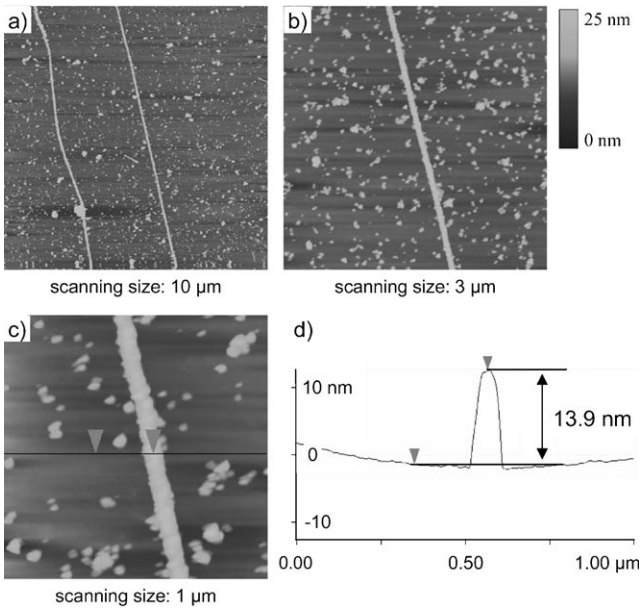



***Figure 4.*** a)–c) AFM analysis of palladium (Pd) nanowires derived from DNA nanotubes. From (a) to (c), the magnification of the images increases. All images have the same height scale, shown on the right. (d) a cross section profile of the Pd nanowire in (c) taken along the black line, the gray arrows in (c) and (d) mark the same positions.

In summary, we have designed a DNA single-strand that self-assembles into multiple-stranded nanotubes, which are 20–45 nm in diameter and up to 60 μm long. We believe such one-strand system may have applications in nanotechnology. For example, the DNA tubes can serve as templates for nanofabrications, as scaffolds to organize nano-objects, and as tracks for nanomotors.[11] Such a system could also serve as a model system to study the assembly mechanism of other 1D nanostructures, including carbon nanotubes.[12]

## Experimental Section

*Oligonucleotides*: DNA sequences were designed by a computer program "SEQUIN".[13] All oligonucleotides were purchased from IDT, Inc. and purified by 20% denaturing polyacrylamide gel electrophoresis (PAGE); bands were cut out of gels and eluted in a solution containing ammonium acetate (500 mM), magnesium acetate (10 mM), and ethylenediamine tetraacetic acid (EDTA; 1 mM).

*Formation of DNA complexes/2D arrays*: DNA arrays were formed by dissolving DNA in Tris-Acetic-EDTA-$Mg^{2+}$ (TAE–$Mg^{2+}$; Tris = tris(hydroxymethyl)aminomethane, Acetic = acetic acid) buffer and slowly cooling DNA solution from 95 °C to 4 °C over 48 h. The final concentration of DNA was between 0.5 and 1.0 μM, and the final volume was 20 μL. The TAE–$Mg^{-2+}$ buffer consisted of Tris base (40 mM, pH 8.0), acetic acid (20 mM), EDTA (2 mM), and $Mg(Ac)_2$ (12.5 mM). For fluorescence imaging, 50% of the DNA was labeled with fluorescein at the 5′ ends.

*Thermal denaturation*: The DNA strand was dissolved to 1 μM concentration in TAE–$Mg^{2+}$ buffer (1 mL, pH 8.0), and annealed as described above. The samples were transferred to quartz cuvettes, and the TAE–$Mg^{2+}$ buffer was used as a blank. Thermal denaturation was monitored at 260 nm on a Varian Cary 100 Bio UV/Visible Spectrophotometer, temperature was incremented at 0.1 °C $min^{-1}$.

*Fabrication of Pd nanowires*: A drop of DNA solution (2 μL) was spotted onto a fresh cleaved mica surface and left to adsorb to the surface for 30 s. On the top of the DNA, saturated aqueous solution OF Palladium Acetate [$Pd(Ac)_2$] (10 μL) was added and allowed to incubate for 10 s, then browed away by compressed air. reducing buffer (10 μL; sodium citrate (25 mg $mL^{-1}$), 85% lactic acid (25 mg $mL^{-1}$), and borane dimethylamine (2.5 mg $mL^{-1}$)) was placed on the surface and incubated for 10–20 s, then browed away. The surface was rinsed twice with doubly distilled $H_2O$ before AFM imaging in air.

*AFM imaging of DNA in TAE–$Mg^{2+}$ buffer*: A drop of DNA sample solution (1 μL) was spotted onto freshly cleaved mica (Ted Pella, Inc.) and left to adsorb to the surface for 30 s, then TAE–$Mg^{2+}$ buffer (50 μL) was placed onto the mica. Imaging was performed by tapping-mode AFM under TAE–$Mg^{2+}$ in a fluid cell on a Multimode NanoScope IIIa, using NP-S tips (Veeco Inc.).

*AFM imaging of Pd nanowires in Air*: Pd nanowires were imaged by tapping-mode AFM on Nanoscope IIIa (Digital Instruments) with NSC15 tips (silicon cantilever, MikroMasch). The tip–surface interaction was minimized by optimizing the scan set-point.

*Fluorescence imaging*: A drop of fluorescein-DNA solution (1 μl) was spotted onto a glass slide, and a coverslip was placed on it immediately, fluorescence images were obtained with a Nikon Fluorescence Microscope E800 at excitation/emission wavelengths of 470/505 (FITC, green).

Received: November 11, 2005
Published online: February 15, 2006

**Keywords:** DNA · nanostructures · palladium · scanning probe microscopy · self-assembly

 © 2006 Wiley-VCH Verlag GmbH & Co. KGaA, Weinheim 

[1] a) S. Zhang, D. M. Marini, W. Hwang, S. Santoso, *Curr. Opin. Chem. Biol.* **2002**, *6*, 865 – 871; b) X. Gao, H. Matsui, *Adv. Mater.* **2005**, *17*, 2037 – 2050.
[2] N. C. Seeman, *Nature* **2003**, *421*, 427 – 431.
[3] a) M. R. Ghadiri, J. R. Granja, R. A. Milligan, D. E. McRee, N. Khazanovich, *Nature* **1993**, *366*, 324 – 327; b) J. D. Hartgerink, E. Beniash, S. I. Stupp, *Science* **2001**, *294*, 1684 – 1688; c) H. Fenniri, B. Deng, A. E. Ribbe, *J. Am. Chem. Soc.* **2002**, *124*, 11064 – 11072.
[4] Note: there are two arguable exceptions: 1) G-wires, that is, guanine-rich DNA strands can associate with each other to form 1D structures through G-quadruplexes. However, they are normally quite short, under than 1 μm, and commonly shorter than 100 nm. Along the wires, there are many defects derived from the imperfect alignment among the DNA strands. We suspect that the defects are responsible for the limited lengths of the G-wires. For related works see: a) M. A. Batalia, E. Protozanova, R. B. Macgregor, Jr., D. A. Erie, *Nano Lett.* **2002**, *2*, 269 – 274; b) E. Protozanova, R. B. Macgregor, Jr., *Biochemistry* **1996**, *35*, 16638 – 16645; c) A. B. Kotlyar, N. Borovok, T. Molotsky, H. Cohen, E. Shapir, D. Porath, *Adv. Mater.* **2005**, *17*, 1901 – 1905. 2) A single 13-mer olionucleotide assembled into 3D lattices through both Watson–Crick base-pairing and non-Watson–Crick interactions (P. J. Paukstelis, J. Nowakowski, J. J. Birktoft, N. C. Seeman, *Chem. Biol.* **2004**, *11*, 1119 – 1126), this study is a very interesting discovery, however, it was not achieved through rational design and it is not clear how this discovery could be generalized into a new design strategy.
[5] a) P. W. K. Rothemund, A. Ekani-Nkodo, N. Papadakis, A. Kumar, D. K. Fygenson, E. Winfree, *J. Am. Chem. Soc.* **2004**, *126*, 16344 – 16352; b) J. C. Mitchell, J. R. Harris, J. Malo, J. Bath, A. J. Turberfield, *J. Am. Chem. Soc.* **2004**, *126*, 16342 – 16343; c) M. Endo, N. C. Seeman, T. Majima, *Angew. Chem.* **2005**, *117*, 6228 – 6231; *Angew. Chem. Int. Ed.* **2005**, *44*, 6074 – 6077.
[6] D. Liu, S. H. Park, J. H. Reif, T. H. LaBean, *Proc. Natl. Acad. Sci. USA* **2004**, *101*, 717 – 722.
[7] H. Yan, S. H. Park, G. Finkelstein, J. H. Reif, T. H. LaBean, *Science* **2003**, *301*, 1882 – 1884.
[8] F. Mathieu, S. Liao, J. Kopatsch, T. Wang, C. Mao, N. C. Seeman, *Nano Lett.* **2005**, *5*, 661 – 665.
[9] a) Y. He, Y. Tian, Y. Chen, Z. Deng, A. E. Ribbe, C. Mao, *Angew. Chem.* **2005**, *117*, 6852 – 6854; *Angew. Chem. Int. Ed.* **2005**, *44*, 6694 – 6696; b) Y. He, Y. Chen, H. Liu, A. E. Ribbe, C. Mao, *J. Am. Chem. Soc.* **2005**, *127*, 12202 – 12203; c) H. Liu, Y. He, A. E. Ribbe, C. Mao, *Biomacromolecules* **2005**, *6*, 2943 – 2945.
[10] Z. Deng, C. Mao, *Nano Lett.* **2003**, *3*, 1545 – 1548.
[11] a) A. P. Alivisatos, K. P. Johnsson, X. Peng, T. E. Wilson, C. J. Loweth, M. P. Bruchez, P. G. Schultz, *Nature* **1996**, *382*, 609 – 611; b) C. A. Mirkin, R. L. Letsinger, R. C. Mucic, J. J. Storhoff, *Nature* **1996**, *382*, 607 – 609; c) C. M. Niemeyer, T. Sano, C. L. Smith, C. R. Cantor, *Nucleic Acids Res.* **1994**, *22*, 5530 – 5539; d) E. Braun, Y. Eichen, U. Sivan, G. Ben-Yoseph, *Nature* **1998**, *391*, 775 – 778; e) Z. Deng, C. Mao, *Angew. Chem.* **2004**, *116*, 4160 – 4162; *Angew. Chem. Int. Ed.* **2004**, *43*, 4068 – 4070; f) Y. Tian, Y. He, Y. Chen, P. Yin, C. Mao, *Angew. Chem.* **2005**, *44*, 4429 – 4432; *Angew. Chem. Int. Ed.* **2005**, *44*, 4355 – 4358.
[12] H. Dai, *Acc. Chem. Res.* **2002**, *35*, 1035 – 1044.
[13] N. C. Seeman, *J. Biomol. Struct. Dyn.* **1990**, *8*, 573 – 581.

 © 2006 Wiley-VCH Verlag GmbH & Co. KGaA, Weinheim 

Reaction Mechanisms

DOI: 10.1002/anie.200503970

# Palladium-Catalyzed Allylation of Alkynes with Allyl Alcohol in Aqueous Media: Highly Regio- and Stereoselective Synthesis of 1,4-Dienes**

*Jingmei Huang, Lei Zhou, and Huanfeng Jiang**

Carbometalation of carbon–carbon multiple bonds is an important process in organometallic chemistry from both theoretical and practical standpoints.[1] In particular, the allylmetalation of alkynes to form 1,4-dienes is an area of growing interest during recent years.[2] However, although allyl alcohols are readily available, they have rarely been employed directly as allylating agents. The transition-metal-catalyzed alkyne/allyl alcohol reaction usually affords β,γ- or γ,δ-unsaturated carbonyl compounds,[3] or hydroalkoxylation products.[4] Thus, it is clear that the scope and synthetic applications of alkyne allylation would be greatly enhanced if methods permitting the direct use of alcohols were developed.

Organic reactions in water have recently attracted much attention, not only because of the unique reactivity observed, but also because water is a safe and economical substitute for conventional organic solvents.[5] Thus, the development of atom-economical reactions in water is one of the most important goals of synthetic chemistry. Herein we disclose that $PdCl_2$ catalyzes the allylation of alkynes with allyl alcohol highly selectively aqueous media with exclusive formation of 1,4-dienes in, and we attribute this finding to a novel catalytic cycle.[6]

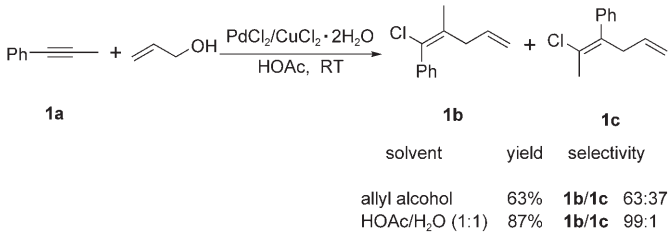
In our studies on the allylation of alkynes with allyl alcohol we found that the reaction of prop-1-ynylbenzene with an excess of allyl alcohol (10 equiv) as the solvent in the presence of $PdCl_2$ (5% mol), $CuCl_2{\cdot}2H_2O$ (2 mmol), and HOAc (2 mmol) afforded 1,4-diene products **1b** and **1c** in 63% yield with a low regioselectivity (63:37, Scheme 1). To our surprise, no trace of aldehyde was detected. A comparative reaction with $CuCl_2$ instead of $CuCl_2{\cdot}2H_2O$ gave 1,4-diene products in a much lower yield. Further studies on

[*] Dr. J. Huang, L. Zhou, Prof. Dr. H. Jiang
The College of Chemistry
South China University of Technology
Guangzhou 510640 (P.R. China)
Fax: (+86) 20-8711-2906
E-mail: jianghf@scut.edu.cn
L. Zhou
Guangzhou Institute of Chemistry
Chinese Academy of Sciences
PO Box 1122, Guangzhou 510650 (P.R. China)
and
Graduate School of the Chinese Academy of Sciences
Beijing 100039 (P.R. China)

[**] We are grateful to the National Natural Science Foundation of China for financial support (Grants: 20172053, 20332030, and 20572027).

Supporting information for this article is available on the WWW under http://www.angewandte.org or from the author.


© 2006 Wiley-VCH Verlag GmbH & Co. KGaA, Weinheim

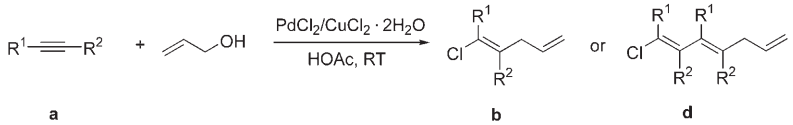


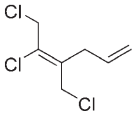
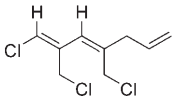
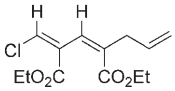
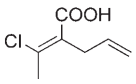
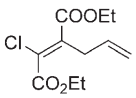
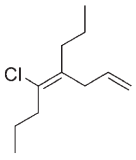
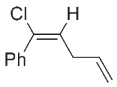
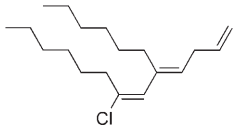
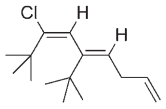
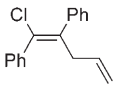

***Scheme 1.*** Comparison of the yield and selectivity of the allylation reaction in different solvents.

optimizing the reaction conditions revealed that changing the solvent to an aqueous mixture (HOAc:$H_2O$, 1:1) afforded a single regioisomer **1b**, the yield of which was increased sharply to 87%.

A range of substrates was explored in the reaction and the results are summarized in Table 1. In most cases, the allylation reactions proceeded smoothly and gave the desired 1,4-dienes in good to excellent yield with extremely high selectivity. It is noteworthy that the terminal acetylenes (entries 4, 5, 10, and 11) gave cotrimerization products from the reaction of two

***Table 1:*** $PdCl_2$-catalyzed allylation of alkynes.




| Entry | $R^1$ | $R^2$ | *t* [h] | Solvent[a] | Product[b] | | Yield[c] [%] |
|---|---|---|---|---|---|---|---|
| 1 | Ph | Me | 12 | allyl alcohol[d] | **1b/1c** 63:37 | | 63 |
| 2 | Ph | Me | 12 | HOAc/$H_2O$ 1:1 | **1b/1c** 99:1 | | 87 |
| 3 | $CH_2Cl$ | $CH_2Cl$ | 6 | HOAc/$H_2O$ 1:1 |  | **3b** | 91 |
| 4 | H | $CH_2Cl$ | 12 | HOAc/$H_2O$ 1:1 |  | **4d** | 59 |
| 5 | H | $CO_2C_2H_5$ | 12 | HOAc/$H_2O$ 1:1 |  | **5d** | 52 |
| 6 | $CH_3$ | COOH | 24 | HOAc/$H_2O$ 1:1 |  | **6b** | 73 |
| 7 | $CO_2C_2H_5$ | $CO_2C_2H_5$ | 12 | HOAc:$H_2O$ 1:1 |  | **7b** | 92 |
| 8 | *n*-$C_3H_7$ | *n*-$C_3H_7$ | 12 | HOAc/$H_2O$ 1:1 |  | **8b** | 71[e] |
| 9 | Ph | H | 12 | HOAc/$H_2O$ 1:1 |  | **9b** | 74 |
| 10 | *n*-$C_6H_{13}$ | H | 10 | HOAc/$H_2O$ 1:1 |  | **10d** | 85 |
| 11 | *t*Bu | H | 14 | HOAc/$H_2O$ 1:1 |  | **11d** | 16 |
| 12 | Ph | Ph | 30 | THF/$H_2O$[f] 5:1 |  | **12b** | 53 |

[a] Standard conditions: alkyne (1 mmol), allyl alcohol (3 mmol), $CuCl_2 \cdot 2H_2O$ (2 mmol), HOAc (1 mL), and $H_2O$ (1 mL), with stirring at RT. [b] The configuration was determined by $^1H$ NMR and $^{13}C$ NMR spectroscopy as well as by NOE studies. [c] Yield of isolated product. [d] HOAc (2 mmol) and allyl alcohol (10 equiv) as solvent. [e] A mixture of **8b**/**8d** (71:29) was obtained. [f] HOAc (2 mmol), allyl alcohol (3 equiv), THF (1 mL), and $H_2O$ (0.2 mL) as solvent.

 © 2006 Wiley-VCH Verlag GmbH & Co. KGaA, Weinheim 

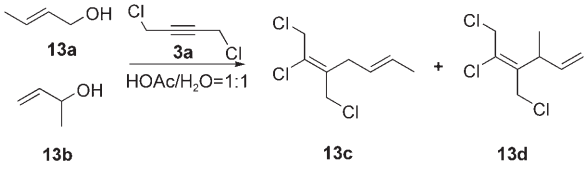
acetylenes and one allyl alcohol. Of special interest is the substrate but-2-ynoic acid (entry 6), which resulted in the introduction of a carboxylic acid moiety directly into the 1,4-diene without the need for functional group protection/deprotection. The low yield of **11d** arose from the dimerization of the terminal alkynes to form 1,4-dihalo-1,3-dienes. In terms of the stereoselectivity, all the products obtained in the presence of an excess of halide ion and acetic acid in a polar solvent resulted from *trans* addition.[7,8] The site of halogen addition to asymmetric acetylenes (entries 1, 2, 4–6, 9–11) was controlled by electronic factors.[8] The consistent preference observed in terms of regio- and stereoselectivity suggests that the reaction might proceed by the initial formation of a vinylpalladium intermediate followed by *trans*-chloropalladation of the alkynes.[7b,9,10]

The exclusive formation of 1,4-dienes in excellent yield prompted us to study the mechanistic aspects of the transformation of allyl alcohol in this reaction. To this end, allyl alcohol was treated with $PdCl_2/CuCl_2 \cdot 2H_2O$ in the presence of $HOAc/H_2O$ at RT without adding any acetylene substrate. No allyl chloride was detected by GC-MS and $^1H$ NMR spectroscopic analysis. Hence, the possibility of an allyl chloride intermediate being involved was clearly ruled out. To our surprise, diallyl ether was observed in the reaction mixture.[11] This result indicated that the reaction proceeded with cleavage of the C–O bond of allyl alcohol to form a vinylpalladium intermediate, followed by the attack of another equivalent of allyl accohol.[5a,12]

Crotyl alcohol (**13a**) and its regioisomer 1-buten-3-ol (**13b**) were employed as the allylic alcohol sources in further studies. Allylation of **13a** and **13b** with 1,4-dichloro-2-butyne (**3a**) in the presence of $PdCl_2/CuCl_2$ in aqueous media ($HOAc:H_2O$, 1:1) gave isomeric 1,4-dienes (**13c** and **13d**, respectively) in moderate yields in both cases (Scheme 2). However, the ratio **13c**/**13d** observed from alcohol **13a** and **13b** is different, thus suggesting that a reaction pathway other than π-allylpalladation might also be involved.

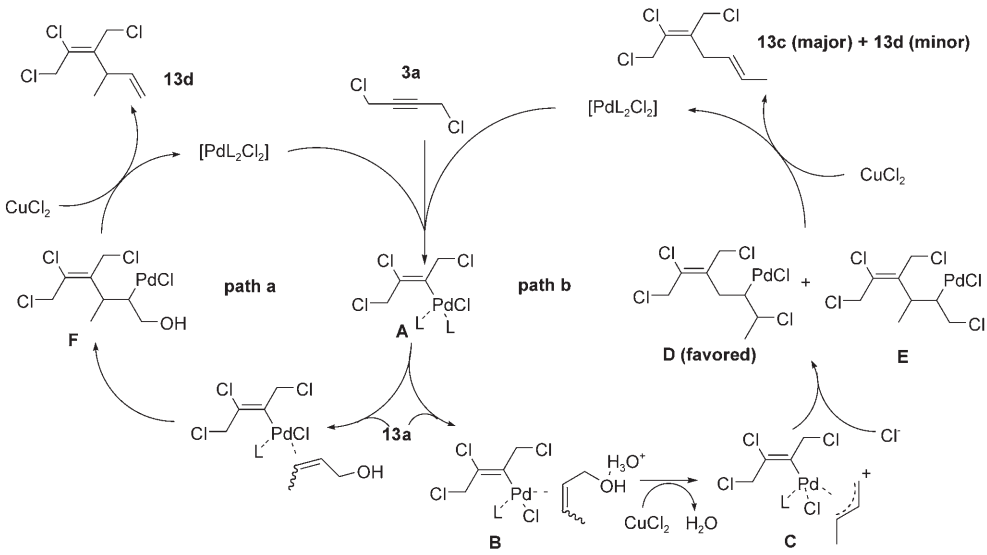
The ratio **13c**/**13d** changed sharply when $CuCl_2$ was replaced by LiCl in the above reaction system: a branched chain product **13d** was obtained predominantly when **13a** was used, while the major isomer was the straight-chain product **13c** when **13b** was used. These results suggested that the reaction with LiCl might proceed through a pathway involving a direct insertion of the allylic alcohol into the vinylpalladium intermediate. Hence, on the basis of the above observation, we hypothesize that $CuCl_2$ may work as a promoter for the formation of a π-allylpalladium species.

A plausible mechanism for the allylation of alkynes in aqueous media ($HOAc/H_2O$, 1:1) catalyzed by $PdCl_2$ is shown in Scheme 3. Vinylpalladium intermediate **A** is initially formed by *trans*-chloropalladation of the alkyne in a polar solvent system[8,13] in the presence of excess halide ions.[14]




| additive salt | alcohol | yield | isomer ratio of product |
|---|---|---|---|
| $CuCl_2$ | from **13a** | 37% | **13c**/**13d**=66:34 |
| | from **13b** | 58% | **13c**/**13d**=90:10 |
| LiCl | from **13a** | 18% | **13c**/**13d**=12:88 |
| | from **13b** | 34% | **13c**/**13d**=98:2 |

***Scheme 2.*** Mechanistic study of the allylation reaction between crotyl alcohol and 1-butyn-3-ol.

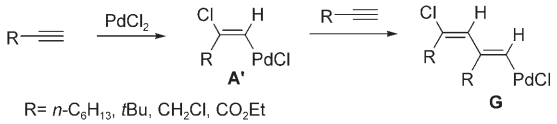



***Scheme 3.*** Mechanistic hypothesis for the palladium-catalyzed allylation of alkynes.

This is followed by a competing reaction between the insertion of crotyl alcohol (path a) and the formation of a π-allylpalladium[15] species in situ by the cleavage of a C–O bond with the aid of acid in water (path b).[5a] The produced intermediates **D** (favored) and **E** in path b subsequently undergo β-halogen elimination to produce **13c** and **13d** and regenerate $PdCl_2$ in the presence of $CuCl_2$.[16] Meanwhile, the alcohol **F** produced in path a undergoes β-OH elimination to produce **13d** and regenerate the catalytic $Pd^{II}$ species in the presence of $CuCl_2$. Hence, since **13c** is the major product from both path a and path b, it is rational that **13c** was obtained in 90% yield when 1-buten-3-ol (**13b**) was employed in the $PdCl_2/CuCl_2$ reaction system. When LiCl was used, the reaction proceeded only minimally by path b, with β-OH elimination to form **13d**. Therefore, $Cu^{II}$ ions are essential to promote the reaction by path b.

 © 2006 Wiley-VCH Verlag GmbH & Co. KGaA, Weinheim 

The terminal alkynes, a group of more-reactive substrates, were prone to undergo an additional alkyne insertion reaction.[17] Under our reaction conditions, intermediate **A′** underwent a consecutive *trans* addition of one more molecule of alkyne to afford a new halopalladium intermediate **G** (Scheme 4). It is noted that an additional alkyne insertion did




***Scheme 4.*** Additional alkyne insertion.

not occur with the terminal alkyne **9a**, where $R^1$ is an aromatic ring (Table 1, entry 9). This result might be a consequence of the coordination of the aromatic ring adjacent to the Pd moiety of the vinylpalladium intermediate **A′**, thus stabilizing the vinylpalladium intermediate **A′** in the catalytic cycle. This stabilization may inhibit further insertion of another molecule of alkyne.[17d]

In conclusion, mild conditions have been developed for the allylation of alkynes by the direct use of allyl alcohol as the allylating agent in aqueous media. A mechanism based on the competition between π-allylpalladation through cleavage of the C–O bond and the insertion of an alkene was employed to explain the unprecedented result. The present procedure provides a new highly stereo- and regioselective method to construct 1,4-dienes in an economical and environmentally benign manner. Further investigation to determine the precise mechanism and expand the scope of this reaction is underway.

## Experimental Section

General procedure for the preparation of **4d**: A test-tube (10 mL) was charged with palladium chloride (10 mg, 0.056 mmol), $CuCl_2$ (343 mg, 2 mmol), allyl alcohol (174 mg, 3 mmol), and HOAc (1 mL). After the resulting mixture had become homogenous through stirring, 3-chloropropyne (74.5 mg, 1 mmol) was added, followed by $H_2O$ (1 mL). The mixture was stirred at RT for 12 h (monitored by TLC). The reaction mixture was dissolved in diethyl ether (10 mL × 2) and washed with brine (5 mL). The organic layer was dried ($MgSO_4$) and concentrated in vacuo. The residue was purified by flash chromatography over silica gel (petroleum ether/ethyl acetate, 15:1) to give **4d** (66 mg, 0.29 mmol, 59%) as a yellow oil.

Received: November 9, 2005
Published online: February 21, 2006

**Keywords:** alkynes · allylation · insertion · palladium · reaction mechanisms

[1] For reviews on carbometalation, see: a) J. F. Normant, A. Alexakis, *Synthesis* **1981**, 841; b) W. Oppolozer, *Angew. Chem.* **1989**, *101*, 39; *Angew. Chem. Int. Ed. Engl.* **1989**, *28*, 38; c) E. Negishi, *Pure Appl. Chem.* **1981**, *53*, 2333; d) P. Knochel in *Comprehensive Organometallic Chemistry II, Vol. 11* (Eds.: E. W. Able, F. G. A. Stone, G. Wilkinson), Pergamon, Oxford, **1995**, p. 159; e) P. Knochel in *Comprehensive Organic Synthesis, Vol. 4* (Eds.: B. M. Trost, I. Fleming), Pergamon, Oxford, **1991**, p. 865; f) Y. Yamamoto, N. Asao, *Chem. Rev.* **1993**, *93*, 2207; g) E. Negishi, D. Y. Kondakov, *Chem. Rev.* **1996**, *96*, 417; h) I. Marek, J. F. Normant in *Metal Catalyzed Cross-Coupling Reactions* (Eds.: F. Diederich, P. Stang), Wiley-VCH, New York, **1998**, p. 271.

[2] a) D. A. Singleton, S. C. Waller, Z. Zang, D. E. Frantz, S.-W. Leung, *J. Am. Chem. Soc.* **1996**, *118*, 9986; b) E. Negishi, J. A. Miller, *J. Am. Chem. Soc.* **1983**, *105*, 6761; c) J. J. Eishi, M. P. Bokslawski, *J. Organomet. Chem.* **1987**, *334*, C1; d) S. H. Yeon, J. S. Han, E. Hong, Y. Do, I. N. Jung, *J. Organomet. Chem.* **1995**, *494*, 159; e) N. Chatani, N. Amishiro, T. Morri, T. Yamashita, S. Murai, *J. Org. Chem.* **1995**, *60*, 1834; f) N. Fujiwara, Y. Yamamoto, *J. Org. Chem.* **1997**, *62*, 2318; g) E. Shirakawa, H. Yoshida, Y. Nakao, T. Hiyama, *Org. Lett.* **2000**, *2*, 2209; h) Y. Matsukawa, A. Asao, H. Kitahara, Y. Yamamoto, *Tetrahedron* **1999**, *55*, 3779; i) E. Yoshikawa, V. Gevorgyan, N. Asao, Y. Yamamoto, *J. Am. Chem. Soc.* **1997**, *119*, 6781; j) S. Shin, T. V. RajanBabu, *J. Am. Chem. Soc.* **2001**, *123*, 8416; k) M. Katsukiyo, F. Naoki, H. Akira, *J. Org. Chem.* **2004**, *69*, 2427.

[3] a) B. M. Trost, J. A. Martinez, R. J. Kulaweic, A. F. Indolese, *J. Am. Chem. Soc.* **1993**, *115*, 10402; b) S. De'rien, P. H. Dixneuf, *J. Chem. Soc. Chem. Commun.* **1994**, 255; c) S. De'rien, D. Jan, P. H. Dixneuf, *Tetrahedron* **1996**, *52*, 5511; d) B. M. Trost, A. Indolese, *J. Am. Chem. Soc.* **1993**, *115*, 4361; e) B. M. Trost, R. J. Kulawiec, *J. Am. Chem. Soc.* **1992**, *114*, 5579; f) X. Lu, G. Zhu, *Organometalics* **1995**, *14*, 4899.

[4] C. Gemel, G. Trimmel, C. Slugovc, S. Kremel, K. Mereiter, R. Schmid, K. Kirchner, *Organometalics* **1996**,*15*, 3998.

[5] a) K. Manabe, S. Kobayashi, *Org. Lett.* **2003**, *52*, 3241; b) *Organic Synthesis in Water* (Ed.: P. A. Grieco), Blackie Academic and Professional, London, **1998**; c) C.-J. Li, T.-H. Chan, *Organic Reactions in Aqueous Media*, Wiley, New York, **1997**; d) U. M. Lindström, *Chem. Rev.* **2002**, *102*, 2751; e) K. Manabe, S. Kobayashi, *Chem. Eur. J.* **2002**, *8*, 4095.

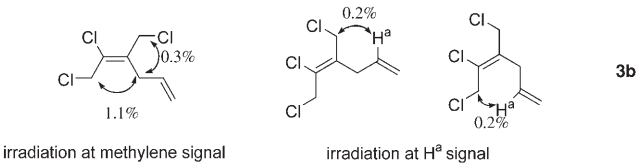
[6] For palladium-catalyzed allylic substitution in water, see: a) D. E. Bergbreiter, Y.-S. Liu, *Tetrahedron Lett.* **1997**, *38*, 7843; b) Y. Uozumi, H. Danjo, T. Hayashi, *Tetrahedron Lett.* **1997**, *38*, 3557; c) Y. Uozumi, H. Danjo, T. Hayashi, *Tetrahedron Lett.* **1998**, *39*, 8303; d) H. Danjo, D. Tanaka, T. Hayashi, Y. Uozumi, *Tetrahedron* **1999**, *55*, 14341; e) S. Kobayashi, W. W.-L. Lam, K. Manabe, *Tetrahedron Lett.* **2000**, *41*, 6115; f) C. Rabeyrin, C. Nguefack, D. Sinou, *Tetrahedron Lett.* **2000**, *41*, 7461; g) T. Hashizume, K. Yonehara, K. Ohe, S. Uemura, *J. Org. Chem.* **2000**, *65*, 5197; h) A. S. Dallas, K. V. Gothelf, *J. Org. Chem.* **2005**, *70*, 3321.

[7] a) R. F. Heck, *Palladium Reagents In Organic Synthesises*, Academic Press, London, **1985**, p. 245; b) J. E. Bäckvall, Y. I. M. Nillson, R. G. P. Gatti, *Organometallics* **1995**, *14*, 4242.

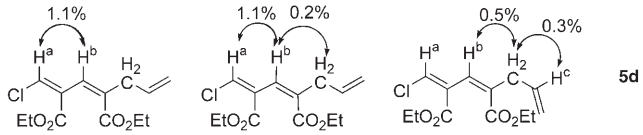
[8] K. Kaneda, T. Uchiyama, Y. Fujiwara, T. Imanaka, S. Teranishi, *J. Org. Chem.* **1979**, *44*, 55.

[9] a) X. Lu, G. Zhu, *J. Org. Chem.* **1995**, *60*, 1087; b) Q. Zhang, X. Lu, X. Han, *J. Org. Chem.* **2001**, *66*, 7676; c) Q. Zhang, W. Xu, X. Lu, *J. Org. Chem.* **2005**, *70*, 1505; d) Z. Zhang, X. Lu, Z. Xu, Q. Zhang, X. Han, *Organometallics* **2001**, *20*, 3724; e) X. Lu, G. Zhu, S. Ma, *Tetrahedron Lett.* **1992**, *33*, 7205.

[10] The configuration of the allylation products was further confirmed by NOE studies on compounds **3b**, **5d**, and **12b**.

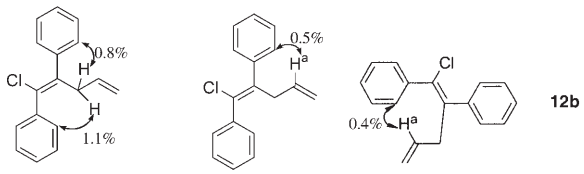



 © 2006 Wiley-VCH Verlag GmbH & Co. KGaA, Weinheim 




5d

irradiation at $H^a$ signal irradiation at $H^b$ signal irradiation at a methylene signal




12b

irradiation at a methylene signal irradiation at $H^a$ signal


[11] Y. Kayaki, T. Koda, T. Ikariya, *J. Org. Chem.* **2004**, *69*, 2595.

[12] a) H. Kinoshita, H. Shinokubo, K. Oshima, *Org. Lett.* **2004**, *6*, 4085; b) Y. Tamaru, *Eur. J. Org. Chem.* **2005**, *13*, 2647; c) N. Tsukada, S. Sugawara, K. Nakaoka, Y. Inoue, *J. Org. Chem.* **2003**, *68*, 5961; d) O. A. Wallner, K. J. Szabo, *J. Org. Chem.* **2003**, *68*, 2934; e) M. Kimura, M. Futamata, R. Mukai, Y. Tamaru, *J. Am. Chem. Soc.* **2005**, *127*, 4592; f) N. T. Patil, Y. Yamamoto, *Tetrahedron Lett.* **2004**, *45*, 3101.

[13] a) T. Wakabayashi, Y. Ishii, T. Murata, Y. Mizobe, M. Hidai, *Tetrahedron Lett.* **1995**, *36*, 5585; b) L. Zhao, X. Lu, *Org. Lett.* **2002**, *4*, 3093.

[14] The presence of excess halide ion leads to *trans* addition and fast reaction; see references [8] and [9c]. In our reaction, 4 equiv of $Cl^-$ (from 2 equiv $CuCl_2$) was employed. A comparative reaction with 0.5 equiv $CuCl_2$ (equals to 1 equiv of $Cl^-$) was carried out with **7a**, and the yield of **7b** was decreased from 92% to 74%.

[15] a) X. Lu, X. Jiang, X. Tao, *J. Organomet. Chem.* **1988**, *344*, 109; b) I. Satoh, M. Ikeda, M. Miura, M. Nomura, *J. Org. Chem.* **1997**, *62*, 4877; c) M. S. Viciu, R. F. Germaneau, N. F. Oscar, E. D. Stevens, S. P. Nolan, *Organomatelics*, **2002**, *21*, 5470; d) D. Alberti, R. Goddard, A. Rufiñska, K. R. Pörschke, *Organometallics* **2003**, *22*, 4025; e) J. Zhang, P. Braunstein, R. Welter, *Inorg. Chem.* **2004**, *43*, 4172; f) M. Bosch, M. Schlaf, *J. Org. Chem.* **2003**, *68*, 5225; g) N. Solin, O. A. Wallner, K. J. Szabo, *Org. Lett.* **2005**, *7*, 689; h) S. Chandrasekhar, V. Jagadeshwar, B. Saritha, C. Narsihmulu, *J. Org. Chem.* **2005**, *70*, 6506; i) F.-X. Felpin, Y. Landais, *J. Org. Chem.* **2005**, *70*, 6441.

[16] A white powder that was insoluble in water was collected after each reaction and identified as CuCl by XRD and IR analysis. It has been reported that $CuCl_2$ may work as an oxidant to assist the cleavage of C–Pd σ bonds; see: a) J. E. Bäckvall, R. E. Nordberg, *J. Am. Chem. Soc.* **1980**, *102*, 393; b) J. Ji, C. Zhang, X. Lu, *J. Org. Chem.* **1995**, *60*, 1160; c) G. Zhu, S. Ma, X. Lu, Q. Huang, *J. Chem. Soc. Chem. Commun.* **1995**, 271 and reference [17f].

[17] a) T. Satoh, S. Ogino, M. Miura, M. Nomura, *Angew. Chem.* **2004**, *116*, 5173; *Angew. Chem. Int. Ed.* **2004**, *43*, 5063; b) S. Kawasaki, T. Satoh, M. Miura, M. Nomura, *J. Org. Chem.* **2003**, *68*, 6836; c) J.-H. Li, Y. Liang, Y.-X. Xie, *J. Org. Chem.* **2004**, *69*, 8125; d) C. Zhou, R. C. Larock, *J. Org. Chem.* **2005**, *70*, 3765; e) X. Zeng, Q. Hu, M. Qian, E.-I. Negishi, *J. Am. Chem. Soc.* **2003**, *125*, 13636; f) J.-H. Li, H.-F. Jiang, M.-C. Chen, *J. Org. Chem.* **2001**, *66*, 3627.


 © 2006 Wiley-VCH Verlag GmbH & Co. KGaA, Weinheim 

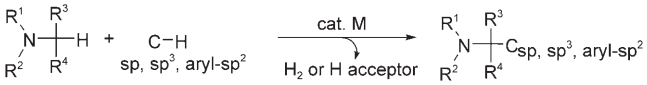
Synthetic Methods

DOI: 10.1002/anie.200503255

# Highly Efficient Cross-Dehydrogenative-Coupling between Ethers and Active Methylene Compounds**

*Yuhua Zhang and Chao-Jun Li**

Transition-metal-catalyzed C–H bond activation and subsequent C–C bond formation provide an alternative to traditional functional-group organic chemistry.[1] With the aim of seeking novel and highly efficient synthetic approaches,[2] our group recently focused on developing cross-dehydrogenative-coupling (CDC) methodologies to construct molecules by directly utilizing C–H bonds. We recently reported three types of CDC reactions (Scheme 1)[3] in which the presence of




***Scheme 1.*** Cross-dehydrogenative-coupling (CDC) of amines to form C–C bonds.

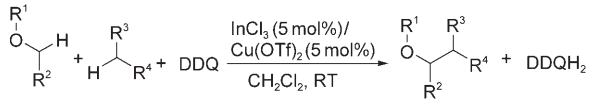
an adjacent nitrogen atom was essential. However, the synthesis of oxygen-containing compounds such as epoxides and ethers are of great interest in industrial and academic research, because these compounds are not only important structural units in many natural products and biologically active compounds,[4] but also highly versatile building blocks in synthetic organic chemistry.[5] Therefore, in an effort to functionalize the C–H bond of ethers and related oxygen-containing compounds directly,[6] we report herein a new type of CDC reaction under mild conditions to construct β-diester ethers catalyzed by a combination of indium[7] and copper[8] catalysts in the presence of 2,3-dichloro-5,6-dicyanobenzoquinone (DDQ). This reaction combines a C($sp^3$)–H bond adjacent to an oxygen atom with a C($sp^3$)–H bond in pronucleophiles, leading to a new C–C bond (Scheme 2).

[*] Dr. Y. Zhang
Department of Chemistry, Tulane University
6400 Freret St., New Orleans, LA 70118 (USA)
Prof. Dr. C.-J. Li
Department of Chemistry, McGill University
801 Sherbrooke St. West, Montreal, PQH3A2K6 (Canada)
Fax: (+1) 514-398-3797
E-mail: cj.li@mcgill.ca

[**] We are grateful to the Canada Research Chair (Tier I) foundation (to C.-J.L.), the NSERC, and the NSF-EPA joint program for a Sustainable Environment for support of our research. Y.Z. thanks McGill University for their hospitality during the aftermath of Hurricane Katrina and Z. Li, L. Zhao, and X. Yao (at McGill University) for their help with NMR spectroscopic and HRMS analysis.

Supporting information for this article is available on the WWW under http://www.angewandte.org or from the author.

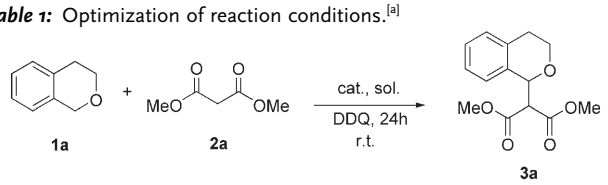

© 2006 Wiley-VCH Verlag GmbH & Co. KGaA, Weinheim




***Scheme 2.*** Cross-dehydrogenative-coupling (CDC) of ethers to form C–C bonds. DDQ = 2,3-dichloro-5,6-dicyanobenzoquinone; Tf = trifluoromethanesulfonyl.

Various transition metals were initially examined as potential catalysts for the desired CDC reaction between isochroman[9] and dimethyl malonate (Table 1). A combination of $InCl_3$ and $Cu(OTf)_2$ provided the best results. No desired product was observed without these catalysts. To improve the yield, we examined various ratios of isochroman, dimethyl malonate, and DDQ. The best yield was obtained when isochroman/malonate/DDQ = 1:1.2:1–1.2. When the amount of DDQ was increased to more than 1.5 equivalents, the yield decreased dramatically. The reaction did not proceed in the absence of DDQ. It was also found that the suitable solvents for this reaction are $CH_2Cl_2$, 1,2-dichloroethane (DCE), and $MeNO_2$. The desired product was not detected when the reaction was performed in THF or $H_2O$. There was no evident difference when the reaction was performed in dry $CH_2Cl_2$ or $CH_2Cl_2$ without drying.

***Table 1:*** Optimization of reaction conditions.[a]

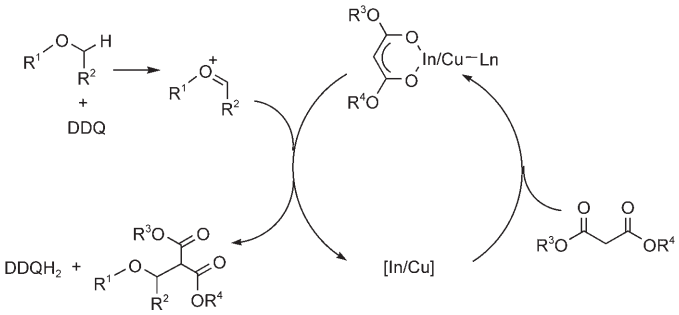



| Entry | Catalyst | Solvent | Conversion (**1a**) [%][b] | Yield (**3a**) [%][b] |
|---|---|---|---|---|
| 1 | $InCl_3$[c] | $CH_2Cl_2$ | 96 | 72 |
| 2 | $In(OAc)_3$[c] | $CH_2Cl_2$ | 100 | n.d.[d] |
| 3 | $In(OTf)_3$[c] | $CH_2Cl_2$ | 94 | 76 |
| 4 | $In(NO_3)_3$[c] | $CH_2Cl_2$ | 100 | n.d.[d] |
| 5 | $In(OH)_3$[c] | $CH_2Cl_2$ | 100 | n.d.[d] |
| 6 | $Cu(OTf)_2$[c] | $CH_2Cl_2$ | 93 | 69 |
| 7 | Cu(OTf)[c] | $CH_2Cl_2$ | 94 | 50 |
| 8 | $InCl_3/Cu(OTf)_2$ (5 mol%/5 mol%) | $CH_2Cl_2$ | 92 | 77 |
| 9 | $InCl_3/Cu(OTf)_2$ (10 mol%/5 mol%) | $CH_2Cl_2$ | 95 | 74 |
| 10 | $InCl_3/Cu(OTf)_2$ (5 mol%/10 mol%) | $CH_2Cl_2$ | 95 | 77 |
| 11 | $InCl_3/Cu(OTf)$[e] | $CH_2Cl_2$ | 96 | 71 |
| 12 | $InCl_3/Cu(OTf)_2$[e] | DCE | 96 | 76 |
| 13 | $InCl_3/Cu(OTf)_2$[e] | $MeNO_2$ | 82 | 66 |
| 14 | $InCl_3/Cu(OTf)_2$[e] | THF | 0 | n.d.[d] |
| 15 | $InCl_3/Cu(OTf)_2$[e] | $H_2O$ | 68 | n.d.[d] |
| 16 | $InCl_3/Cu(OTf)_2$[e] | PhMe | 80 | 43 |
| 17 | $InCl_3/Cu(OTf)_2$[e] | MeCN | 68 | 44 |

[a] Isochroman (0.5 mmol), dimethyl malonate (0.6 mmol), DDQ (0.6 mmol), solvent (2–3 mL). [b] Determined by $^1H$ NMR spectroscopy using an internal standard. [c] Catalyst: 10 mol%. [d] Not detected by $^1H$ NMR spectroscopy. [e] In/Cu (5 mol%/5 mol%).

Several active methylene compounds were then used in the reaction with isochroman derivatives, phthalan, and benzyl methyl ether under the optimized reaction conditions (Table 2). Isochroman and its derivatives were found to be more reactive than phthalan and benzyl methyl ether. A large amount of benzyl methyl ether remained unchanged after the reaction. No desired product was isolated when benzyl phenyl ether was treated with dimethyl malonate, which could be due to the increased steric effect of the bulky phenyl group in the ether. Notably, benzoylnitromethane was also reactive with isochroman. 2,4-Pentanedione and β-ketone esters also reacted effectively with isochroman; however, they generated a rather complicated mixture that is still under investigation.

A likely mechanism of this CDC reaction is shown in Scheme 3. The first step involves a hydride abstraction from the benzylic position of isochroman to generate a cationic species.[10] The malonate is activated by the In/Cu catalyst.[11] Subsequently, the coupling of the two intermediates results in the desired product and regenerates the catalyst. However, it is also possible that the lactol compound is involved as an intermediate and is further converted into the corresponding cross-coupling product. Alternatively, $In^{III}$ may activate DDQ through coordination with its carbonyl oxygen atom, which increases the oxidizing power of DDQ.[12]




***Scheme 3.*** Possible mechanism for the CDC reaction of ether with malonate.

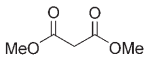
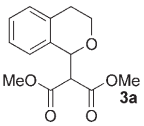
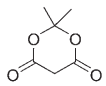
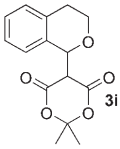
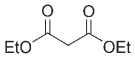
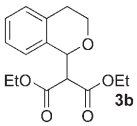
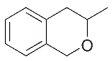
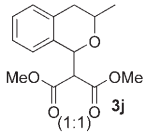
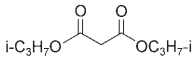
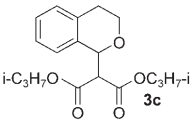
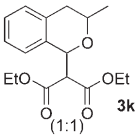
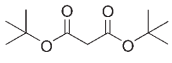
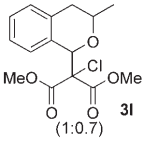
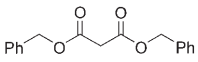
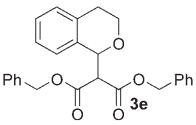
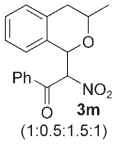
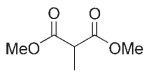
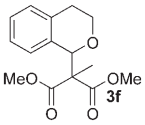
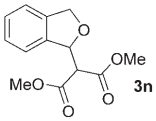
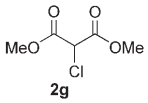
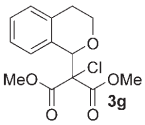
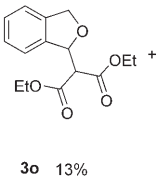
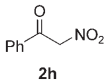
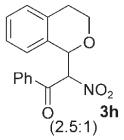
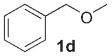
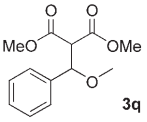
In summary, the first highly efficient cross-dehydrogenative-coupling reaction between a $C(sp^3)$–H bond adjacent to an oxygen atom and a $C(sp^3)$–H bond of a pronucleophile, catalyzed by In/Cu, has been developed to generate a C–C bond. This methodology not only provides the simplest way to construct isochroman derivatives and β-ether diesters, but also opens a new way to build and study more complex oxygen-containing natural products. The advantages of this method include: 1) relatively mild reaction conditions; 2) tolerance of various functional groups; 3) direct use of simple ethers as starting materials; 4) high regioselectivity; and 5) direct use of relatively cheap metals, indium and copper, as catalysts. The scope, mechanism, and synthetic application of this reaction are currently under investigation.

Received: September 13, 2005
Published online: February 15, 2006

**Keywords:** C–C coupling · C–H activation · copper · homogeneous catalysis · indium

 © 2006 Wiley-VCH Verlag GmbH & Co. KGaA, Weinheim 

***Table 2:*** CDC reaction of ethers with active methylene compounds.[a]

| Entry | 1 | 2 | Product | Yield [%][b] | Entry | 1 | 2 | Product | Yield [%][b] |
|---|---|---|---|---|---|---|---|---|---|
| 1 |  1a |  2a |  3a | 71 | 9 | 1a |  2i |  3i | 65 |
| 2 | 1a |  2b |  3b | 66 | 10 |  1b | 2a |  3j | 60 |
| 3 | 1a |  2c |  3c | 63 | 11 | 1b | 2b |  3k | 57 |
| 4 | 1a |  2d | decomp. | | 12 | 1b | 2g |  3l | 40 |
| 5 | 1a |  2e |  3e | 65 | 13 | 1b | 2h |  3m | 65 |
| 6 | 1a |  2f |  3f | 53 | 14[c] |  1c | 2a |  3n | 48 |
| 7 | 1a |  2g |  3g | 64 | 15[d] | 1c | 2b |  3o 13% 3p 15% (1.5:1) | |
| 8 | 1a |  2h |  3h (2.5:1) | 72 | 16 |  1d | 2a |  3q | 17 |

[a] Diethyl ether (0.5 mmol), active methylene compound (0.6 mmol), $InCl_3/Cu(OTf)_2$ (5 mol%/5 mol%), DDQ (0.6 mmol); all reactions were run for 24–36 h. [b] Yields of isolated products based on ethers. [c] Phthalan (0.2 mmol), dimethyl malonate (0.4 mmol), DDQ (0.2 mmol). [d] Phthalan (0.2 mmol), diethyl malonate (0.4 mmol), DDQ (0.24 mmol).


[1] For reviews, see: a) V. Ritleng, C. Sirlin, M. Pfeffer, *Chem. Rev.* **2002**, *102*, 1731–1769; b) G. Dyker, *Angew. Chem.* **1999**, *111*, 1808–1822; *Angew. Chem. Int. Ed.* **1999**, *38*, 1698–1712; c) T. Naota, H. Takaya, S. I. Murahashi, *Chem. Rev.* **1998**, *98*, 2599–2660; for some recent examples, see: d) N. Chatani, T. Asaumi, S. Yorimitsu, T. Ikeda, F. Kakiuchi, S. Murai, *J. Am. Chem. Soc.* **2001**, *123*, 10935–10941; e) L. J. Gooßen, *Angew. Chem.* **2001**, *113*, 3929–3932; *Angew. Chem. Int. Ed.* **2002**, *41*, 3775–3778; f) B. A. Arndtsen, R. G. Bergman, T. A. Mobley, T. H. Peterson, *Acc. Chem. Res.* **1995**, *28*, 154–162; g) H. Chen, S. Schlecht, T. C. Semple, J. F. Hartwig, *Science* **2000**, *287*, 1995; h) A. S. Goldman, *Nature* **1993**, *366*, 514; i) R. H. Crabtree, *J. Organomet. Chem.* **2004**, *689*, 4083–4091; j) C. Jia, T. Kitamura, Y. Fujiwara, *Acc. Chem. Res.* **2001**, *34*, 633–639.

[2] a) C.-J. Li, *Acc. Chem. Res.* **2002**, *35*, 533–538; b) C.-J. Li, *Chem. Rev.* **2005**, *105*, 3095–3166; c) C. Wei, Z. Li, C.-J. Li, *Synlett* **2004**, 1472–1483; d) C.-J. Li, *Chem. Rev.* **1993**, *93*, 2023–2035.

[3] a) Z. Li, C.-J. Li, *J. Am. Chem. Soc.* **2005**, *127*, 6968–6969; b) Z. Li, C.-J. Li, *J. Am. Chem. Soc.* **2005**, *127*, 3672–3673; c) Z. Li, C.-J. Li, *Org. Lett.* **2004**, *6*, 4997–4999; d) Z. Li, C.-J. Li, *J. Am. Chem. Soc.* **2004**, *126*, 11810–11811; e) Z. Li, C.-J. Li, *Eur. J. Org. Chem.* **2005**, 3173–3176; see also: f) S.-I. Murahashi, N. Komiya, H. Terai, T. Nakae, *J. Am. Chem. Soc.* **2003**, *125*, 15312–15313; g) Y. Hatamoto, S. Sakaguchi, Y. Ishii, *Org. Lett.* **2004**, *6*, 4623–4625; h) T. Yokota, M. Tani, S. Sakaguchi, Y. Ishii,


 © 2006 Wiley-VCH Verlag GmbH & Co. KGaA, Weinheim 

*J. Am. Chem. Soc.* **2003**, *125*, 1476 – 1477; i) J. Tsuji, H. Nagashima, *Tetrahedron* **1984**, *40*, 2699 – 2702; j) B. DeBoef, S. J. Pastine, D. Sames, *J. Am. Chem. Soc.* **2004**, *126*, 6556 – 6557; k) K. C. Nicolaou, R. E. Zipkin, N. A. Petasis, *J. Am. Chem. Soc.* **1982**, *104*, 5558 – 5560; l) Z. Li, C.-J. Li, *J. Am. Chem. Soc.* **2006**, *128*, 56 – 57.

[4] a) J. W. Blunt, B. R. Copp, M. H. G. Munro, P. T. Northcote, M. R. Prinsep, *Nat. Prod. Rep.* **2005**, *22*, 15 – 61; b) V. M. Dembitsky, T. A. Gloriozova, V. V. Poroikov, *Mini-Rev. Med. Chem.* **2005**, *5*, 319 – 336; c) T. L. Simmons, E. Andrianasolo, K. McPhail, P. Flatt, W. H. Gerwick, *Mol. Cancer Ther.* **2005**, *4*, 333 – 342; d) D. J. Newman, G. M. Cragg, *J. Nat. Prod.* **2004**, 67, 1216 – 1238; e) L. Bongiorni, F. Pietra, *Chem. Ind.* **1996**, (2), 54 – 58.

[5] a) I. Kadota, Y. Yamamoto, *Acc. Chem. Res.* **2005**, *38*, 423 – 432; b) M. Sasaki, H. Fuwa, *Synlett* **2004**, 1851 – 1874; c) L. F. Tietze, N. Rackelmann, *Pure Appl. Chem.* **2004**, *76*, 1967 – 1983; d) E. Lee, *Pure Appl. Chem.* **1996**, *68*, 631 – 634; e) G. M. Nicholas, A. J. Phillips, *Nat. Prod. Rep.* **2005**, *22*, 144 – 161.

[6] For our early work on an ether-functionalization reaction, see: Y. Zhang, C.-J. Li, *Tetrahedron Lett.* **2004**, *45*, 7581 – 7584.

[7] For representative reviews on indium catalyzed reactions, see: a) P. Cintas, *Synlett* **1995**, 1087 – 1096; b) C.-J. Li, *Tetrahedron* **1996**, *52*, 5643 – 5668; c) J. A. Marshall, *Chemtracts: Org. Chem.* **1997**, *10*, 481; d) I. Coldham, *J. Chem. Soc. Perkin Trans. 1* **1998**, 1343 – 1364; e) C.-J. Li, T.-H. Chan, *Tetrahedron* **1999**, *55*, 11149 – 11176; f) K. K. Chauhan, C. G. Frost, *J. Chem. Soc. Perkin Trans. 1* **2000**, 3015 – 3019; g) B. C. Ranu, *Eur. J. Org. Chem.* **2000**, *55*, 2347 – 2356; h) G. Babu, P. T. Perumal, *Aldrichimica Acta* **2000**, *33*, 16; i) J. A. Marshall, *Chem. Rev.* **1996**, *96*, 31 – 48.

[8] For recent reviews on copper-catalyzed reactions, see: a) I. P. Beletskaya, A. V. Cheprakov, *Coord. Chem. Rev.* **2004**, *248*, 2337 – 2364; b) T. D. Nelson, R. D. Crouch, *Org. React.* **2004**, *63*, 265 – 555; c) K. Kunz, U. Scholz, D. Ganzer, *Synlett* **2003**, 2428 – 2439; d) S. V. Ley, A. W. Thomas, *Angew. Chem.* **2003**, *115*, 5558 – 5607; *Angew. Chem. Int. Ed.* **2003**, *42*, 5400 – 5449; e) B. L. Feringa, R. Naasz, R. Imbos, L. A. Arnold in *Modern Organocopper Chemistry* (Ed.: N. Krause), Wiley-VCH, Weinheim, **2002**, pp. 224 – 258; f) J. Hassan, M. Sevignon, C. Gozzi, E. Schulz, M. Lemaire, *Chem. Rev.* **2002**, *102*, 1359 – 1470; g) C. Hertweck, *J. Prakt. Chem.* **2000**, *342*, 316 – 321.

[9] Such compounds exhibit a wide range of biological activities; for examples, see: a) R. E. Ziegert, J. Toraeng, K. Knepper, S. Bräse, *J. Comb. Chem.* **2005**, *7*, 147 – 169; b) J. D. Hepworth, B. M. Heron, *Prog. Heterocycl. Chem.* **2003**, *15*, 360.

[10] D. Hermeling, Ger. Offen. DE 4201544, A1 19930729, **1993**, p. 5.

[11] a) M. Nakamura, K. Endo, E. Nakamura, *J. Am. Chem. Soc.* **2003**, *125*, 13002 – 13003; b) T. Pei, X. Wang, R. A. Widenhoefer, *J. Am. Chem. Soc.* **2003**, *125*, 648 – 649; c) D. Yang, J. H. Li, Q. Gao, Y. L. Yan, *Org. Lett.* **2003**, *5*, 2869 – 2871; d) J. J. Kennedy-Smith, S. T. Staben, F. D. Toste, *J. Am. Chem. Soc.* **2004**, *126*, 4526 – 4527; e) X. Yao, C.-J. Li, *J. Am. Chem. Soc.* **2004**, *126*, 6884 – 6885; f) R.-V. Nguyen, X. Yao, D. S. Bohle, C.-J. Li, *Org. Lett.* **2005**, *7*, 673 – 675.

[12] H.-B. Zhang, L. Liu, Y.-J. Chen, D. Wang, C.-J. Li, *Adv. Synth. Catal.* **2006**, *348*, 229 – 235.

 © 2006 Wiley-VCH Verlag GmbH & Co. KGaA, Weinheim 

Synthetic Methods

DOI: 10.1002/anie.200504021

# Direct Catalytic Intermolecular α-Allylic Alkylation of Aldehydes by Combination of Transition-Metal and Organocatalysis**

*Ismail Ibrahem and Armando Córdova**

The α-alkylation of carbonyl compounds is a fundamental carbon–carbon bond-forming reaction in organic synthesis.[1] The conventional α-alkylation of carbonyl compounds is performed by utilizing stoichiometric amounts of metal enolates for addition to alkyl halides. In this context, the catalytic direct α-alkylation of nonstabilized aldehydes and ketones is challenging due to competing side reactions, such as aldol condensations, Cannizzaro and Tishchenko reactions, and N- or O-alkylations.[2,3] Therefore, metal-catalyzed methods that rely on the stoichiometric use of preactivated aldehydes and ketones as their metal enolates,[4] silyl enol ethers,[5] enol carbonates,[6] or enamines[7] have been developed. There are a few methods for the catalytic intermolecular α-alkylation of nonactivated aldehydes and ketones. For example, Tamaru and co-workers reported that the α-allylic alkylation of aldehydes is possible in the presence of a catalytic amount of palladium and a slight excess of $Et_3B$.[8] Most recently, transition-metal catalysis was employed in the α-alkylation of ketone enolates with alcohols.[9]

Organocatalysis is a fast forward-moving research field.[10] In this area, phase-transfer catalysis is used in the α-alkylations of glycine derivatives.[11] In addition, palladium catalysis has been combined with chiral phase-transfer catalysis for the α-allylation of glycine imino esters.[11f–g] Moreover, Koga and co-workers have developed oligoamine-mediated α-benzylations of preformed cyclohexanone lithium enolates.[12] Most recently, List and Vignola reported an elegant amino acid catalyzed intramolecular aldehyde α-alkylation reaction.[13] Well-designed, two-component activation systems with Pd that combine metal catalysis and the employment of stoichiometric or catalytic amounts of an organic catalyst have also been successfully employed in allylic alkylation reactions.[14] Herein, we report the first direct intermolecular α-alkylation of aldehydes, which involves catalytic enamine intermediates. The novel catalytic reaction assembles the corresponding α-allylic alkylated

[*] I. Ibrahem, Prof. Dr. A. Córdova
Department of Organic Chemistry
The Arrhenius Laboratory
Stockholm University, 10691 Stockholm (Sweden)
Fax: (+46) 8-154-908
E-mail: acordova@organ.su.se, acordova1a@netscape.net

[**] We gratefully acknowledge the Swedish National Research Council and Wenner-Gren Foundation for financial support and Prof. Jan E. Bäckvall for valuable discussions.

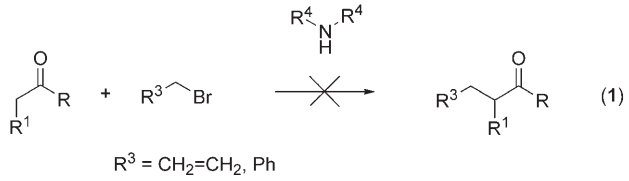
Supporting information for this article is available on the WWW under http://www.angewandte.org or from the author.


WILEY InterScience DISCOVER SOMETHING GREAT
© 2006 Wiley-VCH Verlag GmbH & Co. KGaA, Weinheim

aldehydes and cyclic ketones in high yield and chemoselectivity by combining enamine- and transition-metal-catalysis in one pot.

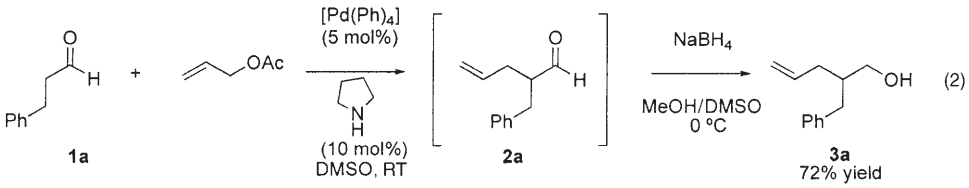
As part of our research program on amine catalysis,[15–16] we have made several attempts to alkylate catalytic enamine intermediates (generated in situ) with allyl or benzyl bromides [Eq. (1)]. However, our initial attempts into the intermolecular α-alkylation of aldehydes and cyclohexanone failed and the N-alkylation of the pyrrolidine and proline catalysts occurred.

Inspired by the work of Trost and Tsuji on allylic alkylations,[5] the use of




previously reported two-component catalyst systems with Pd,[14] and our experience from initial experiments, we decided to pursue a different highly challenging strategy for the α-alkylation of aldehydes and cyclic ketones: the one-pot combination of transition-metal and enamine catalysis (Scheme 1). Thus, the merging of two powerful catalytic cycles would enable both electrophilic and nucleophilic activation, which is not possible by one activation mechanism alone. For example, our reaction design would plausibly enable C–C bond formation by allowing catalytic enamine intermediates generated in situ to attack catalytically generated electrophilic palladium π-allyl complexes. Reductive elimination and subsequent hydrolysis of the iminium intermediate would regenerate the $Pd^0$ and amine catalysts, respectively, and yield the α-allylic alkylated aldehyde or ketone.

In an initial experiment, we treated 3-phenylpropionaldehyde (**1a**; 1.5 mmol) with allyl acetate[17] (0.5 mmol) in the presence of a catalytic amount of $[Pd(PPh_3)_4]$[18] (5 mol%) and pyrrolidine (10 mol%) in dimethyl sulfoxide (DMSO; 2 mL) at room temperature [Eq. (2)]. To our delight, the reaction was highly chemoselective, and we were able to



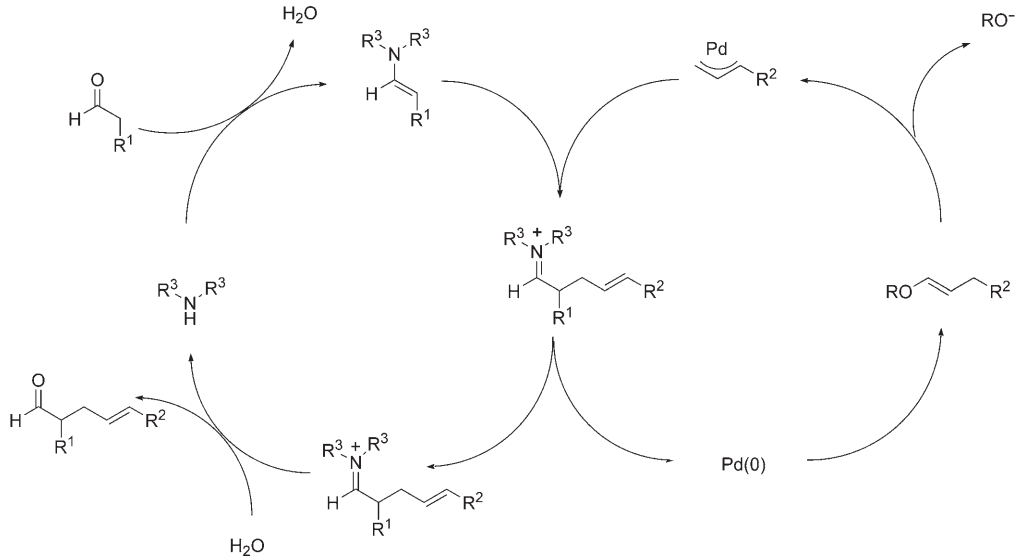

isolate the corresponding α-benzylic alcohol **3a** in 72% yield after 16 h by reduction of the α-allylic alkylated aldehyde **2a** in situ with excess $NaBH_4$.

In addition, we found that other cyclic and acyclic secondary amines catalyzed the direct allylic alkylation reactions between aldehyde **1a** and allyl acetate but with lower efficiency than pyrrolidine (Table 1).

Encouraged by these initial results, we decided to investigate the combined transition-metal- and amine-catalyzed direct allylic alkylation reactions for a set of simple aldehydes **1** (Table 2).

The reactions proceeded smoothly to give the corresponding α-allylic alkylated alcohols **3a–d** after reduction in situ of **2a–d**, respectively, in high yield with high chemoselectivity. In addition, the combined palladium- and amine-catalyzed reactions furnished quaternary carbon centers. For example, the α-allylic alkylated cyclohexanone carboxaldehyde **2e** was isolated in 65% yield. The direct allylic alkylation of cyclic ketones was also investigated (Table 3).

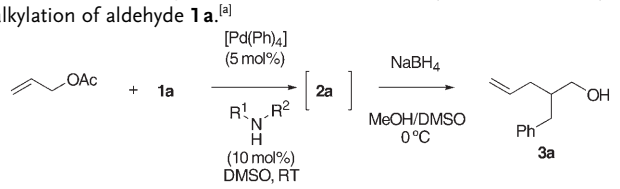
The direct catalytic allylic alkylation reactions were efficient, and the corresponding α-allylic alkylated ketones **5** were isolated in high yield: for example, **5a** was recovered in 95% yield. Thus, the one-pot combination of transition-metal

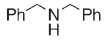



***Scheme 1.*** Combined transition-metal and enamine catalysis.

 © 2006 Wiley-VCH Verlag GmbH & Co. KGaA, Weinheim 

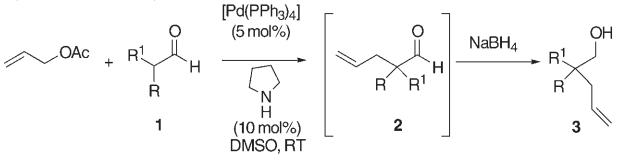
***Table 1:*** Combined palladium- and amine-catalyzed direct α-allylic alkylation of aldehyde **1a**.[a]

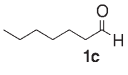
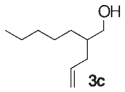
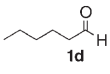
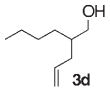



| Entry | Amine catalyst | **3a** | |
|---|---|---|---|
| | | *t* [h] | Yield [%][b] |
| 1 |  | 16 | 72 |
| 2 |  | 16 | 45 |
| 3 |  | 16 | 20 |
| 4 |  | 16 | 37 |

[a] See the Experimental Section for the reaction conditions. [b] Yield of the isolated product after column chromatography on silica gel.

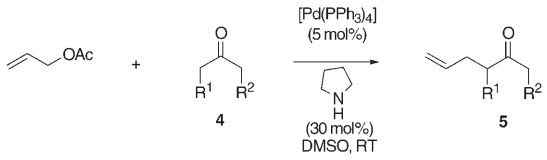
***Table 2:*** Combined palladium- and amine-catalyzed direct α-allylic alkylation of aldehydes **1**.[a]

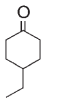
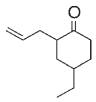
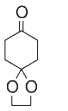
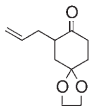
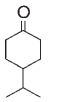
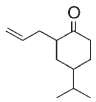
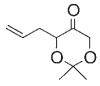



| Entry | Aldehyde | Product | *t* [h] | Yield [%][b] |
|---|---|---|---|---|
| 1 |  **1a** |  **3a** | 16 | 72 |
| 2 |  **1b** |  **3b** | 16 | 70 |
| 3 |  **1c** |  **3c** | 17 | 76 |
| 4 |  **1d** |  **3d** | 17 | 80 |
| 5 |  **1e** |  **2e** | 15 | 65[c] |

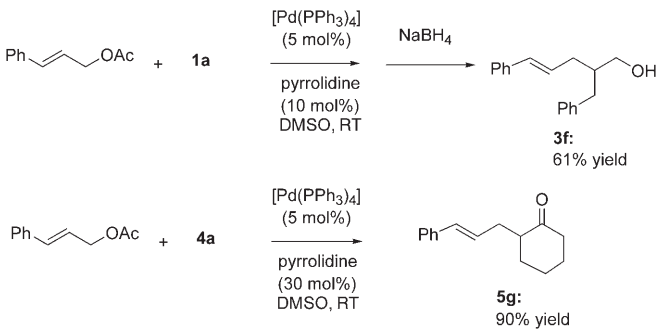
[a] See the Experimental Section for the reaction conditions. [b] Yield of the isolated product of the corresponding alcohol **3** after column chromatography on silica gel. [c] The yield of the isolated product of aldehyde **2e**.

***Table 3:*** Combined palladium- and amine-catalyzed direct allylic α-alkylation of ketones **4**.[a]




| Entry | Ketone | Product | *t* [h] | d.r.[b] | Yield [%][c] |
|---|---|---|---|---|---|
| 1 |  **4a** |  **5a** | 16 | | 95 |
| 2 |  **4b** |  **5b** | 16 | 1:1 | 90 |
| 3 |  **4c** |  **5c** | 16 | 1:1 | 85 |
| 4 |  **4d** |  **5d** | 16 | | 82 |
| 5 |  **4e** |  **5e** | 15 | 2:1 | 70 |
| 6 |  **4f** |  **5f** | 14 | | 65 |

[a] See the Experimental Section for the reaction conditions. [b] Determined by NMR spectroscopic analysis. [c] Yield of the isolated product after column chromatography on silica gel.




***Scheme 2.*** Regioselective catalytic α-allylic alkylation of aldehydes and ketones.

and enamine catalysis is applicable to the synthesis of functional α-allylic alkylated cyclohexanones. Notably, the combined palladium- and amine-catalyzed reactions proceed with excellent regioselectivity when a substituted allylic acetate or carbonate is used as the electrophile. For example, the treatment of aldehyde **1a** or ketone **4a** with cinnamyl acetate furnished α-alkylated alcohol **3f** in 61% yield and ketone **5g** in 90% yield, respectively, as single regioisomers (Scheme 2). Thus, the combined palladium and amine-catalyzed allylic alkylation reaction exhibited excellent regioselectivity with respect to the electrophile.

We also investigated a catalytic asymmetric version of the allylic alkylation reaction. In preliminary studies, inexpensive optically active pyrrolidine derivatives or (*S*)-proline provides α-allylic alkylated alcohol **3a** and ketone **4a** with high

 © 2006 Wiley-VCH Verlag GmbH & Co. KGaA, Weinheim 

enantioselectivity but in moderate yields (see the Supporting Information).

In summary, we have developed a simple method for the direct catalytic allylic alkylation of aldehydes and cyclic ketones. The direct catalytic highly chemo- and regioselective intermolecular α-allylic alkylation reaction is mediated by an unprecedented combination of palladium and enamine catalysis which furnishes α-allylic alkylated aldehydes and cyclic ketones in high yield. Thus, transition-metal and amine catalysis can be efficiently merged for the development of selective reactions. We are currently focusing on the following topics: 1) expansion of the concept of one-pot combinations of transition-metal and enamine catalysis to other metals and electrophiles; 2) the development of catalytic asymmetric allylic alkylation (AAA) reactions by employing simple and inexpensive optically active amine catalysts and/or chiral metal ligands. The initial results will be reported in due course.

## Experimental Section

Typical experimental procedure (Table 1, entry 1): A mixture of allyl acetate (0.5 mmol) and $[Pd(PPh_3)_4]$ (5 mol%) in DMSO (2 mL) was stirred for 5 min. Aldehyde **1a** (1.5 mmol, 3 equiv) and amine (10 mol%) were added to the reaction mixture, which was stirred at room temperature for 15–16 h. The reaction was quenched by reduction of aldehyde **2a** in situ with excess $NaBH_4$ to yield the corresponding alcohol **3a**. Aqueous work up and purification by column chromatography (toluene/EtOAc, 3:1) furnished alcohol **3a** in 72% yield as a clear oil. $^1$H NMR (400 MHz, $CDCl_3$): $\delta = 7.32$–$7.15$ (m, 5H), 5.82 (m, 1H), 5.22 (m, 2H), 3.59–3.52 (m, 2H), 2.69–2.63 (m, 2H), 2.15 (t, $J = 6.8$ Hz, 2H), 1.97–1.90 ppm (m, 1H); $^{13}$C NMR: $\delta =$ 35.7, 37.5, 42.6, 64.9, 116.8, 126.2,128.6, 129.4, 137.1, 140.7 ppm.

Received: November 11, 2005

**Keywords:** aldehydes · allylation · homogeneous catalysis · organocatalysis

[1] a) D. Caine in *Comprehensive Organic Synthesis, Vol. 3* (Eds.: B. M. Trost, I. Fleming), Pergamon, Oxford, **1991**, pp. 1–63; b) S. Carettin, J. Guzman, A. Corma, *Angew. Chem.* **2005**, *117*, 2282; *Angew. Chem. Int. Ed.* **2005**, *44*, 2242; c) *Modern Carbonyl Chemistry* (Ed.: J. Otera), Wiley-VCH, Weinheim, **2000**.

[2] H. O. House, W. C. Liang, P. D. Weeks, *J. Org. Chem.* **1974**, *39*, 3102.

[3] G. Stork, A. Brizzolara, H. Landesman, J. Szmuskovicz, R. Terell, *J. Am. Chem. Soc.* **1963**, *85*, 8829.

[4] a) S.-L. You, X.-L. Hou, L.-X. Dai, X.-Z. Zhu, *Org. Lett.* **2001**, *3*, 149; b) B. M. Trost, G. M. Schroeder, *J. Am. Chem. Soc.* **1999**, *121*, 6759; c) M. Braun, F. Laicher, T. Meier, *Angew. Chem.* **2000**, *112*, 3637; *Angew. Chem. Int. Ed.* **2000**, *39*, 3494; d) B. M. Trost, G. M. Schroeder, *Chem. Eur. J.* **2005**, *11*, 174; e) F.-T. Luo, E. Negishi, *Tetrahedron Lett.* **1985**, *26*, 2177; f) X.-X. Yan, C.-G. Liang, Y. Zhang, W. Hong, B.-X. Cao, L.-X. Dai, X.-L. Hou, *Angew. Chem.* **2005**, *117*, 6702; *Angew. Chem. Int. Ed.* **2005**, *44*, 6544; for catalytic α-arylations of ketone enolates, see: g) J. M. Fox, X. Huang, A. Chieffi, S. L. Buchwald, *J. Am. Chem. Soc.* **2000**, *122*, 1360, and references therein; h) M. Kawatsura, J. F. Hartwig, *J. Am. Chem. Soc.* **1999**, *121*, 1473; i) T. Satoh, Y. Kametani, Y. Terao, M. Miura, M. Nomura, *Tetrahedron Lett.* **1999**, *40*, 5345; for a noncatalytic α-arylation, see: j) V. K. Aggarwal, B. Olofsson, *Angew. Chem.* **2005**, *117*, 2652; *Angew. Chem. Int. Ed.* **2005**, *44*, 5516.

[5] a) J. Tsuji, I. Minami, I. Shimizu, *Chem. Lett.* **1983**, 1325; b) B. M. Trost, E. Keinan, *Tetrahedron Lett.* **1980**, *21*, 2591.

[6] a) B. M. Trost, J. Xu, *J. Am. Chem. Soc.* **2005**, *127*, 2846; b) D. C. Behenna, B. M. Stoltz, *J. Am. Chem. Soc.* **2004**, *126*, 15044.

[7] a) S. Murahashi, Y. Makabe, K. Kurita, *J. Org. Chem.* **1988**, *53*, 4489; b) Y. Huang, X. Lu, *Tetrahedron Lett.* **1988**, *29*, 5663; c) K. Hiroi, J. Abe, K. Suya, S. Sato, T. Koyama, *J. Org. Chem.* **1994**, *59*, 203; d) K. Hiroi, K. Suya, S. Sato, *J. Chem. Soc. Chem. Commun.* **1986**, 469; e) K. Hiroi, J. Abe, K. Suya, S. Sato, *Tetrahedron Lett.* **1989**, *30*, 1543; f) D. Enders, M. Voith, S. J. Ince, *Synthesis* **2002**, 1775, and references therein.

[8] M. Kimura, Y. Horino, R. Mukai, S. Tanaka, Y. Tamaru, *J. Am. Chem. Soc.* **2001**, *123*, 10401.

[9] a) M. S. Kwon, N. Kim, S. H. Seo, I. S. Park, R. K. Cheedrala, J. Park, *Angew. Chem.* **2005**, *117*, 7073; *Angew. Chem. Int. Ed.* **2005**, *44*, 6913, and references therein; b) C. S. Cho, B. T. Kim, M. J. Lee, T.-J. Kim, S. C. Shim, *Angew. Chem.* **2001**, *113*, 984; *Angew. Chem. Int. Ed.* **2001**, *40*, 958; c) K. Taguchi, H. Nagawa, T. Hirabayashi, S. Sakaguchi, Y. Ishii, *J. Am. Chem. Soc.* **2004**, *126*, 72; d) R. Martínez, G.-J. Brand, D. J. Ramón, M. Yus, *Tetrahedron Lett.* **2005**, *46*, 3683.

[10] a) P. I. Dalko, L. Moisan, *Angew. Chem.* **2001**, *113*, 3840; *Angew. Chem. Int. Ed.* **2001**, *40*, 3726; b) B. List, *Tetrahedron* **2002**, *58*, 5573; c) R. O. Duthaler, *Angew. Chem.* **2002**, *114*, 1005; *Angew. Chem. Int. Ed.* **2003**, *42*, 975; d) P. I. Dalko, L. Moisan, *Angew. Chem.* **2004**, *116*, 5248; *Angew. Chem. Int. Ed.* **2004**, *43*, 5138.

[11] For reviews, see: a) K. Maruoka, T. Ooi, *Chem. Rev.* **2003**, *103*, 3013; b) M. O'Donnel in *Catalytic Asymmetric Synthesis* (Ed.: I. Ojima), Wiley-WCH, New York, **2000**; also see: c) B. Lygo, P. G. Wainwright, *Tetrahedron Lett.* **1997**, *38*, 8595; d) E.-J. Corey, F. Xu, M. C. Noe, *J. Am. Chem. Soc.* **1997**, *119*, 12414; e) H.-G. Park, B.-S. Jeong, M.-S. Yoo, J.-H. Lee, M.-K. Park, Y.-J. Lee, M.-J. Kim, S.-S. Jew, *Angew. Chem.* **2002**, *114*, 3162; *Angew. Chem. Int. Ed.* **2002**, *41*, 3036; for a one-pot combination of phase-transfer and palladium catalysis, see: f) M. Nakoji, T. Kanayama, T. Okino, Y. Takemoto, *Org. Lett.* **2001**, *3*, 3329; g) M. Nakoji, T. Kanayama, T. Okino, Y. Takemoto, *J. Org. Chem.* **2002**, *67*, 7418.

[12] M. Imai, A. Hagihara, H. Kawasaki, K. Manabe, K. Koga, *J. Am. Chem. Soc.* **1994**, *116*, 8829.

[13] N. Vignola, B. List, *J. Am. Chem. Soc.* **2004**, *126*, 450.

[14] a) B. G. Jellerichs, J. R. Kong, M. J. Krische, *J. Am. Chem. Soc.* **2003**, *125*, 7758; b) B. M. Trost, E. J. McEachern, F. D. Toste, *J. Am. Chem. Soc.* **1998**, *120*, 12702; c) M. Sawamura, M. Sudoh, Y. Ito, *J. Am. Chem. Soc.* **1996**, *118*, 3309.

[15] a) J. Casas, M. Engqvist, I. Ibrahem, B. Kaynak, A. Córdova, *Angew. Chem.* **2005**, *117*, 1367; *Angew. Chem. Int. Ed.* **2005**, *44*, 1343; b) A. Córdova, H. Sundén, M. Engqvist, I. Ibrahem, J. Casas, *J. Am. Chem. Soc.* **2004**, *126*, 8914; c) A. Córdova, *Acc. Chem. Res.* **2004**, *37*, 102; d) I. Ibrahem, J. Samec, J.-E. Bäckvall, A. Córdova, *Tetrahedron Lett.* **2005**, *46*, 3965; e) A. Bøgevig, H, Sundén, A. Córdova, *Angew. Chem.* **2004**, *116*, 1129; *Angew. Chem. Int. Ed.* **2004**, *43*, 1109; f) H, Sundén, I. Ibrahem, L. Eriksson, A. Córdova, *Angew. Chem.* **2005**, *117*, 4955; *Angew. Chem. Int. Ed.* **2005**, *44*, 4877; g) A. Córdova, *Chem. Eur. J.* **2004**, *10*, 1987; h) A. Córdova, *Synlett* **2003**, 1651, and references therein.

[16] a) A. Bøgevig, K. Juhl, N. Kumaragurubaran, W. Zhuang, K. A. Jørgensen, *Angew. Chem.* **2002**, *114*, 1868; *Angew. Chem. Int. Ed.* **2002**, *41*, 1790; b) B. List, *J. Am. Chem. Soc.* **2002**, *124*, 5656; c) A. Córdova, W. Notz, C. F. Barbas III, *J. Org. Chem.* **2002**, *67*, 301; d) A. Bøgevig, K. Juhl, N. Kumaragurubaran, K. A. Jørgensen, *Chem. Commun.* **2002**, 620; e) A. B. Northrup, D. W. C. MacMillan, *J. Am. Chem. Soc.* **2002**, *124*, 6798; for the pioneering work of the use of amino acids, see: f) Z. G. Hajos, D. R. Parrish, German Patent DE 2102623, July 29, **1971**;

 © 2006 Wiley-VCH Verlag GmbH & Co. KGaA, Weinheim 

g) Z. G. Hajos, D. R. Parrish, *J. Org. Chem.* **1974**, *39*, 1615; h) U. Eder, G. Sauer, R. Wiechert, German Patent DE 2014757, Oct. 7, **1971**; i) U. Eder, G. Sauer, R. Wiechert, *Angew. Chem.* **1971**, *83*, 492; *Angew. Chem. Int. Ed. Engl.* **1971**, *10*, 496.

[17] Allyl carbonates could also be used as electrophiles.

[18] The initial palladium complexes were $[Pd(PPh_3)_4]$ generated in situ, commercially available $[Pd(PPh_3)_4]$, or $[Pd(dppa)_2]$ (dppa = 1,2-bis(diphenylphosphanyl)acetylene).

 © 2006 Wiley-VCH Verlag GmbH & Co. KGaA, Weinheim 

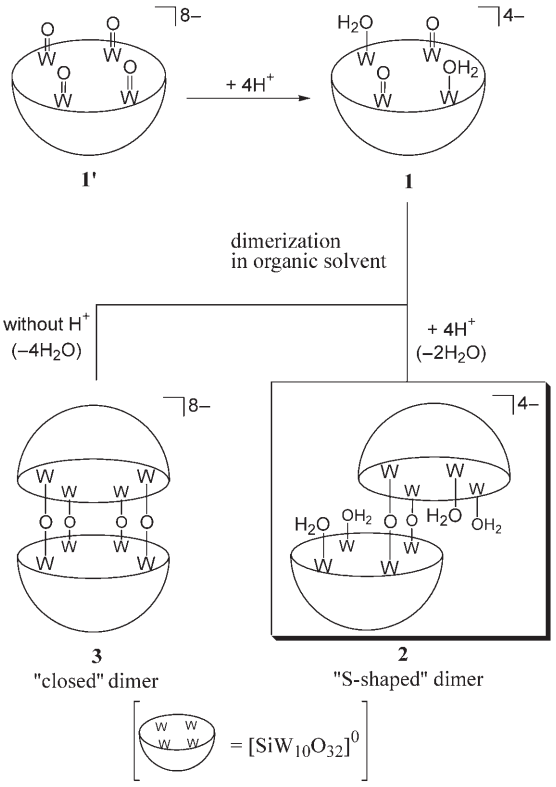
Polyoxometalates

DOI: 10.1002/anie.200502543

# Formation of S-Shaped Disilicoicosatungstate and Efficient Baeyer–Villiger Oxidation with Hydrogen Peroxide**

*Akihiro Yoshida, Masayuki Yoshimura, Kazuhiro Uehara, Shiro Hikichi, and Noritaka Mizuno**

Metal–oxygen clusters, namely, polyoxometalates (POMs), have attracted much attention because of their tunability of composition, size, shape, acid–base properties, and redox potential.[1] The molecular properties lead to the use of POMs in catalysis, medicine, and materials science. Structural variations of POMs may arise from self-assembly of M–O/M–OH components and from isomerization by repetitive hydrolysis and condensation of metal fragments in aqueous media, and these behaviors complicate POM chemistry.[2] Therefore, synthesis, structural characterization, and chemical properties of novel POMs are still attractive in modern chemistry. Lacunary POMs are useful precursors for mixed-metal–oxide clusters and organic–inorganic hybrid compounds.[1] Especially the γ isomer of a divacant Keggin-type silicodecatungstate, namely, $[SiW_{10}O_{36}]^{8-}$ (**1′**),[3] has been used as a molecular replica to synthesize dimetal-substituted POMs with reactive dinuclear $M_2(\mu\text{-}O)_2$ sites.[4] We have also synthesized aqua-ligated divacant silicodecatungstate $[\gamma\text{-}SiW_{10}O_{34}(H_2O)_2]^{4-}$ (**1**) by treatment of **1′** with $H^+$ in aqueous solution at pH 2 (Scheme 1).[5] Single-crystal X-ray structure analysis of **1** indicates that two of four oxo ligands located at the vacant sites are selectively protonated to give the aquatungsten moieties.




***Scheme 1.*** Formation of disilicoicosatungstates **2** and **3**.

Baeyer–Villiger oxidation is well known and widely used in organic synthesis because of its versatility, although it is carried out with expensive and/or hazardous peracids and leads to formation of one equivalent of the corresponding carboxylic acid. Therefore, efforts have been made to develop homogeneous and heterogeneous catalytic systems with hydrogen peroxide or organic peracids generated by the reaction of either the corresponding aldehyde with dioxygen or the carboxylic acid with hydrogen peroxide.[6] Herein we report novel disilicoicosatungstates $[\{\gamma\text{-}SiW_{10}O_{32}(H_2O)_2\}_2(\mu\text{-}O)_2]^{4-}$ (**2**) and $[(\gamma\text{-}SiW_{10}O_{32})_2(\mu\text{-}O)_4]^{8-}$ (**3**), formed by dimerization of **1** by dehydrative condensation in an organic solvent. Interestingly, **2** can catalyze the Baeyer–Villiger oxidation of cycloalkanones with $H_2O_2$ and shows high selectivity ($\geq 90\,\%$) for the corresponding lactones and high turnover numbers ($\geq 1900$), whereas **1** and **3** with the common $[\gamma\text{-}SiW_{10}O_{32}]$ fragment are almost inactive.

The tetra-*n*-butylammonium salt of **1** ($(TBA)_4$[**1**]) was transformed to the TBA salt of **2** (Scheme 1 and Experimental Section). The IR spectrum of **2** was clearly different from that of **1**, and this suggested a structural change of the cluster framework. The molecular structure of **2** was determined by X-ray analysis on a colorless single crystal. As shown in Figure 1 a, **2** has an S-shaped molecular structure composed of

[*] A. Yoshida, M. Yoshimura, Prof. Dr. S. Hikichi, Prof. Dr. N. Mizuno
Department of Applied Chemistry
School of Engineering
The University of Tokyo
7-3-1 Hongo, Bunkyo-ku, Tokyo 113-8656 (Japan)
Fax: (+81) 3-5841-7220
E-mail: tmizuno@mail.ecc.u-tokyo.ac.jp
Dr. K. Uehara, Prof. Dr. S. Hikichi, Prof. Dr. N. Mizuno
Core Research for Evolutional Science and Technology (CREST)
Japan Science and Technology Agency (JST)
4-1-8 Honcho, Kawaguchi, Saitama 332-0012 (Japan)

[**] This work was supported by the CREST program of JST and a Grant-in-Aid for Scientific Research from the Ministry of Education, Culture, Science, Sports, and Technology of Japan.

Supporting information for this article is available on the WWW under http://www.angewandte.org or from the author.


InterScience
© 2006 Wiley-VCH Verlag GmbH & Co. KGaA, Weinheim

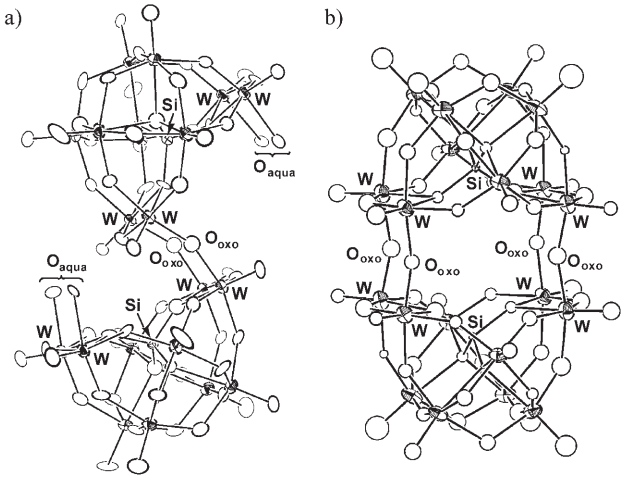
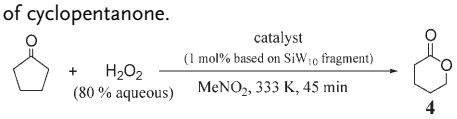



***Figure 1.*** Molecular structures of **2** (a) and **3** (b). The thermal ellipsoid probabilities for **2** and **3** are shown at 30 and 50%, respectively.

of $H_2O_2$ utilization were 99% or higher. The yield of **4** from the oxidation of cyclopentanone in MeCN was 96%, almost the same as that in $MeNO_2$. The yield of **4** from the oxidation of cyclopentanone with 30% aqueous $H_2O_2$ in $MeNO_2$ was 91%. The catalytic activity of **2** was compared with those of **1** and **3** (Table 1). The S-shaped cluster **2** catalyzed the reaction

***Table 1:*** Comparison of the catalytic activities of **1**, **2**, and **3** in the oxidation of cyclopentanone.




| Catalyst | Initial rate [mM$^{-1}$ min$^{-1}$] | Conversion [%] | Selectivity for **4** [%] | Yield of **4** [%] |
|---|---|---|---|---|
| **1** | 0.082 | 2 | ≥99 | 2 |
| **2** | 49 | ≥99 | ≥99 | ≥99 |
| **3** | 0.13 | 4 | ≥99 | 4 |

two neutral divacant γ-Keggin-type $[SiW_{10}O_{32}]^0$ fragments bridged by two oxo ligands. The four unbridged W sites are occupied by aqua ligands (W–$O_{aqua}$ 2.19(3)–2.22(3) Å, W=$O_{oxo}$ 1.62(2)–1.81(3) Å). In other words, **2** is a dimer of the $[SiW_{10}O_{33}(H_2O)_2]^{2-}$ fragment and was formed by the loss of one oxo ligand of **1** by protonation followed by dissociation as water.[7]

It is known that one of two terminal oxo ligands in dioxo complexes of $d^0$ metals ($V^V$, $Mo^{VI}$, $W^{VI}$) is basic enough to react with various protic substrates, and the ligand-exchange reaction then proceeds through dissociation of the protonated oxo (i.e., aqua) ligand. Indeed, several organic-modified POMs have been synthesized by reaction of the W(=O)$_2$ moieties of divacant silicodecatungstate **1′** (unprotonated form of **1**) with protic substrates such as silanols and phosphoric acids.[8] In these organic-modified compounds, however, the tungsten sites are fully occupied. In contrast, **2** retains four vacant sites (terminal W(=O)(OH$_2$) moieties). It is notable that the divacant γ-Keggin framework of the $[SiW_{10}O_{32}]$ fragment of **1** remained unchanged in **2** in spite of the action of strong acid in an aprotic organic solvent during its formation. To date, a sole example of an icosatungstate, namely, $[KP_2W_{20}O_{72}]^{13-}$, has been reported: This diphosphoicosatungstate is composed of two $[\alpha\text{-}PW_9O_{34}]^{9-}$ fragments bridged by two octahedral $WO_6$ units and $K^+$, and therefore the structure is clearly different from those of **2** (S-shaped) and **3** ("closed" cluster; see Figure 1b and below).[9]

In the absence of $H^+$, another type of disilicoicosatungstate **3** was formed by dimerization of **1** (Scheme 1 and Experimental Section). The IR spectrum of **3** was different from those of **1** and **2**, whereas the elemental analyses indicated that the Si:W ratios were all 1:10. Single-crystal X-ray structure analysis of the $[K([18]crown\text{-}6)]^+$ salt revealed that **3** is a "closed" dimer of the $[SiW_{10}O_{34}]^{4-}$ fragment (Figure 1b), formed by dissociation of aqua ligands from **1**.[10]

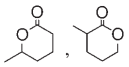
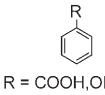
The Baeyer–Villiger oxidation of cyclopentanone with $H_2O_2$ was carried out in the presence of S-shaped dimeric cluster **2**. Oxidation was quantitatively complete after 45 min and the selectivity for δ-valerolactone (**4**) and the efficiency well, whereas monomeric precursor **1** and closed dimer **3** exhibited quite low activities: the initial rate for **2** (49 mM min$^{-1}$) was more than 100 times larger than those for **1** (0.082) and **3** (0.13). Thus, the catalytic activities of **1**–**3** are different, although they all are composed of common [γ-$SiW_{10}O_{32}$] fragments. Peroxotungstates such as $[(PO_4)\{WO(O_2)_2\}_4]^{3-}$ and $[W_2O_3(O_2)_4(H_2O)_2]^{2-}$ were almost inactive under the present reaction conditions. The S-shaped cluster **2** is the first example of a tungsten catalyst for Baeyer–Villiger oxidation with high selectivity for the lactone, high efficiency of $H_2O_2$ utilization, and high turnover number.[11,12] Catalyst **2** is stable under the reaction conditions: the UV/Vis and IR spectra of the recovered catalyst were the same as those of the as-prepared one. The reusability of catalyst **2** was also confirmed by maintenance of activity for the oxygenation of cyclobutanone in repetitive reactions [yields of lactone: ≥99% (first run), 98% (second run), 99% (third run)].

Table 2 summarizes the results for the Baeyer–Villiger oxidation of various cycloalkanones catalyzed by **2** (**2**:$H_2O_2$:substrate = 1:200:1000). Cyclobutanone, cyclopentanone, and 2-adamantanone were quantitatively converted into the corresponding lactones. Even in the oxidation of cyclobutanone and 2-adamantanone under stoichiometric conditions ($H_2O_2$:substrate = 1:1), the yields and selectivities for the corresponding lactones exceeded 95 and 99%, respectively. Acetophenone, which is hard to oxidize, was also converted to the corresponding ester and the hydrolysis products (phenol and benzoic acid).[13,14] The regioselectivity of the oxygenation of 2-methylcyclopentanone depends on the direction of insertion of the oxygen atom.[15] The **2**-mediated oxygenation of 2-methylcyclopentanone afforded δ-methyl-δ-valerolactone:α-methyl-δ-valerolactone = 64:36, and the ratio was clearly different from that observed for stoichiometric oxygenation with *m*-chloroperbenzoic acid (96:4).

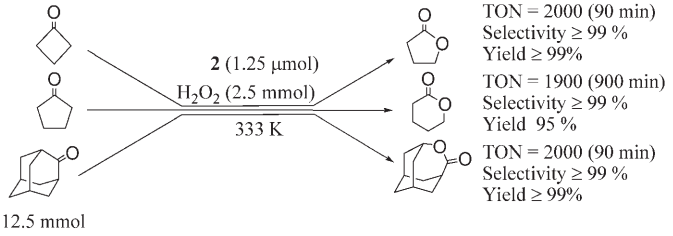
Larger-scale (tenfold scaleup) reactions with cyclobutanone, cyclopentanone, and 2-adamantanone exhibited turnover numbers (based on **2**) of 2000, 1900, and 2000, respectively (Scheme 2). These values are much higher than

 © 2006 Wiley-VCH Verlag GmbH & Co. KGaA, Weinheim 

***Table 2:*** Baeyer–Villiger oxidation of cycloalkanones and acetophenone with $H_2O_2$ catalyzed by **2**.[a]

| Substrate | Product(s) | Reaction time [min] | Conversion [%] | Selectivity for lactone(s) [%] | Yield [%] (Ratio of products) | TON (based on **2**) |
|---|---|---|---|---|---|---|
|  |  | 5 | ≥99 | ≥99 | ≥99 | 200 |
|  |  | 45 | ≥99 | ≥99 | ≥99 | 200 |
|  |  | 45 | 70 | 90 | 63 (64:36) | 126 |
|  |  | 15 | ≥99 | ≥99 | ≥99 | 200 |
|  |  R = COOH,OH,OAc | 135 | 17 | 87[b] | 15 (40:33:27) | 30 |

[a] Reaction conditions: Catalyst (**2**), 1.25 μmol; substrate, 1.25 mmol; $H_2O_2$ (80% aqueous), 0.25 mmol; solvent ($MeNO_2$), 1.0 mL; reaction temperature, 333 K. Conversion, selectivity, and yield were determined by gas chromatography or $^1$H NMR spectroscopy with an internal standard and are based on $H_2O_2$. [b] Selectivity for the ester and the successive hydrolysis products.




***Scheme 2.*** Larger-scale Baeyer–Villiger oxidations with **2** as catalyst.

those reported for Baeyer–Villiger oxidations with $H_2O_2$ and other catalysts:[6,13,15–18] for cyclobutanone: $[Pt^{II}(CF_3)(dppe)(CH_2Cl_2)](BF_4)$ (dppe = 1,4-bis(diphenylphosphanyl)ethane), TON = 333 ),[6b] bis[3,5-bis(trifluoromethyl)phenyl] diselenide (TON = 178);[18b] for 2-adamantanone: Sn-beta zeolite (TON = 140),[13a] bis[3,5-bis(trifluoromethyl)phenyl] diselenide (TON = 198).[18b]

In conclusion, dehydrative condensation of $[SiW_{10}O_{34}(H_2O)_2]^{4-}$ (**1**), which was obtained by partial protonation of $[SiW_{10}O_{36}]^{8-}$ (**1′**), yielded the novel disilicoicosatungstates $[\{\gamma\text{-}SiW_{10}O_{32}(H_2O)_2\}_2(\mu\text{-}O)_2]^{4-}$ (**2**; S-shaped cluster) and $[(\gamma\text{-}SiW_{10}O_{32})_2(\mu\text{-}O)_4]^{8-}$ (**3**; closed cluster). The S-shaped cluster **2** was selectively obtained in the presence of $H^+$ during the dimerization reaction. Baeyer–Villiger oxidation of cycloalkanones to give the corresponding lactones with $H_2O_2$ was efficiently catalyzed by **2** (≥90% selectivity for the lactone and TON ≥ 1900), whereas monomeric precursor **1** and closed cluster **3** exhibited very low activity.

## *Experimental Section*

$(TBA)_4$[**2**]: $(TBA)_4$[**1**] (0.99 g, 0.29 mmol) was dissolved in 1,2-dichloroethane (10 mL) and $CF_3SO_3H$ (80 μL, 0.60 mmol) was added. The insoluble solids were removed by filtration. The solution was kept at 293 K for one week to afford colorless rodlike crystals of $(TBA)_4$[**2**] (0.71 g, 85% yield). Elemental analysis (%) calcd for $(TBA)_4$[**2**]: C 13.18, H 2.63, N 0.96; found: C 13.46, H 2.78, N 0.97. IR (KBr): $\tilde{\nu}$ 2963 (m), 2934 (w), 2874 (m), 1483 (m), 1470 (sh), 1380 (m), 974 (s), 931 (sh), 915 (s), 879 (s), 817 (sh), 794 (s), 741 (sh), 676 (s), 557 (m), 412 (w), 386 (w), 363 (m), 332 (w), 303 $cm^{-1}$ (w). UV/Vis (MeCN): $\lambda$ = 265 nm (sh; $\varepsilon$ = 57920 $M^{-1}cm^{-1}$). Because of the extremely low solubility of **2**, its $^{183}$W and $^{29}$Si NMR spectra in solution could not be measured.

TBA salt of **3**: $(TBA)_4$[**1**] (3.00 g, 0.88 mmol) was dissolved in 1,2-dichloroethane (30 mL) and the resulting solution was stirred under Ar for 72 h at ambient temperature. After the removal of a small amount of insoluble solids by filtration, the filtrate was evaporated to dryness under reduced pressure. Part of the resulting pale yellow solid (0.81 g) was dissolved in 1,2-dichloroethane (2.4 mL) and benzene (0.6 mL) was added. Pale yellow crystals of the TBA salt of **3** (0.39 g, 0.06 mmol) precipitated on allowing the solution to stand for one week at 293 K. Elemental analysis (%) calcd for $(TBA)_7H$[**3**]·$6C_2H_4Cl_2$: C 20.94, H 3.93, N 1.38; found: C 20.75, H 4.02, N 1.38. IR (KBr): $\tilde{\nu}$ 2960 (m), 2934 (w), 2874 (m), 1483 (m), 1470 (sh), 1380 (m), 1152 (w), 1107 (w), 1021 (m), 1001 (m), 959 (s), 930 (s), 901 (s), 872 (s), 789 (s), 755 (sh), 690 (w), 549 (m), 408 (w), 390 (w), 366 (m), 345 (w), 334 (w), 325 (w), 309 (w), 295 $cm^{-1}$ (w). UV/Vis (MeCN): 295 nm (sh; $\varepsilon$ = 39640 $M^{-1}cm^{-1}$).

X-ray crystallography: Single crystals of $(TBA)_4$[**2**]·$5H_2O$ were obtained as follows: $(TBA)_4$[**1**] (0.44 g, 0.12 mmol) was dissolved in nitromethane (2.0 mL), and $CF_3SO_3H$ (19 μL, 0.24 mmol) was added. The solution was kept at 293 K. Colorless crystals were obtained over several hours. The single crystals were collected by filtration and washed with nitromethane (0.5 mL). The yield of $(TBA)_4$[**2**]·$5H_2O$ was 0.14 g (40%). Crystals of the $[K([18]crown\text{-}6)]^+$ salt of **3** were prepared as follows: $K_8$[**1′**]·$12H_2O$ (2.98 g, 1.00 mmol) was dissolved in water (15 mL) and then the pH of this aqueous solution was adjusted to 2 with 2 M $HNO_3$. After stirring this clear solution for 2 min at room temperature, [18]crown-6 (1.062 g, 4 mmol) was added in a single portion. The resulting pale yellow suspension was stirred for 5 min followed by evaporation to dryness to give 1.61 g of a pale yellow powder. A small amount of powder (58 mg) was suspended in MeCN (2.0 mL) and the insoluble solids were removed by filtration. Pale yellow crystals of $[K([18]crown\text{-}6)]_6H_2$·**3**·$8MeOH·8H_2O$ formed in the presence of MeOH vapor at ambient temperature.

Diffraction measurements were made on a Rigaku Saturn CCD detector with graphite-monochromated $Mo_{K\alpha}$ radiation ($\lambda$ = 0.71069 Å; 5 kW). Data were collected and processed with CrystalClear (Rigaku). Neutral scattering factors were obtained from the standard source. In the data reduction, corrections for Lorentzian and polarization effects were made. Structural analyses were performed by using the CrystalClear crystallographic structure-solving program package. The structures were solved by heavy-atom Patterson methods and expanded by Fourier techniques. For $(TBA)_4$[**2**]·$5H_2O$, the tungsten, silicon, and oxygen atoms of **2** and the nitrogen atoms of the TBA ions were refined anisotropically in the final cycle of full-matrix least-squares refinement on *F*. The carbon atoms of one of the four TBA ions and the oxygen atoms of the water molecules were refined isotropically. The positions of the carbon atoms of the remaining disordered TBA ions were fixed, although the isotropic thermal parameters were refined. The hydrogen atoms of the isotropically refined TBA ion were located by using riding models.

 © 2006 Wiley-VCH Verlag GmbH & Co. KGaA, Weinheim 

For $[K([18]crown\text{-}6)]_6H_2\cdot\mathbf{3}\cdot 8MeOH\cdot 8H_2O$, the tungsten atoms were refined anisotropically, and the other atoms, except for one oxygen atom, were refined isotropically. The hydrogen atoms of the [18]crown-6 ligands were located by using riding models.

Crystal data for $(TBA)_4[\mathbf{2}]\cdot 5H_2O$: $C_{64}H_{160}N_4O_{75}Si_2W_{20}$; $M=5921.14$, orthorhombic, space group $P2_12_12_1$ (no. 19), $a=14.09300(10)$, $b=26.7218(3)$, $c=37.7468(4)$ Å, $V=14215.1(2)$ Å$^3$, $Z=4$, $\rho_{calcd}=2.767\ g\,cm^{-3}$, $\mu(Mo_{K\alpha})=162.26$, $R=\Sigma||F_o|-|F_c||/\Sigma|F_o|=0.054$ for 13768 unique data with $I>3.0\sigma(I)$ ($R_w=[\Sigma w(|F_o|-|F_c|)^2/\Sigma wF_o^2]^{1/2}=0.077$) and 1068 parameters used for refinement. Crystal data for $[K([18]crown\text{-}6)]_6H_2[\mathbf{3}]\cdot 8MeOH\cdot 4H_2O$: $C_{80}H_{186}O_{120}K_6Si_2W_{20}$; $M=6972.04$, monoclinic, space group $P2_1/n$ (no. 14), $a=18.547(3)$, $b=16.564(2)$, $c=28.633(4)$ Å, $\beta=99.715(2)°$, $V=8670.4(21)$ Å$^3$, $Z=2$, $\rho_{calcd}=2.670\ g\,cm^{-3}$, $\mu(Mo_{K\alpha})=134.80$, $R=0.047$ for 12297 unique data with $I>3.0\sigma(I)$ ($R_w=0.053$) and 598 parameters used for refinement. CCDC 278955 and CCDC 278956 contain the supplementary crystallographic data for this paper. These data can be obtained free of charge from The Cambridge Crystallographic Data Centre via www.ccdc.cam.ac.uk/data_request/cif.

Baeyer–Villiger oxidation: Catalyst containing 25 μmol of W (i.e., **1**: 2.5 μmol, **2** and **3**: 1.25 μmol), solvent (nitromethane, 1.0 mL), $H_2O_2$ (80% aqueous solution, 0.25 mmol), and substrate (cyclopentanone, 1.25 mmol) were charged to the reaction vial under air. The reaction was carried out at 333 K. The reaction solution was periodically sampled and analyzed by gas chromatography with an internal standard.

Received: July 21, 2005
Revised: December 22, 2005
Published online: February 17, 2006

**Keywords:** homogeneous catalysis · lactones · oxidation · polyoxometalates · tungsten

[1] a) C. L. Hill, C. Chrisina, M. P. McCartha, *Coord. Chem. Rev.* **1995**, *143*, 407–453; b) T. Okuhara, N. Mizuno, M. Misono, *Adv. Catal.* **1996**, *41*, 113–252; c) thematic issue on polyoxometalates (Ed.: C. L. Hill): *Chem. Rev.* **1998**, *98*, 1–390; d) R. Neumann, *Prog. Inorg. Chem.* **1998**, *47*, 317–370; e) *Polyoxometalate Chemistry: From Topology via Self-Assembly to Applications* (Eds.: M. T. Pope, A. Müller), Kluwer, Dordrecht, **2001**; f) *Polyoxometalate Chemistry for Nano-Composite Design* (Eds.: T. Yamase, M. T. Pope), Kluwer, Dordrecht, **2002**; g) I. V. Kozhevnikov, *Catalysis by Polyoxometalates*, Wiley, Chichester, UK, **2002**; h) "Polyoxometalates: Reactivity": C. L. Hill in *Comprehensive Coordination Chemistry II: Transition Metal Groups 3–6, Vol. 4* (Ed.: A. G. Wedd), Elsevier, New York, **2004**, chap. 4.11, pp. 679–759.

[2] a) M. T. Pope, *Heteropoly and Isopoly Oxometalates*, Springer, Berlin, **1983**; b) M. T. Pope, A. Müller, *Angew. Chem.* **1991**, *103*, 56–70; *Angew. Chem. Int. Ed. Engl.* **1991**, *30*, 34–48; c) "Polyoxo Anions: Synthesis and Structure": M. T. Pope in *Comprehensive Coordination Chemistry II: Transition Metal Groups 3–6, Vol. 4* (Ed.: A. G. Wedd), Elsevier, New York, **2004**, chap. 4.10, pp. 635–678.

[3] a) J. Canny, A. Tézé, R. Thouvenot, G. Hervé, *Inorg. Chem.* **1986**, *25*, 2114–2119; b) A. Tézé, G. Hervé, *Inorg. Synth.* **1990**, *27*, 85–96.

[4] a) J. Canny, R. Thouvenot, A. Tézé, G. Hervé, M. Leparulo-Loftus, M. T. Pope, *Inorg. Chem.* **1991**, *30*, 976–981; b) K. Wassermann, H.-J. Lunk, R. Palm, J. Fuchs, N. Steinfeldt, R. Stösser, M. T. Pope, *Inorg. Chem.* **1996**, *35*, 3273–3279; c) X.-Y. Zhang, C. J. O'Connor, G. B. Jameson, M. T. Pope, *Inorg. Chem.* **1996**, *35*, 30–34; d) C. Nozaki, I. Kiyoto, Y. Minai, M. Misono, N. Mizuno, *Inorg. Chem.* **1999**, *38*, 5724–5729.

[5] a) K. Kamata, K. Yonehara, Y. Sumida, K. Yamaguchi, S. Hikichi, N. Mizuno, *Science* **2003**, *300*, 964–966; b) K. Kamata, Y. Nakagawa, K. Yamaguchi, N. Mizuno, *J. Catal.* **2004**, *224*, 224–228.

[6] Reviews of Baeyer–Villiger oxidation: a) G.-J. ten Brick, W. C. E. Arends, R. A. Sheldon, *Chem. Rev.* **2004**, *104*, 4105–4123; b) G. Strukul, *Angew. Chem.* **1998**, *110*, 1256–1267; *Angew. Chem. Int. Ed.* **1998**, *37*, 1198–1209; c) M. Rent, B. Meunier, *Eur. J. Org. Chem.* **1999**, 737–750.

[7] Acidification of the $Ti^{IV}$-containing heteropolytungstate $[PTiW_{11}O_{40}]^{5-}$ leads to the formation of the corresponding dimer $[(PTiW_{11}O_{39})_2(\mu\text{-}OH)]^{7-}$ through protonation of the terminal oxo ligand attached to the titanium center followed by dehydration: O. A. Kholdeeva, G. M. Maksimov, R. I. Maksimovskaya, L. A. Kovaleva, M. A. Fedotov, V. A. Grigoriev, C. L. Hill, *Inorg. Chem.* **2000**, *39*, 3828–3878.

[8] Examples of organic–inorganic hybrid compounds derived from $[SiW_{10}O_{36}]^{8-}$: a) F. Xin, M. T. Pope, *Inorg. Chem.* **1996**, *35*, 5693–5695; b) C. R. Mayer, V. Cabuil, T. Lalot, R. Thouvenot, *Angew. Chem.* **1999**, *111*, 3878–3881; *Angew. Chem. Int. Ed.* **1999**, *38*, 3672–3675; c) C. R. Mayer, P. Herson, R. Thouvenot, *Inorg. Chem.* **1999**, *38*, 6152–6158; d) C. R. Mayer, R. Thouvenot, T. Lalot, *Macromolecules* **2000**, *33*, 4433–4437; e) C. R. Mayer, R. Thouvenot, T. Lalot, *Chem. Mater.* **2000**, *12*, 257–260; f) C. R. Mayer, I. Fournier, R. Thouvenot, *Chem. Eur. J.* **2000**, *6*, 105–110; g) R. C. Schroden, C. F. Blanford, B. J. Melde, B. J. S. Johnson, A. Stein, *Chem. Mater.* **2001**, *13*, 1074–1081; h) M. Bonchio, M. Carraro, G. Scorrano, A. Bagno, *Adv. Synth. Catal.* **2004**, *346*, 648–654.

[9] J. Fuchs, R. Palm, *Z. Naturforsch. B* **1984**, *39*, 757–762.

[10] Formation of the $W_{20}$ clusters **2** and **3** presented herein suggests that larger POMs are likely formed through condensation of lacunary POMs. For example, Wells–Dawson-type clusters $[X_2M_{18}O_{62}]^{n-}$ can be regarded as dimers of trivacant Keggin-type POMs $[XM_9O_{34}]^{n-}$, and the acidification of $K_{10}[\alpha\text{-}SiW_9O_{34}]$ gives $K_{13}[\{K(H_2O)_3\}_2\{K(H_2O)_2\}(Si_2W_{18}O_{66})]$, the structure of which can be described as open Wells–Dawson type: a) N. Laronze, J. Marrot, G. Hervé, *Chem. Commun.* **2003**, 2360–2361; b) N. Leclerc-Laronze, J. Marrot, G. Hervé, *Inorg. Chem.* **2005**, *44*, 1275–1281.

[11] A Baeyer–Villiger oxidation step is suggested to be involved in the oxidation of cyclohexanone to adipic acid with $H_2O_2$ catalyzed by $H_2WO_4$, although the corresponding lactone intermediate has not been detected: a) Y. Usui, K. Sato, *Green Chem.* **2003**, *5*, 373–375. See also the following paper reporting the oxidative transformation of cyclohexene to adipic acid: b) K. Sato, M. Aoki, R. Noyori, *Science* **1998**, *281*, 1646–1647.

[12] In the present system, a peroxide adduct of **2** could not be detected.

[13] The platinum diphosphane complex $[Pt(\mu\text{-}OH)(dppb)]^{2+}$ (dppb = 1,4-bis(diphenylphosphanyl)butane) catalyzes the oxidation of acyclic methyl ketones, but the activity for the oxidation of acetophenone is very low in comparison with those for aliphatic ketones: R. Gavagnin, M. Cataldo, F. Pinna, G. Strukul, *Organometallics* **1998**, *17*, 661–667.

[14] The oxidation of aliphatic and aromatic aldehydes with $H_2O_2$ mediated by the tungsten peroxo complex $[PO_4\{W(O)(O_2)_2\}_4]^{3-}$ has been suggested to proceed by a Baeyer–Villiger-type mechanism, although the products are the corresponding carboxylic acids, and formate esters and/or hydrolysis products (i.e., alcohols and phenols) have not been detected: C. Venturello, M. Gambaro, *J. Org. Chem.* **1991**, *56*, 5924–5931.

[15] For peracid-mediated Baeyer–Villiger oxidation of 2-methylated cycloalkanones, oxygen insertion between the carbonyl group and the more highly substituted neighboring carbon atom is favorable,[6] whereas the regioselectivity for (Lewis and Brønsted) acid-catalyzed oxygenation with $H_2O_2$ is similar to

 © 2006 Wiley-VCH Verlag GmbH & Co. KGaA, Weinheim 

that observed for **2**: Lewis acid catalyzed systems: a) M. Renz, T. Blasco, A. Corma, V. Fornes, R. Jensen, L. Nemeth, *Chem. Eur. J.* **2002**, *8*, 4708 – 4717 (δ-methyl-δ-valerolactone:α-methyl-δ-valerolactone = 67:33 with catalysis by $Sc[N(SO_2C_8F_{17})_2]_3$); b) K. Mikami, M. N. Islam, M. Yamanaka, Y. Itoh, M. Shinoda, K. Kubo, *Tetrahedron Lett.* **2004**, *45*, 3681 – 3683 (ε-methyl-ε-caprolactone:α-methyl-ε-caprolactone = 85:15 with catalysis by Sn-beta zeolite). The $H^+$-mediated ($HClO_4$) reaction also exhibited a similar selectivity to that with **2** (δ-methyl-δ-valerolactone:α-methyl-δ-valerolactone = 57:43). The chemical shift of the carbonyl carbon atom of DMF (7.5 μmol) in $MeNO_2$ (0.6 mL) was 163.9 ppm. A downfield shift (4.7–4.8 ppm) was observed on addition of **2** (5 μmol), whereas no shift was observed on addition of **1**. In addition, **2** was much more active for the Mukaiyama aldol condensation. These facts suggest that **2** is more acidic than **1**. The stronger acidity of **2** possibly explains why **2** is more active than **1** for Baeyer–Villiger oxidation.

[16] Examples of using compounds of early transition metals as catalysts and $H_2O_2$ as oxidant have been reported. Re catalysts: a) W. A. Herrmann, R. W. Fischer, J. D. G. Correia, *J. Mol. Catal.* **1994**, *94*, 213 – 223 (cyclobutanone, TON = 13); b) A. M. F. Phillips, C. Romão, *Eur. J. Org. Chem.* **1999**, 1767 – 1770 (cyclobutanone derivatives, TON = 210–267); c) R. Berinini, A. Coratti, G. Fabrizi, A. Goggiamani, *Tetrahedron Lett.* **2003**, *44*, 8991 – 8994 (cyclobutanone and 2-adamantanone, TON > 49). Mo catalyst: d) S. E. Jacobson, R. Tang, F. Mares, *J. Chem. Soc. Chem. Commun.* **1978**, 888 – 889 (cyclopentanone, TON = 12); e) S. Campestrini, F. D. Furia, *J. Mol. Catal.* **1993**, *79*, 13 – 19 (cyclopentanone, TON = 6).

[17] Examples of using catalysts based on late transition metals and $H_2O_2$ as oxidant: Pt catalysts: a) G. Strukul, A. Varagnolo, F. Pinna, *J. Mol. Catal. A* **1997**, *117*, 413 – 423 (cyclohexanone, TON = 12); b) R. A. Michelin, E. Pizzo, A. Scarso, P. Sgarbossa, G. Strukul, A. Tassan, *Organometallics* **2005**, *24*, 1012 – 1017 (cyclobutanone, TON = 100); Co catalyst: c) T. Uchida, T. Katsuki, *Tetrahedron Lett.* **2001**, *42*, 6911 – 6914 (3-(4-chlorophenyl)cyclobutanone, TON = 15).

[18] Examples of main-group catalysts: a) R. T. Taylor, L. A. Flood, *J. Org. Chem.* **1983**, *48*, 5160 – 5164 (cyclopentanone, TON = 67); b) G.-J. ten Brink, J.-M. Vis, I. W. C. E. Arends, R. A. Sheldon, *J. Org. Chem.* **2001**, *66*, 2429 – 2433 (cyclobutanone, TON = 178; cyclopentanone, TON = 178; 2-adamantanone, TON = 198).

 © 2006 Wiley-VCH Verlag GmbH & Co. KGaA, Weinheim 

Protein-Structure Determination

DOI: 10.1002/anie.200503558

# Sequence-Specific Assignment of Aromatic Resonances of Uniformly $^{13}C$,$^{15}N$-Labeled Proteins by Using $^{13}C$- and $^{15}N$-Edited NOESY Spectra**

*Zhi Lin, Yingqi Xu, Shuai Yang, and Daiwen Yang**

The precision of a protein structure determined by NMR spectroscopy is strongly influenced by the number of long-range NOE interactions per residue. Aromatic and methyl-containing residues are frequently located in the hydrophobic interior of proteins and yield long-range NOE interactions. Methyl groups have become the major focus in the structure determination of large proteins in recent years.[1] On the other hand, aromatic groups have not received equal attention because their sequence-specific assignment is extremely difficult, especially for proteins larger than 25 kDa. In cases in which aromatic proton resonances are well dispersed and the protein is small, assignments can be made on the basis of 2D NOESY experiments (linking resonances between aromatic protons and side-chain $\alpha$ and/or $\beta$ protons) and 2D COSY-type experiments (linking resonances within the ring).[2]

When the chemical shifts of H atoms are degenerate and hence assignment is ambiguous, $^{13}C$-edited experiments allow ambiguities to be resolved through better dispersion of $^{13}C$ spins. In all these $^{13}C$-edited experiments, aromatic protons correlate with aliphatic protons and/or carbon atoms through a multiple-relay or TOCSY scheme.[3] These experiments may fail for larger proteins owing to increased decay of magnetization during the lengthy transfer steps. To improve the sensitivity, a suite of experiments with fewer transfer steps that correlate $C^{\gamma}$ with either $H^{\beta}$ or aromatic protons in two sets of spectra was proposed.[4] With these experiments, about 70% of the aromatic protons of the Phe and Tyr residues in *F. solani pisi* cutinase ($\approx$22 kDa with 1 His, 6 Phe, 1 Trp, and

[*] Z. Lin, Dr. Y. Q. Xu, Prof. D. W. Yang
Department of Biological Sciences
National University of Singapore
14 Science Drive 4, Singapore 117543 (Singapore)
Fax: (+65) 6779-2486
E-mail: dbsydw@nus.edu.sg
S. Yang
Department of Chemistry
National University of Singapore
14 Science Drive 4, Singapore 117543 (Singapore)

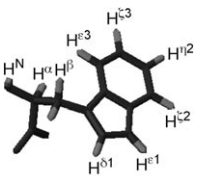
[**] This research was supported by a grant from the Biomedical Research Council (BMRC) and the Agency for Science, Technology, and Research, A*Star of Singapore. D.W.Y. is the recipient of a BMRC Young Investigator Award. The authors thank Prof. L. E. Kay (University of Toronto) for providing the MBP sample and for evaluating the manuscript.

Supporting information for this article is available on the WWW under http://www.angewandte.org or from the author.


WILEY InterScience DISCOVER SOMETHING GREAT

© 2006 Wiley-VCH Verlag GmbH & Co. KGaA, Weinheim

6 Tyr) were assigned, as the assignment relies on the dispersion of $C^{\gamma}$ spins which is generally not excellent for the same type of amino acid residue. Recently, Lohr et al. proposed the assignment of $H^{\delta 2}/C^{\delta 2}$ of His residues and $H^{\varepsilon 1}/N^{\varepsilon 1}$ of Trp by linking these spins with $C^{\beta}$ based on multiple-relay and TROSY schemes.[5] The method was also applied for the assignment of $H^{\varepsilon 1}/N^{\varepsilon 1}$ of Trp residues in large deuterated proteins.



Trp158

Alternatively, aromatic resonances may be assigned by using traditional experiments on selectively labeled protein samples. Reverse-labeled U-$^{12}$C-(Tyr/Phe)/$^{13}$C samples can be used to assign many aromatic ring protons in relatively large proteins with 2D $^{12}$C-filtered NOESY and TOCSY and 3D $^{13}$C-edited/$^{12}$C-filtered NOESY experiments,[6] provided that the resonances of the aromatic protons are well dispersed. In favorable cases, some aromatic spins in perdeuterated proteins in which all H atoms are found in methyl and aromatic groups only can be assigned from methyl/aromatic NOE interactions based on the prior assignment of the methyl groups and initial structures derived from NOE interactions between amide and methyl groups.[7] Very recently, a specific labeling strategy for the regio- and stereoselective preparation of $^{2}$H,$^{13}$C,$^{15}$N-labeled Phe and Tyr was proposed which allowed unambiguous assignment of only $C^{\varepsilon}H^{\varepsilon}$ and $C^{\zeta}H^{\zeta}$ groups of these two types of residues in two different samples (i.e., $\approx$66% and 50% aromatic resonances can be obtained for Phe and Tyr residues, respectively).[8] However, the sample preparation for this method is not straightforward and can be very expensive.

According to statistics on proton–proton distances (see the Supporting Information),[9] we found the following features for aromatic residues: 1) A majority of residues produce observable intraresidue $H_i^{\delta}$–$H_i^{N}$ NOE interactions ($i$ = the $i$th residue in the protein sequence); 2) Most Phe and Tyr residues and many His and Trp residues generate sequential $H_i^{\delta}$–$H_{i+1}^{N}$ NOE interactions; 3) The amide group of an aromatic residue much more likely correlates with the aromatic protons in the same and in preceding residues than in other residues; 4) All $H_i^{\delta}$–$H_i^{\beta}$ and most $H_i^{\delta}$–$H_i^{\alpha}$ NOE interactions are detectable. On the basis of these features, we propose herein a simple strategy to designate aromatic resonances in uniformly $^{13}$C,$^{15}$N-labeled proteins by using 3D $^{15}$N- and $^{13}$C-edited spectra and prior aliphatic assignment.

In a $^{15}$N-edited NOESY spectrum, each amide group correlates with a number of aromatic protons at chemical shifts $\omega(H_j^{aro})$, $\omega(N_i)$, $\omega(H_i^{N})$ ($\omega$ = chemical shift, aro = aromatic). $H_i^{\delta}$ can be assigned from the overlap of intraresidue and sequential $H^{aro}$–$H^{N}$ NOE interactions arising from the amide groups of residues $i$ and $i+1$ or from intraresidue NOE interactions only. This is similar to the assignment strategy for aliphatic spins.[10] The assignment can be further confirmed by the presence of $H_i^{\delta}$–$H_i^{\beta}$ and/or $H_i^{\delta}$–$H_i^{\alpha}$ NOE interactions in a $^{13}$C-edited NOESY spectrum. Simultaneously, the chemical shifts of $C^{\delta}$ spins are obtained. On the basis of the assignment of $H^{\delta}/C^{\delta}$, other aromatic spins can be designated stepwise from $H^{\varepsilon}/C^{\varepsilon}$ to $H^{\zeta}/C^{\zeta}$ and then to $H^{\eta}/C^{\eta}$ by using the $^{13}$C-edited NOESY spectrum. The assignment of some $H^{\varepsilon}$ atoms can be confirmed by using the $^{15}$N-edited spectrum, as some $H_i^{\varepsilon}$–$H_i^{N}$ NOE interactions are also detectable. If there are still any ambiguities in the assignments after using all NOE data, they might be resolved from the structure calculated from available NOE interactions.

We modified a previously published pulse scheme[11] for recording $^{15}$N- and $^{13}$C-edited 3D NOESY spectra in a single experiment (see the Supporting Information). The modified version with optimal water flip-back and minimum delays for transverse $^{1}$H magnetization is more suitable for large proteins. The NOESY-HSQC experiment used in this study is more sensitive than the NOESY-HMQC scheme for both CH and NH groups on an 800-MHz spectrometer owing to the large chemical-shift anisotropy of aromatic $^{13}$C spins, though it is slightly less sensitive for CH groups at lower fields. We applied the scheme and assignment strategy to uniformly $^{13}$C,$^{15}$N-labeled samples of a sterile α motif (SAM, 9 kDa, 0.5 mM), a $Ca^{2+}$-dependent cell-adhesion protein of *Dictyostelium discoideum* (DdCAD-1, 24 kDa, 0.8 mM), and a maltose-binding protein (MBP, 42 kDa, 1.2 mM). The assignment procedure is described below.

For a given peak at chemical shifts $\omega(H_i^{N})$, $\omega(N_j)$, $\omega(H_j^{N})$ (i.e., an $H_i^{N}$–$H_j^{N}$ NOE interaction on the plane located at $\omega(N_j)$), we often find its symmetry-related peak at $\omega(H_j^{N})$, $\omega(N_i)$, $\omega(H_i^{N})$ on the plane at $\omega(N_i)$. In contrast, $H^{aro}$–$H^{N}$ NOE interactions show no such symmetry in the $^{15}$N-edited spectrum. Most $H^{aro}$–$H^{N}$ NOE interactions can be differentiated from $H^{N}$–$H^{N}$ NOE interactions in this manner. If the amide group of a given aromatic residue yields one (or more) $H^{aro}$–$H^{N}$ NOE interaction, the latter (or the most intense) can be tentatively assigned as an intraresidue $H_i^{\delta}$–$H_i^{N}$ correlation (Figure 1b; see also the Supporting Information) as $H_i^{N}$, in most cases, is closer to $H_i^{\delta}$ than to other aromatic protons. If the amide group of the following residue also shows an $H^{aro}$–$H^{N}$ NOE interaction whose $H^{aro}$ shift is identical to $\omega(H_i^{\delta})$ (Figure 1a,b and Supporting Information), the assignment of $H_i^{\delta}$ is considered to be correct. This is because the probability for a non-$H_i^{\delta}$ to correlate with both $H_i^{N}$ and $H_{i+1}^{N}$ is very small. For the three proteins examined in this study, $\approx$20–30% of the $H^{\delta}$ atoms were assigned uniquely by matching the $H_i^{\delta}$–$H_i^{N}$ and $H_i^{\delta}$–$H_{i+1}^{N}$ NOE interactions (Table 1, column B), whereas most Phe and Tyr $H^{\delta}$ atoms gave rise to $H_i^{\delta}$–$H_i^{N}$ NOE interactions as expected from the statistics, leading to tentative assignments. The assignments made in this step can be cross-checked further with a $^{13}$C-edited 3D NOESY experiment.

The chemical shift of $C_i^{\delta}$ is obtained from a $^{13}$C-edited 3D NOESY experiment on the basis of the $H_i^{\delta}$ shift assigned in the first step (Figure 1c and Supporting Information). The observation of an $H_i^{N}$-$H_i^{\delta}$ NOE interaction at $\omega(H_i^{N})$, $\omega(C_i^{\delta})$, $\omega(H_i^{\delta})$ in the $^{13}$C-edited spectrum further confirms the assignment (Figure 1c). This type of symmetry-related NOE interaction also resolves ambiguous assignments of $H_i^{\delta}$ resulting from a lack of sequential $H_i^{\delta}$–$H_{i+1}^{N}$ NOE interactions (Figure 1g). We found that in most cases $\omega(H_i^{\delta})$, $\omega(N_i)$, $\omega(H_i^{N})$ NOE interactions are stronger than their symmetric $\omega(H_i^{N})$, $\omega(C_i^{\delta})$, $\omega(H_i^{\delta})$ NOE interactions, implying that the symmetric pattern may not exist for some NOE interactions.

 © 2006 Wiley-VCH Verlag GmbH & Co. KGaA, Weinheim 

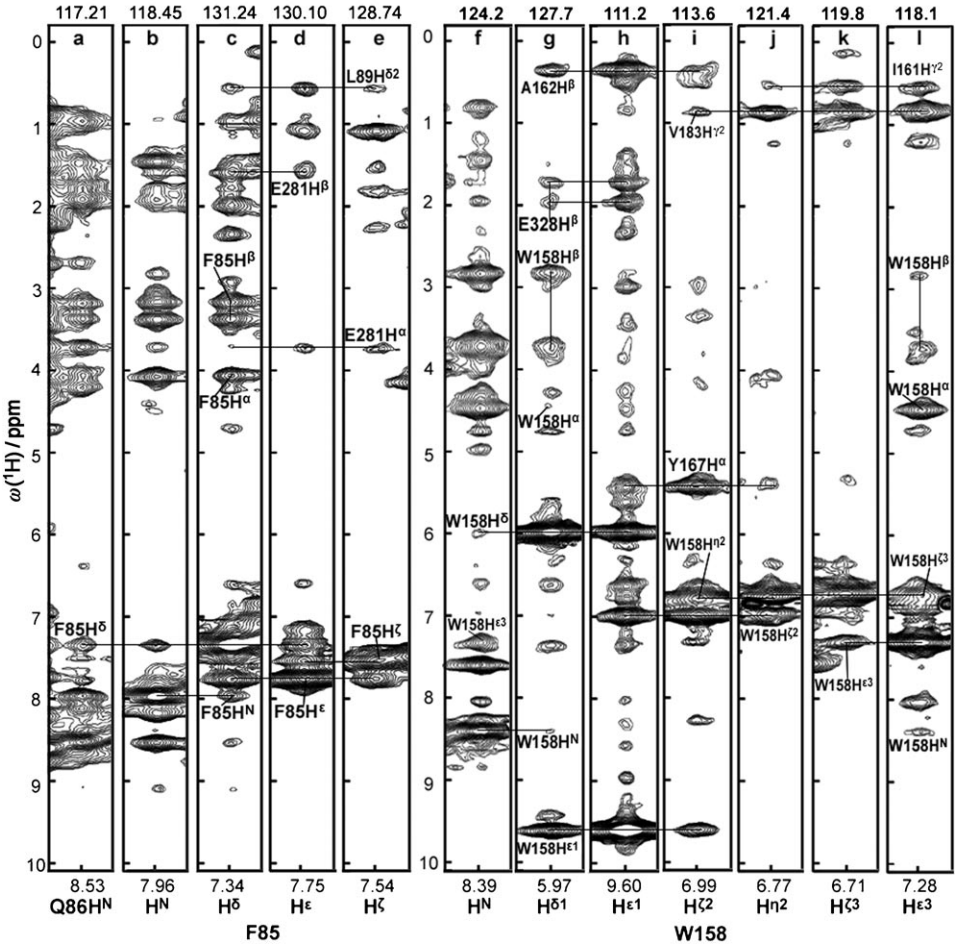



***Figure 1.*** Representative slices from the $^{13}C$- and $^{15}N$-edited NOESY spectra. Each $F_1(^1H)$–$F_3(^1H)$ slice is labeled with proton identities and the $F_2(^{13}C/^{15}N)$ frequency in ppm is indicated at the top of each slice. The experiment was recorded with a 42-kDa $^{13}C,^{15}N$-labeled MBP in $H_2O/D_2O$ (90:10) solution (1.2 mM protein, pH 7, 30 °C) on a Bruker 800-MHz spectrometer with a triple-resonance probe: $80(t_1)\times30(t_2)\times640(t_3)$ complex points were collected with an NOE mixing time of 50 ms, giving $t_{1max}=8.2$ ms, $t_{2Cmax}=5.2$ ms, $t_{2Nmax}=18.1$ ms, $t_{3max}=54$ ms. An interscan delay of 1.3 s with 8 scans per increment was used, resulting in a total experimental time of 60 h.

This can be explained by the magnetization-transfer-efficiency difference between $^1H^N\rightarrow{}^{15}N\rightarrow{}^1H^N$ and $^1H^C\rightarrow{}^{13}C\rightarrow{}^1H^C$ pathways owing to $^{13}C$–$^{13}C$ coupling and relaxation effects. If uncertainty in the assignment of $H^\delta$/$C^\delta$ still exists, intraresidue $H^\delta$–$H^\beta$ and/or $H^\delta$–$H^\alpha$ NOE interactions are used to finalize the assignment (Figure 1c,g). Nearly all $H^\delta$ protons in SAM, DdCAD-1, and MBP undergo $H_i^\delta$–$H_i^\beta$ and $H_i^\delta$–$H_i^\alpha$ NOE interactions. Although only $H^\delta$-$H^\beta$ NOE interactions were observed for some His residues, they were sufficient to allow confirmation of the assignment. After this step, nearly all tentative assignments were unambiguous.

For His and Trp residues, many $H^\delta$ atoms do not show $H_i^\delta$–$H_i^N$ NOE interactions and cannot be assigned with the strategy mentioned above. Fortunately, the $C^\delta$–$H^\delta$ correlations of His and Trp are well dispersed and display an opposite sign with respect to other aromatic correlations in a constant-time $^{13}C$–$^1H$ HSQC (see the Supporting Information). The chemical shifts of a Trp or His $C^\delta H^\delta$ group were obtained from these characteristic HSQC peaks. Thereafter, sequence-specific assignment can be achieved from $H_i^\delta$–$H_i^\beta$ and/or $H_i^\delta$–$H_i^\alpha$ NOE interactions on the plane at $\omega(C_i^\delta)$ based on prior assignment of $H_i^\beta$ and $H_i^\alpha$ of the Trp or His residue (see the Supporting Information). For MBP, four Trp $H^\delta$ atoms and one His $H^\delta$ atom were assigned in this

***Table 1:*** Summary of assignments of aromatic resonances of SAM, DdCAD-1, and MBP.[a]

| | | SAM | | | | DdCAD-1 | | | | MBP | | | |
|---|---|---|---|---|---|---|---|---|---|---|---|---|---|
| | | A | B | C | D | A | B | C | D | A | B | C | D |
| Phe Tyr | $C^\delta H^\delta$(6/21/30) | 6 | 2 | 4 | 6 | 18 | 7 | 10 | 17 | 26 | 7 | 17 | 24 |
| | $C^\varepsilon H^\varepsilon$(6/21/30) | - | - | - | 6 | - | - | - | 15 | - | - | - | 13 |
| | $C^\zeta H^\zeta$(4/14/15) | - | - | - | 4 | - | - | - | 5 | - | - | - | 3 |
| His | $C^{\delta2}H^{\delta2}$(1/3/3) | 1 | 1 | 1 | 1 | 2 | 1 | 2 | 3 | 1 | 1 | 1 | 2 |
| | $C^{\varepsilon1}H^{\varepsilon1}$(1/3/3) | - | - | - | 1 | - | - | - | 3 | - | - | - | 2 |
| Trp | $C^{\delta1}H^{\delta1}$(1/3/8) | 1 | 0 | 1 | 1 | 2 | 1 | 2 | 3 | 5 | 1 | 5 | 6 |
| | $N^{\varepsilon1}H^{\varepsilon1}$(1/3/8) | - | - | - | 1 | - | - | - | 3 | - | - | - | 6 |
| | $C^{\varepsilon3}H^{\varepsilon3}$(1/3/8) | - | - | - | 1 | - | - | - | 2 | - | - | - | 4 |
| | $C^{\zeta2}H^{\zeta2}$(1/3/8) | - | - | - | 1 | - | - | - | 3 | - | - | - | 6 |
| | $C^{\zeta3}H^{\zeta3}$(1/3/8) | - | - | - | 1 | - | - | - | 3 | - | - | - | 4 |
| | $C^{\eta2}H^{\eta2}$(1/3/8) | - | - | - | 1 | - | - | - | 3 | - | - | - | 5 |

[a] Column A: Tentatively assigned with $H_i^N$–$H_i^\delta$ NOE interactions. Column B: Uniquely assigned with intraresidue and sequential $H_{i+1}^N$–$H_i^\delta$ NOE interactions. Column C: Uniquely assigned with $H^\delta$–$H^\beta$/$H^\alpha$ and $H_i^\delta$–$H_i^N$/$H_i^\delta$–$H_{i+1}^N$ NOE interactions. The number of the assignments shown in column B is not included here. Column D: Final assignments. The total number of $C^{aro}H^{aro}$ groups of SAM/DdCAD-1/MBP is indicated in brackets.

 © 2006 Wiley-VCH Verlag GmbH & Co. KGaA, Weinheim 

step. In principle, some unassigned $C^{\delta}H^{\delta}$ groups in Tyr and Phe that display no $H^{\delta}$–$H^{N}$ NOE interactions can be designated from the $^{13}C$–$^{1}H$ HSQC and $^{13}C$-edited NOESY in a similar way. In practice, these $C^{\delta}H^{\delta}$ groups could not be assigned for DdCAD-1 and MBP owing to the poor dispersion of $C^{\delta}$–$H^{\delta}$ chemical shifts, especially for MBP (Supporting Information).

Once the chemical shifts of the $C^{\delta}H^{\delta}$ groups are known, their neighboring $C^{\varepsilon}H^{\varepsilon}$ or $N^{\varepsilon}H^{\varepsilon}$ groups can be assigned. Since the $H^{\delta}$–$H^{\varepsilon}$ distances are $<2.6$ Å, $H^{\delta}$–$H^{\varepsilon}$ NOE interactions should be observable in the $^{13}C$-edited NOESY. The assignment of $C^{\varepsilon}H^{\varepsilon}$ is straightforward from the NOE interactions at $\omega(H_i^{\varepsilon})$, $\omega(C_i^{\delta})$, $\omega(H_i^{\delta})$ and $\omega(H_i^{\delta})$, $\omega(C_i^{\varepsilon})$, $\omega(H_i^{\varepsilon})$ (Figure 1c,d), provided that $H_i^{\delta}$ and $H_i^{\varepsilon}$ are not degenerate, that is, $|\omega(H_i^{\delta})-\omega(H_i^{\varepsilon})|>0.05$ ppm. $H_i^{\delta}$ and $H_i^{\varepsilon}$ often undergo NOE interactions with the same aliphatic protons. This feature can be applied to confirm the assignment of $H_i^{\varepsilon}$ (Figure 1c,d). $N^{\varepsilon}H^{\varepsilon}$ groups are easy to assign for Trp based on the $^{15}N$–$^{1}H$ correlations in an HSQC spectrum and the NOE interactions at $\omega(H_i^{\varepsilon})$, $\omega(C_i^{\delta})$, $\omega(H_i^{\delta})$ and $\omega(H_i^{\delta})$, $\omega(N_i^{\varepsilon})$, $\omega(H_i^{\varepsilon})$ (Figure 1g,h). Similarly, the remaining CH groups in Trp and Phe can be assigned on the basis of strong NOE interactions with neighboring ring protons (Figure 1e,i–l). However, the small difference in chemical shifts between two neighboring ring protons often makes the assignment difficult, especially for Phe. This is the reason why the $C^{\varepsilon}H^{\varepsilon}$ and $C^{\zeta}H^{\zeta}$ groups in Phe and Tyr are not as comprehensively assigned as the $C^{\delta}H^{\delta}$ groups in DdCAD-1 and MBP (Table 1). For the same reason, few aromatic spins of a large protein with many aromatic residues (such as MBP) can be assigned by using a single $^{13}C$-edited NOESY spectrum.

Some $C^{\varepsilon 3}H^{\varepsilon 3}$ groups in Trp can also be assigned from $H_i^{\varepsilon 3}$–$H_i^{N}$ and/or $H_i^{\varepsilon 3}$–$H_{i+1}{}^{N}$ NOE interactions as these can be detected (Figure 1f). The $C^{\varepsilon 3}H^{\varepsilon 3}$ assignment can be further confirmed from the $H_i^{\varepsilon 3}$–$H_i^{\beta}$ and/or $H_i^{\varepsilon 3}$–$H_i^{\alpha}$ NOE interactions (Figure 1l). To assign the $C^{\varepsilon 1}H^{\varepsilon 1}$ groups in His, one has to rely on the structure obtained from available NOEs. The presence of $H^{\varepsilon 1}$–$H^{\delta 2}$, $H^{\varepsilon 1}$–$H^{\alpha}$, and/or $H^{\varepsilon 1}$–$H^{\beta}$ NOE interactions will support the assignment (Supporting Information).

With the above-mentioned procedure, we assigned 100%, 75%, and 57% of the aromatic resonances of SAM, DdCAD-1, and MBP, respectively (Table 1). The degree of completeness of assignment decreases with increasing protein size. Nevertheless, about 80% of the $C^{\delta}H^{\delta}$ groups were assigned for MBP, as these aromatic CH groups gave rise to intraresidue $H^{\delta}$–$H^{N}$ NOE interactions. Without the use of the $^{15}N$-edited NOESY experiments, few aromatic CH groups could be uniquely assigned for MBP. The strategy presented herein often allows more resonance assignments than existing methods for proteins larger than 20 kDa and requires only $^{13}C$,$^{15}N$-labeled samples. More complete assignments might be obtained by using 4D $^{13}C$, $^{15}N$-edited and $^{13}C$,$^{13}C$-edited NOESY spectra, which provide less ambiguities but suffer from longer data collection time. Although the assignment strategy based on $H^{\alpha}/H^{\beta}$–$H^{aro}$ NOE interactions has been used for small proteins, it is shown herein for the first time that a similar strategy based on both $H^{N}$–$H^{aro}$ and $H^{\alpha}/H^{\beta}$–$H^{aro}$ NOE interactions can be applied to proteins up to 42 kDa without using specific or selective isotope labeling.

On average, each aromatic CH group produced $\approx 2.5$ long-range NOE interactions between aromatic and aliphatic protons in the $^{13}C$-edited NOESY as observed in SAM and DdCAD-1. When an assigned aromatic CH group is degenerate with unassigned ones, however, it will be difficult to assign the long-range NOE interactions uniquely. Fortunately, most such assignment ambiguities can be resolved on the basis of an initial structure calculated from unambiguous NOE interactions. Therefore, partial assignment of aromatic resonances from the NOESY spectra necessary for structure determination by NMR—which requires no extra experiments or additional samples—will provide more structural constraints and improve the structure quality, especially for large proteins.

Received: October 7, 2005

**Keywords:** NMR spectroscopy · protein structures · proteins · spectroscopic methods · structure elucidation

[1] a) V. Tugarinov, L. E. Kay, *J. Am. Chem. Soc.* **2003**, *125*, 5701–5706; b) D. W. Yang, Y. Zheng, D. J. Liu, D. F. Wyss, *J. Am. Chem. Soc.* **2004**, *126*, 3710.
[2] K. Wüthrich, *NMR of Proteins and Nucleic Acids*, Wiley, New York, NY, **1986**.
[3] a) T. Yamazaki, J. D. Forman-Kay, L. E. Kay, *J. Am. Chem. Soc.* **1993**, *115*, 11054; b) S. Grzesiek, A. Bax, *J. Am. Chem. Soc.* **1995**, *117*, 6527.
[4] J. J. Prompers, A. Groenewegen, C. W. Hilbers, H. A. M. Pepermans, *J. Magn. Reson.* **1998**, 130, 68.
[5] F. Lohr, V. Katsemi, M. Betz, J. Hartleib, H. Ruterjans, *J. Biomol. NMR* **2002**, 22, 153.
[6] D. S. Garrett, Y. J. Seok, D. I. Liao, A. Peterkofsky, A. M. Gronenborn, G. M. Clore, *Biochemistry* **1997**, *36*, 2517.
[7] S. Park, R. Isaacson, H. T. Kim, P. A. Silver, G. Wagner, *Structure* **2005**, *13*, 995.
[8] T. Torizawa, A. M. Ono, T. Terauchi, M. Kainosho, *J. Am. Chem. Soc.* **2005**, *127*, 12620.
[9] Y. Zheng, D. W. Yang, *Bioinformatics* **2005**, 21, 2925.
[10] Y. Xu, Z. Lin, C. Ho, D. W. Yang, *J. Am. Chem. Soc.* **2005**, *127*, 11920.
[11] a) S. M. Pascal, D. R. Muhandiram, T. Yamazaki, J. D. Forman-Kay, L. E. Kay, *J. Magn. Reson. Ser. B* **1994**, 103, 197; b) Y. Xia, A. Yee, C. H. Arrowsmith, X. Gao, *J. Biomol. NMR* **2003**, 27, 19.

 © 2006 Wiley-VCH Verlag GmbH & Co. KGaA, Weinheim 

Photosynthesis

DOI: 10.1002/anie.200503804

# Cationic State of Accessory Chlorophyll and Electron Transfer through Pheophytin to Plastoquinone in Photosystem II**

*Hiroshi Ishikita, Jacek Biesiadka, Bernhard Loll, Wolfram Saenger, and Ernst-Walter Knapp**

Atmospheric oxygen is generated by the oxidation of water at the $Mn_4Ca$ cluster of the photosynthetic protein–pigment complex, photosystem II (PSII). Light-induced charge separation leads to the formation of an oxidized, positively charged radical $P680^+$ chlorophyll *a* (Chl*a*), while electron transfer (ET) occurs via pheophytin $Pheo_{D1}$ and the primary plastoquinone $Q_A$ in the ET D1 branch rather than the D2 branch to the secondary quinone $Q_B$ (Figure 1). $P680^+$ is re-reduced by the redox-active tyrosine $Y_Z$, which is subsequently reduced by ET from the $Mn_4Ca$ cluster. The D1/D2 proteins of PSII have structural similarity with the L/M subunits of the photosynthetic reaction center (RC) from purple bacteria (bRC).[1] The four Chl*a* $P_{D1}/P_{D2}$ and $Chl_{D1}/Chl_{D2}$ units in the RC of PSII appear in bRC as the four bacteriochlorophyll *a* $P_L/P_M$ and $B_L/B_M$ moieties, respectively. In the bRC from *Rhodobacter sphaeroides*, charge separation initiates at P870, which is the strongly coupled dimer $P_L/P_M$.

Although $P_{D1}/P_{D2}$ in PSII shows a similar dimer geometry as $P_L/P_M$ in bRC (Figure 1), there is no indication that $P_{D1}/P_{D2}$ is a strongly coupled Chl*a* dimer. A number of recent studies imply that P680 is likely a multimeric Chl*a* complex and that $Chl_{D1}$ is the key component of the initial charge separation.[2] Herein, we compute the redox potential ($E_m$) for the one-electron reduction of $Pheo_{D1}/Pheo_{D2}$ ($E_m(Pheo_{D1}/Pheo_{D2})$) and demonstrate the influence of the different charge states of the PSII RC on these $E_m$ values.

[*] Dr. H. Ishikita, Dr. J. Biesiadka, Prof. Dr. W. Saenger, Prof. Dr. E.-W. Knapp
Institut für Chemie und Biochemie
Freie Universität Berlin
Takustrasse 6, 14195 Berlin (Germany)
Fax: (+49) 30-8385-6921
E-mail: knapp@chemie.fu-berlin.de
Dr. B. Loll
Max-Planck-Institut für Medizinische Forschung
Abteilung für Biomolekulare Mechanismen
69115 Heidelberg (Germany)
Dr. H. Ishikita
Department of Chemistry
Pennsylvania State University
104 Chemistry Building, University Park, PA 16802 (USA)

[**] We thank Dr. Donald Bashford and Dr. Martin Karplus for providing the programs MEAD and CHARMM22, respectively. This work was supported by Deutsche Forschungsgemeinschaft through SFB 498, Projects A4 and A5, GRK 80/2, GRK 268, and GRK 788/1. H.I. was supported by DAAD.

Supporting information for this article is available on the WWW under http://www.angewandte.org or from the author.

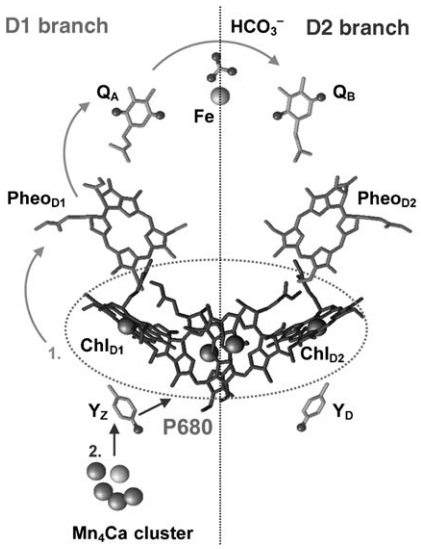



***Figure 1.*** ET pathways from P680 to $Q_B$ and from the $Mn_4Ca$ cluster to P680 in PSII. $Chl_{D1}$ and $Chl_{D2}$ = accessory chlorophyll on the D1 and D2 branches, respectively; $Y_Z$ = redox-active tyrosine; $Y_D$ = symmetry-related redox-inactive tyrosine.

The $E_m(Pheo_{D1})$ value of −600 mV measured by redox titration[3,4] can differ from that relevant to the ET process for two reasons.[5] 1) The reduction of $Pheo_{D1}$ by redox titration also implies the reduction of $Q_A$, thus yielding a downshift in $E_m(Pheo_{D1})$. In our computations, the presence of $Q_A^-$ downshifts $E_m(Pheo_{D1})$ by about 90 mV (Table 1), which is consistent with the estimated downshift of 90 mV in time-resolved photovoltage measurements.[6] 2) As the initial ET and charge-separation process leads to the formation of $P680^+Pheo_{D1}^-$, the $E_m(Pheo_{D1})$ value obtained by redox titration in the presence of uncharged P680 is lower than that derived for $P680^+Pheo_{D1}^-$ by ET kinetic studies. Indeed, for the charge state $Q_A^-$ we obtained $E_m(Pheo_{D1}) = -588$ mV (Table 1), in agreement with the experimental value of −600 mV obtained by redox titration.[3,4]

***Table 1:*** Calculated $E_m$ values [mV] for PSII cofactors.[a]

| Charge state | $E_m(Pheo_{D1})$ | $E_m(Pheo_{D2})$ | $E_m(Q_A)$ |
|---|---|---|---|
| neutral | −499 | −577 | −13 |
| $Q_A^-$ | −588 | n.d. | n.d. |
| $P_{D1}^+$ | −417 | −529 | 4 |
| $Chl_{D1}^+$ | −342 | −549 | 13 |

[a] For the calculated values of $E_m(Q_A)$, see our previous computations.[15] n.d. = not determined.

According to the observations from FTIR[7] and UV/Vis absorption spectra,[8] the cationic state of P680 is delocalized over the $P_{D1}/P_{D2}$ dimer as a consequence of charge separation. However, a number of recent studies suggest that $Chl_{D1}$ is the true primary electron donor in the PSII RC, and that ET is initiated by the formation of the charge pair $Chl_{D1}^+Pheo_{D1}^-$ (for instance, see reference [2]). The calculated $E_m(Pheo_{D1})$ values differ dramatically depending on the charge state of the RC,


WILEY InterScience DISCOVER SOMETHING GREAT
© 2006 Wiley-VCH Verlag GmbH & Co. KGaA, Weinheim

whereas $E_m(Q_A)$ varies only between +13 and −13 mV (Table 1).

Herein, we obtained the driving energy $\Delta G$ for the ET from $Pheo^-_{D1}$ to $Q_A$ as $\Delta G = -e[E_m(Pheo_{D1}) - E_m(Q_A)]$ ($e$ = elementary charge), which yielded −421 and −346 meV for the ET reactions $[P^+_{D1}Pheo^-_{D1}Q^0_A \rightarrow P^+_{D1}Pheo^0_{D1}Q^-_A]$ and $[Chl^+_{D1}Pheo^-_{D1}Q^0_A \rightarrow Chl^+_{D1}Pheo^0_{D1}Q^-_A]$, respectively (Table 1). It was suggested that the measurable $P^0_{D1}Chl^+_{D1}Pheo^-_{D1}$ state transforms to the $P^+_{D1}Chl^0_{D1}Pheo^-_{D1}$ state in 5[2] to 25 ps,[9] which is shorter than the 300 ps[10] measured for the forward ET from $Pheo^-_{D1}$ to $Q_A$. Thus, it is likely that the electron hole has moved from $Chl^+_{D1}$ to $P^+_{D1}$ before the electron transfers from $Pheo^-_{D1}$ to $Q_A$, and the relevant charge state for ET from Pheo to $Q_A$ is $P^+_{D1}Chl^0_{D1}$ rather than $P^0_{D1}Chl^+_{D1}$.

Based on recombination-fluorescence measurements, it was estimated that $\Delta G$ is between −340 and −360 meV.[5,11,12] The computed $\Delta G$ value of the corresponding ET reaction $[P^+_{D1}Pheo^-_{D1} \rightarrow P^+_{D1}Q^-_A]$ is −421 meV, in reasonable agreement with the $\Delta G$ value estimated from measurements. However, $\Delta G = -346$ meV was calculated for $[Chl^+_{D1}Pheo^-_{D1} \rightarrow Chl^+_{D1}Q^-_A]$ and may refer to PSII conditions at low temperatures, where a triplet state is predominantly observed at $Chl_{D1}$ and not at $P_{D1}/P_{D2}$.[13]

Finally, the fact that the value of $E_m(Pheo_{D2})$ is lower than that of $E_m(Pheo_{D1})$ by 80–210 mV (Table 1) indicates that the formation of the $Pheo^-_{D1}$ state is energetically much more favorable than that of $Pheo^-_{D2}$. This finding could also refer to the observation that the formation of $Pheo^-$ and ET occur predominantly in the D1 branch (for instance, see reference [2]). Remarkably, the difference in $E_m$ values between $Pheo_{D1}$ and $Pheo_{D2}$ reaches a maximum of 210 meV at the $Chl^+_{D1}$ state (Table 1), which indicates that this is the best state to facilitate the predominant formation of $Pheo^-_{D1}$ and ET from $Pheo^-_{D1}$ to $Q_A$.

## Experimental Section

The crystal structure of PSII at 3.0-Å resolution (PDB: 2 AXT)[14] from the thermophilic cyanobacterium *Thermosynechococcus elongatus* was used. As in previous applications,[15,16] the hydrogen atom positions were energetically optimized with CHARMM.[17] Atomic partial charges of the amino acids were adopted from the all-atom CHARMM22[17] parameter set. Atomic partial charges from previous applications[15,16] were used for cofactors and residues whose charges were not available in CHARMM22. We used $E_m(Pheo\,a) = -780$ mV versus the normal hydrogen electrode measured in $CH_2Cl_2$ (with the electrolyte tetrabutylammonium perchlorate).[18] The computation of the energetics of the protonation pattern and of $E_m$ was based on the electrostatic continuum model, in which the linearized Poisson–Boltzmann equation was solved by the program MEAD from Bashford and Karplus.[19] Our own program Karlsberg[20] was used to sample the ensemble of protonation patterns by a Monte Carlo (MC) method. The dielectric constant was set to $\varepsilon_P = 4$ inside the protein and $\varepsilon_W = 80$ for solvent and protein cavities corresponding to water. All computations were performed in the S1 state[21] of the $Mn_4Ca$ cluster at 300 K, pH 7.0, and an ionic strength of 100 mM. MC sampling yielded the probabilities $[A_{ox}]$ and $[A_{red}]$ of the oxidized and reduced states of the redox-active compound A, respectively. The values of $E_m(Pheo_{D1}/Pheo_{D2})$ in the protein environment were calculated from the Nernst equation. For convenience, the computed $E_m$ values are given with millivolt accuracy, without implying that the last digit is significant. As the present study was done under the same conditions as in previous computations, further details on error estimates and comparisons with the previous results can be obtained from references [15,16].

Received: October 27, 2005
Published online: February 17, 2006

**Keywords:** cations · chlorophyll · electron transfer · photosynthesis · redox chemistry

[1] H. Michel, J. Deisenhofer, *Biochemistry* **1988**, *27*, 1.
[2] M. L. Groot, N. P. Pawlowicz, L. J. G. W. van Wilderen, J. Breton, I. H. M. van Stokkum, R. van Grondelle, *Proc. Natl. Acad. Sci. USA* **2005**, *102*, 13087.
[3] A. W. Rutherford, J. E. Mullet, A. R. Crofts, *FEBS Lett.* **1981**, *123*, 235.
[4] M. C. W. Evans, Y. E. Atkinson, R. C. Ford, *Biochim. Biophys. Acta* **1985**, *806*, 247.
[5] F. Rappaport, M. Guergova-Kuras, P. J. Nixon, B. A. Diner, J. Lavergne, *Biochemistry* **2002**, *41*, 8518.
[6] K. Gibasiewicz, A. Dobek, J. Breton, W. Leibl, *Biophys. J.* **2001**, *80*, 1617.
[7] T. Noguchi, T. Tomo, Y. Inoue, *Biochemistry* **1998**, *37*, 13614.
[8] B. A. Diner, E. Schlodder, P. J. Nixon, W. J. Coleman, F. Rappaport, J. Lavergne, W. F. J. Vermaas, D. A. Chisholm, *Biochemistry* **2001**, *40*, 9265.
[9] V. I. Prokhorenko, A. R. Holzwarth, *J. Phys. Chem. B* **2000**, *104*, 11563.
[10] H. Dau, K. Sauer, *Biochim. Biophys. Acta* **1996**, *1273*, 175.
[11] R. de Wijn, H. J. van Gorkom, *Biochim. Biophys. Acta* **2002**, *1553*, 302.
[12] M. Grabolle, H. Dau, *Biochim. Biophys. Acta* **2005**, *1708*, 209.
[13] J. P. Dekker, R. van Grondelle, *Photosynth. Res.* **2000**, *63*, 195.
[14] B. Loll, J. Kern, W. Saenger, A. Zouni, J. Biesiadka, *Nature* **2005**, *438*, 1040.
[15] H. Ishikita, E.-W. Knapp, *J. Am. Chem. Soc.* **2005**, *127*, 14714.
[16] H. Ishikita, E.-W. Knapp, *Biochemistry* **2005**, *44*, 14772.
[17] B. R. Brooks, R. E. Bruccoleri, B. D. Olafson, D. J. States, S. Swaminathan, M. Karplus, *J. Comput. Chem.* **1983**, *4*, 187.
[18] R. R. Bucks, T. L. Netzel, I. Fujita, S. G. Boxer, *J. Phys. Chem.* **1982**, *86*, 1947.
[19] D. Bashford, M. Karplus, *Biochemistry* **1990**, *29*, 10219.
[20] B. Rabenstein, *Karlsberg online manual* **1999**, http://agknapp.chemie.fu-berlin.de/karlsberg/.
[21] P. Joliot, A. Joliot, B. Kok, *Biochim. Biophys. Acta* **1968**, *153*, 635.

 © 2006 Wiley-VCH Verlag GmbH & Co. KGaA, Weinheim 

Cyclizations

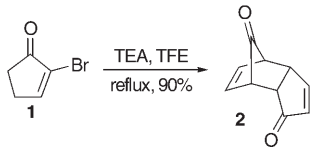
DOI: 10.1002/anie.200503812

# Deantiaromatization as a Driving Force in an Electrocyclic Reaction**

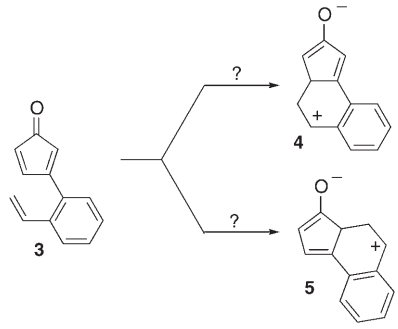
*Michael Harmata,* Pinguan Zheng, Peter R. Schreiner,* and Armando Navarro-Vázquez*

Antiaromatic molecules are characterized by pronounced kinetic instability,[1] which leads to rapid reactions with a variety of reagents and reactants to afford products that are no longer antiaromatic. The dimerizations of cyclobutadienes[2] and cyclopentadienones[3] are classic examples of this behavior. Snapper and co-workers have shown in the intramolecular cycloaddition chemistry of cyclobutadienes that the use of deantiaromatization as a driving force in organic reactions is not only of theoretical interest.[4] We wondered how broadly this concept could be applied and thus have begun a program of study to uncover the scope of deantiaromatization as a driving force in organic reactions.

We recently reported the generation of cyclopentadienones from 2-bromocyclopentenones as a general approach to certain cyclopentadienone dimers (Scheme 1).[5] We surmised that this procedure was one that involved the relatively slow generation of cyclopentadienone, such that this reactive intermediate could be trapped effectively with a reactant other than itself in synthetically useful yields. We chose to examine the electrocyclic ring-closing reaction of cyclopentadienones represented by **3** (Scheme 2). At the outset, we did not know if the cyclization of such a species would be regioselective for the 2- or 4-position or how the intermediates in the reaction would evolve. Indeed, we were not certain that the reaction would work to produce any kind of product, except possibly the corresponding cyclopentadienone dimers.[6]

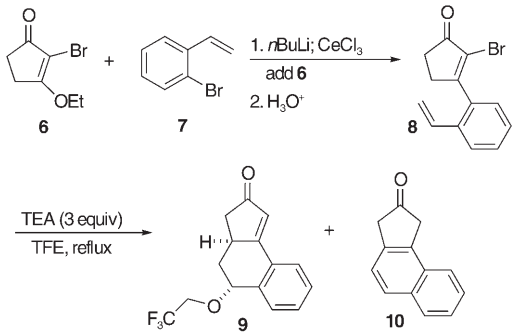



***Scheme 1.*** Formation of the cyclopentadienone dimer. TEA: triethylamine, TFE = trifluoroethanol.




***Scheme 2.*** Possible electrocyclizations of cyclopentadienone **3**.

We began our study by examination of the chemistry of **8**, which was prepared by the addition of an aryl trichlorocerate to 2-bromo-3-ethoxycyclopentenone[7,8] followed by hydrolysis (Scheme 3). The reaction of this compound under our standard conditions for the formation of cyclopentadienone (TEA, TFE, reflux) resulted in the formation of **9** in 63% yield, along with the elimination product **10** (ca. 6%)[9] and recovered starting material (16%). Compound **10** was identified by comparison with reported NMR spectral data. The fact that TFE was incorporated into **9** was clearly evident in both the $^{13}C$ and $^{1}H$ NMR spectra of the product. For example, a quartet appeared at $\delta = 66.1$ ppm ($J = 34.1$ Hz) in the $^{13}C$ NMR spectrum, which is indicative of the trifluoromethyl group. The structural assignment based on this and other NMR data was confirmed by X-ray analysis (Figure 1).[10]




***Scheme 3.*** Electrocyclization of **8** via a cyclopentadienone intermediate.

Excited by this result, we explored other reaction conditions that might minimize the formation of **10**, while

[*] Prof. M. Harmata, P. Zheng
Department of Chemistry
University of Missouri—Columbia
Columbia, MO 65211 (USA)
Fax: (+1) 573-882-2754
E-mail: harmatam@missouri.edu
Prof. Dr. P. R. Schreiner
Institut für Organische Chemie
Justus-Liebig-Universität
Heinrich-Buff-Ring 58, 35392 Giessen (Germany)
Fax: (+49) 641-99-34309
E-mail: prs@org.chemie.uni-giessen.de
Dr. A. Navarro-Vázquez
Departamento de Química Orgánica y Unidad Asociada al CSIC
Facultade de Química
Universidade de Santiago de Compostela
15782 Santiago de Compostela (Spain)

[**] This work was supported by the National Science Foundation to whom we are grateful. We thank Dr. Charles L. Barnes for the acquisition of the X-ray data, the Centro de Supercomputación de Galicia (CESGA) for allocation of computer time, and Halocarbon Products Corp. for fluorinated solvents.

 InterScience © 2006 Wiley-VCH Verlag GmbH & Co. KGaA, Weinheim 

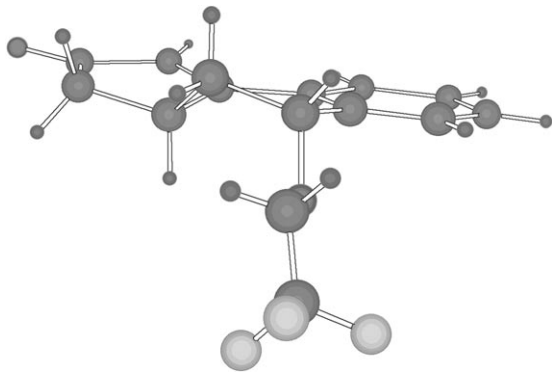
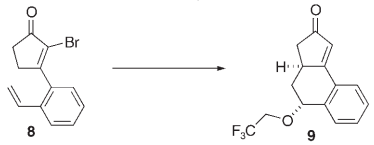


***Figure 1.*** Crystal structure of **9**.

promoting complete conversion of the starting material. The results are summarized in Table 1.

***Table 1:*** Optimization of the electrocyclization reaction of **8**.



**8** **9**

| Entry | Base (equiv) | Solvent | *T* [°C] (time) | Yield [%] |
|---|---|---|---|---|
| 1 | TEA (3) | TFE | reflux (2 days) | 63 |
| 2 | TEA (3) | TFE | 50 (50 h) | 56 |
| 3 | TEA (3) | TFE | 50 (7 days) | 66 |
| 4 | TEA (3) | TFE | 60 (3 days) | 66 |
| 5 | TEA (3) | TFE | 70 (2 days) | 69 |
| 6 | TEA (3) | TFE | 90 (2 days) | 60[a] |
| 7 | TEA (3) | MeCN | reflux, (12 h) | –[b] |
| 8 | TEA (3) | THF | reflux, (12 h) | –[b] |
| 9 | TEA (3) | EtOH | 50 (3 days) | –[b] |
| 10 | TEA (3) | HFIP | 50 (3 days) | –[b] |
| 11 | TEA (3) | HFIP | 50 (7 days) | –[b] |
| 12 | TEEDA (1.2) | TFE | 50 (3 days) | 39 |
| 13 | TEEDA (1.2) | MeCN | reflux, (2 days) | –[b] |
| 14 | DIPEA (1.2) | TFE | 50 (3 days) | 43 |
| 15 | DIPEA (1.2) | MeCN | reflux, (2 days) | [b] |
| 16 | DBU (1.2) | TFE | 50 (2 days) | 63 |
| 17 | DBU (1.2) | MeCN | 50 (2 days) | –[c] |
| 18 | DBU (1.2) | THF | 50 (2 days) | –[c] |
| 19 | HMPP (1.5) | TFE | 70 (2 days) | 54 |

[a] Compound **10** was also isolated in 29% yield. [b] Only the starting material was recovered during the reaction. [c] Only cyclopentadienone dimers were isolated in approximately 30% yield. DBU: 1,8-diazabicyclo-[5.4.0]undec-7-ene; DIPEA: diisopropylethylamine; HMPP: 1,3,4,6,7,8-hexahrdro-1-methyl-2H-pyrimido[1,2-a]pyrimidine; TEEDA: tetraethylethylendiamine; HFIP = hexafluoroisopropanol.

We thought that lowering the reaction temperature might help suppress the formation of **10**, but a correspondingly longer reaction time would be required. Thus, stirring **8** in TFE in the presence of TEA at 50 °C for 50 h afforded **9** in 56% yield, with no evidence of the formation of **10** (Table 1, entry 2). However, $^1$H NMR spectroscopic analysis of the crude reaction mixture showed a 71:29 ratio of **9** to starting material. When the reaction was allowed to proceed for 7 days, this ratio grew to 88:12, and the yield of isolated **9** was 66%. In the hope that small rises in temperature would increase the rate of the reaction without lowering the yield of **9**, we conducted experiments at 60, 70, and 90 °C and found that the reaction at 70 °C for 2 days proceeded to give the product in good yield (69%) with minimal formation of **10**, though some starting material still remained (Table 1, entry 5). The reaction that was run at 60 °C worked reasonably well (Table 1, entry 4), but that at 90 °C afforded significant amounts of **10** (Table 1, entry 6). Interestingly, when **9** was refluxed in TFE in the presence of TEA for 2 days, the formation of **10** was not observed, thus indicating that **9** is not an intermediate in the formation of **10**.

An investigation of other solvents suggested that TFE was the best solvent for the reaction. It was both surprising and interesting to find that no reaction took place in hexafluoroisopropanol. The reasons for this are not clear at this time. Several other bases were examined, but none were superior to TEA (Table 1, entries 12–19). Though DBU also worked effectively, it was not any better than TEA, whose lower cost made it the base of choice.

During our optimization studies, we subjected a number of other substrates to what at the time were our best reaction conditions: TEA, TFE, 50 °C, 7 days. The results are collected in Table 2 along with those for when the reaction was conducted at higher temperature (70 °C) for a shorter time (2 days).

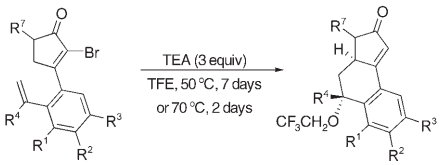
The reaction offers reasonable generality. Electron-rich aromatic systems appear to be better substrates than less-substituted aromatic rings, which is consistent with our mechanistic proposal. In particular, we note that **14** and **16** formed in high yield. While most of the products form with high diastereoselectivity, that of **16** was high at 50 °C (10:1) but deteriorated to 5.4:1 at 70 °C. We attribute this decrease in diastereoselectivity to a slower trapping of the intermediate cation by the solvent, which perhaps allows certain conformational changes to take place, thus resulting in some loss of facial selectivity.

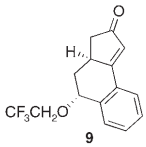
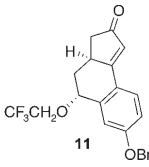
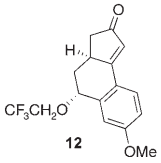
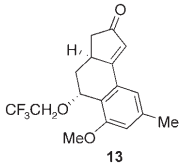
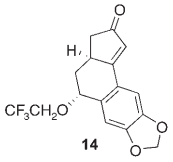
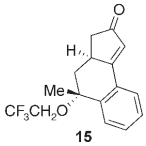
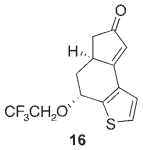
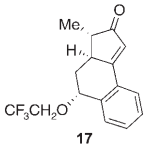
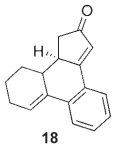
Though the yield of the isolated product was low, the preparation of **17** demonstrated that an electron-donating group on the cyclopentadienone unit does not prevent the cyclization reaction from occurring. We imagine that placement of an electron-withdrawing group would facilitate the reaction, but this has yet to be tested. The structure of **17** was firmly established by X-ray analysis.[10] We have rationalized the formation of the observed products by a mechanism that involves a cyclopentadienone intermediate (Scheme 4). This proposal is based on our previous work and the work of others in which pseudo-cine substitution of a cyclopentadienone was formulated as proceeding via such an intermediate.[11]

We evaluated the feasibility of the proposed mechanism by means of density functional theory (DFT) computations on system **8b**, along with thiophenyl systems **16b** and **19b**. For zwitterionic intermediates and some of the transition structures of biradicaloid character, we used a broken-spin-symmetry unrestricted determinant (UBS)[12] for the DFT computations. All structures were optimized at the B3LYP[13]/6-31G*[14] level of theory;[15] single-point energies were computed at the B3LYP/6-311 + G** level. Solvent effects

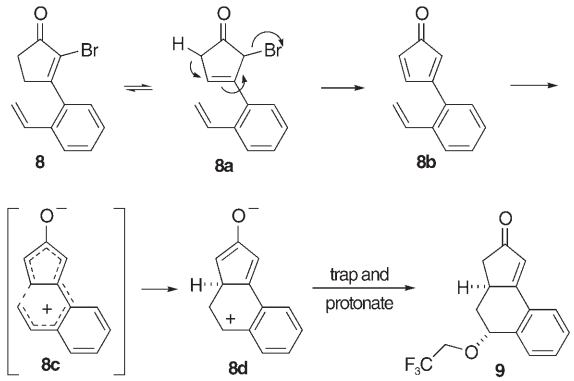
 © 2006 Wiley-VCH Verlag GmbH & Co. KGaA, Weinheim 

***Table 2:*** Electrocyclization of a series of bromocyclopentenones.




| Entry | Product | Yield [%] 50 °C[a] | 70 °C[a] |
|---|---|---|---|
| 1 |  **9** | 56 | 69 |
| 2 |  **11** | 64 | 61 |
| 3 |  **12** | 54 (72) | 64 |
| 4 |  **13** | 39 (58) | 61 (72) |
| 5 |  **14** | 71 | 78 |
| 6 |  **15** | 36 (49) | 50 (71) |
| 7 |  **16** | 84[b] | 86[c] |
| 8 |  **17** | 24 (44)[d] | 33 (67)[e] |
| 9 |  **18** | 23 | – |

[a] Yield in parentheses are based on the recovered starting material. [b] d.r. = 10:1. [c] d.r. = 5.4:1. [d] d.r. = 5.5:1. [e] d.r. = 4.5:1.

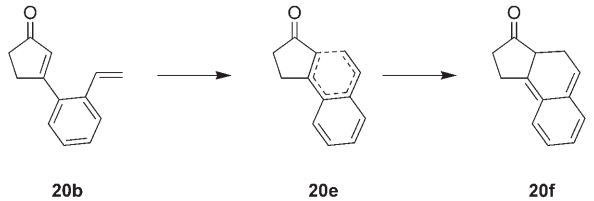



***Scheme 4.*** Proposed mechanism for the conversion of **8**.

were modeled using the polarized continuum model (PCI)[16] and all gas-phase structures were reoptimized at the PCM-B3LYP/6-31G* level. To model the solvation of trifluoroethanol, we employed the ethanol parameters provided with Gaussian03[17] in combination with a relative permittivity $\varepsilon$ of 26.73 and an effective solvent radius of 3.0 Å; single-point energies were computed at the PCM-B3LYP/6-311+G** level as well. Harmonic frequencies were computed on all optimized structures to verify the nature of the stationary points and to obtain thermochemical quantities. Reported free energies $\Delta G_{298.15\,K}$ were obtained by inclusion of B3LYP/6-31G* thermochemical corrections on the B3LYP/6-311+G** computations. NICS[18] values were computed by using the GIAO method[19] on the gas-phase B3LYP/6-311+G** densities at points 1.0 Å over the cyclopentadienone-ring point (we have chosen the less-congested face from the two possibilities; see the Supporting Information for the location of computed points) and reported as NICS(1) values. The ring critical points used for the NICS computations were located by using the AIMPAC program of Bader and co-workers.[20] In excellent agreement with experimental values, we found that the proposed cyclopentadienone intermediate **8b** has a kinetic preference for cyclization at C4 ($\Delta G^{\ddagger}_{298.15\,K} = 25.0$ kcal mol$^{-1}$ in the gas phase) via the conrotatory transition state **8c**, despite the fact that the disrotatory cyclization onto C2 via disrotatory transition state **8e** ($\Delta G^{\ddagger}_{298.15\,K} = 31.6$ kcal mol$^{-1}$ in the gas phase) is enthalpically favored ($\Delta\Delta G_{298.15\,K} = 21.3$ kcal mol$^{-1}$). This preference is due to the closed-shell nature of **8f** (relative to the zwitterionic/open-shell character of **8d**), which is highly unfavorable in the gas phase. Both cyclization modes benefit kinetically and thermodynamically from the inclusion of solvent effects, and this effect is particularly important for the cyclization at C4 ($\Delta\Delta G^{\ddagger}_{298.15\,K} = 11.4$ kcal mol$^{-1}$) because of the stabilization of the partially zwitterionic intermediate **8d** and the transition state **8c**. The thermodynamic preference is also decreased to $\Delta\Delta G^{\ddagger}_{298.15\,K} = 18.9$ kcal mol$^{-1}$.

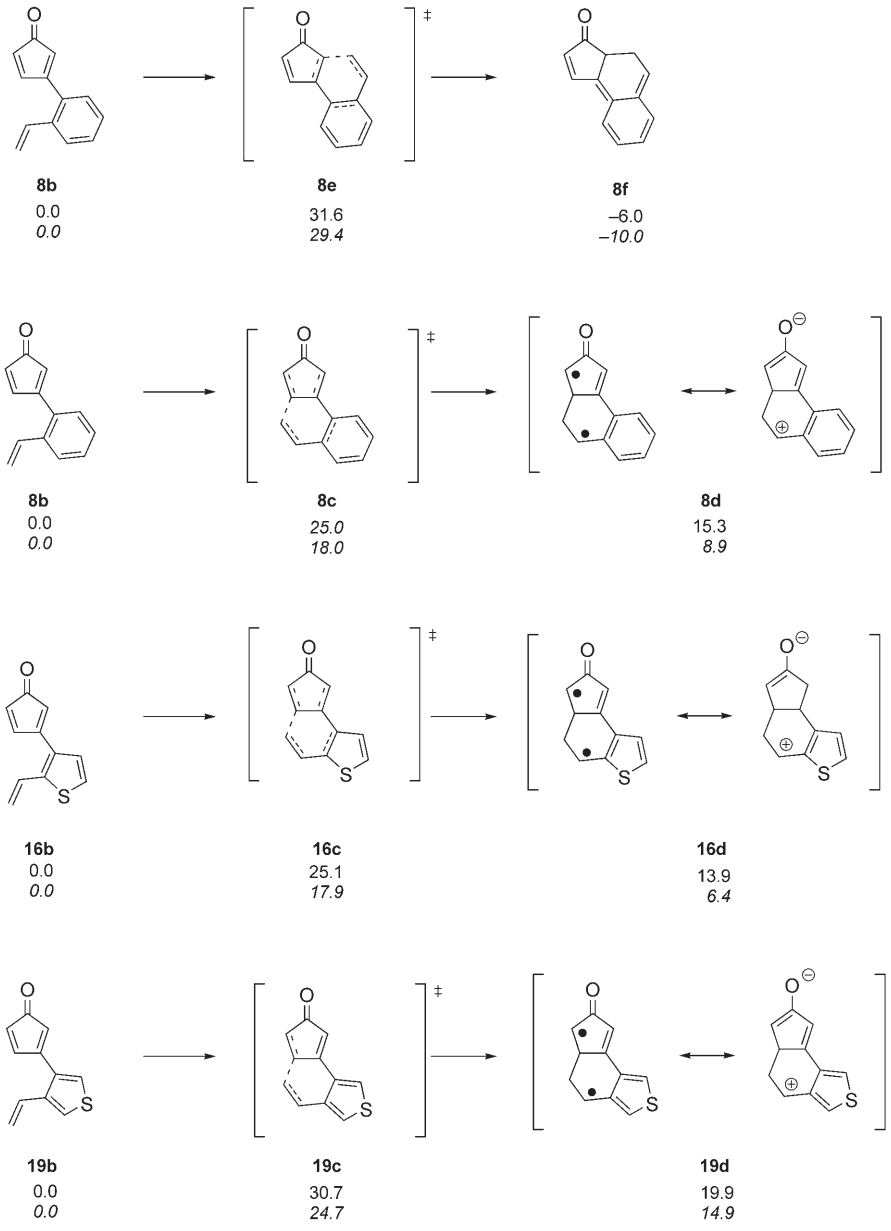
To test the hypothesis that deantiaromatization of the cyclopentadienone moiety[21] is the driving force of the observed cyclizations, we computed the activation and reaction energies for disrotatory cyclization at C2 on the cyclopentenone model system **20b** (Scheme 5). The results strongly support our hypothesis, as this process is both

 © 2006 Wiley-VCH Verlag GmbH & Co. KGaA, Weinheim 




***Scheme 5.*** Computed relative free energies $\Delta G_{298.15\,K}$ (gas phase) for the disrotatory cyclization of **20b**.

thermodynamically ($\Delta\Delta G_{298.15\,K} = 18.7$ kcal mol$^{-1}$) and kinetically ($\Delta\Delta G^{\ddagger}_{298.15\,K} = 8.9$ kcal mol$^{-1}$) much more disfavorable relative to the cyclization at C2 of **8b** (Scheme 6).



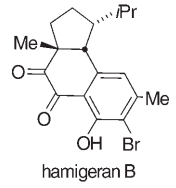

***Scheme 6.*** Computed relative free energies $\Delta G_{298.15\,K}$ values for the proposed reaction pathways. Normal type: gas phase; italic: in a solution of TFE.

NICS(1) computations (Figure 2) agree with the concept of deantiaromatization. Whereas **8b**[22] is moderately antiaromatic (positive NICS(1)), the negative NICS(1) value in transition state **8c** shows the involvement of the cyclopentenone π system in the eight-electron aromatic Möbius arrangement in the cyclization at C4. Clearly, the antiaromatic character of the starting material **8b** is entirely overcome by this pronounced and favorable cyclic delocalization. Quite the opposite is found for transition state **8e** for the cyclization at C2, in which the antiaromatic character is significantly increased. The finding that the aromaticity of the products **8d** and **8f** is virtually the same emphasizes the notion of deantiaromatization as a transition-state effect.

We have also studied the cyclization at C4 of the electron-rich 2-vinylthiophen-3-yl **16b** and 4-vinylthiophen-3-yl **19b** intermediates. The reaction and activation free energies for system **16b** (Scheme 6) are very similar to those computed for the aryl system **8b**. However, the cyclization at C4 of the 4-vinyl system **19b** is disfavored both kinetically and enthalpically by approximately 7 kcal mol$^{-1}$ with respect to the 2-vinyl system. The markedly different behavior of both thiophenyl systems can be attributed to the fact that the thiophene moiety can be considered as an independent, weakly aromatic unit that does not readily share its six π electrons with the rest of the molecule; this behavior is also evident in transition state **19c** (Scheme 6).

In accord with these computational results, we found that treatment of **19** under standard cyclization conditions afforded only the cyclopentadienone dimer **21** in good yield and as a single stereo- and regioisomer (Scheme 7).

In summary, we have demonstrated that an electrocyclic ring closure can occur in synthetically useful yields in an antiaromatic system, and we investigated this process through DFT computations. It should be noted that this reaction is not merely of theoretical interest; for example, the products of the process bear a striking resemblance to certain natural products, such as the antiviral agent hamigeran B.[23]



hamigeran B

Efforts to explore the extent to which these reactions are driven by deantiaromatization, expand the scope of the reaction, apply the meth-

 © 2006 Wiley-VCH Verlag GmbH & Co. KGaA, Weinheim 

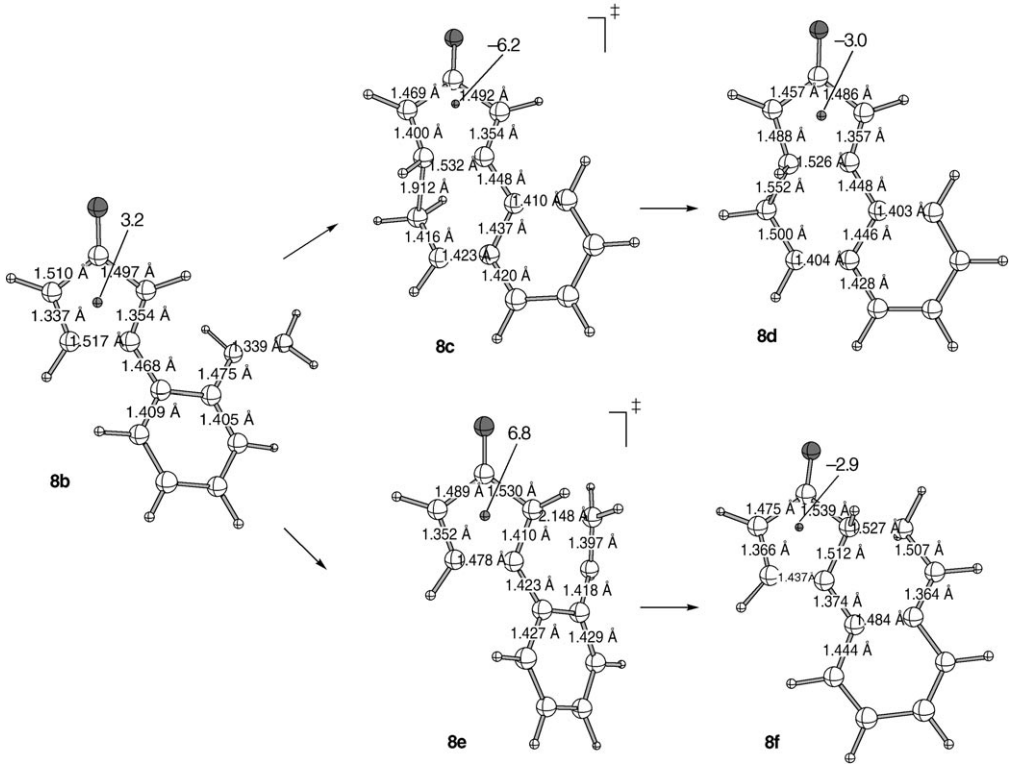
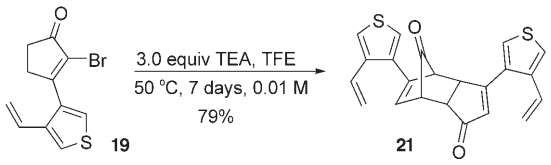



***Figure 2.*** NICS(1) GIAO-B3LYP/6-311+G**//B3LYP/6-31G* computed values in ppm.




***Scheme 7.*** Attempted electrocyclization of the 4-vinylthiophen-3-yl system **19**.

odology to compounds such as hamigeran B, and create new examples of reactions driven by deantiaromatization are in progress. The results will be reported in due course.

Received: October 27, 2005
Published online: February 22, 2006

**Keywords:** antiaromaticity · computational chemistry · cyclopentadienones · electrocyclization · hamigeran B

[1] a) K. B. Wiberg, *Chem. Rev.* **2001**, *101*, 1317; b) A. D. Allen, T. T. Tidwell, *Chem. Rev.* **2001**, *101*, 1333; c) R. Breslow, *Acc. Chem. Res.* **1973**, *6*, 393.

[2] a) G. Maier, *Angew. Chem.* **1988**, *100*, 317; *Angew. Chem. Int. Ed. Engl.* **1988**, *27*, 309; b) T. Bally, S. Masamune, *Tetrahedron* **1980**, *36*, 343; c) A. Efraty, *Chem. Rev.* **1977**, *77*, 691; d) G. Maier, *Angew. Chem.* **1974**, *86*, 491; *Angew. Chem. Int. Ed. Engl.* **1974**, *13*, 425.

[3] M. A. Ogliaruso, M. G. Romanelli, E. I. Becker, *Chem. Rev.* **1965**, *65*, 261.

[4] a) J. Limanto, K. S. Khuong, K. N. Houk, M. L. Snapper, *J. Am. Chem. Soc.* **2003**, *125*, 16310; b) J. Limanto, J. A. Tallarico, J. R. Porter, K. S. Khuong, K. N. Houk, M. L. Snapper, *J. Am. Chem. Soc.* **2002**, *124*, 14748; c) J. Limanto, M. L. Snapper, *J. Am. Chem. Soc.* **2000**, *122*, 8071; d) J. Limanto, M. L. Snapper, *J. Org. Chem.* **1998**, *63*, 6440; e) J. A. Tallarico, M. L. Randall, M. L. Snapper, *J. Am. Chem. Soc.* **1996**, *118*, 9196.

[5] M. Harmata, C. L. Barnes, J. Brackley, G. Bohnert, P. Kirchhoefer, L. Kürti, P. Rashatasakhon, *J. Org. Chem.* **2001**, *66*, 5232.

[6] However, we were aware, of course, that the paths to **4** and **5** were fundamentally different, the former being directly analogous to an electrocyclization of an octatetraene (conrotatory) and the latter being analogous to an electrocyclization of hexatriene (disrotatory). Other things being equal, it is well known that the former electrocyclization proceeds much more rapidly than the latter, so that a competition between the two should favor the conrotatory [8π] electrocyclization; for examples and references, see: a) B. Lecea, A. Arrieta, F. P. Cossío, *J. Org. Chem.* **2005**, *70*, 1035; b) S. Sakai, S.-y. Takane, *J. Phys. Chem.* A **1999**, *103*, 2878.

[7] a) B. B. Kikani, J. R. McKee, M. Zanger, *Synthesis* **1991**, 176; b) W. C. Black, C. Brideau, C.-C. Chan, S. Charleson, N. Chauret, D. Claveau, D. Ethier, R. Gordon, G. Greig, J. Guay, G. Hughes, P. Jolicoeur, Y. Leblanc, D. Nicoll-Griffith, N. Ouimet, D. Riendeau, D. Visco, Z. Wang, L. Xu, P. Prasit, *J. Med. Chem.* **1999**, *42*, 1274.

[8] a) B. A. Narayanan, W. H. Bunnelle, *Tetrahedron Lett.* **1987**, *28*, 6261; b) M. T. Crimmins, D. Dedopoulou, *Synth. Commun.* **1992**, *22*, 1953.

[9] In this experiment, compound **10** was not isolated, but its presence detected in the $^1$H NMR spectrum of the crude reaction mixture; the isolation and characterization of **10** was achieved through other experiments; the $^1$H and $^{13}$C NMR spectra of **10** matched those in the literature: K. K. De Fonseka, J. J. McCullough, A. J. Yarwood, *J. Am. Chem. Soc.* **1979**, *101*, 3277.

[10] CCDC-285951 (**9**) and -285952 (**17**) contain the supplementary crystallographic data for this paper. These data can be obtained

 © 2006 Wiley-VCH Verlag GmbH & Co. KGaA, Weinheim 

free of charge from The Cambridge Crystallographic Data Centre via www.ccdc.cam.ac.uk/data_request/cif.
[11] a) F. G. West, G. U. Gunawardena, *J. Org. Chem.* **1993**, *58*, 5043; b) G. U. Gunawardena, A. M. Arif, F. G. West, *J. Am. Chem. Soc.* **1997**, *119*, 2066.
[12] J. Gräfenstein, E. Kraka, M. Filatov, D. Cremer, *Int. J. Mol. Sci.* **2002**, *3*, 360.
[13] a) A. D. Becke, *J. Chem. Phys.* **1993**, *98*, 5648; b) C. Lee, W. Yang, R. G. Parr, *Phys. Rev. B* **1988**, *37*, 785.
[14] W. Hehre, L. Radom, P. v. R. Schleyer, J. A. Pople, *Ab Initio Molecular Orbital Theory*, Wiley, New York, **1986**.
[15] P. R. Schreiner, A. Navarro-Vázquez, M. Prall, *Acc. Chem. Res.* **2005**, *38*, 29.
[16] S. Miertus, E. Scrocco, J. Tomasi, *Chem. Phys.* **1981**, *55*, 117.
[17] Gaussian 03, Revision B.05, M. J. Frisch et al., Gaussian, Inc., Wallingford, CT, **2004**.
[18] P. v. R. Schleyer, C. Maerker, A. Dransfeld, H. Jiao, N. J. R. v. E. Hommes, *J. Am. Chem. Soc.* **1996**, *118*, 6317.
[19] K. Wolinski, J. F. Hinton, P. Pulay, *J. Am. Chem. Soc.* **1990**, *112*, 8251.
[20] http://www.chemistry.mcmaster.ca/aimpac.
[21] P. Quadrelli, S. Romano, L. Toma, P. Caramella, *J. Org. Chem.* **2003**, *68*, 6035.
[22] K. Najafian, P. v. R. Schleyer, T. T. Tidwell, *Org. Biomol. Chem.* **2003**, *1*, 3410.
[23] D. L. J. Clive, J. Wang, *Org. Prep. Proced. Int.* **2005**, *37*, 1.

 © 2006 Wiley-VCH Verlag GmbH & Co. KGaA, Weinheim 

*Fullerenes*

DOI: 10.1002/anie.200503964

# Selective Synthesis of a Trifluoromethylated Fullerene and the Crystal Structure of $C_{60}(CF_3)_{12}$**

*Sergey I. Troyanov,* Anton Dimitrov, and Erhard Kemnitz**

Like fluorofullerenes, perfluoroalkyl fullerenes are potential compounds in the further derivatization of fullerene and the creation of new materials, including light-harvesting systems.[1] Compared to fluorofullerenes, trifluoromethyl fullerenes are possibly more useful because they have increased electron-withdrawing properties and decreased susceptibility to nucleophilic substitution. There are a limited number of reports on the trifluoromethylation of fullerenes. Known synthetic methods are based on the reaction of fullerenes with compounds that readily release $CF_3$ radicals, such as metal trifluoroacetates[2,3] or $CF_3I$.[4] Up until now, these methods resulted in complex mixtures of $CF_3$ derivatives that needed to be separated by means of fractional sublimation and high-pressure liquid chromatography (HPLC).[5] The latest achievement in the chemistry of trifluoromethylated fullerenes was the synthesis of $C_{60}$ derivatives by reaction with a gas flow of $CF_3I$ with heating.[6] The crystals of one of the $C_{60}(CF_3)_{10}$ isomers were grown after separation by two-stage HPLC, and its molecular structure determined by X-ray crystallographic studies. Analogous methods were used for the preparation of trifluoromethylated $C_{70}$.[6] The separation of $C_{70}(CF_3)_n$ mixtures by HPLC resulted in the isolation of individual compounds and their investigation by mass-spectrometric and NMR spectroscopic analysis. The molecular structures of $C_{70}(CF_3)_8$ and $C_{70}(CF_3)_{10}$ have been recently determined by X-ray crystallography.[7]

Herein, we report the first selective synthesis and X-ray crystallographic study of $C_{60}(CF_3)_{12}$. Remarkably, a single-stage reaction of $C_{60}$ with $CF_3I$ vapor resulted in a high-yield preparation of $C_{60}(CF_3)_{12}$, with high compositional and isomeric purity. The compound possesses a unique molecular and crystal structure which defines its physical properties, such as low solubility and volatility. Typically, $C_{60}$ (36 mg, 0.05 mmol) was placed in a glass ampoule and $CF_3I$ (ca. 0.3 mL, 0.7 g, 0.55 mmol) was condensed into the ampoule with cooling. The ampoule was sealed and a section of the ampoule containing the fullerene heated in an oven at 440(±5) °C for 2 days. [60]Fullerene reacted nearly completely, and the neck of the ampoule (at ca. 400 °C) was clogged with crystalline reaction products. The main product (65 mg, 84 % yield based on the amount of fullerene used) in the form of octahedrally shaped orange crystals was shown to be $C_{60}(CF_3)_{12}$ by single-crystal X-ray crystallography.[8] The next section of the ampoule (at a lower condensation temperature) contained some milligrams of an orange material, which was proven to be a mixture of $C_{60}(CF_3)_{12}$ and several higher trifluoromethylated derivatives according to the MALDI analysis. Furthermore, a large amount of crystalline $I_2$ was condensed; the excess liquid $CF_3I$ was deep violet in color owing to dissolved iodine.

Unusually for trifluoromethylated fullerenes, $C_{60}(CF_3)_{12}$ is insoluble in most organic solvents (benzene, toluene, hexane, *o*-dichlorobenzene, and carbon disulfide) and sparingly soluble in acetone; therefore, it can be readily separated from other $CF_3$ derivatives by washing. The IR spectrum contains several very strong absorption bands at 1160–1260 $cm^{-1}$ (Figure 1), which are characteristic of $CF_3$ groups.[3,5] The most prominent bands, with lower wave numbers, were observed at 1110, 1079, 1009, 988, 940, 886, 767, 758, 743, 737, 714, 679, 604, and 518 $cm^{-1}$. The compound is stable in air, and its complete sublimation in an inert atmosphere proceeds at 400–500 °C.

[*] Prof. Dr. S. I. Troyanov
Chemistry Department
Moscow State University
119992 Moscow (Russia)
Fax: (+7) 95-939-1240
E-mail: troyanov@thermo.chem.msu.ru
Dr. A. Dimitrov, Prof. Dr. E. Kemnitz
Institut für Chemie
Humboldt Universität Berlin
12489 Berlin (Germany)
Fax: (+49) 30-2093-7277
E-mail: erhard.kemnitz@chem.hu-berlin.de

[**] This work was partially supported by the Deutsche Forschungsgemeinschaft (KE 489/26-1) and the Russian Foundation for Basic Research (05-03-04006).

 © 2006 Wiley-VCH Verlag GmbH & Co. KGaA, Weinheim 

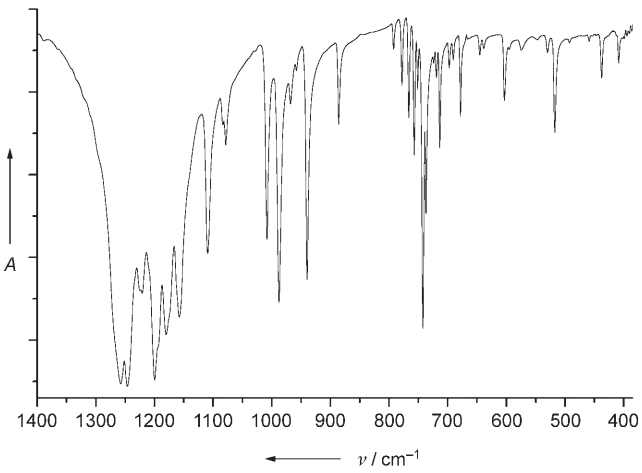



***Figure 1.*** IR spectrum of $S_6$-$C_{60}(CF_3)_{12}$.

The $C_{60}(CF_3)_{12}$ molecule is characterized by the high-symmetry point group $S_6$ (Figure 2), which coincides with the symmetry in the crystal. Twelve $CF_3$ groups form a continuous loop of alternating *para*- and *meta*-$C_6(CF_3)_2$ hexagons. Such an arrangement of 12 atoms/groups on the $C_{60}$ cage (denoted as $PM_hPM_hPM_hPM_hPM_hP$) has been predicted theoretically as the second most stable for $C_{60}Cl_{12}$ and $C_{60}Br_{12}$.[9,10] The most stable arrangement was the structure with two skewed pentagonal pyramids on opposite sides of the molecule. Obviously, the $CF_3$ groups, which are bulkier than Cl or Br atoms, destabilize the skewed pyramidal arrangement because of the presence of 1,2-adjacency. In fact, a low stability of the skewed pyramid for $C_{60}X_6$ compounds has been theoretically predicted for such bulky groups as *t*-Bu[9a] and $CF_3$.[10] Therefore, the experimentally determined structure with a continuous loop of $C_6(CF_3)_2$ hexagons agrees with theoretical expectations. The addition pattern in the $C_{60}$-$(CF_3)_{12}$ molecule differs considerably from that in the $C_1$-$C_{60}(CF_3)_{10}$ molecule,[6] so that the latter can not be considered as a precursor of the former.

The presence of $C_{60}(CF_3)_{12}$ was indicated by mass-spectrometric analysis of mixtures of trifluoromethylated $C_{60}$ obtained by different methods,[2–4,6] but the individual compound $C_{60}(CF_3)_{12}$ has not been isolated and characterized before. Other $C_{60}X_{12}$ compounds have been obtained experimentally, for example, $C_{60}Me_{12}$,[11] $C_{60}Ph_{12}$,[12] and $C_{60}Cl_{12}$.[13] The structure of the former was proposed to be unsymmetrical based on its $^1$H NMR spectrum,[11] whereas there was not enough experimental evidence to establish the structure of the two latter compounds.

There are only 15 independent fullerene C–C bonds (Table 1) owing to the high $S_6$ symmetry. Because of the absence of the fragments with high aromaticity, predominantly the double bonds C–C are short (average length: 1.373 Å), whereas predominantly the single $C(sp^2)$–$C(sp^2)$ bonds have an average length of 1.438 Å, close to the values of 1.391 and 1.455 Å, respectively, for [60]fullerene.[14] The $C(sp^2)$–$C(sp^3)$ bonds are significantly longer (average length: 1.525 Å). The longest C–C bonds in the molecule are the C–$CF_3$ bonds, with an average value of 1.542 Å. The C–F lengths lie in the narrow range of 1.325–1.342 Å; average angles are 111.2° for C-C-F and 107.7° for F-C-F. Both of the independent intramolecular F···F distances are 2.590 Å. All these values correspond well to those found in the $C_1$-$C_{60}(CF_3)_{10}$ molecule.[6]

***Table 1:*** Interatomic distances in $C_{60}(CF_3)_{12}$.

| Bond | *d* [Å] | Bond | *d* [Å] |
|---|---|---|---|
| Double C–C | | Single $C(sp^2)$–$C(sp^3)$ | |
| C(2)–C(3) | 1.357(1) | C(1)–C(2) | 1.548(1) |
| C(4)–C(9) | 1.374(1) | C(1)–C(3′) | 1.512(1) |
| C(5)–C(6) | 1.370(1) | C(1)–C(5) | 1.521(1) |
| C(7)–C(8) | 1.391(1) | C(2)–C(10′) | 1.520(1) |
| | | C(6)–C(10″) | 1.539(1) |
| | | C(9)–C(10) | 1.534(1) |
| Single $C(sp^2)$–$C(sp^2)$ | | C–$CF_3$ | |
| C(3)–C(4) | 1.465(1) | C(1)–C(11) | 1.538(1) |
| C(4)–C(5) | 1.427(1) | C(10)–C(12) | 1.546(1) |
| C(6)–C(7) | 1.429(1) | C-F(ave) | 1.332 |
| C(7)–C(8′) | 1.449(1) | | |
| C(8)–C(9) | 1.422(1) | | |

Analysis of crystal packing could help to understand some properties of the compound (Figure 3). A special feature of the packing is the arrangement of the molecules in linear chains along the c axis at a very short distance of 9.716 Å,

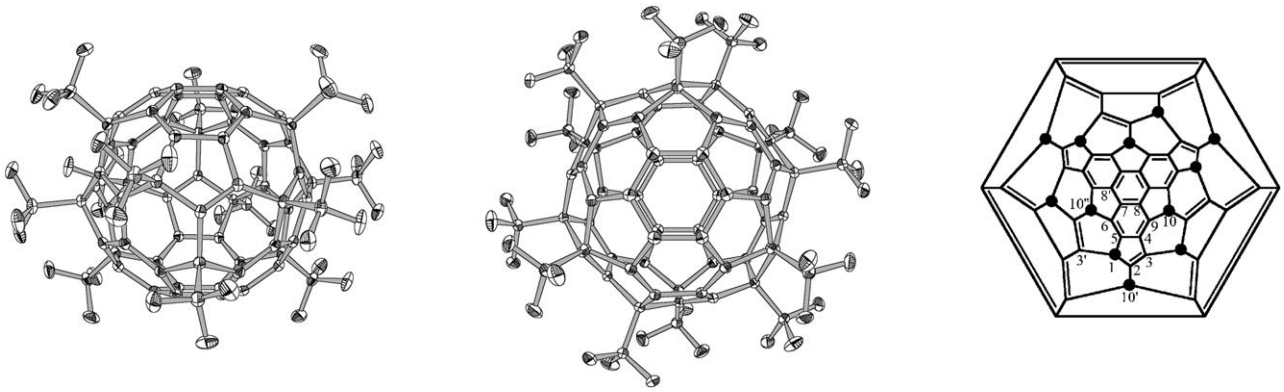



***Figure 2.*** Top and side views of the $C_{60}(CF_3)_{12}$ molecule (65% ellipsoids); Schlegel diagram with a numbering scheme for the carbon atoms of the cage.

 © 2006 Wiley-VCH Verlag GmbH & Co. KGaA, Weinheim 

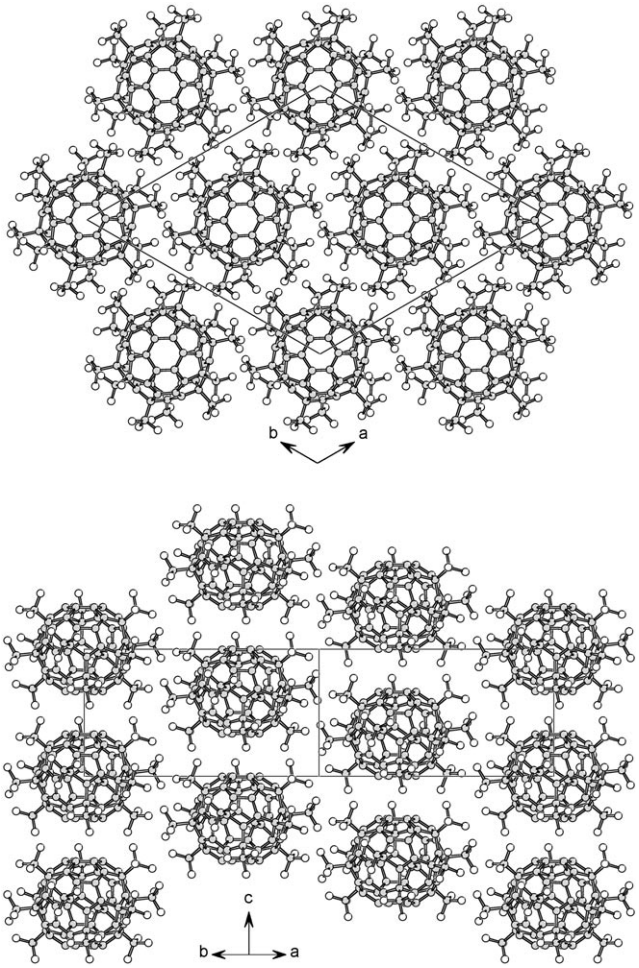



***Figure 3.*** Packing of the $C_{60}(CF_3)_{12}$ molecules in the crystal viewed along the c axis (above); the fragments of four chains in the (110) plane (below).

which is significantly shorter than the usual minimum distance of 10 Å between fullerene molecules (9.94 Å in the ordered cubic phase of $C_{60}$).[14,15] This arrangement is possible because of the absence of $CF_3$ groups at both poles of the molecule. Therefore, the pole hexagons of adjacent molecules are in close contact, separated by 3.316 Å, which is typical for short stacking interactions in the packing of flat aromatic molecules.[16] Notably, triene systems of the adjacent hexagons are rotated by 60° relative to one another, thus allowing effective interaction. Although some F atoms of the $CF_3$ groups are situated beyond the pole hexagons (Figure 2), these do not hinder the proximity of two adjacent molecules because of a relative rotation of 60° (a key–lock relationship). Moreover, six $CF_3$ groups that surround each hexagon–hexagon junction effectively shield it from further contact with the environment. Apparently, such a particular structure of the polymeric $C_{60}(CF_3)_{12}$ chains stabilizes them against being destroyed by dissolution or evaporation. The chains themselves are packed in a parallel hexagonal arrangement at distances of 11.953 Å.

In conclusion, the ampoule reaction between [60]fullerene and gaseous $CF_3I$ at 440 °C resulted in the first selective synthesis of the trifluoromethylated fullerene $C_{60}(CF_3)_{12}$, thus allowing its preparative-scale synthesis. In the $C_{60}(CF_3)_{12}$ molecule, twelve $CF_3$ groups are arranged in a continuous loop of alternating *para*- and *meta*-$C_6(CF_3)_2$ hexagons. In the crystal packing, stacking interactions between the molecules and the shielding effects of the $CF_3$ groups result in the formation of infinite linear chains, thus accounting for the low volatility and solubility of the compound.

Received: November 8, 2005

**Keywords:** fullerenes · regioselectivity · structure elucidation · synthesis design · trifluoromethylation

[1] G. A. Burley, A. G. Avent, I. V. Gol'dt, P. B. Hitchcock, H. Al-Matar, D. Paolucci, F. Paolucci, P. W. Fowler, A. Soncini, J. M. Street, R. Taylor, *Org. Biomol. Chem.* **2004**, *2*, 319–329.

[2] I. S. Uzkikh, E. I. Dorozhkin, O. V. Boltalina, A. I. Boltalin, *Dokl. Chem.* **2001**, *379*, 204–207.

[3] A. D. Darwish, A. K. Abdul-Sada, A. G. Avent, Yu. I. Lyakhovetsky, E. A. Shilova, R. Taylor, *Org. Biomol. Chem.* **2003**, *1*, 3102–3110.

[4] P. J. Fagan, P. J. Krusic, C. N. McEwen, J. Lazar, D. H. Parker, N. Herron, E. Wasserman, *Science* **1993**, *262*, 404–407.

[5] A. A. Goryunkov, I. V. Kuvychko, I. N. Ioffe, D. L. Dick, L. N. Sidorov, S. H. Strauss, O. V. Boltalina, *J. Fluorine Chem.* **2003**, *124*, 61–64.

[6] I. E. Kareev, I. V. Kuvychko, S. F. Lebedkin, S. M. Miller, O. P. Anderson, K. Seppelt, S. H. Strauss, O. V. Boltalina, *J. Am. Chem. Soc.* **2005**, *127*, 8362–8375.

[7] a) A. A. Goryunkov, E. I. Dorozhkin, D. V. Ignat'eva, L. N. Sidorov, E. Kemnitz, G. M. Sheldrick, S. I. Troyanov, *Mendeleev Commun.* **2005**, 225–227; b) I. E. Kareev, I. V. Kuvychko, A. A. Popov, S. F. Lebedkin, S. M. Miller, O. P. Anderson, S. H. Strauss, O. V. Boltalina, *Angew. Chem.* **2005**, *117*, 8198–8201; *Angew. Chem. Int. Ed.* **2005**, *44*, 7984–7987.

[8] The crystal data for $C_{60}(CF_3)_{12}$ were collected on an IPDS diffractometer (Stoe) at 100 K (graphite monochromated $Mo_{K\alpha}$ radiation, $\lambda = 0.71073$ Å); $M_r = 1548.72$, trigonal, $R\bar{3}$, $a = 20.704(1)$, $c = 9.7161(6)$ Å, $V = 3606.8(4)$ Å$^3$, $Z = 3$; 14138 reflections were collected, independent 3507. Structure solution with SHELXS-97. The final anisotropic LS refinement (SHELXL-97) with 163 parameters converged to $wR_2 = 0.097$ and $R_1 = 0.037$. CCDC-286205 contains the supplementary crystallographic data for this paper. These data can be obtained free of charge from The Cambridge Crystallographic Data Centre via www.ccdc.cam.ac.uk/data_request/cif.

[9] a) B. W. Clare, D. L. Kepert, *J. Mol. Struct. (Theochem)* **2003**, *621*, 211–231; b) B. W. Clare, D. L. Kepert, *J. Mol. Struct. (Theochem)* **1995**, *340*, 125–142.

[10] A. A. Goryunkov, I. N. Ioffe, I. V. Kuvychko, T. S. Yankova, V. Yu. Markov, A. A. Streletskii, D. L. Dick, L. N. Sidorov, O. V. Boltalina, S. H. Strauss, *Fullerenes Nanotubes Carbon Nanostruct.* **2004**, *12*, 181–185.

[11] H. Al-Matar, A. K. Abdul-Sada, A. G. Avent, P. W. Fowler, P. B. Hitchcock, K. M. Rogers, R. Taylor, *J. Chem. Soc. Perkin Trans. 2* **2002**, 53–58.

[12] R. Taylor, G. J. Langley, M. F. Meidine, J. P. Parsons, Abdul-Sada, T. J. Dennis, J. P. Hare, H. W. Kroto, D. R. M. Walton, *J. Chem. Soc. Chem. Commun.* **1992**, 667–668.

[13] P. A. Troshin, O. Popkov, R. N. Lyubovskaya, *Fullerenes Nanotubes Carbon Nanostruct.* **2003**, *11*, 165–185.

[14] H.-B. Bürgi, E. Blanc, D. Schwarzenbach, S. Liu, Y. J. Lu, M. Kappes, J. A. Ibers, *Angew. Chem.* **1992**, *104*, 667–669; *Angew. Chem. Int. Ed. Engl.* **1992**, *31*, 640–643.

 © 2006 Wiley-VCH Verlag GmbH & Co. KGaA, Weinheim 

[15] O. A. Dyachenko, A. Graja, *Fullerene Sci. Technol.* **1999**, *7*, 317–385.
[16] a) S. Troyanov, N. Kuzmina, I. Soboleva, N. Chugarov, Chemical vapor deposition. Proceedings of the Fourteenth International Conference and EUROCVD-11, **1997**, pp. 886–892; b) N. Kuzmina, M. Ryazanov, S. Troyanov, *Polyhedron* **1999**, *18*, 2177–2184.

 © 2006 Wiley-VCH Verlag GmbH & Co. KGaA, Weinheim 

Enzyme Fidelity

DOI: 10.1002/anie.200504296

# Remarkable Sensitivity to DNA Base Shape in the DNA Polymerase Active Site**

*Herman O. Sintim and Eric T. Kool**

The mechanisms of DNA synthesis by DNA polymerase enzymes have come under intensive study recently because of their close biological connections to cancer.[1] Replicative polymerases, such as Pol I and Pol III in bacteria, must synthesize DNA with high fidelity to avoid deleterious mutations.[2] Repair polymerases, on the other hand, operate with lower fidelity and serve to replicate DNA beyond damaged and mismatched sites, keeping cells alive while other enzymes act to correct the damage and prevent oncogenic mutations from proliferating.[3] Because of the importance to human health, a focus of research in many labs has been on the factors that govern fidelity in these enzymes.[4]

Recent studies have suggested that steric effects can have strong influences in DNA polymerase enzymes. In early studies with nonpolar nucleoside isosteres,[5] it was observed that purinelike molecular shapes can be selectively paired with pyrimidine shapes,[6] and a large pyrene nucleobase analogue was shown to be selectively replicated against a very small (abasic) nucleoside.[7] Experiments by Hirao and co-workers[8] have lent support to a strong contribution from sterics in DNA replication, and studies by Shultz, Romesberg, and co-workers[9] with methylated and fluorinated synthetic bases have shown differing efficiency with changes in substitution. Furthermore, steric effects in polymerase active sites have also been observed on the level of the sugar–phosphate backbone in experiments by Marx and co-workers.[10]

However, the influence of steric effects in polymerases has remained in question, in part owing to recent experiments by Berdis and co-workers,[11] and by Engels, Kuchta, and co-workers.[12] Berdis and co-workers studied a set of 5-substituted indoles as deoxynucleoside triphosphate derivatives and observed low selectivity for incorporation of the analogues by T4 DNA polymerase opposite the four natural DNA bases. Engels, Kuchta, and co-workers tested compounds with the related benzimidazole skeleton by using the Klenow polymerase and reported little relationship between different substitution patterns and selectivity between natural DNA bases. In both studies, it was concluded that sterics do not play an important role in the activities observed. Thus size and shape effects and their contribution to DNA polymerase fidelity remain in active debate.

We have undertaken a series of studies to begin to address the steric hypothesis in a systematic way. An earlier report evaluated the effects of increasing DNA base size while keeping the shape constant by using nonpolar thymine shape mimics (toluene, difluoro-, dichloro-, dibromo- and diiodotoluene) paired opposite adenine.[13] These compounds varied in size over a small 1.0 Å range, yet experiments showed that there were large differences in efficiency and fidelity across the series.[13c] However, steric effects depend not only on size, but also shape—that is, size at specific positions in a molecule. Herein, we investigate the effects of nucleobase shape in the DNA polymerase I active site through variation in the positions of substitution of H, F, Cl, and Br atoms on the toluene skeleton. We find surprisingly large kinetic effects resulting from subtle changes in substituent size and location.

Design of this new series started with the known 2,4-difluorotoluene deoxyriboside,[5] a nearly perfect isostere of thymidine, and in particular, the recent variant 2,4-dichlorotoluene deoxyriboside[13a] (**6**, Figure 1), which has virtually the same shape but is slightly larger. Both of these molecules are highly active with replicative DNA polymerases and encode replication opposite adenine.[13c,14] To test whether it is shape, size, or other properties of such thymidine-mimicking compounds (and by inference, thymidine itself) that make them active, we have now altered the shapes in regular increments through the substitution of larger and smaller groups along the periphery of the toluene ring. The sets of varied molecular shapes are shown in Figure 1 and Figure 2. Comparison of compounds **1**–**3** preserves the size but varies the position of a single chlorine substituent, whereas compounds **4**–**6**, with varied double substitution, helps to determine the degree to which shape effects are important for the remarkable thymine-like behavior of the 2,4-isomer in pairing and in replication.[13c] Finally, comparisons of four-compound sets allows for slow variation in size at the hypothetically important 2- and 4-positions separately (Figure 2). For example, the series **1**→**9**→**6**→**10** incrementally increases the size of the 4-position with H, F, Cl, and Br atoms,[13a,15] and the **3**→**7**→**6**→**8** series addresses effects at the 2-position in the same way.

A generalized strategy for the preparation of the new C-glycosides involved reacting the appropriate lithiated halotol-

[*] Dr. H. O. Sintim, Prof. Dr. E. T. Kool
Department of Chemistry
Stanford University
Stanford, CA 94305-5080 (USA)
Fax: (+1) 650-725-0259
E-mail: kool@stanford.edu

[**] This work was supported by the US National Institutes of Health (GM072705).

Supporting information for this article is available on the WWW under http://www.angewandte.org or from the author.


InterScience
© 2006 Wiley-VCH Verlag GmbH & Co. KGaA, Weinheim

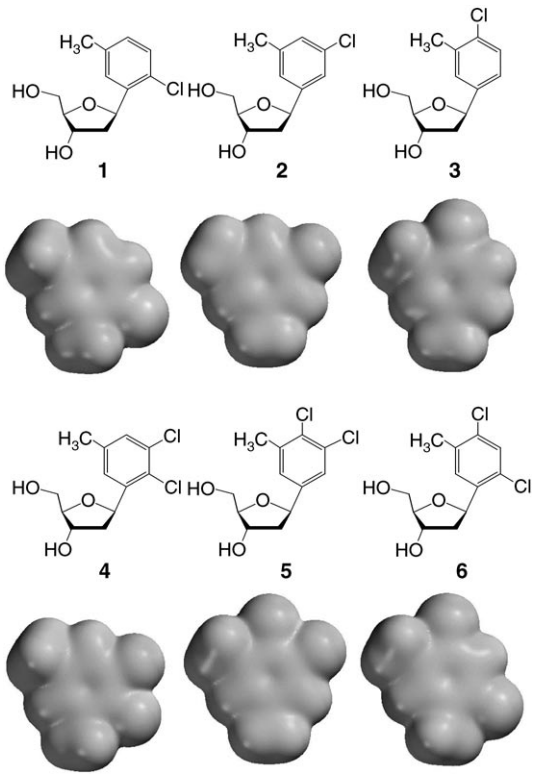
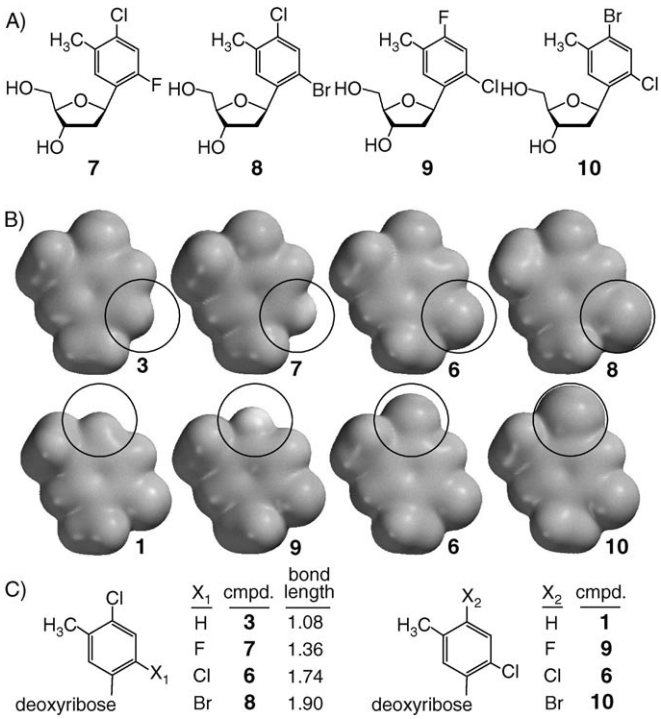



***Figure 1.*** Structures of nonpolar thymidine analogues with systematically varied shape and constant size. Compounds **1**–**3** have a single chlorine substituent at varied positions along the Watson–Crick pairing edge, while **4**–**6** have two substituents. Space-filling models are shown with methyl group replacing deoxyribose.




| $X_1$ | cmpd. | bond length |
|---|---|---|
| H | **3** | 1.08 |
| F | **7** | 1.36 |
| Cl | **6** | 1.74 |
| Br | **8** | 1.90 |

| $X_2$ | cmpd. |
|---|---|
| H | **1** |
| F | **9** |
| Cl | **6** |
| Br | **10** |

***Figure 2.*** Two series of nonpolar thymidine analogues with gradually varied shape. Circles highlight the position with increasing steric demand. A) Structures of deoxyribosides **7**–**10**. B) Space-filling models showing gradual increases in size at the 2-position (**3**→**7**→**6**→**8**) and separately at the 4-position (**1**→**9**→**6**→**10**). Models are shown with a methyl group replacing deoxyribose. C) Expected bond lengths at the variable positions for the two series.[28]

uene (generated through lithium–halogen exchange) with disiloxanediyl-protected deoxyribonolactone[16] **11** followed by triethylsilane reduction under Lewis acid catalysis (see the Supporting Information). We prepared the 5′-dimethoxytrityl-3′ phosphoramidite derivatives (see the Supporting Information) and incorporated them into synthetic 12 mer and 28 mer oligonucleotides by using an automated synthesizer. The 5′-triphosphate derivatives were also prepared following published procedures.[17]

To investigate the small shape effects for pairing in DNA, we evaluated the relative pairing stabilities of compounds **1**–**10** placed opposite each of the four natural DNA bases in a 12 mer duplex context[18] (see the Supporting Information). Optically monitored melting studies were used to evaluate stabilities at pH 7.0 in a buffer solution containing $Mg^{2+}$ (10 mM) and $Na^{+}$ (100 mM). The results showed that, despite their differences in shape, these ten molecules have quite similar pairing properties in this sequence context. With natural bases as partners in the 12 mer duplex, compounds **1**–**10** were all destabilizing relative to a natural T–A pair (also observed previously for **6**[13b] and other low-polarity compounds[18–20]) and generally displayed little pairing selectivity among the natural partners. With the exception of the 3-substituted analogues (**2**, **4**, and **5**) and the 4-chloro compound **3**, some of the new analogues showed a small but significant preference (by approximately 2–4 °C in $T_m$) for adenine as partner. In our previous studies with 2,4-dihalotoluene base analogues[13b] and studies of others,[9] a similar small preference for adenine was also observed; this may be due to the stronger stacking of adenine relative to other DNA bases.[21] Interestingly, two cases, the 2,4-dichloro compound **6** and the 2-chloro-4-bromo compound **7**, showed a stronger preferences for adenine over a mismatch (5–7 °C); this may be owing to a small degree of thymine-like shape preference opposite adenine conferred by the backbone. However, the selectivity was lower than that of thymine (8 °C) and the analogues were both considerably destabilizing overall (by 12 °C and greater), consistent with their low polarity and lack of significant hydrogen bonding ability. Overall, despite their differences in shape, these ten molecules have quite similar pairing properties in this sequence context, which suggests that the DNA backbone confers relatively low shape selectivity.

To determine the DNA polymerase shape selectivity, the properties of the shape-varied compounds in the active site of KF exonuclease-deficient (*exo*$^-$) polymerase were then tested. Preliminary gel analyses of single-nucleotide insertion reactions against each of the four DNA bases showed that all ten compounds were enzymatically paired with adenine and thymine in varied amounts but not significantly with guanine or cytosine (see the Supporting Information). Thus, we proceeded to measure the steady-state kinetic efficiencies when these nonpolar thymine analogues are paired with A or

 © 2006 Wiley-VCH Verlag GmbH & Co. KGaA, Weinheim 

T, wherein pairing with A defines absolute efficiency and pairing with T, the most efficient mismatch, defines selectivity or fidelity.

The kinetics data (shown in Figure 3, Figure 4, and tabulated in the Supporting Information) as a whole showed that the analogues were enzymatically paired with widely varying efficiencies and selectivities. As template-base analogues, the enzyme incorporated dATP opposite the compounds with efficiencies that varied by three orders of magnitude. The most efficient analogues were compounds **6**, **7**, and **10**, which gave efficiencies within error limits of each other and were only 2–3-fold less efficient than natural thymidine as a template. As incoming nucleotide (dNTP) derivatives, the compounds varied in efficiency by an even larger 3500-fold for insertion opposite a template adenine. The most efficient was compound **10**, which was tenfold below natural dTTP in efficiency. Thus a general inspection of the data shows that shape effects are clearly large in magnitude with this enzyme and that a number of the new analogues may be even more efficient as thymidine mimics than any previously reported.[13c,14]

Data for analogues in the monochlorinated series **1**–**3** showed that they were generally more efficient in a template strand than as dNTP derivatives (Figure 3A,B). The 2- and 4-substituted compounds were enzymatically paired opposite adenine preferentially, with efficiencies that were moderate to high. The 2-chloro compound **1** showed greater selectivity for adenine than did the 4-chloro case **3**. The selectivity of **1** was moderate, with a 34-fold to 470-fold preference for adenine over the most efficient mismatch (thymine). In contrast to this, the 3-substituted compound **2** was paired very poorly with adenine, 3–4 orders of magnitude below thymidine, and the selectivity underwent a switch in the template strand with a small preference for being paired with T over A.

The second series (Figure 3C,D) compared enzymatic processing of doubly chlorinated toluenes (**4**–**6**). Of the three, only the 2,4-dichloro compound **6** showed selectivity for adenine (selectivity was high, 64- to 810-fold), as previously reported.[13c] In contrast to this, the other two compounds (**4** and **5**) showed selectivity for thymine over adenine. Thus these two 3-substituted compounds demonstrated a selectivity switch as had the other 3-substituted compound **3**, above.

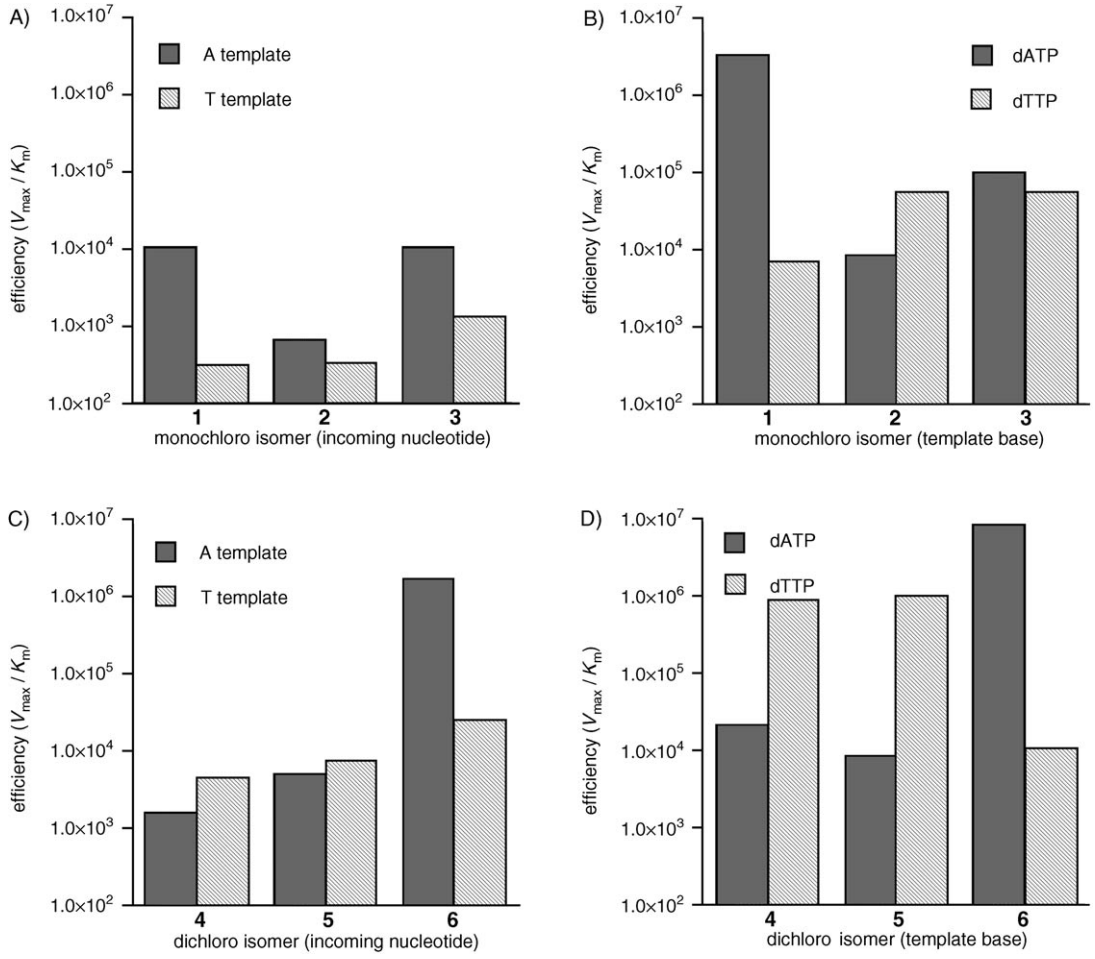



***Figure 3.*** Shape effects on DNA replication, as measured with thymidine analogues having the same size but altered shapes. A) and B) Data for monochlorinated analogues **1**–**3**. C) and D) Data for dichlorinated analogues **4**–**6**. Kinetic efficiencies with the Kf enzyme are plotted on a $\log_{10}$ scale; black columns show data for replication opposite deoxyadenosine (as expected for a thymidine analogue), and striped columns show data for replication against thymidine (the most efficient mismatch). Data are shown both for analogues as incoming nucleotides (A,C) and as template bases (B,D).

 © 2006 Wiley-VCH Verlag GmbH & Co. KGaA, Weinheim 

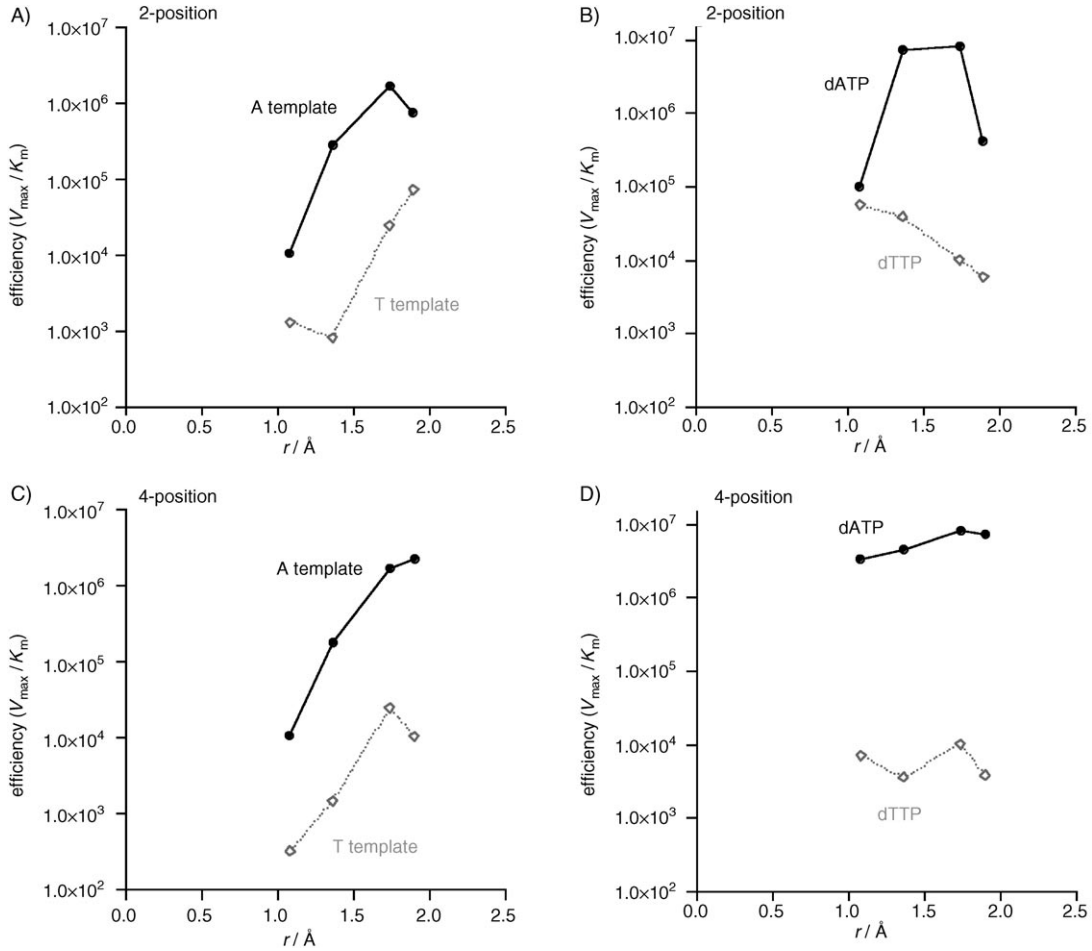



***Figure 4.*** Effects of a gradually altering shape on DNA replication as measured with a series of thymidine analogues with one substituent of varied size (over an 0.8 Å bond length range, Figure 2). Kinetic efficiencies with the Kf enzyme are plotted on a log scale. A) and B) Data for varied size at the 2-position (analogues **3**, **7**, **6**, and **8**). C) and D) Data for varied size at the 4-position (analogues **1**, **9**, **6**, **10**). Black lines show data for replication against deoxyadenosine and gray dashed lines show data for mismatched replication opposite the most efficient mismatch (thymidine). Data are shown both for analogues as incoming nucleotides and as template bases. $r$ = bond length.

The above data suggests strongly that the 2- and 4-positions were important in the determination of thymidine-like pairing behavior. Thus two series of compounds were evaluated to investigate the effects of gradual shape changes at these positions individually, by slowly increasing size (Figure 4 A–D). The data for the 2-position size variation are plotted in Figure 4 A, B and those for 4-position variation are given in Figure 4 C,D.

The incoming nucleotide analogues had gradually varied shapes (Figure 4 A, C), and the results showed that the substituent size preference was strong at both the 2- and 4-positions, with a 110-fold and 210-fold difference over the size range. The maximum efficiency at the 4-position occurred with bromo substitution, and this size preference appeared to be slightly larger than that at the 2-position, wherein the maximum appeared upon chloro substitution. The effects in the template strand (Figure 4 B, D) were somewhat similar in that the 4-position had a larger size preference (chloro/bromo) as compared with the 2-position (fluoro/chloro). However, there was one substantial difference, the 4-position selectivity overall was quite modest with a high efficiency regardless of substituent size (Figure 4 D).

Data were also plotted for the most efficient mismatch (replication opposite thymidine; Figure 4, gray dashed lines), which allowed for evaluation of the effects of gradually altered nucleobase shape on pairing selectivity with this enzyme. As a whole, the analogue with highest fidelity in a template strand was the 2-chloro-4-bromo compound **10**; as incoming nucleotides, fidelities were the same for compound **10** and for the 2-fluoro-4-chloro compound **7**. The overall fidelity of compound **10** as an incoming nucleotide analogue was approximately threefold lower than natural thymidine (230-fold preference for adenine versus 790-fold). In the template strand, however, compound **10** was processed with higher fidelity than thymidine (1900-fold versus 1100-fold) although identity of the most common mismatch was different.

Taken together, the results demonstrate that the Klenow DNA polymerase is highly sensitive to even small differences in nucleobase shape. Overall, the shape analogues in this

 © 2006 Wiley-VCH Verlag GmbH & Co. KGaA, Weinheim 

series displayed a remarkable 3500-fold range in enzymatic efficiency despite the fact that they are all closely related chlorinated toluenes. We showed previously that this same enzyme is responsive to nucleobase analogues with variable size but that maintain thymine-like shape.[13c] The present results are distinct in that they shed light on the importance of the location of steric substitutions rather than on the size of the nucleobase as a whole. Changing a hydrogen substituent to a chlorine (in dNTP analogues) at positions 2 or 4 has a strong positive effect (>100-fold) on the efficiency of insertion opposite adenine (compare **1** with **6**, and **3** with **6**). In marked contrast, making the same steric change at the 3-position has a negative effect on insertion opposite adenine (by a factor of 2–5; compare **1** with **4** and **3** with **5**).

We hypothesize that these local steric preferences are defined by the shape of the base opposite these analogues,[22] and that the magnitude of the shape preferences is enforced by the active-site tightness of the enzyme around the incipient base pair.[23,13c] The kinetic optimization that occurred here with varying shape may reflect the optimal filling of space in the active site; local steric protrusions that clash with adenine (such as at the thymine 3-position) or with the enzyme at other positions would be energetically costly at the closed transition state for phosphodiester bond formation. On the other hand, groups that are smaller than needed to fill the space leave a void in the protein, which is also energetically costly.[24]

We considered whether other factors apart from sterics, such as polarity or electrostatic effects, might explain these enzymatic results. For example, nucleobase dipoles might conceivably influence base pairing or active site binding.[25] However, comparison of members of the analogue series **1**–**3** and **4**–**6** reveals widely varying replication efficiencies with essentially constant dipole strengths. In addition, local electrostatic charges might conceivably contribute. However, examination of data for the increasing size series (**3**→**7**→**6**→**8** and **1**→**9**→**6**→**10**), showed that the maximum efficiencies occur with the largest halogens (bromine and chlorine), whereas the strongest negative charge is associated with fluorine. Moreover, local electrostatic charges associated with chlorine would remain virtually the same in compounds **1**–**4** and in **4**–**6**, but the replication efficiencies vary by orders of magnitude. Thus we conclude that it is the size and location of space-filling substituents, rather than polar factors, that best explains these results.

Earlier experiments with larger nonpolar nucleobase analogues (indoles and benzimidazoles) led to the suggestion that steric effects may not be a dominant factor within this and other enzymes.[11,12] Herein, we offer a steric argument that may explain a number of those findings. The indole and closely related benzimidazole frameworks can exist in an alternative *syn* conformation, such as is found for 8-oxoGuanine in its mispairing opposite adenine.[26] We suggest that 5- and 6- substitution of these molecular skeletons renders them far too large to fit opposite natural bases in canonical base pair geometry. Thus, steric repulsion might cause them to occupy the *syn* conformation instead; in this conformation the 5- and 6-positions project into the open major groove where the enzyme has few steric constraints. This would explain the low selectivity and little difference among the analogues seen by Berdis, as all the molecules would present essentially the same steric environment if they were oriented *syn*. Engels, Kuchta, and co-workers studied closely related 5- and 6-substituted benzimidazole nucleotides, and they observed that nearly all of them gave pairing selectivity for guanine.[12] Once again this could be readily explained if those molecules flipped to the *syn* conformation in the active site, driven by the expected large steric clash of the 5- and 6-substituents with the template base. Importantly, the 9-nitrogen of benzimidazole, if in *syn* orientation, would be analogous to N3 of cytosine. Thus in this alternative conformation, one would expect the best steric complementarity (and also H-bonding complementarity) to guanine, which was the observed replication result. The energetic cost of flipping to the *syn* conformation might help explain the generally low activity of the benzimidazole analogues that were studied.

In conclusion, we have shown that *E. coli* DNA polymerase I (KF *exo*$^-$) can distinguish easily between nucleobases that have the same sizes but different shapes. This enzyme's sensitivity to shape is surpisingly high, with subangstrom changes being readily distinguished. Furthermore, we have shown that the steric requirements of the 2-, 3-, and 4-positions of thymine are all different. The 2- and 4-position steric protrusions play crucial roles in defining the adenine-encoding behavior of thymine, whereas steric substitutions at the 3-position eliminate thymine-like behavior. Taken together, our results suggest that nucleobase shape plays a more prominent role in base-pairing efficiency and selectivity than other factors in this enzyme. The results add insight into the basic mechanisms of DNA replication, and into the origins of mutations that arise during this process. More work is needed, however, to evaluate how other enzymes respond to differences in nucleobase shape and size.

Received: December 2, 2005

**Keywords:** base pairing · DNA replication · enzymes · steric effects

[1] a) J. F. Davidson, H. H. Guo, L. A. Loeb, *Mutat. Res.* **2002**, *509*, 17–21; b) A. Sarasin, *Mutat. Res.* **2003**, *544*, 99–106.
[2] L. A. Loeb, T. A. Kunkel, *Annu. Rev. Biochem.* **1982**, *51*, 429–457.
[3] a) M. F. Goodman, *Annu. Rev. Biochem.* **2002**, *71*, 17–50; b) L. Stojic, R. Brun, J. Jiricny, *DNA Repair* **2004**, *3*, 1091–1101; c) A. Sancar, L. A. Lindsey-Boltz, K. Unsal-Kacmaz, S. Linn, *Annu. Rev. Biochem.* **2004**, *73*, 39–85; d) C. H. McGowan, *Mutat. Res.* **2003**, *27*, 75–84; e) M. Christmann, M. T. Tomicic, W. P. Roos, B. Kaina, *Toxicology* **2003**, *15*, 3–34.
[4] a) H. Echols, M. F. Goodman, *Annu. Rev. Biochem.* **1991**, *60*, 477–511; b) T. A. Kunkel, K. Bebenek, *Annu. Rev. Biochem.* **2000**, *69*, 497–529; c) E. T. Kool, *Annu. Rev. Biophys. Biomol. Struct.* **2001**, *30*, 1–22; d) W. A. Beard, S. H. Wilson, *Structure* **2003**, *11*, 489–496.
[5] a) B. A. Schweitzer, E. T. Kool, *J. Org. Chem.* **1994**, *59*, 7238–7242; b) N. C. Chaudhuri, R. X.-F. Ren, E. T. Kool, *Synlett* **1997**, 341–347.
[6] J. C. Morales, E. T. Kool, *Nat. Struct. Biol.* **1998**, *5*, 950–954.
[7] T. J. Matray, E. T. Kool, *Nature* **1999**, *399*, 704–708.

 © 2006 Wiley-VCH Verlag GmbH & Co. KGaA, Weinheim 

[8] T. Mitsui, M. Kimoto, A. Sato, S. Yokoyama, I. Hirao, *Bioorg. Med. Chem. Lett.* **2003**, *13*, 4515 – 4518.
[9] a) A. K. Ogawa, Y. Q. Wu, M. Berger, P. G. Schultz, F. E. Romesberg, *J. Am. Chem. Soc.* **2000**, *122*, 8803 – 8804; b) S. Matsuda, F. E. Romesberg, *J. Am. Chem. Soc.* **2004**, *126*, 14419 – 14427.
[10] M. Strerath, J. Cramer, T. Restle, A. Marx, *J. Am. Chem. Soc.* **2002**, *124*, 2056 – 2057.
[11] X. Zhang, I. Lee, A. Berdis, *J. Biochem.* **2005**, *44*, 13101 – 13110.
[12] K. Kincaid, J. Beckman, A. Zivkovic, R. L. Halcomb, J. W. Engels, R. D. Kuchta, *Nucleic Acids Res.* **2005**, *33*, 2620 – 2628.
[13] a) T. Kim, E. T. Kool, *Org. Lett.* **2004**, *6*, 3949 – 3952; b) T. Kim, E. T. Kool, *J. Org. Chem.* **2005**, *70*, 2048 – 2053; c) T. Kim, J. C. Delaney, J. M. Essigmann, E. T. Kool, *Proc. Natl. Acad. Sci. USA* **2005**, *102*, 15803 – 15808.
[14] a) S. Moran, R. X.-F. Ren, S. Rumney, E. T. Kool, *J. Am. Chem. Soc.* **1997**, *119*, 2056 – 2057; b) S. Moran, R. X.-F. Ren, E. T. Kool, *Proc. Natl. Acad. Sci. USA* **1997**, *94*, 10506 – 10511.
[15] M. L. Hamm, S. Rajguru, A. M. Downs, R. Cholera, *J. Am. Chem. Soc.* **2005**, *127*, 12220 – 12221.
[16] U. Wichai, S. A. Woski, *Org. Lett.* **1999**, *1*, 1173.
[17] a) M. Yoshikawa, T. Kato, T. Takenishi, *Tetrahedron Lett.* **1967**, *8*, 5065 – 5068; b) T. Kovács, L. Ötvös, *Tetrahedron Lett.* **1988**, *29*, 4525 – 4528.
[18] E. T. Kool, J. C. Morales, K. M. Guckian, *Angew. Chem.* **2000**, *112*, 1046 – 1068; *Angew. Chem. Int. Ed.* **2000**, *39*, 990 – 1009.
[19] Z. Sun, D. Chen, T. Lan, L. W. McLaughlin, *Biopolymers* **2002**, *65*, 211 – 217.
[20] J. Parsch, J. W. Engels, *Nucleosides Nucleotides Nucleic Acids* **2001**, *20*, 815 – 818.
[21] a) K. M. Guckian, R. X.-F. Ren, N. C. Chaudhuri, D. C. Tahmassebi, E. T. Kool, *J. Am. Chem. Soc.* **2000**, *122*, 2213 – 2222; b) S. Bommarito, N. Peyret, J. SantaLucia, *Nucleic Acids Res.* **2000**, *28*, 1929 – 1934.
[22] E. T. Kool, *Biopolymers* **1998**, *48*, 3 – 17.
[23] E. T. Kool, *Annu. Rev. Biochem.* **2002**, *71*, 191 – 219.
[24] A. E. Eriksson, W. A. Baase, X. J. Zhang, D. W. Heinz, M. Blaber, E. P. Baldwin, B. W. Matthews, *Science* **1992**, *255*, 178 – 183.
[25] K. Seio, H. Ukawa, K. Shohda, M. J. Sekine, *J. Biomol. Struct. Dyn.* **2005**, *23*, 735 – 746.
[26] a) L. G. Brieba, B. F. Eichman, R. J. Kokoska, S. Doublie, T. A. Kunkel, T. Ellenberger, *EMBO J.* **2004**, *23*, 3452 – 3461; b) G. W. Hsu, M. Ober, T. Carell, L. S. Beese, *Nature* **2004**, *431*, 217 – 221; c) S. J. Johnson, L. S. Beese, *Cell* **2004**, *116*, 803 – 816.
[27] M. F. Goodman, S. Creighton, L. B. Bloom, J. Petruska, *Crit. Rev. Biochem. Mol. Biol.* **1993**, *28*, 83 – 126.
[28] The values were obtained from the *CRC Handbook of Chemistry and Physics 81st ed.*, *9–2*, *5* (Ed.: David R. Lide), CRC, Florida, **2000–2001**.

 © 2006 Wiley-VCH Verlag GmbH & Co. KGaA, Weinheim 

Cycloadditions

DOI: 10.1002/anie.200503672

# A Highly Enantio- and Diastereoselective Cu-Catalyzed 1,3-Dipolar Cycloaddition of Azomethine Ylides with Nitroalkenes**

*Xiao-Xia Yan, Qian Peng, Yan Zhang, Kai Zhang, Wei Hong, Xue-Long Hou,* and Yun-Dong Wu*

*Dedicated to Professor Wei-Yuan Huang on the occasion of his 85th birthday*

The 1,3-dipolar cycloaddition of azomethine ylides to electron-deficient alkenes is one of the most powerful methods for the construction of highly substituted pyrrolidine rings.[1] Following early research on the preparation of optically active pyrrolidines in the presence of either a stoichiometric amount of a chiral metal complex[2] or a chiral auxiliary,[3] an asymmetric catalytic version of this reaction has been developed recently.[4–8] The groups of Jørgensen,[4a] Zhang,[5a] Schreiber,[6] Zhou,[8a] and Carretero[8b] have reported that the reaction of glycine derivatives with electron-deficient alkenes is highly enantio- and *endo*-selective in the presence of chiral $Zn^{II}$–bisoxazolines, $Ag^{I}$–phosphanes, $Ag^{I}$–quinap, Ag–P,N ligands, and Cu–fesulphos, while the groups of Komatsu and Zhang have reported *exo* selectivity with a Cu–diphosphane complex and P,N ligands as catalyst.[5b,7] Each of these reactions involves derivatives of unsaturated carboxylates as the dipolarophiles and the diastereoselectivity is not switchable.[9a] Herein, we report a $Cu^{I}$–P,N-ferrocene-catalyzed 1,3-dipolar cycloaddition of nitroalkenes to an imino ester derived from glycine and our observation of a dramatic switch in *exo*/*endo* selectivity due to

[*] Dr. X.-X. Yan, Y. Zhang, Prof. Dr. X.-L. Hou
State Key Laboratory of Organometallic Chemistry
Shanghai Institute of Organic Chemistry
Chinese Academy of Sciences
354 Fenglin Road, Shanghai 200032 (China)
Fax: (+86) 21-5492-5100
E-mail: xlhou@mail.sioc.ac.cn

Q. Peng, K. Zhang, W. Hong, Prof. Dr. X.-L. Hou, Prof. Dr. Y.-D. Wu
Shanghai–Hong Kong Joint Laboratory in Chemical Synthesis
Shanghai Institute of Organic Chemistry
Chinese Academy of Sciences,
354 Fenglin Road, Shanghai 200032 (China)

Prof. Dr. Y.-D. Wu
Department of Chemistry
Hong Kong University of Science and Technology
Hong Kong (China)

[**] This research was supported financially by the Major Basic Research Development Program (grant G 200077506), the National Natural Science Foundation of China, the Chinese Academy of Sciences, the Shanghai Committee of Science, and the Technology and Croucher Foundation of Hong Kong. We thank Professors L.-X. Dai, H. N. C. Wong, and T.-L. Ho for their helpful discussions.

Supporting information for this article is available on the WWW under http://www.angewandte.org or from the author.

 © 2006 Wiley-VCH Verlag GmbH & Co. KGaA, Weinheim 

the electronic properties of the chiral ligand. A qualitative model is also proposed to rationalize the observed stereochemistry.

Initially, the reaction of imino ester **1a** with nitroalkene **2a** was examined in the presence of $CuClO_4$ and ligands **3a**[9b] and **3f–h** [Eq. (1)].[10d,11] The results are compiled in Table 1.

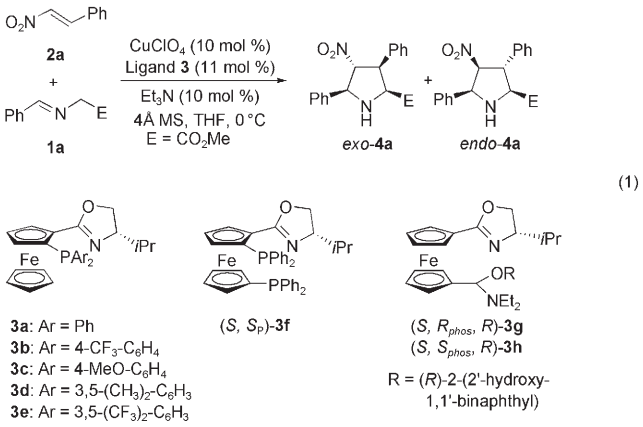



***Table 1:*** Reaction of **1a** with **2a** in the presence of different ligands.[a]

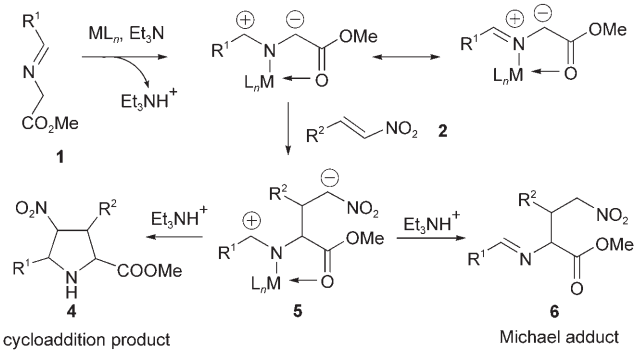
| Entry | Ligand | Yield [%][b] | *exo*/*endo*[c] | *ee* [%] (*exo*/*endo*)[d] |
|---|---|---|---|---|
| 1 | **3a** | 58 | only *exo* | 97 (n.d.) |
| 2 | **3b** | 67 | 73:27 | 95 (84) |
| 3 | **3c** | 65 | only *exo* | 98 (n.d.) |
| 4 | **3d** | 49 | only *exo* | 98 (n.d.) |
| 5 | **3e** | 62 | 18:82 | 88 (97) |
| 6 | **3f** | 37 | 49:51 | 92 (15) |
| 7 | **3g** | 75 | only *endo* | n.d. (17) |
| 8 | **3h** | 60 | 18:82 | n.d. (3) |

[a] Molar ratio of **1a** to **2a** = 1.2:1. [b] Yield of isolated product. [c] Determined by $^1$H NMR spectroscopy. [d] Determined by chiral HPLC. n.d. = not determined.

The reaction with ligand **3a** yielded *exo*-**4a**[12] as the sole product in 58% yield with 97% *ee* (Table 1, entry 1), while the *endo* isomer was obtained with 17% *ee* with ligand **3g** (Table 1, entry 7). A sharp decrease in diastereo- and/or enantioselectivities was observed with ligands **3f** and **3h** (Table 1, entries 6 and 8, respectively).

Encouraged by the result with ligand **3a**, we synthesized a series of P,N-ferrocenyl ligands **3b–e** bearing different aryl groups on the P atom[11,13] and used them in the reaction. As shown in Table 1, a dramatic variation in diastereoselectivity was observed. Ligands **3c** and **3d**, which have electron-donating substituents on the phenyl rings, gave exclusively the *exo* product with excellent enantioselectivity (entries 3 and 4, Table 1), whereas ligand **3b**, which has one electron-withdrawing $CF_3$ group on each phenyl ring, gave a mixture of *exo* and *endo* isomers in a ratio of 73:27 with 95% and 84% *ee*, respectively. Ligand **3e** with two $CF_3$ substituents on each phenyl ring, gave the *endo* isomer as the major product with 97% *ee* (entry 5, Table 1). THF proved to be a better solvent than $CH_2Cl_2$, toluene, $Et_2O$, or $CH_3CN$ in terms of yields and diastereoselectivities. When AgOAc and ligand **3a** were used in THF for the reaction, an 87:13 ratio of *exo* and *endo* isomers (91% and 62% *ee*, respectively) was obtained in an overall yield of 67%.

Although the reaction provides the pyrrolidine derivatives with high *ee*, the yields are only moderate because Michael addition occurs as a side reaction.[12] This supports the stepwise mechanism proposed by Cossío and co-workers.[12,14] As shown in Scheme 1, a zwitterionic species **5** should




***Scheme 1.*** Proposed mechanism of the reaction of **1** with **2**.

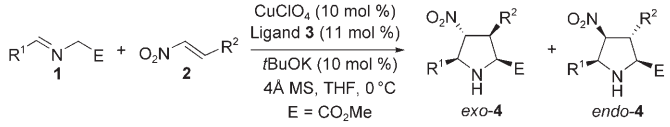
be formed as an intermediate, from which the cycloaddition product **4** is formed. However, **5** can also be protonated by $Et_3NH^+$, the conjugate acid of $Et_3N$, to form the Michael adduct. In this case the yield of pyrrolidine **4** could be improved by using a stronger base (weaker conjugate acid) to slow down the protonation. Indeed, when *t*BuOK was used as the base in the reaction of **1a** and **2a** with **3a** as ligand, the yield of *exo*-**4a** increased from 58% to 87%, albeit with a slight decrease in *ee* (from 97% to 95%).

The 1,3-cycloaddition of different imino esters **1** and nitroalkenes **2** in the presence of ligands **3a** and **3e** was studied under these optimized conditions (Table 2).[15] All reactions in the presence of **3a** provided *exo*-**4** either exclusively (Table 2, entries 1–7) or as the major isomer in a ratio between 88:12 and 92:8 (Table 2, entries 8–11). The yields were always high and the *ee* values for *exo*-**4** ranged from 92% to 98%, except for product **4k** (Table 2, entry 11). An aliphatic nitroalkene was also found to be a suitable dipolarophile; it gave *exo*-**4g** as the sole diastereomer with 98% *ee* (Table 2, entry 7). When ligand **3e** was used, the *endo*-**4** diastereomers were obtained in high yields. The ratio of *endo*-**4** to *exo*-**4** ranged from 70:30 to 94:6 (Table 2, entries 12–19), with *ee* values between 92% and 98% (Table 2, entries 12–16 and 18), with the exception of products **4i** and **4k**, for which the *ee* values were 84 and 88%, respectively (Table 2, entries 17 and 19). After one recrystallization from dichloromethane/petroleum ether, *exo*-**4k** and *endo*-**4k** were obtained with over 99% and 96% *ee*, respectively.

The absolute configurations of *exo*-**4k** and *endo*-**4k** were assigned as (2*S*,3*S*,4*R*,5*R)* and (2*S*,3*R*,4*S*,5*R*), respectively, by X-ray diffraction analysis (Figure 1). The same (2*S*,5*R*) configuration for the two products indicates that the addition

 © 2006 Wiley-VCH Verlag GmbH & Co. KGaA, Weinheim 

***Table 2:*** Enantioselective $Cu^{I}$-catalyzed 1,3-dipolar cycloaddition of azomethine ylides **1** to nitroalkenes **2**.




| Entry | $R^1$ | $R^2$ | Ligand | *exo*/*endo*[a] | Product | Yield [%][b] | *ee* [%][c] |
|---|---|---|---|---|---|---|---|
| 1 | Ph | Ph | **3a** | only *exo* | **4a** | 87 | 95 |
| 2 | Ph | *p*-$NO_2$-$C_6H_4$ | **3a** | only *exo* | **4b** | 70 | 96 |
| 3 | Ph | *p*-MeO-$C_6H_4$ | **3a** | only *exo* | **4c** | 77 | 96 |
| 4 | Ph | *p*-Me-$C_6H_4$ | **3a** | only *exo* | **4d** | 73 | 96 |
| 5 | Ph | *p*-Cl-$C_6H_4$ | **3a** | only *exo* | **4e** | 64 | 92 |
| 6 | Ph | *m*-Cl-$C_6H_4$ | **3a** | only *exo* | **4f** | 74 | 95 |
| 7 | Ph | *i*Pr | **3a** | only *exo* | **4g** | 75 | 98 |
| 8 | *p*-MeO-$C_6H_4$ | Ph | **3a** | 89:11 | **4h** | 96 | 97 |
| 9 | *m*-Cl-$C_6H_4$ | Ph | **3a** | 88:12 | **4i** | 97 | 92 |
| 10 | 2-naphthyl | Ph | **3a** | 92:8 | **4j** | 92 | 92 |
| 11 | *p*-Br-$C_6H_4$ | Ph | **3a** | 86:14 | **4k** | 77 | 83 (99)[d] |
| 12 | Ph | Ph | **3e** | 14:86 | **4a** | 85 | 98 |
| 13 | Ph | *p*-MeO-$C_6H_4$ | **3e** | 30:70 | **4c** | 79 | 95 |
| 14 | Ph | *m*-Cl-$C_6H_4$ | **3e** | 11:89 | **4f** | 82 | 92 |
| 15 | Ph | *i*Pr | **3e** | 6:94 | **4g** | 88[e] | 97 |
| 16 | *p*-MeO-$C_6H_4$ | Ph | **3e** | 18:82 | **4h** | 79 | 96 |
| 17 | *m*-Cl-$C_6H_4$ | Ph | **3e** | 17:83 | **4i** | 98 | 84 |
| 18 | 2-naphthyl | Ph | **3e** | 19:81 | **4j** | 98 | 97 |
| 19 | *p*-Br-$C_6H_4$ | Ph | **3e** | 18:82 | **4k** | 71 | 88 (96)[d] |

[a] Determined by $^1$H NMR spectroscopy. [b] Yield of isolated product. [c] Major product determined by HPLC. [d] The *ee* value obtained after one recrystallization is given in parentheses. [e] Yield of isolated *endo* products.

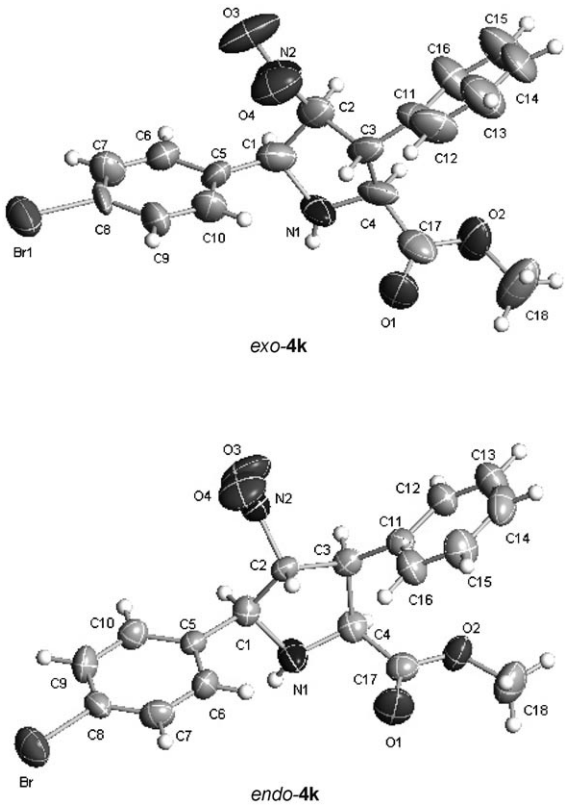



***Figure 1.*** ORTEP diagrams of the X-ray crystal structures of *exo*-**4k** and *endo*-**4k**.

of the nitroalkene occurs at the *Si* face of the Cu-bound imino ester anion with both **3a** and **3e**.

Varying the electronic properties of ligands to fine-tune the stereoselectivity in asymmetric catalysis has been conceptually attractive.[16] Pioneered by Jacobsen[16a] and others, there have since been many reports of improved stereoselectivity by utilizing this electronic effect.[11,16] However, there has been only limited success in switching the stereoselectivity.[16d,h,j–l] Our current finding of a dramatic switch in diastereoselectivity while still keeping high enantioselectivity represents an exceptional example. Our results also indicate that the effect is not due to a π–π interaction (see entries 7 and 15 in Table 2).

A computational study of the complex formed by Cu–**3a** and the anion of the imino ester **1a** was also performed. The two structures were fully optimized with the density functional theory method at the B3LYP/6-31G*(lanldz) level.[17] When these structures assume a distorted tetrahedral geometry with a more or less coplanar Cu-P-N-N array (Figure 2), structure **A** is calculated to be about 4.3 kcal mol$^{-1}$ more stable than **B**.[18] The latter is significantly destabilized by the steric interactions between the phenyl group of the imino ester and one of the phenyl groups of the ligand and the ferrocene. Therefore, the stereoselectivity can be discussed on the basis of the addition of nitroalkene to structure **A**.[19]

The *Re* face of structure **A** is apparently shielded by the isopropyl group, as indicated by the short C1–H1 distance (3.14 Å). On the other hand, the two phenyl groups on the P atom are oriented in such a way that they do not shield the *Si* face. Therefore, it is reasonable to assume that the attack of nitroalkene occurs at the *Si* face of the Cu-bound imino ester anion, in agreement with the experimental observations (Figure 1). As shown by the Newman projections, there are three transition structures with staggered conformations for the *exo* and *endo* diastereomers. Upon nucleophilic addition at C2 of the nitroalkene there should be an accumulation of negative charge at C3. Therefore, we argue that **7c** and **8b** are more favorable transition structures for the *exo* and *endo* products, respectively, because the developing negative charge at C3 can be stabilized by electrostatic interaction with the Cu center. In structure **7c**, the nitro group, which carries partial negative charge, lies away from the valley formed by the two aryl groups of the P ligand, whereas the nitro group in **8b** lies in the valley. Therefore, when the aryl groups are electron-rich, structure **7c** is expected to be more stable than **8b**, which leads to the favorable formation of the

 © 2006 Wiley-VCH Verlag GmbH & Co. KGaA, Weinheim 

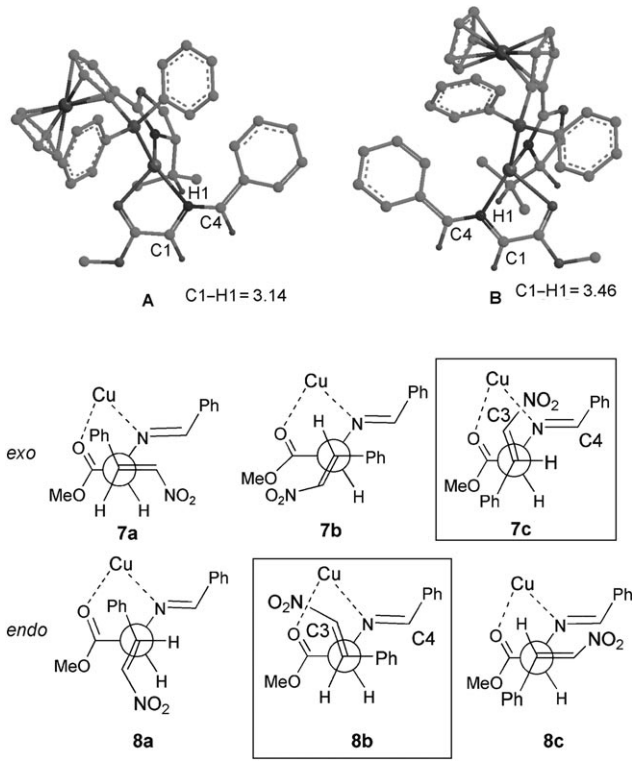



***Figure 2.*** Calculated structures (**A** and **B**) of complexation modes of $Cu^{I}$–**3a** with the anion of imino ester **1a** and staggered transition-structure models of nitrostyrene on the *Si* face of the Cu-bound imino ester anion. Fe brown, Cu black, C green, O red, N blue, H violet.

*exo* product. When the aryl groups are electron-deficient, however, structure **8b** is stabilized by electrostatic interaction, which leads to formation of the *endo* product.

The present report reveals for the first time the $Cu^{I}$-catalyzed asymmetric 1,3-dipolar cycloaddition of azomethine ylides to nitroalkenes.[20] A high yield of either *exo* or *endo* adducts can be achieved, with excellent enantioselectivity, by using electron-rich or electron-deficient aryl groups on the P atom of chiral P,N-ferrocene ligands, respectively. A qualitative model has been proposed to rationalize the observed stereoselectivity. These results point to a new possibility to switch the stereoselectivity of the reaction by varying the electronic properties of the ligands. Furthermore, useful hints for ligand design are revealed. The application of this reaction and the use of other electron-deficient alkenes as dipolarophiles is currently being studied further.

Received: October 17, 2005
Revised: December 30, 2005
Published online: February 21, 2006

**Keywords:** asymmetric catalysis · azomethine ylides · copper · cycloaddition · diastereoselectivity

[1] Reviews: a) C. Nájera, J. M. Sansano, *Angew. Chem.* **2005**, *117*, 6428 – 6432; *Angew. Chem. Int. Ed.* **2005**, *44*, 6272 – 6276; b) K. V. Gothelf in *Cycloaddition Reactions in Organic Synthesis* (Eds.: S. Kobayashi, K. A. Jørgensen), Wiley-VCH, Weinheim, **2002**, pp. 211 – 247; c) K. V. Gothelf, K. A. Jørgensen, *Chem. Rev.* **1998**, *98*, 863 – 909; d) K. V. Gothelf, K. A. Jørgensen, *Chem. Commun.* **2000**, 1449 – 1458.

[2] a) P. Allway, R. Grigg, *Tetrahedron Lett.* **1991**, *32*, 5817 – 5820; b) R. Grigg, *Tetrahedron: Asymmetry* **1995**, *6*, 2475 – 2486; c) J. Casas, R. Grigg, C. Nájera, J. M. Sansano, *Eur. J. Org. Chem.* **2001**, 1971 – 1982.

[3] For examples, see: a) P. Garner, O. Dogan, *J. Org. Chem.* **1994**, *59*, 4 – 6; b) M. E. Kopach, A. H. Fray, A. I. Meyers, *J. Am. Chem. Soc.* **1996**, *118*, 9876 – 9883; c) I. Merino, Y. R. S. Laxmi, J. Florez, J. Barluenga, J. Ezquerra, C. Pedregal, *J. Org. Chem.* **2002**, *67*, 648 – 655; d) J. L. G. Ruano, A. Tito, M. T. Peromingo, *J. Org. Chem.* **2002**, *67*, 981 – 987.

[4] a) A. S. Gothelf, K. V. Gothelf, R. G. Hazell, K. A. Jørgensen, *Angew. Chem.* **2002**, *114*, 4410 – 4412; *Angew. Chem. Int. Ed.* **2002**, *41*, 4236 – 4238; b) C. Alemparte, G. Blay, K. A. Jørgensen, *Org. Lett.* **2005**, *7*, 4569 – 4572.

[5] a) J. M. Longmire, B. Wang, X. Zhang, *J. Am. Chem. Soc.* **2002**, *124*, 13400 – 13401; b) W. Gao, X. Zhang, M. Raghunath, *Org. Lett.* **2005**, *7*, 4241 – 4244.

[6] C. Chen, X. Li, S. L. Schreiber, *J. Am. Chem. Soc.* **2003**, *125*, 10174 – 10175.

[7] Y. Oderaotoshi, W. Cheng, S. Fujitomi, Y. Kasano, S. Minakata, M. Komatsu, *Org. Lett.* **2003**, *5*, 5043 – 5046.

[8] a) W. Zeng, Y. G. Zhou, *Org. Lett.* **2005**, *7*, 5055 – 5058; b) S. Carbrera, R. Gómez, J. C. Carretero, *J. Am. Chem. Soc.* **2005**, *127*, 16394 – 16395.

[9] a) Töke and co-workers have found that the ratio of *endo* and *exo* products is between 1.4:1 and 3.5:1 in the reaction of an azomethine ylide with a nitroalkene in the presence of LiBr as catalyst; this ratio changed to 1.25:1–1:2.3 with AgOAc as catalyst: M. Nyerges, M. Rudas, G. Tóth, B. Herényi, I. Kádas, I. Bitter, L. Töke, *Tetrahedron* **1995**, *51*, 13321 – 13330; b) T. Sammakia, E. L. Stangeland, *J. Org. Chem.* **1997**, *62*, 6104 – 6105.

[10] a) L.-X. Dai, T. Tu, S.-L. You, W.-P. Deng, X.-L. Hou, *Acc. Chem. Res.* **2003**, *36*, 659 – 667; b) W.-P. Deng, X.-L. Hou, L.-X. Dai, X.-W. Dong, *Chem. Commun.* **2000**, 1483 – 1484; c) W.-P. Deng, S.-L. You, X.-L. Hou, L.-X. Dai, Y.-H. Yu, W. Xia, *J. Am. Chem. Soc.* **2001**, *123*, 6508 – 6519; d) S.-L. You, X.-Z. Zhu, Y.-M. Luo, X.-L Hou, L.-X. Dai, *J. Am. Chem. Soc.* **2001**, *123*, 7471 – 7472; e) T. Tu, X. L. Hou, L.-X. Dai, *Org. Lett.* **2003**, *5*, 3651 – 3653; f) X.-L. Hou, N. Sun, *Org. Lett.* **2004**, *6*, 4399 – 4401 (correction: X.-L. Hou, N. Sun, *Org. Lett.* **2005**, *7*, 1435).

[11] T. Tu, W.-P. Deng, X.-L. Hou, L.-X. Dai, X.-C. Dong, *Chem. Eur. J.* **2003**, *9*, 3073 – 3081.

[12] M. Ayerbe, A. Arrieta, F. P. Cossío, *J. Org. Chem.* **1998**, *63*, 1795 – 1805.

[13] See Supporting Information of ref. [5].

[14] S. Vivanco, B. Lecea, A. Arrieta, P. Prieto, I. Morao, A. Linden, F. P. Cossío, *J. Am. Chem. Soc.* **2000**, *122*, 6078 – 6092.

[15] Other Cu and Ag salts, including $Cu(OTf)_2$, CuOTf, $CuBF_4$, AgOTf, $AgClO_4$, and $AgBF_4$, were tested in the reaction of **1a** with **2a** in the presence of ligands **3a** or **3e** under these optimized reaction conditions. All Cu salts gave similar enantio- and diastereoselectivities with comparable yields to the reaction using $CuClO_4$, while Ag salts gave somewhat higher yields of the *endo* product but lower enantioselectivity.

[16] For examples, see: a) E. N. Jacobsen, W. Zhang, M. L. Güler, *J. Am. Chem. Soc.* **1991**, *113*, 6703 – 6704; b) A. Schnyder, L. Hintermann, A. Togni, *Angew. Chem.* **1995**, *107*, 996 – 998; *Angew. Chem. Int. Ed. Engl.* **1995**, *34*, 931 – 933; c) T. V. RajanBabu, A. L. Casalnuovo, *J. Am. Chem. Soc.* **1996**, *118*, 6325 – 6326; d) N. Nomura, Y. C. Mermet-Bouvier, T. V. Rajan-Babu, *Synlett* **1996**, 745 – 746; e) T. V. RajanBabu, T. A. Ayers, G. A. Halliday, K. K. You, J. C. Calabrese, *J. Org. Chem.* **1997**, *62*, 6012 – 6028; f) A. Schnyder, A. Togni, U. Wiesli, *Organometallics* **1997**, *16*, 255 – 260 (correction: A. Schnyder, A. Togni,

 © 2006 Wiley-VCH Verlag GmbH & Co. KGaA, Weinheim 

U. Wiesli, *Organometallics* **1997**, *16*, 2226); g) D. Yang, Y.-C. Yip, J. Chen, K.-K. Cheung, *J. Am. Chem. Soc.* **1998**, *120*, 7659 – 7660; h) D. S. Clyne, Y. C. Mermet-Bouvier, N. Nomura, T. V. Rajan-Babu, *J. Org. Chem.* **1999**, *64*, 7601 – 7611, and references therein; i) C. Gambs, S. Chaloupka, G. Consiglio, A. Togni, *Angew. Chem.* **2000**, *112*, 2602 – 2604; *Angew. Chem. Int. Ed.* **2000**, *39*, 2486 – 2488; j) Z.-Z. Huang, Y.-B. Kang, J. Zhou, Y.-C. Ye, Y. Tang, *Org. Lett.* **2004**, *6*, 1677 – 1679; k) M. P. Sibi, M. Liu, *Curr. Org. Chem.* **2001**, *5*, 719 – 753; l) G. Zanoni, F. Castronovo, M. Franzini, G. Vidari, E. Giannini, *Chem. Soc. Rev.* **2003**, *32*, 115 – 129.

[17] The calculations were performed with the Gaussian 03 program (Gaussian 03, Revision B.03, M. J. Frisch et al.). See Supporting Information for details.

[18] L. Bernardi, A. S. Gothelf, R. G. Hazell, K. A. Jørgensen, *J. Org. Chem.* **2003**, *68*, 2583 – 2591.

[19] The stereochemical course of the reaction can be determined in two reaction steps: the formation of **5** or the formation of **4** (Scheme 1). We assume that formation of **5** is the crucial to stereochemistry because it would be difficult to understand the stereoseclectivity based on the models shown in Figure 2 (that is, **7a** and **8c**) if formation of **4** was the rate-determining step.

[20] Whilst this paper was under review, Carretero and co-workers published a paper that includes one example of the use of a nitroalkene in Cu-catalyzed asymmetric dipolar cycloaddition. See ref. [8b].

 © 2006 Wiley-VCH Verlag GmbH & Co. KGaA, Weinheim 